World Meteorological Organization
Ozone Research and Monitoring – GAW Report No. 278

Scientific Assessment of Ozone Depletion 2022

World Meteorological Organization
7bis avenue de la Paix
Case postale 2300
CH-1211 Geneva 2
Switzerland

United Nations Environment Programme
Ozone Secretariat
P.O. Box 30552
Nairobi, 00100
Kenya

US Department of Commerce
National Oceanic and Atmospheric Administration
14th Street and Constitution Avenue NW
Herbert C. Hoover Building, Room 5128
Washington, D. C. 20230

National Aeronautics and Space Administration
Earth Science Division
NASA Headquarters
300 E. Street SW
Washington, D.C. 20546-0001

European Commission
Directorate-General for Research
B-1049 Bruxelles
Belgium

Published October 2022.
Posted online February 2023.

ISBN: 978-9914-733-97-6

This document should be cited as:
World Meteorological Organization (WMO). *Scientific Assessment of Ozone Depletion: 2022*, GAW Report No. 278, 509 pp.; WMO: Geneva, 2022.

This report is available on the internet at the following locations:
https://ozone.unep.org/science/assessment/sap
https://www.csl.noaa.gov/assessments/ozone/2022

The cover of this book shows an ozonesonde balloon launch conducted in 2018 at South Pole, Antarctica. Photograph by Johannes Werthebach (Ice Cube / NSF). Cover design by Chelsea R. Thompson (NOAA).

ISBN 978-9914-733-97-6
9 789914 733976

World Meteorological Organization
Ozone Research and Monitoring – GAW Report No. 278

Scientific Assessment of Ozone Depletion

2022

World Meteorological Organization
United Nations Environment Programme
National Oceanic and Atmospheric Administration
National Aeronautics and Space Administration
European Commission

Scientific Assessment of Ozone Depletion: 2022

Co-Chairs of the Scientific Assessment Panel (SAP) of the Montreal Protocol and Assessment Co-Chairs

David W. Fahey
Paul A. Newman
John A. Pyle
Bonfils Safari

Assessment Scientific Steering Committee

David W. Fahey
Paul A. Newman
John A. Pyle
Bonfils Safari
Julie Arblaster
Lucy Carpenter
Jianxin Hu
Ken Jucks
David A. Plummer

Assessment Coordinator

Sarah J. Doherty

Graphics and Layout Coordinator

Chelsea R. Thompson

Chapter Lead Authors

Chapter 1: Update on Ozone-Depleting Substances (ODSs) and Other Gases of Interest to the Montreal Protocol

Johannes C. Laube
Susann Tegtmeier

Chapter 2: Hydrofluorocarbons (HFCs)

Qing Liang
Matt Rigby

Chapter 3: Update on Global Ozone: Past, Present, and Future

Birgit Hassler
Paul J. Young

Chapter 4: Polar Stratospheric Ozone: Past, Present, and Future

Martyn P. Chipperfield
Michelle L. Santee

Chapter 5: Stratospheric Ozone Changes and Climate

Hella Garny
Harry Hendon

Chapter 6: Stratospheric Aerosol Injection and Its Potential Effect on the Stratospheric Ozone Layer

James Haywood
Simone Tilmes

Chapter 7: Scenarios and Information for Policymakers

John S. Daniel
Stefan Reimann

Annex: Summary of Abundances, Lifetimes, ODPs, REs, GWPs, and GTPs

James B. Burkholder
Øivind Hodnebrog

The full list of contributors can be found at the end of this book.

REMEMBRANCES

It is with sadness that we note the passing of the following scientists who have played important roles in the international scientific assessments of the ozone layer.

Paul J. Crutzen

(1933–2021) Paul Jozef Crutzen was born in Amsterdam on 3 December 1933. His early working life was as a civil engineer. His appointment as a computer programmer at the Department of Meteorology in what is now Stockholm University was the start of his atmospheric science career. His PhD research established the important role of the oxides of nitrogen in the formation and destruction of ozone in the stratosphere and troposphere. His work pointed to the potential destruction of ozone if the concentration of NO_x radicals, key components in catalytic ozone destruction cycles, increased following enhanced emissions from aviation.This was part of the work for which Paul was awarded the 1995 Nobel Prize in Chemistry, along with Mario Molina and F. Sherwood Rowland. Paul's contributions were wide ranging and hugely influential. They covered work on polar stratospheric clouds, the budget of tropospheric ozone, 'nuclear winter', biomass-burning, cloud chemistry, climate and climate intervention. He worked in Boulder, Colorado, during the 1970s at NOAA Aeronomy Laboratory and the National Center for Atmospheric Research, before moving to be head of the Max Planck Institute for Atmospheric Chemistry in Mainz in 1980. A highlight of his career was originating and promoting the concept of the 'anthropocene' to describe the current period where human activity is having a profound influence on our environment. Paul died on 28 January 2021 in Mainz, Germany.

Mack McFarland

(1947–2022) Mack McFarland was born in Houston, Texas, on 9 September 1947. He received his Bachelor's Degree in chemistry from the University of Texas–Austin and a PhD in chemical physics from the University of Colorado–Boulder in 1973. He completed post-doctoral studies at York University in Canada and became a research scientist in the NOAA Aeronomy Laboratory in Boulder, Colorado. While at NOAA, Mack led innovative measurements of nitrogen oxides (NO_x) on a ship in the remote Pacific Ocean and into the mid stratosphere using balloon-borne chemiluminescence detectors. NO_x chemistry controls ozone amounts in the stratosphere and troposphere. In 1983, he joined DuPont Company to help interpret the emerging scientific information and understanding of ozone depletion and climate change. Mack was involved in many of the quadrennial scientific assessments of ozone depletion that support decision making in the Montreal Protocol and in climate assessments conducted by the Intergovernmental Panel on Climate Change (IPCC). As an atmospheric scientist and industry representative, he was a highly valued contributor to the ozone assessments. Mack's foresight and understanding of how global use of synthetic gases influenced ozone depletion and climate change was an essential resource to the science and policy communities. Mack was the first to describe the importance of future global HFC emissions, which led to the Montreal Protocol Kigali Amendment to phase-down key HFCs in 2016. Mack received numerous awards and honors including the 1999 EPA Climate Protection Award and the 2007 Dupont Pedersen Medal. Mack died on 30 November 2022 in Dallas, Texas.

Mario José Molina

(1943–2020) Mario José Molina was born in Mexico City on 19 March 1943. His father was a diplomat and his early schooling was in Switzerland. He was a chemical engineering undergraduate at the Universidad Nacional Autónoma de México and subsequently studied applied chemistry at the University of Freiburg. After a PhD at the University of California–Berkeley he began work as a post-doctoral researcher with F. Sherwood Rowland at UC Irvine. Their famous Nature paper from 1974 alerted the world to the potential dangers to the stratospheric ozone layer of the build-up in the atmosphere of chlorofluorocarbons, work which led to the award in 1995 of the Nobel Prize in Chemistry to him, F. Sherwood Rowland and Paul Crutzen. Mario was only the third Mexican to win the Nobel Prize and the first for science. After the discovery of the Antarctic ozone hole, Mario's experimental work at the Massachusetts Institute of Technology (MIT) in the US elucidated the mechanism of chlorine activation on polar stratospheric clouds, a key component in understanding why ozone depletion occurs in polar regions. It was at MIT that Mario also started his very important work on megacities, with a focus on Mexico City. He founded the Molina Center for Energy and the Environment (MCE2) after his move to University of California–San Diego. He played important roles in advising policymakers on matters related to climate change, the environment and human health. He died on 7 October 2020 in Mexico City.

Other individuals who have contributed over many years to the scientific understanding of ozone depletion have passed away since our last assessment. We particularly note the death of **William T. Ball** on 29 April 2022 at the age of 39. Will held positions as an assistant professor at the Delft University of Technology in the Netherlands and as a visiting scientist at the Royal Netherlands Meteorological Institute in De Bilt. He was an active Co-author of Chapter 3 in this assessment. Will made important contributions to understanding trends in ozone in the lower stratosphere. His passing is a deep loss to his family and colleagues and has taken away a future leader from the ozone science community.

With the passing of Mario Molina, Paul Crutzen and Sherwood Roland, parties to the Montreal Protocol adopted Decision XXXIV/1 at the 34th Meeting of the Parties in November 2022.

Decision XXXIV/1: Recognition of the achievements of Paul Jozef Crutzen, Mario José Molina and Frank Sherwood Rowland, winners of the Nobel Prize in Chemistry in 1995.

Deeply grateful for the pioneering contributions and the extraordinary, visionary and courageous scientific work of scientists Paul Jozef Crutzen (Netherlands), Mario José Molina (Mexico) and Frank Sherwood Rowland (United States of America) throughout their careers in atmospheric chemistry, and particularly for their work concerning the formation and decomposition of ozone, which led to their being awarded the Nobel Prize in Chemistry in 1995,

Aware that their scientific work paved the way for global action to protect the ozone layer and led to the adoption of the Vienna Convention for the Protection of the Ozone Layer and the Montreal Protocol on Substances that Deplete the Ozone Layer and that, furthermore, their work spurred related action by every United Nations Member State as a party to those global environmental treaties,

Acknowledging the importance of continuing work to restore the ozone layer and the many associated benefits of such work to the planet and therefore to humanity,

1. To express recognition of and gratitude for the invaluable scientific contributions of Paul Jozef Crutzen, Mario José Molina and Frank Sherwood Rowland, which inspired countries around the world to join in solidarity and cooperation to protect the ozone layer from depletion, thus making the planet safer for present and future generations;
2. To uphold their legacy by maintaining mutual trust in and commitment to the work of the Vienna Convention and the Montreal Protocol;
3. To strive to continue to strengthen the institutions that their achievements helped to establish in order to achieve the aims of those institutions and protect the atmosphere for the benefit of all.

CONTENTS

Scientific Assessment of Ozone Depletion: 2022

World Meteorological Organization
Ozone Research and Monitoring – GAW Report No. 278

EXECUTIVE SUMMARY

Scientific Assessment of Ozone Depletion: 2022

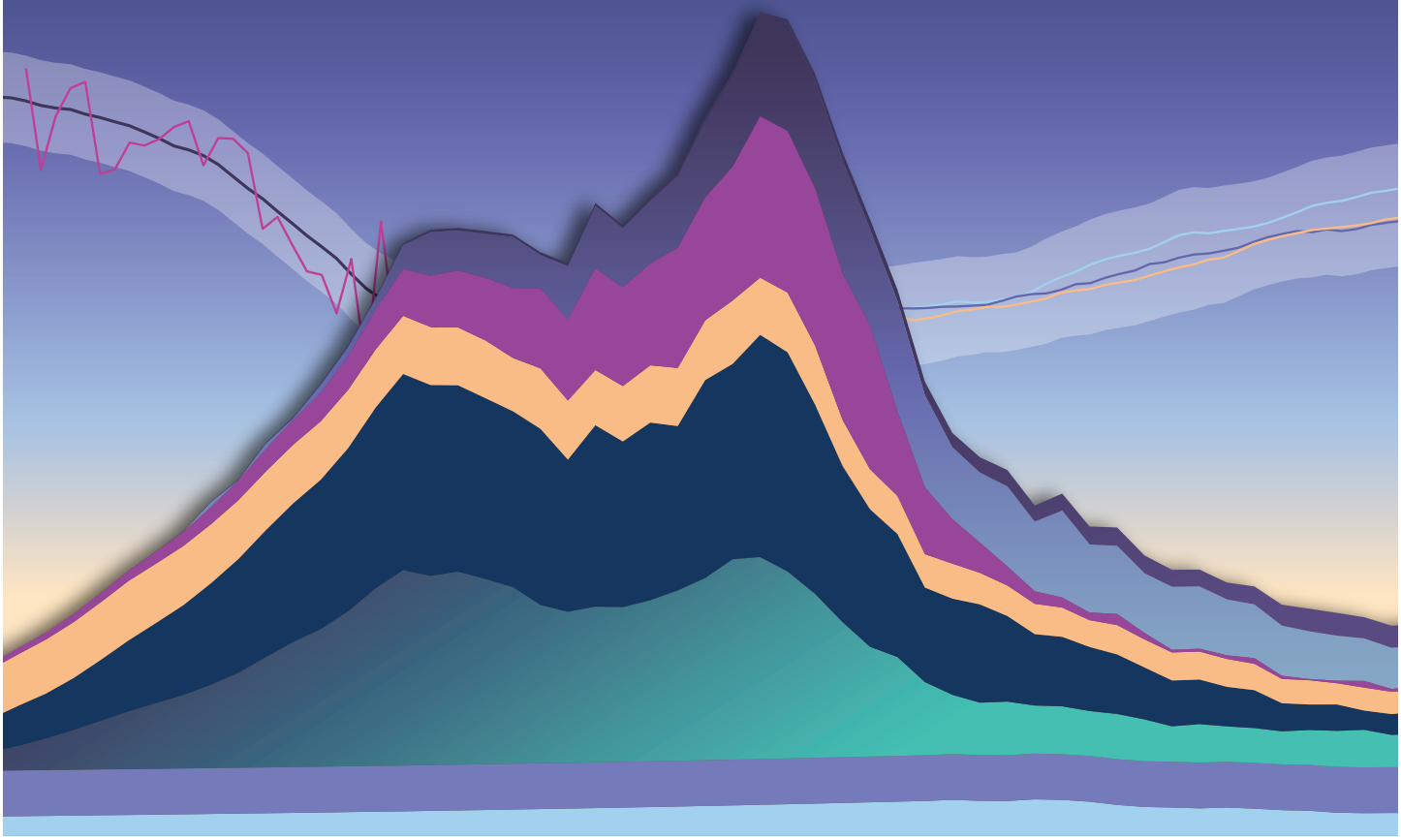

World Meteorological Organization
United Nations Environment Programme
National Oceanic and Atmospheric Administration
National Aeronautics and Space Administration
European Commission

HIGHLIGHTS
of the
SCIENTIFIC ASSESSMENT OF OZONE DEPLETION: 2022

Science has been one of the foundations of the Montreal Protocol's success. This document highlights advances and updates in the scientific understanding of ozone depletion since the 2018 Scientific Assessment of Ozone Depletion and provides policy-relevant scientific information on current challenges and future policy choices.

A. Major achievements of the Montreal Protocol

- Actions taken under the Montreal Protocol continued to decrease atmospheric abundances of controlled ozone-depleting substances (ODSs) and advance the recovery of the stratospheric ozone layer. The atmospheric abundances of both total tropospheric chlorine and total tropospheric bromine from long-lived ODSs have continued to decline since the 2018 Assessment. New studies support previous Assessments in that the decline in ODS emissions due to compliance with the Montreal Protocol avoids global warming of approximately 0.5–1 °C by mid-century compared to an extreme scenario with an uncontrolled increase in ODSs of 3–3.5% per year.
- Actions taken under the Montreal Protocol continue to contribute to ozone recovery. Recovery of ozone in the upper stratosphere is progressing. Total column ozone (TCO) in the Antarctic continues to recover, notwithstanding substantial interannual variability in the size, strength, and longevity of the ozone hole. Outside of the Antarctic region (from 90°N to 60°S), the limited evidence of TCO recovery since 1996 has low confidence. TCO is expected to return to 1980 values around 2066 in the Antarctic, around 2045 in the Arctic, and around 2040 for the near-global average (60°N–60°S). The assessment of the depletion of TCO in regions around the globe from 1980–1996 remains essentially unchanged since the 2018 Assessment.
- Compliance with the 2016 Kigali Amendment to the Montreal Protocol, which requires phase down of production and consumption of some hydrofluorocarbons (HFCs), is estimated to avoid 0.3–0.5 °C of warming by 2100. This estimate does not include contributions from HFC-23 emissions.

B. Current Scientific and Policy Challenges

- The recent identification of unexpected CFC-11 emissions led to scientific investigations and policy responses. Observations and analyses revealed the source region for at least half of these emissions and substantial emissions reductions followed. Regional data suggest some CFC-12 emissions may have been associated with the unreported CFC-11 production. Uncertainties in emissions from banks and gaps in the observing network are too large to determine whether all unexpected emissions have ceased.
- Unexplained emissions have been identified for other ODSs (CFCs-13, 112a, 113a, 114a, 115, and CCl_4), as well as HFC-23. Some of these unexplained emissions are likely occurring as leaks of feedstocks or by-products, and the remainder is not understood.
- Outside of the polar regions, observations and models are in agreement that ozone in the upper stratosphere continues to recover. In contrast, ozone in the lower stratosphere has not shown signs of recovery. Models simulate a small recovery in mid-latitude lower-stratospheric ozone in both hemispheres that is not seen in observations. Reconciling this discrepancy is key to ensuring a full understanding of ozone recovery.
- The existing network of atmospheric monitoring stations provides measurements of global surface concentrations of long-lived ODSs and HFCs resulting from anthropogenic emissions. However, gaps in regional atmospheric monitoring limit the scientific community's ability to identify and quantify emissions of controlled substances from many source regions.
- Several space-borne instruments providing vertically resolved, global measurements of ozone-related atmospheric constituents (e.g., reactive chlorine, water vapor, and long-lived transport tracers) are due to be retired within a few years. Without replacements of these instruments, the ability to monitor and explain changes in the stratospheric ozone layer in the future will be impeded.
- The impact on the ozone layer of stratospheric aerosol injection (SAI), which has been proposed as a possible option to offset global warming, has been assessed following the terms of reference for the 2022 SAP Assessment Report. Important potential consequences, such as deepening of the Antarctic ozone hole and delay in ozone recovery, were identified. Many knowledge gaps and uncertainties prevent a more robust evaluation at this time.
- Heightened concerns about influences on 21st century ozone include impacts of: further increases in nitrous oxide (N_2O), methane (CH_4), and CO_2 concentrations; rapidly expanding ODS and HFC feedstock use and emissions; climate change on TCO in the tropics; extraordinary wildfires and volcanic eruptions; increased frequency of civilian rocket launches and the emissions of a proposed new fleet of supersonic commercial aircraft.

C. Future Policy Considerations

- If ODS feedstock emissions as currently estimated were to be eliminated in future years, the return of mid-latitude Equivalent Effective Stratospheric Chlorine (EESC) to 1980 abundances could be advanced by almost 4 years, largely due to reductions in CCl_4, and thereby reduce total climate forcing from ODSs.
- Eliminating future emissions of methyl bromide (CH_3Br) from quarantine and pre-shipment applications currently allowed by the Montreal Protocol would accelerate the return of mid-latitude EESC to 1980 abundances by two years (as noted in previous Assessments).
- Emissions of anthropogenic very short-lived chlorine substances, dominated by dichloromethane (CH_2Cl_2), continue to grow and contribute to ozone depletion. If CH_2Cl_2 emissions continue at their current level, they will continue to deplete approximately 1 DU of annually averaged global TCO. Elimination of these emissions would rapidly reverse this depletion.
- A 3% reduction in anthropogenic N_2O emissions, averaged over 2023–2070, would lead to an increase in annually averaged global TCO of about 0.5 DU over the same period, and a decrease of about 0.04 Wm^{-2} in radiative forcing, averaged over 2023–2100.
- Global emissions of long-lived HFC-23, which are largely a by-product of HCFC-22 production, are as much as eight times larger than expected and are likely to grow unless abatement increases during HCFC-22 production or feedstock use of HCFC-22 decreases.
- The current combined GWP-weighted emissions of CFCs plus HCFCs are comparable to those of HFCs. Reductions in the future emissions of CFCs and HCFCs requires addressing releases from banks and continuing production and use in allowed manufacturing of feedstocks, in by-products, or in unknown uses, depending upon the compound.

CONTENTS

PREFACE

This document contains information upon which the Parties to the Montreal Protocol on Substances that Deplete the Ozone Layer ("The Parties") will base their future decisions regarding protection of the stratospheric ozone layer and climate from the production and consumption of ozone-depleting substances (ODSs) and their replacements.

The Charge to the Assessment Panels

Specifically, Article 6 of the Montreal Protocol on Substances that Deplete the Ozone Layer states:

> *Beginning in 1990, and at least every four years thereafter, the Parties shall assess the control measures provided for in Article 2 and Articles 2A to 2I on the basis of available scientific, environmental, technical and economic information.*

To provide the mechanisms whereby these assessments are conducted, the Montreal Protocol further states:

> *". . . the Parties shall convene appropriate panels of experts" and "the panels will report their conclusions . . . to the Parties."*

To meet this request, the Scientific Assessment Panel (SAP), the Environmental Effects Assessment Panel, and the Technology and Economic Assessment Panel each prepare, every 4 years, major assessments that update the state of understanding in their purviews. These assessments are made available to the Parties in advance of their annual meetings at which they consider amendments and adjustments to the provisions of the Montreal Protocol.

Sequence of Scientific Assessments

The 2022 Assessment is the latest in a series of assessments prepared by the world's leading experts in the atmospheric sciences and under the auspices of the Montreal Protocol in coordination with the World Meteorological Organization (WMO) and the United Nations Environment Programme (UN Environment). The 2022 Assessment is the tenth in the series of major assessments that have been prepared by the Scientific Assessment Panel as direct input to the Montreal Protocol process. The chronology of the ten scientific assessments of ozone depletion, along with other relevant reports and international policy decisions, are summarized in **Table ES-1**.

2022 Assessment Terms of Reference

The terms of reference of the 2022 Assessment for the SAP were decided at the 31st Meeting of the Parties to the Montreal Protocol in Rome, Lazio, Italy (4–8 November 2019) in their Decision XXXI/2[1] (items 1–3 and 5):

1. To request the Scientific Assessment Panel, the Environmental Effects Assessment Panel and the Technology and Economic Assessment Panel to prepare quadrennial assessment reports and submit them to the Secretariat by 31 December 2022 for consideration by the Open-ended Working Group and the Meeting of the Parties in 2023, and to present a synthesis report by 30 April 2023, noting that the panels should continue to exchange information, during the process of developing their respective reports in order to avoid duplication and provide comprehensive information to the parties to the Montreal Protocol;
2. To request the assessment panels to bring to the notice of the parties any significant developments which, in their opinion, deserve such notice, in accordance with Decision IV/13;
3. To encourage the assessment panels to closely involve relevant scientists from Article 5 parties with a view to promoting gender and regional balance, to the best of their ability, in producing the reports;
5. That the 2022 report of the Scientific Assessment Panel should include:
   a) An assessment of the state of the ozone layer and its future evolution;
   b) An evaluation of global and polar stratospheric ozone, including the Antarctic ozone hole and Arctic winter/spring ozone depletion and the predicted changes in those phenomena;
   c) An evaluation of trends in the top-down derived emissions, abundances and fate in the atmosphere of trace gases of relevance to the Montreal Protocol on Substances that Deplete the Ozone Layer, in particular controlled substances and other substances of importance to the ozone layer, which should include a comparison of bottom-up and top-down estimations of such emissions with a view to addressing unidentified emission sources and discrepancies between reported emissions and observed atmospheric concentrations;
   d) An evaluation of consistency with reported production and consumption of those substances and the likely implications for the state of the ozone layer, including its interaction with the climate system;
   e) An assessment of the interaction between changes in stratospheric ozone and the climate system, including possible future policy scenarios relating to ozone depletion and climate impacts;
   f) Early identification and quantification, where possible, of any other issues of importance to the ozone layer and the climate system consistent with the objectives of the Vienna Convention for the Protection of the Ozone Layer and the Montreal Protocol;
   g) An assessment of information and research related to solar radiation management and its potential effect on the stratospheric ozone layer;
   h) Relevant information on any newly detected substances that are relevant for the Montreal Protocol.

[1] Decision XXXI/2: Potential areas of focus for the 2022 quadrennial reports of the Scientific Assessment Panel, the Environmental Effects Assessment Panel and the Technology and Economic Assessment Panel

The Final Author Meeting was held in Geneva, Switzerland on 25–29 July 2022. Shown is the iconic Jet d'Eau on Lake Geneva.

The Assessment Process

The process of writing the current Assessment started early in 2020. The co-chairs of the Scientific Assessment Panel (SAP) of the Montreal Protocol (David W. Fahey, Paul A. Newman, John A. Pyle, and Bonfils Safari) considered suggestions from the Parties regarding experts from their countries who could participate in the process. A Scientific Steering Committee (SSC), comprising the co-chairs and an ad-hoc international scientific advisory group, was formed to suggest authors and reviewers from the world scientific community and to help craft the Assessment outline. As in previous Assessments, the participants represented experts from the developed and developing world who bring a special perspective to the process and whose involvement in the Assessment contributes to capacity building. The *Authors, Contributors, and Reviewers* section at the end of this document provides a listing of the approximately 230 scientists from 30 countries who contributed to the preparation and review of the Assessment.

An initial letter was sent to a large number of scientists and policymakers in November 2020 soliciting comments and inputs on a draft outline along with suggestions for authors for the 2022 Assessment. This was followed by revisions to the outline and recruitment of lead authors and co-authors. Revised chapter outlines were developed between February and April 2021 through a series of online meetings of the SSC and lead authors. The chapter writing process produced four drafts between August 2021 and September 2022 aided by a virtual meeting of the author team and SSC in March 2022 and an in-person meeting in July 2022 at WMO Headquarters in Geneva, Switzerland. The first drafts of the chapters were formally peer-reviewed by over 100 expert reviewers. The chapters were revised by the author teams based on the extensive review comments (numbering over 3500). Review editors for each chapter provided oversight of the revision process to ensure that all comments were addressed appropriately.

At a meeting in Geneva, Switzerland, held on 25–29 July 2022, the Executive Summary contained herein was prepared and completed by the 74 attendees of the meeting. These attendees included the steering committee, chapter lead authors, review editors, some chapter co-authors (selected by the chapter leads), reviewers (selected by the review editors), and some leading experts invited by the steering committee. The Executive Summary, initially drafted by the Assessment SSC, was reviewed, revised, and approved line-by-line. The section of Assessment highlights was drafted during the meeting.

The success of the 2022 Assessment depended on the combined efforts and commitment of a large international team of scientific researchers who volunteered their time as lead authors, contributors, reviewers, and review editors and on the skills and dedication of the assessment coordinator and the editorial and production staff, who are listed at the end of this report.

David W. Fahey
Paul A. Newman
John A. Pyle
Bonfils Safari

Co-chairs of the Scientific Assessment Panel of the Montreal Protocol

Table ES-1. Chronology of scientific reports and policy decisions related to ozone depletion.

Year	Policy Decisions	Scientific Reports
1981		The Stratosphere 1981: Theory and Measurements. WMO No. 11.
1985	Vienna Convention	Atmospheric Ozone 1985. Three volumes. WMO No. 16.
1987	Montreal Protocol	
1988		International Ozone Trends Panel Report 1988. Two volumes. WMO No. 18.
1989		Scientific Assessment of Stratospheric Ozone: 1989. Two volumes. WMO No. 20.
1990	London Adjustment and Amendment	
1991		Scientific Assessment of Ozone Depletion: 1991. WMO No. 25.
1992		Methyl Bromide: Its Atmospheric Science, Technology, and Economics (Montreal Protocol Assessment Supplement). UNEP (1992)
1992	Copenhagen Adjustment and Amendment	
1994		Scientific Assessment of Ozone Depletion: 1994. WMO No. 37.
1995	Vienna Adjustment	
1997	Montreal Adjustment and Amendment	
1998		Scientific Assessment of Ozone Depletion: 1998. WMO No. 44.
1999	Beijing Adjustment and Amendment	
2002		Scientific Assessment of Ozone Depletion: 2002. WMO No. 47.
2006		Scientific Assessment of Ozone Depletion: 2006. WMO No. 50.
2007	Montreal Adjustment	
2010		Scientific Assessment of Ozone Depletion: 2010. WMO No. 52.
2014		Scientific Assessment of Ozone Depletion: 2014. WMO No. 55.
2016	Kigali Amendment	
2018		Scientific Assessment of Ozone Depletion: 2018. WMO No. 58.
2021		Report on Unexpected Emissions of CFC-11. WMO No. 1268.
2022		Scientific Assessment of Ozone Depletion: 2022. GAW No. 278.

INTRODUCTION

The 1985 Vienna Convention for the Protection of the Ozone Layer is an international agreement in which United Nations States recognized the fundamental importance of preventing damage to the stratospheric ozone layer. The 1987 Montreal Protocol on Substances that Deplete the Ozone Layer and its succeeding amendments, adjustments, and decisions were subsequently negotiated to control the consumption and production of anthropogenic ozone-depleting substances (ODSs) and some hydrofluorocarbons (HFCs). The Montreal Protocol Parties base their decisions on scientific, environmental, technical, and economic information that is provided by their assessment panels. The Protocol requests quadrennial reports from its Scientific Assessment Panel that update the science of the ozone layer. This Executive Summary (ES) highlights the key findings of the Scientific Assessment of Ozone Depletion: 2022, as put together by an international team of scientists. The key findings of each of the seven chapters of the Scientific Assessment have been condensed and formulated to make the ES suitable for a broad audience.

Ozone depletion is caused by human-related emissions of ODSs and the subsequent release of reactive halogen gases, especially chlorine and bromine, in the stratosphere. ODSs include chlorofluorocarbons (CFCs), bromine-containing halons and methyl bromide, hydrochlorofluorocarbons (HCFCs), carbon tetrachloride (CCl_4), and methyl chloroform. The substances controlled under the Montreal Protocol are listed in the various annexes to the agreement (CFCs and halons under Annex A and B, HCFCs under Annex C, and methyl bromide under Annex E)[2]. These ODSs are long-lived (e.g., CFC-12 has a lifetime greater than 100 years) and are also powerful greenhouse gases (GHGs). As a consequence of Montreal Protocol controls, the stratospheric concentrations of anthropogenic chlorine and bromine are declining.

In addition to the longer-lived ODSs, there is a broad class of chlorine- and bromine-containing substances known as very short-lived substances (VSLSs) that are not controlled under the Montreal Protocol and have lifetimes shorter than about 6 months. For example, bromoform ($CHBr_3$) has a lifetime of 24 days, while chloroform ($CHCl_3$) has a lifetime of 149 days. These substances are generally destroyed in the lower atmosphere in chemical reactions. In general, only small fractions of VSLS emissions reach the stratosphere where they contribute to chlorine and bromine levels and lead to increased ozone depletion.

The Montreal Protocol's control of ODSs stimulated the development of replacement substances, firstly HCFCs and then HFCs, in a number of industrial sectors. While HFCs have only a minor effect on stratospheric ozone, some HFCs are powerful GHGs. Previous Assessments have shown that HFCs have been increasing rapidly in the atmosphere over the last decade and were projected to increase further as global development continued in the coming decades. The adoption of the 2016 Kigali Amendment to the Montreal Protocol (see Annex F) will phase down the production and consumption of some HFCs and avoid much of the projected global increase and associated climate change.

Observations of atmospheric ozone are made by instruments on the ground and on board balloons, aircraft, and satellites. This network of observations documented the decline of ozone around the globe, with extreme depletions occurring over Antarctica in each spring and occasional large depletions in the Arctic, and they allowed us to report some indications of recovery in stratospheric ozone in the 2014 and 2018 Assessments. The chemical and dynamical processes controlling stratospheric ozone are well understood, with ozone depletion being fundamentally driven by the atmospheric abundances of chlorine and bromine.

Strong declines in the emissions of ODSs starting in the late 1980s led to a decline in the abundances of chlorine and bromine starting around the turn of the century. As a result, the first indications of ozone recovery are emerging. In addition to ODSs, model simulations demonstrate that stratospheric ozone concentrations are also affected by the chemical and climate effects of greenhouse gases. In particular, increasing concentrations of the GHGs carbon dioxide (CO_2) and methane (CH_4) during this century will cause global ozone levels to increase beyond the natural level of ozone observed in the 1960s, primarily because of the cooling of the upper stratosphere and a change of the stratospheric circulation. On the other hand, the chemical effect of increasing concentrations of nitrous oxide (N_2O), another GHG, is to deplete stratospheric ozone.

This 2022 Assessment is the tenth in a series that is provided to the Montreal Protocol by its Scientific Assessment Panel. Completely new to this Assessment is Chapter 6, on the potential effects on ozone of the intentional addition of aerosols to the stratosphere, known as stratospheric aerosol injection (SAI). SAI has been proposed as a potential method to reduce climate warming by increasing sunlight reflection; an unintended consequence of SAI is that it could also affect stratospheric

[2] Montreal Protocol Handbook, 2018.

temperatures, circulation and ozone production and destruction rates and transport. This new chapter assesses our understanding of these effects based on the SAI strategy and under different climate warming scenarios, as well as identifying sources of uncertainty in these impacts.

In the other six chapters of this Assessment, many of our previous Assessment findings are strengthened and new results are presented. A clear message of the 2022 Assessment is that the Montreal Protocol continues to be effective at reducing the atmospheric abundance of ODSs.

Terminology Used in the Executive Summary

Ozone-depleting substance (ODS)

Here and throughout, the term ozone depleting substances (ODSs) refers to gases containing either chlorine or bromine that are released to the atmosphere as a result of human activity and are controlled under Annexes A, B, C, or E of the Montreal Protocol. These include, among others, chlorofluorocarbons (CFCs), carbon tetrachloride (CCl_4), methyl chloroform (CH_3CCl_3), halons, methyl bromide (CH_3Br) and hydrochlorofluorocarbons (HCFCs). These ODSs typically have sufficiently long atmospheric lifetimes to reach the stratosphere after being emitted at the surface. Methyl bromide is the shortest-lived of the controlled substances and has natural and anthropogenic sources. Other substances contribute chlorine and bromine to the atmosphere but are not controlled under the Montreal Protocol for various reasons.

Ozone depletion potential (ODP) / ODP weighting

The ozone depletion potential (ODP) of a substance is a metric for determining the relative strength of that chemical's ability to destroy ozone. The ODP of a substance is defined as the ratio of the change in global ozone for a given mass emission of the substance to the change in global ozone for the same mass emission of CFC-11 ($CFCl_3$). In order to be able to compare the potential impact on stratospheric ozone of changes in the emissions of different gases, gases are often weighted by their ODP and given as "ODP-weighted emissions", so that the units of these emissions are "Mt CFC-11 equivalent".

Halogenated very short-lived substances (VSLSs)

Halogenated very short-lived substances (VSLSs) have atmospheric lifetimes less than 0.5 year and yet make a contribution to stratospheric chlorine or bromine levels. As short-lived ODSs, a large fraction of VSLS emissions are destroyed in the troposphere, limiting the fraction of emissions that reaches the stratosphere and causes ozone depletion. VSLS emissions that occur in regions with rapid transport to the stratosphere will make an enhanced contribution to stratospheric halogen levels. Hence, the ODP of a VSLS is generally dependent on assumptions about the emission source region and time of the year of the emissions. VSLSs are not controlled under the Montreal Protocol.

Equivalent effective chlorine (EECl) and equivalent effective stratospheric chlorine (EESC)

EECl is a metric for representing ODS levels in the troposphere. It is calculated based upon the surface atmospheric concentrations of individual ODSs, their number of chlorine and bromine atoms, and the relative efficiency of chlorine and bromine at ozone depleting ozone.

EESC is, similarly, a metric for representing ODS levels in the stratosphere. It is calculated based upon the same three factors as EECl, as well as accounting for the time required for the substances to reach different stratospheric regions and break down to release their chlorine and bromine atoms. As EESC continues to decrease in response to Montreal Protocol provisions, stratospheric ozone is expected to increase.

In this Assessment, neither EECl nor EESC include chlorine and bromine from very short-lived substances (VSLSs).

Feedstocks and banks

A "feedstock" is a substance used to synthesize one or more other chemicals through a process of chemical transformation.

The "bank" of a given substance represents the amount of that substance that has been produced, is contained in equipment or products, and has not yet been released to the atmosphere. Banks include substances contained in refrigeration and air conditioning equipment, foams, and fire protection systems. Without intervening actions, some fraction of the substances contained will be gradually released during the equipment or product's lifetime, and some will be released at or after the end-of-life of equipment or products. With an intervention at the end of life, chemicals may be collected, stored, and destroyed, thereby preventing their release into the atmosphere. All releases to the atmosphere, as well as destruction, result in a decrease in the bank size.

Global warming potential (GWP) / GWP weighting

The global warming potential (GWP) is a metric for determining the relative contribution of a substance to climate warming. GWP is defined as the ratio of the radiative forcing for a given mass emission of a substance relative to the same mass emission of CO_2 summed over a given time period (typically 20 or 100 years). In this Assessment, a 100-yr time window is implied unless otherwise stated. As such, the GWP of CO_2 is defined to be unity. In order to be able to compare the potential impact on climate of changes in the emissions of different gases, the emissions are often weighted by their GWP and given as "GWP-weighted emissions", so that the units of these emissions are "Gt CO_2-equivalent".

Representative concentration pathways (RCPs) & shared socioeconomic pathways (SSPs)

Representative concentration pathways (RCPs) and shared socioeconomic pathways (SSPs) were developed by the climate change research community to describe a range of plausible societal futures out to the year 2100. SSPs are the main scenarios assessed in the 6th Intergovernmental Panel on Climate Change (IPCC) reports, replacing the previous generation of scenarios, the RCPs. For better comparability of the projections using SSPs with projections done for the previous IPCC Assessment Report (AR5), we include a description of the RCPs. Both define a timeline of emissions of greenhouse gases (GHGs) expressed in units of $GtCO_2$-eq and describe a range of plausible future climate pathways.

The four RCP pathways, RCP-2.6, RCP-4.5, RCP-6.0, and RCP-8.5, are labeled by the approximate radiative forcing at 2100 (e.g., RCP-2.6 has a global mean radiative forcing from GHGs in 2100 of 2.6 W m^{-2}). RCP-2.6 assumes that GHG emissions peaked before 2020; RCP-4.5 assumes a peak around 2040; RCP-6.0 assumes a peak around 2080; and RCP-8.5 assumes no peak before 2100. Each scenario includes certain socioeconomic assumptions about fossil fuel use and other aspects related to GHG emissions and other factors that affect climate, such as aerosol emissions and land use change. The SSPs adopt similar radiative forcing values at 2100 for consistency with the RCPs, but differ in their exact composition and emission trajectories. For example, methane trajectories are quite different between the two scenario frameworks.

Like the RCPs, the SSPs define a timeline of atmospheric concentrations of GHGs expressed in units of $GtCO_2$-eq. SSPs are developed based on a range of socioeconomic development trajectories, coupled with the expected global mean radiative forcing from GHGs in 2100. The SSPs include scenarios for "Sustainability" (SSP1), "Middle of the Road" (SSP2), "Regional Rivalry" (SSP3), "Inequality" (SSP4) and "Fossil-fueled Development" (SSP5) pathways. So, for example, SSP2-4.5 is a "Middle of the Road" pathway that ends in 2100 with a radiative forcing of 4.5 W m^{-2}. The SSPs also include a new very low emissions scenario which is consistent with staying below 1.5 °C of warming. Here, projections of future ozone abundances are given for the greenhouse gas trajectories given in specific SSPs.

EXECUTIVE SUMMARY

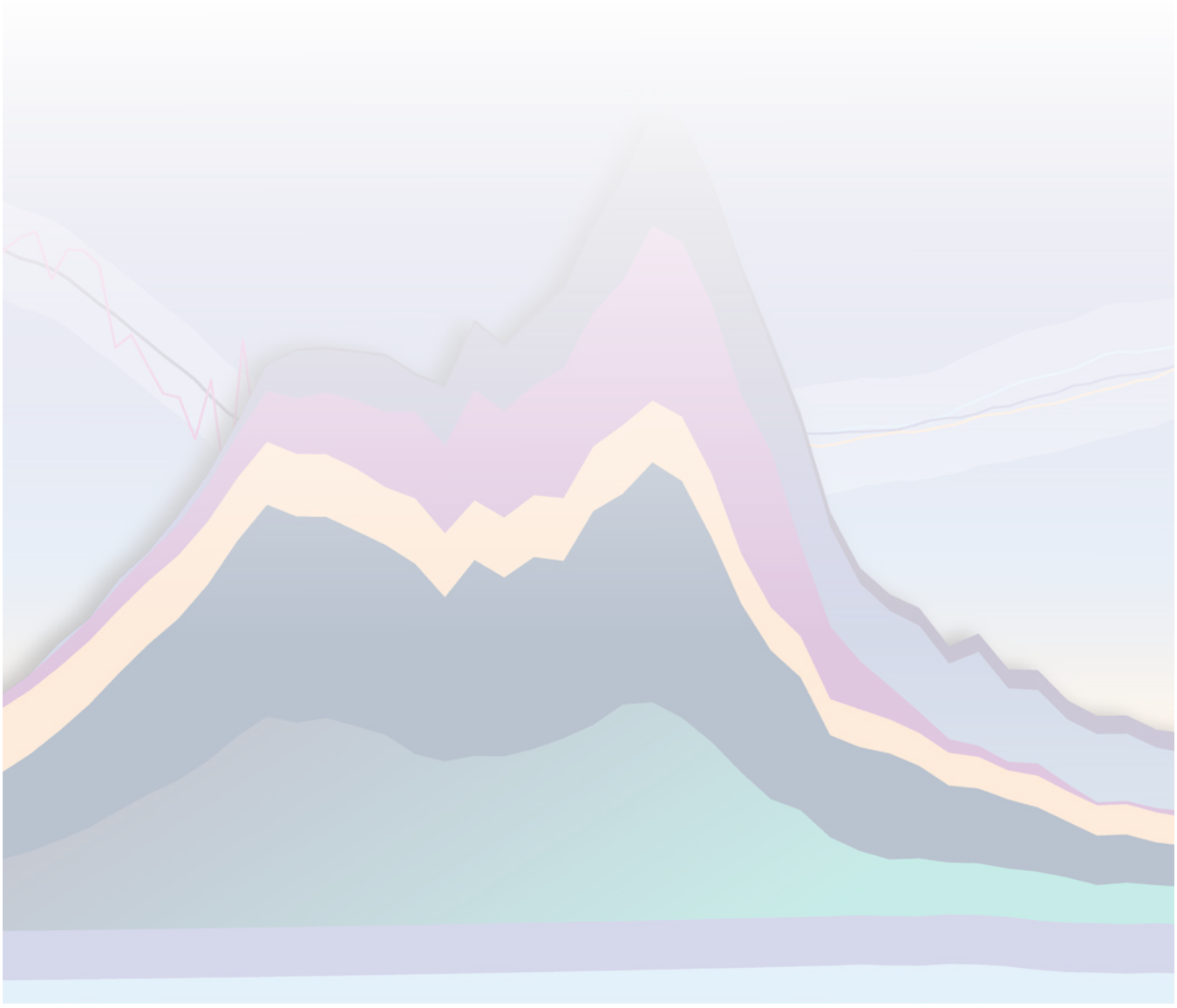

1

ABUNDANCES AND TRENDS IN OZONE-DEPLETING SUBSTANCES (ODSs)

Our confidence in the achievements of the Montreal Protocol continues to be based on sustained networks of measurements of long-lived source gas abundances covering several decades. These measurements allow the determination of global abundances, their interhemispheric differences and their trends. The data allow us to derive emissions that can be compared with emissions derived from data reported to the UN Environment Programme, when combined with lifetime information and atmospheric modelling.

Changes in tropospheric chlorine and bromine over 2016–2020

- **The atmospheric abundances of both tropospheric chlorine (Cl) and bromine (Br), from long-lived ozone-depleting substances (ODSs) controlled under the Montreal Protocol, continued to decline (Figure ES-1).** The observed rate of decline in tropospheric chlorine due to substances controlled under the Montreal Protocol was 15.4 ± 4.1 ppt Cl yr^{-1} (Table ES-2), which is close to the baseline projection from the 2018 Assessment.
- **Tropospheric chlorine from very short-lived gases, whose sources are mainly anthropogenic and which are not controlled under the Montreal Protocol, increased by 2.1 ± 0.6 ppt Cl yr^{-1}.**
- **The observed rate of decline in tropospheric bromine due to controlled substances was 0.18 ± 0.05 ppt Br yr^{-1}, which is close to the baseline projection from the 2018 Assessment.** The majority of this decrease originated from decreases in halon abundances.

Total stratospheric chlorine and bromine

- **Total chlorine entering the stratosphere from controlled and uncontrolled ODSs declined by 420 ± 20 ppt (11.5%) between the 1993 peak (3660 ppt) and 2020 (3240 ppt) (Figure ES-2).** This long-term decrease was largely driven by decreasing abundances of CH_3CCl_3 and CFCs.
- **HCl is the major chlorine component in the upper stratosphere. Its abundance in this region decreased on average by 0.5 ± 0.2 % yr^{-1} during 1997–2020.** The long-term decrease is consistent with the decline in total chlorine entering the stratosphere.
- **Total bromine entering the stratosphere from controlled and uncontrolled ODSs declined by 3.2 ± 1.2 ppt (14.5%) between the 1999 peak (22.1 ppt) and 2020 (18.9 ppt).** This long-term decrease was largely driven by decreasing abundances of CH_3Br and halon-1211.
- **Total stratospheric bromine, as derived from bromine monoxide (BrO) observations, has decreased by 0.18 ± 0.04 ppt Br yr^{-1} (0.8% yr^{-1}) since 2003.** This decrease is consistent with the decline in total bromine entering in the stratosphere.

CFC-11

- **Global CFC-11 emissions declined after 2018, dropping to 45 ± 10 Gg in both 2019 and 2020. This drop suggests the elimination of most of the unexpected emissions occurring in the years after 2012 (Figure ES-3).**
- **A large fraction of the unexpected emissions originated from eastern China.** This finding is based on available regional observations from multiple sites. The decline of CFC-11 emissions from eastern China since 2018 explains 60 ± 30% of the observed global emission decrease.

CFC-12

- **Global CFC-12 abundances continued to decrease during 2016–2020.** Estimates of global CFC-12 emissions were 33 ± 21 Gg yr^{-1} in 2016 and 25 ± 20 Gg yr^{-1} in 2020.
- **CFC-12 emissions from eastern China decreased from 3.3 ± 1.4 Gg yr^{-1} in 2016 to 0.5 ± 0.5 Gg yr^{-1} in 2019.** This decrease is likely associated with the decline in CFC-11 production.

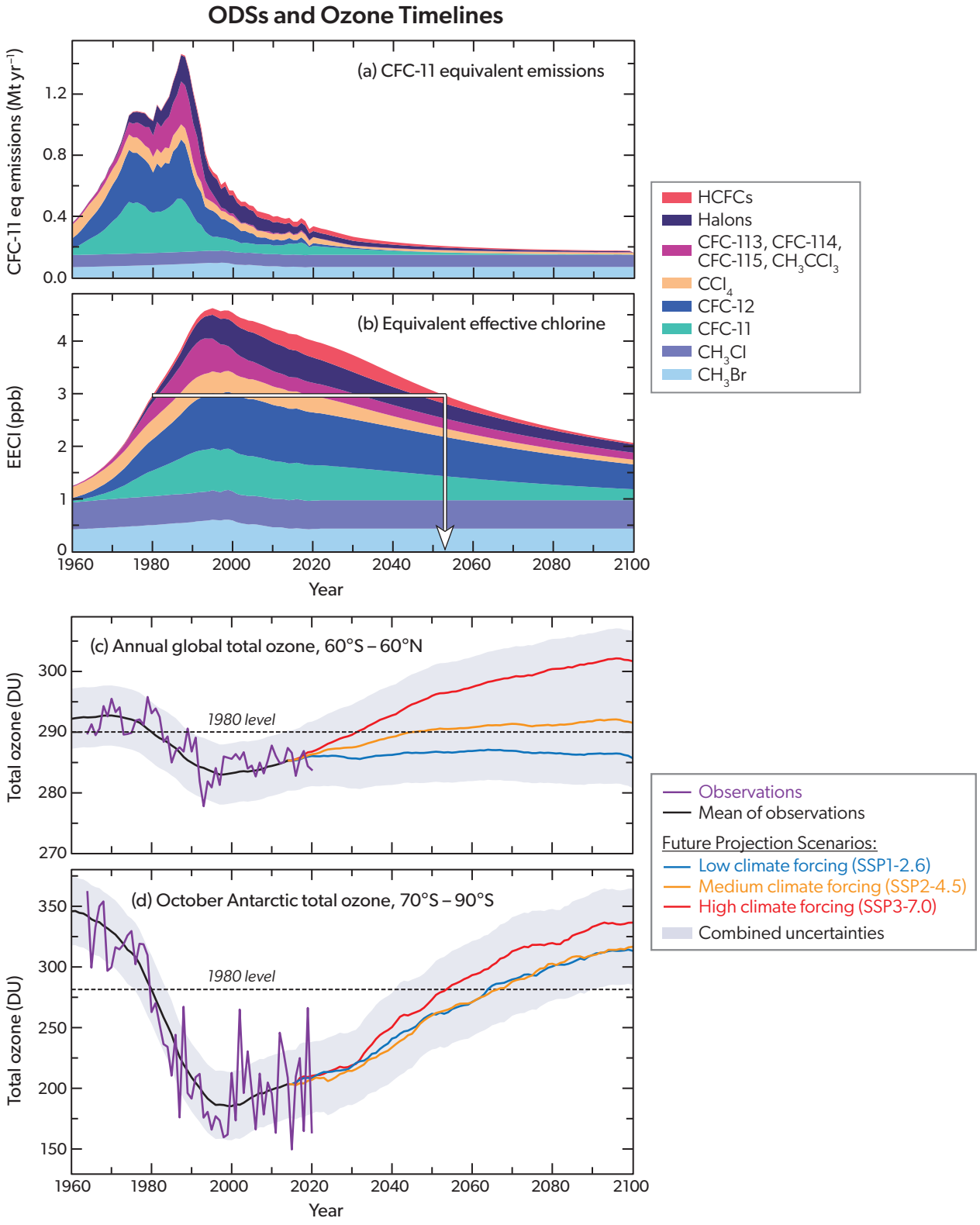

(see caption on facing page)

Other CFCs

- **Global abundances of CFC-13, CFC-112a, CFC-113a, CFC-114a, and CFC-115 increased from 16.0 ± 0.3 ppt in 2016 to a total of 17.2 ± 0.3 ppt ppt Cl in 2020. These changes suggest stable or increasing emissions.** Atmospheric observations confirm that eastern Asia is a substantial source region.

Carbon tetrachloride (CCl_4)

- **The atmospheric abundance of CCl_4 continued to decrease at slower rates than expected, which could be due to underestimated emissions from feedstock production and usage.** Global CCl_4 emission estimates based on atmospheric observations are now more accurate than in the last Assessment due to an improved lifetime estimate, and were on average 44 ± 15 Gg yr^{-1} in both 2016 and 2020.
- **Emissions of CCl_4 in eastern China over the period 2013–2019 show year-to-year variability likely related to CFC-11 production.** Emissions increased after 2013, reaching 11.3 ± 1.9 Gg yr^{-1} in 2016, and decreased to 6.3 ± 1.1 Gg yr^{-1} in 2019.

Hydrochlorofluorocarbons (HCFCs)

- **Tropospheric chlorine from HCFCs has continued to increase, reaching 320 ± 3 ppt in 2020.** The annual average growth rate of chlorine from HCFCs decreased from 5.9 ± 1.3 ppt yr^{-1} reported in the 2018 Assessment to 2.5 ± 1.0 ppt yr^{-1} during 2016–2020.
- **Global emission estimates of HCFC-22 show evidence of a decline in 2020 after a period of relatively constant emissions. HCFC-142b emissions continued to decline, and HCFC-142b abundances have started to decrease. In contrast, HCFC-141b as well as several low-abundance HCFCs (HCFC-31, HCFC-124, HCFC-133a, and the newly detected HCFC-132b) show stable or increasing emissions.**

Halons and methyl bromide (CH_3Br)

- **Bromine from halons has decreased from a peak of 8.5 ± 0.1 ppt in 2006 to 7.3 ± 0.1 in 2020.** Halon-1211, halon-2402, and halon-1202 abundances continued to decline between 2016 and 2020. The rate of change of halon-1301 remained indistinguishable from zero. In 2020 it was the most abundant halon in the atmosphere.
- **Methyl bromide (CH_3Br) abundances have varied annually between 6.5 ppt and 6.9 ppt during 2016–2020 with no clear overall trend.** Most anthropogenically produced CH_3Br has been phased out except for quarantine and pre-shipment (QPS) fumigation, leaving natural emissions as the dominant source. Reported QPS consumption has been relatively stable for more than two decades.

Halogenated very short-lived substances (VSLS)

- **Dichloromethane (CH_2Cl_2), the main component of VSLS chlorine, continued to increase between 2016 and 2020 with a slightly lower growth rate than prior to 2016.** This increase primarily results from growing CH_2Cl_2 emissions in Asia.
- **Tropospheric chlorine based on measurements of VSLS source gases increased by about 10 ppt between 2016 and 2020.** The estimated input of chlorine from VSLSs to the stratosphere also increased by about 10 ppt and amounts to 130 ± 30 ppt in 2020, contributing about 4% of the total chlorine input (Figure ES-2).
- **Chlorinated VSLSs contribute 4% to the total stratospheric chlorine input in 2020 (Figure ES-2).** The VSLS chlorine input is estimated as 130 ± 30 ppt in 2020 compared to 120 ± 40 ppt in 2016.
- **Brominated VSLSs, with mainly natural sources, contribute 5 ± 2 ppt to stratospheric bromine and show no long-term changes.**

Figure ES-1. Timeline of: a) CFC-11-equivalent emissions, b) equivalent effective chlorine (EECl), c) global total ozone, and d) October Antarctic total ozone. Annual CFC-11-equivalent emissions are computed for the ODSs shown in the legend by multiplying mass emissions of a substance by its ODP (panel a). Historical emissions are derived from the measured atmospheric abundances of individual ODSs. The future projections of emissions assume full compliance with the Montreal Protocol and use standard methodologies based on reported production, inventory estimates of the banks, and release rates. The annual abundances of EECl, shown for the global surface, are based on surface abundances (measured or derived from projected emissions and lifetimes) of the chlorine- and bromine-containing substances (panel b). The bromine abundances are weighted by a factor of 65 to account for the greater efficiency of bromine in ozone destruction reactions in the atmosphere. Global total column ozone represents an annual average over 60°N to 60°S latitudes (panel c) and Antarctic total column ozone represents an October average over 70°S to 90°S latitudes (panel d). Panels (c) and (d) include a comparison of chemistry-climate model results (black lines with gray shadings indicating uncertainty ranges) and available observations (purple lines). The chemistry-climate model projections assume compliance with the Montreal Protocol and an increase in greenhouse gases following either the SSP1-2.6 (low climate forcing), SSP2-4.5 (medium climate forcing), or SSP3-7.0 (high climate forcing) scenario, which diverge in 2014. In panel (b),the white line with an arrow marks when EECl returns to its 1980 value. The uncertainty shown in panels (c) and (d) represents the 1-sigma standard deviation about the multi-model mean (MMM), either added to the SSP3-7.0 MMM (upper limit) or subtracted from the SSP1-2.6 MMM (lower limit). [Data sources are: panel (a) mixing ratios in Figure 7-5 and Table 7-6 and ODPs and lifetimes in Table A-1; panel (b) following Figure 7-5 and Table 7-6 with an alpha factor of 65; panel (c) Figure 3-24; and panel (d) Figure 4-24.]

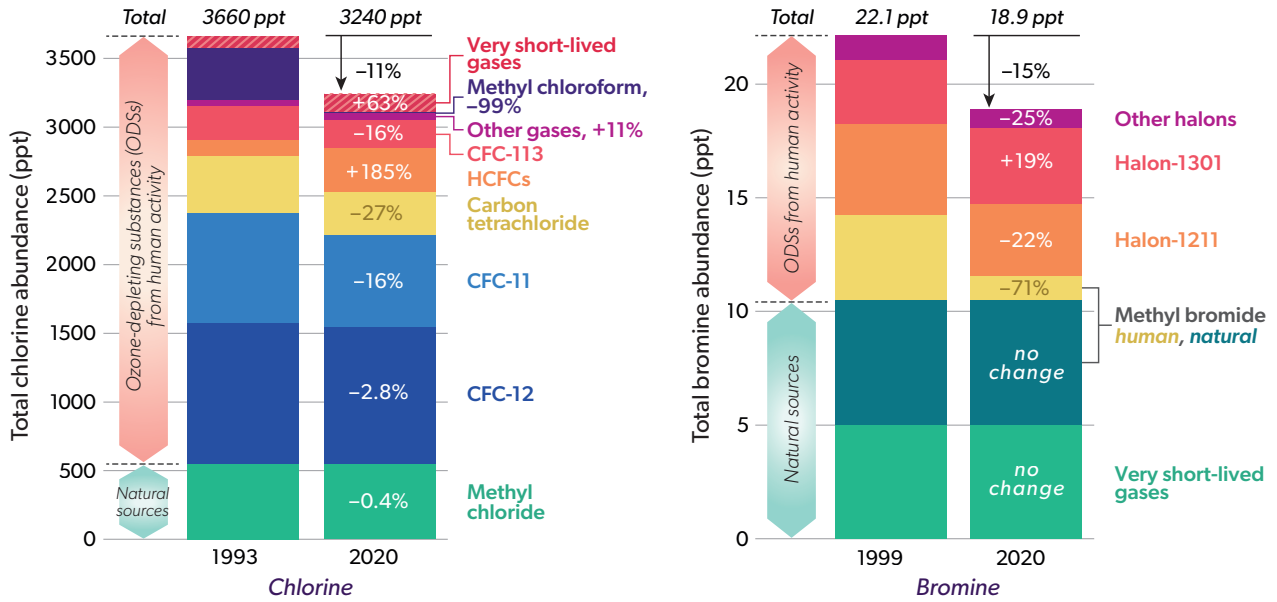

Figure ES-2. Chlorine and bromine input to the stratosphere for a reference year (1993 for chlorine and 1999 for bromine) and for 2020, for different species and classes of compounds. The reference year is the year of maximum chlorine or bromine loading of the troposphere. Mole fractions of long-lived gases were mostly derived from surface observations from global networks (AGAGE and NOAA), except for CH_3Cl before 1995, when observations from both networks were unavailable and values were filled with the simulations from the scenario A1 of the previous Ozone Assessment, which are based on measurements of firn air. The VSLS contributions for bromine are included as a constant 5 ppt, as in previous Assessments. The VSLS chlorine contribution is based on the VSLS input from a model constrained by observed surface boundary conditions. Total VSLS Cl input derived in this way is 80 ppt in 1993 and 130 ppt in 2020. For chlorine, HCFCs include HCFC-22, HCFC-141b, and HCFC-142b; "other" includes contributions from minor CFCs (CFC-13, CFC-112, CFC-113a, CFC-114+CFC-114a, and CFC-115) and halon-1211. For bromine, "other halons" is the sum of bromine contained in halon-1202 and halon-2402. Methyl chloride is counted as having purely natural sources, despite some indications of anthropogenic contributions. The contribution of natural sources to CH_3Br mole fractions was estimated as a constant 5.5 ppt, based on the published firn air and ice core measurements, whereas the anthropogenic contribution was estimated by the global surface mole fractions measured by AGAGE and NOAA minus 5.5 ppt. [See also Figure 1-15]

- **New evidence suggests that iodine from mostly natural sources is entrained into the stratosphere, contributing 0.3–0.9 ppt VSLS iodine in particulate or gas-phase form.** No observational trend estimates exist.

Other gases that influence stratospheric ozone and climate

- Three major greenhouse gases—CH_4, N_2O, and CO_2—cause changes in stratospheric chemistry and dynamics that can affect O_3. An increase in N_2O depletes ozone, and increases in CH_4 and CO_2 tend to increase global stratospheric column ozone. **These gases have increased over the industrial era and continue to increase, and are thus additional factors, beyond ODSs, that control stratospheric O_3 trends.**
- **Anthropogenic N_2O emissions in 2020, when expressed as a CFC-11-equivalent, were more than two times the ODP-weighted emissions from all CFCs in that year, and more than 20% of the CFC emissions in 1987, when the latter were at their peak.**
- **The abundances of many non-ODS, non-HFC, highly fluorinated substances (e.g., SF_6, perfluorocarbons, SO_2F_2, NF_3) have continued to increase.** While these species do not deplete ozone, they are very strong greenhouse gases with long atmospheric residence times. Total direct radiative forcing due to anthropogenic emissions from these species increased from 0.013 W m^{-2} in 2016 to 0.014 W m^{-2} in 2020.
- **Decarbonization of the fossil fuel industry through a transition to molecular hydrogen (H_2) could lead to large increases in atmospheric H_2. Estimates from the few existing studies point to relatively small impacts of H_2 on future global stratospheric ozone.** Global abundances of H_2 increased by about 70% since preindustrial times and have varied between 530 and 550 ppb since the late 20th century.

Table ES-2. Contributions of ODSs controlled under the Montreal Protocol to tropospheric chlorine and bromine in 2020, and annual average trends between 2016 and 2020.

	Contribution to tropospheric chlorine and bromine in 2020[3] (ppt Cl/Br)	Changes in tropospheric chlorine and bromine (ppt Cl or Br per year) from 2016 to 2020
Controlled chlorine substances by group		
Chlorofluorocarbons (CFCs)	1925	−12.9 ± 2.0
Methyl chloroform (CH_3CCl_3)	4.2	−0.90 ± 0.04
Carbon tetrachloride (CCl_4)	308	−3.8 ± 1.0
Hydrochlorofluorocarbons (HCFCs)	319	+2.5 ± 0.4
Halon-1211	3.16	−0.1 ± 0.02
Total chlorine from controlled substances	*2560*	*−15.1 ± 2.4*
Controlled bromine substances by group		
Halons	7.3	−0.11 ± 0.02
Methyl bromide (CH_3Br)[4]	6.6	−0.07 ± 0.02
Total bromine from controlled substances	*13.9*	*−0.18 ± 0.05*

[3] Values are annual averages.

[4] Some anthropogenic uses of CH_3Br are exempted from Montreal Protocol controls, and CH_3Br has natural sources, which results in a natural background concentration.

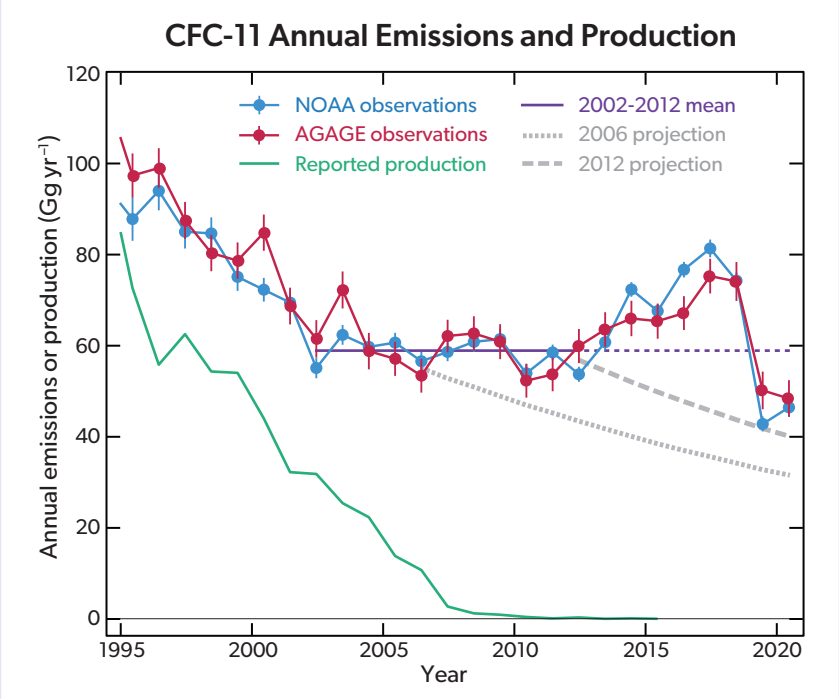

Figure ES-3. CFC-11 global emissions and reported production. Shown are emissions of CFC-11 derived from AGAGE (Advanced Global Atmospheric Gases Experiment; red) and NOAA (National Oceanic and Atmospheric Administration; blue) global network measurements of CFC-11 abundances (see also Figure 1-3 of the Assessment) and a model using a CFC-11 lifetime of 52 years. Also shown is the production history reported to the UN Environment Programme for all uses (green), the average of annual emissions over the 2002–2012 period (horizontal purple line) extended to 2020 (dashed purple line), and scenario projections based on observations through 2006 or through 2012 (grey dotted and dashed lines). These emission projections are calculated using standard methodologies based on reported production, inventory estimates of the bank, and an empirically determined release fraction from the bank over the seven years before 2006 or 2012, which is then applied to subsequent years (see Chapters 1 and 7). Uncertainties in emissions, shown as vertical lines on the data points, include the influence of measurement and model representation uncertainties, and do not include the influence of dynamical variability. The uncertainties are smaller than those presented in Figure 1-3, because uncertainties related to factors constant across the whole time period, such as lifetimes and calibration scale, have been omitted.

2

HYDROFLUOROCARBONS (HFCs)

Hydrofluorocarbons (HFCs) do not contain ozone-depleting chlorine or bromine. Similar to long-lived CFCs and HCFCs, some HFCs have high global warming potentials. The Kigali Amendment to the Montreal Protocol, which was adopted in 2016 and came into force in 2019, sets schedules for the phase-down of production and consumption of specific HFCs. The radiative forcing due to HFCs is currently small, and the Kigali Amendment was designed to avoid uncontrolled radiative forcing growth in coming decades. HFCs were included as one group within the basket of gases of the 1997 Kyoto Protocol and as a result some countries supply annual emission estimates of HFCs to the United Nations Framework Convention on Climate Change (UNFCCC). The Kigali Amendment initiated additional reporting of production and consumption of HFCs and the emissions of HFC-23. HFC-23 is considered separately primarily because it is emitted to the atmosphere largely as a by-product of HCFC-22 production. This reporting will become more complete as more Parties ratify this Amendment.

Observed HFC abundances and associated emissions

- **Global atmospheric abundances and emissions of most HFCs are increasing.** CO_2-equivalent emissions of HFCs derived from observations increased by 18% from 2016 to 2020.
- **Global HFC emissions derived from atmospheric observations are larger than those reported by Annex I Parties to UNFCCC. The gap between these estimates has grown since the previous Assessment.** In 2019, Annex I UNFCCC reporting accounted for approximately one third of the global total emissions derived from atmospheric observations.
- **It is not possible to attribute a substantial fraction of global HFC emissions to individual countries due to limitations in the global monitoring networks and reporting.** Observationally based emission estimates are available for some non-Annex I countries. When these are added to UNFCCC Annex I reports, around 40% of global total CO_2-equivalent emissions (excluding HFC-23) remain unexplained.
- **Global emissions of HFC-23 derived from atmospheric observations increased since the previous Assessment, inconsistent with new information suggesting a substantial rise in abatement independent of Kigali Amendment controls.** The estimated global emissions of HFC-23 were 17.2 ± 0.8 kt yr^{-1} in 2019. This value is substantially higher than the emissions of 2.2 kt yr^{-1} in that year derived from activity-based estimates. These activity-based estimates are derived from UNFCCC emission reports, information on production and abatement submitted under the Montreal Protocol, and the estimated effect of national regulations.
- **Observational evidence suggests that changes are occurring in the use of certain HFCs and their replacements, HFOs (hydrofluoroolefins), because of national regulations, market developments, and actions related to the implementation of the Kigali Amendment.**
  - The 2017–2019 CO_2-eq. emissions of HFCs are approximately 20% lower than those projected in the scenario without national regulations or the controls of the Kigali Amendment.
  - HFOs are increasing in the atmosphere, consistent with their increasing use in place of HFCs. Measurements show that atmospheric background abundances of two HFOs at one central European site have increased by an order of magnitude from 2016 to 2020.
- **The formation in the atmosphere of trifluoroacetic acid (TFA) is expected to increase in the coming decades due to increased use of HFOs and HCFOs.** TFA, a breakdown product of some HFCs, HCFCs, HFOs and HCFOs, is a persistent chemical with potential harmful effects on animals, plants, and humans. The concentration of TFA in rainwater and ocean water is, in general, significantly below known toxicity limits at present. Potential environmental impacts of TFA require future evaluation due to its persistence.

Projections of HFCs and temperature contributions

- **Since the previous Assessment, updated projections**

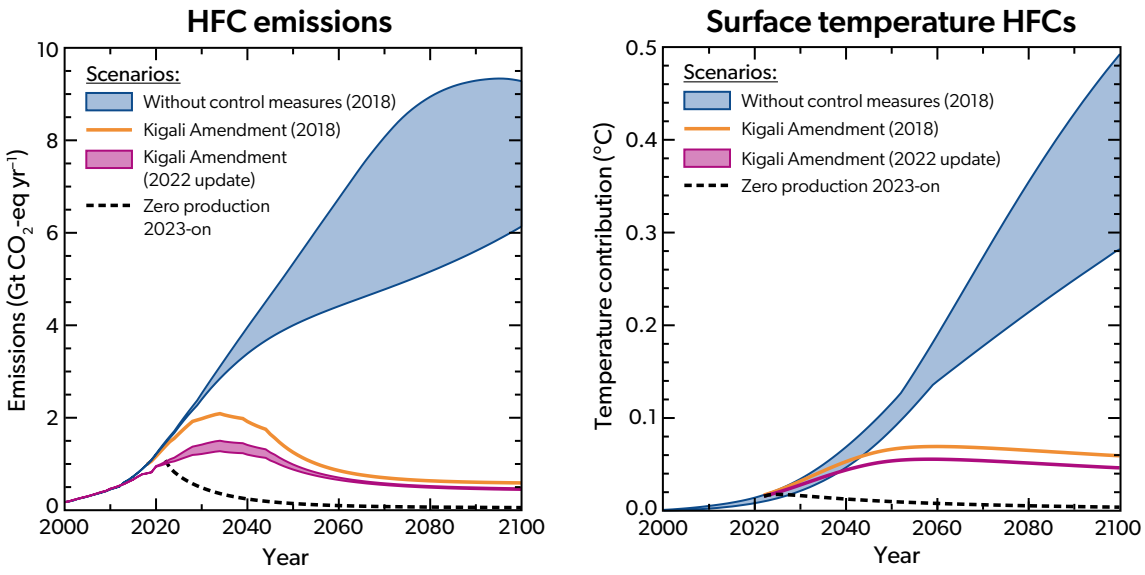

Figure ES-4. HFC emissions (left) and their impact on global average surface temperature (right). Shown is a scenario without global HFC control measures (the 'baseline' scenario from the 2018 Assessment, blue area) and the 2018 and 2022 scenarios assuming full compliance with the Kigali Amendment (orange and pink, respectively). Also shown is a scenario assuming that the global production of HFCs ceased in 2020 (black dashed line). For comparison, the total warming from all greenhouse gases is projected to be 1.4 °C to 4.4 °C by the end of the 21st century, relative to 1850–1900, following IPCC (2021) projections. The contribution from HFC-23 emissions is not included here.

have been made of HFC emissions assuming adherence to the Kigali Amendment (excluding HFC-23). The projected emissions and the associated radiative forcing and temperature change are smaller than estimated previously. The revised projections are based on extended atmospheric observations from 2014 to 2020, updated UNFCCC national emission inventory reports, updated activity data from Annex I countries, and new consumption data from some non-Annex I countries.

- **Concerted efforts to improve the energy efficiency of refrigeration and air conditioning equipment could lead to reductions in greenhouse gas emissions of the same order as those from the global implementation of the Kigali Amendment.** These estimated benefits of improving energy efficiency are highly dependent on the greenhouse gas emission rate from power generation and the pace of decarbonization in the energy sector.

- **Following the controls of the Kigali Amendment, HFC emissions (excluding HFC-23) in 2050 are projected to be 0.9–1.0 Gt CO_2-eq. yr^{-1} in the updated 2022 Kigali Amendment scenario, compared to 4.0–5.3 Gt CO_2-eq yr^{-1} in the 2018 scenario without control measures (Figure ES-4).** The corresponding radiative forcing in 2050 due to HFCs is 0.09–0.10 W m^{-2} with adherence to the Kigali Amendment, compared to 0.22–0.25 W m^{-2} without control measures. Annual average surface warming from HFCs is expected to be 0.04 °C in 2100 under the updated 2022 Kigali Amendment scenario, compared to 0.3–0.5 °C without control measures.

- **Emissions of HFC-23 are expected to grow in the coming decades unless abatement during HCFC-22 production is increased.** This growth is based on an anticipated continued increase in HCFC-22 production, primarily for feedstock use, which is allowed under the Montreal Protocol.

3

STRATOSPHERIC OZONE

The Montreal Protocol and its Amendments and Adjustments have been effective in decreasing the abundance of ODSs in the atmosphere. The clearest signs of corresponding ozone recovery are seen in the upper stratosphere and in the Antarctic lower stratosphere in spring. ODS-related ozone recovery is difficult to detect in other regions due to large natural variability and confounding factors, such as climate change and changes in tropospheric ozone. In the Arctic, for example, severe ozone loss occurs only under cold stratospheric conditions (e.g., in spring 2011 and most recently in spring 2020). An Arctic ozone trend is difficult to detect given the much larger variability than in the Antarctic. Episodic volcanic eruptions and, recently, intense wildfires can increase stratospheric aerosol substantially and hence have the potential to perturb stratospheric ozone. The effects of the Australian wildfires of 2019/2020 and of the large Hunga Tonga-Hunga Ha'apai volcanic eruption in 2022 on ozone are not assessed here and are an area of active research. Ozone in the tropical lower stratosphere shows little response to changes in ODSs, because halogen-driven ozone depletion is comparatively small in this region.

Antarctic and Arctic ozone

- **Recovery of Antarctic stratospheric ozone continues to progress.** New results since the 2018 Assessment support the findings reported at that time that the Antarctic ozone hole has generally diminished in size and depth since the year 2000. New analyses provide additional evidence that September is the period when stratospheric ozone over Antarctica shows the largest sensitivity to decreasing ODSs, and when Antarctic ozone recovery rates are the strongest and the most statistically significant.
- **Antarctic ozone holes observed between 2019 and 2021 exhibited substantial variability in size, strength, and longevity. This behavior is largely dynamically driven, is consistent with our understanding, and does not challenge the evidence for the emergence of recovery.** The 2019 ozone hole was the smallest since 2002. In contrast, both 2020 and 2021 had relatively large and long-lasting late-spring ozone holes.
- **In the Arctic, observed trends in ozone remain small compared to the large year-to-year variability. This precludes the identification of a statistically significant trend in Arctic ozone over the 2000–2021 period.**
- **Arctic total ozone reached exceptionally low values in spring 2020.** A very stable, cold, and long-lived stratospheric polar vortex enabled halogen-catalyzed chemical ozone loss that exceeded the previous record-breaking loss observed in spring 2011. The strong vortex also inhibited dynamical replenishment of polar ozone. The evolution of high-latitude ozone in 2020 is successfully reproduced by model simulations, further substantiating our understanding of polar ozone chemistry.

Global ozone

Changes to date in total column ozone

- **Aggregated ground- and space-based observations indicate an increase of 0.3% decade^{-1} (with a 2-sigma uncertainty of at least ±0.3% decade^{-1}) in near-global (60°S–60°N) total column ozone over the 1996–2020 period.** This trend is consistent with model simulations and our scientific understanding of the processes controlling ozone. Over the same period, trends over broad latitude bands are as follows:
  - Southern Hemisphere mid-latitude (35°S–60°S), total column ozone has increased (0.8 ± 0.7% decade^{-1}).
  - Northern Hemisphere mid-latitudes (35°N–60°N), total column ozone trends are negligible (0.0 ± 0.7% decade^{-1}).
  - Tropical (20°S–20°N) total column ozone shows no clear trend (0.2 ± 0.3% decade^{-1}), likely because lower stratospheric ozone is decreasing while tropospheric ozone is increasing, both unrelated to changes in ODSs.

  The latitudinal pattern of these total column ozone trends is largely consistent with our scientific understanding and is reproduced in the latest set of chemistry-climate models.

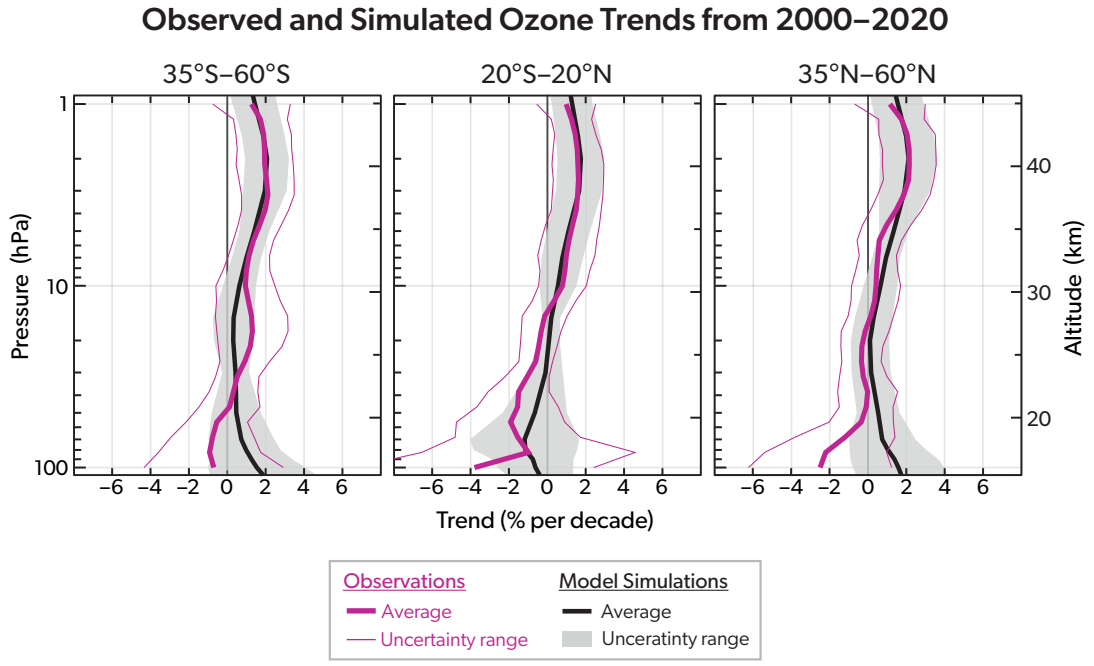

Figure ES-5. Ozone trends in the stratosphere from 2000 to 2020 for three latitude bands. Ozone trends derived from satellite observations (thick magenta lines, with uncertainty ranges given by thin magenta lines) are compared to trends from chemistry-climate models (black lines, with uncertainty ranges given by the grey envelopes). The largest increase has occurred in the upper stratosphere across all three regions, where observations and models are in best agreement. The maximum positive trend of about 2% per decade occurs near 40 km altitude. Uncertainties in the trends become larger below 25 km, where observations in the mid-latitudes suggest a decrease while models suggest an increase. [See also Figures 3-11 and 3-12]

- **Present day (2017–2020) total column ozone as measured from space-based and ground-based observations remains lower than the 1964–1980 average,** by
  - about 2% for the near global average (60°S–60°N)
  - about 4% in the Northern Hemisphere mid-latitudes (35°N–60°N)
  - about 5% in the Southern Hemisphere mid-latitudes (35°S–60°S)
  - about 1% in the tropics (20°S–20°N).

  Within uncertainties associated with natural variability and instrumental accuracy, these values are essentially the same as given in the previous Assessment for the 2014–2017 average.

Changes to date in vertically resolved ozone

*Vertically resolved trends (**Figure ES-5**) are very similar to those given in the last Assessment. With longer records and updates to merged datasets, uncertainties have been reduced.*

- **Measurements show unambiguous increases in upper stratospheric ozone for 2000–2020 outside of the polar regions.** Positive trends have a range of 1.5–2.2% decade^{-1} at mid-latitudes in both the Northern and Southern Hemispheres and 1.1–1.6% decade^{-1} in the tropics.
- **Upper stratospheric ozone increases are due to a combination of decreases in ozone-depleting substances and decreases in stratospheric temperature driven by increases in CO_2.** New model simulations reaffirm this finding from the 2018 Assessment.
- **There are multiple lines of evidence from both observations and models for a small, though uncertain, decrease (1–2% decade^{-1}, with uncertainty up to ±5% decade^{-1}) in tropical lower stratospheric ozone over 2000–2020.** This decrease is consistent with climate change-driven acceleration of the large-scale circulation and has a small impact on total column ozone. Chemical ozone loss from chlorine and bromine is comparatively minor in the tropical lower stratosphere.
- **Observations suggest small decreases in lower stratospheric ozone in the mid-latitudes of both hemispheres for 2000–2020, while chemistry-climate model simulations suggest small increases.** Ozone in mid-latitudes has large year-to-year variability; thus trends have large uncertainties, and they are not robust across all datasets and models. The observed decrease is more evident in the Northern Hemisphere.
- **Outside of polar regions, attribution of total column ozone trends during the period of slow ODS decline requires knowledge of changes in ozone in both the troposphere and stratosphere.** For instance, there is evidence that the lack of a change in total column ozone in the tropics reflects an increase in tropospheric ozone that compensates for the ozone decrease in the tropical lower stratosphere.

Future ozone changes

As reported in the last Assessment, the key drivers of future stratospheric ozone levels continue to be declining ODSs coupled with CO_2-driven cooling in the upper stratosphere and a strengthening of the Brewer-Dobson circulation. Total column ozone will also be affected by changes in the tropospheric ozone burden.

- **New estimates for the year of return of total column ozone outside of polar regions to 1980 values are broadly consistent with the last Assessment. Also similar to the 2018 Assessment, these modeled return dates vary considerably depending on the assumed future greenhouse gas scenario.** Total column ozone returns to 1980 values sooner for scenarios that assume larger emissions of greenhouse gases than scenarios with smaller greenhouse gas emissions. Broadly, the return dates for a middle-of-the-road (SSP2-4.5) scenario are consistent with previous Assessments:
  - around 2040 for near global mean (60°S–60°N) annually averaged column ozone;
  - around 2045 for Southern Hemisphere (60°S–35°S) annually averaged column ozone; and
  - around 2035 for Northern Hemisphere (35°N–60°N) annually averaged column ozone.
- **For scenarios that assume strong reductions in the emission of tropospheric ozone precursors, the resulting reductions in tropospheric ozone can be important for total column ozone trends.** Under such scenarios, total column ozone in the tropics is projected to remain below the 1980 values until at least 2100. As discussed in the last Assessment, tropical total column ozone under high greenhouse gas (GHG) scenarios will be below 1980 values in 2100 due to circulation-driven changes affecting lower stratospheric ozone.
- **The Antarctic ozone hole is expected to gradually close, with springtime total column ozone returning to 1980 values shortly after mid-century (about 2065).** Updated chemistry-climate model projections suggest that ozone hole recovery may depend on the future climate change scenario, with projections of return around 2050 for the low climate change mitigation scenarios. This sensitivity of Antarctic recovery to climate change scenario differs from the findings in previous Assessments and may be due to the use of a smaller number of updated models, as well as the models being forced with different evolutions of GHGs.
- **Arctic springtime total ozone is expected to return to 1980 values slightly before mid-century (about 2045).** Substantial Arctic ozone loss will occur in cold winters/springs as long as ODS concentrations are well above natural levels. While dynamical changes associated with increasing GHGs lead to an earlier recovery of Arctic ozone, increasing stratospheric water vapor abundances and CO_2-driven cooling of the lower stratosphere may increase the potential for the formation of polar stratospheric clouds in dynamically undisturbed Arctic winters, leading to ozone loss.
- **The unreported production of CFC-11 over 2012–2019 is estimated to delay polar ozone return to 1980 values by up to 3 years.** For global total column ozone, the delay is about 1 year.
- **Exceptional events can temporarily perturb chemical and dynamical processes that affect stratospheric ozone amounts.** Since the last Assessment, these include the 2019/2020 wildfires in Australia, the eruption of the Hunga Tonga-Hunga Ha'apai volcano, and disruptions to the quasi-biennial oscillation of the tropical winds. In particular, intense wildfires have become more frequent. Their potential impacts on the stratosphere are not yet well quantified and are a subject of active research.
- **The impending loss of vertically resolved, global space-borne measurements of ozone-related atmospheric constituents (e.g., reactive chlorine, water vapor, and long-lived transport tracers) will impede the ability to monitor and explain changes in the stratospheric ozone layer in the future.**

4

STRATOSPHERIC OZONE CHANGE AND ITS INFLUENCE ON CLIMATE

Stratospheric ozone has a wide-ranging influence on the Earth system. Antarctic ozone depletion caused an expansion of the tropics and a poleward shift of the jet stream and storm tracks in the Southern Hemisphere that lead to pronounced changes in summertime surface climate, as summarized in the previous Assessments. Continuing ozone recovery and increases in atmospheric greenhouse gas (GHG) concentrations will be key drivers of future Southern Hemisphere climate changes. The relative importance of ozone recovery for future Southern Hemisphere climate will depend on the magnitude and rate of atmospheric GHG concentration changes.

Evolution of stratospheric climate

- **The estimated rate of long-term cooling in the global middle and upper stratosphere (0.6 K decade^{-1}) is similar to previous Assessments.** The evolution of stratospheric temperatures continues to follow the behavior expected from the well understood effects of natural and anthropogenic forcings. The long-term trends are primarily driven by changing CO_2 and stratospheric ozone. Global temperature in the lower stratosphere has been near constant since the late 1990s.
- **In the future, increasing GHGs and the effects of ozone recovery would have opposing effects on stratospheric temperature and circulation.** For a moderate GHG emission scenario (RCP6.0), stratospheric cooling and the acceleration of the global stratospheric transport circulation (the Brewer-Dobson Circulation) driven by increasing GHGs dominate over opposing effects from ozone recovery. Under both moderate (RCP4.5/SSP2-4.5) and high emission (RCP8.5/SSP5-8.5) scenarios, the delayed breakdown of the austral springtime polar vortex that was driven by ozone depletion in the late 20th century will persist due to the effect of increasing GHGs.

Influence on tropospheric and surface climate

- **New evidence suggests that ozone recovery has caused changes in the observed trends of the Southern Hemisphere atmospheric circulation between the ozone depletion and recovery periods.** Model simulations support the attribution of these changes to ozone recovery. These results provide evidence that Southern Hemisphere circulation trends have responded to the recovery of Antarctic ozone due to the Montreal Protocol (see Figure ES-6).
- **While there are no detectable surface impacts of long-term Arctic ozone changes, new evidence shows that for individual years low springtime Arctic ozone can amplify existing stratospheric circulation anomalies and their influence on tropospheric circulation and surface climate.**

Influence on the Southern Hemisphere ocean and cryosphere

- **New evidence confirms that ozone depletion is unlikely to have driven the observed high-latitude sea-surface temperature cooling and changes in Antarctic sea ice since 1979.** There is no robust link between ozone depletion and net Southern Ocean carbon uptake, which exhibits large decadal variations.

Radiative forcing from past ODS, HFC, and stratospheric ozone changes

- **The calculated total direct radiative forcing due to CFCs, HCFCs, halons, CCl_4 and CH_3CCl_3 decreased by 0.006 W m^{-2} since 2016 and was 0.337 W m^{-2} in 2020.** This forcing is approximately 16% of the radiative forcing of CO_2. CO_2-equivalent emissions (in Gt CO_2-eq yr^{-1}) in 2020 were, for species where estimates are available, 0.7 ± 0.4 for CFCs, 0.7 ± 0.1 for HCFCs, 0.09 ± 0.03 for CCl_4 and CH_3CCl_3 combined, and 0.02 ± 0.01 for halons.
- **The best estimate of radiative forcing from stratospheric ozone changes over 1850–2011 is –0.02 W m^{-2}, with an uncertainty of ± 0.13 W m^{-2}.** Hence, the combined radiative forcing from ODSs and historical stratospheric ozone changes is positive (around 0.3 Wm^{-2}), consistent with previous Assessments.
- **Radiative forcing from measured HFCs continues to increase.** The radiative forcing due to the HFCs reached 0.044 ± 0.006 W m^{-2} in 2020, an increase of around one-third since

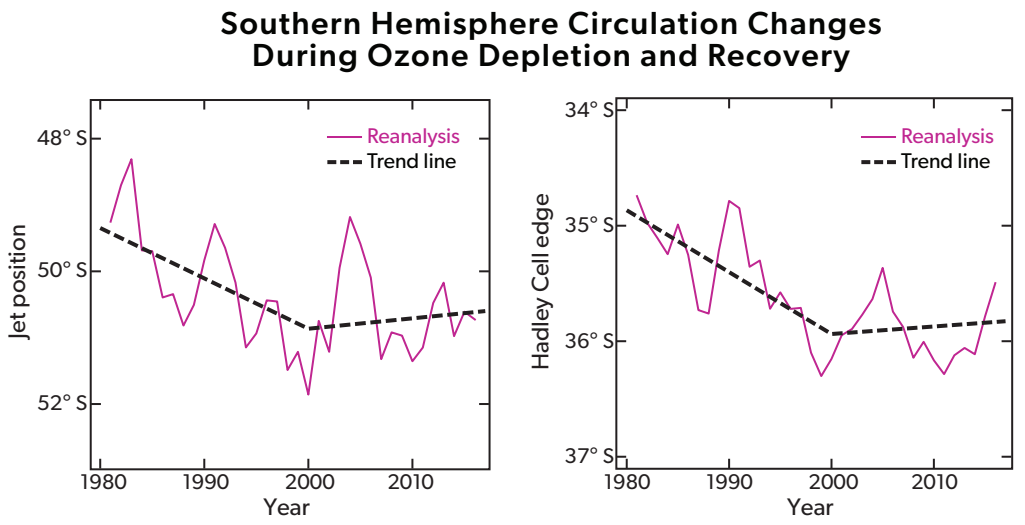

Figure ES-6. Antarctic ozone recovery has caused changes in the observed trends of the Southern Hemisphere atmospheric circulation between the ozone depletion and recovery periods (see Figure ES-1 panel d). Shown are the positions (in latitude) of a) the Southern Hemisphere midlatitude jet and b) Hadley Cell edge, which indicates the poleward extent of the subtropical dry zone, in austral summer (December–February). Solid lines are 3-year running means derived from four different meteorological reanalyses. The dashed lines are piece-wise linear trends computed over the two periods 1980–2000 and 2000–2017. [Figure adapted from Figure 5-14].

2016. The most important contributor to HFC radiative forcing was HFC-134a (44%), and HFC-125 (18%) overtook HFC-23 (15%) as the second largest contributor. Together, the HFCs represent approximately 2% of the radiative forcing of CO_2. Total CO_2-equivalent emissions in 2020 were 1.22 ± 0.05 Gt CO_2-eq yr^{-1}.

Climate impacts of the control of ODSs by the Montreal Protocol

- **New studies support previous Assessments that the decline in ODS emissions due to the implementation of the Montreal Protocol avoids an additional global warming of approximately 0.5–1 K by mid-century compared to an extreme scenario with an uncontrolled increase in ODSs of 3–3.5% per year and the resulting changes in ozone.** New evidence suggests an additional avoided warming by mid-century due to prevention of UV radiation damage to the terrestrial carbon sink, as such damage would cause additional CO_2 to remain in the atmosphere.

5

STRATOSPHERIC AEROSOL INJECTION AND POTENTIAL IMPACTS ON OZONE

Global warming has now reached approximately 1.2 °C above preindustrial levels. Climate model scenarios considered by IPCC (2021) indicate continued future warming in the next few decades even with ambitious mitigation and decarbonization, leading to further climate impacts. Stratospheric Aerosol Injection (SAI) has the potential to limit the rise in global surface temperatures by increasing the concentrations of particles in the stratosphere. These particles reflect a fraction of sunlight back to space, in a process similar to that evident after large volcanic eruptions. However, SAI comes with significant risks and can cause unintended consequences. The 2022 Assessment is the first to dedicate a chapter to assess the potential impacts on stratospheric ozone in possible SAI scenarios in the coming decades based on the limited number of model simulations that have been performed to date.

- **Stratospheric Aerosol Injection (SAI) has the potential to reduce global mean temperatures. However, SAI cannot fully offset the widespread effects of global warming and produces unintended consequences, including effects on ozone. Details of these effects depend on the specifics of the SAI scenario and SAI injection strategy.**
  - In different SAI scenarios, the modeled effects of SAI on future ozone depend on the specific details of future climate change, and on the amount, timing and duration of SAI applied. Offsetting an ever-increasing global warming with an ever-increasing SAI ("strong SAI") has been shown to lead to increasing environmental risks.
  - In a world with limited mitigation of greenhouse gas emissions, global mean temperatures continue to increase significantly in the future (**Figure ES-7**, black line). This future warming would be reduced by aggressive decarbonization (orange line). An SAI peakshaving scenario offsets the overshoot of surface temperature above a certain threshold until greenhouse gases have been reduced (purple line).
  - Different SAI strategies, such as the altitude and latitude of injection, and type of material, have been developed to mitigate some of the unintended climate impacts of SAI. In modelling studies, the principal injected material is sulfur. Different strategies would have different effects on stratospheric ozone.
- **Model simulations of SAI reveal large differences in surface cooling per unit sulfur injected, which are attributed to differences in representing key processes. Explosive volcanic eruptions serve as natural analogs to aid evaluation of these models.**
  - Very few Earth System Models resolve complex stratospheric processes, including detailed aerosol microphysics coupled with chemistry, radiation, and dynamics. In addition, the sparsity of current existing model simulations limits the confidence in the quantification of many impacts.
  - Injection rates vary between 8 and 16 Mt of sulfur dioxide (SO_2) per year to cool the Earth by 1 °C (an injection amount approximately equivalent to that of the Mount Pinatubo eruption in 1991), based on simulations with seven Earth System Models.
  - Explosive volcanic eruptions sporadically emit millions of tonnes of SO_2 into the stratosphere and provide useful, albeit imperfect, natural analogs for evaluating the global models used to conduct SAI simulations.
- **The net effects of large-scale SAI on stratospheric ozone are mainly driven by i) increases in aerosol surface area, ii) stratospheric halogen and nitrogen concentrations, and iii) aerosol-induced heating of the stratosphere, which change both stratospheric ozone chemistry and stratospheric dynamics. These simulated changes are strongly model dependent.**
  - Enhanced stratospheric sulfate aerosol increases stratospheric heterogeneous chemical reaction rates, leading to enhanced or depleted stratospheric ozone depending on altitude, latitude, and season. Details depend on the SAI-induced aerosol surface area distribution, the current stratospheric halogen and nitrous oxide concentrations, and SAI-induced changes in stratospheric water vapor.
  - Increased sulfate aerosols in SAI scenarios heat the lower tropical stratosphere by 4.6 ± 2.7 °C per 1°C surface

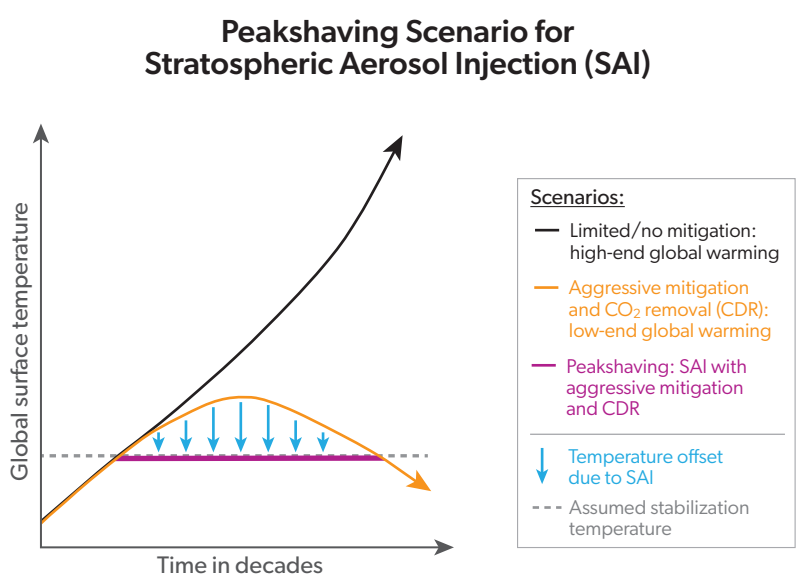

Figure ES-7. Schematic diagram representing the concept of "Peakshaving". Different lines illustrate global mean surface temperatures for future scenarios: a limited or no mitigation scenario leading to strong future global warming (black line); a so-called "overshoot scenario" that assumes strong mitigation and Carbon Dioxide Removal (CDR), and leads to a temporary overshoot of global mean temperatures above sustainable limits for some time (orange); a Peakshaving scenario that applies temporary SAI to the overshoot scenario in order to prevent the increase in global mean temperature from exceeding these sustainable limits (purple line). The blue arrows represent the approximate relative magnitude of the temperature impact of the applied SAI.

cooling based on results from different models and injection scenarios. Resulting changes in stratospheric composition and transport depend on the details of the injection strategy and are strongly model dependent.

- **Additional ozone depletion due to SAI is simulated in spring over Antarctica, with magnitudes dependent on the injection rate and timing. Simulations of strong SAI show an increase in total column ozone (TCO) in mid-latitudes (40–60°N) in the winter Northern Hemisphere.**
  - For October over Antarctica, SAI simulations that achieve a global mean surface cooling of 0.5 °C in the first 20 years, show a reduction of TCO of around 58 ± 20 DU, assuming 2020–2040 halogen conditions. This reduction brings TCO values close to the observed minimum in the 1990s. Less ozone loss would be expected for a later SAI start date, when halogen concentrations are projected to be lower.
  - Beyond the first 20 years, the continued application of strong SAI, to offset almost 5 °C of warming by 2100, reduces Antarctic ozone in October by similar amounts (55 ± 20 DU) throughout the 21st century despite declining abundances of ozone-depleting substances (ODS). In this case, ozone hole recovery from ODSs is delayed by between 25 and 50 years. A peakshaving scenario potentially leads to less ozone depletion.
  - Under stronger SAI scenarios, ozone is significantly enhanced in NH mid-latitudes in winter owing to stratospheric heating from injected sulfur, which leads to increased equator to poleward transport of ozone.
  - Ozone loss within the Arctic polar vortex has not yet been robustly quantified for SAI.
- **The injection of aerosols other than sulfate is expected to change the effects on ozone via associated changes in heterogeneous chemistry, dynamics and transport.** Aerosol types that are more chemically inert and absorb less solar radiation may reduce chemical and dynamical impacts on stratospheric ozone respectively. However, the laboratory studies and climate model simulations sufficient to quantify these effects have yet to be performed.

6

POLICY-RELEVANT SCENARIOS AND INFORMATION

*Changes in total column ozone and in average radiative forcing in response to various control measures using alternative scenarios and bounding test cases are shown in **Figure ES-8**. The baseline scenario used here assumes full compliance with the Montreal Protocol. The hypothetical alternative scenarios assessed here include the elimination of banks, production, and emissions of gases that are both controlled and uncontrolled by the Montreal Protocol and are intended to demonstrate the impacts on climate and ozone relevant to policy actions.*

- **The unexpected emissions of CFC-11 over 2012–2019 have led to a delay in the return of mid-latitude EESC to 1980 abundances by about 1 year.** The reduction in emissions since 2018, based on global and regional observations, have prevented a longer delay.
- **The CFC-11 production that led to these observed unexpected emissions has most likely increased global banks.** Assuming these emissions were associated with the production of insulating foams, it is estimated that they account for 25% to 45% of the unreported production. This suggests a potential increase in the CFC-11 bank of 146–1320 kt from unreported production between 2012 and 2019. For reference, a 1000 kt increase in the 2020 bank would further delay the return of mid-latitude EESC to 1980 levels by almost 4 years (**Figure ES-8**).
- **If it were possible to eliminate all future long-lived anthropogenic ODS emissions in 2023, this would bring forward the return of mid-latitude EESC to 1980 abundances by about 16 years and increase the average of global stratospheric ozone in the period 2023–2070 by about 2 DU.** This provides an upper limit for the reduction of EESC through control measures. These emissions are dominated by the release from current banks, with additional contributions from controlled future production and consumption of ODSs, production for feedstock use, and quarantine and preshipment uses of CH_3Br.
- **The projected return of mid-latitude EESC is delayed by 6 years compared with the previous Assessment due mostly to larger assessed banks in the current baseline scenario.**The larger bank estimates primarily arise from the use of a new modelling approach to assess the banks.
- **Total production of controlled substances for feedstock use is increasing. If all future feedstock-related emissions were eliminated, this would bring forward the return of mid-latitude EESC to 1980 levels by almost 4 years when compared to the baseline scenario.** Reported feedstock production has increased by 75% by mass over the last decade. Assuming that the fraction of emissions related to feedstock production has not changed, emissions have increased accordingly. Additionally, feedstock usage has led to the emission of a range of ODS by-products and intermediates.
- **The CCl_4 emissions from feedstock production and use currently dominate the ODS influence on ozone from all feedstocks. The elimination of these CCl_4 emissions accomplishes much of the projected 4-year accelerated return in EESC noted above.** This usage of CCl_4 is expected to continue increasing primarily because of its application in the growing production of HFOs, and could roughly double CCl_4 abundances in 2100 compared to the baseline scenario.
- **If future emissions of methyl bromide (CH_3Br) from quarantine and preshipment (QPS) applications could be eliminated, this would accelerate the return of mid-latitude EESC by about 2 years.** Production for QPS use has remained nearly unchanged over the last two decades. It now constitutes almost 99% of the reported production of CH_3Br, with critical use exemptions (CUEs) making up the remaining reported production. The importance of QPS CH_3Br has been noted in previous Assessments.

Abundances of several gases not controlled by the Montreal Protocol have been increasing due primarily to anthropogenic emissions and have direct effects on stratospheric ozone, for example dichloromethane (CH_2Cl_2) and N_2O.

- **Emissions of CH_2Cl_2, the dominant anthropogenic VSLS chlorine gas, continue to increase and augment ozone-depleting chlorine in the atmosphere.** Future projections are uncertain due to the highly variable emissions over the past few years. If CH_2Cl_2 emissions continue at their current level, they will continue to deplete approximately

1 DU of global, annual average ozone. Elimination of these emissions would rapidly reverse this depletion (Figure ES-8).

- **A 3% reduction in anthropogenic N_2O emissions, averaged over 2023–2070, leads to an increase in global ozone of about 0.5 DU averaged over the same period, and a decrease of about 0.40 W m^{-2} in radiative forcing, averaged over 2023–2100 (Figure ES-8).** This reduction is the amount obtained when comparing the baseline N_2O scenario (SSP2-4.5) to the strongest N_2O mitigation scenario of the SSPs (SSP1-1.9).

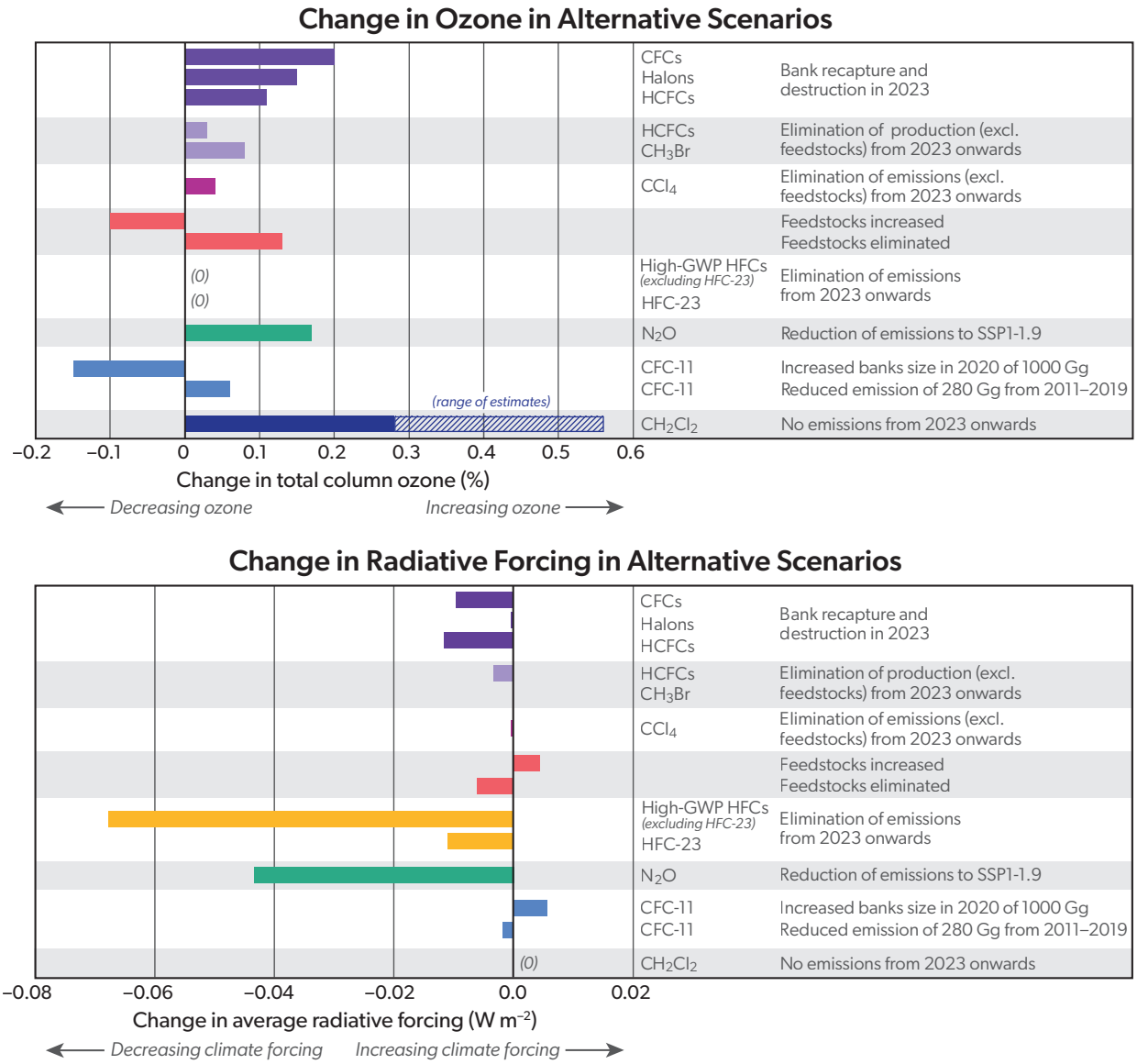

Figure ES-8. Impacts of various alternative scenarios and test cases on total column ozone (averaged over 2020 through 2070) and radiative forcing of climate (averaged over 2023 through 2100) compared with the baseline scenario. The scenarios and cases include reduced N_2O emissions (SSP1-1.9 scenario), elimination of emissions for HFCs, HFC-23, CH_2Cl_2, and CCl_4 (excluding emissions from feedstock production and usage) starting in 2023, elimination of future production of CH_3Br and HCFCs starting in 2023 (excluding feedstock production and usage), and elimination and destruction of banks of halons, HCFCs and CFCs in 2023. Also considered are the unexpected CFC-11 emissions over 2012–2019 (assumed to be 280 Gg in total), an additional 1000 Gg in the 2020 CFC-11 bank, elimination of all feedstock-related emissions starting in 2023, and a case in which feedstock-related emissions are allowed to grow at their current growth rates through 2030 and are then held constant. Potential climate benefits from improved energy efficiency in the refrigeration and air conditioning sector are not included here, and are thought to have the potential to have an impact much larger than that of any of the scenarios and cases considered here. For reference, current total column ozone depletion is about 2% when averaged over 60°S–60°N, and the current radiative forcing from CO_2 is about 2 W m^{-2}.

SCIENTIFIC SUMMARIES OF THE CHAPTERS

Chapter 1:

Update on Ozone-Depleting Substances (ODSs) and Other Gases of Interest to the Montreal Protocol

This chapter concerns atmospheric changes in ozone-depleting substances (ODSs), such as chlorofluorocarbons (CFCs), halons, chlorinated solvents (e.g., carbon tetrachloride [CCl_4] and methyl chloroform [CH_3CCl_3]) and hydrochlorofluorocarbons (HCFCs), which are controlled under the Montreal Protocol. Furthermore, the chapter updates information about ODSs not controlled under the Protocol, such as methyl chloride (CH_3Cl) and very short-lived substances (VSLSs). In addition to depleting stratospheric ozone, many ODSs are potent greenhouse gases.

Mole fractions of ODSs and other species are primarily measured close to the surface by global or regional monitoring networks. The surface data can be used to approximate a mole fraction representative of the global or hemispheric tropospheric abundance. Changes in the tropospheric abundance of an ODS result from a difference between the rate of emissions into the atmosphere and the rate of removal from it.

- **The total amount of chlorine and bromine from ODSs that were controlled under the original Montreal Protocol is continuing to decline, as the overall emissions are smaller than the rate at which these ODSs are destroyed. Abundances of many of the first-stage replacement compounds, HCFCs, are now increasing very slowly or not at all.**

Tropospheric Chlorine (Cl)

Total tropospheric chlorine is a metric used to quantify the combined globally averaged abundance of chlorine in the troposphere due to the major chlorine-containing ODSs. The contribution of each ODS to total tropospheric chlorine is the product of its global mean tropospheric mole fraction and the number of chlorine atoms it contains.

- **Total tropospheric chlorine from ODSs continued to decrease between 2016 and 2020.** Total tropospheric chlorine in 2020 was 3220 ppt (where ppt refers to parts per trillion as a dry air mole fraction), about 1.8% lower than in 2016 and 12% lower than its peak value in 1993. Of the 2020 total, CFCs accounted for about 60%, CH_3Cl for about 17%, and CCl_4 and HCFCs each for about 10%. The contribution from CH_3CCl_3 has now decreased to 0.1%. Very short-lived source gases (VSL SGs), as measured in the lower troposphere, contributed approximately 3.5%.
    - During the period 2016–2020, the observed rate of decline in tropospheric chlorine due to controlled substances was 15.1 ± 2.4[5] ppt Cl yr^{-1}, which is larger than during the 2012–2016 period (12.8 ± 0.8 ppt Cl yr^{-1}). This rate of decrease was close to the projections in the previous Assessment. The net rate of change was the result of a slightly slower than projected decrease in CFCs and a slower HCFC increase than in the 2018 A1 projection scenario.
    - When substances not controlled under the Montreal Protocol are also included, the overall decrease in tropospheric chlorine was 15.1 ± 3.6 ppt Cl yr^{-1} during 2016–2020. This is larger than the rate of decline during the 2012–2016 period (3.6 ± 4.7 ppt Cl yr^{-1}) and comparable to the rate of decline in controlled substances. Changes in the predominantly anthropogenic dichloromethane (CH_2Cl_2) and the largely natural CH_3Cl largely canceled each other out, resulting in almost no net change in Cl from uncontrolled substances during this period.
- **Starting around 2018, the rate at which the CFC-11 mole fraction was declining in the atmosphere accelerated again, following a slowdown since 2013. These recent changes are largely due to a decrease in emissions originating mostly from northeastern China.** Assuming no

[5] Uncertainties in absolute changes of atmospheric abundances were derived using the 1 standard deviation measurement uncertainties (where appropriate combined as the square root of the sum of their squares) and the bootstrap algorithm described in Barreto and Howland (2006). Similar to the procedure described in Leedham Elvidge et al. (2018), and to represent atmospheric variability, data was converted to a dataset comprised of 1) original data, 2) original data minus measurement uncertainty and 3) original data plus measurement uncertainty. This dataset was then resampled (with replacement) 1000 times to derive a standard deviation that is a realistic representation of the uncertainty of the entirety of the original data.

impact from changes in atmospheric circulation, global emissions increased from about 57 Gg yr^{-1} (= kt yr^{-1}) in 2012 to around 78 Gg yr^{-1} in 2017; after 2018, they then decreased, to approximately 47 Gg yr^{-1} in 2020. Emissions from northeastern China explain 60 ± 40% of the 2012–2018 increase and 60 ± 30% of the subsequent decrease. There is evidence that other recent significant emission regions include the Arabian and Indian subcontinents. If these renewed global emissions are associated with uses that substantially increase the size of the CFC-11 bank, further emissions resulting from this production would be expected in the future.

- **During 2016–2020, mole fractions of CFC-12 decreased by about 2.8%, which is comparable to the decrease during 2012–2016 (~2.3%).** Estimates of global CFC-12 emissions in 2016 and 2020 were similar within uncertainties, at 33 ± 21 Gg yr^{-1} and 25 ± 20 Gg yr^{-1}, respectively. CFC-11 and CFC-12 are often co-produced, and atmospheric observations have confirmed a decrease in CFC-12 emissions from northeastern China from 3.3 ± 1.4 Gg yr^{-1} in 2016 to 0.5 ± 0.5 Gg yr^{-1} in 2019.
- **The CFC-113 global mole fraction has continued to decrease**, but emissions remained constant within uncertainties at around 6 ± 6 Gg yr^{-1} between 2016 and 2020.
- **Mole fractions of CFC-114 remained stable during 2016–2020, whereas those of CFC-13, CFC-113a, and CFC-115 continued to rise, and mole fractions of CFC-112a and CFC-114a exhibited positive growth after previously showing near-zero change.** Total Cl from the latter five CFCs increased from 16.0 ± 0.3 ppt in 2016 to a total of 17.2 ± 0.3 ppt Cl in 2020. These findings likely indicate an increase or stabilization of the emissions of these relatively low abundance compounds. While some of these emissions are known to originate from eastern China, the primary processes responsible are unknown.
- **The rate at which CCl_4 has declined in the atmosphere remains slower than expected from its reported use as a feedstock and its removal rate from the atmosphere, which indicates ongoing emissions of around 44 ± 15 Gg yr^{-1}.** This is likely, at least in part, due to feedstock emissions from the production of chloromethanes and perchloroethylene and from chlor-alkali plants. Global CCl_4 emission estimates based on atmospheric observations are now more accurate than in the last Assessment due to an improved lifetime estimate.
- **Emissions of CCl_4 in eastern China over the period 2013–2019 show year-to-year variability likely related to CFC-11 production.** Emissions increased after 2013, reaching 11.3 ± 1.9 kt yr^{-1} in 2016, and decreasing to 6.3 ± 1.1 kt yr^{-1} in 2019.
- **Total tropospheric chlorine from HCFCs has continued to increase, reaching 320 ± 3 ppt in 2020.** There is evidence of a slowdown of this increase, as the annual average growth rate of total chlorine from HCFCs decreased from 5.9 ± 1.3 ppt yr^{-1} during 2012–2016 to 2.5 ± 0.4 ppt yr^{-1} during 2016–2020.
- **Combined emissions of the major HCFCs have declined since the previous Assessment.** Emissions of HCFC-22 and HCFC-142b likely declined between 2016 and 2020, while emissions of HCFC-141b, after an initial drop, likely rose year-on-year since 2017, amounting to a total rise of ~4.5 Gg during 2017–2020. These findings are consistent with a sharp drop in reported HCFC consumption after 2012, particularly from Article 5 countries.
- Continued emissions of the compounds HCFC-124, HCFC-31, HCFC-132b, and HCFC-133a have been inferred from atmospheric measurements. HCFC-132b is yet another newly detected HCFC, and its atmospheric mole fractions, while currently small, continue to increase.

Tropospheric Bromine (Br)

Total tropospheric bromine is defined in analogy to total tropospheric chlorine. Even though the abundance of bromine is much smaller than that of chlorine, it has a significant impact on stratospheric ozone because it is around 60–65 times more efficient than chlorine as an ozone-destroying catalyst.

- **Total tropospheric bromine from controlled ODSs (halons and methyl bromide [CH_3Br]) continued to decrease, and was 13.9 ppt by 2020, 3.2 ppt below the peak levels observed in 1999.** From 2012 to 2016, total controlled bromine declined at a rate of 0.15 ± 0.14 ppt Br yr^{-1} (about 1% yr^{-1}). This rate increased to 0.18 ± 0.05 ppt Br yr^{-1} during 2016–2020, with halons contributing about 60% to the overall decline.
- **The mole fractions of halon-1211, halon-2402, and halon-1202 continued to decline between 2016 and 2020. There was no significant change in the mole fraction of halon-1301 between 2016 and 2020. This ODS is, at ~3.3 ppt, now the most abundant halon in the atmosphere.** Emissions of halon-2402, halon-1301, and halon-1211, as derived from atmospheric observations, declined or remained stable between 2016 and 2020.
- **CH_3Br annually averaged mole fractions showed little net change between 2016 and 2020. The small increase (2–3%) observed between 2015 and 2016 was compensated by a small decrease (4%) largely taking place during 2016–2017.** The 2020 mole fraction was around 6.6 ppt, a reduction of 2.6 ppt from peak levels measured between 1996 and 1998. Reported quarantine and pre-shipment (QPS) consumption was relatively stable from 1996 to 2020.

Halogenated Very Short-Lived Substances (VSLSs)

VSLSs are defined as trace gases whose local lifetimes are shorter than 0.5 years and have non-uniform tropospheric abundances. These local lifetimes typically vary substantially over time and space. Of the very short-lived source gases (VSL SGs) identified in the atmosphere, brominated and iodinated species are predominantly of oceanic origin, while chlorinated species have significant anthropogenic sources. VSLSs that reach the stratosphere will release the halogen they contain almost immediately and will thus play an important role for lower-stratospheric ozone in particular. Due to their short lifetimes and their atmospheric variability, the quantification of their contribution is much more difficult and has much larger uncertainties than for long-lived compounds.

- **Total tropospheric chlorine from VSL SGs in the background lower atmosphere is dominated by anthropogenic sources. It continued to increase between 2016 and 2020, but its contribution to total stratospheric chlorine remained small.** Global mean chlorine from VSLSs in the troposphere has increased from about 103 ppt in 2016 to about 113 ppt in 2020. The relative contribution of VSLS to the stratospheric chlorine input amounted to 4% in 2020, compared to 3.6% in 2016.
- **Dichloromethane (CH_2Cl_2), with predominantly anthropogenic sources, is the main contributor to total chlorine from VSLSs. It accounted for the majority of the change in VSLS chlorine between 2016 and 2020.** The CH_2Cl_2 global mean abundance reached approximately 40–45 ppt in 2020, which is more than a doubling compared to the early part of the century. The rate of increase slowed after 2016 but remained substantial. Regional CH_2Cl_2 emissions from Asia most likely account for most of this increase and more than offset a small decrease in European and North American emissions.
- **Brominated VSLSs contribute 5 ± 2 ppt to stratospheric bromine; this constitutes about 27% of total stratospheric bromine in 2020.** The main sources for brominated VSLSs are natural, and no long-term change is observed. Due to the decline in the abundance of controlled bromine compounds, the relative contribution of VSLSs to total stratospheric bromine increased by about 1% since 2016.
- **New evidence suggests that natural iodinated VSLSs contribute 0.3–0.9 ppt iodine to the stratosphere.** A rapid shift in the partitioning between gas-phase and particulate iodine has been detected in the upper troposphere. This mechanism can enable iodine entrainment into the stratosphere in particulate form in addition to the entrainment in gas form. No observational trend estimates exist.

Stratospheric chlorine and bromine

In the stratosphere, chlorine and bromine can be released from organic source gases to form inorganic species, which participate in ozone depletion. In addition to estimates of the stratospheric input derived from the tropospheric observations, measurements of inorganic halogen loading in the stratosphere are used to determine trends of stratospheric chlorine and bromine.

- **The total chlorine input to the stratosphere for 2020 was 3240 ppt, which is 11.5% below the 1993 peak value, equivalent to a decline of 420 ± 20 ppt.** This long-term decrease was largely driven by decreasing abundances of CH_3CCl_3 and CFCs. The chlorine input for 2020 is derived from measurements of long-lived ODSs at the surface and estimates of stratospheric entrainment of VSLSs.
- **Hydrogen chloride (HCl) is the major reservoir of inorganic chlorine (Cl_y). Middle-stratosphere profile and total column measurements of HCl show a long-term decrease for the period 1997–2020 of around 0.5 ± 0.2% yr^{-1}.** If the evaluations are constrained to the shorter period 2005–2020 the satellite records show a rate of decrease of around 0.3 ± 0.2% yr^{-1}. This latter rate of decline in stratospheric HCl for the more recent period is in good agreement with expectations from the decline in tropospheric chlorine, which slowed after 2000.
- **Total bromine input to the stratosphere of 18.9 ppt is derived for 2020 by combining 13.9 ppt from long-lived gases and 5 ppt from VSLSs not controlled under the Montreal Protocol.** The total input declined by 14.5% between 1999 peak values and 2020. Anthropogenic emissions of all brominated long-lived gases are controlled, but as CH_3Br also has natural sources, more than 50% of the bromine reaching the stratosphere is now estimated to be from sources not controlled under the Montreal Protocol.
- **Total stratospheric bromine, derived from observations of bromine monoxide (BrO), has decreased at a rate of about 0.8% yr^{-1} since 2003.** This decline is consistent with the decrease in total tropospheric organic bromine, based on measurements of CH_3Br and the halons. There is no indication of a long-term change in natural sources of stratospheric bromine.

Equivalent Effective Stratospheric Chlorine (EESC)

EESC is the chlorine-equivalent sum of chlorine and bromine derived from ODS tropospheric abundances, weighted to reflect their expected depletion of stratospheric ozone. The growth and decline in EESC depend on a given tropospheric abundance propagating to the stratosphere with varying time lags (on the order of years) associated with transport to different regions of the stratosphere. Therefore, the EESC abundance, its peak timing, and its rate of decline are different in different regions of the stratosphere.

- **By 2020, EESC had declined from peak values by about 11% for polar winter conditions and by about 15% for mid-latitude conditions.** This drop to 1607 ppt is 37% of the decrease required for EESC in mid-latitudes to return to the 1980 benchmark level. In polar regions, the drop to 3710 ppt is about 23% of the decrease required to return to the 1980 benchmark level. However, regional estimates have indicated that EESC might be higher in some parts of the stratosphere, with an additional 200–300 ppt predominantly originating from CH_3Cl and CH_3Br. Contributions from the ozone-depleting VSLSs and nitrous oxide (N_2O) are currently not included in EESC calculations.

Tropospheric and Stratospheric Fluorine (F)

While fluorine has no direct impact on stratospheric ozone, many fluorinated gases are strong greenhouse gases, and their emissions are often related to the replacement of chlorinated substances controlled under the Montreal Protocol. For this reason, trends in fluorine are also assessed in this report.

- **The main sources of fluorine in the troposphere and in the stratosphere are CFCs, HCFCs, and HFCs (hydrofluorocarbons). In contrast to total chlorine, total fluorine in the troposphere continued to increase between 2016 and 2020, at a rate of 1.71% yr^{-1}.** This increase shows the decoupling of the temporal trends in fluorine and chlorine due to the increasing emissions of HFCs (see Chapter 2). The ODS contribution to the fluorine budget has started to decline, so that the fluorine trend due to ODSs alone became negative after 2016. In contrast, the fluorine trend due to HFCs has constantly increased, causing the total fluorine trend to increase as well. The Northern Hemisphere stratospheric abundance

of inorganic fluorine has continued to increase at a rate of about 0.8% yr^{-1} since 2004.

Effect of ODSs on climate

- **The total direct radiative forcing of CFCs continues to be distinctly higher than that of HCFCs, with CFCs contributing around 68% of the total forcing from ODSs.** Radiative forcing from CFCs has dropped by 0.007 W m^{-2} since 2016 to about 0.257 W m^{-2} in 2020, while radiative forcing from HCFCs increased from 0.062 W m^{-2} to 0.064 W m^{-2} from 2016 to 2020. The total direct radiative forcing due to CFCs, HCFCs, halons, CCl_4, and CH_3CCl_3 was 0.337 W m^{-2} in 2020 (approximately 16% that of CO_2).
- **CO_2-equivalent emissions of CFCs and HCFCs were again approximately equal in 2020.** Based on 100-year time horizon global warming potentials (GWPs), the CO_2-equivalent emissions (in Gt CO_2-eq yr^{-1}) in 2020 were, for species where estimates are available, 0.7 ± 0.4 for CFCs, 0.7 ± 0.1 for HCFCs, 0.09 ± 0.03 for CCl_4 and CH_3CCl_3 combined, and 0.02 ± 0.01 for halons. The CO_2-equivalent emissions from the sum of CFCs, HCFCs, halons, CCl_4, and CH_3CCl_3 remained similar to the value reported in the last Assessment at approximately 1.5 Gt CO_2-eq in 2020.

Other gases that affect ozone and climate

- **Mole fractions of many other gases that affect both ozone and climate (including the three major greenhouse gases CH_4, N_2O, and CO_2) have changed since the last Assessment.** The atmospheric abundance of methane (CH_4) has continued to increase following a period of stagnation in the early 2000s. The drivers of the changing trend are likely largely anthropogenic.
- **Mole fractions of N_2O, which is an ODS, continue to grow in the atmosphere, with growth rates exceeding some of the highest projections.** When expressed as a CFC-11-equivalent, anthropogenic N_2O emissions in 2020 were equal to more than two times the ODP-weighted emissions from all CFCs in that year. When compared to the CFC emission peak from 1987, those 2020 anthropogenic N_2O emissions were equal to more than 20% of the ODP-weighted emissions from CFCs in that year. Almost half of the N_2O emissions in recent years are anthropogenic in origin.
- **The global mole fractions of many non-ODS, non-HFC, highly fluorinated substances have continued to grow** (e.g., sulfur hexafluoride [SF_6], carbon tetrafluoride [CF_4], hexafluoroethane [C_2F_6], sulfuryl fluoride [SO_2F_2], and nitrogen trifluoride [NF_3]). These species contributed 0.014 W m^{-2} to anthropogenic radiative forcing in 2020. In contrast, the abundance of the sulfur-containing compound sulfur dioxide (SO_2) has not changed substantially, while carbonyl sulfide (COS) has shown a small negative trend.
- **Molecular hydrogen (H_2) is included in the Assessment for the first time, due to its potential future effects on stratospheric ozone. The decarbonization of the fossil fuel industry could lead to drastically increasing atmospheric mole fractions of H_2. The resulting future effects on ozone are currently not well understood but are expected to be small.** Atmospheric abundances of H_2 have increased from ~330 ppb during the mid-to-late 1800s to the present levels of 530–550 ppb in the late 20th and early 21st centuries.

Chapter 2:
Hydrofluorocarbons (HFCs)

Hydrofluorocarbons (HFCs) have been increasingly produced and used in applications such as refrigeration, air-conditioning, and foam blowing following the phasedown of ozone-depleting substances (ODSs). In addition to emissions resulting from these uses, some HFCs, particularly HFC-23, are released as by-products during the manufacture of other compounds. While being benign for the stratospheric ozone layer and generally having lower radiative efficiencies than the most abundant ODSs, long-lived HFCs are potent greenhouse gases. Therefore, HFCs were included in the basket of substances controlled by the 1997 Kyoto Protocol under the United Nations Framework Convention on Climate Change (UNFCCC). Subsequently, certain HFCs were brought into the Montreal Protocol framework by the Kigali Amendment in 2016. The Kigali Amendment, which came into force in January 2019 for parties who ratified the Amendment, seeks to limit the production and consumption of a selection of HFCs. For HFC-23, the Kigali Amendment seeks to limit emissions formed as a by-product of HCFC (hydrochlorofluorocarbon) and HFC production to the extent practicable using approved technologies.

For all the most abundant HFCs (HFC-134a, HFC-23, HFC-32, HFC-125, and HFC-143a) and some of the more minor HFCs, atmospheric observations have been available for several years or decades. Observations in the remote atmosphere can be used to derive "top-down" global emissions. These emissions can be compared to the sum of "bottom-up" estimates derived from accounting methods for Annex I parties to the UNFCCC, who are required to report their emissions annually. For some parts of the

world, atmospheric observations exist in sufficient density to derive top-down emissions estimates at regional scales. These can be compared to bottom-up estimates reported by the countries in these regions.

Based on the historical emissions trends derived from atmospheric data and estimates of future consumption, projections of future emissions can be derived under different policy scenarios. These emissions scenarios can be used to estimate the climate impact of various HFC policies in terms of future radiative forcing and temperature change.

The key findings of this chapter are as follows:

- **Global mean abundances of each of the major HFCs have increased since 2016.** Radiative forcing due to the HFCs reached 44.1 ± 0.6 mW m^{-2} in 2020, an increase of around one-third since 2016. HFC-134a remained the largest contributor to the overall radiative forcing due to HFCs (44%), and HFC-125 (18%) overtook HFC-23 (15%) as the second-largest contributor.
- **Total CO_2-equivalent HFC emissions inferred from observations increased through 2020.** The total carbon dioxide-equivalent emissions (CO_2-eq, calculated using 100-year global warming potentials, GWPs) due to HFCs was 1.22 ± 0.05 Pg CO_2-eq yr^{-1} in 2020 (1 Pg = 1 Gt), 19% higher than in 2016. Of this total, HFC-134a was responsible for approximately 30%, HFC-125 for 28%, HFC-23 for 20%, and HFC-143a for 15%. Emissions of the majority of the most abundant HFCs grew between 2016 and 2020, except for HFC-143a, HFC-152a, HFC-365mfc, and HFC-43-10mee, for which emissions remained roughly constant. In 2020, global total CO_2-eq emissions due to HFCs were 60–70% higher than those of CFCs (chlorofluorocarbons) or HCFCs.
- **The gap between total CO_2-eq HFC emissions reported by Annex I countries to the UNFCCC and global estimates derived from atmospheric data has grown.** The emissions reported by Annex I countries in common reporting format (CRF) are approximately constant in the period 2015–2019, while atmospheric observations in the background atmosphere suggest continued growth in global total emissions. In 2019, UNFCCC reports accounted for only 31% (including HFC-23 in the analysis) or 37% (excluding HFC-23) of the global total CO_2-eq emissions derived from observations. Regional top-down emissions estimates for Europe, the USA, and Australia are similar to reported bottom-up emissions, suggesting that underreporting by these Annex I countries likely does not explain this discrepancy. Inverse modeling studies have been carried out for China and India (both non-Annex I countries) and find that around one-third of the emissions gap (excluding HFC-23) could be explained by sources in these countries. However, approximately 40% of global total HFC CO_2-eq emissions (excluding HFC-23) remain unaccounted for by Annex I reports or top-down estimates for non-Annex I parties. Top-down regional emissions estimates are available from only a relatively small number of countries based on the existing measurement network, whereas global top-down estimates reflect the aggregate of all emissions (for longer-lived HFCs). Therefore, the unattributed emissions probably occur in countries that are not monitored by atmospheric measurements and/or that do not report to the UNFCCC in CRF.
- **The global inferred CO_2-eq HFC emissions are less than the emissions in the 2018 Assessment HFC baseline scenario. They are about 20% lower for 2017–2019.** It is too early to link this directly to the provisions of the Kigali Amendment, since the first step in the scheduled phasedown was in 2019. The lower emissions can be explained by lower reported consumption in several countries following national regulations.
- **The ratio of global HFC-23 emissions inferred from atmospheric observations to reported HCFC-22 production has increased between 2010 and 2019, despite reports of substantial new emissions abatement since 2015.** Top-down estimates of global HFC-23 emissions were 17.2 ± 0.8 Gg yr^{-1} in 2019 (1 Gg = 1 kt). This is substantially larger than a bottom-up estimate of 2.2 Gg yr^{-1} derived from UNFCCC reports for Annex I countries (1.6 Gg yr^{-1}), HCFC-22 production reported to the United Nations Environment Programme (UNEP), and national abatement programs in India and China. The contribution to the global atmospheric HFC-23 budget of photolysis of trifluoroacetaldehyde (CF_3CHO), a minor degradation product of some fluorinated compounds, is assessed to be negligible.
- **Some HFCs and unsaturated HFCs (hydrofluoroolefins [HFOs]) degrade in the environment to produce trifluoroacetic acid (TFA), a persistent toxic chemical.** HFO-1234yf has been increasingly used to replace HFC-134a as a mobile air conditioner (MAC) refrigerant. Measurements show that atmospheric background abundances of HFO-1234yf at Jungfraujoch, Switzerland have grown from less than 0.01 ppt before 2016 to annual median levels of 0.10 ppt in 2020. At the 2020 level, the oxidation of HFO-1234yf is likely producing a comparable, or potentially larger, amount of TFA than the oxidation of HFC-134a locally near Jungfraujoch. The measured and model simulated concentrations of TFA from the use of HFO-1234yf and other relevant HFOs, HFCs, HCFCs, and hydrochlorofluoroolefins (HCFOs) is, in general, significantly below known toxicity limits at present. However, the production of TFA in the atmosphere is expected to increase due to increased use of HFOs and HCFOs. Potential environmental impacts of TFA require future evaluation due to its persistence.
- **Projected emissions of HFCs based on current trends in consumption and emissions, national policies in several countries, and the Kigali Amendment are lower than those projected in the 2018 Assessment.** The 2020–2050 cumulative emissions in the 2022 updated Kigali Amendment scenario are 14–18 Pg CO_2-eq lower than the corresponding scenario in the previous Assessment. The 2050 radiative forcing in a scenario that assumes no controls on HFCs, is 220–250 mW m^{-2} (termed the Baseline scenario in the previous Assessment). Radiative forcing in 2050 is reduced to 90–100 mW m^{-2} in the 2022 Kigali Amendment scenario, 30 mW m^{-2} lower than projected in the 2018 Kigali Amendment scenario. The new scenario follows national controls on the consumption and production of HFCs in non-Article 5 countries, reflects lower reported consumption in China, is based on updated historical information on the use of HFCs in non-Article 5 countries, uses observed mixing ratios through 2020 as a constraint, and includes assumptions about reduced use of HFCs for commercial and industrial refrigeration. The new

scenario also assumes that all countries adhere to the provisions of the Kigali Amendment.

- **Under the provisions of the Kigali Amendment, current trends in consumption and emissions, and national policies, the contribution of HFCs to global annual average surface warming is projected to be 0.04 °C in 2100.** This is substantially lower than under the scenario without HFC control measures, for which a contribution of 0.3–0.5 °C was projected.
- **Concerted efforts to improve energy efficiency of refrigeration and air-conditioning equipment could lead to reductions in greenhouse gas emissions of the same order as those from global implementation of the Kigali Amendment.** These estimated benefits of improving energy efficiency are highly dependent on greenhouse gas emissions from local electric grids and the pace of decarbonization in the energy sector.

Chapter 3:
Update on Global Ozone: Past, Present, and Future

This chapter presents our current understanding of global ozone outside of the polar regions. The increase of ozone-depleting substance (ODS) concentrations caused the large ozone decline observed from the early satellite era (circa 1980) to the mid-1990s. Since the late 1990s, concentrations of ODSs have been declining due to the successful implementation of the Montreal Protocol and its Amendments and adjustments. Since the last Assessment, the longer observational records show a small increase in near-global total column ozone (TCO) with reduced uncertainty, but this trend is not yet statistically significant. A small increase in TCO is seen in the Southern Hemisphere (SH) mid-latitudes but not yet in the Northern Hemisphere (NH) mid-latitudes or tropics. Different processes operating at different altitudes complicate the attribution of the overall total column trend. However, a significant increase in upper-stratospheric ozone noted in the previous Assessment continues, driven by declines in ozone-depleting substances and increases in greenhouse gases (GHGs). Model simulations support our overall understanding of these trends.

Over this century, we expect an increase in global stratospheric ozone as the concentrations of ODSs decline. The future evolution for different latitudes and vertical levels depends on the future concentrations of GHGs and precursors of tropospheric ozone. These other influences may lead to TCO levels that remain below 1980 values in some regions, even after concentrations of ODSs have declined to pre-1980 levels.

Changes to date in total column ozone

- **Aggregated ground- and space-based observations indicate an increase of 0.3% decade^{-1} (with a 2-sigma uncertainty of at least ±0.3% decade^{-1}) in near-global (60°S–60°N) TCO over the 1996–2020 period.** This trend is consistent with model simulations and our scientific understanding of the processes controlling ozone.
- Over the same 1996–2020 period, the TCO trends in broad latitude bands are as follows:
  - SH mid-latitude (60–35°S) TCO has increased (0.8 ± 0.7% decade^{-1}).
  - NH mid-latitude (35–60°N) TCO trends are negligible (0.0 ± 0.7% decade^{-1}).
  - Tropical (20°S–20°N) TCO shows no clear trend (0.2 ± 0.3% decade^{-1}), likely because stratospheric ozone is decreasing while tropospheric ozone is increasing, both unrelated to changes in ODSs.

  The latitudinal pattern of these TCO trends is largely consistent with our scientific understanding and is reproduced in the latest set of chemistry-climate models (CCMs).
- Present-day (2017–2020) TCO as measured from space-based and ground-based observations remains lower than the 1964–1980 average by
  - about 2% for the near-global average (60°S–60°N),
  - about 4% in the NH mid-latitudes (35–60°N),
  - about 5% in the SH mid-latitudes (35–60°S), and
  - about 1% in the tropics (20°S–20°N).

  Within uncertainties associated with natural variability and instrumental accuracy, these values are essentially the same as given in the previous Assessment for the 2014–2017 average.

Changes to date in vertically resolved ozone

Vertically resolved trends are very similar to those given in the last Assessment. However, with longer records and updated merged datasets, recovery trends are now statistically significant in more locations.

- **Measurements show unambiguous increases in upper-stratospheric ozone for 2000–2020.** Positive trends have a range of ~1.5–2.2% decade^{-1} at mid-latitudes in both the Northern and Southern Hemispheres and ~1–1.5% decade^{-1} in the tropics.

- **Upper stratospheric ozone increases are due to a combination of decreases in ODSs and decreases in stratospheric temperature driven by increases in carbon dioxide (CO_2).** New CCM simulations affirm this finding from the last Assessment.
- **There are multiple lines of evidence from both observations and models for a small though uncertain decrease (1–2% decade^{-1}, with uncertainty up to ±5% decade^{-1}) in tropical lower stratospheric ozone over 2000–2020.** This decrease is consistent with climate change-driven acceleration of the large-scale circulation and has a small impact on TCO. Chemical ozone loss from chlorine and bromine is comparatively minor in the tropical lower stratosphere.
- **Observations suggest small decreases in lower stratospheric ozone in the mid-latitudes of both hemispheres for 2000–2020, while chemistry-climate model simulations suggest small increases.** Ozone in mid-latitudes has large year-to-year variability; thus, trends have large uncertainties, and they are not robust across all datasets and models. The observed decrease is more evident in the Northern Hemisphere.
- **Attribution of TCO trends during the period of slow ODS decline requires knowledge of changes in ozone in both the troposphere and stratosphere.** For instance, there is evidence that the lack of a change in TCO in the tropics reflects an increase in tropospheric ozone that compensates for the ozone decrease in the tropical lower stratosphere. This decrease, due to a climate change-driven acceleration of the large-scale circulation, is expected based on modeling studies. Depletion due to ODSs, on the other hand, is very minor in the tropical lower stratosphere. Nevertheless, analyses of these changes using different observational datasets indicate significant remaining uncertainty.

Future ozone changes

Projections of future stratospheric ozone are available from new model simulations that follow new emissions scenarios: the shared socioeconomic pathways (SSPs). These scenarios all assume compliance with the Montreal Protocol and its Amendments and adjustments for ODSs but span a wider range in future GHG and pollutant emissions pathways than the scenarios used in the previous Assessment, although there are fewer models from which to draw results. As in the last Assessment, the key drivers of future stratospheric ozone levels continue to be declining ODS concentrations coupled with CO_2-driven cooling in the upper stratosphere and a strengthening of the Brewer-Dobson circulation. TCO will also be affected by changes in the tropospheric ozone burden.

- **New estimates for the year of return of near-global TCO to its 1980 value are broadly consistent with the last Assessment. Also similar to the last Assessment, these modeled return dates vary considerably depending on the assumed future scenario.** TCO returns to its 1980 value sooner for scenarios that assume larger emissions of GHGs than scenarios with smaller GHG emissions. The return dates for a middle-of-the-road (SSP2-4.5) scenario are:
  - around 2040 for near global mean (60°S–60°N) annually averaged column ozone;
  - around 2045 for SH (60–35°S) annually averaged column ozone; and
  - around 2035 for NH (35–60°N) annually averaged column ozone.
- **For scenarios that assume strong reductions in the emission of tropospheric ozone precursors, the resulting reductions in tropospheric ozone can be important for TCO trends.** Under such scenarios, TCO in the tropics is projected to remain below the 1980 values until at least 2100. As discussed in the last Assessment, tropical TCO under high GHG scenarios will be below 1980 values at 2100 due to circulation-driven changes affecting lower stratospheric ozone.
- **Future ozone recovery and the expected strengthening of the Brewer–Dobson circulation will most likely increase the proportion of ozone of stratospheric origin in the troposphere.** A new analysis has quantified the contribution of stratosphere-to-troposphere transport of ozone in models under scenarios with limited GHG mitigation (RCP6.0 and RCP8.5). While stratosphere-to-troposphere transport remains highly variable between models and is strongly scenario-dependent, the projected increase is robust, suggesting increases of stratospheric ozone in the troposphere of 10–50% over the 21st century, depending on the model and scenario. Nonetheless, in situ chemistry involving air pollutants remains the largest production term for the simulated tropospheric ozone budget.
- The unreported production of CFC-11 over 2012–2019 (see Chapter 1) is estimated to delay global TCO recovery to 1980 levels by ~1 year.

Emerging Issues

- **Exceptional events can temporarily perturb chemical and dynamical processes that affect stratospheric ozone amounts.** Since the last Assessment, these include the 2019/2020 wildfires in Australia, the eruption of the Hunga Tonga-Hunga Ha'apai volcano, and disruptions to the quasi-biennial oscillation of the tropical winds. In particular, intense wildfires have become more frequent. Their potential impacts on the stratosphere are not yet well quantified and are a subject of active research.
- **The impending loss of vertically resolved, global space-borne measurements of ozone-related atmospheric constituents (e.g., reactive chlorine, water vapor, and long-lived transport tracers) will impede the ability to monitor and explain changes in the stratospheric ozone layer in the future.**

Chapter 4:
Polar Stratospheric Ozone: Past, Present, and Future

The chemical and dynamical processes controlling polar ozone are well understood. Polar ozone depletion is fundamentally driven by anthropogenic chlorine and bromine, with the severity of the chemical loss each year in both polar regions strongly modulated by meteorological conditions (temperatures and winds) and, to a lesser extent, by the stratospheric aerosol loading and the solar cycle. As noted in previous Assessments, the stratospheric halogen concentration resulting from the emissions of ozone-depleting substances (ODSs) reached its peak in the polar regions around the turn of the century and has been gradually declining since then in response to actions taken under the Montreal Protocol and its Amendments and adjustments. The 2018 Assessment reported for the first time that signs of the onset of ozone recovery from the effects of ODSs had been detected over the Antarctic. More varied and more robust signs of the onset of recovery are now beginning to emerge; as the observational record lengthens, ozone hole recovery trends are expected to continue to become clearer against the background of natural variability. Nevertheless, the Antarctic ozone hole will continue to be a recurring phenomenon until the middle of the century, although with a decreasing average size and some interannual variability. The Arctic is more dynamically variable, precluding identification of a significant increase in Arctic ozone. Cold conditions conducive to substantial stratospheric ozone loss occur in some Arctic winter/spring seasons and are expected to continue to do so, interspersed with warmer years with little or no ozone depletion. Chemistry–climate model (CCM) projections largely confirm previous studies that, in both hemispheres, springtime polar total column ozone (TCO) will return to 1980 historical levels around the middle of this century. For the Antarctic, the timing of this return depends mainly on the declining stratospheric halogen concentrations from decreasing ODS emissions, and the impact of climate change is small. In the Arctic, TCO is expected to return to 1980 levels earlier than in the Antarctic. This is because in the Arctic, springtime stratospheric ozone has a stronger dependence on the future greenhouse gas (GHG) emissions scenarios.

Observed changes in polar ozone

- **The Antarctic ozone hole continued to appear each spring during the 2018–2021 period.** The occurrence and character of recent ozone holes are consistent with the current concentrations of ODSs and their small overall downward trend.
- **Recent Antarctic ozone holes exhibited substantial interannual variability in size, strength, and longevity: the 2019 ozone hole was the smallest since 2002, whereas 2020 saw a deep ozone hole of record duration.** In 2019, a strong minor sudden stratospheric warming disrupted the evolution of the ozone hole, leading to the early termination of chemical ozone depletion and relatively high TCO. In contrast, in 2020 and 2021, weak atmospheric wave activity resulted in exceptionally persistent polar vortices. Despite decreasing ODS concentrations, the unusual dynamical state of the stratosphere in 2020 and 2021 induced large and long-lasting late spring ozone holes.
- **Recovery of Antarctic stratospheric ozone continues to progress.** New results since the 2018 Assessment support the findings reported at that time that the Antarctic ozone hole has diminished in size and depth since the year 2000. The remarkable Antarctic ozone holes in 2019, 2020, and 2021 do not challenge the findings of the emergence of recovery.
- **Arctic total ozone reached exceptionally low values in spring 2020.** A very stable, cold, and long-lived stratospheric polar vortex enabled halogen-catalyzed chemical ozone loss exceeding that observed during the previous record-breaking spring of 2011. The strong vortex also inhibited dynamical replenishment of ozone. The evolution of high-latitude ozone in 2020 is successfully reproduced by model simulations, further substantiating our understanding of polar ozone chemistry.
- **No statistically significant signature of recovery in Arctic stratospheric ozone over the 2000–2021 period has yet been detected.** Observed Arctic ozone trends remain small compared to the year-to-year dynamical variability.

Understanding of factors controlling polar ozone

- **An updated vortex-wide climatology of polar stratospheric cloud (PSC) occurrence and composition based on satellite data enabled advances in the understanding of particle formation mechanisms and trends.** Evidence that heterogeneous nucleation on preexisting ice particles or foreign nuclei, such as meteoritic particles, is the typical formation process for the nitric acid trihydrate (NAT) particles that lead to denitrification has been strengthened. PSC occurrence in the Arctic early winter significantly increased between the 1980s (1978–1989) and the recent past (2006–2018), while in the Antarctic, PSC occurrence was very similar in the two periods.
- **The broad range of polar springtime TCO in recent years in both hemispheres is largely explained by differences in the magnitude of the dynamical forcing.** Both the weak Antarctic ozone hole in 2019 and the record-low Arctic ozone in spring 2020 resulted from atypical dynamical conditions in the respective winters. Although exceptional, the evolution of polar ozone in both years was in line with current understanding of the chemical and dynamical factors controlling its abundance.
- **September, and especially the first half of that month, is the period when the impact of ODSs on stratospheric ozone over Antarctica can be quantified with the**

greatest certainty, and thus it represents the most suitable time window for monitoring ozone recovery. Until recently, most studies of Antarctic ozone depletion trends focused on longer time windows or later ones that included the months of October and November. New analyses indicate that September ozone has the largest sensitivity to decreasing ODSs, and September observations show the strongest and the statistically most significant Antarctic ozone recovery rates.

- **Model simulations with historical emissions scenarios indicate that decreasing atmospheric amounts of ODSs can explain the observed increase in Antarctic springtime ozone over the last two decades.** Model simulations indicate that if ODS concentrations had remained at the peak values attained in the late 1990s, recent polar springtime ozone loss in both hemispheres would have been ~20 DU (~10%) larger than currently observed. Model simulations of unabated ODS emissions (i.e., allowing for a 3–3.5% yr^{-1} increase in emissions since the mid-1980s) indicate that conditions similar to those currently observed over Antarctica would have occurred in the Arctic in years with unusually stable and long-lived stratospheric vortices, such as 2011 and 2020.
- **Future commercial supersonic or hypersonic aircraft fleets would cause stratospheric ozone depletion.** Both types of aircraft would potentially release substantial amounts of water vapor and nitrogen oxides (NO_x) into the stratosphere, with concomitant strong effects on stratospheric ozone arising primarily through enhancement of NO_x catalytic ozone destruction at cruise altitudes. This could reduce total column ozone by as much as 10%, depending on aircraft type and injection altitude, and would be most pronounced in the Northern Hemisphere polar region in spring and fall.

Future evolution of polar ozone

- **The Antarctic ozone hole is expected to gradually close. September multi-model mean (MMM) TCO from updated CCM projections, based on full compliance with the Montreal Protocol and assuming the baseline estimate of the future evolution of GHGs (SSP2-4.5), returns to 1980 values shortly after mid-century (about 2066, with a range between 2049 and 2077 arising from the spread in modeled dynamical variability).** The October TCO MMM returns two years earlier, with a similar uncertainty range.
- **The timing of the recovery of the ozone hole may be affected by anthropogenic climate change, with the MMM from updated CCM projections recovering approximately 15 years earlier for both SSP3-7.0 and SSP5-8.5 GHG scenarios.** This sensitivity of Antarctic return date to different climate change scenarios was not evident in projections presented in previous Assessments. The small set of CMIP6 models included in this Assessment makes interpretation of this scenario sensitivity difficult.
- **Arctic springtime total ozone is expected to return to 1980 values near mid-century (about 2045, with a range between 2029 and 2051), based on full compliance with the Montreal Protocol and assuming the baseline estimate of the future evolution of GHGs (SSP2-4.5).** This return date is around a decade later than projected by simulations in the previous Assessment using a different set of models and scenarios, but with considerable overlap of the large range. The timing of the recovery of Arctic TCO in spring will be affected by anthropogenic climate change. Consistent with previous Assessments, the new model simulations confirm that in the Arctic, dynamical changes induced by enhanced GHG concentrations cause an earlier return of TCO to historical values than do reductions in ODSs alone.
- **Future ozone depletion will be substantial in the Arctic during cold winters/springs as long as ODS concentrations are well above natural levels.** The projected strong increase in GHGs will cause cooling in the stratosphere. This effect, coupled with increases in stratospheric humidity from GHG warming of the tropical tropopause and increases in future tropospheric CH_4 emissions, will increase the potential for formation of PSCs in Arctic winter, leading to ozone loss.
- **Noncompliant production (e.g., of CFC-11) could delay the recovery of ozone to 1980 values by several years by slowing the rate of decline of stratospheric chlorine.** The magnitude of the delay depends on the total additional emissions. Additional emissions of 120–440 Gg of CFC-11 over the period 2012–2019 are estimated to delay the return to 1980 levels for Antarctic column ozone by 0.5–3.1 years. Emissions of uncontrolled very short-lived substances (VSLSs; e.g., chloroform [$CHCl_3$], dichloromethane [CH_2Cl_2]) could also extend the timeframe for polar ozone recovery by the same mechanism, with the impact dependent on the amount of chlorine delivered to the stratosphere. The future magnitudes of emissions from noncompliant production and anthropogenic VSLSs are highly uncertain.

Chapter 5:
Stratospheric Ozone Changes and Climate

Since the last Assessment, new research has continued to quantify, attribute and improve the understanding of long-term changes in stratospheric climate. New studies are assessed that quantify the effects of ozone-depleting substances and ozone changes on the climate system, including atmospheric temperatures and circulation, the ocean and the cryosphere. The new results support the main conclusions from the previous Assessment.

Changes in stratospheric climate

- **Stratospheric Temperature: The global middle and upper stratosphere continues to cool at a rate of ~–0.6 K decade^{-1} because of growing levels of well-mixed greenhouse gases (GHGs; primarily carbon dioxide [CO_2]) and evolving stratospheric ozone in response to changing ozone-depleting substances (ODSs).** Lower-stratospheric temperatures have been near constant since the late 1990s. The overall evolution is consistent with the well-understood effects of ozone, ODSs, GHGs, stratospheric aerosols, and solar variability. This is in agreement with previous Assessments.
- **Stratospheric Water Vapor: Since the last Assessment, the understanding of processes that influence water vapor entry into the stratosphere has strengthened.** Interannual variations in lower-stratospheric water vapor are quantitatively consistent with observed tropical tropopause temperatures, with small contributions from monsoon circulations and overshooting convection. Models predict small multi-decadal increases in tropopause temperature and lower-stratospheric water vapor as a response to GHG increases, but these changes are still not evident within the variability of the observational records.
- **Brewer-Dobson Circulation[6] (BDC):**
  - **The BDC in the lower stratosphere has accelerated in recent decades and is predicted to continue to accelerate in the future given continued increases in GHG abundances.** This result is confirmed by models, observations, and reanalyses. New studies since the last Assessment confirm the attribution of the BDC acceleration by models to increases in GHGs and ODS-induced ozone depletion over the last decades of the 20th century. Model simulations indicate that the decline of ODSs and subsequent recovery of ozone should have acted to reduce the rate of BDC acceleration after the year 2000, but there is not yet sufficient analysis to determine whether this change has been detectable outside of the natural variability in the BDC.
  - **Estimates of past BDC trends in the middle and upper stratosphere based on observations continue to be opposite in sign from modeled trends.** However, new observationally based estimates since the last Assessment bring observed trends closer to modeled trends.
- **Polar Vortex Trends and Variability: Recent extreme polar vortex events in both hemispheres caused strong variations of polar ozone. However, currently there is no evidence for a systematic trend toward more frequent polar vortex disruptions in either hemisphere.**
  - Two sudden stratospheric warming (SSW)[7] events have been observed in the Southern Hemisphere (SH) since the start of comprehensive satellite records in 1979. New model studies show that this is consistent with model simulations, and no change in SSW frequency is necessary to explain this occurrence rate. The delay of the austral polar vortex breakup date, which in the past was driven by ozone depletion, is not expected to fully reverse by the end of the 21st century, due to the opposing effect of GHG increases under moderate and high emission scenarios.
  - In the Northern Hemisphere (NH), new studies confirm that changes in SSW frequency and in polar vortex strength are not robustly detected in the historical record, and future changes are not robust across models.
- **Quasi-Biennial Oscillation (QBO)[8]: Since the last Assessment, there is more confidence that the amplitude of the QBO will weaken in the future as a result of acceleration of the BDC**, but there is still large uncertainty about any change in its periodicity and the associated ozone variability.
  - New model studies infer that further disruptions of the QBO, such as occurred in 2016 and 2019, might become more likely as a result of increasing GHGs.

Ozone and ODS effects on climate

- **Ozone and ODS Radiative Forcing (RF): New estimates confirm previous Assessments in that the RF from ODSs, including the indirect effect on ozone abundances, has been positive over the second half of the 20th century, contributing to anthropogenic GHG forcing.** The newest best estimate of stratosphere-adjusted RF over the period 1850–2011 from stratospheric ozone changes is –0.02 W m^{-2}, with an uncertainty of ± 0.13 W m^{-2}. The range in this RF remains smaller than the RF from ODSs (0.337 W m^{-2}). However, new studies reveal uncertainties in the estimation of radiative forcing, due to 1) rapid adjustments arising from tropospheric circulation changes and 2) uncertainties in modeled ozone

[6] The global zonal mean circulation that transports mass, heat, and tracers in the stratosphere.

[7] Based on an adapted SSW definition in the Southern Hemisphere; see Chapter 5, Section 5.2.6.1.

[8] Quasi-periodic (period ~28 months) oscillation of stratospheric equatorial winds from easterly to westerly.

trends. Since the late 1990s, the RF from ODSs and changes in stratospheric ozone abundances has remained approximately constant as a consequence of the Montreal Protocol.

- **ODS Effects on Climate:** There is new evidence since the last Assessment that suggests that the direct radiative effects of ODSs on climate not only contributed to global warming but also enhanced Arctic amplification[9] in the late 20th century.
- **Role of Stratospheric Ozone in the Climate Response to GHG Forcing:** Evidence suggests that GHG-induced ozone changes act to dampen the GHG-induced surface temperature warming. New estimates since the last Assessment confirm that this climate feedback by stratospheric ozone is negative but smaller than previously estimated. In addition, there is new evidence for an influence of stratospheric ozone on the tropospheric and stratospheric circulation response to GHGs via ozone-circulation coupling.
- **Relevance of Stratospheric Ozone-Circulation Coupling for Trends and Interannual Variability:**
  - Two-way ozone-circulation coupling modulates the effects of ozone depletion and recovery on SH stratospheric circulation trends, as well as stratospheric interannual variability in the tropics and extratropics in both hemispheres.
  - There have been no detectable effects of long-term ODS-driven ozone trends in the Arctic on tropospheric and surface climate. Yet, new evidence shows that for individual years low springtime Arctic ozone can amplify existing stratospheric circulation anomalies and their subsequent influence on tropospheric circulation and surface climate.
- **Signature of Ozone Recovery in the Southern Hemisphere Circulation:**
  - **Antarctic ozone depletion led to pronounced changes in the SH atmospheric circulation, as summarized in the previous Assessments.** New evidence suggests that the recovery of Antarctic ozone is now evident as changes in SH atmospheric circulation trends between the ozone depletion and recovery eras (the eras before and after roughly the year 2000, respectively). The observed changes in circulation trends are significant at stratospheric altitudes but on the fringe of significance in the troposphere; model simulations support the hypothesis that the changes in atmospheric circulation trends are driven by the onset of ozone recovery.
  - Climate simulations suggest that in the future the effects of ozone recovery will compete with the effects of GHG increases on SH tropospheric circulation changes, resulting in a poleward shift of the mid-latitude jet in all seasons under high GHG emissions scenarios but little change or even an equatorward shift of the jet in austral summer under low GHG emissions scenarios.
- **Ozone-Induced Impacts on the SH Ocean and Cryosphere:**
  - **Ocean and Sea Ice**: Observed upper Southern Ocean warming and freshening since the 1950s is driven primarily by increasing GHGs. Stratospheric ozone depletion plays a secondary role in the warming. In agreement with previous Assessments, ozone trends are unlikely to have driven the observed high-latitude sea surface temperature cooling and weak sea ice changes since 1979. Ocean eddies continue to remain a source of uncertainty in the ocean's response to wind changes.
  - **Carbon Uptake**: The Southern Ocean carbon uptake exhibits strong decadal variations. Ozone changes are unlikely to have substantially contributed to the observed net change in Southern Ocean carbon uptake, consistent with the conclusion from the previous Assessment.
  - **Antarctic Ice Sheet**: New modeling evidence suggests that stratospheric ozone depletion could potentially have influenced the surface mass balance of the Antarctic ice sheet by enhancing precipitation over the continent in the latter part of the 20th century. However, the underlying processes whereby stratospheric ozone depletion influences continentwide precipitation are poorly constrained; further, observed Antarctic surface mass balance shows large variability.

Climate impacts of the Montreal Protocol

- New evidence since the last Assessment shows that the decline in ODS emissions due to the implementation of the Montreal Protocol has already had an influence on SH circulation trends due to the stabilization and slow recovery of the Antarctic ozone hole, leading to a change in trends in the austral summer tropospheric circulation.
- Recent modeling studies estimate that the Montreal Protocol has already resulted in the avoidance of 0.17 ± 0.06 K global surface warming and 0.45 ± 0.23 K of Arctic surface warming in 2020, and will likely avoid about 0.5–1 K (0.79 ± 0.24 K) of global surface warming by the mid-21st century compared to a scenario with uncontrolled ODS emissions.
- New evidence since the last Assessment suggests that the Montreal Protocol has also potentially avoided an additional 0.5–1.0 K globally averaged surface warming by the end of the 21st century by protecting the terrestrial carbon sink from ultraviolet (UV) radiation damage, which would cause additional CO_2 to remain in the atmosphere.

[9] Arctic amplification refers to the ratio of Arctic warming (60–90°N) to global warming over a given time period.

Chapter 6:
Stratospheric Aerosol Injection and Its Potential Effect on the Stratospheric Ozone Layer

Since the 2018 Ozone Assessment global warming has continued, having now reached approximately 1.2 °C above preindustrial levels. All climate model scenarios considered by IPCC (2021) indicate continued future warming beyond 1.5 °C above the preindustrial level, a limit that has been proposed to prevent further detrimental impacts. Ambitious mitigation and decarbonization efforts are required to minimize the likely overshoot of temperatures above this limit and to stabilize global surface temperatures in the future. However, with a temperature overshoot, irreversible impacts on the climate system may still occur. Stratospheric aerosol injection (SAI) has been suggested as a potential mechanism for reflecting sunlight back to space, thereby offsetting some of the surface warming. Evidence from explosive volcanic eruptions and various model simulations has shown that increasing stratospheric sulfate aerosols can substantially cool the planet. SAI and other solar radiation modification (SRM) approaches may therefore be the only option to keep the global surface temperature below the limit of 1.5 °C. The amount and duration of SAI required would depend on how fast atmospheric greenhouse gas (GHG) concentrations are lowered through mitigation and decarbonization efforts.

While SAI could reduce some of the impacts of global warming, it cannot restore past climatic conditions and would very likely cause unintended consequences, including changes in stratospheric ozone concentrations. To date, Earth system models (ESMs) have performed simulations to provide information on the climate impacts, benefits, and risks of SAI. Little research has been done to quantify the effects of SAI on the stratospheric composition and total column ozone (TCO) in a multi-model setting, and even fewer studies have examined the effects of aerosol types other than sulfate. While existing studies do not suggest a deepening of the ozone hole beyond that already experienced, current shortcomings in model representation of required processes limit confidence in the results.

This new chapter of the Ozone Assessment assesses the impacts of SAI on stratospheric ozone through SAI-related changes in stratospheric chemistry and transport. The dependence of SAI effects on future climate change scenarios and injection strategies, as well as uncertainties in our current understanding and model shortcomings, are assessed. Side effects and risks beyond the effects on stratospheric ozone are only briefly covered. It is well recognized that any potential future deployment of SAI is fundamentally linked to complex moral, ethical, and governance issues. These aspects are of critical importance but beyond the scope of this chapter, which will focus solely on physical science.

Framing SAI scenarios and strategies

- **Based on the observed cooling after large volcanic eruptions and various model studies, stratospheric aerosol injection (SAI) has the potential to reduce global mean temperatures. However, SAI cannot fully offset the widespread effects of global warming and produces unintended consequences, including effects on ozone. Details of these effects depend on the specifics of the SAI scenario and injection strategies.** SAI uses stratospheric aerosols to reflect sunlight back to space, thereby cooling the planet. A straightforward offsetting of global warming from greenhouse gases (GHGs) cannot be achieved because SAI reduces a fraction of the incoming sunlight, which is seasonally and latitudinally dependent, while GHGs interact with terrestrial radiation and warm the planet more uniformly across latitudes and seasons. In addition, aerosol heating of the lowermost stratosphere by SAI using sulfate would result in further residual impacts, including changes in regional temperatures, precipitation, and stratospheric ozone. Details of the future climate scenario, the SAI scenario (i.e., the degree of SAI cooling applied), and applied SAI strategy (i.e., the specifics of injection location, timing, and material for achieving predefined climate goals) determine the specifics of the resulting impacts and risks.
  - **Changes in future ozone using SAI depend on details of future climate change and the degree of SAI cooling applied. The three different SAI scenarios considered in this report (Figure 6-2, reproduced here) result in significantly different future ozone.** The "peakshaving" scenario (Panel A in Fig. 6-2) assumes delayed and then aggressive mitigation and carbon dioxide removal (CDR). SAI offsets the overshoot of the surface temperature target until greenhouse gases have been sufficiently reduced. The "strong SAI" scenario (Panel B) assumes a limited or no-mitigation high-warming future scenario, requiring continuously increasing SAI to keep surface temperatures from exceeding the climate target (dashed line). The "medium SAI" scenario (Panel C) assumes a limited or no-mitigation high-warming future scenario in which global warming is reduced to that of a moderate mitigation scenario (red line) by the deployment of SAI. A qualitative illustration of the required injection amounts for each scenario is shown in Panel D. The impacts on ozone of many other possible SAI scenarios have not been comprehensively studied to date. These scenarios currently do not include any socioeconomic feedbacks related to SAI.
  - **In model simulations, different injection strategies have been developed to mitigate some of the unintended climate impacts of SAI.** For the same scenario, the specifics of the injection strategy, including location, timing, and material, can be adjusted to better achieve desired global and regional climate targets and minimize regional changes. Some models include a feedback control algorithm to modulate annual stratospheric sulfur injections in order to reach predefined climate temperature

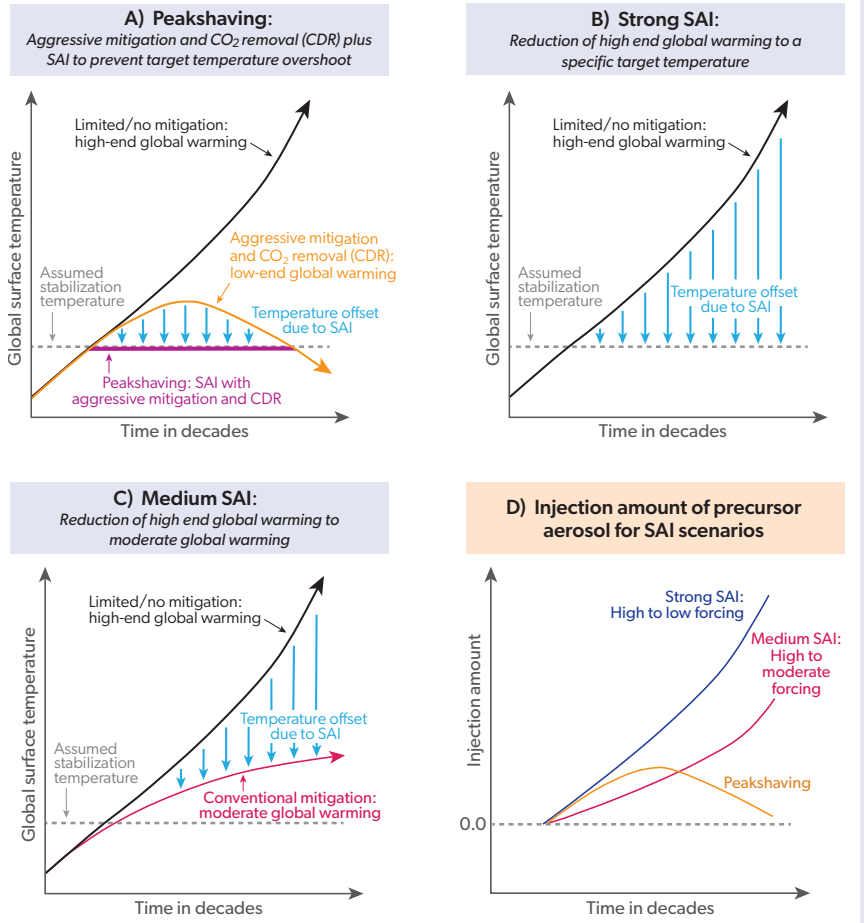

Figure 6-2. Schematic diagram representing the concept of three policy-relevant SAI scenarios: peakshaving scenario, strong SAI scenario, and medium SAI scenario. Different lines illustrate global mean surface temperatures for future scenarios: a limited or no mitigation scenario leading to strong future global warming (black line); a so-called "overshoot scenario" that assumes strong mitigation and Carbon Dioxide Removal (CDR), and leads to a temporary overshoot of global mean temperatures above sustainable limits for some time (orange); a peakshaving scenario that applies temporary SAI to the overshoot scenario in order to prevent the increase in global mean temperature from exceeding these sustainable limits (purple line); and a moderate warming scenario (red). The blue arrows represent the approximate relative magnitude of the temperature impact of the applied SAI. The bottom right panel shows the stratospheric injection that is applied under each of these three scenarios.

goals and other impact-relevant targets. Adjustments of sulfur injection to account for climate feedback help in managing uncertainties and limiting some of the side effects of SAI. Different strategies change the effectiveness of SAI and its effects on stratospheric ozone.

SAI effects on radiation and temperature

- **Multi-model comparisons reveal large uncertainties in forcing and surface cooling per unit of sulfur injected, which are attributed to differences in model complexity in representing key processes and details of SAI strategies.** Using sulfate aerosol, the efficacy of the radiative forcing ranges between −0.04 and −0.1 W m^{-2} per Tg SO_2 yr^{-1}, and the resulting surface cooling ranges from 0.04 to 0.14 °C per Tg SO_2 yr^{-1} based on a multi-model analysis. Continuous annual injection rates vary between 8 and 16 Tg of SO_2 yr^{-1} to cool the Earth by 1 °C; this range is approximately equivalent to the estimated injection amount from Mount Pinatubo in 1991, which resulted in less than 0.5 °C global surface cooling. The significant uncertainties associated with these values are attributed to differences in model representations of stratospheric chemistry, transport, radiation, and aerosol microphysical processes, including differences in model resolution. The choices of SAI injection location, timing, and material influence the resulting stratospheric aerosol mass, optical depth, and surface area density (SAD), which determine both cooling efficacy and impacts on stratospheric ozone.

Mechanisms for SAI impacts on ozone

- **Despite the limited number of model studies, some robust impacts of SAI on ozone have been identified. The combined effects of large-scale, long-term SAI on ozone are driven by 1) an increase in aerosol surface area, 2) stratospheric halogen concentrations, and 3) aerosol-induced heating of the stratosphere, which changes both stratospheric ozone chemistry and stratospheric dynamics.** SAI impacts on total column ozone (TCO) are regionally and seasonally dependent and result in ozone reduction in spring over Antarctica due to the increase in chemical ozone depletion. In contrast, an increase in TCO is possible (with increasing SAI amount) in the tropics, as well as in the winter Northern Hemisphere (NH) in mid- and high latitudes, due to increased tropical chemical ozone production rates and increased poleward transport.
  - **Enhanced stratospheric sulfate aerosol increases stratospheric heterogeneous chemical reaction rates and can enhance or deplete ozone depending on the altitude, latitude, and season.** Net chemical ozone production rates decrease in the lower polar

stratosphere in winter and spring where halogen and hydrogen catalytic cycles are most important but increase in the tropical mid-stratosphere where the nitrogen cycle is most important. The magnitude and sign of ozone changes depend on the details of the SAI aerosol distribution and the current stratospheric halogen and nitrous oxide concentrations, as well as on any changes in stratospheric water vapor due to changes in transport and temperature that occur in response to SAI.

- **Enhanced stratospheric sulfate aerosol also impacts stratospheric temperature, transport, and chemistry, causing a general increase of ozone concentrations in the tropics and mid- to high latitudes through enhanced transport from the tropics to high latitudes.** Increased sulfate aerosols in SAI scenarios heat the lower tropical stratosphere by 4.6 ± 2.7 °C per 1 °C surface cooling, with variation across models and injection strategy. The heating induced by aerosols changes the vertical and horizontal transport in the stratosphere and polar vortex dynamics and leads to an acceleration of the lower branch of Brewer-Dobson Circulation (BDC). The stronger transport of ozone to high latitudes with SAI can overcompensate for the effects of ozone depletion, especially in the Northern Hemisphere winter in the strong SAI scenario. Heating of the tropopause results in increases in stratospheric water vapor. For any given scenario, the impacts of SAI on stratospheric temperature, transport, and dynamics are strongly model dependent.

SAI impacts on ozone in the future

- **Future changes in TCO resulting from SAI would be in addition to changes driven by future climate conditions and stratospheric halogen burden, as described in Chapters 3, 4, and 5. The SAI-related TCO changes depend on the required SAI injection rate, which is different for the three defined SAI scenarios (Figure 6-2). Compared to conditions without SAI, significant TCO reductions are expected in October over Antarctica for any SAI applications within the 21st century that are sufficient to appreciably impact climate warming.**
  - **In October over Antarctica, aerosol injection rates sufficient to achieve a 0.5 °C global cooling over the period 2020–2040 result in a reduction of TCO of around 58 ± 20 DU compared to no SAI. Smaller initial injection rates to achieve cooling of 0.2 °C between 2020 and 2040 result in a modeled reduction in TCO of 17 ± 9 DU.** Large injection rates based on the peakshaving and strong SAI scenarios starting in 2020 bring TCO close to the minimum values observed between 1990 and 2000, while smaller injection rates in the medium SAI scenario lead to less TCO reduction. The initial phase-in of SAI leads to relatively larger reductions in TCO over Antarctica in spring compared to a case without SAI because of nonlinearities in microphysical processes.
  - **In October over Antarctica, the magnitude of TCO changes in the second half of the 21st century increase with increasing injection rates. Injection rates and the resulting TCO reductions are scenario, strategy, and model dependent.** Under the strong SAI scenario, with injections starting in 2020, model simulations suggest that Antarctic TCO is reduced by around 55 ± 20 DU in October throughout the 21st century and the ozone hole recovery is delayed between 25 and 50 years. In this case, the effect of continually increasing injections is offset by the simultaneously declining chlorine burden in response to Montreal Protocol provisions. SAI, therefore, counters some of the super recovery of TCO above 1980 values driven by increasing greenhouse gases. The medium SAI scenario results in a smaller TCO reduction of between 9 and 29 DU (based on three models), and the peakshaving scenario results in no significant ozone loss by 2100 due to SAI (based on one model).
  - **In the Arctic in spring, SAI starting in 2020 to achieve global cooling of 0.5 °C by 2040 results in TCO reductions between 13 DU ± 10 DU and 22 ± 21 DU compared to no SAI, with no significant changes after 2040, based on results from two different models. The change in TCO for smaller initial injection rates is not significant.** In the Arctic, chemical changes are in part offset by changes in dynamics, resulting in smaller SAI-induced changes of TCO compared to Antarctica. As a result, SAI only slightly offsets the super recovery of TCO in a high-GHG scenario. Modeled impacts on TCO in the Arctic under the medium SAI scenario are smaller and not significant. These results, which are based on ensemble means of zonal and monthly mean TCO comparisons, do not reflect possible larger regional ozone changes that may occur within the Arctic polar vortex for years with warm and cold vortex conditions.
  - **In NH mid-latitudes in winter, increasing SAI toward the end of the century in both the strong and medium SAI scenarios can lead to a significant TCO increase relative to that in a scenario with no GHG mitigation and without SAI.** In both SAI scenarios, the increased heating in the tropical lower stratosphere causes increased transport of ozone from the tropics to mid- and high latitudes, resulting in a greater increase in TCO with injection amount. SAI, therefore, enhances the super recovery of TCO for a high-GHG scenario. No significant TCO changes occur in NH mid-latitudes in the peakshaving scenario.

Other side effects, risks, and limitations of SAI

- **Limited aerosol injections in a peakshaving scenario minimize SAI-induced side effects and climate risks, including reductions in global precipitation, while climate impacts and risks increase in scenarios with less mitigation and more SAI.** A portfolio of climate responses, including effective mitigation and decarbonization, limits the amount of SAI needed to maintain the global surface temperature below specific targets. Since SAI offsets the warming from atmospheric GHGs, limiting SAI would reduce the risks associated with a potential abrupt termination of SAI. Such an abrupt termination would result in a rapid (within 10 years) return of climate to the non-SAI climate base state if SAI was not restarted. Other side effects induced by SAI, such as Eurasian winter warming and associated precipitation impacts and a

significant weakening of the Asian monsoon, depend on the amount of SAI. Ocean acidification depends mostly on atmospheric carbon dioxide (CO_2) concentrations and is impacted only to a small extent by SAI.

SAI using aerosols other than sulfates

- **The use of aerosols other than sulfate is expected to change the effects on ozone via changes in heterogeneous chemistry and dynamics and transport. Comprehensive climate model simulations to quantify these effects have yet to be performed.** Other aerosol types that absorb less solar radiation would heat the tropical lower stratosphere much less than sulfate. They are also potentially more chemically inert and less impactful on stratospheric ozone. Materials that have been considered include calcium carbonate, titanium dioxide, aluminum oxide, and diamond. The effects on ozone are less certain for these alternate materials owing to the paucity of laboratory and modeling studies investigating them and the lack of natural analogs.

Evaluation of models

- **The study of SAI is aided by natural analogs. Volcanic eruptions and pyrocumulonimbus events are useful, albeit imperfect, natural analogs for assessing SAI.** Present-day Earth system models may not accurately simulate the effects of stratospheric aerosol perturbations on ozone and other side effects. Remote sensing and in situ observations of volcanic eruptions and pyrocumulonimbus (pyroCb) formation provide essential information on the stratospheric evolution of injected sulfur dioxide and resultant sulfate aerosol, which can be used to assess and improve SAI models. However, remote and in situ observations valuable for evaluating the effects of injected aerosols on the ozone layer are generally lacking. SAI scenarios with continuous aerosol (precursor) injections will produce different stratospheric aerosol distributions than pulse injections that occur with natural analogs; therefore, accurately simulating these natural events is a necessary but not sufficient constraint on model fidelity in representing SAI.

Chapter 7:
Scenarios and Information for Policymakers

In its evaluation of future scenarios, this chapter uses reduced complexity models to calculate future impacts on ozone and climate. These models supplement the results from more complex models discussed in Chapters 3–6, with the added advantage that the simpler framework allows exploration of a greater number of scenarios and sensitivity experiments.

Post-Kigali Information of Interest

- **The Kigali Amendment to the Montreal Protocol, along with regional and national regulatory and voluntary actions taken before Kigali entered into force, is expected to substantially limit future climate forcing by HFCs.** Assuming global compliance with the Kigali Amendment, it is expected that HFCs will cause a peak radiative forcing of about 100 mW m^{-2} by mid-century. This may be compared to some past projections of forcing absent the Kigali Amendment or regulation under another convention, the highest being in excess of 400 mW m^{-2} in 2050, with substantial increases after that. Given the regional and national regulatory and voluntary actions taken before Kigali entered into force, and assuming global adherence to the Kigali Amendment to the Montreal Protocol, the contribution of HFCs to global annual average warming is projected to be 0.04 °C in 2100 (Chapter 2), with a continued decline after that time.
- **The elimination of all long-lived HFC emissions (including HFC-23) from 2023 onward represents an extreme example of the potential opportunities for future HFC reductions and would reduce the average radiative forcing over 2023–2100 by 79 mW m^{-2}**, with additional benefits continuing after 2100. This is more than twice the benefit of eliminating all controlled ODS emissions from the baseline scenario and would reduce the warming attributable to all HFCs to less than 0.01 °C by 2100. Of the 79 mW m^{-2}, 51 mW m^{-2} arises from future production and usage of long-lived HFCs (excluding HFC-23), 16 mW m^{-2} comes from future emissions from current banks, and 11 mW m^{-2} comes from emissions of HFC-23.
- **If emissions of HFC-23, a potent greenhouse gas, remain at the current relative level compared with HCFC-22 production, HFC-23 has the potential to cause about half of the climate forcing (30 mW m^{-2}) of all the other HFCs, combined, by 2100.** HFC-23 is emitted into the atmosphere mainly as a by-product from the production of HCFC-22. Its emissions relative to the amounts of HCFC-22 produced have not changed much in recent years and are higher than would be expected if state-of-the-art destruction had been performed during the HCFC-22 production process. While the Kigali Amendment to the Montreal Protocol requires that HFC-23 be "destroyed to the extent practicable," this requirement and the connected reporting of emissions went into effect only on 1 January 2020, and thus reporting is still incomplete and the global response is unclear. Through 2019,

the emissions of HFC-23 as a fraction of HCFC-22 production indicate that a considerable part of the produced HFC-23 was still being released unabated into the atmosphere.

- **Other sources of HFC-23 emissions to the atmosphere may exist and could contribute to its atmospheric burden.** There could be contributions to HFC-23 abundances through formation and loss during the production of tetrafluoroethene (TFE) and from the incineration of HCFC-22. Furthermore, direct emissions could grow from the use of HFC-23 in low-temperature refrigerants, although it is not the only refrigerant used in this application.
- **The Kigali Amendment's control of high-GWP HFCs is expected to lead to overwhelmingly positive climate benefits. Nevertheless, there is a potential for certain negative side effects.** Hydrofluoroolefins (HFOs) are increasingly used for replacing high-global warming potential (GWP) HFCs in refrigeration, foam blowing, and various other applications. This replacement leads to less climate change. However, high-volume usage of CCl_4 (carbon tetrachloride) as a feedstock in the production of HFOs, a usage and production not controlled by the Montreal Protocol, could lead to sustained elevated abundances of CCl_4 if current techniques are continued and some fraction of feedstock production continues to be emitted. A second side effect is that HFO-1234yf emitted into the atmosphere will be fully converted to the stable trifluoroacetic acid (TFA; see below).
- **Trifluoroacetic acid (TFA), which is produced in the atmosphere from the degradation of HFCs, HCFCs, HFOs, and HCFOs, is not expected to harm the environment over the next few decades, although some regional concerns have been raised; periodic evaluation of this assessment is suggested, as important gaps in our understanding remain.** This assessment is based on updated estimates of the TFA formation from current atmospheric concentrations of HFCs and HCFCs (hydrochlorofluorocarbons) and their projected decline, as well as the expected increasing abundance of HFOs as HFC and HCFC replacements within the next years. With long-lived HFCs being replaced with high-TFA-producing, short-lived HFOs, more TFA will be formed in the atmosphere. Because of the shorter lifetime of HFOs, this TFA is expected to be deposited nearer to the location of emissions. Other anthropogenic sources of TFA, such as the incineration of polytetrafluoroethene (PTFE), could also contribute. In view of changing and potential unknown sources, concentrations of TFA should be monitored for changes in different parts of the environment, with a special focus on highly populated regions and on the remote ocean.

Updates on the Climate Impact of Gases Controlled by the Montreal Protocol

- **In the baseline scenario, future emissions of HFCs (excluding HFC-23), HFC-23, HCFCs, and CFCs contribute approximately 68, 11, 9, and 9 mW m^{-2} to radiative forcing, respectively, averaged over the 2023–2100 period.** Of the 68 mW m^{-2} from HFCs, 51 mW m^{-2} arise from future production. For reference, CO_2 (carbon dioxide) emissions from fossil fuel usage over this time period are projected to contribute an average of about 3250 mW m^{-2} in the SSP2-4.5 scenario. The total radiative forcing from CFCs, HCFCs, and their HFC replacements is projected to continue to remain roughly constant for the next decade or two. After about 2040, the ODS and HFC restrictions of the Montreal Protocol, if adhered to, are expected to ensure a continued decline in the total RF from ODSs and their replacements. Previous expected increases in RF driven by projected HFC increases throughout the century are now mitigated by assumed compliance with the Kigali Amendment.
- **The effective radiative forcing of the halocarbons has been revised to encompass lower values due to a larger range of estimated negative forcing from the ozone depletion they cause.** This offset of the halocarbon direct radiative forcing remains highly uncertain.

Ozone-Depleting Substances (ODSs) and Their Replacements: Impacts on Ozone and Climate

Below, we discuss potential trajectories of equivalent effective stratospheric chlorine (EESC; a proxy for ozone depletion) and radiative forcing (a proxy for climate change) that result from our current understanding of the emissions of individual gases or groups of gases and the processes that lead to these emissions. We reference these potential changes to the so-called baseline scenario, which should be considered a plausible future pathway for these gases that is consistent with the controls of the Montreal Protocol. The specific assumptions made in the baseline scenario can be extremely important to the results. Note that the combined impact of changing assumptions is not always simply the addition of each of the changes. It is also important to recognize that the return date of EESC to 1980 levels is quite sensitive to any change in the EESC concentration because of the relatively small rate at which the EESC is projected to decline around the middle of this century. While a change in the return date to 1980 EESC levels measured in tenths of years or even a few years cannot be discerned in the atmosphere, primarily due to natural variability, this metric can be useful for comparing various alternative ODS scenarios.

It should also be noted that the EESC formalism adopted here is the same one that was applied in Appendix 6C of the 2018 Assessment and reflects our improved scientific understanding of EESC (see Section 7.3). This alters the time evolution of EESC and dates when EESC returns to 1980 levels when compared with the older approach used in the main part of Chapter 6 of the 2018 Assessment, but it has little effect on the relative impacts of the various alternative future scenarios. If EESC comparisons are made with the 2018 Assessment, it is most appropriate to compare to those found in Appendix 6C rather than Table 6-5 of that Assessment.

- **Changes in the current baseline scenario lead to a delay in the return of mid-latitude and polar EESC to 1980 levels by 4 years and 7 years, respectively, compared with the baseline scenario in the previous Assessment. This is due mainly to a larger assessed CFC-11 bank, and to a lesser degree, to a larger assessed CFC-12 bank.** The larger bank for CFC-11 does not include any explicit increase due to unreported production over the past decade, as that amount is highly uncertain.
- **The unexpected emissions of CFC-11 declined after 2018. The continued elimination of this emission and**

the production that has caused it will prevent a substantial impact on ozone and climate. Cumulative unexpected emissions over 2012–2019 have been estimated at 120–440 Gg. Since then, these annual emissions have diminished substantially from their peak amount. The integrated emissions over this period are calculated to lead to a delay in the return of mid-latitude EESC to 1980 levels by about one year and to cause an additional radiative forcing of 2 mW m^{-2} averaged over 2023–2100. It is unclear how much of the production that led to these emissions has gone into banks, as opposed to having already been emitted. If the unexpected emissions over 2012–2019 were associated with the production of insulating foams, it is estimated that they would have accounted for 25% to 45% of the unreported production, with the rest (146–1320 Gg) going into the CFC-11 bank. The impact of any increase in the bank can be estimated from knowing that a hypothetical 1000 Gg added to the 2020 bank delays the return of mid-latitude EESC to 1980 levels by almost four years and leads to an additional averaged radiative forcing over 2023–2100 of about 6 mW m^{-2}.

- **The hypothetical elimination of all future ODS emissions would bring forward the return of mid-latitude and polar EESC to 1980 levels by 16 years and 19 years, respectively, and increase the average of global stratospheric ozone levels in the period 2020–2070 by about 2 DU.** It would also reduce average radiative forcing by 31 mW m^{-2} averaged over 2023–2100. These emissions are dominated by the release from current banks, with a smaller contribution from future production of ODSs that is controlled by the Montreal Protocol and emissions associated with production intended for feedstock purposes. Estimates of bank sizes are highly uncertain though; the bank approach used in the scenarios here has resulted in substantially larger 2020 banks than estimated in the previous Assessment.
- **In the baseline scenario, future emissions from current CFC banks contribute more to EESC than do emissions from either HCFC banks or halon banks.** However, given the uncertainty in estimates of current bank sizes, these differences are likely not statistically significant. An elimination of the emissions from the CFC banks are calculated to bring forward the return of mid-latitude EESC to 1980 levels by about 5 years. In this chapter, there is no evaluation made regarding the accessibility of various banks in terms of recapture and destruction.
- **In the baseline scenario, future emissions from current HCFC banks contribute more to climate change than do future emissions from either CFC banks or halon banks.** However, the differences in the climate impacts between the banks of HCFCs and CFCs are likely not statistically significant. Again, there is no evaluation made regarding the accessibility of various banks in terms of recapture and destruction.
- **Elimination of future emissions of methyl bromide (CH_3Br) from quarantine and preshipment (QPS) applications, not controlled by the Montreal Protocol, would accelerate the return of mid-latitude and polar EESC to 1980 levels by about two years and would increase globally averaged total ozone by 0.2 DU when averaged over 2020–2070.** Production for QPS use has remained relatively stable over the last two decades and now constitutes almost 99% of reported production of CH_3Br, since emissions from other uses have declined dramatically. Non-QPS applications of CH_3Br were completely phased out in 2015, except for approved critical use exemptions (CUEs). These CUEs have declined by a factor of ~200 since 2005 and make up the remaining ~1% of reported production. CH_3Br has little direct impact on climate.
- **Otherwise-controlled ODSs have increasingly been used as feedstocks. With estimated emission rates of 2–4% (4.3% for CCl_4) from the produced ODSs, this has resulted in estimated emissions associated with ODS feedstock applications of 37–59 Gg (15–19 ODP-Gg) in 2019. The influence on ozone of these emissions was dominated by emissions from the feedstock use of CCl_4. When compared to the baseline scenario, in which these emissions continue at current levels, an elimination of emissions associated with feedstock use would bring forward the return of mid-latitude and polar EESC to 1980 levels by about 4 and 5 years, respectively.** Between 2009 and 2019, the mass of ODSs used as feedstocks, which is not controlled under the Protocol, increased by 75%. When expressed in units of Gg ODP (Gg multiplied by the ozone depletion potential), the increase in feedstock-linked production was only 41% over the same period, as HCFC-22, with a relatively low ODP, was responsible for the highest growth. Eliminating all these emissions in the future would reduce averaged radiative forcing by 6 mW m^{-2} compared with the baseline scenario.
- **Of the feedstock production reported, estimated emissions from CCl_4 and HCFC production dominate the impact on climate over the coming decades. These two groups lead to an increased average radiative forcing over 2023–2100 of 5 mW m^{-2} in the baseline scenario.** The size of this climate effect is dependent on the assumptions made in the baseline scenario regarding feedstock production growth.
- **CCl_4 feedstock production and usage increased by a factor of about two within the last decade. If CCl_4 emissions associated with these allowed uses continue to grow through 2030 as they have been growing over the past decade, future CCl_4 atmospheric concentrations will decline more slowly and will be about twice as high (+20 ppt) in 2100 than in the baseline scenario, in which feedstock-related emissions remain constant.** As reported in the 2018 Assessment, CCl_4 emissions inferred from atmospheric observations continue to be considerably higher than those estimated from feedstock uses, as reported to the United Nations Environment Programme (UNEP), and other known sources. CCl_4 emissions related to its feedstock production and usage have been assessed to be 4.3% of the produced amount of CCl_4, with a relatively large associated uncertainty. Calculated as ODP-weighted emissions, the emissions from feedstock use of CCl_4 in 2019 was 11.2 ODP-Gg yr^{-1}, or 60–74% of all feedstock-related emissions. This is important, as the usage of CCl_4 is projected to continue to increase because of its application in the growing production of HFOs in the replacement of the long-lived HFCs. An elimination of all future CCl_4 emissions associated with feedstock usage would reduce radiative forcing by about 2 mW m^{-2} compared with the baseline scenario when averaged over 2023–2100.

- **In addition to CCl_4, the most important contributions to ODP-weighted emissions from other ODSs used as feedstock are from CFC-113 and CFC-114 (2.3–4.6 ODP-Gg), from HCFC-22 (0.5–1.1 ODP-Gg), and from the sum of other HCFCs (0.1–0.3 ODP-Gg), with the highest contribution from HCFC-142b.** These are based on estimated emissions of 2–4% relative to the production amount. The increased use of HCFC-22 and other HCFCs as feedstocks for fluoropolymer production within the last decades is expected to continue into the future. On the other hand, the usage of feedstock chemicals for the production of HFCs will likely decline because of the Kigali Amendment.
- **The production and usage of short-lived chlorinated solvents is not controlled by the Montreal Protocol, and some are used in large amounts. Their impact on stratospheric ozone, and their ODPs, vary depending on the season and location of emissions and could grow in the future even as emissions from long-lived ODSs decline.** More than 1600 Gg of $CHCl_3$ (chloroform) are used as feedstock in the production of HCFC-22. Emissions from $CHCl_3$ used as a feedstock are comparable to its solvent emissions. CH_2Cl_2 (dichloromethane), TCE (trichloroethene), and PCE (perchloroethene) are also used as feedstock chemicals, although their emissions are dominated by emissive uses (e.g., from solvents).
- **Sustained increases in anthropogenic chlorinated very short-lived substance (VSLS) emissions, as seen for CH_2Cl_2 over the last two decades, would lead to more stratospheric ozone depletion in the future.** While observed growth rates of CH_2Cl_2 have been highly variable and future projections are believed to be highly uncertain, emissions have continued to increase since the last Assessment. If emission rates remain constant at their present level into the future, CH_2Cl_2 is projected to deplete 0.8–1.7 DU averaged over 2020 to 2070 compared to a case of zero future emissions. Any reduction in the production and consumption of CH_2Cl_2 would have a rapid impact on ozone, since this VSLS is both emitted soon after production and is cleansed out of the stratosphere within a few years.
- **A reduction in future N_2O emissions from that in the baseline scenario (SSP2-4.5) to that in the SSP scenario with the strongest N_2O mitigation (SSP1-1.9) results in a 0.5 DU increase in ozone averaged over 2020 to 2070, or about one-quarter of the impact of eliminating all emissions from controlled ODSs beginning in 2023.** This emission reduction also leads to a radiative forcing reduction of 43 mW m^{-2} averaged over 2023–2100. The magnitude of this N_2O reduction represents a decrease in anthropogenic N_2O emissions of 3% compared with the baseline scenario when averaged over 2020–2070.

Impacts of Mitigation Options and Particular Scenarios

Figure 7.1 (also shown as Figure ES-8 in this document) shows the ozone and climate-relevant changes that would occur if various actions were to be taken. These changes are shown as the differences in global total column ozone averaged over 2020–2070 and in radiative forcing averaged over 2023–2100, both relative to the baseline scenario, which includes the Kigali Amendment controls for HFCs in Annex F, Group 1. The options available to hasten the recovery of the ozone layer are somewhat limited, mostly because past actions have already been very successful at reducing emissions of ODSs and their replacements.

- For the ODSs, the single most effective ozone depletion and climate change mitigation option, not considering technical feasibility, is bank recapture and destruction of the CFC banks; however, large uncertainties in the CFC-11 and CFC-12 banks have been reported in the literature, with the recent production associated with the unexpected emissions of CFC-11 further adding to uncertainties in the bank sizes. Furthermore, no assessment has been made here regarding the fraction of the banks that are accessible for capture or the fraction that are active.
- For CH_3Br, elimination of production for currently uncontrolled QPS applications is shown.
- For CCl_4, the impact of eliminating emissions from controlled production starting in 2023 is shown.
- For CH_2Cl_2, an uncontrolled ozone-depleting gas with an atmospheric lifetime of ~180 days, future emissions continue to have the potential to lead to more ozone depletion than emissions from many of the other alternative scenarios explored here. CH_2Cl_2 is emitted mainly from Asia, and emissions and concentrations have been growing steadily in recent years.
- For N_2O, the impacts of a strong mitigation scenario (SSP1-1.9) are compared to the base-line scenario (SSP2-4.5).
- For HFCs, the impact of a hypothetical complete global phaseout of production (excluding HFC-23) starting in 2023 is shown. An additional scenario is included in which HFC-23 emissions are reduced to virtually zero, consistent with the current best practice of incineration, rather than the assumed emissions rate of 1.6% of HCFC-22 production included in the baseline scenario, in order to show the effect of nearly eliminating by-product emissions.

Updates on Impacts of Greenhouse Gases and Other Processes on Future Stratospheric Ozone

In this section, we summarize potentially important impacts on the future of the ozone layer that could result from anthropogenic activity not associated with ODS or replacement production and consumption and thus that is not controlled by the Montreal Protocol. Net stratospheric cooling, which is projected in many scenarios due to increases in greenhouse gas concentrations, is predicted to lead to increases in upper-stratospheric ozone at all latitudes, with a more complex pattern of ozone changes in the lower stratosphere, including a decrease at tropical latitudes driven by changes in dynamics and transport; these processes are discussed in detail in Chapters 3 and 4. Potential climate intervention activities that may affect ozone are discussed in Chapter 6.

- **Our ability to accurately predict future changes in the ozone layer continues to be limited more by uncertainties in the future levels of CO_2, CH_4 (methane), and N_2O than by uncertainties in the levels of ODSs.** Global mean tropospheric warming, as well as stratospheric cooling, will

drive ozone changes through both atmospheric circulation and chemistry, while changing CH_4 and N_2O will lead to further changes in the chemistry associated with stratospheric ozone. Future ozone levels depend on the path of greenhouse gas emissions and aerosol abundances, as well as the sensitivity of the climate system to these emissions.

- **Rocket launches presently have a small effect on total stratospheric ozone (much less than 0.1%). However, rocket systems using new propellants (e.g., hydrogen and methane) could exert a substantial influence in the future.** The future scenarios of space industry emissions consider the potential for a significant increase in launch rates, the adoption of new launch-vehicle propellants, and an increase in middle-atmosphere aerosol and the production of NO (nitrogen monoxide) by reentering space debris. Many of the impacts of rocket activity involve chemistry and radiative interactions that are poorly understood and, in some cases, not yet studied. Furthermore, the planned development of massive low-Earth orbit satellite constellations (megaconstellations) could cause particulates resulting from space debris reentry to become comparable to that from launch emissions; little is known about the impacts of reentry particles, and their accumulation in the stratosphere has not been modeled. The uncertainties in these processes and in any potential new emission sources limit the confidence level of predictions of present and future impacts of space industry emissions on stratospheric ozone. Periodic assessment and critical knowledge gap identification are warranted.
- **The influence of hydrogen as an energy carrier on stratospheric ozone remains uncertain.** Hydrogen-based energy will likely play a role in a future non- or reduced-fossil economy. However, if it is not a dominant energy carrier, it is unlikely that it will significantly affect ozone. This statement should be reevaluated periodically.
- **The impacts of supersonic aircraft on stratospheric ozone are discussed in Chapter 4.**
- **Climate intervention approaches that affect the stratospheric ozone layer are discussed in Chapter 6.**

Errata (February 2023)

Executive Summary Introduction:

- The definition of Ozone Depleting Substances was corrected in the Terminology.

Chapter 3, Appendix 3A, Table 3A-3:

- The entry for SBUV NASA (MOD) was corrected from S-NPP OMPS NP NOAA v2.8 to S-NPP OMPS NP NASA v2.8.
- The entry for SBUV NOAA (COH) was corrected from S-NPP OMPS NP NASA v2.6 to S-NPP OMPS NP NOAA v3r2.

CHAPTER 1

Update on Ozone-Depleting Substances (ODSs) and Other Gases of Interest to the Montreal Protocol

About the cover image:
The Jungfraujoch research station in Switzerland is one of many observatories in the Advanced Global Atmospheric Gases Experiment (AGAGE) network from which scientists monitor changes in atmospheric composition that affect both ozone depletion and climate change.

Photo credit: Paedii Luchs via Stocksy

CHAPTER 1

Update on Ozone-Depleting Substances (ODSs) and Other Gases of Interest to the Montreal Protocol

Lead Authors : Johannes C. Laube
Susann Tegtmeier

Coauthors : Rafael P. Fernandez
Jeremy Harrison
Lei Hu
Paul Krummel
Emmanuel Mahieu
Sunyoung Park
Luke Western

Contributing Authors : Elliot Atlas
Peter Bernath
Carlos A. Cuevas
Geoff Dutton
Lucien Froidevaux
Ryan Hossaini
Timo Keber
Theodore K. Koenig
Stephen A. Montzka
Jens Mühle
Simon O'Doherty
David E. Oram
Klaus Pfeilsticker
Maxime Prignon
Birgit Quack
Matthew Rigby
Meike Rotermund
Takuya Saito
Isobel J. Simpson
Dan Smale
Martin K. Vollmer
Dickon Young

Review Editors : Andreas Engel
Bo Yao

CONTENTS

Chapter 1: Update on Ozone-Depleting Substances (ODSs) and Other Gases of Interest to the Montreal Protocol

SCIENTIFIC SUMMARY

This chapter concerns atmospheric changes in ozone-depleting substances (ODSs), such as chlorofluorocarbons (CFCs), halons, chlorinated solvents (e.g., carbon tetrachloride [CCl_4] and methyl chloroform [CH_3CCl_3]) and hydrochlorofluorocarbons (HCFCs), which are controlled under the Montreal Protocol. Furthermore, the chapter updates information about ODSs not controlled under the Protocol, such as methyl chloride (CH_3Cl) and very short-lived substances (VSLSs). In addition to depleting stratospheric ozone, many ODSs are potent greenhouse gases.

Mole fractions of ODSs and other species are primarily measured close to the surface by global or regional monitoring networks. The surface data can be used to approximate a mole fraction representative of the global or hemispheric tropospheric abundance. Changes in the tropospheric abundance of an ODS result from a difference between the rate of emissions into the atmosphere and the rate of removal from it.

- **The total amount of chlorine and bromine from ODSs that were controlled under the original Montreal Protocol is continuing to decline, as the overall emissions are smaller than the rate at which these ODSs are destroyed. Abundances of many of the first-stage replacement compounds, HCFCs, are now increasing very slowly or not at all.**

Tropospheric Chlorine (Cl)

Total tropospheric chlorine is a metric used to quantify the combined globally averaged abundance of chlorine in the troposphere due to the major chlorine-containing ODSs. The contribution of each ODS to total tropospheric chlorine is the product of its global mean tropospheric mole fraction and the number of chlorine atoms it contains.

- **Total tropospheric chlorine from ODSs continued to decrease between 2016 and 2020.** Total tropospheric chlorine in 2020 was 3220 ppt (where ppt refers to parts per trillion as a dry air mole fraction), about 1.8% lower than in 2016 and 12% lower than its peak value in 1993. Of the 2020 total, CFCs accounted for about 60%, CH_3Cl for about 17%, and CCl_4 and HCFCs each for about 10%. The contribution from CH_3CCl_3 has now decreased to 0.1%. Very short-lived source gases (VSL SGs), as measured in the lower troposphere, contributed approximately 3.5%.
    - During the period 2016–2020, the observed rate of decline in tropospheric chlorine due to controlled substances was 15.1 ± 2.4[1] ppt Cl yr^{-1}, which is larger than during the 2012–2016 period (12.8 ± 0.8 ppt Cl yr^{-1}). This rate of decrease was close to the projections in the previous Assessment. The net rate of change was the result of a slightly slower than projected decrease in CFCs and a slower HCFC increase than in the 2018 A1 projection scenario.
    - When substances not controlled under the Montreal Protocol are also included, the overall decrease in tropospheric chlorine was 15.1 ± 3.6 ppt Cl yr^{-1} during 2016–2020. This is larger than the rate of decline during the 2012–2016 period (3.6 ± 4.7 ppt Cl yr^{-1}) and comparable to the rate of decline in controlled substances. Changes in the predominantly anthropogenic dichloromethane (CH_2Cl_2) and the largely natural CH_3Cl largely canceled each other out, resulting in almost no net change in Cl from uncontrolled substances during this period.
- **Starting around 2018, the rate at which the CFC-11 mole fraction was declining in the atmosphere accelerated again, following a slowdown since 2013. These recent changes are largely due to a decrease in emissions originating mostly from northeastern China.** Assuming no impact from changes in atmospheric circulation, global emissions increased from about 57 Gg yr^{-1} (= kt yr^{-1}) in 2012 to around 78 Gg yr^{-1} in 2017; after 2018, they then decreased to approximately 47 Gg yr^{-1} in 2020. Emissions from northeastern China explain 60 ± 40% of the 2012–2018 increase and 60 ± 30% of the subsequent decrease. There is evidence that other recent significant emission regions include the Arabian and Indian subcontinents. If these renewed global emissions are associated with uses that substantially increase the size of the CFC-11 bank, further emissions resulting from this production would be expected in the future.
- **During 2016–2020, mole fractions of CFC-12 decreased by about 2.8%, which is comparable to the decrease during 2012–2016 (~2.3%).** Estimates of global CFC-12 emissions in 2016 and 2020 were similar within uncertainties, at 33 ± 21 Gg yr^{-1} and 25 ± 20 Gg yr^{-1}, respectively. CFC-11 and CFC-12 are often co-produced, and atmospheric observations have confirmed a decrease in CFC-12 emissions from northeastern China from 3.3 ± 1.4 Gg yr^{-1} in 2016 to 0.5 ± 0.5 Gg yr^{-1} in 2019.
- **The CFC-113 global mole fraction has continued to decrease**, but emissions remained constant within uncertainties at around 6 ± 6 Gg yr^{-1} between 2016 and 2020.
- **Mole fractions of CFC-114 remained stable during 2016–2020, whereas those of CFC-13, CFC-113a, and CFC-115 continued to rise, and mole fractions of CFC-112a and CFC-114a exhibited positive growth after previously showing near-zero change.** Total Cl from the latter five CFCs increased from 16.0 ± 0.3 ppt in 2016 to a total of 17.2 ± 0.3 ppt Cl in 2020. These findings likely indicate an increase

[1] Uncertainties in absolute changes of atmospheric abundances were derived using the 1 standard deviation measurement uncertainties (where appropriate combined as the square root of the sum of their squares) and the bootstrap algorithm described in Barreto and Howland (2006). Similar to the procedure described in Leedham Elvidge et al. (2018), and to represent atmospheric variability, data was converted to a dataset comprised of 1) original data, 2) original data minus measurement uncertainty and 3) original data plus measurement uncertainty. This dataset was then resampled (with replacement) 1000 times to derive a standard deviation that is a realistic representation of the uncertainty of the entirety of the original data.

or stabilization of the emissions of these relatively low abundance compounds. While some of these emissions are known to originate from eastern China, the primary processes responsible are unknown.

- **The rate at which CCl_4 has declined in the atmosphere remains slower than expected from its reported use as a feedstock and its removal rate from the atmosphere, which indicates ongoing emissions of around 44 ± 15 Gg yr^{-1}.** This is likely, at least in part, due to feedstock emissions from the production of chloromethanes and perchloroethylene and from chlor-alkali plants. Global CCl_4 emission estimates based on atmospheric observations are now more accurate than in the last Assessment due to an improved lifetime estimate.
- **Emissions of CCl_4 in eastern China over the period 2013–2019 show year-to-year variability likely related to CFC-11 production.** Emissions increased after 2013, reaching 11.3 ± 1.9 Gg yr^{-1} in 2016, and decreasing to 6.3 ± 1.1 Gg yr^{-1} in 2019.
- **Total tropospheric chlorine from HCFCs has continued to increase, reaching 320 ± 3 ppt in 2020.** There is evidence of a slowdown of this increase, as the annual average growth rate of total chlorine from HCFCs decreased from 5.9 ± 1.3 ppt Cl yr^{-1} during 2012–2016 to 2.5 ± 0.4 ppt Cl yr^{-1} during 2016–2020.
- **Combined emissions of the major HCFCs have declined since the previous Assessment.** Emissions of HCFC-22 and HCFC-142b likely declined between 2016 and 2020, while emissions of HCFC-141b, after an initial drop, likely rose year-on-year since 2017, amounting to a total rise of ~4.5 Gg during 2017–2020. These findings are consistent with a sharp drop in reported HCFC consumption after 2012, particularly from Article 5 countries.
- Continued emissions of the compounds HCFC-124, HCFC-31, HCFC-132b, and HCFC-133a have been inferred from atmospheric measurements. HCFC-132b is yet another newly detected HCFC, and its atmospheric mole fractions, while currently small, continue to increase.

Tropospheric Bromine (Br)

Total tropospheric bromine is defined in analogy to total tropospheric chlorine. Even though the abundance of bromine is much smaller than that of chlorine, it has a significant impact on stratospheric ozone because it is around 60–65 times more efficient than chlorine as an ozone-destroying catalyst.

- **Total tropospheric bromine from controlled ODSs (halons and methyl bromide [CH_3Br]) continued to decrease, and was 13.9 ppt by 2020, 3.2 ppt below the peak levels observed in 1999.** From 2012 to 2016, total controlled bromine declined at a rate of 0.15 ± 0.14 ppt Br yr^{-1} (about 1% yr^{-1}). This rate increased to 0.18 ± 0.05 ppt Br yr^{-1} during 2016–2020, with halons contributing about 60% to the overall decline.
- **The mole fractions of halon-1211, halon-2402, and halon-1202 continued to decline between 2016 and 2020. There was no significant change in the mole fraction of halon-1301 between 2016 and 2020. This ODS is, at ~3.3 ppt, now the most abundant halon in the atmosphere.** Emissions of halon-2402, halon-1301, and halon-1211, as derived from atmospheric observations, declined or remained stable between 2016 and 2020.
- **CH_3Br annually averaged mole fractions showed little net change between 2016 and 2020. The small increase (2–3%) observed between 2015 and 2016 was compensated by a small decrease (4%) largely taking place during 2016–2017.** The 2020 mole fraction was around 6.6 ppt, a reduction of 2.6 ppt from peak levels measured between 1996 and 1998. Reported quarantine and pre-shipment (QPS) consumption was relatively stable from 1996 to 2020.

Halogenated Very Short-Lived Substances (VSLs)

VSLs are defined as trace gases whose local lifetimes are shorter than 0.5 years and have non-uniform tropospheric abundances. These local lifetimes typically vary substantially over time and space. Of the very short-lived source gases (VSL SGs) identified in the atmosphere, brominated and iodinated species are predominantly of oceanic origin, while chlorinated species have significant anthropogenic sources. VSLs that reach the stratosphere will release the halogen they contain almost immediately and will thus play an important role for lower-stratospheric ozone in particular. Due to their short lifetimes and their atmospheric variability, the quantification of their contribution is much more difficult and has much larger uncertainties than for long-lived compounds.

- **Total tropospheric chlorine from VSL SGs in the background lower atmosphere is dominated by anthropogenic sources. It continued to increase between 2016 and 2020, but its contribution to total stratospheric chlorine remained small.** Global mean chlorine from VSLs in the troposphere has increased from about 103 ppt in 2016 to about 113 ppt in 2020. The relative contribution of VSLs to the stratospheric chlorine input amounted to 4% in 2020, compared to 3.6% in 2016.
- **Dichloromethane (CH_2Cl_2), with predominantly anthropogenic sources, is the main contributor to total chlorine from VSLs. It accounted for the majority of the change in VSLS chlorine between 2016 and 2020.** The CH_2Cl_2 global mean abundance reached approximately 40–45 ppt in 2020, which is more than a doubling compared to the early part of the century. The rate of increase slowed after 2016 but remained substantial. Regional CH_2Cl_2 emissions from Asia most likely account for most of this increase and more than offset a small decrease in European and North American emissions.
- **Brominated VSLSs contribute 5 ± 2 ppt to stratospheric bromine; this constitutes about 27% of total stratospheric bromine in 2020.** The main sources for brominated VSLSs are natural, and no long-term change is observed. Due to the decline in the abundance of controlled bromine compounds, the relative contribution of VSLSs to total stratospheric bromine increased by about 1% since 2016.
- **New evidence suggests that natural iodinated VSLSs contribute 0.3–0.9 ppt iodine to the stratosphere.** A rapid shift in the partitioning between gas-phase and particulate iodine has been detected in the upper troposphere. This

mechanism can enable iodine entrainment into the stratosphere in particulate form in addition to the entrainment in gas form. No observational trend estimates exist.

Stratospheric chlorine and bromine

In the stratosphere, chlorine and bromine can be released from organic source gases to form inorganic species, which participate in ozone depletion. In addition to estimates of the stratospheric input derived from the tropospheric observations, measurements of inorganic halogen loading in the stratosphere are used to determine trends of stratospheric chlorine and bromine.

- **The total chlorine input to the stratosphere for 2020 was 3240 ppt, which is 11.5% below the 1993 peak value, equivalent to a decline of 420 ± 20 ppt.** This long-term decrease was largely driven by decreasing abundances of CH_3CCl_3 and CFCs. The chlorine input for 2020 is derived from measurements of long-lived ODSs at the surface and estimates of stratospheric entrainment of VSLSs.
- **Hydrogen chloride (HCl) is the major reservoir of inorganic chlorine (Cl_y). Middle-stratosphere profile and total column measurements of HCl show a long-term decrease for the period 1997–2020 of around 0.5 ± 0.2% yr^{-1}.** If the evaluations are constrained to the shorter period 2005–2020 the satellite records show a rate of decrease of around 0.3 ± 0.2% yr^{-1}. This latter rate of decline in stratospheric HCl for the more recent period is in good agreement with expectations from the decline in tropospheric chlorine, which slowed after 2000.
- **Total bromine input to the stratosphere of 18.9 ppt is derived for 2020 by combining 13.9 ppt from long-lived gases and 5 ppt from VSLSs not controlled under the Montreal Protocol.** The total input declined by 14.5% between 1999 peak values and 2020. Anthropogenic emissions of all brominated long-lived gases are controlled, but as CH_3Br also has natural sources, more than 50% of the bromine reaching the stratosphere is now estimated to be from sources not controlled under the Montreal Protocol.
- **Total stratospheric bromine, derived from observations of bromine monoxide (BrO), has decreased at a rate of about 0.8% yr^{-1} since 2003.** This decline is consistent with the decrease in total tropospheric organic bromine, based on measurements of CH_3Br and the halons. There is no indication of a long-term change in natural sources of stratospheric bromine.

Equivalent Effective Stratospheric Chlorine (EESC)

EESC is the chlorine-equivalent sum of chlorine and bromine derived from ODS tropospheric abundances, weighted to reflect their expected depletion of stratospheric ozone. The growth and decline in EESC depend on a given tropospheric abundance propagating to the stratosphere with varying time lags (on the order of years) associated with transport to different regions of the stratosphere. Therefore, the EESC abundance, its peak timing, and its rate of decline are different in different regions of the stratosphere.

- **By 2020, EESC had declined from peak values by about 11% for polar winter conditions and by about 15% for mid-latitude conditions.** This drop to 1607 ppt is 37% of the decrease required for EESC in mid-latitudes to return to the 1980 benchmark level. In polar regions, the drop to 3710 ppt is about 23% of the decrease required to return to the 1980 benchmark level. However, regional estimates have indicated that EESC might be higher in some parts of the stratosphere, with an additional 200–300 ppt predominantly originating from CH_3Cl and CH_3Br. Contributions from the ozone-depleting VSLSs and nitrous oxide (N_2O) are currently not included in EESC calculations.

Tropospheric and Stratospheric Fluorine (F)

While fluorine has no direct impact on stratospheric ozone, many fluorinated gases are strong greenhouse gases, and their emissions are often related to the replacement of chlorinated substances controlled under the Montreal Protocol. For this reason, trends in fluorine are also assessed in this report.

- **The main sources of fluorine in the troposphere and in the stratosphere are CFCs, HCFCs, and HFCs (hydrofluorocarbons). In contrast to total chlorine, total fluorine in the troposphere continued to increase between 2016 and 2020, at a rate of 1.71% yr^{-1}.** This increase shows the decoupling of the temporal trends in fluorine and chlorine due to the increasing emissions of HFCs (see *Chapter 2*). The ODS contribution to the fluorine budget has started to decline, so that the fluorine trend due to ODSs alone became negative after 2016. In contrast, the fluorine trend due to HFCs has constantly increased, causing the total fluorine trend to increase as well. The Northern Hemisphere stratospheric abundance of inorganic fluorine has continued to increase at a rate of about 0.8% yr^{-1} since 2004.

Effect of ODSs on climate

- **The total direct radiative forcing of CFCs continues to be distinctly higher than that of HCFCs, with CFCs contributing around 68% of the total forcing from ODSs.** Radiative forcing from CFCs has dropped by 0.007 W m^{-2} since 2016 to about 0.257 W m^{-2} in 2020, while radiative forcing from HCFCs increased from 0.062 W m^{-2} to 0.064 W m^{-2} from 2016 to 2020. The total direct radiative forcing due to CFCs, HCFCs, halons, CCl_4, and CH_3CCl_3 was 0.337 W m^{-2} in 2020 (approximately 16% that of CO_2).
- **CO_2-equivalent emissions of CFCs and HCFCs were again approximately equal in 2020.** Based on 100-year time horizon global warming potentials (GWPs), the CO_2-equivalent emissions (in Gt CO_2-eq yr^{-1}) in 2020 were, for species where estimates are available, 0.7 ± 0.4 for CFCs, 0.7 ± 0.1 for HCFCs, 0.09 ± 0.03 for CCl_4 and CH_3CCl_3 combined, and 0.02 ± 0.01 for halons. The CO_2-equivalent emissions from the sum of CFCs, HCFCs, halons, CCl_4, and CH_3CCl_3 remained similar to the value reported in the last Assessment at approximately 1.5 Gt CO_2-eq in 2020.

Other gases that affect ozone and climate

- **Mole fractions of many other gases that affect both ozone and climate (including the three major greenhouse gases CH_4, N_2O, and CO_2) have changed since the last Assessment.** The atmospheric abundance of methane (CH_4) has continued to increase following a period of

stagnation in the early 2000s. The drivers of the changing trend are likely largely anthropogenic.

- **Mole fractions of N_2O, which is an ODS, continue to grow in the atmosphere, with growth rates exceeding some of the highest projections.** When expressed as a CFC-11-equivalent, anthropogenic N_2O emissions in 2020 were equal to more than two times the ODP-weighted emissions from all CFCs in that year. When compared to the CFC emission peak from 1987, those 2020 anthropogenic N_2O emissions were equal to more than 20% of the ODP-weighted emissions from CFCs in that year. Almost half of the N_2O emissions in recent years are anthropogenic in origin.
- **The global mole fractions of many non-ODS, non-HFC, highly fluorinated substances have continued to grow** (e.g., sulfur hexafluoride [SF_6], carbon tetrafluoride [CF_4], hexafluoroethane [C_2F_6], sulfuryl fluoride [SO_2F_2], and nitrogen trifluoride [NF_3]). These species contributed 0.014 W m^{-2} to anthropogenic radiative forcing in 2020. In contrast, the abundance of the sulfur-containing compound sulfur dioxide (SO_2) has not changed substantially, while carbonyl sulfide (COS) has shown a small negative trend.
- **Molecular hydrogen (H_2) is included in the Assessment for the first time, due to its potential future effects on stratospheric ozone. The decarbonization of the fossil fuel industry could lead to drastically increasing atmospheric mole fractions of H_2. The resulting future effects on ozone are currently not well understood but are expected to be small.** Atmospheric abundances of H_2 have increased from ~330 ppb during the mid-to-late 1800s to the present levels of 530–550 ppb in the late 20th and early 21st centuries.

1.0 INTRODUCTION

This chapter provides an update on the emissions rates and abundances of ozone depleting substances (ODSs) and other species of interest to the Montreal Protocol. In addition to the brief definitions given in the Scientific Summary, we describe the source of these data and how the metrics used in this chapter are derived. Observations of ODSs and other species of interest to the Montreal Protocol, as well as relevant quantities derived from those observations, are presented not only in this section but throughout *Chapters 1 and 2*. These observations have been carried out over multiple decades by several groups and networks with different sampling and measurement strategies. Independent and regularly compared and improved calibration scales have been derived, as highlighted in **Box 1-1**.

Globally and hemispherically representative abundances are mean dry air mole fractions and are expressed here also, and interchangeably, as mixing ratios (mostly in ppt). These abundances are derived using data from networks with ground-based air sampling stations that are distributed around the world: the Advanced Global Atmospheric Gases Experiment (AGAGE) network, the United States National Oceanic and Atmospheric Administration (NOAA) network, and the University of California, Irvine (UCI) network. For species that are primarily anthropogenic in origin, the difference between Northern and Southern Hemisphere (NH, SH) mole fractions is related to the global emission rate because their sources are concentrated in the Northern Hemisphere.

Further data representative of regional or hemispheric scales are available for some species from the National Institute for Environmental Studies (NIES) and the University of East Anglia/Forschungszentrum Jülich (UEA/FZJ). These networks maintain independent calibration scales and employ different measurement techniques, as well as different sampling locations and frequencies. As such, small differences (typically on the order of a few percent or less) in the burdens and trends estimated from each dataset are often observed. Therefore, for much of this section, global abundance trends and inferred emissions (using an atmospheric transport model, uncertainties of which are explained in **Box 1-2**) are given separately for each network. Data from regionally representative (e.g., Southern Hemisphere) sites are used when independent calibration scales exist (see **Box 1-1**) or global network data are not available. Particularly for species with atmospheric lifetimes of several years or more, these data can be extrapolated to derive global-scale mole fractions or emissions.

In terms of the atmospheric lifetimes of the species covered in this chapter, few manuscripts have been published since the last Assessment (e.g., Orkin et al., 2020; Suntharalingam et al., 2019; Burkholder et al., 2019), and these updates have been incorporated into emissions estimates only if they represent a significant change in understanding. Emission sources for many of the species covered in this chapter (especially the longer-lived ones) have been well known for some time, and the reader is therefore referred to the previous Assessment for a comprehensive overview. In this chapter, sources are covered only if substantial new evidence has been published since the last Assessment or if such coverage is necessary for the narrative of the particular section. Also note that all annually averaged data presented in this chapter are centered around the middle of that year.

As the ozone-depleting efficiency of the different halogen families is different, bromine and iodine "alpha" (scaling) factors are used to quantify the efficiency of ozone loss mediated by a single bromine or iodine atom relative to the loss caused by a single chlorine atom. Although the relative efficiency of these different species in destroying ozone depends on location, height, and season, average alpha factors are usually integrated for the polar and extra-polar (i.e., tropical and mid-latitudes) total column annual mean, with typical values ranging between 60 and 75 for bromine and between 150 and 300 for iodine (Ko, Poulet et al., 2003; Sinnhuber et al., 2009; Engel, Rigby et al., 2018; Klobas et al., 2021). Consistent with the last Assessment, we here use a bromine alpha factor of 60 for mid-latitudes and 65 for polar latitudes.

The number of observed species relevant for this chapter has been growing with each Assessment. Here, species with an average equivalent chlorine (ECl, using an alpha factor of 60 for bromine) contribution of less than 1 ppt near the surface in 2020 have been excluded from tables and figures. These species will be mentioned in the text only briefly in order to help maintain a focus on the more abundant ODSs and VSLSs. For species that do not directly affect stratospheric ozone, their relevance is largely determined by their impact on global warming. Therefore, compounds with a radiative forcing (RF) of less than 0.1 mW m^{-2} in 2020 are also excluded from tables and figures, with two exceptions: Carbonyl sulfide (COS) is included due to its relevance for stratospheric aerosol, and molecular hydrogen (H_2) is included due to its potential future relevance. To ensure that a consistent list of species is used for calculations of total F, Cl, and Br we have also included HCFC-124 throughout as the only species that does not fulfill the ECl criterion but contributes more than 0.1 mW m^{-2} to RF. The full list of species used in tables and figures is therefore as follows: CFCs: 11, 12, 13, 112, 113, 113a, 114, 114a, and 115; HCFCs: 22, 141b, 142b; halons: 1202, 1211, 1301, and 2402; solvents and methyl halides: CCl_4, CH_3CCl_3, CH_3Cl, and CH_3Br, VSLSs: CH_2Cl_2, $CHCl_3$, C_2Cl_4, all Br-VSLSs, and CH_3I; other fluorinated species: CF_4, C_2F_6, C_3F_8, *c*-C_4F_8, *n*-C_6F_{14}, SF_6, NF_3, SO_2F_2, and desflurane.

Total column and upper-tropospheric and stratospheric abundance observations are available for some species based on ground-based or satellite-based remote sensing methods.

Emissions, along with global and hemispheric mean mole fractions, are estimated using a 12-box model of atmospheric transport and chemistry, constrained using baseline atmospheric data and following a Bayesian inverse method described in Rigby et al. (2011; 2014). The model parameterizes the advection and eddy diffusion of trace gases between four zonal-mean boxes (separated at the equator and 30° N and S) for three vertical levels (separated at 500 and 200 hPa; e.g., Cunnold et al., 1983; Rigby et al., 2013). Trace gas lifetimes in the 12-box model are calculated based on rate constants for the reaction with the hydroxyl radical given in Burkholder et al. (2019), hydroxyl radical abundances described in Rigby et al. (2013), and steady-state stratospheric lifetimes as described in the *Annex* unless a different reference is given. The box model has undergone some minor changes since the previous Assessment, most notably the removal of some smoothing constraints on the emissions. Consequently, emissions and global mole fractions reported here may differ slightly from those reported in previous Assessments or in previously published literature. Similarly, other small differences primarily resulted from updated calibrations and usage of different datasets

Box 1-1. Methods for Determining Atmospheric Abundances

As noted by Hall et al. (2014), "there are many factors that can lead to differences in the data records collected by different groups…. Perhaps the most fundamental of these is the calibration scale upon which the measurements are based." The purpose of this box is to highlight the importance of calibration methods and to give insight into some of the basic principles. For the observational data presented in this chapter, there are two principal calibration approaches, depending on whether these observations are based on in situ (including flask collection-based) or remote sensing measurements (**Box 1-1 Figure 1**).

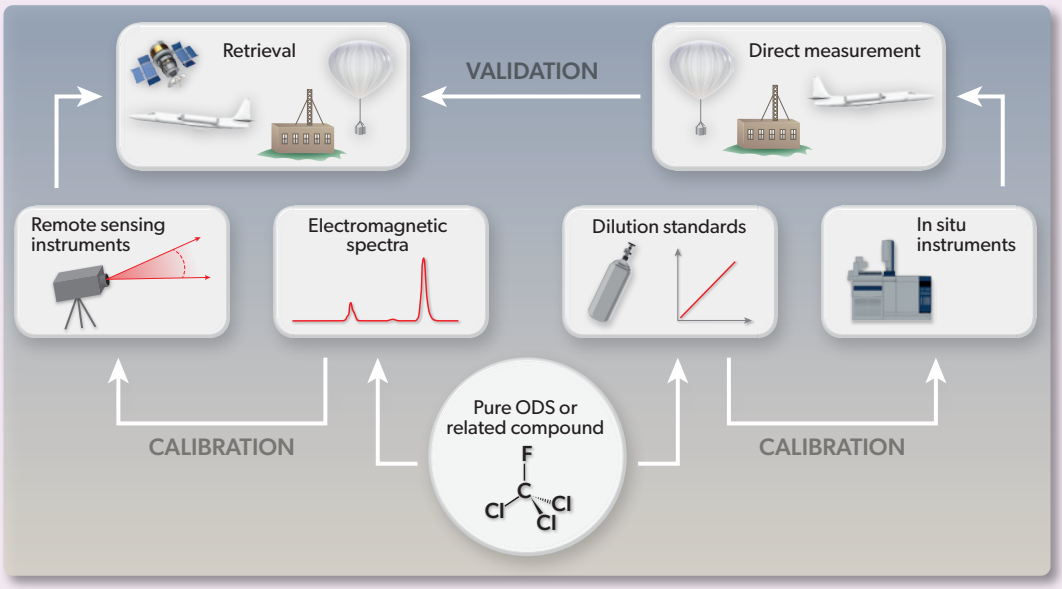

Box 1-1 Figure 1. Schematic of the processes used to calibrate global observations.

In situ measurement calibrations (e.g., Prinn et al., 2000; Laube et al., 2010) are typically based on the dilution of pure chemicals with gases containing virtually no trace species, such as oxygen-free nitrogen or synthetic air mixtures. Such a dilution can be static (i.e., mixing in canisters or other enclosures) or dynamic (i.e., in a continuous gas stream), the latter often being the preferred option for more reactive species, as these can be unstable when stored in canisters over longer periods. Due to the very low abundances of many of the ODSs and related species in the atmosphere, most dilutions have to take place over 10 to 13 orders of magnitude in order to reach a relevant concentration range. The determination of the amount of the to-be-calibrated species that is present initially is therefore of utmost importance. This includes ensuring and, if necessary, improving the purity of said substance (e.g., through freeze-drying cycles), as well as very accurate and precise methods of quantifying weight or volume (the latter being an approximation to mass-calibrated measurements after considerations of molar volume and ideal gas behavior). Often, one or several species with well-established calibration scales are also added as an "internal reference." Once diluted, the mixture is then analyzed with common measurement techniques such as cryogenic extraction from the main air components, followed by gas chromatographic separation and, for instance, detection with a mass spectrometer or an electron capture detector.

These calibration scales can then be transferred onto so-called "secondary standards," which are measured close in time and often consist of compressed tropospheric air samples in 30–50 L metal cylinders with passivated internal surfaces. For the long-term operation of global networks, it can be necessary to transfer the calibration scales further onto tertiary and even quaternary standards to ensure that results from all instruments on each field station are consistent with each other.

Remote sensing techniques use quantitative molecular spectroscopy to convert the strength of an absorption or emission feature in an atmospheric spectrum into abundances or concentrations, in line with the Beer-Lambert law. Concentrations of the halogenated species measured by remote sensing techniques (in **Table 1-2**) were derived using reference spectroscopy recorded in the laboratory, in particular air-broadened measurements of the target gas over a range of appropriate atmospheric temperatures and pressures. Spectroscopic parameters are made available in databases such as HITRAN (Gordon et al., 2021) or GEISA (Delahaye et al., 2022), which include uncertainty estimates on these reported parameters. Further work involves direct comparisons of in situ and remote sensing time series of trace gas abundances in ambient air, but the intercalibration of the respective scales is often complicated by the fact that these techniques give access to different quantities, e.g., surface concentrations in comparison to vertical profiles in the upper troposphere/lower stratosphere (UTLS), or to partial or total column abundances. However, advances have been made more recently for approaching these comparisons, as reported, e.g., in Prignon et al. (2019) for HCFC-22.

The enormous efforts that have gone into comparing, harmonizing, and improving calibration scales and quantifying and resolving potential differences between networks and groups (e.g., Jones et al., 2011; Hall et al., 2014; and the work of WMO Global Atmosphere Watch Calibration Centres) have been vital for ensuring the quality and comparability of the data underlying this and previous Assessments (**Figures 1-1** and **1-2**). The existence of several independent calibration scales for a given species is an essential part of the independent verification approach that is a key component of advancing scientific understanding, especially for monitoring the impacts of the Montreal Protocol and its subsequent Amendments. Some recent examples that also highlight the continued importance of these efforts are the comparison of long-term trends in the upper troposphere and stratosphere based on the ACE-FTS (Atmospheric Chemistry Experiment - Fourier Transform Spectrometer) satellite instrument (Steffen et al., 2019; Bernath et al., 2020; Bernath et al., 2021) with ground-based observations, the reevaluation and concentration range expansion of known species' calibrations such as CFC-11 or *c*-C_4F_8 (Montzka et al., 2018; Mühle et al., 2019), the quantification of isomeric impurities in more abundant species (Laube et al., 2016; Droste et al., 2020), and the detection of new species (Vollmer et al., 2019, 2021).

for calculation of hemispheric and global annual mole fractions. There are also small differences in global steady-state lifetimes, compared to the values reported in the *Annex*, due to differences in the model hydroxyl radical concentration and model transport.

For the long-lived species that are primarily of anthropogenic origin, we can use these global mole fraction and emissions estimates, as well as ozone depletion potentials (ODPs) as summarized in the *Annex*, to estimate radiative forcing, CO_2-equivalent emissions, and, for ODSs, CFC-11-equivalent emissions. As explained in detail in **Box 5-1**, we use the term "radiative forcing" to mean "stratosphere-adjusted radiative forcing" throughout this Assessment. For *Chapters 1* and *2*, estimates of the global radiative forcing due to most trace gases are derived as the global mean lower-tropospheric mole fraction multiplied by the radiative efficiency for each gas, using, for consistency with previous Assessments, stratosphere-adjusted radiative forcing values from the *Annex*. For methane (CH_4), nitrous oxide (N_2O), and CF_4 (for the latter we assume a preindustrial mole fraction of 40 ppt) we use the expression for radiative forcing from Ramaswamy et al. (2001). CO_2-equivalent emissions are calculated as the product of the emissions of each trace gas and its global warming potential (GWP) over a 100-year time horizon (also taken from the *Annex*). While other metrics are available to compare the climate impact of the emissions of different HFC species (e.g., Forster et al., 2021, we have used 100-year GWPs here because they are widely used, including in the Kigali Amendment. Uncertainties in radiative forcing and CO_2-equivalent emissions are due to the uncertainty in the atmospheric observations and trace gas lifetimes. They do not include uncertainties in radiative efficiencies or GWPs. Note that we use the recently updated radiative efficiencies from Hodnebrog et al. (2020) and Andersen et al. (2021) based on improved stratospheric estimates by Shine and Myhre (2020); this has resulted in higher GWPs for many species.

The production and emission of ODSs are closely linked to so-called "banks" of these compounds, a term that refers to an existing quantity of an ODSs that is contained in, e.g., equipment or stockpiles, and will eventually be released to the atmosphere if no action to the contrary is taken. Banks are only briefly mentioned here; for a more extensive discussion, we point the reader to *Chapter 7*. Finally, we are not aware of any peer-reviewed literature quantifying the impact of the COVID-19 pandemic on global or regional ODS abundances or emissions.

1.1 SUMMARY OF FINDINGS FROM THE PREVIOUS OZONE ASSESSMENT

Chapter 1 of the 2018 Assessment (Engel, Rigby et al., 2018) provided updates on ozone-depleting substances (ODSs) and other gases of interest to the Montreal Protocol, except for hydrofluorocarbons (HFCs), which were covered in Chapter 2.

During the five-year period 2012–2016, total tropospheric chlorine from substances controlled under the Montreal Protocol was declining at a rate of 12.7 ± 0.9 ppt yr^{-1}, with a slower-than-projected decrease in chlorofluorocarbon (CFC) concentrations and a slower-than-projected increase in first-stage replacement compounds (i.e., HCFCs) as compared to the 2014 A1 scenario. An increase in global CFC-11 emissions after 2012 was documented, suggesting new production not reported to the United Nations Environment Programme (UNEP). Stable or even increasing emissions of some of the low-abundance CFCs were also noted. The growth rate of chlorine from HCFCs declined relative to previous years and was comparable to values observed in the early 2000s.

The decrease of chlorine from controlled substances between 2012 and 2016 was partly offset by increases in the mainly natural CH_3Cl and mainly anthropogenic very short-lived gases (VSLSs), which are not controlled under the Montreal Protocol. Dichloromethane (CH_2Cl_2) was found to account for most of the rise in total tropospheric chlorine from VSLSs, and a substantial fraction of its global emissions were attributed to southern and eastern Asia.

Total chlorine entering the stratosphere from long-lived ODSs was reported to have declined by 405 ppt (12%) between the 1993 peak and 2016. While the VSLS contributions increased over the 2012–2016 period, their contribution to total chlorine remained below 4%. Hydrogen chloride (HCl), the major chlorine component in the upper stratosphere, decreased by about 6% between 2005 and 2016, consistent with the decline in total chlorine entering the stratosphere.

Total tropospheric bromine from controlled substances was reported to decline at a rate of 0.15 ± 0.04 ppt yr^{-1} between 2012 and 2016, primarily driven by a decline in atmospheric halons, with a smaller contribution from a decrease in methyl bromide (CH_3Br) abundance. Despite its overall decreasing trend, CH_3Br increased during 2015–2016 for the first time in a decade, most

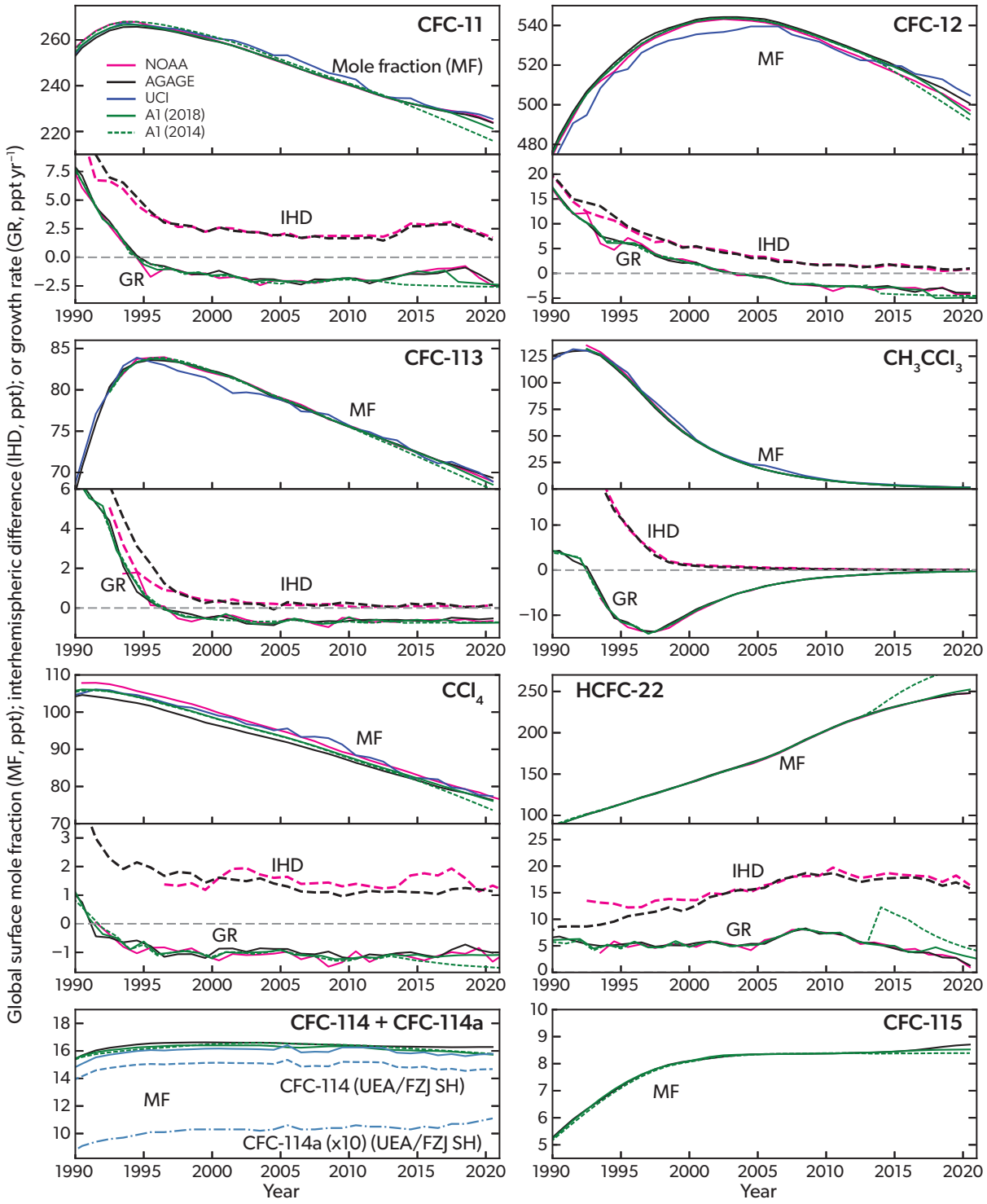

Figure 1-1. Annual mean mole fractions (MF) between 1990 and 2020 of ozone-depleting substances (except minor species; see *Introduction*), as measured from ground-based sampling networks and as simulated from the A1 scenarios of the previous two Ozone Assessments (dashed green line, Harris, Wuebbles et al., 2014; solid green line, Carpenter, Daniel et al., 2018). Mole fractions from the NOAA (red), AGAGE (black), and UCI (blue) networks were calculated as mid-year-centered global annual mole fractions. Annual mole fractions from UEA/FZJ (steel blue) represent mid-year-centered annual mole fractions observed in unpolluted whole-air flask samples collected at Cape Grim, Australia. Annual mean mole fractions from the A1 scenarios are interpolations from the simulated January-centered annual mole fractions. For some gases, we also show inter-hemispheric differences (IHD; defined as NH minus SH mole fraction; dashed lines) and growth rates (GR; ppt yr^{-1}; solid lines) in the lower panels, using the same color scheme as in the corresponding upper panels. Note that, compared to values reported in the last Assessment,

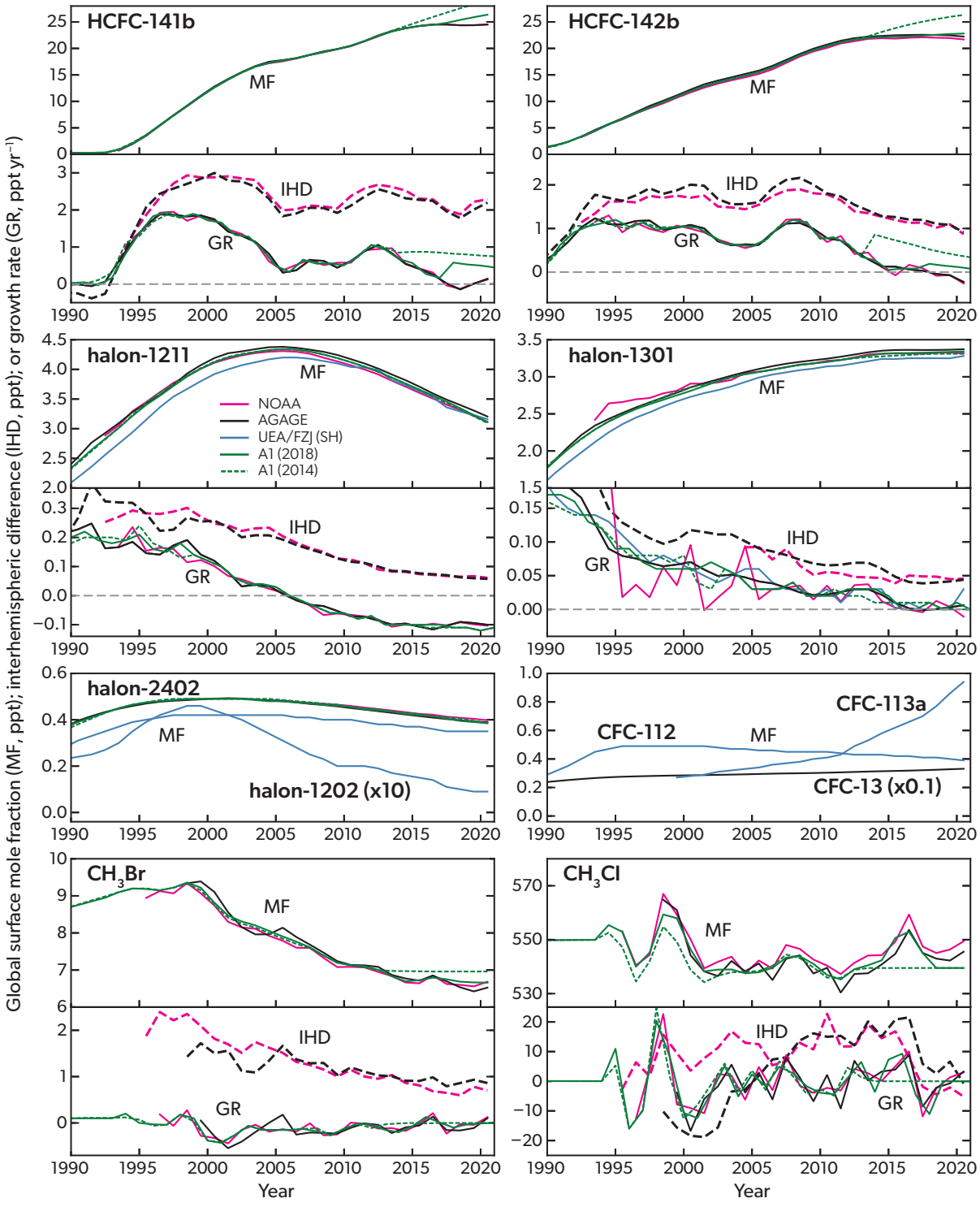

there were several changes in the NOAA reported global annual mean mole fractions associated with termination or changing instrumentations and updates in calibrations: The global annual mean mole fractions for CCl_4 were calculated from NOAA in situ measurements in this Assessment, whereas NOAA flask and in situ measurements were included for the calculation for the previous Assessments; the calibration of NOAA in situ measurements of CFC-12 were reassessed since the last Assessment, and the reported mole fractions of halon-1301 were scaled by a factor of 1.015 to be consistent with measurements from a new instrument. AGAGE CFC-113 data prior to approximately 2011 were measured by GC-ECD and likely contain a small fraction (0.2–0.4 ppt) of CFC-113a. Global GRs and IHDs derived from UCI data are not plotted because they show much higher variability, likely related to more regional influence on this sampling network.

likely not related to anthropogenic sources. Total bromine entering the stratosphere from well-mixed ODSs also continued to decline, with a total decrease of 2.4 ppt (15%) between the 1998 peak and 2016. Brominated VSLSs, of primarily natural origin, were found to contribute about 25% to total bromine in 2016 and showed no long-term changes. Total stratospheric bromine derived from bromine monoxide (BrO) observations decreased by about 8% from 2004 to 2014, which is again consistent with the decline in total bromine entering the stratosphere.

Equivalent effective stratospheric chlorine (EESC) was assessed to have declined from its maximum value in polar regions by about 9% and in mid-latitudes by about 13–17%. The rate at which EESC was decreasing had slowed, in accordance with a slowdown of the decrease in tropospheric chlorine. A new and improved methodology for estimating EESC was found to result in smaller recovery rates of stratospheric halogen loading with respect to their maximum peak, especially in mid-latitudes.

The influence of CFC and HCFC emissions on climate was assessed in terms of their equivalent in gigatonnes of carbon dioxide (CO_2-equivalent emissions) using 100-year GWPs. While the direct radiative forcing of CFCs continued to be much higher than for HCFCs, the CO_2-equivalent emissions of CFCs and HCFCs were roughly equal in 2016.

1.2 ABUNDANCES, TRENDS, LIFETIMES, AND EMISSIONS OF LONGER-LIVED HALOGENATED SOURCE GASES

1.2.1 Chlorofluorocarbons (CFCs)

Observations of Atmospheric Abundance. Global mole fractions of the two most abundant CFCs, i.e., CFC-12 (CCl_2F_2) and CFC-11 (CCl_3F), continued to decline since 2016, reaching approximately 499 ppt and 224 ppt, respectively, in 2020 (**Figure 1-1**). The atmospheric abundance of CFC-12 has fallen increasingly rapidly throughout this period, with the rate of decline increasing from 3.3 ppt yr^{-1} in 2015–2016 to around 4.0 ppt yr^{-1} in 2019–2020 (**Figure 1-1** and **Table 1-1**). For CFC-11, a slowdown in the rate at which the global abundance was falling after 2012 had been reported in the last Assessment (Engel, Rigby et al., 2018; Montzka et al., 2018). A major driver of this slowdown from around 2 ppt yr^{-1} to around 1.3 ppt yr^{-1} has now been identified as renewed emissions from eastern China (Rigby et al., 2019; Adcock et al., 2020), with satellite-based evidence also indicating CFC-11 sources in the vicinity of the Indian and Arabian peninsulas adding to the slowdown over 2013–2018 (Chen et al., 2020). More recently, Park et al. (2021) and Montzka et al. (2021) reported another turnaround, i.e., an increase in the rate of decline in CFC-11 abundance since 2018 that is equivalent to a return to pre-2012 values. A thorough and detailed overview on all recent findings related to atmospheric CFC-11 can be found in the *"Report on the Unexpected Emissions of CFC-11"* (WMO, 2021). As an update to the findings of that report, global CFC-11 mole fractions decreased from 2019 to 2020 even faster than from 2018 to 2019, by an unprecedentedly large amount of 2.3 ppt yr^{-1}. In addition, several observation-based publications have since confirmed unusually high abundances of various CFCs, most notably CFC-11 and CFC-12, in different parts of China during 2009–2019 (Zeng et al., 2020; Yang et al., 2021; Benish et al., 2021; Huang et al., 2021; Lin et al., 2021). However, it should be noted that quantitative conclusions from these latter studies are limited due to one or more factors, such as scarcity of the data, lack of regional background mole fractions, higher uncertainties, and potential calibration or measurement biases indicated by reported CFC mole fractions lower than their global background levels in the same time intervals. The inter-hemispheric differences (IHDs) derived for the two main CFCs are consistent with the

Table 1-1. Annual mean mole fractions, mole fraction changes, global emissions, and CO_2-equivalent emissions (based on 100-year GWPs) of ozone-depleting gases measured from ground-based sampling networks (except minor species; see *Introduction*). Emission uncertainties are given as 1 standard deviation (1-sigma) and more specific details can be found in the footnote.

General footnote: Mole fractions in this table represent independent estimates based on air sampling at Earth's surface from different research groups for the years indicated. Results in bold text are estimates of globally averaged annual mole fractions. Regional data from relatively unpolluted sites are shown (in italics) where global estimates are not available, where global estimates are available from only one network, or where data from global networks do not represent independent calibration scales. Absolute changes (ppt yr^{-1}) are calculated by subtracting the 2019 annual mole fractions from the 2020 annual mole fractions; relative changes (% yr^{-1}) are this difference relative to the 2019 value. Annual mole fractions reported by AGAGE were calculated based on the simulated surface mole fractions using a 12-box inverse model (e.g., Cunnold et al., 1983; Rigby et al., 2013) that were optimized to represent the AGAGE in situ observations made at remote locations. Annual mole fractions reported by NOAA are weighted annual averages from the measured monthly mole fractions from whole-air flask measurements made at remote locations, except for CFC-11, CFC-12, and CFC-113, which include both NOAA in situ and flask measurements at those remote locations, and CCl_4, which includes only NOAA in situ measurements. Differences to the 2016 values reported in the last Assessment primarily result from either minor box model changes (AGAGE data: <0.2 ppt for all species except CFC-12 and CH_3Cl <1.6 ppt) or updated calibrations and usage of different datasets for the calculation of hemispheric and global annual mole fractions (NOAA data: <0.3 ppt); i.e., the calibration of NOAA in situ CFC-12 measurements was adjusted to improve the overall consistency among the six sampling and measurement locations. Mole fractions reported by UEA/FZJ are annual averages of measured mole fractions from whole-air flask samples collected at Cape Grim, Australia, and are based on volumetric calibration scales, except for halon-1211 and halon-1301 (NOAA-based). Mole fractions reported by NIES are annual average mole fractions from in situ measurements made in Japan and are based on a gravimetric calibration scale. Mole fractions reported by UCI are based on flask air samples in the Pacific region spanning both hemispheres and are based on volumetric calibration scales. Reported global annual emissions were calculated based on the AGAGE and NOAA observations using the 12-box model mentioned above; "n.a." indicates that emissions were not available. These observations are updated from the following sources: Butler et al. (1998); Laube et al. (2014); Laube et al. (2016); Miller et al. (2008); Montzka et al. (2003); Montzka et al. (2015); Montzka et al. (2021); Newland et al. (2013); O'Doherty et al. (2004); Prinn et al. (2018); Rigby et al. (2014); Simmonds et al. (2017); Simpson et al. (2007); Vollmer et al. (2016); Vollmer et al. (2018); Yokouchi et al. (2006); AGAGE (agage.eas.gatech.edu); NOAA (gml.noaa.gov/dv/site); UCI (data.ess-dive.lbl.gov/view/doi:10.3334/CDIAC/ATG.002).

Notes:
[1] AGAGE calibrations were specified in Prinn et al. (2018).
[2] The NOAA data used the same calibrations as those published in the previous Assessment, except for H-1301 (see caption of **Figure 1-1**).
[3] Measurements of CFC-114 from AGAGE are a combination of CFC-114 and the CFC-114a isomer.
[4] CFC-114 and CFC-114a are quantified separately by UEA/FZJ.

Table 1-1. *See caption on facing page.*

Chemical	Mole Fraction (ppt)		Change (2019–2020)		Emissions (Gg yr^{-1})		CO_2-eq. Emissions (Tg yr^{-1})	Network
	2016	2020	(ppt yr^{-1})	(% yr^{-1})	2016	2020	2020	
CFCs								
CCl_3F (CFC-11)	229.4	223.8	–2.2	–1.0	67 ± 10	48 ± 10	310 ± 64	AGAGE[1]
	230.0	224.0	–2.5	–1.1	77 ± 10	46 ± 10	298 ± 62	NOAA[2]
	230.0	225.5	–2.0	–0.9	n.a.	n.a.	n.a.	UCI
CCl_2F_2 (CFC-12)	514.5	500.7	–3.9	–0.8	30 ± 21	27 ± 21	334 ± 268	AGAGE
	511.9	497.2	–4.2	–0.8	36 ± 21	23 ± 20	282 ± 252	NOAA
	515.6	504.7	–3.7	–0.7	n.a.	n.a.	n.a.	UCI
$CClF_3$ (CFC-13)	3.18	3.32	0.04	1.1	0.5 ± 0.2	0.6 ± 0.2	10 ± 3	AGAGE
CCl_2FCCl_2F (CFC-112)	*0.42*	*0.39*	*–0.01*	*–1.8*	*n.a.*	*n.a.*	*n.a.*	UEA/FZJ
CCl_2FCClF_2 (CFC-113)	71.5	69.4	–0.5	–0.7	6.5 ± 6.4	6.9 ± 6.0	45 ± 39	AGAGE
	71.5	68.9	–0.7	–1.0	5.5 ± 5.0	6.4 ± 4.8	42 ± 32	NOAA
	71.1	70.0	–1.1	–1.6	n.a.	n.a.	n.a.	UCI
CCl_3CF_3 (CFC-113a)	*0.66*	*0.94*	*0.09*	*10*	*n.a.*	*n.a.*	*n.a.*	UEA/FZJ
$CClF_2CClF_2$ (CFC-114)	16.28	16.28	–0.01	–0.03	2.3 ± 0.9	2.6 ± 0.9	24 ± 8	AGAGE[3]
	14.64	*14.68*	*0.03*	*0.2*	*n.a.*	*n.a.*	*n.a.*	UEA/FZJ[4]
CCl_2FCF_3 (CFC-114a)	*1.04*	*1.11*	*0.02*	*1.7*	*n.a.*	*n.a.*	*n.a.*	UEA/FZJ[4]
$CClF_2CF_3$ (CFC-115)	8.50	8.71	0.03	0.4	1.5 ± 0.5	1.0 ± 0.6	10 ± 5	AGAGE
	8.62	*8.86*	*–0.02*	*–0.2*	*n.a.*	*n.a.*	*n.a.*	NIES
HCFCs								
$CHClF_2$ (HCFC-22)	237.5	248.0	1.3	0.5	375 ± 53	348 ± 55	664 ± 104	AGAGE
	237.4	247.8	1.0	0.4	373 ± 51	337 ± 53	643 ± 102	NOAA
	242.3	256.1	3.3	3.1	n.a.	n.a.	n.a.	UCI
CH_3CCl_2F (HCFC-141b)	24.49	24.52	0.14	0.58	60 ± 9	58 ± 9	47 ± 7	AGAGE
	24.53	24.50	0.12	0.5	62 ± 8	56 ± 8	45 ± 7	NOAA
	24.6	25.8	–0.2	–0.8	n.a.	n.a.	n.a.	UCI
CH_3CClF_2 (HCFC-142b)	22.54	22.23	–0.23	–1.0	24 ± 4	19 ± 4	41 ± 10	AGAGE
	22.02	21.69	–0.26	–1.2	25 ± 4	19 ± 4	41 ± 10	NOAA
	23.2	22.8	0.00	0.0	n.a.	n.a.	n.a.	UCI
Halons								
CBr_2F_2 (halon-1202)	*0.014*	*0.009*	*–0.000*	*0.0*	*n.a.*	*n.a.*	*n.a.*	UEA/FZJ
$CBrClF_2$ (halon-1211)	3.59	3.21	–0.10	–3.0	3.2 ± 1.8	2.9 ± 1.6	6 ± 3	AGAGE
	3.51	3.11	–0.10	–3.2	3.4 ± 1.8	2.9 ± 1.6	6 ± 3	NOAA
	3.70	3.36	–0.09	–2.6	n.a.	n.a.	n.a.	UCI
	3.53	*3.16*	*–0.07*	*–2.3*	*n.a.*	*n.a.*	*n.a.*	UEA/FZJ
$CBrF_3$ (halon-1301)	3.36	3.37	0.01	0.18	1.2 ± 0.6	1.4 ± 0.6	10 ± 4	AGAGE
	3.31	3.32	–0.01	–0.3	1.3 ± 0.3	1.1 ± 0.5	9 ± 3	NOAA
	3.25	*3.28*	*0.03*	*0.8*	*n.a.*	*n.a.*	*n.a.*	UEA/FZJ
$CBrF_2CBrF_2$ (halon-2402)	0.41	0.39	0.00	–1.0	0.4 ± 0.1	0.5 ± 0.1	1.1 ± 0.3	AGAGE
	0.42	0.40	–0.01	–1.5	0.4 ± 0.1	0.4 ± 0.1	0.9 ± 0.3	NOAA
	0.36	*0.35*	*–0.00*	*0.0*	*n.a.*	*n.a.*	*n.a.*	UEA/FZJ
Chlorocarbons								
CH_3Cl (methyl chloride)	553.6	545.5	3.3	0.6	4699 ± 960	4720 ± 946	28 ± 6	AGAGE
	559.3	549.4	3.0	0.6	4756 ± 975	4718 ± 959	28 ± 6	NOAA
CCl_4 (carbon tetrachloride)	79.92	76.34	–1.01	–1.3	42 ± 15	41 ± 14	89 ± 30	AGAGE
	81.31	77.10	–1.32	–1.7	45 ± 15	46 ± 14	99 ± 31	NOAA
	81.9	77.4	–0.3	–0.4	n.a.	n.a.	n.a.	UCI
CH_3CCl_3 (methyl chloroform)	2.62	1.42	–0.23	–14	2.2 ± 2.0	2.3 ± 1.1	0.4 ± 0.2	AGAGE
	2.60	1.40	–0.22	–14	2.9 ± 1.8	2.2 ± 1.0	0.4 ± 0.2	NOAA
	3.05	1.47	–0.26	–15	n.a.	n.a.	n.a.	UCI
Bromocarbons								
CH_3Br (methyl bromide)	6.85	6.52	0.10	1.6	135 ± 21	131 ± 20	0.26 ± 0.04	AGAGE
	6.85	6.68	0.12	1.9	136 ± 20	134 ± 20	0.27 ± 0.04	NOAA

aforementioned accelerated mole fraction changes, as they have also been decreasing after 2018 (**Figure 1-1**).

Measurements of the 2014–2020 trends in northern hemisphere (NH) CFC-11 and CFC-12 abundances made using ground-based Fourier transform infrared (FTIR) spectroscopy at Jungfraujoch, Switzerland, agree within uncertainties with those derived using surface-based in situ observations (**Table 1-2** and **Figure 1-2**). Upper-tropospheric NH trends derived from ACE-FTS measurements are slightly less negative than their ground-based counterparts (**Table 1-2**). The causes for these differences are not entirely clear; however, it should be noted that due to the irregularity of the ACE-FTS sampling, trends tend to be more robust over longer time periods. Recently it has been shown that long-term CFC-11 near-surface abundances can be extracted from the nadir-viewing AIRS (Atmospheric InfraRed Sounder) instrument; the retrieved trends agree with those derived from ground observations within their 95% confidence intervals (Chen et al., 2020). This approach opens up the possibility of monitoring CFC-11 via other nadir sounders such as the Cross-track Infrared Sounder (CrIS) and the Infrared Atmospheric Sounding Interferometer (IASI), both of which offer a greater density of global coverage relative to ACE-FTS.

CFC-113 (CCl_2FCClF_2) near-surface global mole fractions also have continued to decline, from 72 ppt in 2016 to 69 ppt in 2020. The rate of decline in CFC-113 has remained relatively constant at around 0.6 ppt yr^{-1}, and its IHD has remained approximately stable (**Figure 1-1**). The 2014–2020 trends in NH CFC-113 from the ACE-FTS retrievals do not agree well with surface measurement–derived values (**Table 1-2**). The ACE-FTS retrieval of CFC-113 has a number of artifacts that contribute toward this trend bias; in Bernath et al. (2021), the ACE-FTS trend is ~70% more negative than that derived from near-surface observations.

The previous Assessment reported a slowdown in the decline of the combined mole fraction of the CFC-114 ($CClF_2CClF_2$) and CFC-114a (CCl_2FCF_3) isomers. This has continued, such that there has been virtually no change in global abundance between 2016 and 2020 (**Figure 1-1** and **Table 1-1**; update from Vollmer et al., 2018). In 2020, the global mean mole fraction of combined CFC-114 and CFC-114a was still approximately 16 ppt, while the mole fraction of CFC-114a (only available from measurements in the Southern Hemisphere) increased slightly from 1.0 ppt to 1.1 ppt since 2016 (update of Laube et al., 2016). On a regional scale, enhanced mole fractions of CFC-114 have been observed in air masses above China (Zeng et al., 2020; Yang et al., 2021; Benish et al., 2021), though the portions of these signals caused by its hard-to-separate isomer CFC-114a are not quantified.

In the 2018 Assessment, it was reported that the mole fraction of CFC-115 ($CClF_2CF_3$) had grown since 2012, reaching 8.5 ppt in 2016 (update from Vollmer et al., 2018). This trend has continued, with CFC-115 reaching 8.7 ppt in 2020. For CFC-13 ($CClF_3$), the previously reported slow growth has also continued, and the global mole fraction increased from 3.18 ppt in 2016 to 3.32 ppt in 2020 (update from Vollmer et al., 2018).

Since the last Assessment, CFC-112 (CCl_2FCCl_2F), which had a southern hemisphere (SH) mole fraction of 0.42 ppt in 2016, has continued to decline in the atmosphere, to 0.39 ppt in 2020. The abundance of its isomer CFC-112a ($CClF_2CCl_3$) has, however, started to increase recently in the SH, from 0.07 to 0.08 ppt between 2016 and 2020 (update of Laube et al., 2014). In addition, CFC-113a (CCl_3CF_3) mole fraction increases have accelerated for a second time in the Southern Hemisphere (first around 2012, and then again after 2016), reaching 0.95 ppt in 2020 (compared to 0.66 ppt in 2016) (update from Adcock et al., 2018; **Table 1-1**).

For CFC-216ba ($CClF_2CClFCF_3$), no significant change in SH abundance was observed since the last Assessment (0.04 ppt, update from Kloss et al., 2014), and there is no update available for CFC-216ca ($CClF_2CF_2CClF_2$; 2016: 0.02 ppt).

Emissions, Lifetimes, and Radiative Forcings. Atmospheric lifetimes of CFCs have not been reevaluated since the 2014 Assessment, although one recent publication has assessed the influence of the oceanic reservoir to be currently of no significant importance to the CFC-11 lifetime (Wang et al., 2021). Therefore, the lifetime estimates used here—which underpin all emission estimates—are again still largely based on SPARC (2013), with small

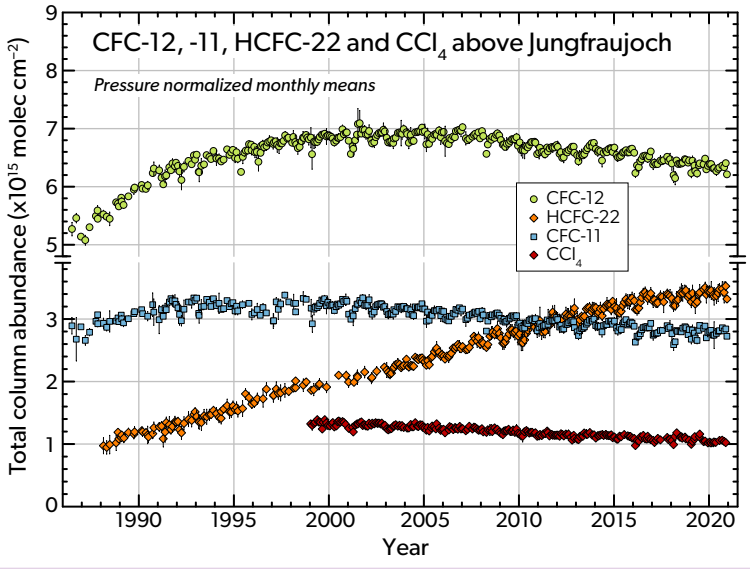

Figure 1-2. Monthly mean total vertical column abundance time series of CFC-12, CFC-11, HCFC-22, and CCl_4 derived from the long-term FTIR monitoring program conducted at the Jungfraujoch station, Switzerland (46.5°N), from 1986 to 2021 (updated from Zander et al., 2008; Gardiner et al., 2008; Rinsland et al., 2012; and Prignon et al., 2019). Note the discontinuity in the vertical scale.

Table 1-2. Annual trends of selected ODSs, CF_4, and SF_6 for the 2014–2020 time period derived from surface measurements as well as ground-based and satellite remote sensing observations. Trends derived from in situ measurements were based on linear regression of the hemispheric annual mole fractions calculated from the NOAA and AGAGE observations for 30–90°N. Their associated uncertainties were calculated from uncertainties in the slopes and the differences in the relative trends derived from NOAA and AGAGE observations. For CF_4, only AGAGE data were used. For ground-based remote sensing observations, relative annual rates of change were computed from FTIR observations at Jungfraujoch station, Switzerland, with the bootstrap resampling tool described in Gardiner et al. (2008). All uncertainties are estimated at 2-sigma. For satellite remote sensing observations, the ACE-FTS trends were determined for 0–60°N, from the least-squares linear regression of averaged mixing ratios in molecule-dependent upper-tropospheric altitude ranges (updated from Bernath et al., 2021). For CF_4, the trend was calculated over the altitude range 25.5–40.5 km due to problems with the retrieval in the troposphere. Trend uncertainties were calculated from uncertainties in the slopes and intercepts of the regression lines. As opposed to the in situ-based mole fractions, those derived from ACE-FTS and FTIR are volume-based and not dry air, which may account for part of the differences.

Annual Trend 2014 – 2020 (% yr^{-1} relative to 2017)			
Substance	**In situ (surface)**	**Remote sensing ground-based (total column)[1,2]**	**Remote sensing satellite (upper troposphere)[3,4]**
CFC-11	–0.61 ± 0.10	–0.72 ± 0.19	–0.46 ± 0.04
CFC-12	–0.69 ± 0.02	–0.72 ± 0.09	–0.59 ± 0.04
CFC-113	–0.84 ± 0.04	N/A	–1.58 ± 0.05
CCl_4	–1.24 ± 0.12	–1.31 ± 0.22	–1.14 ± 0.05
HCFC-22	1.19 ± 0.19	1.36 ± 0.13	1.43 ± 0.15
HCFC-141b	0.23 ± 0.24	N/A	–0.82 ± 0.29
HCFC-142b	–0.24 ± 0.22	0.50 ± 0.73	0.61 ± 0.34
CF_4	1.07 ± 0.02	0.93 ± 0.07	1.07 ± 0.06
SF_6	3.56 ± 0.11	3.86 ± 0.14	3.73 ± 0.15

Notes:
[1] The Jungfraujoch FTIR trends are based on observations of CFC-11, CFC-12 (updated from Zander et al., 2008), CCl_4 (updated from Rinsland et al., 2012), HCFC-22 (updated from Prignon et al., 2019), HCFC-142b (updated from Mahieu et al., 2017), CF_4 (updated from Mahieu et al., 2014b), SF_6 (updated from Zander et al., 2008). Note that the HCFC-142b trend is not significant at 2-sigma uncertainty.
[2] The methods used for the determination of the uncertainties affecting the retrieved trends for remote sensing–based observations benefited from recent research developments that account for the autocorrelation and heteroskedasticity (i.e., changing variance with time) that are often present in such geophysical time series. Previous statistical tools used random permutations of the residuals (differences between the fitted function and the observations) in order to assess the trend distribution and associated uncertainty (Gardiner et al., 2008). This approach has the disadvantage of failing to preserve the possible autocorrelation and heteroskedasticity of the residuals, since they are randomly resampled. More recent studies (Friedrich et al., 2020a, 2020b) present improved statistical tools based on the autoregressive wild bootstrap method that do not involve any permutation of the residuals. They are therefore more appropriate for geophysical time series and are expected to provide a more reliable estimate of the uncertainties associated with the trends. This is particularly important when dealing with small rates of change.
[3] Uncertainties are also 2-sigma but currently not derived in a way that is comparable to the other data shown in this table.
[4] Remote sensing satellite trends are taken solely from ACE-FTS measurements (updated from Bernath et al., 2021).

changes due to reaction rate updates (Burkholder et al., 2019), and are given in the *Annex*.

CFC emissions to the atmosphere have for several years been expected to be due only to leakage from banks and therefore to decline with time as the size of the banks decreases. This appears to be qualitatively the case for CFC-12, as its emissions have continued to decrease since the previous Assessment. The aforementioned *"Report on the Unexpected Emissions of CFC-11"* (WMO, 2021) also included research on CFC-12, as the two species are often co-produced. Similar to CFC-11, a slowdown in the decline of emissions was also observed for CFC-12 between 2010 and 2017, followed by a small but not significant emission reduction between 2017 and 2019. In 2020, the fall in CFC-12 emissions continued, reaching a new all-time minimum of approximately 25 Gg yr^{-1} (**Table 1-1**, **Figure 1-3**).

Concurrent with the recent accelerated decrease in CFC-11 atmospheric abundances, CFC-11 emissions have declined markedly in recent years: from 72 Gg yr^{-1} in 2016 to 47 Gg yr^{-1} in both 2019 and 2020 (**Table 1-1**), corresponding to a drop of more than 30%. Importantly, the research carried out after the renewed increases in emissions of CFC-11 were observed (Montzka et al., 2018) highlighted several factors that currently limit the ability to accurately estimate when emissions of CFCs and other long-lived controlled species diverge from expectations. Among these factors are uncertainties in emissions from banks (e.g., Lickley et al., 2020; see also *Chapter 7*) and variability in air transport to and from their main sink region in the stratosphere (Montzka et al., 2018; Ray et al., 2020; Laube et al., 2020; Lickley et al., 2021; Ruiz et al., 2021). Also challenging, in terms of pinpointing the sources of such emissions, is the lack of precise, accurate, frequent, and regular measurements in many regions of the world (Rigby et al., 2019). Emission uncertainties are highlighted in **Box 1-2**.

Emissions of CFC-113 are estimated at 6.0 Gg yr^{-1} in 2016 and 6.6 Gg yr^{-1} in 2020. However, since these annual estimates have relatively large uncertainties of around 5–6 Gg yr^{-1}, this is not a significant change. Importantly, CFC-113 emissions remain much lower than in the 1990s; nevertheless, a significant further decrease should be detectable over longer timescales, and its absence has been notable for some time (Lickley et al., 2020; **Figure 1-3**).

Of the less abundant CFCs, CFC-13 emissions plateaued at around 0.5 ± 0.2 Gg yr^{-1} in the decade leading up to the last

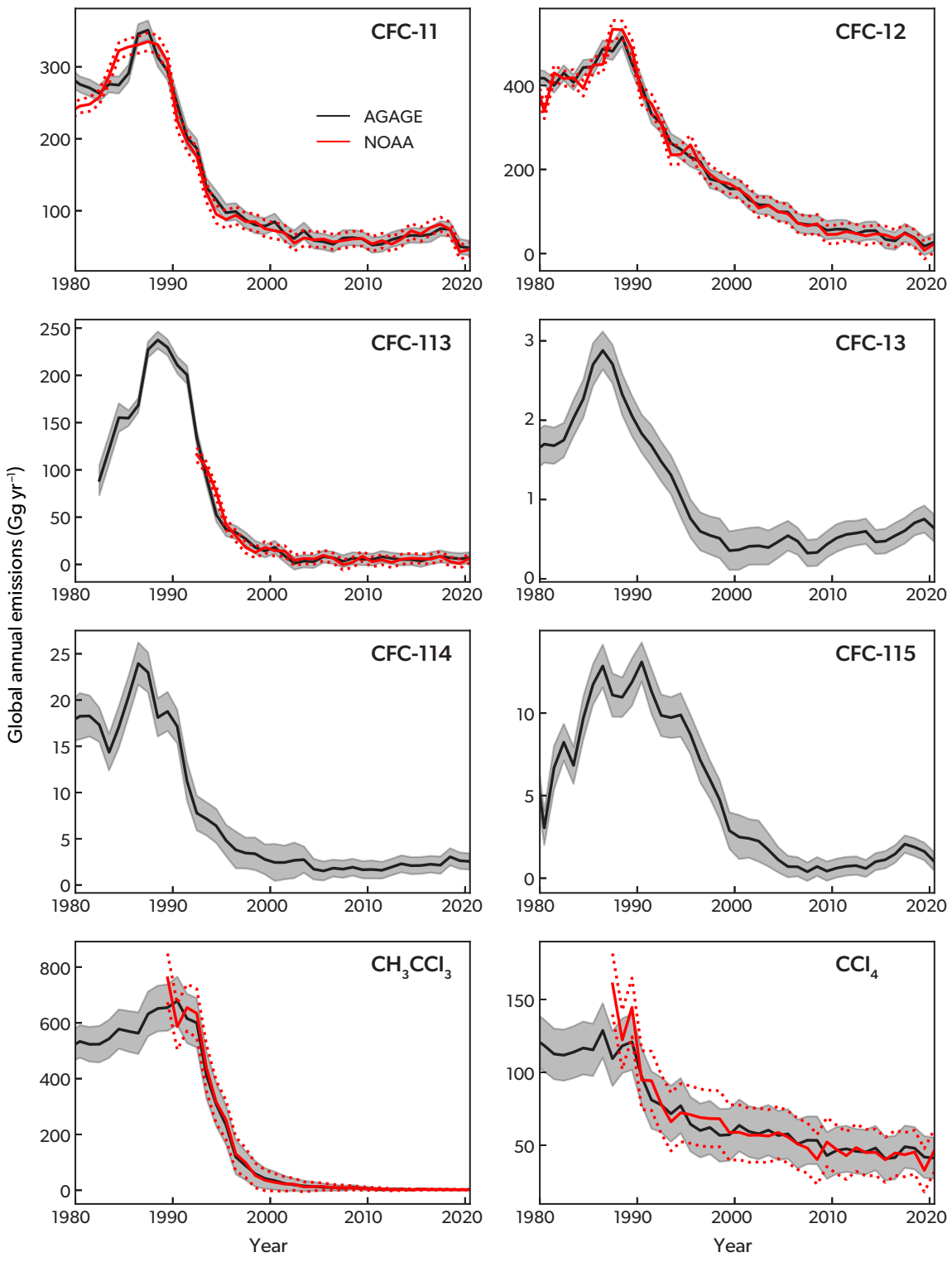

Figure 1-3. *Continued on next page.*

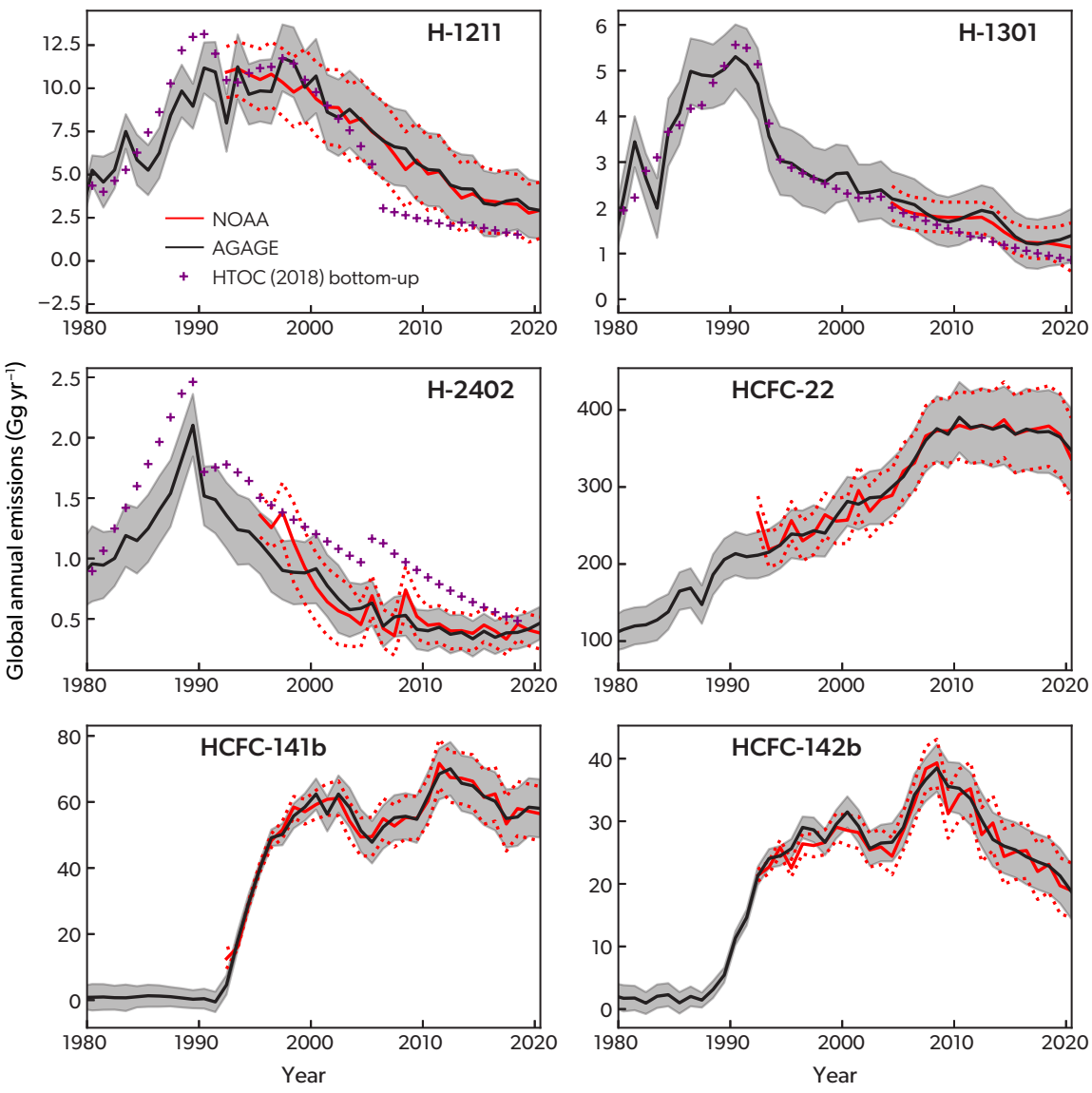

Figure 1-3. *Continued from previous page.*
Atmospheric observation-based "top-down" global emission estimates (Gg yr^{-1}) for long-lived ozone-depleting substances with equivalent chlorine at the surface greater than 1 ppt in 2020, and emission inventory-based "bottom-up" global emissions estimates for H-1211, H-1301, and H-2402. Top-down emissions were calculated using a global 12-box model and a Bayesian inverse modeling framework (Cunnold et al., 1983; Rigby et al., 2013) using atmospheric data from AGAGE (black) and NOAA (red) measurement networks. For top-down estimates, losses for CFCs were assumed to occur only in the stratosphere (but no dynamical correction to account for changes in stratosphere-troposphere fluxes, as in Montzka et al., 2021, is included here), and total lifetimes were taken from the *Annex*. For other gases, OH rate constants were taken from Burkholder et al. (2019), and stratospheric lifetimes were taken from the *Annex*, with the exception of CCl_4, which was taken from SPARC (2016) but using the oceanic lifetime from Suntharalingham et al. (2019). Global steady-state lifetimes for each species (in years) were as follows: CFC-11 (55), CFC-12 (103), CFC-113 (95), CFC-13 (640), CFC-114 (191), CFC-115 (664), CH_3CCl_3 (4.8), CCl_4 (29.9), H-1211 (16.0), H-1301 (71.8), H-2402 (28.0), HCFC-22 (11.3), HCFC-141b (8.7) and HCFC-142b (17.1). Small differences may appear between global lifetimes presented in the *Annex* and those calculated by the 12-box model due to assumed OH and model transport. The gray shading and dotted red lines show the 1-standard deviation uncertainties. The Bayesian approach uses bottom-up emissions estimates as an a priori constraint. Details of the a priori constraints used are detailed in Rigby et al. (2013), Rigby et al. (2014), Simmonds et al. (2017), Vollmer et al. (2016), and Vollmer et al. (2018), where the year-to-year prior constraint on emissions was assumed to be 20% of the maximum emissions. Uncertainties in the lifetimes are taken from SPARC (2013) and applied using the method presented in Rigby et al. (2014). Bottom-up estimates have been updated for the halons using data from HTOC (2018) and are shown as purple crosses.

Assessment, and this has continued with an estimate of 0.6 ± 0.2 Gg yr^{-1} for 2020 (update of Vollmer et al., 2018). This is contrary to the expectation of CFC-13 bank-related emissions decreasing with time.

Emissions from the combination of the CFC-114/CFC-114a isomers also plateaued in the decade leading up to 2016. Estimates for 2016 have been adjusted upwards, from 1.9 Gg yr^{-1} to 2.2 Gg yr^{-1}, which is well within the uncertainty range of ±0.9 Gg yr^{-1} and also not significantly different from the 2020 emissions of 2.6 Gg yr^{-1} (**Table 1-1**; update from Vollmer et al., 2018). Emission estimates from the independent record of Laube et al. (2016), in which the two isomers were separated, have not been updated. It should be noted, though, that the observed increases in CFC-114a abundance imply an emission increase, thus highlighting further that the sources of the two isomers are not identical.

For CFC-113a, in addition to the emission increase observed between 2009 and 2012 (to 1.7 Gg yr^{-1} in 2012–2016; Adcock et al., 2018), observations indicate that emissions have increased again since 2018, although no quantitative estimate is currently available.

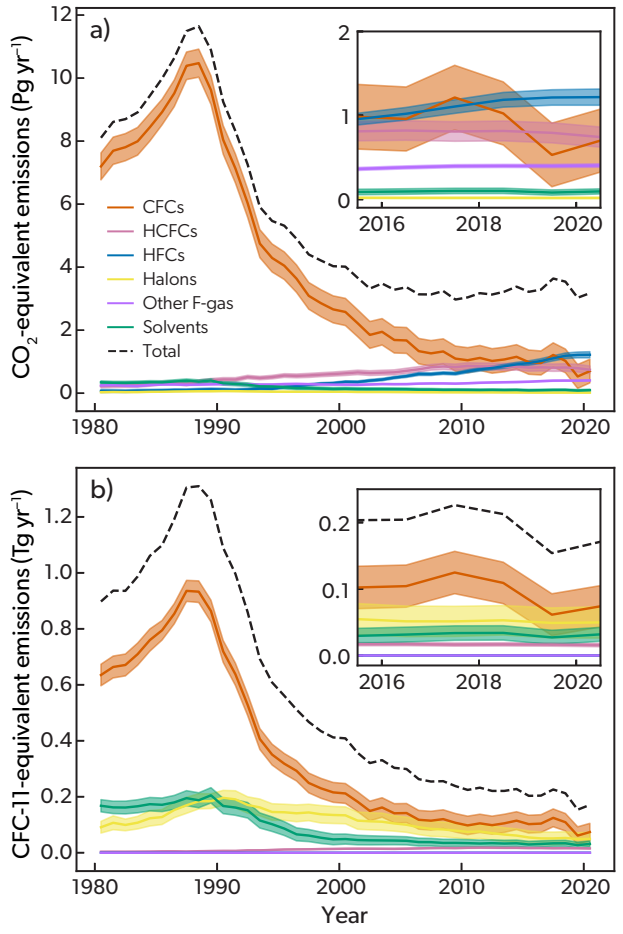

Figure 1-4. (a) 100-year GWP-weighted (CO_2-equivalent) emissions and (b) ODP-weighted (CFC-11-equivalent) emissions. CO_2- and CFC-11-equivalents are taken from the *Annex*. Solvents are defined as CCl_4 and CH_3CCl_3, and other F-gases include SF_6, CF_4, C_2F_6, C_3F_8, *c*-C_4F_8, *n*-C_6F_{14}, NF_3, and SO_2F_2 (minor species not included; see *Introduction*). Shading shows the 1-standard deviation uncertainty.

An increase in the global emissions of CFC-115 to 1.14 ± 0.5 Gg yr^{-1} for 2015–2016 was reported in the previous Assessment (Vollmer et al., 2018; **Figure 1-3**). More recently, these emissions have varied within uncertainties and are estimated at 1.0 Gg yr^{-1} for 2020. As for several other CFCs, the cause of these persisting emissions remains uncertain.

Recent regional studies examining CFC emissions using atmospheric observations (i.e., top-down estimates) have focused largely on CFC-11 and CFC-12, and the reader is again referred to the *"Report on the Unexpected Emissions of CFC-11"* (WMO, 2021) for more detail. Briefly, individual studies have found that Indian and Australian emissions are thought to be negligible in comparison to the global total (Say et al., 2019; Fraser et al., 2020). In contrast, emissions of CFC-11 (and, to a lesser degree, CFC-12) from within China were found to have been substantially enhanced from 2012 to 2018, after which they declined very rapidly (Montzka et al., 2021; Park et al., 2021; Yi et al., 2021). The decline of CFC-11 emissions from eastern China, however, explain only 60 ± 30% (10 ± 3 Gg yr^{-1}) of the observed global emission decrease (Park et al., 2021). In addition to the aforementioned CFC-11 Report, Hu et al. (2022) recently examined continental-scale contributions to the increase in global CFC-11 emissions between 2012 and 2017 by inferring emissions from campaign-based observations during the HIAPER Pole-to-Pole Observation (HIPPO), the Atmospheric Tomography Mission (ATom), and NOAA's global CFC-11 measurements. They found that Asia, including temperate eastern Asia, temperate western Asia, and tropical Asia, accounted for 86 (59–115) % of the global CFC-11 emission rise between 2012 and 2017. Rust et al. (2022) also reported regional emissions of 28 halocarbons for Switzerland, but all of these are very minor in a global context (e.g., around 0.05 Gg yr^{-1} for CFC-11 in 2019), which is why we do not specifically mention this study in any of the following sections. In terms of regional emissions of CFC-12, atmospheric observations have confirmed a decrease in emissions from northeastern China from 3.3 ± 1.4 Gg yr^{-1} in 2016 to 0.5 ± 0.5 Gg yr^{-1} in 2019 (Park et al., 2021).

In summary, global emissions of most CFCs remain well below their peak levels (**Figure 1-3**), with CFC-11 (and to a lesser degree CFC-12) accelerating its decline substantially since the last Assessment and now being much closer to previous baseline scenarios. This is largely due to a recent reduction in Chinese emissions. Of note are the continuing and, in some cases, increasing emissions of several of the more minor CFCs (as evidenced by an increase in chlorine from the five increasing CFCs, from 16.0 ± 0.3 ppt in 2016 to 17.2 ± 0.3 ppt Cl in 2020), for which the only known emission regions are in eastern Asia (updates from Laube et al., 2016; Adcock et al., 2018; Vollmer et al., 2018). Total ODP-weighted emissions for all CFCs dropped from 98 ± 33 Gg yr^{-1} CFC-11-equivalent in 2016 to 77 ± 32 Gg yr^{-1} in 2020 (**Figure 1-4**).

With respect to their influence on climate, in 2020 CFCs contributed 76% of the total direct radiative forcing due to ODSs controlled under the Montreal Protocol, with a combined radiative forcing of 257 mW m^{-2} in 2020 (**Figure 1-5**). The radiative forcing due to CFCs declined by 2.6% between 2016 and 2020, driven primarily by the reduction in abundance of CFC-11 and CFC-12;

over this five-year period, the radiative forcing due to these two gases declined by 6 mW m^{-2}. Consequently, when the combined emissions of all CFCs are expressed as CO_2-equivalent, a decline has again been observed since the last Assessment (**Figure 1-4**). CO_2-equivalent emissions of CFCs were 0.9 ± 0.4 Pg yr^{-1} and 0.7 ± 0.4 Pg yr^{-1} in 2016 and 2020, respectively. This means that HFCs, which contributed 1.25 ± 0.10 Pg yr^{-1} in 2020, are now the highest contributor among the halogenated species in terms of CO_2-equivalent emissions in 2020 (see also *Chapter 2*). Where available, CO_2-equivalent emissions of individual species for 2020 can be found in **Table 1-1**.

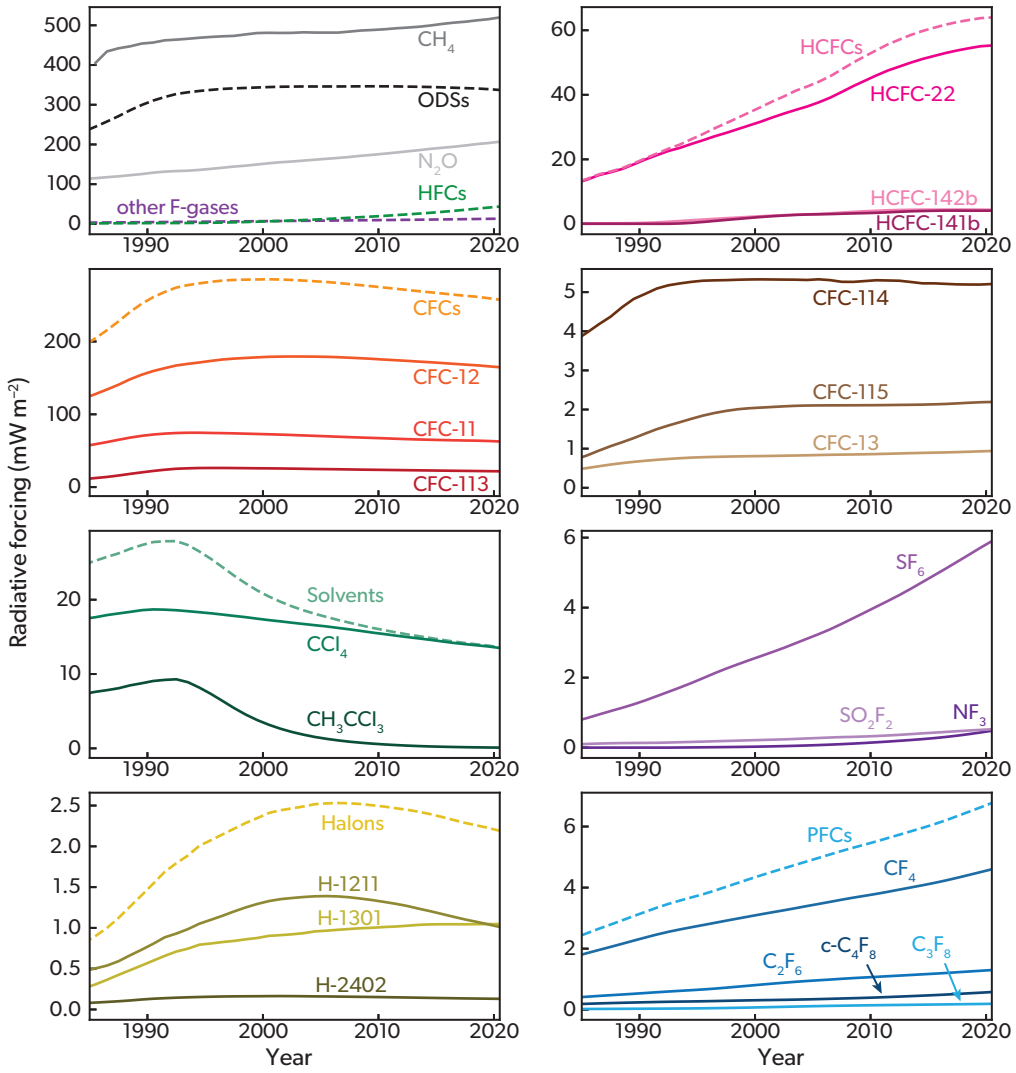

Figure 1-5. Direct radiative forcing based on the lower-tropospheric atmospheric mole fractions of ODSs and selected greenhouse gases, if their radiative forcing in 2020 was 0.1 mW m^{-2} or higher. Groupings of gases are shown with dashed lines, and selected compounds are shown with solid lines. The ODS group here refers to combined CFCs, HCFCs, halons, and solvents (minor species not included; see *Introduction*). HFCs include the species HFC-23, HFC-32, HFC-134a, HFC-143a, HFC-125, HFC-152a, HFC-4310mee, HFC-227ea, HFC-365mfc, HFC-236fa, and HFC-245fa. Other F-gases are defined as the sum of PFCs, SF_6, SO_2F_2, and NF_3. Radiative forcings for individual HFCs are not shown as these can be found in *Chapter 2*. Individual lines for HCFC-124 and *n*-C_6F_{14} have been omitted for clarity. The radiative forcing for CH_3CCl_3 in 2020 is less than 0.1 mW m^{-2} but has been included due to historical significance. Lower tropospheric annual mean mole fractions were taken from merged NOAA, AGAGE, and UEA/FZJ data. Radiative forcings are calculated following the approach of Ramaswamy et al. (2001) using the radiative efficiencies from the *Annex*. Preindustrial (in 1750) mole fractions are assumed to be zero for all gases except for CH_4 (722 ppb), N_2O (270 ppb), and CF_4 (40 ppt). For comparison, the radiative forcing due to CO_2 was approximately 2111 mW m^{-2} in 2020 (Butler and Montzka, 2021).

Box 1-2. Uncertainties in Atmospheric Observation-Based Emission Estimates

Uncertainties in atmospheric observation-based global emission estimates

Global emissions of a trace gas can be derived from the annual rate of change in its atmospheric burden and its atmospheric lifetime, as described in detail in the last Assessment. Uncertainties in such estimates are often dominated by uncertainties of the atmospheric lifetime of the trace gas. Atmospheric lifetimes for the majority of trace gases considered in this Assessment were inferred from satellite observations, in situ measurements of tracer-tracer correlations, photochemical model simulations, and estimates of oceanic and terrestrial fluxes. Uncertainties in atmospheric lifetimes for many trace gases considered here are on the order of ±10% to ±30%.

In addition to atmospheric lifetimes, uncertainties of atmospheric burdens (B) also contribute to the overall uncertainty of such global emission estimates. B is generally estimated from the NOAA and AGAGE atmospheric mole fraction measurements made near Earth's surface in locations that are far away from emissive sources, so that the measured mole fractions are deemed as good representations of zonal average tropospheric mole fractions at measurement locations. However, the representativeness of those surface measurements for zonal averages is an additional factor that can augment inaccuracies in global means derived from a small number of remote surface sites. Furthermore, the Quasi-Biennial Oscillation (QBO) of tropical zonal winds, previously known as a climate phenomenon that strongly affects the variability of trace gas concentrations in the stratosphere, can also influence trace gas levels at Earth's surface (Ray et al., 2020; Montzka et al., 2021; Ruiz et al., 2021). This influence is on one- to five-year timescales and can impact global annual emission estimates. However, when averaging global annual emissions over five years or more, the impact of QBO on the multiyear global average emission estimate is reduced.

In this Assessment, global emissions of ODSs (and of HFCs, discussed in *Chapter 2*) are derived from the AGAGE 12-box model (Cunnold et al., 1994; Rigby et al., 2013) rather than a one-box model. Because the transport in the 12-box model relies on parameterized mixing and advection between boxes, additional uncertainties of global emissions from this approach arise from uncertainties in the parameterized transport in the 12-box model.

Uncertainties in atmospheric observation-based regional emission estimates

Atmospheric observation-based regional emission estimates compiled in this Assessment are mostly derived from Bayesian inverse modeling of regional atmospheric trace gas mole fraction measurements. The fundamental assumption in this modeling technique is that there is a linear relationship between regional emissions (s) and enhancements (z) in mole fractions measured within or closely downwind of this region. This linear operator, or the sensitivity of these atmospheric observations to upwind emissions (H), is often computed from atmospheric transport models. The Bayesian technique requires an initial guess on regional emissions (a priori, s_p). It assumes errors between the prior guess and the unknown "true" emissions (or prior emission errors) and errors between observed mole fraction enhancements and simulated mole fraction enhancements with the chosen transport model (or model-observation mismatch errors) follow Gaussian distributions. The Bayesian solution of regional emissions was obtained by minimizing the following cost function (L), such that it reflects the most likely magnitudes and distributions of regional emissions, given the observed mole fraction enhancements in space and time, prior emission assumptions, and atmospheric transport simulations.

$$L = \frac{1}{2}(z - Hs)^T R^{-1}(z - Hs) + \frac{1}{2}(s - s_p)^T Q^{-1}(s - s_p)$$

Here, R and Q represent the covariance matrices of model-observation mismatch errors and prior emission errors.

The first order of uncertainties in such estimates originate from biases in atmospheric transport simulations, assumptions in prior emissions, and the estimated upwind boundary values that were subtracted from atmospheric observations to derive regional mole fraction enhancements. To incorporate such uncertainties into regional emission estimates, some atmospheric inversion analyses implement an ensemble approach, where multiple transport simulations, prior emissions, and boundary value estimates are considered (e.g., Hu et al., 2017; Rigby et al., 2019; Park et al., 2021). The range of emissions derived from these multiple inversion runs are used for calculating the final mean and uncertainties of regional emissions.

The locations, density, and frequency of atmospheric trace gas measurements used for deriving regional emissions also contribute to the overall uncertainties of regional emission estimates. In general, more measurements within and closely downwind of emissive regions will enable a more accurate inference of regional emissions that have less dependence on prior assumptions. For example, the current atmospheric sampling network has a good sensitivity for emissions from North America, western Europe, and eastern Asia (**Box 1-2 Figure 1**), enabling robust estimates of regional emissions from such an approach (Graziosi et al., 2015; Hu et al., 2015, 2016, 2017; Maione et al., 2014; Park et al., 2021; Rigby et al., 2019; Simmonds et al., 2020). In contrast, huge gaps exist in many developing countries (Weiss et al., 2021), resulting in challenges in understanding their contributions to global emissions of important controlled substances and their compliance to the Montreal Protocol.

Besides the factors mentioned above, assumptions about error covariances in prior emissions and model–observation mismatch errors (Q and R in the equation above) also influence the final Bayesian solution of emissions. This is because these assumptions determine the relative weights between atmospheric observations and prior emission assumptions in the final solution. In the early

Bayesian regional inversion studies, scientists often used "expert judgment" to arbitrarily assign error covariance matrices, whereas recent techniques (Ganesan et al., 2014; Hu et al., 2015; Lickley et al., 2021) allow direct quantification of error covariances from atmospheric observations, enabling a more objective derivation of regional emissions.

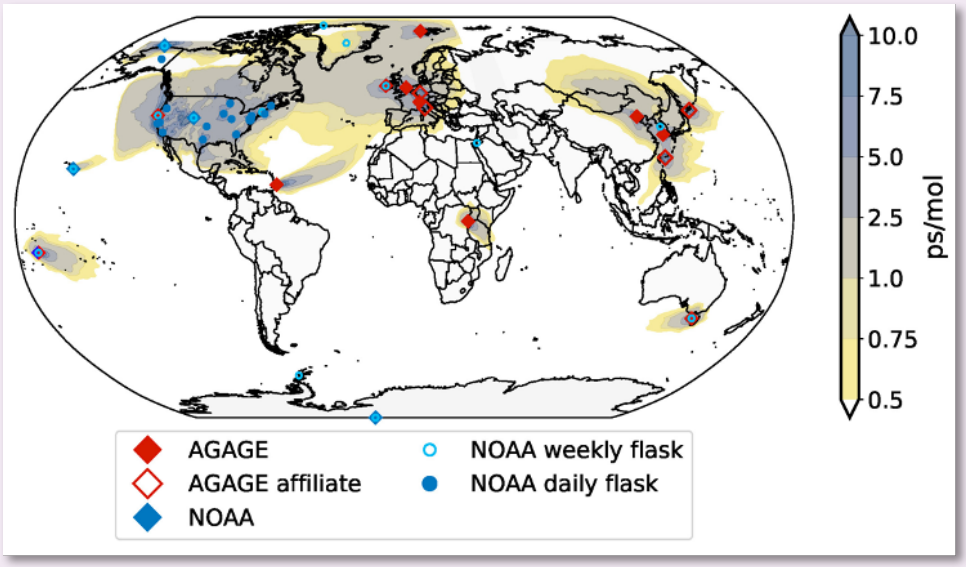

Box 1-2 Figure 1. Current atmospheric sampling for measurements of ozone-depleting substances and their substitutes from the NOAA and AGAGE networks. Displayed in color shading are mean footprints, which are a measure of the contribution to the above-baseline mole fraction made by a unit emission. [Figure from WMO, 2021.]

1.2.2 Halons

Observations of Atmospheric Abundance. Halon-1211 ($CBrClF_2$), halon-2402 ($CBrF_2CBrF_2$), and halon-1202 (CBr_2F_2) abundances continued to decline from their peak values, which were observed in the early and mid-2000s. Global surface mean mole fractions of approximately 3.2 ppt and 0.40 ppt were observed for halon-1211 and halon-2402, respectively, in 2020, and SH mole fractions of approximately 0.009 ppt were recorded for halon-1202 (**Table 1-1** and **Figure 1-1**; updates from Newland et al., 2013; Vollmer et al., 2016). Halon-1301 ($CBrF_3$) growth rates, which were reported as <0.01 ppt yr^{-1} in 2016, remained close to zero. A 2020 global mean mole fraction of 3.37 ppt and 3.32 ppt was derived from AGAGE and NOAA, respectively, which means that halon-1301 has now become the most abundant halon in the atmosphere. Abundances of halon-2311 ($CF_3CHBrCl$) remained below 0.01 ppt.

Emissions, Lifetimes, and Radiative Forcings. Emissions of halon-1211 estimated from observed atmospheric abundances show signs of a continuing decline since the last Assessment, from 3.3 ± 1.8 Gg yr^{-1} in 2016 to 2.9 ± 1.6 Gg yr^{-1} in 2020. These top-down estimates continue to be higher than the bottom-up emission estimates in the *Halons Technical Options Committee 2018 Assessment Report* (HTOC, 2018; **Figure 1-3**). For halon-2402, emissions remain low at around 0.4 Gg yr^{-1}, with no indications of a change since 2016. There is now good agreement with HTOC-based bottom-up estimates for this ODS, as the latter declined substantially between 2016 and 2020. Halon-1301 emissions have also remained stable at around 1.3 Gg yr^{-1} during 2016–2020, with HTOC estimates slightly lower than those based on atmospheric observations. No update is available for halon-1202 and halon-2311, although the most recently reported mole fractions (<0.01 ppt in both cases) indicate that the contributions from these two species are likely small.

Halons have high ODPs, so as a group their ODP-weighted emissions still make the second-highest contribution to CFC-11-equivalent emissions relative to those of other ODS groups (**Figure 1-4**). Due to their low GWPs, the direct contribution of halons to global radiative forcing is small. At 2.2 mW m^{-2} in 2020, halons contribute only 0.6% of the radiative forcing of CFCs (**Figure 1-4**). When their influence on ozone depletion is also considered, net radiative forcing due to halons is negative (Daniel et al., 1995).

1.2.3 Carbon Tetrachloride (CCl_4) and Methyl Chloroform (CH_3CCl_3)

Observations of Atmospheric Abundance. The abundance of carbon tetrachloride (CCl_4) has continued to decline at a rate similar to that reported in the previous Assessment. AGAGE observations showed a mole fraction of 79.9 ppt in 2016 and 76.3 ppt in 2020, while NOAA reported a mole fraction of 81.3 ppt in 2016 and 77.1 ppt in 2020 (**Table 1-1** and **Figure 1-1**). These differences are likely related to known calibration-scale differences, although a higher discrepancy between inter-hemispheric differences derived from observations by the two networks has emerged since around 2018 (**Figure 1-1**). Data from UCI show a similar decline, from 81.9 ppt to 77.4 ppt, between these years. Ground-based remote sensing observations of CCl_4 from Jungfraujoch also show a very similar rate of decline between

2014 and 2020 as compared to the average of the global surface-based measurements from the AGAGE and NOAA networks (**Table 1-2**).

Methyl chloroform (1,1,1-trichloroethane, CH_3CCl_3) global mean mole fractions decreased from 2.6 ± 0.7 ppt in 2016 to 1.4 ppt in 2020 (**Table 1-1**), i.e., reaching 1% of its maximum value. This is reflected also in long-term atmospheric CH_3CCl_3 measurements at seven background stations in China and confirmed by a record of 12 years showing a continuous decline (Yu et al., 2020).

Emissions, Lifetimes, and Radiative Forcings. Since the last Assessment, Suntharalingam et al. (2019) reevaluated the partial lifetime of CCl_4 with respect to the ocean sink and derived an estimate of 124 (110–150) years. This is shorter than the previously used estimate of 183 (147–241) years (Butler et al., 2016) and implies higher emissions of 5–7 Gg yr^{-1}. Given the numerous improvements in the methodology of the new study, the revised partial lifetime has been incorporated into emission estimates in this Assessment. One further study examined the atmospheric lifetime of CH_3CCl_3 (Orkin et al., 2020), but its main focus was on improving estimations of the atmospheric lifetimes of other species using an improved scaling method in combination with modeling and kinetic data. They derive a partial lifetime of 6.0 years with respect to loss from reaction with the OH radical, but this is only slightly lower than, and not significantly different from, the currently used 6.1 years (Engel, Rigby et al., 2018).

Global emissions of CCl_4 are estimated at 44 ± 14 Gg yr^{-1} in 2020, virtually unchanged from the estimate of 43 ± 15 Gg yr^{-1} during 2016. As noted by Liang et al. (2016) and in the previous Assessment, there are still indications for a gap between bottom-up (based on emissions reporting) and atmospheric observation–derived emissions. This gap is discussed further in *Chapter 7*, although it should also be noted that the uncertainty ranges of the two emission estimates currently overlap (**Table 1-1**). As for regional estimates, emissions of CCl_4 in eastern China over the period 2013–2019 show year-to-year variability likely related to CFC-11 production (which is not surprising as CCl_4 is a feedstock for CFC-11 production). Emissions were found to have increased after 2013, reaching 11.3 ± 1.9 kt yr^{-1} in 2016, and to have then decreased to 6.3 ± 1.1 kt yr^{-1} in 2019 (Park et al., 2021).

CH_3CCl_3 emissions are stable at about 2.3 Gg yr^{-1} in 2020, although there are differences in the emissions reported for 2016 between the AGAGE (2.2 Gg yr^{-1}) and NOAA networks (2.9 Gg yr^{-1}). However, when considering the uncertainty ranges, the 2016 and 2020 emission estimates are indistinguishable (**Table 1-1**). In terms of regional studies, Say et al. (2019) derived CCl_4 emissions of 2.3 (1.5–3.4) Gg yr^{-1} and CH_3CCl_3 emissions of 0.07 (0.04–0.10) Gg yr^{-1} for northern and central India during an aircraft campaign in June and July 2016. The studies focusing on China report a temporal evolution of CCl_4 emissions similar to those of CFC-11 and CFC-12, with an increase from about 2012 onwards, followed by a decrease that started approximately during 2016–2017, and 2019 emissions being comparable to those in 2011 (Lunt et al., 2018; Park et al., 2021).

Radiative forcing due to CCl_4 declined to 13 mW m^{-2} in 2020, equivalent to 5% of the radiative forcing due to CFCs. The radiative forcing due to CH_3CCl_3 remains negligible (**Figure 1-4**).

1.2.4 Hydrochlorofluorocarbons (HCFCs)

Observations of Atmospheric Abundance. The global surface mean mole fraction of HCFC-22 ($CHClF_2$) has continued to increase, from around 237 ppt in 2016 to around 248 ppt in 2020 (**Figure 1-1** and **Table 1-1**). However, its annual growth rate has decreased even further and is now about 0.5% (2019–2020) as compared to 1.8% in 2015–2016. In contrast, growth rates of HCFC-141b (CH_3CCl_2F) and HCFC-142b (CH_3CClF_2) have not continued their decline since 2016 (**Figure 1-1**). Their global abundances were 24.5 ppt and 22 ppt in 2016, respectively; i.e., within uncertainties they are identical to the 2020 values. Nevertheless, higher growth rates of these three HCFCs had been projected in the previous two Assessments, which is reflected in the higher abundances in the A1-2014 and A1-2018 scenarios (**Figure 1-1**). These near-surface observations of abundances are in excellent agreement with FTIR-based abundances and trends (**Figure 1-2** and **Table 1-2**; Prignon et al., 2019), whereas upper-tropospheric trends derived from the ACE-FTS satellite instrument are lower (HCFC-141b) or higher (HCFC-142b) than the other available trend estimates. It should be noted, however, that no comprehensive uncertainty analysis has been carried out for these satellite-based trends.

Of the less abundant HCFCs, mole fractions of HCFC-124 ($CHClFCF_3$) were not reported in the last Assessment. These have since become available, changing from 1.1 ppt in 2016 to 0.9 ppt in 2020 (update from Simmonds et al., 2017). Vollmer et al. (2021) reported in situ observations of the newly detected HCFC-132b ($CH_2ClCClF_2$), which included a reconstruction of its historical atmospheric trends and abundances. This ODS first appeared in the atmosphere during the late 1990s, exhibiting a growth period until 2013, reaching 0.15 ppt in the NH. A brief period of decline was followed by another increase from around 2016 onwards to arrive at a global mole fraction of 0.14 ppt in 2020.

HCFC-133a (CF_3CH_2Cl) SH mole fractions remained stable at around 0.39 ppt between 2016 and 2020 (update from Laube et al., 2014) and globally were at 0.45 ppt in 2020. The abundances of HCFC-31 (CH_2ClF) increased slightly from 0.09 ppt in 2016 to 0.11 ppt in 2020 (update from Vollmer et al., 2021). No update is available for HCFC-225ca ($CF_3CF_2CHCl_2$), which in 2012 was reported at 0.02 ppt.

Emissions, Lifetimes, and Radiative Forcings. Global emissions of HCFC-22 may have started to decline in 2020 after a period of relatively constant emissions, with 2020 emissions of 348 ± 53 Gg yr^{-1} and 337 ± 53 Gg yr^{-1} inferred using AGAGE and NOAA measurements, respectively, compared to 2016 emissions of 375 ± 50 Gg yr^{-1} and 373 ± 51 Gg yr^{-1}, respectively. HCFC-142b emissions show indications of a decline by a total of 5–6 Gg (22–25%) between 2016 and 2020, though the uncertainties of the estimates for these two years overlap. HCFC-142b emissions in 2020 were around 19 Gg yr^{-1}. Global emissions of HCFC-141b of 58.1 ± 8.8 Gg yr^{-1} and 56.4 ± 8.2 Gg yr^{-1} from AGAGE and NOAA respectively in 2020 were smaller than in 2016, although, after an initial drop, emissions rose year on year since 2017, amounting to a total rise of ~4.5 Gg. Again, this is not a significant increase when considering the uncertainties (**Table 1-1**). However, the emission changes for those three HCFCs are consistent with a sharp drop in reported HCFC consumption after 2012, particularly from Article 5 countries. Emissions of HCFC-124 have continued to decline since 2016, with 2020 emissions of 3.0 ± 0.7 Gg yr^{-1}. The 2020 emissions were, however, slightly larger (up to ~0.4 Gg yr^{-1}) than those in the three preceding years.

A number of HCFCs with no known purposeful end use

Table 1-3. Regional emissions estimates for HCFCs (mainly focusing on new estimates published since the last Assessment) for years where data are available. Uncertainties are given as the 68% uncertainty range or 1 standard deviation where available. Note that some estimates of HCFC-22, HCFC-141b, HCFC-142b, and HCFC-124 emissions are derived using a bottom-up method, while other estimates use a top-down approach. Estimates for India use measurements made only during June and July.

Region	Year									
	2011	2012	2013	2014	2015	2016	2017	2018	2019	2020
HCFC-22 (Gg yr^{-1})										
China[a]	139 ± 35	154 ± 51	172 ± 37	159 ± 34	146 ± 44	147 ± 36	147 ± 26			
China[b*]	107 (79–129)	116 (87–142)	112 (91–153)	127 (95–161)	130 (124–131)	134 (127–135)	131 (124–135)	126 (116–132)	121 (108–131)	116 (100–130)
Europe[c*]	18.6	16.1								
Europe[c]	15.2 ± 3.1	12.1 ± 2.0								
India[d]						7.8 (6.0–9.9)				
South Africa[e]							3.0 (1.6 – 4.4)			
USA[f]	48.8 ± 9.4	42.8 ± 3.1	41.1 ± 4.4	40.0 ± 5.9						
USA[g*]	80	76	73	69	58	54	51	47	43	
HCFC-141b (Gg yr^{-1})										
China[a]	24 ± 5	22 ± 6	18 ± 6	16 ± 7	15 ± 6	15 ± 3	15 ± 2			
China[h]	13.1	14.3	14.2	15.7	15.5	10.3	10.6	11.6	10.9	
China[i*]	15.3	16.4	15.8	15.7	17.4	18.4	20.0	23.1	23.6	24.0
India[d]						1.0 (0.7–1.5)				
HCFC-142b (Gg yr^{-1})										
China[a]	11 ± 3	11 ± 4	11 ± 4	11 ± 3	9 ± 3	8 ± 2	6 ± 1			
China[h]	10.8	13.4	12.8	11.4	8.1	7.2	6.5	5.8	6.0	
China[i*]	12.7	14.6	12.3	12.1	12.6	12.6	12.5	12.2	11.9	11.7
India[d]						0.10 (0.06–0.14)				

*Bottom-up; [a] Fang et al. (2019c); [b] Li et al. (2016); [c] Graziozi et al. (2015); [d] Kuyper et al. (2019) [e] Say et al. (2019); [f] Hu et al. (2017); [g] US EPA (2021); [h] Yi et al. (2021); [i] Wang et al. (2015); [j] Han et al. (2014)

continue to be emitted. Emissions of HCFC-133a remained at around 2 Gg yr^{-1} between 2017 and 2020 (update from Vollmer et al., 2021), which follows emissions of 2.8 ± 0.4 Gg yr^{-1} in 2016. HCFC-31 emissions between 2018 and 2020 were around 1 Gg yr^{-1}, following a rise from 0.9 ± 0.2 Gg yr^{-1} to 1.3 ± 0.2 Gg yr^{-1} between 2016 and 2017. The newly discovered HCFC-132b reached an all-time high in emissions in 2020 of 1.2 ± 0.5 Gg yr^{-1}, up from 0.8 ± 0.3 Gg yr^{-1} in 2016.

Regional emission estimates of the three most abundant HCFCs are summarized in **Table 1-3**. A top-down study of India's HCFC emissions was carried out using measurements made during an aircraft campaign in June and July 2016 (Say et al., 2019). Measurements included HCFC-22, HCFC-141b, and HCFC-142b. The derived emissions were extrapolated to the whole of 2016, and show that India was reportedly responsible for 2.1% (1.6–2.7%, one standard deviation) of global HCFC-22 emissions. In contrast, India was estimated to be responsible for 7% of global HCFC-22 production in 2017 (Stanley et al., 2020), making it one of the primary global HCFC-22 manufacturers at the time. The relative contribution of India to global emissions is smaller for the other two HCFCs, at 1.8 (1.2–2.6) % of HCFC-141b and 0.4 (0.2–0.6) % of HCFC-142b.

The first top-down HCFC-22 emission estimates from Africa, using the first high-frequency halocarbon measurements made on the continent, show that South African emissions in 2017 were 3.0 (1.6–4.4) Gg yr^{-1} (Kuyper et al., 2019), around 40% of those estimated from India in the previous year.

Recently published top-down emissions estimates for China show that HCFC-22 emissions peaked at 172 ± 37 Gg yr^{-1} in 2013, although there was no statistically significant increase or decrease in emissions over the period 2011–2017 (Fang et al., 2019c). These estimates are generally in agreement with bottom-up emission estimates for China (Li et al., 2016), although uncertainties are comparably large. A reported rise in global HFC-23 emissions (Stanley et al., 2020; see *Chapter 2* for more details) has been linked to HCFC-22 production (as a by-product) in developing countries. There was previously a reported discrepancy (of ~23 Gg yr^{-1} in 2014, Hu et al., 2017) between top-down and bottom-up derived emissions in the United States; it is currently not known whether this persisted after 2014.

Top-down emission estimates of HCFC-141b in China declined from 24 ± 5 Gg yr^{-1} in 2011 to 15 ± 2 Gg yr^{-1} in 2017, and emissions of HCFC-142b declined from 11 ± 3 Gg yr^{-1} in 2011 to 6 ± 1 Gg yr^{-1} in 2017 (Fang et al., 2019c). A separate study, using an interspecies-correlation method (Yi et al., 2021, correlated to HCFC-22), also shows a decline in China's HCFC-141b emissions from 13.1 Gg yr^{-1} in 2011 to 10.9 Gg yr^{-1} in 2019 (peaking at 15.7 Gg yr^{-1} in 2015), and a decline in emissions of HCFC-142b from 10.8 Gg yr^{-1} in 2011 to 6.0 Gg yr^{-1} in 2019 (peaking at 13.4 Gg yr^{-1} in 2012), though not all of China's industrial centers are covered. From 2016 onwards, top-down estimates of HCFC-142b are significantly smaller than those projected using bottom-up methods (i.e., in Han et al., 2014, by around 50%), whereas prior to 2016 the top-down and bottom-up estimates were all in good

agreement. The top-down estimates for HCFC-141b in China generally show a decline in emissions. However, a bottom-up estimate projected that those emissions should increase by 6.6 Gg yr^{-1} between 2015 and 2020 (Wang et al., 2015).

HCFC-124 emissions in China are estimated to have remained largely constant between 2011 and 2017 at around 0.8 Gg yr^{-1} (Fang et al., 2019c), with no statistically significant year-to-year variation. Emissions of two minor HCFCs, HCFC-133a and HCFC-132b, were shown to originate almost entirely from East Asia, and since 2016 the majority of these have been emitted from eastern China (Vollmer et al., 2021).

Emissions of all HCFCs, in terms of their combined CFC-11-equivalent, have continued to decline since 2016, supporting the previous Assessment's suggestion that the 2007 adjustment to the Montreal Protocol has been effective in limiting HCFC emissions. The 2020 CFC-11-equivalent emissions of HCFCs (16 ± 3 Gg CFC-11 yr^{-1}) are only around 21% of those from CFCs.

A similar decline has continued for the HCFCs in terms of their combined CO_2-equivalence. HCFC emissions were 0.7 Pg CO_2-equivalent yr^{-1} in 2020, similar to those from CFCs. Radiative forcing for all HCFCs remains dominated by HCFC-22, which contributed 86% of HCFC radiative forcing in 2020. Overall radiative forcing for HCFCs has risen by 4% since 2016 and is, at 64.0 mW m^{-2}, equivalent to 25% of the forcing of CFCs in 2020.

1.2.5 Methyl Chloride (CH_3Cl)

Observations of Atmospheric Abundance. CH_3Cl is not controlled under the Montreal Protocol and is largely natural in origin, although some direct (feedstock, coal combustion; e.g., Li et al., 2017) and indirect (biomass burning; e.g., Mead et al., 2008) anthropogenic sources are known. The 2020 global mean mole fraction determined from the AGAGE and NOAA global networks was 546 and 549 ppt, respectively (**Table 1-1**). These values are around 1–2% lower than the 2016 values reported in the previous Assessment, and changes of this magnitude are well within historically observed variability since ongoing measurements commenced in the 1990s (**Figure 1-1**). It should be noted, though, that observations of CH_3Cl abundances in the upper troposphere have repeatedly shown that the global values from ground-based networks may represent an underestimation by approximately 50–100 ppt of the amount of CH_3Cl entering the stratosphere (Umezawa et al., 2014, 2015; Adcock et al., 2021). This may be related to the nature of some of its sources (and also its terrestrial sink), as biomass burning tends to lift air rapidly, and many emissions in the tropics and in the source regions near the Asian monsoon (i.e., two main input regions for air to the stratosphere) are not well captured due to the locations of the network stations (see also **Box 1-2**).

Emissions, Lifetime, and Radiative Forcing. Global emissions of CH_3Cl are estimated at around 4.7 Tg yr^{-1} both in 2016 and 2020. In terms of regional emission estimates, anthropogenic emissions from China were previously estimated to average 363 ± 85 Gg yr^{-1} between 2008 and 2012 (Li et al., 2017), equivalent to about 7% of current global emissions. More recent evidence linked some of these emissions directly to iron and steel industrial processes, as unexpectedly high concentrations were found to be emitted in the sintering processes (Ding et al., 2020). Another study reported that based on new kinetic isotope measurements of the main sink reactions of CH_3Cl in combination with modeling, the tropical rainforest source of this gas might be much smaller than previously believed, i.e., 670 ± 200 Gg yr^{-1} instead of around 2 Tg yr^{-1} (Bahlmann et al., 2019). This would in turn mean that a major CH_3Cl source is missing.

In terms of regional emissions, southwest South African emissions were estimated for the first time by an observation-based study at 9.7 (6.0–13.5) Gg yr^{-1} during 2017 by Say et al. (2020). In a more process-oriented study, Macdonald et al. (2020) reported consumption of CH_3Cl from the forefield of a retreating Arctic glacier, although this is unlikely to be a significant sink, given the relatively small fluxes and surface area. This could, however, be of future importance as the Arctic is one of the most rapidly warming regions of the Earth, and this additional sink process might become more significant. Other recently reported minor

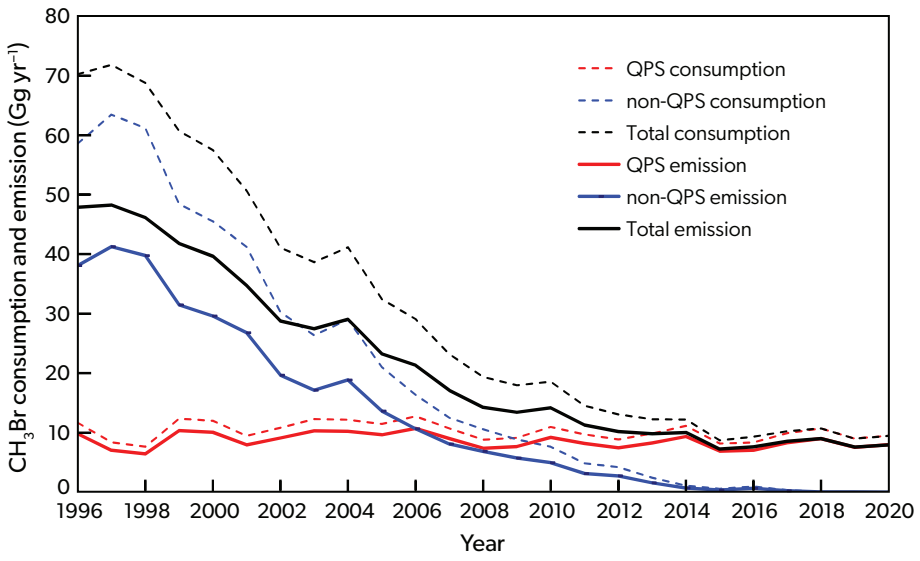

Figure 1-6. CH_3Br consumption (dashed lines), as reported in the UNEP database (UNEP, 2022), for non-QPS uses (blue) and QPS uses (red), and emissions (solid lines) from non-QPS uses (blue) and QPS uses (red). Total consumption and emissions are shown as black dashed and solid lines, respectively. As in previous Assessments, soil fumigation emission rates are estimated as 65% of reported consumption, and QPS emission rates are estimated as 84% of reported consumption (based on UNEP, 2006, where uses are weighted averages with mean emission factors and the smallest non-QPS source, i.e., soil injection without a tarp, is removed from the calculation).

or unquantified sources of CH_3Cl include tropical mangroves (4–7 Gg yr^{-1}; Koluso et al., 2018), rapeseed crops (~5 Gg yr^{-1}; Jiao et al., 2020), advancing saltmarsh due to sea level rise (with the nearby degraded forest wetland acting as a net sink; Jiao et al., 2018), animal excrements on coastal Antarctic tundra soils (with those soils otherwise acting as a sink; Zhang et al., 2020), and copper-based chemical usage (2.5 ± 0.7 Gg yr^{-1}; Jiao et al., 2022).

With regard to its direct influence on anthropogenic-induced global warming, the effect from CH_3Cl emissions on climate is small relative to other long-lived halogenated gases due to its very low radiative impact (GWP-100 of 5.54; Smith et al., 2021) and large natural emissions contributing to its current abundance.

1.2.6 Methyl Bromide (CH_3Br)

Observations of Atmospheric Abundance. CH_3Br has the shortest atmospheric lifetime of all the controlled ODSs in this chapter (*Annex*), and its 2020 global mean surface mole fractions from the AGAGE and NOAA networks, respectively, were 6.52 ppt and 6.68 ppt (**Figure 1-1** and **Table 1-1**). This is about 30% lower than the peak observed between 1996 and 1998 and around 20% higher than the preindustrial SH mole fraction of 5.5 ± 0.2 ppt derived from ice core measurements (Carpenter, Reimann et al., 2014). The global mean mole fraction had briefly grown around 2015–2016, but subsequently reverted to a slow decrease until about 2017, followed by a period with little overall change. The 2020 global CH_3Br abundances were 0.33 ppt (AGAGE) or 0.17 ppt (NOAA) lower than the 2016 value of 6.85 ppt. The cause of these difference between the networks is unclear, but it could arise from the various source and sink processes of this ODS and the partly different locations of the observing sites for these networks, in combination with its relatively short atmospheric lifetime causing a less even distribution throughout the global troposphere. It should also be noted that a comparison with 2016 global mole fractions is somewhat misleading, as abundances in 2014 and 2015 were considerably lower (between 6.5 and 6.6 ppt, respectively), resulting in, e.g., no significant decrease when comparing abundances in 2015 and 2020.

Emissions, Lifetime, and Radiative Forcing. Global CH_3Br emissions were relatively unchanged between 2016 (135 ± 21 Gg yr^{-1}) and 2020 (131 ± 20 Gg yr^{-1}; **Table 1-1**). This ODS is emitted by both natural and anthropogenic sources, including biomass and biofuel burning, oceanic emissions, fumigation, crops, and other vegetation (e.g., Montzka et al., 2003; Deventer et al., 2018; Jiao et al., 2020; Nicewonger et al., 2022). Among the anthropogenic sources, the fumigation of soils, post-harvest storage of commodities, and the fumigation of structures are controlled under the Montreal Protocol. Production of CH_3Br for use in quarantine and pre-shipment (QPS) for pest control in the transport of agricultural products, on the other hand, is exempt from the phaseout. The non-QPS consumption (i.e., other usage) dropped to 0.01 Gg in 2019, around 0.03% of its peak value (UNEP, 2022; **Figure 1-6**).

The reported consumption for QPS had been relatively stable for about two decades, from 1996 to 2016, as discussed in the previous Assessment. The temporal evolution between 2016 and 2020 was similar, with increases from about 8.2 Gg yr^{-1} in 2015 to about 10.7 Gg yr^{-1} in 2018, followed by a slight drop to 9.5 Gg in 2020 (**Figure 1-6**). These relatively small fluctuations in reported consumption cannot explain the observed slowdown in the decline rates of both atmospheric mole fraction and IHD as observed by both the AGAGE and NOAA networks (**Figure 1-1**).

In terms of regional emissions, CH_3Br from eastern China has been reported to have remained relatively constant at 4.1 ± 1.3 Gg yr^{-1} for the period 2008–2019 (Choi et al., 2022). The estimated emissions peaked in 2010 at 7.1 ± 1.3 Gg yr^{-1} and then decreased to 2.4 ± 1.3 Gg yr^{-1} in 2012, followed by a small positive trend in later years. This slight increase from 2014 to 2018 seems to reflect the impact of increased QPS use in traded commodities as reported to UNEP. There was, however, a significant discrepancy of 2.9 ± 1.3 Gg yr^{-1} on average between the observation-inferred estimates and bottom-up emission estimates based on the consumption data reported to UNEP in 2008–2019. After the potential contributions of the rapeseed industry and biomass burning were assessed, the remaining discrepancy of about 1.4 Gg yr^{-1} is likely due to fumigation use that was not reported and/or inaccurately reported, or to emissions from unknown sources in eastern China.

As for recent vegetation-focused emission studies, several smaller sources have been investigated or revisited. Deventer et al. (2018) estimated the global salt marsh source to be 1.0 to 7.8 Gg yr^{-1}, based on a latitudinal examination of all the published salt marsh studies, while Jiao et al. (2020) reassessed the global source from rapeseed, downscaling the prior estimate of 5.2 Gg yr^{-1} to 2.8 ± 0.7 Gg yr^{-1}. Advancing salt marshes due to sea level rise do not seem to change CH_3Br emissions (Jiao et al., 2018), which is in contrast to emissions of CH_3Cl. In addition, Jiao et al. (2022) reported CH_3Br production induced by Cu(II)-based chemical usage, with a preliminary estimate of the global emissions from that process of 4.1 ± 1.9 Gg yr^{-1}.

After accounting for the decline due to anthropogenic emissions, changes in the interannual variability of the global mean atmospheric CH_3Br have been found to be largely driven by El Niño-Southern Oscillation (ENSO)-related changes in fire emissions, suggesting that climate variability may affect the future CH_3Br budget (Nicewonger et al., 2022). The imbalance between CH_3Br sources and sink terms of more than 30 Gg yr^{-1} reported for the late 1990s (e.g., Yvon-Lewis and Butler, 2002; Yvon-Lewis et al., 2009) has declined to 20 Gg yr^{-1} from unknown sources, based on NOAA observations and a 6-box ocean-atmosphere model (Saltzman et al., 2022). Time dependence and latitudinal distribution of the budget gap based on the model inversion suggests that it can be partitioned into a time-invariant natural source and a smaller time-varying component that scales with anthropogenic emissions during phaseout. Similar to CH_3Cl, CH_3Br emissions also have a very low direct radiative impact (GWP-100 of 2.43; Smith et al., 2021).

1.3 HALOGENATED VERY SHORT-LIVED SUBSTANCES (VSLSs)

VSLSs are defined as trace gases whose local lifetimes are shorter than 0.5 years and consist of organic and inorganic halogenated source gases (SGs) and product gases (PGs). The SGs include all VSLSs present in the atmosphere in the form they were emitted. Brominated and iodinated SGs are predominantly of natural oceanic origin, whereas chlorinated species have mostly anthropogenic sources. The halogenated PGs can arise from SG degradation and other sources of tropospheric halogens.

In contrast to longer-lived ODSs, which account for most of the present-day stratospheric halogen loading, VSLSs are not controlled by the Montreal Protocol (see **Box 1-3** for commonalities and differences between VSLSs and ODSs). There is convincing evidence that VSLSs now contribute about 25% to stratospheric bromine and 3–4% to stratospheric chlorine (Carpenter, Reimann et al., 2014; Engel, Rigby et al., 2018). Even though the VSLS contribution to total stratospheric chlorine is relatively small, it has shown a strong positive trend over the last decades (Hossaini et al., 2019). Recent studies have suggested that tropospheric iodine can also reach the stratosphere (Koenig et al., 2020) and contribute to halogen-driven ozone loss (Cuevas et al., 2022).

The overall contribution of VSLSs to stratospheric halogen loading and ozone destruction depends strongly on the spatial and temporal variability of their sources, transport pathways, and chemical transformation. In this section, we apply data from global networks to assess the mean surface mixing ratios and emissions, whereas observations close to the tropopause are used to infer the input of VSLSs to the stratosphere.

1.3.1 Tropospheric Abundance, Trends, and Emissions of Very Short-Lived Source Gases (VSL SGs)

Halogenated VSLSs are partially broken down during their transport to the stratosphere and show large spatial variability due to their nonuniform emission distributions and relatively short atmospheric lifetimes. A detailed compilation of chlorinated, brominated, and iodinated SG seasonal lifetimes was given in Table 1-5 of Carpenter, Reimann et al. (2014) and is updated in the *Annex* of this Assessment. Any interpretation of measurements from regional campaigns and global networks needs to take into account potential issues arising from the scarce spatial coverage and representativeness of the data.

Since the last Assessment, updated global network observations of chlorinated VSLSs have led to new emission estimates. Long-term changes of these emissions can show pronounced regional differences. For brominated VSLSs, emission estimates have remained largely unchanged, with some reduction of the upper and lower limits. Emissions of iodinated VSLSs are now considered to include inorganic iodine sources, which dominate the tropospheric iodine budget.

1.3.1.1 Chlorine-Containing VSL SGs

This section focuses on the chlorinated VSLSs most widely reported in the background atmosphere: dichloromethane (CH_2Cl_2), chloroform (trichloromethane, $CHCl_3$), tetrachloroethene (perchloroethylene, CCl_2CCl_2, shortened to C_2Cl_4), and 1,2-dichloroethane (CH_2ClCH_2Cl). In particular, CH_2Cl_2 and $CHCl_3$ have received much attention in the scientific literature in recent years due to increasing emission estimates. Long-term measurements of CH_2Cl_2 and C_2Cl_4 are available from both the NOAA and AGAGE surface networks, while measurements of $CHCl_3$ are available only from AGAGE. Hemispheric mean mole fractions from these globally distributed measurements and emissions derived with a 12-box model are given in **Table 1-4** and shown in **Figure 1-7**, together with regional emissions based on inverse modeling approaches (Claxton et al., 2020; An et al., 2021).

Dichloromethane (CH_2Cl_2) has shown steadily increasing mole fractions since the beginning of this century. Global mean mole fractions in 2020 amount to 38.3 and 45.5 ppt based on AGAGE and NOAA networks, respectively (**Table 1-4**). Differences between the global means of the two CH_2Cl_2 datasets of about 7 ppt in 2020 cannot be fully explained by the known calibration difference of ~10% (Carpenter, Reimann et al., 2014) and likely arise from differences in sampling locations between the networks. Large industrial sources lead to pronounced spatial variability (e.g., Claxton et al., 2020), which is also apparent in the strong IHDs with NH CH_2Cl_2 mole fractions being up to a factor of 3.5 larger than those in the SH (**Figure 1-7**). Global mean mole fractions increased by 3.2% yr^{-1} and 3.0% yr^{-1} for 2019–2020 based on AGAGE and NOAA, respectively (**Table 1-4**). These increase rates are smaller than the four-year mean increase rates for 2016–2020 of 4.3% yr^{-1} (AGAGE) and 4.6% yr^{-1} (NOAA). They are also considerably smaller than the peak growth rates of 6.7% yr^{-1} (AGAGE) and 6.6% yr^{-1} (NOAA) found for 2012–2016, thus confirming a slow flattening of the strong positive trends that occurred after 2010.

Anthropogenic sources of CH_2Cl_2 have been estimated to account for roughly 90% of global emissions (Montzka, Reimann et al., 2010). Natural marine sources of CH_2Cl_2 might also play a role; however, oceanic emission estimates have large uncertainties due to the paucity of observational data (e.g., Claxton et al., 2020). Measurements from the AGAGE and NOAA networks

Table 1-4. Annual global mean mole fractions of chlorinated VSL SGs and estimated emissions (including 1-sigma uncertainties) from the global networks. Emissions based on AGAGE and NOAA surface data were calculated using a global 12-box model (Cunnold et al., 1983; Rigby et al., 2013), identical to the global emissions shown in **Figure 1-3** for longer-lived ODSs. The calculations assume parameterized global steady-state total lifetimes of 0.54, 0.52, and 0.40 years for CH_2Cl_2, $CHCl_3$, and C_2Cl_4, respectively.

Compound	Annual Mean Mole Fraction (ppt)			Growth (2019–2020)		Annual Global Emissions (Gg yr^{-1})			Network
	2016	2019	2020	ppt yr^{-1}	% yr^{-1}	2016	2019	2020	
CH_2Cl_2	32.7	37.1	38.3	1.2	3.2	943 (±179)	1061 (±203)	1130 (±211)	AGAGE
	38.4	44.2	45.5	1.3	3.0	1126 (±204)	1328 (±235)	1328 (±242)	NOAA
$CHCl_3$	9.0	8.7	8.7	0.0	0.0	345 (±70)	335 (±69)	339 (±70)	AGAGE
C_2Cl_4	1.07	1.05	1.01	–0.04	–3.8	83 (±42)	86 (±40)	80 (±39)	AGAGE
	1.21	1.19	1.12	–0.07	–5.9	102 (±50)	98 (±49)	91 (±47)	NOAA

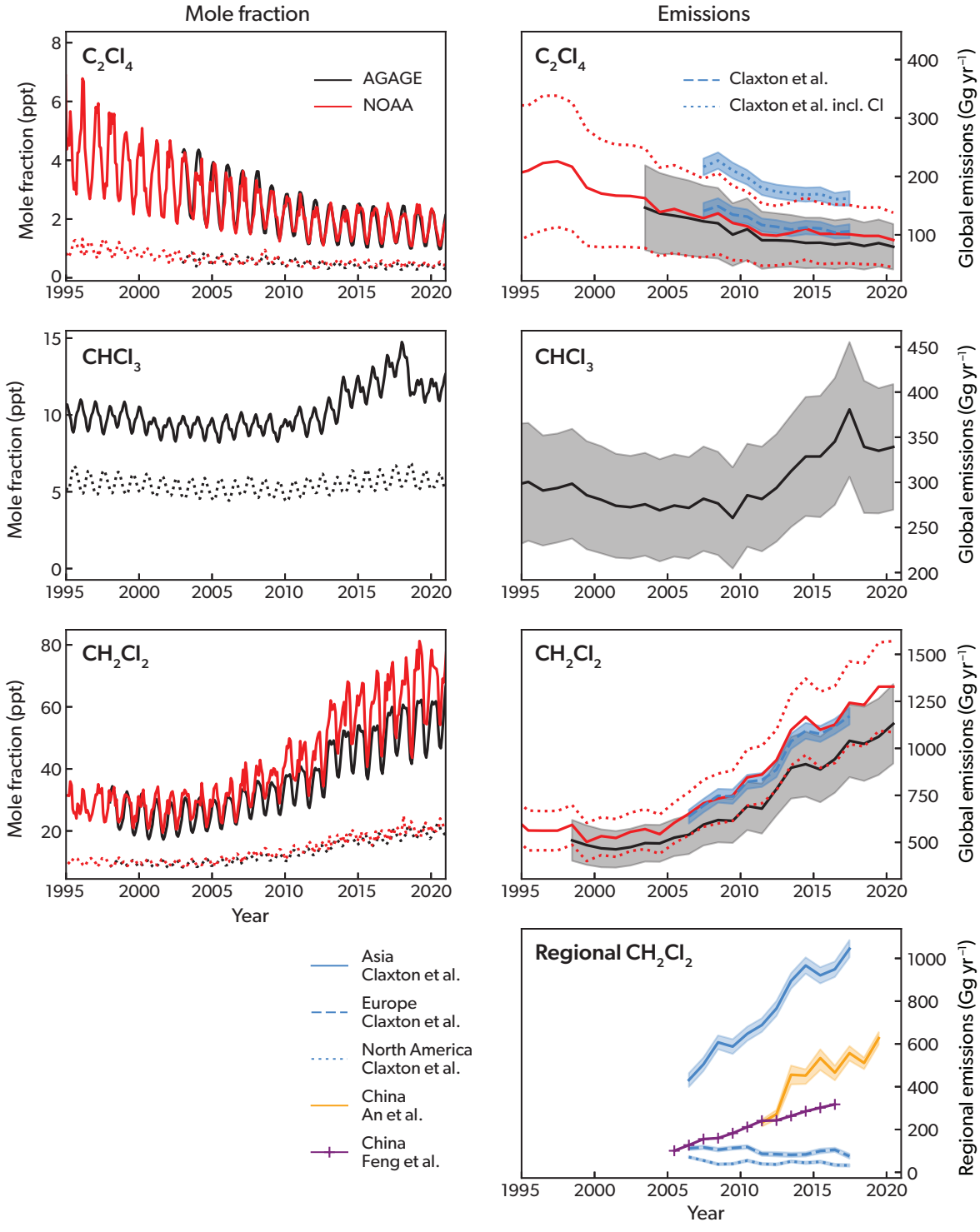

Figure 1-7. *(left three panels)* Monthly hemispheric mean mole fractions of C_2Cl_4, $CHCl_3$, and CH_2Cl_2 derived from AGAGE (black) and NOAA (red) observations in the Northern (solid lines) and Southern (dotted lines) Hemispheres. *(right three upper panels)* Global emissions estimates (Gg yr^{-1}) calculated using a global 12-box model (using methods described in **Figure 1-3**), with 1-sigma uncertainties indicated by shading (AGAGE) or dotted lines (NOAA). Global emissions for C_2Cl_4 from Claxton et al. (2020) are reported with loss due to only OH and photolysis and including an additional chlorine sink (incl. Cl). *(bottom right panel)* Regional estimates for Asia, Europe, and North America (Claxton et al., 2020, blue), as well as China (Feng et al., 2018, purple; An et al., 2021, yellow), are also shown together with 1-sigma uncertainties (shading). Estimates for China from Feng et al. (2018) use a bottom-up approach; all other regional estimates use a top-down methodology.

suggest global CH_2Cl_2 emissions for 2020 of 1130 (±211) Gg yr^{-1} and 1328 (±242) Gg yr^{-1} (**Table 1-4**), respectively, corresponding to a factor 2.5 increase compared to 2000.

Regional emission estimates have highlighted the influence of CH_2Cl_2 emissions from Asia, and in particular from China, on the global estimates and their long-term changes. Based on surface observations and chemistry-transport modeling, Asian emissions have been suggested to account for about 90% of global emissions in 2017 (Claxton et al., 2020). The global emission estimates from that study show a total increase between 2006 and 2017 of 534 Gg yr^{-1}, which is in very good agreement with other estimates of global long-term changes (**Figure 1-7**). Regional CH_2Cl_2 emissions from Asia account for an increase of 615 Gg yr^{-1}, more than offsetting the small decrease in European and North American emissions over the same time period (**Figure 1-7**). A substantial fraction of the Asian emission increase is driven by China, with a 217 Gg yr^{-1} increase estimated for 2005–2016 based on a bottom-up emission inventory (Feng et al., 2018). A combined top-down and bottom-up CH_2Cl_2 emission estimate suggests an even larger role for emissions from China, with an increase of 395 Gg yr^{-1} for 2011–2019 completely accounting for the global emission increase over the same time period (An et al., 2021). On a local scale, strongly enhanced mole fractions have been observed in China, potentially due to enhanced local emissions (Benish et al., 2021; Zeng et al., 2020). In addition, emissions from India appeared to have experienced a pronounced increase of 77 Gg yr^{-1} from 2008 to 2016 (Say et al., 2019).

Global chloroform ($CHCl_3$) mole fractions (**Table 1-4**) slightly decreased from 9.0 ppt in 2016 to 8.7 ppt in 2020 (AGAGE). Interestingly, NH surface concentrations increased quite rapidly between 2011 and 2017 (**Figure 1-7**), by 4.9% yr^{-1}; however, around 2018, concentrations dropped in a steplike manner back down to 2015 levels. A detailed analysis focusing on 2010–2015 revealed that the background $CHCl_3$ concentrations increased at nearly all stations, but the number of pollution events with highly elevated $CHCl_3$ only increased at stations in Asia, suggesting nearby sources (Fang et al., 2019a).

Atmospheric $CHCl_3$ stems from natural and anthropogenic emissions, with the contribution from each source term currently being debated and anthropogenic emission estimates ranging from 10% (McCulloch, 2003) to at least 50% (Worton et al., 2006) of the total emissions. In addition to the known natural sources (e.g., phytoplankton, peatlands, soils, and plants), $CHCl_3$ emissions from Antarctic tundra (Zhang et al., 2021), Dead Sea landscapes (Schechner et al., 2019), and coastal wetlands degraded by sea level rise (Jiao et al., 2018) were recently identified. Measurements from the AGAGE network suggest total global $CHCl_3$ emissions for 2020 of 339 (±70) Gg yr^{-1} (**Table 1-4**). Consistent with the global mole fractions, emissions increased until 2017 and dropped sharply afterwards back to 2015 values (**Figure 1-7**). Regional emission estimates for 2010–2015 suggest that the global emission increase of 44 Gg over this time period can be explained entirely by increasing emissions from eastern China (Fang et al., 2019a; 2019b).

Atmospheric C_2Cl_4 has continued to decrease over the past few decades (**Figure 1-7**). Global mean mole fractions in 2020 amount to 1.01 and 1.12 ppt based on the AGAGE and NOAA networks, respectively (**Table 1-4**). Decrease rates of 3.8% yr^{-1} (AGAGE) and 5.9% yr^{-1} (NOAA) for 2019–2020 are similar to values provided in the last Assessment for 2015–2016, suggesting that while the decreasing trend has slowed down when compared to the first decade of this century, it is still ongoing.

In consequence, global C_2Cl_4 emission estimates also show a slow decline, reaching values of 80 (±39) Gg yr^{-1} and 91 (±47) Gg yr^{-1} for AGAGE and NOAA, respectively (**Table 1-4**). The long-term decline of C_2Cl_4 emissions based on the 12-box model is in good agreement with estimates based on chemistry-transport modeling if the termolecular loss reaction of C_2Cl_4 with Cl atoms is not included (**Figure 1-7**). The latter approach suggests similar emissions from North America, Europe, and Asia, which together account for the total global emissions (Claxton et al., 2020). It also demonstrates the sensitivity of the emission estimates to the atmospheric C_2Cl_4 lifetime by showing that global emissions are ~1.5 times higher if an uncertain chlorine sink is included. Regional top-down emission estimates suggest modest contributions from India (2.9 ± 0.5 Gg yr^{-1}) and South Africa (0.8 ± 0.2 Gg yr^{-1}), accounting for 3.5% and 1% of the global emissions, respectively (Say et al., 2019; 2020).

No 1,2-dichloroethane (CH_2ClCH_2Cl) measurements have been published for either the AGAGE or the NOAA network; as a result, its budget and emissions are poorly constrained. Based on 2013/14 aircraft observations, boundary layer CH_2ClCH_2Cl mole fractions are of the order ~10–20 ppt in the NH (Engel, Rigby et al., 2018), with SH mole fractions a factor of ~6 lower (Hossaini et al., 2016), indicative of dominant anthropogenic sources.

For other minor chlorinated VSLS compounds such as chloroethane (C_2H_5Cl) and 1,2-dichloropropane ($C_3H_6Cl_2$), noteworthy mole fractions have been observed in and above the planetary boundary over a highly industrialized region in China during spring 2016 (Benish et al., 2021). No global background values are available for either of the two gases. While C_2H_5Cl and $C_3H_6Cl_2$ abundances were significantly lower than that of CH_2Cl_2, they were of the same magnitude as $CHCl_3$ and CH_2ClCH_2Cl, with all chlorinated VSL SGs being enhanced in this region compared to their global tropospheric background levels.

Short-lived halogenated unsaturated hydrocarbons (halogenated olefins), including the hydrofluoroolefins (HFOs) and the hydrochlorofluoroolefins (HCFOs), have been introduced as alternatives to HCFCs and HFCs due to their low GWP. While the HFOs are included in *Chapter 2*, the HCFOs are discussed as part of the VSLSs in this section. The only atmospheric record of HCFOs currently available is that for HCFO-1233zd(E) (E-CF_3CH=CHCl) from central Europe, where it has been detectable in all samples since 2016. A mean mole fraction of 0.03 ppt observed at the Jungfraujoch station in 2016 has increased to 0.19 ppt in 2020 (update from Vollmer et al., 2015a), which under the assumption of linear growth corresponds to an increase of 36% yr^{-1}. Based on these observations, HCFO-1233zd(E) emission estimates from Switzerland of 6 Mg yr^{-1} were derived for 2019/20 (Rust et al., 2022).

1.3.1.2 Bromine-Containing VSL SGs

The most abundant brominated VSLSs, bromoform ($CHBr_3$) and dibromomethane (CH_2Br_2), are largely produced by marine organisms such as macroalgae and phytoplankton (e.g., Carpenter and Liss, 2000; Leedham et al., 2013; Keng et al., 2021). $CHBr_3$ also has some anthropogenic sources resulting from the chemical treatment of sea water used in cooling units, industry, and desalination plants, as well as for ship ballast water

Box 1-3. Metrics for ODSs and VSLSs

Halogenated long-lived ozone-depleting substances (ODSs; lifetimes >0.5 yr) and very short-lived substances (VSLSs; lifetimes <0.5 yr) both contribute to stratospheric ozone depletion. However, the two groups of gases differ substantially in terms of their sources, emissions, and tropospheric processing. Some of the existing metrics traditionally used to evaluate long-lived ODSs cannot be directly applied to VSLSs without considering additional adjustments.

Commonalities and differences

Long-lived ODSs have largely anthropogenic sources, resulting from their past use and from current inadvertent by-product formation. Some gases have accumulated substantial banks over the past decades, which can delay emission reductions. Only a small fraction of ODSs stem from natural sources such as oceanic and terrestrial ecosystems. VSLSs have both natural and anthropogenic sources, with brominated and iodinated VSLSs being mostly produced naturally in the ocean and some smaller anthropogenic contributions from coastal power plants and ships (Maas et al., 2021). In contrast, chlorinated VSLSs originate largely from industrial processes, and their atmospheric abundances have increased strongly over the last two decades due to growing industrial emissions (Claxton et al., 2020). Noteworthy natural VSLS emissions can be impacted by anthropogenically driven oceanographic, meteorological, and air quality changes (*Chapter 7*). In consequence, there could be future changes in VSLS emissions resulting from direct anthropogenic emissions or anthropogenically altered natural emissions. Distinguishing between these two source terms will be a challenge, due to the existing large uncertainties in emission estimates and the paucity of observational data (see **Box 1-2**).

Most long-lived ODSs persist in the atmosphere for decades to centuries and are therefore well mixed throughout the troposphere. Irrespective of the geographic location of their emissions, nearly all long-lived ODSs are eventually injected into the stratosphere, where they release their ozone-depleting chlorine and bromine. In consequence, their impact on stratospheric ozone is largely independent of changes in emission location and troposphere-stratosphere transport patterns. In contrast, VSLSs can undergo rapid chemical degradation with pronounced lifetime variations depending on the distribution of tropospheric oxidants (e.g., Rex et al., 2014) and background conditions such as temperature and solar flux (e.g., Hossaini et al., 2010). In consequence, the impact of VSLSs on stratospheric ozone depends on a complex interplay between emission location, transport patterns, efficiency of deposition processes, and chemical processing, with enhanced transport in the tropics being of particular importance. In addition, VSLSs in inorganic form can impact tropospheric chemistry, thus contributing to tropospheric and stratospheric ozone depletion.

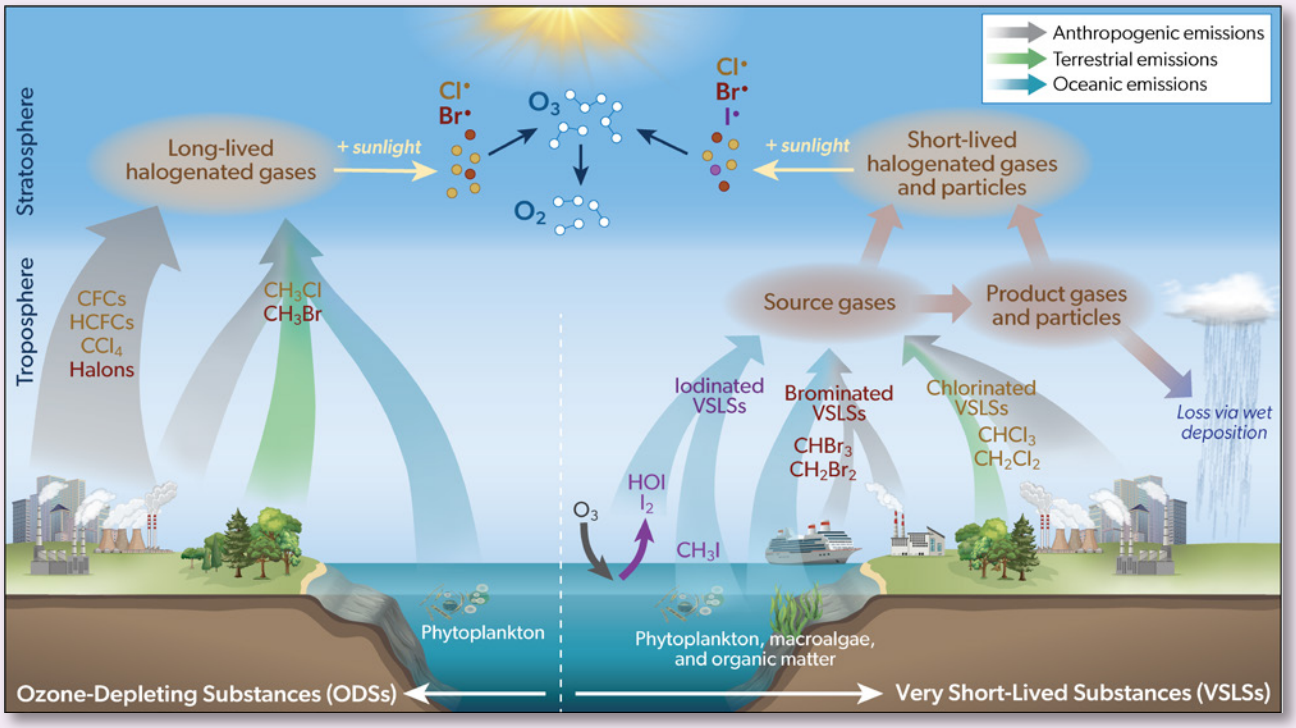

Box 1-3 Figure 1. Schematic of long-lived ozone-depleting substances (ODSs) and halogenated very short-lived substances (VSLSs).

Conventional metrics and their adjustments

Ozone depletion potential (ODP) was introduced as a metric for assessing a compound's ability to destroy stratospheric ozone (Wuebbles, 2015) and has been used extensively in policy frameworks, including the Montreal Protocol. The original concept was developed for long-lived ODSs and, given their uniform distribution and negligible chemical loss in the troposphere, is based on a single-value index independent of emission location and season. Moreover, the original ODP concept, having been developed for long-lived gases that do not impact tropospheric ozone, is based on the total column ozone change.

The more recent application of the ODP concept to VSLSs has led to some modifications of the original definition. As the ODP of a VSLS can change by a factor of up to 30 depending on where the emissions occur, ODP estimates for VSLSs must be reported as a function of season and location of emissions (e.g., Ko, Poulet et al., 2003; Brioude et al., 2010). Furthermore, the contribution of VSLSs to tropospheric ozone destruction needs to be excluded when calculating their ODP (Pisso et al., 2010; Claxton et al., 2019), prompting the introduction of the term stratospheric ODP (SODP, Zhang et al., 2020). Maps of SODP-weighted emissions and their global averages allow for the direct comparisons of the impact of short- and long-lived halogens on stratospheric ozone (Tegtmeier et al., 2015). For long-lived gases, ODP and SODP have nearly the same values, whereas for VSLSs, the difference between these two metrics provides a measure of their influence on tropospheric ozone (Zhang et al., 2020).

Quantitative intercomparisons of the total chlorine and bromine contributions to the stratospheric halogen loading also suffer from inconsistencies. For example, chlorinated VSLSs are taken into account when estimating the total tropospheric organic chlorine (*Section 1.4.1.1*), whereas brominated VSLSs are not included in the calculation of the total tropospheric organic bromine (*Section 1.4.2.1*). While this approach does not alter existing tropospheric halogen trends, brominated VSLSs may be of growing interest for trend estimates in coming years, given their highly uncertain future changes (*Chapter 7*).

A metric of the total amount of halogen-driven stratospheric ozone depletion is the equivalent effective stratospheric chlorine (EESC; *Section 1.4.4*). Current formulations of EESC (Engel et al., 2018) do not include the impact of VSLSs on stratospheric ozone and thus do not reflect their changing emissions over time. Given the highly variable tropospheric lifetimes of VSLSs, quantifying their contribution to EESC requires a seasonally resolved stratospheric injection function taking into account their tropical tropopause abundance, instead of the global annual surface mean values usually considered for ODSs.

Overall, large improvements in the understanding of VSLS emissions and tropospheric processing have been made over the recent decades. This has led to adjustments of some of the existing metrics, providing a basic framework for consistent intercomparison of VSLS and ODS impacts on stratospheric ozone. Other metrics continue to include only ODSs and might change in the future once detailed VSLS distribution estimates are available.

(Boudjellaba et al., 2016; Maas et al., 2019; 2021; Quivet et al., 2022). Their marine boundary layer mole fractions amount to 1.2 ppt ($CHBr_3$) and 0.9 ppt (CH_2Br_2) on average (**Table 1-5**), with a pronounced spatial variability.

Air-sea fluxes of brominated VSLSs show large spatiotemporal variations driven by changes in primary marine productivity, biogeochemical cycling, anthropogenic sources, sea surface temperature, and meteorology. Ship-based and land-based observations suggest high fluxes in coastal and upwelling regions with steep gradients toward the open ocean (e.g., Ziska et al., 2013). Given this large variability and the lack of adequate seasonal and spatial coverage of observational data, brominated VSLS emission inventories are not well constrained, with bottom-up estimates being a factor of two lower than top-down estimates. For $CHBr_3$, the range of global emission estimates of 120–820 Gg Br yr^{-1} given in the last Assessment (Engel, Rigby et al., 2018) has been changed to 150–820 Gg Br yr^{-1}, reflecting an update of the Ziska et al. (2013) emission climatology (Fiehn et al., 2018). The updated inventory shows enhanced $CHBr_3$ emissions in the tropical Indian Ocean and subtropical northern Atlantic, with emissions in the west Indian Ocean being almost twice as large as previous estimates. A new $CHBr_3$ emission inventory from a data-oriented machine-learning algorithm suggests an oceanic source of 385 Gg Br yr^{-1}, falling in the middle of the range of existing estimates (Wang et al., 2019). The study derived very high regional $CHBr_3$ emissions for the Bay of Bengal and South China Sea; the authors pointed out that these might be overestimated due to the lack of data in these regions and therefore require further confirmation.

Anthropogenic sources of $CHBr_3$ from the chlorination of coastal power plant cooling water in East and Southeast Asia have been estimated to amount to 25–75 Gg Br yr^{-1} (Maas et al., 2021). As such industrial sources are not included in any of the existing bottom-up emission inventories, they could explain some of the discrepancies between different approaches. For CH_2Br_2, the range from the last Assessment (57–280 Gg Br yr^{-1}) has been reduced to 54–100 Gg Br yr^{-1} when taking the new machine-learning algorithm estimates into account. This is consistent with a model sensitivity study showing more realistic CH_2Br_2 abundances in the lower-stratosphere NH high latitudes if the lower emission scenarios (i.e., Liang et al., 2010; Ordóñez et al., 2012) are used (Keber et al., 2020). Potential future changes of brominated VSLS emissions are discussed in *Chapter 7*.

1.3.1.3 Iodine-Containing VSL SGs

Iodinated VSLSs include the group of organic SGs, which stem from biotic (e.g., phytoplankton and cyanobacteria) and abiotic (e.g., photochemical breakdown of dissolved organic matter) oceanic sources. For the first time, this section also discusses inorganic iodine emissions, as new studies suggest that both organic and inorganic sources can contribute iodine to the stratosphere. Consequently, and differing from other VSLS

and ODS sources, iodine SGs include both organic (i.e., carbon-bonded) and inorganic (i.e., HOI, I_2), gas-phase emissions from the surface. However, since inorganic iodine plays an active role in tropospheric chemistry (i.e., recycling back and forth among reactive and reservoir species), the inorganic iodine SGs are expected to be completely recycled to inorganic PGs before they reach the upper troposphere (*Section 1.3.2.3*).

Methyl iodide (CH_3I) is the main organic iodine-containing source gas, with a mean mole fraction of 0.8 ppt in the marine atmospheric boundary layer (**Table 1-5**). Air-sea fluxes of CH_3I from coastal and open-ocean environments have been estimated to cause an input of 157–550 Gg I yr^{-1} to the atmosphere (Butler et al., 2007; Ziska et al., 2013), which is unchanged compared to the last two Assessments. CH_3I has been proposed as a replacement of CH_3Br as it is very effective in controlling a wide variety of soil pests and weeds (Waggoner et al., 2000). However, environmental and health concerns have limited its use as fumigant, and no current emission estimates from such sources exist. Other iodinated VSLSs, such as CH_2I_2, CH_2IBr, and, CH_2ICl account for an additional 340 Gg I yr^{-1}. Iodotrifluoromethane (CF_3I), currently under consideration as a replacement for halon in fire suppression

Table 1-5. Summary of observed mole fractions (in ppt) of VSL SGs from the marine atmospheric boundary layer (MBL) to the tropical tropopause layer (TTL) and above. Note that many of the upper-tropospheric measurements were made at least one decade ago in the case of brominated and iodinated SGs. As chlorinated SGs have significant anthropogenic sources and some show trends, data are based only on measurements from 2015 onwards.

	Marine Boundary Layer		Lower TTL		LZRH(z_0)[1]		Upper TTL		Tropical Tropopause	
Height Range			12 – 14 km		14.5 – 15.5 km		15.5 – 16.5 km		16.5 – 17.5 km	
Potential Temperature Range			340 – 355 K		355 – 365 K		365 – 375 K		375 – 385 K	
	Median[2]	Range[4]	Mean[3]	Range[4]	Mean[3]	Range[4]	Mean[3]	Range[4]	Mean[3]	Range[4]
Chlorinated VSLSs Based on Measurements from 2015 Onwards										
CH_2Cl_2			36.9	30.4–59.3	37.1	29.2–55.7	41.6	30.8–68.4	41.3	33.4–56.9
$CHCl_3$			7.7	5.8–8.4	7.7	6.0–8.6	7.8	5.7–8.5	6.7	5.4–7.8
C_2Cl_4			0.77	0.42–1.02	0.66	0.32–0.95	0.55	0.15–0.90	0.31	0.07–0.71
CH_2ClCH_2Cl			8.3	3.3–11.4	8.7	3.3–13.6	7.2	1.9–12.1	4.0	1.0–8.4
Brominated and Iodinated VSLSs Based on Measurements from 2004 Onwards										
$CHBr_3$	1.2	0.4–4.0	0.61	0.22–1.51	0.45	0.05–1.60	0.35	0.02–1.20	0.18	0.01–0.54
CH_2Br_2	0.9	0.6–1.7	0.93	0.61–1.15	0.81	0.49–1.08	0.72	0.30–1.11	0.59	0.17–0.89
CH_2BrCl	0.10	0.07–0.12	0.22	0.07–0.45	0.19	0.08–0.45	0.22	0.10–0.42	0.18	0.07–0.40
$CHBr_2Cl$	0.3	0.1–0.8	0.13	0.06–0.23	0.10	0.04–0.19	0.09	0.02–0.16	0.06	0.00–0.14
$CHBrCl_2$	0.3	0.1–0.9	0.23	0.14–0.55	0.17	0.08–0.40	0.15	0.07–0.31	0.11	0.05–0.32
CH_3I	0.8	0.3–2.1	0.16	0.00–0.49	0.10	0.00–0.32	0.05	0.00–0.32	0.03	0.00–0.14
Total VSLS Halogen Budgets Based on Estimates Above										
Total Cl			118	87–173	118	85–170	124	84–191	113 (105)[5]	86–158 (85–125)[5]
Anthrop. Cl[6]			98	72–147	99	70–144	104	69–164	94	71–134
Total Br	6.5	2.8–18.0	4.4	2.2–8.3	3.5	1.3–8.3	3.0	0.9–6.9	2.1	0.5–4.4
Total I	0.8	0.3–2.1	0.16	0.00–0.49	0.10	0.00–0.32	0.05	0.00–0.32	0.03	0.00–0.14

Notes:
[1] LZRH (z_0) corresponds to the level of zero clear-sky radiative heating (see **Box 1-3** of Carpenter, Reimann et al., 2014). As in the previous Assessment, this level is at about 15 km or 360 K, where there is a transition from clear-sky radiative cooling to clear-sky radiative heating.
[2] In the MBL, abundances are median values. For tropical MBL CH_2Cl_2, $CHCl_3$, CH_2ClCH_2Cl, and C_2Cl_4, no updates exist to the data from the CAST and CONTRAST missions presented in the last Assessment. MBL $CHBr_3$, CH_2Br_2, and CH_3I data are based on tropical data from the HalOcAt campaign (Ziska et al., 2013). MBL CH_2BrCl, $CHBr_2Cl$, and $CHBrCl_2$ data are from the previous Assessment (Carpenter, Reimann et al., 2014).
[3] In the TTL, abundances are mean values. For brominated VSLSs and CH_3I, data have been compiled from observations obtained during the Pre-AVE, CR-AVE, TC4, HIPPO, SHIVA, CONTRAST, and ATTREX aircraft campaigns (Navarro et al., 2015; Pan et al., 2017; Sala et al., 2014; Wofsy et al., 2011) and from balloon observations (Brinckmann et al., 2012). ATTREX values used here differ from those used in Wales et al. (2018), as they have been filtered by altitude instead of applying any tracer-tracer correlation. For chlorinated VSLSs, data are from the VIRGAS (2015) and POSIDON (2016) missions in 2015/16 only. (See below for definitions of field mission acronyms.) Note that calibration scales for VSLSs may differ among different research groups (e.g., Hall et al., 2014; Jones et al., 2011). Intercalibration of standards during CAST, CONTRAST, and ATTREX revealed generally good agreement between VSLS measurements performed by different instruments (relative standard deviation of <10%), although losses in aircraft sampling lines can add a major source of uncertainty (Andrews et al., 2016).
[4] In the MBL, the stated observed range is 10th to 90th percentile. In the TTL, the stated observed range represents the smallest mean minus 1 standard deviation and the largest mean plus 1 standard deviation.
[5] Values for 2019 are based on updated model simulations first described in Hossaini et al. (2019), which is used to derive total stratospheric VSL source gas injection for chlorine, as explained in *Section 1.3.2.1*. Model values are used in order to reduce variability from individual campaigns in assessing total Cl input to the stratosphere.
[6] The anthropogenic fraction of VSLS (Anthrop. Cl) is approximate and has been calculated from the sum of 90% of CH_2Cl_2, 50% of $CHCl_3$, and 100% of other compounds. Anthropogenic $CHCl_3$ source contributions are highly uncertain and have been chosen here as the upper range estimate of 50%.

Pre-AVE = Pre-Aura Validation Experiment (2004); CR-AVE = Costa Rica-Aura Validation Experiment (2006); TC4 = Tropical Composition, Cloud, and Climate Coupling missions (2007); HIPPO = HIAPER (High-Performance Instrumented Airborne Platform for Environmental Research) Pole-to-Pole Observations (2009–2011); SHIVA = Stratospheric Ozone: Halogen Impacts in a Varying Atmosphere (2011); ATTREX = Airborne Tropical TRopopause EXperiment (2011, 2013, and 2014); CAST = Coordinated Airborne Studies in the Tropics (2014); CONTRAST = Convective Transport of Active Species in the Tropics (2014); VIRGAS = Volcano-plume Investigation Readiness and Gas-phase and Aerosol Sulfur (2015); POSIDON = Pacific Oxidants, Sulfur, Ice, Dehydration, and cONvection (2016).

systems, has been estimated to have very little impact on stratospheric ozone due to its short lifetime (Zhang et al., 2020).

Inorganic iodine emissions occur in the form of hypoiodous acid (HOI) and molecular iodine (I_2) fluxes when ocean surface iodide (I^-) dissolved in the seawater reacts with deposited gas-phase ozone (Carpenter et al., 2013). Emission estimates of inorganic iodine depend strongly on surface I^- concentrations, which can vary by more than two orders of magnitude and are difficult to parameterize in regions that lack observational data (e.g., Wadley et al., 2020). A high-resolution dataset of sea-surface I^- estimates based on a machine learning algorithm suggests highest I^- concentrations in the tropics (Sherwen et al., 2019; Carpenter et al., 2021). Another uncertainty arises from the effect of the sea surface microlayer on I_2 solubility and emissions, which is currently not fully understood (Tinel et al., 2020). Global estimates of oceanic inorganic iodine emissions stem from modeling studies and range between 1.9 Tg I yr^{-1} (Prados-Roman et al., 2015) and 2.1 Tg I yr^{-1} (Sherwen et al., 2016). In consequence, inorganic iodine sources dominate the tropospheric iodine budget (Prados-Roman et al., 2015) and can account for a large fraction of tropospheric iodine oxide (IO) levels in the tropical Atlantic (Read et al., 2008; Lawler et al., 2014) and eastern Pacific (MacDonald et al., 2014), although they fail to adequately explain IO measurements in the Indian and Southern Oceans (Inamdar et al., 2020). Potential future changes of iodinated VSLS emissions are discussed in *Chapter 7*.

1.3.2 Input of VSLS Halogen to the Stratosphere

During transport from their surface sources to the stratosphere, halogenated SGs can undergo chemical degradation mainly through reaction with OH or photolysis. The originating halogenated PGs can experience dry and wet scavenging during transit to the stratosphere. We differentiate between stratospheric halogen input in the form of the emitted source gases (source gas injection [SGI]) and in the form of product gases (product gas injection [PGI]). While PGI has been traditionally based on gas-phase inorganic halogens, it can now also include

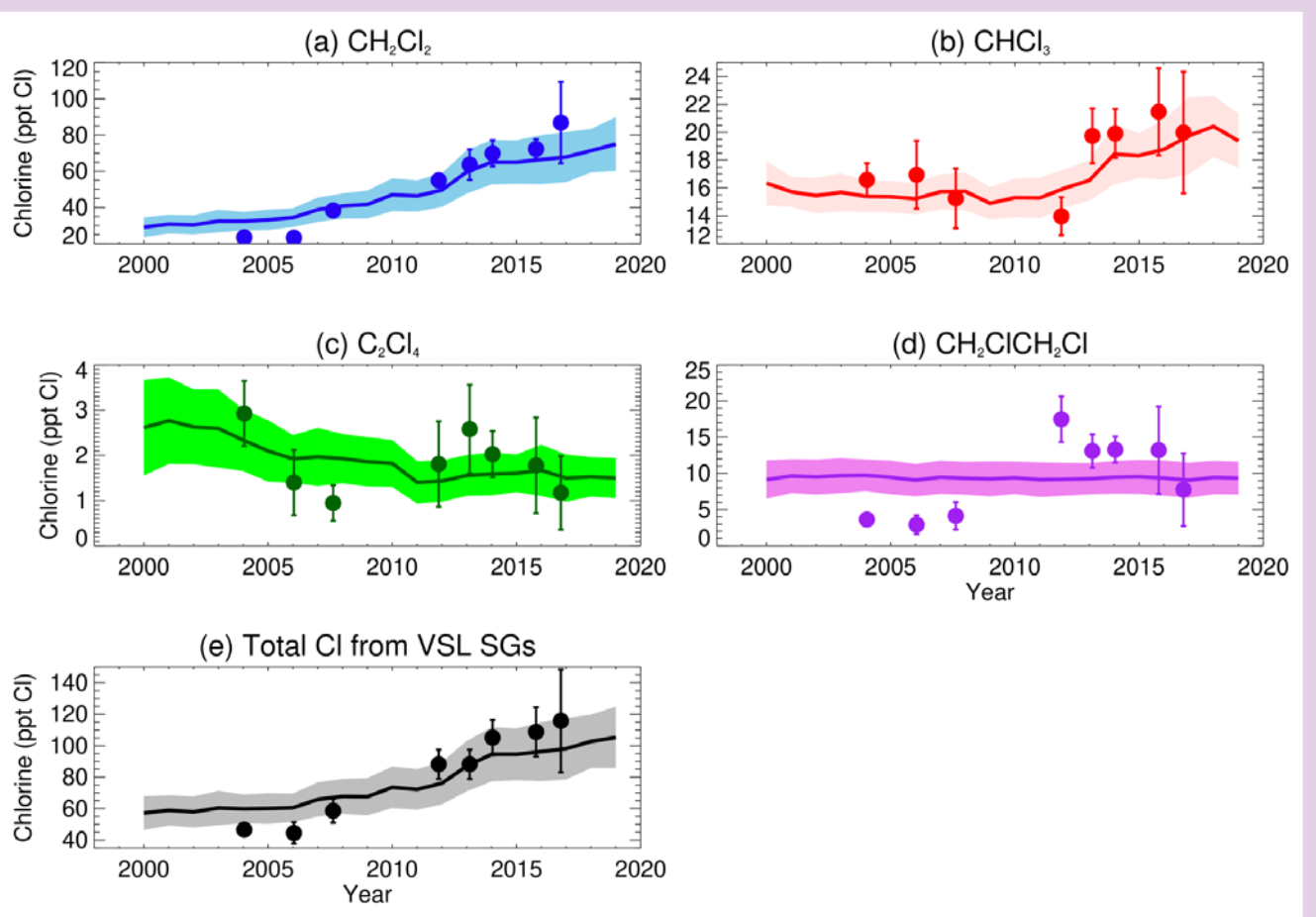

Figure 1-8. Stratospheric chlorine source gas injection (ppt Cl) from (a) CH_2Cl_2, (b) $CHCl_3$, (c) C_2Cl_4, (d) CH_2ClCH_2Cl, and (e) total. Model results (solid lines) with the ±1-sigma uncertainty (shading) are tropical mean (20°N–20°S) values derived from simulations with the offline 3-D chemistry-transport model TOMCAT/SLIMCAT constrained by observed surface abundances of these source gases. Observed tropopause quantities (filled circles) are averages (vertical bars denote ±1-sigma) for available aircraft data between 16.5 and 17.5 km in the tropics from Pre-AVE in 2004; CR-AVE in 2006; TC4 in 2007; ATTREX in 2011, 2013, and 2014; VIRGAS in 2015; and POSIDON in 2016 (campaign acronyms are provided in **Table 1-5**). [Updated from Hossaini et al., 2019.]

carbon-bonded compounds (e.g., phosgene) and particulate iodine (iodine taken up in particles). The relative contributions of SGI and PGI are different for each compound and depend on source distributions, tropospheric loss rates, timescales of troposphere-to-stratosphere transport, heterogeneous recycling processes, and removal by precipitation or sedimentation.

SGI is estimated from the global average halogen SG mixing ratios transported into the stratosphere and has been quantified from measurements around the tropical tropopause (~17 km), complemented by model simulations. PGI is estimated as the global average inorganic halogen mixing ratio injected into the stratosphere and has been derived mostly from global, Lagrangian, and box-modeling studies oriented to reproduce aircraft and balloon observations close to the tropopause.

1.3.2.1 Input of VSLS Chlorine to the Stratosphere

The input of VSLS chlorine to the stratosphere amounts to a total of 130 ± 30 ppt Cl in 2020. The underlying SGI and PGI contributions are estimated based on model data constrained by surface observations as well as aircraft and satellite observations, as explained below.

Observation-based chlorine SGI from VSLSs was estimated as 113 (86–158) ppt Cl based on measurements from the two tropical campaigns VIRGAS (2015) and POSIDON (2016; Table 1-5). CH_2Cl_2, $CHCl_3$, and CH_2ClCH_2Cl account for ~73%, ~18%, and ~7% of this total, respectively; the remaining ~1% stems from C_2Cl_4. Total chlorine SGI has increased by 13 ppt Cl (12%) compared to observational estimates given in the last Assessment and based on 2013/14 aircraft missions, with most of this difference (10 ppt Cl) driven by anthropogenic VSLS changes. It is noteworthy that the campaign-derived estimates might not reflect tropical average SGI trends, given the significant spatiotemporal variability in VSLS transport and lifetimes. For instance, aircraft measurements in the Asian summer monsoon anticyclone region during the StratoClim campaign (2015/16) showed significantly enhanced levels of CH_2Cl_2, CH_2ClCH_2Cl, and $CHCl_3$ (Adcock et al., 2021). In total, the three gases add up to 169–393 ppt Cl, which is more than two times the abundances observed over the West Pacific and Gulf of Mexico region, highlighting that the anticyclone acts as a rapid transport mechanism of nearby surface emissions into the stratosphere. Observations above Europe and the Atlantic during the WISE aircraft campaign (2017) detected up to a 150% (100%) enhancement in CH_2Cl_2 ($CHCl_3$) in air masses that entered the extratropical UTLS via the Asian summer monsoon anticyclone (Lauther et al., 2022). On a global scale, the enhanced entrainment has been estimated to contribute between 0.3 and 34.9 ppt to total equivalent chlorine in the NH lower stratosphere (Adcock et al., 2021; Ploeger et al., 2017).

Model-based chlorine SGI from VSLSs in 2019 is 105 (85–125) ppt (**Table 1-5**), showing good agreement with the observational data (**Figure 1-8**; update of Hossaini et al., 2019), with differences largely explained by limited sampling during individual campaigns. The chemistry-transport model simulations based on the latest and most up-to-date model version give an updated value of 96 (77–115) ppt for chlorine SGI in 2016. Consistent with the observed surface mole fractions, which are used to drive the simulations, the SGI model estimates show a continuous positive trend due to growing CH_2Cl_2, with slower growth after 2014 compared to earlier years.

Chlorinated PGI have been estimated based on TTL observations of phosgene ($COCl_2$) and hydrogen chloride (HCl), which can arise from chlorinated VSLS PGI or from recirculation of stratospheric air. Based on observations of $COCl_2$ (up to 32 ppt Cl) and HCl (up to 20 ppt Cl), chlorinated VSLS PGI was estimated as 25 ppt in the last Assessment (Engel, Rigby et al., 2018). The contribution of VSLSs to satellite measurements of $COCl_2$ between 2004 and 2016 changed from 20% to 27% (Harrison et al., 2019), consistent with model-derived long-term trends of chlorine PGI over the same time period (Hossaini et al., 2015). This trend is suspected to be driven by the growth of the CH_2Cl_2 degradation products, which are the largest contributors to the overall PGI (Hossaini et al., 2019).

Chlorinated VSLS PGI estimates are also available from model simulations, with the complexity of the involved chemical processes being one of the major challenges. Hossaini et al. (2019) determined a non-zero chlorine PGI from VSLSs of ~18 (±5) ppt Cl, which increases to ~34 (±7) ppt Cl if no tropospheric wet removal of chlorinated PGs is assumed. Following the methodology of the last Assessment, we derive a best estimate of 25 (13–50) ppt Cl PGI from VSLSs (**Table 1-6**), with the lower limit reflecting the lower limit from modeling work (Hossaini et al., 2019) and the mean value and upper limit reflecting the observational estimates.

In summary, a total of 130 (100–160) ppt Cl is injected into the stratosphere, according to our best estimates (**Table 1-6**). The contribution from SGI accounts for 105 (85–125) ppt Cl and is based on model data constrained by surface observations

Table 1-6. Summary of estimated VSL source gas injection (SGI) and product gas injection (PGI) contributions to stratospheric halogens (based on observations and model results).

VSLS Best Estimate (ppt)	SGI[1]	PGI[2]	Total (SGI + PGI)[3]
Chlorine	105 (85–125)	25 (13–50)	130 (100–160)
Bromine	2.1 (0.5–4.4)	2.8 (1.8–4.2)	5 (3–7)
Iodine	0–0.1	0.3–0.8	0.3–0.9

Notes:
[1] The SGI estimate for chlorinated SGs, which show increasing trends, is representative of the year 2019 based on model data (see **Table 1-5**). SGI for bromine and iodine represent the global mean from 2004 onwards, as there are no reports of long-term trends.
[2] PGI for chlorine has been estimated from observations based on HCl and $COCl_2$ and modeling studies and is representative of the year 2020. PGI for bromine has been estimated by box- and global-modeling studies based on BrO measurements from 2004 onwards.
[3] The SGI and PGI lower/upper limits are not strictly additive, because whenever SGI increases (e.g., due to rapid lifting), the correspondent PGI arising from SG photodecomposition decreases (and vice versa).

(update of Hossaini et al., 2019) in order to avoid the seasonal and regional variability of individual campaign-based estimates. The contribution from PGI accounts for 25 (13–50) ppt Cl. Compared to 2016 estimates based on the same methodology, chlorine VSLS injection to the stratosphere has increased by 10 ppt. While this increase is not significant, given the large uncertainties of the total VSLS injection, it is consistent with increasing abundances of tropospheric CH_2Cl_2. Model-derived long-term trends suggest that the relative contribution of VSLSs to total stratospheric chlorine increased from ~2% in 2000 to ~3.4% in 2017, reflecting VSLS growth and decreases in long-lived halocarbons (Hossaini et al., 2019).

1.3.2.2 Input of VSLS Bromine to the Stratosphere

Since the previous Assessment, the two tropical campaigns VIRGAS (2015) and POSIDON (2016) have confirmed existing estimates of stratospheric injections of bromine VSL SGs, which range from 0.5 to 4.4 ppt (**Table 1-5**). Most of the stratospheric injection of $CHBr_3$ was modeled to occur over the southern tip of India during boreal summer and over the Western Pacific in boreal winter, with an interannual variability of up to 20% due to the coupled ocean-atmosphere circulation system (Fiehn et al., 2018; Butler et al., 2018; Tegtmeier et al., 2020).

Taking into account all tropical measurements performed during the last two decades under the assumption of no long-term changes of brominated VSLSs, the current estimate for bromine SGI amounts to 2.1 (0.5–4.4) ppt Br, dominated by $CHBr_3$ and CH_2Br_2 (**Table 1-5**). The wider uncertainty range with respect to the last Assessment is in agreement with recent modeling studies that highlight the significant dependence of bromine SGI on the seasonal and regional variability of surface emissions (Fiehn et al., 2017; 2018; Tegtmeier et al., 2012; Keber et al., 2020), as well as on the variable photochemical degradation lifetime of VSL SGs over shallow and rapid convective regions (Aschmann and Sinnhuber, 2013; Fernandez et al., 2014; Butler et al., 2018; Filus et al., 2020).

At the NH extratropical tropopause, total organic bromine from VSLSs of up to 4.0 ± 1.2 ppt (fall) and 5.2 ± 1.3 ppt (winter) was detected during the TACTS (2012), WISE (2017), and PGS (2015/16) aircraft campaigns (**Figure 1-9**; Keber et al., 2020). These observations indicate that the seasonal SG troposphere-to-stratosphere transport over the NH mid- to high latitudes is significantly higher than the annual mean tropical injection of 2.1 (0.5–4.4) ppt (**Table 1-5**). The increase of SG mixing ratios with latitude, in particular during winter (**Figure 1-9**; Keber et al., 2020), is most probably related to the lifetime variations with season and latitude (*Annex*), although the influence of higher regional or seasonal sources cannot be excluded.

Stratospheric injection of bromine PGI across the extratropical tropopause was estimated as 1.5 ± 0.6 ppt, with a range of 0.2–3.3 ppt, depending on latitude (Rotermund et al., 2021). No new tropical PG observations have become available since the last Assessment. Global modeling studies confirm that a

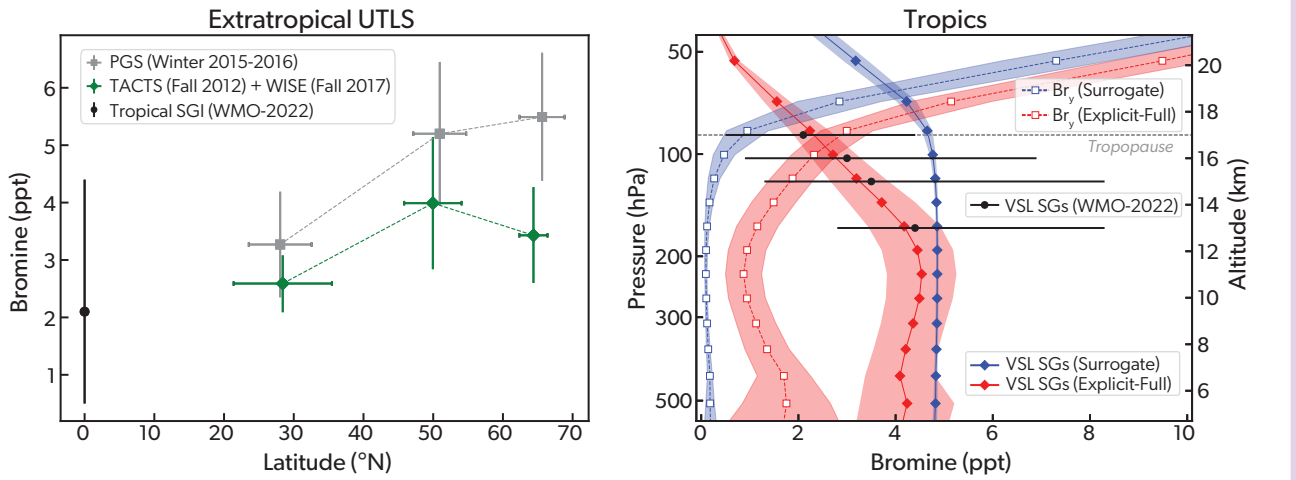

Figure 1-9. *(left panel)* Latitudinal cross section of total brominated VSL SGs observed during the PGS (gray) and WISE+TACTS (green) extratropical aircraft campaigns, binned by latitude just below the local tropopause (error bars denote 1-sigma uncertainty). Tropical SGI of 2.1 ppt Br is also shown (black; **Table 1-6**). Adapted from Keber et al. (2020). *(right panel)* Tropical vertical profile of brominated VSL SGs (filled diamonds) and inorganic bromine (Br_y; empty squares) for two different tropospheric chemical schemes: a simplified approach considering long-lived CH_3Br as a surrogate for VSL SGs (blue) and an explicit mechanism considering major and minor VSL SGs, as well as a full chemical treatment of Br_y processing in the troposphere (red). Note that at and below the tropopause, VSL PGs are assumed to be equal to Br_y, whereas above the tropopause Br_y also accounts for long-lived ODS bromine degradation. Shaded areas represent the annual spatiotemporal variability (mean ± 1-sigma) within the tropics (20°N–20°S). Black filled circles and bars show the assessed total brominated VSL SGs observational mean ± range within the TTL (see **Table 1-5**). WISE = Wave-driven ISentropic Exchange; TACTS = Transport and Composition in the Upper Troposphere/Lowermost Stratosphere; PGS = POLSTRACC (The Polar Stratosphere in a Changing Climate), GW-LCYCLE (Investigation of the Life cycle of gravity waves) and SALSA (Seasonality of Air mass transport and origin in the Lowermost Stratosphere). [Adapted from Fernandez et al., 2021.]

significant fraction of the VSLS bromine input to the stratosphere occurs via PGI, with tropical mean annual values ranging from 2.3 to 3.5 ppt (Tegtmeier et al., 2020; Fernandez et al., 2021). Model simulations with different degrees of complexity demonstrate that an explicit chemical modeling of tropospheric VSLSs is required to reproduce VSL SG observations in the TTL (**Figure 1-9**). The explicit modeling approach suggests significant enhancement of the VSL PG contribution to the total inorganic bromine (Br_y) in the lower stratosphere. Since inorganic PGs can directly destroy ozone, while the organic SGs first have to undergo chemical degradation, these relative contributions are important when analyzing the VSLS impact on stratospheric ozone.

In summary, a total of 5 (3–7) ppt bromine is injected to the stratosphere, with a contribution from SGI accounting for 2.1 (0.5–4.4) ppt Br and the remaining fraction of 2.8 (1.8–4.2) ppt Br delivered via PGI (**Table 1-6**). The new assessed range is very similar to the one provided in previous Assessments and indicates that the trend in the VSLS contribution to stratospheric bromine, if any, is very small (Tegtmeier et al., 2020).

1.3.2.3 Input of VSLS Iodine to the Stratosphere

In previous Assessments, stratospheric injection of iodinated VSLSs have considered only gas-phase iodine. As new evidence suggests a rapid shift in the partitioning between gas-phase and particulate iodine (Koenig et al., 2020), in this Assessment iodinated PG entrainment also includes the contribution of particulate iodine (inorganic iodine taken up in particles). The transport of particulate iodine across the tropopause can enable inorganic iodine, either from recycled inorganic SGs or from photodecomposed organic SGs, to reach the stratosphere. Given the larger stratospheric ozone destruction efficiency of a single iodine atom compared with that of bromine and chlorine (Klobas et al., 2021), small amounts of iodine reaching the stratosphere can contribute to stratospheric ozone loss (Koenig et al., 2020; Cuevas et al., 2022; see *Chapter 4*).

The contribution of iodine VSL SGs in the form of CH_3I to the stratospheric halogen loading remains identical to previous Assessments (0–0.1 ppt). Estimates derived from observations (**Table 1-5**) and global modeling studies suggest that CH_3I mixing ratios rapidly decay to close to zero just before reaching the tropical tropopause (Saiz-Lopez et al., 2015; Tegtmeier et al., 2013). The CH_3I decomposition has been suggested to make up for 30–40% of the inorganic iodine injection to the stratosphere (Koenig et al., 2020). The dominant fraction arises from the inorganic iodine SGs (i.e., HOI and I_2) released from the ocean surface and rapidly processed during their transport to the stratosphere (see *Section 1.3.1.3*).

Current quantitative measurements of IO radicals and particulate iodine performed during tropical and subtropical campaigns (TORERO, CONTRAST, and ATom) suggest that 0.77 ± 0.10 ppt of total iodine PGI can reach the tropopause (**Figure 1-10**; Koenig et al., 2020). In the upper troposphere, gas-phase iodine dominates, and observations are compatible with model simulations only if ice recycling is assumed (Saiz-Lopez et al.,

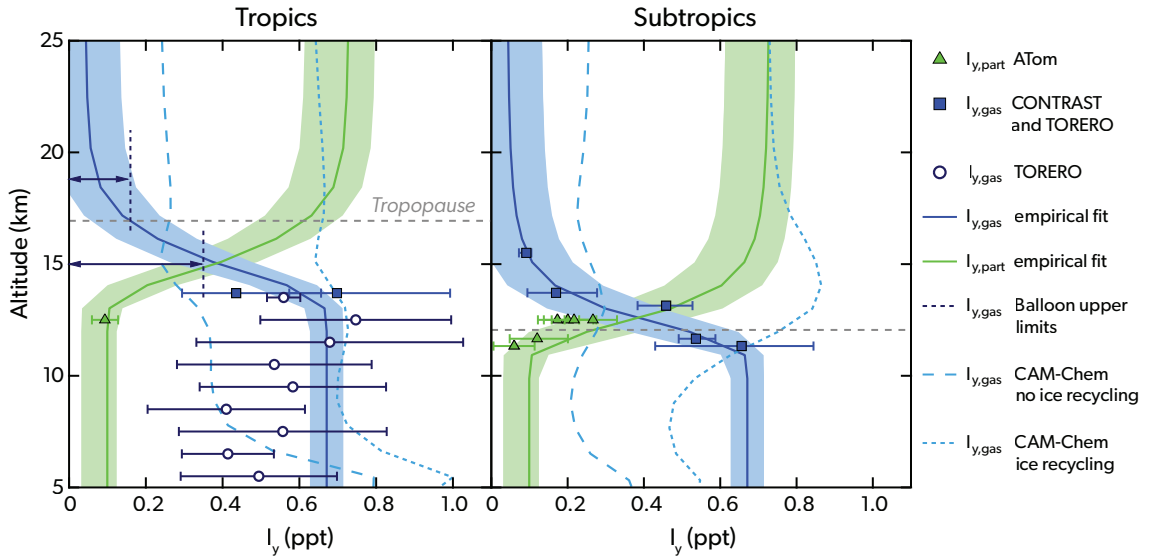

Figure 1-10. Vertical profiles of iodinated VSLSs within the tropics (20°N–20°S; left) and subtropics (20–60°N and 20–60°S; right). Aircraft-based total gas-phase iodine ($I_{y,gas}$, blue) and particulate iodine ($I_{y,part}$, green) mixing ratios are shown with different symbols depending on the campaign (ATom, CONTRAST, and TORERO [Tropical Ocean tRoposphere Exchange of Reactive halogen species and Oxygenated VOC]). Filled symbols indicate values in the UTLS, while tropospheric profiles are shown with empty symbols (error bars denote 1-sigma of observations plus 30% of box-model uncertainty, added in quadrature). Dark-blue vertical dashed-lines in the left panel indicate balloon-borne $I_{y,gas}$ upper-limit estimations during twilight (Butz et al., 2009) above and below the tropopause (light-gray horizontal dashed lines). Blue and green solid lines represent an empirical fit based on observed H_2O/O_3 ratios (shading denotes 1-sigma uncertainty) assuming a constant total stratospheric iodine abundance ($I_{y,gas}$ + $I_{y,part}$ = 0.77 ppt). CAM-Chem model output considering only gas-phase iodine with two different chemical schemes are shown in cyan. [Adapted from Koenig et al., 2020 and Saiz-Lopez et al., 2015.]

2015). However, in the upper TTL, empirical fits of the new observations suggest that the efficient gas-to-particle multiphase repartitioning results in particulate iodine being the dominant contribution of the 0.77 ± 0.10 ppt iodine injection (Koenig et al., 2020). The particulate iodine formation results in a net reduction of gas-phase iodine consistent with balloon-borne upper limits of the latter (Bosch et al., 2003; Butz et al., 2009). Given the large uncertainties and unknowns regarding iodine uptake and sedimentation on stratospheric aerosols, the overall gas-to-particle PGI partitioning currently cannot be distinguished. Estimations of the iodine entrainment into the stratosphere, and consequently of the iodine impact on the ozone layer, should be taken with caution.

Based on the available compendium of iodine measurements, we provide a new range of VSLS iodine input to the stratosphere of 0.3–0.9 ppt (**Table 1-6**), which is higher than the range of 0–0.8 ppt given in the last Assessment (Engel, Rigby et al., 2018). Stratospheric iodine input is dominated by inorganic

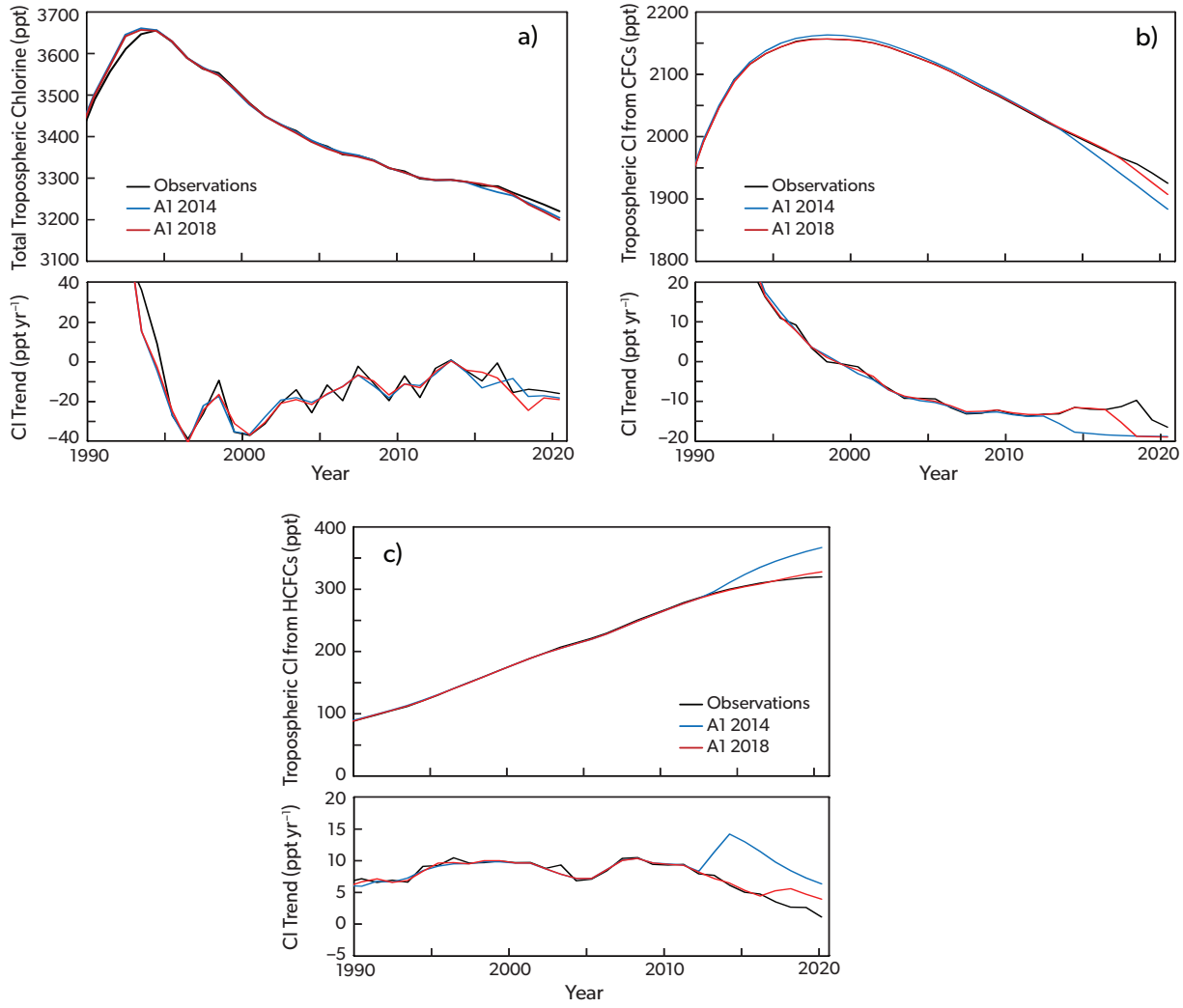

Figure 1-11. (a) Near-surface total tropospheric organic chlorine from the combined global ground-based measurement networks (black line), in comparison to the A1 scenarios from the 2014 (blue line) and 2018 (red line) Assessments. The observed global annual mole fractions of CFC-11, CFC-12, CFC-113, CH_3CCl_3, CCl_4, CH_3Cl, HCFC-22, HCFC-141b, HCFC-142b, and halon-1211 were determined from NOAA and AGAGE data. The observed global annual mole fractions of CFC-114, CFC-112, and CFC-113a were derived from AGAGE and UEA/FZJ data. Values for CFC-115 and CFC-13 were from AGAGE only. Total organic chlorine also includes contributions from VSL SGs (AGAGE and NOAA: CH_2Cl_2, and C_2Cl_4; AGAGE only: $CHCl_3$; see also **Table 1-6**). Continuous observations of these three species from AGAGE and NOAA are available only back to the mid-1990s. Between 1990 and 1995, the same constant mixing ratio as in the 2018 Assessment was used for CH_2Cl_2. Contributions from $CHCl_3$ and C_2Cl_4 before 1995 were not considered, as no in situ measurements are available. For species that are not included in the calculation of the scenarios (some minor ODSs and VSLSs), the observed values were added to the scenario totals in order to provide a comparison based on the same set of compounds. Panels (b) and (c) show the same as panel (a) for the sum of the tropospheric chlorine contents of the CFCs and the tropospheric chlorine content of all HCFCs, respectively.

Table 1-7. Contributions of long-lived ODSs and VSL SGs to total chlorine in the troposphere. Chlorine mid-year mole fractions were derived using AGAGE, NOAA, and UEA/FZJ data. Shown are absolute and relative contributions to total Cl over five-year periods, as indicated. For the average rate of change, the values in parentheses represent the standard deviation of the annual growth rates during the respective period, which reflects the observed variability (1 standard deviation). Changes in total chlorine were calculated relative to values at the beginning of each period (e.g., for 2008–2012, relative to 3342 ppt total chlorine in 2008). We refer to these periods as five-year periods, as they are based on annual average values, e.g., from the beginning of 2016 to the end of 2020. Values for past years differ slightly from previous Assessments because of updated calibration information, different methods for determining global mean mole fractions, and rounding errors.

Compound	Total Cl (ppt)			Contribution to Total Cl (%)			Average Rate of Change of Total Cl (ppt yr^{-1})		
	2012	2016	2020	2012	2016	2020	2008–2012	2012–2016	2016–2020
All CFCs	2026	1977	1925	61.5	60.3	59.8	–13.0 (0.7)	–12.1 (0.7)	–13.0 (3.1)
CCl_4	340	322	307	10.3	9.8	9.6	–4.7 (0.3)	–4.4 (0.3)	–3.9 (0.5)
HCFCs	286	310	320	8.7	9.4	9.9	9.0 (0.7)	5.9 (1.3)	2.5 (1.0)
CH_3CCl_3	16	7.8	4.2	0.48	0.24	0.13	–4.1 (0.9)	–2.0 (0.5)	–0.9 (0.2)
Halon-1211	3.96	3.55	3.16	0.12	0.11	0.1	–0.07 (0.01)	–0.10 (0.00)	–0.10 (0.01)
Total Controlled Cl	2672	2621	2559	81.1	79.9	79.5	–12.9 (0.1)	–12.8 (0.8)	–15.1 (2.4)
CH_3Cl	539	556	547	16.4	17	17	–1.5 (5.4)	4.3 (3.7)	–2.3 (5.7)
VSLSs[1]	84	103	113	2.5	3.1	3.5	2.3 (3.1)	4.9 (5.2)	2.5 (3.3)
Total Cl	3295	3281	3220				–12.1 (8.0)	–3.6 (4.7)	–15.1 (3.6)

[1] Not including CH_2ClCH_2Cl (due to the absence of near-surface long-term trends), as well as SGI.

iodine plus a minor contribution from organic iodine. The non-zero minimum edge is obtained assuming that total iodine in the lower stratosphere is not preserved (Koenig et al., 2020), whereas no central value is provided due to the very large uncertainties regarding the gas-to-particle iodine partitioning. If the upper limit of the range is considered, the impact of iodine on tropical lower-stratospheric ozone could be as large as that of brominated VSLSs.

1.4 CHANGES IN ATMOSPHERIC HALOGENS

1.4.1 Tropospheric and Stratospheric Chlorine Changes

1.4.1.1 Tropospheric Chlorine Changes

The total amount of chlorine from ODSs that were controlled under the original Montreal Protocol is continuing to decline, as the overall emissions are smaller than the rate at which these ODSs are destroyed. Total tropospheric chlorine has been decreasing continuously since its peak abundance observed during 1993–1994 (**Figure 1-11a**). The maximum annual average total chlorine observed from controlled and uncontrolled substances was about 3660 ppt in 1994. The rate of decrease slowed from 39 ppt yr^{-1} in 1995–1996 to 3.6 ppt yr^{-1} between 2012 and 2016, then accelerated again to an average 15.1 ± 3.6 ppt yr^{-1} between 2016 and 2020. This recent acceleration is predominantly due to changes in substances not controlled by the Montreal Protocol, namely CH_3Cl and VSLSs. The concentrations of tropospheric chlorine shown in **Figure 1-11a** do not include several minor species (i.e., any species contributing less than 1 ppt of chlorine; see *Introduction*), but these have very little influence on the total or its trend. When looking at total chlorine from controlled ODSs only, there is still a recent acceleration in the rate of decline (though much less pronounced), from an average rate of 12.8 ± 0.8 ppt yr^{-1} between 2012 and 2016 to 15.4 ± 2.4 ppt yr^{-1} between early 2016 and late 2020 (**Table 1-7**). **Figure 1-11b and c** show the temporal evolution of combined tropospheric chlorine from CFCs and HCFCs, respectively. It is apparent that the former has not declined as rapidly as expected in the A1 scenarios from the 2014 and 2018 Assessments, although there is a more recent CFC-11-driven reduction in the growth rate; in contrast, the latter has not increased as rapidly as expected and is approaching near-zero growth rates in 2020. The tropospheric chlorine contribution from HCFCs has continued to increase, reaching 320 ± 3 ppt in 2020. However, the annual average growth rate of chlorine from HCFCs decreased from 5.9 ± 1.3 ppt yr^{-1} reported in the 2018 Assessment to 2.5 ± 1.0 ppt yr^{-1} during 2016–2020. Total tropospheric chlorine (including uncontrolled substances) reached 3220 ppt in 2020, which is equivalent to a 12% reduction from the previous maximum, and about 1.8% lower than in 2016.

1.4.1.2 Stratospheric Chlorine Changes

Long-term changes in stratospheric inorganic chlorine are driven by changes in tropospheric chlorine and transport variability. The total organic chlorine in the troposphere has been declining since the early 1990s (**Figure 1-11**), and as a consequence, a decline in stratospheric inorganic chlorine is also expected. The timing of the trend reversal is shifted between the two atmospheric regions according to timescales of transport and photochemical conversion. Details of the stratospheric trend will also be impacted by changes in the stratospheric circulation and the relative contributions of SGs.

Total column abundance for hydrogen chloride (HCl) and chlorine nitrate ($ClONO_2$) and their summation (Cl_y) at Jungfraujoch (46.5°N) and Lauder (45.0°S) are presented in **Figure 1-12**, with the corresponding trends listed in **Table 1-8**. HCl shows a statistically significant decrease from 1997 to 2020 at the two stations of –0.41 ± 0.15% yr^{-1} and –0.56 ± 0.12% yr^{-1}, respectively (updated from Mahieu et al., 2014a), similar to the trend reported in the last

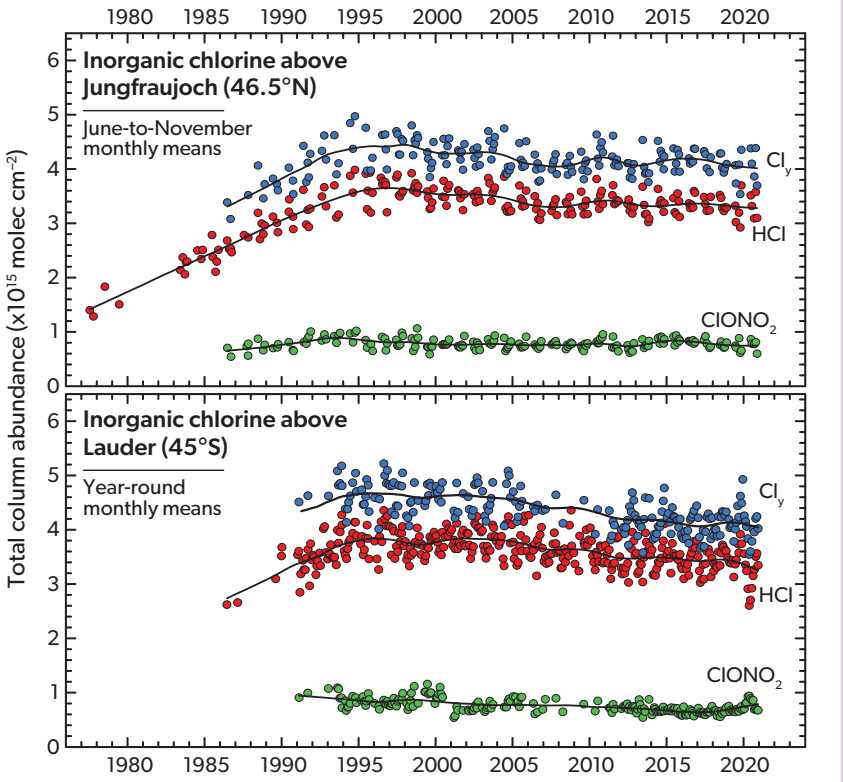

Figure 1-12. Time series of monthly mean total column abundances for the two main stratospheric chlorine reservoirs HCl (red circles) and $ClONO_2$ (green circles) derived at two mid-latitude stations, Jungfraujoch (46.5°N) and Lauder (45.0°S), in the framework of the NDACC network. The HCl and $ClONO_2$ sum is a good proxy of total inorganic chlorine and is denoted as Cl_y (blue circles). For Jungfraujoch, the datasets are restricted to June through November in an effort to limit the variability caused by atmospheric transport and subsidence during winter and spring. The continuous lines come from non-parametric least-squares fits involving an integration time of about three years and help to visualize the non-monotonic and non-linear changes in stratospheric chlorine.

Table 1-8. Observed inorganic chlorine trends for the total column and for the upper atmosphere. Trends (% yr^{-1}) of HCl and $ClONO_2$ and their summation (Cl_y) are based on the FTIR column time series shown in **Figure 1-12**. Near-global (60°S–60°N) trends in HCl averaged over the middle stratosphere are based on trend profiles from GOZCARDS, Aura MLS, and ACE-FTS, and trends of $ClONO_2$ are from ACE-FTS. All uncertainties are estimated at 2-sigma.

Data Source/Location	Cl_y Species	Altitude Region	Rate of Change (% yr^{-1})	Time Period
FTIR NDACC Jungfraujoch (46.5°N)	HCl	Total column	−0.41 ± 0.15	1997–2020
	$ClONO_2$		−0.07 ± 0.39	
	Cl_y		−0.34 ± 0.15	
FTIR NDACC Lauder (45.0°S)	HCl	Total column	−0.56 ± 0.12	1997–2020
	$ClONO_2$		−0.97 ± 0.41	
	Cl_y		−0.65 ± 0.11	
GOZCARDS1 (60°S–60°N)	HCl	68 to 10 hPa	−0.56 ± 0.26	1997–2020
Aura MLS (60°S–60°N)			−0.28 ± 0.21	2005–2020
ACE-FTS (60°S–60°N)	HCl	68 to 10 hPa	−0.30 ± 0.17	2004–2020
	$ClONO_2$	23–8 hPa	−0.53 ± 0.14	2004–2020

[1] GOZCARDS trends are derived from merged HCl data (updated from Froidevaux et al., 2015) based on a multi-linear regression model that accounts for seasonal and shorter-period cycles, as well as longer-term variations relating to the QBO, ENSO, and solar flux (Froidevaux et al., 2019). From 2011 onwards, no ACE-FTS data are used in GOZCARDS. The 2-sigma error bars are based on a bootstrap residual resampling method.
[2] MLS trends are based on version 4 Aura MLS data derived with the regression model and bootstrap method described in footnote 1 of this table.
[3] ACE-FTS trends are based on version 4.1 data (HCl data updated from Bernath and Fernando, 2018; $ClONO_2$ data updated from Bernath et al., 2021). Trends are derived from a linear trend calculation applied to seasonally averaged data with the dynamical variability removed based on a regression model that includes N_2O time series in the fitting. The errors are 2-sigma estimates, taking into account the autocorrelation of the residuals.

Assessment for 1997–2016. In contrast, $ClONO_2$ shows a significant decrease only at the SH station (–0.97 ± 0.41% yr^{-1}), while at the NH station the time series is flat with no significant trend (–0.07 ± 0.39% yr^{-1}). Interestingly, the SH $ClONO_2$ abundance in 2020 was higher than during any previous year since 2014.

The long-term decreases in HCl and $ClONO_2$ lead to a significant negative trend in Cl_y, which is stronger in the SH (–0.65 ± 0.11% yr^{-1}) than in the NH (–0.34 ± 0.15% yr^{-1}). Shorter-term temporal variability in inorganic chlorine (e.g., increasing values at Jungfraujoch between 2005 and 2011) have been attributed to circulation changes in the NH (Mahieu et al., 2014a). Such fluctuations seem to appear somewhat regularly for the NH HCl and Cl_y data (**Figure 1-12**). Transport anomalies are known to influence stratospheric gases in different ways in the two hemispheres. HCl columns have been found to be sensitive to variations in the lower-stratospheric age of air and have been used to infer differences in lower-stratospheric age of air between the NH and SH (Strahan et al., 2020; Prignon et al., 2021).

Stratospheric HCl trends from limb-viewing satellite observations (**Table 1-8**) confirm the FTIR-based findings for the near-global scale (60°S–60°N). The merged satellite record from the Global OZone Chemistry And Related trace gas Data records for the Stratosphere (GOZCARDS) yields decreasing HCl of –0.56 ± 0.26% yr^{-1} for 1997–2020 (updated from Froidevaux et al., 2015), consistent with the FTIR column trends. If the evaluations are constrained to a shorter time period, the satellite records from the Aura Microwave Limb Sounder (MLS) and the Atmospheric Chemistry Experiment-Fourier Transform Spectrometer (ACE-FTS) suggest trends of –0.28 ± 0.21% yr^{-1} (2005–2020) and –0.30 ± 0.17% yr^{-1} (2004–2020), respectively (updated from Froidevaux et al., 2015, 2019; Bernath and Fernando, 2018; Bernath et al., 2021). These provide convincing evidence that the rate of decline in middle-stratospheric HCl slowed down considerably after 2004. Taking into account the time shift between the troposphere and the middle/upper stratosphere of about four years, this is in good agreement with surface chlorine abundances, which decreased by –0.50 ± 0.03% yr^{-1} for 1992–2016 and slowed down to a decrease of –0.36 ± 0.02% yr^{-1} for 2000–2016. ACE-FTS measurements suggest that the upper-stratospheric HCl (and thus Cl_y) decline slowed even further after around 2010, when the rapid initial decline of species with shorter atmospheric lifetimes, such as CH_3CCl_3, became smaller (Bernath and Fernando, 2018; Bernath et al., 2020). In addition, model simulations in good agreement with satellite observations suggest that this HCl decline is about 15% slower than it would be without the contribution from chlorinated VSLSs (Hossaini et al., 2019), demonstrating that VSLSs have offset a portion of stratospheric chlorine reductions since the mid-2000s.

1.4.2 Tropospheric and Stratospheric Bromine Changes

1.4.2.1 Tropospheric Bromine Changes

The total amount of bromine from ODSs that were controlled under the original Montreal Protocol is continuing to decline, as the overall emissions are smaller than the rate at which these ODSs are destroyed. Results from the AGAGE and NOAA networks indicate that total tropospheric bromine from the controlled substances (CH_3Br and halons) reached a maximum in 1999, with an annual average value of 17.1 ppt. Both the timing and the

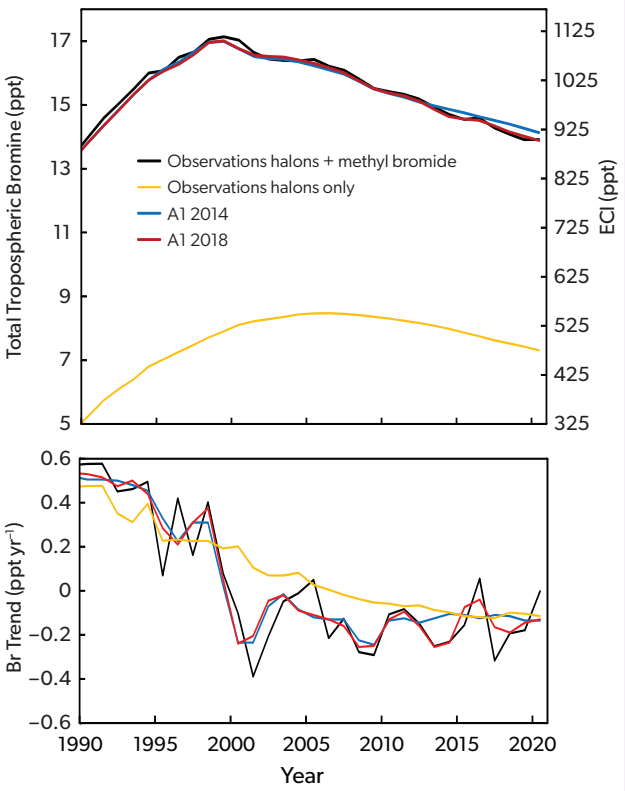

Figure 1-13. Time series of near-surface tropospheric bromine mole fractions (sum of halons and CH_3Br, black line) and those of halons only (yellow line) in comparison to the A1 scenarios from the 2014 (blue line) and 2018 (red line) Assessments. Long-term global surface observations are not available for brominated VSLSs, and therefore their contribution is not included here. Values in the upper panel are also expressed as equivalent chlorine (right-hand axis), using a value of α = 65 to account for the higher efficiency of bromine in catalyzing ozone destruction. All values are derived from a merged dataset based on NOAA, AGAGE, and UEA/FZJ data.

mole fraction are slightly different than those given in previous Assessments (i.e., 16.9 ppt in 1998) due to the effects detailed in the *Introduction*. Since 1999, the abundance of tropospheric bromine has been decreasing continuously (**Figure 1-13**), reaching a value of 13.9 ppt by 2020. While CH_3Br has been decreasing since the late 1990s (except for the brief increase in 2015–2016 and the stable period after 2017; see *Section 1.2.7*), bromine from halons started decreasing only around 2006. From 2012 to 2016, total controlled bromine declined at a rate of 0.15 ± 0.14 ppt yr^{-1} (1% yr^{-1}), and this rate increased to 0.18 ± 0.05 ppt yr^{-1} during 2016–2020. Halons contributed ~64% to this decline (2012–2016: ~70%), with CH_3Br accounting for the remainder. Similar to the last Assessment, the decrease in total bromine over the past five-year period was therefore again dominated by a decrease in halon abundances. The observed decrease in total controlled bromine is in overall good agreement with the decrease projected by the A1 scenario from the last Assessment (Carpenter, Daniel et al., 2018). Note that the tropospheric bromine total discussed

here does not include contributions from brominated VSLSs of around 5 ppt (see *Section 1.4.2.2*), as no trends from AGAGE or NOAA surface measurements of these gases are available.

1.4.2.2 Stratospheric Bromine Changes

Total stratospheric inorganic bromine (Br_y) originates from long-lived ODSs, mainly CH_3Br and halons, as well as from VSLSs, both in organic and inorganic forms. Estimates of stratospheric Br_y rely on two different methods. The first method (SG-based) sums up all bromine in the form of ODSs and VSL SGs found at the stratospheric entry level (e.g., Brinckmann et al., 2012; Navarro et al., 2015). This approach provides the contribution from the measured species at a high accuracy, but any bromine entering the stratosphere in inorganic form needs to be added to this to get true total bromine. The second method infers Br_y from atmospheric measurements of bromine oxide (BrO) coupled with photochemical modeling of the Br_y partitioning (e.g., Dorf et al., 2008; Parrella et al., 2013; Werner et al., 2017) or, following an equivalent methodology, from measurements of bromine nitrate ($BrONO_2$; Höpfner et al., 2021). This approach is ideally applied in the middle and upper stratosphere, where all bromine is present in inorganic form. If the method is applied in the lower stratosphere, additional measurements of the organic bromine from long-lived ODSs and VSL SGs are needed to determine total bromine (Wales et al., 2018; Werner et al., 2017). Uncertainties can also arise from the BrO or $BrONO_2$ measurements, as well as from the model-derived partitioning of Br_y, and depend on the measurement technique and probed photochemical regime.

Time series of Br_y estimates derived from the two methods are shown in **Figure 1-14a**. For the SG-based method, observations of the long-lived CH_3Br and halons were added to time-invariant and current best estimates of SG and PG injections from brominated VSLSs (5 ± 2 ppt; **Table 1-6**) to derive Br_y estimates (blue lines). Given that CH_3Br and halons are sufficiently long-lived to be transported into the stratosphere, the amounts of their stratospheric injection are taken as global mean surface values (**Figure 1-13**). For the BrO-based method, total column and vertically resolved BrO measurements were used to obtain Br_y estimates and plotted against the "year of stratospheric entry" (symbols in **Fig. 1-14a**). Ground-based measurements from the NH station Harestua (60°N) suggest a very slow decline with some year-to-year variability. Values measured in 2020, and mapped to a stratospheric entry in 2016, suggest 19.6 ppt of total bromine, in excellent agreement with the SG-based method assuming a

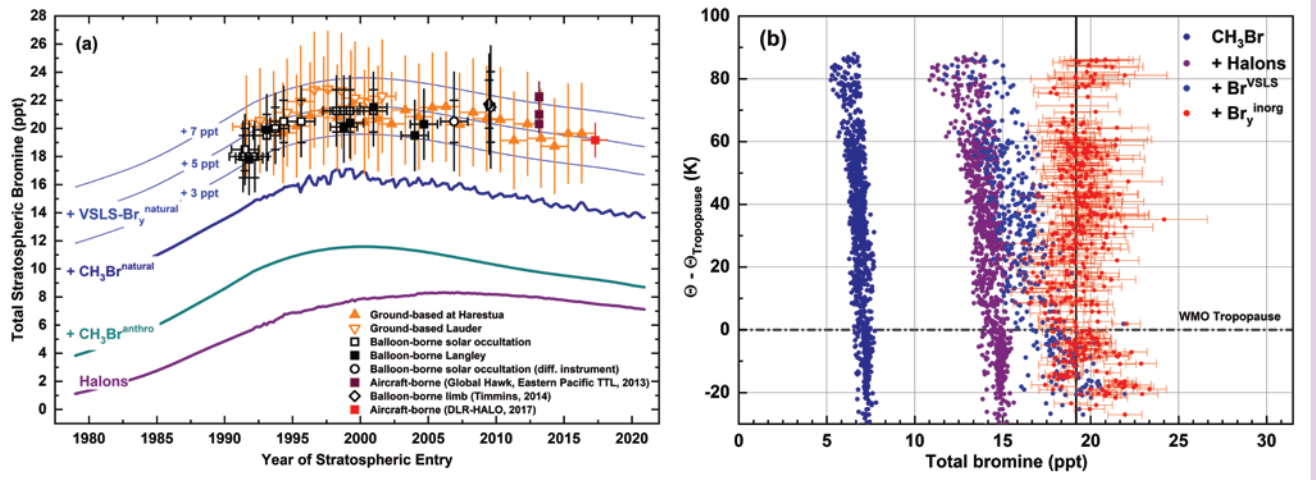

Figure 1-14. (a) Changes in total stratospheric Br_y (ppt) derived from balloon-borne (black open and filled symbols; update of Dorf et al., 2006) and airborne (purple filled squares from Werner et al., 2017; red filled square from Rotermund et al., 2021) BrO observations and from ground-based UV-visible measurements of stratospheric BrO made at Harestua (60°N) and Lauder (45°S) stations (filled and open orange triangles, respectively; adapted from Hendrick et al., 2007, 2008). All UV-visible measurements of stratospheric BrO were evaluated using a common BrO absorption cross section (based on Wahner et al., 1988), frequency-shifted to match the wavelength scale (Wilmouth et al., 1999). For the balloon-borne observations, exclusive of those using the Langley method, the outer and inner capping of the error bars correspond to the precision and accuracy of the estimates, respectively. For the ground-based measurements (triangles), the error bars correspond to the total uncertainties in the Br_y estimates. For stratospheric data, the date corresponds to the time when the air was last in the troposphere, i.e., sampling date minus estimated mean age of the stratospheric air parcel. Time series of halons and CH_3Br, with the latter split into the natural and anthropogenic fraction, have been updated (NOAA data only; see Carpenter, Reimann et al., 2014, for details). The blue lines show the expected stratospheric Br_y, assuming an additional input of 3, 5, and 7 ppt of brominated VSLSs, respectively. For tropospheric data, the date corresponds to the sampling time. This figure updates Figure 1-16 from the previous Assessment (Engel, Rigby et al., 2018). (b) Inferred total bromine as a function of potential temperature distance from the WMO tropopause during the WISE campaign in fall 2017. The organic bromine species are summed up according to their Br atomicity: CH_3Br (dark blue), sum of four halons (purple), and brominated VSLSs (light blue). The inferred inorganic Br_y is subsequently added (red), resulting in the UTLS total bromine. The solid black line represents the LS weighted mean total bromine of 19.2 ± 1.2 ppt. [Adapted from Rotermund et al., 2021.]

VSLS contribution of 5 ppt. Long-term changes based on ground-based BrO measurements indicate a slow decline of total bromine of –0.18 ± 0.04 ppt yr^{-1} (–0.8% yr^{-1}) since 2003. This decrease is in very good agreement with trends in tropospheric bromine, which have ranged between 0 and –0.4 ppt yr^{-1} since the early 2000s (**Figure 1-13**). The $BrONO_2$-based MIPAS satellite estimates focus on the period of maximum Br_y loading, with 21.2 ± 1.4 ppt Br at mid-latitudes corresponding to stratospheric entry between 1997 and 2006 and no significant long-term trend.

Data from the Global Hawk during the ATTREX campaign in the Eastern Pacific in 2013 suggests slightly higher Br_y concentrations of up to 22.3 ppt (purple filled square, **Figure 1-14a**) for air masses directly measured in the tropical tropopause region (Werner et al., 2017). Measurements during the 2017 WISE campaign also found elevated bromine values in the TTL, with a Br_y estimate of 21.6 ± 0.7 ppt (Rotermund et al., 2021), somewhat larger than the Br_y of 19.2 ± 1.2 ppt found in the extratropical and polar lower stratosphere. Both campaigns indicate slightly enhanced total Br_y in the upwelling part of the stratospheric Brewer-Dobson circulation in the tropics compared to those measured in its subsistence region at mid- and high latitudes, in agreement with earlier studies (Navarro et al., 2015; Werner et al., 2017; Wales et al., 2018). The cause of this difference is presently unclear, although it is conceivable that some bromine is heterogeneously taken up on the cold aerosols and cloud particles in the TTL and ultimately removed by sedimentation (Sinnhuber and Folkins, 2006). In addition, the Br_y estimates for both campaigns include directly measured VSLS contributions, which are known to show pronounced spatiotemporal variability in the TTL, with ranges of 0.5–4.4 and 1.8–4.2 ppt for brominated SGI and PGI, respectively (**Table 1-6**).

Observations of total bromine at mid- to high latitudes during the WISE campaign have demonstrated the large impact of transport-related variations on the Br_y budget in this region (**Figure 1-14b**; Rotermund et al., 2021). Bromine-rich air masses from the tropics were found to persistently protrude into the mid-latitude lowermost stratosphere during the boreal summer, causing a pronounced variability in Br_y, with a high bromine region of 20.9 ± 0.8 ppt exceeding the mean value of 19.2 ± 1.2 ppt.

1.4.3 Tropospheric and Stratospheric Iodine Changes

Tropospheric iodine stems mostly from oceanic emissions of

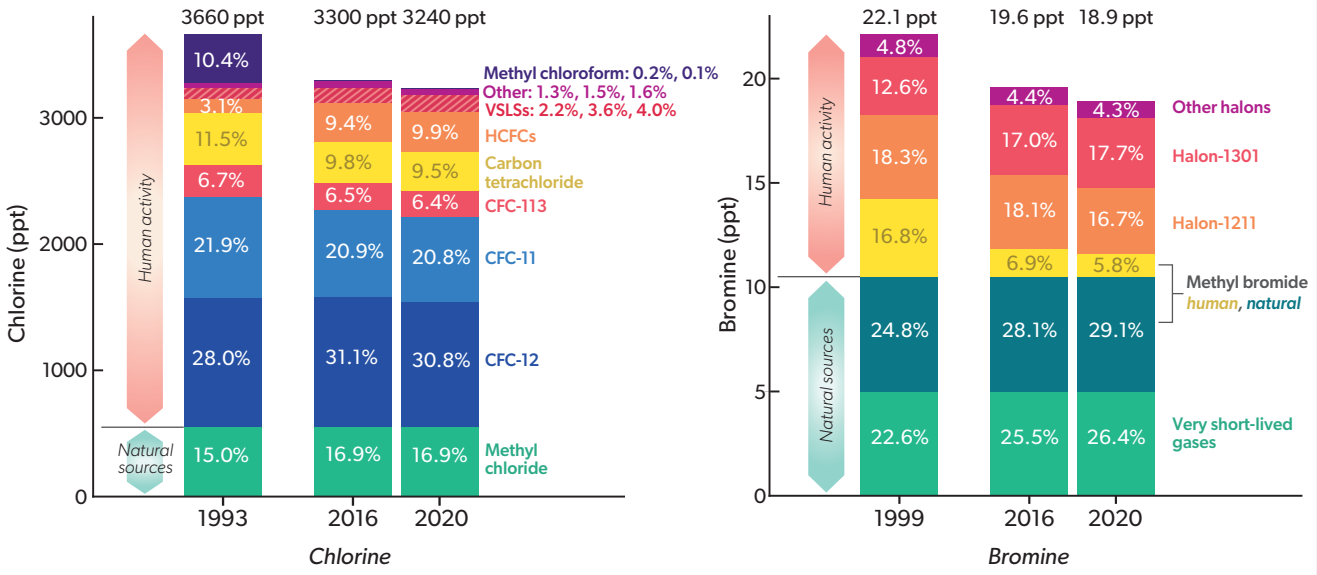

Figure 1-15. Chlorine and bromine input to the stratosphere for a reference year (1993 for chlorine and 1999 for bromine), 2016, and 2020 for different species and classes of compounds. The reference is close to the maximum of chlorine or bromine loading of the troposphere. Mole fractions of long-lived gases were mostly derived from surface observations from global networks (AGAGE and NOAA), except for CH_3Cl before 1995, when observations from both networks were unavailable and values were filled with the simulations from scenario A1 of the previous Assessment (Carpenter, Daniel et al., 2018) as derived from firn air measurements (Montzka, Fraser et al., 2003). The VSLS contributions for bromine are included as a constant 5 ppt, as in previous Assessments. The VSLS chlorine contribution is based on the VSL SG input from a model constrained by observed surface boundary conditions (update of Hossaini et al., 2015). Total VSLS Cl input derived in this way is 80 ppt, 120 ppt, and 130 ppt for years 1993, 2016, and 2020, respectively. For chlorine, HCFCs include HCFC-22, HCFC-141b, HCFC-142b, and HCFC-124; "other" includes contributions from minor CFCs (CFC-13, CFC-112, CFC-113a, CFC-114+CFC-114a, and CFC-115) and halon-1211. For bromine, "other halons" is the sum of bromine contained in halon-1202 and halon-2402. Methyl chloride is counted as having purely natural sources, despite some indications of anthropogenic contributions. The contribution of natural sources to CH_3Br mole fractions was estimated as a constant 5.5 ppt, based on the published firn air and ice core measurements (Butler et al., 1999; Trudinger et al., 2004; Saltzman et al., 2004; 2008), whereas the anthropogenic contribution was estimated by the global surface mole fractions measured by AGAGE and NOAA minus 5.5 ppt.

inorganic iodine in the form of hypoiodous acid (HOI) and molecular iodine (I_2). These emissions are driven by the reaction of ozone with iodide (I^-) at the ocean surface. Since tropospheric ozone over the NH has increased over the last decades, oceanic emissions as well as tropospheric levels of inorganic iodine are likely to have increased in response. Observations reveal a positive trend in iodine in spruce tree rings in the Tibet Plateau (Zhao et al., 2019), as well as in Greenland and Alpine ice cores, with the latter showing a tripling in iodine since 1950 (Legrand et al., 2018). This iodine increase can be explained by model-derived oceanic iodine emissions in the North Atlantic and their increase over the latter half of the 20th century (Cuevas et al., 2018). While observations and models agree on increasing tropospheric iodine levels, it should be noted that the results are accompanied by large uncertainties due to the lack of observational constraints on ozone changes, iodide levels, flux parameterizations, and tropospheric iodine chemistry (Carpenter et al., 2021).

Tropospheric iodine also stems from oceanic emissions of organic iodine in the form of CH_3I. Earlier measurements at remote sites in the western and northern Pacific from the late 1990s to 2011 reported long-term decadal oscillations of atmospheric CH_3I, possibly related to natural oscillations of sea surface temperature (Yokouchi et al., 2012). These results suggest that climate change can impact oceanic trace gas emissions. However, very little updated data on CH_3I tropospheric trends exist to further investigate such impacts. One of the few available datasets consists of observations in the Greater Pearl River Delta region of China during 2001–2018 and shows a significant increase in CH_3I over the measurement period, of 0.08 ± 0.02 ppt yr^{-1}. Given the proximity to densely populated regions, these trends could be related to anthropogenic sources, based on the use of CH_3I as a methylating agent (Zeng et al., 2020).

For stratospheric iodine, no observational trend estimates exist. Assuming iodine injections in particulate form is a plausible entrainment mechanism (Koenig et al., 2020), changes in oceanic emissions and aerosol iodine content could also influence stratospheric iodine levels. Given the large uncertainties in the processes controlling tropospheric particulate iodine formation and reactive transport to the stratosphere, any model-based stratospheric iodine trend can also be expected to have large uncertainties.

1.4.4 Changes in Ozone-Depleting Halogen Abundance in the Stratosphere

Figure 1-15 illustrates the contributions of different ODSs or ODS groups to chlorine and bromine input to the stratosphere during the respective peak years (Cl: 1993, Br: 1999), as well as in 2016 and 2020. In contrast to *Sections 1.4.1.1* and *1.4.2.1*, VSLS tropopause estimates are included here, as these species have strong sinks in the troposphere and therefore ground-based measurements do not reflect the actual amounts reaching the stratosphere. In 2020, total chlorine and bromine entering the stratosphere from controlled and uncontrolled ODSs reached values of 3240 ppt and 18.9 ppt, respectively. Thus, the chlorine and bromine inputs have declined by 11.5% (420 ± 20 ppt) and 14.5% from their peak abundances, respectively, with 1.6% and 3.2% of this decline between 2016 and 2020.

Equivalent effective stratospheric chlorine (EESC) also generally follows the changes in tropospheric ODSs but additionally includes calculations 1) reflecting the ability of bromine to destroy more ozone than chlorine (α-factors of 60 and 65 were used here for mid-latitude and polar winter conditions, respectively; see **Figure 1-16**), 2) addressing the influence of stratospheric lifetime differences between ODSs, and 3) taking into account effects from the transport of air in the stratosphere (timescales of years), which is much slower than in the free troposphere (days to months). As noted in the last Assessment, the traditional use of EESC in 1980 as a benchmark is somewhat arbitrary, as 1) anthropogenically induced ozone loss occurred prior to 1980, and 2) a return to 1980 EESC levels does not imply a recovery of the ozone layer to the 1980 state, ozone being influenced by many additional parameters (e.g., greenhouse gas abundances,

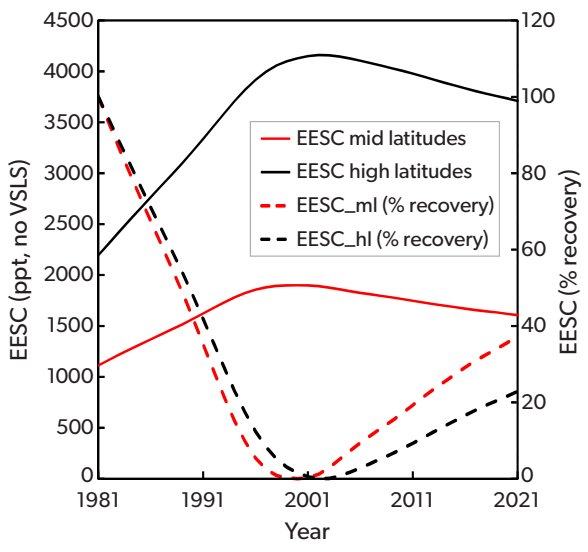

Figure 1-16. Level of EESC (left y-axis) and its percentage recovery toward 1980 benchmark values (right y-axis) using the improved EESC calculation from the 2018 Assessment (Engel, Rigby et al., 2018), which is based on the method by Engel et al. (2018). Solid lines show the EESC at 3 (red) and 5.5 (black) years of mean age, representative of mid-latitude conditions and polar winter conditions, respectively. The dashed lines indicate the percentage of recovery at those same years of mean age, but are shown relative to 1980 levels (defined as 100% recovery) and EESC maxima (defined as 0% recovery). In all cases, the different age spectra were parameterized as suggested by Newman et al. (2007) using half of the mean age as the width of the age spectrum and an inverse Gaussian function as the shape of the age spectrum. The age spectrum has been integrated over a time period of 20 years. Fractional release factors were calculated as in the last Assessment, based on the work by Ostermöller et al. (2017). The same tropospheric data were used as in *Sections 1.4.1.1* and *1.4.2.1*. VSLS contributions to EESC are not included in this calculation, and the higher efficiency of bromine to destroy stratospheric ozone is taken into account (factors of 60 for mid-latitude and 65 for polar winter conditions).

changes in stratospheric dynamics and chemistry). For EESC calculations, an average stratospheric transit time, or mean age, of 5.5 years is again used to reflect typical polar winter conditions, and a three-year mean age for mid-latitude conditions. Here we exclusively use the new and improved formulation of EESC suggested by Engel et al. (2018), introduced in the last Assessment, which also included a comparison to the previously used formulation by Newman et al. (2007). A limitation of the EESC metric is that it does not include contributions from VSLSs (also see **Box 1-3** on VSLS metrics) or nitrous oxide (N_2O), with the latter having an unknown but certainly substantial impact on stratospheric ozone (Ravishankara et al., 2009). Also, more recently, regional variability in EESC has been observed based on observations in the vicinity of the Asian monsoon (e.g., it is between 200 to 300 ppt higher at a mean age of three years; Adcock et al., 2021), which raises some questions on the applicability of this concept for the entire stratosphere, especially for relatively short-lived ODSs with large regional emissions close to stratospheric input regions such as CH_3Cl and CH_3Br (see also *Sections 1.2.5* and *1.2.6*). In addition, a recent study has highlighted the shortcomings of a simple α-factor for bromine, as it does not take into account the global chemistry-climate state, and it suggested the future introduction of an equivalent effective stratospheric benchmark-normalized chlorine (EESBnC) to reflect changes in the rates of bromine- and chlorine-mediated ozone loss (Klobas et al., 2020).

As is shown in **Figure 1-16** and **Table 1-9**, the previously reported decline in EESC has continued. For mid-latitude conditions, we derive an average recovery rate of 37% relative to the 1980 benchmark. This compares to 31% recovery in 2016 reported in the last Assessment. For polar winter conditions, recovery has progressed from 18% in 2016 to 23% in 2020, again relative to 1980, confirming that a full recovery, even only to the 1980 EESC levels, is not expected in the near future.

1.4.5 Tropospheric and Stratospheric Fluorine Changes

Atmospheric fluorine results from the photodissociation of fluorine-bearing source gases including CFCs, halons, HCFCs, HFCs, PFCs, and other compounds. The resulting inorganic fluorine reservoir gas HF is very stable in the atmosphere, and as a consequence, fluorine does not contribute to stratospheric ozone depletion. The primary interest in monitoring inorganic fluorine (F_y) is to provide an independent measure of the accumulation of the associated source gases, many of which are potent greenhouse gases. Among the source gases, HFCs (*Chapter 2*) are of growing interest because their increasing atmospheric abundance is a direct consequence of the restrictions on ODS production and consumption. The regulation of HFCs has been added to the Montreal Protocol in the framework of the Kigali Amendment, in part because they are replacement compounds for substances already regulated under the Protocol.

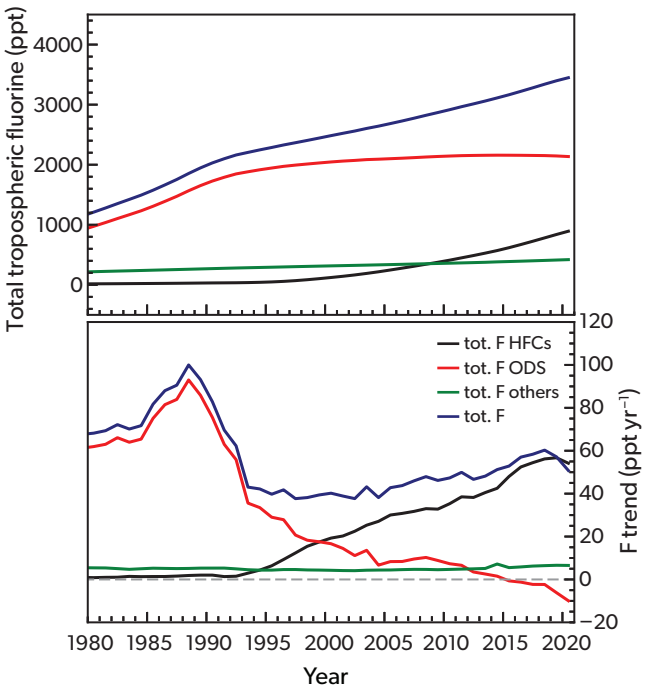

Figure 1-17. *(top)* Tropospheric total fluorine time series and *(bottom)* annual changes from long-lived gases, separated by contributions due to ODSs, HFCs (see *Chapter 2*), and other fluorinated gases (such as SF_6, NF_3, CF_4, not including minor species; see *Introduction*). Mole fractions for ODSs and other fluorinated gases were derived from a merged dataset based on NOAA, AGAGE, and UEA/FZJ data. HFC mole fractions were derived from AGAGE and NOAA data. HFC records prior to regular global measurements were supplemented with estimates from Vollmer et al. (2011), Vollmer et al. (2015b), and the simulated mole fractions from the A1 scenarios in the previous Assessment (Carpenter, Daniel et al., 2018).

Changes in tropospheric fluorine concentrations result from changes in tropospheric concentrations of long-lived ODSs (*Section 1.2*) and HFCs (*Chapter 2*), as well as PFCs and other compounds (*Section 1.5.4*), as shown in **Figure 1-17**. In contrast

Table 1-9. EESC values for 1980 and 2020 as well as when EESC was at its maximum. Values are given for 3 and 5.5 years of mean age (representative of mid-latitude and polar winter conditions, respectively) and are based on the improved method of Engel et al. (2018). Also shown are percentage changes achieved by early 2020 with respect to the maximum and the percentage recovery with respect to the 1980 values.

	EESC 1980 (ppt)	EESC Maximum (ppt) [year]	EESC 2020 (ppt)	Change from Maximum (%)	Recovery to 1980 Level (%)
Mid-Latitude Conditions	1113	1900 [1999]	1607	–15	37
Polar Winter Conditions	2196	4160 [2001]	3710	–11	23

Table 1-10. Observed inorganic fluorine trends for the total column (FTIR) and for the upper atmosphere (ACE-FTS). Trends (% yr^{-1}) of HF and $2xCOF_2$ and their summation (F_y), which represents most of the inorganic fluorine in the stratosphere, are based on mid-latitude FTIR column and ACE-FTS time series shown in **Figure 1-18**. Trends relative to 2004 have been derived for the common time period of observations 2004–2020. All uncertainties are estimated at 2-sigma.

Species	Rate of Change 2004–2020 (% yr^{-1})			
	ACE-FTS (40–50°N)	FTIR (Jungfraujoch, 46.5°N)	ACE-FTS (40–50°S)	FTIR (Lauder, 45.0°S)
F_y	0.87 ± 0.22	0.72 ± 0.19	0.48 ± 0.26	0.05 ± 0.25
HF	0.88 ± 0.20	0.66 ± 0.21	0.59 ± 0.30	0.31 ± 0.22
$2xCOF_2$	1.22 ± 0.49	0.89 ± 0.34	0.28 ± 0.25	–0.45 ± 0.40

to chlorine, total tropospheric fluorine has continued to increase, with a 2016–2020 trend of 57.1 ± 0.8 ppt yr^{-1} corresponding to 1.71 ± 0.02% yr^{-1}. Similarity with the trend reported in the last Assessment (1.7 ± 0.07% yr^{-1} for 2012–2016) suggests stable growth rates of total fluorine. The contributions of the different compound classes to the tropospheric fluorine trend have changed over time. The ODS contribution to the fluorine budget remained relatively constant between 2005 and 2015 and started to decline afterwards. As a result, the fluorine trend due to ODSs alone became negative after 2016, reaching –10 ppt yr^{-1} in 2020. In contrast, the fluorine trend due to HFCs alone increased constantly between 1995 and 2019 and only flattened in 2020, reaching 55 ppt yr^{-1} in 2020.

A good proxy for the total inorganic fluorine (F_y) in the stratosphere is calculated as the weighted sum of the two most abundant fluorinated reservoirs, i.e., hydrogen fluoride (HF) and two times carbonyl fluoride (COF_2). Total column F_y, based on FTIR HF and COF_2 measurements at two mid-latitude stations, has increased steadily since 1989, with a stronger positive trend over the first 15 years of the record (**Figure 1-18**). ACE-FTS satellite data, available since 2004, are mostly consistent with the FTIR data but suggest slightly stronger positive trends. The largest discrepancies exist for the SH, where COF_2 from FTIR measurements has been decreasing, inconsistent with the ACE-FTS satellite record. This is possibly related to transport variability impacting the long-term changes in the two datasets in different ways. In total, F_y in the NH stratosphere has increased at a rate of 0.87 ± 0.22% yr^{-1} (ACE-FTS) and 0.72 ± 0.19% yr^{-1} (FTIR) over the 2004–2020 time period (**Table 1-10**). This long-term change is smaller than tropospheric trends over 2000–2016 of 1.53 ± 0.02% yr^{-1}. While changes in inorganic stratospheric fluorine are largely driven by changes in total tropospheric fluorine, they are also impacted by the efficiency of the fluorine release from the different compound classes. As the relative contributions from different compounds

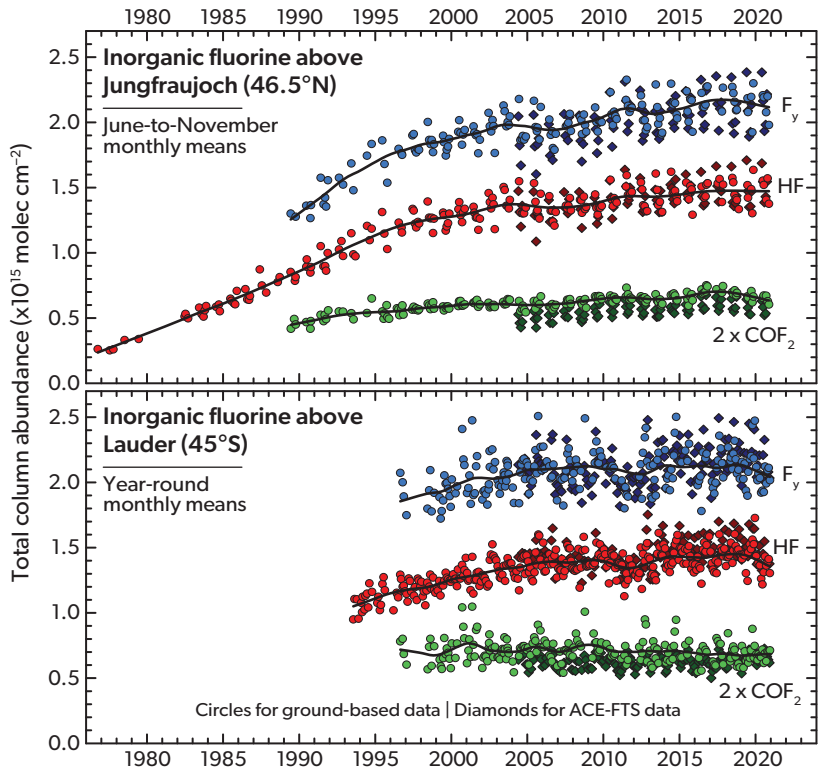

Figure 1-18. Multi-decadal monthly mean total column time series of the two main stratospheric fluorine reservoirs, HF and COF_2, and their summation, F_y, derived at two mid-latitude stations (Jungfraujoch, 46.5°N, and Lauder, 45.0°S) in the framework of the NDACC network and from ACE-FTS occultation measurements (40–50°S and 40–50°N). HF monthly means are reproduced as red symbols; 2 x COF_2 as green symbols. Their summation (blue symbols) is a good proxy of total inorganic fluorine. The satellite and ground-based data are given as diamonds and circles, respectively. Note that the ACE-FTS time series for Fy also includes the contribution of COCIF, a species that cannot be measured from the ground. Finally, non-parametric fits to the FTIR data are shown as continuous thick curves. [Adapted and updated from Prignon et al., 2021.]

have changed over time, a direct correlation of stratospheric and tropospheric fluorine changes is not necessarily expected.

1.5 CHANGES IN OTHER TRACE GASES THAT INFLUENCE OZONE AND CLIMATE

In this section, gases that are not covered by the Montreal Protocol but that indirectly affect stratospheric ozone are discussed. These include long-lived greenhouse gases such as methane (CH_4) and nitrous oxide (N_2O), aerosol precursor gases such as carbonyl sulfide (COS) and sulfur dioxide (SO_2), and other fluorinated chemicals such as sulfur hexafluoride (SF_6) and perfluorocarbons (PFCs). As in the last Assessment, HFCs are covered in *Chapter 2*; while carbon dioxide (CO_2), even though it induces temperature changes that directly alter the chemical rates that produce and destroy ozone, is not included due to its coverage in great detail in the recent IPCC report (IPCC, 2021).

1.5.1 Nitrous Oxide (N_2O) and Methane (CH_4)

Observations of Atmospheric Abundance. N_2O and CH_4 cause the release of chemicals into the stratosphere that catalytically produce and destroy ozone. For an extensive and comprehensive overview of the emissions and abundances of both gases up to 2019, see the recently published IPCC report (IPCC, 2021). In summary, their global abundances have continued to increase, reaching 332.1 ± 0.4 ppb (N_2O) and 1866.3 ± 3.3 ppb (CH_4) in 2019. As an update to the IPCC report, N_2O increased by a further 1.1 ppb between 2019 and 2020 (**Table 1-11**), which is distinctly higher than the average growth rate between 2012 and 2019 of 0.96 ± 0.05 ppb yr^{-1} (IPCC, 2021). CH_4 increased, on average, by 9.3 ± 2.4 ppb yr^{-1} between 2014 and 2019; the recent 2019–2020 change of 10–13 ppb yr^{-1} is at the upper end of this range (**Table 1-11**).

Emissions, Lifetimes, and Radiative Forcings. Several recent publications have found that global N_2O emission increases have been accelerating over the last two decades and by now exceed some of the highest projections (Thompson et al., 2019; Tian et al., 2020; IPCC, 2021). These increases are driven by anthropogenic emissions (mainly from nitrogen additions to croplands), which account for nearly half of the global N_2O emissions in recent years. Due to its much shorter lifetime and its multitude of source and sink processes, the derivation of atmospheric emissions of CH_4 is generally more complex. However, recent increases are likely mainly driven directly (agriculture and fossil fuels) or indirectly (prolonged El Niño conditions) by anthropogenic activities (see Box 5.2 in IPCC, 2021).

In particular, the accelerating increase of N_2O abundances and emissions is a serious threat for stratospheric ozone, as it is the main driver of NO_x-induced ozone depletion and by far the most abundant ODS (Ravishankara et al., 2009; Müller et al., 2021). To illustrate these effects, we here use the maximum range of potential N_2O ODPs from 0.015 to 0.030 as derived by Revell et al. (2015) for various atmospheric scenarios between the years 2000 and 2100. When deriving CFC-11-equivalent emissions from this range, we estimate between 461 and 922 Gg yr^{-1} for 2020, i.e., 5–10 times the ODP-weighted emissions from all CFCs in that year. In addition, the increase in N_2O emissions translates to an increase of 52–104 Gg of CFC-11 equivalent emissions between 2016 and 2020. Anthropogenic emissions N_2O were driving that increase, and these alone (43%, Tian et al., 2020) were equal to more than two times the ODP-weighted emissions from all CFCs in 2020. For context, when compared to the CFC emission peak from 1987, those 2020 anthropogenic N_2O emissions were equal to more than 20 % the ODP-weighted emissions from CFCs in that year.

The direct radiative forcing effects from N_2O and CH_4 in 2020 are estimated at 207 mW m^{-2} and 520 mW m^{-2}, respectively.

1.5.2 Aerosol Precursors: Carbonyl Sulfide (COS) and Sulfur Dioxide (SO_2)

The sulfur-containing gases COS and SO_2 act as precursor gases of stratospheric sulfate aerosol, which can influence halogen chemistry. Stratospheric COS and SO_2 injections occur regularly via troposphere-stratosphere air mass transport or sporadically via explosive volcanic eruptions.

Carbonyl Sulfide (COS). NOAA measurements have reported global mean COS mole fractions of 497 ppt for 2020 and trends of –1.5% yr^{-1} for 2019–2020 (**Table 1-11**) and –1.3% yr^{-1} for the four-year time period 2016–2020. These small negative trends are of opposite sign compared to the small positive trends reported for 2012–2016 in the previous Assessment.

COS is one of the major sources of stratospheric sulfate aerosols, contributing between 40% (Feinberg et al., 2019) and 70% (Brühl et al., 2012) to the stratospheric sulfur budget during volcanically quiescent periods. Satellite observations confirm model-derived values of ~0.45 ppb COS around the tropical tropopause (Brühl et al., 2015). Current estimates of the source and sink terms do not balance the atmospheric observations and imply that there may be a large missing COS source of 235 to 800 Gg S yr^{-1} (e.g., Lennartz et al., 2017; Ma et al., 2021; Whelan et al., 2018). Sulfur isotope measurements have recently been used to better constrain atmospheric COS sources and have identified the main source to be the ocean (Davison et al., 2021), anthropogenic activities (Hattori et al., 2020), or both (Angert et al., 2019). Overall, there is no consensus on the cause of the COS imbalance.

Sulfur Dioxide (SO_2). SO_2 is short-lived with highly variable mole fractions in the troposphere, and it can be entrained into the stratosphere through volcanic eruptions and direct transport. Large uncertainties exist in how efficiently SO_2 is transported from major anthropogenic emission regions into the stratosphere, mostly due to poorly known heterogeneous SO_2 loss processes occurring during uplift. Aircraft campaign measurements in the tropical Pacific and Gulf of Mexico region have reported relatively low SO_2 mixing ratios in the tropical tropopause layer (TTL), suggesting zonally averaged SO_2 at the tropical tropopause of around 5 ppt (Rollins et al., 2017; Rollins et al., 2018). These measurements are in good agreement with some model simulations and MIPAS satellite data (Brühl et al., 2015), indicating that on a global scale the direct transport of SO_2 into the stratosphere is a minor source of stratospheric aerosols. However, zonal asymmetries of SO_2 injections can be expected primarily in outflow regions of the Asian summer monsoon convection, where upper troposphere SO_2 of more than 100 ppt was observed (Lelieveld et al., 2018). The overall impact of such enhanced injections on the stratospheric SO_2 budget remains to be clarified.

Table 1-11. Annual mean mole fractions, mole fraction changes, and global emissions of selected fluorinated compounds with radiative forcing greater than 0.1 mW m^{-2} (see *Introduction*) and other gases of interest (uncertainties are 1-sigma), measured from ground-based sampling networks. The measured mole fractions are expressed in dry air mole fractions as ppt or ppb.

Chemical	Mole Fraction (ppt)		Change (2019–2020)		Emissions (Gg yr^{-1})		Network
	2016	2020	(ppt yr^{-1})	(% yr^{-1})	2016	2020	
Perfluorocarbon (PFCs)							
CF_4 (PFC-14)	**82.8**	**86.4**	**0.9**	**1.1**	**13 ± 1**	**15 ± 1**	AGAGE
C_2F_6 (PFC-116)	**4.57**	**4.94**	**0.09**	**1.9**	**2.1 ± 0.1**	**2.2 ± 0.1**	AGAGE
	3.98	*4.34*	*0.07*	*1.7*	*n.a.*	*n.a.*	UEA/FZJ
C_3F_8 (PFC-218)	**0.63**	**0.7**	**0.02**	**2.7**	**0.5 ± 0.0**	**0.6 ± 0.1**	AGAGE
	0.60	*0.66*	*0.01*	*1.3*	*n.a.*	*n.a.*	UEA/FZJ
c-C_4F_8 (PFC-318)	**1.56**	**1.82**	**0.07**	**3.8**	**2.1 ± 0.1**	**2.5 ± 0.2**	AGAGE
	1.44	*1.69*	*0.06*	*3.6*	*n.a.*	*n.a.*	UEA/FZJ
n-C_6F1_4 (PFC-5-1-14	*0.22*	*0.22*	*0.00*	*0.0*	*n.a.*	*n.a.*	UEA/FZJ
Other Fluorinated Compounds							
SF_6 (sulfur hexafluoride)	**8.9**	**10.3**	**0.3**	**3.5**	**8.8 ± 0.3**	**9.0 ± 0.3**	AGAGE
	8.9	**10.3**	**0.3**	**3.3**	**n.a.**	**n.a.**	NOAA
NF_3 (nitrogen trifluoride)	**1.5**	**2.3**	**0.2**	**11.5**	**2.0 ± 0.1**	**3.0 ± 0.1**	AGAGE
SO_2F_2 (sulfuryl fluoride)	**2.2**	**2.6**	**0.09**	**3.7**	**2.9 ± 0.4**	**2.9 ± 0.4**	AGAGE
$CHF_2OCHFCF_3$ (desflurane)	*0.35*	*0.37*	*–0.01*	*–2.7*	*n.a.*	*n.a.*	AGAGE[1]
Other Compounds							
CH_4 (methane) (ppb, Tg yr^{-1})	**1842**	**1878**	**12**	**0.7**	**551 ± 74**	**576 ± 76**	AGAGE
	1843	**1879**	**13**	**0.7**	**n.a.**	**n.a.**	NOAA
	1840	**1872**	**11**	**0.6**	**n.a.**	**n.a.**	UCI
	1841	**1872**	**10**	**0.5**	**n.a.**	**n.a.**	CSIRO
N_2O (nitrous oxide) (ppb, Tg yr^{-1})	**329.4**	**333.5**	**1.1**	**0.3**	**27 ± 2**	**31 ± 2**	AGAGE
	329.0	**333.0**	**1.1**	**0.3**	**n.a.**	**n.a.**	NOAA
	328.6	**332.6**	**1.1**	**0.3**	**n.a.**	**n.a.**	CSIRO
COS (carbonyl sulfide)	**497**	**472**	**–7**	**–1.5**	**n.a.**	**n.a.**	NOAA
H_2 (hydrogen) (ppb)	**533**	**542**	**3**	**0.6**	**n.a.**	**n.a.**	AGAGE
	536	**546**	**4**	**0.7**	**n.a.**	**n.a.**	CSIRO

General footnote: Mole fractions in this table represent independent estimates based on air sampling collected at Earth's surface from different research groups for the years indicated. Results in bold text are estimates of globally averaged annual mole fractions and are derived on gravimetric calibration scales. As in **Table 1-1**, UEA/FZJ data from whole-air flask samples collected at Cape Grim, Australia (CGO), which are based on volumetric calibration scales, are shown in italics. Absolute changes (ppt yr^{-1}) are calculated by subtracting the 2019 annual mole fractions from the 2020 annual mole fractions; relative changes (% yr^{-1}) are the same difference relative to the 2019 value. Annual mole fractions and global emissions reported by AGAGE were generally calculated using a 12-box inverse model (e.g., Cunnold et al., 1983; Rigby et al., 2013) that were optimized to represent the AGAGE in situ observations made at remote locations, except for H_2. The global H_2 mole fractions from AGAGE were calculated as the average mole fractions between measurements made at Mace Head, Ireland (MHD), and at CGO. Annual mole fractions reported by NOAA are global annual averages from whole-air flask measurements except for SF_6, which used both in situ and flask measurements. Annual mole fractions reported by CSIRO are global annual averages from whole-air flask measurements.

The presented values are updates from AGAGE (agage.mit.edu) with calibrations as specified in Prinn et al. (2018) and related primary publications; NOAA (gml.noaa.gov/dv/site/); CSIRO data archived at WDCGG (gaw.kishou.go.jp); UCI (data.ess-dive.lbl.gov/view/doi:10.3334/CDIAC/ATG.002); and the following publications: Leedham Elvidge et al., 2018; Droste et al., 2020.

Notes:
[1]Values are based on measurements made only at Jungfraujoch, Switzerland.

1.5.3 Other Fluorine-Containing Species (SF_6, Perfluorocarbons, NF_3, SO_2F_2, SF_5CF_3, Hydrofluoroethers)

Most of the other fluorine-containing species exhibit increasing global mole fractions. The total direct radiative forcing due to these substances increased from 12.7 mW m^{-2} in 2016 to 14.3 mW m^{-2} in 2020.

Sulfur Hexafluoride (SF_6). The atmospheric global surface mean mole fraction of SF_6 increased from 8.9 to 10.3 ppt between 2016 and 2020 (**Table 1-1**1 and **Figure 1-19**), which is comparable to the increase of 1.3 ppt during 2012–2016 reported in the last Assessment. While the concentrations from ground-based networks agree very well, FTIR measurements of air above the Jungfraujoch station in the Swiss Alps show a slightly higher increase of 3.86 ± 0.14% yr^{-1} between 2014 and 2020 (compared to 3.56 ± 0.11% yr^{-1} from the near-surface measurements); trends from the ACE-FTS satellite-based measurements are between the two at 3.73% ± 0.15 yr^{-1} (**Table 1-2**). Some of these differences (especially those between the in situ network global trend and the European FTIR record) can probably be attributed to the main sources of SF_6 being located in the NH.

Global emissions of SF_6 were 8.8 Gg yr^{-1} in 2016 and 9.0 Gg yr^{-1} in 2020. Simmonds et al. (2020) estimated Chinese, Korean, and Western European emissions of SF_6, with the former accounting for 36 (29–42) % of total global emissions in 2018, and the latter two being about 10 times smaller in comparison. The radiative forcing of SF_6 is estimated at 5.9 mW m^{-2} in 2020, representing an increase of 0.8 mW m^{-2} since 2016.

Perfluorocarbons (PFCs). PFCs consist exclusively of carbon and fluorine and, in the case of alkane and cycloalkane derivatives, typically have very long lifetimes and high radiative efficiencies. Long-term observation-based trends and mole fractions are available for 10 PFCs: CF_4, C_2F_6, C_3F_8 *c*-C_4F_8, *n*-C_4F_{10}, *n*-C_5F_{12}, *i*-C_6F_{14}, *n*-C_6F_{14}, *n*-C_7F_{16}, and *n*-C_8F_{18}. Improved estimates of PFC radiative efficiencies have recently been published by Hodnebrog et al. (2020), leading to higher GWPs in all cases. Since 2016, atmospheric abundances of all PFCs have continued to increase, albeit at very different rates (**Table 1-11** and **Figure 1-19**).

CF_4 is the most abundant PFC. Its mole fraction increased from 82.8 ppt to 86.4 ppt between 2016 and 2020 (update from Say et al., 2021), which is higher than the 3 ppt increase previously reported between 2012 and 2016. When comparing these observations with FTIR-based remote sensing observations at Jungfraujoch between 2014 and 2020, the increase of 0.93 ± 0.07% yr^{-1} from the latter is slightly lower than the rate of 1.06 ± 0.02% yr^{-1} derived from ground-based measurements (**Table 1-2**). ACE-FTS-based upper-tropospheric growth during that period was 1.07 ± 0.06% yr^{-1}, i.e., very similar to the in situ record-based rate.

Emissions of CF_4 are estimated to have increased on a global basis, from 13 ± 1 Gg yr^{-1} in 2016 to 15 ± 1 Gg yr^{-1} in 2020, confirming that the period of increasing CF_4 emissions first reported by Trudinger et al. (2016), and recently updated by Say et al. (2021), is continuing. Estimates of northwestern European emissions did not change significantly during 2010–2019 and are equivalent to 0.7% of the global total in 2018 (Say et al., 2021). Emissions from East Asia are estimated at 4–5 Gg yr^{-1}, and there is evidence that the global CF_4 emission increase between 2012 and 2019 is likely driven by increased emissions from that region (Kim et al., 2021). Part of these emissions likely originate from Chinese rare earth metal production (Cai et al., 2018). Radiative

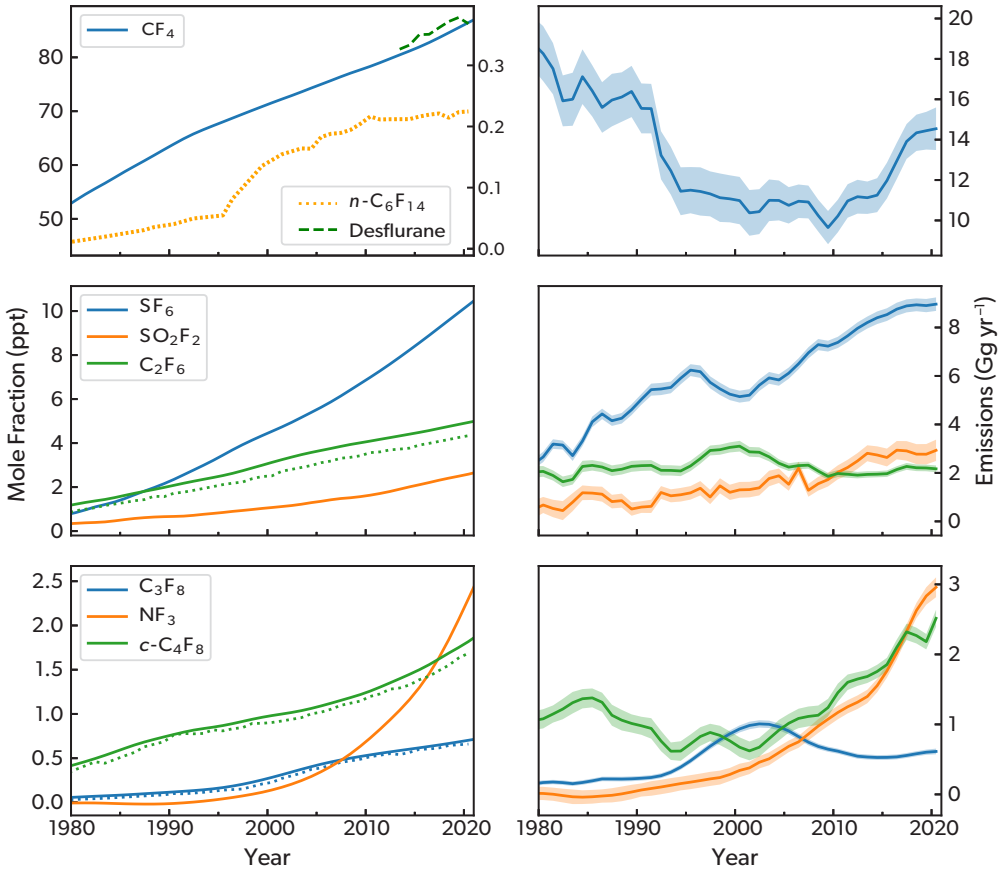

Figure 1-19. Global mean surface mole fraction (*left*) and emissions estimates (*right*) for the same fluorinated greenhouse gases as in **Table 1-11** (excluding CFCs, halons, HCFCs and HFCs). Solid lines show global mole fractions and emissions derived using AGAGE measurement data and a 12-box model, as described in **Figure 1-3**. Shading indicated the 1 standard deviation uncertainty in emissions. Dotted lines show annual mean mole fractions measured at Cape Grim, Australia, by UEA/FZJ. A dashed line in the top-left panel shows the annual mean mole fractions (since 2013) of desflurane measured at Jungfraujoch, Switzerland, by Empa. The left axis in the top-left panel is for CF_4, and the right axis is for *n*-C_6F_{14} and desflurane.

forcing from anthropogenic CF_4 increased from 4.2 mW m^{-2} to 4.6 mW m^{-2} between 2016 and 2020.

Over the 2016 to 2020 period, global mole fractions of hexafluoroethane (C_2F_6) and octafluoropropane (C_3F_8) increased from 4.57 ppt to 4.94 ppt, and from 0.63 to 0.70 ppt, respectively (updates from Say et al., 2021). Both increases are similar to those observed between 2012 and 2016. This translates to global emissions of 2.2 ± 0.1 Gg yr^{-1} for C_2F_6 in 2020, i.e., practically unchanged since 2016 (**Table 1-11**), and of 0.6 ± 0.0 Gg yr^{-1} for C_3F_8, an increase from 0.5 ± 0.0 Gg yr^{-1} in 2016. Northwestern European emissions were estimated to be somewhat higher contributors to the global total, with contributions of 1.6% for C_2F_6 and, notably, 5.1% for C_3F_8 in 2018 (Say et al., 2021). For recent years, a much larger fraction of global C_2F_6 emissions (~1.2 Gg yr^{-1}) has been estimated to originate from East Asia (Kim et al., 2021), again with likely contributions from rare earth metal production (Cai et al., 2018). Radiative forcing from the two gases increased from 1.20 mW m^{-2} to 1.30 mW m^{-2} (C_2F_6) and from 0.17 mW m^{-2} to 0.19 mW m^{-2} (C_3F_8) over the 2016–2020 period.

For octafluorocyclobutane (*c*-C_4F_8), Mühle et al. (2019) presented a comprehensive overview of global observations, including a full reconstruction of its atmospheric history. Based on evidence from firn air, atmospheric abundances were near zero (<0.02 ppt) from the early 1900s to the early 1960s, which is in agreement with the current understanding that there are no natural sources of this PFC. Global *c*-C_4F_8 mole fractions have increased monotonically since. This is qualitatively in line with the previously published records of Saito et al. (2010) and Oram et al. (2012), including a temporary slowdown during the 1990s and early 2000s, although some differences exist. These are probably at least in part related to independent calibration scales. The SH Oram et al. record was recently updated by Droste et al. (2020), and the results from that study agree with those of Mühle et al. (2019) in that both report abundances to be accelerating over approximately the two decades leading up to 2020 (**Figure 1-19**). Mole fractions of *c*-C_4F_8 reached 1.69 ppt in the SH (update from Droste et al., 2020) and 1.82 ppt globally (update from Mühle et al., 2019) in 2020. In terms of emissions, the recent increases in *c*-C_4F_8 mole fractions translate to 2.1 ± 0.1 Gg yr^{-1} in 2016, and 2.5 ± 0.1 Gg yr^{-1} in 2020 (update from Mühle et al., 2019), with the AGAGE emission estimates for 2016 slightly higher than those of Droste et al. (2020), i.e., 1.9 Gg yr^{-1}. Regional inverse methods and observations were used to estimate emissions from eastern Asia (0.73 Gg yr^{-1} in 2017, 31 ± 4% of global emissions, predominantly from eastern China), northern and central India (0.14 ± 0.06 Gg yr^{-1} in mid-2016), northwestern Europe, and Australia (about 1% and 0.7% of the global total, respectively), as well as indications that two Russian facilities might possibly be contributing between 5% and 26% of the global total (Mühle et al., 2019). Atmospheric sources were previously thought to be mainly from the semiconductor industry, but PTFE (polytetrafluoroethylene) and HFP (hexafluoropropylene) production is likely a more dominant contributor (Mühle et al., 2019). In support of this theory, Mühle et al. (2022) reported that *c*-C_4F_8 emissions are highly correlated with the production of HCFC-22 for feedstock uses, as almost all of this is pyrolyzed to produce PTFE and HFP. In 2020, *c*-C_4F_8 contributed 0.58 mW m^{-2} to global radiative forcing.

Updated trends of five less abundant longer-chain PFCs, i.e., *n*-C_4F_{10}, *n*-C_5F_{12}, *n*-C_6F_{14}, *n*-C_7F_{16}, and the newly detected perfluoro-2-methylpentane (*i*-C_6F_{14}), were recently reported by Droste et al. (2020). This included a new calibration of all species except *n*-C_5F_{12} due to the identification and separation of isomers present in the atmosphere. All PFCs continued to increase between 2016 and 2020, though at relatively slow rates, i.e., from 0.194 ppt to 0.202 ppt (*n*-C_4F_{10}), from 0.148 ppt to 0.149 ppt (*n*-C_5F_{12}; increase not significant within uncertainties), from 0.220 ppt to 0.225 ppt (*n*-C_6F_{14}), from 0.110 ppt to 0.116 ppt (*n*-C_7F_{16}), and from 0.065 ppt to 0.072 ppt (*i*-C_6F_{14}). No update is available for abundances of *n*-C_8F_{18} (which in 2011 was 0.09 ppt; Ivy et al., 2012). Global emissions of the five former PFCs were estimated by Droste et al. (2020) to have remained constant between 2013 and 2017 at 0.09 Gg yr^{-1} (*n*-C_4F_{10}), 0.06 Gg yr^{-1} (*n*-C_5F_{12}), 0.14 Gg yr^{-1} (*n*-C_6F_{14}), 0.18 Gg yr^{-1} (*n*-C_7F_{16}), and 0.09 Gg yr^{-1} (*i*-C_6F_{14}). Expressed as radiative forcing, the combined contribution of all six PFCs (at their last-known abundances) amounted to 0.38 mW m^{-2} in 2020.

Nitrogen Trifluoride (NF_3). Between 2016 and 2020, global mole fractions of NF_3 increased from 1.5 ppt to 2.3 ppt, thus maintaining its annual growth rate of >10% (update from Arnold et al., 2013; **Table 1-11** and **Figure 1-19**). NF_3 emissions also continued to increase, from 2.0 ± 0.1 Gg yr^{-1} to 3.0 ± 0.1 Gg yr^{-1}, with radiative forcing concurrently increasing by almost 60%, to 0.48 mW m^{-2} in 2020.

Sulfuryl Fluoride (SO_2F_2). SO_2F_2 is mainly used as a substitute for CH_3Br. Its rate of growth has declined since the previous Assessment, with global mole fractions of 2.2 ppt in 2016 and 2.6 ppt in 2020. This is, however, still equivalent to a very rapid growth of about 18% from 2016 to 2020, compared to the 25% increase between 2012 and 2016 (update from Mühle et al., 2009, and Gressent et al., 2021; **Table 1-11** and **Figure 1-19**). SO_2F_2 global emissions reported in this Assessment are 2.9 ± 0.4 Gg yr^{-1} in both 2016 and 2020. In terms of regional SO_2F_2 emissions, North America was recently identified as the major global emitter (Gressent et al., 2021), and the reported long-term increase in emissions is partly due to the expanded use of SO_2F_2 for post-harvest treatment, although soil fumigation remains another main source. Radiative forcing from this gas increased from 0.45 mW m^{-2} to 0.52 mW m^{-2} between 2016 and 2020.

(Trifluoromethyl) Sulfur Pentafluoride (SF_5CF_3). SH observations confirm that mole fractions of SF_5CF_3 are virtually unchanged, with 0.152 ppt reported for 2016 and 0.155 ppt for 2020 (update from Sturges et al., 2012), corresponding to no renewed emissions of this species. Consequently, SF_5CF_3 radiative forcing remained at 0.09 mW m^{-2}.

Halogenated Ethers (HFEs). Atmospheric abundances, trends, and emissions of desflurane (HFE-236ea2, $CHF_2OCHFCF_3$), isoflurane (HCFE-235da2, $CHF_2OCHClCF_3$), and sevoflurane (HFE-347 isomer, $(CF_3)_2CHOCH_2F$) were first reported by Vollmer et al. (2015c), who determined global mean mole fractions in 2014 of 0.30 ppt, 0.097 ppt, and 0.13 ppt, respectively. An update is available only for desflurane, for which mole fractions derived from observations at the Jungfraujoch station in Switzerland increased slightly, from 0.35 ppt in 2016 to 0.37 ppt in 2020, equivalent to an increase from 0.17 mW m^{-2} to 0.18 mW m^{-2} in 2020. In the absence of updated atmospheric abundances, the best estimates of radiative forcing from isoflurane and sevoflurane remain at 0.04 mW m^{-2} for both anesthetics (using the recent GWP update from Andersen et al., 2021, for sevoflurane). No updated emission estimates are available for any of the three species.

In addition, Vollmer et al. (2019) reported the first observations of the potent greenhouse gas octafluorooxolane (*c*-C_4F_8O). The radiative efficiency of this HFE is relatively high at 0.47 W m^{-2} ppb^{-1}, but atmospheric mole fractions remain low at 0.074 ppt in the NH in 2018. Emissions, which are thought to originate predominantly from usage as a solvent in the semiconductor industry, peaked at 0.15 ± 0.04 Gg yr^{-1} in 2004 and have since declined to <0.015 Gg yr^{-1} in 2018.

1.5.4 Molecular Hydrogen (H_2)

H_2 is an abundant atmospheric trace gas with both natural and anthropogenic emission sources and a relatively complex biogeochemical cycle. It is relevant for this Assessment as a stratospheric source gas for hydrogen oxide radicals (HO_x), and also adds stratospheric water vapor (H_2O) when oxidized. In addition, its atmospheric impacts may well become more important in the near future due to its use in fuel cells and internal combustion engines and related emerging applications. Few publications have estimated the potential decrease in ozone levels from such hydrogen emissions. These studies all have large uncertainties, but they indicate that the resulting impacts on global ozone are likely small (<1%) even in the case of an extreme leakage scenario (Schultz et al., 2003; Tromp et al., 2003; Feck et al., 2008; Vogel et al., 2011).

Observations of Atmospheric Abundance. Atmospheric abundances of H_2 have increased from ~330 ppb during the mid-to-late 1800s to the present levels of 530–550 ppb in the late 20th and early 21st centuries, an increase of about 70% (Patterson et al., 2020; Patterson et al., 2021). The increase in atmospheric H_2 is primarily attributed to increasing anthropogenic emissions and production from the oxidation of methane over the 20th century (Patterson et al., 2021).

Global mole fractions of H_2 in 2020 were approximately 544 ppb (**Table 1-11**). The increase in the atmospheric abundance of H_2 from 2016 to 2020 was around 10 ppb, with about 4 ppb of this occurring between 2019 and 2020 alone. There is a small inter-hemispheric gradient in the atmospheric H_2 mole fractions due to the major sink being biological uptake on land. This results in approximately 3% higher concentrations in the Southern Hemisphere (Ehhalt and Rohrer, 2009).

Emissions, Lifetimes, and Radiative Forcings. The largest source of H_2 in the atmosphere is from the photolysis of formaldehyde, which is formed by the photochemical oxidation (reaction with the hydroxyl radical) of methane and other organic compounds. Recent reviews and updates estimate this source to be in the range of 30–77 Tg yr^{-1} (Ehhalt and Rohrer, 2009; Zgonnik, 2020). The second largest source is from incomplete combustion processes, through fossil fuel combustion and biomass burning. Carbon monoxide (CO) is formed during incomplete combustion, which then reacts with water vapor to produce carbon dioxide (CO_2) and H_2. Estimates for fossil fuel sources range from 11 to 20 Tg yr^{-1}, while estimates for biomass burning range from 10–20 Tg yr^{-1}. Hydrogen is also emitted from geological sources, including volcanoes, with a recent review suggesting this may be as high as 23 Tg yr^{-1} (Zgonnik, 2020). Lastly, H_2 is emitted by nitrogen fixation on land, and in the ocean, with emissions estimated to be 3–6 Tg yr^{-1} for oceans and 0–6 Tg yr^{-1} for land (Ehhalt and Rohrer, 2009; Zgonnik, 2020).

There are two major sinks of atmospheric H_2, with the largest one being uptake by soil microorganisms as a fuel source and the other oxidation of H_2 by the hydroxyl radical (OH). Estimates for the soil uptake sink range from 55–88 Tg yr^{-1}, while the sink for oxidation by OH ranges from 8–19 Tg yr^{-1} (Ehhalt and Rohrer, 2009; Zgonnik, 2020).

The atmospheric lifetime of H_2 is estimated to be about two years (Ehhalt and Rohrer, 2009). Even though H_2 is not a greenhouse gas, Derwent et al. (2020) estimate that it has an indirect GWP_{100} of about 5 ± 1. This is primarily due to its reaction with tropospheric OH, which depletes the oxidizing capacity of the troposphere, resulting in a longer methane lifetime, and through the production of ozone in the troposphere.

REFERENCES

Adcock, K., C.E. Reeves, L.J. Gooch, E.L. Elvidge, P.J. Fraser, R. Langenfelds, C.A.M. Brenninkmeijer, J.-L. Wang, C.-F. Ou-Yang, T. Röckmann, S. O'Doherty, W.T. Sturges, D.E. Oram, M.J. Ashfold, N.M. Hanif, and J.C. Laube, CFC-113a (CF_3CCl_3) in the atmosphere: an update of distributions, trends, emissions and potential source, ***Atmos. Chem. Phys.***, ***18***, 4737–4751, doi:10.5194/acp-18-4737-2018, 2018.

Adcock, K.E., M.J. Ashfold, C.C-K. Chou, L.J. Gooch, N. Mohd Hanif, J.C. Laube, D.E. Oram, C.F. Ou-Yang, M. Panagi, W.T. Sturges, and C.E. Reeves, Investigation of East Asian emissions of CFC-11 using atmospheric observations in Taiwan, ***Environ. Sci. Technol.***, ***54*** (7), 3814–3822, doi:10.1021/acs.est.9b06433, 2020.

Adcock, K.E., P.J. Fraser, B.D. Hall, R.L. Langenfelds, G. Lee, S.A. Montzka, D.E. Oram, T. Röckmann, F. Stroh, W.T. Sturges, B. Vogel, and J.C. Laube, Aircraft-based observations of ozone-depleting substances in the upper troposphere and lower stratosphere in and above the Asian summer monsoon, ***J. Geophys. Res. Atmos.***, ***126*** (1), 1–18, doi:10.1029/2020JD033137, 2021.

An, M., L.M. Western, D. Say, L. Chen, T. Claxton, A.L. Ganesan, R. Hossaini, P.B. Krummel, A.J. Manning, J. Mühle, S. O'Doherty, R.G. Prinn, R.F. Weiss, D. Young, J. Hu, B. Yao, and M. Rigby, Rapid increase in dichloromethane emissions from China inferred through atmospheric observations, ***Nat. Commun.***, ***12*** (1), 7279, doi:10.1038/s41467-021-27592-y, 2021.

Andersen, M.P.S., O.J. Nielsen, and J.D. Sherman, The global warming potentials for anesthetic gas sevoflurane need significant corrections, ***Environ. Sci. Technol.***, ***55*** (15), 10,189–10,191, doi:10.1021/acs.est.1c02573, 2021.

Andrews, S.J., L.J. Carpenter, E.C. Apel, E. Atlas, V. Donets, J.R. Hopkins, R.S. Hornbrook, A.C. Lewis, R.T. Lidster, R. Lueb, J. Minaeian, M. Navarro, S. Punjabi, D. Riemer, and S. Schauffler, A comparison of very short-lived halocarbon (VSLS) and DMS aircraft measurements in the tropical west Pacific from CAST, ATTREX and CONTRAST, ***Atmos. Meas. Tech.***, 9(10), 5213–5225, doi:10.5194/amt-9-5213-2016, 2016.

Angert, A., W. Said-Ahmad, C. Davidson, and A. Amrani, Sulfur isotopes ratio of atmospheric carbonyl sulfide constrains its sources, ***Sci. Rep.***, ***9***, 741, doi:10.1038/s41598-018-37131-3, 2019.

Arnold, T., C.M. Harth, J. Mühle, A.J. Manning, P.K. Salameh, J. Kim, D.J. Ivy, L.P. Steele, V.V. Petrenko, J.P. Severinghaus, D. Baggenstos, and R.F. Weiss, Nitrogen trifluoride global emissions estimated from updated atmospheric measurements, ***Proc. Natl. Acad. Sci.***, ***110*** (6), 2029–2034, doi:10.1073/pnas.1212346110, 2013.

Aschmann, J., and B.M. Sinnhuber, Contribution of very short-lived substances to stratospheric bromine loading: uncertainties and constraints, ***Atmos. Chem. Phys.***, ***13*** (3), 1203–1219, doi:10.5194/acp-13-1203-2013, 2013.

Bahlmann, E., F. Keppler, J. Wittmer, M. Greule, H.F. Schöler, R. Seifert, and C. Zetzsch, Evidence for a major missing source in the global chloromethane budget from stable carbon isotopes, ***Atmos. Chem. Phys.***, ***19*** (3), 1703–1719, doi:10.5194/acp-19-1703-2019, 2019.

Barreto, H. and F. Howland: Introductory Econometrics. Using Monte Carlo Simulation with Microsoft Excel, Cambridge University Press, New York, 2006.

Benish, S.E., R.J. Salawitch, X. Ren, H. He, and R.R. Dickerson, Airborne observations of CFCs over Hebei Province, China in spring 2016, ***J. Geophys. Res. Atmos.***, ***126*** (18), doi:10.1029/2021JD035152, 2021.

Bernath, P., and A.M. Fernando, Trends in stratospheric HCl from the ACE satellite mission, ***J. Quant. Spectrosc. Radiat. Trans., 217***, 126–129, doi:10.1016/j.jqsrt.2018.05.027, 2018.

Bernath, P.F., J. Steffen, J. Crouse, and C.D. Boone, Sixteen-year trends in atmospheric trace gases from orbit, ***J. Quant. Spectrosc. Radiat. Trans.***, ***253***, 107178, doi:10.1016/j.jqsrt.2020.107178, 2020.

Bernath, P.F., J. Crouse, R.C. Hughes, and C.D. Boone, The atmospheric chemistry experiment Fourier transform spectrometer (ACE-FTS) version 4.1 retrievals: Trends and seasonal distributions, ***J. Quant. Spectrosc. Radiat. Trans., 259***, 107409, doi:10.1016/j.jqsrt.2020.107409, 2021.

Bosch, H., C. Camy-Peyret, M.P. Chipperfield, R. Fitzenberger, H. Harder, U. Platt, and K. Pfeilsticker, Upper limits of stratospheric IO and OIO inferred from center-to-limb-darkening-corrected balloon-borne solar occultation visible spectra: Implications for total gaseous iodine and stratospheric ozone, ***J. Geophys. Res.***, ***108*** (D15), doi:10.1029/2002JD003078, 2003.

Boudjellaba, D., J. Dron, G. Revenko, C. Demelas, and J.L. Boudenne, Chlorination by-product concentration levels in seawater and fish of an industrialised bay (Gulf of Fos, France) exposed to multiple chlorinated effluents, ***Sci. Total Environ.***, ***541***, 391–399, doi:10.1016/j.scitotenv.2015.09.046, 2016.

Brinckmann, S., A. Engel, H. Bonisch, B. Quack, and E. Atlas, Short-lived brominated hydrocarbons–observations in the source regions and the tropical tropopause layer, ***Atmos. Chem. Phys.***, ***12*** (3), 1213–1228, doi:10.5194/acp-12-1213-2012, 2012.

Brioude, J., R.W. Portmann, J.S. Daniel, O.R. Cooper, G.J. Frost, K.H. Rosenlof, C. Granier, A.R. Ravishankara, S.A. Montzka, and A. Stohl, Variations in ozone depletion potentials of very short-lived substances with season and emission region, ***Geophys. Res. Lett.***, ***37*** (19), doi:10.1029/2010GL044856, 2010.

Brühl, C., J. Lelieveld, P.J. Crutzen, and H. Tost, The role of carbonyl sulphide as a source of stratospheric sulphate aerosol and its impact on climate, ***Atmos. Chem. Phys.***, ***12*** (3), 1239–1253, doi:10.5194/acp-12-1239-2012, 2012.

Brühl, C., J. Lelieveld, H. Tost, M. Höpfner, and N. Glatthor, Stratospheric sulfur and its implications for radiative forcing simulated by the chemistry climate model EMAC, ***J. Geophys. Res. Atmos., 120*** (5), 2103–2118, doi:10.1002/2014JD022430, 2015.

Burkholder, J.B., S.P. Sander, J. Abbatt, J.R. Barker, C. Cappa, J.D. Crounse, T.S. Dibble, R.E. Huie, C.E. Kolb, M.J. Kurylo, V.L. Orkin, C.J. Percival, D.M. Wilmouth, and P.H. Wine, ***Chemical Kinetics and Photochemical Data for Use in Atmospheric Studies***, Evaluation No. 19, JPL Publication 19-5, Jet Propulsion Laboratory, Pasadena, California, [available at: https://jpldataeval.jpl.nasa.gov/pdf/NASA-JPL%20Evaluation%2019-5.pdf], 2019.

Butler, J.H., S.A. Montzka, A.D. Clarke, J.M. Lobert, and J.W. Elkins, Growth and distribution of halons in the atmosphere, ***J. Geophys. Res. Atmos.***, ***103*** (D1), 1503–1511, doi:10.1029/97JD02853, 1998.

Butler, J., M. Battle, M.L. Bender, S.A. Montzka, A.D. Clarke, E.S. Saltzman, C.M. Sucher, J.P. Severinghaus, and J.W. Elkins, A record of atmospheric halocarbons during the twentieth century from polar firn air, ***Nature***, ***399***, 749–755, doi:10.1038/21586, 1999.

Butler, J.H., D.B. King, J.M. Lobert, S.A. Montzka, S.A. Yvon-Lewis, B.D. Hall, N.J. Warwick, D.J. Mondeel, M. Aydin, and J.W. Elkins, Oceanic distributions and emissions of short- lived halocarbons, Glob. Biogeochem. Cycles, ***21*** (1), doi:10.1029/2006GB002732, 2007.

Butler, J.H., S.A. Yvon-Lewis, J.M. Lobert, D.B. King, S.A. Montzka, J.L. Bullister, V. Koropalov, J.W. Elkins, B.W. Hall., L. Hu, and Y. Liu, A comprehensive estimate for loss of atmospheric carbon-tetrachloride (CCl_4) to the ocean, ***Atmos. Chem. Phys.***, ***16*** (17), 10,899–10,910, doi:10.5194/acp-16-10899-2016, 2016.

Butler, R., P.I. Palmer, L. Feng, S.J. Andrews, E.L. Atlas, L.J. Carpenter, V. Donets, N.R.P. Harris, S.A. Montzka, L.L. Pan, R.J. Salawitch, and S.M. Schauffler, Quantifying the vertical transport of $CHBr_3$ and CH_2Br_2 over the western Pacific, ***Atmos. Chem. Phys.***, ***18*** (17), 13,135–13,153, doi:10.5194/acp-18-13135-2018, 2018.

Butler, J.H., and S.A. Montzka, The NOAA Annual Greenhouse Gas Index (AGGI), ***NOAA Earth System Research Laboratory***, Boulder, Colorado, [available at: https://gml.noaa.gov/aggi/aggi.html], 2021.

Butz, A., H. Bosch, C. Camy-Peyret, M.P. Chipperfield, M. Dorf, S. Kreycy, L. Kritten, C. Prados-Roman, J. Schwarzle, and K. Pfeilsticker, Constraints on inorganic gaseous iodine in the tropical upper troposphere and stratosphere inferred from balloon-borne solar occultation observations, ***Atmos. Chem. Phys.***, ***9*** (18), 7229–7242, doi:10.5194/acp-9-7229-2009, 2009.

Cai, B., H. Liu, F. Kou, Y. Yang, B. Yao, X. Chen, D.S. Wong, L. Zhang, J. Li, G. Kuang, L. Chen, J. Zheng, D. Guan, and Y. Shan, Estimating perfluorocarbon emission factors for industrial rare earth metal electrolysis, ***Resour. Conserv. Recycl.***, ***136***, 315–323, doi:10.1016/j.resconrec.2018.04.018, 2018.

Carpenter, L.J., and P.S. Liss, On temperate sources of bromoform and other reactive organic bromine gases, ***J. Geophys. Res. Atmos.***, ***105*** (D16), 20,539–20,547, doi:10.1029/2000JD900242, 2000.

Carpenter, L.J., S.M. MacDonald, M.D. Shaw, R. Kumar, R.W. Saunders, R. Parthipan, J. Wilson, and J.M. C. Plane, Atmospheric iodine levels influenced by sea surface emissions of inorganic iodine, ***Nat. Geosci., 6***, 108–111, doi:10.1038/ngeo1687, 2013.

Carpenter, L.J., and S. Reimann (Lead authors), J.B. Burkholder, C. Clerbaux, B.D. Hall, R. Hossaini, J.C. Laube, and S.A. Yvon-Lewis, Ozone-Depleting Substances (ODSs) and Other Gases of Interest to the Montreal Protocol, Chapter 1 in ***Scientific Assessment of Ozone Depletion: 2014***, Global Ozone Research and Monitoring Project–Report No. 55, World Meteorological Organization, Geneva, Switzerland, 2014.

Carpenter, L.J., and J.S. Daniel (Lead authors), E.L. Fleming, T. Hanaoka, J. Hu, A.R. Ravishankara, M.N. Ross, S. Tilmes, T.J. Wallington, and D.J. Wuebbles, Scenarios and Information for Policymakers, Chapter 6 in ***Scientific Assessment of Ozone Depletion: 2018***, Global Ozone Research and Monitoring Project–Report No. 58, World Meteorological Organization, Geneva, Switzerland, 2018.

Carpenter, L.J., R.J. Chance, T. Sherwen, T.J. Adams, S.M. Ball, M.J. Evans, H. Hepach, L.D.J. Hollis, C. Hughes, T.D. Jickells, A. Mahajan, D.P. Stevens, L. Tinel, and M.R. Wadley, Marine iodine emissions in a changing world, ***Proc. R. Soc. A***, ***477*** (2247), doi:10.1098/rspa.2020.0824, 2021.

Chen, X., X. Huang, and L.L. Strow, Near-global CFC-11 trends as observed by atmospheric infrared sounder from 2003 to 2018**,** ***J. Geophys. Res. Atmos.***, ***125*** (22), e2020JD033051, doi:10.1029/2020JD033051, 2020.

Chipperfield, M.P., M.I. Hegglin, S.A. Montzka, P.A. Newman, S. Park, S. Reimann, M. Rigby, A. Stohl, G.J. M. Velders, H. Walter-Terrinoni, and B. Yao, ***Report on the Unexpected Emissions of CFC-11***, Ozone Research and Monitoring, WMO No. 1268, World Meteorological Organization, Geneva, Switzerland, 2021.

Choi, H., M.-K. Park, P.J. Fraser, H. Park, S. Geum, J. Mühle, J. Kim, I. Porter, P.K. Salameh, C.M. Harth, B.L. Dunse, P.B. Krummel, R.F. Weiss, S. O'Doherty, D. Young, and S. Park, Top-down and bottom-up estimates of anthropogenic methyl bromide emissions from eastern China, ***Atmos. Chem. Phys.***, ***22***, 5157–5173, doi:10.5194/acp-22-5157-2022, 2022.

Claxton, T., R. Hossaini, O. Wild, M.P. Chipperfield, and C. Wilson, On the regional and seasonal ozone depletion potential of chlorinated very short lived substances, ***Geophys. Res. Lett.***, ***46*** (10), 5489–5498, doi:10.1029/2018GL081455, 2019.

Claxton, T., R. Hossaini, C. Wilson, S.A. Montzka, M.P. Chipperfield, O. Wild, E.M. Bednarz, L.J. Carpenter, S.J. Andrews, S.C. Hackenberg, J. Mühle, D. Oram, S. Park, M. Park, E. Atlas, M. Navarro, S. Schauffler, D. Sherry, M. Vollmer, T. Schuck, A. Engel, P.B. Krummel, M. Maione, J. Arduini, T. Saito, Y. Yokouchi, S. O'Doherty, D. Young, and C. Lunder, A synthesis inversion to constrain global emissions of two very short lived chlorocarbons: dichloromethane, and perchloroethylene**,** ***J. Geophys. Res. Atmos.***, ***125*** (12), e2019JD031818, doi:10.1029/2019JD031818, 2020.

Cuevas, C.A., N. Maffezzoli, J.P. Corella, A. Spolaor, P. Vallelonga, H.A. Kjær, M. Simonsen, M. Winstrup, B. Vinter, C. Horvat, R.P. Fernandez, D. Kinnison, J.-F. Lamarque, C. Barbante, and A. Saiz-Lopez, Rapid increase in atmospheric iodine levels in the North Atlantic since the mid-20th century, ***Nat. Commun.***, ***9*** (1452), doi:10.1038/s41467-018-03756-1, 2018.

Cuevas C.A., Fernandez R.P., Kinnison D.E., Li Q., Lamarque J.F., Trabelsi T., Francisco J.S., Solomon S., Saiz-Lopez A. The influence of iodine on the Antarctic stratospheric ozone hol**e,** ***Proc. Natl. Acad. Sci.***, 119(7), doi: 10.1073/pnas.2110864119, 2022.

Cunnold, D.M., R.G. Prinn, R.A. Rasmussen, P.G. Simmonds, F.N. Alyea, C.A. Cardelino, A.J. Crawford, P.J. Fraser, and R.D. Rosen, The atmospheric lifetime experiment: 3. lifetime methodology and application to 3 years of $CFCl_3$ data, ***J. Geophys. Res. Oceans***, ***88*** (C13), 8379–8400, doi:10.1029/JC088iC13p08379, 1983.

Cunnold, D.M., P.J. Fraser, R.F. Weiss, R.G. Prinn, P.G. Simmonds, B.R. Miller, F.N. Alyea, and A.J. Crawford, Global trends and annual releases of CCl_3F and CCl_2F_2 estimated from ALE/GAGE and other measurements from July 1978 to June 1991, ***J. Geophys. Res. Atmos.***, ***99*** (D1), 1107–1126, doi:10.1029/93JD02715, 1994.

Daniel, J.S., S. Solomon, and D.L. Albritton, On the evaluation of halocarbon radiative forcing and global warming potentials, ***J. Geophys. Res. Atmos.***, ***100*** (D1), 1271–1285, doi:10.1029/94JD02516, 1995.

Delahaye, T., R. Armante, N.A. Scott, N. Jacquinet-Husson, A. Chédin, L. Crépeau, C. Crevoisier, V. Douet, A. Perrin, A. Barbe, V. Boudon, A. Campargue, L.H. Coudert, V. Ebert, J.M. Flaud, R.R. Gamache, D. Jacquemart, A. Jolly, F. Kwabia Tchana, A. Kyuberis, G. Li, O.M. Lyulin, L. Manceron, S. Mikhailenko, N. Moazzen-Ahmadi, H.S.P. Müller, O.V. Naumenko, A. Nikitin, V.I. Perevalov, C. Richard, E. Starikova, S.A. Tashkun, V.G. Tyuterev, J. Vander Auwera, B. Vispoel, A. Yachmenev, and S. Yurchenko, The 2020 edition of the GEISA spectroscopic database, ***J. Mol. Spectrosc.***, ***380***, 111510, doi:10.1016/J.JMS.2021.111510, 2021.

Derwent, R.G., D.S. Stevenson, S.R. Utembe, M.E. Jenkin, A.H. Khan, and D.E. Shallcross, Global modelling studies of hydrogen and its isotopomers using STOCHEM-CRI: Likely radiative forcing consequences of a future hydrogen economy, ***Int. J. Hydrog. Energy***, ***45***, 9211–9221, doi:10.1016/j.ijhydene.2020.01.125, 2020.

Deventer, M.J., Y. Jiao, S.H. Knox, F. Anderson, M.C. Ferner, J.A. Lewis, and R.C. Rhew, Ecosystem-scale measurements of methyl halide fluxes from a brackish tidal marsh invaded with perennial pepperweed (Lepidium latifolium), ***J. Geophys. Res. Biogeosci.***, ***123*** (7), 2104–2120, doi:10.1029/2018JG004536, 2018.

Ding, X., Q. Ling, Y. Huo, Y. Liang, H. Wang, J. Zhang, S. Wang, T. Wang, X. Ye, and J. Chen, Gaseous and particulate chlorine emissions from typical iron and steel industry in China, ***J. Geophys. Res. Atmos.***, ***125*** (15), doi:10.1029/2020JD032729, 2020.

Dorf, M., A. Butz, C. Camy-Peyret, M.P. Chipperfield, L. Kritten, and K. Pfeilsticker, Bromine in the tropical troposphere and stratosphere as derived from balloon-borne BrO observations, ***Atmos. Chem. Phys.***, ***8*** (23), 7265–7271, doi:10.5194/acp-8-7265-2008, 2008.

Dorf, M., J.H. Butler, A. Butz, C. Camy-Peyret, M.P. Chipperfield, L. Kritten, S.A. Montzka, B. Simmes, F. Weidner, and K. Pfeilsticker, Long-term observations of stratospheric bromine reveal slow down in growth, ***Geophys. Res. Lett.***, ***33*** (24), doi:10.1029/2006GL027714, 2006.

Droste, E.S., K.E. Adcock, M.J. Ashfold, C. Chou, Z. Fleming, P.J. Fraser, L.J. Gooch, A.J. Hind, R.L. Langenfelds, E.L Elvidge, N.M. Hanif, S. O'Doherty, D.E. Oram, C. Ou-Yang, M. Panagi, C.E. Reeves, W.T. Sturges, and J.C. Laube, Trends and emissions of six perfluorocarbons in the Northern Hemisphere and Southern Hemisphere, ***Atmos. Chem. Phys., 20*** (8), 4787–4807, doi:10.5194/acp-20-4787-2020, 2020.

Ehhalt, D.H., and F. Rohrer, The tropospheric cycle of H_2: a critical review, ***Tellus B: Chem. Phys. Meteorol.***, ***61*** (3), 500–535, doi:10.1111/j.1600-0889.2009.00416.x, 2009.

Engel, A., H. Bönisch, J. Ostermöller, M.P. Chipperfield, S. Dhomse, and P. Jöckel, A refined method for calculating equivalent effective stratospheric chlorine, ***Atmos. Chem. Phys.***, ***18*** (2), 601–609, doi:10.5194/acp-18-601-2018, 2018.

Engel, A., and M. Rigby (Lead Authors), J.B. Burkholder, R.P. Fernandez, L. Froidevaux, B.D. Hall, R. Hossaini, T. Saito, M.K. Vollmer, and B. Yao, Update on Ozone-Depleting Substances (ODSs) and Other Gases of Interest to the Montreal Protocol, Chapter 1 in ***Scientific Assessment of Ozone Depletion: 2018***, Global Ozone Research and Monitoring Project–Report No. 58, World Meteorological Organization, Geneva, Switzerland, 2018.

Fang, X., S. Park, T. Saito, R. Tunnicliffe, A.L. Ganesan, M. Rigby, S. Li, Y. Yokouchi, P.J. Fraser, C.M. Harth, P.B. Krummel, J. Mühle, S. O'Doherty, P.K. Salameh, P.G. Simmonds, R.F. Weiss, D. Young, M.F. Lunt, A.J. Manning, A. Gressent, and R.G. Prinn, Rapid increase in ozone-depleting chloroform emissions from China, ***Nat. Geosci.***, ***12***, 89–93, doi:10.1038/s41561-018-0278-2, 2019a.

Fang, X., J.A. Pyle, M.P. Chipperfield, J.S. Daniel, S. Park, and R.G. Prinn, Challenges for the recovery of the ozone layer, ***Nat. Geosci.***, ***12***, 592–596, doi:10.1038/s41561-019-0422-7, 2019b.

Fang, X., B. Yao, M.K. Vollmer, S. Reimann, L. Liu, L. Chen, R.G. Prinn, and J. Hu, Changes in HCFC emissions in China during 2011–2017, ***Geophys. Res, Lett.***, ***46*** (16), 10,034–10,042, doi:10.1029/2019GL083169, 2019c.

Feck, T., J.-U. Grooß, and M. Riese, Sensitivity of Arctic ozone loss to stratospheric H_2O, ***Geophys. Res. Lett.***, ***35*** (1), doi:10.1029/2007GL031334, 2008.

Feinberg, A., T. Sukhodolov, B.-P. Luo, E. Rozanov, L.H.E. Winkel, T. Peter, and A. Stenke, Improved tropospheric and stratospheric sulfur cycle in the aerosol–chemistry–climate model SOCOL-AERv2, ***Geosci. Model Dev.***, ***12***, 3863–3887, doi:10.5194/gmd-12-3863-2019, 2019.

Feng, Y., P. Bie, Z. Wang, L. Wang, and J. Zhang, Bottom-up anthropogenic dichloromethane emission estimates from China for the period 2005–2016 and predictions of future emissions, ***Atmos. Environ.***, ***186***, 241–247, doi:10.106/j.atmosenv.2018.05.039, 2018.

Fernandez, R.P., R.J. Salawitch, D.E. Kinnison, J.F. Lamarque, and A. Saiz-Lopez, Bromine partitioning in the tropical tropopause layer: Implications for stratospheric injection, ***Atmos. Chem. Phys.***, ***14*** (24), 13,391–13,410, doi:10.5194/acp-14-13391-2014, 2014.

Fernandez, R.P., J.A. Barrera, A.I. López-Noreña, D.E. Kinnison, J. Nicely, R.J. Salawitch, P.A. Wales, B.M. Toselli, S. Tilmes, J.-F. Lamarque, C.A. Cuevas, and A. Saiz-Lopez, Intercomparison between surrogate, explicit and full treatments of VSL bromine chemistry within the CAM-Chem chemistry-climate model, ***Geophys. Res. Lett.***, ***48*** (4), doi:10.1029/2020GL091125, 2021.

Fiehn, A., B. Quack, H. Hepach, S. Fuhlbrugge, S. Tegtmeier, M. Toohey, E. Atlas, and K. Krüger, Delivery of halogenated very short-lived substances from the west Indian Ocean to the stratosphere during the Asian summer monsoon, ***Atmos. Chem. Phys.***, ***17*** (11), 6723–6741, doi:10.5194/acp-17-6723-2017, 2017.

Fiehn A., B. Quack, I. Stemmler, F. Ziska, and K. Krüger, Importance of seasonally resolved oceanic emissions for bromoform delivery from the tropical Indian Ocean and west Pacific to the stratosphere, ***Atmos. Chem. Phys., 18***, 11,973–11,990, doi:10.5194/acp-18-11973-2018, 2018.

Filus, M.T., E.L. Atlas, M.A. Navarro, E. Meneguz, D. Thomson, M.J. Ashfold, L.J. Carpenter, S.J. Andrews, and N.R.P. Harris, Transport of short-lived halocarbons to the stratosphere over the Pacific Ocean, ***Atmos. Chem. Phys.***, ***20*** (2), 1163–1181, doi:10.5194/acp-20-1163-2020, 2020.

Forster, P., T. Storelvmo, K. Armour, W. Collins, J.-L. Dufresne, D. Frame, D.J. Lunt, T. Mauritsen, M.D. Palmer, M. Watanabe, M. Wild, and H. Zhang, The Earth's Energy Budget, Climate Feedbacks, and Climate Sensitivity, Chapter 7, In: ***Climate Change 2021: The Physical Science Basis***, Contribution of Working Group I to the Sixth Assessment Report of the Intergovernmental Panel on Climate Change, [Masson-Delmotte, V., P. Zhai, A. Pirani, S.L. Connors, C. Péan, S. Berger, N. Caud, Y. Chen, L. Goldfarb, M.I. Gomis, M. Huang, K. Leitzell, E. Lonnoy, J.B.R. Matthews, T.K. Maycock, T. Waterfield, O. Yelekçi, R. Yu, and B. Zhou (eds.)], Cambridge University Press, Cambridge, United Kingdom and New York, NY, USA, 923–1054 pp., doi:10.1017/9781009157896.009, 2021.

Fraser, P.J., B.L. Dunse, P.B. Krummel, L.P. Steele, N. Derek, B. Mitrevski, C.E. Allison, Z. Loh, A.J. Manning, A. Redington, and M. Rigby, Australian chlorofluorocarbon (CFC) emissions: 1960–2017, ***Enviro. Chem.***, 17 (8), 525–544, doi:10.1071/EN19322, 2020.

Friedrich, M., S. Smeekes, and J.-P. Urbain, Autoregressive wild bootstrap inference for nonparametric trends, ***J. Econom.***, ***214*** (1), 81–109, doi:10.1016/j.jeconom.2019.05.006, 2020a.

Friedrich, M., E. Beutner, H. Reuvers, S. Smeekes, J.-P. Urbain, W. Bader, B. Franco, B. Lejeune, and E. Mahieu, A statistical analysis of time trends in atmospheric ethane, ***Clim. Change***, ***162***, 105–125, doi:10.1007/s10584-020-02806-2, 2020b.

Froidevaux, L., J. Anderson, H.-J. Wang, R.A. Fuller, M.J. Schwartz, M.L. Santee, N.J. Livesey, H.C. Pumphrey, P.F. Bernath, J.M. Russell III, and M.P. McCormick, Global ozone chemistry and related trace gas data records for the Stratosphere (GOZCARDS): methodology and sample results with a focus on HCl, H_2O, and O_3, ***Atmos. Chem. Phys.***, ***15*** (18), 10,471–10,507, doi:10.5194/acp-15-10471-2015, 2015.

Froidevaux, L., D.E. Kinnison, R. Wang, J. Anderson, and R.A. Fuller, Evaluation of CESM1 (WACCM) free-running and specified dynamics atmospheric composition simulations using global multispecies satellite data records, ***Atmos. Chem. Phys.***, ***19*** (7), 4783–4821, doi:10.5194/acp-19-4783-2019, 2019.

Ganesan, A.L., M. Rigby, A. Zammit-Mangion, A.J. Manning, R.G. Prinn, P.J. Fraser, C.M. Harth, K.-R. Kim, P.B. Krummel, S. Li, J. Mühle, S.J. O'Doherty, S. Park, P.K. Salameh, L.P. Steele, and R.F. Weiss, Characterization of uncertainties in atmospheric trace gas inversions using hierarchical Bayesian methods, ***Atmos. Chem. Phys.***, ***14***, 3855–3864, doi:10.5194/acp-14-3855-2014, 2014.

Gardiner, T., A. Forbes, M. de Mazière, C. Vigouroux, E. Mahieu, P. Demoulin, V. Velazco, J. Notholt, T. Blumenstock, F. Hase, I. Kramer, R. Sussmann, W. Stremme, J. Mellqvist, A. Strandberg, K. Ellingsen, and M. Gauss, Trend analysis of greenhouse gases over Europe measured by a network of ground-based remote FTIR instruments, ***Atmos. Chem. Phys.***, ***8*** (22), 6719–6727, doi:10.5194/acp-8-6719-2008, 2008.

Gordon I.E., L.S. Rothman, R.J. Hargreaves, R. Hashemi, E.V. Karlovets, F.M. Skinner, E.K. Conway, C. Hill, R.V. Kochanov, Y. Tan, P. Wcisło, A.A. Finenko, K. Nelson, P.F. Bernath, M. Birk, V. Boudon, A. Campargue, K.V. Chance, A. Coustenis, B.J. Drouin. J.–M. Flaud, R.R. Gamache, J.T. Hodges, D. Jacquemart, E.J. Mlawer, A.V. Nikitin, V.I. Perevalov, M. Rotger, J. Tennyson, G.C. Toon, H. Tran, V.G. Tyuterev, E.M. Adkins, A. Baker, A. Barbe, E. Canè, A.G. Császár, A. Dudaryonok, O. Egorov, A.J. Fleisher, H. Fleurbaey, A. Foltynowicz, T. Furtenbacher, J.J. Harrison, J.–M. Hartmann, V.–M. Horneman, X. Huang, T. Karman, J. Karns, S. Kassi, I. Kleiner, V. Kofman, F. Kwabia–Tchana, N.N. Lavrentieva, T.J. Lee, D.A. Long, A.A. Lukashevskaya, O.M. Lyulin, V.Yu. Makhnev, W. Matt, S.T. Massie, M. Melosso, S.N. Mikhailenko, D. Mondelain, H.S.P. Müller, O.V. Naumenko, A. Perrin, O.L. Polyansky, E. Raddaoui, P.L. Raston, Z.D. Reed, M. Rey, C. Richard, R. Tóbiás, I. Sadiek, D.W. Schwenke, E. Starikova, K. Sung, F. Tamassia, S.A. Tashkun, J. Vander Auwera, I.A. Vasilenko, A.A. Vigasin, G.L. Villanueva, B. Vispoel, G. Wagner, A. Yachmenev, and S.N. Yurchenko, The HITRAN2020 molecular spectroscopic database, ***J. Quant. Spectrosc. Radiat. Transf.***, ***277***, 107949, doi:10.1016/j.jqsrt.2021.107949, 2022.

Graziosi, F., J. Arduini, F. Furlani, U. Giostra, L.J.M. Kuijpers, S.A. Montzka, B.R. Miller, S.J. O'Doherty, A. Stohl, P. Bonasoni, and M. Maione, European emissions of HCFC-22 based on eleven years of high frequency atmospheric measurements and a Bayesian inversion method, ***Atmos. Environ.***, ***112***, 196–207, doi:10.1016/j.atmosenv.2015.04.042, 2015.

Gressent, A., M. Rigby, A.L. Ganesan, R.G. Prinn, A.J. Manning, J. Mühle, P.K. Salameh, P.B. Krummel, P.J. Fraser, L.P. Steele, B. Mitrevski, R.F. Weiss, C.M. Harth, R.H. Wang, S. O'Doherty, D. Young, S. Park, S. Li, B. Yao, S. Reimann, M.K. Vollmer, M. Maione, J. Arduini, and C.R. Lunder, Growing atmospheric emissions of sulfuryl fluoride, ***J. Geophys. Res. Atmos.***, ***126*** (9), e2020JD034327, doi:10.1029/2020JD034327, 2021.

Hall, B.D., A. Engel, J. Muhle, J.W. Elkins, F. Artuso, E. Atlas, M. Aydin, D. Blake, E.G. Brunke, S. Chiavarini, P.J. Fraser, J. Happell, P.B. Krummel, I. Levin, M. Loewenstein, M. Maione, S.A. Montzka, S. O'Doherty, S. Reimann, G. Rhoderick, E.S. Saltzman, H.E. Scheel, L.P. Steele, M.K. Vollmer, R.F. Weiss, D. Worthy, and Y. Yokouchi, Results from the International Halocarbons in Air Comparison Experiment (IHALACE), ***Atmos. Meas. Tech.***, ***7*** (2), 469–490, doi:10.5194/amt-7-469-2014, 2014.

Han, J.R., L. Li, S.S. Su, J. Wu, X.K. Fang, S.L. Jia, J.B. Zhang, and J.X. Hu, Estimated HCFC-142b emissions in China: 2000-2050, ***Chinese Sci. Bull.***, ***59*** (24), 3046–3053, doi:10.1007/s11434-014- 0337-z, 2014.

Harris, N.R.P., and D. Wuebbles (Lead Authors), J.S. Daniel, J. Hu, L.J. M. Kuijpers, K.S. Law, M.J. Prather, and R. Schofield, Scenarios and information for policymakers, Chapter 5 in ***Scientific Assessment of Ozone Depletion: 2014***, Global Ozone Research and Monitoring Project–Report No. 55, World Meteorological Organization, Geneva, Switzerland, 2014.

Harrison, J.J., M.P. Chipperfield, R. Hossaini, C.D. Boone, S. Dhomse, W. Feng, and P.F. Bernath, Phosgene in the upper troposphere and lower stratosphere: a marker for product gas injection due to chlorine-containing very short lived substances, ***Geophys. Res. Lett.***, ***46*** (2), 1032–1039, doi:10.1029/2018GL079784, 2019.

Hattori, S., K. Kamezaki, and N. Yoshida, Constraining the atmospheric OCS budget from sulfur isotopes, ***Proc. Natl. Acad. Sci.***, ***117*** (34), 20,447–20,452; doi:10.1073/pnas.2007260117, 2020.

Hendrick, F., M. Van Roozendael, M.P. Chipperfield, M. Dorf, F. Goutail, X. Yang, C. Fayt, C. Hermans, K. Pfeilsticker, J.P. Pommereau, J.A. Pyle, N. Theys, and M. De Mazière, Retrieval of stratospheric and tropospheric BrO profiles and columns using ground-based zenith-sky DOAS observations at Harestua, 60° N, ***Atmos. Chem. Phys.***, ***7*** (18), 4869–4885, doi:10.5194/acp-7-4869-2007, 2007.

Hendrick, F., P.V. Johnston, M. De Mazière, C. Fayt, C. Hermans, K. Kreher, N. Theys, A. Thomas, and M. Van Roozendael, One-decade trend analysis of stratospheric BrO over Harestua (60°N) and Lauder (45°S) reveals a decline, ***Geophys. Res. Lett.***, ***35*** (14), doi:10.1029/2008GL034154, 2008.

Hodnebrog, Ø., B. Aamaas, J.S. Fuglestvedt, G. Marston, G. Myhre, C.J. Nielsen, M. Sandstad, K.P. Shine, and T.J. Wallington, Updated global warming potentials and radiative efficiencies of halocarbons and other weak atmospheric absorbers, ***Rev. Geophys.***, ***58*** (3), e2019RG000691, doi:10.1029/2019RG000691, 2020.

Höpfner, M., O. Kirner, G. Wetzel, B.-M. Sinnhuber, F. Haenel, S. Johansson, J. Orphal, R. Ruhnke, G. Stiller, and T. von Clarmann, The Michelson Interferometer for Passive Atmospheric Sounding global climatology of $BrONO_2$ 2002–2012: a test for stratospheric bromine chemistry, ***Atmos. Chem. Phys.***, ***21***, 18,433–18,464, doi:10.5194/acp-21-18433-2021, 2021.

Hossaini, R., M.P. Chipperfield, B.M. Monge-Sanz, N.A.D. Richards, E. Atlas, and D.R. Blake, Bromoform and dibromomethane in the tropics: A 3-D model study of chemistry and transport, ***Atmos. Chem. Phys.***, 10 (2), 719–735, doi:10.5194/acp-10-719-2010, 2010.

Hossaini, R., M.P. Chipperfield, A. Saiz-Lopez, J.J. Harrison, R. von Glasow, R. Sommariva, E. Atlas, M. Navarro, S.A. Montzka, W. Feng, S. Dhomse, C. Harth, J. Mühle, C. Lunder, S. O'Doherty, D. Young, S. Reimann, M.K. Vollmer, P.B. Krummel, and P.F. Bernath, Growth in stratospheric chlorine from short-lived chemicals not controlled by the Montreal Protocol, ***Geophys. Res. Lett.***, ***42*** (11), 4573–4580, doi:10.1002/2015gl063783, 2015.

Hossaini, R., M.P. Chipperfield, A. Saiz-Lopez, R. Fernandez, S. Monks, W. Feng, P. Brauer, and R. von Glasow, A global model of tropospheric chlorine chemistry: Organic versus inorganic sources and impact on methane oxidation, ***J. Geophys. Res. Atmos.***, ***121*** (23), 14,271–14,297, doi:10.1002/2016JD025756, 2016.

Hossaini, R., E. Atlas, S.S. Dhomse, M.P. Chippefield, P.F. Bernath, A.M. Fernando, J. Mühle, A.A. Leeson, S.A. Montzka, W. Feng, J.J. Harrison, P. Krummel, M.K. Vollmer, S. Reimann, S. O'Doherty, D. Young, M. Maione, J. Arduini, and C.R. Lunder, Recent trends in stratospheric chlorine from very short-lived substances,

J. Geophys. Res. Atmos., *124* (4), 2318–2335, doi:10.1029/2018JD029400, 2019.

HTOC (Halons Technical Options Committee), ***2018 Assessment Report***, United Nations Environment Programme, Ozone Secretariat, Nairobi, Kenya, [available at: https://ozone.unep.org/sites/default/files/Assessment_Panel/Assessment_Panels/TEAP/Reports/HTOC/HTOC_assessment_2018.pdf], 2018.

Hu, L., S.A. Montzka, J.B. Miller, A.E. Andrews, S.J. Lehman, B.R. Miller, K. Thoning, C. Sweeney, H. Chen, D.S. Godwin, K. Masarie, L. Bruhwiler, M.L. Fischer, S.C. Biraud, M.S. Torn, M. Mountain, T. Nehrkorn, J. Eluszkiewicz, S. Miller, R.R. Draxler, A.F. Stein, B.D. Hall, J.W. Elkins, and P.P. Tans, U.S. emissions of HFC-134a derived for 2008–2012 from an extensive flask-air sampling network, *J. Geophys. Res. Atmos.*, *120*, 801–825, doi:10.1002/2014JD022617, 2015.

Hu, L., S.A. Montzka, B.R. Miller, A.E. Andrews, J.B. Miller, S.J. Lehman, B.R. Miller, C. Sweeney, S.M. Miller, K. Thoning, C. Siso, E.L. Atlas, D.R. Blake, J. de Gouw, J.B. Gilman, G. Dutton, J.W. Elkins, B. Hall, H. Chen, M.L. Fischer, M.E. Mountain, T. Nehrkorn, S.C. Biraud, F.L. Moore, and P.P. Tans, Continued emissions of carbon tetrachloride from the United States nearly two decades after its phaseout for dispersive uses, *Proc. Natl. Acad. Sci.*, *113* (11), 2880–2885, doi:10.1073/pnas.1522284113, 2016.

Hu, L., S.A. Montzka, S.J. Lehman, D.S. Godwin, B.R. Miller, A.E. Andrews, K. Thoning, J.B. Miller, C. Sweeney, C. Siso, J.W. Elkins, B.D. Hall, D.J. Mondeel, D. Nance, T. Nehrkorn, M. Mountain, M.L. Fischer, S.C. Biraud, H. Chen, and P.P. Tans, Considerable contribution of the Montreal Protocol to declining greenhouse gas emissions from the United States, *Geophys. Res. Lett.*, *44*, 8075–8083, doi:10.1002/2017GL074388, 2017.

Hu, L., S.A. Montzka, F. Moore, E. Hinsta, G. Dutton, M.C. Siso, K. Thoning, R.W. Portmann, K. McKain, C. Sweeney, I. Vimount, D. Nance, B. Hall, and S. Wofsy, Continental-scale contributions to the global CFC-11 emission increase between 2012 and 2017, *Atmos. Chem. Phys.*, *22* (4), 2891–2907, doi:10.5194/acp-2021-793, 2022.

Huang, X., Y. Zhang, L. Xue, J. Tang, W. Song, D.R. Blake, and X. Wang, Constraining emission estimates of CFC-11 in Eastern China based on local observations at Surface Stations and Mount Tai, *Environ. Sci. Technol. Lett.*, *8*, 940−946, doi:10.1021/acs.estlett.1c00539, 2021.

Inamdar, S., Tinel, L., Chance, R., Carpenter, L. J., Sabu, P., Chacko, R., Tripathy, S. C., Kerkar, A. U., Sinha, A. K., Bhaskar, P. V., Sarkar, A., Roy, R., Sherwen, T., Cuevas, C., Saiz-Lopez, A., Ram, K., and Mahajan, A. S.: Estimation of reactive inorganic iodine fluxes in the Indian and Southern Ocean marine boundary layer, *Atmos. Chem. Phys.*, 20, 12093–12114, https://doi.org/10.5194/acp-20-12093-2020, 2020.

IPCC (Intergovenmental Panel on Climate Change), ***Climate Change 2021: The Physical Science Basis. Contribution of Working Group I to the Sixth Assessment Report of the Intergovernmental Panel on Climate Change,*** edited by V. Masson-Delmotte, P. Zhai, A. Pirani, S.L. Connors, C. Péan, S. Berger, N. Caud, Y. Chen, L. Goldfarb, M.I. Gomis, M. Huang, K. Leitzell, E. Lonnoy, J.B.R. Matthews, T.K. Maycock, T. Waterfield, O. Yelekçi, R. Yu, and B. Zhou, Cambridge University Press, Cambridge, United Kingdom and New York, NY, USA, In press, doi:10.1017/9781009157896.

Ivy, D.J., T. Arnold, C.M. Harth, L.P. Steele, J. Mühle, M. Rigby, P.K. Salameh, M. Leist, P.B. Krummel, P.J. Fraser, R.F. Weiss, and R.G. Prinn, Atmospheric histories and growth trends of C_4F_{10}, C_5F_{12}, C_6F_{14}, C_7F_{16} and C_8F_{18}, *Atmos. Chem. Phys.*, *12* (9), 4313–4325, doi:10.5194/acp-12-4313-2012, 2012.

Jiao, Y., A. Ruecker, M.J. Deventer, A.T. Chow, and R.C. Rhew, Halocarbon emissions from a degraded forested wetland in coastal South Carolina impacted by sea level rise, *ACS Earth Space Chem.*, *2* (10), 955–967, doi:10.1021/acsearthspacechem.8b00044, 2018.

Jiao Y., J. Acdan, R. Xu, M.J. Deventer, W. Zhang, and R.C. Rhew, Global methyl halide emissions from rapeseed (Brassica napus) using life cycle measurements, *Geophys. Res. Lett.*, *47* (19), e2020GL089373, doi:10.1029/2020GL089373, 2020.

Jiao, Y., W. Zhang, J.Y.R. Kim, M.J. Deventer, J. Vollering, and R.C. Rhew, Application of copper (II)-based chemicals induces CH3Br and CH3Cl emissions from soil and seawater, *Nat. Commun.*, *13* (1), 1–8, doi:10.1038/s41467-021-27779-3, 2022.

Jones, C.E., S.J. Andrews, L.J. Carpenter, C. Hogan, F.E. Hopkins, J.C. Laube, A.D. Robinson, T.G. Spain, S.D. Archer, N.R.P. Harris, P.D. Nightingale, S.J. O'Doherty, D.E. Oram, J.A. Pyle, J.H. Butler, and B.D. Hall, Results from the first national UK inter-laboratory calibration for very short-lived halocarbons, *Atmos. Meas. Tech.*, *4* (5), 865–874, doi:10.5194/amt-4-865-2011, 2011.

Keber, T., H. Bönisch, C. Hartick, M. Hauck, F. Lefrancois, F. Obersteiner, A. Ringsdorf, N. Schohl, T. Schuck, R. Hossaini, P. Graf, P. Jöckel, and A. Engel, Bromine from short-lived source gases in the extratropical northern hemispheric upper troposphere and lower stratosphere (UTLS), *Atmos. Chem. Phys.*, *20* (7), 4105–4132, doi:10.5194/acp-20-4105-2020, 2020.

Keng, F.S.-L., S.-M. Phang, N. Abd Rahman, H.-Y. Yeong, G. Malin, E. Leedham Elvidge, W. Sturges, Halocarbon emissions by selected tropical seaweeds exposed to different temperatures, *Phytochemistry*, *190*, 112869, doi:10.1016/j.phytochem.2021.112869, 2021.

Kim, J., R. Thompson, H. Park, S. Bogle, J. Mühle, M. Park, Y. Kim, C.M. Harth, P.K. Salameh, R. Schmidt, D. Ottinger, S. Park, and R.F. Weiss, Emissions of tetrafluoromethane (CF4) and hexafluoroethane (C2F6) from East Asia: 2008 to 2019, *J. Geophys. Res. Atmos.*, *126* (16), doi:10.1029/2021jd034888, 2021.

Klobas, J.E., D.K. Weisenstein, R.J. Salawitch, and D.M. Wilmouth, Reformulating the bromine alpha factor and equivalent effective stratospheric chlorine (EESC): evolution of ozone destruction rates of bromine and chlorine in future climate scenarios, *Atmos. Chem. Phys.*, *20* (15), 9459–9471, doi:10.5194/acp-20-9459-2020, 2020.

Klobas, J.E., J. Hansen, D.K. Weisenstein, R.P. Kennedy, and D.M. Wilmouth, Sensitivity of iodine-mediated stratospheric ozone loss chemistry to future chemistry-climate scenarios, *Front. Earth Sci.*, *9*, 617586, doi:10.3389/feart.2021.617586, 2021.

Kloss, C., M.J. Newland, D.E. Oram, P.J. Fraser, C.A.M. Brenninkmeijer, T. Rockmann, and J.C. Laube, Atmospheric abundances, trends and emissions of CFC-216ba, CFC-216ca and HCFC-225ca, *Atmosphere*, *5* (2), 420–434, doi:10.3390/atmos5020420, 2014.

Ko, M.K.W., and G. Poulet (Lead Authors), D.R. Blake, O. Boucher, J.H. Burkholder, M. Chin, R.A. Cox, C. George, H.-F. Graf, J.R. Holton, D.J. Jacob, K.S. Law, M.G. Lawrence, P.M. Midgley, P.W. Seakins, D.E. Shallcross, S.E. Strahan, D.J. Wuebbles, and Y. Yokouchi, Very short-lived halogen and sulfur substances, Chapter 2 in ***Scientific Assessment of Ozone Depletion: 2002***, Global Ozone Research and Monitoring Project–Report No. 47, World Meteorological Organization, Geneva, Switzerland, 2003.

Koenig T.K., S. Baidar, P. Campuzano-Jost, C.A. Cuevas, B. Dix, R.P. Fernandez, H. Guo, S.R. Hall, D. Kinnison, B. Nault, K. Ullmann, J.L. Jimenez, S.-L. Alfonso, and R. Volkamer, Quantitative detection of iodine in the stratosphere, *Proc. Natl. Acad. Sci.*, *117* (4) 1860–1866; doi:10.1073/pnas.1916828117, 2020.

Koluso, S.R., S.H. Schlünzen, D. Grawe, and R. Seifert, Determination of chloromethane and dichloromethane in a tropical terrestrial mangrove forest in Brazil by measurements and modelling, *Atmos. Environ.*, *173*, 185–197, doi:10.1016/j.atmosenv.2017.10.057, 2018.

Kuyper, B., D. Say, C. Labuschagne, T. Lesch, W.R. Joubert, D. Martin, D. Young, M.A.H. Khan, M. Rigby, A.L. Ganesan, and M.F. Lunt, Atmospheric HCFC-22, HFC-125, and HFC-152a at Cape Point, South Africa, *Environ. Sci. Technol.*, *53* (15), 8967–8975, doi:10.1021/acs.est.9b01612, 2019.

Laube, J.C., P. Martinerie, E. Witrant, T. Blunier, J. Schwander, C.A.M. Brenninkmeijer, T.J. Schuck, M. Bolder, T. Röckmann, C. van der Veen, H. Bönisch, A. Engel, G.P. Mills, M.J. Newland, D.E. Oram, C.E. Reeves, and W.T. Sturges, Accelerating growth of HFC-227ea (1,1,1,2,3,3,3-heptafluoropropane) in the atmosphere, *Atmos. Chem. Phys.*, *10* (13), 5903–5910, doi:10.5194/acp-10-5903-2010, 2010.

Laube, J.C., M.J. Newland, C. Hogan, C.A.M. Brenninkmeijer, P.J. Fraser, P. Martinerie, D.E. Oram, C.E. Reeves, T. Rockmann, J. Schwander, E. Witrant, and W.T. Sturges, Newly detected ozone-depleting substances in the atmosphere, *Nat. Geosci.*, *7* (4), 266–269, doi:10.1038/ngeo2109, 2014.

Laube, J.C., N.M. Hanif, P. Martinerie, E. Gallacher, P.J. Fraser, R. Langenfelds, C.A.M. Brenninkmeijer, J. Schwander, E. Witrant, J.L. Wang, C.F. Ou-Yang, L.J. Gooch, C.E. Reeves, W.T. Sturges, and D.E. Oram, Tropospheric observations of CFC-114 and CFC-114a with a focus on long-term trends and emissions, *Atmos. Chem. Phys.*, *6* (23), 15,347–15,358, doi:10.5194/acp-16-15347-2016, 2016.

Laube, J.C., E.C.L. Elvidge, K.E. Adcock, B. Baier, C.A.M. Brenninkmeijer, H. Chen, E.S. Droste, J.-U. Grooß, P. Heikkinen, A.J. Hind, R. Kivi, A. Lojko, S.A. Montzka, D.E. Oram, S. Randall, T. Röckmann, W.T. Sturges, C. Sweeney, M. Thomas, E. Tuffnell, and F. Ploeger, Investigating stratospheric changes between 2009 and 2018 with halogenated trace gas data from aircraft, AirCores, and a global model focusing on CFC-11, *Atmos. Chem. Phys.*, *20* (16), 9771–9782, doi:10.5194/acp-20-9771-2020, 2020.

Lauther, V., B. Vogel, J. Wintel, A. Rau, P. Hoor, V. Bense, R. Müller, and C.M. Volk, In situ observations of CH_2Cl_2 and $CHCl_3$ show efficient transport pathways for very short-lived species into the lower stratosphere via the Asian and the North American summer monsoon, *Atmos. Chem. Phys.*, *22* (3), 2049–2077, doi:10.5194/acp-22-2049-2022, 2022.

Lawler, M.J., A.S. Mahajan, A. Saiz-Lopez, and E.S. Saltzman, Observations of I_2 at a remote marine site, ***Atmos. Chem. Phys.***, ***14*** (5), 2669–2678, doi:10.5194/acp-14-2669-2014, 2014.

Leedham, E.C., C. Hughes, F.S. L. Keng, S.-M. Phang, G. Malin, and W.T. Sturges, Emission of atmospherically significant halocarbons by naturally occurring and farmed tropical macroalgae, ***Biogeosciences***, ***10***, 3615–3633, doi:10.5194/bg-10-3615-2013, 2013.

Leedham Elvidge, E., H. Bönisch, C.A.M. Brenninkmeijer, A. Engel, P.J. Fraser, E. Gallacher, R. Langenfelds, J. Mühle, D.E. Oram, E.A. Ray, A.R. Ridley, T. Röckmann, W.T. Sturges, R.F. Weiss, and J.C. Laube, Evaluation of stratospheric age of air from CF_4, C_2F_6, C_3F_8, CHF_3, HFC-125, HFC-227ea and SF_6: Implications for the calculations of halocarbon lifetimes, fractional release factors and ozone depletion potentials, ***Atmos. Chem. Phys.***, ***18*** (5), 3369–3385, doi:10.5194/acp-18-3369-2018, 2018.

Legrand, M., J.R. McConnell, S. Preunkert, M. Arienzo, N. Chellman, K. Gleason, T. Sherwen, M.J. Evans, and L.J. Carpenter, Alpine ice evidence of a three-fold increase in atmospheric iodine deposition since 1950 in Europe due to increasing oceanic emissions, ***Proc. Natl. Acad. Sci.***, ***115*** (48), 12,136–12,141, doi:10.1073/pnas.1809867115, 2018.

Lelieveld, J., E. Bourtsoukidis, C. Brühl, H. Fischer, H., Fuchs, H. Harder, A. Hofzumahaus, F. Holland, D. Marno, M. Neumaier, A. Pozzer, H. Schlager, J. Williams, A. Zahn, and H. Ziereis, The South Asian monsoon—pollution pump and purifier, ***Science***, ***361*** (6399), 270–273, doi:10.1126/science.aar2501, 2018.

Lennartz, S.T., C.A. Marandino, M. von Hobe, P. Cortes, B. Quack, R. Simo, D. Booge, A. Pozzer, T. Steinhoff, D.L. Arevalo-Martinez, C. Kloss, A. Bracher, R. Röttgers, E. Atlas, and K. Krüger, Direct oceanic emissions unlikely to account for the missing source of atmospheric carbonyl sulfide, ***Atmos. Chem. Phys.***, ***17***, 385–402, doi:10.5194/acp-17-385-2017, 2017.

Li, Z., P. Bie, Z. Wang, Z. Zhang, H. Jiang, W. Xu, J. Zhang, and J. Hu, Estimated HCFC-22 emissions for 1990–2050 in China and the increasing contribution to global emissions, ***Atmos. Environ., 132***, 77–84, doi:10.1016/j.atmosenv.2016.02.038, 2016.

Li, S., M.-K. Park, C.O. Jo, and S. Park, Emission estimates of methyl chloride from industrial sources in China based on high frequency atmospheric observations, ***J. Atmos. Chem.***, ***74***, 227–243, doi:10.1007/s10874-016-9354-4, 2017.

Liang, Q., R.S. Stolarski, S.R. Kawa, J.E. Nielsen, J.M. Rodriguez, A.R. Douglass, J.M. Rodriguez, D.R. Blake, E.L. Atlas, and L.E. Ott, Finding the missing stratospheric Bry: A global modeling study of $CHBr_3$ and CH_2Br_2, ***Atmos. Chem. Phys.***, ***10*** (5), 2269–2286, doi:10.5194/acp-10-2269-2010, 2010.

Liang, Q., P.A. Newman, and S. Reimann, SPARC Report on the Mystery of Carbon Tetrachloride, SPARC Report No. 7, WCRP-13/2016, [available at: https://www.wcrp-climate.org/WCRP-publications/2016/SPARC_Report7_2016.pdf], 2016.

Lickley, M., S. Solomon, S. Fletcher, G.J.M. Velders, J. Daniel, M. Rigby, S.A. Montzka, L.J.M. Kuijpers, and K. Stone, Quantifying contributions of chlorofluorocarbon banks to emissions and impacts on the ozone layer and climate, ***Nat. Commun.***, ***11*** (1380), doi:10.1038/s41467-020-15162-7, 2020.

Lickley, M., S. Solomon, D. Kinnison, P. Krummel, J. Mühle, S, O'Doherty, S., R. Prinn, M. Rigby, K.A. Stone, P. Wang, R. Weiss, and D. Young , Quantifying the imprints of stratospheric contributions to interhemispheric differences in tropospheric CFC-11, CFC-12, and N_2O abundances, ***Geophys. Res. Lett.***, ***48*** (15), e2021GL093700, doi:10.1029/2021GL093700, 2021.

Lin, Y., D. Gong, S. Lv, Y. Ding, G. Wu, H. Wang, Y. Li, Y. Wang, L. Zhou, and B. Wang, Observations of high levels of ozone-depleting CFC-11 at a remote mountain-top site in Southern China, ***Environ. Sci. Technol. Lett.***, ***6*** (3), 114–118, doi:10.1021/acs.estlett.9b00022, 2019.

Lunt, M.F., S. Park, S. Li, S. Henne, A.J. Manning, A.L. Ganesan, I.J. Simpson, D.R. Blake, Q. Liang, S. O'Doherty, C.M. Harth, J. Mühle, P.K. Salameh, R.F. Weiss, P.B. Krummel, P.J. Fraser, R.G. Prinn, S. Reimann, and M. Rigby, Continued emissions of the ozone-depleting substance carbon tetrachloride from eastern Asia, ***Geophys. Res. Lett.***, ***45*** (20), 11,423–11,430, doi:10.1029/2018GL079500, 2018

Ma, J., L.M.J. Kooijmans, A. Cho, S.A. Montzka, N. Glatthor, J.R. Worden, L. Kuai, E.L. Atlas, and M.C. Krol, Inverse modelling of carbonyl sulfide: implementation, evaluation and implications for the global budget, ***Atmos. Chem. Phys.***, ***21*** (5), 3507–3529, doi:10.5194/acp-21-3507-2021, 2021.

Maas, J., S. Tegtmeier, B. Quack, A. Biastoch, J.V. Durgadoo, S. Rühs, S. Gollasch, and M. David, Simulating the spread of disinfection by-products and anthropogenic bromoform emissions from ballast water discharge in Southeast Asia, ***Ocean Sci.***, ***15*** (4), 891–904, doi:10.5194/os-15-891-2019, 2019.

Maas, J., S. Tegtmeier, Y. Jia, B. Quack, J.V. Durgadoo, and A. Biastoch, Simulations of anthropogenic bromoform indicate high emissions at the coast of East Asia, ***Atmos. Chem. Phys.***, 21, 4103–4121, doi:10.5194/acp-21-4103-2021, 2021.

Mahieu, E., M.P. Chipperfield, J. Notholt, T. Reddmann, J. Anderson, P.F. Bernath, T. Blumenstock, M.T. Coffey, S.S. Dhomse, W. Feng, B. Franco, L. Froidevaux, D.W.T. Griffith, J.W. Hannigan, F. Hase, R. Hossaini, N.B. Jones, I. Morino, I. Murata, H. Nakajima, M. Palm, C. Paton-Walsh, J.M. Russell, M. Schneider, C. Servais, D. Smale, and K.A. Walker, Recent Northern Hemisphere stratospheric HCl increase due to atmospheric circulation changes, ***Nature***, ***515*** (7525), 104–107, doi:10.1038/nature13857, 2014a.

Mahieu, E., R. Zander, G.C. Toon, M.K. Vollmer, S. Reimann, J. Mühle, W. Bader, B. Bovy, B. Lejeune, C. Servais, P. Demoulin, G. Roland, P.F. Bernath, C.D. Boone, K.A. Walker, and P. Duchatelet, Spectrometric monitoring of atmospheric carbon tetrafluoride (CF_4) above the Jungfraujoch station since 1989: evidence of continued increase but at a slowing rate, ***Atmos. Meas. Tech.***, ***7*** (1), 333–344, doi:10.5194/amt-7-333-2014, 2014b.

Mahieu, E., B. Lejeune, B. Bovy, C. Servais, G.C. Toon, P.F. Bernath, C.D. Boone, K.A. Walker, S. Reimann, M.K. Vollmer, and S. O'Doherty, Retrieval of HCFC-142b (CH_3CClF_2) from ground-based high-resolution infrared solar spectra: Atmospheric increase since 1989 and comparison with surface and satellite measurements, ***J. Quant. Spectrosc. Radiat. Trans.***, ***186***, 96–105, doi:10.1016/j.jqsrt.2016.03.017, 2017.

Macdonald, M.L., J.L. Wadham, D. Young, C.R. Lunder, O. Hermansen, G. Lamarche-Gagnon, and S. O'Doherty, Consumption of CH_3Cl, CH_3Br, and CH_3I and emission of $CHCl_3$, $CHBr_3$, and CH_2Br_2 from the forefield of a retreating Arctic glacier, ***Atmos. Chem. Phys.***, ***20*** (12), 7243–7258, doi:10.5194/acp-20-7243-2020, 2020.

MacDonald, S.M., J.C. Gómez Martín, R. Chance, S. Warriner, A. Saiz-Lopez, L.J. Carpenter, and J.M.C. Plane, A laboratory characterisation of inorganic iodine emissions from the sea surface: dependence on oceanic variables and parameterisation for global modelling, ***Atmos. Chem. Phys.***, ***14*** (11), 5841–5852, doi:10.5194/acp-14-5841-2014, 2014.

Maione, M., F. Graziosi, J. Arduini, F. Furlani, U. Giostra, D.R. Blake, P. Bonasoni, X. Fang, X., S.A. Montzka, S.J. O'Doherty, S. Reimann, A. Stohl, and M.K. Vollmer, Estimates of European emissions of methyl chloroform using a Bayesian inversion method, ***Atmos. Chem. Phys.***, ***14***, 9755–9770, doi:10.5194/acp-14-9755-2014, 2014.

Manley, S.L., N.-Y. Wang, M.L. Walser, and R.J. Cicerone, Methyl halide emissions from greenhouse-grown mangroves, ***Geophys. Res. Lett.***, ***34*** (1), doi:10.1029/2006GL027777, 2007.

McCulloch, A., Chloroform in the environment: occurrence, sources, sinks and effects, ***Chemosphere***, ***50*** (10), 1291–1308, doi:10.016/S0045-6535(02)00697-5, 2003.

Mead, M.I., M.A.H. Khan, I.R. White, G. Nickless, D.E. Shallcross, Methyl halide emission estimates from domestic biomass burning in Africa, ***Atmos. Environ.***, ***42*** (21), 5241–5250, doi:10.1016/j.atmosenv.2008.02.066, 2008.

Miller, B.R., R.F. Weiss, P.K. Salameh, T. Tanhua, B.R. Greally, J. Muhle, and P.G. Simmonds, Medusa: A sample preconcentration and GC/MS detector system for ***in situ*** measurements of atmospheric trace halocarbons, hydrocarbons, and sulfur compounds, ***Anal. Chem.***, ***80*** (5), 1536–1545, doi:10.1021/ac702084k, 2008.

Montzka, S.A., J.H. Butler, B.D. Hall, D.J. Mondeel, and J.W. Elkins, A decline in tropospheric organic bromine, ***Geophys. Res. Lett.***, ***30*** (15), 1826–1826, doi:10.1029/2003GL017745, 2003.

Montzka, S.A., and P.J. Fraser (Lead Authors), J.H. Butler, P.S. Connell, D.M. Cunnold, J.S. Daniel, R.G. Derwent, S. Lal, A. McCulloch, D.E. Oram, C.E. Reeves, E. Sanhueza, L.P. Steele, G.J.M. Velders, R.F. Weiss, and R.J. Zander, Controlled substances and other source gases, Chapter 1 in Scientific Assessment of Ozone Depletion: 2002, Global Ozone Research and Monitoring Project–Report No. 47, Geneva, Switzerland, 2003.

Montzka, S.A., and S. Reimann, (Coordinating Lead Authors) A. Engel, K. Krüger, S. O`Doherty, and W.T. Sturges, Ozone-Depleting Substances (ODSs) and Related Chemicals, Chapter 1 in ***Scientific Assessment of Ozone Depletion: 2010***, Global Ozone Research and Monitoring Project–Report No. 52, World Meteorological Organization, Geneva, Switzerland, 2010.

Montzka, S.A., M. McFarland, S.O. Andersen, B.R. Miller, D.W. Fahey, B.D. Hall, L. Hu, C. Siso, and J.W. Elkins, Recent trends in global emissions of hydrochlorofluorocarbons and hydrofluorocarbons: Reflecting on the 2007 adjustments to the Montreal Protocol, ***J. Phys. Chem. A***, ***119*** (19), 4439–4449, doi:10.1021/jp5097376, 2015.

Montzka, S.A., G.S. Dutton, P. Yu, E. Ray, R.W. Portmann, J.S. Daniel, L. Kuijpers, B.D. Hall, D. Mondeel, C. Siso, J.D. Nance, M. Rigby, A.J. Manning, L. Hu, F. Moore, B.R. Miller, and J.W. Elkins, An unexpected and persistent increase in global emissions of ozone-depleting CFC-11, ***Nature, 557***, 413–417, doi:10.1038/s41586-018-0106-2, 2018.

Montzka, S.A., G.S. Dutton, R.W. Portmann, M.P. Chipperfield, S. Davis, W. Feng, A.J. Manning, E. Ray, M. Rigby, B.D. Hall, C. Siso, J.D. Nance, P.B. Krummel, J. Mühle, D. Young, S. O'Doherty, P.K. Salameh, C.M. Harth, R.G. Prinn, R.F. Weiss, J. W. Elkins, H. Walter-Terrinoni, and C. Theodoridi, A decline in global CFC-11 emissions during 2018–2019, ***Nature, 590***, 428–432, doi:10.1038/s41586-021-03260-5, 2021.

Mühle, J., J. Huang, R.F. Weiss, R.G. Prinn, B.R. Miller, P.K. Salameh, C.M. Harth, P.J. Fraser, L.W. Porter, B.R. Greally, S. O'Doherty, and P.G. Simmonds, Sulfuryl fluoride in the global atmosphere, ***J. Geophys. Res. Atmos.***, ***114*** (D5), doi:10.1029/2008JD011162, 2009.

Mühle, J., C.M. Trudinger, L.M. Western, M. Rigby, M.K. Vollmer, S. Park, A.J. Manning, D. Say, A. Ganesan, L.P. Steele, D.J. Ivy, T. Arnold, S. Li, A. Stohl, C.M. Harth, P.K. Salameh, A. McCulloch, S. O'Doherty, M.-K. Park, C.O. Jo, D. Young, K.M. Stanley, P.B. Krummel, B. Mitrevski, O. Hermansen, C. Lunder, N. Evangeliou, B. Yao, J. Kim, B. Hmiel, C. Buizert, V.V. Petrenko, J. Arduini, M. Maione, D.M. Etheridge, E. Michalopoulou, M. Czerniak, J.P. Severinghaus, S. Reimann, P.G. Simmonds, P.J. Fraser, R.G. Prinn, and R.F. Weiss, Perfluorocyclobutane (PFC-318, c-C_4F_8) in the global atmosphere, ***Atmos. Chem. Phys.***, ***19*** (15), 10,335–10,359, doi:10.5194/acp-19-10335-2019, 2019.

Mühle, J., L.J.M. Kuijpers, K.M. Stanley, M. Rigby, L.M. Western, J. Kim, S. Park, C.M. Harth, P.B. Krummel, P.J. Fraser, S. O'Doherty, P.K. Salameh, R. Schmidt, D. Young, R.G. Prinn, R.H.J. Wang, and R.F. Weiss, Global emissions of perfluorocyclobutane (PFC-318, c-C4F8) resulting from the use of hydrochlorofluorocarbon-22 (HCFC-22) feedstock to produce polytetrafluoroethylene (PTFE) and related fluorochemicals, ***Atmos. Chem. Phys.***, ***22***, 3371–3378, doi:10.5194/acp-22-3371-2022, 2022.

Müller, R., The impact of the rise in atmospheric nitrous oxide on stratospheric ozone, ***Ambio***, ***50***, 35–39, doi:10.1007/s13280-020-01428-3, 2021

Navarro, M.A., E.L. Atlas, A. Saiz-Lopez, X. Rodriguez-Lloveras, D.E. Kinnison, J.F. Lamarque, S. Tilmes, M. Filus, N.R.P. Harris, E. Meneguz, M.J. Ashfold, A.J. Manning, C.A. Cuevas, S.M. Schauffler, and V. Donets, Airborne measurements of organic bromine compounds in the Pacific tropical tropopause layer, ***Proc. Natl. Acad. Sci.***, ***112*** (45), 13,789–13,793, doi:10.1073/pnas.1511463112, 2015.

Newland, M.J., C.E. Reeves, D.E. Oram, J.C. Laube, W.T. Sturges, C. Hogan, P. Begley, and P.J. Fraser, Southern hemispheric halon trends and global halon emissions, 1978–2011, ***Atmos. Chem. Phys.***, ***13*** (11), 5551–5565, doi:10.5194/acp-13-5551-2013, 2013.

Newman, P.A., J.S. Daniel, D.W. Waugh, and E.R. Nash, A new formulation of equivalent effective stratospheric chlorine (EESC), ***Atmos. Chem. Phys.***, ***7*** (17), 4537–4552, doi:10.5194/acp-7-4537-2007, 2007.

Nicewonger, M. R., E.S. Saltzman, and S. A. Montzka, ENSO-driven fires cause large interannual variability in the naturally emitted, ozone-depleting trace gas CH_3Br, ***Geophys. Res. Lett.***, 49, e2021GL094756, doi:10.1029/2021GL094756, 2022.

O'Doherty, S., D.M. Cunnold, A. Manning, B.R. Miller, R.H.J. Wang, P.B. Krummel, P.J. Fraser, P.G. Simmonds, A. McCulloch, R.F. Weiss, P. Salameh, L.W. Porter, R.G. Prinn, J. Huang, G. Sturrock, D. Ryall, R.G. Derwent, and S.A. Montzka, Rapid growth of hydrofluorocarbon 134a and hydrochlorofluorocarbons 141b, 142b, and 22 from advanced global atmospheric gases experiment (AGAGE) observations at Cape Grim, Tasmania, and Mace Head, Ireland, ***J. Geophys. Res.***, ***109*** (D6), D06310, doi:10.1029/2003JD004277, 2004.

Oram, D.E., F.S. Mani, J.C. Laube, M.J. Newland, C.E. Reeves, W.T. Sturges, S.A. Penkett, C.A.M. Brenninkmeijer, T. Rockmann, and P.J. Fraser, Long-term tropospheric trend of octafluorocyclobutane (c-C_4F_8 or PFC-318), ***Atmos. Chem. Phys.***, ***12*** (1), 261–269, doi:10.5194/acp-12-261-2012, 2012.

Ordóñez, C., J.-F. Lamarque, S. Tilmes, D.E. Kinnison, E.L. Atlas, D.R. Blake, G. Sousa Santos, G. Brasseur, and A. Saiz-Lopez, Bromine and iodine chemistry in a global chemistry-climate model: Description and evaluation of very short-lived oceanic sources, ***Atmos. Chem. Phys.***, ***12*** (3), 1423-1447, doi:10.5194/acp-12-1423-2012, 2012.

Orkin, V.L., M.J. Kurylo, and E.L. Fleming, Atmospheric lifetimes of halogenated hydrocarbons: Improved estimations from an analysis of modeling results, ***J. Geophys. Res.***, ***125*** (16), e2019JD032243, doi:10.1029/2019JD032243, 2020.

Ostermöller, J., H. Bönisch, P. Jöckel, and A. Engel, A new time-independent formulation of fractional release, ***Atmos. Chem. Phys.***, ***17 (***6), 3785–3797, doi:10.5194/acp-17-3785-2017, 2017.

Pan, L.L., E.L. Atlas, R.J. Salawitch, S.B. Honomichl, J.F. Bresch, W.J. Randel, E.C. Apel, R.S. Hornbrook, A J. Weinheimer, D.C. Anderson, S.J. Andrews, S. Baidar, S.P. Beaton, T.L. Campos, L.J. Carpenter, D. Chen, B. Dix, V. Donets, S.R. Hall, T.F. Hanisco, C.R. Homeyer, L.G. Huey, J.B. Jensen, L. Kaser, D.E. Kinnison, T.K. Koenig, J.F. Lamarque, C. Liu, J. Luo, Z.J. Luo, D.D. Montzka, J.M. Nicely, R.B. Pierce, D.D. Riemer, T. Robinson, P. Romashkin, A. Saiz-Lopez, S. Schauffler, O. Shieh, M.H. Stell, K. Ullmann, G. Vaughan, R. Volkamer, and G. Wolfe, The convective transport of active species in the tropics (CONTRAST) experiment, ***Bull. Am. Meteorol. Soc.***, ***98*** (1), 106–128, doi:10.1175/bams-d-14-00272.1, 2017.

Park, S., L.M. Western, T. Saito, A.L. Redington, S. Henne, X. Fang, R.G. Prinn, A.J. Manning, S.A. Montzka, P.J. Fraser, A.L. Ganesan, C.M. Harth, J. Kim, P.B. Krummel, Q. Liang, J. Mühle, S. O'Doherty, H. Park, M.-K. Park, S. Reimann, P.K. Salameh, R.F. Weiss, and M. Rigby, A decline in emissions of CFC-11 and related chemicals from eastern China, ***Nature, 590***, 433–437, doi:10.1038/s41586-021-03277, 2021.

Parrella, J.P., K. Chance, R.J. Salawitch, T. Canty, M. Dorf, and K. Pfeilsticker, New retrieval of BrO from SCIAMACHY limb: an estimate of the stratospheric bromine loading during April 2008, ***Atmos. Meas. Tech.***, ***6*** (10), 2549–2561, doi:10.5194/amt-6-2549-2013, 2013.

Patterson, J.D., M. Aydin, A.M. Crotwell, G. Pétron, J.P. Severinghaus, and E.S. Saltzman, Atmospheric history of H_2 over the past century reconstructed from South Pole firn air, ***Geophy. Res. Lett.***, ***47*** (14), e2020GL087787, doi:10.1029/2020GL087787, 2020.

Patterson, J.D., M. Aydin, A.M. Crotwell, G. Pétron, J.P. Severinghaus, P.B. Krummel, R.L. Langenfelds, and E.S. Saltzman, H_2 in Antarctic firn air: atmospheric reconstructions and implications for anthropogenic emissions, ***Proc. Natl. Acad. Sci.***, ***118*** (36), e2103335118, doi:10.1073/pnas.2103335118, 2021.

Pisso, I., P.H. Haynes, and K.S. Law, Emission location dependent ozone depletion potentials for very short-lived halogenated species, ***Atmos. Chem. Phys.***, ***10***, 12,025–12,036, doi:10.5194/acp-10-12025-2010, 2010.

Ploeger, F., P. Konopka, K. Walker, and M. Riese: Quantifying pollution transport from the Asian monsoon anticyclone into the lower stratosphere, ***Atmos. Chem. Phys.***, 17, 7055–7066, doi:10.5194/acp-17-7055-2017, 2017.

Prados-Roman, C., C.A. Cuevas, R.P. Fernandez, D.E. Kinnison, J.-F. Lamarque, and A. Saiz-Lopez, A negative feedback between anthropogenic ozone pollution and enhanced ocean emissions of iodine, ***Atmos. Chem. Phys.***, ***15*** (4), 2215–2224, doi:10.5194/acp-15-2215-2015, 2015.

Prignon, M., S. Chabrillat, D. Minganti, S. O'Doherty, C. Servais, G. Stiller, G.C. Toon, M.K. Vollmer, and E. Mahieu, Improved FTIR retrieval strategy for HCFC-22 (CHClF 2), comparisons with in situ and satellite datasets with the support of models, and determination of its long-term trend above Jungfraujoch, ***Atmos. Chem. Phys.***, ***19*** (19), 12,309–12,324, doi:10.5194/acp-19-12309-2019, 2019.

Prignon, M., S. Chabrillat, M. Friedrich, D. Smale, S.E. Strahan, P.F. Bernath, M.P. Chipperfield, S.S. Dhomse, W. Feng, D. Minganti, C. Servais, and E. Mahieu, Stratospheric fluorine as a tracer of circulation changes: Comparison between infrared remote-sensing observations and simulations with five modern reanalyses, ***J. Geophys. Res.***, ***126*** (19), e2021JD034995. doi:10.1029/2021JD034995, 2021.

Prinn, R.G., R.F. Weiss, P.J. Fraser, P.G. Simmonds, D.M. Cunnold, F.N. Alyea, S. O'Doherty, P. Salameh, B.R. Miller, J. Huang, R.H.J. Wang, D.E. Hartley, C. Harth, L.P. Steele, G. Sturrock, P.M. Midgley, and A. McCulloch, A history of chemically and radiatively important gases in air deduced from ALE/GAGE/AGAGE, ***J. Geophys. Res.***, ***105*** (D14), 17,751–17,792, doi:10.1029/2000JD900141, 2000.

Prinn, R.G., R.F. Weiss, J. Arduini, T. Arnold, H.I. DeWitt, P.J. Fraser, A.L. Ganesan, J. Gasore, C.M. Harth, O. Hermansen, J. Kim, P.B. Krummel, S. Li, Z. M. Loh, C.R. Lunder, M. Maione, A.J. Manning, B.R. Miller, B. Mitrevski, J. Mühle, S. O'Doherty, S. Park, S. Reimann, M. Rigby, T. Saito, P.K. Salameh, R. Schmidt, P.G. Simmonds, L.P. Steele, M.K. Vollmer, R.H. Wang, B. Yao, Y. Yokouchi, D. Young, and L. Zhou, History of chemically and radiatively important atmospheric gases from the Advanced Global Atmospheric Gases Experiment (AGAGE), ***Earth Syst. Sci. Data***, ***10*** (2), 985–1018, doi:10.5194/essd-10-985-2018, 2018.

Quivet, E., P. Höhener, B. Temime-Roussel, J. Dron, G. Revenko, M. Verlande, K. Lebaron, C. Demelas, L. Vassalo, and J.-L. Boudenne, Underestimation of anthropogenic bromoform released into the environment?, ***Environ. Sci. Technol.***, ***56*** (3), 1522–1533, doi:10.1021/acs.est.1c05073, 2022.

Ramaswamy, V., O. Boucher, J.D. Haigh, D.A. Hauglustaine, J.M. Haywood, G. Myrhe, T. Nakajima, G.Y. Shi, and S. Solomon, Radiative Forcing of Climate Change, Chapter 6, in ***Climate Change 2001: The Scientific Basis, Contribution of Working Group I to the Third Assessment Report of the Intergovernmental Panel on Climate Change***, edited by F. Joos, and J. Srinivasan, Cambridge University Press,

Cambridge, United Kingdom and New York, NY, 68 pp., [available at: https://www.ipcc.ch/site/assets/uploads/2018/03/TAR-06.pdf], 2001.

Ravishankara, A.R., J.S. Daniel, and R.W. Portmann, Nitrous oxide (N2O): The dominant ozone-depleting substance emitted in the 21st century, ***Science***, ***326***, 123–125, doi:10.1126/science.1176985, 2009.

Ray, E.A., R.W. Portmann, P. Yu, J. Daniel, S.A. Montzka, G.S. Dutton, B.D. Hall, F.L. Moore, and K.H. Rosenlof, The influence of the stratospheric Quasi-Biennial Oscillation on trace gas levels at the Earth's surface, ***Nat. Geosci.***, ***13***, 22–27, doi:10.1038/s41561-019-0507-3, 2020.

Read, K.A., A.S. Mahajan, L.J. Carpenter, M.J. Evans, B.V.E. Faria, D.E. Heard, J.R. Hopkins, J.D. Lee, S.J. Moller, A.C. Lewis, L.M. Mendes, J.B. McQuaid, H. Oetjen, A. Saiz-Lopez, M.J. Pilling, and J.M.C. Plane, Extensive halogen-mediated ozone destruction over the tropical Atlantic Ocean, ***Nature***, ***453***, 1232–1235, doi:10.1038/nature07035, 2008.

Revell, L.E., Tummon, F., Salawitch, R.J., Stenke, A., and T. Peter, The changing ozone depletion potential of N_2O in a future climate, ***Geophys. Res. Lett.***, ***42***, 10,047–10,055, doi:10.1002/2015GL06570, 2015.

Rex, M., I. Wohltmann, T. Ridder, R. Lehmann, K. Rosenlof, P. Wennberg, D. Weisenstein, J. Notholt, K. Kruger, V. Mohr, and S. Tegtmeier, A tropical West Pacific OH minimum and implications for stratospheric composition, ***Atmos. Chem. Phys.***, ***14*** (9), 4827–4841, doi:10.5194/acp-14-4827-2014, 2014.

Rigby, M., A.L. Ganesan, and R.G. Prinn, Deriving emissions time series from sparse atmospheric mole fractions, ***J. Geophys. Res.***, ***116*** (D8), D08306, doi:10.1029/2010jd015401, 2011.

Rigby, M., R.G. Prinn, S. O'Doherty, S.A. Montzka, A. McCulloch, C.M. Harth, J. Mühle, P.K. Salameh, R.F. Weiss, D. Young, P.G. Simmonds, B.D. Hall, G.S. Dutton, D. Nance, D.J. Mondeel, J.W. Elkins, P.B. Krummel, L.P. Steele, and P.J. Fraser, Re-evaluation of the lifetimes of the major CFCs and CH_3CCl_3 using atmospheric trends, ***Atmos. Chem. Phys.***, ***13*** (5), 2691–2702, doi:10.5194/acp-13-2691-2013, 2013.

Rigby, M., R.G. Prinn, S. O'Doherty, B.R. Miller, D. Ivy, J. Mühle, C.M. Harth, P.K. Salameh, T. Arnold, R.F. Weiss, P.B. Krummel, L.P. Steele, P.J. Fraser, D. Young, and P.G. Simmonds, Recent and future trends in synthetic greenhouse gas radiative forcing, ***Geophys. Res. Lett.***, ***41*** (7), 2623–2630, doi:10.1002/2013GL059099, 2014.

Rigby, M., S. Park, T. Saito, L.M. Western, A.L. Redington, X. Fang, S. Henne, A.J. Manning, R.G. Prinn, G.S. Dutton, P.J. Fraser, A.L. Ganesan, B.D. Hall, C.M. Harth, J. Kim, K.-R. Kim, P.B. Krummel, T. Lee, S. Li, Q. Liang, M.F. Lunt, S.A. Montzka, J. Mühle, S. O'Doherty, M.-K. Park, S. Reimann, P.K. Salameh, P. Simmonds, R.L. Tunnicliffe, R.F. Weisse, Y. Yokouchi, and D. Young, Increase in CFC-11 emissions from eastern China based on atmospheric observations, ***Nature***, ***569***, 546–550, doi:10.1038/s41586-019-1193-4, 2019.

Rinsland, C.P., E. Mahieu, P. Demoulin, R. Zander, C. Servais, and J.-M. Hartmann, Decrease of the carbon tetrachloride (CCl_4) loading above Jungfraujoch, based on high resolution infrared solar spectra recorded between 1999 and 2011, ***J. Quant. Spectrosc. Radiat. Trans.***, ***113*** (11), 1322–1329, doi:10.1016/j.jqsrt.2012.02.016, 2012.

Rollins, A.W., T.D. Thornberry, L.A. Watts, P. Yu, K.H. Rosenlof, M.J. Mills, E. Baumann, F.R. Giorgetta, T.V. Bui, M. Höpfner, K.A. Walker, C. Boone, P.F. Bernath, P.R. Colarco, P.A. Newman, D.W. Fahey, and R.S. Gao, The role of sulfur dioxide in stratospheric aerosol formation evaluated by using ***in situ*** measurements in the tropical lower stratosphere, ***Geophy. Res. Lett.***, ***44*** (9), 4280–4286, doi:10.1002/2017GL072754, 2017.

Rollins, A.W., T.D. Thornberry, E. Atlas, M. Navarro, S. Schauffler, F. Moore, J.W. Elkins, E. Ray, K. Rosenlof, V. Aquila, and R.-S. Gao, SO_2 observations and sources in the western Pacific tropical tropopause region, ***J. Geophys. Res. Atmos.***, ***123*** (23), 13,549–13,559, doi:10.1029/2018JD029635, 2018.

Rotermund, M.K., V. Bense, M.P. Chipperfield, A. Engel, J.-U. Grooß, P. Hoor, T. Hüneke, T., Keber, F. Kluge, B. Schreiner, T. Schuck, B. Vogel, A. Zahn, and K. Pfeilsticker, Organic and inorganic bromine measurements around the extratropical tropopause and lowermost stratosphere: Insights into the transport pathways and total bromine, ***Atmos. Chem. Phys.***, ***21***, 15,375–15,407, doi:10.5194/acp-21-15375-2021, 2021.

Ruiz, D.J., M.J. Prather, S.E. Strahan, R.L. Thompson, L. Froidevaux, and S.D. Steenrod, How atmospheric chemistry and transport drive surface variability of N_2O and CFC-11, ***J. Geophys. Res. Atmos.***, ***126*** (8), e2020JD033979, doi:10.1029/2020JD033979, 2021.

Rust, D., I. Katharopoulos, M.K. Vollmer, S. Henne, S. O'Doherty, D. Say, L. Emmenegger, R. Zenobi, and S. Reimann, Swiss halocarbon emissions for 2019 to 2020 assessed from regional atmospheric observations, ***Atmos. Chem. Phys.***, ***22*** (4), 2447–2466, doi:10.5194/acp-2021-633, 2022.

Saito, T., Y. Yokouchi, A. Stohl, S. Taguchi, and H. Mukai, Large emissions of perfluorocarbons in East Asia deduced from continuous atmospheric measurements, ***Environ. Sci. Technol.***, ***44*** (11), 4089–4095, doi:10.1021/es1001488, 2010.

Saiz-Lopez, A., S. Baidar, C.A. Cuevas, T.K. Koenig, R.P. Fernandez, B. Dix, D.E. Kinnison, J.F. Lamarque, X. Rodriguez-Lloveras, T.L. Campos, and R. Volkamer, Injection of iodine to the stratosphere, ***Geophys. Res. Lett.***, ***42*** (16), 6852–6859, doi:10.1002/2015GL064796, 2015.

Sala, S., H. Bonisch, T. Keber, D.E. Oram, G. Mills, and A. Engel, Deriving an atmospheric budget of total organic bromine using airborne ***in situ*** measurements from the western Pacific area during SHIVA, ***Atmos. Chem. Phys.***, ***14*** (13), 6903–6923, doi:10.5194/acp-14-6903-2014, 2014.

Saltzman, E.S., M. Aydin, W.J. De Bruyn, D.B. King, and S.A. Yvon-Lewis, Methyl bromide in preindustrial air: Measurements from an Antarctic ice core, ***J. Geophys. Res.***, ***109***, D05301, doi:10.1029/2003JD004157. 2004.

Saltzman, E.S., M. Aydin, C. Tatum, and M.B. Williams, 2,000-year record of atmospheric methyl bromide from a South Pole ice core, ***J. Geophys. Res.***, ***113***, D05304, doi:10.1029/2007JD008919. 2008.

Saltzman, E.S., M.R. Nicewonger, S.A. Montzka, and S.A. Yvon-Lewis, A post-phase-out retrospective reassessment of the global methyl bromide budget, ***J. Geophys. Res.***, ***127*** (3), e2021JD035567 doi:10.1029/2021JD035567, 2022.

Say, D., A.L. Ganesan, M.F. Lunt, M. Rigby, S. O'Doherty, C. Harth, A.J. Manning, P.B. Krummel, and S. Bauguitte, Emissions of halocarbons from India inferred through atmospheric measurements, ***Atmos. Chem. Phys.***, ***19*** (15), 9865–9885, doi:10.5194/acp-19-9865-2019, 2019.

Say D., B. Kuyper, L. Western, M.A.H. Khan, T. Lesch, C. Labuschagne, D. Martin, D. Young, A.J. Manning, S. O'Doherty, M. Rigby, P.B. Krummel, M.T. Davies-Coleman, A.L. Ganesan, and D.E. Shallcross, Emissions and marine boundary layer concentrations of unregulated chlorocarbons measured at Cape Point, South Africa, ***Environ. Sci. Technol.***, ***54*** (17), 10,514–10,523, doi:10.1021/acs.est.0c02057, 2020.

Say, D., A.J. Manning, L.M. Western, D. Young, A. Wisher, M. Rigby, S. Reimann, M.K. Vollmer, M. Maione, J. Arduini, P.B. Krummel, J. Mühle, C.M. Harth, B. Evans, R.F. Weiss, R.G. Prinn, and S. O'Doherty, Global trends and European emissions of tetrafluoromethane (CF_4), hexafluoroethane (C_2F_6) and octafluoropropane (C_3F_8), ***Atmos. Chem. Phys.***, ***21***, 2149–2164, 2021 doi:10.5194/acp-21-2149-2021, 2021.

Schultz, M.G., T. Diehl, G.P. Brasseur, and W. Zittel, Air pollution and climate-forcing impacts of a global hydrogen economy, ***Science***, ***302*** (5645), 624–627, doi:10.1126/science.1089527, 2003.

Shechner, M., A. Guenther, R. Rhew, A. Wishkerman, Q. Li, D. Blake, G. Lerner, and E. Tas, Emission of volatile halogenated organic compounds over various Dead Sea landscapes, ***Atmos. Chem. Phys.***, ***19***, 7667–7690, doi:10.5194/acp-19-7667-2019, 2019.

Sherwen, T., J.A. Schmidt, M.J. Evans, L.J. Carpenter K. Großmann, S.D. Eastham, D.J. Jacob, B. Dix, T.K. Koenig, R. Sinreich, I. Ortega, R. Volkamer, A. Saiz-Lopez, C. Prados-Roman, A.S. Mahajan, and C. Ordóñez, Global impacts of tropospheric halogens (Cl, Br, I) on oxidants and composition in GEOS-Chem, ***Atmos. Chem. Phys.***, ***16*** (18), 12,239–12,271, doi:10.5194/acp-16-12239-2016, 2016.

Sherwen T., R.J. Chance, L. Tinel, D. Ellis, M.J. Evans, and L.J. Carpenter, A machine learning-based global sea-surface iodide distribution, ***Earth Syst. Sci. Data, 11*** (3), 1239–1262, doi:10.5194/essd-11-1239-2019, 2019.

Shine, K.P., and G. Myhre, The spectral nature of stratospheric temperature adjustment and its application to halocarbon radiative forcing, ***J. Adv. Model. Earth Syst.***, ***12*** (3), e2019MS001951, doi:10.1029/2019MS001951, 2020.

Simmonds, P.G., M. Rigby, A. McCulloch, S. O'Doherty, D. Young, J. Mühle, P.B. Krummel, P. Steele, P.J. Fraser, A.J. Manning, R.F. Weiss, P.K. Salameh, C.M. Harth, R.H.J. Wang, and R.G. Prinn, Changing trends and emissions of hydrochlorofluorocarbons (HCFCs) and their hydrofluorocarbon (HFCs) replacements, ***Atmos. Chem. Phys.***, ***17*** (7), 4641–4655, doi:10.5194/acp-17-4641-2017, 2017.

Simmonds, P.G., M. Rigby, A.J. Manning, S. Park, K.M. Stanley, A. McCulloch, S. Henne, F. Graziosi, M. Maione, J. Arduini, S. Reimann, M.K. Vollmer, J. Mühle, S. O'Doherty, D. Young, P.B. Krummel, P.J. Fraser, R.F. Weiss, P.K. Salameh, C.M. Harth, M.-K. Park, H. Park, T. Arnold, C. Rennick, L.P. Steele, B. Mitrevski, R.H.J. Wang, and R.G. Prinn, The increasing atmospheric burden of the greenhouse gas sulfur hexafluoride (SF_6), ***Atmos. Chem. Phys.***, ***20*** (12), 7271–7290, doi:10.5194/acp-20-7271-2020, 2020.

Simpson, I.J., N.J. Blake, D.R. Blake, S. Meinardi, M.P.S. Andersen, and F.S. Rowland, Strong evidence for negligible methyl chloroform (CH_3CCl_3) emissions from biomass burning, ***Geophys. Res. Lett.***, ***34*** (10), doi:10.1029/2007GL029383, 2007.

Sinnhuber, B.-M., and I. Folkins, Estimating the contribution of bromoform to stratospheric bromine and its relation to dehydration in the tropical tropopause layer, ***Atmos. Chem. Phys.***, ***6*** (12), 4755–4761, doi:10.5194/acp-6-4755-2006, 2006.

Sinnhuber, B.-M., N. Sheode, M. Sinnhuber, M.P. Chipperfield, and W. Feng, The contribution of anthropogenic bromine emissions to past stratospheric ozone trends: A modelling study, ***Atmos. Chem. Phys.***, 9, 2863–2871, doi:10.5194/acp-9-2863-2009, 2009.

Smith, C., Z.R.J. Nicholls, K. Armour, W. Collins, P. Forster, M. Meinshausen, M.D. Palmer, and M. Watanabe, The Earth's Energy Budget, Climate Feedbacks, and Climate Sensitivity Supplementary Material, Chapter 7, in ***Climate Change 2021: The Physical Science Basis, Contribution of Working Group I to the Sixth Assessment Report of the Intergovernmental Panel on Climate Change*** edited by V. Masson-Delmotte, P. Zhai, A. Pirani, S.L. Connors, C. Péan, S. Berger, N. Caud, Y. Chen, L. Goldfarb, M.I. Gomis, M. Huang, K. Leitzell, E. Lonnoy, J.B.R. Matthews, T.K. Maycock, T. Waterfield, O. Yelekçi, R. Yu, and B. Zhou, Cambridge University Press, Cambridge, United Kingdom and New York, NY, USA, [available at: https://www.ipcc.ch/], 2021.

SPARC (Stratosphere-troposphere Processes And their Role in Climate), ***SPARC Report on the Lifetimes of Stratospheric Ozone-Depleting Substances, Their Replacements, and Related Species***, edited by M.K.W. Ko, P.A. Newman, S. Reimann, and S.E. Strahan, SPARC Report No. 6, WCRP-15/2013, 255 pp., [available at: https://www.sparc-climate.org/fileadmin/customer/6_Publications/SPARC_reports_PDF/6_SPARC_LifetimeReport_Web.pdf], 2013.

SPARC (Stratosphere-troposphere Processes And their Role in Climate), ***SPARC Report on the Mystery of Carbon Tetrachloride***, edited by Q. Liang, P.A. Newman, and S. Reimann, SPARC Report No. 7, WCRP-13/2016, 67 pp., [available at: https://www.wcrp-climate.org/WCRP-publications/2016/SPARC_Report7_2016.pdf], 2016.

Stanley, K.M., D. Say, J. Mühle, C.M. Harth, P.B. Krummel, D. Young, S.J. O'Doherty, P.K. Salameh, P.G. Simmonds, R.F. Weiss, R.G. Prinn, P.J. Fraser, and M. Rigby, Increase in global emissions of HFC-23 despite near-total expected reductions, ***Nat. Commun.***, ***11*** (397), doi:10.1038/s41467-019-13899-4, 2020.

Steffen, J., P.F. Bernath, and C.D. Boone, Trends in halogen-containing molecules measured by the Atmospheric Chemistry Experiment (ACE) satellite, ***J. Quant. Spectrosc. Radiat. Transf.***, ***238***, 106619, doi:10.1016/j.jqsrt.2019.106619, 2019.

Strahan, S.E., D. Smale, A.R. Douglass, T. Blumenstock, J.W. Hannigan, F. Hase, N.B. Jones, E. Mahieu, J. Notholt, L.D. Oman, I. Ortega, M. Palm, M. Prignon, J. Robinson, M. Schneider, R. Sussmann, and V.A. Velazco, Observed hemispheric asymmetry in stratospheric transport trends from 1994 to 2018, ***Geophys. Res. Lett.***, ***47*** (17), e2020GL088567, doi:10.1029/2020GL088567, 2020.

Sturges, W.T., D.E. Oram, J.C. Laube, C.E. Reeves, M.J. Newland, C. Hogan, P. Martinerie, E. Witrant, C.A.M. Brenninkmeijer, T.J. Schuck, and P.J. Fraser, Emissions halted of the potent greenhouse gas SF_5CF_3, ***Atmos. Chem. Phys.***, ***12*** (8), 3653–3658, doi:10.5194/acp-12-3653-2012, 2012.

Suntharalingam, P., E. Buitenhuis, L.J. Carpenter, J.H. Butler, M.J. Messias, S.J. Andrews, and S.C. Hackenberg, Evaluating oceanic uptake of atmospheric CCl_4: A combined analysis of model simulations and observations, ***Geophys. Res. Lett.***, ***46*** (1), 472–482, doi:10.1029/2018GL080612, 2019.

Tegtmeier, S., E. Atlas, B. Quack, F. Ziska, and K. Krüger, Variability and past long-term changes of brominated very short-lived substances at the tropical tropopause, Atmos. Chem. Phys., 20(11), 7103–7123, doi:10.5194/acp-20-7103-2020, 2020.

Tegtmeier, S., F. Ziska, I. Pisso, B. Quack, G. J. M. Velders, X. Yang, and K. Krüger, Oceanic bromoform emissions weighted by their ozone depletion potential, Atmos. Chem. Phys., 15, 13647–13663, doi:10.5194/acp-15-13647-2015, 2015.

Tegtmeier, S., K. Kruger, B. Quack, E. Atlas, D. R. Blake, H. Boenisch, A. Engel, H. Hepach, R. Hossaini, M. A. Navarro, S. Raimund, S. Sala, Q. Shi, and F. Ziska, The contribution of oceanic methyl iodide to stratospheric iodine, Atmos. Chem. Phys., 13(23), 11869–11886, doi:10.5194/acp-13-11869-2013, 2013.

Tegtmeier, S., K. Kruger, B. Quack, E. L. Atlas, I. Pisso, A. Stohl, and X. Yang, Emission and transport of bromocarbons: From the West Pacific Ocean into the stratosphere, Atmos. Chem. Phys., 12(22), 10633–10648, doi:10.5194/acp-12-10633-2012, 2012.

Thompson, R.L., L. Lassaletta, P.K. Patra, C. Wilson, K.C. Wells, A. Gressent, E.N. Koffi, M.P. Chipperfield, W. Winiwarter, E.A. Davidson, H. Tian, and J.G. Canadell, Acceleration of global N_2O emissions seen from two decades of atmospheric inversion, ***Nat. Clim. Change***, ***9***, 993–998, doi:10.1038/s41558-019-0613-7, 2019.

Tian, H., R. Xu, J.G. Canadell, R.L. Thompson, W. Winiwarter, P. Suntharalingam, E.A. Davidson, P. Ciais, R.B. Jackson, G. Janssens-Maenhout, M.J. Prather, P. Regnier, N. Pan, S. Pan, G.P. Peters, H. Shi, F.N. Tubiello, S. Zaehle, F. Zhou, A. Arneth, G. Battaglia, S. Berthet, L. Bopp, A.F. Bouwman, E.T. Buitenhuis, J. Chang, M.P. Chipperfield, S.R.S. Dangal, E. Dlugokencky, J.W. Elkins, B.D. Eyre, B. Fu, B. Hall, A. Ito, F. Joos, P.B. Krummel, A. Landolfi, G.G. Laruelle, R. Lauerwald, W. Li, S. Lienert, T. Maavara, M. MacLeod, D.B. Millet, S. Olin, P.K. Patra, R.G. Prin, P.A. Raymond, D.J. Ruiz, G.R. van der Werf, N. Vuichard, J. Wang, R.F. Weiss, K.C. Wells, C. Wilson, J. Yang, and Y. Yao, A comprehensive quantification of global nitrous oxide sources and sinks, ***Nature***, ***586***, 248–256, doi:10.1038/s41586-020-2780-0, 2020.

Tinel, L., T.J. Adams, L.D. J. Hollis, A.J.M. Bridger, R.J. Chance, M.W. Ward, S.M. Ball, and L.J. Carpenter, Influence of the sea surface microlayer on oceanic iodine emissions, ***Environ. Sci. Technol.***, ***54*** (20), 13,228–13,237, doi: 10.1021/acs.est.0c02736, 2020.

Tromp, T.K., R.-L. Shia, M. Allen, J.M. Eiler, and Y.L. Yung, Potential environmental impact of a hydrogen economy on the stratosphere, ***Science***, ***300***, 1740–1722, doi:10.1126/science.1085169, 2003.

Trudinger, C.M., D.M. Etheridge, G.A. Sturrock, P.J. Fraser, P.B. Krummel, and A. McCulloch, Atmospheric histories of halocarbons from analysis of Antarctic firn air: Methyl bromide, methyl chloride, chloroform, and dichloromethane, ***J. Geophys. Res.***, ***109***, D22310, doi:10.1029/2004JD004932, 2004.

Trudinger, C.M., P.J. Fraser, D.M. Etheridge, W.T. Sturges, M.K. Vollmer, M. Rigby, P. Martinerie, J. Mühle, D.R. Worton, P.B. Krummel, L.P. Steele, B.R. Miller, J. Laube, F.S. Mani, P.J. Rayner, C.M. Harth, E. Witrant, T. Blunier, J. Schwander, S. O'Doherty, and M. Battle, Atmospheric abundance and global emissions of perfluorocarbons CF_4, C_2F_6 and C_3F_8 since 1800 inferred from ice core, firn, air archive and ***in situ*** measurements, ***Atmos. Chem. Phys.***, ***16*** (18), 11,733–11,754, doi:10.5194/acp-16-11733-2016, 2016.

Umezawa, T., A.K. Baker, D. Oram, C. Sauvage, D. O'Sullivan, A. Rauthe-Schöch, S.A. Montzka, A. Zahn, and C.A.M. Brenninkmeijer, Methyl chloride in the upper troposphere observed by the CARIBIC passenger aircraft observatory: Large-scale distributions and Asian summer monsoon outflow, ***J. Geophys. Res. Atmos.***, ***119*** (9), 5542–5558, doi:10.1002/2013JD021396, 2014.

Umezawa, T., A.K. Baker, C.A.M. Brenninkmeijer, A. Zahn, D.E. Oram, and P.F.J. van Velthoven, Methyl chloride as a tracer of tropical tropospheric air in the lowermost stratosphere inferred from IAGOS-CARIBIC passenger aircraft measurements, ***J. Geophys. Res. Atmos.***, ***120*** (23), doi:10.1002/2015JD023729, 2015.

UNEP (United Nations Environment Programme), Report of the Methyl Bromide Technical Options Committee, United Nations Environment Programme, Ozone Secretariat, Nairobi, Kenya, 2006.

UNEP (United Nations Environment Programme), data from Ozone Secretariat Country Data Centre, United Nations Environment Programme, Nairobi, Kenya [available at: https://ozone.unep.org/countries/data-table], 2022.

U.S. EPA (U.S. Environmental Protection Agency), ***Inventory of U.S. Greenhouse Gas Emissions and Sinks: 1990-2019***, U.S. Environmental Protection Agency, [available at: https://www.epa.gov/ghgemissions/inventory-us-greenhouse-gas-emissions-and-sinks-1990-2019], 2021.

Vogel, B., T. Feck, and J.-U. Grooß, Impact of stratospheric water vapor enhancements caused by CH_4 and H_2O increase on polar ozone loss, ***J. Geophys. Res. Atmos.***, ***116*** (D5), doi:10.1029/2010JD014234, 2011.

Vollmer, M.K., B.R. Miller, M. Rigby, S. Reimann, J. Mühle, P.B. Krummel, S. O'Doherty, J. Kim, T.S. Rhee, R.F. Weiss, P.J. Fraser, P.G. Simmonds, P.K. Salameh, C.M. Harth, R.H.J. Wang, L.P. Steele, D. Young, C.R. Lunder, O. Hermansen, D. Ivy, T. Arnold, N. Schmidbauer, K.-R. Kim, B.R. Greally, M. Hill, M. Leist, A. Wenger, and R.G. Prinn, Atmospheric histories and global emissions of the anthropogenic hydrofluorocarbons HFC-365mfc, HFC-245fa, HFC-227ea, and HFC-236fa, ***J. Geophys. Res.***, ***116*** (D8), D08304, doi:10.1029/2010JD015309, 2011.

Vollmer, M.K., S. Reimann, M. Hill, and D. Brunner, First observations of the fourth generation synthetic halocarbons HFC-1234yf, HFC-1234ze(E), and HCFC-1233zd(E) in the atmosphere, ***Environ. Sci. Technol.***, ***49*** (5), 2703–2708, doi:10.1021/es505123x, 2015a.

Vollmer, M.K., M. Rigby, J.C. Laube, S. Henne, T.S. Rhee, L.J. Gooch, A. Wenger, D. Young, L.P. Steele, R.L. Langenfelds, C.A.M. Brenninkmeijer, J.L. Wang, C.F. Ou-Yang, S.A. Wyss, M. Hill, D.E. Oram, P.B. Krummel, F. Schoenenberger, C. Zellweger, P.J. Fraser, W.T. Sturges, S. O'Doherty, and S. Reimann, Abrupt reversal in emissions and atmospheric abundance of HCFC-133a (C_3FCH_2Cl), ***Geophys. Res. Lett.***, ***42*** (20), 8702–8710, doi:10.1002/2015GL065846, 2015b.

Vollmer, M.K., T.S. Rhee, M. Rigby, D. Hofstetter, M. Hill, F. Schoenenberger, and S. Reimann, Modern inhalation anesthetics: Potent greenhouse gases in the global atmosphere, ***Geophys. Res. Lett.***, ***42*** (5), 1606–1611, doi:10.1002/2014GL062785, 2015c.

Vollmer, M.K., J. Mühle, C.M. Trudinger, M. Rigby, S.A. Montzka, C.M. Harth, B.R. Miller, S. Henne, P.B. Krummel, B.D. Hall, D. Young, J. Kim, J. Arduini, A. Wenger, B. Yao., S. Reimann., S. O'Doherty, M. Maione, D.M. Etheridge, S. Li, D.P. Verdonik, S. Park, G.S. Dutton, L.P. Steele, C.P. Lunder, T.S. Rhee, O. Hermansen, N. Schmidbauer , R.H.J. Wang, M. Hill, P.K. Salameh, R.L. Langenfelds, Z.L.X. Zhou, T. Blunier, J. Schwander, J.W. Elkins, J.H. Butler, P.G. Simmonds, R.F. Weiss, R.G. Prinn, and P.J. Fraser, Atmospheric histories and global emissions of halons H-1211 ($CBrClF_2$), H-1301 ($CBrF_3$), and H-2402 ($CBrF_2CBrF_2$), ***J. Geophys. Res. Atmos.***, ***121***, 3663–3686, doi:10.1002/2015JD0024488, 2016.

Vollmer, M.K., D. Young, C.M. Trudinger, J. Mühle, S. Henne, M. Rigby, S. Park, S. Li, M. Guillevic, B. Mitrevski, C.M. Harth, B.R. Miller, S. Reimann, B. Yao, L.P. Steele, S.A. Wyss, C.R. Lunder, J. Arduini, A. McCulloch, S. Wu, T.S. Rhee, R.H.J. Wang, P.K. Salameh, O. Hermansen, M. Hill, R.L. Langenfelds, D. Ivy, S. O'Doherty, P.B. Krummel, M. Maione, D.M. Etheridge, L. Zhou, P.J. Fraser, R.G. Prinn, R.F. Weiss, and P.G. Simmonds, Atmospheric histories and emissions of chlorofluorocarbons CFC-13 ($CClF_3$), ΣCFC-114 ($C_2Cl_2F_4$), and CFC-115 (C_2ClF_5), ***Atmos. Chem. Phys.***, ***18*** (2), 979–1002, doi:10.5194/acp-18-979-2018, 2018.

Vollmer, M.K., F. Bernard, B. Mitrevski, L.P. Steele, C.M. Trudinger, S. Reimann, R.L. Langenfelds, P.B. Krummel, P.J. Fraser, D.M. Etheridge, M.A.J. Curran, and J.B. Burkholder, Abundances, emissions, and loss processes of the long-lived and potent greenhouse gas octafluorooxolane (octafluorotetrahydrofuran, c-C_4F_8O) in the atmosphere, ***Atmos. Chem. Phys.***, ***19*** (6), 3481–3492, doi:10.5194/acp-19-3481-2019, 2019.

Vollmer, M.K., J. Mühle, S. Henne, D. Young, M. Rigby, B. Mitrevski, S. Park, C.R. Lunder, T.S. Rhee, C.M. Harth, M. Hill, R.L. Langenfelds, M. Guillevic, P.M. Schlauri, O. Hermansen, J. Arduini, R.H.J. Wang, P.K. Salameh, M. Maione, P.B. Krummel, S. Reimann, S. O'Doherty, P.G. Simmonds, P.J. Fraser, R.G. Prinn, R.F. Weiss, and L.P. Steele, Unexpected nascent atmospheric emissions of three ozone-depleting hydrochlorofluorocarbons, ***Proc. Natl. Acad. Sci.***, ***118*** (5), doi:10.1073/pnas.2010914118, 2021.

Wadley, M.R., D.P. Stevens, T.D. Jickells, C. Hughes, R. Chance, H. Hepach, L. Tinel, and L.J. Carpenter, A global model for iodine speciation in the upper ocean, ***Global Biogeochem. Cycles***, ***34*** (9), doi:10.1029/2019GB006467, 2020.

Waggoner, M., H.D. Ohr, C. Adams, J.J. Sims, and D. Gonzalez, Methyl iodide: an alternative to methyl bromide for insectary fumigation, ***J. Appl. Entomol.***, ***124*** (2), 113–117, doi:10.1046/j.1439-0418.2000.00437.x, 2000.

Wahner, A., A.R. Ravishankara, S.P. Sander, and R.R. Friedl, Absorption cross section of BrO between 312 and 385 nm AT 298 and 223 K, ***Chem. Phys. Lett.***, ***152***, 507–510, doi:10.1016/0009-2614(88)80450-0, 1988.

Wang, Z.Y., H.H. Yan, X.K. Fang, L.Y. Gao, Z.H. Zhai, J.X. Hu, B.Y. Zhang, and J.B. Zhang, Past, present, and future emissions of HCFC-141b in China, ***Atmos. Environ.***, ***109***, 228–233, doi:10.1016/j. atmosenv.2015.03.019, 2015.

Wang, S., D. Kinnison, S.A. Montzka, E.C. Apel, R.S. Hornbrook, A.J. Hills, D.R. Blake, B. Barletta, S. Meinardi, C. Sweeney, F. Moore, M. Long, A. Saiz-Lopez, R.P. Fernandez, S. Tilmes, L.K. Emmons, and J.-F. Lamarque, Ocean biogeochemistry control on the marine emissions of brominated very short-lived ozone-depleting substances: a machine-learning approach, ***J. Geophys. Res. Atmos.***, ***124*** (22), 12,319–12,339, doi:10.1029/2019JD031288, 2019.

Wang, P., J.R. Scott, S. Solomon, J. Marshall, A.R. Babbin, M. Lickley, D.W.J. Thompson, T. DeVries, Q. Liang, and R.G. Prinn, On the effects of the ocean on atmospheric CFC-11 lifetimes and emissions, ***Proc. Natl. Acad. Sci.***, ***118*** (12), doi:10.1073/pnas.2021528118, 2021.

Wales, P.A., R.J. Salawitch, J.M. Nicely, D.C. Anderson, T.P. Canty, S. Baidar, B. Dix, T.K. Koenig, R. Volkamer, D. Chen, L.G. Huey, D.J. Tanner, C.A. Cuevas, R.P. Fernandez, D.E. Kinnison, J.-F Lamarque, A. Saiz-Lopez, E.L. Atlas, S.R. Hall, M.A. Navarro, L.L. Pan, S.M. Schauffler, M. Stell, S. Tilmes, K. Ullmann, A.J. Weinheimer, H. Akiyoshi, M.P. Chipperfield, M. Deushi, S.S. Dhomse, W. Feng, P. Graf, R. Hossaini, P. Jöckel, E. Mancini, M. Michou, O. Morgenstern, L.D. Oman, G. Pitari, D.A. Plummer, L.E. Revell, E. Rozanov, D. Saint-Martin, R. Schofield, A. Stenke, K.A. Stone, D. Visioni, Y. Yamashita, and G. Zeng, Stratospheric injection of brominated very short-lived substances: Aircraft observations in the Western Pacific and representation in global models, ***J. Geophys. Res. Atmos.***, ***123*** (10), 5690–5719, doi:10.1029/2017JD027978, 2018.

Whelan, M.E., S.T. Lennartz, T.E. Gimeno, R. Wehr, G. Wohlfahrt, Y. Wang, L.M.J. Kooijmans, T.W. Hilton, S. Belviso, P. Peylin, R. Commane, W. Sun, H. Chen, L. Kuai, I. Mammarella, K. Maseyk, M. Berkelhammer, K.-F. Li, D. Yakir, A. Zumkehr, Y. Katayama, J. Ogée, F.M. Spielmann, F. Kitz, B. Rastogi, J. Kesselmeier, J. Marshall, K.-M. Erkkilä, L. Wingate, L.K. Meredith, W. He, R. Bunk, T. Launois, T. Vesala, J.A. Schmidt, C.G. Fichot, U. Seibt, S. Saleska, E.S. Saltzman, S.A. Montzka, J.A. Berry, and J.E. Campbell, Reviews and syntheses: Carbonyl sulfide as a multi-scale tracer for carbon and water cycles, ***Biogeosciences***, ***15***, 3625–3657, doi:10.5194/bg-15-3625-2018, 2018.

Weiss, R.F., A.R. Ravishankara, and P.A. Newman, Huge gaps in detection networks plague emissions monitoring, ***Nature***, ***595*** (7868), 491–493, doi:10.1038/d41586-021-01967-z, 2021.

Werner, B., J. Stutz, M. Spolaor, L. Scalone, R. Raecke, J. Festa, S.F. Colosimo, R. Cheung, C. Tsai, R. Hossaini, M.P. Chipperfield, G.S. Taverna, W. Feng, J.W. Elkins, D.W. Fahey, R.-S. Gao, E.J. Hintsa, T.D. Thornberry, F.L. Moore, M.A. Navarro, E. Atlas, B.C. Daube, J. Pittman, S. Wofsy, and K. Pfeilsticker, Probing the subtropical lowermost stratosphere and the tropical upper troposphere and tropopause layer for inorganic bromine, ***Atmos. Chem. Phys.***, ***17*** (2), 1161–1186, doi:10.5194/acp-17-1161-2017, 2017.

Wilmouth, D.M., T.F. Hanisco, N.M. Donahue, and J.G. Anderson, Fourier transform ultraviolet spectroscopy of the A 2Π3/2← X 2Π3/2 transition of BrO, ***J. Phys. Chem. A***, ***103*** (45), 8935–8945, doi:10.1021/jp991651o, 1999.

WMO (World Meteorological Organization), ***Scientific Assessment of Ozone Depletion: 2018***, Global Ozone Research and Monitoring Project–Report No. 58, 588 pp., Geneva, Switzerland, 2018.

Wofsy, S.C., HIAPER Pole-to-Pole Observations (HIPPO): fine-grained, global-scale measurements of climatically important atmospheric gases and aerosols, ***Philos. Trans. R. Soc. A***, ***369*** (1943), 2073–2086, doi:10.1098/rsta.2010.0313, 2011.

Worton, D.R., W.T. Sturges, J. Schwander, R. Mulvaney, J.-M. Barnola, and J. Chappellaz, 20th century trends and budget implications of chloroform and related tri-and dihalomethanes inferred from firn air, ***Atmos. Chem. Phys.***, ***6*** (10), 2847–2863, doi:10.5194/acp-6-2847-2006, 2006.

Wuebbles, D.J., Ozone Depletion and Related Topics | Ozone Depletion Potentials, ***Encycl. Atmos. Sci. (2nd Ed.)***, 364–369, doi:10.1016/B978-0-12-382225-3.00293-0, 2015.

Yang, M., F. Yang, H. Li, T. Li, F. Cao, X. Nie, J. Zhen, P. Li, and Y. Wang, CFCs measurements at high altitudes in northern China during 2017–2018: concentrations and potential emission source regions, ***Sci. Tot. Environ.***, ***754*** (17), 142290, doi:10.1016/j.scitotenv.2020.142290, 2021.

Yi, L., J. Wu, M. An, W. Xu, X. Fang, B. Yao, Y. Li, D. Gao, X. Zhao, and J. Hu, The atmospheric concentrations and emissions of major halocarbons in China during 2009–2019, ***Environ. Pollut.***, ***284***, 117190, doi:10.1016/j.envpol.2021.117190, 2021.

Yokouchi, Y., S. Taguchi, T. Saito, Y. Tohjima, H. Tanimoto, and H. Mukai, High frequency measurements of HFCs at a remote site in east Asia and their implications for Chinese emissions, ***Geophys. Res. Lett.***, ***33*** (21), doi:10.1029/2006GL026403, 2006.

Yokouchi, Y., Y. Nojiri, D. Toom-Sauntry, P. Fraser, Y. Inuzuka, H. Tanimoto, H. Nara, R. Murakami, and H. Mukai, Long-term variation of atmospheric methyl iodide and its link to global environmental change, ***Geophys. Res. Lett.***, ***39*** (23), doi:10.1029/2012GL053695, 2012.

Yu, D., B. Yao, W. Lin, M.K. Vollmer, B. Ge, G. Zhang, Y. Li, H. Xu, S. O'Doherty, L. Chen, and S. Reimann, Atmospheric CH_3CCl_3 observations in China: Historical trends and implications, ***Atmos. Res.***, 231, 104658, doi:10.1016/j.atmosres.2019.104658, 2020.

Yvon-Lewis, S.A., and J.H. Butler, Effect of oceanic uptake on atmospheric lifetimes of selected trace gases, ***J. Geophys. Res.***, ***107*** (D20), 4414, doi:10.1029/2001JD001267, 2002.

Yvon-Lewis, S.A., E.S. Saltzman, and S.A. Montzka, Recent trends in atmospheric methyl bromide: analysis of post-Montreal Protocol variability, ***Atmos. Chem. Phys.***, ***9***, 5963–5974, doi:10.5194/acp-9-5963-2009, 2009.

Zander R., E. Mahieu, P. Demoulin, P. Duchatelet, G. Roland, C. Servais, M. De Mazière, S. Reimann, and C.P. Rinsland, Our changing atmosphere: evidence based on long-term infrared solar observations at the Jungfraujoch since 1950, ***Sci. Tot. Environ.***, ***391*** (1-2), 184–195, doi:10.1016/j.scitotenv.2007.10.018, 2008.

Zeng, L., J. Dang, H. Guo, X. Lyu, I.J. Simpson, S. Meinardi, Y. Wang, L. Zhang, and D.R. Blake, Long-term temporal variations and source changes of halocarbons in the Greater Pearl River Delta region, China, ***Atmos. Environ.***, ***234*** (40), 117550, doi:10.1016/j.atmosenv.2020.117550, 2020.

Zhang, J., D.J. Wuebbles, D.E. Kinnison, and A. Saiz-Lopez, Revising the ozone depletion potentials metric for short-lived chemicals such as CF_3I and CH_3I, ***J. Geophys. Res. Atmos.***, ***125*** (9), e2020JD032414, doi:10.1029/2020JD032414, 2020.

Zhang, W., Y. Jiao, R. Zhu, and R.C. Rhew, Methyl chloride and methyl bromide production and consumption in coastal Antarctic tundra soils subject to sea animal activities, ***Environ. Sci. Technol.***, ***54***, 13354–13363, 2020.

Zhang, W., Y. Jiao, R. Zhu, R.C. Rhew, B. Sun, and H. Dai, Chloroform ($CHCl_3$) emissions from coastal Antarctic tundra, ***Geophys. Res. Lett.***, ***48*** (18), e2021GL093811, doi:10.1029/2021GL093811, 2021.

Zhao, X., X. Hou, and W. Zhou, Atmospheric iodine (127I and 129I) record in spruce tree rings in the northeast Qinghai–Tibet Plateau, ***Environ. Sci. Technol.***, ***53*** (15), 8706–8714, doi:10.1021/acs.est.9b01160, 2019.

Ziska, F., B. Quack, K. Abrahamsson, S.D. Archer, E. Atlas, T. Bell, J.H. Butler, L.J. Carpenter, C.E. Jones, N.R.P. Harris, H. Hepach, K.G. Heumann, C. Hughes, J. Kuss, K. Kruger, P. Liss, R.M. Moore, A. Orlikowska, S. Raimund, C.E. Reeves, W. Reifenhauser, A.D. Robinson, C. Schall, T. Tanhua, S. Tegtmeier, S. Turner, L. Wang, D. Wallace, J. Williams, H. Yamamoto, S. Yvon-Lewis, and Y. Yokouchi, Global sea-to-air flux climatology for bromoform, dibromomethane and methyl iodide, ***Atmos. Chem. Phys.***, ***13*** (17), 8915–8934, doi:10.5194/acp-13-8915-2013, 2013.

Zgonnik, V., The occurrence and geoscience of natural hydrogen: A comprehensive review, ***Earth Sci. Rev.***, ***203***, 103140, doi:10.1016/j.earscirev.2020.103140, 2020.

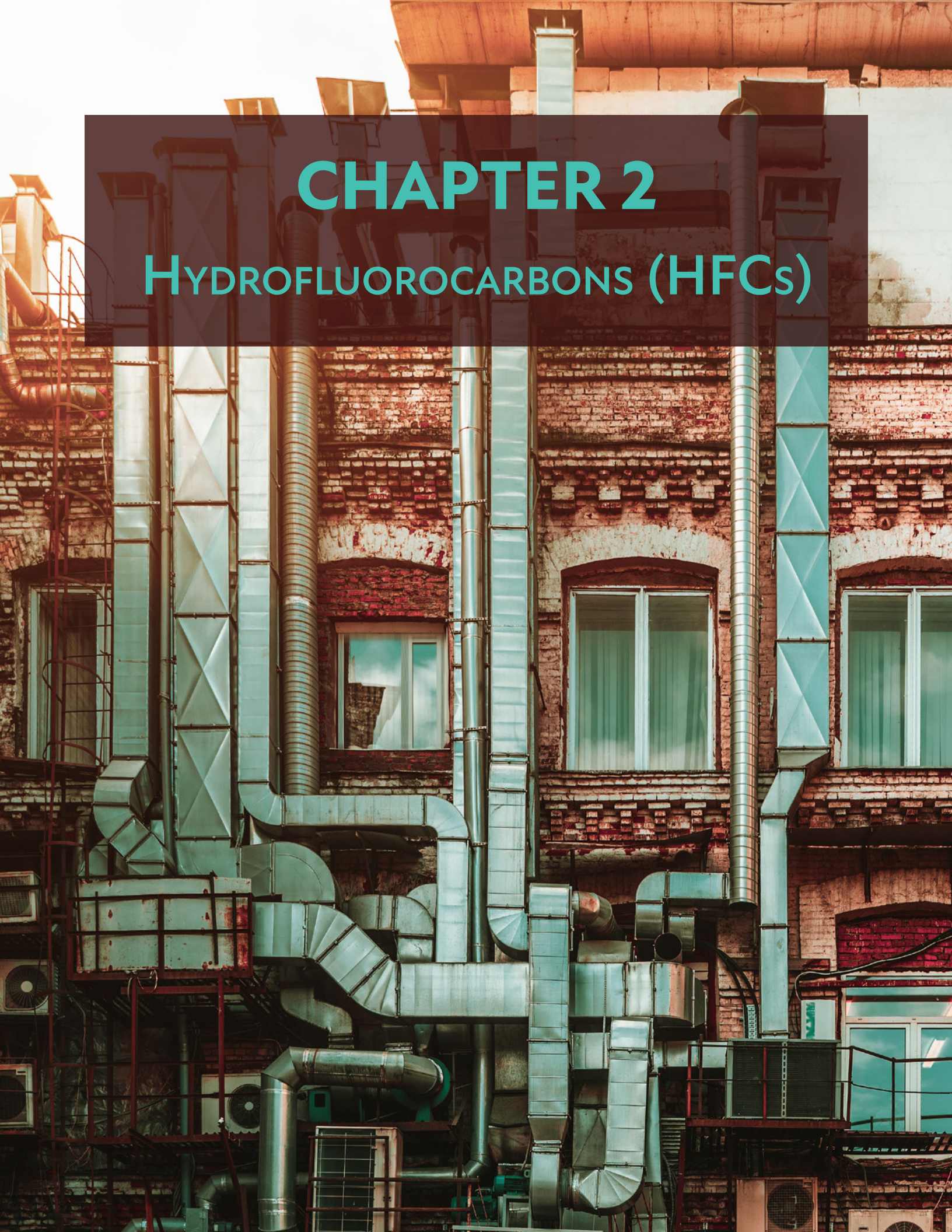

CHAPTER 2

Hydrofluorocarbons (HFCs)

About the cover image:
Hydrofluorocarbons (HFCs), widely used in the air conditioning and refrigeration sectors, are now controlled under the Kigali Amendment of the Montreal Protocol.

Photo credit: Adapted from image by skyNext via Adobe Stock

CHAPTER 2

Hydrofluorocarbons (HFCs)

Lead Authors : Qing Liang
Matthew Rigby

Coauthors : Xuekun Fang
David Godwin
Jens Mühle
Takuya Saito
Kieran M. Stanley
Guus J. M. Velders

Contributing Authors : Peter Bernath
Nada Derek
Stefan Reimann
Isobel J. Simpson
Luke Western

Review Editors : Stephen A. Montzka
Martin K. Vollmer

CONTENTS

Chapter 2: Hydrofluorocarbons (HFCs)

SCIENTIFIC SUMMARY

Hydrofluorocarbons (HFCs) have been increasingly produced and used in applications such as refrigeration, air-conditioning, and foam blowing following the phasedown of ozone-depleting substances (ODSs). In addition to emissions resulting from these uses, some HFCs, particularly HFC-23, are released as by-products during the manufacture of other compounds. While being benign for the stratospheric ozone layer and generally having lower radiative efficiencies than the most abundant ODSs, long-lived HFCs are potent greenhouse gases. Therefore, HFCs were included in the basket of substances controlled by the 1997 Kyoto Protocol under the United Nations Framework Convention on Climate Change (UNFCCC). Subsequently, certain HFCs were brought into the Montreal Protocol framework by the Kigali Amendment in 2016. The Kigali Amendment, which came into force in January 2019 for parties who ratified the Amendment, seeks to limit the production and consumption of a selection of HFCs. For HFC-23, the Kigali Amendment seeks to limit emissions formed as a by-product of HCFC (hydrochlorofluorocarbon) and HFC production to the extent practicable using approved technologies.

For the most abundant HFCs (HFC-134a, HFC-23, HFC-32, HFC-125, and HFC-143a) and some of the less abundant HFCs, atmospheric observations have been available for several years or decades. Observations in the remote atmosphere can be used to derive "top-down" global emissions. These emissions can be compared to the sum of "bottom-up" estimates derived from accounting methods for Annex I parties to the UNFCCC, who are required to report their emissions annually. For some parts of the world, atmospheric observations exist in sufficient density to derive top-down emissions estimates at regional scales. These can be compared to bottom-up estimates reported by the countries in these regions.

Based on the historical emissions trends derived from atmospheric data and estimates of future consumption, projections of future emissions can be derived under different policy scenarios. These emissions scenarios can be used to estimate the climate impact of various HFC policies in terms of future radiative forcing and temperature change.

The key findings of this chapter are as follows:

- **Global mean abundances of each of the major HFCs have increased since 2016.** Radiative forcing due to the HFCs reached 44.1 ± 0.6 mW m^{-2} in 2020, an increase of around one-third since 2016. HFC-134a remained the largest contributor to the overall radiative forcing due to HFCs (44%), and HFC-125 (18%) overtook HFC-23 (15%) as the second-largest contributor.
- **Total CO_2-equivalent HFC emissions inferred from observations increased through 2020.** The total carbon dioxide-equivalent emissions (CO_2-eq, calculated using 100-year global warming potentials, GWPs) due to HFCs was 1.22 ± 0.05 Pg CO_2-eq yr^{-1} in 2020 (1 Pg = 1 Gt), 19% higher than in 2016. Of this total, HFC-134a was responsible for approximately 30%, HFC-125 for 28%, HFC-23 for 20%, and HFC-143a for 15%. Emissions of the majority of HFCs grew between 2016 and 2020, except for HFC-143a, HFC-152a, HFC-365mfc, and HFC-43-10mee, for which emissions remained roughly constant. In 2020, global total CO_2-eq emissions due to HFCs were 60–70% higher than those of CFCs (chlorofluorocarbons) or HCFCs.
- **The gap between total CO_2-eq HFC emissions reported by Annex I countries to the UNFCCC and global estimates derived from atmospheric data has grown.** The emissions reported by Annex I countries in common reporting format (CRF) are approximately constant in the period 2015–2019, while atmospheric observations in the background atmosphere suggest continued growth in global total emissions. In 2019, UNFCCC reports accounted for only 31% (including HFC-23 in the analysis) or 37% (excluding HFC-23) of the global total CO_2-eq emissions derived from observations. Regional top-down emissions estimates for Europe, the USA, and Australia are similar to reported bottom-up emissions, suggesting that underreporting by these Annex I countries likely does not explain this discrepancy. Inverse modeling studies have been carried out for China and India (both non-Annex I countries) and find that around one-third of the emissions gap (excluding HFC-23) could be explained by sources in these countries. However, approximately 40% of global total HFC CO_2-eq emissions (excluding HFC-23) remain unaccounted for by Annex I reports or top-down estimates for non-Annex I parties. Top-down regional emissions estimates are available from only a relatively small number of countries based on the existing measurement network, whereas global top-down estimates reflect the aggregate of all emissions (for longer-lived HFCs). Therefore, the unattributed emissions probably occur in countries that are not monitored by atmospheric measurements and/or that do not report to the UNFCCC in CRF.
- **The global inferred CO_2-eq HFC emissions are less than the emissions in the 2018 Assessment HFC baseline scenario. They are about 20% lower for 2017–2019.** It is too early to link this directly to the provisions of the Kigali Amendment, since the first step in the scheduled phasedown was in 2019. The lower emissions can be explained by lower reported consumption in several countries following national regulations.
- **The ratio of global HFC-23 emissions inferred from atmospheric observations to reported HCFC-22 production has increased between 2010 and 2019, despite reports of substantial new emissions abatement since 2015.** Top-down estimates of global HFC-23 emissions were 17.2 ± 0.8 Gg yr^{-1} in 2019 (1 Gg = 1 kt). This is substantially larger than a bottom-up estimate of 2.2 Gg yr^{-1} derived from UNFCCC reports for Annex I countries (1.6 Gg yr^{-1}), HCFC-22 production reported to the United Nations Environment Programme (UNEP), and national abatement programs in India and China. The contribution to the global atmospheric

HFC-23 budget of photolysis of trifluoroacetaldehyde (CF_3CHO), a minor degradation product of some fluorinated compounds, is assessed to be negligible.

- **Some HFCs and unsaturated HFCs (hydrofluoroolefins [HFOs]) degrade in the environment to produce trifluoroacetic acid (TFA), a persistent toxic chemical.** HFO-1234yf has been increasingly used to replace HFC-134a as a mobile air conditioner (MAC) refrigerant. Measurements show that atmospheric background abundances of HFO-1234yf at Jungfraujoch, Switzerland have grown from less than 0.01 ppt before 2016 to annual median levels of 0.10 ppt in 2020. At the 2020 level, the oxidation of HFO-1234yf is likely producing a comparable, or potentially larger, amount of TFA than the oxidation of HFC-134a locally near Jungfraujoch. The measured and model simulated concentrations of TFA from the use of HFO-1234yf and other relevant HFOs, HFCs, HCFCs, and hydrochlorofluoroolefins (HCFOs) is, in general, significantly below known toxicity limits at present. However, the production of TFA in the atmosphere is expected to increase due to increased use of HFOs and HCFOs. Potential environmental impacts of TFA require future evaluation due to its persistence.
- **Projected emissions of HFCs based on current trends in consumption and emissions, national policies in several countries, and the Kigali Amendment are lower than those projected in the 2018 Assessment.** The 2020–2050 cumulative emissions in the 2022 updated Kigali Amendment scenario are 14–18 Pg CO_2-eq lower than the corresponding scenario in the previous Assessment. The 2050 radiative forcing in a scenario that assumes no controls on HFCs, is 220–250 mW m^{-2} (termed the Baseline scenario in the previous Assessment). Radiative forcing in 2050 is reduced to 90–100 mW m^{-2} in the 2022 Kigali Amendment scenario, 30 mW m^{-2} lower than projected in the 2018 Kigali Amendment scenario. The new scenario follows national controls on the consumption and production of HFCs in non-Article 5 countries, reflects lower reported consumption in China, is based on updated historical information on the use of HFCs in non-Article 5 countries, uses observed mixing ratios through 2020 as a constraint, and includes assumptions about reduced use of HFCs for commercial and industrial refrigeration. The new scenario also assumes that all countries adhere to the provisions of the Kigali Amendment.
- **Under the provisions of the Kigali Amendment, current trends in consumption and emissions, and national policies, the contribution of HFCs to global annual average surface warming is projected to be 0.04 °C in 2100.** This is substantially lower than under the scenario without HFC control measures, for which a contribution of 0.3–0.5 °C was projected.
- **Concerted efforts to improve energy efficiency of refrigeration and air-conditioning equipment could lead to reductions in greenhouse gas emissions of the same order as those from global implementation of the Kigali Amendment.** These estimated benefits of improving energy efficiency are highly dependent on greenhouse gas emissions from local electric grids and the pace of decarbonization in the energy sector.

2.1 INTRODUCTION

2.1.1 Summary of Findings from Previous Assessments

The previous Ozone Assessment reported the continuing rise of hydrofluorocarbon (HFC) emissions through 2016 and the accelerating growth of HFC atmospheric abundances. Radiative forcing due to HFCs was estimated to be 0.030 W m^{-2} in 2016, 1% of the total anthropogenic forcing for all long-lived greenhouse gases. Global CO_2-equivalent (CO_2-eq) HFC emissions were estimated to be 0.88 ± 0.07 Pg CO_2-eq yr^{-1} in 2016, 23% higher than in 2012. The magnitude of the rise in total HFC CO_2-eq emissions was found to be larger than the decline from chlorofluorocarbons (CFCs) and hydrochlorofluorocarbon (HCFCs). This was driven primarily by increases in HFC-134a, HFC-125, HFC-23, and HFC-143a, the four most abundant HFCs in the atmosphere. Emissions reported to the United Nations Framework Convention on Climate Change (UNFCCC) accounted for less than half of the global total derived from atmospheric measurements in 2016. The remaining emissions were thought to have originated primarily from non-Annex 1 countries. Global emissions of HFC-23 were found to have varied substantially, primarily due to changing levels of abatement in non-Annex 1 countries brought about by the UNFCCC Clean Development Mechanism (CDM). Emissions of HFC-23 inferred from atmospheric observations or from inventories generally agreed well. Future emissions scenarios suggested that the Kigali Amendment and national and regional regulations could more than halve radiative forcing due to all HFCs, excluding HFC-23, by 2050, compared to the baseline scenario.

2.1.2 Scope

Following the controls on CFC and HCFC production and use under the terms of the Montreal Protocol, the production and use of HFCs, which do not contribute to ozone depletion, increased substantially. HFCs are primarily used in refrigeration, air-conditioning, and foam blowing. Minor applications include use as firefighting agents and propellants (see **Table 2-1**). Post-production emissions of HFCs can occur months to decades following their manufacture, depending on the application. Once emitted, many HFCs persist in the atmosphere for several years or longer, where they absorb outgoing infrared radiation and therefore contribute to radiative forcing of climate.

Owing to their influence on climate, HFCs are subject to a range of regulations and international protocols. While HFCs were included in a basket of compounds controlled under the Kyoto Protocol to the UNFCCC, limits were not placed on their emissions explicitly as controls related to the aggregated total greenhouse gas emissions from individual parties. In some regions, national or regional regulations are in place to limit HFC use (e.g., European F-gas regulations; EU, 2014). In 2019, the Kigali Amendment to the Montreal Protocol came into force (**Box 2-1**). The Amendment sets out a phasedown schedule for production and consumption of a select group of HFCs, with differing time frames for non-Article 5 [non-A5] and Article 5 [A5] parties. For HFC-23, which is primarily a by-product of HCFC-22 production, the Kigali Amendment states that emissions should be controlled to the maximum extent practicable using proven technologies.

In this chapter, updates are provided for observations of the atmospheric abundance of HFCs. Global emissions are inferred based on these observations, estimates of their atmospheric lifetimes, and simulations of their dispersion throughout the atmosphere. These "top-down" emissions are compared to UNFCCC reports and other inventory-based ("bottom-up") methods. Furthermore, recent scientific literature is assessed regarding regional top-down and bottom-up emissions estimates and factors affecting the atmospheric lifetime and breakdown products of HFCs. Global emissions estimates are compared to earlier projections and emissions scenarios, and new scenarios are developed, constrained by updated atmospheric data. Information is also presented on new uses of HFCs, HFC alternatives, and energy efficiency improvements.

In 2017, Decision XXIX/12 was adopted, requesting that the Assessment Panels provide information on production and consumption of certain HFCs not listed as controlled substances under Annex F of the Montreal Protocol. The HFCs that are the subject of this decision have Global Warming Potentials (GWPs) at least as large as that of the controlled HFC with the lowest GWP (that of HFC-152). Of the 162 HFCs listed in the Annex, about 110 species meet this criterion. However, since there is no information available on the production, consumption, or atmospheric abundance of these compounds, they are not addressed in this Assessment.

2.2 ATMOSPHERIC OBSERVATIONS AND DERIVED EMISSIONS ESTIMATES

The abundance of HFCs in the atmosphere is regularly monitored by global networks such as the Advanced Global Atmospheric Gases Experiment (AGAGE; e.g., Prinn et al., 2018) and the National Oceanic and Atmospheric Administration (NOAA; e.g., Montzka et al., 2015). These networks maintain independent calibration scales, which typically agree within a few percent. Global measurements of HFC-134a are also provided by the University of California, Irvine (UCI; Simpson et al., 2014). The historical abundance of many HFCs, before routine ambient measurements began, has been reconstructed by AGAGE and the University of East Anglia from measurements of the Cape Grim Air Archive and archived Northern Hemispheric air samples (e.g., Prinn et al., 2018 and references therein; Oram et al., 2017; Laube et al., 2010; Leedham Elvidge et al., 2018). Complementing these surface-based observations, satellite data from the Atmospheric Chemistry Experiment Fourier Transform Spectrometer (ACE-FTS) onboard SCISAT provide estimates of upper-tropospheric abundance of HFC-23 and HFC-134a (Fernando et al., 2019; Bernath et al., 2021; Harrison et al., 2021).

In this section, updates of surface- and space-based measurements of atmospheric HFC abundances are provided through 2020. Based on the data from the AGAGE and NOAA surface networks, updates of top-down (atmospheric data-based) global annual mean emissions estimates are provided. The methodology for deriving global emissions, global lower-tropospheric mean abundances, CO_2-equivalent (CO_2-eq) emissions, and radiative forcing (defined as stratosphere-adjusted radiative forcing as outlined in **Box 5-1**) are described in detail in *Section 1.0*. Unless otherwise specified, all ranges given here correspond to 1-sigma uncertainties.

Global emissions estimates are presented here through 2020, the year in which socioeconomic activity was reduced

Box 2-1. The Kigali Amendment (2016) to the Montreal Protocol

The phasedown of chlorofluorocarbons (CFCs) and hydrochlorofluorocarbons (HCFCs) under the Montreal Protocol has led to substantial benefits to climate (e.g., Velders et al., 2007). Growth in the use of hydrofluorocarbons (HFCs) as replacements for CFCs and HCFCs could offset some of these climate benefits (Velders et al., 2012). To preserve the benefits by minimizing future growth in radiative forcing due to HFCs, parties to the Montreal Protocol agreed to an Amendment in Kigali, Rwanda, in October 2016. The Kigali Amendment added 18 HFCs to the Montreal Protocol as controlled substances and set out a schedule to phase down their production and consumption, or, in the case of HFC-23, reduce by-product emissions. The Amendment, which entered into force on 1 January 2019, outlines an 80–85% reduction in global production and consumption by 2047, with respect to baselines as defined in the caption to **Box 2-1 Figure 1**. By September 2022, 138 parties had ratified, approved, or accepted the Kigali Amendment.

HFCs controlled by the Kigali Amendment include HFC-23, HFC-134, HFC-134a, HFC-143, HFC-245fa, HFC365mfc, HFC-227ea, HFC-236cb, HFC-236ea, HFC-236fa, HFC-245ca, HFC-43-10mee, HFC-32, HFC-125, HFC-143a, HFC-41, HFC-152, and HFC-152a. The Amendment specifies that emissions of HFC-23 generated during production of HCFCs or HFCs be destroyed to the extent practicable beginning January 2020.

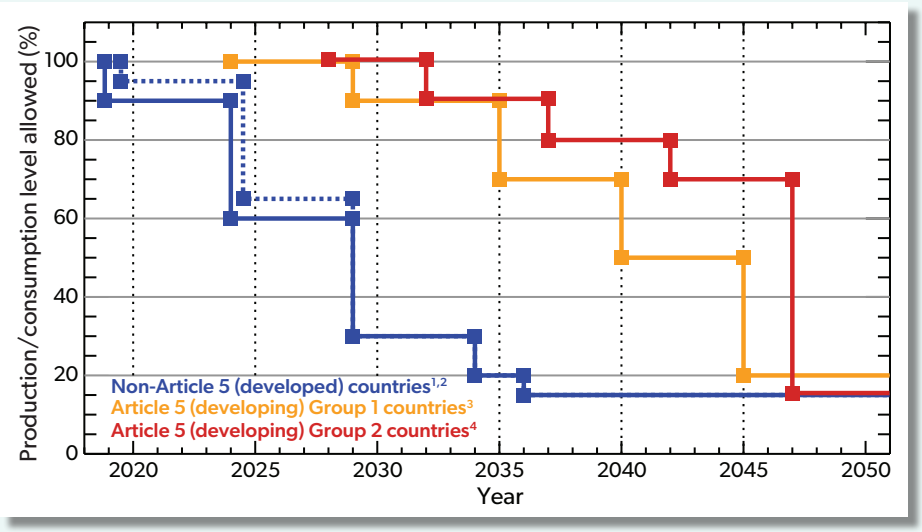

Box 2-1 Figure 1. Phasedown schedule for allowed production and consumption, in percentages with respect to defined baselines, of controlled HFCs, expressed as CO_2-equivalents (CO_2-eq), under the Kigali Amendment. The schedule for non-Article 5 (non-A5) countries is shown in blue[1,2], and the schedule for Article 5 (A5) countries is shown in orange[3] or red[4].

[1] Non-A5 countries also referred to as Article 2 countries (Article 2J of the Montreal Protocol). Baseline for non-A5 countries is defined as average HFC CO_2-eq production/consumption for 2011–2013 plus 15% of HCFC baseline in CO_2-eq production/consumption.
[2] For the non-A5 countries Belarus, Russian Federation, Kazakhstan, Tajikistan, and Uzbekistan, the baseline is defined as average HFC CO_2-eq production/consumption for 2011–2013 plus 25% of HCFC baseline CO_2-eq production/consumption (blue dotted line).
[3] Group 1: A5 countries not part of Group 2 (Article 5 of the Montreal Protocol). Baseline for A5 Group 1 countries is defined as average HFC CO_2-eq production/consumption for 2020–2022 plus 65% of HCFC baseline CO_2-eq production/consumption.
[4] Group 2: A5 countries are Bahrain, the Islamic Republic of Iran, Iraq, Kuwait, Oman, Pakistan, Qatar, Saudi Arabia, and the United Arab Emirates. Baseline for A5 Group 2 countries is defined as average HFC CO_2-eq production/consumption for 2024–2026 plus 65% of HCFC baseline CO_2-eq production/consumption.

in large parts of the world due to the COVID-19 pandemic. At present, there are very few peer-reviewed studies examining the influence of these restrictions on HFC emissions. Therefore, in this section, we do not speculate on the potential effect of the pandemic on HFC emissions.

Top-down regional emissions estimates are possible in parts of the world with sufficiently dense atmospheric measurement networks. In contrast to global inverse modeling, top-down regional emissions estimates of long-lived HFCs are insensitive to uncertainties in atmospheric lifetimes because transport timescales between emissions and measurement are small compared to their rate of removal in the atmosphere (**Box 1-2**). Uncertainties in derived regional emissions are typically dominated by uncertainties in the 3-D chemical transport models used to simulate atmospheric dispersion and uncertainties in the meteorological fields used to drive the models.

In the following section, recent literature on top-down and bottom-up regional emissions are assessed and compared to emissions reported by Annex I Parties to the UNFCCC, where available. The Annex I UNFCCC reports contain annual bottom-up estimates of emissions from those countries. In most of these reports, emissions estimates are available for several individual HFC species. However, reported emissions for some species from some parties are grouped together as an "unspecified mix" of compounds. For many individual species and for aggregated totals, statistically significant differences are found

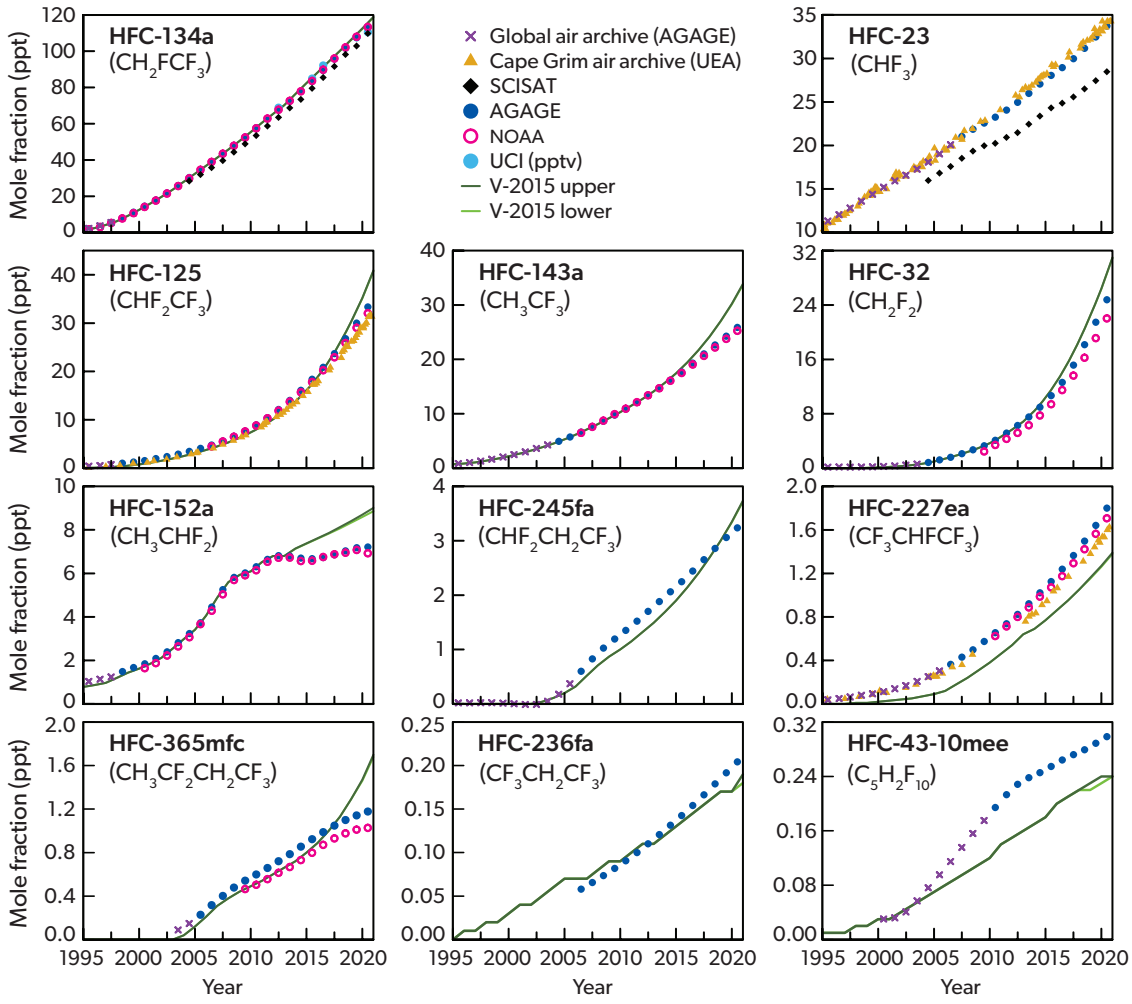

Figure 2-1. Annual mean mole fractions and recent projections. Global annual mean values from the independent ground-based AGAGE, NOAA, and UCI networks are shown as blue filled circles, magenta open circles, and light blue filled circles, respectively. AGAGE and NOAA values are based on monthly mean baseline measurements assimilated into the AGAGE global 12-box model (e.g., Rigby et al., 2014). Purple crosses represent global annual mole fractions based on AGAGE measurements of the Cape Grim Air Archive (CGAA) incorporated into the 12-box model. Gold triangles show Southern Hemisphere mole fractions from the CGAA measured by the University of East Anglia (UEA). Descriptions of these data can be found in Prinn et al. (2018) for AGAGE; Montzka et al. (2015) for NOAA; Simpson et al. (2014) for UCI; and Oram et al. (1998), Laube et al. (2010), and Leedham Elvidge et al. (2018) for UEA. UCI HFC-134a data are reported as pptv (parts per trillion, volume based). In contrast, AGAGE and NOAA data are reported as ppt (dry air mole fraction). Differences are expected to be small at the reported abundances compared to the stated 10% uncertainty of the UCI HFC-134a scale. Upper-tropospheric measurements from ACE-FTS aboard SCISAT represent averages for 60°S–60°N in the altitude range of 5.5–8.5 km for HFC-23 and 45°S–45°N in the altitude range of 10.5–14.5 km for HFC-134a (black diamonds, Fernando et al., 2019; Boone et al., 2020; Bernath et al., 2021). Since the previous Assessment, the ACE-FTS processing algorithm has been updated (Boone et al., 2020), which changed some trend values compared to previous versions (Bernath et al., 2021). ACE-FTS data are reported as wet air mole fractions. A water vapor correction was not applied to the ACE data as its influence is thought to be small compared to the other uncertainties. Also shown are projections from Velders et al. (2015; dark and light green lines).

between summed Annex I emissions reports and global top-down emissions, even when available regional top-down estimates of non-Annex I emissions are added to the Annex I reports. These gaps may arise from substantial emissions in non-reporting countries and, potentially from underreporting of emissions in reporting countries (although, as discussed below, where top-down estimates are available, substantial underreporting has not yet been identified).

Updates relating to the atmospheric lifetime and degradation products of HFCs are discussed in *Section 2.3*.

Table 2-1. Lifetimes, the 100-year time horizon GWP, and main applications of the HFCs with the highest atmospheric abundances.

Name	Formula	Lifetime (yr)	GWP-100	Main Applications
HFC-134a	CH_2FCF_3	14	1470	• Refrigerant for mobile and for domestic refrigerators/freezers • Blend component for stationary air-conditioning and commercial refrigeration • Propellant for pharmaceutical aerosols and for industrial aerosols • Blowing agent
HFC-23	CHF_3	228	14,700	• By-product in production of HCFC-22 • Low-temperature specialist refrigerant • Firefighting agent
HFC-32	CH_2F_2	5.4	749	• Blend component for air-conditioning equipment and commercial refrigeration and heat pumps
HFC-125	CHF_2CF_3	30	3820	• Blend component for stationary air-conditioning and commercial refrigeration and heat pumps • Firefighting agent
HFC-143a	CH_3CF_3	51	5900	• Blend component for commercial refrigeration
HFC-152a	CH_3CHF_2	1.6	153	• Propellant for specialized industrial aerosols • Blowing agent component for extruded polystyrene foams
HFC-245fa	$CHF_2CH_2CF_3$	7.9	966	• Foam blowing agent for polyurethane foams • Working fluid for organic Rankine cycles
HFC-365mfc	$CH_3CF_2CH_2CF_3$	8.9	969	• Foam blowing agent for polyurethane and phenolic foams • Blend component for solvents
HFC-227ea	CF_3CHFCF_3	36	3580	• Propellant for pharmaceutical aerosols • Firefighting agent
HFC-236fa	$CF_3CH_2CF_3$	213	9120	• Firefighting agent
HFC-43-10mee	$CF_3CHFCHFCF_2CF_3$	17	1610	• Solvent for specialized applications

Table 2-2. Global atmospheric mole fractions and emissions of hydrofluorocarbons estimated by surface air sampling networks.

Species	Network	Annual Mean Mole Fraction (ppt)			Change (2019–2020)		Emissions (2020)	
		2016	2019	2020	ppt yr^{-1}	% yr^{-1}	Gg yr^{-1}	Tg CO_2-eq yr^{-1}
HFC-134a	AGAGE	89.4	108	113	5.5	5.1	247 ± 28	364 ± 41
	NOAA	89.8	108	113	5.4	5.0	243 ± 27	358 ± 39
	UCI (pptv)	92.1	108	111	3.3	3.1		
HFC-23	AGAGE	28.9	32.5	33.7	1.3	3.9	17 ± 0.8	243 ± 12
HFC-125	AGAGE	20.9	30	33.3	3.3	11	92 ± 6	352 ± 23
	NOAA	20.2	29	32	3.0	10	83 ± 5	319 ± 20
HFC-143a	AGAGE	19.3	24.3	25.9	1.6	6.7	31 ± 2	185 ± 12
	NOAA	19	23.8	25.2	1.5	6.2	29 ± 2	169 ± 10
HFC-32	AGAGE	12.6	21.5	24.8	3.3	15	70 ± 7	53 ± 5
	NOAA	11.5	19.1	22	2.9	15	62 ± 6	47 ± 5
HFC-152a	AGAGE	6.73	7.18	7.21	0.032	0.44	54 ± 8	8.3 ± 1.2
	NOAA	6.75	7.08	6.92	–0.15	–2.1	49 ± 8	7.5 ± 1.1
HFC-245fa	AGAGE	2.44	3.06	3.24	0.18	5.9	14 ± 2	13 ± 2
HFC-227ea	AGAGE	1.24	1.64	1.8	0.16	9.7	6.3 ± 0.7	23 ± 3
	NOAA	1.17	1.56	1.71	0.14	9.1	5.8 ± 0.6	21 ± 2
HFC-365mfc	AGAGE	0.989	1.14	1.18	0.035	3.1	4.3 ± 1	4.1 ± 0.9
	NOAA	0.87	1.01	1.03	0.015	1.5	3.4 ± 0.7	3.3 ± 0.7
HFC-236fa	AGAGE	0.154	0.192	0.204	0.013	6.6	0.39 ± 0.09	3.5 ± 0.8
HFC-43-10mee	AGAGE	0.264	0.289	0.299	0.0099	3.4	1.2 ± 0.3	1.9 ± 0.5

Notes: Averages represent annual calendar-year global means for each independent measurement network. The AGAGE and NOAA networks share only a few common measurement sites; most measurements occur at different sites. Differences in the 2016 values since WMO (2018) are due to calibration scale changes and differences in methodology used to estimate global means. The observations are updated from Prinn et al. (2018) and Montzka et al. (2015). They are available at http://agage.mit.edu/ for AGAGE data and gml.noaa.gov/dv/site/ for NOAA data. Global means are estimated by assimilating data into the AGAGE 12-box model (Cunnold et al., 1983; Rigby et al., 2013), using the methodology of Rigby et al. (2014). UCI HFC-134a data are reported as pptv (parts per trillion, volume based; Simpson et al., 2014). In contrast, other data are reported as ppt (molar based). Differences are expected to be small at the reported abundances compared to the stated 10% uncertainty of the UCI HFC-134a scale.

2.2.1 Global and Regional HFC Abundances and Emissions

In this section, we provide updates to the abundance and emissions of each HFC species. Species are grouped in subsections based broadly on their application or production route and are ordered, approximately, by their contribution to radiative forcing.

2.2.1.1 HFC-134a (CH_2FCF_3)

HFC-134a is the most abundant HFC and contributes the most to total HFC radiative forcing. Its lifetime in the atmosphere is approximately 14 years, and its 100-year Global Warming Potential (GWP) is approximately 1470 (*Annex*). It is used as a refrigerant in mobile and domestic refrigerators and freezers, a blend component for stationary air-conditioning and commercial refrigeration, a foam-blowing agent, and a propellant for pharmaceutical and industrial aerosols (**Table 2-1**). In some applications, lower-GWP refrigerants, such as HFO-1234yf and HFO-1234ze(E), are starting to replace HFC-134a (UNEP, 2017).

The global annual mean mole fraction reached 113 ± 2 ppt in 2020, up from 89 ± 1 ppt in 2016 (average of AGAGE and NOAA data; UCI results over this period are 111 ± 2 ppt in 2020, up from 92 ± 2 ppt in 2016; **Table 2-2** and **Figure 2-1**). The change in mole fraction between 2016 and 2020 was 24 ± 2 ppt (26 ± 2%), which is similar, within uncertainty, to that during the four-year period (2012–2016) examined in the previous Assessment. This observed increase in global mole fraction is similar to that projected in Velders et al. (2015). The global abundance in 2020 contributed to a radiative forcing of 19.5 ± 0.3 mW m^{-2}, the highest of any HFC.

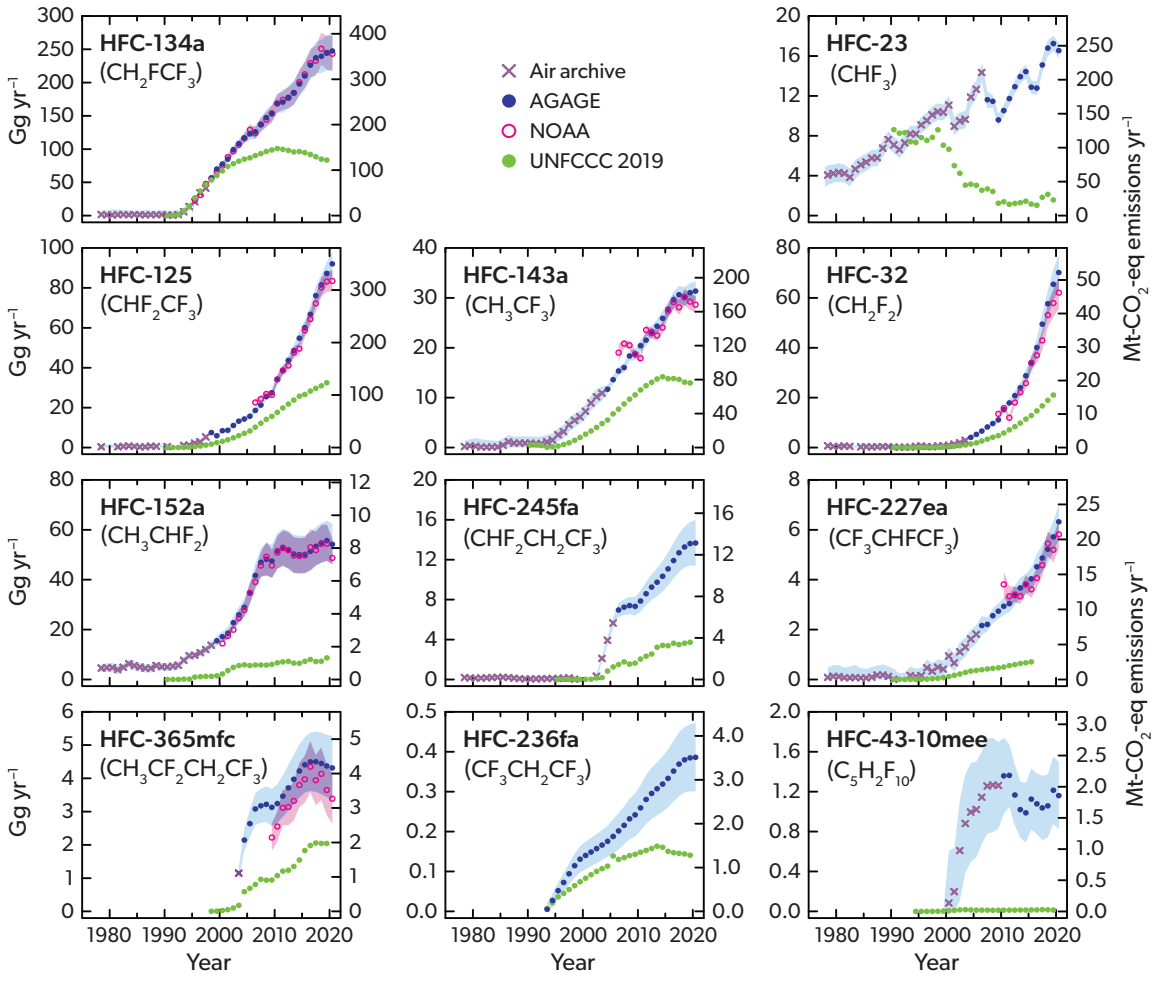

Figure 2-2. Global emissions derived from background atmospheric measurements and Annex I emissions reports to the UNFCCC. Emissions shown as blue circles are derived from five background AGAGE stations, filtered to remove measurements that are strongly influenced by regional sources. Purple crosses show global emissions derived from AGAGE measurements of the Cape Grim Air Archive. Red open circles show emissions derived from NOAA measurements in the remote atmosphere. Global emissions are derived from the AGAGE 12-box model, with steady state lifetimes as in **Table 2-1** and the *Annex*, using the method described in Rigby et al. (2014). Left-hand axes show emissions in Gg yr^{-1}, and the right-hand axes show CO_2-eq emissions. Shading indicates 1-sigma uncertainties and includes contributions from measurement and model error, as well as due to lifetime and calibration scale uncertainty. Green filled circles show the total emissions from Annex I countries reported to the UNFCCC (2019).

Upper-tropospheric distributions of HFC-134a between 45°S and 45°N in the altitude range 10.5–14.5 km are measured from orbit as mole fractions by ACE-FTS (Fernando et al., 2019; Bernath et al., 2021). The latitude and altitude ranges are different from those used in the previous Assessment (60°S to 60°N) due to ACE-FTS retrieval problems below 10 km. These observations indicate that HFC-134a in the upper troposphere increased from 85.5 ± 0.3 ppt in 2016 to 109.8 ± 0.2 ppt in 2020 (**Figure 2-1**; Fernando et al., 2019; Bernath et al., 2020; Harrison et al., 2021). Uncertainties in these quantities represent the standard deviation in the mean and do not include potential systematic errors, which are likely to be substantially larger. The upper-tropospheric trend observed from ACE-FTS is consistent with the trends derived from the surface-based AGAGE and NOAA measurements.

Total global emissions of HFC-134a estimated from inverse analysis of mole fractions at remote sites increased from 228 ± 21 Gg yr^{-1} in 2016 to 245 ± 27 Gg yr^{-1} in 2020 (average of AGAGE and NOAA inversions, which differ from each other by about 1%; **Table 2-2** and **Figure 2-2**). Previous Assessments noted a near-linear rise in HFC-134a emissions since the early 1990s. The updated observations indicate that the growth in emissions has slowed substantially since the previous Assessment (Montzka, Velders et al., 2018); the increase in emissions between 2016 and 2020 was approximately 18 ± 3 Gg yr^{-1} (8 ± 1%), compared to a rise of 51 ± 3 Gg yr^{-1} (28 ± 2%) between 2012 and 2016. The 2020 HFC-134a emissions were equivalent to 361 ± 40 Tg CO_2-eq yr^{-1}.

While global top-down emissions of HFC-134a have grown, the totals reported to the UNFCCC by Annex I countries have declined from 92 Gg yr^{-1} in 2016 to 84 Gg yr^{-1} in 2019 (the last year available at the time of writing). Therefore, the discrepancy between the UNFCCC reported emissions and global top-down values, noted in the previous Assessment, has increased to around 160 Gg yr^{-1} in 2019. This gap is approximately three times the total reported emissions (**Figure 2-3**). Montzka, Velders et al. (2018) described numerous regional top-down studies, which indicated that emissions from the major reporting regions, primarily the USA and Europe, were similar to, or slightly lower than, the emissions estimates reported to UNFCCC by these two regions. Therefore, it was proposed that the gap was most likely due to emissions from non-reporting countries, although it is possible that underreporting has occurred from Annex I countries that are not well observed by atmospheric measurement networks.

Atmospheric measurement–based emissions estimates for the USA and Europe were discussed in the previous Assessment. Since then, additional studies have become available that support the conclusion that underreporting by UNFCCC Annex I countries does not explain the discrepancy with global top-down estimates. In Europe, new measurements of HFC-134a were carried out on the island of Crete, and these were combined with long-term measurements in Ireland, Switzerland, and Italy (Schoenenberger et al., 2018). These measurements allowed new estimates to be made of emissions from central and western Europe and the eastern Mediterranean. The top-down estimates of aggregated HFC-134a emissions for reporting countries in the domain were 51% (37–69%) lower than the UNFCCC reports (total top-down emissions were 18.6 [16.7–20.6] Gg yr^{-1} for this domain). In Australia, top-down emissions of around 1 Gg yr^{-1} were derived, around half of the value reported to the UNFCCC (Dunse et al., 2018) and only ~0.4% of global total emissions.

For non-Annex I countries, new top-down and bottom-up estimates have become available for India and China only. Two

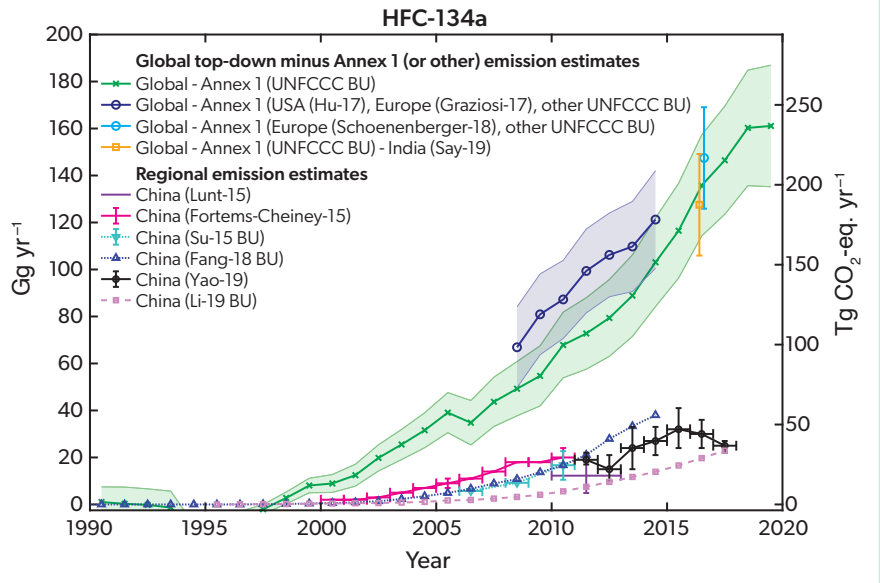

Figure 2-3. Difference between global HFC-134a emissions derived from atmospheric observations (AGAGE and NOAA mean) and UNFCCC reports from Annex I countries (green line and crosses with shading represent 1-sigma uncertainty). The dark blue line with open circles and shading shows the same but with UNFCCC reports for the USA and Europe replaced by regional inversion results from Hu et al. (2017) and Graziosi et al. (2017), respectively. Similarly, the light blue circle and error bar shows the global difference but with European UNFCCC reports replaced by top-down values from Schoenenberger et al. (2018). A set of bottom-up or top-down regional emissions estimates are shown for China in broken or solid lines, respectively. Top-down estimates are from Lunt et al. (2015) in purple, Fortems-Cheiney et al. (2015) in magenta, and Yao et al. (2019) in black. Bottom-up estimates are from Su et al. (2015) in dotted cyan, Fang et al. (2018) in dotted blue with triangular points, and Li et al. (2019) in a light pink dashed line with square data points. The contribution of emissions from India is indicated in the gold square and error bar, which represents the global top-down/UNFCCC difference minus the Indian emissions estimate from Say et al. (2019).

bottom-up studies by Li et al. (2019) and Fang et al. (2018) estimate rapidly increasing emissions of HFC-134a in China through 2017 and 2014, respectively (**Figure 2-4**). However, the estimates by Li et al. (2019) are about half that by Fang et al. (2018), at 14 Gg yr^{-1} and 38 Gg yr^{-1} in 2014, respectively. Top-down estimates by Yao et al. (2019) use flask and in situ measurements from seven observatories in China between 2011 and 2017. The top-down estimates also exhibit an increase during this period, although with substantial interannual variability. The average top-down emissions estimate from this study falls between the two bottom-up estimates, with emissions of 25 (22–27) Gg yr^{-1} for 2017. In India, air samples were collected at low altitudes during an aircraft campaign in June and July 2016 (Say et al., 2019). National emissions of HFC-134a derived from these observations were 8.2 (6.1–10.7) Gg yr^{-1}. Based on these top-down studies, India and China could account for around 25% of the difference between global top-down HFC-134a emissions estimates and UNFCCC reports (**Figure 2-3**). The remaining missing emissions probably occur in countries for which sparse atmospheric monitoring precludes the estimation of regional emissions and/or that do not report to the UNFCCC.

2.2.1.2 HFC-23 (CHF_3)

The radiative forcing due to HFC-23 was the third largest of the HFCs in 2020 (down from the second largest in the previous Assessment). It has the longest lifetime (228 years) and highest 100-year GWP (14,700) of the HFCs described here (*Annex*). In contrast to the other, more abundant HFCs, the majority of HFC-23 in the atmosphere has not been released following its intentional use (**Table 2-1**). Instead, it is primarily a by-product that is vented during the production of other compounds. The major focus of previous work on HFC-23 has been its emissions during the production of HCFC-22 (e.g., Oram et al., 1998; Miller et al., 2010; Miller and Kuijpers, 2011; Simmonds et al., 2018; Stanley et al., 2020). There is also evidence that HFC-23 can be released during the production of tetrafluoroethylene (TFE) and hexafluoropropylene (HFP) from HCFC-22 (Sung et al., 2006; Ebnesajjad, 2015; *Section 7.2.2.1*). However, there has not been an assessment of the quantities recycled within production facilities or potential contributions of these sources to global total emissions. Compared to by-product emissions from HCFC-22 production, smaller emissions are associated with the use of HFC-23 as a feedstock for halon-1301 production, as a plasma etching chemical and chamber-cleaning agent in the semiconductor industry, as a

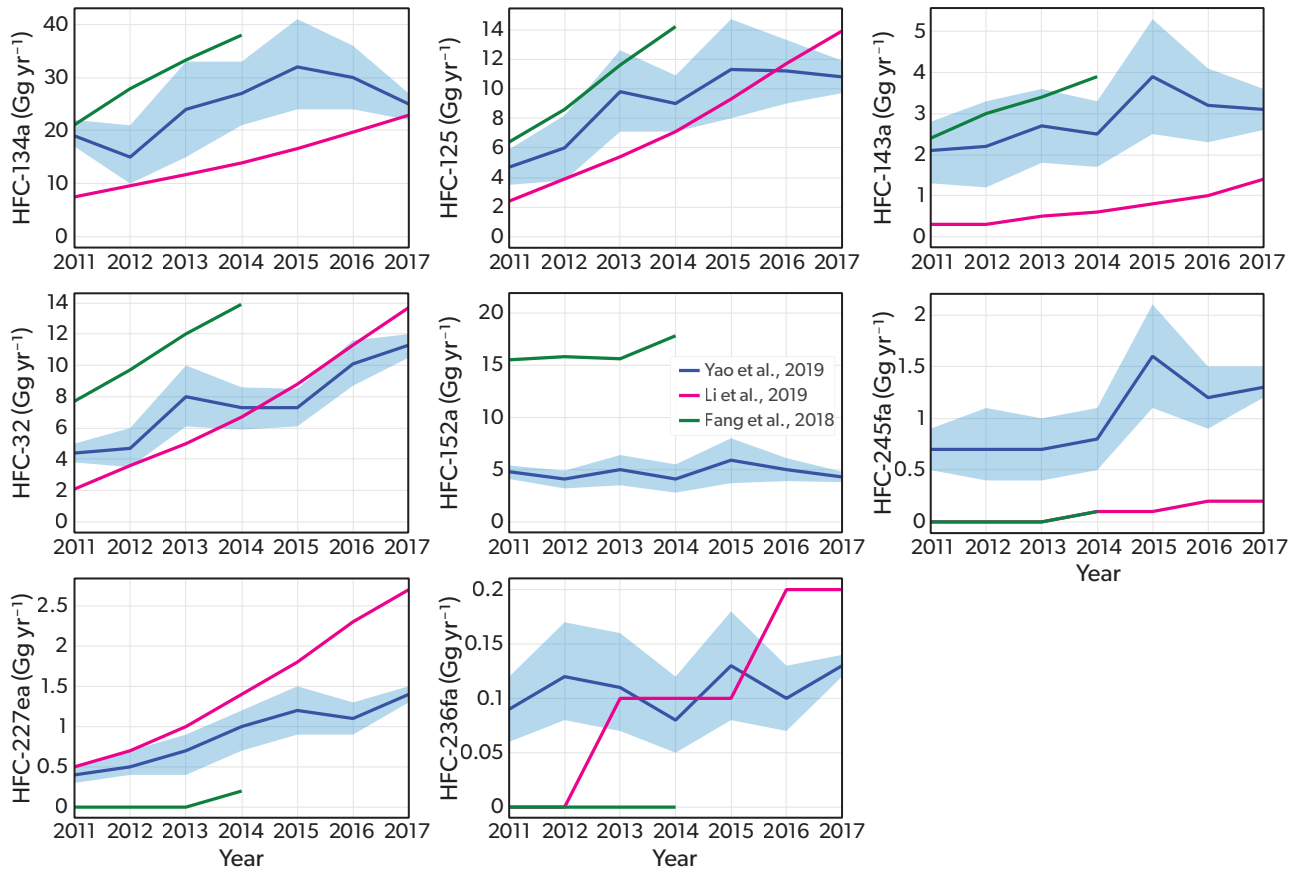

Figure 2-4. Emissions of the major HFCs (excluding HFC-23 and HFC-43-10mee) from China. Top-down estimates from Yao et al. (2019) are shown in blue, including 1-sigma uncertainties as shaded areas. Bottom-up estimates are from Li et al. (2019) in red and Fang et al. (2018) in green.

very low-temperature refrigerant, and as a specialty fire-suppression agent.

The abundance of HFC-23 continues to increase in the global atmosphere and reached 33.7 ± 0.9 ppt in 2020, compared to 28.9 ± 0.7 ppt in 2016 (AGAGE data; **Table 2-2** and **Figure 2-1**). The previous Assessment (Montzka, Velders et al., 2018) noted a reduction in growth rate from around 1.1 ppt yr^{-1} to 0.9 ppt yr^{-1} between 2014 and 2016. This trend has since reversed, with growth reaching 1.3 ppt yr^{-1} around 2018/19, the highest rate yet recorded (Stanley et al., 2020). The overall change in mole fraction between 2016 and 2020 was 4.8 ± 1.1 ppt (17 ± 4%), compared to 4.0 ± 1.0 ppt (16 ± 4%) between 2012 and 2016. The radiative forcing due to HFC-23 was 6.5 ± 0.2 mW m^{-2} in 2020.

HFC-23 concentrations in the upper troposphere from ACE-FTS through 2020 are shown in **Figure 2-1** (Fernando et al., 2019; Bernath et al., 2021). These upper-tropospheric means for latitudes 60°S and 60°N were approximately 15–20% lower than surface-based estimates from the AGAGE network. The ACE-FTS growth rate was also smaller than that observed in the AGAGE network, with an increase from 2016 to 2020 of 3.6 ± 0.1 ppt (14 ± 1%). As with HFC-134a, the uncertainties quoted here represent the standard deviation in the mean and do not include potential systematic errors, which are likely to be substantially larger. Ground-based column-average observations of HFC-23 based on FTIR measurements at Rikubetsu, Japan, and Syowa Station, Antarctica (Takeda et al., 2021), exhibited similar trends to those based on the AGAGE measurements at similar latitudes, but the column mole fractions were around 15% lower on average.

The previous Assessment (Montzka, Velders et al., 2018) noted a decline in emissions derived from remote AGAGE measurements between 2014 and 2016. Stanley et al. (2020) found that this trend had since reversed and that emissions had grown to 15.9 ± 0.9 Gg yr^{-1} in 2018. Updates presented here show an additional rise to 17.2 ± 0.8 Gg yr^{-1} in 2019, and a similar value of 16.5 ± 0.8 Gg yr^{-1} in 2020 (**Table 2-2** and **Figures 2-2** and **2-5**). The 2020 emissions of HFC-23 were equivalent to 243 ± 12 Tg CO_2-eq yr^{-1}.

Global inventory-based (bottom-up) emissions estimates are derived from publicly accessible information, as outlined in Stanley et al. (2020) and shown in **Figure 2-5**. For Annex I parties to the UNFCCC, annual HFC-23 emissions reports are available (UNFCCC, 2021). For countries not obliged to report to the UNFCCC, HFC-23 by-product generation is calculated by multiplying reported HCFC-22 production by estimates of HFC-23 by-product formation per mass of HCFC-22 produced. From these totals, reported abatement is subtracted, based on information from the UNFCCC Clean Development Mechanism (CDM) or national programs.

For Annex I parties to the UNFCCC, reported emissions have been relatively low during the last decade. Other than in 2018, reported emissions have remained below 2 Gg yr^{-1} since 2008. Between 2016 and 2018 growth was reported, predominantly driven by emissions from fluorochemical production. However, a decrease to 1.6 Gg yr^{-1} was subsequently reported in 2019 (**Figure 2-2**).

HCFC-22 production totals and HFC-23 by-product weights were taken from information provided to UNEP under Article 7 of the Montreal Protocol and made publicly available through reports of the UN Multilateral Fund (MLF; UNEP, 2018a, 2018b) and the Technology and Economic Assessment panel (TEAP; UNEP, 2020b). The TEAP report suggests that China is the largest producer of HCFC-22, accounting for 61% of global production in 2018; India is the next largest, accounting for less than 10% (UNEP, 2020b). The HCFC-22 production amounts from China suggest the generation of 14 Gg yr^{-1} of HFC-23 by-product in 2018 (UNEP, 2020a).

Between 2006 and 2014, the amount of HFC-23 by-product abated before reaching the atmosphere was taken from CDM reports (Stanley et al., 2020). Since 2015, China has reported to the MLF increasing HFC-23 abatement at its HCFC-22 production facilities, reaching 45%, 93%, 98%, and 99.8% HFC-23 destruction in 2015, 2016, 2017 and 2018, respectively (UNEP, 2018a, 2018b, 2020c). An executive order in India required HCFC-22 producers to destroy all HFC-23 by-product from October 2016 onward (MEFCC, 2016).

These bottom-up considerations suggest an overall growth of HFC-23 by-product generation from non-Annex I countries between 1990 and 2019 (**Figure 2-5**, dashed red line), reflecting an increase in global total HCFC-22 production. However, when abatement is considered, a substantial reduction in emissions to the atmosphere is estimated during the CDM period (2006–2014) and from 2015 (**Figure 2-5**, top panel, solid red line). Updated global bottom-up emissions were 2.2 Gg yr^{-1} in 2019. The previous Assessment (Montzka, Velders et al., 2018) presented substantially lower bottom-up HFC-23 emissions in 2014 and 2015 (based on Simmonds et al., 2018) than is shown here. This disagreement is due to revisions in reported HCFC-22 production and HFC-23 by-product weights that resulted from verification programs that occurred since the last Assessment (UNEP, 2018a, 2018b, 2020c). Furthermore, it was assumed in the estimates used in the previous Assessment that abatement installed during the CDM period would continue after the scheme closed, whereas the updated estimates rely only on reported abatement amounts.

Up until 2013, global bottom-up emissions track (within ± 2 Gg yr^{-1}) the global emissions derived from atmospheric measurements (**Figure 2-5**, top panel; Miller et al., 2010; Simmonds et al., 2018; Stanley et al., 2020). Similarly, up until 2013, the ratio of HFC-23 emissions to HCFC-22 production (E_{23}/P_{22}) derived from atmospheric data closely matched that derived from bottom-up estimates (**Figure 2-5**, bottom panel). As reported in Stanley et al. (2020), between 2013 and 2015, top-down emissions grew more slowly than expected based on HCFC-22 production data and the decline in abatement reported under the CDM, which had been operating since 2006. They proposed that this change can be explained by new emissions from newly installed, and at least partly unabated, HCFC-22 production capacity, combined with the switching off of some, but not all, abatement installed before or during the CDM period. Between 2015 and 2019, as reported abatement increased dramatically in China and India, bottom-up emissions and E_{23}/P_{22} declined substantially (**Figure 2-5**). However, emissions and E_{23}/P_{22} derived from atmospheric data increased. By 2019, the difference between top-down and bottom-up emissions and E_{23}/P_{22} was the largest since atmospheric records began. Stanley et al. (2020) concluded that this discrepancy was most likely the result of the reported emissions abatement, primarily from China, not being fully realized, or substantial new unreported HCFC-22 production. Stanley et al.

(2020) estimated that only 27% of the reported global abatement capacity was achieved in 2018.

A small number of regional top-down studies have provided additional information on the spatial distribution of global HFC-23 emissions. However, none of these studies can explain the discrepancy between bottom-up and top-down global emissions after 2016. Using aircraft data collected over India in June and July 2016 (prior to the Indian government's executive order to incinerate HFC-23 by-product from HCFC-22 production), Say et al. (2019) derived emissions of 1.2 Gg yr^{-1} for a region in the northern part of the country comprising 72% of the Indian population and four of five known HCFC-22 manufacturing plants. In China, Pu et al. (2020) carried out observations in the Yangtze River Delta region between 2012 and 2016. They estimated that their measurements were sensitive to the Shanghai, Zhejiang, Jiangsu, and Anhui provinces, as well as to nine fluorine chemistry plants producing HCFC-22, comprising around 46% of national emissions. Using a tracer ratio method, with carbon monoxide as the reference tracer, emissions of 2.4 ± 1.4 Gg yr^{-1} were derived for this region. Manning et al. (2021) derived United Kingdom (UK) emissions of HFC-23 that were not statistically different from zero for most years between 2008 and 2020. The derived emissions were broadly consistent with the UK National Inventory Report, which suggests very small emissions (<0.1 Gg yr^{-1}).

2.2.1.3 HFC-32 (CH_3F_2), HFC-125 (CHF_2CF_3), HFC-143a (CH_3CF_3)

Current radiative forcing due to HFC-32, HFC-125, and HFC-143a, which are primarily used as HCFC substitutes in refrigerants (**Table 2-1**), are the fifth, second, and fourth largest of the HFCs, respectively. They have lifetimes of 5.4, 30, and 51 years and 100-year GWPs of 749, 3820, and 5900 (*Annex*). The abundances of all three compounds have increased in the background atmosphere since the previous Assessment, with global surface mean mole fractions in 2020 of 23.4 ± 0.7 ppt for HFC-32, 32.7 ± 1.6 ppt for HFC-125, and 25.6 ± 0.8 ppt for HFC-143a (AGAGE and NOAA mean; **Figure 2-1** and **Table 2-2**). The increases between 2016 and 2020 were 11.4 ± 0.8 ppt (94 ± 4%), 12.1 ± 1.9 ppt (59 ± 7%), and 6.4 ± 1.0 ppt (33 ± 4%), respectively. Except for HFC-143a, these increases are larger, in absolute terms, than the change between 2012 and 2016. However, they are smaller than the increases projected by Velders et al. (2015; second row of **Figure 2-1**), which was the basis for the baseline scenario for HFC projections in the previous Assessment. The radiative forcings in 2020 due to these species were 3.0 ± 0.1 mW m^{-2} (HFC-32), 8.0 ± 0.4 mW m^{-2} (HFC-125), and 4.4 ± 0.1 mW m^{-2} (HFC-143a).

Global top-down emissions in 2020 were 66 ± 7 Gg yr^{-1} for HFC-32, 88 ± 6 Gg yr^{-1} for HFC-125, and 30 ± 2 Gg yr^{-1} for HFC-143a (mean of AGAGE and NOAA inversions, **Figure 2-2**). The increases in their emissions between 2016 and 2020 were 28 ± 1 Gg yr^{-1} (72 ± 2%), 22 ± 1 Gg yr^{-1} (34 ± 1%), and 0.6 ± 0.9 Gg yr^{-1} (2 ± 3%), respectively. The year-to-year emissions growth rate declined during this four-year period for all three compounds. HFC-143a exhibited the most marked slowdown, with overall growth not significantly different from zero between 2016 and 2020. The 2020 emissions of these substances were equivalent to 50 ± 5 Tg CO_2-eq yr^{-1} (HFC-32), 335 ± 22 Tg CO_2-eq yr^{-1} (HFC-125), and 177 ± 11 Tg CO_2-eq yr^{-1} (HFC-143a).

Since the previous Assessment, emissions reported to the UNFCCC have increased for HFC-32 and HFC-125 (reaching 21

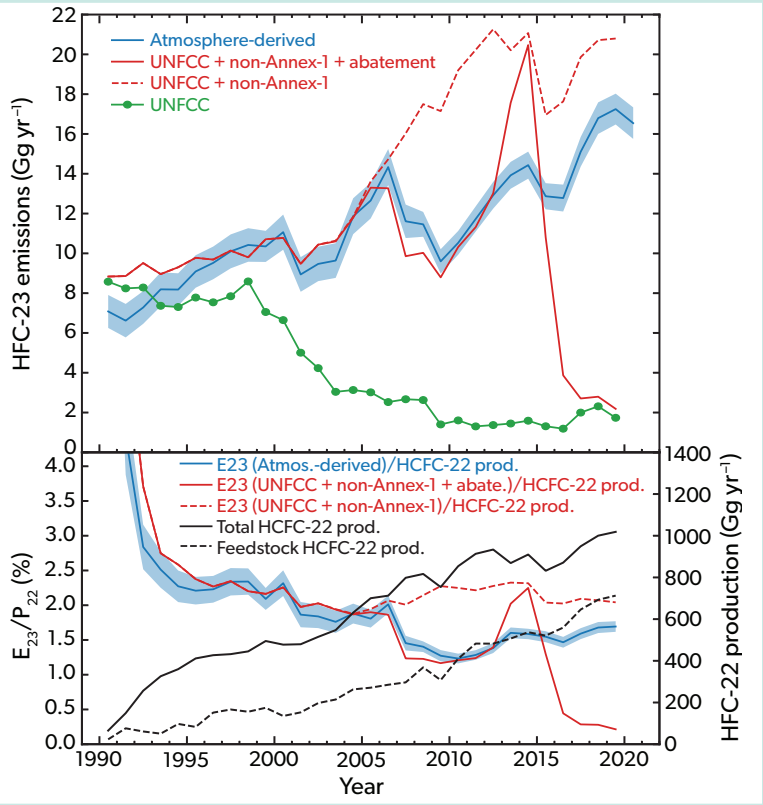

Figure 2-5. HFC-23 global emissions and HFC-23/HCFC-22 production ratio (updated from Stanley et al., 2020). *(top panel)* Top-down emissions estimates derived from AGAGE data are shown in blue (1-sigma uncertainty shown in blue shading). The dashed red line shows the sum of emissions reported to the UNFCCC and a bottom-up estimate for non-Annex I countries based on HCFC-22 production reported to the Multilateral Fund (MLF) and an HFC-23 emissions factor. The solid red line shows the same but includes abatement of HCFC-22 production-related emissions. Abatement estimates are derived from reports under the UNFCCC Clean Development Mechanism, reports to the MLF of abatement after 2015 by China and the assumed complete abatement of HCFC-22 production emissions in India due to an executive order in 2016. Emissions reported to the UNFCCC (2021) are shown in green. *(lower panel)* Total (solid black line) and feedstock (dashed black line) production of HCFC-22 (right-hand axis). The blue line shows the ratio of top-down HFC-23 emissions to HCFC-22 production (E23/P22). The solid and dashed red lines show the same, but for E23 derived from bottom-up methods either with (solid) or without (dashed) the reported abatement, respectively.

Gg yr^{-1} and 32 Gg yr^{-1} in 2019, respectively), and have slightly fallen for HFC-143a (13 Gg yr^{-1} in 2019). The drop in reported emissions for HFC-143a likely follows from a reduction in its use in the European Union (EU) ahead of its 2020 phaseout in favor of lower-GWP alternatives in commercial refrigeration (Velders, et al., 2022; *Section 2.4.1*). The gap between these reports and global emissions derived from atmospheric observations has grown for all three species (**Figures 2-6** to **2-8**). For 2019, UNFCCC reports represented 34%, 38%, and 43% of global top-down emissions for HFC-32, HFC-125, and HFC-143a, respectively.

Updated top-down emissions have been derived for several UNFCCC Annex I countries. These studies support the conclusions of the previous Assessment that the gap between reported and top-down emissions could not be explained by underreporting to the UNFCCC for countries that are monitored by atmospheric observations. Top-down estimated emissions of HFC-125 and HFC-143a in 2013 were smaller than, or consistent with, the reported emissions for central and western Europe and the eastern Mediterranean (Schoenenberger et al., 2018). For the UK, top-down emissions estimates were lower than inventory-based estimates for HFC-125 and HFC-32 from the early 2000s to 2018 (Manning et al., 2021). For HFC-143a, the top-down values were similar to the UNFCCC reported emissions between 2010 and 2016, but in the subsequent years, top-down values rose above inventory estimates. For all three gases, UK emissions were estimated to be less than 2% of the global total derived from AGAGE and NOAA observations. Similarly, top-down emissions for Australia were estimated to be less than 2% of global emissions for each of these gases between the early 2000s and 2016 (Dunse et al., 2018). Substantial over-reporting of HFC-125 was found in the Australian inventory (top-down values around 50% lower) and underreporting for HFC-32 and HFC-143a (top-down estimates two to three times higher).

Among non-Annex I countries that do not regularly report to the UNFCCC, top-down or bottom-up studies have been conducted in China, India, and South Africa. These studies suggest that some, but not all, of the gap between the global top-down estimates and UNFCCC reports can be explained by emissions from these countries (**Figures 2-6** to **2-8**). In China, growing top-down emissions of HFC-32, HFC-125, and HFC-143a were derived for 2011 to 2017, reaching 11.3 (10.5–12.0) Gg yr^{-1}, 10.8 (9.7–11.9) Gg yr^{-1}, and 3.1 (2.6–3.6) Gg yr^{-1}, respectively, at the end of the study period (Yao et al., 2019). These emissions could explain around 20–40% of the difference between UNFCCC reports and the global top-down estimates for these gases. Similar to HFC-134a, the top-down estimates for HFC-125 and HFC-143a emissions from China of Yao et al. (2019) mostly fall between inventory-based estimates of Li et al. (2019) and Fang et al. (2018), while the HFC-32 emissions estimates are slightly lower in recent years. Based on a spatially and temporally sparse aircraft dataset collected during the summer of 2016, Say et al. (2019) estimated Indian emissions of 6.4 (5.2–7.8) Gg yr^{-1} for HFC-125 and 0.8 (0.4–1.2) Gg yr^{-1} for HFC-143a. These emissions could account for around 5–17% of the global difference between top-down estimates and UNFCCC reports for these two species. For HFC-32, Say et al. (2019) derived Indian emissions that were only ~2% of the gap. Using measurements from Cape Point, Kuyper et al. (2019) estimated small emissions of HFC-125 from South Africa (~1% of global emissions, after extrapolation of emissions derived in the vicinity of Cape Point to the whole country based on population density).

2.2.1.4 HFC-152a (CH_3CHF_2)

HFC-152a is the seventh-largest contributor to radiative forcing of the HFCs. Compared to the other major HFCs, it has a relatively short atmospheric lifetime of 1.6 years and a low GWP (relative to other HFCs) of 153 over a 100-year time horizon (*Annex*). This species is mainly used as a propellant for specialized industrial aerosols, as a blowing agent component for extruded polystyrene foams, and recently as a replacement for HFC-134a in some automobile air-conditioning systems (**Table 2-1**).

As reported in the previous Assessment (Montzka, Velders et al., 2018), the growth of HFC-152a in the background atmosphere slowed substantially between 2012 and 2016 compared to the preceding decade. This trend has continued, with HFC-152a exhibiting a relatively small increase of 0.33 ± 0.29 ppt (5 ± 4%) between 2016 and 2020, reaching 7.1 ± 0.2 ppt in 2020 (mean of AGAGE and NOAA data; **Figure 2-1** and **Table 2-2**). This slowdown contrasts with the projected continuing growth during this period in Velders et al. (2015). The radiative forcing of climate due to HFC-152a was 0.9 ± 0.03 mW m^{-2} in 2020.

Global emissions of HFC-152a derived from observations in the background atmosphere did not change significantly between 2016 and 2020. They were 51 ± 8 Gg yr^{-1} in 2020, a change of –0.7 ± 0.9 Gg yr^{-1} (–1 ± 2%) relative to 2016 (AGAGE and NOAA mean; **Figure 2-2**). Although HFC-152a has the fourth-largest mass emissions of the HFCs because of its relatively short lifetime and lower (relative to other HFCs) GWP, the CO_2-equivalent emissions of HFC-152a were only the ninth largest in 2020, at 8 ± 1 Tg CO_2-eq yr^{-1}.

Emissions of HFC-152a reported to the UNFCCC have increased slightly since those reported in the previous Assessment (8.6 Gg yr^{-1} in 2019 compared to 7.3 Gg yr^{-1} in 2015; **Figure 2-2**), but the substantial discrepancy between top-down and reported emissions remains, at 46 Gg yr^{-1} in 2019. The UNFCCC reports accounted for 16% of the global top-down values in that year. As noted in the previous Assessment, much of this difference could be attributed to the USA not reporting HFC-152a emissions explicitly but instead aggregating them with several other compounds (including HFC-227ea, HFC-245fa, and HFC-43-10mee). Regional top-down studies confirmed that substantial emissions (~10–30 Gg yr^{-1}) originated from the USA around the period 2004–2012 (Stohl et al., 2009; Miller et al., 2012; Barletta et al., 2011; Lunt et al., 2015; Simmonds et al., 2016).

Recent top-down studies in Europe, the eastern Mediterranean, and Australia have confirmed that these regions are relatively small contributors to global total HFC-152a emissions. Emissions for western and central Europe and the eastern Mediterranean were inferred to be 2.8 (2.3–3.3) Gg yr^{-1} in 2013 (Schoenenberger et al., 2018), accounting for around 5% of global emissions. For Annex I countries in the domain, emissions were consistent with, or lower than, those reported to the UNFCCC. Emissions of less than 0.1 Gg yr^{-1} (or around 0.1% of global emissions) were inferred for Australia between 2003 and 2016 (Dunse et al., 2018).

Regional inverse estimates from the non-Annex I countries China and India suggest that emissions from these regions do not contribute substantially to the difference between the top-down global total and the global UNFCCC reports. Yao et al. (2019) made a top-down estimate of HFC-152a emissions in China, and these were generally consistent with top-down estimates

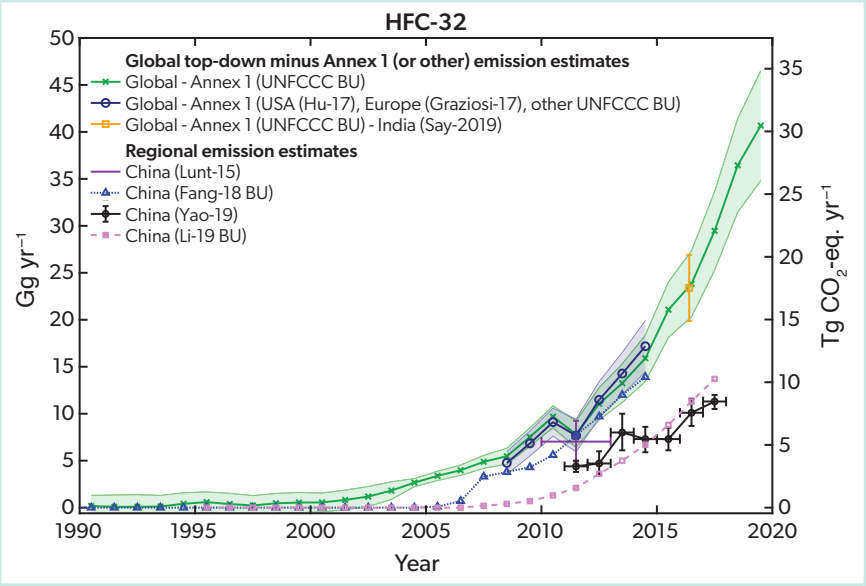

Figure 2-6. As in **Figure 2-3**, but for HFC-32.

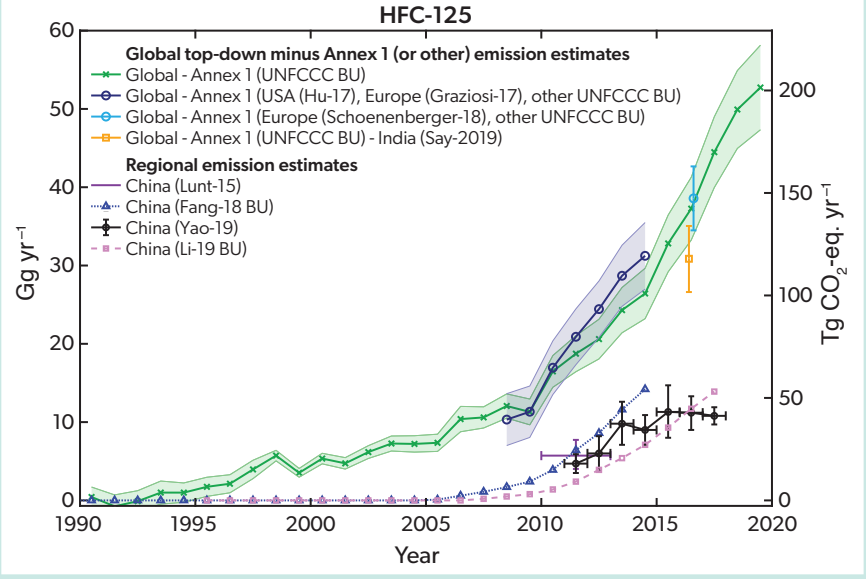

Figure 2-7. As in **Figure 2-3**, but for HFC-125.

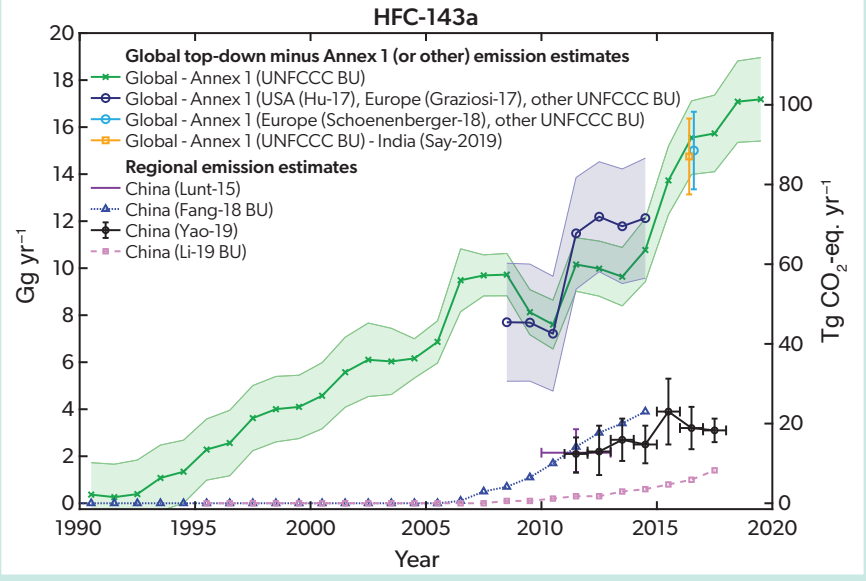

Figure 2-8. As in **Figure 2-3**, but for HFC-143a.

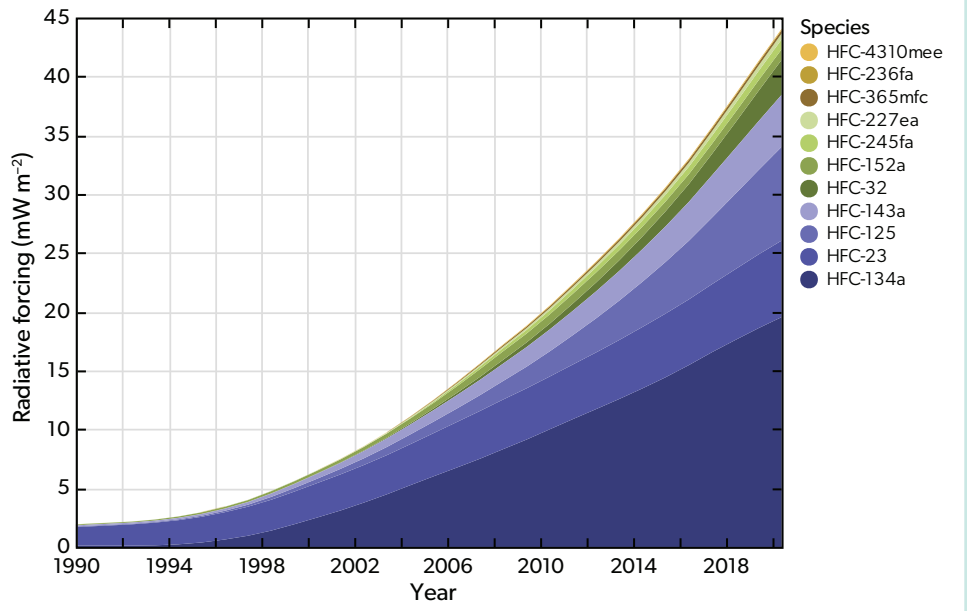

Figure 2-9. Radiative forcing due to HFCs derived from AGAGE mole fractions and the radiative efficiencies given in the *Annex*.

presented in the previous Assessment (Montzka, Velders et al., 2018). Both were substantially lower than the emissions from the bottom-up studies of Fang et al. (2016, 2018) (**Figure 2-4**). Top-down Chinese HFC-152a emissions were found to be relatively stable at ~5 Gg yr^{-1} (~10% of global emissions) during the 2011–2017 period (Yao et al., 2019). Based on measurements from an aircraft campaign in June and July 2016, Say et al. (2019) estimate that HFC-152a emissions from India were 1.2 (0.9–1.4) Gg yr^{-1}, contributing around 2% to global emissions.

2.2.1.5 HFC-245fa ($CHF_2CH_2CF_3$), HFC-365mfc ($CH_3CF_2CH_2CF_3$), HFC-227ea (CF_3CHFCF_3), HFC-236fa ($CF_3CH_2CF_3$)

HFC-245fa, HFC-365mfc, HFC-227ea, and HFC-236fa are present in the atmosphere at lower abundances than the above species (<5 ppt in 2020). Correspondingly, they have relatively small radiative forcings, making between the 6th and 11th most important contributions to overall HFC radiative forcing. Their lifetimes span a wide range, from 7.9 (HFC-245fa) to 213 years (HFC-236fa), and 100-year GWPs range from 969 (HFC-365mfc) to 9120 (HFC-236fa) (*Annex*). HFC-245fa and HFC-365mfc are used primarily as blowing agents replacing HCFC-141b and others in the production of foam products (**Table 2-1**). HFC-227ea is used as a fire suppressant, primarily replacing halon-1211 in streaming applications and halon-1301 in total flooding situations. HFC-227ea is also used with HFC-134a as a propellant in metered dose inhalers and, with HFC-365mfc, in foam blowing to reduce flammability. HFC-236fa is used in niche refrigeration applications.

The abundances of all four compounds have grown since the previous Assessment, reaching 3.2 ± 0.3 ppt (HFC-245fa; AGAGE data), 1.1 ± 0.2 ppt (HFC-365mfc; AGAGE and NOAA), 1.8 ± 0.1 ppt (HFC-227ea; AGAGE and NOAA) and 0.20 ± 0.04 ppt (HFC-236fa; AGAGE) in 2020 (**Figure 2-1** and **Table 2-2**). The growth of HFC-245fa, HFC-227ea, and HFC-236fa is roughly consistent with the projections of Velders et al. (2015), but the projected growth of HFC-365mfc was higher than has been observed. Together, these species contributed 1.6 mW m^{-2} to radiative forcing of climate in 2020.

Global emissions derived from atmospheric observations in the background atmosphere have increased since the previous Assessment for HFC-245fa, HFC-227ea, and HFC-236fa, while those of HFC-365mfc may have decreased slightly. Emissions in 2020 were 13.7 ± 2.3 Gg yr^{-1} (HFC-245fa; AGAGE), 6.1 ± 0.6 Gg yr^{-1} (HFC-227ea; AGAGE and NOAA), 3.9 ± 0.9 Gg yr^{-1} (HFC-365mfc; AGAGE and NOAA), and 0.39 ± 0.09 Gg yr^{-1} (HFC-236fa; AGAGE). The sum of the 2020 emissions of these four compounds was equivalent to approximately 42 Tg CO_2-eq yr^{-1}.

Emissions reported to the UNFCCC represented only a fraction of the global top-down estimates for each of these compounds. For HFC-245fa, HFC-227ea, HFC-365mfc, and HFC-236fa, Annex I reports represented 27%, 23%, 51%, and 37% of their global top-down total, respectively. However, as noted in the previous Assessment, much of this discrepancy likely stems from the fact that many countries report these species aggregated with others as an "unspecified mix" without sufficient information to disaggregate the mix.

Regional estimates of emissions from China, the UK, and Australia have become available since the last Assessment (Montzka, Velders et al., 2018). For China, top-down estimates were about 10–40% of the global total for these HFCs in 2017 (Yao et al., 2019; **Figure 2-4**). For HFC-245fa, the top-down values were substantially higher than the bottom-up estimates of Li et al. (2019) and Fang et al. (2018). For HFC-227ea, the top-down values were between the two bottom-up studies, and for HFC-236fa, they were similar to the bottom-up estimates of Li et al. (2019). (Fang et al., 2018, estimated zero emissions of HFC-236fa until the end of the study period in 2014.) Top-down Australian emissions estimates account for less than 2% of the global total in 2016 for all four compounds (Dunse et al., 2018). Similarly, top-down UK emissions estimates of HFC-227ea were around 1% of the global top-down value in 2018 (Manning et al., 2021). The UK

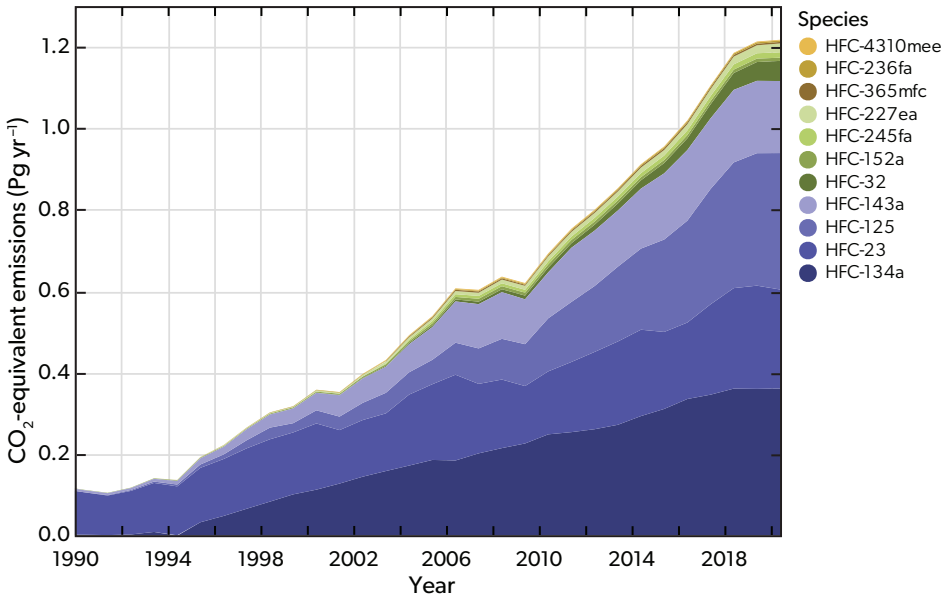

Figure 2-10. CO_2-equivalent emissions of the HFCs, as derived from AGAGE and NOAA concentration data and the 100-year GWPs from **Table 2-1** and in the *Annex*.

top-down emissions were around half of those reported by the UK to the UNFCCC.

2.2.1.6 HFC-43-10mee ($CF_3CHFCHFCF_2CF_3$)

HFC-43-10mee is the 10th-largest contributor to HFC radiative forcing, with a lifetime of 17 years and a 100-year GWP of 1610. It is used as a solvent in electronics and precision cleaning, replacing CFC-113 and methyl chloroform (**Table 2-1**). Its abundance in the atmosphere continues to increase, growing by 0.03 ± 0.03 ppt (13 ± 12%) between 2016 and 2020 and reaching 0.30 ± 0.02 ppt in 2020 (AGAGE data, **Table 2-2** and **Figure 2-1**). The radiative forcing due to HFC-43-10mee in 2020 was 0.11 ± 0.01 mW m^{-2}. Emissions derived from observed concentrations at remote AGAGE stations have not changed significantly since 2016 and were 1.2 ± 0.3 Gg yr^{-1} in 2020 (**Figure 2-2**), about 80 times higher than the most recent bottom-up UNFCCC reports. The 2020 emissions were equivalent to 1.9 ± 0.5 Tg CO_2-eq yr^{-1}.

2.2.2 Summed Radiative Forcing and CO_2-eq Emissions for HFCs

The summed radiative forcing due to the HFCs has increased by around one-third (11.0 ± 0.7 mW m^{-2}) since the previous Assessment, reaching 44.1 ± 0.6 mW m^{-2} in 2020 (**Figure 2-9**; AGAGE data). HFC-134a accounts for around 44% of this total, with the next-largest contributions coming from HFC-125 (18%), HFC-23 (15%), and HFC-143a (10%). Since the previous Assessment, radiative forcing due to HFC-125 has overtaken that of HFC-23. The radiative forcing due to the HFCs was around 13% that of the ODSs in 2020 (*Chapter 1*) and approximately 2% of that of CO_2 (https://gml.noaa.gov/aggi/aggi.html).

Total CO_2-eq emissions due to the HFCs were 1.22 ± 0.05 Pg CO_2-eq yr^{-1} in 2020, 19% higher than in 2016 (**Figure 2-10**). Of this total, HFC-134a was responsible for approximately 30%, HFC-125 for 28%, HFC-23 for 20%, and HFC-143a for 15%. The remaining species contributed less than 5% each. Chapter 2 of the last Assessment (Montzka, Velders et al., 2018) noted that GWP-weighted emissions from HFCs, HCFCs, and CFCs were similar in 2016. In 2020, because of the continuing decline in CFC and HCFC emissions and the growth of HFCs, CO_2-equivalent total emissions due to HFCs were 60–70% higher than those of CFCs or HCFCs (see *Chapter 1*).

2.2.3 Aggregate Emissions of HFCs Reported to the UNFCCC and Contributions from Non-reporting Countries

In the above subsections, the gap between top-down emissions and those reported to the UNFCCC is described for each species. For all the HFCs for which UNFCCC reports are available, this gap has grown since the previous Assessment (except for HFC-365mfc, for which the gap slightly declined). When considered in aggregate CO_2-eq emissions, the 2019 UNFCCC reports explain 31% (including HFC-23) or 37% (excluding HFC-23) of the top-down global total, down from 38% or 45% in 2015, respectively (**Figure 2-11**).

The cause of the gap between UNFCCC reports and global top-down emissions estimates is not well understood. The gap is likely dominated by emissions from non-Annex I countries, which are not required to report emissions to the UNFCCC. As also described in the previous Assessment and above, regional inverse modeling studies have not found evidence of underreporting of aggregate HFC emissions from Europe, the USA, or Australia (e.g., Lunt et al., 2015; Hu et al., 2017; Schoenenberger et al., 2019; Manning et al., 2021; Dunse et al., 2018). The measurement network used to infer top-down emissions is not sensitive to all reporting countries, but because the USA and Europe accounted for approximately three-quarters of total reported Annex I emissions in 2019, it is unlikely that underreporting in the remaining Annex I countries can account for a substantial fraction of the overall emissions gap. For non-Annex I countries, top-down emissions by Yao et al. (2019) suggest that, excluding HFC-23, around 21% of the 2017 gap (and 25% of the 2016 gap) could be explained by emissions from China (**Figure 2-11**). Top-down

emissions from India (Say et al., 2019) suggest that around 9% of the 2016 gap (both excluding or including HFC-23) could be explained by emissions from India, although there may be large uncertainty in this estimate, as it is based on a single aircraft sampling campaign that took place over a limited time period (approximately two months) and did not sample air representative of emissions from the entire country. Total emissions from South Africa in 2017, for HFC-125 and HFC-152a only, contribute less than 1% of the gap (Kuyper et al., 2019). For 2016, the year with emissions estimates for both China and India, the origin of around 40% of global CO_2-equivalent HFC emissions remained unaccounted for by UNFCCC reporting and atmospheric measurement-based regional emissions estimates (excluding HFC-23, for which top-down estimates are not available for China). These emissions likely originate primarily from non-Annex I countries where a lack of inventory reporting and sparse or non-existent atmospheric sampling preclude the robust quantification of regional emissions.

2.2.4 Next-Generation Substitutes

Unsaturated HFCs, known as hydrofluoroolefins (HFOs), have been increasingly used as lower-GWP alternatives to saturated HFCs or in blends with high-GWP HFCs. Although these compounds have GWPs similar to that of CO_2 (*Annex*), their atmospheric lifetimes are on the order of days (*Annex*), much shorter than saturated HFCs. These species are not subject to the controls of the Kigali Amendment to the Montreal Protocol.

To the best of our knowledge, there are no comprehensive global datasets on the production and consumption of HFOs. However, some atmospheric observations indicate growing regional emissions. Vollmer et al. (2015) reported atmospheric measurements of HFO-1234yf and HFO-1234ze(E) at an urban (Dubendorf) and a remote (Jungfraujoch) site in Switzerland. They also reported on measurements of the unsaturated HCFC (hydrochlorofluoroolefin) HCFO-1233zd(E) (see *Chapter 1*). Here, the Jungfraujoch measurements are updated through 2020 (**Figure 2-12**). The measurements show that the background atmospheric abundances of both compounds in central Europe have continued to grow, from less than 0.01 ppt before 2016 to annual median levels of 0.10 and 0.14 ppt for HFO-1234yf and HFO-1234ze(E), respectively, in 2020.

2.3 ATMOSPHERIC CHEMISTRY OF HFCs

2.3.1 Update on Kinetics and Lifetimes

HFCs are removed from the atmosphere primarily by reaction with the hydroxyl radical (OH) in the troposphere. Reaction with electronically excited atomic oxygen ($O(^1D)$) and OH in the stratosphere also contributes to the loss of long-lived HFCs and impacts their lifetimes slightly. Other loss processes include photolysis at the Lyman-α wavelength (mainly 121.6 nm) and dissolution into the ocean. The photochemical degradation at the Lyman-α wavelength is applicable to extremely long-lived species that can reach the mesosphere, and the oceanic loss is applicable only to a few soluble species, such as HFC-134a, HFC-125, and HFC-23 (Yvon-Lewis and Butler, 2002). Both processes have negligible impacts on total atmospheric lifetime of HFCs and therefore are not considered in the lifetime calculation. A comprehensive list of atmospheric lifetimes of HFCs, as well as HFOs, can be found in the *Annex*. The best-estimate lifetimes for major HFCs remain unchanged since the last Assessment.

2.3.2 Chemical Reactions and Impact on Atmospheric Composition

Following OH-initiated destruction of HFCs and HFOs in the atmosphere, carbon dioxide (CO_2) and hydrogen fluoride (HF) are the major stable breakdown products. Some of these

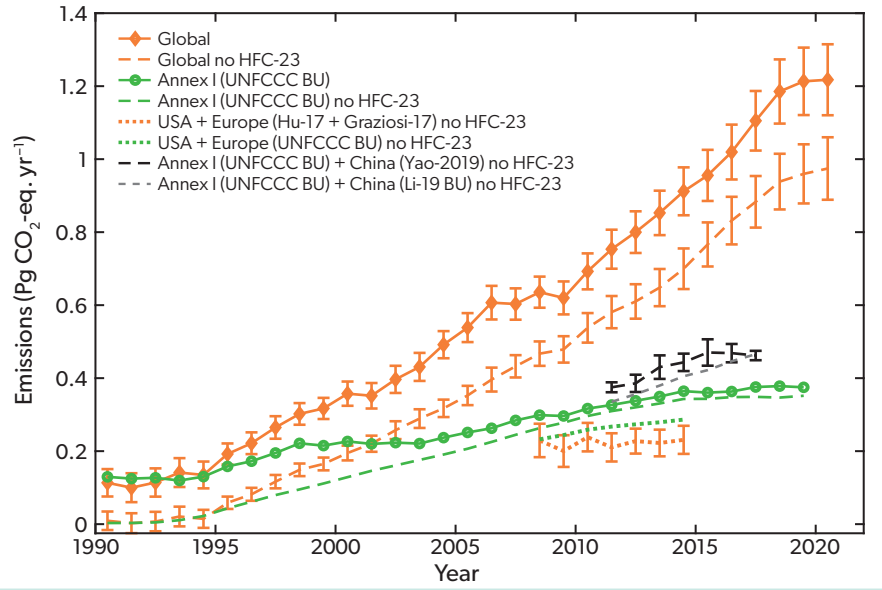

Figure 2-11. Summed CO_2-eq emissions from top-down estimates compared to those using UNFCCC reported emissions. Global aggregated HFC emissions derived from AGAGE and NOAA data are shown as the orange lines (solid, including HFC-23; dashed, excluding HFC-23). Emissions reported by Annex I countries to the UNFCCC are shown as the green lines (solid, including HFC-23; dashed, excluding HFC-23). Summed reported HFC emissions for the USA and Europe (excluding HFC-23) are shown as the dotted green line, and top-down estimate for the same regions are shown as the orange dotted line (Graziosi et al., 2017; Hu et al., 2017). The sum of the UNFCCC reported emissions (excluding HFC-23) and top-down (Yao et al., 2019) or bottom-up (Li et al., 2019) emissions from China are shown as black dashed or gray dashed lines, respectively. Error bars represent 1-sigma uncertainties.

fluorocarbons also produce trifluoroacetic acid (TFA; CF_3COOH), trifluoroacetaldehyde (CF_3CHO), and, potentially, HFC-23 as products.

2.3.2.1 Trifluoroacetic Acid (TFA, CF_3COOH) Formation

Some HFCs, as well HCFCs, HFOs, and HCFOs, degrade in the atmosphere to produce TFA. TFA abundance and its environmental impacts have been assessed in many previous Assessments (e.g., Montzka, Reimann et al., 2011; Montzka, Velders et al., 2018; Carpenter, Daniel et al., 2018). Previous Assessments concluded that the environmental effects of TFA due to the breakdown of HCFCs and HFCs are too small to be a risk to the environment over the next few decades based on the projected future use of hydrocarbons, HCFCs, and HFOs. However, they also recommended that environmental effects of TFA produced from these gases be reevaluated regularly because their emissions are increasing and sources and sinks of TFA are uncertain (Montzka, Reimann et al., 2011; Montzka, Velders et al., 2018; Carpenter, Daniel et al., 2018).

HFOs that have atmospheric lifetimes on the order of days are used as lower-GWP alternatives to the long-lived HFCs (lifetime >1 year, see *Annex*). In particular, HFO-1234yf has been increasingly used as an HFC-134a replacement refrigerant in mobile air conditioners (MAC). If the same amount of short-lived HFOs were used as replacement for the long-lived HFCs, their atmospheric breakdown would occur at a much faster rate and at locations much closer to where they were emitted. As a result, the deposition of TFA formed from degradation of these compounds would be much larger over a shorter time frame and become more localized. In this section, we assess the impact of this transition from HCFCs and long-lived HFCs to short-lived HFOs and focus on the HFC-134a to HFO-1234yf transition and how this affects TFA abundance. Projected future global production of TFA and its deposition rate related to projected HFC-134a and HFO-1234yf emissions for 2020–2100 are presented in *Chapter 7*.

TFA is highly soluble and is scavenged from the atmosphere via rain, fog, and snow, as well as dry deposition. Some fraction of the TFA dissolved in cloud water can partition back into the gas phase when the cloud water evaporates. More than 90% of TFA is physically removed from the atmosphere via wet and dry deposition (about 80% via wet deposition and 10% via dry deposition; Holland et al., 2021), with an estimated global mean deposition lifetime of about 5–10 days (Hurley et al., 2004; Holland et al., 2021). TFA is also chemically destroyed in the atmosphere by OH. This is estimated to be a minor loss channel (about 6%; Holland et al., 2021), with a global mean partial lifetime against OH of ~4 months (Chiappero et al., 2006). Criegee intermediate chemistry, under which ozone reacts with biogenic emissions of alkenes (Chhantyal-Pun et al., 2017), is a minor contribution to overall global TFA loss (<1%) but is important near the surface in the forested regions where biogenic emissions are high (Holland et al., 2021). Once in contact with soil or surface water, TFA reacts with minerals to form salt. TFA in salt form is extremely stable and persistent in the hydrosphere, with a hydrospheric half-life of centuries or greater (Solomon et al., 2016), so it accumulates in lakes and the ocean.

TFA is present ubiquitously in the hydrosphere in small concentrations. In surface freshwater, TFA levels are typically 10–300 ng L^{-1} (Carpenter, Daniel et al., 2018). TFA in freshwater is most likely a result of industrialization, as no detectable level (<2–5 ng L^{-1}) of TFA was found in very old groundwater or in preindustrial freshwater samples (Berg et al., 2000; Nielsen et al., 2001). This is consistent with the findings from ice core samples (Pickard et al., 2020), where deposition of TFA to the Arctic environment was essentially absent until the 1970s and increased substantially after the onset of HFC-134a production and emissions. New rainwater TFA concentration measurements have been reported for Germany (Freeling et al., 2020). During a nationwide 12-month field monitoring campaign in Germany, the mean TFA concentration was 703 ng L^{-1} in 1187 collected and analysed precipitation samples (Freeling et al., 2020). TFA enters the environment directly and indirectly through industrial uses. It is manufactured as an industrial chemical and is widely used. It can also be formed during the breakdown of many ODSs and ODS substitutes that contain a CF_3 group (Solomon et al., 2016). Molar yields of TFA are estimated to be 100% for HFC-1234yf (Burkholder et al., 2015; Lindley et al., 2019) and HCFC-124 (Burkholder et al., 2015), 7–20% for HFC-134a (Wallington et al., 1994), and 60% for HCFC-133a (Burkholder et al., 2015). TFA is also formed from CF_3CHO, another degradation product of some HFCs, HFOs, and HCFOs (Chiappero et al., 2006). Formation of TFA from CF_3CHO can also occur in the aqueous phase. Research shows that about 20–33% of CF_3CHO will enter the water phase and is quickly hydrated (Rayne and Forest, 2016). A recent study suggests that after remobilization into the gas phase, hydrated aldehydes in cloud droplets can be converted to organic acids by reaction with OH radicals (Franco et al., 2021). This mechanism can potentially convert hydrated CF_3CHO to form TFA. For the time being, no global modeling study is available that fully accounts for all processes in the contribution of CF_3CHO to TFA formation.

TFA is present in the ocean even at great depths and in remote locations (Frank et al., 2002; Solomon et al., 2016; UNEP 2014). The reported consistent concentration of TFA at around 200 ng L^{-1} regardless of location or depth, down to the deepest parts of ocean (Frank et al., 2002), suggests small but ubiquitous natural sources in seawater. In contrast, Scott et al. (2005) found parts of the oceans that contained very little TFA, less than 10 ng L^{-1}. However, it is unclear how representative these measurements are for the global abundance of TFA in seawater. A comprehensive review of published TFA measurements in preindustrial and other environmental examples pointed out that there were limited analytical details and uncertainties in these earlier measurements (Joudan et al., 2021). As more sources of TFA are being identified and new plausible mechanisms are proposed that can potentially transport TFA into the deep ocean on decadal timescales or faster, the presence of TFA in the deep ocean may not provide sufficient evidence that TFA occurs naturally (Joudan et al., 2021).

Since the previous Assessment, there have been new global 3-D chemical transport modeling studies to assess TFA formation in hypothetical scenarios in which refrigerants in all MACs in existence today were assumed to contain solely HFO-1234yf. These studies estimated TFA formation and deposition in the USA, Europe, China, India, and the Middle East (Wang et al., 2018; David et al., 2021). In these studies, the global total deposition of TFA produced from HFO-1234yf degradation was estimated to be approximately 60 Gg yr^{-1}. The model-simulated annual total TFA deposition rates were 7.5 Gg yr^{-1} in the USA (Wang et al.,

2018), 5.9 Gg yr^{-1} in the EU (Wang et al., 2018), 19–24 Gg yr^{-1} in China (Wang et al., 2018; David et al., 2021), 12–21 Gg yr^{-1} in India (David et al., 2021), and 10–19 Gg yr^{-1} in the Middle East (David et al., 2021). The simulated TFA rainwater concentrations show large variation, but the regional mean concentrations were below the "no observable effect" concentration for most of the areas around the globe, suggesting that the environmental impacts are insignificant (David et al., 2021). In some parts of North Africa and the Middle East where precipitation is scarce, simulated TFA rainwater concentrations exceeded the no-effect level for the most sensitive algae (1.2×10^5 ng L^{-1}) (Solomon et al., 2016; Wang et al., 2018). However, this finding is based on a single model study, and there are large uncertainties in model-calculated precipitation amounts and TFA rainwater concentrations in regions with very low precipitation.

In Chapter 6 of the last Assessment (Carpenter, Daniel et al., 2018), HFC-134a was estimated to make the largest contribution of the HCFCs and HFCs to TFA formation globally. Atmospheric measurements in central Europe show that the mean background molar fraction of HFC-1234yf at Jungfraujoch has increased from <1 parts per quadrillion (ppq) in 2014 (Vollmer et al., 2015) to about 0.10 ± 0.07 ppt in 2020 (**Figure 2-12**, updated from Vollmer et al., 2015). With an abundance of about 0.10 ± 0.07 ppt, an atmospheric lifetime of 14 days, and 100% TFA molar yield, the breakdown of HFC-1234yf is estimated to form a comparable, or possibly larger, amount of TFA near Jungfraujoch than from the breakdown of HFC-134a (mean background abundance of 120.7 ± 2.9 ppt at Jungfraujoch in 2020, lifetime of 14 years, 7–20% TFA molar yield). Like HFC-1234yf, the atmospheric annual mean background concentrations of HFO-1234ze(E) and HCFO-1233zd(E) at Jungfraujoch have increased rapidly in the recent years to around 0.1 ppt in 2020 (*Section 2.2.4* and *Section 1.3.1.1*). If their atmospheric levels continue to grow in the coming years, their contributions to TFA formation need to be considered in the atmospheric TFA budget estimate. Due to the limited representativeness of Jungfraujoch measurements and the large spatial variability and uncertainties related to short-lived HFOs and their atmospheric chemical loss, it is difficult to assess the contribution of HFC-1234yf, and similarly HFO-1234ze(E) and HCFO-1233zd(E), to TFA formation on a global scale. Currently, the measured and model-simulated concentrations of TFA from the use of HFOs, HFCs, HCFCs, and HCFOs for present-day conditions in general remain significantly below known toxicity limits, but continued work is needed as updates to science are made, particularly for the regions that could be vulnerable to adverse impacts in future.

The transition from use of HFCs to HFOs will lead to more TFA and less HF formation. Both are substances considered potential contributors to acidification. Lindley et al. (2019) compared the acidification potential of HFCs, HFOs and HCFOs emissions in the EU and concluded that the relative acidification potential of these compounds is very similar and that these compounds contribute less than 0.5% of the main acidification air pollutants—sulfur dioxide (SO_2), nitrogen oxides (NO_x) and ammonia (NH_3)—resulting in an insignificant contribution to acidification both presently and up to at least 2030.

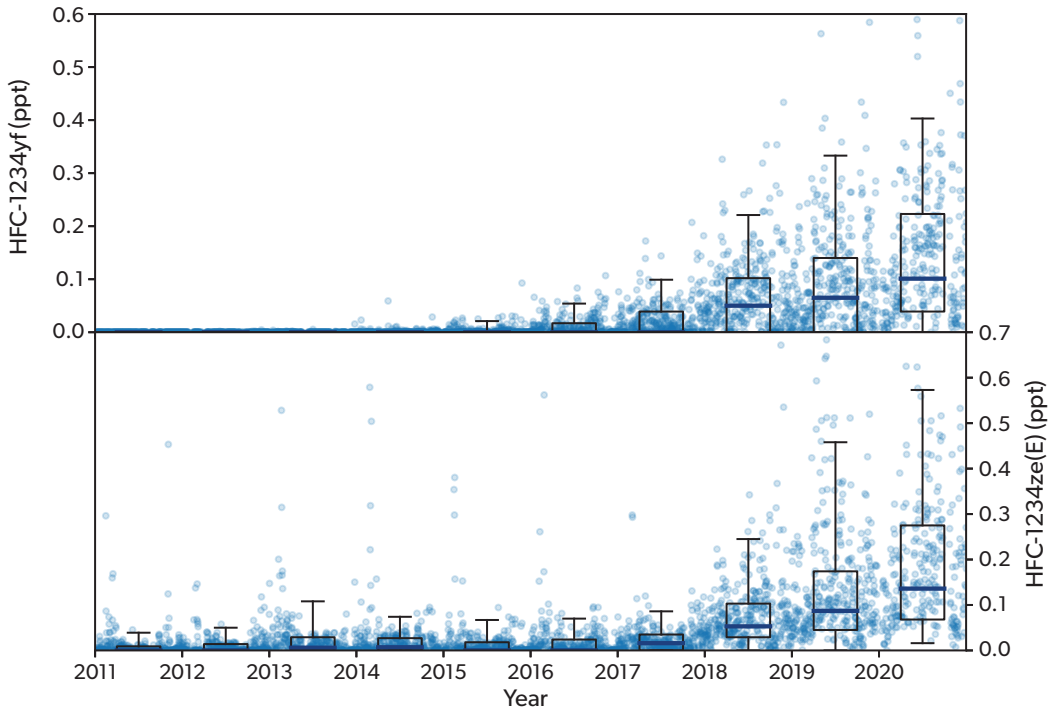

Figure 2-12. Measurements of HFO-1234yf and HFO-1234ze(E) at Jungfraujoch. Points show daily averages of data collected approximately every two hours. Boxes indicate the 25th and 75th percentiles of the two-hourly data within each year, and the whiskers show the 5th and 95th percentiles. The median is indicated by the thick gray line inside each box. [Updated from Vollmer et al., 2015.]

2.3.2.2 Trifluoroacetaldehyde (CF_3CHO) Formation and Impact

CF_3CHO is a minor degradation product of some fluorinated compounds and is linked to TFA chemistry (see above). CF_3CHO is primarily formed in the atmosphere during the degradation of HFC-143a, HFO-1234ze(E), and HCFO-1233zd(E), with a 100% CF_3CHO molar yield from each compound (Sulbaek Andersen et al., 2018; Burkholder et al., 2015). Photolysis of CF_3CHO can potentially form HFC-23 in the atmosphere (Chiappero et al., 2006; Burkholder, et al., 2015), although the significance of HFC-23 formation via this mechanism is not well quantified at present.

CF_3CHO is primarily removed from the atmosphere via photolysis, with a photolysis lifetime of a few days (Chiappero et al., 2006). Loss of CF_3CHO can also occur through reaction with OH radicals, with an OH partial lifetime of ~24 days (Scollard et al., 1993; Sellevåg et al., 2004). It has an additional minor loss mechanism by reacting with Cl radicals (Scollard et al., 1993; Burkholder, et al., 2015). CF_3CHO photolysis can proceed via three pathways at solar radiation wavelengths >290 nm (Chiappero et al., 2006; Burkholder, et al., 2015):

$$CF_3CHO + hv \longrightarrow CF_3 + HCO \quad \textit{(pathway 1)}$$
$$\longrightarrow CHF_3 + CO \quad \textit{(pathway 2)}$$
$$\longrightarrow CF_3CO + H \quad \textit{(pathway 3)}$$

Chiappero et al. (2006) reported a CF_3CHO total quantum yield of 0.17 ± 0.03 for pathway 1. The quantum yield of a photochemical reaction describes the number of molecules undergoing a photochemical event per absorbed photon. The quantum yield for pathway 2 is <0.02 at 308 nm, suggesting this is a negligible HFC-23 source (Chiappero et al., 2006). Updated photolysis experiments also found no detectable (<0.3%) production of CHF_3 during the photolysis of CF_3CHO under conditions representative of the troposphere (ambient pressures of air, N_2, or O_2 and with wavelengths ranging from 400 nm to 290–300 nm; Sulbaek Anderson and Nielsen, 2022).

Measurements at central European stations show an atmospheric mean background molar fraction of ~0.20 ppt for HFO-1234ze(E) and ~0.18 ppt for HCFO-1233zd(E) (update from Vollmer et al., 2015). Since HFO-1234ze(E) and HCFO-1233zd(E), like the long-lived HFCs, are predominantly destroyed by OH oxidation in the troposphere, with background concentrations of ~0.2 ppt (lower in more remote regions) and assuming a <0.3% CHF_3 formation rate during CF_3CHO photolysis, their contribution to HFC-23 formation in the atmosphere is negligible. With a global concentration of 25.8 ppt and a lifetime of 51 years, the contribution of HFC-143a to CF_3CHO and subsequent HFC-23 formation is also negligible.

2.3.2.3 Impact on Tropospheric Ozone

The atmospheric degradation of HFCs can contribute to tropospheric ozone formation, but their photochemical ozone creation potentials are very small (Montzka, Velders et al., 2018). There are no updates since the previous Assessment, and the impact of HFCs on tropospheric ozone formation are still estimated to be negligible. A recent modeling analysis by Sulbaek Andersen et al. (2018) assessed the impact on ozone formation of commercially relevant ODSs and HFCs replacing HFOs and HCFOs, including HCFO-1233zd, and concluded that they too will have a small impact.

2.4 POTENTIAL FUTURE CHANGES

In Chapter 2 of the previous Assessment (Montzka, Velders et al., 2018), scenarios were presented with projections of HFC consumption, emissions, and radiative forcing through 2050. These consisted of scenarios without national or international regulations on the use of HFCs (from Velders et al., 2015, and termed "baseline" scenarios in the previous Assessment) and scenarios with a phasedown of HFC production and consumption according to the 2016 Kigali Amendment to the Montreal Protocol (Montzka, Velders et al., 2018). In *Section 2.4.1* these scenarios are compared with emissions inferred from HFC observations through 2020. In *Section 2.4.2*, an updated Kigali Amendment scenario is presented based on updated consumption data, on updated emissions inferred from observations, on national policies in place in the EU, USA, and Japan, and on the phasedown schedule of the 2016 Kigali Amendment. Also presented are zero-production and zero-emissions scenarios, used to illustrate the hypothetical limit of the effects of further global policy options.

2.4.1 Comparison of WMO (2018) Scenarios with Inferred Emissions

The scenarios presented in Chapter 2 of the previous Assessment (Montzka, Velders et al., 2018) were based on HFC emissions and activity data reported to the UNFCCC up to 2011, HCFC consumption data reported to UNEP up to 2013, observations of HFC mixing ratios up to 2013, assumptions about growth in demand for HFCs, and assumptions on how much of this demand would be met by HFCs or not-in-kind alternatives (Velders et al., 2015). In **Figure 2-13**, the global CO_2-eq emissions from the 2018 scenario without control measures are compared with emissions inferred from measured global HFC concentration trends from the AGAGE and NOAA networks from 2010 to 2020. In contrast to *Section 2.2*, in this section, top-down global annual emissions were calculated using a 1-box atmospheric model, as in Velders et al. (2015), rather than the 12-box model. Because this model estimates annual emissions from the difference in mole fraction between subsequent Januarys, estimates are provided through 2019, rather than 2020. The global total HFC CO_2-eq emissions projected in the 2018 scenario without control measures exceed those derived from atmospheric observations by about 20% for the 2017–2019 period (**Figure 2-13**).

The smaller inferred emissions, compared to the 2018 scenario with no control measures, result largely from lower emissions of HFC-125 and HFC-143a (**Figure 2-14**). Top-down emissions are lower than those in the 2018 scenario without control measures for HFC-32, HFC-125, and HFC-143a: HFC-32 is 19% below the scenario averaged over 2017–2019; HFC-125, 25% below; and HFC-143a, about 40% below. The global top-down emissions of HFC-143a slowly increased up to 2015 and then were approximately constant from 2016 to 2019. HFC-143a is used mainly in the blend R-404A[2] in industrial and commercial refrigeration (ICR) applications. In the scenario without control measures, it was assumed that global consumption would increase following the growing demand for refrigeration applications, mainly in

[2] R404A is a blend, by mass, of 44% HFC-125, 52% HFC-143a, and 4% HFC-134a. Using the GWPs in the Kigali Amendment, it has a GWP of 3921.6.

developing countries, and the phaseout of HCFC-22 following the Montreal Protocol provisions. The fact that the global emissions of HFC-143a are significantly below the scenario and were approximately constant from 2016 to 2019 indicates that during the ongoing phaseout of HCFC-22, the ICR sector turned away from HFC-143a and employed non-HFC alternatives or switched to lower-GWP blends in larger amounts.

According to data reported to the UNFCCC (2021), the EU and USA have the largest reported use of HFC-143a of all Annex I countries (Velders et al., 2022). The use in the EU decreased by about 60% in 2017 compared to 2010. This decrease preceded the prohibition on the use of HFCs with a GWP larger than 2500 for commercial refrigeration applications, which is in effect from 2020 (EU, 2014). This is in line with a finding from TEAP (2019) that in Europe, R-404A has already been replaced by an HFC blend (R-452A[3]) without HFC-143a. In the USA, the use of HFC-143a increased by 14% in 2017 compared to 2010, and small increases are also seen in other developed countries. The net effect is that in 2017,the total Annex I use decreased by about 8% compared to 2010. Based on the decreased use of HFC-143a in developed countries and the trend in observed emissions, additional lines are added to **Figures 2-13** and **2-14** in which the 2018 scenario without control measures is adjusted for the period 2013–2020. In this adjusted scenario, the projected use of HFCs in ICR is reduced for developed countries following the UNFCCC reported reduction in HFC-143a use, and the use of HFCs in ICR in developing countries is held constant at the 2013 level. With these adjustments, the baseline emissions of HFC-143a and HFC-125 are close to the emissions inferred from observations (**Figure 2-14**). The adjusted emissions scenario ("Reduced HFC use in ICR" in **Figures 2-13** and **2-14**) more closely follow the emissions inferred from observations (NOAA and AGAGE in **Figures 2-13** and **2-14**).

2.4.2 Scenario Based on National Policies and the Kigali Amendment

An updated HFC scenario is constructed for the period 2019–2050, which takes into account updated trends in consumption and emissions, national regulations in place by 1 January 2021, and the provisions of the Kigali Amendment. The national regulations include the EU F-gas regulation (EU, 2014) and MAC directive (EU, 2006), the HFC phasedown in the USA (US EPA, 2021a), and regulations in Japan (METI, 2015). This scenario uses the same procedure as the baseline scenario in Velders et al. (2015).

The updated 2022 Kigali Amendment scenario starts with a consumption scenario without any national regulation or international protocols, after which the national regulations are applied, followed by the provisions of the Kigali Amendment. The scenario is based on detailed information reported by Annex I countries to the UNFCCC (2021) for individual HFCs per use sector from 1990 to 2018, HCFC consumption data from 1989 to 2019 reported by non-A5 and A5 countries to UNEP (2021), and observations of HFC mixing ratios up to 2020. In addition, data are used from historical HFC consumption in China for 1995–2017 derived from Chinese statistical data (Li et al., 2019) and HFC emissions of India for 2016 estimated from observed mixing ratios (Say et al., 2019).

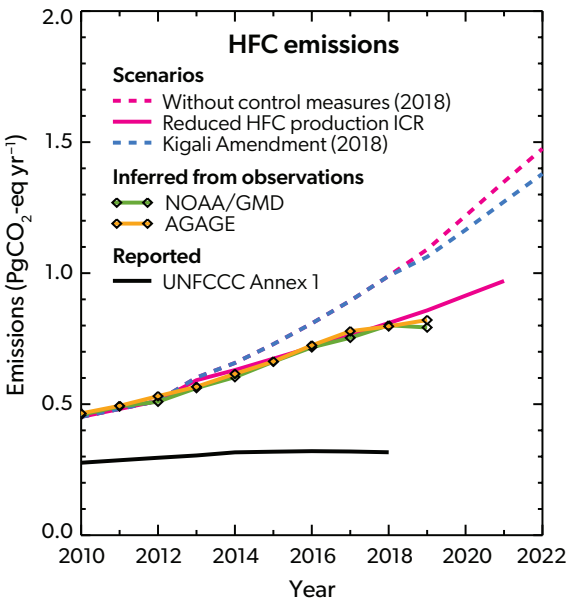

Figure 2-13. Global average HFC emissions ($PgCO_2$-eq yr^{-1}) from the WMO (2018) scenario without control measures (previously called the "baseline" scenario in Montzka, Velders et al., 2018, originating from Velders et al., 2015), from the 2018 Kigali Amendment scenario (Montzka, Velders et al., 2018), and from emissions inferred from observed mixing ratios from the AGAGE and NOAA networks. The solid red line shows an adjusted scenario with reduced HFC production for industrial and commercial refrigeration (ICR) from 2013 onward. The 2018 scenarios were constrained by the emissions inferred from observed mixing ratios up to 2013. Also shown are the emissions reported to the UNFCCC by Annex I countries. The curves contain the sum of all HFC emissions except HFC-23. [Figure from Velders et al., 2022.]

An upper and lower range of this scenario is constructed using the same assumptions for growth in demand for HFCs and not-in-kind alternatives in non-A5 and A5 countries as for the baseline scenarios from the previous Assessment (Velders et al., 2015; Montzka, Velders et al., 2018; Velders et al., 2022). As such, the demand in A5 countries grows proportionally with gross domestic product, and the demand in non-A5 countries grows proportional to the growth in population. Assumptions (see Velders et al., 2015) about how much of this demand was met by HFCs or not-in-kind alternatives follow those in the previous Assessment, except for the use of HFCs for ICR applications because the trends in observed mixing ratios indicate smaller use of HFCs in this sector (*Section 2.4.1*). Therefore, for A5 countries, the use of HFCs for ICR in the lower range is kept constant at the 2018 level. In non-A5 countries, the use of HFCs for ICR grows only slightly, following growth in population, as in the scenario without control measures of WMO (2018). The growth in some sectors might be underestimated in the scenarios when they are driven by new

[3] R-452A is a blend, by mass, of 11% HFC-32, 59% HFC-125, and 30% HFO-1234yf. Using the GWPs in the Kigali Amendment, it has a GWP of 2139.25.

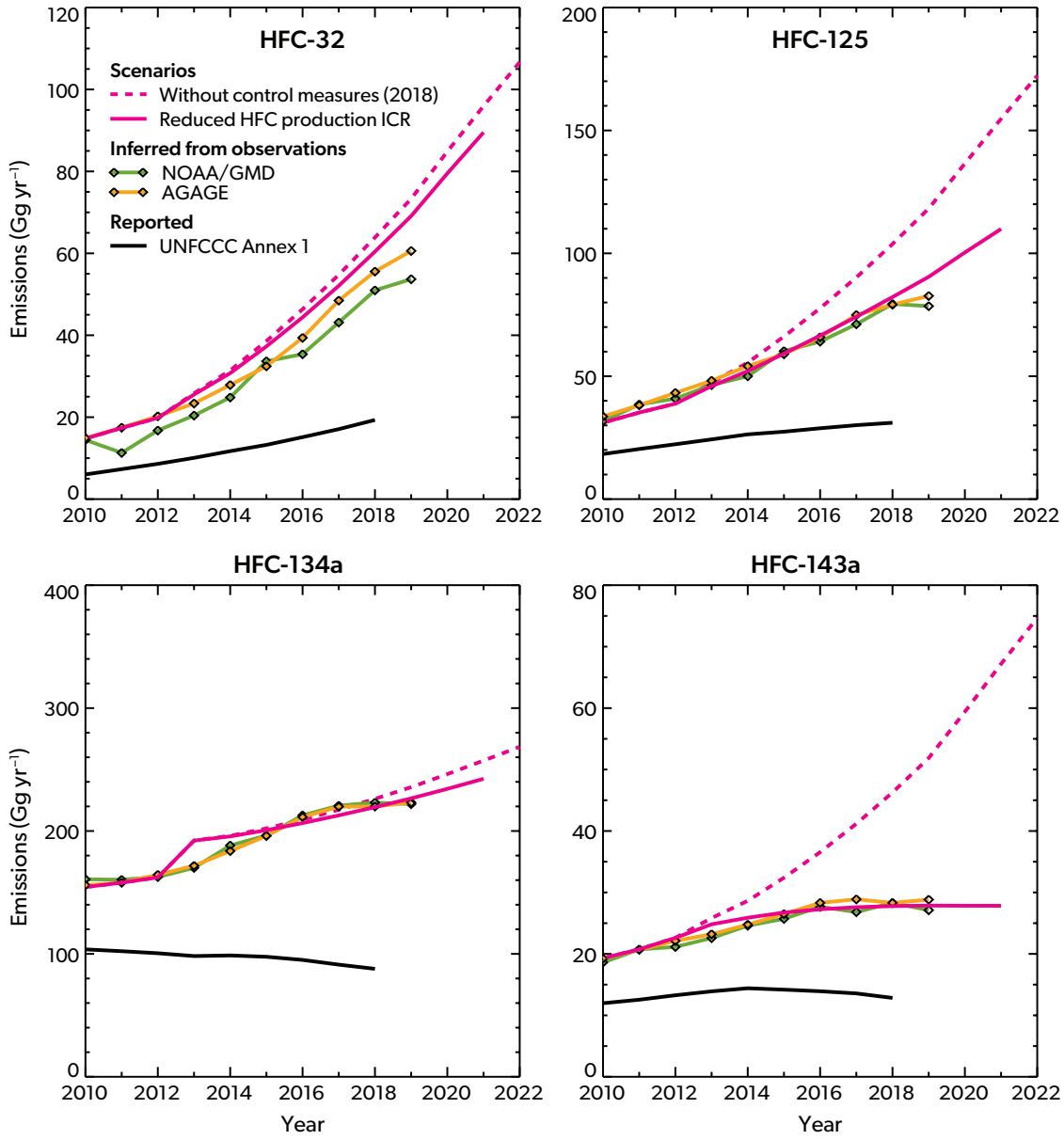

Figure 2-14. Global average HFC emissions (Gg yr^{-1}) from the 2018 scenario without control measures (previously called the "baseline" scenario) compared with emissions inferred from observed mixing ratios from the AGAGE and NOAA networks. The solid red line shows an adjusted scenario with reduced HFC production for industrial and commercial refrigeration (ICR) from 2013 onward. Also shown are the emissions reported to the UNFCCC by Annex I countries. The scenarios were constrained by the emissions inferred from observed mixing ratios up to 2013. [Figure from Velders et al., 2022.]

and strongly growing markets. An example could be heat pumps that replace gas boilers for heating buildings. See Velders et al. (2022) for details of the scenarios.

The policies already in place in the EU, USA, and Japan are applied to the scenario limiting the production and consumption in these (groups of) countries. The provisions of the 2016 Kigali Amendment are then applied. Any HFC consumption in excess of the limits of the national policies or the Kigali Amendment is assumed to be replaced by low-GWP alternative substances or alternative technologies.

The Kigali Amendment (2022 update) scenario is shown in **Figures 2-15** and **2-16**. The regional and sectoral contributions to HFC CO_2-eq emissions for the upper range of the scenario are shown in **Figure 2-15**, while the contributions of the different HFCs to global emissions by mass and weighted by their GWP in the upper range of the Kigali Amendment scenario are shown in **Figure 2-16**. The largest 2050 contributions are projected to be from China and other A5 countries. Stationary air-conditioning

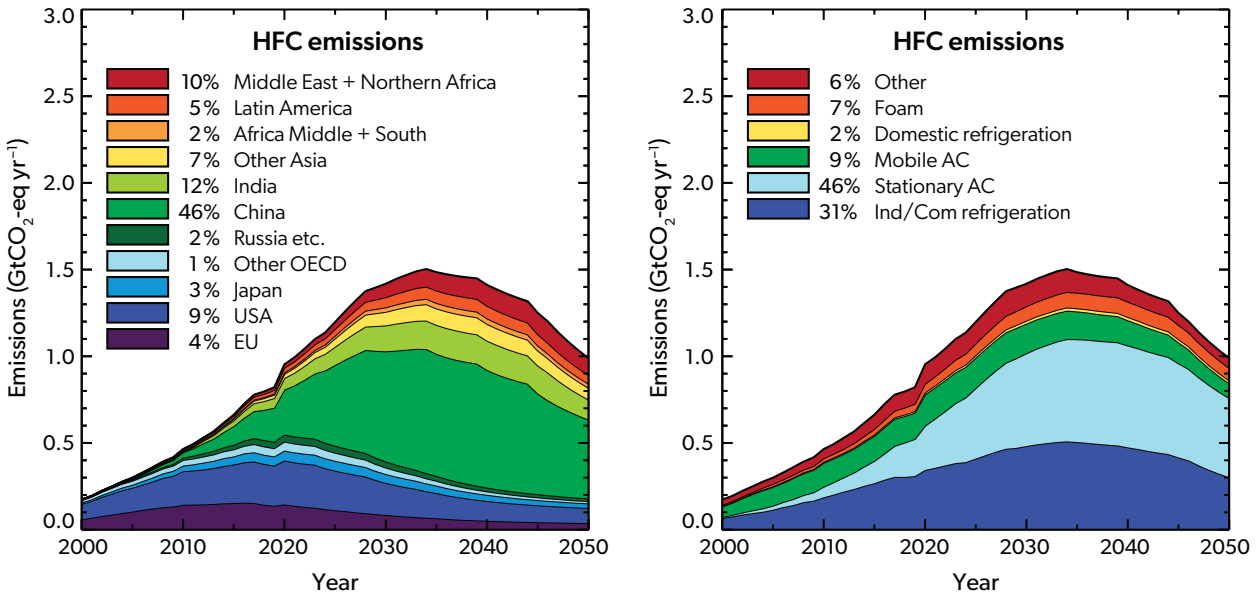

Figure 2-15. Contributions of the HFCs in 11 regions *(left)* and 6 use sectors *(right)* to the CO_2-eq emissions from the 2022 Kigali Amendment scenario based on updated observations and reported consumption, national policies, and the provisions of the Kigali Amendment (upper-range scenario). The percentages in the legend refer to the relative contributions in 2050. The regions are the EU and UK, USA, Japan, other Organization for Economic Co-operation and Development (OECD) countries, states of the former Soviet Republics (Russia) and Yugoslavia, China, India, other Asian countries, central and southern Africa, Latin America, and the Middle East plus Northern Africa. The use sectors are: 1) industrial, commercial (open compressor), commercial (hermetically sealed compressor), and transport refrigeration; 2) stationary air-conditioning; 3) mobile air-conditioning; 4) domestic refrigeration; 5) foams (extruded polystyrene, polyurethane, and open cell foams); and 6) other (aerosol products, fire extinguishing systems, and solvents). The data before 2020 are partly based on observed mixing ratios, while from 2020 to 2050 the data are based on the 2022 Kigali Amendment scenario, which causes some discontinuity around 2020. Contributions from HFC-23 are not included. The CO_2-eq emissions shown here are based on the GWPs from WMO (2018). Scenarios are from Velders et al. (2022).

and ICR are projected to give the largest sector contributions. The difference between the upper and lower ranges of these scenarios is small compared to that of the scenario without control measures.

Emissions from the Kigali Amendment (2022 update) scenario, assuming global adoption, are projected to be 0.9–1.0 Pg CO_2-eq yr^{-1} in 2050, compared to 4.0–5.3 Pg CO_2-eq yr^{-1} from the 2018 scenario without control measures (**Figure 2-17**). The corresponding radiative forcing in the 2018 "without control measures" scenario of 0.22–0.25 W m^{-2} is reduced to 0.09–0.10 W m^{-2} in 2050 under the Kigali Amendment (2022 update) scenario. The updated projections of the emissions and radiative forcing are lower than the Kigali Amendment scenario presented in the 2018 Assessment. Compared to that scenario, the 2020–2050 cumulative emissions are reduced by 14–18 Pg CO_2-eq and the 2050 radiative forcing is reduced by 0.03 W m^{-2}. In scenarios with a cessation in global production or emissions of HFCs in 2023, the projected emissions and radiative forcing are further reduced. If production of HFCs were to cease in 2023, the radiative forcing would be reduced to about 0.03 W m^{-2} in 2050, and would decline thereafter. Cumulative 2020–2050 emissions would be reduced by 21–26 Pg CO_2-eq relative to the Kigali Amendment (2022 update) scenario. If all emissions (from new production and from banks) ceased in 2023, radiative forcing due to HFCs would decline to 0.01 W m^{-2} by 2050, with cumulative emissions being reduced by 32–37 Pg CO_2-eq relative to the updated Kigali Amendment scenario (**Figure 2-17**). These scenarios are not necessarily achievable, but they provide useful information on the lower limits of future radiative forcing due to HFCs.

2.4.2.1 HFC-23 Scenarios

Unlike other HFCs, which have a phasedown schedule that extends over several decades, the Kigali Amendment mandates that "Each country manufacturing HCFC-22 or HFCs shall ensure that starting in 2020 the emissions of HFC-23 generated in production facilities are destroyed to the extent practicable using technology approved by the Montreal Protocol" (UNEP, 2016). Without abatement, HFC-23 emissions were projected to increase to ~20 Gg yr^{-1} by 2016 and ~24 Gg yr^{-1} by 2035 (Miller and Kuijpers, 2011). Emissions for 2020, derived from atmospheric observations, were 16.5 ± 0.9 Gg yr^{-1}, below the worst-case scenario in Miller and Kuijpers (2011) but above the best-practice scenario, which was 0 Gg yr^{-1} in 2020 (and substantially higher than bottom-up estimates based on recent abatement reports; *Section 2.2.1.2*).

As outlined in *Section 2.2.1.2*, *Chapter 7*, and Stanley et al. (2020), only a minor quantity of the theoretical possible

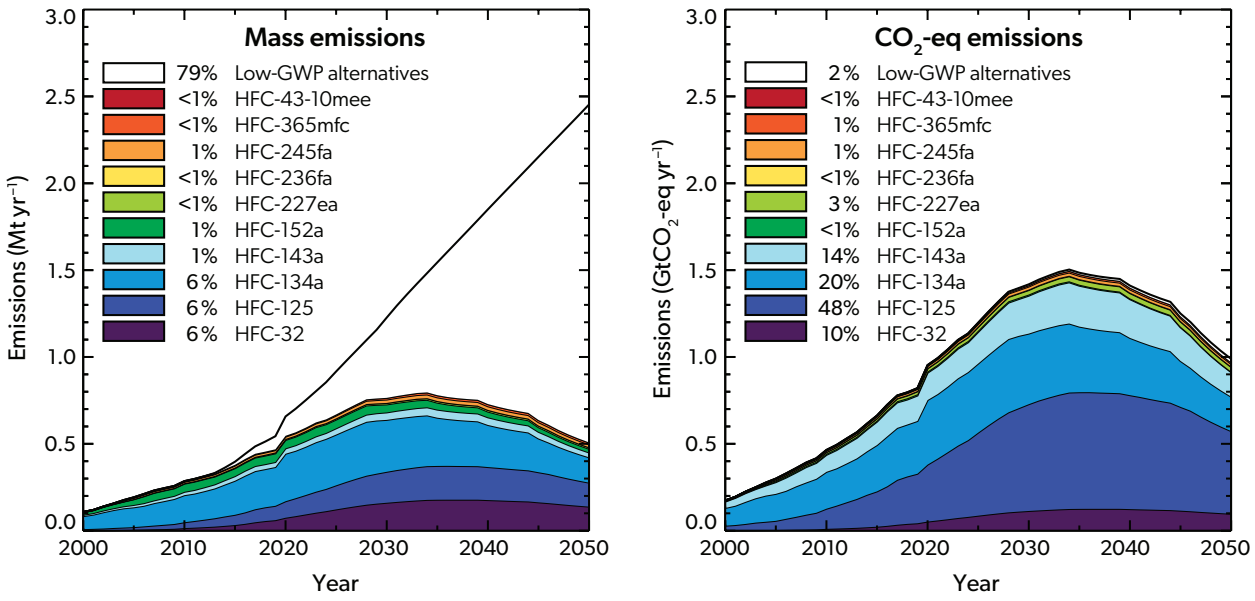

Figure 2-16. Contributions of the different HFCs to global emissions (in Tg yr^{-1} and Pg CO_2-eq yr^{-1}) from the 2022 Kigali Amendment scenario based on updated observations and reported consumption, national policies, and the provisions of the Kigali Amendment (upper-range scenario). Also shown are the contributions from alternative substances and/or technologies used to replace HFCs, indicated as "low-GWP alternative." The percentages refer to the relative contributions in 2050. The CO_2-eq emissions shown here are based on the GWPs from WMO (2018). [Adapted from Velders et al., 2022.]

abatement capacity seems to have been realised in the most recent years. Two different scenarios have been developed in *Chapter 7* to project future HFC-23 emissions within this Assessment. Both scenarios are outlined in *Section 7.2.2.1* and assume similar increases in HCFC-22 production. The first scenario assumes the widespread use of abatement such that emissions of HFC-23 are only 0.08% relative to the produced HCFC-22 (97% effective destruction capacity of HFC-23 by-product plus small emissions related to failures and maintenance of destruction systems). The second scenario assumes business-as-usual behavior (1.8% emissions relative to HCFC-22 production), where destruction capacities are only partly exploited.

Under the business-as-usual scenario, if the current fractional rate of HFC-23 destruction continues into the future, radiative forcing due to HFC-23 is expected to reach 0.015 W m^{-2} in 2050. Under the scenario in which there is widespread destruction of HFC-23 by-product, the contribution of HFC-23 to overall HFC radiative forcing will be small (*Section 7.2.2.1*).

2.4.3 Surface Temperature Contributions from HFCs

Radiative forcing contributes to global surface warming, changes in atmospheric circulation, sea level rise, and other warming-related climate changes. The contribution of HFCs (**Figure 2-17**) to surface warming is shown in **Figure 2-18**. For this calculation, the scenarios are extended to 2100, based on the same assumptions as used for 2020–2050. In the new scenario following current trends, national policies, and the provisions of the Kigali Amendment, the HFCs are projected to contribute 0.04°C to the global average surface warming in 2100, compared to 0.3–0.5°C in the baseline scenarios of the previous Assessment (Montzka, Velders et al., 2018; Velders et al., 2022). The updated Kigali Amendment scenario leads to a temperature rise that is slightly lower than that of the previous Assessment. For comparison, all greenhouse gases (GHGs) are projected to contribute 1.4–4.4°C to surface warming by the end of the 21st century, following the IPCC scenarios (best estimate for 2081–2100; IPCC, 2021). In hypothetical scenarios with a cease in global production or emissions of HFCs in 2023, the contribution to surface warming is reduced to no more than 0.01°C in 2100.

2.4.4 New and Expanding Uses of HFCs

Since the previous Assessment, HFC use may have expanded to similar uses or into a higher percentage of markets where competing non-HFC technologies exist. Most of the HFC uses and emissions continue to come from end uses that traditionally used ODSs. In this section, we briefly describe several technologies that traditionally did not rely on ODSs.

There is a growth in use of HFCs in vapor-compression cycles for air and/or water heating. Devices that use this process, for both cooling and heating, have been used for several decades and have typically been referred to as "heat pumps." This same terminology is also used to refer to newer equipment types that are designed to provide heating and that are often not reversible to provide cooling. In space heating, e.g., for occupant comfort, such heat pumps typically replace boilers or electric resistance heating. In addition to the potential gains in energy efficiency, the use of heat pumps will decarbonize (except for any HFC leakage) the heating at the building or central plant site, although the emissions from the power supply need to be considered in any full life-cycle analysis.

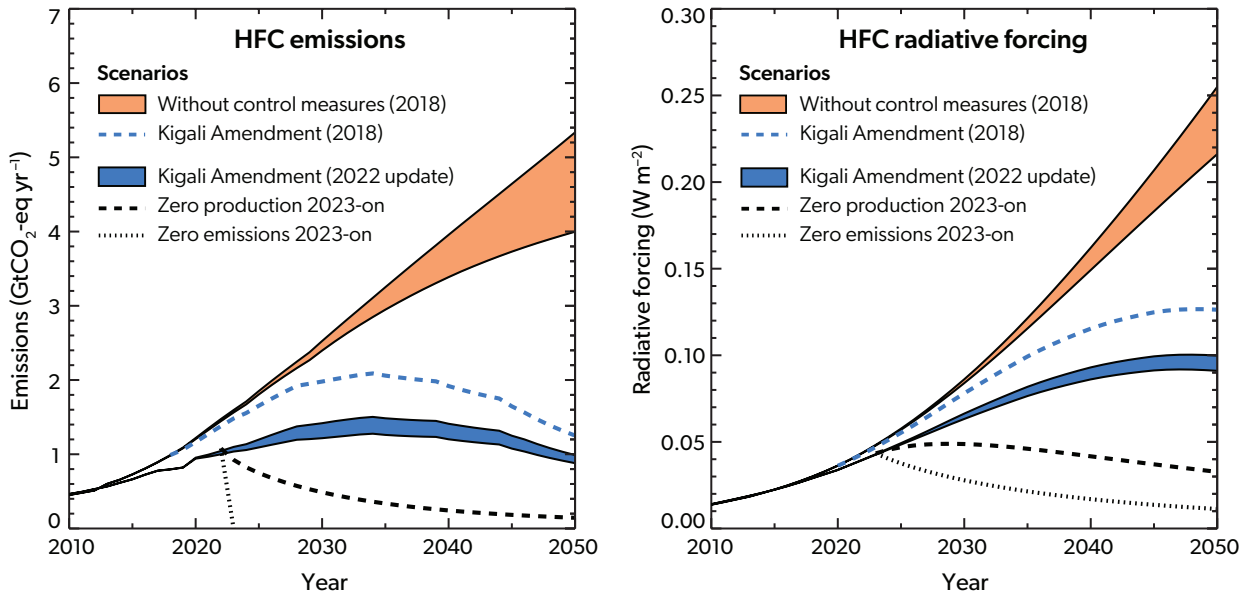

Figure 2-17. Global average HFC emissions (Pg CO_2-eq yr^{-1}) (*left*) and radiative forcing *(right)* ranges from the 2018 scenario without control measures (Montzka and Velders et al., 2018, based on Velders et al., 2015; orange) and on scenarios based on updated observations and reported consumption, national policies, and the Kigali Amendment provisions (blue shading). Also shown is a scenario that follows the phasedown schedules of the Kigali Amendment from the 2018 Assessment (blue dashed lines). Scenarios in which the global HFC production ceases in 2023 or the global HFC emissions cease in 2023 are given in black dashed and dotted lines, respectively. The data shown use the lifetimes, GWPs, and radiative efficiencies from WMO (2018). The curves contain the contributions of all HFCs except HFC-23 (see *Sections 2.4.2.1* and *7.2.2.1*). Scenarios from Velders et al. (2022).

For water heating, a heat pump provides hot, potable water that can be supplied for typical uses (showers, dish washing, laundry, etc.), utilized in radiator systems for space heating, or used in a combination system that performs both functions. R-410A[4] and HFC-134a dominate the market for these types of technologies (UNEP, 2018c). National and regional HFC controls may cause the market to shift to lower-GWP refrigerants if reductions in other sectors do not adequately provide the reductions necessary to allow for the increase in this use.

Heat pump technology has also been introduced as an energy-efficient option for clothes drying, replacing the typical tumble dryer that uses electric resistance heating. HFC-134a is the primary refrigerant used; models using R-407C[5] and R-290 (propane) are also available. R-450A[6] has also been used (EFTC, 2021). The primary market for these units has been in non-A5 countries (UNEP, 2018c).

There may be additional use of HFC cooling in electric vehicles, for passenger comfort and to provide cooling to the electric battery (UNEP, 2018c). In some instances, two separate systems are employed for the two functions; in others, a heat pump is used for both. These systems require refrigerant charges 30–50% higher than mobile air-conditioning in internal combustion engine vehicles. With the growing number of electric vehicles, this would lead to an increased use of high-GWP HFCs (e.g., HFC-134a) if such systems are not transitioned to low-GWP alternatives (e.g., HFO-1234yf or carbon dioxide [CO_2]).

HFC-134a is used as a solvent for the extraction of oil from dry biomass. This is currently applied in the cannabis oil industry (Timatic, 2021a), which is seen as a growing market due to the increase in the legalization of marijuana use. The same process has also been applied to the production of a large range of aromatic and flavoring agents, such as chocolate, cinnamon, lemon peels, and vanilla bean (Costello, 2021; MMV, 2006).

HFCs have been used in small quantities in other applications that did not previously rely on ODSs. In magnesium production and processing, there is minor use and emissions of HFC-134a as part of a proprietary blend sold under the trade name AM-cover™. This option and others (CO_2, FK-5-1-12) replace the high-GWP cover gas typically used—sulfur hexafluoride (SF_6) mixed with dry air and/or CO_2. HFC emissions from this source are small, for example, amounting to 0.1 Tg CO_2-eq yr^{-1} in the USA for the past five years (US EPA, 2021b).

Other potential applications—such as cork poppers, desk ornaments (such as dunking birds), and airsoft pistols—use minimal amounts of HFCs, having generally shifted to other alternatives

[4] R-410A is a blend, by mass, of 50% HFC-32 and 50% HFC-125. Using the GWPs in the Kigali Amendment, it has a GWP of 2087.5.
[5] R-407C is a blend, by mass, of 23% HFC-32, 25% HFC-125, and 52% HFC-134a. Using the GWPs in the Kigali Amendment, it has a GWP of 1773.85.
[6] R-450A is a blend, by mass, of 42% HFC-134a and 58% HFO-1234ze(E). Using the GWPs in the Kigali Amendment, it has a GWP of 600.6.

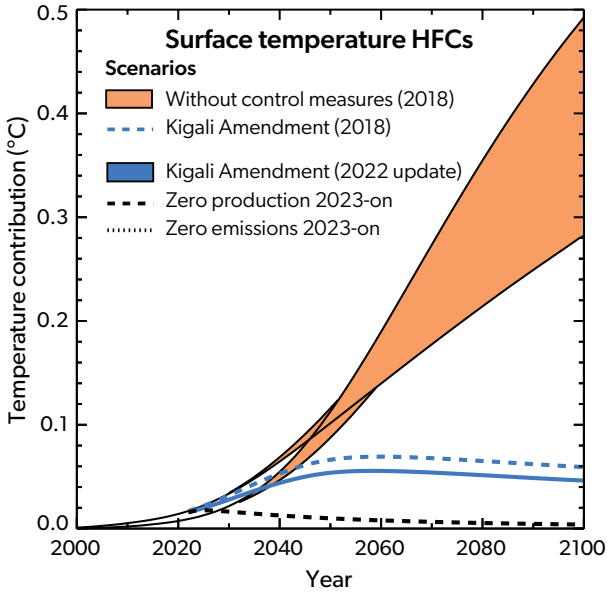

Figure 2-18. Contribution of HFCs to the global average surface warming for the 2018 scenarios without control measures (orange) and for the updated 2022 Kigali Amendment scenario based on updated observations and reported consumption, national regulations, and the Kigali Amendment provisions (solid blue line). The scenarios without control measures are from the previous Assessment and are based on Xu et al. (2013) and Velders et al. (2015). Also shown are the effects of the provisions of the Kigali Amendment presented in the 2018 Assessment (dashed blue line) and scenarios assuming that the global production or emissions of HFCs would cease in 2023 (dashed black line). No range is shown for the updated 2022 Kigali Amendment since the lower and upper range scenarios virtually coincide. The surface temperature change for the Kigali Amendment scenarios is calculated using the MAGICC6 model. Lifetimes, GWPs, and radiative efficiencies are taken from WMO (2018). The curves contain the contributions of all HFCs except HFC-23 (see *Sections 2.4.2.1* and *7.2.2.1*). [Adapted from Velders et al., 2022.]

including argon, dichloromethane (CH_2Cl_2; also known as methylene chloride), and propane, respectively.

2.4.5 Alternatives to High-GWP HFCs

The mandate to phase down high-GWP HFCs has triggered a major effort to find and implement more environmentally benign alternatives. HFOs and blends that contain HFOs were identified as the most promising replacements (McLinden et al., 2020). For example, in non-A5 countries, HFO-1234yf is now used in most new automotive air-conditioning systems as a replacement for HFC-134a, and it is expected to be used universally in the coming years in the EU, USA, and Japan. HFO-1234ze(E) and HFO-1336mzz(Z) have been used as foam-blowing agents and as refrigerants in chillers. Other HFOs that are being developed include HFO-1132a as a feedstock for fluoropolymers and HFO-1123 as a replacement for R-410A, by blending it with HFC-32. Many of these are slightly flammable, presenting trade-offs between safety and environmental considerations. None of the HFOs are a direct replacement for R-410A. Instead, non-flammable blends—which often contain some combination of HFO-1234yf, HFO-1234ze(E), HFC-32, HFC-134a, and HFC-125—have been proposed to replace R-410A (Kujak and Schultz, 2019). HFC-32 is also used as a single-component refrigerant replacement for R-410A in some equipment.

Nonfluorinated refrigerants, primarily ammonia, carbon dioxide, propane, and isobutane, are seeing renewed interest as alternatives to ODSs and HFCs in a wide range of applications and may have contributed to the slower-than-projected rise in emissions from 2013–2020 (**Figure 2-13**). These refrigerants all have zero ozone depletion potential (ODP) and very low global warming potential (GWP) compared to fluorinated refrigerants, making them environmentally attractive possibilities. Ammonia is considered to be a superior refrigerant because of its thermodynamic properties, and application is relatively easy in large, low-temperature systems (McLinden et al., 2020). However, due to its toxicity and flammability, ammonia may not be appropriate in some systems. Carbon dioxide is being used across a wide range of systems such as supermarkets, ice rinks, heat pump water heaters, data center cooling, automotive air-conditioning, and industrial freezers (McLinden et al., 2020). However, engineering CO_2-based systems to be efficient, especially in warmer climates, requires them to be very complex compared to traditional equipment, which also makes them more expensive to construct and maintain. Hydrocarbons are used for refrigeration in oil refineries, where the flammability hazard of a hydrocarbon refrigerant is readily addressed, as well as in very small systems such as domestic refrigerators. Based on research findings, safety standards are changing, allowing larger amounts of hydrocarbons in additional equipment types.

2.4.6 Energy Efficiency

As discussed in Chapter 2 of the last Assessment (Montzka, Velders et al., 2018), the climate impact of the expanding base of air-conditioning and refrigeration equipment will depend on several factors. These can be divided into a "direct effect" from refrigerant leakage (unless a zero-GWP refrigerant is used) and an "indirect effect" resulting from the production and transmission of energy (generally, electricity) to operate the product. The indirect effect is highly variable depending on the local energy supply, which changes as different energy sources are deployed over the day and throughout the seasons. It is important to understand the assumptions used when assessing the GHG emissions reduction potential from energy efficiency improvements, because such emissions reduction benefits may decrease in the future as the energy supply is decarbonized.

Changing the refrigerant alone would not drive significant energy efficiency improvements compared to the equipment used today (UNEP, 2018d). Depending on the equipment or system in use with a high-GWP refrigerant, UNEP (2018d) expected only about ±10% change in energy efficiency from switching to a low-GWP refrigerant (i.e., without concurrent changes to the equipment). However, the transition to new refrigerants provides

an opportunity to implement energy-efficient design changes. Such change could lead to energy efficiencies, compared to current equipment, in the range of 10–70% (UNEP, 2018d). UNEP (2020d) found that highly energy-efficient products using low-GWP alternatives are available, but accessibility to these technologies is low in many A5 countries and in some non-A5 countries. Looking at the situation in seven A5 countries, four non-A5 countries, and Europe as a whole, the study found that the market average energy efficiency was typically far below the best energy efficiency available in each country (or region).

TEAP (2021) reviewed and summarized several studies of the potential benefits of phasing down high-GWP HFCs while improving equipment efficiency. TEAP has reported that technology has developed rapidly, and there is now availability of refrigeration and air conditioning equipment with enhanced energy efficiency and lower GWP refrigerants in all sectors covered in its report. These technologies are increasingly accessible worldwide. Peters (2018) analyzed the growth of cooling equipment (space cooling, stationary refrigeration, and mobile cooling), finding that under a "current technology progress" scenario, energy use alone would lead to emissions of 7.4 Pg CO_2-eq yr^{-1} by 2050. With no assumptions of refrigerant changes, this scenario found an additional 1.5 Pg CO_2-eq yr^{-1} from refrigerant emissions. In a "cooling for all" scenario (i.e., high proliferation of air-conditioning in regions that experience high temperatures), emissions were projected to rise to 18.8 Pg CO_2-eq yr^{-1} by 2050. With significant improvements in energy efficiency and use of low-GWP refrigerants, emissions could be limited to 13.3 Pg CO_2-eq yr^{-1} by 2050 under that scenario. UNEP and IEA (2020d) also examined the increasing demand for cooling technologies and discussed policies and financing strategies to address the consequent environmental effect, including international initiatives, implementation of minimum energy performance standards, improved building design to reduce demand, and cessation of the resale of obsolete and inefficient equipment. The report suggested that by improving energy efficiency while phasing down high-GWP HFCs in refrigeration and air-conditioning, global GHG emissions of up to 210–460 Pg CO_2-eq would be avoided over the next four decades, depending on future rates of decarbonization of the power grid.

Shah et al. (2019), Dreyfus et al. (2020), and Purohit et al. (2020) quantified the overall benefits to climate that could be achieved through the integration of lower-GWP refrigerant adoption with deployment of more efficient equipment. These studies projected benefits of similar orders of magnitude from energy efficiency improvements and from moving to lower-GWP refrigerants, assuming both policies are pursued at the same time. Projecting near-universal saturation of air-conditioning in all warm areas, Shah et al. (2019) estimated avoidance by 2050 of up to 240.1 Pg CO_2-eq in GHG emissions under efficiency improvements (of ~30%) that the authors deemed as low-cost and up to 373 Pg CO_2-eq using best-available technologies. Dreyfus et al. (2020) found similar results, estimating that widespread adoption of the best currently available technologies could reduce the climate emissions from stationary air-conditioning and refrigeration by 130–260 Pg CO_2-eq by 2050 and 210–460 Pg CO_2-eq by 2060. The energy efficiency improvements in Dreyfus's scenarios account for about 75% of the benefits seen. Purohit et al.

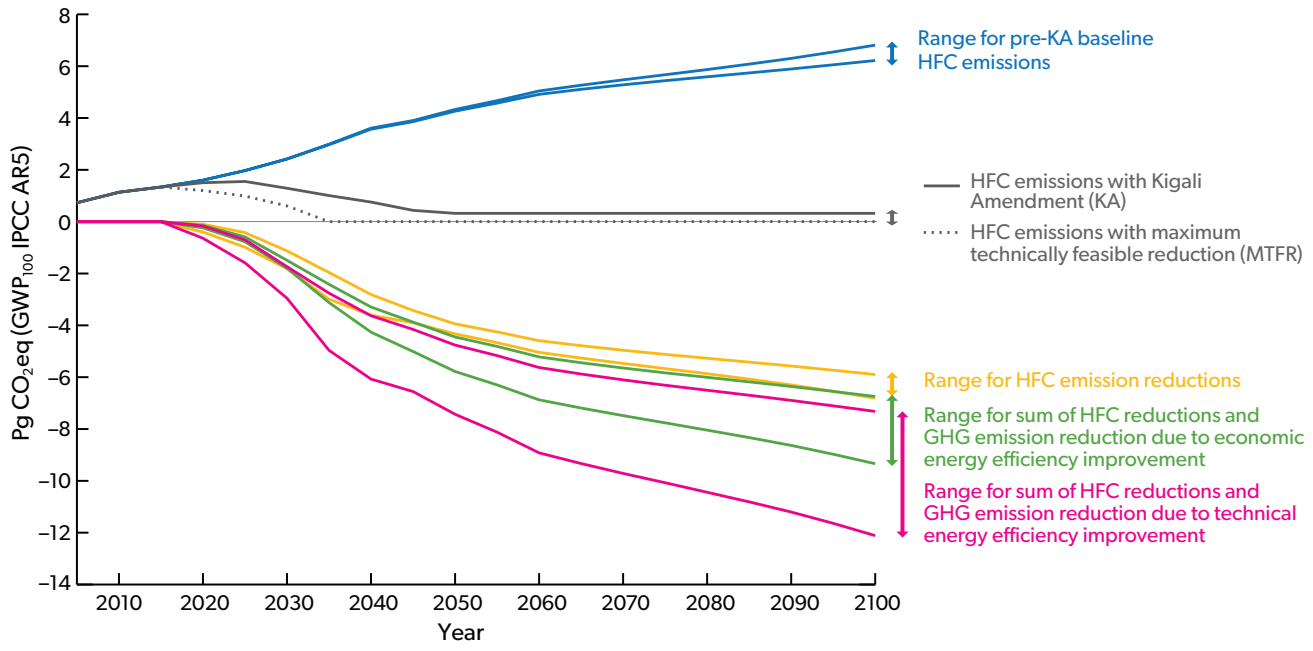

Figure 2-19. Full range of HFC CO_2-eq emissions under scenarios that either do not account for the effects of the Kigali Amendment (blue) or that do account for the Kigali Amendment and maximum technically feasible reduction scenarios (grey). Also shown are the range of mitigation potential (i.e., potential avoided emissions) (yellow) and the summed emissions benefits (Pg CO_2-eq yr^{-1}) due to HFC reductions and other greenhouse gas mitigation under technical or economic energy efficiency improvements (red and green, respectively). [Adapted from Purohit et al., 2020, Figure 7.]

(2020) incorporated a change in fuel mix (i.e., a lower CO_2-eq kWh^{-1} emissions factor from electric supply) along with an HFC phasedown and energy efficiency improvements, finding that the combination could prevent 411–631 Pg CO_2-eq emissions from stationary cooling equipment between 2018 and 2100 (**Figure 2-19**). Purohit et al. (2020) found that climate benefits from improved energy efficiency in stationary cooling technologies are about the same magnitude as those from the HFC phasedown.

REFERENCES

Barletta, B., Nissenson, P., Meinardi, S., Dabdub, D., Sherwood Rowland, F., VanCuren, R. A., Pederson, J., Diskin, G. S., Blake, D. R.. HFC-152a and HFC-134a emission estimates and characterization of CFCs, CFC replacements, and other halogenated solvents measured during the 2008 ARCTAS campaign (CARB phase) over the South Coast Air Basin of California. ***Atmospheric Chemistry and Physics***, ***11***(6), 2655–2669. https://doi.org/10.5194/acp-11-2655-2011, 2011.

Berg, M., S.R. Müller, J. Mühlemann, A. Wiedmer, and R.P. Schwarzenbach, Concentrations and mass fluxes of chloroacetic acids and trifluoroacetic acid in rain and natural waters in Switzerland, ***Environ. Sci. Technol.***, ***34*** (13), 2675–2683, doi:10.1021/es990855f, 2000.

Bernath, P.F., J. Steffen, J. Crouse, and C.D. Boone, Sixteen-year trends in atmospheric trace gases from orbit, ***J. Quant. Spect. Rad. Trans.***, ***253***, 107178, doi:10.1016/j.jqsrt.2020.107178, 2020.

Bernath, P.F., J. Crouse, R.C. Hughes, and C.D. Boone, The Atmospheric Chemistry Experiment Fourier transform spectrometer (ACE-FTS) version 4.1 retrievals: Trends and seasonal distributions, ***J. Quant. Spect. Rad. Trans.***, ***259***, 107409, doi:10.1016/j.jqsrt.2020.107409, 2021.

Boone, C.D., P.F. Bernath, D. Cok, S.C. Jones, and J. Steffen, Version 4 retrievals for the atmospheric chemistry experiment Fourier transform spectrometer (ACE-FTS) and imagers, ***J. Quant. Spect. Rad. Trans., 247***, 106939, doi:10.1016/j.jqsrt.2020.106939, 2020.

Burkholder, J.B., S.P. Sander, J. Abbatt, J.R. Barker, R.E. Huie, C.E. Kolb, M.J. Kurylo, V.L. Orkin, D.M. Wilmouth, and P.H. Wine, ***Chemical Kinetics and Photochemical Data for Use in Atmospheric Studies***, Evaluation No. 18, JPL Publication 15-10, Jet Propulsion Laboratory, National Aeronautics and Space Administration, Pasadena, California, [available at: http://jpldataeval.jpl.nasa.gov], 2015.

Carpenter, L.J., and J.S. Daniel (Lead Authors), E.L. Fleming, T. Hanaoka, J. Hu, A.R. Ravishankara, M.N. Ross, S. Tilmes, T.J. Wallington, and D.J. Wuebbles, Scenarios and Information for Policymakers, Chapter 6 in ***Scientific Assessment of Ozone Depletion: 2018***, Global Ozone Research and Monitoring Project–Report No. 58, World Meteorological Organization, Geneva, Switzerland, 2018.

Chiappero, M.S., F.E. Malanca, G.A. Argüello, S.T. Wooldridge, M.D. Hurley, J.C. Ball, T.J. Wallington, R.L. Waterland, and R.C. Buck, Atmospheric chemistry of perfluoroaldehydes ($C_xF_{2x+1}CHO$) and fluorotelomer aldehydes ($C_xF_{2x+1}CH_2CHO$): Quantification of the important role of photolysis, ***J. Phys. Chem. A***, ***110*** (43), 11,944–11,953, doi:10.1021/jp064262k, 2006.

Chhantyal-Pun, R., M. R. McGillen, J. M. Beames, M. A. H. Khan, C. J. Percival, D. E. Shallcross, A. J. Orr-Ewing, Temperature-Dependence of the Rates of Reaction of Trifluoroacetic Acid with Criegee Intermediates, ***Angew. Chem. Int. Ed.***, 56, 9044, doi:10.1002/anie.201703700, 2017.

Costello, ***Advanced Pytonics Extraction Technology using HFC-134a***, Costello, [available at: https://rccostello.com/extraction.html], 2021.

Cunnold, D.M., R.G. Prinn, R.A. Rasmussen, P.G. Simmonds, F.N. Alyea, C.A. Cardelino, A.J. Crawford, P.J. Fraser, and R.D. Rosen, The atmospheric lifetime experiment: 3. Lifetime methodology and application to three years of CFCl3 data, ***J. Geophys. Res., 88*** (C13), 8379–8400, doi:10.1029/Jc088ic13p08379, 1983.

David, L.M., M. Barth, L. Höglund-Isaksson, P. Purohit, G.J.M. Velders, S. Glaser, and A.R. Ravishankara, Trifluoroacetic acid deposition from emissions of HFO-1234yf in India, China, and the Middle East, ***Atmos. Chem. Phys.***, ***21*** (19), 14,833–14,849, doi:10.5194/acp-21-14833-2021, 2021.

Dreyfus, G., N. Borgford-Parnell, J. Christensen, D.W. Fahey, B. Motherway, T. Peters, R. Picolotti, N. Shah, and Y. Xu, ***Assessment of Climate and Development Benefits of Efficient and Climate-Friendly Cooling***, Climate & Clean Air Coalition and Institute for Governance & Sustainable Development, Molina, M., and D. Zaelke (Steering Committee co-chairs), [available at: https://ccacoalition.org/en/resources/assessment-climate-and-development-benefits-efficient-and-climate-friendly-cooling], 2020.

Dunse, B.L., N. Derek, P.J. Fraser, P.B. Krummel, and L.P. Steele, ***Australian and global HFC, PFC, sulfur hexafluoride nitrogen trifluoride and sulfuryl fluoride emissions***, Report prepared for Australian Government Department of the Environment and Energy, CSIRO Oceans and Atmosphere, Aspendale, Australia, iv, 33 pp., [available at: http://www.environment.gov.au/protection/ozone/publications/csiro-report-australian-global-sgg], 2018.

Ebnesajjad, S., Preparation of Tetrafluoroethylene and Other Monomers, In: ***Fluoroplastics (2nd Edition)***, William Andrew Publishing, Oxford, 48–75 pp., 2015.

EFTC (European Fluorocarbon Technical Committee), ***Heat Pumps***, [available at: https://www.fluorocarbons.org/applications/heat-pumps/], 2021.

EU (European Union), Directive 2006/40/EC of the European parliament and of the council of 17 May 2006 relating to emissions from air-conditioning systems in motor vehicles. Official J. EU L161, 12-18, [available at: https://eur-lex.europa.eu/legal-content/EN/TXT/?uri=CELEX%3A32006L0040], 2006.

EU (European Union), Regulation (EU) No 517/2014 of the European Parliament and of the Council of 16 April 2014 on fluorinated greenhouse gases and repealing Regulation (EC) No 842/2006 Text with EEA relevance, ***Off. J. Eur. Union***, ***150***, 195–230, [available at: http://data.europa.eu/eli/reg/2014/517/oj], 2014.

Fang, X., G.J.M. Velders, A.R. Ravishankara, M.J. Molina, J. Hu, and R.G. Prinn, Hydrofluorocarbons (HFCs) emissions in China: an inventory for 2005–2013 and projections to 2050, ***Environ. Sci. Technol.***, ***50*** (4), 2027–2034, doi:10.1021/acs.est.5b04376, 2016.

Fang, X., A.R. Ravishankara, G.J.M. Velders, M.J. Molina, S. Su, J. Zhang, J. Hu, and R.G. Prinn, Changes in emissions of ozone-depleting substances from China due to implementation of the Montreal Protocol, ***Environ. Sci. Technol.***, ***52*** (19), 11,359–11,366, doi:10.1021/acs.est.8b01280, 2018.

Fernando, A.M., P.F. Bernath, and C.D. Boone, Trends in atmospheric HFC-23 (CHF3) and HFC-134a abundances, ***J. Quant. Spectrosc. Radiat. Transf.***, ***238***, 106540, doi:10.1016/j.jqsrt.2019.06.019, 2019.

Franco, B., T. Blumenstock, C. Cho, L. Clarisse, C. Clerbaux, P.-F. Coheur, M. De Mazière, I. De Smedt, H.-P. Dorn, T. Emmerichs, H. Fuchs, G. Gkatzelis, D. W. T. Griffith, S. Gromov, J. W. Hannigan, F. Hase, T. Hohaus, N. Jones, A. Kerkweg, A. Kiendler-Scharr, E. Lutsch, E. Mahieu, A. Novelli, I. Ortega, C. Paton-Walsh, M. Pommier, A. Pozzer, D. Reimer, S. Rosanka, R. Sander, M. Schneider, K. Strong, R. Tillmann, M. Van Roozendael, L. Vereecken, C. Vigouroux, A. Wahner, and D. Taraborrelli, Ubiquitous atmospheric production of organic acids mediated by cloud droplets, ***Nature, 593*** (7858), 233–237, doi:10.1038/s41586-021-03462-x, 2021.

Frank, H., E.H. Christoph, O. Holm-Hansen, and J.L. Bullister, Trifluoroacetate in ocean waters, ***Environ. Sci. Technol.***, ***36*** (1), 12–15, doi:10.1021/es0101532, 2002.

Freeling, F., D. Behringer, F. Heydel, M. Scheurer, T.A. Ternes, and K. Nödler, Trifluoroacetate in precipitation: deriving a benchmark data set, ***Environ. Sci. Technol.***, ***54*** (18), 11,210–11,219, doi:10.1021/acs.est.0c02910, 2020.

Forster, P., T. Storelvmo, K. Armour, W. Collins, J.-L. Dufresne, D. Frame, D.J. Lunt, T. Mauritsen, M.D. Palmer, M. Watanabe, M. Wild, and H. Zhang, The Earth's Energy Budget, Climate Feedbacks, and Climate Sensitivity, Chapter 7 in ***Climate Change 2021: The Physical Science Basis, Contribution of Working Group I to the Sixth Assessment Report of the Intergovernmental Panel on Climate Change***, edited by V. Masson-Delmotte, P. Zhai, A. Pirani, S.L. Connors, C. Péan, S. Berger, N. Caud, Y. Chen, L. Goldfarb, M.I. Gomis, M. Huang, K. Leitzell, E. Lonnoy, J.B.R. Matthews, T.K. Maycock, T. Waterfield, O. Yelekçi, R. Yu, and B. Zhou, Cambridge University Press, Cambridge, United Kingdom and New York, NY, USA, 131 pp., doi:10.1017/9781009157896.009, 2021.

Fortems-Cheiney, A., M. Saunois, I. Pison, F. Chevallier, P. Bousquet, C. Cressot, S.A. Montzka, P.J. Fraser, M.K. Vollmer, P.G. Simmonds, D. Young, S. O'Doherty, R.F. Weiss, F. Artuso, B. Barletta, D.R. Blake, S. Li, C. Lunder, B.R. Miller, S. Park, R. Prinn, T. Saito, L.P. Steele, and Y.C.J. Yokouchi, Increase in HFC-134a emissions in response to the success of the Montreal Protocol, ***J. Geophys. Res. Atmos.***, ***120*** (22), 11,728–11,742, doi:10.1002/2015jd023741, 2015.

Graziosi, F., J. Arduini, F. Furlani, U. Giostra, P. Cristofanelli, X. Fang, O. Hermanssen, C. Lunder, G. Maenhout, S. O'Doherty, S. Reimann, N. Schmidbauer, M.K. Vollmer, D. Young, and M. Maione, European emissions of the powerful greenhouse gases

hydrofluorocarbons inferred from atmospheric measurements and their comparison with annual national reports to UNFCCC, ***Atmos. Environ.***, ***158***, 85–97, doi:10.1016/j.atmosenv.2017.03.029, 2017.

Harrison, J.J., M.P. Chipperfield, C.D. Boone, S.S. Dhomse, and P.F. Bernath, Fifteen years of HFC-134a satellite observations: comparisons with SLIMCAT calculations, ***J. Geophys. Res.***, ***126*** (8), e2020JD033208, doi:10.1029/2020jd033208, 2021.

Höglund-Isaksson, L., A. Gómez-Sanabria, Z. Klimont, P. Rafaj, and W. Schöpp, Technical potentials and costs for reducing global anthropogenic methane emissions in the 2050 timeframe–results from the GAINS model, ***Environ. Res. Commun.***, ***2*** (2), 025004, doi:10.1088/2515-7620/ab7457, 2020.

Holland, R., M.A.H. Khan, I. Driscoll, R. Chhantyal-Pun, R.G. Derwent, C.A. Taatjes, A.J. Orr-Ewing, C.J. Percival, and D.E. Shallcross, Investigation of the production of trifluoroacetic acid from two halocarbons, HFC-134a and HFO-1234yf and its fates using a global three-dimensional chemical transport model, ***ACS Earth Space Chem.***, ***5*** (4), 849–857, doi:10.1021/acsearthspacechem.0c00355, 2021.

Hu, L., S.A. Montzka, S.J. Lehman, D.S. Godwin, B.R. Miller, A.E. Andrews, K. Thoning, J.B. Miller, C. Sweeney, C. Siso, J.W. Elkins, B.D. Hall, D.J. Mondeel, D. Nance, T. Nehrkorn, M. Mountain, M.L. Fischer, S.C. Biraud, H. Chen, and P.P. Tans, Considerable contribution of the Montreal Protocol to declining greenhouse gas emissions from the United States, ***Geophys. Res. Lett.***, ***44*** (15), 8075–8083, doi:10.1002/2017GL074388, 2017.

Hurley, M.D., M.P. Sulbaek Andersen, T.J. Wallington, D.A. Ellis, J.W. Martin, and S.A. Mabury, Atmospheric chemistry of perfluorinated carboxylic acids: reaction with OH radicals and atmospheric lifetimes, ***J. Phys. Chem. A***, ***108*** (4), 615–620, doi:10.1021/jp036343b, 2004.

IPCC, Changing State of the Climate System, in Climate Change 2021: The Physical Science Basis. Contribution of Working Group I to the Sixth Assessment Report of the Intergovernmental Panel on Climate Change, edited by V. Masson-Delmotte, P. Zhai, A. Pirani, S. L. Connors, C. Péan, S. Berger, N. Caud, Y. Chen, L. Goldfarb, M. I. Gomis, M. Huang, K. Leitzell, E. Lonnoy, J. B. R. Matthews, T. K. Maycock, T. Waterfield, O. Yelekçi, R. Yu and B. Zhou (eds.), Cambridge University Press., 2021.

Joudan, S., A.O. De Silva, and C.J. Young, Insufficient evidence for the existence of natural trifluoroacetic acid, ***Environ. Sci. Process. Impacts***, ***23*** (11), 1641–1649, doi:10.1039/d1em00306b, 2021.

Kujak, S., and K. Schultz, Examination of a novel R410A replacement, ***ASHRAE Trans.***, ***125*** (2), 264–272, [available at: https://link.gale.com/apps/doc/A616448773/AONE?u=anon~8471483c&sid=googleScholar&xid=f29cece1], 2019.

Kuyper, B., D. Say, C. Labuschagne, T. Lesch, W.R. Joubert, D. Martin, D. Young, M.A.H. Khan, M. Rigby, A.L. Ganesan, M.F. Lunt, C. O'Dowd, A.J. Manning, S. O'Doherty, M.T. Davies-Coleman, and D.E. Shallcross, Atmospheric HCFC-22, HFC-125, and HFC-152a at Cape Point, South Africa, ***Environ. Sci. Technol.***, ***53*** (15), 8967–8975, doi:10.1021/acs.est.9b01612, 2019.

Laube, J.C., P. Martinerie, E. Witrant, T. Blunier, J. Schwander, C.A.M. Brenninkmeijer, T.J. Schuck, M. Bolder, T. Röckmann, C. van der Veen, H. Bönisch, A. Engel, G.P. Mills, M.J. Newland, D.E. Oram, C.E. Reeves, and W.T. Sturges, Accelerating growth of HFC-227ea (1,1,1,2,3,3,3-heptafluoropropane) in the atmosphere, ***Atmos. Chem. Phys.***, ***10*** (13), 5903–5910, doi:10.5194/acp-10-5903-2010, 2010.

Leedham Elvidge, E., H. Bönisch, C.A.M. Brenninkmeijer, A. Engel, P.J. Fraser, E. Gallacher, R. Langenfelds, J. Mühle, D.E. Oram, E.A. Ray, A.R. Ridley, T. Röckmann, W.T. Sturges, R.F. Weiss, and J.C. Laube, Evaluation of stratospheric age of air from CF_4, C_2F_6, C_3F_8, CHF_3, HFC-125, HFC-227ea and SF_6; implications for the calculations of halocarbon lifetimes, fractional release factors and ozone depletion potentials, ***Atmos. Chem. Phys.***, ***18*** (5), 3369–3385, doi:10.5194/acp-18-3369-2018, 2018.

Li, Y.X., Z.Y. Zhang, M.D. An, D. Gao, L.Y. Yi, and J.X. Hu, The estimated schedule and mitigation potential for hydrofluorocarbons phase-down in China, ***Adv. Clim. Chang. Res.***, ***10*** (3), 174–180, doi:10.1016/j.accre.2019.10.002, 2019.

Lindley, A., A. McCulloch, and T. Vink, Contribution of hydrofluorocarbons (HFCs) and hydrofluoro-Olefins (HFOs) atmospheric breakdown products to acidification ("Acid Rain") in the EU at present and in the future, ***Open J. Air Pollut.***, ***8*** (4), 81–95, doi:10.4236/ojap.2019.84004, 2019.

Lunt, M.F., M. Rigby, A.L. Ganesan, A.J. Manning, R.G. Prinn, S. O'Doherty, J. Mühle, C.M. Harth, P.K. Salameh, T. Arnold, R.F. Weiss, T. Saito, Y. Yokouchi, P.B. Krummel, L.P. Steele, P.J. Fraser, S. Li, S. Park, S. Reimann, M.K. Vollmer, C. Lunder, O. Hermansen, N. Schmidbauer, M. Maione, J. Arduini, D. Young, and P.G. Simmonds, Reconciling reported and unreported HFC emissions with atmospheric observations, ***Proc. Natl. Acad. Sci.***, ***112*** (19), 5927–5931, doi:10.1073/pnas.1420247112, 2015.

Manning, A.J., A.L. Redington, D. Say, S. O'Doherty, D. Young, P.G. Simmonds, M.K. Vollmer, J. Mühle, J. Arduini, G. Spain, A. Wisher, M. Maione, T.J. Schuck, K. Stanley, S. Reimann, A. Engel, P.B. Krummel, P.J. Fraser, C.M. Harth, P.K. Salameh, R.F. Weiss, R. Gluckman, P.N. Brown, J.D. Watterson, and T. Arnold, Evidence of a recent decline in UK emissions of hydrofluorocarbons determined by the InTEM inverse model and atmospheric measurements, ***Atmos. Chem. Phys.***, ***21*** (16), 12,739–12,755, doi:10.5194/acp-21-12739-2021, 2021.

McLinden, M.O., C.J. Seeton, and A. Pearson, New refrigerants and system configurations for vapor-compression refrigeration, ***Science***, ***370*** (6518), 791–796, doi:10.1126/science.abe3692, 2020.

MEFCC (Ministry of Environment, Forest and Climate Change), ***Control of Emission/Venting of Hydrofluorocarbon (HFC)-23, Produced as By-product While Manufacturing of Hydrochlorofluorocarbon (HCFC)-22, in the Atmosphere***, Ministry of Environment, Forest and Climate Change, New Dehli, India, [available at: http://ozonecell.nic.in/wp-content/uploads/2018/09/1482401969634-ORDER-13-OCTOBER-2016.pdf], 2016.

METI, Act on the rational use and proper management of fluorocarbons (Act no. 64 of 2001), Ministry of Economy, Trade and Industry, Japan, Tokyo., [available at: http://conf.montreal-protocol.org/meeting/workshops/hfc_management/presentations/Statements by Heads of Delegations/4-Masafumi Ohki_session_4.ppt], 2015.

Miller, B.R., M. Rigby, L.J.M. Kuijpers, P.B. Krummel, L.P. Steele, M. Leist, P.J. Fraser, A. McCulloch, C. Harth, P. Salameh, J. Mühle, R.F. Weiss, R.G. Prinn, R.H.J. Wang, S. O'Doherty, B.R. Greally, and P.G. Simmonds, HFC-23 (CHF_3) emission trend response to HCFC-22 ($CHClF_2$) production and recent HFC-23 emission abatement measures, ***Atmos. Chem. Phys.***, ***10*** (16), 7875–7890, doi:10.5194/acp-10-7875-2010, 2010.

Miller, B.R., and L.J.M. Kuijpers, Projecting future HFC-23 emissions, ***Atmos. Chem. Phys.***, ***11*** (24), 13,259–13,267, doi:10.5194/acp-11-13259-2011, 2011.

Miller, J. B., Lehman, S. J., Montzka, S. a., Sweeney, C., Miller, B. R., Karion, A., Wolak, C., Dlugokencky, E., Southon, J., Turnbull, J. C., Tans, P. P.. Linking emissions of fossil fuel CO2 and other anthropogenic trace gases using atmospheric 14CO2. ***Journal of Geophysical Research***, ***117***(D8). https://doi.org/10.1029/2011JD017048, 2012.MMV (Medicines for Malaria Venture), ***Comparative Assessment of Technologies for Extraction of Artemisinin***, Summary report commissioned through the Malalaria Medicines Venture, 17 pp., Geneva, Switzerland, [available at: https://www.mmv.org/sites/default/files/uploads/docs/publications/8_-_1_ArtemisiaExtractionStudy_3.pdf], 2006.

Montzka, S.A., and S. Reimann, (Lead Authors), A. Engel, K. Krüger, S. O`Doherty, and W.T. Sturges, Ozone-Depleting Substances (ODSs) and Related Chemicals, Chapter 1 in ***Scientific Assessment of Ozone Depletion: 2010,*** Global Ozone Research and Monitoring Project–Report No. 52, World Meteorological Organization, Geneva, Switzerland, 2011.

Montzka, S.A., M. McFarland, S.O. Andersen, B.R. Miller, D.W. Fahey, B.D. Hall, L. Hu, C. Siso, and J.W. Elkins, Recent trends in global emissions of hydrochlorofluorocarbons and hydrofluorocarbons: Reflecting on the 2007 adjustments to the Montreal Protocol, ***J. Phys. Chem. A***, ***119*** (19), 4439–4449, doi:10.1021/jp5097376, 2015.

Montzka, S.A., and G.J.M. Velders (Lead Authors), P.B. Krummel, J. Mühle, V.L. Orkin, S. Park, N. Shah, H. Walter-Terrinoni, P. Bernath, C. Boone, L. Hu, M.J. Kurylo, E.L. Elvidge, M. Maione, B.R. Miller, S. O'Doherty, M. Rigby, I.J. Simpson, M.K. Vollmer, R.F. Weiss, L.J.M. Kuijpers, and W.T. Sturges, Hydrofluorocarbons (HFCs), Chapter 2 in ***Scientific Assessment of Ozone Depletion: 2018***, Global Ozone Research and Monitoring Project–Report No. 58, World Meteorological Organization, Geneva, Switzerland, 2018.

Nielsen, O.J., B.F. Scott, C. Spencer, T.J. Wallington, and J.C. Ball, Trifluoroacetic acid in ancient freshwater, ***Atmos. Environ.***, ***35*** (16), 2799–2801, doi:10.1016/S1352-2310(01)00148-0, 2001.

Oram, D.E., W.T. Sturges, S.A. Penkett, A. Mc-Culloch, and P.J. Fraser, Growth of fluoroform (CHF_3, HFC-23) in the background atmosphere, ***Geophys. Res. Lett.***, ***25*** (1), 35–38, doi:10.1029/97GL03483, 1998.

Oram, D.E., M.J. Ashfold, J.C. Laube, L.J. Gooch, S. Humphrey, W.T. Sturges, E. Leedham-Elvidge, G.L. Forster, N.R.P. Harris, M.I. Mead, A.A. Samah, S.M. Phang, C.F. Ou-Yang, N.H. Lin, J.L. Wang, A.K. Baker, C.A.M. Brenninkmeijer, and D. Sherry, A growing threat to the ozone layer from short-lived anthropogenic chlorocarbons, Atmos. Chem. Phys., 17 (19), 11929-11941, doi:10.5194/acp-17-11929-2017, 2017.

Peters, T., ***A Cool World: Defining the Energy Conundrum of Cooling for All***, University of Birmingham, Birmingham Energy Institute, and the Institute for Global

Innovation, Birmingham, United Kingdom, 19 pp., [available at: https://www.birmingham.ac.uk/Documents/college-eps/energy/Publications/2018-clean-cold-report.pdf], 2018.

Pickard, H.M., A.S. Criscitiello, D. Persaud, C. Spencer, D.C.G. Muir, I. Lehnherr, M.J. Sharp, A.O. De Silva, and C.J. Young, Ice core record of persistent short-chain fluorinated alkyl acids: Evidence of the impact from global environmental regulations, ***Geophys. Res. Lett.***, ***47*** (10), e2020GL087535, doi:10.1029/2020gl087535, 2020.

Prinn, R.G., R.F. Weiss, J. Arduini, T. Arnold, H.L. DeWitt, P.J. Fraser, A.L. Ganesan, J. Gasore, C.M. Harth, O. Hermansen, J. Kim, P.B. Krummel, S. Li, Z.M. Loh, C.R. Lunder, M. Maione, A.J. Manning, B.R. Miller, B. Mitrevski, J. Mühle, S. O'Doherty, S. Park, S. Reimann, M. Rigby, T. Saito, P.K. Salameh, R. Schmidt, P.G. Simmonds, L.P. Steele, M.K. Vollmer, R.H. Wang, B. Yao, Y. Yokouchi, D. Young, and L. Zhou, History of chemically and radiatively important atmospheric gases from the Advanced Global Atmospheric Gases Experiment (AGAGE), ***Earth Syst. Sci. Data***, ***10*** (2), 985–1018, doi:10.5194/essd-10-985-2018, 2018.

Pu, J., H. Xu, B. Yao, Y. Yu, Y. Jiang, Q. Ma, and L. Chen, Estimate of hydrofluorocarbon emissions for 2012–16 in the Yangtze River Delta, China, ***Adv. Atm. Sci.***, ***37*** (6), 576–585, doi:10.1007/s00376-020-9242-3, 2020.

Purohit, P., L. Höglund-Isaksson, J. Dulac, N. Shah, M. Wei, P. Rafaj, and W. Schöpp, Electricity savings and greenhouse gas emission reductions from global phase-down of hydrofluorocarbons, ***Atmos. Chem. Phys.***, ***20*** (19), 11,305–11,327, doi:10.5194/acp-20-11305-2020, 2020.

Rayne, S., and K. Forest, Aqueous phase hydration and hydrate acidity of perfluoroalkyl and n:2 fluorotelomer aldehydes, ***J. Environ. Sci. Health A***, ***51*** (7), 579–582, doi:10.1080/10934529.2016.1141625, 2016.

Rigby, M., R.G. Prinn, S. O'Doherty, S.A. Montzka, A. McCulloch, C.M. Harth, J. Mühle, P.K. Salameh, R.F. Weiss, D. Young, P.G. Simmonds, B.D. Hall, G.S. Dutton, D. Nance, D.J. Mondeel, J.W. Elkins, P.B. Krummel, L.P. Steele, and P.J. Fraser, Re-evaluation of the lifetimes of the major CFCs and CH_3CCl_3 using atmospheric trends, ***Atmos. Chem. Phys.***, ***13*** (5), 2691–2702, doi:10.5194/acp-13-2691-2013, 2013.

Rigby, M., R.G. Prinn, S. O'Doherty, B.R. Miller, D. Ivy, J. Mühle, C.M. Harth, P.K. Salameh, T. Arnold, R.F. Weiss, P.B. Krummel, L.P. Steele, P.J. Fraser, D. Young, and P.G. Simmonds, Recent and future trends in synthetic greenhouse gas radiative forcing, ***Geophys. Res. Lett.***, ***41*** (7), 2623–2630, doi:10.1002/2013GL059099, 2014.

Say, D., A.L. Ganesan, M.F. Lunt, M. Rigby, S. O'Doherty, C. Harth, A.J. Manning, P.B. Krummel, and S. Bauguitte, Emissions of halocarbons from India inferred through atmospheric measurements, ***Atmos. Chem. Phys.***, ***19*** (15), 9865–9885, doi:10.5194/acp-2018-1146, 2019.

Schoenenberger, F., S. Henne, M. Hill, M.K. Vollmer, G. Kouvarakis, N. Mihalopoulos, S. O'Doherty, M. Maione, L. Emmenegger, T. Peter, and S. Reimann, Abundance and sources of atmospheric halocarbons in the Eastern Mediterranean, ***Atmos. Chem. Phys.***, ***18*** (6), 4069–4092, doi:10.5194/acp-18-4069-2018, 2018.

Scollard, D.J., J.J. Treacy, H.W. Sidebottom, C. Balestra-Garcia, G. Laverdet, G. LeBras, H. MacLeod, and S. Teton, Rate constants for the reactions of hydroxyl radicals and chlorine atoms with halogenated aldehydes, ***J. Phys. Chem.***, ***97***, 4683–4688, doi:10.1021/j100120a021, 1993.

Scott, B.F., R.W. Macdonald, K. Kannan, A. Fisk, A. Witter, N. Yamashita, L. Durham, C. Spencer, and D.C.G. Muir, Trifluoroacetate profiles in the Arctic, Atlantic, and Pacific oceans, ***Environ. Sci. Technol.***, ***39*** (17), 6555–6560, doi:10.1021/es047975u, 2005.

Sellevåg, S.R., T. Kelly, H. Sidebottom, and C.J. Nielsen, A study of the IR and UV-Vis absorption cross-sections, photolysis and OH-initiated oxidation of CF_3CHO and CF_3CH_2CHO, ***Phys. Chem. Chem. Phys.*** ***6*** (6), ***1243***–1252, doi:10.1039/B315941H, 2004.

Shah, N., M. Wei, V. Letschert, and A. Phadke, ***Benefits of Energy Efficient and Low-Global Warming Potential Refrigerant Cooling Equipment***, No. LBNL-2001229, Lawrence Berkley National Laboratory, Berkeley, California, doi:10.2172/1559243, 2019.

Simmonds, P.G., M. Rigby, A.J. Manning, M.F. Lunt, S. O'Doherty, A. McCulloch, P.J. Fraser, S. Henne, M.K. Vollmer, J. Mühle, R.F. Weiss, P.K. Salameh, D. Young, S. Reimann, A. Wenger, T. Arnold, C.M. Harth, P.B. Krummel, L.P. Steele, B.L. Dunse, B.R. Miller, C.R. Lunder, O. Hermansen, N. Schmidbauer, T. Saito, Y. Yokouchi, S. Park, S. Li, B. Yao, L.X. Zhou, J. Arduini, M. Maione, R.H.J. Wang, D. Ivy, and R.G. Prinn, Global and regional emissions estimates of 1,1-difluoroethane (HFC-152a, CH3CHF2) from in situ and air archive observations, Atmos. Chem. Phys., 16 (1), 365-382, doi: 10.5194/acp-16-365-2016, 2016.

Simmonds, P.G., M. Rigby, A. McCulloch, M.K. Vollmer, S. Henne, J. Mühle, S. O'Doherty, A.J. Manning, P.B. Krummel, P.J. Fraser, D. Young, R.F. Weiss, P.K. Salameh, C.M. Harth, S. Reimann, C.M. Trudinger, P. Steele, R.H.J. Wang, D.J. Ivy, R.G. Prinn, B. Mitrevski, and D.M. Etheridge, Recent increases in the atmospheric growth rate and emissions of HFC-23 (CHF_3) and the link to HCFC-22 ($CHClF_2$) production, ***Atmos. Chem. Phys.***, ***18*** (6), 4153–4169, doi:10.5194/acp-18-4153-2018, 2018.

Simpson, I.J., O.S. Aburizaiza, A. Siddique, B. Barletta, N.J. Blake, A. Gartner, H. Khwaja, S. Meinardi, J. Zeb, and D.R. Blake, Air quality in Mecca and surrounding holy places in Saudi Arabia during Hajj: initial survey, ***Environ. Sci. Technol.***, ***48*** (15), 8529–8537, doi:10.1021/es5017476, 2014.

Solomon, K.R., G.J.M. Velders, S.R. Wilson, S. Madronich, J. Longstreth, P.J. Aucamp, and J.F. Bornman, Sources, fates, toxicity, and risks of trifluoroacetic acid and its salts: Relevance to substances regulated under the Montreal and Kyoto Protocols, ***J. Toxicol. Environ. Health B***, ***19*** (7), 289–304, doi:10.1080/10937404.2016.1175981, 2016.

Stanley, K.M., D. Say, J. Mühle, C.M. Harth, P.B. Krummel, D. Young, S.J. O'Doherty, P.K. Salameh, P.G. Simmonds, R.F. Weiss, R.G. Prinn, P.J. Fraser, and M. Rigby, Increase in global emissions of HFC-23 despite near-total expected reductions, ***Nature Commun.***, ***11*** (1), 397, doi:10.1038/s41467-019-13899-4, 2020.

Stohl, A., Seibert, P., Arduini, J., Eckhardt, S., Fraser, P., Greally, B. R., Lunder, C., Maione, M., Mühle, J., O'Doherty, S., Prinn, R. G., Reimann, S., Saito, T., Schmidbauer, N., Simmonds, P. G., Vollmer, M. K., Weiss, R. F., Yokouchi, Y. An analytical inversion method for determining regional and global emissions of greenhouse gases : Sensitivity studies and application to halocarbons. ***Atmospheric Chemistry and Physics***, ***9***(5), 1597–1620. https://doi.org/10.5194/acp-9-1597-2009, 2009.

Su, S., X. Fang, L. Li, J. Wu, J. Zhang, W. Xu, and J. Hu, HFC-134a emissions from mobile air conditioning in China from 1995 to 2030, ***Atmos. Environ.***, ***102***, 122–129, doi:10.1016/j.atmosenv.2014.11.057, 2015.

Sulbaek Andersen, M.P., J.A. Schmidt, A. Volkova, and D.J. Wuebbles, A three-dimensional model of the atmospheric chemistry of E and Z-CF_3CH=CHCl (HCFO-1233(zd) (E/Z)), ***Atmos. Environ.***, ***179***, 250–259, doi:10.1016/j.atmosenv.2018.02.018, 2018.

Sulbaek Andersen, M.P., and O.J. Nielsen, Tropospheric photolysis of CF_3CHO, ***Atmos. Environ.***, ***272***, 118935, doi:10.1016/j.atmosenv.2021.118935, 2022.

Sung, D.J., D.J. Moon, J. Kim, S. Moon, and S.-I. Hong, Production of TFE by catalytic pyrolysis of chlorodifluoromethane ($CHClF_2$), ***Stud. Surf. Sci. Catal.***, ***159***, 233–236, doi:10.1016/S0167-2991(06)81576-4, 2006.

Takeda, M., H. Nakajima, I. Murata, T. Nagahama, I. Morino, G.C. Toon, R.F. Weiss, J. Mühle, P.B. Krummel, P.J. Fraser, and H.-J. Wang, First ground-based FTIR observations of HFC-23 at Rikubetsu, Japan, and Syowa Station, Antarctica, ***Atmos. Meas. Tech.***, ***14*** (9), 5955–5976, doi:10.5194/amt-2020-505, 2021.

TEAP (Technology and Economic Assessment Panel), Montreal Protocol on Substances that Deplete the Ozone Layer, ***Decision XXXI/7 - Continued Provision of Information on Energy-efficient and Low-global-warming-potential Technologies***, ISBN: 978-9966-076-88-5, [available at: https://ozone.unep.org/system/files/documents/TEAP-EETF-report-may2021.pdf], 2021.

Timatic, ***Timatic Extraction Equipment and Processes: FC Extractor Models***, Timatic USA, [available at: https://timaticusa.com/fcextractioninfo], 2021a.

UNEP (United Nations Environment Programme), Environmental Effects Assessment Panel, ***Environmental Effects of Ozone Depletion and its Interactions with Climate Change: 2014 Assessment***, United Nations Environment Programme, Nairobi, Kenya, [available at: https://ozone.unep.org/sites/default/files/2019-05/eeap_report_2014.pdf], 2014.

UNEP (United Nations Environment Programme), ***Report of the Twenty-Eighth Meeting of the Parties to the Montreal Protocol on Substances that Deplete the Ozone Layer***, UNEP/OzL.Pro.28/12, United Nations Environment Programme, Kigali, Rwanda, [available at: https://ozone.unep.org/sites/default/files/2019-08/MOP-28-12E.pdf], 2016.

UNEP (United Nations Environment Programme), ***2017 Progress Report of the Technology and Economic Assessment Pane***l, coordinated by Maranion, B., M. Pizano, and A. Woodcock, United Nations Environment Programme, Vol. 1, 105 pp., Nairobi, Kenya, [available at: https://ozone.unep.org/sites/default/files/2019-05/TEAP-Progress-Report-May2017.pdf], 2017.

UNEP (United Nations Environment Programme), Executive Committee of the Multilateral Fund for the Implementation of the Montreal Protocol, ***Cost-effective***

Options for Controlling HFC-23 By-product Emissions (Decision 81/68(e)), United Nations Environment Programme, Montreal, Canada, [available at: http://multilateralfund.org/82/English/1/8268.pdf], 2018a.

UNEP (United Nations Environment Programme), Executive Committee of the Multilateral Fund for the Implementation of the Montreal Protocol, *Corrigendum: Cost-effective Options for Controlling HFC-23 By-product Emissions (Decision 81/68(e))*, United Nations Environment Programme, Montreal, Canada, [available at: http://multilateralfund.org/82/English/1/8268c1.pdf], 2018b.

UNEP (United Nations Environment Programme), *Refrigeration, Air Conditioning and Heat Pumps Technical Options Committee: 2018 Assessment Report*, United Nations Environment Programme, ISBN: 978-9966-076-58-8, 300 pp., Nairobi, Kenya, [available at: https://ozone.unep.org/sites/default/files/2019-04/RTOC-assessment-report-2018_0.pdf], 2018c.

UNEP (United Nations Environment Programme), Report of the Technology and Economic Assessment Panel, *Decision XXIX/10--Task Force on Issues Related to Energy Efficiency While Phasing Down Hydrofluorocarbons*, United Nations Environment Programme, Vol. 5, 90 pp., ISBN: 978-9966-076-42-7, Nairobi, Kenya, [available at: https://ozone.unep.org/sites/default/files/2019-04/TEAP_DecisionXXIX-10_Task_Force_EE_May2018.pdf], 2018d.

UNEP (United Nations Environment Programme), Report of the Technology and Economic Assessment Panel, *Decision XXXI/7—Continued Provision of Information on Energy-Efficient and Low-Global-Warming-Potential Technologies*, United Nations Environment Programme, Vol. 2, 127 pp., ISBN: 978-9966-076-86-1, Nairobi, Kenya, [available at: https://ozone.unep.org/sites/default/files/assessment_panels/TEAP_dec-XXXI-7-TFEE-report-september2020.pdf], 2020a.

UNEP (United Nations Environment Programme), Report of the Technology and Economic Assessment Panel, *Assessment of the Funding Requirement for the Replenishment of the Multilateral Fund for the Period 2021-2023*, United Nations Environment Programme, Vol. 3, 108 pp., ISBN: 978-9966-076-84-7, Nairobi, Kenya, [available at: https://ozone.unep.org/system/files/documents/TEAP_decision_XXXI-1_replenishment-task-force-report_may2020.pdf], 2020b.

UNEP (United Nations Environment Programme), Executive Committee of the Multilateral Fund for the Implementation of the Montreal Protocol, *Report of the sub-group on the production sector*, United Nations Environment Programme, Montreal, Canada, [available at: http://multilateralfund.org/84/English/1/8474ri.pdf], 2020c.

UNEP (United Nations Environment Programme) and IEA (International Energy Agency), *Cooling Emissions and Policy Synthesis Report: Benefits of cooling efficiency and the Kigali Amendment*, United Nations Environment Programme, 50 pp., Nairobi, Kenya and Paris, France, [available at: https://iea.blob.core.windows.net/assets/71c8db7e-1137-41ef-99c3-8f2c8d3a5d86/Cooling_Emissions_and_Policy_Synthesis_Report.pdf], 2020d.

UNEP (United Nations Environment Programme), *Production and consumption of ozone depleting substances under the Montreal Protocol*, United Nations Environment Programme, Nairobi, Kenya, [available at: http://ozone.unep.org], 2021.

UNFCCC (United Nations Framework Convention on Climate Change), *National Inventory Submissions 2020 to the United Nations Framework Convention of Climate Change*, UNFCCC Secretariat, Bonn, Germany, [available at: https://unfccc.int/ghg-inventories-annex-i-parties/2020], 2021.

UNFCCC (United Nations Framework Convention on Climate Change), National Inventory Submissions 2019 (eds.), p. last access: May 2019, https://unfccc.int/process-and-meetings/transparency-and-reporting/reporting-and-review-under-the-convention/greenhouse-gas-inventories-annex-i-parties/national-inventory-submissions-2019, 2019.

UNFCCC (United Nations Framework Convention on Climate Change), National Inventory Submissions 2021, https://unfccc.int/ghg-inventories-annex-i-parties/2021, 2021.

US EPA (Environmental Protection Agency), *Phasedown of Hydrofluorocarbons: Establishing the Allowance Allocation and Trading Program Under the American Innovation and Manufacturing Act*, U.S. Environmental Protection Agency, [https://www.federalregister.gov/documents/2021/10/05/2021-21030/phasedown-of-hydrofluorocarbons-establishing-the-allowance-allocation-and-trading-program-under-the], 2021a.

US EPA (U.S. Environmental Protection Agency), *Inventory of U.S. Greenhouse Gas Emissions and Sinks: 1990-2019*, U.S. Environmental Protection Agency, [available at: https://www.epa.gov/ghgemissions/inventory-us-greenhouse-gas-emissions-and-sinks-1990-2019], 2021b.

Velders, G.J.M., S.O. Andersen, J.S. Daniel, D.W. Fahey, and M. McFarland, The importance of the Montreal Protocol in protecting climate, *Proc. Natl. Acad. Sci.*, 104 (12), 4814-4819, doi:10.1073/pnas.0610328104, 2007.

Velders, G.J.M., A.R. Ravishankara, M.K. Miller, M.J. Molina, J. Alcamo, J.S. Daniel, D.W. Fahey, S.A. Montzka, and S. Reimann, Preserving Montreal Protocol Climate Benefits by Limiting HFCs, *Science*, 335 (6071), 922-923, doi:10.1126/science.1216414, 2012.

Velders, G.J.M., D.W. Fahey, J.S. Daniel, S.O. Andersen, and M. McFarland, Future atmospheric abundances and climate forcings from scenarios of global and regional hydrofluorocarbon (HFC) emissions, *Atmos. Environ., 123*, 200–209, doi:10.1016/j.atmosenv.2015.10.071, 2015.

Velders, G.J.M., J.S. Daniel, S.A. Montzka, I. Vimont, M. Rigby, P.B. Krummel, J. Muhle, S. O'Doherty, R.G. Prinn, R.F. Weiss, and D. Young, Projections of hydrofluorocarbon (HFC) emissions and the resulting global warming based on recent trends in observed abundances and current policies, *Atmos. Chem. Phys.*, *22* (9), 6087–6101, doi:10.5194/acp-22-6087-2022, 2022.

Vollmer, M.K., S. Reimann, M. Hill, and D. Brunner, First observations of the fourth generation synthetic halocarbons HFC-1234yf, HFC-1234ze(E), and HCFC-1233zd(E) in the atmosphere, *Environ. Sci. Technol., 49* (5), 2703–2708, doi:10.1021/es505123x, 2015.

Wallington, T.J., W.F. Schneider, D.R. Worsnop, O.J. Nielsen, J. Sehested, W.J. Debruyn, and J.A. Shorter, The environmental impact of CFC replacements HFCs and HCFCs, *Environ. Sci. Technol.*, *28* (7), 320A–326A, doi:10.1021/es00056a714, 1994.

Wang, Z., Y. Wang, J. Li, S. Henne, B. Zhang, J. Hu, and J. Zhang, Impacts of the degradation of 2, 3, 3, 3-tetrafluoropropene into trifluoroacetic acid from its application in automobile air conditioners in China, the United States, and Europe, *Environ. Sci. Technol., 52* (5), 2819–2826, doi:10.1021/acs.est.7b05960, 2018.

WMO (World Meteorological Organization), *Scientific Assessment of Ozone Depletion: 2018*, Global Ozone Research and Monitoring Project–Report No. 58, 588 pp., Geneva, Switzerland, 2018.

Xu, Y., D. Zaelke, G.J.M. Velders, and V. Ramanathan, The role of HFCs in mitigating 21st century climate change, *Atmos. Chem. Phys.*, *13* (12), 6083–6089, doi:10.5194/acp-13-6083-2013, 2013.

Yao, B., X. Fang, M.K. Vollmer, S. Reimann, L. Chen, S. Fang, and R.G. Prinn, China's hydrofluorocarbon emissions for 2011–2017 inferred from atmospheric measurements, *Environ. Sci. Technol. Lett.*, *6* (8), 479–486, doi:10.1021/acs.estlett.9b00319, 2019.

Yvon-Lewis, S.A., and J.H. Butler, Effect of oceanic uptake on atmospheric lifetimes of selected trace gases, *J. Geophys. Res.*, *107* (D20), 4414, doi:10.1029/2001JD001267, 2002.

CHAPTER 3

Update on Global Ozone: Past, Present, and Future

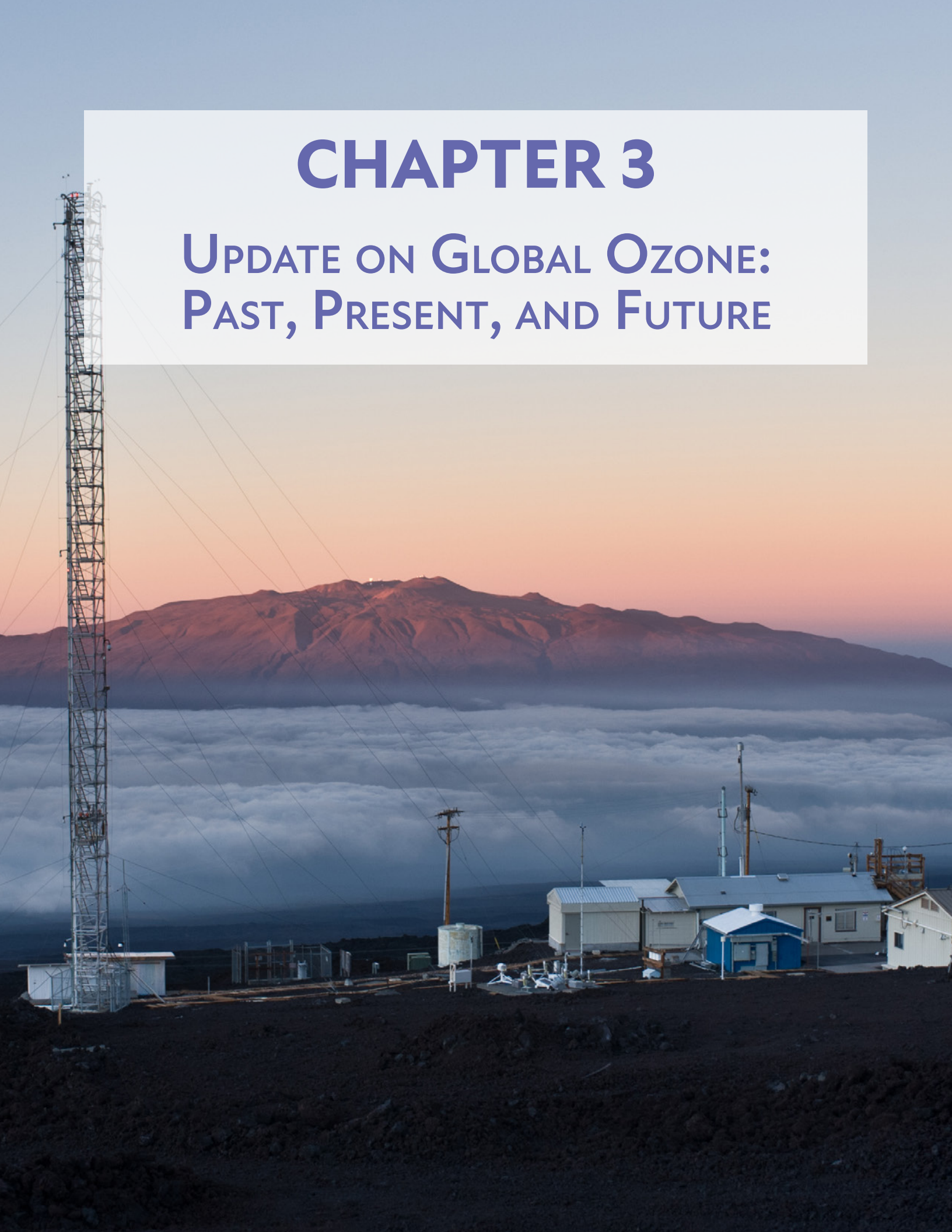

About the cover image:
The Mauna Loa Observatory in Hawai'i is a principal remote site for monitoring changes in atmospheric composition that affect both ozone depletion and climate change.

Photo credit: Jonathan Kingston

CHAPTER 3

Update on Global Ozone: Past, Present, and Future

Lead Authors : Birgit Hassler
Paul J. Young

Coauthors : William T. Ball
Robert Damadeo
James Keeble
Elaine Maillard Barras
Viktoria Sofieva
Guang Zeng

Contributing Authors : Matt Amos
Niramson Azouz
Melanie Coldewey-Egbers
Lawrence Coy
Simone Dietmüller
Sandip S. Dhomse
Sophie Godin-Beekman
Daan Hubert
Mahesh Kovilakam
Paul A. Newman
Clara Orbe
Irina Petropavlovskikh
William J. Randel
Wolfgang Steinbrecht
Monika E. Szeląg
Kleareti Tourpali
Corinne Vigouroux
Mark Weber

Review Editors : Jessica Neu
Wolfgang Steinbrecht

Errata (February 2023)

Chapter 3, Appendix 3A, Table 3A-3:

- The entry for SBUV NASA (MOD) was corrected from S-NPP OMPS NP NOAA v2.8 to S-NPP OMPS NP NASA v2.8.
- The entry for SBUV NOAA (COH) was corrected from S-NPP OMPS NP NASA v2.6 to S-NPP OMPS NP NOAA v3r2.

CONTENTS

Chapter 3: Update on Global Ozone: Past, Present, and Future

SCIENTIFIC SUMMARY

This chapter presents our current understanding of global ozone outside of the polar regions. The increase of ozone-depleting substance (ODS) concentrations caused the large ozone decline observed from the early satellite era (circa 1980) to the mid-1990s. Since the late 1990s, concentrations of ODSs have been declining due to the successful implementation of the Montreal Protocol and its Amendments and adjustments. Since the last Assessment, the longer observational records show a small increase in near-global total column ozone (TCO) with reduced uncertainty, but this trend is not yet statistically significant. A small increase in TCO is seen in the Southern Hemisphere (SH) mid-latitudes but not yet in the Northern Hemisphere (NH) mid-latitudes or tropics. Different processes operating at different altitudes complicate the attribution of the overall total column trend. However, a significant increase in upper-stratospheric ozone noted in the previous Assessment continues, driven by declines in ozone-depleting substances and increases in greenhouse gases (GHGs). Model simulations support our overall understanding of these trends.

Over this century, we expect an increase in global stratospheric ozone as the concentrations of ODSs decline. The future evolution for different latitudes and vertical levels depends on the future concentrations of GHGs and precursors of tropospheric ozone. These other influences may lead to TCO levels that remain below 1980 values in some regions, even after concentrations of ODSs have declined to pre-1980 levels.

Changes to date in total column ozone

- **Aggregated ground- and space-based observations indicate an increase of 0.3% decade^{-1} (with a 2-sigma uncertainty of at least ±0.3% decade^{-1}) in near-global (60°S–60°N) TCO over the 1996–2020 period.** This trend is consistent with model simulations and our scientific understanding of the processes controlling ozone.
- Over the same 1996–2020 period, the TCO trends in broad latitude bands are as follows:
  - SH mid-latitude (60–35°S) TCO has increased (0.8 ± 0.7% decade^{-1}).
  - NH mid-latitude (35–60°N) TCO trends are negligible (0.0 ± 0.7% decade^{-1}).
  - Tropical (20°S–20°N) TCO shows no clear trend (0.2 ± 0.3% decade^{-1}), likely because stratospheric ozone is decreasing while tropospheric ozone is increasing, both unrelated to changes in ODSs.

  The latitudinal pattern of these TCO trends is largely consistent with our scientific understanding and is reproduced in the latest set of chemistry-climate models (CCMs).
- Present-day (2017–2020) TCO as measured from space-based and ground-based observations remains lower than the 1964–1980 average by
  - about 2% for the near-global average (60°S–60°N),
  - about 4% in the NH mid-latitudes (35–60°N),
  - about 5% in the SH mid-latitudes (35–60°S), and
  - about 1% in the tropics (20°S–20°N).

  Within uncertainties associated with natural variability and instrumental accuracy, these values are essentially the same as given in the previous Assessment for the 2014–2017 average.

Changes to date in vertically resolved ozone

Vertically resolved trends are very similar to those given in the last Assessment. However, with longer records and updated merged datasets, recovery trends are now statistically significant in more locations.

- **Measurements show unambiguous increases in upper-stratospheric ozone for 2000–2020.** Positive trends have a range of ~1.5–2.2% decade^{-1} at mid-latitudes in both the Northern and Southern Hemispheres and ~1–1.5% decade^{-1} in the tropics.
- **Upper stratospheric ozone increases are due to a combination of decreases in ODSs and decreases in stratospheric temperature driven by increases in carbon dioxide (CO_2).** New CCM simulations affirm this finding from the last Assessment.
- **There are multiple lines of evidence from both observations and models for a small though uncertain decrease (1–2% decade^{-1}, with uncertainty up to ±5% decade^{-1}) in tropical lower stratospheric ozone over 2000–2020.** This decrease is consistent with climate change–driven acceleration of the large-scale circulation and has a small impact on TCO. Chemical ozone loss from chlorine and bromine is comparatively minor in the tropical lower stratosphere.
- **Observations suggest small decreases in lower stratospheric ozone in the mid-latitudes of both hemispheres for 2000–2020, while chemistry-climate model simulations suggest small increases.** Ozone in mid-latitudes has large year-to-year variability; thus, trends have large uncertainties, and they are not robust across all datasets and models. The observed decrease is more evident in the Northern Hemisphere.
- **Attribution of TCO trends during the period of slow ODS decline requires knowledge of changes in ozone in both the troposphere and stratosphere.** For instance, there is evidence that the lack of a change in TCO in the tropics reflects an increase in tropospheric ozone that compensates for the ozone decrease in the tropical lower stratosphere. This decrease, due to a climate change–driven acceleration of the large-scale circulation, is expected based on modeling studies. Depletion due to ODSs, on the other hand, is very minor in the tropical lower stratosphere. Nevertheless, analyses of

these changes using different observational datasets indicate significant remaining uncertainty.

Future ozone changes

Projections of future stratospheric ozone are available from new model simulations that follow new emissions scenarios: the shared socioeconomic pathways (SSPs). These scenarios all assume compliance with the Montreal Protocol and its Amendments and adjustments for ODSs but span a wider range in future GHG and pollutant emissions pathways than the scenarios used in the previous Assessment, although there are fewer models from which to draw results. As in the last Assessment, the key drivers of future stratospheric ozone levels continue to be declining ODS concentrations coupled with CO_2-driven cooling in the upper stratosphere and a strengthening of the Brewer-Dobson circulation. TCO will also be affected by changes in the tropospheric ozone burden.

- **New estimates for the year of return of near-global TCO to its 1980 value are broadly consistent with the last Assessment. Also similar to the last Assessment, these modeled return dates vary considerably depending on the assumed future scenario.** TCO returns to its 1980 value sooner for scenarios that assume larger emissions of GHGs than scenarios with smaller GHG emissions. The return dates for a middle-of-the-road (SSP2-4.5) scenario are:
  - around 2040 for near global mean (60°S–60°N) annually averaged column ozone;
  - around 2045 for SH (60–35°S) annually averaged column ozone; and
  - around 2035 for NH (35–60°N) annually averaged column ozone.
- **For scenarios that assume strong reductions in the emission of tropospheric ozone precursors, the resulting reductions in tropospheric ozone can be important for TCO trends.** Under such scenarios, TCO in the tropics is projected to remain below the 1980 values until at least 2100. As discussed in the last Assessment, tropical TCO under high GHG scenarios will be below 1980 values at 2100 due to circulation-driven changes affecting lower stratospheric ozone.
- **Future ozone recovery and the expected strengthening of the Brewer–Dobson circulation will most likely increase the proportion of ozone of stratospheric origin in the troposphere.** A new analysis has quantified the contribution of stratosphere-to-troposphere transport of ozone in models under scenarios with limited GHG mitigation (RCP6.0 and RCP8.5). While stratosphere-to-troposphere transport remains highly variable between models and is strongly scenario-dependent, the projected increase is robust, suggesting increases of stratospheric ozone in the troposphere of 10–50% over the 21st century, depending on the model and scenario. Nonetheless, in situ chemistry involving air pollutants remains the largest production term for the simulated tropospheric ozone budget.
- The unreported production of CFC-11 over 2012–2019 (see *Chapter 1*) is estimated to delay global TCO recovery to 1980 levels by ~1 year.

Emerging Issues

- **Exceptional events can temporarily perturb chemical and dynamical processes that affect stratospheric ozone amounts.** Since the last Assessment, these include the 2019/2020 wildfires in Australia, the eruption of the Hunga Tonga-Hunga Ha'apai volcano, and disruptions to the quasi-biennial oscillation of the tropical winds. In particular, intense wildfires have become more frequent. Their potential impacts on the stratosphere are not yet well quantified and are a subject of active research.
- **The impending loss of vertically resolved, global space-borne measurements of ozone-related atmospheric constituents (e.g., reactive chlorine, water vapor, and long-lived transport tracers) will impede the ability to monitor and explain changes in the stratospheric ozone layer in the future**

3.1 INTRODUCTION

This chapter assesses our current knowledge and understanding of past and potential future changes in near-global (60°S–60°N) ozone, updating the corresponding chapter from the previous Assessment (Braesicke, Neu et al., 2018). Our current state of knowledge regarding past-to-present ozone changes and trends is assessed, including attribution, confidence, and uncertainty regarding the drivers of the changes and trends, both from statistical modeling approaches and comprehensive chemistry-climate models (CCMs). The chapter also describes how ozone is expected to change in the future, given scenarios for emissions of greenhouse gases (GHGs), air pollutants and ozone-depleting substances (ODSs), which will affect the composition, chemistry, and climate of the atmosphere. As in past assessments, the key benchmark is ozone's return to its mean value at the reference time of 1980, near the beginning of observed ozone loss.

3.1.1 Summary of Findings from the Previous Ozone Assessment

The 2018 Assessment (Braesicke, Neu et al., 2018) examined the evidence for ozone recovery, drawing on updated statistical methods with more rigorous treatment of uncertainties. Evidence for significant ozone increases of 1–3% decade^{-1} was reported for the upper stratosphere (35–45 km), with the most robust trends in the Northern Hemisphere mid-latitudes. Simulations from CCMs attributed approximately half of this trend to the reductions in emissions of ODSs under the Montreal Protocol, with the other half coming from slowing of gas-phase chemistry caused by GHG-induced cooling. A reported decrease in lower-stratospheric ozone, particularly in the tropics, was found to be sensitive to the ozone dataset analyzed and the start and end years of the analyzed period. CCM simulations supported the hypothesis that any apparent trend was linked to dynamical variability. Small increases (0.3–1.2% decade^{-1}) in the near-global total ozone column were reported, although these were not statistically significant, given the uncertainties in the data and the large year-to-year dynamical variability (up to 5%). The importance of accurately quantifying tropospheric ozone changes was highlighted because they can be important for the total column ozone (TCO) trend and they are necessary to establish consistency between total column and profile data.

CCM projections of ozone recovery showed that for a baseline scenario with weak climate change mitigation (RCP6.0), global and Southern Hemisphere (SH) mid-latitude ozone should recover by the middle of the century, while the Northern Hemisphere (NH) mid-latitude ozone would do so by around 2035. With negligible halogen-driven ozone destruction, future projections of the ozone layer were found to be most sensitive to the greenhouse gas scenario: elevated GHG concentrations strengthen the stratospheric overturning circulation and impact ozone chemical loss through stratospheric cooling (see *Chapter 5*). Furthermore, the projected strengthening of the circulation results in scenario-dependent stratospheric ozone decreases in the tropics, while the overall column change also depends on the tropospheric ozone trends. Outside of long-term trends, the last Assessment also described how the slow decline of ODSs means that stratospheric injection of sulfate aerosols (e.g., from a large volcanic eruption) could still result in substantial near-term ozone losses.

3.1.2 Major New Developments Since 2018

As with past Assessments, an extended observational record facilitates revisiting the evidence for positive ozone trends, as well as their attribution to declining levels of halogenated ODSs controlled by the Montreal Protocol. In addition to the extended records, several merged, vertically resolved datasets have been updated and/or improved, and new ones developed (*Section 3.1.3* and *Appendix 3A*). Moreover, new statistical approaches have been developed and new model simulations have been conducted, both of which provide new insight on the drivers of recent trends.

The Long-term Ozone Trends and Uncertainties in the Stratosphere (LOTUS) initiative (SPARC/IO3C/GAW, 2019) has left a legacy of robust methods for trend detection and uncertainty calculation, from which this chapter draws heavily. New developments since the last Assessment include extending the methodology to diagnose trends by season, as well as demonstrating the utility of dynamic linear models (DLMs) in detecting trends and quantifying uncertainties. The growing use of advanced data science techniques, such as DLMs, is surveyed in **Box 3-1**. Moreover, new longitudinally resolved datasets of total column and vertically resolved ozone trends facilitate new comparisons and validations of ground-based and remotely sensed measurement data.

New simulations and analyses of CCMs have proceeded along two fronts: 1) coordinated multi-model experiments for hindcasts and future projections and 2) detailed investigations of specific issues, often with a single model. For the former, this chapter mostly makes use of simulations from Phase 6 of the Coupled Model Intercomparison Project (CMIP6; Eyring et al., 2016), covering 1850–2100 and including several future scenarios. However, compared to the Chemistry-Climate Model Initiative Phase 1 (CCMI-1) simulations (Morgenstern et al., 2017) used in the previous Assessment, the CMIP6 experiment does not mandate archiving the same degree of ozone-relevant model output and, moreover, includes fewer models that have a sophisticated treatment of atmospheric chemistry processes. For the more detailed studies, this chapter particularly benefits from new investigations into ozone trends in the upper troposphere and lower stratosphere, which, together with extended observations, enable better understanding of the drivers of the trends in this important region. Finally, several models have performed simulations targeted at quantifying the impact of recent unregulated CFC-11 emissions on the current state and future recovery of the ozone layer (WMO, 2021).

3.1.3 Data Sources, Quality, and Methods

The analyses and results presented in this Assessment rely on essentially the same ground-based and satellite ozone datasets as were used for the 2018 Assessment. The data records have been extended, and some of them have been partly or fully revised or reprocessed. An overview of the different data sources with more details about specific updates and revision efforts are given in *Appendix 3A*. Since the last Assessment, two new space-based instruments that measure ozone have been deployed, both launched in 2017: SAGE III on the International Space Station (ISS) and TROPOMI on the Sentinel 5 Precursor. SAGE III/ISS provides vertically resolved profiles using solar and lunar occultation (Szatkowski et al., 1999; Cisewski et al., 2014), while TROPOMI is

Box 3-1. Emerging Data Science Methods for Stratospheric Ozone Analysis

"Data science" is a broad term applied to the "principled extraction of information and knowledge from data" (Provost and Fawcett, 2013) and is a phrase whose use in the environmental sciences has been growing in recent years (e.g., Blair et al., 2019). While data science could be a label to describe statistical methods that have long been a staple for ozone analysis, the term is also used more particularly to refer to the adoption and development of more advanced approaches, including artificial intelligence (AI) and machine learning (ML). These have only recently been exploited in this field, thanks to increasing computational power and the wider availability of codes from the statistical and computer science research communities.

Many of the new approaches employ Bayesian inference. In contrast to frequentist approaches, where probabilities are derived from long-run frequency distributions, Bayesian approaches start with a prior hypothesis, such as for model parameters, whose probabilities are updated as additional information becomes available. This forms the basis of, for instance, dynamic linear modeling (DLM) methods, which have been used to understand ozone trends (*Section 3.2.2*). Bayesian approaches are well suited to data-sparse situations, although as data volume increases, inferences from frequentist and Bayesian analyses tend to converge (**Figure 3-5**).

This box briefly highlights some relevant emerging data science advances in three key areas: 1) creating new merged datasets, 2) emulating complex models, and 3) making better use of model output.

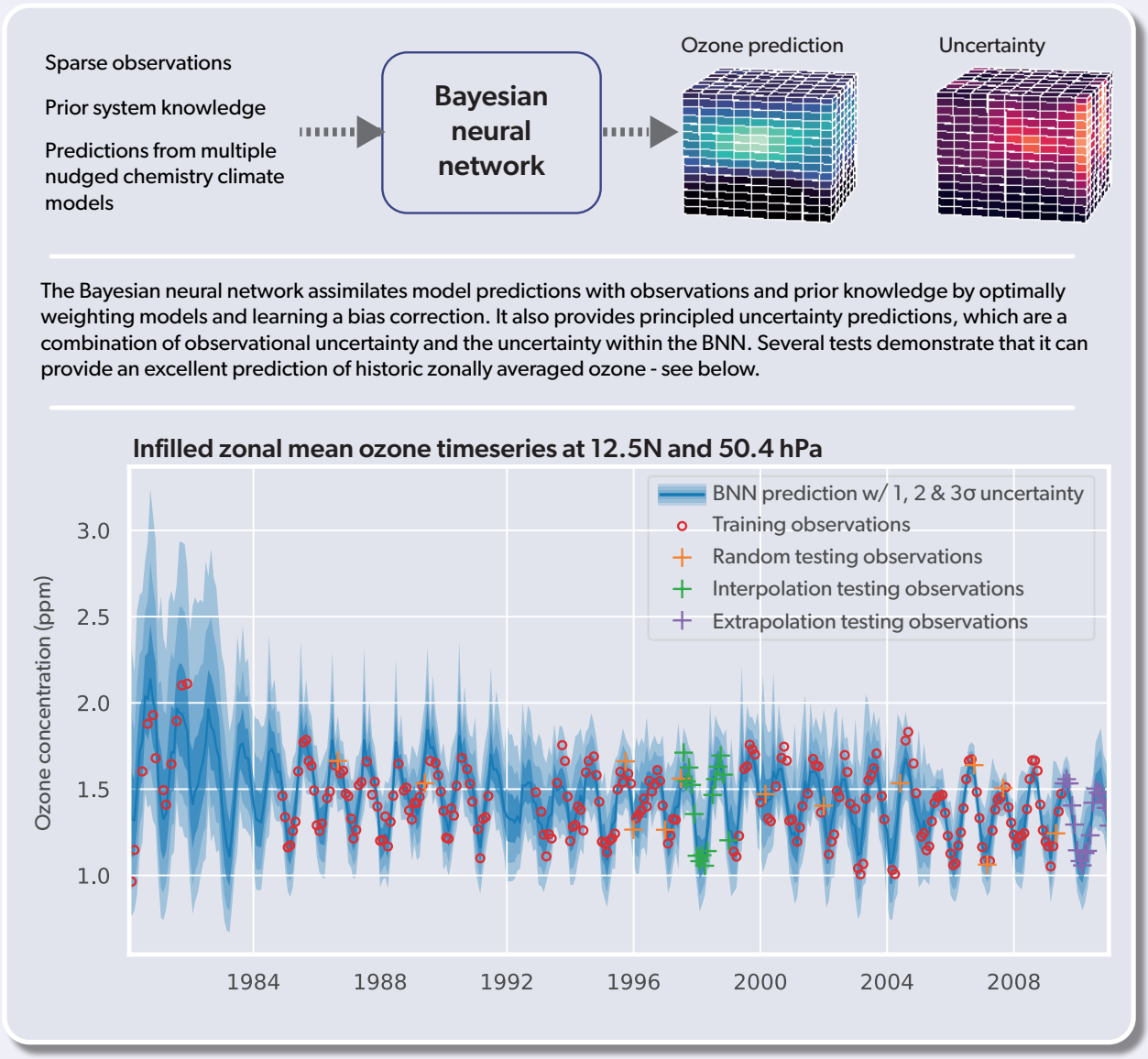

Box 3.1 Figure 1. Schematic of the Bayesian neural network (BNN). [Based on Sengupta et al., 2020.]

Creating New Datasets: Model-Measurement Fusion

Statistical techniques have long been employed to join different instrumental records into a complete time series, as well as to spatially and temporally infill sparse datasets, often using multiple linear regression (MLR)-based approaches (e.g., Bodeker et al., 2013; Davis et al., 2016), and now also with more advanced techniques (Loyola and Coldewey-Egbers, 2012; Ball et al., 2017; Bodeker et al., 2020; Dhomse et al., 2021). One different approach is the Bayesian neural network (BNN), which can be used to fuse data from chemistry-climate models (CCMs) and observations (Sengupta et al., 2020). A BNN can learn which weighted combination of CCM data is appropriate to use for a given location and time (rather than using fixed weights) and provide a principled treatment of uncertainty. A schematic of the BNN is given in the **Box 3.1 Figure 1**.

Complex Model Emulation

CCMs are computationally expensive and time consuming to run, which places practical limits on the number of simulations that can be completed. This limits both our exploration of model uncertainty, such as through alternative parameter choices to simulate chemical and physical processes, and the investigation of a wider range of possible future scenarios. One way to address this is to emulate the complex model with a sophisticated but computationally cheaper statistical approach. Approaches include building an emulator by fitting Gaussian processes to a set of carefully chosen calibration simulations, which can then be exploited to explore what would be simulated by the complex model across a multidimensional parameter space (e.g., Revell et al., 2018; Wild et al., 2020). Other studies have emulated CCM output using a variety of ML approaches, which have been used to explore a wide range of future scenarios (Keeble et al., 2021b), or they have proposed the adoption of ML-based algorithms within a CCM to replace more computationally expensive chemistry solvers (Nowack et al., 2018). Nevertheless, application of these newer approaches to stratospheric ozone research is still in its infancy, and CCMs in their current form remain our best tools for analyzing past ozone trends and generating future projections.

Approaches to Make Better Use of Model Output

Given the same input scenarios for greenhouse gases and ozone-depleting substances, different CCMs simulate a wide range of outputs. While some of this model spread represents irreducible uncertainty due to the chaotic nature of the climate system (which can be approximated as "weather noise"), different models will have varying levels of skill in reproducing reality. Moreover, this variation in simulation skill will likely be a function of, e.g., geographical region and season, atmospheric composition, and the prevailing climate. Different models are also seldom independent (e.g., Knutti et al., 2013). This varying model skill and intermodel commonality means that the commonly used multi-model mean does not provide the best estimate of the past, current, or future state of the atmosphere. Recent approaches have sought to improve on this by providing weighted multi-model means, where model weighting is based on a measure of model independence and the performance of the model when compared to observations (Amos et al., 2020; Sengupta et al., 2020). In the broader climate literature, other studies have developed and exploited "causal networks" for a novel process-based model evaluation (Runge et al., 2019; Nowack et al., 2020). This is a sophisticated data science approach to identify causal links through spatiotemporal correlations in observational data. These can then be examined to produce metrics to evaluate models and understand model-observation and model-model differences.

a nadir sounder that provides total and tropospheric column information as well as vertical profiles (Veefkind et al., 2012). Early validation efforts for both SAGE III/ISS (Wang et al., 2020) and TROPOMI (Hubert et al., 2021; Mettig et al., 2021) suggest the data are well suited to provide valuable information about long-term changes, and these data are already being incorporated into commonly used merged datasets.

Several currently operational spaceborne instruments are well beyond their design lifetimes, and some are scheduled to be decommissioned in the next few years. Instruments whose data have been used as part of this Assessment (see **Tables 3A-3** and **3A-4**) or previous Assessments (see Table 3A-1 of WMO (2014)) that will likely cease operations by the end of the 2026 Ozone Assessment process include the Aura Microwave Limb Sounder (MLS), the SciSat Atmospheric Chemistry Experiment Fourier Transform Spectrometer (ACE-FTS), the Odin Optical Spectrograph and Infrared Imager System (OSIRIS), and the Odin Sub-Millimetre Radiometer (SMR). With the loss of current limb-viewing capabilities, vertically resolved global measurements of many trace gases relevant for stratospheric chemistry and dynamics will no longer be available. These trace gases include reactive (chlorine monoxide, ClO) and reservoir (hydrochloric acid, HCl; chlorine nitrate, $ClONO_2$) chlorine species, water vapor, nitric acid (HNO_3), and long-lived transport tracers (e.g., nitrous oxide, N_2O; methane, CH_4; carbon monoxide, CO; methyl chloride, CH_3Cl). The recent Report of the Ozone Research Managers of the Parties to the Vienna Convention (ORM, 2021) identifies the need to "continue limb emission and infrared solar occultation observations from space" that are "necessary for global vertical profiles of many ozone- and climate-related trace gases" as one of the "key systematic observations recommendations." Indeed, the impending cessation of these measurements, many of which have been taken continuously over the last several decades, will hamper the ability to reduce key uncertainties that remain in understanding stratospheric ozone depletion, including the lack of emergence of a clear signature of recovery in the Arctic, the potential influence of volcanic and wildfire emissions, the role of very short-lived substances (VSLSs), and the impact of strengthening of the Brewer-Dobson circulation, among others.

In addition to the multiple merged datasets that were the

basis for most of the long-term, zonally averaged variability and trends discussed in the last Assessment, an additional dataset was created recently: SAGE II-SCIAMACHY-OMPS (Arosio et al., 2019). This includes a slightly different combination of satellite measurements than in previous merged datasets; however, since different merged datasets share underlying data sources, trends calculated using these datasets are not independent. Also, since the last Assessment the community has created new (gridded) latitudinally, longitudinally, and vertically resolved ozone datasets: an expanded version of the SAGE II-SCIAMACHY-OMPS dataset (Arosio et al., 2019) and MEGRIDOP (Sofieva et al., 2021). So far, only a few merged datasets provide gridded ozone profiles, which allow more detailed analyses of spatially and vertically resolved trends.

Data quality remains one of the key drivers of trend uncertainties, and specific topics, such as instrument drifts, biases, and sampling, were discussed in detail in the last Assessment. Considerable effort has since been made to improve individual instrument records as well as merged datasets. For example, ground-based vertical profile records were improved through homogenization of ozone soundings in the framework of the Tropospheric Ozone Assessment Report Phase 2 (TOAR II) project, homogenization of Umkehr and lidar records, and reprocessing of Dobson, Brewer, and FTIR records (see *Appendix 3A*). Satellite measurements have been improved by updating retrieval algorithms and by enhancing the consistency and stability between individual datasets. These advances in data quality, and the additional four years of data, have led to a more consistent picture of trends derived from ground-based and satellite measurements since the last Assessment. In addition to data quality, the methodology used to determine trends can also affect the resulting uncertainties. Not much has changed with respect to the most commonly applied multi-linear regression models for trend detection since the last Assessment, but alternative statistical models (e.g., dynamic linear models) are seeing greater use by the community and provide a robust alternative method of trend detection.

With the publication of the SPARC Reanalysis Intercomparison Project Report (SPARC, 2022), a comprehensive evaluation and intercomparison of meteorological reanalyses is now available, complete with recommendations on how to best use reanalysis data for long-term trend and variability analyses. For this reason, **Box 3-2** provides a discussion about the usability of reanalyses to calculate reliable ozone trends. However, the recommended practices have not yet been widely adopted by the community, and therefore trend studies based on reanalysis data are again not highlighted in this Assessment.

3.2 NATURAL VARIATION AND TREND MODELS

Ozone varies on seasonal, interannual, and decadal timescales as a result of both natural and anthropogenic forcing. Careful determination of long-term trends requires accurately attributing the other major sources of variability. The most common method of quantifying the trends is through statistical techniques involving linear regression (WMO, 2018; SPARC/IO3C/GAW, 2019, and references therein). Various regression techniques adopt different statistical approaches to evaluate trends and their uncertainties. Two common approaches in ozone analysis are multiple linear regression (MLR) and dynamic linear models (DLMs). The application of these linear regression techniques assumes that ozone is linearly dependent on predictor time series (or proxies) that dictate how it varies with time. The following sections present the different sources of variability and their proxies (*Section 3.2.1*), the different methodologies applied to calculate long-term ozone trends (*Section 3.2.2*), and (briefly) how significance is assigned to the calculated trends (*Section 3.2.3*).

3.2.1 Natural Variability

The primary influences on the global distribution of ozone are sunlight, chemistry, and transport of either ozone itself or any reactive species important for ozone chemistry. The proxies that describe these sources of variability are often empirical, rather than having a simple functional form, and are often not completely independent, as the processes can interact with each other or simply have similarities in their temporal dependence. This lack of

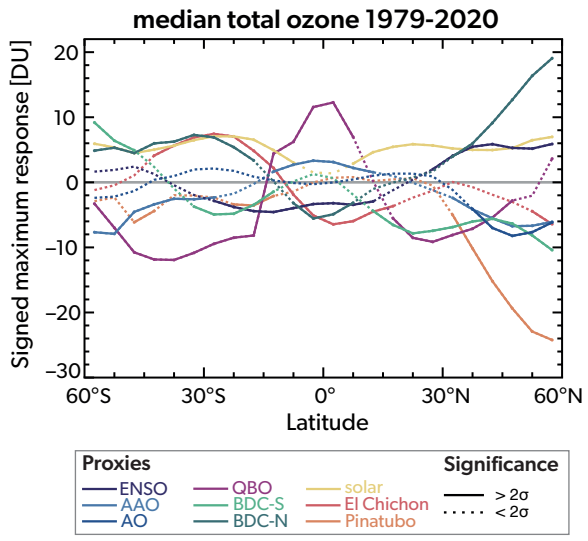

Figure 3-1. Maximum contribution of different sources of natural variability (as proxies) in a multiple linear regression analysis applied to the median of five TCO datasets as a function of latitude (Weber et al., 2022). Each colored line shows the response (i.e., deviation in Dobson units, or DU) of ozone resulting from a different proxy in the regression (see legend), with the sign indicating whether the ozone response is positively or negatively correlated with the proxy. A solid line indicates that the response to a given proxy is significant at the 5% level, whereas a dashed line indicates that it is not significant at the 5% level. [Adapted from Weber et al., 2022.]

Box 3-2. Can Reanalyses Be Used to Calculate Robust Ozone Trends?

Diverse methods are used to create ozone datasets from different sources or to fill gaps in existing datasets, including merging observations with simulated data. One of the goals is to provide ozone datasets suitable for trend analyses. Merging techniques are updated and further developed. Lately, machine learning techniques have also been applied to datasets with sporadic coverage (see **Box 3-1**). Reanalysis, which integrates physics-based prognostic meteorological models with observational data in an iterative way, is another approach. Both one-directional coupling (meteorology modifying prognostic ozone fields) and bi-directional coupling (ozone fields also modifying meteorological fields via radiation) are applied in reanalyses. As such, ozone estimates from reanalyses depend on both continued high-quality observations and the skill and accuracy of the underlying forecasting model.

In almost all current reanalysis systems, ozone is included as a prognostic variable. How well the ozone fields and their variability are represented in the different reanalyses depends on the assimilated observations and the chemical and microphysical model parametrizations. Primarily, total column ozone observations or measurements of broad vertically weighted averages are assimilated, but more recent reanalyses also assimilate observations with a higher vertical resolution (Davis et al., 2017). Problems for ozone trend analyses based on reanalysis data occur when the different assimilated data contain internal drifts or steplike changes (Wargan et al., 2020) and/or biases between the datasets (Wargan et al., 2018). Approaches to account for internal drifts and biases exist (van der A et al., 2010, 2015) but have so far not been widely applied. Additionally, assimilation of radiances and other parameters might introduce step changes in stratospheric temperatures and wind fields that directly influence the estimated ozone distribution (Stauffer et al., 2019), and inhomogeneities and discontinuities can be introduced by a changing number of assimilated datasets over time (Sterl, 2004; Simmons et al., 2014; Shangguan et al., 2019).

For these reasons, there has been reluctance to use ozone from reanalysis datasets for trend studies despite successful use in ozone-related process studies (e.g., Banerjee et al., 2020; Orr et al., 2021). Recent developments in data assimilation methodology do seek to address the continuity issues outlined above. Some reanalyses currently include bias correction or ozone data homogenization algorithms (van der A et al., 2010, 2015; Hersbach et al., 2020; Wargan et al., 2020). Additionally, several recently developed reanalysis products focus specifically on atmospheric composition and use sophisticated chemistry models that help correctly propagate observational data in space and time by providing stable priors for data assimilation (Flemming et al., 2017; Errera et al., 2019; Inness et al., 2019a, 2019b; Huijnen et al., 2020).

There is, therefore, a tension between some clear advantages that reanalyses provide for studies of long-term trends and variability, and current limitations. The SPARC Reanalysis Intercomparison Project (S-RIP) has made substantial progress in providing advice to users and feedback to reanalysis centers. The S-RIP report (SPARC, 2022) provides a comprehensive evaluation and intercomparison of 12 major meteorological reanalyses with a focus on the representation of stratospheric processes and assimilated fields, including ozone. An overview of the skill level demonstrated in different reanalysis datasets for different metrics of ozone trends and variability, as analyzed with S-RIP, is shown in **Box 3-2 Figure 1**. Several recommendations emerged from this evaluation: 1) trends from reanalyses should be treated with caution; 2) an understanding of the reanalysis systems is necessary for interpretation; 3) studies should use multiple reanalyses and, where possible, other data to help assess result robustness and estimate uncertainties; and 4) the use of several specific, now-outdated reanalyses is discouraged.

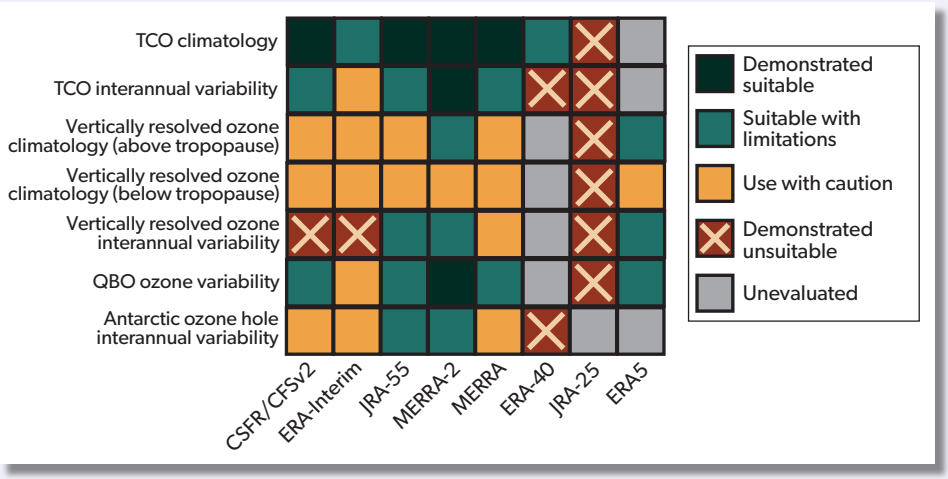

Box 3.2 Figure 1. Overview of analyzed ozone diagnostics with a variety of recent and commonly used meteorological reanalysis data, with recommendations on where the data can be used most appropriately. [Adapted from Davis, Hegglin et al., 2021, in SPARC, 2022.]

orthogonality between the proxies can sometimes make it difficult to attribute variability in ozone directly to one source or another. Furthermore, since the 2018 Assessment, new behavior has been observed that raises questions about the suitability of some of the proxies that are typically used, with concerns regarding how well they represent the actual variability of ozone. **Table 3A-1** lists the sources of data for different proxies, while **Figure 3-1** illustrates a comparison of the relative impact that some of the different sources of variability described here have on total column ozone (TCO) as a function of latitude.

3.2.1.1 The Quasi-Biennial Oscillation (QBO)

The Quasi-Biennial Oscillation (QBO) is a pattern of alternating zonal winds in the tropical stratosphere that affects ozone through transport and chemistry. It is characterized by an oscillating pattern of easterly and westerly winds in the stratosphere, with a variable (24–32 month) period over which it progressively descends through the stratosphere (**Figure 3-2a**). These oscillating wind shear patterns induce oscillating vertical motions in both the tropics and extratropics that are opposite in direction to each other along with corresponding meridional transport in between (Baldwin et al., 2001). The response of ozone to the QBO is strongest in the tropical lower stratosphere, with secondary maxima in the middle stratosphere in both the tropics and low-latitude (<40°) extratropics (Zawodny and McCormick, 1991).

The QBO is the dominant source of variability of stratospheric ozone in the tropics, particularly in the lower stratosphere, and it is a modulator of variability at higher latitudes (Anstey and Shepherd, 2014). It is vital that its influence be accurately represented in trend analyses. The vertical and meridional transport and chemical influence of the QBO on ozone are represented using tropical zonal wind data as a proxy. This usually takes one of two forms: a pair of time series of zonal wind measurements from two different pressure levels that are roughly out of phase from each other, or the leading two empirical orthogonal functions (EOFs) derived from this data (Wallace et al., 1993; Randel and Wu, 1996). The latter is preferable since EOFs are explicitly constructed to better represent the variability present in all of the source data. The proxies typically represent over 90% of the QBO's variability but are limited in their ability to fully represent the effect of the QBO on ozone. For example, the seasonal cycle modulates the QBO at higher latitudes (Tung and Yang, 1994), creating a nonlinear effect that must be adequately captured in regression analyses, such as by using seasonal cross-terms in the regression (Randel and Wu, 1996; Damadeo et al., 2014). Not accounting for this can make trend analyses particularly sensitive to the endpoints (Ball et al., 2019a).

The typical pattern of the QBO has been fairly stable and repeatable over the first six decades of observations of tropical zonal winds, which started in the early 1950s. The last Assessment highlighted the first-ever disruption to the QBO in 2015/16 (Newman et al., 2016; Osprey et al., 2016; Tweedy et al., 2017), and since then another disruption happened in 2019/20 (Saunders et al., 2020; Anstey et al., 2021), as illustrated in **Figure 3-2a**. In both cases, large horizontal momentum fluxes originating from the extratropics propagated to the tropics, where they interfered with the normal momentum transfer associated with the QBO (Coy et al., 2017; Lin et al., 2019; Saunders et al., 2020; Anstey et al., 2021). This resulted in the introduction of westward winds at around 40 hPa (~35 km) during the eastward phase and lifting of the eastward winds. The changing wind shear patterns associated with these disruptions drove correlated changes in stratospheric ozone resulting from changes in upwelling. While the impacts were similar in the two cases, the origin of each disruption was different. The 2015/16 disruption was caused by the coincidence of a particularly strong El Niño event in the Northern Hemisphere (Coy et al., 2017; Lin et al., 2019), while the 2019/20 event was the result of strong wave forcing from the Southern Hemisphere in the absence of any El Niño event (Saunders et al., 2020; Anstey et al., 2021).

These disruptions present an additional challenge as to the representativeness of the QBO proxies used in regression analyses. During such disruptions, the amount of QBO variance explained by the two leading EOFs is substantially reduced and higher-order EOFs are necessary to fully capture the variability (**Figure 3-2b**). It has not yet been determined if these higher-order EOFs can adequately capture the correlated variability in ozone during the disruptions. In addition, while these were unprecedented in the observational record, they may not be isolated incidents. Accounting for QBO disruptions may become necessary for both current and future trend analyses.

3.2.1.2 El Niño-Southern Oscillation (ENSO)

The El Niño-Southern Oscillation (ENSO) is a pattern of alternating warm and cold sea surface temperatures (SSTs) of the tropical eastern and western Pacific Ocean, which influence tropospheric circulation and stratosphere-troposphere exchange. Warmer El Niño phases increase tropical upwelling, resulting in negative ozone anomalies in the tropical upper troposphere/lower stratosphere (UTLS), whereas colder La Niña phases decrease tropical upwelling and result in positive ozone anomalies (Domeisen et al., 2019); ozone anomalies also occur at mid-latitudes, which may differ separately by hemisphere with the ENSO phase (Ziemke et al., 2010; Oman et al., 2013). Ultimately, ENSO can substantially affect stratospheric circulation as a whole by influencing other transport mechanisms such as the QBO or the Brewer-Dobson circulation (BDC; Domeisen et al., 2019, and references therein). For example, the QBO propagates downward more rapidly during an El Niño phase, and El Niño leads to a strengthened BDC associated with tropical stratospheric cooling, warmer poles (Randel et al., 2009), and weaker stratospheric polar vortex (Ermakova et al., 2019). These interconnections make ENSO an important process controlling the interannual variations of stratospheric ozone but complicate any regression analyses that assume all proxies are orthogonal to each other.

The ENSO-related proxies used for long-term trend analyses are computed as an index that is derived from a number of possible oceanic and/or atmospheric parameters (Domeisen et al., 2019). Among them are the Niño 3.4 Index, which derives directly from a time series of Pacific SST anomalies over a region in the tropical Pacific (Huang et al., 2017), and the multivariate ENSO index (MEI), computed from a principal component analysis of SSTs, surface air temperatures, sea level pressures, surface winds, and radiation over the tropical Pacific (Wolter and Timlin, 1998). These simple indices may capture the general ENSO pattern that correlates with ozone variability but do not account for the more subtle impacts of ENSO on circulation patterns. Stratospheric ozone anomalies and large SST anomalies are found not only during El Niño and La Niña but also during the transition phases (Lin and Qian, 2019). However, sometimes SST anomalies are not

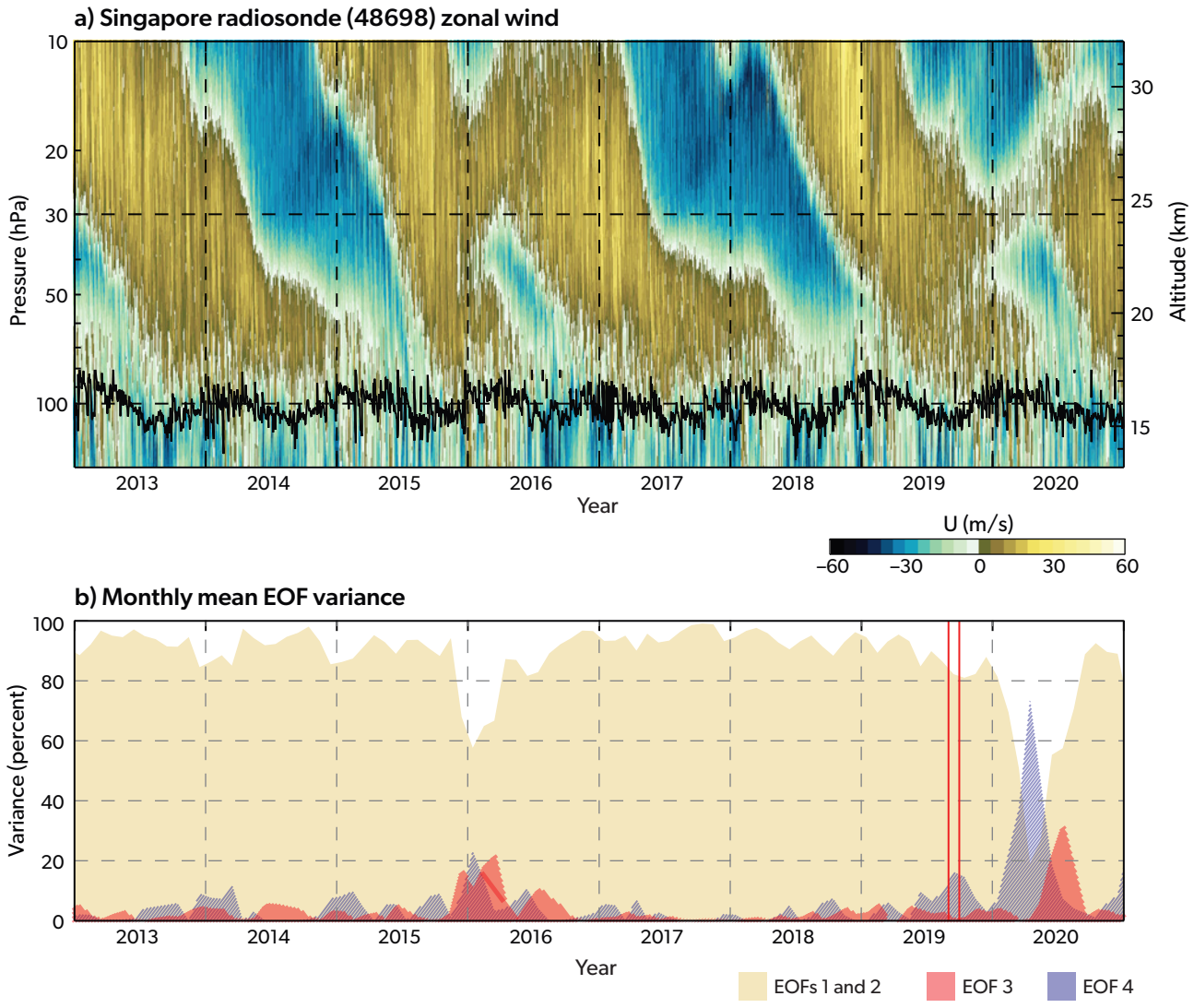

Figure 3-2. (a) Zonal winds observed from radiosondes at Singapore (blue to gold shading) and the lapse-rate tropopause (black line). Disruptions in the zonal winds are noticeable by the ascending gold shading above 40 hPa in 2016 and 2020 that breaks the descending blue shading. (b) Amount of variance explained over time by the first two EOFs (light orange shading), the third EOF (dark orange), and the fourth EOF (blue), computed from the Singapore wind data excluding the two disruptions. Typically, 80% or more of the QBO variability can be represented by the leading two EOFs, but the disruptions illustrate that additional EOFs are required to adequately capture the variability during these time periods. The two vertical red lines bracket September 2019. [Adapted from Anstey et al., 2021.]

accompanied by corresponding atmospheric anomalies; these events are called uncoupled El Niño warming (Hu et al., 2020).

The potential disconnect between an ENSO proxy and ozone anomalies exists in part because ENSO's influence is the by-product of the propagation of highly regionalized effects to the rest of the atmosphere. Moreover, the remote impacts depend on the location and intensity of ENSO events. The SST anomalies are not always simply warm or cold in the eastern Pacific ("canonical ENSO") but are sometimes warm in the Central Pacific ("ENSO Modoki"; Ashok et al., 2007) or even double-peaked with warm centers in both regions (Shin et al., 2021). These subtle differences can result in noticeable changes in stratospheric ozone. For example, the warm phase of canonical ENSO has been found to be associated with negative ozone anomalies in the SH lower stratosphere and positive ozone anomalies in the NH lower stratosphere, while the warm phase of ENSO Modoki results in the opposite (Lu et al., 2019).

Both the simplicity of the ENSO proxy and the way it is implemented can affect long-term trend analyses. ENSO indices are a single time series, meaning they cannot alone account for any lag in the response. The response of stratospheric ozone to the phase of an ENSO index derived from tropospheric data is often delayed by several months, with the strongest anomaly appearing in the NH winter one year after El Niño (Lin and Qian, 2019). Another aspect of trend analysis implementation is the spatial coordinate system of the ozone data. For instance, when ozone is gridded

with respect to the location of the subtropical jet, its variability in the UTLS shows a stronger correlation with ENSO variability than if it was analyzed in the usual latitude/longitude/altitude coordinate system, although this is still an active area of study (Olsen et al., 2019). Including the QBO in the analysis shows that ENSO generally dominates ozone variability around the subtropical jet, while the magnitudes of the QBO and ENSO impacts are more comparable at mid-latitudes.

3.2.1.3 Aerosols

The term "aerosols," which is strictly defined as fine particles suspended in a gas, is essentially a catch-all term for everything in the atmosphere that is not a gas or cloud, although the focus is generally on the particle component. Aerosols exhibit many different compositions and originate from a variety of natural and anthropogenic sources (Kremser et al., 2016, and references therein), but the most common form of aerosol in the stratosphere is an aqueous suspension of sulfuric acid (Junge et al., 1961). The last Assessment went into detail regarding the sources and impacts of aerosols on ozone. In brief, aerosols affect ozone through two main mechanisms. The first is by offering a surface for heterogeneous chemistry that leads to denitrification and primarily leads to ozone destruction/enhancement in the presence/absence of chlorine. The second is by cooling the Earth's surface and heating the stratosphere, which both alters chemical reaction rates and modifies circulation. The first mechanism is influential at the location of the aerosol, while the second mechanism can have impacts beyond that. (See *Chapter 6* for the potential ozone impacts of stratospheric aerosol from climate interventions.)

Stratospheric aerosol proxies for use with long-term ozone trend analyses are derived from long-term aerosol data records (e.g., Chouza et al., 2020; Kovilakam et al., 2020), which are composed of individual satellite- and ground-based measurements. Since the last Assessment, several of these instrument records have been improved, including OMPS (Chen et al., 2018), OSIRIS (Rieger et al., 2019), and CALIPSO (Kar et al., 2019); a new instrument, SAGE III/ISS (Chen et al., 2020; Wang et al., 2020), has also been deployed, as mentioned in *Section 3.1.3*. These updated and new datasets have been used to generate a more consistent long-term multi-instrument stratospheric aerosol record with version 2.0 of the GloSSAC (Kovilakam et al., 2020). As an improvement over version 1.0 (Thomason et al., 2018), version 2.0 uses the new SAGE III/ISS data to recalibrate the bias correction of OSIRIS and CALIPSO data so that they better align with the native aerosol extinction measurement of SAGE II and SAGE III/ISS for a more consistent multi-decadal record.

While sulfate makes up the majority of stratospheric aerosol, and volcanic eruptions are the primary source, some other sources of stratospheric aerosol include black and brown/organic carbon components, which will impact the properties of the injected aerosol. Normally, carbonaceous aerosols do not make it into the stratosphere in appreciable levels, but the time since the last Assessment has seen the two largest fire-fueled thunderstorms (pyroCbs; see also *Chapter 6*) ever recorded, and both resulted in smoke injection into the stratosphere. These fires were in Canada in 2017 (Bourassa et al., 2019; Kloss et al., 2019; Yu et al., 2019) and Australia in 2020 (Kablick et al., 2020; Khaykin et al., 2020; Schwartz et al., 2020; Yu et al., 2021). Smoke aerosols are typically larger than stratospheric sulfate particles, so they have more surface area to facilitate chemical processes. They also heat the stratosphere more efficiently, particularly black carbon, through absorption of both outgoing infrared and incoming solar radiation. The 2020 Australian wildfires resulted in denoxification typically seen with volcanic eruptions (Solomon et al., 2022) and unprecedented chlorine partitioning (Santee et al., 2022) that cannot be explained by existing sulfate aerosol-based modelling (Strahan et al., 2022), as well as the first major impact to global lower-stratospheric temperature (>0.5 °C) since the 1991 Mount Pinatubo eruption (Rieger et al., 2021; see *Chapters 5* and *6*). At the same time, stratospheric ozone was reduced by 0.1–0.2 ppm throughout the SH mid-latitudes starting several months after the fires, an amount comparable to the impact of the 2015 Calbuco eruption (**Figure 3-3**). However, as a relatively recent occurrence with few published studies, there is still some debate as to how much of this observed low ozone was a result of the smoke injected into the stratosphere (Rieger et al., 2021; Solomon et al., 2022; Bernath et al., 2022) versus expected as a result of transport from unperturbed natural variability (Santee et al., 2022; Strahan et al., 2022).

Differences in the type of aerosol contributing to stratospheric aerosol perturbations can have implications for the nature of the aerosol proxy that is used and how it relates to changes in ozone. For example, aerosol surface area density would correlate quite well to chemistry, but smoke aerosol and sulfate aerosol of the same size would have substantially different radiative impacts. Similarly, smoke and sulfate aerosol can have appreciably different particle size distributions and thus similar aerosol optical depth at one wavelength but very different at another. For ozone trend analyses across periods where smoke aerosol becomes the dominant aerosol influence, this may pose a problem for the usefulness of aerosol proxies that assume stratospheric aerosol is dominated by sulfate. However, the different impact of wildfires may be a problem only when an aerosol proxy is applied to data after the mid- to late 1990s, as the large ozone response to the Mount Pinatubo eruption in late 1991 will dominate any potential erroneous response to much smaller stratospheric aerosol injections that occurred after the early 2000s.

Another example of an atypical stratospheric aerosol injection event are the January 2022 eruptions of the Hunga Tonga-Hunga Ha'apai volcano. These eruptions injected large amounts of water vapor into the stratosphere and are a topic of ongoing research but are expected to have some impact on stratospheric ozone, perhaps unlike that of previous eruptions of similar size (see **Box 5-1**).

3.2.1.4 Solar Radiation

Variations in the sun's irradiance affect ozone through photochemical processes in the upper and middle stratosphere, as well as through possible associated dynamical feedbacks (Haigh, 1994; Hood and Soukharev, 2003). Solar fluxes as a function of wavelength (spectral solar irradiance [SSI]) are needed to describe this forcing. Ultraviolet (UV) wavelengths shorter than 242 nm are particularly important as they drive the primary production of ozone from oxygen photolysis. However, direct, stable, long-term UV observations are not available due to the short lifetime of observing satellites and in-flight instrument degradation, making an accurate representation of solar UV changes on decadal timescales a challenge. Solar UV variability is highly correlated with solar radio fluxes in the 10.7 and 30 cm ranges. While both are used, recent analyses indicate that in the context of attribution

studies, the 30 cm radio flux is a better representative of solar UV variability than the 10.7 cm flux (Dudok de Wit et al., 2014; Dudok de Wit and Bruinsma, 2017). Solar energetic particles are also important for stratospheric ozone, and these are discussed in *Chapter 4*.

In the last Assessment, consistency in the estimated effects of solar forcing on ozone over the past decade was low. This was due to different derived responses of ozone to solar variability between different ozone datasets, as well as surprising observations of the 11-year solar cycle, which indicated much larger variability for some UV wavelengths compared to previous observations. Progress has been made in these areas.

Since the previous Assessment, new analyses and corrected ozone datasets have led to closer agreement on the magnitude and location of the ozone response to the solar cycle. The last Assessment reported that the observed ozone/solar cycle response had reduced to ~1% in the upper stratosphere (Dhomse et al., 2016; Maycock et al., 2016), with estimates from SBUV MOD v8.6 mixing ratio data showing a smaller signal than the SAGE II v7.0 number density data. While it was further noted that estimates from number density data (**Figure 3-4a**) were more robust (Ball et al., 2019b), unexplained differences remained. More recent studies now suggest the smaller solar-ozone response from SBUV data is likely a result of a satellite drift (Li et al., 2016; Ball et al., 2019b). Accounting for this, new SBUV and SAGE II-based composites agree that the magnitude of the maximum solar response in the tropics is ~2% (2σ uncertainty of 1%) and occurs at ~7 hPa (35 km; **Figure 3-4b**), although the peak is vertically broad (5–10 hPa or ~32–38 km). This is a lower altitude than in some earlier studies (Soukharev and Hood, 2006; Dhomse et al., 2016; **Figure 3-4a**).

While these results include data from the Aura MLS satellite (operational since 2004), they are also in broad agreement with a recent study that used Aura MLS data alone (Dhomse et al., 2022), factoring in the magnitude of the solar cycle and associated uncertainties. This recent study covers a period (2005–2020) of monotonic changes in equivalent effective stratospheric chlorine (EESC) and few volcanic eruptions that could substantially influence the stratosphere (see *Section 3.2.1.3*). It found an ozone response of ~3% with a single broad peak at ~5 hPa (~38 km) in the tropical stratosphere. A secondary ozone peak in the tropical lower stratosphere, discussed in the previous Assessment and thought to be a dynamical response to the solar cycle, was found to be notably smaller than in previous estimates when considering Aura MLS data alone (Dhomse et al., 2022). These results are robust across several multiple linear regression approaches (see *Section 3.2.2*).

The previous Assessment also reported that, at the time, the latest measurements showed much larger variability across solar cycles for some UV wavelengths than previous observations.

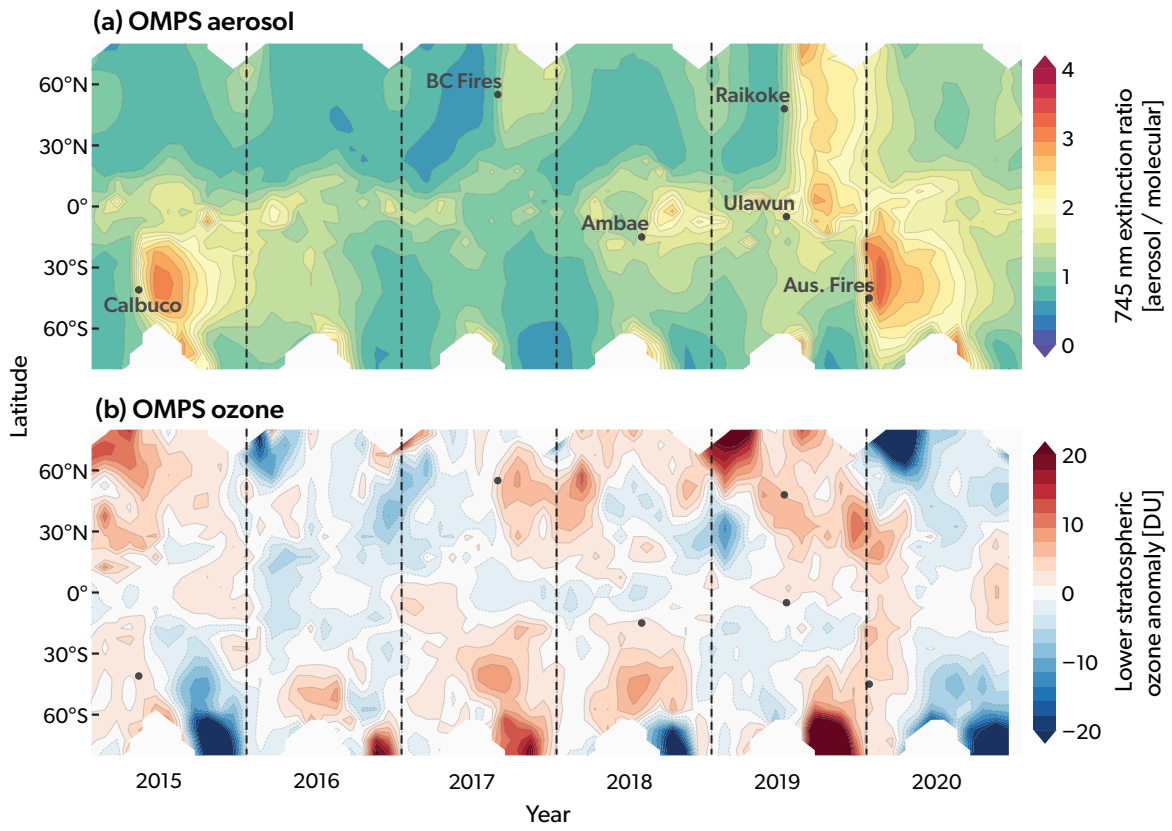

Figure 3-3. (a) Ratio of OMPS-LP lower-stratospheric aerosol extinction at 745 nm to molecular scattering, an indicator of the presence of aerosols. Major sources of stratospheric aerosol during 2015–2020 are indicated. (b) Deseasonalized lower-stratospheric ozone anomaly from OMPS-LP. [Adapted from Rieger et al., 2021.]

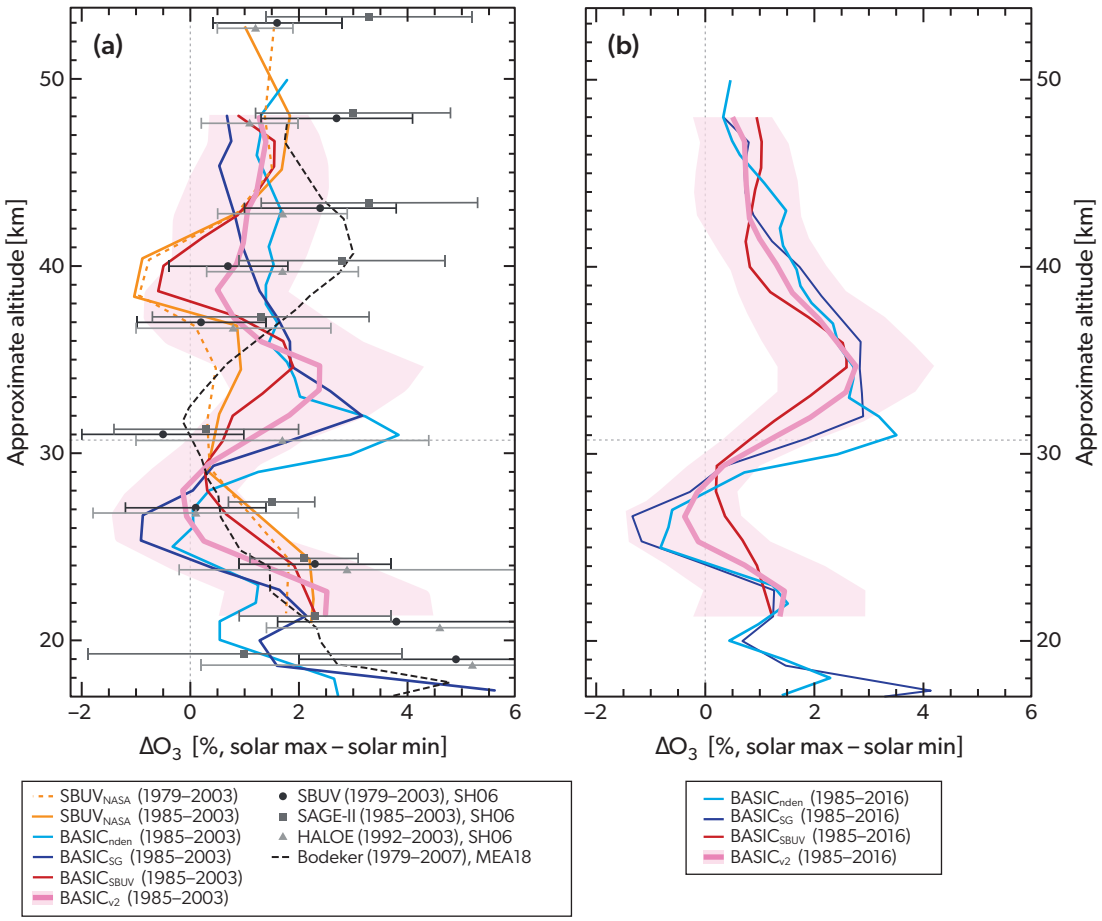

Figure 3-4. The response in upper-stratospheric tropical (25°S–25°N) ozone due to solar cycle forcing (solar maximum minus solar minimum) for different datasets and time periods. (a) Analyses performed over different periods (between 1979 and 2007) by Maycock et al. (2018) ("MEA18"; dashed), using ozone data from Bodeker Scientific ("Bodeker"; Bodeker et al., 2013); Soukharev and Hood (2006) ("SH06"), using ozone data from SBUV (black circles), SAGE-II (dark gray squares), and HALOE (light-gray triangles); and sensitivity analyses for periods that end in 2003 using the SBUV NASA (MOD) data only (orange, solid/dashed) and using different versions of the BASIC dataset (Ball et al., 2017, 2019b; light blue, blue, red, pink). (b) Analyses performed with the SBUV and BASIC ozone datasets for the full analysis period, 1985–2016 (colors in legend represent the same datasets as in the legend in [a]). [Adapted from Ball et al., 2019b.]

However, observed and reconstructed SSI datasets driven by analysis of new SSI observations from the SORCE satellite mission are now converging, reducing uncertainties in the attribution of ozone variability to SSI variability. Variability in UV fluxes in cycle 24 (1996–2008) reported early in the SORCE mission was larger than previous estimates (Harder et al., 2009) and has been regularly revised down. In cycle 25 (2008–2019), SORCE observations showed relatively lower variability, in better agreement with that of the two main SSI reconstructions (Krivova et al., 2010; Yeo et al., 2014; Coddington et al., 2016). These reconstructions have been merged to form the climate model forcing data for the latest generation of multi-model experiments (e.g., CMIP6; see **Box 3-4**; Matthes et al., 2017). Moreover, retrievals from TSIS, SORCE's successor, also display similar behavior to these solar irradiance reconstructions, albeit only within uncertainties and for a short overlap period (Mauceri et al., 2020).

Finally, since the previous Assessment, there have been additional chemistry-climate model (CCM) simulations of the solar-ozone response in the tropical lower stratosphere. The response in ozone was as high as 6% in earlier analyses (Austin et al., 2008); in the new simulations, the response is smaller, ~2%, and more consistent across CCMs (Maycock et al., 2018). However, some differences in the solar response remain in CCMs, attributable to remaining uncertainties in solar cycle SSI changes and structural uncertainty in the models (Kunze et al., 2020).

3.2.1.5 Other Dynamical Influence Factors

Patterns of atmospheric circulation and transport have a marked effect on the distribution of ozone around the globe. In addition to sources of transport already discussed as part of other natural variability proxies, some of the largest influences on ozone variability are the BDC, atmospheric jets and waves, and the direct exchange of air between the lower stratosphere and upper troposphere. Some of the more influential examples of these different mechanisms are discussed here.

The BDC describes the global-scale meridional circulation in the stratosphere. It largely dictates the distribution of stratospheric ozone through transport and chemistry and is driven by atmospheric waves originating in the troposphere (e.g., Butchart, 2014). While long-term trends in the BDC (*Chapter 5*) will impact long-term ozone trends, variability at shorter timescales is also important. For example, ozone trends calculated in BDC-sensitive locations (such as the tropics at ~35 km) vary considerably depending on the time period analyzed, and this has been attributed to sub-decadal variation in the strength of the BDC (Arosio et al., 2019; Galytska et al., 2019). At multi-decadal timescales, BDC strength may be coupled to the Interdecadal Pacific Oscillation (IPO; e.g., Henley et al., 2015). Model simulations suggest that the IPO could explain up to 50% of the decadal variability in tropical mid-stratosphere ozone (Iglesias-Suarez et al., 2021).

Year-to-year variability of the polar vortex strength also influences the ozone distribution not only in polar regions but also at mid-latitudes. This is especially important for the Northern Hemisphere, where the polar vortex is often disturbed by planetary wave activity. In particular, the anticipated ozone recovery in late winter has been shown to be sensitive not only to ODS decline but also to the polar vortex changes, and late-winter ozone recovery could be substantially delayed in some regions of the NH extratropics due to trends in the polar vortex driven by climate change (Zhang et al., 2018; von der Gathen et al., 2021; see also *Chapter 4*).

Another source of ozone variability in the lower stratosphere are intrusions of tropospheric air. The uplift of tropospheric air occurs along the ascending warm conveyor belt of the cyclonic structure (Stohl, 2001). Most tropospheric intrusions do not reach high altitudes, predominantly staying within the UTLS layer, where their impact on ozone concentrations is comparatively small. However, deep intrusions can even lead to the formation of intermittent ozone "mini-holes" (Reutter et al., 2015; Sofiev et al., 2020). A recent example of tropospheric influence is the persistent smoke-charged vortex generated by the 2019/20 Australian wildfires, which caused an ozone mini-hole (Khaykin et al., 2020). Currently, tropospheric intrusions do not have a noticeable impact on ozone trends, but the impact could increase if such events became more frequent in the future (see also *Section 3.2.1.3*).

The previous Assessment detailed dynamical proxies that can be used in the ozone trend analysis-eddy heat flux (EHF), tropopause pressure, the Arctic Oscillation (AO), the North Atlantic Oscillation (NAO), the Antarctic Oscillation (AAO), and an index for the upper branch of the BDC (UBDC)—with more recent studies also using proxies related to the Indian Ocean Dipole (Krzyścin, 2017; Thompson et al., 2021; **Table 3A-1**). Using dynamical proxies can improve the regression fit in some regions, but they can only partly explain the complicated and intermittent structure of dynamical variability. Moreover, since changes in dynamics can also be a response to a long-term driver, the use of these proxies requires care in interpreting what is driving and what is responding to long-term perturbations. However, at least for the middle and upper stratosphere, zonally averaged ozone trends outside of the polar regions are not very sensitive to the inclusion of EHF, NAO/AO, and AAO indices. (SPARC/IO3C/GAW, 2019; see also *Section 3.2.2*).

3.2.2 Long-Term Trends and Trend Models

In addition to proxies for natural variability, regression model approaches for understanding changes in ozone also include a long-term trend component (Laine et al., 2014; Weber et al., 2018; SPARC/IO3C/GAW, 2019). This component does not necessarily have a well-defined form or cause. Obvious candidates are long-term changes in ODSs or temperature, but any long-term changes in transport mechanisms or concentrations of non-halide species involved in regular ozone chemistry can play a role.

The statistical approach to modeling ozone determines how the long-term changes are captured. In multiple linear regression (MLR; e.g., see WMO, 2018), the form of long-term changes is prescribed, usually being either linear or chemistry based. Linear forms, such as the piecewise linear trend (PWLT; Newchurch et al., 2003) and independent linear trend (ILT; WMO, 2014; Weber et al., 2018; SPARC/IO3C/GAW, 2019), allow for the possibility of a turnaround in the trend but will not follow the curvature of ODS-related changes. Chemistry based forms, such as the EESC proxy (Newman et al., 2007) or EOFs based on it (Damadeo et al., 2014), assume a turnaround in the long-term trend related to the mean age-of-air, which itself may be variable over time (Li et al., 2018). However, these will be ineffective (single proxy) or less effective (2 x EOF proxy) in representing monotonic trends. On the other hand, dynamic linear model (DLM; Laine et al., 2014; Ball et al., 2018; Alsing, 2019) or ensemble empirical model decomposition (EEMD; Bai et al., 2017; Boleti et al., 2020) approaches can estimate a smoothly varying background trend without assuming its shape. These trend models allow the freedom to accurately represent the nonlinearity of long-term changes, whether they have a turnaround or are monotonic. However, the curvature near the beginning or end of the analysis period is less constrained and subject to larger influence from interannual variability, especially when this is not well represented by the proxies, although such

Table 3-1. Comparison of five different trend models for ozone. Abbreviations are defined as follows (see also *Section 3.2.2*): piecewise linear trend (PWLT), independent linear trend (ILT), effective equivalent stratospheric chlorine (EESC), EESC empirical orthogonal functions (EESC EOFs), and dynamic linear model (DLM).

	PWLT	ILT	EESC	EESC EOFs	DLM
Allows for a variable turnaround date	No	Yes	No	Yes	Yes
Allows for monotonic trends	Yes	Yes	No	Yes	Yes
Can follow nonlinearity of chemical changes	No	No	Yes	Yes / Not as well when monotonic	Yes
Local trend affected by end data (relative comparison between methods)	Middle	Middle	Smallest	High	Highest
Comparative computational cost	Low	Low	Low	Low	High

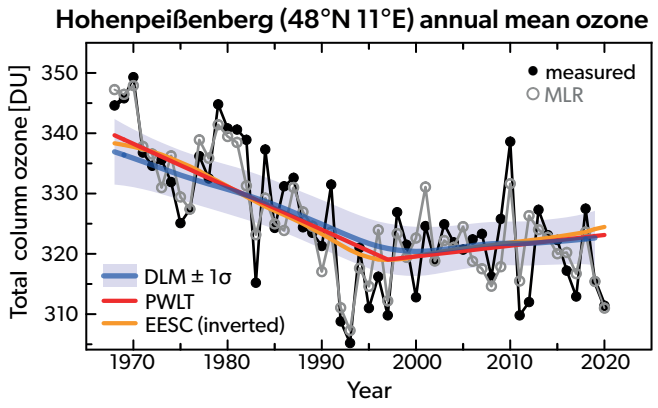

Figure 3-5. Example comparison between different trend models fitted to annual mean TCO at Hohenpeißenberg. Observations (solid black circles) are fitted with an MLR regression model including a PWLT and proxies for the QBO, solar cycle, Arctic Oscillation, and stratospheric aerosol with chlorine weighting (open gray circles). Also shown are different trends: an MLR-based trend result using a PWLT (red line), a single EESC-based trend (orange line), and a DLM-based trend (blue line) with its 1σ-uncertainties (blue shading). Despite differences over shorter timescales in the representation of the nonlinearity of changes in the data, the overall trends are similar among the three trend models. [Adapted and updated from Steinbrecht et al., 2011.]

influence is encompassed by larger uncertainties during these periods. The pros and cons of the different trend models are outlined in **Table 3-1**, but it is important to note that when applied to decades of data, trends are usually well represented by all of the models (**Figure 3-5**), with varying levels of uncertainty.

While the choice of trend model is important, the methodology of the applied analysis is equally, if not more, important. Trend analyses rely on widely accepted statistical regression techniques that are becoming increasingly sophisticated (e.g., more aspects of variability, more detailed uncertainty analysis). The most commonly applied technique is MLR, but DLM-like techniques have become increasingly popular, especially with the availability of pre-written code (Alsing, 2019), and are being explored in community-wide efforts like LOTUS (SPARC/IO3C/GAW, 2019). Current implementations of both MLR and DLMs are similar in their underlying construction and assumption of a linear dependence of the regressed data on proxies. However, they differ fundamentally in their underlying statistical principles (Bayesian versus frequentist; see **Box 3-1**) and in how they model the time evolution of the data.

DLMs are underpinned by a Kalman filter framework and have advantages over traditional MLR approaches (Alsing, 2019): they allow 1) a flexible, time-varying background trend, 2) seasonal and regressor variables to modulate in time, 3) a better treatment of auto-regressive processes, and 4) a better treatment of time-varying errors. While many of these can be incorporated into ever-more complex MLR models, it is the smoothly varying trend, with no assumption of when or how many inflection points might occur, that has the most obvious advantage over MLR (**Figure 3-5**). For this reason, DLM approaches are more flexible and provide more information about how ozone evolves over time, particularly for the seasonal and trend components.

Ultimately, both techniques are useful for long-term trend analyses, with each having its own benefits and caveats. Although increasing the complexity of statistical models comes at the cost of a substantial increase in the required computing power (especially for DLMs or similar), these more complex models can be applied to gain more insightful and robust results.

3.2.3 Trend Significance

No value carries substantial meaning without an associated uncertainty. It is important to know whether the result is different from zero by greater than some margin of uncertainty (known as statistical significance). Statistical significance offers a convenient way to display in a single figure both the magnitude of trends and their "importance." The most commonly used metric of significance is the 95% confidence interval, assuming a Gaussian distribution (2σ for most statistical applications), but the choice is somewhat arbitrary. Results that are significant at the 90% (or lower) confidence interval, for instance, may still be valid and worthy of discussion. Moreover, multiple significance tests (e.g., trends at different grid points) alter the calculation of significance (Wilks, 2006). Note that studies that take a Bayesian perspective on data analysis will quote "credible intervals"; while these require a slightly different interpretation, they can be regarded in a similar way (**Box 3-1**).

For the sake of comparison with previous Assessments, uncertainties shown throughout this chapter are the 2σ uncertainties, unless otherwise stated. However, it is important to note that trend results displayed where uncertainties encompass zero may still be indicative of meaningful change and may be worth discussing. Finally, unless otherwise stated, uncertainties reported here are random statistical uncertainties and do not consider the potential influence of data quality complications (e.g., sampling biases or instrumental drifts; see *Section 3.1*) as these are generally not included or quantified in the referenced studies.

3.3 PAST OZONE

Investigating past changes in ozone in observations and in models is critical to both understanding the impacts of natural and anthropogenic forces on ozone in Earth's atmosphere and evaluating the efficacy of the Montreal Protocol. Analysis of past ozone is performed on two representations of ozone: total column ozone (TCO) and vertical profiles. Total column measurements encompass all ozone from the surface to the top of the atmosphere and are useful because they best represent changes in how much damaging solar UV radiation reaches Earth's surface. To fully understand why these changes occur requires knowledge of the vertical distribution of ozone, provided by vertical profile measurements or partial columns. Analysis of profile observations is focused primarily on the stratosphere, where the ozone layer is located and where global satellite observations are of highest quality.

Analyses of long-term stratospheric ozone trends have traditionally been broken down into two periods: before and after the late-1990s/early-2000s. As reported in previous Assessments, ozone exhibits a noticeable decrease in the stratosphere at almost every altitude and latitude from the time when global observations started in the late 1970s until the late 1990s, after which it appears to flatten out or even increase (see also *Section 3.3.2.1*). While the magnitude of the pre-1990s decrease varies by location, the primary contributor to the decrease was the increase of ozone-depleting substances (ODSs) in the stratosphere, the concentration of which peaked in the late 1990s (*Chapter 1*). The results of trend analyses on this "pre-turnaround" period have been extensively discussed in prior Assessments and have not changed appreciably, even with the addition of new analysis techniques. As such, the discussion here mainly focuses on the period after the peak of ODSs in the stratosphere.

This section assesses changes in TCO (*Section 3.3.1*) and the vertical distribution of ozone (*Section 3.3.2*). In addition, special focus is given to the upper troposphere/lower stratosphere (UTLS) region, where a large fraction of atmospheric ozone resides, where the dynamical variability is largest, and where there has been considerable uncertainty in the ozone trends and discrepancies with models (*Section 3.3.3*). Finally, attention is also given to model simulations of past ozone changes and their use in attributing different drivers of ozone trends (*Section 3.3.4*). Information on the measurement datasets can be found in *Appendix 3A* and the associated tables (**Tables 3A-2 to 3A-5**).

3.3.1 Changes in Total Column Ozone

3.3.1.1 Interannual Variability

Since the mid-1990s, there has been only a small long-term trend in TCO, with substantial year-to-year variability. The time series of annual mean TCO are shown in **Figure 3-6** for the near-global average (60°S–60°N) and three selected broad-latitude bands (35–60°N, 20°S–20°N, 60–35°S; Weber et al.,

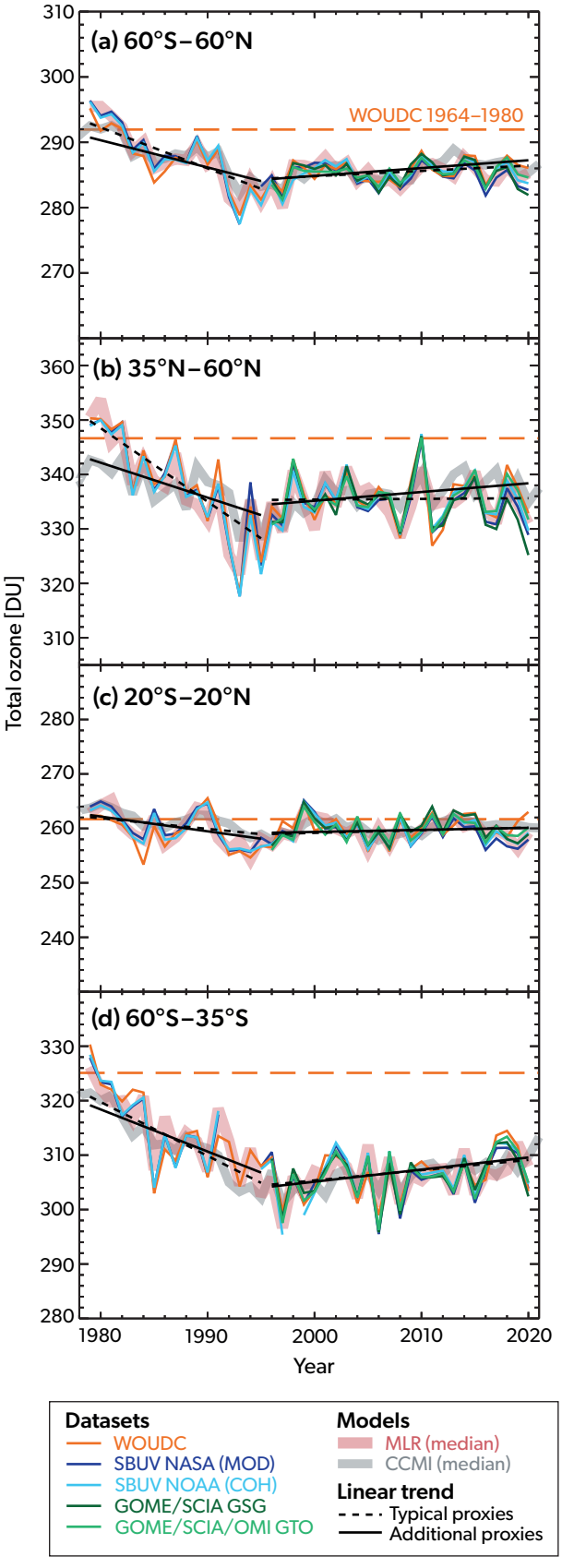

Figure 3-6. Time series of annual mean TCO (in DU), for 1979–2020, and linear trends, for 1979–1995 and 1996–2020, in four zonal bands: near global (60°S–60°N), NH mid-latitudes (35–60°N), tropics (20°S–20°N), and SH mid-latitudes (60–35°S). Data are from WOUDC ground-based measurements combining Brewer, Dobson, SAOZ, and filter spectrometer (orange); the BUV/SBUV/SBUV2 v8.7/OMPS merged products from NASA (MOD v8.7, dark blue) and NOAA (COH, light blue); the GOME/SCIAMACHY/GOME-2 products from University of Bremen (GSG; dark green); and the GOME/SCIAMACHY/GOME-2/OMI products from ESA/DLR (GTO; light green). See *Appendix 3A* for the references associated with these datasets. All five datasets have been bias-corrected by subtracting averages for the reference period 1998–2008 and adding back the mean of these averages. The dashed lines in each panel show the average ozone level for 1964–1980 calculated from the WOUDC data. The thick red lines show the median of MLR models. The black dashed lines are the linear trend as calculated with an MLR trend model using typical proxies, whereas the solid black lines are the linear trends as calculated with an MLR with additional dynamical proxies (see *Section 3.3.1.2*). [Adapted from Weber et al., 2022.]

2022). On average, the current (2017–2020) TCO is about 2.3% below the 1964–1980 mean (reference mean) in the near-global average, about 1.1% below the reference mean in the tropics, and about 3.6% and about 4.7% below the reference mean in the NH and SH mid-latitudes, respectively (**Figure 3-6**).

Most of the anomaly pattern in the annually averaged ozone in years since the previous Assessment is well understood and can be explained with varying combinations of dynamical influences (Matthes et al., 2010; Domeisen et al., 2019; Coldewey-Egbers et al., 2020; Section 3.2). For example, the influence of the Quasi-Biennial Oscillation (QBO) on ozone can be seen in the 2018 anomalies. Compared to the annual means observed in the last decade, NH and SH mid-latitude TCO values were high and the tropical values were low, all associated with the easterly phase of the QBO at 50 hPa. Moreover, an assessment of the impact of major sources of natural variability on recent ozone interannual variability is consistent with established correlations in ozone anomalies with the QBO at 30 hPa, El Niño-Southern Oscillation (ENSO), and solar cycle signals (Coldewey-Egbers et al., 2020).

In 2019, the SH mid-latitude TCO anomalies remained high. A persistent, weak polar vortex (perturbed by a SH stratospheric warming event; *Chapter 4*) associated with a strong hemispheric Brewer-Dobson circulation (BDC) led to more ozone being transported into SH mid-latitudes (Weber et al., 2020). The 2020 annual near-global mean and the annual mid-latitude mean in both hemispheres are below the decadal average of 1998–2008 (Weber et al., 2022). This negative anomaly, which is still within the variability observed in recent years, is due to a combination of very low polar ozone during the Arctic winter/spring (Weber et al., 2022), a large and stable Antarctic ozone hole during that year (see *Chapter 4*), and potentially the impact of the Australian wildfires on the stratosphere (*Section 3.2.1.3*).

The disruption of the downward propagation of the QBO westerly phase in 2019/20 is similar in many aspects to the one observed in 2016 (WMO, 2018; SPARC/IO3C/GAW, 2019, and references therein) but was initiated by horizontal momentum transport from the Southern Hemisphere (see *Section 3.2.1.1*). Some influence of this event might have contributed to the observed 2020 TCO anomalies, which are similar to 2016 and are consistent with our understanding of QBO-induced air mass transport (Weber et al., 2022). Overall, with four more years of data, our understanding of interannual TCO variability remains robust and unchanged compared to the previous Assessment.

3.3.1.2 Trends

The TCO trend estimates for the time series shown in **Figure 3-6** are based on a multiple linear regression (MLR) method (fit shown as black lines) that uses the typical proxies (see *Section 3.2.1*

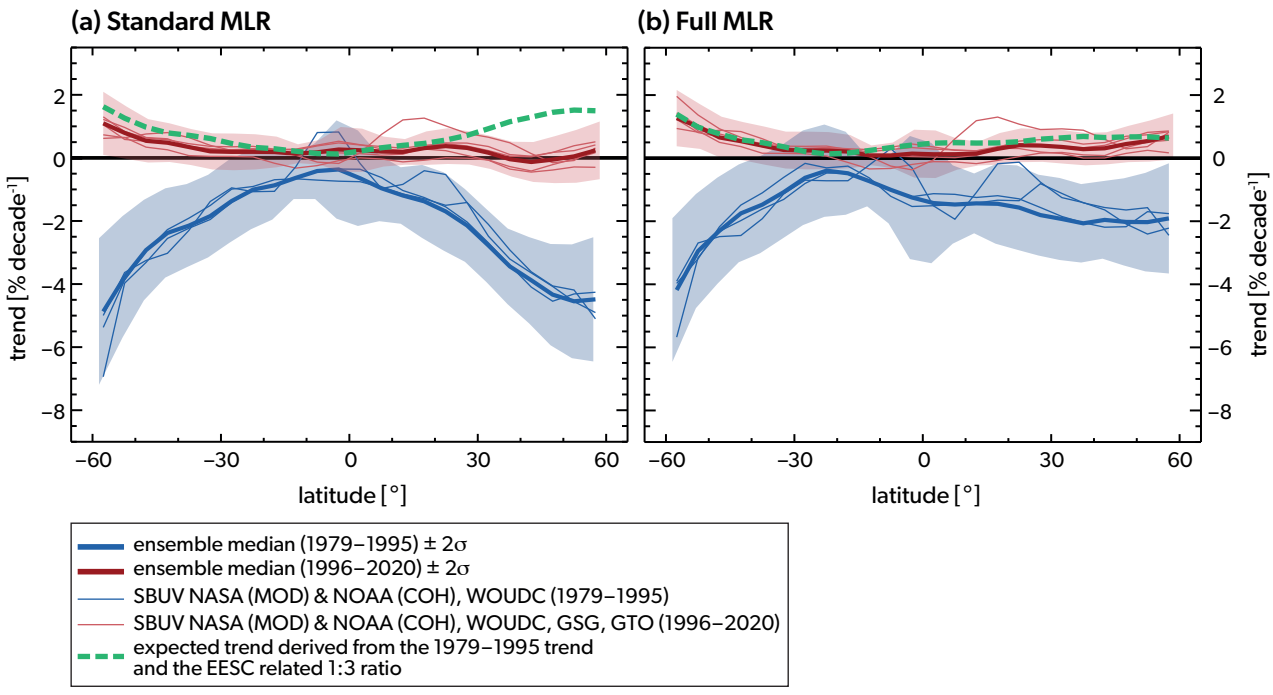

Figure 3-7. TCO linear trend in % decade^{-1} as a function of latitude for 1979–1995 (blue) and 1996–2020 (red), estimated using SBUV NASA (MOD), SBUV NOAA (COH), GTO, GSG, and WOUDC datasets, with (a) an MLR model that includes typical proxies and (b) an MLR model that includes additional dynamical proxies (see *Section 3.3.1.2*). Trends shown are the linear trend (% decade^{-1}) of the ensemble median (thick blue and red lines), as well as the 2σ uncertainty (blue and red shading) from the regression. Overlayed thin lines show trends from individual datasets without their uncertainties. Also shown (dashed green line) is the expected trend from changes in ODSs alone. This is derived from the 1979–1995 ODS trend, as represented by EESC, and by applying a scaling to account for the rate of change in EESC post-1996 relative to pre-1996 (i.e., "EESC-related 1:3 ratio"). [From Weber et al., 2022.]

and **Table 3A-1**) and the independent linear trend (ILT) model (**Table 3-1**) (Weber et al., 2022). Trend estimates are derived for the near-global (60°S–60°N) annual mean and for annual mean zonal-mean data in the same three latitude bands considered for the TCO year-to-year variability. Near-global 1996–2020 trends are on the verge of a significant increase (+0.3 ± 0.3% decade^{-1}; Weber et al., 2022), whereas trends in different latitude bands do not show a uniform picture. In the SH mid-latitudes, the trend is significant at the 2σ level (+0.8 ± 0.7% decade^{-1}), while the trend in NH mid-latitudes is negligible and not significant (+0.0 ± 0.7% decade^{-1}), and there is only a small non-significant trend after 1996 in the tropics (+0.2 ± 0.3% decade^{-1}). Similar trend values were reported in the last Assessment (see also SPARC/IO3C/GAW, 2019), although with four more years of data and an updated trend model, the near-global mean and SH mid-latitude trend become significant. The apparent discrepancy in the significance of near-global and latitudinally resolved trends is a result of different causes for variability in the three latitude bands, which can compensate for each other when aggregated globally (see also Coldewey-Egbers et al., 2014; Steinbrecht et al., 2018; Weber et al., 2018).

Latitude-dependent TCO trends are shown in **Figure 3-7a** in 5° latitude bins for the 1979–1995 and 1996–2020 periods. The pre-1996 decreases, which have been discussed extensively in previous Assessments, show a latitudinal dependence, with values ranging from nearly zero in the tropics to statistically significant negative trends at mid-latitudes in both hemispheres. The latitude-dependent trends after 1996 are largely consistent with the results for the broader zonal bands and with those given in the last Assessment (see also Weber et al., 2018), even with an additional four years of data. There are small (<1% decade^{-1}), mostly positive trends in the SH mid-latitudes and near zero (<0.5% decade^{-1}) trends in the tropics and NH mid-latitudes. Almost all the trends are statistically insignificant.

While computing trends in TCO is important, understanding what causes these trends is equally so. An attempt at isolating trends from ODS-induced changes only is shown in **Figure 3-7b**. The trends shown in **Figure 3-7** are derived from nearly identical MLR analyses (Weber et al., 2022), with both incorporating explanatory variables for natural variability (i.e., QBO, ENSO, solar, and aerosol) and ILT-proxy trends, but differing in that **Figure 3-7b** also includes AO (Arctic Oscillation), AAO (Antarctic Oscillation), and BDC proxies (**Table 3A-1**). These additional dynamical proxies have a trend themselves, meaning the resulting trend from the regression is no longer representative of all long-term changes in TCO. An independent estimate of the "expected" ODS-related post-1996 changes, which is based on equivalent effective stratospheric chlorine (EESC), is shown as dashed green lines in **Figure 3-7**. ODS concentrations, as represented by EESC, are expected to decrease at about one-third of the rate they increased before the 1990s (Dhomse et al., 2006; Weber et al., 2018), and so the magenta lines are simply the pre-1996 trends multiplied by –⅓, illustrating what the post-1996 trends would look like assuming they were purely driven by ODS changes. The derived post-1996 trends in both the Northern and Southern Hemisphere are in much better, though not complete, agreement with the estimated ODS-based trends when the additional explanatory variables (**Figure 3-7b**) are used in the regression. This suggests that the linear trends from **Figures 3-6** and **3-7b** are to a large part attributable to ODS changes only, demonstrating the success of the Montreal Protocol and its Amendments and adjustments at protecting stratospheric ozone. It also implies that the additional proxies are useful in capturing important components of dynamical variability, including how possible trends in dynamics impact long-term changes in ozone. The difference between the derived post-1996 trends in **Figures 3-7a** and **3-7b** suggests that the long-term changes in dynamics, as captured by the AO, AAO, and BDC proxies, are contributing to negative trends of up to 0.5% decade^{-1} in TCO, offsetting the positive ODS related trends, particularly in NH mid-latitudes.

When the MLR, including the additional dynamical proxies, is applied to the data for the broad-latitude bands (**Figure 3-6**, black solid line), trends and significance for the latitude bands change compared to the results of the MLR without these proxies. Trends for the near-global (+0.4 ± 0.2% decade^{-1}) and SH mid-latitude (+0.7 ± 0.6% decade^{-1}) TCO are significant (Weber et al., 2022), and the NH mid-latitude trends are on the verge of significance (+0.5 ± 0.5% decade^{-1}), but the tropical trends are still not significant, even with the additional proxies considered.

Besides the differences in latitudinally resolved trends, TCO trends, derived from the period 1997–2020, also show a longitudinal dependence. Trends derived from a recently updated dataset based on GOME-type (GTO) satellite measurements (Coldewey-Egbers et al., 2022), with a MLR trend model where dynamical proxies for the AO and AAO are included, are positive in most parts of the globe (**Figure 3-8**) and statistically non-significant (at 0.3 ± 0.6% decade^{-1}) in the tropics but significant (at 1.0 ± 0.9 % decade^{-1}) for some regions of the SH mid-latitudes. The largest positive trends of about 1.5% ± 1.0% decade^{-1} are found in in the NH in the northwestern part of Europe and in the North Atlantic region and in the SH higher latitudes (up to 2.8 ± 2.6 % decade^{-1}) in the region of the Southern Ocean, while non-significant trends are estimated above Eurasia (–1.0 ± 1.0 % decade^{-1}). GTO-derived trends are consistent with the latitude band picture given by WOUDC and SBUV datasets (see **Figure 3-7**), where TCO trends during the recovery period are only significant in the SH mid-latitudes (Coldewey-Egbers et al., 2022).

In a different study, zonally asymmetric TCO trends estimated using principal component analysis on a dataset combining TOMS, GOME, SBUV, and OMI for the 1997–2015 period are reported as negative and significant over the North Pacific and positive and significant over northwestern North America in February (Zhang et al., 2019). This asymmetric behavior is attributable to a polar vortex shift, which causes not only interannual variability of regional TCO but also a significant reduction of TCO over the central Eurasian continent (**Figure 3-8**). This effect is opposite to the expected increase in ozone due to reduced atmospheric ODS concentrations and is an example of how dynamical changes could affect the timing of TCO recovery in different regions (Zhang et al., 2018).

Ground-based FTIR measurements provide total column ozone and ozone partial columns for the period 2000–2020. Post-2000 TCO trends estimated from five different FTIR measurement sites are consistent, within their uncertainties, with trends estimated from the WOUDC and SBUV datasets as determined by MLR with the typical proxies (see **Figure 3-7**). TCO trends over 2000–2020 at FTIR stations within the NH mid-latitudes and in the tropics are slightly negative but non-significant, while the trend at a station in the SH mid-latitudes is positive and significant at 1.1 ± 0.9% decade^{-1} (updated from Vigouroux et al., 2015).

Seasonally resolved post-1997 TCO trends have also been derived from the GTO 5° × 5° gridded dataset. The seasonality in the trend is not very pronounced, and most of the regions show trends that are not significant at the 95% confidence level. In the Northern Hemisphere, a strong trend over the North Atlantic is significant and positive for all seasons and varies in intensity, and a negative trend over Eurasia is significant except in winter (December to February). In the Southern Hemisphere, regions of significant positive trends are reported throughout the year in the extratropics but are stronger between March and May in the mid-latitudes (the Pacific region, south of Africa, and south of Australia; Coldewey-Egbers et al., 2022).

3.3.2 Changes in the Vertical Distribution of Ozone

3.3.2.1 Time Series

The ozone decline in the 1980s and 1990s, caused by increasing atmospheric concentrations of ODSs, has now transitioned to a slow ozone increase in both hemispheres (SPARC/IO3C/GAW, 2019). This is consistent among the ground- and satellite-based measurements and model simulations from the Chemistry-Climate Model Initiative (CCMI-1; REF-C2 experiment: see Morgenstern et al., 2017) for all latitude bands and in the middle and upper stratosphere, despite the larger variability of the ground-based measurements. This is apparent in the evolution of observed and modeled annual mean deseasonalized ozone anomalies, relative to the 1998–2008 climatology of each individual plotted dataset, in the upper stratosphere (42 km or 2 hPa) and in the lower stratosphere (19 km or 70 hPa), as shown in **Figure 3-9**. A direct comparison of individual years between the CCMI-1 output and measured anomalies is not possible as natural forcings and variability in the REF-C2 simulations used in this comparison are either absent or are not as observed (e.g., volcanoes, QBO).

Ozone anomalies over 2017–2020 in the upper stratosphere from most datasets are positive relative to the 1998–2008 average, consistent with expectations from the CCMI-1 simulations. This is true for the NH and SH mid-latitudes and to a lesser extent for the tropics. In contrast, lower-stratospheric ozone anomalies over 2017–2020 continue to be about the same as for the 1998–2008 average. In 2019 and 2020, stratospheric ozone values were lower than in previous years and below the level expected from model simulations (Weber et al., 2020). The particularly low 2020 annual mean is the result of a very weak BDC and a large and stable Antarctic ozone hole (Klekociuk et al., 2021; Weber et al., 2021). Such large variability, driven by variations in meteorology and transport (Chipperfield et al., 2018), is typical for the lower stratosphere and impedes drawing definite conclusions about long-term trends, especially for the mid-latitudes (30°–60°) in both hemispheres (see *Section 3.3.3*).

3.3.2.2 Trends as a Function of Latitude

Estimates of vertically resolved trends as a function of latitude are possible from seven merged satellite ozone datasets, which include the six datasets used in the last Assessment and by LOTUS (SPARC/IO3C/GAW, 2019) alongside the new SAGE II-SCIAMACHY-OMPS dataset (Godin-Beekmann et al., 2022). Altitude-latitude cross sections of ozone trends for 2000–2020 (**Figure 3-10**) are similar to those reported in the last Assessment, with the new SAGE II-SCIAMACHY-OMPS dataset yielding results that are similar to those from the other SAGE-containing datasets. All the datasets show positive and statistically significant trends for the post-2000 period in the upper stratosphere, in the range of about 2–7% decade^{-1}, with more pronounced trends at mid-latitudes than in the tropics in both hemispheres. Except for SBUV MOD, all results indicate positive tropical trends in the upper stratosphere (above ~40 km), although the trends are somewhat smaller and not always statistically significant. Trends in the middle stratosphere (25–40 km) are slightly positive (0–3% decade^{-1}) in most datasets at SH mid-latitudes and slightly negative (−2–0% decade^{-1}) at NH mid-latitudes and in the tropics, although these are typically not statistically significant. Estimated trends in the lower stratosphere (tropopause to 25 km) are mostly negative but are also rarely statistically significant. The trends were determined using the ILT regression model (*Section 3.2.2*), which was applied to the full available observational period (1984–2020).

Profiles of ozone trends in broad-latitude bands for the same seven datasets (**Figure 3-11**) all show significant positive ozone trends in the upper stratosphere at mid-latitudes in both hemispheres (60–35°S and 35–60°N), in the range of 1–3% decade^{-1} (mean ~1.9% decade^{-1} in the Southern Hemisphere and ~2.2% decade^{-1} in the Northern Hemisphere) for the post-2000 period. In the tropical (20°S–20°N) upper stratosphere, the trends

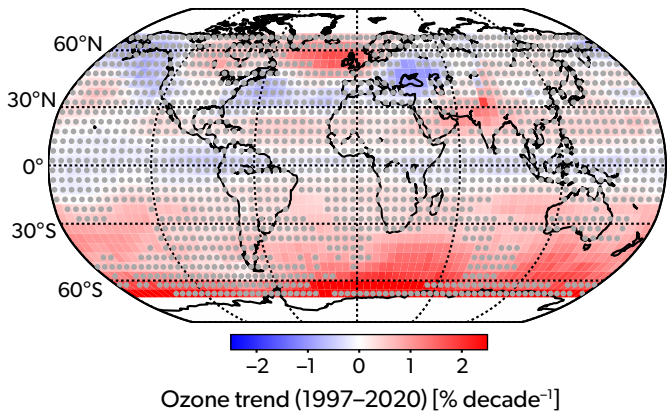

Figure 3-8. Latitude- and longitude-dependent TCO trends (5° × 5° resolution) derived using MLR (including AAO/AO but not the BDC) for the 1997–2020 period, in % decade^{-1}. Trends are from GOME-type satellites (GTO), which include measurements from GOME, SCIAMACHY, OMI, and TROPOMI. Gray dots denote locations where the trends are not significant at the 95% confidence level. [Figure from Coldewey-Egbers et al., 2022].

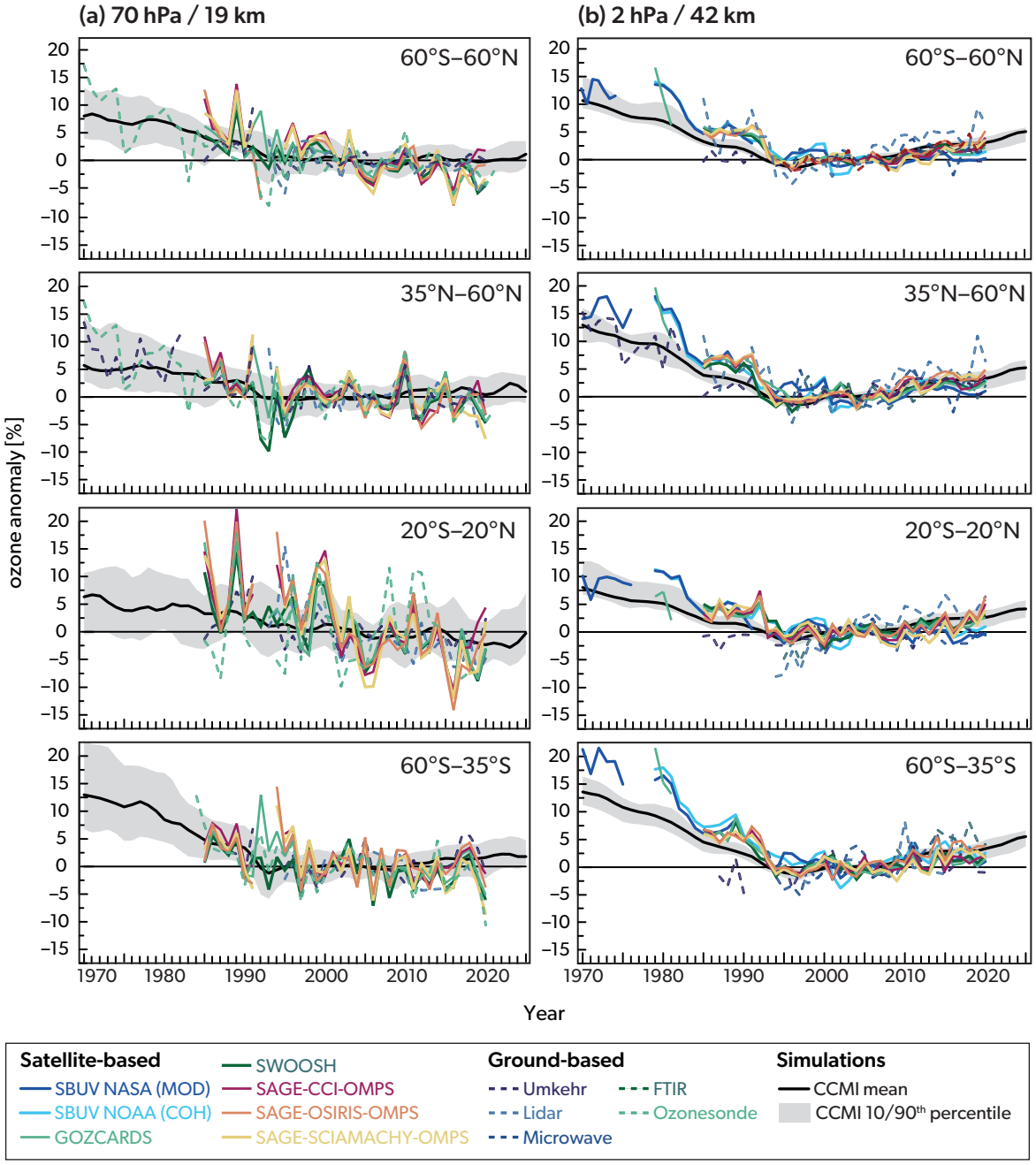

Figure 3-9. Annual mean anomalies of ozone in (a) the lower stratosphere, near 19 km altitude (70 hPa pressure) and (b) the upper stratosphere, near 42 km (2 hPa), for four latitude bands: 60°S–60°N, 35–60°N, 20°S–20°N (tropics), and 60–35°S. Anomalies are referenced to a 1998–2008 baseline. Colored lines are long-term records obtained by merging data from different nadir (SBUV NASA (MOD) and SBUV NOAA (COH)) or limb-viewing (GOZCARDS, SWOOSH, SAGE-CCI-OMPS, SAGE-OSIRIS-OMPS, SAGE-SCIAMACHY-OMPS) satellite instruments. Dashed colored lines are long-term records from ground-based observations (Umkehr, lidar, microwave, FTIR and ozonesondes); see Steinbrecht et al. (2017), WMO (2018), and Arosio et al. (2018) for details on the various datasets. The gray shaded areas show the range (10th and 90th percentiles) of 16 CCM simulations performed as part of the CCMI-1 REF-C2 experiment (see Morgenstern et al., 2017) with the black line indicating the median. [Adapted from SPARC/IO3/GAW, 2019, and updated from the last Assessment.]

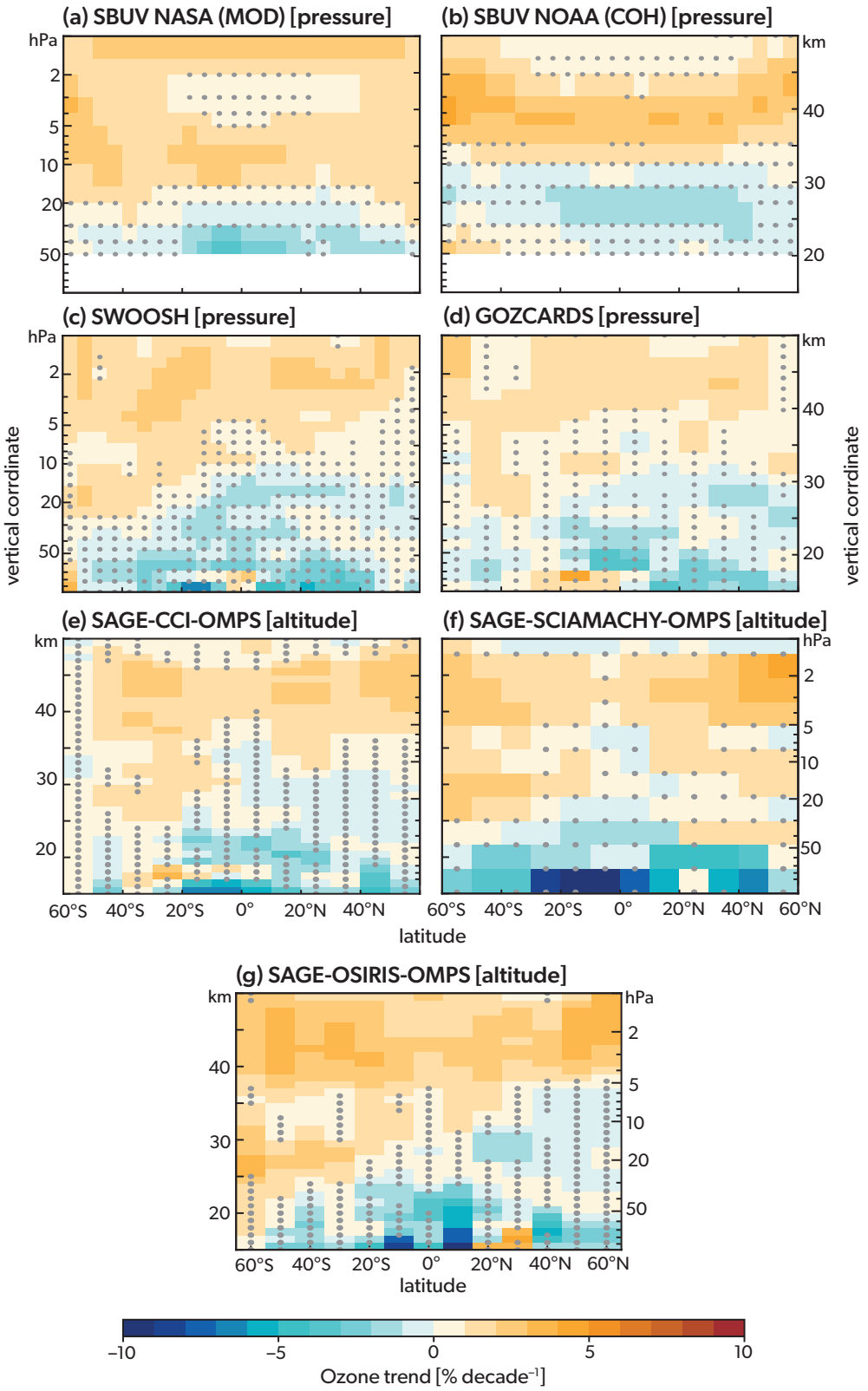

Figure 3-10. Ozone trends (% decade^{-1}) for the period 2000–2020 estimated from seven merged satellite data records using an independent linear trend model. Trends are shown for the (a) SBUV NASA (MOD), (b) SBUV NOAA (COH), (c) SWOOSH, (d) GOZCARDS, (e) SAGE-CCI-OMPS, (f) SAGE-SCIAMACHY-OMPS, and (g) SAGE-OSIRIS-OMPS datasets. Gray stippling denotes results that are not significant at the 2σ level. Data are presented on the vertical coordinates (lefthand axis; square brackets in title) and latitudinal grid associated with each dataset. [Adapted from Godin-Beekmann et al., 2022.]

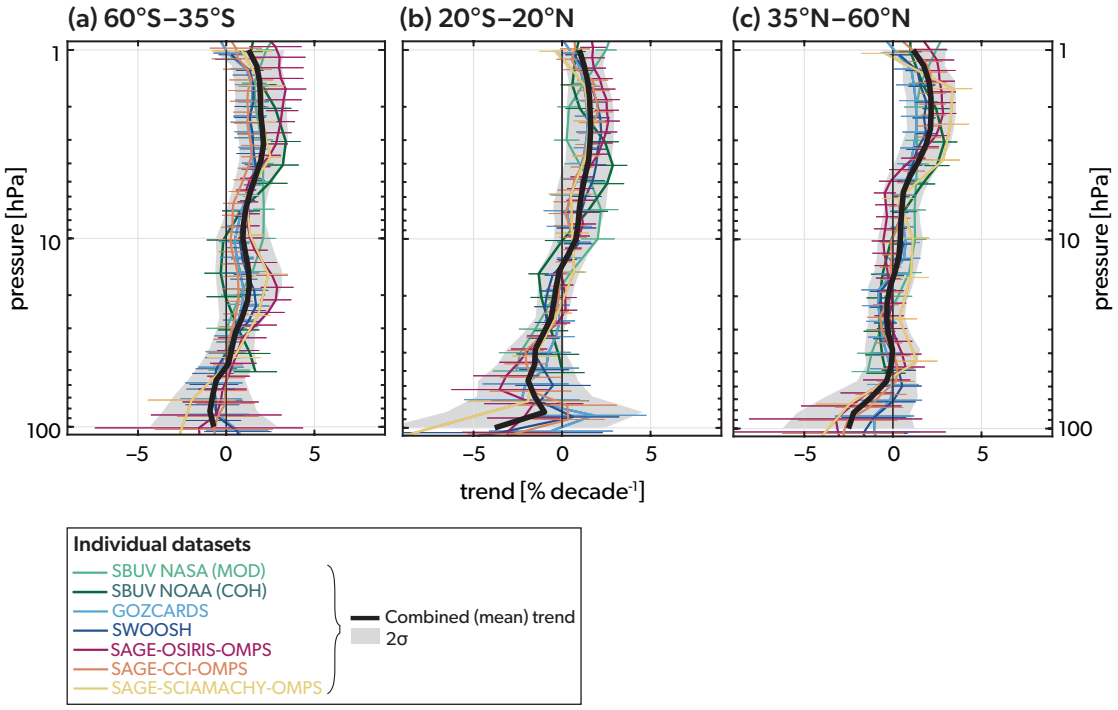

Figure 3-11. Ozone profile trends with 2σ uncertainties for the period 2000–2020 for latitude bands 35–60°S *(left panel)*, 20°S–20°N *(center panel)*, and 35–60°N *(right panel)*. Colored lines are the trend estimates from seven individual merged datasets on their original vertical grid (SBUV NASA (MOD), SBUV NOAA (COH), GOZCARDS, SWOOSH, SAGE-OSIRIS-OMPS, SAGE-CCI-OMPS, and SAGE-SCIAMACHY-OMPS). Black lines represent the mean (combined) trends and gray shading indicates the 2σ uncertainty intervals for the combined trends, estimated using the method for combining trends from different observational datasets outlined in SPARC/IO3C/GAW (2019). [Adapted from Godin-Beekmann et al., 2022.]

are also positive but smaller (~1–2% decade^{-1}; mean ~1.5% decade^{-1}) and are statistically significant for all merged datasets except SBUV MOD. Most datasets indicate negative trends in the lower stratosphere, but all trend estimates, either from individual merged datasets or combined trends, have large uncertainties and therefore are not statistically significant. The estimated trends in these profiles from individual merged satellite datasets agree better with each other than reported in the previous Assessment, resulting in a more robust assessment of vertically resolved trends. Note that the mean trend shown in **Figure 3-11** is a combination of the individually derived satellite trends and is shown with its 2σ uncertainty, estimated in the same way as reported in the last Assessment (see SPARC/IO3C/GAW, 2019). In brief, these uncertainties include both a simple error propagation, which captures uncertainties associated with trend estimates from individual merged datasets, and the standard error of the mean, which captures the spread of trend estimates due to systematic uncertainties, such as those induced by possible drift in some datasets used in the combined products (see *Section 3A.3*).

Comparing the 2000–2020 trend profiles with the 2000–2016 trends from the previous Assessment (from SPARC/IO3C/GAW, 2019), the overall trends are almost identical (**Figure 3-12**). The uncertainties of the mean trend estimates, however, are now smaller at most altitudes. This reduction is mainly due to the additional four years of data available from observations and the fact that the trend estimates from individual merged datasets are now more consistent, as noted above. In addition, the updated trend is based on trends from seven, rather than six, merged satellite data products (Godin-Beekmann et al., 2022).

Multi-model mean trends estimated from the CCMI-1 simulations are very similar to the satellite mean ozone trends in the upper stratosphere (**Figure 3-12**). In the lower stratosphere, the models and observations agree on negative ozone trends in the tropics; in the mid-latitudes, however, the multi-model mean suggests positive ozone trends, whereas the satellite observations indicate negative trends (**Figure 3-12**). However, none of the trends in the lower stratosphere are statistically significant. For more details on the ozone trends in the UTLS, see *Section 3.3.3*. Note that individual model trends are estimated using the ILT regression method and using the same approach as for the satellite data, with the necessary proxies either being calculated directly from the individual model simulations (e.g., QBO, ENSO) or taken from the external forcings provided to the models before they are combined into a multi-model mean.

3.3.2.3 Regional and Longitudinally Resolved Trends

Since the last Assessment, a new development has been to investigate ozone trends at finer spatial and temporal resolutions. In particular, two studies have focused on longitude- and latitude-dependent trends in ozone profiles to obtain a finer

regional perspective. These studies used the longitudinally resolved merged datasets SAGE II-SCIAMACHY-OMPS (Arosio et al., 2019) and MEGRIDOP (Sofieva et al., 2021) and evaluated the trends using the MLR method for the period 2003–2018. Both studies consistently show a strong longitudinal dependence to ozone trends at high and mid-latitudes in the Northern Hemisphere, with a dipole pattern of increasing trends over Scandinavia and decreasing trends over Siberia below 40 km and stronger increasing trends over Scandinavia at 40 and 45 km (**Figure 3-13**). This spatial feature is thought to be related to changes in dynamical processes that are associated with the BDC (see Arosio et al., 2019, and references therein), but this hypothesis has yet to be fully confirmed.

When longitudinally resolved trends are derived from gridded satellite datasets, their magnitude and significance vary with longitude and differ spatially compared to latitude band trends derived from the same datasets (Arosio et al., 2019; Sofieva et al., 2021). This fact calls into question the common practice of using latitude band data to estimate the agreement between vertically resolved trends from satellite data and ground-based records (SPARC/IO3C/GAW, 2019). When compared to their corresponding SBUV zonal means, lidar monthly mean data at different stations show correlations of 0.1 to 0.6 (Zerefos et al., 2018). The trends estimated at individual ground-based stations may not be representative of their respective large latitude bands and may be relevant only on a regional, longitudinally resolved scale in the mid- and lower stratosphere.

Different ground-based observation methods vary in their measurement record length, vertical and temporal sampling, and the spatial distribution of station locations. Trends estimated from these different ground-based records may be more sensitive to regional atmospheric conditions (SPARC/IO3C/GAW, 2019). This can lead to a high variability in trends from ground-based measurements. Disagreements between the trends estimated from collocated measurements can be used to reveal the presence of uncorrected drift in the ground-based records. Consideration of data uncertainties and inhomogeneities in the regression model can affect the resulting trends and improve their consistency, as has been demonstrated for collocated lidar and microwave radiometer measurements (Bernet et al., 2020). If the measurement times are at regular intervals, temporal sampling can be excluded from the factors responsible for trend discrepancies, as has been demonstrated with microwave radiometers (Maillard Barras et al., 2020).

Post-2000 trend profiles derived using MLR (SPARC/IO3C/GAW, 2019) at three selected Network for the Detection of Atmospheric Composition Change (NDACC) locations from different latitude regions are shown in **Figure 3-14**. The selected locations provide measurements from several ground-based instruments at the same station or multiple measurements at nearby stations (Godin-Beekmann et al., 2022). The European "site" combines measurements from the Alpine stations Haute Provence (France; OHP, 43.9°N, 5.7°E), Hohenpeißenberg (Germany; HOH, 47.8°N, 11.0°E), and Arosa (Switzerland; ARO,

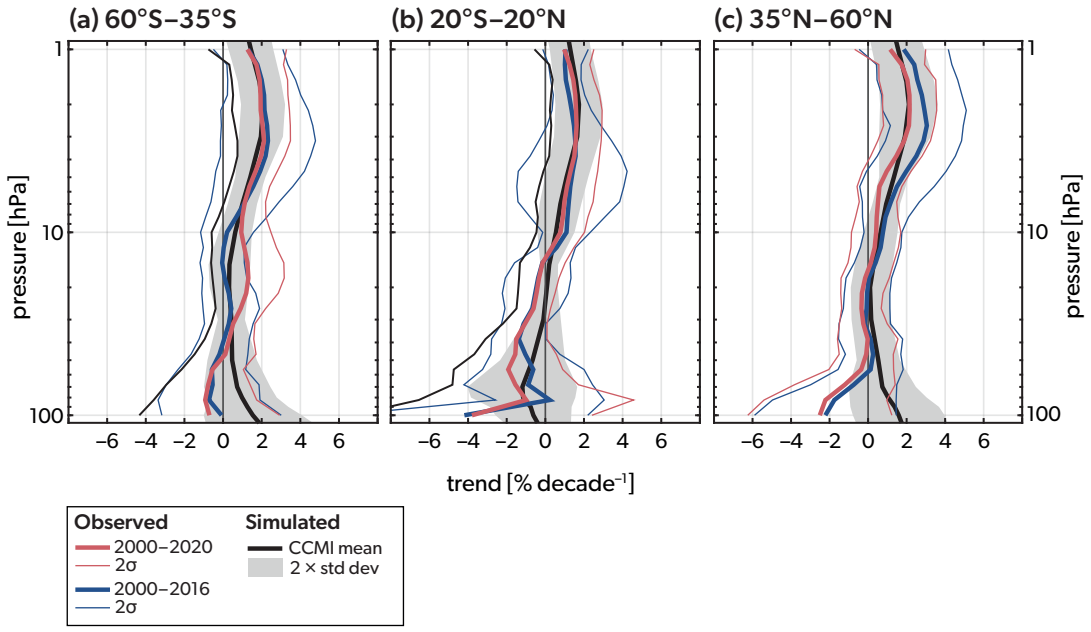

Figure 3-12. Comparison of simulated and observed post-2000 ozone trend profiles for the latitude bands 35–60°S *(left panel)*, 20°S–20°N *(center panel)*, and 35–60°N *(right panel)*. Observed trends from the last Assessment (the period 2000–2016) are shown in blue, and results for the updated period 2000–2020 are shown in red, with the trend values based on combining different merged satellite datasets and their 2σ uncertainties, all estimated using the method outlined by SPARC/IO3C/GAW (2019) and as also shown in **Figure 3-11**. The black line is the multi-model mean trend calculated from 16 CCMI-1 REF-C2 simulations (Morgenstern et al., 2017), with the spread of the individual model trends (±2 standard deviations) indicated by the gray shading. [Adapted from Godin-Beekmann et al., 2022.]

46.8°N, 6.9°E). All three stations are located within a single grid cell in the MEGRIDOP, SBUV MOD, and SWOOSH satellite-based datasets. Mauna Loa (Hawai'i, USA; 19.5°N, 155.6°W) and Lauder (New Zealand; 45.0°S, 169.7°E) are single-station sites located in the tropics and the SH mid-latitudes, respectively. For the three locations, the agreement with trends estimated from the gridded satellite datasets is good, taking into account that the SBUV MOD and SWOOSH cells are larger (in longitude) than the MEGRIDOP cells.

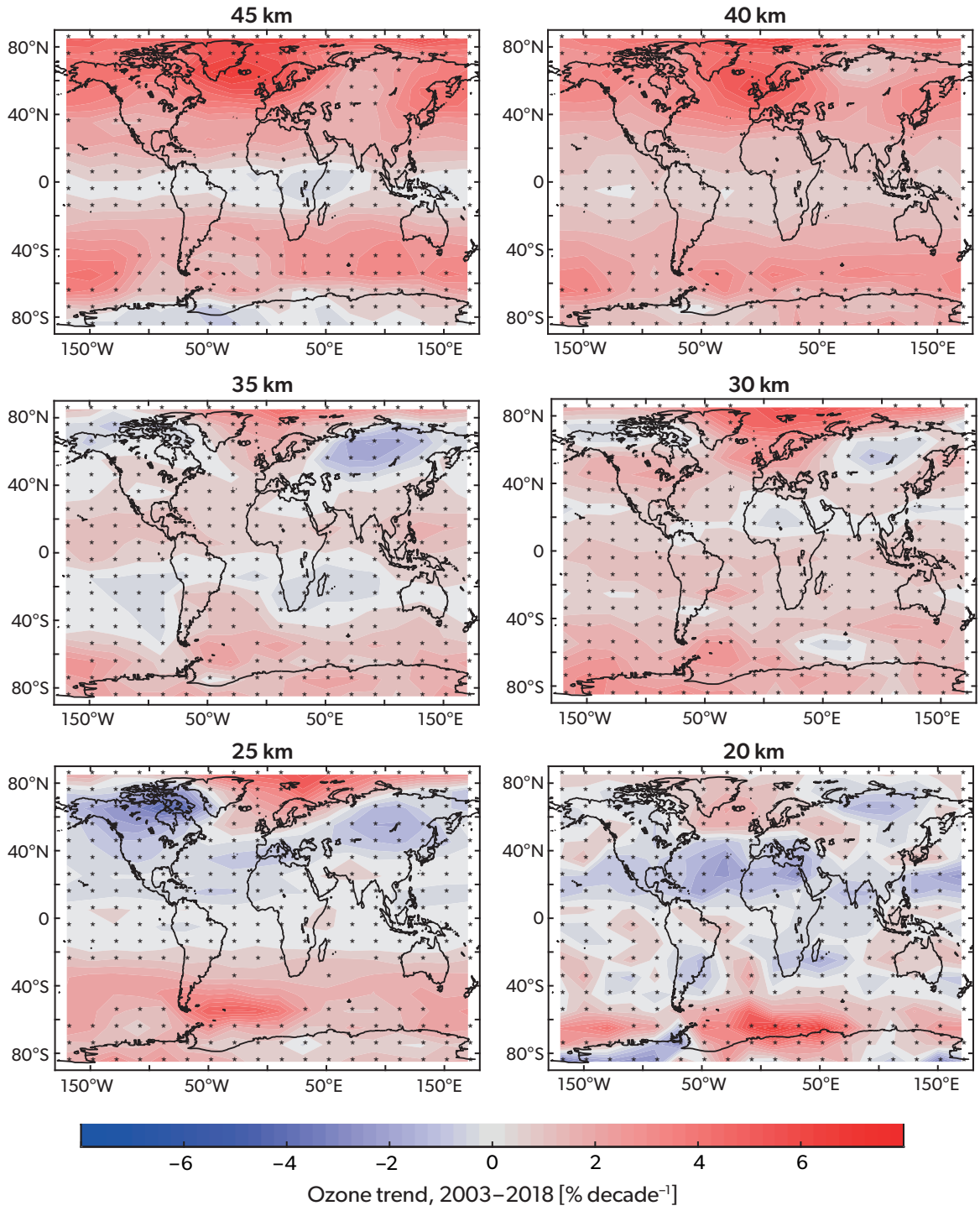

Figure 3-13. Latitude- and longitude-dependent ozone trends (% decade^{-1}) derived for the period 2003–2018 for six different altitude levels, based on the MEGRIDOP dataset (Sofieva et al., 2021). Gray stars indicate regions where the trends are not statistically significant at the 2σ level. [Adapted from Sofieva et al., 2021.]

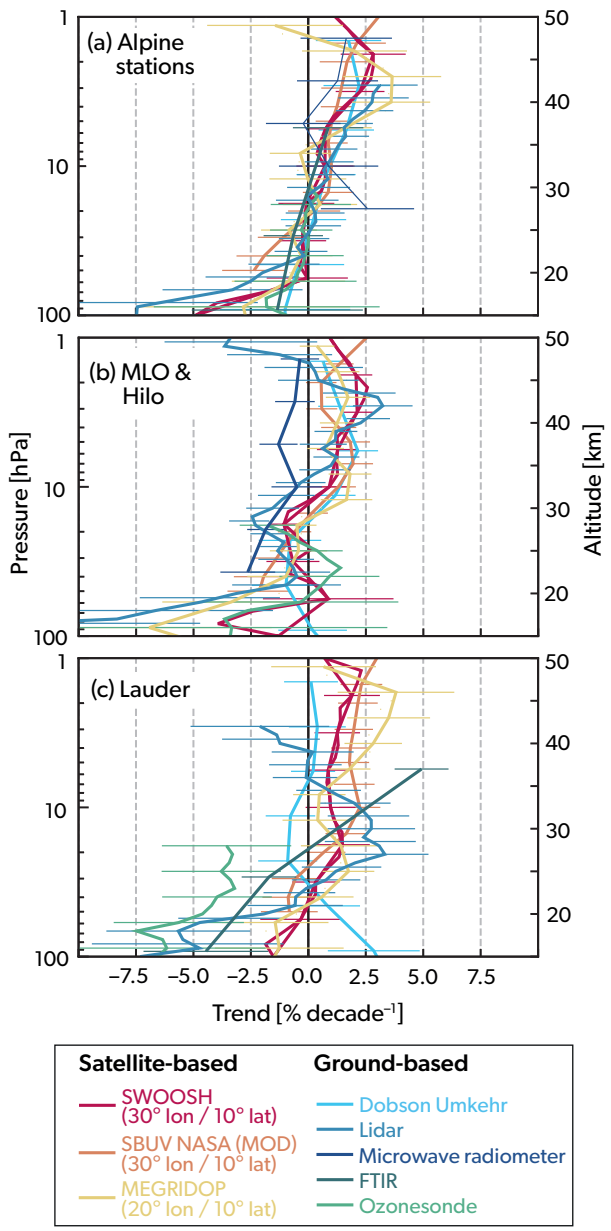

Figure 3-14. Ozone trend profiles (% decade^{-1}) for 2000–2020 at selected NDACC locations: (a) a European "site" that combines measurements from the Alpine stations Haute Provence (France), Hohenpeißenberg and Zugspitze (Germany), and Jungfraujoch, Payerne and Arosa (Switzerland); (b) a site that combines Mauna Loa (Hawaii, USA; MLO) and Hilo (Japan; just ozonesonde data); and (c) Lauder (New Zealand). Trend profiles are shown for Dobson Umkehrs (light blue), ground-based lidars (medium blue), microwave radiometers (dark blue), FTIR (dark green), and ozonesondes (light green), although not all measurements appear at all locations. Also shown are trend profiles estimated from the SWOOSH (red), SBUV NASA (MOD) (orange), and MEGRIDOP (yellow) gridded satellite products, using the nearest grid boxes. Error bars represent the 95% confidence intervals. [Adapted from Godin-Beekmann et al., 2022.]

The ground-based trend profiles are in general agreement with the gridded satellite trends, within their respective uncertainties (**Figure 3-14**). Disagreements likely reflect inhomogeneities in the different measurement time series that are not properly considered or the need for data curation, which is currently in process. Significant positive trends are found in the upper stratosphere for nearly all datasets, except for four that show negative and non-significant trends. The lower-stratospheric picture is not as clear but is representative of the actual state of our knowledge within that vertical range (see *Section 3.3.3*). Since the last Assessment, the European ozonesondes have been homogenized under the framework of the Tropospheric Ozone Assessment Report Phase 2 (TOAR II) project (*Section 3A.2*), and, within uncertainties, their trends show agreement with the trend of the gridded satellites and the collocated ground-based instruments (**Figure 3-14**). Although the comparison of ground-based trends at the three selected NDACC locations and longitudinally resolved satellite trends is made at a more appropriate spatial resolution than with broad zonal-mean bands derived from satellite data, the overall conclusion is the same for both comparisons: trend profiles from ground-based measurements and satellite data agree within the limits given by the different spatial representations and the homogeneity problems of the datasets.

The seasonal dependence of ozone trends in the stratosphere has been examined in a new study using four long-term merged satellite datasets in three broad-latitude bands (60–30°S, 10°S–10°N, 30–60°N; Szeląg et al., 2020). All four datasets show qualitatively similar trends, although there are some minor differences, mostly in trend magnitude (**Figure 3-15**). In the upper stratosphere, the 2000–2018 trends are positive throughout all seasons and most latitudes. The largest upper-stratospheric ozone trends are observed in the mid-latitudes during local winter in the Northern Hemisphere (up to 6% decade^{-1}) and at the equinoxes in the Southern Hemisphere (up to 3% decade^{-1}). In the equatorial region, there is a very strong seasonal dependence of ozone trends at all altitudes: the trends are negative in the upper stratosphere during boreal winter (−1 to −2% decade^{-1}) and in the lower stratosphere during boreal spring (−2 to −4% decade^{-1}), while the mid-stratosphere (30–35 km) has positive trends in boreal spring (2 to 3% decade^{-1}) and negative trends (–0.5 to –2% decade^{-1}) in boreal fall. The tropical trends below 25 km are negative and maximize during summer (up to −2% decade^{-1}) and spring (up to −3% decade^{-1}). There is a hemispheric asymmetry in the mid-latitude lower stratosphere (Szeląg et al., 2020): during local summers and equinoxes, positive trends are observed in the Southern Hemisphere (1–2% decade^{-1}), while negative trends are observed in the Northern Hemisphere (–1% to –2% decade^{-1}). A comparison of the seasonally dependent ozone trends with available analyses of the seasonally dependent stratospheric temperature trends reveals a positive correlation (trends in the same direction) in the dynamically controlled lower stratosphere and negative correlation (trends in opposite directions) above 30 km, where photochemical processes dominate.

3.3.2.4 Consistency of Total Column Ozone Trends and Partial Column Trends

In past Assessments, trends in TCO have been a gauge of the efficacy of the Montreal Protocol in halting stratospheric ozone layer losses. Since 1998–2000, the previous rapid decline in TCO, which had been primarily driven by stratospheric ozone losses,

has halted. However, it is only now that significant increases in TCO are being detected, and only at some latitudes (*Section 3.3.1* and **Figure 3-6**). Since the last Assessment, there have been further investigations into the contribution of different vertical regions to TCO trends, particularly the contribution of tropospheric changes (see **Box 3-3**). Overall, these findings raise questions about whether TCO is the best metric for determining ozone recovery in the context of the Montreal Protocol.

Stratospheric ozone represents ~90% of the total column, but it may no longer reflect the bulk of the long-term changes. Although analyses of some satellite datasets indicate a decline in tropospheric ozone since the early 2000s (e.g., some analyses shown by Gaudel et al., 2018), several estimates of tropospheric ozone changes conservatively suggest increases of ~1.5 DU decade^{-1} (~5% of the tropospheric column) globally since the early 2000s (Ball et al., 2018; Ziemke et al., 2019; Gaudel et al., 2018, 2020), and this is supported by modeling studies (Zhang et al., 2016, 2021). Where TCO changes match or are smaller than the tropospheric ozone trends (*Section 3.3.1*), post-2000 stratospheric column ozone changes may be zero or even negative. For example, focusing on observations at Irene, South Africa (~26°S), one recent study found that local TCO increases may be driven by tropospheric increases (Bencherif et al., 2020). Separating stratospheric ozone trends into partial column components isolates stratospheric trends. Such analyses indicate that the magnitude and significance of post-2000 ozone increases in the upper stratosphere (above 32 km) are strengthening with additional years (Ball et al., 2019a; *Sections 3.3.2.2* and *3.3.2.3*).

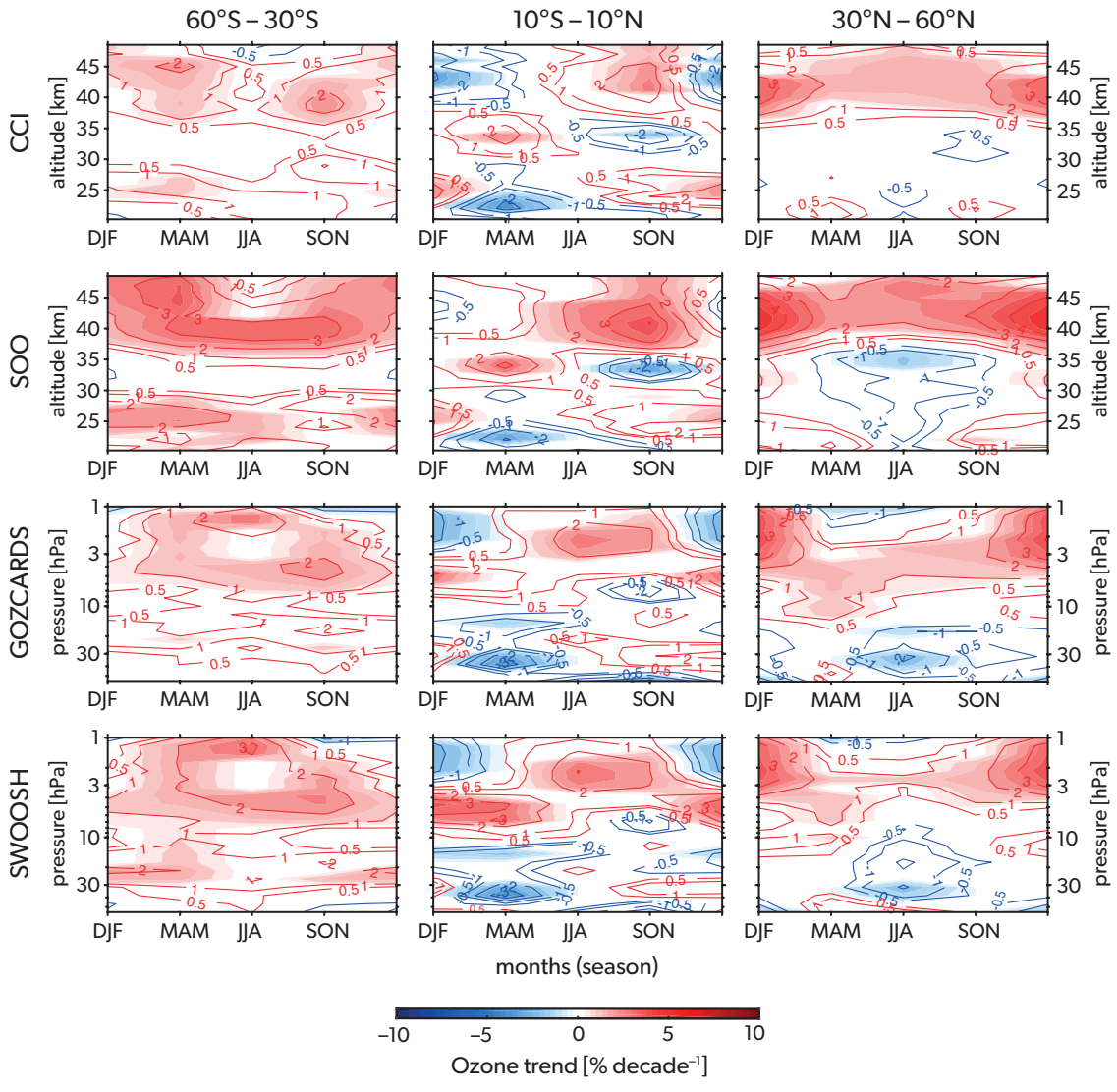

Figure 3-15. Altitude-season variation of linear trends for four merged ozone datasets (top to bottom, SAGE II-CCI-OMPS [CCI], SAGE II-OSIRIS-OMPS [SOO], GOZCARDS, and SWOOSH) calculated over the period 2000–2018 for three selected latitudinal bands (left to right, 60–30°S, 10°S–10°N, and 30–60°N). Data are presented on their natural vertical coordinate: altitude grid for CCI and SOO and pressure grid for GOZCARDS and SWOOSH. The colored shading denotes where the trends are significant at the 95% confidence level. [From Szeląg et al., 2020.]

Box 3-3. The Importance of the Troposphere for Total Column Ozone

A key conclusion of this Assessment is that it is more difficult than in the past to interpret total column ozone (TCO) changes due to the different trends and processes that contribute to the overall column. In particular, the contribution from tropospheric ozone changes is highlighted for both current (*Section 3.3.2.4*) and future (*Section 3.4.3*) total column trends, despite the modest contribution (~10%) of the tropospheric column to the total amount of ozone in the column.

Production of ozone in the stratosphere results from the photolysis of molecular oxygen (O_2) and subsequent reaction of atomic oxygen with O_2. In contrast, tropospheric ozone is produced from photochemical reactions involving its precursors, nitrogen oxides (NO and NO_2; NO_x), carbon monoxide (CO), and volatile organic compounds, with an additional source from net stratosphere-to-troposphere transport. It is lost through additional chemical reactions as well as through deposition at the surface (e.g., Monks et al., 2015). Tropospheric ozone levels depend on highly temporally and spatially variable natural and anthropogenic precursor emissions, different local surfaces that impact dry deposition rates, and tropospheric weather. There are substantial challenges in fully understanding its distribution and changes using both measurements (Gaudel et al., 2018; Tarasick et al., 2019) and simulations (Young et al., 2018). Community efforts such as the Tropospheric Ozone Assessment Report (TOAR) are improving our understanding, while also making previously unpublished measurements available (Schultz et al., 2017). Community modeling efforts (e.g., CCMI; Morgenstern et al., 2017) also seek to evaluate models and better characterize and understand their deficiencies.

Despite these difficulties, models demonstrate skill in comparisons against observations, reproducing the tropospheric ozone burden, distribution, and trends (e.g., Young et al., 2018; **Box 3-3 Figure 1**). Model studies of the historical period (1850–present) find that increases in anthropogenic precursors have dominated the simulated ~30–35% increase in tropospheric ozone (e.g., Young et al., 2013; Griffiths et al., 2021), which is consistent with the 40% change inferred from ice core–based constraints (Yeung et al., 2019). Between 1980 and 2000, the same simulations suggest a ~5% increase in tropospheric ozone, broadly in agreement with observational constraints (Gaudel et al., 2018) and occurring at the same time as the most notable ODS-driven stratospheric ozone depletion. Since 2000, there have been spatially heterogeneous trends in precursor emissions and, consequently, tropospheric ozone (Zhang et al., 2016; Gaudel et al., 2018, 2020; Zhang et al., 2021). This complicates our understanding and interpretation of both the overall tropospheric trends and those of TCO.

Projected future changes in tropospheric ozone strongly depend on the future scenario of precursor emissions and, to a lesser degree, on the projected state of stratospheric ozone and climate (see **Box 3-1 Figure 1**; Stevenson et al., 2013; Young et al., 2013; Griffiths et al., 2021; see also *Section 3.4.3*). Because current and future tropospheric ozone changes may contribute substantially to TCO changes, or offset stratospheric ozone changes (Ball et al., 2018; Bencherif et al., 2020), they must be considered as an integral part of this Assessment.

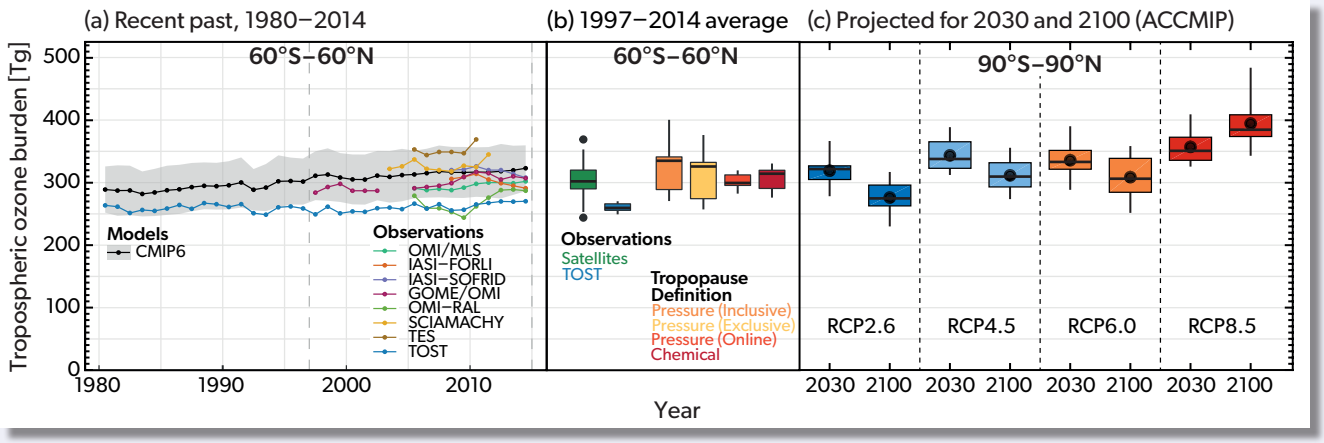

Box 3-3 Figure 1. The evolution of the global tropospheric ozone burden in simulations (1980–2100) and observations (1980–2014), showing (a) a comparison of the CMIP6 models (black; see **Box 3-4**) against observational estimates (colored lines) for 1980–2014, (b) a comparison of the 1997–2014 average tropospheric ozone burden in observations (green and blue boxes) and simulations (orange, yellow and red; with different definitions of the tropopause), and (c) the projected tropospheric ozone burden from the ACCMIP simulations (Lamarque et al., 2013) for 2030 and 2100 time slices for four different future climate scenarios (the Representative Concentration Pathways [RCPs]). [Adapted from Young et al., 2013 and Griffiths et al., 2021; see those references for further details.]

Partial column trends do not always show strong agreement with those derived from highly resolved vertical profiles, especially in terms of significance. This is primarily due to the poorly characterized small-scale and/or short-term variability in regression analyses (*Section 3.2*) that contribute to larger trend uncertainties. These issues become more pronounced for trends derived at higher vertical resolutions since vertical integration averages out some variability (*Section 3.3.3*), particularly if the partial columns are chosen for that purpose. On the other hand, if the vertical integration is performed over the entire column, a significant detection at some finer-resolution vertical levels may be averaged out if trends of opposite sign are present within the column integration. There can also be complications in integrating resolved data into partial columns (such as how data gaps are dealt with). There are few analyses investigating the consistency of TCO with respect to its partial column components in a holistic way.

3.3.3 Understanding Trends in the UTLS Region

Since the previous Assessment, additional observations and new CCM simulations have furthered our understanding of trends in the upper troposphere / lower stratosphere (UTLS) region, with a focus on the tropics (30°S–30°N) and SH and NH mid-latitudes (30–60°). The overall conclusion, discussed in detail below, is that ozone is decreasing in the tropical UTLS, consistent with understood changes in the stratospheric circulation. At mid-latitudes, the picture is more complex. Ozone is decreasing in the mid-latitudes, but 1) this trend has a magnitude and significance that is not consistent across different datasets and time periods, 2) the trend is not generally captured in chemistry-climate model (CCM) simulations, and 3) there is no clear consensus as to what might be driving it. Trends in the UTLS are difficult to assess due to high variability and the fact that there are only two decades of data available. Additionally, the quality of satellite-based observations is usually substantially reduced in the UTLS region compared to the middle and upper stratosphere, while ground-based observations, which do have good data in this region, provide only sparse coverage.

Findings and trends for the tropical lower stratosphere remain consistent with the previous Assessment. This region consistently displays significant, or near-significant, negative trends between the start years of ~1995–2000 and end years of 2013–2019 (Dietmüller et al., 2021; see also **Figure 3-16**). Modeling studies indicate these negative trends are to be expected, as tropical upwelling in the BDC strengthens in response to increasing greenhouse gases (Eyring et al., 2010; Dhomse et al., 2018; see also *Section 3.4* and *Chapter 5*), as reported in previous Assessments. This finding is further supported by a recent analysis of ozonesonde data, which found that ozone trends became insignificant after accounting for changes in tropopause height, suggesting that chemical ozone loss is not a driving factor in long-term changes in this region (Thompson et al., 2021). Separately, a recent model study of the 2016 Indonesian wildfires suggests that tropical UTLS ozone reductions can result from such events due to the gas-phase chemistry of reactive volatile organic compound emissions, although the magnitude of the effect is dependent on model assumptions (Rosanka et al., 2021). Trends and variability in the tropical UTLS are particularly important since this region is a large contributor to quasi-global (60°S–60°N) lower-stratospheric ozone changes.

The mid-latitude lower-stratospheric ozone declines over 1998–2016 reported in the last Assessment (Ball et al., 2017, 2018; Wargan et al., 2018) persist with additional years of data (**Figure 3-16**), both for analyses that are spatially resolved and for partial columns (Dietmüller et al., 2021). While temperature trends, which are expected to change alongside ozone, support this tendency of the ozone trends (Ball et al., 2020; Szeląg et al., 2020), the lower stratosphere is subject to large, dynamically driven interannual variability, and it remains difficult to make robust conclusions. Indeed, earlier studies using fewer data and with end years prior to 2017 also show a decline of ozone in this region, although in those cases the trend is not statistically significant (Bourassa et al., 2014, 2018; Sofieva et al., 2017; Steinbrecht et al., 2017). Trends are sensitive to large variability in the analyzed data, especially near the end of short time series, although

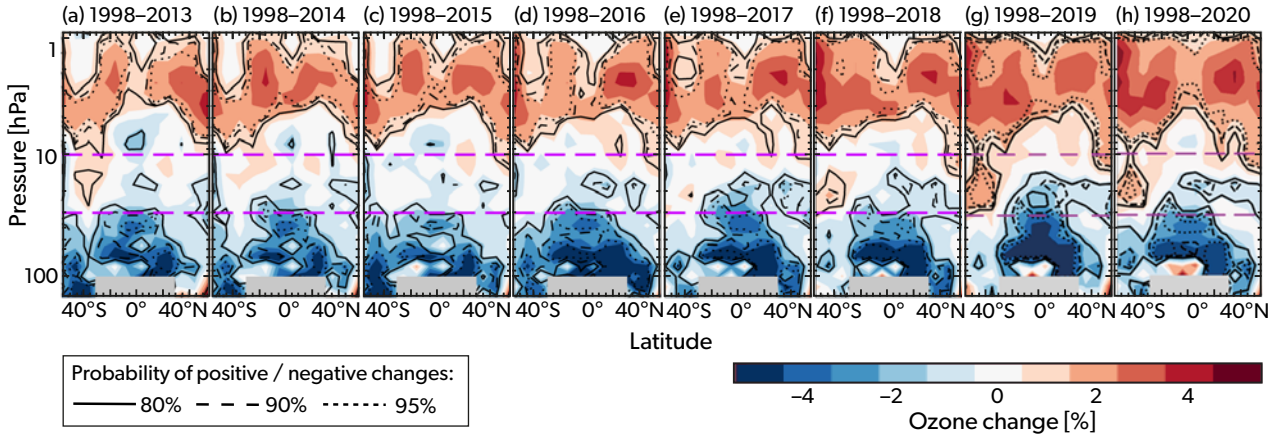

Figure 3-16. Zonal-mean ozone trends using the BASIC dataset (which is based on the GOZCARDS and SWOOSH datasets) starting in 1998 and finishing in years ranging from 2013 to 2020, moving from (a) to (h). Red regions indicate an ozone increase, while blue regions indicate a decrease. Confidence levels in the trends are indicated by solid (80%), dashed (90%), and dotted (95%) lines. [Updated from Ball et al., 2019a.]

the negative trends across the lower stratosphere are persistent even when the end years (**Figure 3-16**) and start years (Dietmüller et al., 2021) are varied. For instance, the large year-on-year ozone increase between 2016 and 2017 in the mid-latitude SH UTLS has been found to fully (Chipperfield et al., 2018) or partially (Ball et al., 2019a) offset the negative ozone trend over 1998–2016. Extended into 2018, the ozone changes in the SH lower stratosphere remain negative but become statistically insignificant (Ball et al., 2019a). Besides large short-term dynamical variability, natural variability (e.g., related to sea surface temperatures) can interfere on interannual (Rosanka et al., 2021) and decadal (Garfinkel et al., 2013; Ball et al., 2020; Iglesias-Suarez et al., 2021) timescales. Both timescales are relevant to understanding the limited observational period and future projections.

Since the previous Assessment, new studies of multiple ozone datasets (Ball et al., 2019a) and CCM simulations (Orbe et al., 2020) have explored the hemispheric pattern in the mid-latitude UTLS ozone trends in more detail. These have demonstrated that lower-stratospheric ozone in the Southern Hemisphere appears to display larger interannual variability than in the Northern Hemisphere, which is partly why trend significance there remains low. Negative changes in the Northern Hemisphere are both more persistent and have smaller uncertainties than in the Southern Hemisphere, although they are still statistically non-significant. The relative contributions of changes in mixing versus circulation to NH lower-stratospheric ozone changes remain an open question. While a model-based tracer budget analysis (over 1998–2018) found that decreases in NH ozone are primarily associated with changes in the meridional transport (poleward expansion of tropical upwelling and reduced downwelling in the northern subtropical region; Orbe et al., 2020), changes in meridional mixing are also important (Wargan et al., 2018; Ball et al., 2020; Orbe et al., 2020). However, it is worth noting that even recent studies that have made use of historical CCM runs with accurate real-world (e.g., sea surface temperature) variability only cover up to 2010 or 2014 (e.g., Orbe et al., 2020), which means comparisons of models with observations beyond this year are problematic.

A different approach to using CCM output is to examine the distribution of trends across an ensemble of free-running simulations, i.e., those where the long-term drivers of ODSs and greenhouse gases are the same but are unconstrained by observed interannual variability. However, statistical analysis of mid-latitude UTLS ozone trends across 31 such CCMI-1 simulations demonstrates that the observed trends represent an extreme value of the CCM probability distribution, indicating that it is between ~75% and 96% probable that the models are not capturing the mid-latitude lower-stratospheric changes (**Figure 3-17**; Dietmüller et al., 2021). Similarly, negative trends were found in both the tropics and mid-latitudes up to present day in only 2 out of 13 models that contributed to the older CCMVal-2 report (Ball et al., 2020). Moreover, simulated mid-latitude lower stratosphere trends remain positive even after accounting for variations in the start and end years (Dietmüller et al., 2021). There is a possibility that the lack of negative mid-latitude lower-stratospheric trends in the models is related to weaker-than-observed tropical BDC trends in climate models (Ball et al., 2020; Orbe et al., 2020; see also Stone et al., 2018).

Finally, we note that there is a spread among the UTLS ozone trends calculated for the available datasets. Most of the results

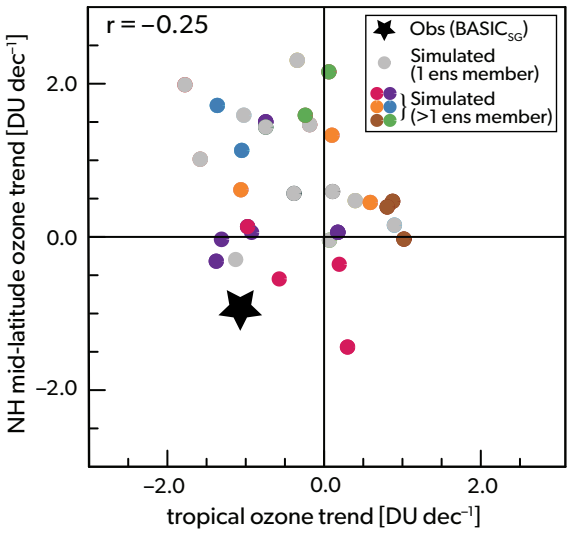

Figure 3-17. Scatter plot of lower stratosphere ozone column trends for the NH mid-latitudes (30–50°N; 150–30 hPa) against the tropics (20°S–20°N, 100–30 hPa) calculated over the period 1998–2018 for observations from the BASICSG dataset (star; Ball et al., 2018) and 31 CCMI REF-C2 simulations (circles; Morgenstern et al., 2017). All ensemble members of a particular model are shown in the same color, whereas simulations with only one ensemble member are shown in gray. Also shown is the correlation between the tropical and NH mid-latitude trends in the simulations. [Adapted from Dietmüller et al., 2021.]

discussed here have relied on observational data from SWOOSH and GOZCARDS, which are constructed using similar underlying satellite data, or on the BASIC dataset, which integrates both of these (Ball et al., 2017, 2018; Chipperfield et al., 2018; Wargan et al., 2018; Ball et al., 2020; Dietmüller et al., 2021; *Section 3A.3*). However, there is not consistency between trends from partial columns with those calculated from resolved profiles, particularly with respect to uncertainties, which are larger in the resolved profiles (SPARC/IO3C/GAW, 2019; Weber et al., 2020; **Figures 3-11** and **3-12**; *Section 3.3.2.4*). It should be emphasized that as data are ever more resolved (vertically, spatially, and/or temporally), higher uncertainties are expected (see *Section 3.3.2.4*), and confidence and consistency with more spatially and temporally smoothed partial columns will decrease (**Figures 3-11** and **3-12**; Bourassa et al., 2018; Arosio et al., 2019; SPARC/IO3C/GAW, 2019; Szeląg et al., 2020; Sofieva et al., 2021; Weber et al., 2021).

3.3.4 Past Ozone in Models and Trend Attribution

Since the previous Assessment, the latest generation of climate models (including some CCMs) have performed new simulations as part of the Coupled Model Intercomparison Project Phase 6 (CMIP6) experiment (Eyring et al., 2016), conducted in support of the Intergovernmental Panel on Climate Change. CMIP6 defines some simulations that are aimed at either identifying the drivers of past changes or exploring future changes under different emissions scenarios (see **Box 3-4** and *Section 3.4.1*).

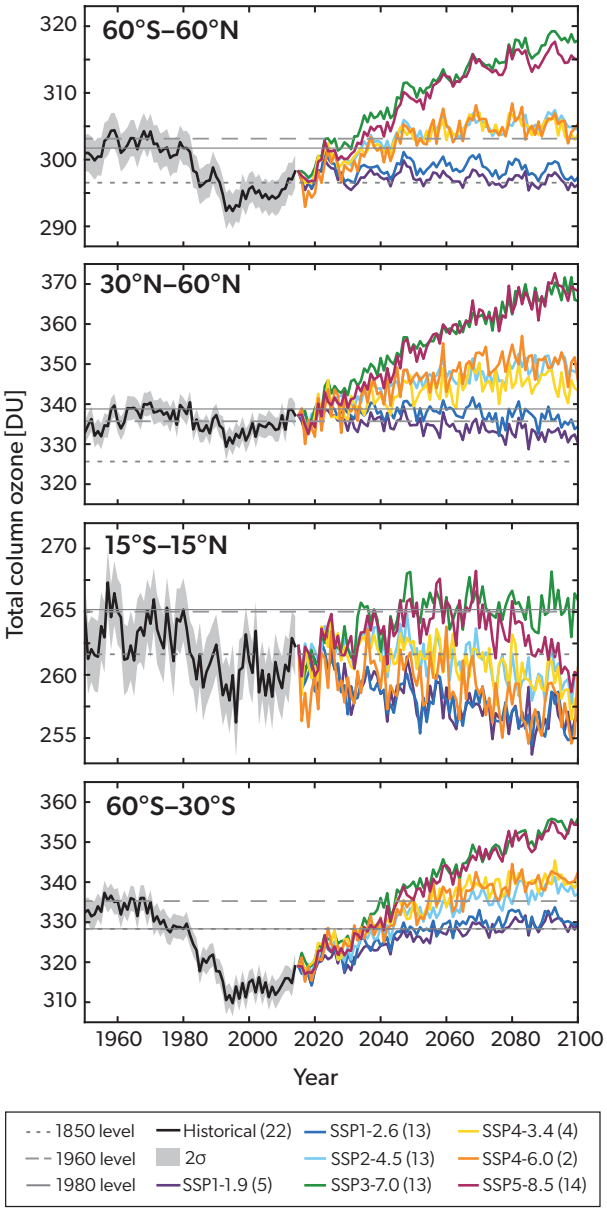

Figure 3-18. CMIP6 multi-model mean, annual mean TCO projections for the historical simulation (black line) and different shared socioeconomic pathways (SSPs; colored lines; see **Box 3-4**) for different latitude bands: near global (60°S–60°N), NH mid-latitudes (30–60°N), tropics (15°S–15°N), and SH mid-latitudes (60–30°S). The light gray envelope indicates the 95% confidence interval for the multi-model mean for the historical simulations. Simulated TCO values for the 1850, 1960, and 1980 annual means are given by the dotted, dashed, and solid horizontal gray lines, respectively. The number of models performing each simulation is provided in parentheses in the legend. Many of the models provided ozone output for a core set of SSPs (SSP1-2.6, SSP2-4.5, SSP3-7.0, and SSP5-8.5), while a smaller number provided data for other SSPs (SSP1-1.9, SSP4-3.4, and SSP4-6.0). [Adapted from Keeble et al., 2021a.]

3.3.4.1 Past Ozone in Models

The individual CMIP6 models span a range of model complexity, from models using interactive chemistry schemes to calculate ozone changes within the model (i.e., in response to changing chemical and physical conditions) to those using a time-evolving ozone field from a pre-prepared dataset (i.e., where the ozone does not interact with the simulation). While the prescribed ozone field is from the same source for all models in the latter category, it is not implemented consistently, with the result that different models have different TCO values (Keeble et al., 2021a).

In contrast to the CCMI-1 simulations (Dhomse et al., 2018) discussed in the last Assessment, which started in 1960, the CMIP6 simulations extend back to 1850. This allows additional exploration of several decades preceding ozone depletion, which can be used to benchmark simulated future changes. In terms of long-term changes in TCO, the simulated near-global (60°S–60°N), annual multi-model mean increases by ~2% between 1850 and 1960 (Keeble et al., 2021a) before rapidly declining through the 1980s and 1990s due to emissions of halogenated ODSs (**Figure 3-18**). TCO reaches a minimum in the late 1990s before increasing again as ODS levels decrease.

Simulated TCO changes for different latitude bands are similar to those for the near-global mean (**Figure 3-18**), although the 1850–1960 ozone increase (not shown) is larger in the Northern Hemisphere and tropics and less prominent in the Southern Hemisphere. This difference is driven by simulated increases in NH tropospheric ozone between the preindustrial period (1850) and present day, as seen in the changes in zonal-mean ozone mixing ratios (**Figure 3-19**; see also *Section 3.3.4.3* and **Box 3-3**; Griffiths et al., 2021; Keeble et al., 2021a). While stratospheric ozone levels have decreased between the preindustrial and present day, particularly in the upper stratosphere and Antarctic polar lower stratosphere due to changes in chlorine-catalyzed ozone depletion, tropospheric ozone has significantly increased during this same period (**Figure 3-19**; Tarasick et al., 2019; Yeung et al., 2019). The impact of these combined changes is that despite stratospheric ozone depletion linked to ODS emissions, the simulated NH mid-latitude TCO is higher in the 1990s than in the preindustrial period (**Figure 3-18**). Although the simulated increase remains to be validated against (the very limited) available observations (e.g., Rieder et al., 2010), this nonetheless highlights the problem of using TCO as a metric for stratospheric ozone changes (see **Box 3-3** and *Sections 3.3.2.4* and *3.4.2*).

TCO over 1980–2014 is ~10 DU higher in the CMIP6 multi-model mean compared to observations when all models are included (Keeble et al., 2021a). Using only those models that explicitly simulate chemical processes, bias-correcting their TCO (to the 1964–1980 average) and then smoothing it using an 11-point boxcar filter (as per Dhomse et al., 2018), the observed TCO trend (**Figure 3-20**) is well captured by the multi-model mean in the 60°S–60°N region and in the mid-latitudes. It is less well captured in the tropics (see also *Section 3.3.3*). Good agreement has also been shown for TCO trends over the period 1979–2000 between the multi-model mean of CMIP6 models that use interactive chemistry schemes and observations at most latitudes (Morgenstern et al., 2020). However, for some locations, there is a large spread in the simulated ozone trends between individual models, and our understanding of the reasons behind this is currently lacking (see also the discussion in *Section 3.4.1*).

Box 3-4. Models and Scenarios: CMIP6 and SSPs

Coordinated model intercomparison projects are a key method for bringing information from multiple model simulations and research groups into climate and ozone assessments. This Assessment makes use of the Coupled Model Intercomparison Project Phase 6 (CMIP6), an international activity that consists of a suite of climate model experiments designed to explore the impacts of past and future emissions changes on the long-term evolution of the Earth system (Eyring et al., 2016).

Of particular interest to this Assessment are the CMIP6 historical simulations, as well as sensitivity simulations performed for the Aerosol Chemistry Model Intercomparison Project (AerChemMIP; Collins et al., 2017) and the projections performed for the Scenario Model Intercomparison Project (ScenarioMIP; O'Neill et al., 2016). The ScenarioMIP simulations use a new set of future climate scenarios, the Shared Socioeconomic Pathways (SSPs; Riahi et al., 2017). SSPs replace Representative Concentration Pathways (RCPs) explored in the previous Assessment but serve the same purpose: to provide a range of future emissions scenarios that assume different socioeconomic trajectories and different levels of climate change mitigation. SSP5-3.4-OS is slightly different from the others in that it is an "overshoot" scenario, following the SSP5-8.5 (high climate forcing) scenario until 2040, with aggressive mitigation thereafter. This scenario informs the Assessment in *Chapter 6*.

Compared to the RCPs, the SSPs explore a much wider range of possible future emissions pathways for well-mixed greenhouse gases, such as CO_2 (carbon dioxide), N_2O (nitrous oxide), and CH_4 (methane), in addition to changes to the emissions of near-term climate forcers (NTCFs), which include tropospheric ozone precursors and aerosols (Gidden et al., 2019). For long-lived halogenated ozone-depleting substances (ODSs), all SSPs assume compliance with the Montreal Protocol and its Amendments and adjustments. However, as models are run with surface mixing ratios as input, rather than emissions, the levels of ODSs do differ marginally between SSPs due to the impacts of different climate trajectories on their lifetime (see also *Chapter 4*). Finally, hydrofluorocarbons (HFCs; *Chapter 2*) differ more markedly between SSPs than do controlled ODSs, as each scenario has different compliance rates with the Kigali Amendment (Meinshausen et al., 2020).

Box 3-4 Table 1. Description of the relevant CMIP6 simulations discussed in this Assessment report (GHGs = greenhouse gases, ODSs = ozone-depleting substances, NTCFs = near-term climate forcers, SSTs = sea surface temperatures, SICs = sea ice concentrations).

Simulation Name(s)	Type	Purpose	Features
historical	Hindcast simulation of the period 1850–2014	To produce realistic simulations of the past atmospheric state	GHGs, ODSs, volcanic aerosol, solar variability, ozone, and aerosol precursors are prescribed from observations. Uses a coupled ocean model for SSTs and SICs
histSST	Historical atmosphere-only transient simulation of the period 1850–2014	Control experiment for AerChemMIP historical perturbation experiments	As "historical," but with SSTs and SICs prescribed from the "historical" experiment rather than using a coupled ocean model.
histSST-piNTCF histSST-piCH4 histSST-piN2O histSST-1950HC	Series of historical atmosphere-only transient perturbation simulations of the period 1850–2014 based on histSST	To assess the impact of NTCFs, CH_4, N_2O, and halocarbon (HC) emissions on the past evolution of atmospheric composition and climate change	As histSST, but with either NTCF, CH_4, or N_2O emissions held at their preindustrial ("pi") levels, or with HCs held at their 1950 levels, while all other emissions evolve as in "historical"
SSP1-1.9 SSP1-2.6 SSP2-4.5 SSP3-7.0 SSP4-3.4 SSP4-6.0 SSP5-8.5 SSP5-3.4-OS	Future simulations of the period 2015–2100	To produce estimates of future atmospheric composition and climate changes given specific emissions assumptions. Named for the radiative forcing level by 2100 (1.9 Wm^{-2}, 2.6 Wm^{-2}, etc.)	GHGs, ODSs, volcanic aerosol, ozone, and aerosol precursors are prescribed following the named SSP scenario (SSP1-1.9, etc.); uses coupled ocean model for SSTs and SICs

The CMIP6 models span a range of complexity, particularly with regard to the simulation of atmospheric chemistry. In contrast to phase 1 of the Chemistry Climate Model Initiative (CCMI-1; Morgenstern et al., 2017), which was used extensively in the last Assessment and includes exclusively those models with interactive chemistry schemes, CMIP6 includes both models with interactive chemistry and those that prescribe ozone fields from a shared dataset. As a result, there is a smaller number of CMIP6 models suitable for exploration of ozone return dates (*Section 3.4.1*) than have been shown in previous Assessments. However, these models have performed simulations following a larger number of potential future emissions pathways.

All of the relevant CMIP6 simulations are described in detail in **Box 3-4 Table 1**, coupled with **Box 3-4 Figure 1** showing the evolution of surface concentrations for selected long-lived greenhouse gases for different SSPs.

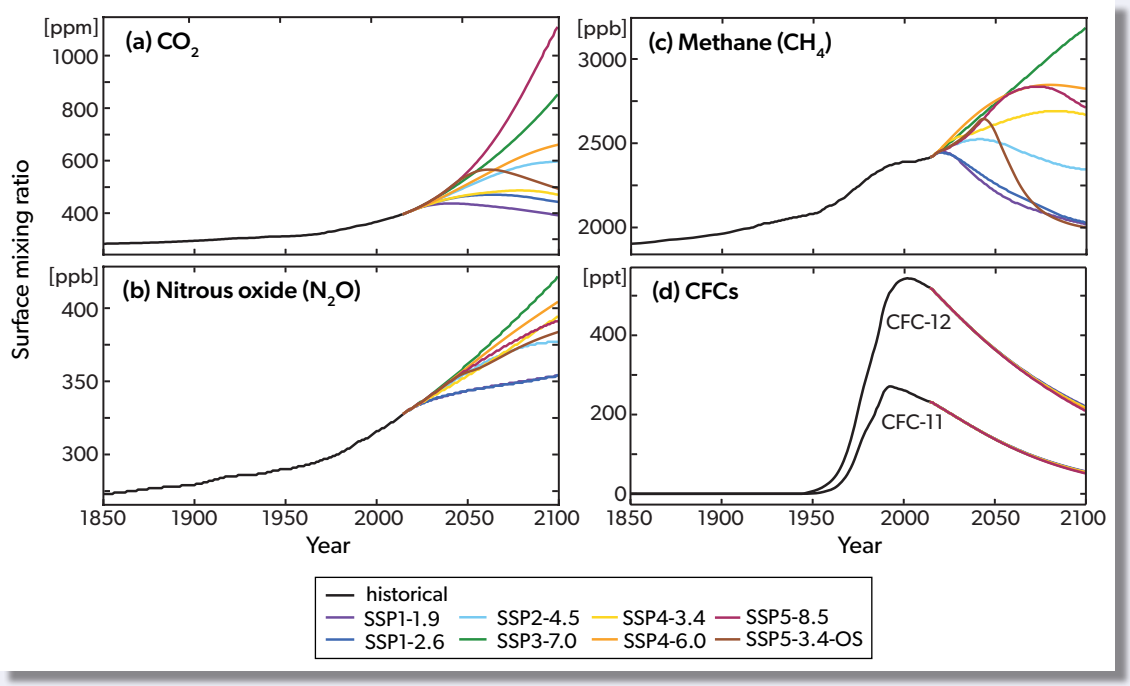

Box 3-4 Figure 1. Evolution of the surface mixing ratios of (a) carbon dioxide (CO_2; in parts per million, ppm), (b) nitrous oxide (N_2O; in parts per billion, ppb), (c) methane (CH_4; in parts per billion, ppb), and (d) the ODSs CFC-11 and CFC-12 (in parts per trillion, ppt) from 1850–2100 for the historical period (black lines) and within different SSPs (colored lines). CFC-11 and CFC-12 surface mixing ratios differ between scenarios but only marginally. See **Box 3-4 Table 1** for more information.

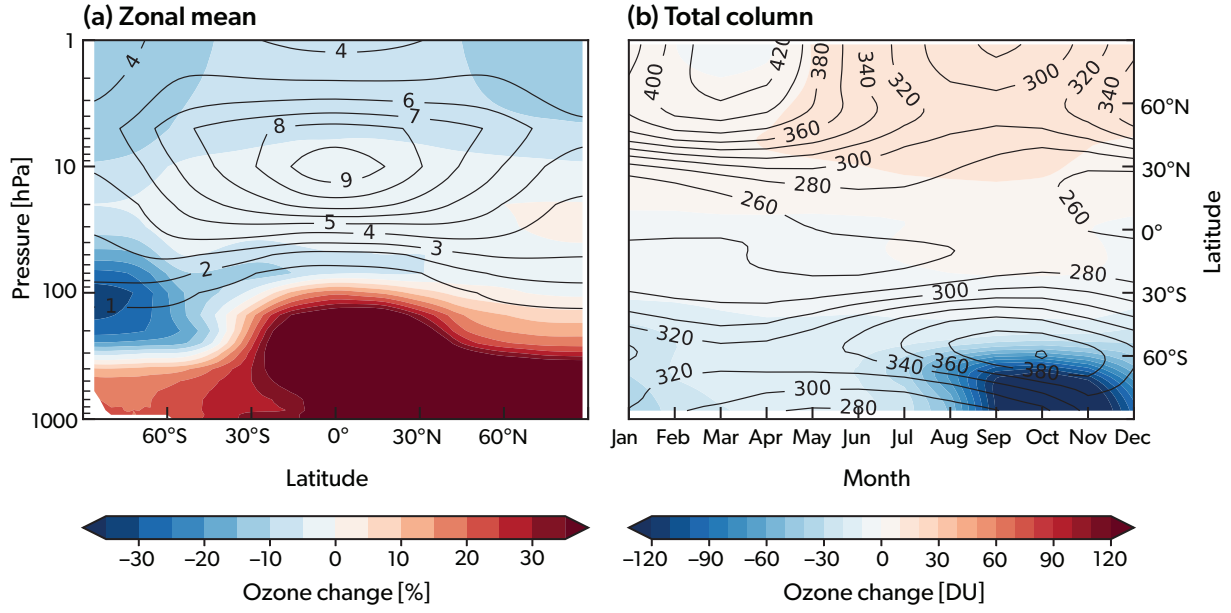

Figure 3-19. Simulated changes in ozone from the preindustrial (1850–1864 average) to present day (2000–2014 average) for the CMIP6 multi-model mean. Color fills show (a) the change in annual and zonal-mean ozone mixing ratios (%) and (b) the change in monthly and zonal-mean TCO (DU). Black contour lines in each panel show the present-day climatology as (a) mixing ratio (ppm) and (b) DU. [Adapted from Keeble et al., 2021.]

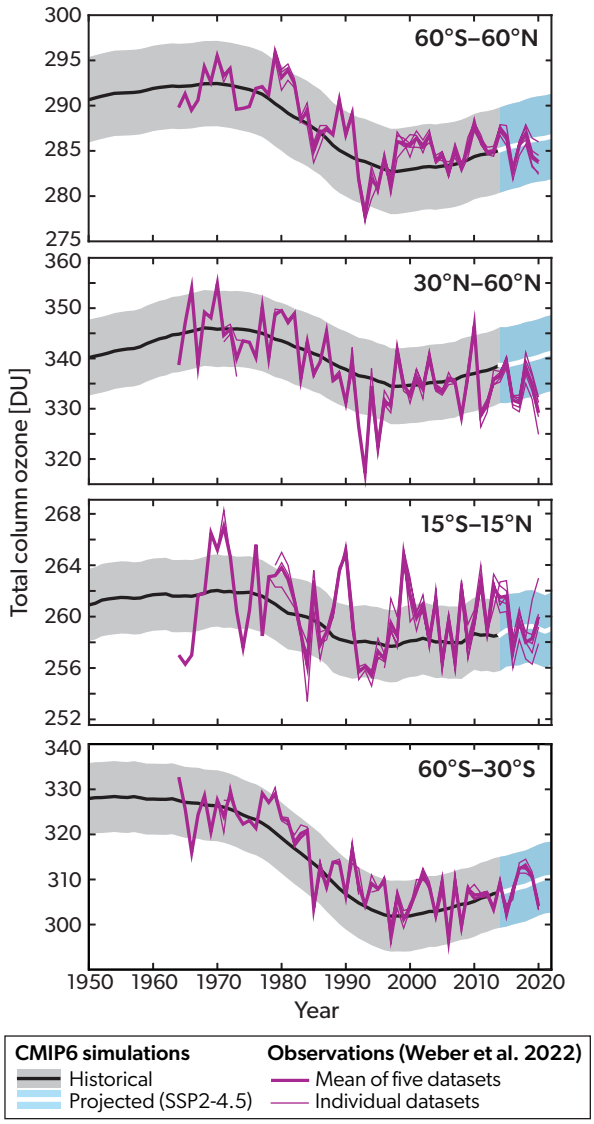

Figure 3-20. TCO for the CMIP6 multi-model mean from 1950 to 2022 (historical to 2014 in black and then extended with SSP2-4.5 in white; see **Box 3-4**) and the five individual observational datasets from **Figure 3-6** (thin purple lines) and their mean (thick purple line) from 1964–2020. Data shown are annual mean values for four different latitude bands: near global (60°S–60°N), NH mid-latitudes (35–60°N), tropics (20°S–20°N), and SH mid-latitudes (60–35°S). The CMIP6 multi-model mean is calculated as an unweighted mean of the five CMIP6 models available that include interactive chemistry schemes. Each model is first bias corrected to the observations averaged over the period 1964–1980, before being smoothed with an 11-point boxcar smoothing. The gray and light blue envelopes show the spread between the individual models that make up the CMIP6 multi-model mean and are calculated as the ±1 standard deviation of the bias-corrected, smoothed model values, averaged 1850–2100 excluding the years 1954–1990, during which time the model variance becomes artificially low due to the bias correction step. [Adapted from Keeble et al., 2021a.]

3.3.4.2 Simulated Impacts of Very Short-Lived Substances

Chlorine and bromine from very short-lived substances (VSLSs; halogenated ozone-depleting substances with lifetimes shorter than six months) contribute to ozone depletion, particularly in the lower stratosphere, where their present-day contribution may be up to half as large as that from long-lived ODSs (e.g., Hossaini et al., 2015; see also *Chapter 1*). Overall, while model sensitivity experiments show that the contribution of past trends in short-lived chlorine species to recent ozone changes is small (e.g., Chipperfield et al., 2018; see also *Section 3.3.3*), the long-term impact of continued VSLS increases on stratospheric ozone recovery remains to be quantified (see also Barrera et al., 2020).

Although VSLSs are not routinely included in all CCMs, the previous Assessment reported how simulations of recent ozone changes can be improved by the inclusion of VSLSs. Since the last Assessment, model studies have sought to quantify the amount of chlorine and bromine from VSLSs in the stratosphere, including highlighting the important role of transport to the stratosphere in the Asian summer monsoon (Adcock et al., 2021). One modeling study estimated that the total amount of stratospheric chlorine from VSLSs has increased from 69 ± 14 ppt in 2000 to 111 ± 22 ppt in 2017 (Hossaini et al., 2019). Due to decreases in long-lived ODSs over the same period, the increase in chlorine from VSLSs has led to their relative contribution to total stratospheric chlorine, increasing from ~2% in 2000 to ~3.4% in 2017. Another CCM study (Barrera et al., 2020) found that brominated VSLSs account for 8 DU (3%), 2.5 DU (1%), and 5.5 DU (2%) additional ozone loss for the SH mid-latitudes, tropics, and NH mid-latitudes, respectively. The same study also noted that the inclusion of 5 ppt biogenic bromine results in a realistic stratospheric bromine loading and improves the agreement between the modeled and observed mid-latitude TCO over the period 1980–2015, consistent with previous findings (Sinnhuber and Meul, 2015).

3.3.4.3 Attributing Drivers of Past Ozone Changes

New sensitivity simulations from the Aerosol and Chemistry Model Intercomparison Project (AerChemMIP; Collins et al., 2017), part of CMIP6 (**Box 3-4**), can be used to attribute past ozone changes to a broader range of individual drivers than was possible using the CCMI-1 models in the last Assessment. These drivers include emissions of non-methane near-term climate forcers (NTCFs; precursors of tropospheric ozone and aerosol; lifetimes <10 years), methane (CH_4), nitrous oxide (N_2O), and halogenated ODSs. AerChemMIP also includes simulations over a longer historical time period (1850–2014 versus 1960–2014). The individual roles of changes in NTCFs, CH_4, N_2O, and halogenated ODSs on historical ozone column changes can be determined by contrasting the AerChemMIP sensitivity simulations (with individual forcing agents held at their preindustrial levels) against an "all-forcing" simulation, where all forcings evolve (histSST; **Box 3-4**; Zeng et al., 2022). In contrast to the seven CCMI-1 models in the previous Assessment, there are only between three and five AerChemMIP models with suitable output to assess the contributions of the different drivers.

In close agreement with the CMIP6 simulations (**Figure 3-18**), the all-forcing multi-model mean of the four AerChemMIP models with interactive stratospheric and tropospheric chemistry

shows a gradual increase of near-global mean TCO during ~1900–1970, mainly due to the increase in tropospheric ozone (**Figure 3-21**). TCO decreases rapidly after the 1970s until the late 1990s, when stratospheric ozone depletion dominates its decrease in all regions. The largest decrease occurs in the SH mid-latitudes. However, in the NH mid-latitudes and the tropics, the continuous increase of the tropospheric ozone column from the 1950s contributes to long-term TCO changes, offsetting the reduction in stratospheric ozone in these regions. The model spread is particularly large in the stratospheric ozone changes that contribute to the uncertainty in TCO changes, particularly in mid-latitudes.

As in previous Assessments, the sensitivity simulations—where individual forcing agents are turned off—can be used to quantify the roles of individual drivers in ozone trends. These runs reveal the dominant role of ODS-induced stratospheric ozone depletion for the global TCO decrease from the 1970s to the late 1990s (**Figure 3-22**). During this ozone depletion period, individual models differ substantially in simulating the stratospheric ozone response to ODS increases; this is the main cause of large intermodel differences in the simulated TCO trend. In contrast, tropospheric column ozone increases can be attributed to the monotonic increases in NTCFs and CH_4 (**Box 3-4 Figure 1**), particularly from the 1950s to the late 1990s. NTCFs contribute to TCO increases largely through increased tropospheric columns (**Box 3-3**), particularly in the tropics and the NH mid-latitudes. Methane contributes to total column increases both through the tropospheric column (as a tropospheric ozone precursor) and the stratospheric column (through its reaction with chlorine, which reduces ozone depletion from ODSs), particularly in the mid-latitudes over 1970–2000. The impact of increased N_2O is to decrease TCO through its role as an ODS in the stratosphere, even though it increases ozone in the tropical lower stratosphere (due to "self-healing," arising from increased UV fluxes as a result from a depleted ozone layer aloft), consistent with the CCMI-1 models (Morgenstern et al., 2018; **Figure 3-22**). Note, this impact is estimated based on only three AerChemMIP models, as the other two did not perform the relevant simulations, and there is a large model spread and large interannual variation.

No simulations directly targeted the impact of carbon dioxide (CO_2) increases on ozone, but this can be estimated from the residual of the other effects, i.e., the difference between the impact from all forcings (histSST) and the combined impact from the other single-forcing perturbations (NTCFs, CH_4, halogenated ODSs, and N_2O), although only for the three models with the required simulations. The impact of CO_2 on simulated TCO is dominated by changes in the stratospheric partial columns (**Figure 3-22**). This includes a slight increase in stratospheric column ozone prior to the 1970s due to CO_2-induced stratospheric cooling (*Chapter 5*), which reduces stratospheric ozone loss, mainly in the NH mid-latitudes, and a sharp decrease after the late 1970s, when ODSs increase and stratospheric cooling leads to enhanced ODS-driven ozone depletion. However, this approach of deriving the impact of CO_2 is associated with large uncertainties, as it involves several simulations and cannot account for couplings between forcing agents.

These sensitivity simulations can also be used to attribute the drivers of vertically resolved ozone trends (**Figure 3-23**). In agreement with previous Assessments, the simulated negative trend in stratospheric ozone is predominantly driven by ODSs during the depletion period (1979–1999). Both the trend

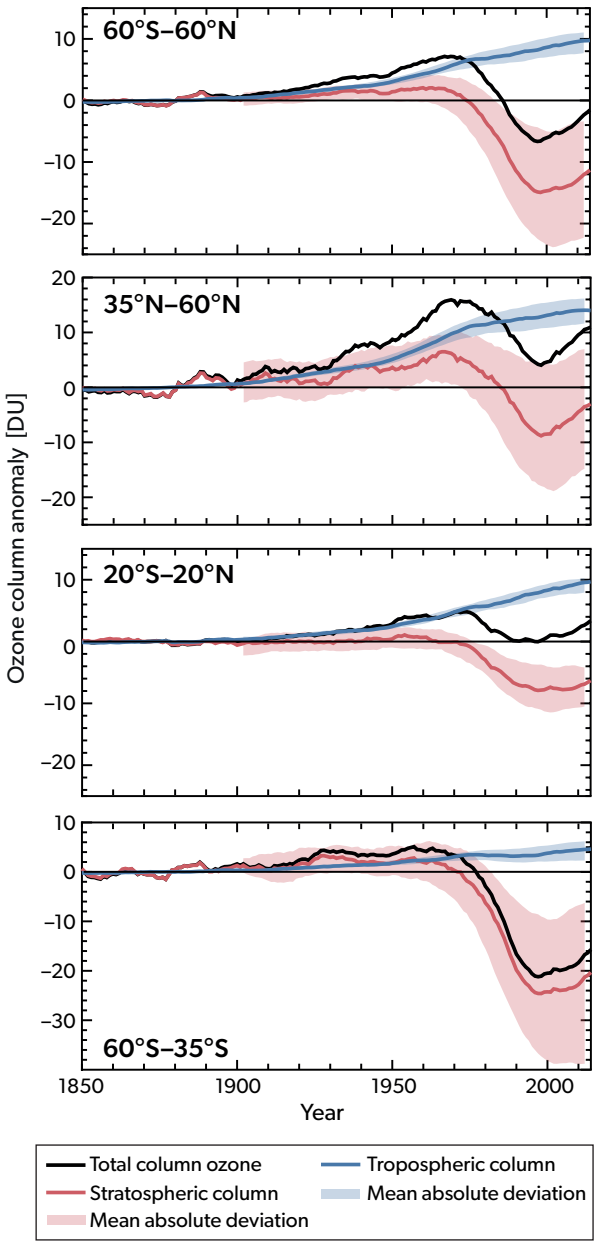

Figure 3-21. Annual multi-model mean TCO (black) and the stratospheric (red) and tropospheric (blue) partial column ozone anomalies (relative to 1850–1900 base period) for 1850 to 2014 from the AerChemMIP histSST simulation (**Box 3-4**), for the near-global mean (60°S–60°N), NH mid-latitudes (35–60°N), the tropics (20°S–20°N), and the SH mid-latitudes (60–35°S). Four models (CESM2-WACCM, GFDL-EM4, MRI-ESM2-0, and UKESM1-0-LL) are included in the ensemble, and the shaded areas are the mean absolute deviation from the multi-model mean. The annual means are smoothed using a 20-year boxcar filter. For the partial columns, the tropopause is defined using the WMO lapse rate definition in each model. [Adapted from Zeng et al., 2022.]

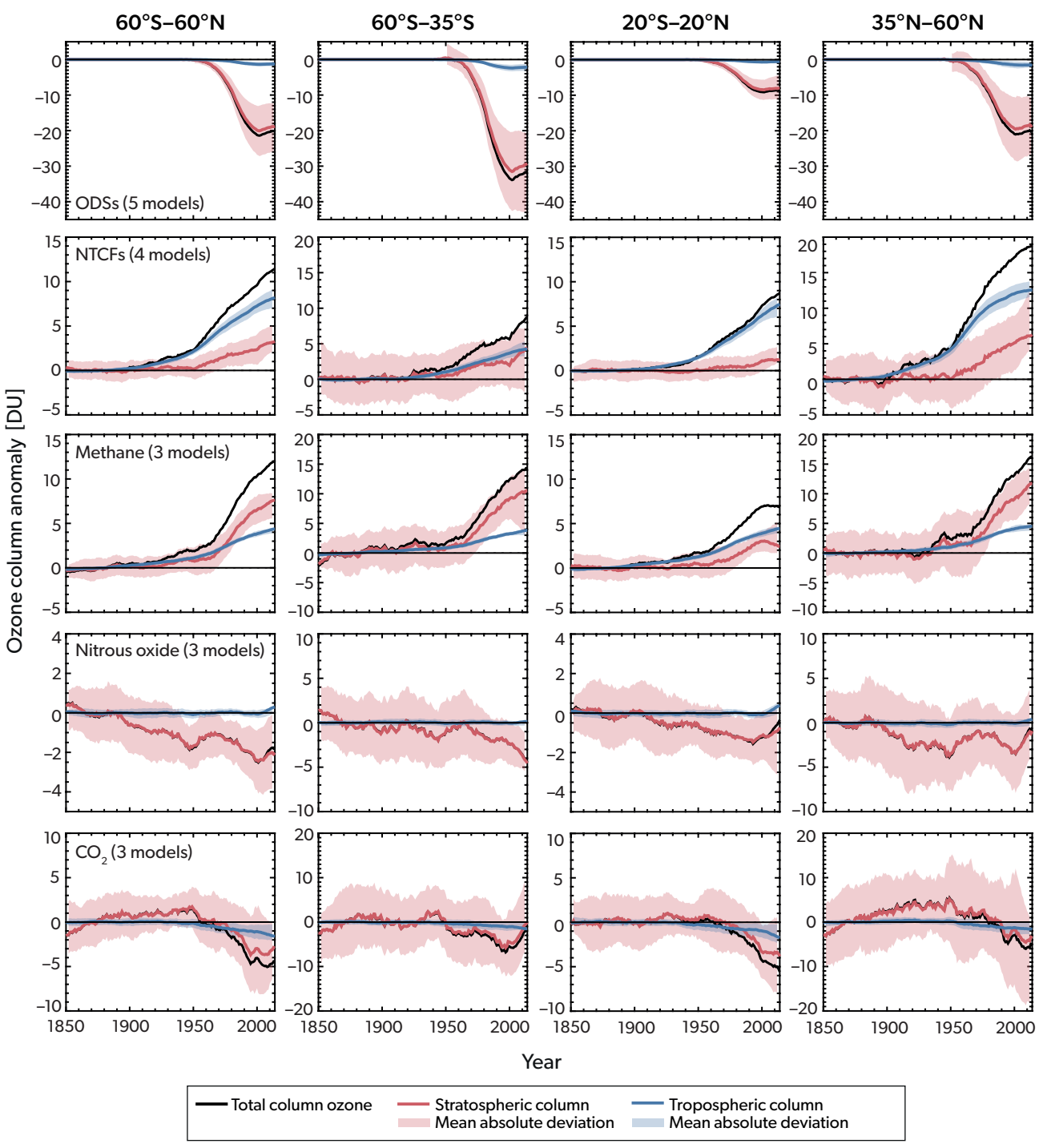

Figure 3-22. Attribution of total column (black), stratospheric column (red), and tropospheric column (blue) ozone changes to *(top to bottom)* halogenated ODSs, near-term climate forcers (NTCFs), methane (CH_4), nitrous oxide (N_2O), and carbon dioxide (CO_2), shown *(left to right)* for the near-global (60°S–60°N), SH mid-latitude (60–35°S), tropical (20°S–20°N), and NH mid-latitude (35–60°N) means. Time series are the smoothed annual mean (20-year boxcar filter) AerChemMIP multi-model mean deviation of ozone columns from their preindustrial values (1850–1900). Except for CO_2, the impact of each forcing (X) on ozone is calculated by subtracting a simulation with a forcing held fixed at the preindustrial level (histX) from one where all forcings evolve (histSST – histX; **Box 3-4**). The impact of CO_2 is derived from subtracting the sum of all single-forcing perturbations (i.e., ODSs, NTCF, CH_4, and N_2O) from the all-forcing (histSST) simulation. Shaded areas are the mean absolute deviations from the multi-model mean. The tropopause is defined by the WMO lapse rate definition. [Adapted from Zeng et al., 2022.]

in ozone and its attribution to ODSs are significant at the 95% confidence level throughout the SH mid-latitudes, a large part of the NH mid-latitudes, and above 20 hPa in the tropics. Methane (CH_4) plays a significant role in driving the positive ozone trend in the mid-latitude middle to upper stratosphere and in the tropical upper stratosphere. The combined impact of N_2O and CO_2 on ozone is predominantly negative and is significant (at the 95% confidence level) in the middle stratosphere over the NH mid-latitudes and the upper tropical stratosphere. The net impact of greenhouse gases (GHGs) on stratospheric ozone during that period is largely insignificant (at the 95% confidence level) due to the opposing effects of CH_4 versus that of CO_2 and N_2O.

Between 2000 and 2014, the ozone trends from the all-forcing simulation are largely positive and significant in the upper stratosphere, due mainly to the decline in ODSs. The individual forcings do not result in any significant trends in stratospheric ozone due to the brevity of the simulation period and a large model uncertainty. The increase in GHGs as well as declining ODSs drive the positive ozone trend in the middle to upper stratosphere (**Figure 3-23**), in agreement with the last Assessment. The trend in ozone in the middle and upper stratosphere due to CH_4 increases is negative during this period (although generally not significant at the 95% confidence level), reflecting a coupling with now decreasing ODSs.

In the lower stratosphere, the ozone trends due to all forcings and individual forcings are masked by large dynamical

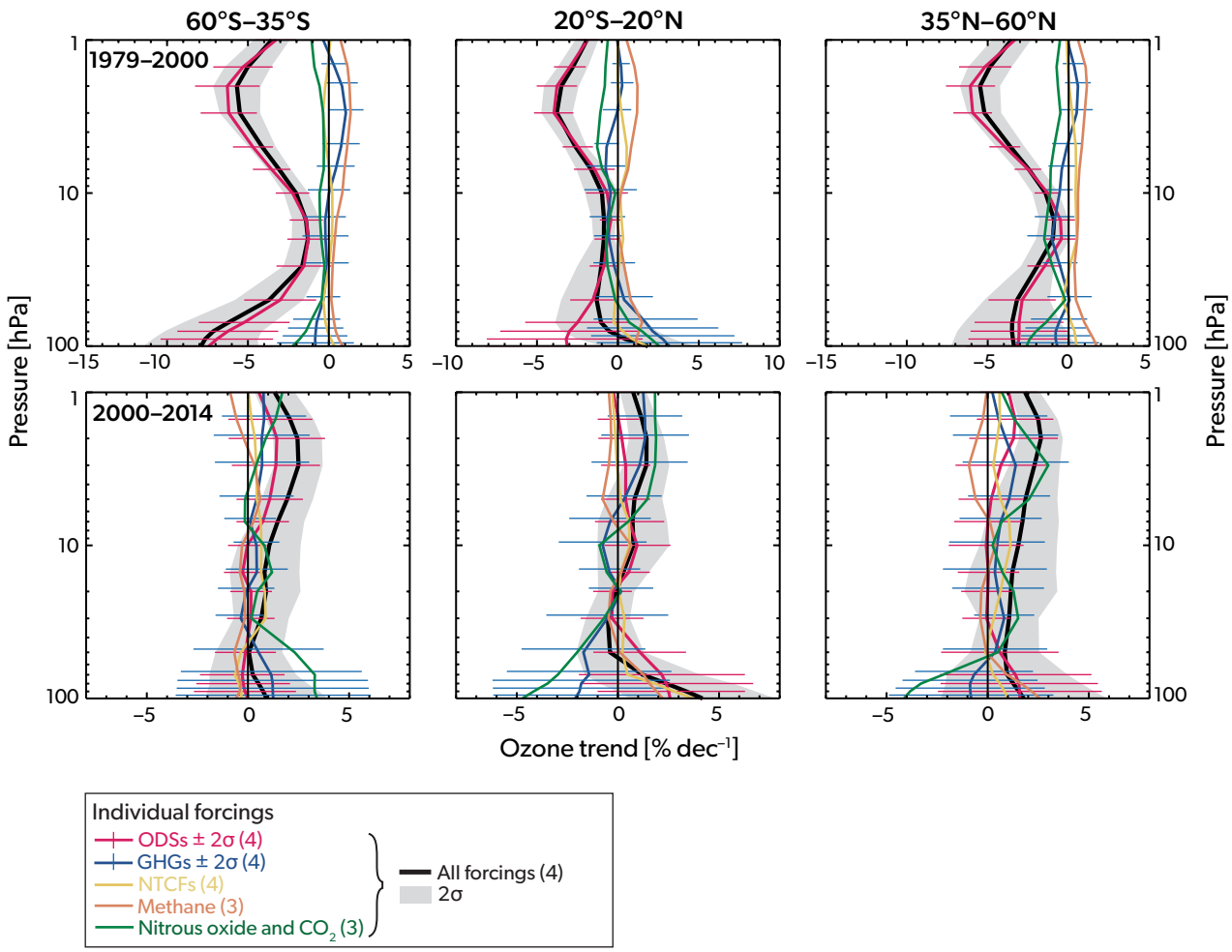

Figure 3-23. Attribution of stratospheric ozone trends along a vertical profile as a function of pressure as simulated by the AerChemMIP models, for *(left to right)* SH mid-latitudes (60–35°S), tropics (20°S–20°N), and NH mid-latitudes (35–60°N), calculated over the periods *(top panels)* 1979–1999 and *(bottom panels)* 2000–2014. The black lines show the vertically resolved trends in the multi-model mean ozone from the histSST simulation (**Box 3-4**), which includes all forcings, with the 2σ uncertainty range shaded in gray (accounting for statistical and model uncertainty). Colored lines show the contributions to the trends from ODSs (red), the combined greenhouse gases (CO_2, N_2O, and CH_4; dark blue), NTCFs (yellow), CH_4 (orange), and combined N_2O and CO_2 (green). The 2σ uncertainty ranges are indicated for ODSs and combined greenhouse gases as error bars. The impact from the combined greenhouse gases is derived by subtracting the impact from ODSs and NTCFs from the all-forcing histSST simulation. Numbers in parentheses next to the labels are the number of the models included in the ensemble. [Adapted from Zeng et al., 2022.]

variability, as was shown for the CCMI-based results presented in the last Assessment. Although the ozone trend due to all forcings here is small and insignificant, contributions from individual forcings are much larger, but there is some offsetting and cancellation between them. The increase in CO_2 drives a strengthening of the BDC (*Sections 3.3.3* and *3.4*; see also *Chapter 5*), which leads to an ozone reduction in the tropical lower stratosphere. Meanwhile, the increases in NTCFs, CH_4, and N_2O lead to lower-stratospheric ozone increases mainly through chemical processes, although this is outweighed overall by the impact of CO_2 on the circulation. Significant trends in ozone occur only in the lowermost tropical stratosphere, driven by NTCF increases over this period.

3.4 PROJECTED OZONE CHANGES

While past changes in ozone can be evaluated using a combination of observations and models, detailed projections of ozone rely on simulations performed using chemistry–climate models (CCMs). This section discusses future ozone recovery, including its impacts on the troposphere, using new simulations that have become available since the last Assessment. The ozone impact of potential future supersonic and hypersonic transport is discussed in *Section 4.3.5.3*, as this issue is most relevant for polar ozone.

3.4.1 Model Projections and Their Uncertainty

CCMs provide projections of ozone recovery under different future emissions scenarios, often as part of a coordinated, multi-model activity where the different models follow the same protocols to perform a comparable set of simulations (**Box 3-4**). As in the previous Assessment, three types of uncertainty for these future ozone projections can be considered: internal variability of the climate system (sometimes called "weather noise"); structural uncertainty from the way the models are built, with the result that different models may not respond consistently to identical inputs; and scenario uncertainty, which is the spread in simulated atmospheric composition and climate from following different scenarios. The relative importance of these uncertainties varies at different spatial and temporal scales and for different variables (Hawkins and Sutton, 2009, 2010). Analysis from an earlier model intercomparison project (Charlton-Perez et al., 2010) indicates that, compared to scenario uncertainty, internal variability and structural uncertainty are larger drivers of uncertainty in global ozone projections over the first two-thirds of this century. Typically, the spread in model results from these two uncertainties is reduced by simple averaging across ensemble members to form a multi-model mean. While this potentially reduces the uncertainty from internal variability (assuming there is no bias in that quantity), a simple unweighted mean does not account for known differences in model skill across the ensemble (e.g., Dhomse et al., 2018). Statistical methods have been demonstrated to account for variable model skill in projections of stratospheric ozone (Amos et al., 2020), but these methods have not been assessed outside the polar regions, and additional evidence is required to evaluate best practices (see also **Box 3-1**).

Scenario uncertainty is outside the control of the models and arises from the ultimately unknowable future trajectories of greenhouse gas (GHG) and pollutant emissions and the societal changes that underpin them (although there is considerable debate as to what futures are "likely"; e.g., Hausfather and Peters, 2020). Since the last Assessment, CMIP6 model simulations following a new set of future emissions scenarios, the Shared Socioeconomic Pathways (SSPs), have been run (see **Box 3-4**). All these scenarios assume future compliance with the Montreal Protocol and its Amendments and adjustments, meaning that the future emissions of controlled ozone-depleting substances (ODSs) are the same across the SSPs. At the same time, the SSPs cover a range of future changes in well-mixed GHGs (such as CO_2, N_2O, and CH_4) and near-term climate forcers (NTCFs, which include precursors to tropospheric ozone and aerosols; Gidden et al., 2019). It is well known that projections of total column ozone (TCO) are sensitive to the emissions of these species (e.g., Dhomse et al., 2018; Morgenstern et al., 2018). However, the SSPs necessarily represent only a limited number of trajectories, excluding, for instance, future unregulated emissions of ODSs banned by the Montreal Protocol (*Section 3.4.4*), future very short-lived substance (VSLS) emissions (*Section 3.3.3.2*), volcanic eruptions (*Section 3.2.1.3*), hydrogen emissions from a future where hydrogen plays a large role as an energy source (*Chapter 1*), future supersonic and hypersonic transport (*Chapter 4*), and the impacts of stratospheric climate interventions (*Chapter 6*).

Finally, there are no standard simulations targeted at understanding and characterizing the response of CCMs to idealized ODS emissions, allowing comparison between different models and between different multi-model experiments (cf. the $2\times CO_2$ simulations that form part of the so-called DECK experiments in CMIP; Meehl et al., 2014). This hampers our ability to compare projected ozone and ozone recovery metrics across different assessments, as the scenarios are refined or changed.

3.4.2 Total Column Ozone and Expected Return to 1980 Levels

The simulated evolution of 21st-century annual mean TCO strongly depends on the SSP scenario and latitude band considered (**Figure 3-18**; Keeble et al., 2021a). For scenarios with stabilizing or slightly declining GHG levels (SSP2-4.5, SSP4-3.4, and SSP4-6.0), near-global mean (60°S–60°N) TCO is projected to return to mid/late-20th century levels by the middle of the 21st century and remain at those levels until 2100. For scenarios with continued GHG increases (SSP3-7.0 and SSP5-8.5), near-global TCO is projected to return to mid/late-20th century levels sooner and significantly exceed these levels throughout the latter half of the 21st century. In contrast, despite the assumption that halogenated ODSs will continue to decline throughout this century, near-global TCO is not projected to return to mid/late-20th century levels under scenarios with the strongest GHG and NTCF mitigation (SSP1-1.9 and SSP1-2.6) due to the NTCF-driven reductions in tropospheric ozone.

A long-standing milestone on the road to ozone recovery is the year at which TCO is projected to return to 1980 values. Only the five CMIP6 models that include interactive chemistry schemes are used for the calculation of the TCO return dates discussed here, since their ozone fields are consistent with both the future emissions scenario and internal model dynamical fields. This is a relatively small number of models compared to that used in the previous Assessment, which drew on the projections from 19 models, meaning that here structural uncertainty is under sampled. On the other hand, this Assessment presents return dates for four scenarios (SSP1-2.6, SSP2-4.5, SSP3-7.0, and SSP5-8.5)

as opposed to the one from the last Assessment (RCP6.0). Each scenario assumes the same future emissions of species regulated under the Montreal Protocol and its subsequent amendments, and so any difference in return dates between scenarios is due to the impacts of other emitted species, such as GHGs and tropospheric ozone precursors.

TCO return dates are calculated following the approach used in the previous Assessment (and described in detail by Dhomse et al., 2018). In brief, the individual CMIP6 models are first bias-corrected to match the observations (in this case the NIWA-BS dataset; Bodeker et al., 2020) averaged over 1980–1984. They are then smoothed with an 11-point boxcar filter to reduce internal variability. The bias-corrected, smoothed time series for each of the five models are then averaged together to give a single multi-model mean time series for each SSP scenario. The return date is defined as the first time this multi-model mean TCO reaches an annual mean value equal to or higher than the 1980 TCO value. Uncertainty estimates for the return dates are given by the first and last times at which the ±1 standard deviation envelope (calculated from the individual model time series) crosses the 1980 TCO value. The process is illustrated in **Figure 3-24a**, which shows two hypothetical TCO projections: one where TCO recovers rapidly and exceeds the 1980 value by the end of the century (FastRecovery), and another where TCO recovers slowly and only slightly exceeds the 1980 value (SlowRecovery). Both

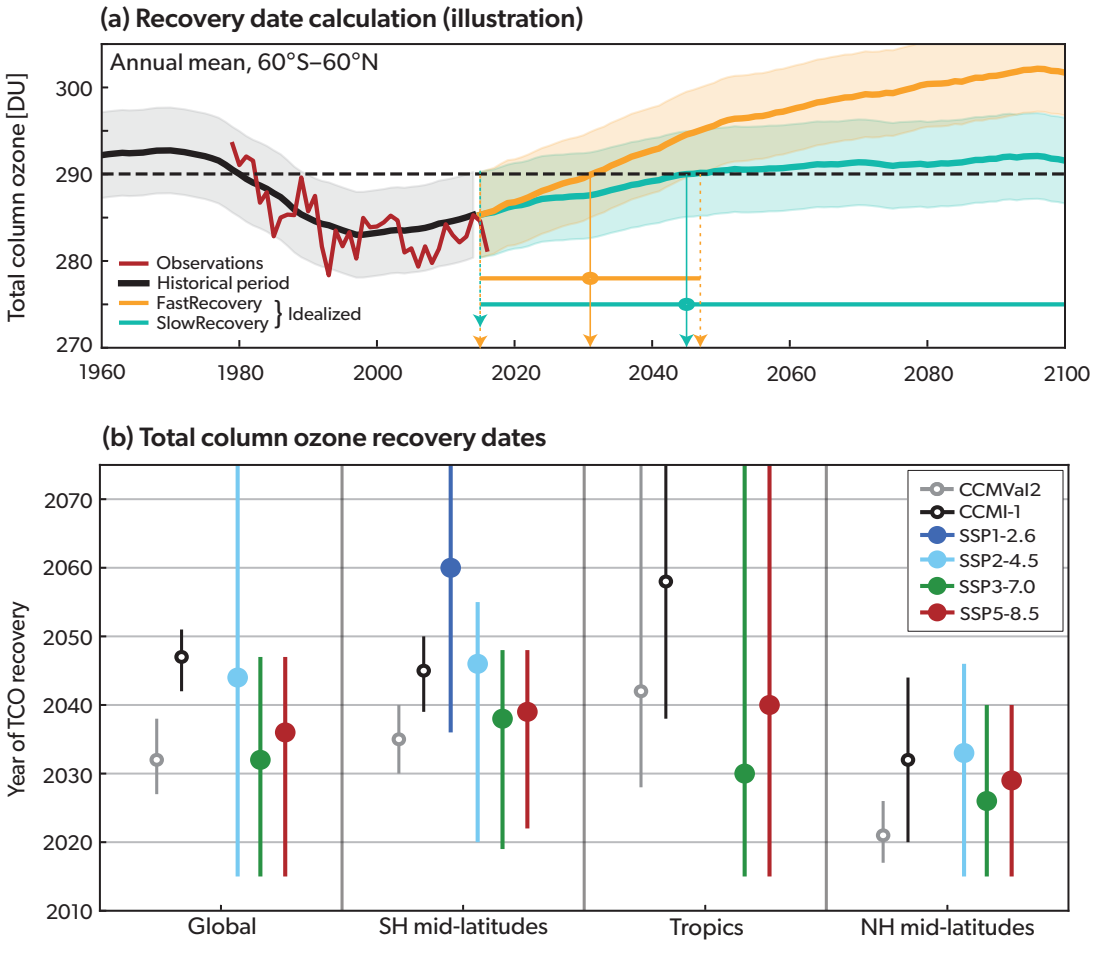

Figure 3-24. Year at which TCO recovers to its 1980 value. (a) Recovery date and error bar calculation for two different idealized scenarios of ozone recovery: FastRecovery (yellow) and SlowRecovery (green). The recovery date is when the multi-model mean (thick lines) meets the 1980 value (arrows with solid lines; 1980 value indicated by dashed black line), with the upper and lower bounds of its uncertainty corresponding to when, respectively, the top and bottom of the 1 standard deviation envelope (from the spread of the individual means; indicated by shading) also meet the 1980 value (arrows with dotted lines). (b) TCO recovery dates for different latitude bands and for four SSPs, calculated using five CMIP6 models (thicker lines, solid circles; uncertainty indicated by bars calculated as per panel [a]), as well as models from the CCMVal2 (SPARC, 2010) and CCMI-1 (Morgenstern et al., 2017) experiments (thinner lines, unfilled circles; error bars for CCMI-1 as per SSPs, whereas CCMVal-2 are the 95% confidence interval based on the individual model simulations), as shown in the previous Assessment and documented by Dhomse et al. (2018). The multi-model mean TCO does not return to its 1980 value by 2100 for the global, tropics, and NH mid-latitudes for SSP1-2.6, and for the tropics for SSP2-4.5. Global return dates are calculated using data averaged from 60°S–60°N for the CCMI-1 and SSP simulations and from 90°S–90°N for CCMVal2.

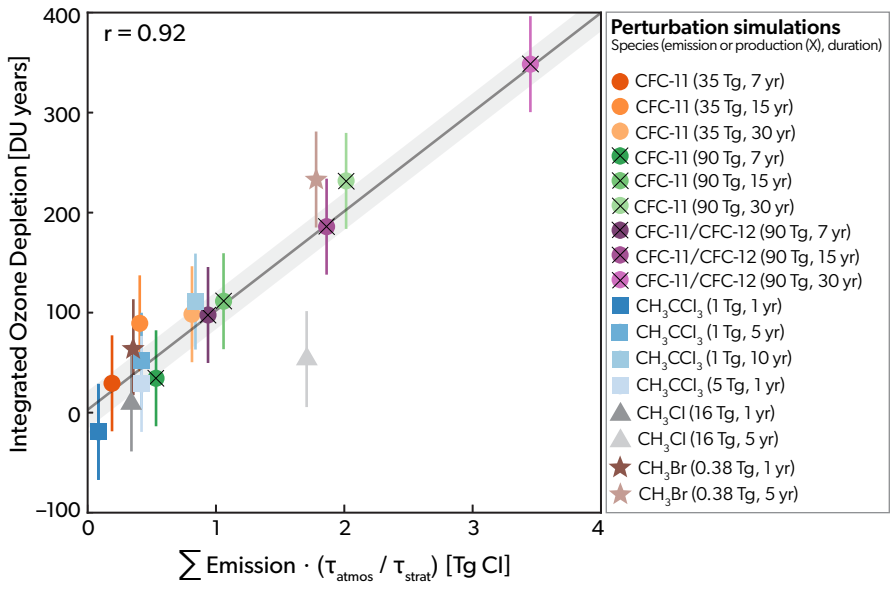

Figure 3-25. Integrated ozone depletion (IOD; units of DU years) from different CCM simulations performed with the UM-UKCA chemistry-climate model, plotted against the cumulative emissions of a halogenated source gas (quantified in units of Tg Cl) multiplied by the dimensionless ratio of the whole-atmospheric lifetime to the stratospheric lifetime of that halogenated source gas. The different colored points correspond to CCM experiments with different emitted species (different shapes), the magnitude of the annual emissions or production (with an "X"; includes a major portion that goes in banks) of that species, and the duration of the emissions. [Adapted from Pyle et al., 2022.]

have the same variance. The FastRecovery scenario clearly recovers to the 1980 value sooner than SlowRecovery and so has an earlier return date. There is also a much smaller uncertainty associated with the FastRecovery return date, despite the identical variances, since the lower bound on the projected TCO remains above the 1980 value from the late 2040s onward. In contrast, the lower bound for TCO remains below the 1980 value beyond 2100 for the SlowRecovery scenario. TCO projections that only slightly exceed the 1980 TCO value therefore have large uncertainty ranges in their return dates.

Generally, TCO return dates from CMIP6 models using the SSPs are consistent with those from previous modeling activities (**Figure 3-24b**). Under the SSP2-4.5 scenario, which assumes more modest increases in GHGs, near-global mean (60°S–60°N) TCO is projected to return to 1980s values before the middle of the century (around 2040). In contrast, under scenarios with the least mitigation for GHGs and NTCFs (SSP3-7.0 and SSP5-8.5), near-global mean TCO is projected to return to 1980 values earlier (around 2030). However, as noted above, for the scenario with the strongest mitigation (SSP1-2.6), the total column is not projected to return to 1980 values before 2100. Recovery happens for all analyzed SSPs in the SH mid-latitudes (where the levels of tropospheric ozone precursors are already low), but ozone does not return to 1980 values in the tropics for the two SSPs with the strongest (SSP1-2.6) and comparatively strong (SSP2-4.5) mitigation (**Figure 3-24b**). In addition, tropical TCO recovery for the SSP with weakest GHG mitigation (SSP5-8.5) does not last the whole century (**Figure 3-24b**), as the strengthened Brewer–Dobson circulation (BDC; see *Chapter 5*) reduces the column beyond 1980 levels after about 2070 (**Figure 3-18**). Finally, some of the return dates are associated with very large uncertainty estimates, particularly the near-global return date under the SSP2-4.5 scenario and the tropical return dates under the SSP3-7.8 and SSP5-8.5 scenarios (**Figure 3-24b**). This is because TCO remains close to the 1980 value for several decades on either side of the return date for those scenarios, and interannual variability means that it may rise above and fall below the return threshold.

While the 1980 return date has been widely used as a metric of ozone recovery in this and previous Assessments and remains an important milestone on the road to ozone recovery, it has some shortcomings. In addition to the fact that significant ozone depletion occurred before 1980 (Shepherd et al., 2014; Langematz et al., 2016), future ozone changes in some regions may be dominated by changes in other processes, such as stratospheric temperature and circulation changes following increases to GHGs or changes happening in the troposphere (**Box 3-3**). Overall, this can mean that despite reductions in stratospheric halogens, the total column never returns to historical values. Return dates also do not measure the overall integrated decrease in ozone prior to that date, which may be more relevant for some impacts (e.g., changes in surface UV). This is particularly true for short-lived halogenated ODSs (*Section 3.3.4.2*), which, owing to their short atmospheric lifetimes, may substantially deplete stratospheric ozone without affecting TCO return dates.

Recognizing these shortcomings, a new ozone recovery metric has recently been proposed to use alongside return dates: integrated ozone depletion (IOD; Pyle et al., 2022). IOD measures the time integrated TCO difference between separate future ozone projections, each following different halogen emissions scenarios. For example, a hypothetical, large, short-duration emission of a halogenated species with a short lifetime (e.g., methyl chloride [CH_3Cl] or methyl bromide [CH_3Br]) would result in substantial ozone depletion, and therefore a large IOD, but potentially no change in the return date if the additional emitted halogen is removed from the atmosphere before the total column has returned to historical values. Conversely, additional emissions of a long-lived species like CFC-11 could result in TCO reductions of a few Dobson units for several decades, which may lead to large delays in ozone return dates, but only a small IOD. Using CCM simulations, it has been shown that there is a linear relationship between IOD and the product of the time-integrated additional emissions (in Tg chlorine) of a halogenated species and the ratio of the species' whole-atmospheric lifetime to its stratospheric lifetime (**Figure 3-25**). There is scope to exploit this

empirical relationship to estimate IOD values without the need for CCM simulations, allowing simple predictions of the impact of halogenated emissions on ozone recovery.

3.4.3 Vertically Resolved Ozone Projections

Vertically resolved changes over the 21st century also depend strongly on the future scenario. Zonal-mean ozone differences between the end of the 21st century (2086–2100 average) and the present day (2000–2014 average) are shown in **Figure 3-26** for a range of SSPs (SSP1-2.6, SSP2-4.5, SSP3-7.0, and SSP5-8.5) and a subset of the CMIP6 models (after Keeble et al., 2021a). The zonal-mean picture is complemented by the future evolution of TCO and the stratosphere and troposphere partial columns (**Figure 3-27**). Ozone mixing ratios in the upper stratosphere and SH polar lower stratosphere are projected to increase for all the SSPs shown, consistent with the decline in halogenated ODSs. The upper-stratospheric increases in ozone grow in magnitude as the GHG emissions increase across the scenarios (moving from SSP1-2.6 to SSP5-8.5) due to the resulting CO_2-induced cooling of the stratosphere (e.g., Isaksen et al., 1980).

Significant differences between the scenarios are seen in the troposphere and tropical lower stratosphere. Tropospheric ozone mixing ratios decrease in the scenarios with large reductions in the emissions of ozone precursors (SSP1-2.6 and SSP2-4.5). In particular, under SSP1-2.6 the decreases in tropospheric ozone are particularly strong in the Northern Hemisphere, while the increases in stratospheric ozone outside of the Antarctic polar lower stratosphere are smaller than in other scenarios (consistent with less CO_2-induced cooling). The strong emissions mitigation in these scenarios slow or prevent the return of TCO to its historical levels (*Section 3.4.2*).

In contrast, ozone mixing ratios are projected to increase throughout much of the troposphere and upper stratosphere in the SSPs with weak or little mitigation (SSP3-7.0 and SSP5-8.5), leading to the projected super-recovery of the mid- and high-latitude TCO by the end of the century (**Figure 3-18**). However, ozone mixing ratios are projected to be lower in the tropical

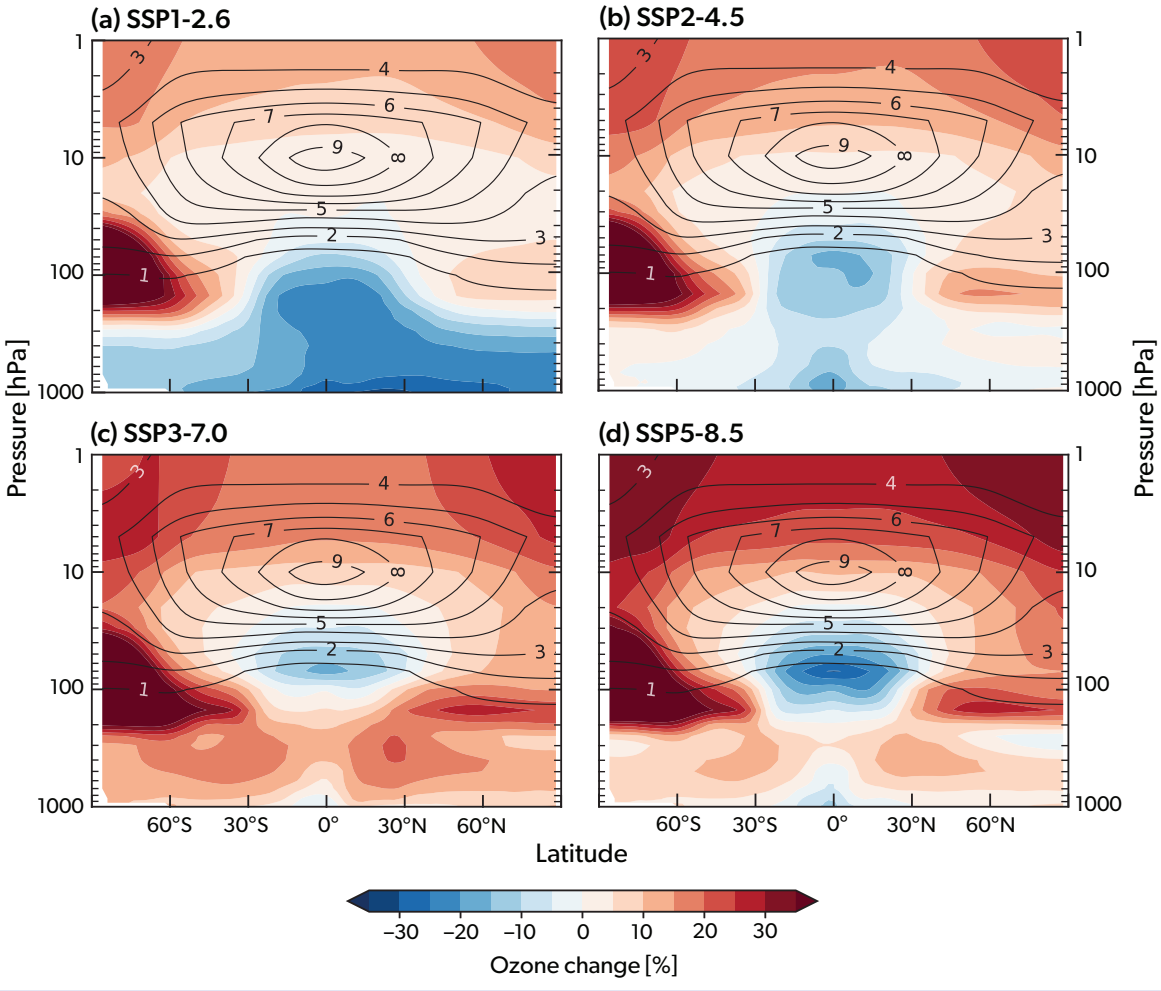

Figure 3-26. Simulated CMIP6 multi-model mean (12 models) and zonal-mean ozone changes (%) between the beginning (2000–2014 average) and end (2086–2100 average) of the 21st century. The present-day (2000–2014) zonal mean ozone climatology (as mixing ratio, in ppmv) is also shown as black contour lines. Changes are shown for the (a) SSP1-2.6, (b) SSP2-4.5, (c) SSP3-7.0, and (d) SSP5-8.5 scenarios (see **Box 3-4**). [Adapted from Keeble et al., 2021a.]

lower stratosphere by the end of the century (**Figure 3-26**) for these scenarios. As noted in the last Assessment, this is due to the acceleration of the BDC, resulting in decreases in tropical lower-stratospheric ozone and the reduced production of ozone, due to a thicker overhead column ozone (Eyring et al., 2013; Iglesias-Suarez et al., 2016; Meul et al., 2016; Keeble et al., 2017). This decrease in lower-stratospheric ozone offsets increases at higher altitudes, leading to renewed TCO decreases in the latter half of the 21st century for the SSP with the strongest GHG increases (SSP5-8.5), despite projected reductions in stratospheric halogens under the Montreal Protocol (**Figure 3-18**; *Section 3.4.2*).

3.4.4 Impacts of Unregulated CFC-11 Emissions on Ozone Recovery

Since the last Assessment, a new source of CFC-11 emissions was identified in East Asia (Montzka et al., 2018; Rigby et al., 2019; see also *Chapter 1*). Given the well-established effectiveness of chlorofluorocarbon-derived chlorine at depleting stratospheric ozone, several recent model studies have estimated the impacts of increased CFC-11 emissions on the trajectory of stratospheric ozone recovery (Dameris et al., 2019; Dhomse et al., 2019; Fleming et al., 2020, 2021; Keeble et al., 2020; WMO, 2021). In contrast to the CMIP6 simulations, which explored future ozone

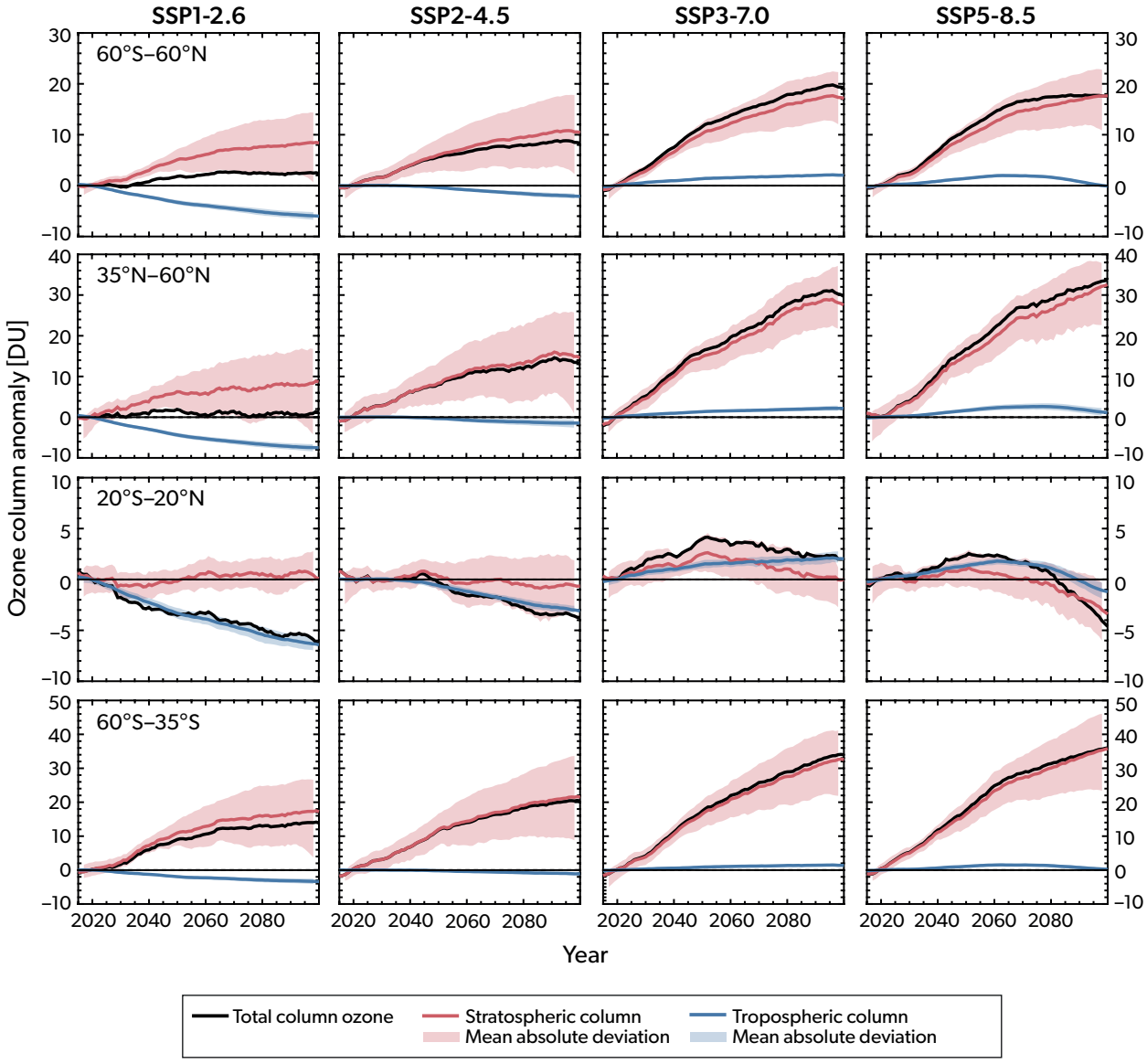

Figure 3-27. Time series of annual and CMIP6 multi-model mean anomalies (four models; relative to 2015) for TCO (black) and stratospheric (red) and tropospheric (blue) partial column ozone for the *(left to right)* SSP1-2.6, SSP2-4.5, SSP3-7.0 and SSP5-8.5 scenarios (see **Box 3-4**), shown for *(top to bottom)* the near-global mean (60°S–60°N), NH mid-latitudes (35–60°N), tropics (20°S–20°N), and SH mid-latitudes (60–35°S). Shaded areas, for the stratospheric and tropospheric ozone columns, are the mean absolute deviations from the multi-model mean. [Updated from results published by Keeble et al., 2021a.]

changes for specific emissions scenarios, there are no common scenarios that consider noncompliance with the Montreal Protocol, and, instead, individual studies followed different assumptions for CFC-11 emissions. Nevertheless, a key result that emerges from combining these studies is a linear relationship between the cumulative amount of CFC-11 emitted and metrics of stratospheric ozone recovery: global total column depletion and the delay in return dates (Keeble et al., 2020; Fleming et al., 2021; WMO, 2021). This allows an estimate of the impact of the actual emissions of CFC-11 identified through observations, even if that specific scenario has not been performed with a chemistry model.

Using the linear relationship, given the estimated additional 120–440 Gg CFC-11 emissions over the period 2012–2019 (WMO, 2021), and applying a decrease of 0.4–0.7 DU per 1000 Gg cumulative CFC-11 emissions (Keeble et al., 2020; Fleming et al., 2021), the estimated global mean total column depletion is 0.05–0.31 DU. This is supported by further simulations run from 2000 to 2017 with and without an additional 230 Gg (cumulative) CFC-11 emissions. These runs simulate the impact of the additional CFC-11 emissions specifically on polar ozone, where the response is expected to be largest, and even here the impact is small (Dhomse et al., 2019; WMO, 2021). Together, these studies indicate that the impact of increased emissions of CFC-11 to date have had a small impact on TCO, and, for instance, do not explain the recent lower-stratosphere ozone trends (see *Section 3.3.3*).

Finally, as with TCO, a linear relationship between the additional CFC-11 emissions and the delay of total ozone recovery to 1980 values can be estimated from the simulations, with the delay varying between 0.9 and 4.2 years per 1000 Gg cumulative CFC-11 emissions (**Figure 3-28**). Based on the estimated 120–440 Gg cumulative additional CFC-11 emissions for 2012–2019, the estimated delay to global ozone recovery is 0.4–1.3 years. While this further supports the fact that the additional CFC-11 emissions to date will have only a modest impact on stratospheric ozone recovery, it is clear from the linear relationships that if additional unregulated CFC-11 emissions were to continue in the future, noticeable delays to ozone return dates could result.

3.4.5 Impacts of Stratospheric Ozone Recovery on Tropospheric Ozone

Changes in the stratosphere will impact tropospheric ozone (Zeng et al., 2010) both dynamically, mainly via enhanced stratosphere-to-troposphere (STT) transport through a strengthened BDC (Butchart, 2014; *Chapter 5*), and chemically, such as through changes in photolysis rates via UV radiation changes due to changes in overhead ozone columns (Voulgarakis et al., 2013). The resulting impact on tropospheric ozone depends strongly on the scenario.

The influence of a future stratosphere on tropospheric ozone has been explored in four CMIP6 models running a weak mitigation scenario (SSP3-7.0; Griffiths et al., 2021; **Figure 3-29**). For these models, STT increases over the 21st century, consistent with the stratospheric ozone recovery (due to the reduction in ODSs) and a strengthened BDC (due to increased GHGs; **Figure 3-29**). There is, however, a large model spread in the magnitude of the STT increase. By the end of this century, STT exceeds pre-depletion levels in all models except the one that shows the strongest ozone depletion over 1980–2000 (UKESM1-LL-0). Moreover, the strongest STT increase is seen in the model that shows the weakest ozone depletion (MRI-ESM2.0). Confidence in the magnitudes of these changes in STT is low, however. STT was not directly diagnosed by the models and is instead inferred as a residual of other fields by assuming that tropospheric chemical production and the net influx from STT balances tropospheric chemical loss and dry deposition to the surface, and this is somewhat sensitive to how the tropopause is defined (Young et al., 2018; Griffiths et al., 2021).

STT has also been explored in other CCMs, giving broadly consistent results to the CMIP6 models. Since the last Assessment,

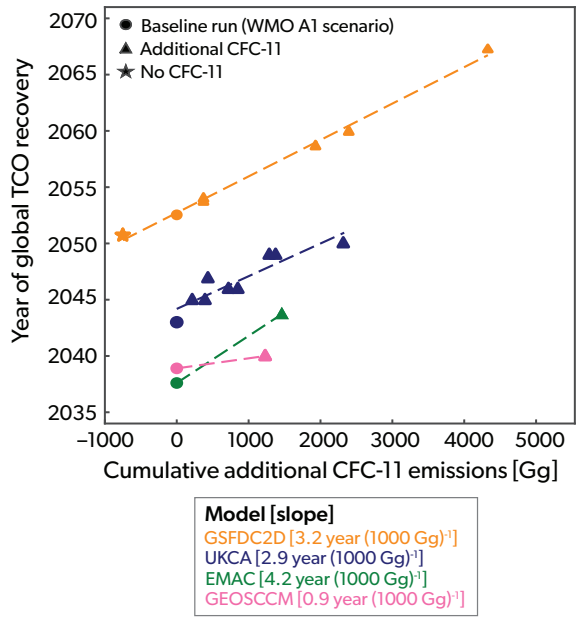

Figure 3-28. Dependence of global (90°S–90°N) annual mean TCO 1980 return dates on cumulative additional equivalent CFC-11 emissions (Gg), emitted up to the return date for each simulation, for various models. Colors represent different models and symbols represent different simulations. Each model performed a baseline simulation (circles) with the WMO A1 scenario for ODS halogen loadings (WMO, 2018). On top of this baseline scenario, the models performed perturbation simulations (stars and triangles) with different assumptions of additional CFC-11 emissions (and in some cases CFC-12, which are converted to equivalent CFC-11 emissions) shown by the x-axis. The dashed lines show the best linear fits to the simulations for each model, with the slope giving the delay in global TCO recovery in units of years per 1000 Gg. For consistent plotting, the simulated return dates for EMAC (which ignores some replacement chlorine compounds and produces early recovery) and GEOSCCM have been moved later by 20 years and 5 years, respectively. [Adapted from WMO, 2021.]

there has been further analysis of a subset of seven CCMI-1 CCMs, providing a more detailed exploration of the potential impact of future stratospheric ozone changes on the tropospheric ozone burden using a stratospheric ozone tracer (Abalos et al., 2020). This stratospheric transport tracer (O_3S) is a diagnostic that is directly related to the ozone concentration in the stratosphere, but in the troposphere its value is affected by photochemical destruction and deposition, meaning that it can be used as a marker of the fraction of tropospheric ozone that originated in the stratosphere. For the RCP6.0 scenario (which has lower emissions than the SSP3-7.0 scenario), the O_3S tropospheric column increases from the year 2000 to around 2060, consistent with stratospheric ozone recovery and an enhanced BDC, which both contribute to enhanced STT (Abalos et al., 2020; **Figure 3-30a**). The proportion of the tropospheric ozone column attributable to O_3S (i.e., ozone sourced from the stratosphere) increases monotonically in all models. However, there is a large spread in the absolute value of this proportion between the models, ranging from 22 to 45% at the start of the 21st century and 25 to 55% at the end of the century (Abalos et al., 2020; **Figure 3-30b**). In terms of attributing drivers to the STT trends, the CCMI analysis found that ODS-induced stratospheric ozone changes overwhelm the greenhouse gas effect on the BDC between 2000 and 2100 (Abalos et al., 2020). Although the decline of ODSs has been projected to weaken the BDC (Polvani et al., 2019; see also *Chapter 5*), the increased ozone reservoir in the stratosphere dominates the future ozone STT trends (Abalos et al., 2020).

The relative contributions to future STT from ODSs and GHG changes will depend on the emissions scenario, with a potentially bigger contribution from an enhanced BDC in higher GHG emissions scenarios. A single model study has projected a 53% increase in STT between 2000 and 2100 under a high emissions scenario (RCP8.5), attributing 46% of this to the effects of increasing GHGs and 7% to the effects of decreasing ODSs. This results in the ratio of O_3S to the total tropospheric ozone increasing from 43 to 46% in the Northern Hemisphere and from 48 to 52% in the Southern (Meul et al., 2018). The same single model study also explored a scenario with weak mitigation (RCP6.0) and found that the ratio of O_3S to tropospheric column ozone had a similar increase despite a smaller STT increase. This underlines that the relative impact of stratospheric ozone on tropospheric ozone depends on the evolution of tropospheric ozone under different future GHG and ozone precursor scenarios. Nevertheless, a robust result from the simulations is that a projected future increase in STT associated with higher GHG emissions will have a detectable impact on tropospheric ozone.

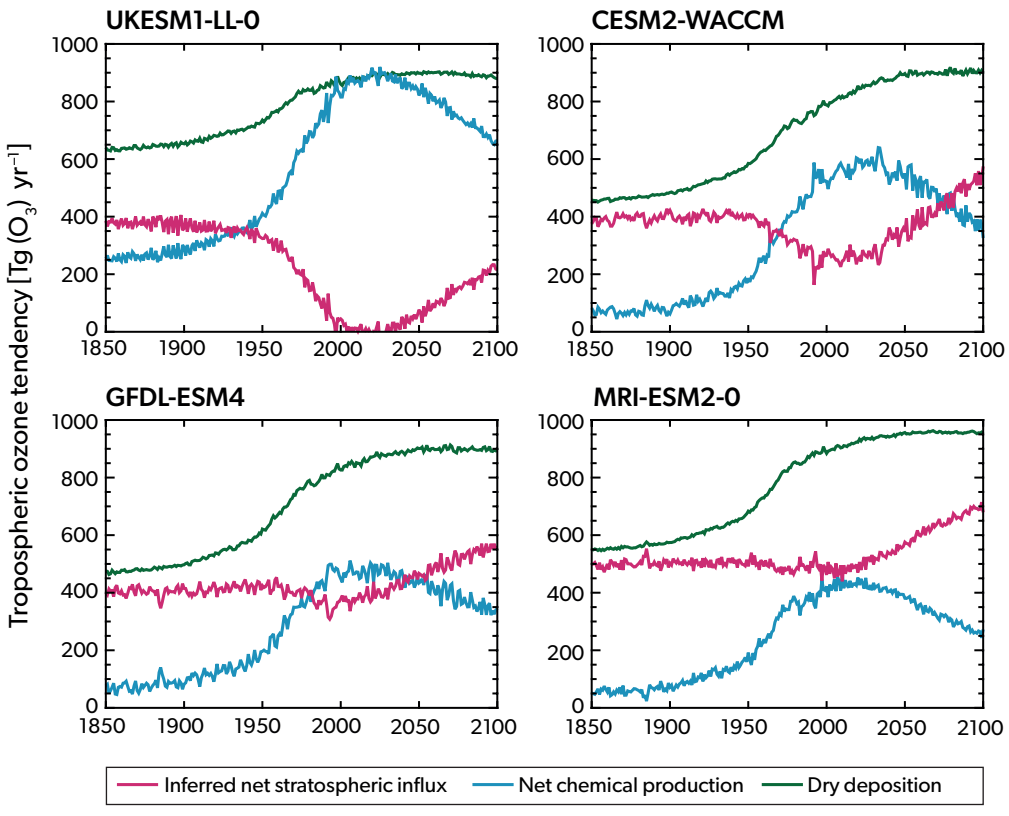

Figure 3-29. Time series of the simulated tropospheric ozone budget terms over 1850–2100 in four CMIP6 models from the historical (1850–2014) and SSP3-7.0 (2015–2100) simulations, showing dry deposition (green), net chemical production (NCP, blue), and the residual (dry deposition minus NCP, assumed to be net stratospheric influx; red). The troposphere is delimited using the WMO tropopause definition. The budget terms are shown for the four CMIP6 models with the required output: UKESM1-0-LL, CESM2-WACCM, GFDL-ESM4, and MRI-ESM2-0. [Adapted from Griffiths et al., 2021.]

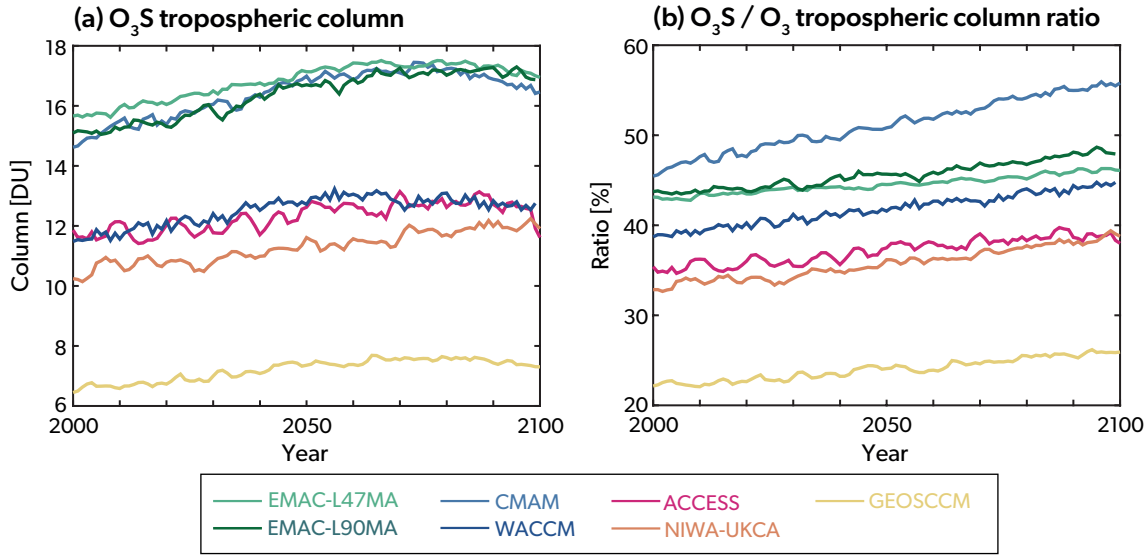

Figure 3-30. Time series for 2000–2100 of (a) the tropospheric column contribution of the stratospheric ozone tracer (O_3S) and (b) the ratio of O_3S to the global tropospheric ozone column, from the REF-C2 simulations of seven CCMs from the CCMI-1 experiment (Morgenstern et al., 2017). [Adapted from Abalos et al., 2020.]

Finally, the last Assessment noted that future changes in tropospheric ozone are likely to be dominated by changes in precursor emissions, with the stratosphere playing a relatively minor role in the increasing tropospheric ozone abundance. However, given that most tropospheric ozone precursors decrease under the new SSPs (apart from methane, which follows a range of trajectories; **Box 3-4**), STT plays an increasingly important role in tropospheric ozone changes. Indeed, recent improvements in diagnostic and modeling tools provide new evidence that the stratosphere has had a much larger influence than previously thought over the most recent climatological period (1980–2010; Williams et al., 2019). Moreover, a new accounting method proposed for the tropospheric budget also suggests an increased importance for ozone of stratospheric origin (Bates and Jacob, 2020). If these tools and methods are assessed in additional models and applied more generally, it could lead to a reappraisal of the role of the stratosphere in current and projected tropospheric ozone budgets.

APPENDIX 3A : DATA SOURCES

3A.1 PROXIES USED IN DIFFERENT PUBLISHED OZONE TREND MODELS

The proxies, parameters used for the proxies, and their data sources are listed in **Table 3A-1**.

3A.2 GROUND-BASED DATASETS

The total column ozone (TCO) and profile trends assessed in this report are based on datasets listed in **Table 3A-2** for ozone observations by ground-based techniques. Most ground-based data records have been simply extended in time since the 2018 Assessment and are archived in the WOUDC or NDACC databases. This is the case for Dobson and Brewer spectrophotometers, SAOZ spectrometers, FTIR spectrometers, microwave radiometers, lidars, balloon-borne ozonesondes, and aircraft-mounted sensors (see WMO, 2018, and references therein).

Since the last Assessment, several records have been revised to detect and correct for inhomogeneities. The four NOAA Dobson Umkehr datasets of Boulder, Lauder, Observatoire de Haute-Provence (OHP), and Mauna Loa have been optimized through a day-to-day comparison with Umkehr profiles simulated by a chemical transport model (Petropavlovskikh et al., 2022), resulting in a noticeable bias reduction compared to MLS and the combined SBUV and OMPS records.

There is a seasonal dependence to the difference between TCO measurements by Dobson and Brewer spectrophotometers that is attributed to the temperature sensitivity of the ozone absorption coefficient of the Dobson instrument (Redondas et al., 2014). The Arosa datasets have been reprocessed using a newer ozone absorption cross section (Serdyuchenko et al., 2014) in conjunction with an effective ozone temperature dataset. This has reduced the seasonal dependence of the difference to 1% (Gröbner et al., 2021). The quality of the world's longest ozone column measurements time series has been assessed, with the conclusion that any bias induced by the automatization and the relocation of the Dobson instrument is not statistically significant (Stübi et al., 2021).

Table 3A-1. Proxies used in different published ozone trend models, including representative data sources. Those used in the different trend analyses presented in *Section 3.3* are highlighted in bold text.

Proxy	Parameter	Data Sources
Solar Cycle	**10.7 cm solar radio flux**	**National Research Council Canada Dominion Radio Astrophysical Observatory: www.spaceweather.gc.ca/forecast-prevision/solar-solaire/solarflux/sx-en.php**
	30 cm solar radio flux	CNES Collecte Localisation Satellites Space Weather Services: spaceweather.cls.fr/services/radioflux/
	Core-to-wing ratio of Mg II doublet (280 nm)	**University of Bremen: www.iup.uni-bremen.de/UVSAT/Datasets/mgii**
QBO	**EOF1 and EOF2 of tropical zonal winds**	**Free University of Berlin: www.geo.fu-berlin.de/en/met/ag/strat/produkte/qbo/**
	Tropical zonal winds at 2 pressure levels (e.g., 30 and 50 hPa; 10 and 30 hPa)	**NOAA National Weather Service Climate Prediction Center: www.cpc.ncep.noaa.gov/data/indices/**
ENSO	**Multivariate ENSO index (v1 superseded by v2 from December 2018)**	**NOAA Earth System Research Laboratory: www.esrl.noaa.gov/psd/enso/mei/**
	Niño 3.4 index	NOAA National Weather Service Climate Prediction Center: www.cpc.ncep.noaa.gov/data/indices www.cpc.ncep.noaa.gov/products/precip/CWlink/MJO/enso.shtml
	Southern Oscillation index	
Aerosol	**Aerosol extinction, optical depth, and properties**	**NASA EarthData ASDC: asdc.larc.nasa.gov/project/GloSSAC/GloSSAC_2.0**
	Aerosol extinction	Chouza et al. (2020)
	Aerosol optical depth	**NASA Goddard Institute for Space Studies: data.giss.nasa.gov/modelforce/strataer (terminates in 2012)**
Other Dynamical Proxies	Brewer–Dobson circulation (BDC): eddy heat flux (EHF) at 100 hPa	NOAA National Weather Service Climate Prediction Center: www.cpc.ncep.noaa.gov/products/stratosphere/polar/polar_body.html
	North Atlantic Oscillation (NAO) index	NOAA National Weather Service Climate Prediction Center: www.cpc.ncep.noaa.gov/products/precip/CWlink/pna/nao.shtml
	Arctic Oscillation (AO) index	**NOAA National Weather Service Climate Prediction Center: www.cpc.ncep.noaa.gov/products/precip/CWlink/daily_ao_index/ao.shtml**
	Antarctic Oscillation (AAO) index	**NOAA National Weather Service Climate Prediction Center: www.cpc.ncep.noaa.gov/products/precip/CWlink/daily_ao_index/aao/aao.shtml**
	Tropopause pressure (TP)	NOAA Earth System Research Laboratory: www.esrl.noaa.gov/psd/data/gridded/data.ncep.reanalysis.tropopause.html NASA Global Modeling and Assimilation Office: disc.gsfc.nasa.gov/datasets?project=MERRA-2
	Upper BDC index (UBDC)	Ball et al. (2016)
	Indian Ocean Dipole Mode Index (IOD MI)	psl.noaa.gov/gcos_wgsp/Timeseries/DMI/

Ongoing efforts are being conducted by the ozonesonde community to quantify the uncertainties and biases of those measurements (Tarasick et al., 2021) in the framework of the ASOPOS 2.0 project (Smit and Thompson, 2021). There is also an effort to homogenize the individual ozonesonde datasets, performed either by the station scientists themselves or in the broader framework of the Tropospheric Ozone Assessment Report Phase 2 (TOAR II) project (42 of the stations have been processed [R. van Malderen, personal communication] and are used in the zonal-mean anomalies time series and trends in this Assessment; see **Table 3A-2**). However, comparisons between TCO from ECC ozonesondes and OMI and OMPS TCO show a decrease in TCO and stratospheric ozone up to 6% for one-third of the 37 stations after 2013. This decline is attributed to ozone measured by the ECC instruments, although no single property of the ozonesondes explains the findings (Stauffer et al., 2020). The post-2013 datasets of the affected sites should not be used for trend estimation and are not used in this Assessment.

The Izaña FTIR record has been reprocessed using an improved retrieval algorithm that optimizes the selection of ozone spectral micro windows and simultaneously retrieves the temperature (García et al., 2022). This enhances the precision and accuracy of the FTIR ozone total column by 0.1–0.2% and results in better agreement with coincident Brewer observations.

Since the 2018 Assessment, European ozone lidars have been evaluated in two campaigns (Wing et al., 2020, 2021), with the conclusion that there is good agreement between all ozone lidar measurements in the range of 15–41 km, with relative differences between collocated ozone profiles of less than ±10%.

3A.3 MERGED AND INDIVIDUAL SATELLITE DATASETS

3A.3.1 Total Column Ozone

Since the last ozone Assessment, TCO time series have been updated and reported as zonal-mean and global mean datasets

Table 3A-2. TCO and ozone profiles measured by ground-based techniques used in the monthly zonal-mean data considered in this Assessment. Datasets marked with an asterisk (*) have been homogenized since the last Assessment. Datasets in square brackets are sonde stations that have not been corrected for 2013 drop-off.

Instruments	Altitude Range Vertical Resolution Units	Station (Start of Data Record)		
		60–35°S	20°S–20°N	35–60°N
Ozonesonde	0–30 km ~150 m mPa	Lauder (1986), Macquarie Island (1994), Broadmeadows (1999)	*Hilo (1982), [*Samoa (1986)], *Izaña (1995), [Ascension (1998)], [*Fiji (1997)], Irene (1998), [Nairobi (1998)], [Natal (1998)], Reunion (1998), Kuala Lumpur (1998), *Paramaribo (1999), Hong Kong Observatory (2000), Hanoi (2004), [Costa Rica (2005)]	*Goose Bay (1963), *Payerne (1966), *Hohenpeißenberg (1966), *Boulder (1967), Tateno (1968), *Uccle (1969), *Edmonton (1970), [*Churchill (1973)], Lindenberg (1975), Legionowo (1979), Praha (1979), *Boulder (1991), *OHP (1991), *De Bilt (1992), Lerwick (1992), Madrid (1994), Valentia (1994), Wallops Island (1995), *Trinidad Head (1997), *Yarmouth (2003), *Kelowna/Port Hardy (2003)
Lidar	15–50 km 1–10 km number density	Lauder (1994)	Mauna Loa (1993)	OHP (1986), Hohenpeißenberg (1987), Table Mountain (1988)
Microwave Radiometer (MWR)	20–70 km 8–15 km ppm	Lauder (1992)	Mauna Loa (1995)	Bern (1994), Payerne (2000)
FTIR Spectrometer	0–50 km 8–20 km molec cm^{-2} Total column by integrating ozone profiles	Wollongong (1996), Lauder (2001)	Izaña (1999)	Jungfraujoch (2000)
Dobson and Brewer Umkehr	0–50 km 5–10 km DU	Perth (1984), *Lauder (1987)	*Mauna Loa (1984)	*Arosa/Davos (1956), *Boulder (1984), *OHP (1984), Fairbanks (1994)
Dobson Brewer SAOZ UV-VIS Filter Ozone Meters Ozonesondes	Total column ozone DU Integrated ozone profiles	worldwide (1926)		

(Weber et al., 2020, 2022). As described below, four merged and homogenized datasets are used in this report. See further details in **Table 3A-3**.

There are integrated vertical ozone profiles from two different versions of merged datasets from the series of SBUV and SBUV-2 satellite instruments and OMPS (NASA SBUV MOD v8.7 and NOAA SBUV Merge v8.7). The NASA SBUV MOD v8.7 is now a monthly mean zonal (5°) and gridded average product, including both profiles and TCO data. OMPS v2.6 data have been included since 2012 and have been intercalibrated to the SBUV series based on overlap comparisons with NOAA 19 SBUV/2 (McPeters et al., 2019).

There are two merged datasets based on the series of European satellite spectrometers (GOME, SCIAMACHY, and GOME-2A), which use different retrieval algorithms and slightly different merging approaches (University of Bremen GSG and ESA/DLR GTO datasets). The ozone retrieval algorithm (GODFIT v4) and the merging approach of the GTO dataset were improved since the last Assessment, and three more sensors were added (OMI/Aura, GOME-2/MetOp-B, and TropOMI/Sentinel-5P; Garane et al., 2018). Comparisons with adjusted MERRA-2 reanalysis data indicate a mean bias of −0.9 ± 1.5% on the monthly mean TCO (Coldewey-Egbers et al., 2020), with a change of ~2% in 2004 when OMI data are included in both GTO and MERRA-2 (Zhao et al., 2021).

3A.3.2 Profiles

Information about the zonally averaged merged datasets of ozone profiles, which are used in this Assessment, is listed in **Table 3A-4**. Since the last Assessment, these datasets have been extended until December 2020 (Froidevaux et al., 2015; Davis et al., 2016; Bourassa et al., 2018; Sofieva et al., 2017; Arosio et al., 2019; Ball et al., 2019a). Additional efforts were made to improve the consistency and stability of the SBUV datasets (Frith et al., 2017; Wild et al., 2016). Several merged datasets with a gridded structure (latitudinally and longitudinally resolved) have been the focus of recent developments (Sofieva et al., 2021; Arosio et al., 2019; Davis et al., 2016; Frith et al., 2017; **Table 3A-5**). They are the basis of the regionally and seasonally dependent trend analyses discussed in this chapter.

Several studies have compared the consistency, biases, and stability between different individual satellite ozone datasets, which are incorporated in the merged datasets used in this Assessment (Rahpoe et al., 2015; Hubert et al., 2016; Hegglin et al., 2021).

Table 3A-3. Satellite-based merged TCO datasets used in this Assessment.

Merged Dataset	Instruments and Data Version	Ozone Representataion	Latitude Coverage and Sampling	Temporal Coverage
SBUV NASA (MOD)	Nimbus 4 BUV v8.7 Nimbus 7 SBUV v8.7 NOAA 11 SBUV/2 v 8.7 NOAA 14 SBUV/2 v8.7 NOAA 16 SBUV/2 v8.7 NOAA 17 SBUV/2 v8.7 NOAA 18 SBUV/2 v8.7 NOAA 19 SBUV/2 v8.7 S-NPP OMPS NP NASA v2.8	Integrated vertical ozone profile in DU	80°S–80°N, 5° latitude bands	1970–2020
SBUV NOAA (COH)	Nimbus 7 SBUV v8.6 NOAA 11 SBUV/2 v 8.6 NOAA 14 SBUV/2 v8.6 NOAA 16 SBUV/2 v8.6 NOAA 17 SBUV/2 v8.6 NOAA 18 SBUV/2 v8.6 NOAA 19 SBUV/2 v8.6 S-NPP OMPS NP NOAA v3r2	Integrated vertical ozone profile in DU	80°S–80°N, 5° latitude bands	1978–2020
GTO	GOME/ERS-2 SCIAMACHY/Envisat GOME-2/MetOp-A OMI/Aura GOME-2/MetOp-B TropOMI/Sentinel-5P	mol m^{-2} or DU	90°S–90°N, 1° × 1°	1995–2020
GSG	GOME/ERS-2 SCIAMACHY/Envisat GOME-2/MetOp-A	mol m^{-2} or DU	90°S–90°N, 1° × 1.25°, (5° latitude bands)	1995–2020

Table 3A-4. Merged satellite vertical ozone profile datasets used in this Assessment (monthly zonal-mean data).

Merged Dataset	Instruments and Data Version	Ozone Representation	Latitude Coverage and Sampling	Vertical Range and Sampling	Temporal Coverage
SBUV NASA (MOD)	Nimbus 4 BUV v8.7 Nimbus 7 SBUV v8.7 NOAA 11 SBUV/2 v 8.7 NOAA 14 SBUV/2 v8.7 NOAA 16 SBUV/2 v8.7 NOAA 17 SBUV/2 v8.7 NOAA 18 SBUV/2 v8.7 NOAA 19 SBUV/2 v8.7 S-NPP OMPS NP NOAA v2.8	Mixing ratio on pressure levels	80°S–80°N, 5° latitude bands	15 pressure levels between 50 and 0.5 hPa	1970–2020
SBUV NOAA (COH)	Nimbus 7 SBUV v8.6 NOAA 11 SBUV/2 v 8.6 NOAA 14 SBUV/2 v8.6 NOAA 16 SBUV/2 v8.6 NOAA 17 SBUV/2 v8.6 NOAA 18 SBUV/2 v8.6 NOAA 19 SBUV/2 v8.6 S-NPP OMPS NP NASA v2.6	Mixing ratio on pressure levels	80°S–80°N, 5° latitude bands	15 pressure levels between 50 and 0.5 hPa	1978–2020
SWOOSH	SAGE II v7.0 HALOE v19 UARS MLS v5 SAGE III v4 Aura MLS v4.2	Mixing ratio on pressure levels	90°S–90°N, 10°, 5°, 2.5° latitude bands	316–1 hPa, ~3 km	1984–2020
SAGE II-CCI- OMPS	SAGE II v7 OSIRIS v5.10 MIPAS v7 SCIAMACHY UBr v3.5 GOMOS ALGOM 2s ACE-FTS v3.5/3.6 OMPS USask v1.1.0	Number density (anomalies) on altitude levels	90°S–90°N, 10° latitude bands	10–50 km, 1 km	1984–2020
SAGE II-OSIRIS-OMPS	SAGE II v7 OSIRIS v5.10 OMPS USask v1.1.0	Number density (anomalies) on altitude levels	60°S–60°N, 10° latitude bands	0–50 km, 1 km	1984–2020
SAGE II-SCIAMACHY-OMPS	SAGE II v7 SCIAMACHY UBr v3.5 OMPS UBr	Number density (anomalies) on altitude levels	90°S–90°N, 10° latitude bands	9–64 km, 3–4 km	1984–2020
$BASIC_{SG}$	SWOOSH v2.6 GOZCARDS v2.20	Mixing ratio on pressure levels	60°S–60°N, 10° latitude bands	147–1 hPa ~3 km	1985–2020

REFERENCES

Abalos, M., C. Orbe, D.E. Kinnison, D. Plummer, L.D. Oman, P. Jöckel, O. Morgenstern, R.R. Garcia, G. Zeng, K.A. Stone, and M. Dameris, Future trends in stratosphere-to-troposphere transport in CCMI models, ***Atmos. Chem. Phys.***, ***20***, 6883–6901, doi:10.5194/acp-20-6883-2020, 2020.

Adcock, K.E., P.J. Fraser, B.D. Hall, R.L. Langenfelds, G. Lee, S.A. Montzka, D.E. Oram, T. Röckmann, F. Stroh, W.T. Sturges, B. Vogel, and J.C. Laube, Aircraft based observations of ozone depleting substances in the upper troposphere and lower stratosphere in and above the Asian summer monsoon, ***J. Geophys. Res.***, ***126*** (1), doi:10.1029/2020jd033137, 2021.

Alsing, J., dlmmc: Dynamical linear model regression for atmospheric time-series analysis, ***J. Open Source Softw.***, ***4*** (37), 1157, doi:10.21105/joss.01157, 2019.

Amos, M., P.J. Young, J.S. Hosking, J.-F. Lamarque, N.L. Abraham, H. Akiyoshi, A.T. Archibald, S. Bekki, M. Deushi, P. Jöckel, D. Kinnison, O. Kirner, M. Kunze, M. Marchand, D.A. Plummer, D. Saint-Martin, K. Sudo, S. Tilmes, and Y. Yamashita, Projecting ozone hole recovery using an ensemble of chemistry–climate models weighted by model performance and independence, ***Atmos. Chem. Phys.***, ***20***, 9961–9977, doi:10.5194/acp-20-9961-2020, 2020.

Anstey, J.A., and T.G. Shepherd, High-latitude influence of the quasi-biennial oscillation, ***Quart. J. Roy. Meteor. Soc.***, ***140***, 1–21, doi:10.1002/qj.2132, 2014.

Anstey, J.A., T.P. Banyard, N. Butchart, L. Coy, P.A. Newman, S. Osprey, and C.J. Wright, Prospect of increased disruption to the QBO in a changing climate, ***Geophys. Res. Lett.***, ***48*** (15), doi:10.1029/2021gl093058, 2021.

Arosio, C., A. Rozanov, E. Malinina, K.-U. Eichmann, T. von Clarmann, and J.P. Burrows, Retrieval of ozone profiles from OMPS limb scattering observations, ***Atmos. Meas. Tech.***, ***11***, 2135–2149, doi:10.5194/amt-11-2135-2018, 2018.

Arosio, C., A. Rozanov, E. Malinina, M. Weber, and J.P. Burrows, Merging of ozone profiles from SCIAMACHY, OMPS and SAGE II observations to study stratospheric ozone changes, ***Atmos. Meas. Tech.***, ***12***, 2423–2444, doi:10.5194/amt-12-2423-2019, 2019.

Ashok, K., S.K. Behera, S.A. Rao, H. Weng, and T. Yamagata, El Niño Modoki and its possible teleconnection, ***J. Geophys. Res.***, ***112*** (C11), doi:10.1029/2006jc003798, 2007.

Austin, J., K. Tourpali, E. Rozanov, H. Akiyoshi, S. Bekki, G. Bodeker, C. Brühl, N. Butchart, M. Chipperfield, M. Deushi, V.I. Fomichev, M.A. Giorgetta, L. Gray, K. Kodera, F. Lott, E. Manzini, D. Marsh, K. Matthes, T. Nagashima, K. Shibata, R.S. Stolarski, H. Struthers, and W. Tian, Coupled chemistry climate model simulations of the solar cycle in ozone and temperature, ***J. Geophys. Res.***, ***113*** (D11), doi:10.1029/2007jd009391, 2008.

Bai, K., N.-B. Chang, R. Shi, H. Yu, and W. Gao, An intercomparison of multidecadal observational and reanalysis data sets for global total ozone trends and variability analysis, ***J. Geophys. Res.***, ***122***, 7119–7139, doi:10.1002/2016JD025835, 2017.

Baldwin, M.P., L.J. Gray, T.J. Dunkerton, K. Hamilton, P.H. Haynes, W.J. Randel, J.R. Holton, M.J. Alexander, I. Hirota, T. Horinouchi, D.B.A. Jones, J.S. Kinnersley, C. Marquardt, K. Sato, and M. Takahashi, The quasi-biennial oscillation, ***Rev. Geophys.***, ***39***, 179–229, doi:10.1029/1999rg000073, 2001.

Ball, W.T., A. Kuchař, E.V. Rozanov, J. Staehelin, F. Tummon, A.K. Smith, T. Sukhodolov, A. Stenke, L. Revell, A. Coulon, W. Schmutz, and T. Peter, An upper-branch Brewer–Dobson circulation index for attribution of stratospheric variability and improved ozone and temperature trend analysis, ***Atmos. Chem. Phys.***, ***16***, 15,485–15,500, doi:10.5194/acp-16-15485-2016, 2016.

Ball, W.T., J. Alsing, D.J. Mortlock, E.V. Rozanov, F. Tummon, and J.D. Haigh, Reconciling differences in stratospheric ozone composites, ***Atmos. Chem. Phys.***, ***17***, 12,269–12,302, doi:10.5194/acp-17-12269-2017, 2017.

Ball, W.T., J. Alsing, D.J. Mortlock, J. Staehelin, J.D. Haigh, T. Peter, F. Tummon, R. Stübi, A. Stenke, J. Anderson, A. Bourassa, S.M. Davis, D. Degenstein, S. Frith, L. Froidevaux, C. Roth, V. Sofieva, R. Wang, J. Wild, P. Yu, J.R. Ziemke, and E.V. Rozanov, Evidence for a continuous decline in lower stratospheric ozone offsetting ozone layer recovery, ***Atmos. Chem. Phys.***, ***18*** (2), 1379–1394, doi:10.5194/acp-18-1379-2018, 2018.

Ball, W.T., J. Alsing, J. Staehelin, S.M. Davis, L. Froidevaux, and T. Peter, Stratospheric ozone trends for 1985–2018: sensitivity to recent large variability, ***Atmos. Chem. Phys.***, ***19***, 12,731–12,748, doi:10.5194/acp-19-12731-2019, 2019a.

Ball, W.T., E.V. Rozanov, J. Alsing, D.R. Marsh, F. Tummon, D.J. Mortlock, D. Kinnison, and J.D. Haigh, The upper stratospheric solar cycle ozone response, ***Geophys. Res. Lett.***, ***46***, 1831–1841, doi:10.1029/2018gl081501, 2019b.

Ball, W.T., G. Chiodo, M. Abalos, J. Alsing, and A. Stenke, Inconsistencies between chemistry–climate models and observed lower stratospheric ozone trends since 1998, ***Atmos. Chem. Phys.***, ***20***, 9737–9752, doi:10.5194/acp-20-9737-2020, 2020.

Banerjee, A., J.C. Fyfe, L.M. Polvani, D. Waugh, and K.-L. Chang, A pause in Southern Hemisphere circulation trends due to the Montreal Protocol, ***Nature***, ***579***, 544–548, doi:10.1038/s41586-020-2120-4, 2020.

Barrera, J.A., R.P. Fernandez, F. Iglesias-Suarez, C.A. Cuevas, J.-F. Lamarque, and A. Saiz-Lopez, Seasonal impact of biogenic very short-lived bromocarbons on lowermost stratospheric ozone between 60° N and 60° S during the 21st century, ***Atmos. Chem. Phys.***, ***20***, 8083–8102, doi:10.5194/acp-20-8083-2020, 2020.

Bates, K.H., and D.J. Jacob, An expanded definition of the odd oxygen family for tropospheric ozone budgets: Implications for ozone lifetime and stratospheric influence, ***Geophys. Res. Lett.***, ***47***, doi:10.1029/2019gl084486, 2020.

Bencherif, H., A.M. Toihir, N. Mbatha, V. Sivakumar, D.J. du Preez, N. Bègue, and G. Coetzee, Ozone variability and trend estimates from 20-years of ground-based and satellite observations at Irene Station, South Africa, ***Atmosphere***, ***11*** (11), 1216, doi:10.3390/atmos11111216, 2020.

Bernath, P., C. Boone, and J. Crouse, Wildfire smoke destroys stratospheric ozone, ***Science***, ***375***, 1292–1295, doi:10.1126/science.abm5611, 2022.

Bernet, L., I. Boyd, G. Nedoluha, R. Querel, D. Swart, and K. Hocke, Validation and trend analysis of stratospheric ozone data from ground-based observations at Lauder, New Zealand, ***Remote Sens.***, ***13*** (1), 109, doi:10.3390/rs13010109, 2020.

Blair, G.S., P. Henrys, A. Leeson, J. Watkins, E. Eastoe, S. Jarvis, and P.J. Young, Data science of the natural environment: a research roadmap, ***Front. Environ. Sci.***, ***7***, 121, doi:10.3389/fenvs.2019.00121, 2019.

Bodeker, G.E., B. Hassler, P.J. Young, and R.W. Portmann, A vertically resolved, global, gap-free ozone database for assessing or constraining global climate model simulations, ***Earth Syst. Sci. Data***, ***5***, 31–43, doi:10.5194/essd-5-31-2013, 2013.

Bodeker, G.E., J. Nitzbon, J.S. Tradowsky, S. Kremser, A. Schwertheim, and J. Lewis, A global total column ozone climate data record, ***Earth Syst. Sci. Data***, ***13*** (8), 3885–3906, doi:10.5194/essd-2020-218, 2020.

Boleti, E., C. Hueglin, S.K. Grange, A.S.H. Prévôt, and S. Takahama, Temporal and spatial analysis of ozone concentrations in Europe based on timescale decomposition and a multi-clustering approach, ***Atmos. Chem. Phys.***, ***20***, 9051–9066, doi:10.5194/acp-20-9051-2020, 2020.

Bourassa, A.E., D.A. Degenstein, W.J. Randel, J.M. Zawodny, E. Kyrölä, C.A. McLinden, C.E. Sioris, and C.Z. Roth, Trends in stratospheric ozone derived from merged SAGE II and Odin-OSIRIS satellite observations, ***Atmos. Chem. Phys.***, ***14***, 6983–6994, doi:10.5194/acp-14-6983-2014, 2014.

Bourassa, A.E., C.Z. Roth, D.J. Zawada, L.A. Rieger, C.A. McLinden, and D.A. Degenstein, Drift-corrected Odin-OSIRIS ozone product: algorithm and updated stratospheric ozone trends, ***Atmos. Meas. Tech.***, ***11***, 489–498, doi:10.5194/amt-11-489-2018, 2018.

Bourassa, A.E., L.A. Rieger, D.J. Zawada, S. Khaykin, L.W. Thomason, and D.A. Degenstein, Satellite limb observations of unprecedented forest fire aerosol in the stratosphere, ***J. Geophys. Res.***, ***124***, 9510–9519, doi:10.1029/2019jd030607, 2019.

Braesicke, P., and J. Neu, (Lead Authors), V. Fioletev, S. Godin-Beekman, D. Hubert, I. Petropalovskikh, M. Shiotani, and B.-M. Sinnhuber, Update on Global Ozone: Past, present, and Future, Chapter 3 in ***Scientific Assessment of Ozone Depletion: 2018***, World Meteorological Organization, 78 pp., Geneva, Switzerland, 2018.

Butchart, N., The Brewer-Dobson circulation, ***Rev. Geophys.***, ***52***, 157–184, doi:10.1002/2013rg000448, 2014.

Charlton-Perez, A.J., E. Hawkins, V. Eyring, I. Cionni, G.E. Bodeker, D.E. Kinnison, H. Akiyoshi, S.M. Frith, R. Garcia, A. Gettelman, J.F. Lamarque, T. Nakamura, S. Pawson, Y. Yamashita, S. Bekki, P. Braesicke, M.P. Chipperfield, S. Dhomse, M. Marchand, E. Mancini, O. Morgenstern, G. Pitari, D. Plummer, J.A. Pyle, E. Rozanov, J. Scinocca, K. Shibata, T.G. Shepherd, W. Tian, and D.W. Waugh, The potential to narrow uncertainty in projections of stratospheric ozone over the 21st century, ***Atmos. Chem. Phys.***, ***10*** (19), 9473–9486, doi:10.5194/acp-10-9473-2010, 2010.

Chen, Z., P.K. Bhartia, R. Loughman, P. Colarco, and M. DeLand, Improvement of stratospheric aerosol extinction retrieval from OMPS/LP using a new aerosol model, ***Atmos. Meas. Tech.***, ***11***, 6495–6509, doi:10.5194/amt-11-6495-2018, 2018.

Chen, Z., P.K. Bhartia, O. Torres, G. Jaross, R. Loughman, M. DeLand, P. Colarco, R. Damadeo, and G. Taha, Evaluation of the OMPS/LP stratospheric aerosol extinction product using SAGE III/ISS observations, ***Atmos. Meas. Tech.***, ***13***, 3471–3485, doi:10.5194/amt-13-3471-2020, 2020.

Chipperfield, M.P., S. Dhomse, R. Hossaini, W. Feng, M.L. Santee, M. Weber, J.P. Burrows, J.D. Wild, D. Loyola, and M. Coldewey-Egbers, On the cause of recent variations in lower stratospheric ozone, ***Geophys. Res. Lett.***, ***45***, 5718–5726, doi:10.1029/2018gl078071, 2018.

Chouza, F., T. Leblanc, J. Barnes, M. Brewer, P. Wang, and D. Koon, Long-term (1999–2019) variability of stratospheric aerosol over Mauna Loa, Hawaii, as seen by two co-located lidars and satellite measurements, ***Atmos. Chem. Phys.***, ***20***, 6821–6839, doi:10.5194/acp-20-6821-2020, 2020.

Cisewski, M., J. Zawodny, J. Gasbarre, R. Eckman, N. Topiwala, O. Rodriguez-Alvarez, D. Cheek, and S. Hall, The stratospheric aerosol and gas experiment (SAGE III) on the International Space Station (ISS) Mission, in ***Sensors, Systems, and Next-Generation Satellites XVIII***, ***9241***, 59–65, doi:10.1117/12.2073131, 2014.

Coddington, O., J.L. Lean, P. Pilewskie, M. Snow, and D. Lindholm, A solar irradiance climate data record, ***Bull. Am. Meteorol. Soc.***, ***97***, 1265–1282, doi:10.1175/BAMS-D-14-00265.1, 2016.

Coldewey-Egbers, M., D.G. Loyola R., P. Braesicke, M. Dameris, M. van Roozendael, C. Lerot, and W. Zimmer, A new health check of the ozone layer at global and regional scales, ***Geophys. Res. Lett.***, ***41***, 4363–4372, doi:10.1002/2014gl060212, 2014.

Coldewey-Egbers, M., D.G. Loyola, G. Labow, and S.M. Frith, Comparison of GTO-ECV and adjusted MERRA-2 total ozone columns from the last 2 decades and assessment of interannual variability, ***Atmos. Meas. Tech.***, ***13***, 1633–1654, doi:10.5194/amt-13-1633-2020, 2020.

Coldewey-Egbers, M., D.G. Loyola, C. Lerot, and M. Van Roozendael, Global, regional and seasonal analysis of total ozone trends derived from the 1995–2020 GTO-ECV climate data record, ***Atmos. Chem. Phys.***, ***22*** (10), 6861–6878, doi:10.5194/acp-2021-1047, 2022.

Collins, W.J., J.-F. Lamarque, M. Schulz, O. Boucher, V. Eyring, M.I. Hegglin, A. Maycock, G. Myhre, M. Prather, D. Shindell, and S.J. Smith, AerChemMIP: Quantifying the effects of chemistry and aerosols in CMIP6, ***Geosci. Model Dev.***, ***10***, 585–607, doi:10.5194/gmd-10-585-2017, 2017.

Coy, L., P.A. Newman, S. Pawson, and L.R. Lait, Dynamics of the disrupted 2015/16 Quasi-Biennial Oscillation , ***J. Clim.***, ***30***, 5661–5674, doi:10.1175/JCLI-D-16-0663.1, 2017.

Damadeo, R.P., J.M. Zawodny, and L.W. Thomason, Reevaluation of stratospheric ozone trends from SAGE II data using a simultaneous temporal and spatial analysis, ***Atmos. Chem. Phys.***, ***14***, 13,455–13,470, doi:10.5194/acp-14-13455-2014, 2014.

Dameris, M., P. Jöckel, and M. Nützel, Possible implications of enhanced chlorofluorocarbon-11 concentrations on ozone, ***Atmos. Chem. Phys.***, ***19***, 13,759–13,771, doi:10.5194/acp-19-13759-2019, 2019.

Davis, S.M., K.H. Rosenlof, B. Hassler, D.F. Hurst, W.G. Read, H. Vömel, H. Selkirk, M. Fujiwara, and R. Damadeo, The Stratospheric Water and Ozone Satellite Homogenized (SWOOSH) database: a long-term database for climate studies, ***Earth Syst. Sci. Data***, ***8***, 461–490, doi:10.5194/essd-8-461-2016, 2016.

Davis, S.M., M.I. Hegglin, M. Fujiwara, R. Dragani, Y. Harada, C. Kobayashi, C. Long, G.L. Manney, E.R. Nash, G.L. Potter, S. Tegtmeier, T. Wang, K. Wargan, and J.S. Wright, Assessment of upper tropospheric and stratospheric water vapor and ozone in reanalyses as part of S-RIP, ***Atmos. Chem. Phys.***, ***17***, 12,743–12,778, doi:10.5194/acp-17-12743-2017, 2017.

Davis, S.M., and M.I. Hegglin (Lead Authors), R. Dragani, M. Fujiwara, Y. Harada, C. Kobayashi, C. Long, G.L. Manney, E.R. Nash, G.L. Potter, S. Tegtmeier, T. Wang, K. Wargan, and J.S. Wright, Overview of ozone and water vapour, in ***SPARC Reanalysis Intercomparison Project (S-RIP) Final Report***, edited by M. Fujiwara, G.L.M.L. Gray, and J.S. Wright, SPARC Report No. 10, WCRP-6/2021, 121–162, doi:10.17874/800dee57d13, 2021.

Dhomse, S., M. Weber, I. Wohltmann, M. Rex, and J.P. Burrows, On the possible causes of recent increases in northern hemispheric total ozone from a statistical analysis of satellite data from 1979 to 2003, ***Atmos. Chem. Phys.***, ***6***, 1165–1180, doi:10.5194/acp-6-1165-2006, 2006.

Dhomse, S.S., M.P. Chipperfield, R.P. Damadeo, J.M. Zawodny, W.T. Ball, W. Feng, R. Hossaini, G.W. Mann, and J.D. Haigh, On the ambiguous nature of the 11 year solar cycle signal in upper stratospheric ozone, ***Geophys. Res. Lett.***, ***43***, 7241–7249, doi:10.1002/2016gl069958, 2016.

Dhomse, S.S., D. Kinnison, M.P. Chipperfield, R.J. Salawitch, I. Cionni, M.I. Hegglin, N.L. Abraham, H. Akiyoshi, A.T. Archibald, E.M. Bednarz, S. Bekki, P. Braesicke, N. Butchart, M. Dameris, M. Deushi, S. Frith, S.C. Hardiman, B. Hassler, L.W. Horowitz, R.-M. Hu, P. Jöckel, B. Josse, O. Kirner, S. Kremser, U. Langematz, J. Lewis, M. Marchand, M. Lin, E. Mancini, V. Marécal, M. Michou, O. Morgenstern, F.M. O'Connor, L. Oman, G. Pitari, D.A. Plummer, J.A. Pyle, L.E. Revell, E. Rozanov, R. Schofield, A. Stenke, K. Stone, K. Sudo, S. Tilmes, D. Visioni, Y. Yamashita, and G. Zeng, Estimates of ozone return dates from Chemistry-Climate Model Initiative simulations, ***Atmos. Chem. Phys.***, ***18***, 8409–8438, doi:10.5194/acp-18-8409-2018, 2018.

Dhomse, S.S., W. Feng, S.A. Montzka, R. Hossaini, J. Keeble, J.A. Pyle, J.S. Daniel, and M.P. Chipperfield, Delay in recovery of the Antarctic ozone hole from unexpected CFC-11 emissions, ***Nat. Commun.***, ***10***, 5781, doi:10.1038/s41467-019-13717-x, 2019.

Dhomse, S.S., C. Arosio, W. Feng, A. Rozanov, M. Weber, and M.P. Chipperfield, ML-TOMCAT: machine-learning-based satellite-corrected global stratospheric ozone profile data set from a chemical transport model, ***Earth Syst. Sci. Data***, ***13***, 5711–5729, doi:10.5194/essd-13-5711-2021, 2021.

Dhomse, S.S., M.P. Chipperfield, W. Feng, R. Hossaini, G.W. Mann, M.L. Santee, and M. Weber, A single-peak-structured solar cycle signal in stratospheric ozone based on Microwave Limb Sounder observations and model simulations, ***Atmos. Chem. Phys.***, ***22***, 903–916, doi:10.5194/acp-22-903-2022, 2022.

Dietmüller, S., H. Garny, R. Eichinger, and W.T. Ball, Analysis of recent lower-stratospheric ozone trends in chemistry climate models, ***Atmos. Chem. Phys.***, ***21***, 6811–6837, doi:10.5194/acp-21-6811-2021, 2021.

Domeisen, D.I.V., C.I. Garfinkel, and A.H. Butler, The teleconnection of El Niño southern oscillation to the stratosphere, ***Rev. Geophys.***, ***57*** (1), 5–47, doi:10.1029/2018rg000596, 2019.

Dudok de Wit, T., S. Bruinsma, and K. Shibasaki, Synoptic radio observations as proxies for upper atmosphere modelling, ***J. Space Weather Space Clim.***, ***4***, A06, doi:10.1051/swsc/2014003, 2014.

Dudok de Wit, T., and S. Bruinsma, The 30 cm radio flux as a solar proxy for thermosphere density modelling, ***J. Space Weather Space Clim.***, ***7***, A9, doi:10.1051/swsc/2017008, 2017.

Ermakova, T.S., O.G. Aniskina, I.A. Statnaia, M.A. Motsakov, and A.I. Pogoreltsev, Simulation of the ENSO influence on the extra-tropical middle atmosphere, ***Earth Planets Space***, ***71*** (1), 1–9, doi:10.1186/s40623-019-0987-9, 2019.

Errera, Q., S. Chabrillat, Y. Christophe, J. Debosscher, D. Hubert, W. Lahoz, M.L. Santee, M. Shiotani, S. Skachko, T. von Clarmann, and K. Walker, Technical note: Reanalysis of Aura MLS chemical observations, ***Atmos. Chem. Phys.***, ***19***, 13,647–13,679, doi:10.5194/acp-19-13647-2019, 2019.

Eyring, V., I. Cionni, G.E. Bodeker, A.J. Charlton-Perez, D.E. Kinnison, J.F. Scinocca, D.W. Waugh, H. Akiyoshi, S. Bekki, M.P. Chipperfield, M. Dameris, S. Dhomse, S.M. Frith, H. Garny, A. Gettelman, A. Kubin, U. Langematz, E. Mancini, M. Marchand, T. Nakamura, L.D. Oman, S. Pawson, G. Pitari, D.A. Plummer, E. Rozanov, T.G. Shepherd, K. Shibata, W. Tian, P. Braesicke, S.C. Hardiman, J.F. Lamarque, O. Morgenstern, J.A. Pyle, D. Smale, and Y. Yamashita, Multi-model assessment of stratospheric ozone return dates and ozone recovery in CCMVal-2 models, ***Atmos. Chem. Phys.***, ***10***, 9451–9472, doi:10.5194/acp-10-9451-2010, 2010.

Eyring, V., J.M. Arblaster, I. Cionni, J. Sedláček, J. Perlwitz, P.J. Young, S. Bekki, D. Bergmann, P. Cameron-Smith, W.J. Collins, G. Faluvegi, K.D. Gottschaldt, L.W. Horowitz, D.E. Kinnison, J.F. Lamarque, D.R. Marsh, D. Saint-Martin, D.T. Shindell, K. Sudo, S. Szopa, and S. Watanabe, Long-term ozone changes and associated climate impacts in CMIP5 simulations, ***J. Geophys. Res.***, ***108***, 5029–5060, doi:10.1002/jgrd.50316, 2013.

Eyring, V., S. Bony, G.A. Meehl, C.A. Senior, B. Stevens, R.J. Stouffer, and K.E. Taylor, Overview of the Coupled Model Intercomparison Project Phase 6 (CMIP6) experimental design and organization, ***Geosci. Model Dev.***, ***9*** (5), 1937–1958, doi:10.5194/gmd-9-1937-2016, 2016.

Fleming, E.L., P.A. Newman, Q. Liang, and J.S. Daniel, The impact of continuing CFC-11 emissions on stratospheric ozone, ***J. Geophys. Res.***, ***125*** (3), doi:10.1029/2019jd031849, 2020.

Fleming, E.L., Q. Liang, L.D. Oman, P.A. Newman, F. Li, and M.M. Hurwitz, Stratospheric impacts of continuing CFC 11 emissions simulated in a chemistry climate model, ***J. Geophys. Res.***, ***126*** (9), doi:10.1029/2020jd033656, 2021.

Flemming, J., A. Benedetti, A. Inness, R.J. Engelen, L. Jones, V. Huijnen, S. Remy, M. Parrington, M. Suttie, A. Bozzo, V.-H. Peuch, D. Akritidis, and E. Katragkou, The CAMS interim reanalysis of carbon monoxide, ozone and aerosol for 2003–2015, ***Atmos. Chem. Phys.***, ***17***, 1945–1983, doi:10.5194/acp-17-1945-2017, 2017.

Frith, S.M., R.S. Stolarski, N.A. Kramarova, and R.D. McPeters, Estimating uncertainties in the SBUV Version 8.6 merged profile ozone data set, ***Atmos. Chem. Phys.***, ***17***, 14,695–14,707, doi:10.5194/acp-17-14695-2017, 2017.

Froidevaux, L., J. Anderson, H.-J. Wang, R.A. Fuller, M.J. Schwartz, M.L. Santee, N.J. Livesey, H.C. Pumphrey, P.F. Bernath, J.M. Russell III, and M.P. McCormick, Global OZone chemistry and related trace gas data records for the stratosphere (GOZCARDS): Methodology and sample results with a focus on HCl, H2O, and O3, ***Atmos. Chem. Phys.***, ***15*** (18), 10,471–10,507, doi:10.5194/acp-15-10471-2015, 2015.

Galytska, E., A. Rozanov, M.P. Chipperfield, S.S. Dhomse, M. Weber, C. Arosio, W. Feng, and J.P. Burrows, Dynamically controlled ozone decline in the tropical mid-stratosphere observed by SCIAMACHY, ***Atmos. Chem. Phys.***, ***19***, 767–783, doi:10.5194/acp-19-767-2019, 2019.

Garane, K., C. Lerot, M. Coldewey-Egbers, T. Verhoelst, M.E. Koukouli, I. Zyrichidou, D.S. Balis, T. Danckaert, F. Goutail, J. Granville, D. Hubert, A. Keppens, J.-C. Lambert, D. Loyola, J.-P. Pommereau, M. Van Roozendael, and C. Zehner, Quality assessment of the Ozone_cci Climate Research Data Package (release 2017) – Part 1: Ground-based validation of total ozone column data products, ***Atmos. Meas. Tech.***, ***11***, 1385–1402, doi:10.5194/amt-11-1385-2018, 2018.

García, O.E., E. Sanromá, M. Schneider, F. Hase, S.F. León-Luis, T. Blumenstock, E. Sepúlveda, A. Redondas, V. Carreño, C. Torres, and N. Prats, Improved ozone monitoring by ground-based FTIR spectrometry, ***Atmos. Meas. Tech.***, ***15***, 2557–2577, doi:10.5194/amt-15-2557-2022, 2022.

Garfinkel, C.I., D.W. Waugh, L.D. Oman, L. Wang, and M.M. Hurwitz, Temperature trends in the tropical upper troposphere and lower stratosphere: Connections with sea surface temperatures and implications for water vapor and ozone, ***J. Geophys. Res.***, ***118***, 9658–9672, doi:10.1002/jgrd.50772, 2013.

Gaudel, A., O.R. Cooper, G. Ancellet, B. Barret, A. Boynard, J.P. Burrows, C. Clerbaux, P.-F. Coheur, J. Cuesta, E. Cuevas, S. Doniki, G. Dufour, F. Ebojie, G. Foret, O. Garcia, M.J. Granados-Muñoz, J.W. Hannigan, F. Hase, B. Hassler, G. Huang, D. Hurtmans, D. Jaffe, N. Jones, P. Kalabokas, B. Kerridge, S. Kulawik, B. Latter, T. Leblanc, E. Le Flochmoën, W. Lin, J. Liu, X. Liu, E. Mahieu, A. McClure-Begley, J.L. Neu, M. Osman, M. Palm, H. Petetin, I. Petropavlovskikh, R. Querel, N. Rahpoe, A. Rozanov, M.G. Schultz, J. Schwab, R. Siddans, D. Smale, M. Steinbacher, H. Tanimoto, D.W. Tarasick, V. Thouret, A.M. Thompson, T. Trickl, E. Weatherhead, C. Wespes, H.M. Worden, C. Vigouroux, X. Xu, G. Zeng, and J. Ziemke, Tropospheric Ozone Assessment Report: Present-day distribution and trends of tropospheric ozone relevant to climate and global atmospheric chemistry model evaluation, ***Elementa (Wash., DC)***, ***6***, 39, doi:10.1525/elementa.291, 2018.

Gaudel, A., O.R. Cooper, K.-L. Chang, I. Bourgeois, J.R. Ziemke, S.A. Strode, L.D. Oman, P. Sellitto, P. Nédélec, R. Blot, V. Thouret, and C. Granier, Aircraft observations since the 1990s reveal increases of tropospheric ozone at multiple locations across the Northern Hemisphere, ***Sci. Adv.***, ***6*** (34), doi:10.1126/sciadv.aba8272, 2020.

Gidden, M.J., K. Riahi, S.J. Smith, S. Fujimori, G. Luderer, E. Kriegler, D.P. van Vuuren, M. van den Berg, L. Feng, D. Klein, K. Calvin, J.C. Doelman, S. Frank, O. Fricko, M. Harmsen, T. Hasegawa, P. Havlik, J. Hilaire, R. Hoesly, J. Horing, A. Popp, E. Stehfest, and K. Takahashi, Global emissions pathways under different socioeconomic scenarios for use in CMIP6: a dataset of harmonized emissions trajectories through the end of the century, ***Geosci. Model Dev.***, ***12***, 1443–1475, doi:10.5194/gmd-12-1443-2019, 2019.

Godin-Beekmann, S., N. Azouz, V. Sofieva, D. Hubert, I. Petropavlovskikh, P. Effertz, G. Ancellet, D. Degenstein, D. Zawada, L. Froidevaux, S. Frith, J. Wild, S. Davis, W. Steinbrecht, T. Leblanc, R. Querel, K. Tourpali, R. Damadeo, E. Maillard-Barras, R. Stübi, C. Vigouroux, C. Arosio, G. Nedoluha, I. Boyd, and R. van Malderen, Updated trends of the stratospheric ozone vertical distribution in the 60° S–60° N latitude range based on the LOTUS regression model, ***Atmos. Chem. Phys. Discuss.***, 1–28, doi:10.5194/acp-2022-137, 2022.

Griffiths, P.T., L.T. Murray, G. Zeng, Y.M. Shin, N.L. Abraham, A.T. Archibald, M. Deushi, L.K. Emmons, I.E. Galbally, B. Hassler, L.W. Horowitz, J. Keeble, J. Liu, O. Moeini, V. Naik, F.M. O'Connor, N. Oshima, D. Tarasick, S. Tilmes, S.T. Turnock, O. Wild, P.J. Young, and P. Zanis, Tropospheric ozone in CMIP6 simulations, ***Atmos. Chem. Phys.***, ***21***, 4187–4218, doi:10.5194/acp-21-4187-2021, 2021.

Gröbner, J., H. Schill, L. Egli, and R. Stübi, Consistency of total column ozone measurements between the Brewer and Dobson spectroradiometers of the LKO Arosa and PMOD/WRC Davos, ***Atmos. Meas. Tech.***, ***14***, 3319–3331, doi:10.5194/amt-14-3319-2021, 2021.

Haigh, J.D., The role of stratospheric ozone in modulating the solar radiative forcing of climate, ***Nature***, ***370***, 544–546, doi:10.1038/370544a0, 1994.

Harder, J.W., J.M. Fontenla, P. Pilewskie, E.C. Richard, and T.N. Woods, Trends in solar spectral irradiance variability in the visible and infrared, ***Geophys. Res. Lett.***, ***36*** (7), doi:10.1029/2008gl036797, 2009.

Hausfather, Z., and G.P. Peters, Emissions – the "business as usual" story is misleading, ***Nature***, ***577***, 618–620, doi:10.1038/d41586-020-00177-3, 2020.

Hawkins, E., and R. Sutton, The potential to narrow uncertainty in regional climate predictions, ***Bull. Am. Meteorol. Soc.***, ***90*** (8), 1095–1108, doi:10.1175/2009BAMS2607.1, 2009.

Hawkins, E., and R. Sutton, The potential to narrow uncertainty in projections of regional precipitation change, ***Clim. Dyn.***, ***37***, 407–418, doi:10.1007/s00382-010-0810-6, 2010.

Hegglin, M.I., S. Tegtmeier, J. Anderson, A.E. Bourassa, S. Brohede, D. Degenstein, L. Froidevaux, B. Funke, J. Gille, Y. Kasai, E.T. Kyrölä, J. Lumpe, D. Murtagh, J.L. Neu, K. Pérot, E.E. Remsberg, A. Rozanov, M. Toohey, J. Urban, T. von Clarmann, K.A. Walker, H.-J. Wang, C. Arosio, R. Damadeo, R.A. Fuller, G. Lingenfelser,, C. McLinden, D. Pendlebury, C. Roth, N.J. Ryan, C. Sioris, L. Smith, and K. Weigel, Overview and update of the SPARC Data Initiative: comparison of stratospheric composition measurements from satellite limb sounders, ***Earth Syst. Sci. Data***, ***13***, 1855–1903, doi:10.5194/essd-13-1855-2021, 2021.

Henley, B.J., J. Gergis, D.J. Karoly, S. Power, J. Kennedy, and C.K. Folland, A tripole index for the interdecadal Pacific oscillation, ***Clim. Dyn.***, ***45***, 3077–3090, doi:10.1007/s00382-015-2525-1, 2015.

Hersbach, H., B. Bell, P. Berrisford, S. Hirahara, A. Horányi, J. Muñoz-Sabater, J. Nicolas, C. Peubey, R. Radu, D. Schepers, A. Simmons, C. Soci, S. Abdalla, X. Abellan, G. Balsamo, P. Bechtold, G. Biavati, J. Bidlot, M. Bonavita, G. Chiara, P. Dahlgren, D. Dee, M. Diamantakis, R. Dragani, J. Flemming, R. Forbes, M. Fuentes, A. Geer, L. Haimberger, S. Healy, R.J. Hogan, E. Hólm, M. Janisková, S. Keeley, P, Laloyaux, P. Lopez, C. Lupu, G. Radnoti, P. Rosnay, I. Rozum, F. Vamborg, S. Villaume, and J.-N. Thépaut, The ERA5 global reanalysis, ***Quart. J. Roy. Meteor. Soc.***, ***146***, 1999–2049, doi:10.1002/qj.3803, 2020.

Hood, L.L., and B.E. Soukharev, Quasi-decadal variability of the tropical lower stratosphere: The role of extratropical wave forcing, ***J. Atmos. Sci.***, ***60***, 2389–2403, doi:10.1175/1520-0469(2003)060<2389:QVOTTL>2.0.CO;2, 2003.

Hossaini, R., M.P. Chipperfield, S.A. Montzka, A. Rap, S. Dhomse, and W. Feng, Efficiency of short-lived halogens at influencing climate through depletion of stratospheric ozone, ***Nat. Geosci.***, ***8***, 186–190, doi:10.1038/ngeo2363, 2015.

Hossaini, R., E. Atlas, S.S. Dhomse, M.P. Chipperfield, P.F. Bernath, A.M. Fernando, J. Mühle, A.A. Leeson, S.A. Montzka, W. Feng, J.J. Harrison, P. Krummel, M.K. Vollmer, S. Reimann, S. O'Doherty, D. Young, M. Maione, J. Arduini, and C.R. Lunder, Recent trends in stratospheric chlorine from very short lived substances, ***J. Geophys. Res.***, ***124***, 2318–2335, doi:10.1029/2018JD029400, 2019.

Hu, Z.-Z., M.J. McPhaden, A. Kumar, J.-Y. Yu, and N.C. Johnson, Uncoupled El Niño warming, ***Geophys. Res. Lett.***, ***47*** (7), doi:10.1029/2020gl087621, 2020.

Huang, B., P.W. Thorne, V.F. Banzon, T. Boyer, G. Chepurin, J.H. Lawrimore, M.J. Menne, T.M. Smith, R.S. Vose, and H.-M. Zhang, Extended reconstructed sea surface temperature, version 5 (ERSSTv5): upgrades, validations, and intercomparisons, ***J. Clim.***, ***30***, 8179–8205, doi:10.1175/JCLI-D-16-0836.1, 2017.

Hubert, D., J.-C. Lambert, T. Verhoelst, J. Granville, A. Keppens, J.-L. Baray, A.E. Bourassa, U. Cortesi, D.A. Degenstein, L. Froidevaux, S. Godin-Beekmann, K.W. Hoppel, B.J. Johnson, E. Kyrölä, T. Leblanc, G. Lichtenberg, M. Marchand, C.T. McElroy, D. Murtagh, H. Nakane, T. Portafaix, R. Querel, J.M. Russell III, J. Salvador, H.G.J. Smit, K. Stebel, W. Steinbrecht, K.B. Strawbridge, R. Stübi, D.P.J. Swart, G.

Taha, D.W. Tarasick, A.M. Thompson, J. Urban, J.A.E. van Gijsel, R. Van Malderen, P. von der Gathen, K.A. Walker, E. Wolfram, and J.M. Zawodny, Ground-based assessment of the bias and long-term stability of 14 limb and occultation ozone profile data records, ***Atmos. Meas. Tech.***, ***9***, 2497–2534, doi:10.5194/amt-9-2497-2016, 2016.

Hubert, D., K.-P. Heue, J.-C. Lambert, T. Verhoelst, M. Allaart, S. Compernolle, P.D. Cullis, A. Dehn, C. Félix, B.J. Johnson, A. Keppens, D.E. Kollonige, C. Lerot, D. Loyola, M. Maata, S. Mitro, M. Mohamad, A. Piters, F. Romahn, H.B. Selkirk, F.R. da Silva, R.M. Stauffer, A.M. Thompson, J.P. Veefkind, H. Vömel, J.C. Witte, and C. Zehner, TROPOMI tropospheric ozone column data: geophysical assessment and comparison to ozonesondes, GOME-2B and OMI, ***Atmos. Meas. Tech.***, ***14***, 7405–7433, doi:10.5194/amt-14-7405-2021, 2021.

Huijnen, V., K. Miyazaki, J. Flemming, A. Inness, T. Sekiya, and M.G. Schultz, An intercomparison of tropospheric ozone reanalysis products from CAMS, CAMS interim, TCR-1, and TCR-2, ***Geosci. Model Dev.***, ***13***, 1513–1544, doi:10.5194/gmd-13-1513-2020, 2020.

Iglesias-Suarez, F., P.J. Young, and O. Wild, Stratospheric ozone change and related climate impacts over 1850–2100 as modelled by the ACCMIP ensemble, ***Atmos. Chem. Phys.***, ***16***, 343–363, doi:10.5194/acp-16-343-2016, 2016.

Iglesias Suarez, F., O. Wild, D.E. Kinnison, R.R. Garcia, D.R. Marsh, J. Lamarque, E.M. Ryan, S.M. Davis, R. Eichinger, A. Saiz Lopez, and P.J. Young, Tropical stratospheric circulation and ozone coupled to pacific multi decadal variability, ***Geophys. Res. Lett.***, ***48*** (11), doi:10.1029/2020gl092162, 2021.

Inness, A., J. Flemming, K.-P. Heue, C. Lerot, D. Loyola, R. Ribas, P. Valks, M. van Roozendael, J. Xu, and W. Zimmer, Monitoring and assimilation tests with TROPOMI data in the CAMS system: near-real-time total column ozone, ***Atmos. Chem. Phys.***, ***19***, 3939–3962, doi:10.5194/acp-19-3939-2019, 2019a.

Inness, A., M. Ades, A. Agustí-Panareda, J. Barré, A. Benedictow, A.-M. Blechschmidt, J.J. Dominguez, R. Engelen, H. Eskes, J. Flemming, V. Huijnen, L. Jones, Z. Kipling, S. Massart, M. Parrington, V.-H. Peuch, M. Razinger, S. Remy, M. Schulz, and M. Suttie, The CAMS reanalysis of atmospheric composition, ***Atmos. Chem. Phys.***, ***19***, 3515–3556, doi:10.5194/acp-19-3515-2019, 2019b.

Isaksen, I.S.A., E. Hesstvedt, and F. Stordal, Influence of stratospheric cooling from CO2 on the ozone layer, ***Nature***, ***283***, 189–191, doi:10.1038/283189a0, 1980.

Junge, C.E., C.W. Chagnon, and J.E. Manson, Stratospheric aerosols, ***J. Atmos. Sci.***, ***18*** (1), 81–108, doi:10.1175/1520-0469(1961)018<0081:SA>2.0.CO;2, 1961.

Kablick III, G.P., D.R. Allen, M.D. Fromm, and G.E. Nedoluha, Australian PyroCb smoke generates synoptic scale stratospheric anticyclones, ***Geophys. Res. Lett.***, ***47*** (13), doi:10.1029/2020gl088101, 2020.

Kar, J., K.-P. Lee, M.A. Vaughan, J.L. Tackett, C.R. Trepte, D.M. Winker, P.L. Lucker, and B.J. Getzewich, CALIPSO level 3 stratospheric aerosol profile product: version 1.00 algorithm description and initial assessment, ***Atmos. Meas. Tech.***, ***12***, 6173–6191, doi:10.5194/amt-12-6173-2019, 2019.

Keeble, J., E.M. Bednarz, A. Banerjee, N.L. Abraham, N.R.P. Harris, A.C. Maycock, and J.A. Pyle, Diagnosing the radiative and chemical contributions to future changes in tropical column ozone with the UM-UKCA chemistry–climate model, ***Atmos. Chem. Phys.***, ***17***, 13,801–13,818, doi:10.5194/acp-17-13801-2017, 2017.

Keeble, J., N.L. Abraham, A.T. Archibald, M.P. Chipperfield, S. Dhomse, P.T. Griffiths, and J.A. Pyle, Modelling the potential impacts of the recent, unexpected increase in CFC-11 emissions on total column ozone recovery, ***Atmos. Chem. Phys.***, ***20***, 7153–7166, doi:10.5194/acp-20-7153-2020, 2020.

Keeble, J., B. Hassler, A. Banerjee, R. Checa-Garcia, G. Chiodo, S. Davis, V. Eyring, P.T. Griffiths, O. Morgenstern, P. Nowack, G. Zeng, J. Zhang, G. Bodeker, S. Burrows, P. Cameron-Smith, D. Cugnet, C. Danek, M. Deushi, L.W. Horowitz, A. Kubin, L. Li, G. Lohmann, M. Michou, M.J. Mills, P. Nabat, D. Olivié, S. Park, Ø. Seland, J. Stoll, K.-H. Wieners, and T. Wu, Evaluating stratospheric ozone and water vapour changes in CMIP6 models from 1850 to 2100, ***Atmos. Chem. Phys.***, ***21***, 5015–5061, doi:10.5194/acp-21-5015-2021, 2021a.

Keeble, J., Y.Y.S. Yiu, A.T. Archibald, F. O'Connor, A. Sellar, J. Walton, and J.A. Pyle, Using machine learning to make computationally inexpensive projections of 21st Century stratospheric column ozone changes in the tropics, ***Front Earth Sci.***, ***8***, 591, doi:10.3389/feart.2020.592667, 2021b.

Khaykin, S., B. Legras, S. Bucci, P. Sellitto, L. Isaksen, F. Tencé, S. Bekki, A. Bourassa, L. Rieger, D. Zawada, J. Jumelet, and S. Godin-Beekmann, The 2019/20 Australian wildfires generated a persistent smoke-charged vortex rising up to 35 km altitude, ***Commun. Earth Environ.***, ***1*** (1), 1–12, doi:10.1038/s43247-020-00022-5, 2020.

Klekociuk, A.R., M.B. Tully, P.B. Krummel, S.I. Henderson, D. Smale, R. Querel, S. Nichol, S.P. Alexander, P.J. Fraser, and G. Nedoluha, The Antarctic ozone hole during 2018 and 2019, ***J. South. Hemisphere Earth Syst. Sci.***, ***71***, 66–91, doi:10.1071/ES20010, 2021.

Kloss, C., G. Berthet, P. Sellitto, F. Ploeger, S. Bucci, S. Khaykin, F. Jégou, G. Taha, L.W. Thomason, B. Barret, E. Le Flochmoen, M. von Hobe, A. Bossolasco, N. Bègue, and B. Legras, Transport of the 2017 Canadian wildfire plume to the tropics via the Asian monsoon circulation, ***Atmos. Chem. Phys.***, ***19***, 13,547–13,567, doi:10.5194/acp-19-13547-2019, 2019.

Knutti, R., D. Masson, and A. Gettelman, Climate model genealogy: Generation CMIP5 and how we got there, ***Geophys. Res. Lett.***, ***40***, 1194–1199, doi:10.1002/grl.50256, 2013.

Kovilakam, M., L.W. Thomason, N. Ernest, L. Rieger, A. Bourassa, and L. Millán, The global space-based stratospheric aerosol climatology (version 2.0): 1979–2018, ***Earth Syst. Sci. Data***, ***12***, 2607–2634, doi:10.5194/essd-12-2607-2020, 2020.

Kremser, S., L.W. Thomason, M. von Hobe, M. Hermann, T. Deshler, C. Timmreck, M. Toohey, A. Stenke, J.P. Schwarz, R. Weigel, S. Fueglistaler, F.J. Prata, J.-P., Vernier, H. Schlager, J.E. Barnes, J.-C. Antuña-Marrero, D. Fairlie, M. Palm, E. Mahieu, J. Notholt, M. Rex, C. Bingen, F. Vanhellemont, A. Bourassa, J.M.C. Plane, D. Klocke, S.A. Carn, L. Clarisse, T. Trickl, R. Neely, A.D. James, L. Rieger, J.C. Wilson, and B. Meland, Stratospheric aerosol—Observations, processes, and impact on climate, ***Rev. Geophys.***, ***54***, 278–335, doi:10.1002/2015rg000511, 2016.

Krivova, N.A., L.E.A. Vieira, and S.K. Solanki, Reconstruction of solar spectral irradiance since the Maunder minimum, ***J. Geophys. Res.***, ***115*** (A12), doi:10.1029/2010ja015431, 2010.

Krzyścin, J.W., El Niño-Southern Oscillation and Indian Ocean Dipole contribution to the zonal mean total ozone in the Northern Hemisphere, ***Int. J. Climatol.***, ***37***, 3517–3524, doi:10.1002/joc.4933, 2017.

Kunze, M., T. Kruschke, U. Langematz, M. Sinnhuber, T. Reddmann, and K. Matthes, Quantifying uncertainties of climate signals in chemistry climate models related to the 11-year solar cycle – Part 1: Annual mean response in heating rates, temperature, and ozone, ***Atmos. Chem. Phys.***, ***20***, 6991–7019, doi:10.5194/acp-20-6991-2020, 2020.

Laine, M., N. Latva-Pukkila, and E. Kyrölä, Analysing time-varying trends in stratospheric ozone time series using the state space approach, ***Atmos. Chem. Phys.***, ***14***, 9707–9725, doi:10.5194/acp-14-9707-2014, 2014.

Lamarque, J.F., D.T. Shindell, B. Josse, P.J. Young, I. Cionni, V. Eyring, D. Bergmann, P. Cameron-Smith, W.J. Collins, R. Doherty, S. Dalsoren, G. Faluvegi, G. Folberth, S.J. Ghan, L.W. Horowitz, Y.H. Lee, I.A. MacKenzie, T. Nagashima, V. Naik, D. Plummer, M. Righi, S.T. Rumbold, M. Schulz, R.B. Skeie, D.S. Stevenson, S. Strode, K. Sudo, S. Szopa, A. Voulgarakis, and G. Zeng, The Atmospheric Chemistry and Climate Model Intercomparison Project (ACCMIP): overview and description of models, simulations and climate diagnostics, ***Geosci. Model Dev.***, ***6***, 179–206, doi:10.5194/gmd-6-179-2013, 2013.

Langematz, U., F. Schmidt, M. Kunze, G.E. Bodeker, and P. Braesicke, Antarctic ozone depletion between 1960 and 1980 in observations and chemistry–climate model simulations, ***Atmos. Chem. Phys.***, ***16***, 15,619–15,627, doi:10.5194/acp-16-15619-2016, 2016.

Li, F., P. Newman, S. Pawson, and J. Perlwitz, Effects of greenhouse gas increase and stratospheric ozone depletion on stratospheric mean age of air in 1960-2010, ***J. Geophys. Res.***, ***123***, 2098–2110, doi:10.1002/2017jd027562, 2018.

Li, K.-F., Q. Zhang, K.-K. Tung, and Y.L. Yung, Resolving a long-standing model-observation discrepancy on ozone solar cycle response, ***Earth Space Sci.***, ***3***, 431–440, doi:10.1002/2016ea000199, 2016.

Lin, J., and T. Qian, Impacts of the ENSO lifecycle on stratospheric ozone and temperature, ***Geophys. Res. Lett.***, ***46***, 10,646–10,658, doi:10.1029/2019gl083697, 2019.

Lin, P., I. Held, and Y. Ming, The early development of the 2015/16 quasi-biennial oscillation disruption, ***J. Atmos. Sci.***, ***76***, 821–836, doi:10.1175/JAS-D-18-0292.1, 2019.

Loyola, D.G., and M. Coldewey-Egbers, Multi-sensor data merging with stacked neural networks for the creation of satellite long-term climate data records, ***EURASIP J. Adv. Signal Process.***, ***2012*** (1), 1–10, doi:10.1186/1687-6180-2012-91, 2012.

Lu, J., F. Xie, W. Tian, J. Li, W. Feng, M. Chipperfield, J. Zhang, and X. Ma, Interannual variations in lower stratospheric ozone during the period 1984–2016, ***J. Geophys. Res.***, ***124***, 8225–8241, doi:10.1029/2019jd030396, 2019.

Maillard Barras, E., A. Haefele, L. Nguyen, F. Tummon, W.T. Ball, E.V. Rozanov, R.

Rüfenacht, K. Hocke, L. Bernet, N. Kämpfer, G. Nedoluha, and I. Boyd, Study of the dependence of long-term stratospheric ozone trends on local solar time, ***Atmos. Chem. Phys.***, ***20***, 8453–8471, doi:10.5194/acp-20-8453-2020, 2020.

Matthes, K., D.R. Marsh, R.R. Garcia, D.E. Kinnison, F. Sassi, and S. Walters, Role of the QBO in modulating the influence of the 11 year solar cycle on the atmosphere using constant forcings, ***J. Geophys. Res.***, ***115*** (D18), doi:10.1029/2009jd013020, 2010.

Matthes, K., B. Funke, M.E. Andersson, L. Barnard, J. Beer, P. Charbonneau, M.A. Clilverd, T. Dudok de Wit, M. Haberreiter, A. Hendry, C.H. Jackman, M. Kretzschmar, T. Kruschke, M. Kunze, U. Langematz, D.R. Marsh, A.C. Maycock, S. Misios, C.J. Rodger, A.A. Scaife, A. Seppälä, M. Shangguan, M. Sinnhuber, K. Tourpali, I. Usoskin, M. van de Kamp, P.T. Verronen, and S. Versick, Solar forcing for CMIP6 (v3.2), ***Geosci. Model Dev.***, ***10***, 2247–2302, doi:10.5194/gmd-10-2247-2017, 2017.

Mauceri, S., E. Richard, P. Pilewskie, D. Harber, O. Coddington, S. Béland, M. Chambliss, and S. Carson, Degradation correction of TSIS SIM, ***Solar Phys., 295*** (11), doi:10.1007/s11207-020-01707-y, 2020.

Maycock, A.C., K. Matthes, S. Tegtmeier, R. Thiéblemont, and L. Hood, The representation of solar cycle signals in stratospheric ozone – Part 1: A comparison of recently updated satellite observations, ***Atmos. Chem. Phys.***, ***16***, 10,021–10,043, doi:10.5194/acp-16-10021-2016, 2016.

Maycock, A.C., K. Matthes, S. Tegtmeier, H. Schmidt, R. Thiéblemont, L. Hood, H. Akiyoshi, S. Bekki, M. Deushi, P. Jöckel, O. Kirner, M. Kunze, M. Marchand, D.R. Marsh, M. Michou, D. Plummer, L.E. Revell, E. Rozanov, A. Stenke, Y. Yamashita, and K. Yoshida, The representation of solar cycle signals in stratospheric ozone – Part 2: Analysis of global models, ***Atmos. Chem. Phys.***, ***18***, 11,323–11,343, doi:10.5194/acp-18-11323-2018, 2018.

McPeters, R., S. Frith, N. Kramarova, J. Ziemke, and G. Labow, Trend quality ozone from NPP OMPS: the version 2 processing, ***Atmos. Meas. Tech.***, ***12***, 977–985, doi:10.5194/amt-12-977-2019, 2019.

Meehl, G.A., R. Moss, K.E. Taylor, V. Eyring, R.J. Stouffer, S. Bony, and B. Stevens, Climate model intercomparisons: Preparing for the next phase, ***Eos Trans. AGU***, ***95*** (9), 77–78, doi:10.1002/2014EO090001, 2014.

Meinshausen, M., Z.R.J. Nicholls, J. Lewis, M.J. Gidden, E. Vogel, M. Freund, U. Beyerle, C. Gessner, A. Nauels, N. Bauer, J.G. Canadell, J.S. Daniel, A. John, P.B. Krummel, G. Luderer, N. Meinshausen, S.A. Montzka, P.J. Rayner, S. Reimann, S.J. Smith, M. van den Berg, G.J.M. Velders, M.K. Vollmer, and R.H.J. Wang, The shared socio-economic pathway (SSP) greenhouse gas concentrations and their extensions to 2500, ***Geosci. Model Dev.***, ***13***, 3571–3605, doi:10.5194/gmd-13-3571-2020, 2020.

Mettig, N., M. Weber, A. Rozanov, C. Arosio, J.P. Burrows, P. Veefkind, A.M. Thompson, R. Querel, T. Leblanc, S. Godin-Beekmann, R. Kivi, and M.B. Tully, Ozone profile retrieval from nadir TROPOMI measurements in the UV range, ***Atmos. Meas. Tech.***, ***14***, 6057–6082, doi:10.5194/amt-14-6057-2021, 2021.

Meul, S., M. Dameris, U. Langematz, J. Abalichin, A. Kerschbaumer, A. Kubin, and S. Oberländer-Hayn, Impact of rising greenhouse gas concentrations on future tropical ozone and UV exposure, ***Geophys. Res. Lett.***, ***43*** (6), 2919–2927, doi:10.1002/2016GL067997, 2016.

Meul, S., U. Langematz, P. Kröger, S. Oberländer-Hayn, and P. Jöckel, Future changes in the stratosphere-to-troposphere ozone mass flux and the contribution from climate change and ozone recovery, ***Atmos. Chem. Phys.***, ***18***, 7721–7738, doi:10.5194/acp-18-7721-2018, 2018.

Monks, P.S., A.T. Archibald, A. Colette, O. Cooper, M. Coyle, R. Derwent, D. Fowler, C. Granier, K.S. Law, G.E. Mills, D.S. Stevenson, O. Tarasova, V. Thouret, E. von Schneidemesser, R. Sommariva, O. Wild, and M.L. Williams, Tropospheric ozone and its precursors from the urban to the global scale from air quality to short-lived climate forcer, ***Atmos. Chem. Phys.***, ***15***, 8889–8973, doi:10.5194/acp-15-8889-2015, 2015.

Montzka, S.A., G.S. Dutton, P. Yu, E. Ray, R.W. Portmann, J.S. Daniel, L. Kuijpers, B.D. Hall, D. Mondeel, C. Siso, J.D. Nance, M. Rigby, A.J. Manning, L. Hu, F. Moore, B.R Miller, and J.W. Elkins, An unexpected and persistent increase in global emissions of ozone-depleting CFC-11, ***Nature***, ***557***, 413–417, doi:10.1038/s41586-018-0106-2, 2018.

Morgenstern, O., M.I. Hegglin, E. Rozanov, F.M. O'Connor, N.L. Abraham, H. Akiyoshi, A.T. Archibald, S. Bekki, N. Butchart, M.P. Chipperfield, M. Deushi, S.S. Dhomse, R.R. Garcia, S.C. Hardiman, L.W. Horowitz, P. Jöckel, B. Josse, D. Kinnison, M. Lin, E. Mancini, M.E. Manyin, M. Marchand, V. Marécal, M. Michou, L.D. Oman, G. Pitari, D.A. Plummer, L.E. Revell, D. Saint-Martin, R. Schofield, A. Stenke, K. Stone, K. Sudo, T.Y. Tanaka, S. Tilmes, Y. Yamashita, K. Yoshida, and G. Zeng, Review of the global models used within phase 1 of the Chemistry–Climate Model Initiative (CCMI), ***Geosci. Model Dev.***, ***10***, 639–671, doi:10.5194/gmd-10-639-2017, 2017.

Morgenstern, O., K.A. Stone, R. Schofield, H. Akiyoshi, Y. Yamashita, D.E. Kinnison, R.R. Garcia, K. Sudo, D.A. Plummer, J. Scinocca, L.D. Oman, M.E. Manyin, G. Zeng, E. Rozanov, A. Stenke, L.E. Revell, G. Pitari, E. Mancini, G.D. Genova, D. Visioni, S.S. Dhomse, and M.P. Chipperfield, Ozone sensitivity to varying greenhouse gases and ozone-depleting substances in CCMI-1 simulations, ***Atmos. Chem. Phys.***, ***18***, 1091–1114, doi:10.5194/acp-18-1091-2018, 2018.

Morgenstern, O., F.M. O'Connor, B.T. Johnson, G. Zeng, J.P. Mulcahy, J. Williams, J. Teixeira, M. Michou, P. Nabat, L.W. Horowitz, V. Naik, L.T. Sentman, M. Deushi, S.E. Bauer, K. Tsigaridis, D.T. Shindell, and D.E. Kinnison, Reappraisal of the climate impacts of ozone depleting substances, ***Geophys. Res. Lett.***, ***47*** (20), doi:10.1029/2020gl088295, 2020.

Newchurch, M.J., E.-S. Yang, D.M. Cunnold, G.C. Reinsel, J.M. Zawodny, and J.M. Russell III, Evidence for slowdown in stratospheric ozone loss: First stage of ozone recovery, ***J. Geophys. Res.***, ***108*** (D16), doi:10.1029/2003jd003471, 2003.

Newman, P.A., J.S. Daniel, D.W. Waugh, and E.R. Nash, A new formulation of equivalent effective stratospheric chlorine (EESC), ***Atmos. Chem. Phys.***, ***7***, 4537–4552, doi:10.5194/acp-7-4537-2007, 2007.

Newman, P.A., L. Coy, S. Pawson, and L.R. Lait, The anomalous change in the QBO in 2015-2016, ***Geophys. Res. Lett.***, ***43***, 8791–8797, doi:10.1002/2016gl070373, 2016.

Nowack, P., P. Braesicke, J. Haigh, N.L. Abraham, J. Pyle, and A. Voulgarakis, Using machine learning to build temperature-based ozone parameterizations for climate sensitivity simulations, ***Environ. Res. Lett.***, ***13*** (10), 104016, doi:10.1088/1748-9326/aae2be, 2018.

Nowack, P., J. Runge, V. Eyring, and J.D. Haigh, Causal networks for climate model evaluation and constrained projections, ***Nat. Commun.***, ***11*** (1), doi:10.1038/s41467-020-15195-y, 2020.

Olsen, M.A., G.L. Manney, and J. Liu, The ENSO and QBO impact on ozone variability and stratosphere troposphere exchange relative to the subtropical jets, ***J. Geophys. Res.***, ***124*** (13), 7379–7392, doi:10.1029/2019jd030435, 2019.

Oman, L.D., A.R. Douglass, J.R. Ziemke, J.M. Rodriguez, D.W. Waugh, and J.E. Nielsen, The ozone response to ENSO in Aura satellite measurements and a chemistry-climate simulation, ***J. Geophys. Res.***, ***118***, 965–976, doi:10.1029/2012jd018546, 2013.

O'Neill, B.C., C. Tebaldi, D.P. van Vuuren, V. Eyring, P. Friedlingstein, G. Hurtt, R. Knutti, E. Kriegler, J.-F. Lamarque, J. Lowe, G.A. Meehl, R. Moss, K. Riahi, and B.M. Sanderson, The scenario model intercomparison project (ScenarioMIP) for CMIP6, ***Geosci. Model Dev.***, ***9***, 3461–3482, doi:10.5194/gmd-9-3461-2016, 2016.

Orbe, C., K. Wargan, S. Pawson, and L.D. Oman, Mechanisms linked to recent ozone decreases in the northern hemisphere lower stratosphere, ***J. Geophys. Res.***, ***125*** (9), doi:10.1029/2019jd031631, 2020.

ORM (Ozone Research Managers), ***Report of Part II of the Eleventh Meeting of the Ozone Research Managers of the Parties to the Vienna Convention for the Protection of the Ozone Layer***, GAW (Global Atmospheric Watch)–Report No. 271, 538 pp., Geneva, Switzerland, 2021.

Orr, A., H. Lu, P. Martineau, E.P. Gerber, G.J. Marshall, and T.J. Bracegirdle, Is our dynamical understanding of the circulation changes associated with the Antarctic ozone hole sensitive to the choice of reanalysis dataset?, ***Atmos. Chem. Phys.***, ***21***, 7451–7472, doi:10.5194/acp-21-7451-2021, 2021.

Osprey, S.M., N. Butchart, J.R. Knight, A.A. Scaife, K. Hamilton, J.A. Anstey, V. Schenzinger, and C. Zhang, An unexpected disruption of the atmospheric quasi-biennial oscillation, ***Science***, ***353***, 1424–1427, doi:10.1126/science.aah4156, 2016.

Petropavlovskikh, I., K. Miyagawa, A. McClure-Beegle, B. Johnson, J. Wild, S. Strahan, K. Wargan, R. Querel, L. Flynn, E. Beach, G. Ancellet, and S. Godin-Beekmann, Optimized Umkehr profile algorithm for ozone trend analyses, ***Atmos. Meas. Tech.***, ***15***, 1849–1870, doi:/10.5194/amt-15-1849-2022, 2022.

Polvani, L.M., L. Wang, M. Abalos, N. Butchart, M.P. Chipperfield, M. Dameris, M. Deushi, S.S. Dhomse, P. Jöckel, D. Kinnison, M. Michou, O. Morgenstern, L.D. Oman, D.A. Plummer, and K.A. Stone, Large impacts, past and future, of ozone-depleting substances on Brewer-Dobson circulation trends: A multi-model assessment, ***J. Geophys. Res.***, ***124***, 6669–6680, doi:10.1029/2018JD029516, 2019.

Provost, F., and T. Fawcett, Data science and its relationship to big data and data-driven decision making, ***Big Data, 1*** (1), 51–59, doi:10.1089/big.2013.1508, 2013.

Pyle, J.A., J. Keeble, N.L. Abraham, M.P. Chipperfield, and P.T. Griffiths, Integrated ozone depletion as a metric for ozone recovery, ***Nature***, ***608***, 719–723, doi:10.17863/CAM.86155, 2022.

Rahpoe, N., M. Weber, A.V. Rozanov, K. Weigel, H. Bovensmann, J.P. Burrows, A. Laeng, G. Stiller, T. von Clarmann, E. Kyrölä, V.F. Sofieva, J. Tamminen, K. Walker, D. Degenstein, A.E. Bourassa, R. Hargreaves, P. Bernath, J. Urban, and D.P. Murtagh, Relative drifts and biases between six ozone limb satellite measurements from the last decade, ***Atmos. Meas. Tech.***, ***8***, 4369–4381, doi:10.5194/amt-8-4369-2015, 2015.

Randel, W.J., and F. Wu, Isolation of the ozone QBO in SAGE II data by singular-value decomposition, ***J. Atmos. Sci.***, ***53***, 2546–2559, doi:10.1175/1520-0469(1996)053<2546:IOTOQI>2.0.CO;2, 1996.

Randel, W.J., R.R. Garcia, N. Calvo, and D. Marsh, ENSO influence on zonal mean temperature and ozone in the tropical lower stratosphere, ***Geophys. Res. Lett.***, ***36*** (15), doi:10.1029/2009gl039343, 2009.

Redondas, A., R. Evans, R. Stuebi, U. Köhler, and M. Weber, Evaluation of the use of five laboratory-determined ozone absorption cross sections in Brewer and Dobson retrieval algorithms, ***Atmos. Chem. Phys.***, ***14***, 1635–1648, doi:10.5194/acp-14-1635-2014, 2014.

Reutter, P., B. Škerlak, M. Sprenger, and H. Wernli, Stratosphere–troposphere exchange (STE) in the vicinity of North Atlantic cyclones, ***Atmos. Chem. Phys.***, ***15***, 10,939–10,953, doi:10.5194/acp-15-10939-2015, 2015.

Revell, L.E., A. Stenke, F. Tummon, A. Feinberg, E. Rozanov, T. Peter, N.L. Abraham, H. Akiyoshi, A.T. Archibald, N. Butchart, M. Deushi, P. Jöckel, D. Kinnison, M. Michou, O. Morgenstern, F.M. O'Connor, L.D. Oman, G. Pitari, D.A. Plummer, R. Schofield, K. Stone, S. Tilmes, D. Visioni, Y. Yamashita, and G. Zeng, Tropospheric ozone in CCMI models and Gaussian process emulation to understand biases in the SOCOLv3 chemistry-climate model, ***Atmos. Chem. Phys.***, ***18***, 16,155–16,172, doi:10.5194/acp-18-16155-2018, 2018.

Riahi, K., D.P. van Vuuren, E. Kriegler, J. Edmonds, B.C. O'Neill, S. Fujimori, N. Bauer, K. Calvin, R. Dellink, O. Fricko, W. Lutz, A. Popp, J.C. Cuaresma, S. Kc, M. Leimbach, L. Jiang, T. Kram, S. Rao, J. Emmerling, K. Ebi, T. Hasegawa, P. Havlik, F. Humpenöder, L.A. Da Silva, S. Smith, E. Stehfest, V. Bosetti, J. Eom, D. Gernaat, T. Masui, J. Rogelj, J. Strefler, L. Drouet, V. Krey, G. Luderer, M. Harmsen, K. Takahashi, L. Baumstark, J.C. Doelman, M. Kainuma, Z. Klimont, G. Marangoni, H. Lotze-Campen, M. Obersteiner, A. Tabeau, and M. Tavoni, The shared socioeconomic pathways and their energy, land use, and greenhouse gas emissions implications: an overview, ***Glob. Environ. Change***, ***42***, 153–168, doi:10.1016/j.gloenvcha.2016.05.009, 2017.

Rieder, H.E., J. Staehelin, J.A. Maeder, T. Peter, M. Ribatet, A.C. Davison, R. Stübi, P. Weihs, and F. Holawe, Extreme events in total ozone over Arosa – Part 2: Fingerprints of atmospheric dynamics and chemistry and effects on mean values and long-term changes, ***Atmos. Chem. Phys.***, ***10***, 10,033–10,045, doi:10.5194/acp-10-10033-2010, 2010.

Rieger, L.A., D.J. Zawada, A.E. Bourassa, and D.A. Degenstein, A multiwavelength retrieval approach for improved OSIRIS aerosol extinction retrievals, ***J. Geophys. Res.***, ***124*** (13), 7286–7307 doi:10.1029/2018jd029897, 2019.

Rieger, L.A., W.J. Randel, A.E. Bourassa, and S. Solomon, Stratospheric temperature and ozone anomalies associated with the 2020 Australian New Year fires, ***Geophys. Res. Lett.***, ***48*** (24), doi:10.1029/2021gl095898, 2021.

Rigby, M., S. Park, T. Saito, L.M. Western, A.L. Redington, X. Fang, S. Henne, A.J. Manning, R.G. Prinn, G.S. Dutton, P.J. Fraser, A.L. Ganesan, B.D. Hall, C.M. Harth, J. Kim, K.-R. Kim, P.B. Krummel, T. Lee, S. Li, Q. Liang, M.F. Lunt, S.A. Montzka, J. Mühle, S. O'Doherty, M.-K. Park, S. Reimann, P.K. Salameh, P. Simmonds, R.L. Tunnicliffe, R.F. Weiss, Y. Yokouchi, and D. Young, Increase in CFC-11 emissions from eastern China based on atmospheric observations, ***Nature***, ***569***, 546–550, doi:10.1038/s41586-019-1193-4, 2019.

Rosanka, S., B. Franco, L. Clarisse, P.-F. Coheur, A. Pozzer, A. Wahner, and D. Taraborrelli, The impact of organic pollutants from Indonesian peatland fires on the tropospheric and lower stratospheric composition, ***Atmos. Chem. Phys.***, ***21***, 11,257–11,288, doi:10.5194/acp-21-11257-2021, 2021.

Runge, J., P. Nowack, M. Kretschmer, S. Flaxman, and D. Sejdinovic, Detecting and quantifying causal associations in large nonlinear time series datasets, ***Sci. Adv.***, ***5*** (11), doi:10.1126/sciadv.aau4996, 2019.

Santee, M.L., A. Lambert, G.L. Manney, N.J. Livesey, L. Froidevaux, J.L. Neu, M.J. Schwartz, L.F. Millán, F. Werner, W.G. Read, M. Park, R.A. Fuller, and B.M. Ward, Prolonged and pervasive perturbations in the composition of the southern hemisphere midlatitude lower stratosphere from the Australian new year's fires, ***Geophys. Res. Lett.***, ***49*** (4), doi:10.1029/2021gl096270, 2022.

Saunders, M.A., A.S.R. Lea, and J.R. Smallwood, The quasi-biennial oscillation: A second disruption in four years, ***Earth Space Sci. Open Archive***, doi:10.1002/essoar.10504326.1, 2020.

Schultz, M.G., S. Schröder, O. Lyapina, O. Cooper, I. Galbally, I. Petropavlovskikh, E. Von Schneidemesser, H. Tanimoto, Y. Elshorbany, M. Naja, R. Seguel, U. Dauert, P. Eckhardt, S. Feigenspahn, M. Fiebig, A.-G. Hjellbrekke, Y.-D. Hong, P.C. Kjeld, H. Koide, G. Lear, D. Tarasick, M. Ueno, M. Wallasch, D. Baumgardner, M.-T. Chuang, R. Gillett, M. Lee, S. Molloy, R. Moolla, T. Wang, K. Sharps, J.A. Adame, G. Ancellet, F. Apadula, P. Artaxo, M. Barlasina, M. Bogucka, P. Bonasoni, L. Chang, A. Colomb, E. Cuevas, M. Cupeiro, A. Degorska, A. Ding, M. Fröhlich, M. Frolova, H. Gadhavi, F. Gheusi, S. Gilge, M.Y. Gonzalez, V. Gros, S.H. Hamad, D. Helmig, D. Henriques, O. Hermansen, R. Holla, J. Huber, U. Im, D.A. Jaffe, N. Komala, D. Kubistin, K.-S. Lam, T. Laurila, H. Lee, I. Levy, C. Mazzoleni, L. Mazzoleni, A. McClure-Begley, M. Mohamad, M. Murovic, M. Navarro-Comas, F. Nicodim, D. Parrish, K.A. Read, N. Reid, L. Ries, P. Saxena, J.J. Schwab, Y. Scorgie, I. Senik, P. Simmonds, V. Sinha, A. Skorokhod, G. Spain, W. Spangl, R. Spoor, S.R. Springston, K. Steer, M. Steinbacher, E. Suharguniyawan, P. Torre, T. Trickl, L. Weili, R. Weller, X. Xu, L. Xue, and M. Zhiqiang, Tropospheric ozone assessment report: Database and metrics data of global surface ozone observations, ***Elementa (Wash., DC)***, ***5***, 58, doi:10.1525/elementa.244, 2017.

Schwartz, M.J., M.L. Santee, H.C. Pumphrey, G.L. Manney, A. Lambert, N.J. Livesey, L. Millán, J.L. Neu, W.G. Read, and F. Werner, Australian new year's PyroCb impact on stratospheric composition, ***Geophys. Res. Lett.***, ***47*** (24), doi:10.1029/2020gl090831, 2020.

Sengupta, U., M. Amos, J.S. Hosking, C.E. Rasmussen, M. Juniper, and P.J. Young, Ensembling geophysical models with Bayesian neural networks, ***Adv. Neural Inf. Process. Syst.***, ***33***, 1205–1217, doi:10.48550/arXiv.2010.03561, 2020.

Serdyuchenko, A., V. Gorshelev, M. Weber, W. Chehade, and J.P. Burrows, High spectral resolution ozone absorption cross-sections – Part 2: Temperature dependence, ***Atmos. Meas. Tech.***, ***7***, 625–636, doi:10.5194/amt-7-625-2014, 2014.

Shangguan, M., W. Wang, and S. Jin, Variability of temperature and ozone in the upper troposphere and lower stratosphere from multi-satellite observations and reanalysis data, ***Atmos. Chem. Phys.***, ***19***, 6659–6679, doi:10.5194/acp-19-6659-2019, 2019.

Shepherd, T.G., D.A. Plummer, J.F. Scinocca, M.I. Hegglin, V.E. Fioletov, M.C. Reader, E. Remsberg, T. von Clarmann, and H.J. Wang, Reconciliation of halogen-induced ozone loss with the total-column ozone record, ***Nat. Geosci.***, ***7***, 443–449, doi:10.1038/ngeo2155, 2014.

Shin, N.-Y., J.-S. Kug, F.S. McCormack, and N.J. Holbrook, The double-peaked El Niño and its physical processes, ***J. Clim.***, ***34***, 1291–1303, doi:10.1175/JCLI-D-20-0402.1, 2021.

Simmons, A.J., P. Poli, D.P. Dee, P. Berrisford, H. Hersbach, S. Kobayashi, and C. Peubey, Estimating low-frequency variability and trends in atmospheric temperature using ERA-Interim, ***Quart. J. Roy. Meteor. Soc.***, ***140***, 329–353, doi:10.1002/qj.2317, 2014.

Sinnhuber, B.-M., and S. Meul, Simulating the impact of emissions of brominated very short lived substances on past stratospheric ozone trends, ***Geophys. Res. Lett.***, ***42***, 2449–2456, doi:10.1002/2014gl062975, 2015.

Smit, H.G.J., and A.M. Thompson, ***Ozonesonde measurement principles and best operational practices: ASOPOS 2.0 (Assessment of Standard Operating Procedures for Ozonesondes)***, World Meteorological Organization, GAW Report No. 268, 173 pp., Geneva, Switzerland, 2021.

Sofiev, M., R. Kouznetsov, R. Hänninen, and V.F. Sofieva, Technical note: Intermittent reduction of the stratospheric ozone over northern Europe caused by a storm in the Atlantic Ocean, ***Atmos. Chem. Phys.***, ***20***, 1839–1847, doi:10.5194/acp-20-1839-2020, 2020.

Sofieva, V.F., E. Kyrölä, M. Laine, J. Tamminen, D. Degenstein, A. Bourassa, C. Roth, D. Zawada, M. Weber, A. Rozanov, N. Rahpoe, G. Stiller, A. Laeng, T. von Clarmann, K.A. Walker, P. Sheese, D. Hubert, M. van Roozendael, C. Zehner, R. Damadeo, J. Zawodny, N. Kramarova, and P.K. Bhartia, Merged SAGE II, Ozone_cci and OMPS ozone profile dataset and evaluation of ozone trends in the stratosphere, ***Atmos. Chem. Phys.***, ***17***, 12,533–12,552, doi:10.5194/acp-17-12533-2017, 2017.

Sofieva, V.F., M. Szeląg, J. Tamminen, E. Kyrölä, D. Degenstein, C. Roth, D. Zawada, A. Rozanov, C. Arosio, J.P. Burrows, M. Weber, A. Laeng, G.P. Stiller, T. von Clarmann, L. Froidevaux, N. Livesey, M. van Roozendael, and C. Retscher, Measurement report: regional trends of stratospheric ozone evaluated using the MErged GRIdded Dataset of Ozone Profiles (MEGRIDOP), ***Atmos. Chem. Phys.***, ***21***, 6707–6720, doi:10.5194/acp-21-6707-2021, 2021.

Solomon, S., K. Dube, K. Stone, P. Yu, D. Kinnison, O.B. Toon, S.E. Strahan, K.H. Rosenlof, R. Portmann, S. Davis, W. Randel, P. Bernarth, C. Boone, C.G. Bardeen, A. Bourassa, D. Zawada, and D. Degenstein, On the stratospheric chemistry of mid-latitude wildfire smoke, ***Proc. Natl. Acad. Sci.***, ***118*** (10), doi:10.1073/pnas.2117325119, 2022.

Soukharev, B.E., and L.L. Hood, Solar cycle variation of stratospheric ozone: Multiple regression analysis of long-term satellite data sets and comparisons with models, ***J. Geophys. Res.***, ***111*** (D20), doi:10.1029/2006jd007107, 2006.

SPARC (Stratospheric Processes And their Role in Climate), ***SPARC CCMVal Report on the Evaluation of Chemistry-Climate Models***, edited by V. Eyring, T. Shepherd, and D. Waugh, SPARC Report No. 5, WCRP-30/2010, WMO/TD – No. 40, [available at: www.sparc-climate.org/publications/sparc-reports/], 2010.

SPARC/IO3C/GAW, ***SPARC/IO3C/GAW Report on Long-term Ozone Trends and Uncertainties in the Stratosphere***, edited by I. Petropavlovskikh, S. Godin-Beekmann, D. Hubert, R. Damadeo, B. Hassler, and V. Sofieva, SPARC Report No. 9, GAW Report No. 241, WCRP-17/2018, doi:10.17874/f899e57a20b, 2019.

SPARC (Stratospheric Processes And their Role in Climate), ***SPARC Reanalysis Intercomparison Project (S-RIP) Final Report***, edited by M. Fujiwara, G.L. Manney, L.J. Gray, and J.S. Wright, SPARC Report No. 10, WCRP-17/2020, doi:10.17874/800dee57d13, 2022.

Stauffer, R.M., A.M. Thompson, L.D. Oman, and S.E. Strahan, The effects of a 1998 observing system change on MERRA 2 based ozone profile simulations, ***J. Geophys. Res.***, ***124*** (13), 7429–7441 doi:10.1029/2019jd030257, 2019.

Stauffer, R.M., A.M. Thompson, D.E. Kollonige, J.C. Witte, D.W. Tarasick, J. Davies, H. Vömel, G.A. Morris, R. Van Malderen, B.J. Johnson, R.R. Querel, H.B. Selkirk, R. Stübi, and H.G.J. Smit, A post 2013 dropoff in total ozone at a third of global ozonesonde stations: Electrochemical concentration cell instrument artifacts?, ***Geophys. Res. Lett.***, ***47*** (11), doi:10.1029/2019gl086791, 2020.

Steinbrecht, W., U. Köhler, H. Claude, M. Weber, J.P. Burrows, and R.J. van der A, Very high ozone columns at northern mid-latitudes in 2010, ***Geophys. Res. Lett.***, ***38*** (6), doi:10.1029/2010gl046634, 2011.

Steinbrecht, W., L. Froidevaux, R. Fuller, R. Wang, J. Anderson, C. Roth, A. Bourassa, D. Degenstein, R. Damadeo, J. Zawodny, S. Frith, R. McPeters, P. Bhartia, J. Wild, C. Long, S. Davis, K. Rosenlof, V. Sofieva, K. Walker, N. Rahpoe, A. Rozanov, M. Weber, A. Laeng, T. von Clarmann, G. Stiller, N. Kramarova, S. Godin-Beekmann, T. Leblanc, R. Querel, D. Swart, I. Boyd, K. Hocke, N. Kämpfer, E. Maillard Barras, L. Moreira, G. Nedoluha, C. Vigouroux, T. Blumenstock, M. Schneider, O. García, N. Jones, E. Mahieu, D. Smale, M. Kotkamp, J. Robinson, I. Petropavlovskikh, N. Harris, B. Hassler, D. Hubert, and F. Tummon, An update on ozone profile trends for the period 2000 to 2016, ***Atmos. Chem. Phys.***, ***17***, 10,675–10,690, doi:10.5194/acp-17-10675-2017, 2017.

Steinbrecht, W., M.I. Hegglin, N. Harris, and M. Weber, Is global ozone recovering?, ***C. R. Geosci.***, ***350***, 368–375, doi:10.1016/j.crte.2018.07.012, 2018.

Sterl, A., On the (in) homogeneity of reanalysis products, ***J. Clim.***, ***17***, 3866–3873, doi:10.1175/1520-0442(2004)017<3866:OTIORP>2.0.CO;2, 2004.

Stevenson, D.S., P.J. Young, V. Naik, J.F. Lamarque, D.T. Shindell, A. Voulgarakis, R.B. Skeie, S.B. Dalsøren, G. Myhre, T.K. Berntsen, G.A. Folberth, S.T. Rumbold, W.J. Collins, I.A. MacKenzie, R.M. Doherty, G. Zeng, T.P.C. van Noije, A. Strunk, D. Bergmann, P. Cameron-Smith, D.A. Plummer, S.A. Strode, L. Horowitz, Y.H. Lee, S. Szopa, K. Sudo, T. Nagashima, B. Josse, I. Cionni, M. Righi, V. Eyring, A. Conley, K.W. Bowman, O. Wild, and A. Archibald, Tropospheric ozone changes, radiative forcing and attribution to emissions in the Atmospheric Chemistry and Climate Model Intercomparison Project (ACCMIP), ***Atmos. Chem. Phys.***, ***13*** (6), 3063–3085, doi:10.5194/acp-13-3063-2013, 2013.

Stohl, A., A 1 year Lagrangian "climatology" of airstreams in the Northern Hemisphere troposphere and lowermost stratosphere, ***J. Geophys. Res.***, ***106*** (D7), 7263–7279, doi:10.1029/2000jd900570, 2001.

Stone, K.A., S. Solomon, and D.E. Kinnison, On the identification of ozone recovery, ***Geophys. Res. Lett.***, ***45***, 5158–5165, doi:10.1029/2018gl077955, 2018.

Strahan, S. D. Smale, S. Solomon, G. Taha, M.R. Damonm S.D. Steerod, N. Jones, B. Liley, R. Querel, and J. Robinson, Unexpected repartitioning of stratospheric inorganic chlorine after the 2020 Australian wildfires, ***Geophys. Res. Lett.***, ***49*** (14), doi: 10.1029/2022GL098290, 2022.

Stübi, R., H. Schill, E. Maillard Barras, J. Klausen, and A. Haefele, Quality assessment of Dobson spectrophotometers for ozone column measurements before and after automation at Arosa and Davos, ***Atmos. Meas. Tech.***, ***14***, 4203–4217, doi:10.5194/amt-14-4203-2021, 2021.

Szatkowski, L.S., O.H. Bradley Jr, L.E. Mauldin III, M.B. Wusk, W.P. Chu, L.C. Farwell II, and P. Galeone, Stratospheric aerosol and gas experiment III (SAGE III) mission aboard the International Space Station, in ***Optical Spectroscopic Techniques and Instrumentation for Atmospheric and Space Research III***, ***3756,*** 164–171, doi:10.1117/12.366370, 1999.

Szeląg, M.E., V.F. Sofieva, D. Degenstein, C. Roth, S. Davis, and L. Froidevaux, Seasonal stratospheric ozone trends over 2000–2018 derived from several merged data sets, ***Atmos. Chem. Phys.***, ***20***, 7035–7047, doi:10.5194/acp-20-7035-2020, 2020.

Tarasick, D., I.E. Galbally, O.R. Cooper, M.G. Schultz, G. Ancellet, T. Leblanc, T.J. Wallington, J. Ziemke, X. Liu, M. Steinbacher, J. Staehelin, C. Vigouroux, J.W. Hannigan, O. García, G. Foret, P. Zanis, E. Weatherhead, I. Petropavlovskikh, H. Worden, M. Osman, J. Liu, K.-L. Chang, A. Gaudel, M. Lin, M. Granados-Muñoz, A.M. Thompson, S.J. Oltmans, J. Cuesta, G. Dufour, V. Thouret, B. Hassler, T. Trickl, and J.L. Neu, Tropospheric Ozone Assessment Report: Tropospheric ozone from 1877 to 2016, observed levels, trends and uncertainties, ***Elementa (Wash., DC)***, ***7***, 39, doi:10.1525/elementa.376, 2019.

Tarasick, D.W., H.G.J. Smit, A.M. Thompson, G.A. Morris, J.C. Witte, J. Davies, T. Nakano, R. Van Malderen, R.M. Stauffer, B.J. Johnson, R. Stübi, S.J. Oltmans, and H. Vömel, Improving ECC ozonesonde data quality: Assessment of current methods and outstanding issues, ***Earth Space Sci.***, ***8*** (3), doi:10.1029/2019ea000914, 2021.

Thomason, L.W., N. Ernest, L. Millán, L. Rieger, A. Bourassa, J.-P. Vernier, G. Manney, B. Luo, F. Arfeuille, and T. Peter, A global space-based stratospheric aerosol climatology: 1979–2016, ***Earth Syst. Sci. Data***, ***10***, 469–492, doi:10.5194/essd-10-469-2018, 2018.

Thompson, A.M., R.M. Stauffer, K. Wargan, J.C. Witte, D.E. Kollonige, and J.R. Ziemke, Regional and seasonal trends in tropical ozone from SHADOZ profiles: Reference for models and satellite products, ***J. Geophys. Res.***, ***126*** (22), doi:10.1029/2021jd034691, 2021.

Tung, K.K., and H. Yang, Global QBO in circulation and ozone. Part I: Reexamination of observational evidence, ***J. Atmos. Sci.***, ***51***, 2699–2707, doi:10.1175/1520-0469(1994)051<2699:GQICAO>2.0.CO;2, 1994.

Tweedy, O.V., N.A. Kramarova, S.E. Strahan, P.A. Newman, L. Coy, W.J. Randel, M. Park, D.W. Waugh, and S.M. Frith, Response of trace gases to the disrupted 2015–2016 quasi-biennial oscillation, ***Atmos. Chem. Phys.***, ***17***, 6813–6823, doi:10.5194/acp-17-6813-2017, 2017.

van der A, R.J., M.A.F. Allaart, and H.J. Eskes, Multi sensor reanalysis of total ozone, ***Atmos. Chem. Phys.***, ***10***, 11,277–11,294, doi:10.5194/acp-10-11277-2010, 2010.

van der A, R.J., M.A.F. Allaart, and H.J. Eskes, Extended and refined multi sensor reanalysis of total ozone for the period 1970–2012, ***Atmos. Meas. Tech.***, ***8***, 3021–3035, doi:10.5194/amt-8-3021-2015, 2015.

Veefkind, J.P., I. Aben, K. McMullan, H. Förster, J. de Vries, G. Otter, J. Claas, H.J. Eskes, J.F. de Haan, Q. Kleipool, M. van Weele, O. Hasekamp, R. Hoogeveen, J. Landgraf, R. Snel, P. Tol, P. Ingmann, R. Voors, B. Kruizinga, R. Vink, H. Visser, and P.F. Levelt, TROPOMI on the ESA Sentinel-5 Precursor: A GMES mission for global observations of the atmospheric composition for climate, air quality and ozone layer applications, ***Remote Sens. Environ.***, ***120***, 70–83, doi:10.1016/j.rse.2011.09.027, 2012.

Vigouroux, C., T. Blumenstock, M. Coffey, Q. Errera, O. García, N.B. Jones, J.W. Hannigan, F. Hase, B. Liley, E. Mahieu, J. Mellqvist, J. Notholt, M. Palm, G. Persson, M. Schneider, C. Servais, D. Smale, L. Thölix, and M. De Mazière, Trends of ozone total columns and vertical distribution from FTIR observations at eight NDACC stations around the globe, ***Atmos. Chem. Phys.***, ***15***, 2915–2933, doi:10.5194/acp-15-2915-2015, 2015.

von der Gathen, P., R. Kivi, I. Wohltmann, R.J. Salawitch, and M. Rex, Climate change favours large seasonal loss of Arctic ozone, ***Nat. Commun.***, ***12***, 3886, doi:10.1038/s41467-021-24089-6, 2021.

Voulgarakis, A., D.T. Shindell, and G. Faluvegi, Linkages between ozone-depleting substances, tropospheric oxidation and aerosols, ***Atmos. Chem. Phys.***, ***13*** (9), 4907–4916, doi:10.5194/acp-13-4907-2013, 2013.

Wallace, J.M., R. Lee Panetta, and J. Estberg, Representation of the equatorial stratospheric quasi-biennial oscillation in EOF phase space, ***J. Atmos. Sci.***, ***50***, 1751–1762, doi:10.1175/1520-0469(1993)050<1751:ROTESQ>2.0.CO;2, 1993.

Wang, H.J.R., R. Damadeo, D. Flittner, N. Kramarova, G. Taha, S. Davis, A.M. Thompson, S. Strahan, Y. Wang, L. Froidevaux, D. Degenstein, A. Bourassa, W. Steinbrecht, K.A. Walker, R. Querel, T. Leblanc, S. Godin-Beekmann, D. Hurst, and E. Hall, Validation of SAGE III/ISS solar occultation ozone products with correlative satellite and ground-based measurements, ***J. Geophys. Res.***, ***125***, doi:10.1029/2020jd032430, 2020.

Wargan, K., C. Orbe, S. Pawson, J.R. Ziemke, L.D. Oman, M.A. Olsen, L. Coy, and K.E. Knowland, Recent decline in extratropical lower stratospheric ozone attributed to circulation changes, ***Geophys. Res. Lett.***, ***45***, 5166–5176, doi:10.1029/2018GL077406, 2018.

Wargan, K., N. Kramarova, B. Weir, S. Pawson, and S.M. Davis, Toward a reanalysis of stratospheric ozone for trend studies: Assimilation of the aura microwave limb sounder and ozone mapping and profiler suite limb profiler data, ***J. Geophys. Res.***, ***125*** (4), doi:10.1029/2019jd031892, 2020.

Weber, M., M. Coldewey-Egbers, V.E. Fioletov, S.M. Frith, J.D. Wild, J.P. Burrows, C.S. Long, and D. Loyola, Total ozone trends from 1979 to 2016 derived from five merged observational datasets – the emergence into ozone recovery, ***Atmos. Chem. Phys.***, ***18***, 2097–2117, doi:10.5194/acp-18-2097-2018, 2018.

Weber, M., W. Steinbrecht, C. Arosio, R. van der A, S.M. Frith, J. Anderson, M. Coldewey-Egbers, S. Davis, D. Degenstein, V.E. Fioletov, L. Froidevaux, D. Hubert, C.S. Long, D. Loyola, A. Rozanov, C. Roth, V. Sofieva, K. Tourpali, R. Wang, and J.D. Wild, Stratospheric ozone, in [State of the Climate in 2019], ***Bull. Am. Met. Soc.***, ***101*** (8), S78–S81, doi:10.1175/BAMS-D-20-0104.1, 2020.

Weber, M., W. Steinbrecht, C. Arosio, R. van der A, S.M. Frith, J. Anderson, L. Castia, M. Coldewey-Egbers, S. Davis, D. Degenstein, V.E. Fioletov, L. Froidevaux, D. Hubert, D. Loyola, C. Roth, A. Rozanov, V. Sofieva, K. Tourpali, R. Wang, and J.D. Wild, Stratospheric ozone, [State of the Climate in 2020], ***Bull. Am. Met. Soc.***, ***102*** (8), S92–S95, doi:10.1175/2021BAMSStateoftheClimate.1, 2021.

Weber, M., C. Arosio, M. Coldewey-Egbers, V. Fioletov, S.M. Frith, J.D. Wild, K. Tourpali, J.P. Burrows, and D. Loyola, Global total ozone recovery trends derived from five merged ozone datasets, ***Atmos. Chem. Phys.***, ***22***, 6843–6859, doi:10.5194/acp-22-6843-2022, 2022.

Wild, J.D., S.-K. Yang, and C.S. Long, Ozone Profile Trends: An SBUV/2 Perspective (QOS2016-133), in ***Proceedings of the Quadrennial Ozone Symposium***, Edinburgh, Scotland, 2016.

Wild, O., A. Voulgarakis, F. O'Connor, J.-F. Lamarque, E.M. Ryan, and L. Lee, Global sensitivity analysis of chemistry–climate model budgets of tropospheric ozone and OH: exploring model diversity, ***Atmos. Chem. Phys.***, ***20***, 4047–4058, doi:10.5194/acp-20-4047-2020, 2020.

Wilks, D.S., On "field significance" and the false discovery rate, ***J. Appl. Meteorol. Climatol.***, ***45***, 1181–1189, doi:10.1175/JAM2404.1, 2006.

Williams, R.S., M.I. Hegglin, B.J. Kerridge, P. Jöckel, B.G. Latter, and D.A. Plummer, Characterising the seasonal and geographical variability in tropospheric ozone, stratospheric influence and recent changes, ***Atmos. Chem. Phys.***, ***19***, 3589–3620, doi:10.5194/acp-19-3589-2019, 2019.

Wing, R., W. Steinbrecht, S. Godin-Beekmann, T.J. McGee, J.T. Sullivan, G. Sumnicht, G. Ancellet, A. Hauchecorne, S. Khaykin, and P. Keckhut, Intercomparison and evaluation of ground- and satellite-based stratospheric ozone and temperature profiles above Observatoire de Haute-Provence during the Lidar Validation NDACC Experiment (LAVANDE), ***Atmos. Meas. Tech.***, ***13***, 5621–5642, doi:10.5194/amt-13-5621-2020, 2020.

Wing, R., S. Godin-Beekmann, W. Steinbrecht, T.J. McGee, J.T. Sullivan, S. Khaykin, G. Sumnicht, and L. Twigg, Evaluation of the new DWD ozone and temperature lidar during the Hohenpeißenberg Ozone Profiling Study (HOPS) and comparison of results with previous NDACC campaigns, ***Atmos. Meas. Tech.***, ***14***, 3773–3794, doi:10.5194/amt-14-3773-2021, 2021.

WMO (World Meteorological Organization), ***Scientific Assessment of Ozone Depletion: 2014***, Global Ozone Research and Monitoring Project–Report No. 55, 416 pp., Geneva, Switzerland, 2014.

WMO (World Meteorological Organization), ***Scientific Assessment of Ozone Depletion: 2018***, Global Ozone Research and Monitoring Project–Report No. 58, 588 pp., Geneva, Switzerland, 2018.

WMO (World Meteorological Organization), ***Report on the Unexpected Emissions of CFC-11***, Ozone Research and Monitoring, WMO-No. 1268, 84 pp., Geneva, Switzerland, 2021.

Wolter, K., and M.S. Timlin, Measuring the strength of ENSO events: How does 1997/98 rank?, ***Weather***, ***53*** (9), 315–324, doi:10.1002/j.1477-8696.1998.tb06408.x, 1998.

Yeo, K.L., N.A. Krivova, S.K. Solanki, and K.H. Glassmeier, Reconstruction of total and spectral solar irradiance from 1974 to 2013 based on KPVT, SoHO/MDI, and SDO/HMI observations, ***Astron. Astrophys. Suppl. Ser.***, ***570***, A85, doi:10.1051/0004-6361/201423628, 2014.

Yeung, L.Y., L.T. Murray, P. Martinerie, E. Witrant, H. Hu, A. Banerjee, A. Orsi, and J. Chappellaz, Isotopic constraint on the twentieth-century increase in tropospheric ozone, ***Nature***, ***570***, 224–227, doi:10.1038/s41586-019-1277-1, 2019.

Young, P.J., A.T. Archibald, K.W. Bowman, J.F. Lamarque, V. Naik, D.S. Stevenson, S. Tilmes, A. Voulgarakis, O. Wild, D. Bergmann, P. Cameron-Smith, I. Cionni, W.J. Collins, S.B. Dalsøren, R.M. Doherty, V. Eyring, G. Faluvegi, L.W. Horowitz, B. Josse, Y.H. Lee, I.A. MacKenzie, T. Nagashima, D.A. Plummer, M. Righi, S.T. Rumbold, R.B. Skeie, D.T. Shindell, S.A. Strode, K. Sudo, S. Szopa, and G. Zeng, Pre-industrial to end 21st century projections of tropospheric ozone from the Atmospheric Chemistry and Climate Model Intercomparison Project (ACCMIP), ***Atmos. Chem. Phys.***, ***13*** (4), 2063–2090, doi:10.5194/acp-13-2063-2013, 2013.

Young, P.J., V. Naik, A.M. Fiore, A. Gaudel, J. Guo, M.Y. Lin, J.L. Neu, D.D. Parrish, H.E. Rieder, J.L. Schnell, S. Tilmes, O. Wild, L. Zhang, J.R. Ziemke, J. Brandt, A. Delcloo, R.M. Doherty, C. Geels, M.I. Hegglin, L. Hu, U. Im, R. Kumar, A. Luhar, L. Murray, D. Plummer, J. Rodriguez, A. Saiz-Lopez, M.G. Schultz, M.T. Woodhouse, and G. Zeng, Tropospheric Ozone Assessment Report: Assessment of global-scale model performance for global and regional ozone distributions, variability, and trends, ***Elementa (Wash., DC)***, ***6***, 10, doi:10.1525/elementa.265, 2018.

Yu, P., O.B. Toon, C.G. Bardeen, Y. Zhu, K.H. Rosenlof, R.W. Portmann, T.D. Thornberry, R.-S. Gao, S.M. Davis, E.T. Wolf, J. de Gouw, D.A. Peterson, M.D. Fromm, and A. Robock, Black carbon lofts wildfire smoke high into the stratosphere to form a persistent plume, ***Science***, ***365***, 587–590, doi:10.1126/science.aax1748, 2019.

Yu, P., S.M. Davis, O.B. Toon, R.W. Portmann, C.G. Bardeen, J.E. Barnes, H. Telg, C. Maloney, and K.H. Rosenlof, Persistent stratospheric warming due to 2019–2020 Australian wildfire smoke, ***Geophys. Res. Lett.***, ***48*** (7), doi:10.1029/2021gl092609, 2021.

Zawodny, J.M., and M.P. McCormick, Stratospheric Aerosol and Gas Experiment II measurements of the quasi-biennial oscillations in ozone and nitrogen dioxide, ***J. Geophys. Res.***, ***96*** (D5), 9371–9377, doi:10.1029/91jd00517, 1991.

Zeng, G., O. Morgenstern, P. Braesicke, and J.A. Pyle, Impact of stratospheric ozone recovery on tropospheric ozone and its budget, ***Geophys. Res. Lett.***, ***37*** (9), L09805, doi:10.1029/2010GL042812, 2010.

Zeng, G., O. Morgenstern, J.H.T. Williams, F.M. O'Connor, P.T. Griffiths, J. Keeble, M. Deushi, L.W. Horowitz, V. Naik, L.K. Emmons, N.L. Abraham, A.T. Archibald, S.E. Bauer, B. Hassler, M. Michou, M.J. Mills, L.T. Murray, N. Oshima, L.T. Sentman, S. Tilmes, K. Tsigaridis, and P.J. Young, Attribution of stratospheric and tropospheric ozone changes between 1850 and 2014 in CMIP6 models, ***J. Geophys. Res.***, ***127*** (16), e2022JD036452, doi:10.1029/2022JD036452, 2022.

Zerefos, C., J. Kapsomenakis, K. Eleftheratos, K. Tourpali, I. Petropavlovskikh, D. Hubert, S. Godin-Beekmann, W. Steinbrecht, S. Frith, V. Sofieva, and B. Hassler, Representativeness of single lidar stations for zonally averaged ozone profiles, their trends and attribution to proxies, ***Atmos. Chem. Phys.***, ***18***, 6427–6440, doi:10.5194/acp-18-6427-2018, 2018.

Zhang, J., W. Tian, F. Xie, M.P. Chipperfield, W. Feng, S.-W. Son, N.L. Abraham, A.T. Archibald, S. Bekki, N. Butchart, M. Deushi, S. Dhomse, Y. Han, P. Jöckel, D. Kinnison, O. Kirner, M. Michou, O. Morgenstern, F.M. O'Connor, G. Pitari, D.A. Plummer, L.E. Revell, E. Rozanov, D. Visioni, W. Wang, and G. Zeng, Stratospheric ozone loss over the Eurasian continent induced by the polar vortex shift, ***Nat. Commun.***, ***9***, 206, doi:10.1038/s41467-017-02565-2, 2018.

Zhang, J., W. Tian, F. Xie, W. Sang, D. Guo, M. Chipperfield, W. Feng, and D. Hu, Zonally asymmetric trends of winter total column ozone in the northern middle latitudes, ***Clim. Dyn.***, ***52***, 4483–4500, doi:10.1007/s00382-018-4393-y, 2019.

Zhang, Y., O.R. Cooper, A. Gaudel, A.M. Thompson, P. Nédélec, S.-Y. Ogino, and J.J. West, Tropospheric ozone change from 1980 to 2010 dominated by equatorward redistribution of emissions, ***Nat. Geosci.***, ***9***, 875–879, doi:10.1038/ngeo2827, 2016.

Zhang, Y., J.J. West, L.K. Emmons, J. Flemming, J.E. Jonson, M.T. Lund, T. Sekiya, K. Sudo, A. Gaudel, K.-L. Chang, P. Nédélec, and V. Thouret, Contributions of world regions to the global tropospheric ozone burden change from 1980 to 2010, ***Geophys. Res. Lett.***, ***48*** (1), doi:10.1029/2020gl089184, 2021.

Zhao, X., V. Fioletov, M. Brohart, V. Savastiouk, I. Abboud, A. Ogyu, J. Davies, R. Sit, S.C. Lee, A. Cede, M. Tiefengraber, M. Müller, D. Griffin, and C. McLinden, The world Brewer reference triad – updated performance assessment and new double triad, ***Atmos. Meas. Tech.***, ***14***, 2261–2283, doi:10.5194/amt-14-2261-2021, 2021.

Ziemke, J.R., S. Chandra, L.D. Oman, and P.K. Bhartia, A new ENSO index derived from satellite measurements of column ozone, ***Atmos. Chem. Phys.***, ***10***, 3711–3721, doi:10.5194/acp-10-3711-2010, 2010.

Ziemke, J.R., L.D. Oman, S.A. Strode, A.R. Douglass, M.A. Olsen, R.D. McPeters, P.K. Bhartia, L. Froidevaux, G.J. Labow, J.C. Witte, A.M. Thompson, D.P. Haffner, N.A. Kramarova, S.M. Frith, L.-K. Huang, G.R. Jaross, C.J. Seftor, M.T. Deland, and S.L. Taylor, Trends in global tropospheric ozone inferred from a composite record of TOMS/OMI/MLS/OMPS satellite measurements and the MERRA-2 GMI simulation, ***Atmos. Chem. Phys.***, ***19***, 3257–3269, doi:10.5194/acp-19-3257-2019, 2019.

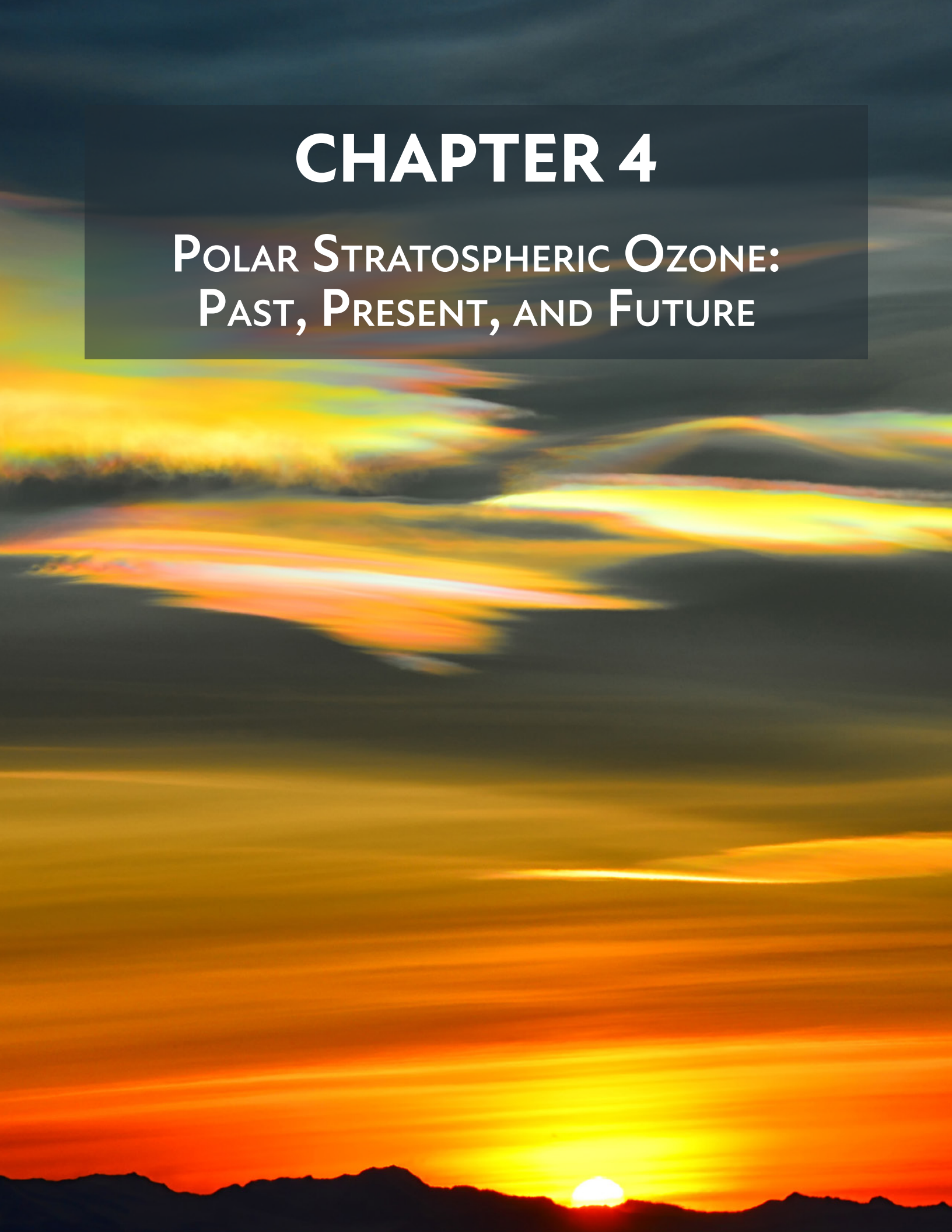

CHAPTER 4

Polar Stratospheric Ozone: Past, Present, and Future

About the cover image:
Polar Stratospheric Clouds (PCSs) form in the winter stratosphere at very low temperatures and can become visible with the arrival of sunlight in late winter. Chemical reactions on the surfaces of PSCs release halogen compounds which cause stratospheric ozone depletion in polar regions.

Photo credit: Ryan Skorecki, NSF via U.S. Antarctic Program Photo Library

CHAPTER 4

Polar Stratospheric Ozone: Past, Present, and Future

Lead Authors : Martyn P. Chipperfield
Michelle L. Santee

Coauthors : Simon P. Alexander
A. T. J. de Laat
Doug E. Kinnison
Jayanarayanan Kuttippurath
Ulrike Langematz
Krzysztof Wargan

Contributing Authors : Sandip S. Dhomse
Jens-Uwe Grooß
James Keeble
Zachary D. Lawrence
Gloria L. Manney
Rolf Müller
Eric Nash
Paul A. Newman
David A. Plummer
Sarah Safieddine
Ines Tritscher
Peter von der Gathen
Mark Weber
Ingo Wohltmann

Review Editors : Susan Solomon
Mark Weber

CONTENTS

Chapter 4: Polar Stratospheric Ozone: Past, Present, and Future

SCIENTIFIC SUMMARY

The chemical and dynamical processes controlling polar ozone are well understood. Polar ozone depletion is fundamentally driven by anthropogenic chlorine and bromine, with the severity of the chemical loss each year in both polar regions strongly modulated by meteorological conditions (temperatures and winds) and, to a lesser extent, by the stratospheric aerosol loading and the solar cycle. As noted in previous Assessments, the stratospheric halogen concentration resulting from the emissions of ozone-depleting substances (ODSs) reached its peak in the polar regions around the turn of the century and has been gradually declining since then in response to actions taken under the Montreal Protocol and its Amendments and adjustments. The 2018 Assessment reported for the first time that signs of the onset of ozone recovery from the effects of ODSs had been detected over the Antarctic. More varied and more robust signs of the onset of recovery are now beginning to emerge; as the observational record lengthens, ozone hole recovery trends are expected to continue to become clearer against the background of natural variability. Nevertheless, the Antarctic ozone hole will continue to be a recurring phenomenon until the middle of the century, although with a decreasing average size and some interannual variability. The Arctic is more dynamically variable, precluding identification of a significant increase in Arctic ozone. Cold conditions conducive to substantial stratospheric ozone loss occur in some Arctic winter/spring seasons and are expected to continue to do so, interspersed with warmer years with little or no ozone depletion. Chemistry-climate model (CCM) projections largely confirm previous studies that, in both hemispheres, springtime polar total column ozone (TCO) will return to 1980 historical levels around the middle of this century. For the Antarctic, the timing of this return depends mainly on the declining stratospheric halogen concentrations from decreasing ODS emissions, and the impact of climate change is small. In the Arctic, TCO is expected to return to 1980 levels earlier than in the Antarctic. This is because in the Arctic, springtime stratospheric ozone has a stronger dependence on the future greenhouse gas (GHG) emissions scenarios.

Observed changes in polar ozone

- **The Antarctic ozone hole continued to appear each spring during the 2018–2021 period.** The occurrence and character of recent ozone holes are consistent with the current concentrations of ODSs and their small overall downward trend.
- **Recent Antarctic ozone holes exhibited substantial interannual variability in size, strength, and longevity: the 2019 ozone hole was the smallest since 2002, whereas 2020 saw a deep ozone hole of record duration.** In 2019, a strong minor sudden stratospheric warming disrupted the evolution of the ozone hole, leading to the early termination of chemical ozone depletion and relatively high TCO. In contrast, in 2020 and 2021, weak atmospheric wave activity resulted in exceptionally persistent polar vortices. Despite decreasing ODS concentrations, the unusual dynamical state of the stratosphere in 2020 and 2021 induced large and long-lasting late spring ozone holes.
- **Recovery of Antarctic stratospheric ozone continues to progress.** New results since the 2018 Assessment support the findings reported at that time that the Antarctic ozone hole has diminished in size and depth since the year 2000. The remarkable Antarctic ozone holes in 2019, 2020, and 2021 do not challenge the findings of the emergence of recovery.
- **Arctic total ozone reached exceptionally low values in spring 2020.** A very stable, cold, and long-lived stratospheric polar vortex enabled halogen-catalyzed chemical ozone loss exceeding that observed during the previous record-breaking spring of 2011. The strong vortex also inhibited dynamical replenishment of ozone. The evolution of high-latitude ozone in 2020 is successfully reproduced by model simulations, further substantiating our understanding of polar ozone chemistry.
- **No statistically significant signature of recovery in Arctic stratospheric ozone over the 2000–2021 period has yet been detected.** Observed Arctic ozone trends remain small compared to the year-to-year dynamical variability.

Understanding of factors controlling polar ozone

- **An updated vortex-wide climatology of polar stratospheric cloud (PSC) occurrence and composition based on satellite data enabled advances in the understanding of particle formation mechanisms and trends.** Evidence that heterogeneous nucleation on preexisting ice particles or foreign nuclei, such as meteoritic particles, is the typical formation process for the nitric acid trihydrate (NAT) particles that lead to denitrification has been strengthened. PSC occurrence in the Arctic early winter significantly increased between the 1980s (1978–1989) and the recent past (2006–2018), while in the Antarctic, PSC occurrence was very similar in the two periods.
- **The broad range of polar springtime TCO in recent years in both hemispheres is largely explained by differences in the magnitude of the dynamical forcing.** Both the weak Antarctic ozone hole in 2019 and the record-low Arctic ozone in spring 2020 resulted from atypical dynamical conditions in the respective winters. Although exceptional, the evolution of polar ozone in both years was in line with current understanding of the chemical and dynamical factors controlling its abundance.
- **September, and especially the first half of that month, is the period when the impact of ODSs on stratospheric ozone over Antarctica can be quantified with the greatest certainty, and thus it represents the most suitable time window for monitoring ozone recovery.** Until recently, most studies of Antarctic ozone depletion trends focused on longer time windows or later ones that included

the months of October and November. New analyses indicate that September ozone has the largest sensitivity to decreasing ODSs, and September observations show the strongest and the statistically most significant Antarctic ozone recovery rates.

- **Model simulations with historical emissions scenarios indicate that decreasing atmospheric amounts of ODSs can explain the observed increase in Antarctic springtime ozone over the last two decades.** Model simulations indicate that if ODS concentrations had remained at the peak values attained in the late 1990s, recent polar springtime ozone loss in both hemispheres would have been ~20 DU (~10%) larger than currently observed. Model simulations of unabated ODS emissions (i.e., allowing for a 3–3.5% yr^{-1} increase in emissions since the mid-1980s) indicate that conditions similar to those currently observed over Antarctica would have occurred in the Arctic in years with unusually stable and long-lived stratospheric vortices, such as 2011 and 2020.
- **Future commercial supersonic or hypersonic aircraft fleets would cause stratospheric ozone depletion.** Both types of aircraft would potentially release substantial amounts of water vapor and nitrogen oxides (NO_x) into the stratosphere, with concomitant strong effects on stratospheric ozone arising primarily through enhancement of NO_x catalytic ozone destruction at cruise altitudes. This could reduce total column ozone by as much as 10%, depending on aircraft type and injection altitude, and would be most pronounced in the Northern Hemisphere polar region in spring and fall.

Future evolution of polar ozone

- **The Antarctic ozone hole is expected to gradually close. September multi-model mean (MMM) TCO from updated CCM projections, based on full compliance with the Montreal Protocol and assuming the baseline estimate of the future evolution of GHGs (SSP2-4.5), returns to 1980 values shortly after mid-century (about 2066, with a range between 2049 and 2077 arising from the spread in modeled dynamical variability).** The October TCO MMM returns two years earlier, with a similar uncertainty range.
- **The timing of the recovery of the ozone hole may be affected by anthropogenic climate change, with the MMM from updated CCM projections recovering approximately 15 years earlier for both SSP3-7.0 and SSP5-8.5 GHG scenarios.** This sensitivity of Antarctic return date to different climate change scenarios was not evident in projections presented in previous Assessments. The small set of CMIP6 models included in this Assessment makes interpretation of this scenario sensitivity difficult.
- **Arctic springtime total ozone is expected to return to 1980 values near mid-century (about 2045, with a range between 2029 and 2051), based on full compliance with the Montreal Protocol and assuming the baseline estimate of the future evolution of GHGs (SSP2-4.5).** This return date is around a decade later than projected by simulations in the previous Assessment using a different set of models and scenarios, but with considerable overlap of the large range. The timing of the recovery of Arctic TCO in spring will be affected by anthropogenic climate change. Consistent with previous Assessments, the new model simulations confirm that in the Arctic, dynamical changes induced by enhanced GHG concentrations cause an earlier return of TCO to historical values than do reductions in ODSs alone.
- **Future ozone depletion will be substantial in the Arctic during cold winters/springs as long as ODS concentrations are well above natural levels.** The projected strong increase in GHGs will cause cooling in the stratosphere. This effect, coupled with increases in stratospheric humidity from GHG warming of the tropical tropopause and increases in future tropospheric CH_4 emissions, will increase the potential for formation of PSCs in Arctic winter, leading to ozone loss.
- **Noncompliant production (e.g., of CFC-11) could delay the recovery of ozone to 1980 values by several years by slowing the rate of decline of stratospheric chlorine.** The magnitude of the delay depends on the total additional emissions. Additional emissions of 120–440 Gg of CFC-11 over the period 2012–2019 are estimated to delay the return to 1980 levels for Antarctic column ozone by 0.5–3.1 years. Emissions of uncontrolled very short-lived substances (VSLSs; e.g., chloroform [$CHCl_3$], dichloromethane [CH_2Cl_2]) could also extend the timeframe for polar ozone recovery by the same mechanism, with the impact dependent on the amount of chlorine delivered to the stratosphere. The future magnitudes of emissions from noncompliant production and anthropogenic VSLSs are highly uncertain.

4.1 INTRODUCTION

This chapter presents and assesses our knowledge of the past, present, and future of stratospheric ozone in Earth's polar regions (poleward of 60° latitude) based on the latest results from the peer-reviewed literature. It builds on the long series of similar chapters in previous Assessments. Substantial scientific effort has been dedicated to observing and understanding polar ozone changes, especially in the nearly 40 years since the discovery of the Antarctic ozone hole. Polar ozone remains an issue of great interest to policymakers and the general public alike. The focus of this chapter is to provide a concise update of new observations and understanding, including new results from numerical modeling, since Langematz, Tully et al. (2018), without repeating general background information that can be found in previous Assessments.

4.1.1 Summary of Findings from the Previous Ozone Assessment

Equivalent effective stratospheric chlorine (EESC; see *Chapter 1*) peaked around the year 2000 in the polar regions and has been slowly declining since then. At current EESC levels, interannual variability in the size and depth of the Antarctic springtime ozone hole is predominantly driven by meteorological conditions. Langematz, Tully et al. (2018) reported that the characteristics of recent ozone holes had continued to generally fall within the range observed since the early 1990s. However, a warm and unusually disturbed stratospheric polar vortex led to a weak ozone hole in 2017, whereas a cold and undisturbed vortex facilitated a strong and long-lasting hole in 2015. Aerosols from the Calbuco volcanic eruption in April of 2015 may have also contributed to the strong ozone depletion. Despite the severe hole in 2015, by the time of the 2018 Assessment, several lines of evidence had begun to emerge that indicated an increase in observed stratospheric ozone in the Antarctic during September, along with a decrease in the annual maximum ozone hole size and depth. Although the large degree of natural variability makes attribution of these changes challenging, the weight of evidence from statistical analyses and other observational and modeling studies suggested that the decline in EESC in response to controls on ozone-depleting substances (ODSs) under the Montreal Protocol and its Amendments and adjustments played a substantial role in those trends. In the Arctic, large year-to-year dynamical variations precluded robust detection of any recovery trend over the 2000–2016 period. Extreme meteorological conditions early in the 2015/16 winter induced rapid Arctic ozone loss, but a sudden stratospheric warming (SSW) at the beginning of March 2016 curtailed further chemical processing and kept ozone abundances from reaching values as low as those observed in spring 2011. Model simulations demonstrated that in both hemispheres, substantial benefit had already accrued from the controls imposed on ODS production. In the absence of the Montreal Protocol, a deep hole in the ozone layer would have developed during the exceptionally cold 2011 Arctic winter, smaller Arctic ozone holes would have occurred regularly, and the Antarctic ozone hole would have expanded considerably.

Knowledge of the processes controlling polar ozone continued to be refined in the 2018 Assessment (Langematz, Tully et al., 2018). Despite the fact that some detailed aspects of polar stratospheric cloud formation, the heterogeneous reactions that take place on their surfaces, and the cycles of catalytic ozone loss they enable remained unresolved, chemical transport models (CTMs) were generally able to successfully reproduce observed conditions, in particular the amount of ozone loss. Very short-lived substances (VSLSs) were found to make an important contribution to stratospheric halogen loading (e.g., around 25% of total bromine) and thus polar ozone destruction. Understanding of the dynamical control of polar ozone, especially the role of variability in planetary wave driving and the factors giving rise to that variability, had advanced since the 2014 Assessment. The impact of SSWs on Arctic ozone loss was specifically highlighted. The influence of energetic particle precipitation (EPP) related to solar variability, which can lead to substantial (10–15%) ozone loss in the middle and upper stratosphere, was also discussed. Although the resulting variation in total column ozone (TCO) is typically only a few percent, effects can persist for two to three years. Such EPP effects on ozone are not fully accounted for in most current chemistry-climate models (CCMs).

The 2018 Assessment (Langematz, Tully et al., 2018) made use of a new set of CCM simulations to provide updated estimates of the future evolution of polar ozone. These simulations confirmed previous findings on the expected behavior of ozone in both polar regions, with updates in the details of the timing of ozone recovery due to revised ODS scenarios. As in past Assessments, the return of polar ozone to 1980 levels was used as the principal metric for recovery. For the Antarctic, this was projected to occur around 2060. There was little influence from different climate scenarios because of the dominant signal of chemical depletion linked to stratospheric levels of chlorine and bromine and therefore ODSs. In contrast, Arctic springtime ozone showed a much earlier return to 1980 levels (2030s) due to dynamical influences, with a much larger dependence on assumed future climate change due to increasing greenhouse gases (GHGs).

Despite the detection of the onset of recovery in the Antarctic, and the CCM projections of a return to 1980 polar ozone levels by 2030–2060, Langematz, Tully et al. (2018) repeated the point made in earlier Assessments that under meteorological conditions conducive to chemical processing, the potential for large seasonal polar ozone depletion remained high in the near future in both hemispheres. The 2018 Assessment also noted that in the latter half of this century, the evolution of Arctic ozone will become increasingly dominated by GHGs through their climate and, in the case of methane (CH_4) and nitrous oxide (N_2O), chemical impacts.

4.1.2 Scope of Chapter

This chapter provides a concise update of the state of our knowledge of ozone in the polar regions of both hemispheres. The long-term record of meteorological conditions and ozone depletion in the polar vortices of both hemispheres is presented and updated for the years following the 2018 Assessment. The exceptional winter/spring seasons of 2019, 2020, and 2021 in the Antarctic and 2019/20 in the Arctic, characterized by anomalous dynamical states in the atmosphere, are considered in more detail. Progress in the understanding of the many chemical and physical processes underlying and influencing polar ozone depletion is then briefly summarized. Recent studies seeking to identify a statistically significant trend due to declining anthropogenic halogen levels (known as the second stage of Antarctic

ozone recovery, as set out in WMO, 2007) are discussed. Finally, the chapter presents a summary of the latest CCM projections of polar ozone over the 21st century from a combination of simulations performed under the auspices of different programs, including the WCRP Coupled Modelled Intercomparison Project 6 (CMIP6) and the SPARC/IGAC Chemistry-Climate Model Initiative (CCMI).

4.2 RECENT POLAR OZONE CHANGES

4.2.1 Measurements of Ozone and Related Constituents

Scientific study of polar ozone relies on the long-term record of measurements of ozone and related constituents from ground-based, balloon-borne, airborne, and satellite instruments, in conjunction with meteorological reanalyses. These measurement programs have largely been maintained since the previous Assessment.

Long-standing ground-based and balloon measurements of both total column and vertically resolved ozone have continued under the WMO Global Atmosphere Watch and its contributing network, NDACC (Network for the Detection of Atmospheric Composition Change). Observational data from these networks are freely available from the NDACC database (http://ndacc-demo.org) and the World Ozone and Ultraviolet Radiation Data Centre (www.woudc.org). (See also **Table 3A-2** for a list of ground-based ozone total column and profile measurements considered in *Chapter 3*.)

A summary of available satellite measurements of ozone and related constituents in polar regions was provided in Table 3A-1 of Dameris, Godin-Beekmann et al. (2014), with only a few changes in availability since then. However, as noted in more detail in *Section 3.1.3*, it is expected that a number of currently operational spaceborne instruments whose measurements have been central to the Assessment process will have ceased collecting data by the time of the 2026 Assessment. In particular, the loss of vertically resolved satellite measurements of many trace gases relevant for polar chemistry and dynamics, including ozone itself during polar night, will hinder the ability to monitor and explain changes in polar stratospheric ozone in the future.

4.2.2 Evolution of Polar Temperatures and Vortex Characteristics

4.2.2.1 Use of Reanalyses in Polar Process Studies

Lower-stratospheric polar processes (i.e., polar stratospheric cloud [PSC] formation, denitrification and dehydration, heterogeneous chlorine activation and deactivation) and chemical ozone loss are "threshold" phenomena that depend critically on meteorological conditions. Therefore, polar processing studies often rely heavily on global meteorological datasets, generally using reanalysis datasets as input or as a constraint. Atmospheric reanalysis systems provide gridded datasets representing the best estimates of the past state of the atmosphere (e.g., temperature, wind, humidity, and other meteorological parameters) that are generated by combining information from global forecast models with observations. It is thus essential to understand the accuracy and reliability of reanalysis data for polar processing studies. The WCRP SPARC Reanalysis Intercomparison Project (S-RIP) recently coordinated a comprehensive intercomparison of a broad set of representative diagnostics in major global atmospheric reanalysis datasets (e.g., Fujiwara et al., 2017; SPARC, 2022). One focus of S-RIP was to evaluate diagnostics relevant to polar chemical processing and dynamics, primarily targeting winter conditions in the lower stratosphere, to examine five modern reanalyses: MERRA, MERRA-2, ERA-Interim, JRA-55, and CFSR/CFSv2 (see Fujiwara et al., 2017, for a detailed overview of these reanalysis systems, including key references). The main findings from that evaluation are summarized here. (See also Figure 10.26 of SPARC (2022) for a table encapsulating the overall performance of each reanalysis for many of the polar processing diagnostics considered.)

Any of the recent full-input reanalyses (i.e., systems that assimilate surface and upper-air conventional and satellite data) can be used with confidence in studies of lower-stratospheric polar processing. Temperature biases and other artifacts in older meteorological reanalyses often rendered them unsuitable for investigations of polar stratospheric chemical processing and dynamics; in particular, ERA-40, NCEP-NCAR R1, and NCEP-DOE R2 (e.g., Fujiwara et al., 2017, and references therein) are obsolete and should no longer be used in such studies. However, polar winter temperatures from modern reanalyses agree much more closely with one another than did those from older systems, with a marked convergence to better agreement, especially in the Southern Hemisphere, after 1999, when reanalysis systems switched from assimilating TOVS to ATOVS radiances. Reanalyses generally match well in the Antarctic for many polar temperature and vortex diagnostics. With their extremely cold conditions and relatively small interannual variability, Antarctic winters tend to have similar chemical processing potential and duration every year, keeping sensitivity to differences in meteorological conditions between the reanalyses low. Average absolute differences from the reanalysis ensemble mean in wintertime daily minimum temperatures poleward of 40°S are usually less than 0.5 K in the post-1999 period. Similarly, in recent years, average absolute differences in the area of the Southern Hemisphere with temperatures below PSC thresholds (A_{PSC}) are within ±0.5% of the area of the hemisphere, or ~5% of the typical Antarctic A_{PSC} of 10% of the hemisphere, and average relative differences from the reanalysis ensemble mean in the fraction of the vortex volume with temperatures below PSC thresholds are ~10% of typical values (Lawrence et al., 2018). In contrast, wintertime meteorological conditions in the Arctic are frequently marginal for PSC formation, and interannual variability is large, increasing the sensitivity of polar temperature and vortex diagnostics to reanalysis differences. Average relative differences from the reanalysis ensemble mean in the area and volume of the Northern Hemisphere with temperatures below PSC thresholds are ~10% and ~15% of typical values, respectively (Lawrence et al., 2018).

To explore how the spatially and temporally varying differences between reanalyses interact to affect the bottom-line conclusions of typical polar processing studies, SPARC (2022) examined simulations from a single CTM driven by different reanalyses. Although the individual model realizations show largely similar behavior through most of the season in both polar regions for most species, substantial disparities between model runs using different reanalyses develop where composition gradients are largest. For example, comparisons with satellite long-lived

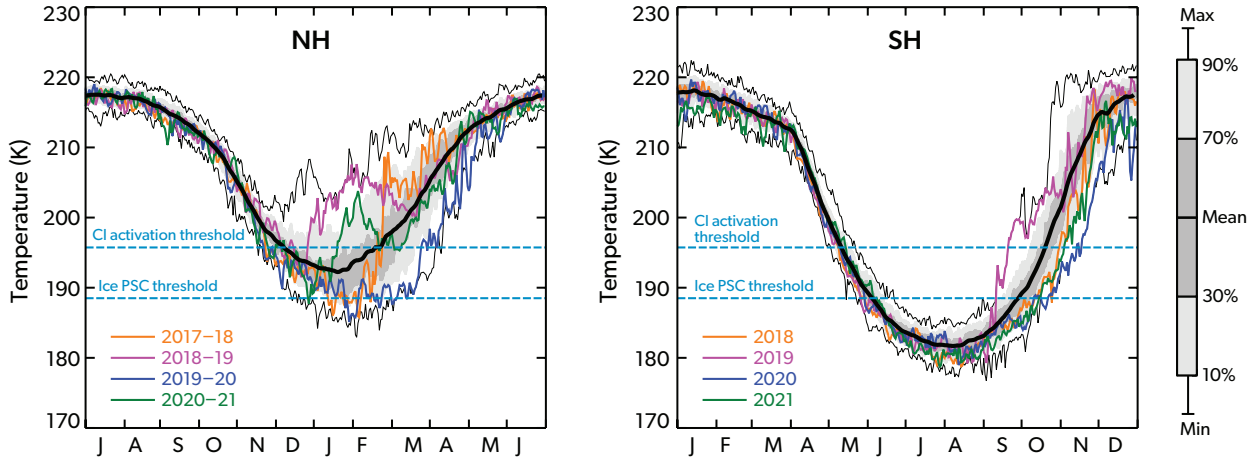

Figure 4-1. The annual cycle and variability of 50 hPa minimum temperature for the *(left)* Northern Hemisphere (NH; 50–90°N) and *(right)* Southern Hemisphere (SH; 50–90°S) polar caps, from MERRA-2 reanalysis data (Gelaro et al., 2017). The thick black line indicates the mean of observations since 1979, while light (dark) shading indicates the 10–90% (30–70%) percentiles. Thin black lines show the record maximum and minimum values. Horizontal blue lines indicate the chlorine activation threshold and ice PSC formation threshold. Data are for 1978/79–2020/21 for the Northern Hemisphere and 1979–2021 for the Southern Hemisphere. [Updated from Figure 4-1 in the 2018 Assessment, with data sourced from ozonewatch.gsfc.nasa.gov.]

tracer measurements indicate that the CTM underestimates the strength of confined diabatic descent inside both winter polar vortices for most of the reanalyses, compromising the fidelity of simulated trace gas distributions. Finally, SPARC (2022) reported results from a case study comparing measured and modeled Antarctic ozone loss. Estimates of chemical ozone loss based on satellite measurements were found to be relatively insensitive to the choice of reanalysis used to interpolate the data to isentropic surfaces and to identify the vortex boundary. However, forcing the same model with different reanalyses yields differences in simulated loss in the Antarctic vortex core that can reach as high as ~25 DU (~20–30%), depending on the specific reanalyses being compared.

Although agreement in polar temperatures is generally good, substantial differences between reanalyses are found for some diagnostics. Therefore, whenever feasible it is best to employ multiple reanalyses, even in studies involving recent winters, for which differences between reanalyses are usually small. Use of more than one reanalysis dataset is of particular value for quantities that cannot be directly compared with observations, as it allows estimation of uncertainties and their potential impact on the results. In light of the limitations in earlier reanalyses, some modeling studies have enacted systematic temperature adjustments of 1–2 K or more in an attempt to reproduce observed conditions. Given the accuracy of current polar reanalysis temperatures, strong justification is needed in any studies seeking to ascribe deficiencies in modeled polar processing or ozone loss to reanalysis temperature biases. Finally, reanalysis temperatures are generally unsuitable for quantification of long-term trends in temperature-based diagnostics, especially those encompassing years prior to 1999. Diagnostics that aggregate low temperatures over months and/or vertical levels (e.g., the winter-mean fraction of the vortex volume with air cold enough for PSCs to exist; see *Section 4.2.2.2*) are particularly problematic as they are highly sensitive to the specific temperature thresholds used to define polar processing potential. The differences between the reanalyses in such diagnostics reflect not only any overall temperature biases but also the differing morphology and spatial gradients of the reanalysis fields (as well as the seasonal evolution and interannual variability thereof). Consequently, winter-mean derived diagnostics can vary widely from one reanalysis to another even if differences in the reanalysis temperatures themselves are relatively small (Lawrence et al., 2018).

4.2.2.2 Temperatures and PSC Volume

The annual cycle of polar ozone depletion depends strongly on stratospheric temperature. Low temperatures present in the winter stratosphere permit the formation of PSCs, upon whose surfaces heterogeneous reactions occur. **Figure 4-1** shows the annual temperature cycle over the satellite era (1979–present) of the 50 hPa polar cap temperature. The four recent winters are highlighted in colors for both the Arctic and Antarctic.

The larger interannual variability in polar temperatures in the Arctic than in the Antarctic is well known and understood in terms of planetary-scale atmospheric dynamics. Recent Arctic winter polar temperatures have been outside the 10–90% percentile envelope. The warm and disturbed 2018/19 vortex was followed by a cold and stable 2019/20 vortex (Lawrence et al., 2020), with 50 hPa polar cap temperatures in 2019/20 hovering around the ice PSC formation temperature for extended periods of time. The 2017/18 and 2020/21 vortex temperatures were closer to the mean, although warming during midwinter 2020/21 and a cold midwinter vortex during 2017/18 were observed.

The more stable nature of the Antarctic vortex during midwinter is clearly apparent in the less variable temperatures. An exception to this pattern occurred in 2019, when the Antarctic vortex was unusually warm and disturbed. In that year, a minor sudden stratospheric warming (SSW; Newman et al., 2020; Klekociuk et al., 2021) resulted in polar temperatures setting record warm

levels during September, exceeding those observed during the 2002 major SSW. The 2019 warming was classified as a minor SSW because the 10 hPa zonal-mean zonal winds did not reverse. The following year, 2020, had a very cold, stable, and long-lasting vortex, with record-low temperatures persisting for much of the spring (into December; Klekociuk et al., 2022).

The potential for ozone depletion throughout the season can be quantified by the time-integrated PSC volume, V_{PSC}, which is calculated between the 400 K and 700 K isentropic surfaces, where heterogeneous ozone loss typically occurs (e.g., Rex et al., 2006; Strahan et al., 2016). Interannual variability in V_{PSC} is large in the Arctic (**Figure 4-2**), reflecting the interannual variability of Arctic vortex-wide temperatures and, specifically, variability in when those temperatures fall below the PSC formation threshold. It is also evident from **Figure 4-2** that recent cold Arctic winters, with a large V_{PSC} and relatively severe ozone depletion (e.g., 2019/20), are interspersed with warmer winters with much lower V_{PSC} (e.g., 2018/19).

The long-term evolution of PSC volume in the Arctic has been a topic of discussion in the last several Assessments. The 2006 Assessment (Newman, Rex et al., 2007) discussed analyses indicating that cold Arctic winters had become colder over the preceding 40 years, resulting in larger V_{PSC} and more chemical ozone loss. Absent a new maximum in V_{PSC} in the intervening years, it was not possible to confirm the continuation of increasingly severe extreme V_{PSC} values in the 2010 Assessment (Douglass, Fioletov et al., 2011). By the time of the 2014 Assessment (Dameris, Godin-Beekmann et al., 2014), several studies had cast doubt on the statistical robustness of the long-term trend in extreme V_{PSC} values discussed by Newman, Rex et al. (2007). Noting that no in-depth analyses had been undertaken since 2014, the 2018 Assessment stated that large interannual variability precluded detection of a significant trend in V_{PSC} (Langematz, Tully et al., 2018). A recent study revisited the issue of whether the coldest Arctic winters are getting colder by examining trends in PSC formation potential (PFP), which represents the number of days a volume of air equal to the volume of the polar vortex is exposed to conditions cold enough to allow the existence of PSCs in a given Arctic ozone-loss season (von der Gathen et al., 2021). Analyzing data from four meteorological reanalyses (see also **Figure 4-2**), they found statistically significant positive trends in maximum PFP values. Von der Gathen et al. (2021) concluded that the vortex has tended to experience conditions conducive to PSC formation for 3.5 to 4.8 more days per decade during the coldest Arctic winters over the past half-century.

4.2.2.3 Polar Vortex Breakup Dates

The polar vortex decays and breaks up during spring as a result of the return of sunlight warming the stratosphere and by planetary wave forcing. As noted in previous Assessments (e.g., Langematz, Tully et al., 2018), various metrics are used to define when the final warming (or vortex breakup date) occurs (e.g., Nash et al., 1996; Charlton and Polvani, 2007; Haigh and Roscoe, 2009; Hu et al., 2014; Lawrence et al., 2018; Butler et al., 2019; Butler and Domeisen, 2021; Hauchecorne et al., 2022). These metrics include a vortex area threshold, a wind speed along the vortex edge threshold, and the timing of the complete and final wind reversal to easterlies at 10 hPa. Defining the vortex breakup date as the last day on which the vortex area exceeds 1% of the hemispheric area, Lawrence et al. (2018) reported larger differences between reanalyses in breakup date above the Antarctic than above the Arctic, which they attributed to differences in vortex area between the reanalyses. A recent study of the seasonal evolution of the Antarctic vortex edge based on reanalysis data found later breakup dates (and, to a lesser extent, earlier onset dates) during the 1980s and 1990s, at the time the ozone hole was intensifying (Lecouffe et al., 2022).

Figure 4-3 shows the vortex breakup date for both polar caps. Here the breakup date is calculated using a threshold for the average wind speed along the vortex edge, following Nash et al.

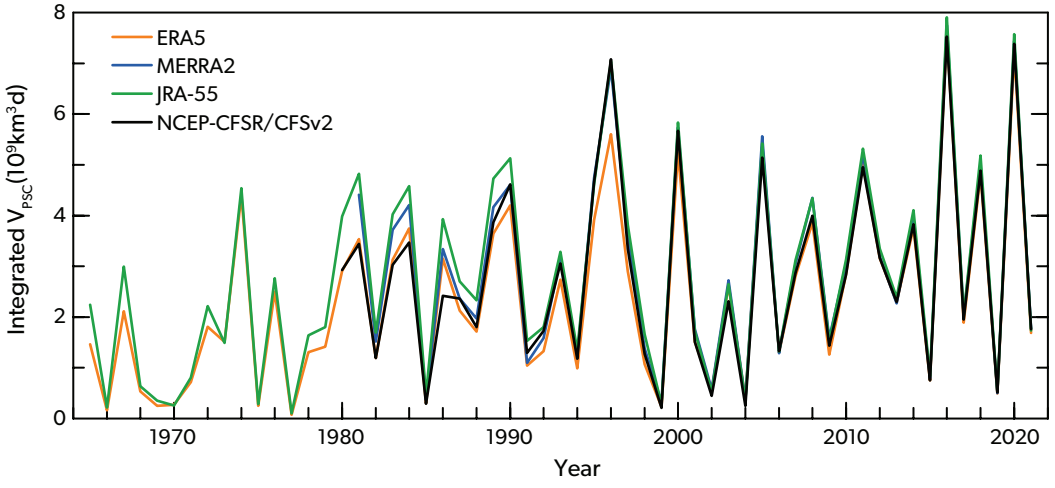

Figure 4-2. The Arctic time-integrated PSC volume, V_{PSC}, calculated using the method of Rex et al. (2006) for the four indicated reanalysis products. The V_{PSC} values are integrated from 1 November until 30 April for each Arctic PSC season. The ERA5 result is a combination of ERA5-BE (preliminary version, prior to 1979), ERA5, and ERA5.1 (2000–2006). [Updated from Figure 4-2 in Langematz, Tully et al., 2018.]

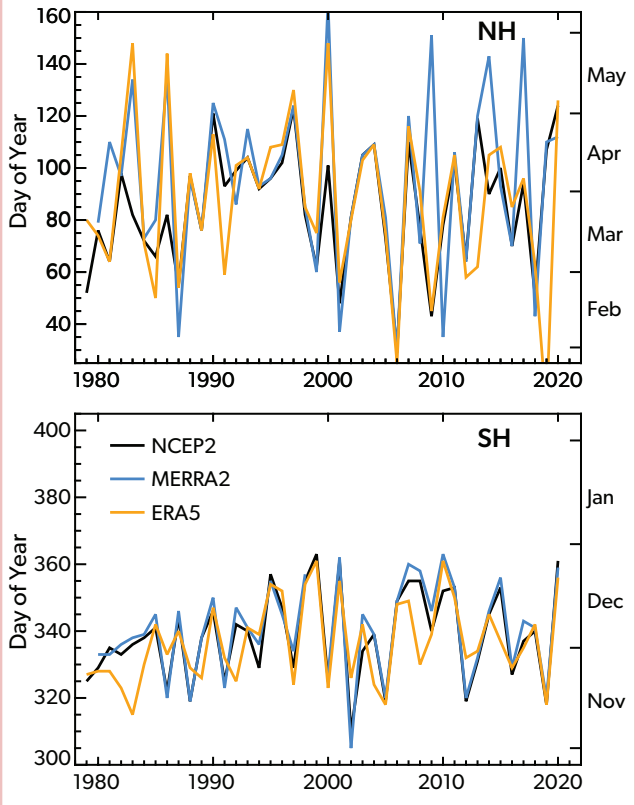

Figure 4-3. The Arctic and Antarctic vortex breakup dates, defined as the date on which the wind speed on the 500 K isentropic surface falls below 15.2 m s^{-1}, following Nash et al. (1996). Reanalysis data are from ERA5 (Hersbach et al., 2020) except for the period 2000–2006, for which data are from ERA5.1; MERRA-2 (Gelaro et al., 2017); and NCEP/CFSR (Saha et al., 2010). [Updated from Figure 4-3 in Langematz, Tully et al., 2018.]

(1996). The interannual variability of both polar vortices' breakup dates remains similar to that reported in the previous Assessment (Langematz, Tully et al., 2018). For some Arctic winters, the breakup dates are markedly different between the reanalyses, likely because of their differences in stratospheric winds (Butler et al., 2017), resulting in differences in the dates that a specific wind threshold is reached.

4.2.3 Ozone Depletion in Recent Antarctic Springs (2018–2021)

Figures 4-4 to **4-6** show updates for both hemispheres of several diagnostics of the multidecadal evolution of springtime polar ozone that have been discussed in previous Assessments. The agreement among the data from the different satellite sensors used to generate these figures is generally within 2% (McPeters et al., 2008, 2015). This range is much less than the interannual variability of the diagnostics shown. **Figure 4-4** shows the evolution of TCO averaged over the polar cap, poleward of 63°S/N, in October for the Antarctic and in March for the Arctic. The edge of the lower-stratospheric portion of the polar vortex, which encloses the ozone hole, typically lies near 63°S in October, except in years when the vortex is strongly deformed. This is not the case in the Northern Hemisphere, where dynamical variability in the springtime stratosphere is large. Highly variable contributions from mid-latitude air masses affect daily average polar cap ozone and, to some degree, the March averages shown in **Figure 4-4**.

Springtime chemical ozone depletion occurs within the polar vortex. To account for dynamical variations of the vortex edge, Dameris, Godin-Beekmann et al. (2014) introduced a dynamical diagnostic of polar ozone defined as the October/March minimum of the daily total ozone averaged poleward of 63° equivalent latitude (Butchart and Remsberg, 1986), which approximates the edge of the polar vortex in the lower stratosphere. The 63° equivalent latitude contour encloses the same area as the 63° parallel, but its shape and position are dynamical and follow the movements and undulations of the polar vortex. **Figure 4-5** shows an updated version of the time series of this quantity. While each metric is useful for specific applications, the equivalent latitude-based minimum average ozone was found to better correlate, on interannual time scales, with chemical ozone depletion than does the polar cap average (Müller et al., 2008). A more extensive discussion of these diagnostics and their limitations is given in Dameris, Godin-Beekmann et al. (2014).

Three additional diagnostics (**Figure 4-6**) are presented here in order to characterize other aspects of long-term changes and interannual variability in springtime Antarctic ozone in relation to changing ODS concentrations. These are as follows: time-averaged ozone hole area, total ozone minimum, and ozone mass deficit (OMD). The last is the amount of ozone in units of mass needed to bring the total column up to 220 DU and, therefore, combines information about the area and depth of ozone holes. Also shown in **Figure 4-6** are quadratic fits of these quantities to EESC. Several other metrics of the long-term evolution of Antarctic ozone have also been proposed (e.g., Pazmiño et al., 2018; Stone et al., 2021). Starting with the 2014 Assessment, the question of which metrics are the most appropriate for detecting and quantifying Antarctic ozone recovery has been the subject of extensive scientific debate. For example, it is important to consider the calendar periods over which such metrics are calculated, because results based on a single month are not necessarily representative of the entire season, nor are they sufficient for comprehensive analyses of long-term changes. The ongoing scientific debate seeks to reevaluate some of the standard polar ozone diagnostics and identify ones that are best suited for trend studies in the period of ozone recovery. *Section 4.4.2* summarizes the background and the current state of this debate. To provide context for the most recent Antarctic and Arctic springs, the standard metrics shown in **Figures 4-4** to **4-6** are sufficient. They are used in this chapter only as a starting point of a more comprehensive analysis of specific years and provide the added value of connecting the present discussions with previous Assessments.

Evident in **Figures 4-4** to **4-6** is the well-known decline in Antarctic ozone during the 1980s and 1990s, followed by two decades of increased interannual variability and no readily discernible trend in most of the diagnostics. Only OMD exhibits a clear decrease since around 2000 that, together with the initial increase, follows the evolution in EESC (see *Section 4.4.2* for a detailed discussion of Antarctic ozone trends). Compared to **Figure 4-4**, **Figure 4-5** exhibits less variability in the Southern Hemisphere. This is expected because, unlike time-averaged quantities, minima are less sensitive to the dynamically controlled

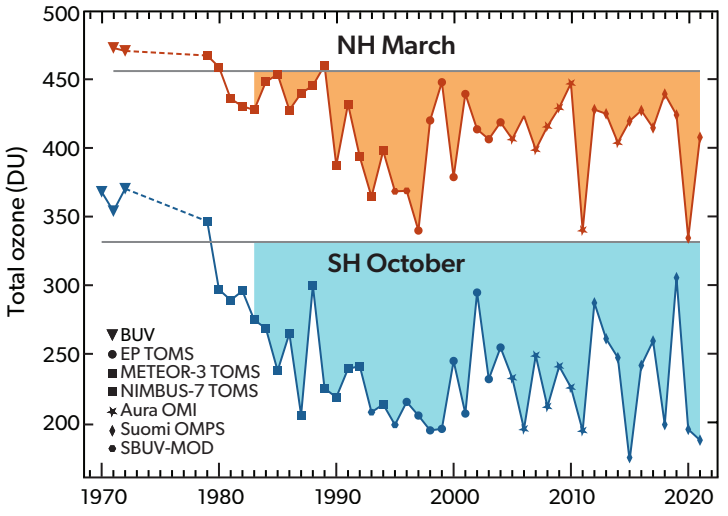

Figure 4-4. Total column ozone (Dobson units) averaged over 63–90° latitude in March (Northern Hemisphere [NH]) and October (Southern Hemisphere [SH]). Symbols indicate the satellite data that have been used in different years. The horizontal gray lines represent the average total ozone for the years prior to 1983 in March for the NH and in October for the SH. [Updated from Figure 4-4 in Langematz, Tully et al., 2018.]

and highly variable ozone evolution throughout the month. In addition, the use of equivalent rather than geographic latitude reduces the contributions to the daily averages of air masses outside the polar vortex.

Average October polar cap ozone was particularly high in 1988, 2002, 2012, and 2019 because of anomalously high lower-stratospheric temperatures. In 2002, the warmer temperatures were associated with the only major SSW (defined as a reversal of the 10 hPa zonal-mean zonal wind at 60° latitude) ever observed in the Southern Hemisphere. The minimum of daily ozone (**Figure 4-5**) was anomalously high in 1988, 1993, 2002, and 2019 because of high wave activity in the mid-latitude stratosphere in these years (*Section 4.3.4*). A peak is also present in 2012 but is less pronounced; this is consistent with the observed total ozone values, which were only slightly elevated at the beginning of October 2012 and then increased rapidly shortly thereafter, thus affecting the monthly mean but not the minimum. The lowest October mean polar cap total ozone was observed in 2015 (**Figure 4-4**). This low anomaly is attributed to enhanced heterogeneous chemistry on sulfate aerosols from the Calbuco volcanic eruption in April within the setting of a very cold and stable polar vortex that resulted from weak wave activity between July and October (Langematz, Tully et al., 2018). The most extreme year, when all of these metrics are considered, was 2019, when a minor SSW led to the highest values of Antarctic polar cap ozone (**Figure 4-4**), the highest minimum of the daily average in equivalent latitude (**Figure 4-5**), and the highest time-averaged daily ozone minimum as well as the smallest ozone hole and the lowest OMD in the 21st century (**Figure 4-6**). See *Section 4.2.3.2* for further discussion of the 2019 Antarctic winter.

Since the last Assessment, springtime Antarctic ozone exhibited significant year-to-year dynamically driven variations. The polar cap total ozone ranged from anomalously low in 2018 and 2020 to record high in 2019 (Kramarova et al., 2019, 2020; Wargan et al., 2020; Safieddine et al., 2020). To assist in analyzing the development of the most recent ozone holes in the

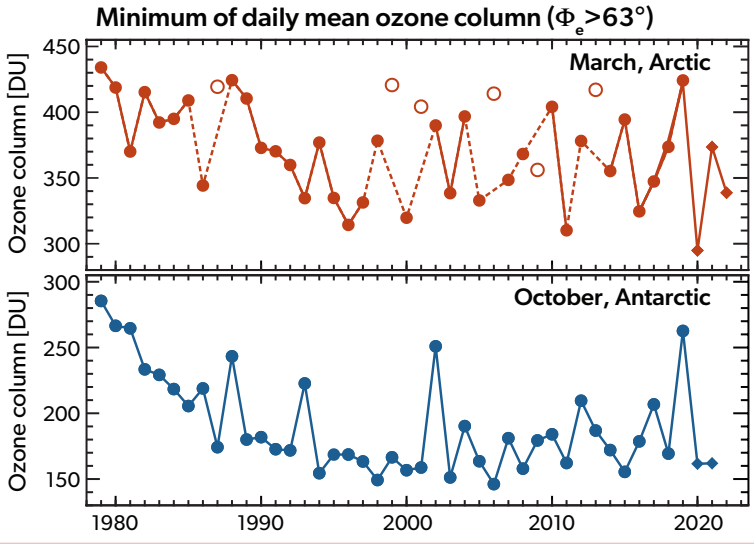

Figure 4-5. Minimum of the daily average total column ozone (Dobson units) poleward of the 63° contour of equivalent latitude (Φ_e) in *(top)* March in the Arctic and *(bottom)* October in the Antarctic. Arctic winters in which the polar vortex broke up before March (1987, 1999, 2001, 2006, 2009, and 2013) are shown by open symbols; dotted lines connect surrounding years. [Adapted from Langematz, Tully et al., 2018. Updated using the Bodeker Scientific combined total column ozone database (version 3.5.1, circles; Müller et al., 2008) until 2019 and Aura OMI measurements thereafter (diamonds).]

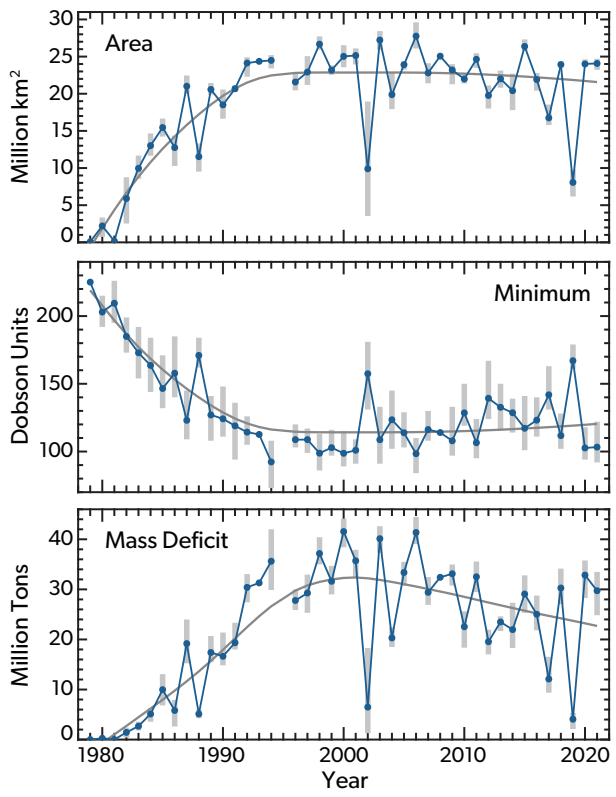

Figure 4-6. *(top)* Antarctic ozone hole area for 1979–2021, averaged from daily total ozone area values contained by the 220 DU contour for 21–30 September. *(middle)* An average of daily minimum total column ozone values over Antarctica during the period from 21 September to 16 October. *(bottom)* Ozone mass deficit averaged over the 21–30 September period. For all three panels, the vertical gray bars indicate the range of values over the same periods. The dark gray curves show the quadratic fits of each quantity to EESC as described in Newman et al. (2004). The EESC is derived as in Newman et al. (2007), updated with the current A1 baseline scenario. A mean age of 5.5 years, an age spectrum width of 2.75 years, and a bromine-scaling factor of 65 are assumed. In the polar regions, this EESC estimate is very similar to that derived by Engel et al. (2018) and used in *Chapter 1*. This figure was generated from TOMS (1979–2004), Aura OMI (2005–2015), and Suomi NPP OMPS (2016–2021) data. [Updated from Figure 4-6 in Langematz, Tully et al., 2018.]

following subsections, two additional figures are shown. **Figure 4-7** plots the daily values of OMD (top panel) for the years 2018 to 2021, as well as for the anomalous year 2002, along with their climatological statistics. This figure is a modified and updated version of plots shown in previous Assessments. In addition to the climatological range, the present version of the graph includes selected percentile envelopes, where all statistics are calculated over the 1980–2021 period. This differs from previous Assessments, for which the statistics were calculated starting in 1990 and the three most recent years in each case were excluded.

Figure 4-8 shows the evolution of several key species involved in chemical processing inside the lower-stratospheric polar vortex and in ozone depletion. In addition to ozone (O_3), the figure plots daily vortex-average concentrations of nitric acid (HNO_3), water vapor (H_2O), hydrogen chloride (HCl), and chlorine monoxide (ClO). Changes in HNO_3 and H_2O are sensitive to temperature: At sufficiently low temperatures, gas-phase HNO_3 and H_2O undergo condensation, leading to the formation of PSCs (see *Section 4.3.1*), which in turn can lead to denitrification and dehydration of the polar lower stratosphere. Changes in HCl and ClO quantify chlorine activation, with low HCl and high ClO indicating the presence of ozone-destroying active chlorine.

4.2.3.1 Antarctic Spring 2018: Moderately Large Ozone Hole

The 2018 ozone hole area, daily minimum, and OMD, while indicative of below-average ozone, are all within the range of values observed during the other years of last decade (**Figure 4-6**). In September, OMD began to diverge from its climatological mean, reached the 70th percentile by mid-month, and remained relatively high until late October (**Figure 4-7**). The evolution of the ozone hole area followed a similar trajectory, with values consistently higher than the long-term average (Wargan et al., 2020). These relatively high values of OMD and area are consistent with the meteorological conditions in the stratosphere in 2018. Minimum high-latitude temperatures were below average for parts of the austral winter and almost all of October (**Figure 4-1**), leading to high PSC volumes in July and August (Kramarova et al., 2019).

Stratospheric temperatures and the strength of the polar vortex on seasonal time scales are largely controlled by extratropical wave activity (*Section 4.3.4*). The lower panel of **Figure 4-7** shows time series of eddy heat flux between 45 and 75°S. This metric serves as a measure of upward propagation of Rossby waves in the lower stratosphere. The weakly negative values between August and October 2018 indicate low wave activity and are consistent with a strong, large, and cold polar vortex. Despite low temperatures and significant PSC volume, HCl and ClO in the Antarctic in 2018 were well within the 2005–2017 range throughout the winter/spring season, with no evidence of unusually strong chlorine activation (**Figure 4-8**). This suggests that the observed low ozone anomaly was at least in part the result of anomalous transport, likely with weak ozone resupply from higher altitudes, consistent with low wave activity.

Model simulations with the Global Modeling Initiative chemistry model driven by assimilated meteorology realistically reproduce the development of the 2018 ozone hole after accounting for a known constant bias. The same model setup but with the EESC values held constant at their maximum surface levels in 1995 produces an ozone hole more than 4 million km^2 (17%) larger than observed, highlighting the role of the Montreal Protocol and its Amendments and adjustments in reducing the severity of the 2018 ozone hole (Kramarova et al., 2019; see also *Section 4.4.4*).

4.2.3.2 Antarctic Spring 2019: Impact of the Strong Minor Sudden Stratospheric Warming

A significant disturbance of the typically quiescent Antarctic stratosphere commenced at the end of August 2019 with a wavenumber-1 displacement of the middle and upper portion of the

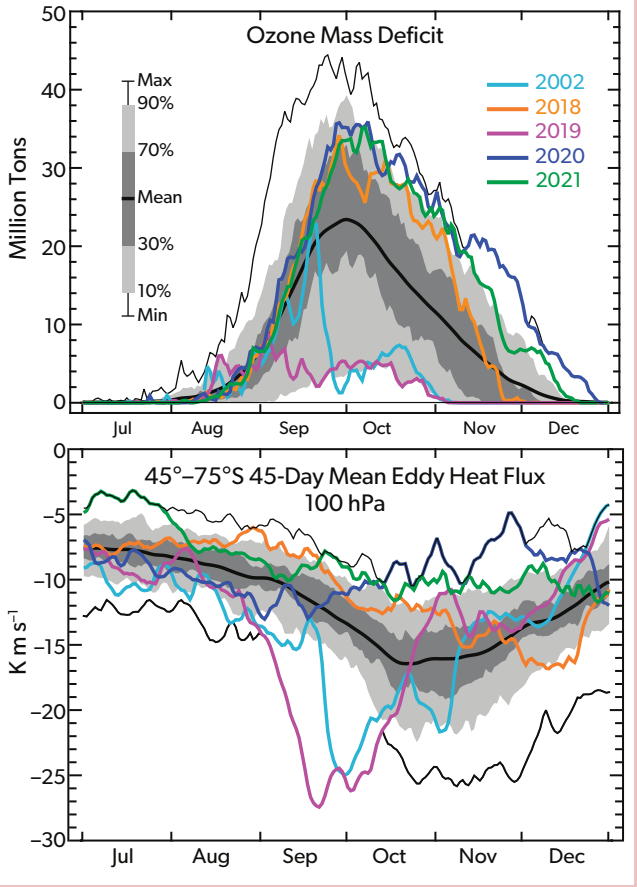

Figure 4-7. *(top)* Daily ozone mass deficit (OMD) for various years compared with selected percentiles calculated over the period 1980–2021 (gray shaded areas) and the maximum values for the same period (thin black lines). The thick black line shows the 1980–2021 OMD average. OMD was calculated using data from TOMS, Aura OMI, and Suomi NPP OMPS. [Updated from Figure 4-7 in Langematz, Tully et al. (2018).] *(bottom)* As above but for the 45-day mean eddy heat flux at 100 hPa averaged between 45°S and 75°S. Eddy heat flux at this level is a metric of upward wave propagation in the stratosphere. Highly negative values correspond to strong wave activity. The heat fluxes are derived from MERRA-2. The results from this particular reanalysis serve as an illustrative example.

polar vortex that was accompanied by a significant reduction in vortex size (Hendon et al., 2019; Yamazaki et al., 2020; Liu et al., 2022). This strong, albeit formally minor, SSW resulted in anomalously high polar ozone and a small ozone hole area (**Figures 4-4** to **4-7**; Safieddine et al., 2020; Wargan et al., 2020; Kramarova et al., 2020; Bodeker and Kremser, 2021; Klekociuk et al., 2021). Average ozone hole area, daily ozone minimum, and OMD in 2019 all exhibited larger anomalies than observed following the major (that is, characterized by a reversal of the zonal-mean zonal wind at 60° latitude in the middle stratosphere) SSW of 2002. While declining ODS concentrations contributed to the high Antarctic ozone in 2019, the SSW was the primary cause of the anomaly (Kramarova et al., 2020).

In 2019, the SSW was preceded by a poleward shift of the polar night jet around the stratopause, resulting in a persistent easterly anomaly that started in early winter (Lim et al., 2021). The minor warming in late August was triggered by a strong upward propagating wave flux of tropospheric origin amplified by constructive interference with climatological wave-one pattern (Shen et al., 2020). Energy and momentum were provided by a strong and long-lived mid-latitude circumpolar Rossby wave train in the troposphere in 2019. This wave train is attributed to sustained convection over the subtropics resulting from warm sea surface temperature anomalies associated with a simultaneous occurrence of a positive phase of the Indian Ocean Dipole and El Niño-like conditions in the Pacific (Shen et al., 2020; Rao et al., 2020). It is estimated that the wave driving in 2019 was stronger than that in 2002 (Liu et al., 2022). The SSW was enabled by a favorable phase of the quasi-biennial oscillation and solar minimum conditions (Rao et al., 2020). The existence of these precursor conditions allows long lead-time predictability of the SSW (up to 18 days), underscoring a highly accurate representation of the underlying mechanisms in modern subseasonal-to-seasonal ensemble prediction models (Rao et al., 2020). The unusually high wave activity and its effects on ozone are seen in **Figure 4-7** (bottom and top panel, respectively). The 2019 event was the strongest disturbance of the Antarctic stratospheric polar vortex since 2002, when the only SSW in the Southern Hemisphere classified as major was observed (Newman, Rex et al., 2007). The two events exerted comparable and significant impacts on ozone. This important observation implies that, as has been demonstrated previously for the Northern Hemisphere (Manney et al., 2015), the classification of SSWs as major or minor, while useful, does not automatically characterize the magnitude of their impacts on ozone. The 2019 ozone hole was the smallest in the 21st century and one of the smallest ever observed in October (**Figures 4-4** and **4-6**). The minimum of the daily average total column ozone (TCO; **Figure 4-5**) was also very high, in part because the polar vortex edge was no longer well approximated by the 63°S equivalent latitude contour after the SSW.

Figure 4-9 (top panel) shows the evolution of the Southern Hemisphere polar (60–90°S) TCO during the 2019 austral winter and spring, along with the 2008–2018 values (Safieddine et al., 2020). Antarctic total ozone sharply increased following the onset of the SSW, reaching 380 DU in mid-September, compared with the multiyear average of less than 250 DU. This anomalous behavior resulted from the reduced size of the polar vortex and its distorted geometry, with ozone-rich air masses transported from the mid-latitudes overlying the lower portion of the vortex, leading to a significant increase of the vertically integrated ozone concentrations (Wargan et al., 2020). These aspects of the 2019 Antarctic winter are similar to the situation in 2002 (Newman, Rex et al., 2007). The wave-induced distortions of the vortex and their effect on the ozone hole are illustrated in the bottom panel of **Figure 4-9**, which shows the evolution of the ozone hole and the polar vortex edge at selected isentropic levels in 2019 and 2018 for comparison.

While the transport-related increase in total ozone was extreme during the first two weeks of September 2019, the rate of chemical ozone depletion was not significantly different from that in 2018. Ozone concentrations at ~18 km were, in fact, lower in 2019 until the end of September (**Figure 4-8**). Lower-stratospheric temperatures began to increase in early September

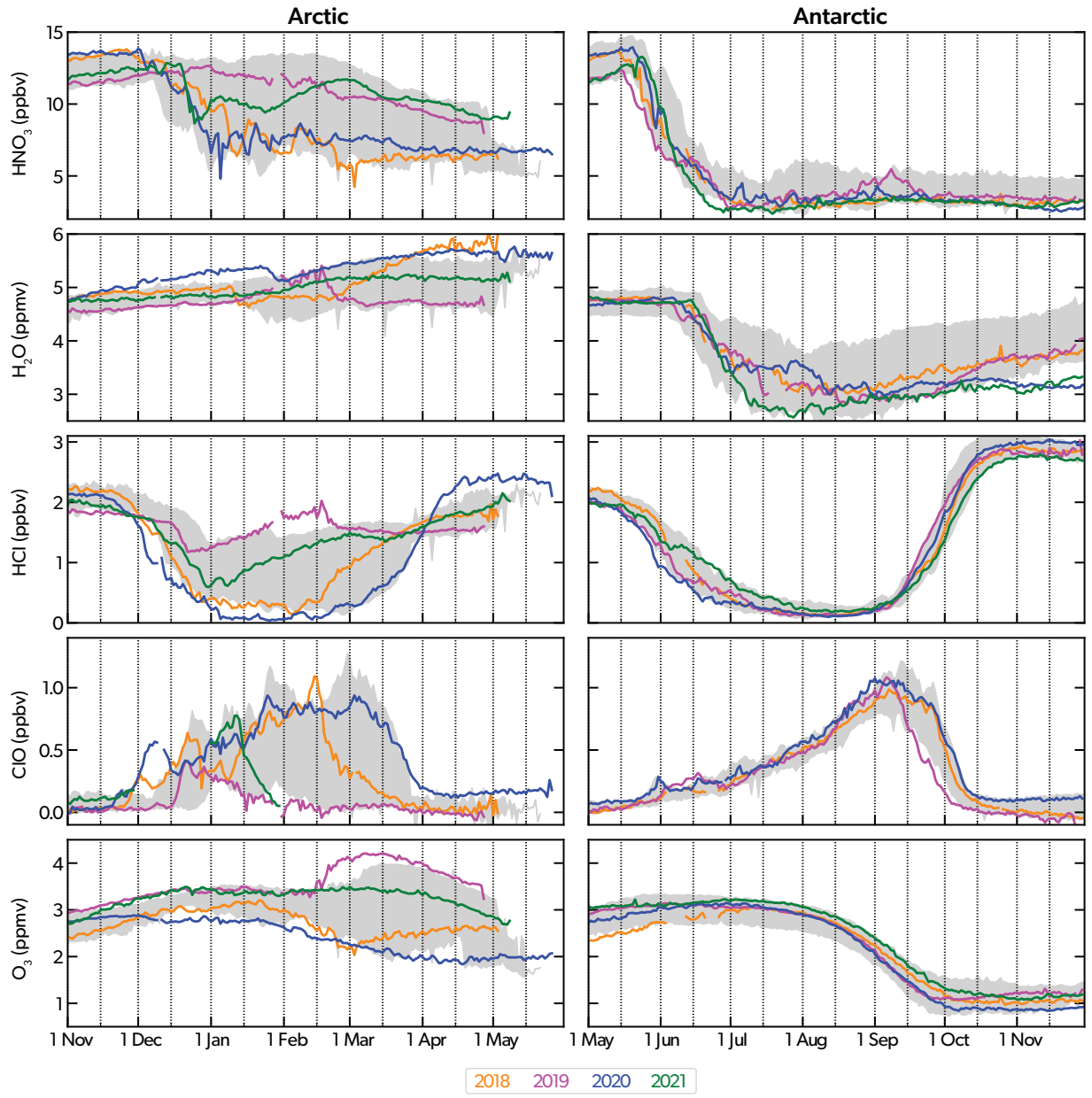

Figure 4-8. Evolution of daily HNO_3, H_2O, HCl, ClO, and O_3 from the Aura Microwave Limb Sounder (MLS) averaged within the polar vortex on the 480 K potential temperature surface (approximately 18 km) for the Arctic (November–May; *left*) and the Antarctic (May–November; *right*). Gray shading marks the range of values observed by Aura MLS over the 2005–2017 period. For ClO, only daytime (ascending node) observations are used so that near-zero ClO concentrations during local night do not contribute to the averages. The recent four winter/spring seasons are shown as colored lines as given in the legend; for the Arctic, the year given refers to the spring. [Update of figure first introduced in Dameris, Godin-Beekman et al. (2014) and updated in Langematz, Tully et al. (2018), where only results for the Arctic were shown.]

because of compression warming from the SSW-induced accelerated descent of vortex air, leading to early chlorine deactivation that began to affect ozone chemistry in the second half of September (Wargan et al., 2020; Smale et al., 2021). The daily minimum temperatures at 50 hPa exceeded the nominal threshold for chlorine activation around mid-September (**Figure 4-1**). At that time, ClO decreased to the lowest values ever observed by MLS during the Antarctic late winter. The evolution of lower-stratospheric vortex-averaged ozone shown in **Figure 4-8** indicates a slow increase starting in late September, which was a combined effect of the cessation of chemical depletion and ozone resupply from higher altitudes. The ozone hole closed at the beginning of November, about a month early compared to typical Antarctic springs.

Even though the 2019 SSW did not meet the criteria of a major SSW, it involved a deceleration of the zonal-mean zonal wind at 60°S at 10 hPa of more than 60 m s^{-1}, dropping from 80 m s^{-1} to about 15 m s^{-1} over the course of two weeks. A decrease of the same magnitude in the Northern Hemisphere would lead to a zonal wind reversal and thus constitute a major SSW (Wargan et al., 2020; Rao and Garfinkel, 2020). Disruptions of the polar vortex can impact surface weather. While the effects of the 2019 strong minor SSW on Southern Hemisphere weather have yet to be fully evaluated, hot and dry conditions over parts of Australia observed during the austral summer 2019/20 are consistent with the expected response to a weak polar vortex event (Lim et al., 2019; Baldwin et al., 2021; Lim et al., 2021). See *Chapter 5* for a discussion of connections between the Southern Hemisphere stratospheric circulation and conditions at the surface, including the role of ozone feedbacks.

4.2.3.3 Antarctic Springs 2020 and 2021: Exceptionally Persistent Ozone Holes

In contrast to 2019, the 2020 and 2021 Antarctic springs were characterized by strong and long-lasting polar vortices and significant ozone depletion. In both years, the ozone hole area reached a maximum of over 24 million km^2, about 5 million km^2 above the 1979–2021 average. In late September of 2020 and

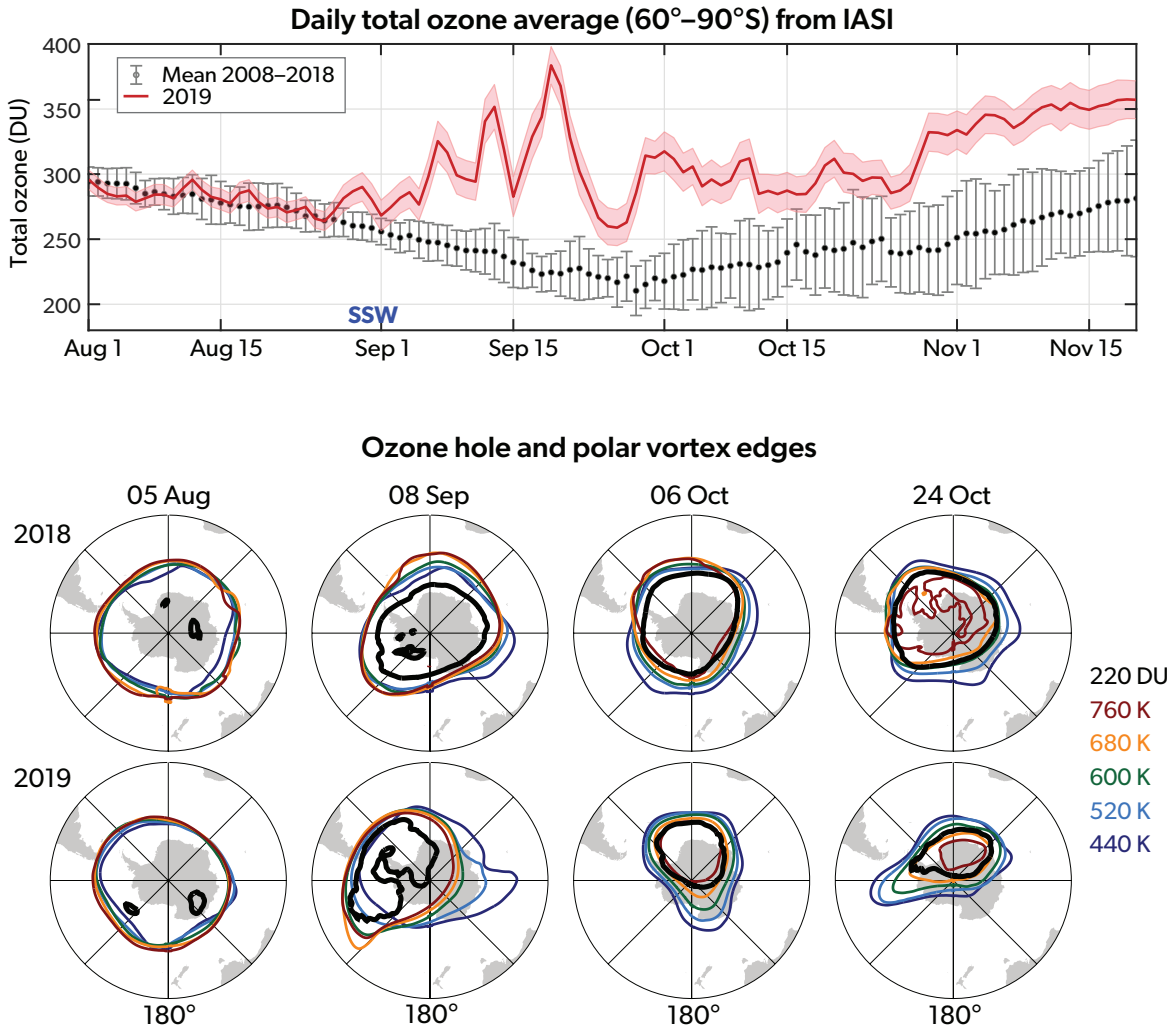

Figure 4-9. *(top)* Time series of daily total column ozone from Infrared Atmospheric Sounding Interferometer (IASI) observations, averaged between 60°S and 90°S for 2019 (red). The shading represents the estimated error. Black dots and error bars show the 2008–2018 average of the same quantity and the 11-year standard deviation, respectively. The onset of the SSW is noted as "SSW" in blue text. [Adapted from Safieddine et al., 2020.] *(bottom)* 220 DU contours of total ozone (black lines), defining the edge of the ozone hole, and the edges of the polar vortex (colored lines) on selected surfaces of potential temperature between 440 and 760 K (approximately 17 to 28 km) on four dates between 5 August and 24 October in 2018 and 2019. The vortex edges are defined using threshold values of scaled potential vorticity. The dynamical and ozone fields are from a specified dynamics experiment forced by MERRA-2 meteorology. [Adapted from Wargan et al., 2020.]

2021, both the OMD and the average minimum ozone, while not extreme, exhibited values more in line with those in the first decade of the 21st century than in recent years (**Figure 4-6**). One remarkable feature of the 2020 ozone hole was its record duration (Klekociuk et al., 2022). Areas with ozone below 220 DU persisted until late December 2020, several weeks longer than in a typical austral spring (**Figure 4-7**). The November and December averages of OMD and ozone hole area in 2020 were higher than previously observed. The 2021 ozone hole closed in mid-December, also significantly later than average (**Figure 4-7**).

The relatively large sizes and the extreme longevity of the 2020 and 2021 ozone holes are consistent with the unusual dynamical states of the stratosphere in both years. Wave activity, slightly elevated during the austral winter of 2020, weakened to record-low levels between October and mid-December (**Figure 4-7**). As a result, the springtime increase of vortex temperature, typically driven by a combination of radiative and dynamical warming, was slow relative to other years. Minimum temperatures at 50 hPa remained below the chlorine activation threshold until mid-November, about one month longer than usual (**Figure 4-1**). The vortex breakup occurred almost one month later than average (*Section 4.2.2.3*; Lecouffe et al., 2022). Chlorine deactivation was likely complete by the end of October (as seen at 480 K in **Figure 4-8**), but ozone remained low as OMD decreased at a relatively slow rate (**Figure 4-7**). Debate is ongoing about potential impacts of the Australian New Year's bushfires on the Southern Hemisphere polar ozone in 2020. The current state of this discussion is summarized in *Section 4.3.5.3*.

In 2021, wave activity was also very weak between late September and late November, although not as weak as that in 2020 (**Figure 4-7**). The minimum vortex temperatures, while higher than those in 2020, were well below average in 2021, and active chlorine in the polar vortex at 480 K followed very similar trajectories in 2020 and 2021 (**Figure 4-8**). Correlation analysis of recent measurements suggests that high levels of sulfate aerosols injected into the stratosphere during the eruption of La Soufrière in April 2021 might have contributed to the large size of the ozone hole in that year (Yook et al., 2022). Further research is needed to investigate the dynamical, chemical, and climatic conditions in 2020 and 2021 that led to the prolonged periods of suppressed wave activity and long-lasting ozone holes.

4.2.4 Ozone Depletion in Arctic Springs (2018–2021)

The polar vortex in the Northern Hemisphere is more dynamically variable than that in the Southern (*Section 4.3.4.1* and **Figure 4-13**), with major SSWs typically occurring several times per decade (Butler et al., 2017) and minor vortex disruptions being commonplace. The interannual variability of springtime Arctic ozone is driven by dynamical effects on transport and chemistry (Tegtmeier et al., 2008; Manney et al., 2011a; Strahan et al., 2016; de la Cámara et al., 2018; Bahramvash Shams et al., 2022). The main contributions to Northern Hemisphere ozone variability are variations in the dynamical resupply of ozone-rich air through downward transport and year-to-year differences in the amount of mixing across the polar vortex edge. Dynamics also controls variations in chemical ozone depletion on interannual time scales (*Section 4.3.4*). Major SSWs occurred in three of the four most recent Arctic winters: 2018, 2019, and 2021 (Rao et al., 2018, 2019; Butler et al., 2020; Lee, 2021; Pérot and Orsolini, 2021; Wright et al., 2021; Bahramvash Shams et al., 2022). In contrast, the 2020 winter was characterized by an exceptionally strong and stable polar vortex and record-low ozone.

Coupling between the stratospheric polar vortex in the Northern Hemisphere and surface conditions is a subject of ongoing research. For a summary of the current understanding of the stratosphere-troposphere interactions, including Arctic ozone feedbacks, see *Chapter 5*.

4.2.4.1 Arctic Springs 2018, 2019, and 2021: Impacts of Disturbed Polar Vortices

In 2018, wavenumber-2 forcing reversed the 60°N zonal winds on 12 February and split the polar vortex, causing an abrupt deceleration of the zonal-mean winds and rapid temperature increases within a deep layer extending down to at least 70 hPa. Prior to the event, minimum temperatures at 50 hPa (in the lower part of the vortex) were significantly below the average throughout January and the first half of February (**Figure 4-1**). The low temperatures provided conditions for intense PSC formation and chemical processing prior to the SSW. **Figure 4-2** shows that the time-integrated volume of air below the chlorine activation threshold was relatively high in 2018. Concentrations of vortex HNO_3 were close to the lower end of the range (**Figure 4-8**), indicative of substantial PSC formation. Observations of HCl and ClO indicate that chlorine activation began in late November, two weeks earlier than usual, and produced high concentrations of active chlorine that would not become fully deactivated until late March (**Figure 4-8**). In early February, prior to the SSW, polar cap total ozone was only about 350 DU, in the low 10th percentile for that time period. As a result of the high concentrations of active chlorine, chemical ozone loss was significant and continued after the vortex split occurred (Bernhard et al., 2019), such that lower-stratospheric vortex ozone in early March 2018 was one of the lowest in the MLS record (**Figure 4-8**). However, because of the SSW and the associated influx of ozone-rich air in the middle and upper stratosphere, the relatively intense chemical destruction did not significantly affect March polar cap total ozone (**Figure 4-4**). Average minimum daily ozone north of 63°N equivalent latitude (**Figure 4-5**) was within the 21st-century range.

The 2019 SSW, which began on 2 January, about 40 days earlier in the season than the 2018 event, had a significant impact on polar chemistry (Bernhard et al., 2020). Unlike the rapid development observed in 2018, the onset of the 2019 SSW was preceded by gradual weakening and displacement of the polar vortex by wavenumber-1 forcing after mid-December (Butler et al., 2020; Lee and Butler, 2020). Minimum vortex temperatures at 50 hPa increased above the threshold for chlorine activation as early as late December (**Figure 4-1**). Vortex HNO_3 on 2 January was above its November levels (**Figure 4-8**), indicating very little PSC formation. Following a brief period of chlorine activation in mid-December 2018, average ClO concentrations gradually declined, while HCl increased and reached values above the 2005–2017 maximum in late January. By the end of January, chlorine deactivation was complete, and chemical ozone loss due to chlorine catalytic cycles ceased. Dynamical effects of the slowly downward propagating vortex disturbance led to a further significant increase of ozone concentrations in mid-February. The March polar cap TCO in 2019 was slightly above the typical values seen in the past two decades (**Figure 4-4**), and the average minimum daily ozone north of 63°N equivalent latitude was one of the highest in the

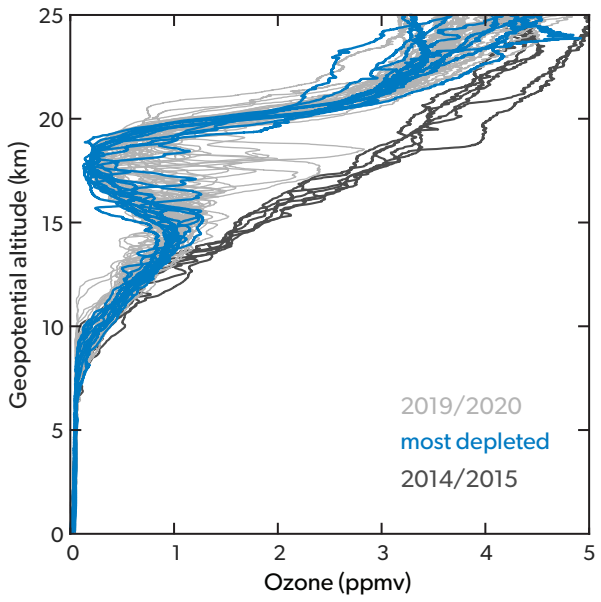

Figure 4-10. Ozone profiles inside the polar vortex from 17 March to 17 April 2020 as a function of altitude. A set of 12 sondes was chosen from all measurements to represent the air masses most depleted in ozone (blue lines). All other profiles from 2019/20 are shown in light gray. For comparison, profiles inside the polar vortex from the warm winter 2014/15 (24 March to 9 April) are shown in black. [Adapted from Wohltmann et al., 2020.]

past three decades (**Figure 4-5**), further underscoring the critical role of dynamical effects on ozone variability in the Arctic.

The onset of the 2021 SSW occurred on 5 January (Wright et al., 2021). Unlike in 2019, minimum temperatures at 50 hPa remained below the chlorine activation threshold until mid-January (**Figure 4-1**). A moderate decrease in HNO_3 observed by MLS indicates PSC formation in late December (**Figure 4-8**). High ClO concentrations in early January suggest that some chemical ozone depletion occurred initially, but by the end of the month, chlorine was fully deactivated. Vortex-averaged ozone concentrations at 18 km were at the upper end of the 2005–2017 range already in November and remained relatively high throughout the winter and spring (**Figure 4-8**). Nonetheless, likely because of partial compensation from below-average ozone at higher altitudes and outside of the vortex, polar cap total ozone in March was one of the lowest in the last 20 years (**Figure 4-4**), excluding the extreme cases of 2011 and 2020. The minimum of daily averages within the area prescribed by 63°N equivalent latitude (**Figure 4-5**) was typical for recent decades.

While major SSWs occurred in all three years, their effects on ozone varied significantly, as is evident from **Figures 4-4**, **4-5**, and **4-8**. This variability arises from differences in the timing of the SSWs and their dynamical evolution that, in turn, impact the concentrations of active chlorine within the polar vortex and the amount of solar illumination of the chemically processed air within the vortex.

4.2.4.2 Arctic Spring 2020: Record-Low Arctic Stratospheric Ozone

Record-low ozone was observed in the Arctic spring of 2020. The only other two years that saw comparable extremes were 1997 and 2011. As was the case in those years, the exceptionally low ozone anomaly in 2020 was a consequence of a prolonged period of very low temperatures and high stability of the polar vortex, which strongly enhanced chemical depletion while inhibiting ozone resupply through transport (Manney et al., 2020; Lawrence et al., 2020; Inness et al., 2020; Dameris et al., 2021; Feng et al., 2021; Weber et al., 2021; Grooß and Müller, 2021). Pronounced ozone minima occurred within the stratospheric polar vortex at altitudes between 15 and 20 km (**Figure 4-10**). Polar cap ozone during most of the late winter and early spring of 2020 was the lowest on record, with values reaching about 90 DU below the 1979–2021 March average. The February–April mean TCO near the North Pole was about 120 DU below the long-term mean (**Figure 4-11a**). Regions where TCO fell below 220 DU were observed between January and March (Dameris et al., 2021; Kuttippurath et al., 2021), prompting media reports of an "Arctic ozone hole." However, these patches of low ozone lacked almost any defining characteristics of Antarctic ozone depletion (Wohltmann et al., 2020). With areas under 1 million km^2, they were small compared to ozone holes, which regularly exceed 20 million km^2 in size. Daily total ozone minima in March ranged between 205 and 240 DU, about 50 DU below the average. By comparison, typical minimum TCO over Antarctica in October ranges between 100 and 160 DU (**Figure 4-6**), with ozone concentrations near zero in the most depleted layer in the lower stratosphere (e.g., Solomon et al., 2014; Kuttippurath et al., 2018). Minimum ozone concentrations measured by ozonesondes in March and April 2020 were generally between 0.15 and 0.2 ppmv and occurred at altitudes around 18 km, with the lowest reported value being 0.13 ppmv (Wohltmann et al., 2020; **Figure 4-10**). These values are lower than previously observed in any other Arctic spring, including 2011, but are still an order of magnitude higher than minima observed over Antarctica (Solomon et al., 2014).

The 2019/20 northern winter/spring has been intensely studied. None of the results published to date challenge our now well-established understanding of polar ozone chemistry. Chemistry models constrained by real-world meteorology from reanalyses accurately reproduce the extreme chemical ozone loss of 2020. This has been demonstrated explicitly with the CLaMS (Grooß and Müller, 2021) and the TOMCAT (Feng et al., 2021; Weber et al., 2021) chemistry models.

Similar to the winter/spring seasons of 1996/97, 2010/11, and, to some extent, 2015/16, the prolonged period of very low minimum polar vortex temperatures that lasted from December through April (**Figure 4-1**) and the high vortex strength resulted primarily from exceptionally low wave activity in the stratosphere. **Figure 4-11b** shows an approximately linear relationship between the amount of wave driving, represented by the vertical component of the Eliassen-Palm flux, and the Northern Annular Mode (NAM) index, which quantifies vortex strength. The springs of 1997, 2011, and 2020 are near the lower-right corner of the plot, with the lowest wintertime wave activity and the strongest polar vortex occurring in 2020. Another feature of the 2020 spring was a strong coupling between the polar vortex and tropospheric meteorology, as manifested in a highly zonal circulation

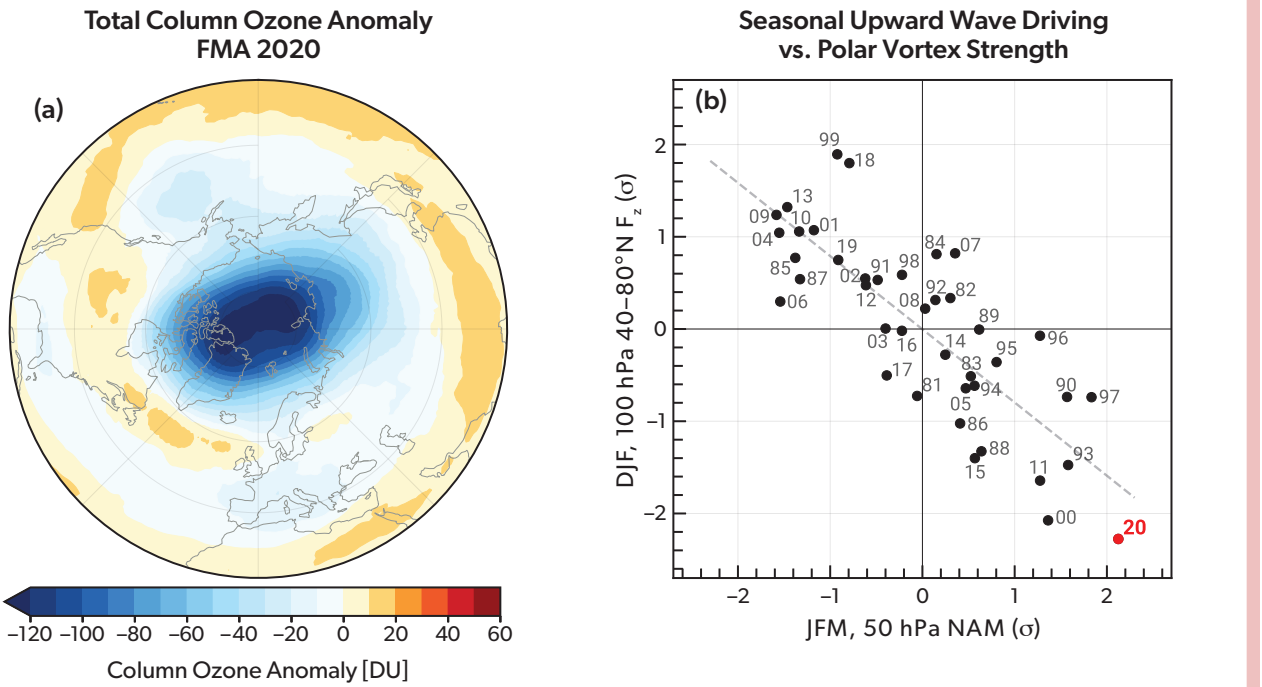

Figure 4-11. (a) Northern Hemisphere February–April (FMA) total ozone anomaly with respect to the 1979–2020 average. (b) December–February (DJF) 100 hPa 40–80°N averaged vertical component of the Eliassen-Palm flux (F_z) versus the January–March (JFM) 50 hPa Northern Annular Mode (NAM) index. The record year 2020 in (b) is marked in red. The ozone data are from the Ozone Mapping and Profiling Suite Nadir Mapper; the dynamical metrics are derived from the MERRA-2 reanalysis. [Adapted from Lawrence et al., 2020.]

throughout the depth of the stratosphere and troposphere down to the surface (Lawrence et al., 2020).

The extremely low Arctic ozone in the spring of 2020 arose as a combined effect of anomalous transport and exceptionally strong chemical depletion, both caused by the unusual dynamical conditions described above. While chemical destruction in 2020 (discussed below) was significant, weak ozone resupply was the other key factor in the occurrence of the extremely low observed values of TCO in the spring of 2020. When wave activity is less intense, as it was in 2020, the Brewer-Dobson Circulation (BDC) slows down, and ozone replenishment is less effective (*Section 4.3.4*). Furthermore, assimilated meteorological fields from reanalyses provide evidence of downward wave reflection and associated anomalous upwelling between January and March 2020 (Lawrence et al., 2020). The phenomenon of planetary wave reflection was highlighted in Langematz, Tully et al. (2018) as a factor in slowing down the BDC, leading to a colder polar vortex and inhibiting vertical transport. In the winter/spring of 2019/20, the rate of ozone resupply into the lower stratosphere was significantly reduced. Dynamical replenishment over the polar cap in March 2020 was only about 60 DU, compared to the climatological average of 150 DU (Feng et al., 2021).

The extreme stability of the stratospheric polar vortex significantly impacted polar chemistry in 2020. Minimum temperatures remained below the threshold for chlorine activation until mid-March (Lawrence et al., 2020; Wohltmann et al., 2020; Dameris et al., 2021). The time-integrated NAT (nitric acid trihydrate) PSC volume (V_{PSC}) reached the second-highest value on record (**Figure 4-2**). Based on satellite measurements, the maximum area covered by PSCs was 8–10 million km^2, comparable to typical Southern Hemisphere values (DeLand et al., 2020). These conditions enabled long-lasting chlorine activation and chemical ozone loss. Vortex-averaged chlorine monoxide (ClO) in the lower stratosphere was persistently high, while the chlorine reservoir compound hydrogen chloride (HCl) was the lowest since at least 2005 for most of the season (**Figure 4-8**). Chlorine activation and ozone depletion began earlier than in any previously observed winter, with evidence of some chemical ozone loss as early as November (Manney et al., 2020). High levels of active chlorine and bromine and significant denitrification are also indicated in satellite measurements of chlorine dioxide (OClO) slant columns and of nitrogen dioxide (NO_2) total columns (Weber et al., 2021) and in ground-based observations of bromine monoxide (BrO), chlorine nitrate ($ClONO_2$), and nitric acid (HNO_3) columns (Bognar et al., 2021). Chlorine deactivation occurred around the March/April boundary, much later than in typical Arctic springs, apart from 2011. The prolonged exposure of chemically processed air to sunlight contributed to the significant chemical ozone depletion in 2020 (Wohltmann et al., 2021). By early April, HCl concentrations increased to record levels, indicating an Antarctic-like deactivation pathway, whereby Cl is incorporated predominantly into this nitrogen-free compound rather than into $ClONO_2$, as typically observed in the Northern Hemisphere (Manney et al., 2020; Grooß and Müller, 2021; Wohltmann et al., 2021).

Box 4-1. What is a 'Polar Vortex' and Why Does it Matter?

As most recently discussed by Manney et al. (2022), there is considerable confusion both within and outside the atmospheric science community about the usage of the term "polar vortex." For instance, in January 2014, a cold air outbreak (CAO) extending through the southern central and eastern United States set new record-low minimum temperatures as far south as Georgia and Texas (e.g., Screen et al., 2015). As discussed by, e.g., Lillo et al. (2021), this CAO was described in the media as "the polar vortex," and this language became commonplace in the popular press. At the time, the term polar vortex in scientific literature most commonly described the stratospheric polar vortex, often without explicit qualification (e.g., Wang et al., 2014); some studies also used "polar" or "circumpolar" vortex to describe a "tropospheric polar vortex" without further qualification (e.g., Wallace et al., 2014; Yu and Zhang, 2015). Waugh et al. (2017) sought to dispel myths about the polar vortex. They described the stratospheric and tropospheric "circumpolar" vortices as the terms had been commonly used in scientific literature, highlighted their differences and relationships to extreme weather events, and provided recommendations for describing them in public forums. Unfortunately, while this work is widely cited, the two concepts are still often conflated or not clearly distinguished, sometimes on educational sites, in studies on climate change communication, or within the atmospheric science community (e.g., Shepherd, 2016; Lyons et al., 2018; UC Davis, 2019; UCAR, 2021; Bushra and Rohli, 2021; Dai et al., 2021; Kömüşcü and Oğuz, 2021).

Box 4-1 Figure 1 shows examples on two dates (chosen during periods in which CAOs were described in the popular press as polar vortex "outbreaks" or "attacks") depicting the stratospheric polar vortex and the upper-tropospheric jet streams (the dynamical features most closely aligned with common definitions of a "tropospheric polar vortex"). **Box 4-1 Table 1** summarizes key differences between the tropospheric and stratospheric circulations in relation to the "polar vortex."

The stratospheric polar vortex is consistently defined as bounded by the polar night jet, the strong band of eastward winds throughout the stratosphere that forms in the fall and weakens and reverses in spring. Several diagnostics can be used to define the stratospheric polar vortex edge (Lawrence and Manney, 2018, and references therein), any of which pick out approximately the same physically meaningful boundary from the lowermost into the upper stratosphere. ***The stratospheric polar vortex is a single persistent feature that dominates the circulation of and transport throughout the polar stratosphere in fall through spring.***

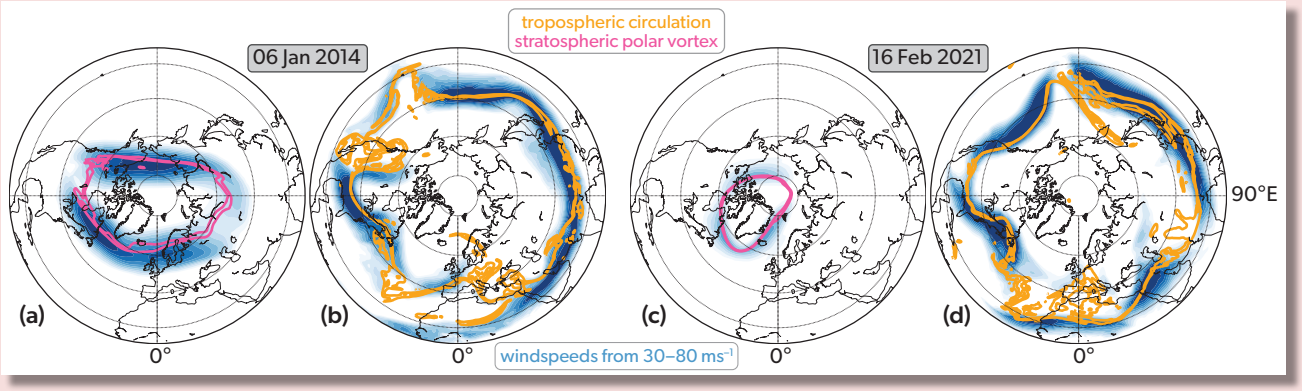

Box 4-1 Figure 1. Maps showing the (a, c) stratospheric polar vortex and (b, d) upper-tropospheric jet stream wind speeds (blue color fill) and "vortex edge" contours (magenta for stratosphere, orange for troposphere) on dates during CAOs in two Arctic winters. [Adapted from Manney et al., 2022.]

There is no consensus on the definition of a "tropospheric polar vortex" or on the altitude(s) at which it is defined. Waugh et al. (2017), and articles they cite, used one common method that defined the tropospheric polar vortex such that its edge approximately follows the axis of an upper tropospheric jet stream. These jets have maxima that are very localized in altitude compared to the stratospheric polar night jet, and they vary strongly with longitude (e.g., Manney et al., 2011b, 2014; and references therein; **Box 4-1 Figure 1b, d**). Because smaller-scale motions dominate tropospheric dynamics, ***a "tropospheric polar vortex" by any definition is not a single coherent circumpolar circulation that plays a central role in tropospheric dynamics and transport***.

The stratospheric polar vortices profoundly affect ozone distributions via their role as transport barriers, isolating species involved in ozone depletion from mid-latitude air. This results in strong ozone gradients across those vortex edges, which in turn lead to very different ozone concentrations inside and outside the stratospheric polar vortices. Polar stratospheric chemical processing and ozone destruction are commonly analyzed from a vortex-centered perspective (e.g., *Sections 4.2.3* and *4.2.4*), and the amount of polar ozone loss in a given spring is controlled by the strength and coldness of the winter/springtime stratospheric polar vortex. In contrast, upper troposphere/lower stratosphere (UTLS) ozone variability is dominated by regional variations in stratosphere-troposphere exchange and differences in the amount of ozone in the lower stratosphere that can be transported into the troposphere (e.g., Albers et al., 2018; Olsen et al., 2019; Breeden et al., 2021). The former depends critically on regional variations

in the upper-tropospheric jets and tropopause, and the latter on stratospheric variability (and thus on stratospheric polar vortex conditions). Unlike in the stratosphere, ozone in the troposphere does not show strong gradients on a hemispheric scale, except at the subtropical boundary that separates higher-ozone stratospheric air at mid-latitudes from lower-ozone tropospheric air at low latitudes (e.g., Manney et al., 2022).

CAOs are described as "polar vortex events" in the media and in venues such as peer-reviewed papers on communication of climate change risks (e.g., Lyons et al., 2018), but, based on the dynamical processes involved, they are best described as excursions of the upper-tropospheric jet stream, such as southward advection of cold Arctic air. While they are sometimes described as "local" variations of the tropospheric polar vortex "edge," they are not generally correlated with the strength of the globally defined tropospheric polar vortex (e.g., Celliti et al., 2006; Waugh et al., 2017; Bushra and Rohli, 2021; and references therein), so the usefulness of that description is limited at best. Sudden stratospheric warmings (SSWs, which weaken/disrupt the stratospheric polar vortex) have been linked to some CAOs (e.g., Butler et al., 2017; Domeisen and Butler, 2020; Huang et al., 2021; and references therein), and the media often hails reports of an SSW with warnings that "the polar vortex is coming" and predicts a CAO. That connection is, however, probabilistic, and CAOs may be associated with either strong (**Box 4-1 Figure 1a, b**; January 2014) or weak (**Box 4-1 Figure 1c, d**; February 2021, following an SSW) stratospheric polar vortices. The effects of the stratospheric polar vortex depend on the location of the CAOs and other characteristics of the stratospheric polar vortex in addition to its strength (e.g., Kretschmer et al., 2018; Lee et al., 2019; Cohen et al., 2021).

It is thus clear that, as discussed by Manney et al. (2022), describing the stratospheric polar vortex as the primary factor dominating stratospheric variability and influencing the surface (with probabilistic links to extreme weather events) is accurate and useful. On the other hand, the most relevant features of the tropospheric circulation, particularly those linked to extreme weather events, are best described as local excursions of the tropospheric jet streams. The term "polar vortex" is best used to denote the stratospheric cool-season circulation. However, because that term often is used inappropriately for other atmospheric features, the more precise term "stratospheric polar vortex" should be used for clarity.

Box 4-1 Table 1. Key differences between the stratospheric and tropospheric polar vortices.

Stratospheric Circulation / Stratospheric Polar Vortex	Tropospheric Circulations / Upper-Tropospheric Jet Streams
Deep feature extending from the tropopause (about 12–15 km) to the stratopause (about 50–60 km).	Circulation influence of extratropical upper-tropospheric jets is limited by vertically localized wind speed maxima that are strongest in a few-km region centered near 12 km (9 km) altitude at lower (higher) latitudes. No consensus on level at which a "tropospheric polar vortex" is defined.
Unique feature whose variations in strength, size, and position dominate the stratospheric circulation in late fall through spring.	No single global feature dominates the circulation; impactful circulation systems / weather (e.g., winter storms) primarily linked to local jet stream excursions rather than to an overall strong or weak circumpolar vortex.
Trace gas transport is closely aligned with the vortex; the vortex edge is a global transport barrier whose strength determines the degree of mixing across it.	Transport controlled by upper-tropospheric jet and tropopause variations; jets represent a transport barrier only in regions where they are strong, not around the globe.
Provides the "containment vessel" in which lower-stratospheric chemical ozone loss occurs; thus variations in strength/coldness dominate interannual variability in ozone.	Upper-tropospheric ozone variability primarily controlled by ozone abundances in the lowermost stratospheric reservoir and local jet / tropopause variations that lead to stratosphere-troposphere exchange.

Several methods of estimating chemical ozone loss have been used in polar ozone studies (for a concise summary, see Newman, Rex et al., 2007), all of which are subject to considerable uncertainties (Livesey et al., 2015; Griffin et al., 2019). Estimates of chemical ozone loss in the Arctic in 2020 are nonetheless in broad agreement in that they all indicate exceptional depletion. The peak chemical loss occurred around the 450 K potential temperature surface, which corresponds to about 16–18 km above the surface. Estimates of the cumulative chemical ozone destruction at that level range between 2.2 and 3.4 ppmv (Wohltmann et al., 2020; Manney et al., 2020; Kuttippurath et al., 2021), at least 75% of the initial ozone abundance. The maximum loss within the vortex core was higher and is estimated to be as large as 93% (Wohltmann et al., 2020). These values are similar to those for 2011, although the maximum depletion in 2020 occurred at a lower altitude, amounting to a larger ozone mass loss in 2020. These maximum values significantly exceed ozone destruction during a typical Arctic spring and approach the range characteristic for the Antarctic, although in the Antarctic, such severe depletion affects a broader range of altitudes and a larger portion of the polar vortex (Wohltmann et al., 2020; Solomon et al., 2014; Livesey et al., 2015). Observation and model-based estimates of the vortex-averaged and vertically integrated loss in the lower stratosphere range between 105 and 131 DU (Weber et al., 2021; Wohltmann et al., 2020; Grooß and Müller, 2021), where the latter value is limited to the vortex core and includes a small amount of chemical loss that occurred in November. Estimates of the total column net ozone loss (implicitly including middle- and upper-stratospheric photochemical ozone production) are 88 and 106 DU, depending on the method used (Weber et al., 2021). These estimates of column ozone loss are quantitatively similar to those for 2011. However, because the March polar vortex area in 2020 was about 25% larger than that in 2011, ozone loss integrated over the vortex was more extensive in 2020 (Weber et al., 2021).

4.3 UNDERSTANDING OF POLAR OZONE PROCESSES

The chemical and dynamical processes controlling polar stratospheric ozone are generally well understood and have been discussed in detail in previous Assessments (e.g., Dameris, Godin-Beekmann et al., 2014; Langematz, Tully et al., 2018). Since the last Assessment, research has focused on refining our understanding of both chemical and dynamical influences on polar ozone, thus reducing uncertainties in model projections of future polar ozone in a changing climate. For example, the fundamental understanding of polar stratospheric cloud (PSC) formation pathways and particle characteristics has progressed, and multi-decadal trends in PSC occurrence could be analyzed for the first time (*Section 4.3.1*). High-resolution measurements obtained from research aircraft campaigns in the UTLS provided new insight into chlorine chemistry (*Section 4.3.2*). *Section 4.3.3* raises the potential but still rather uncertain role of iodine as a halogenated very short-lived substance (VSLS) contributing to chemical ozone depletion. New pathways of dynamical forcing of Arctic ozone associated with future Arctic sea ice decline and North Pacific sea surface temperature anomalies (SSTAs) are addressed in *Section 4.3.4*. Other factors influencing polar stratospheric ozone (*Section 4.3.5*) include, in particular, the role

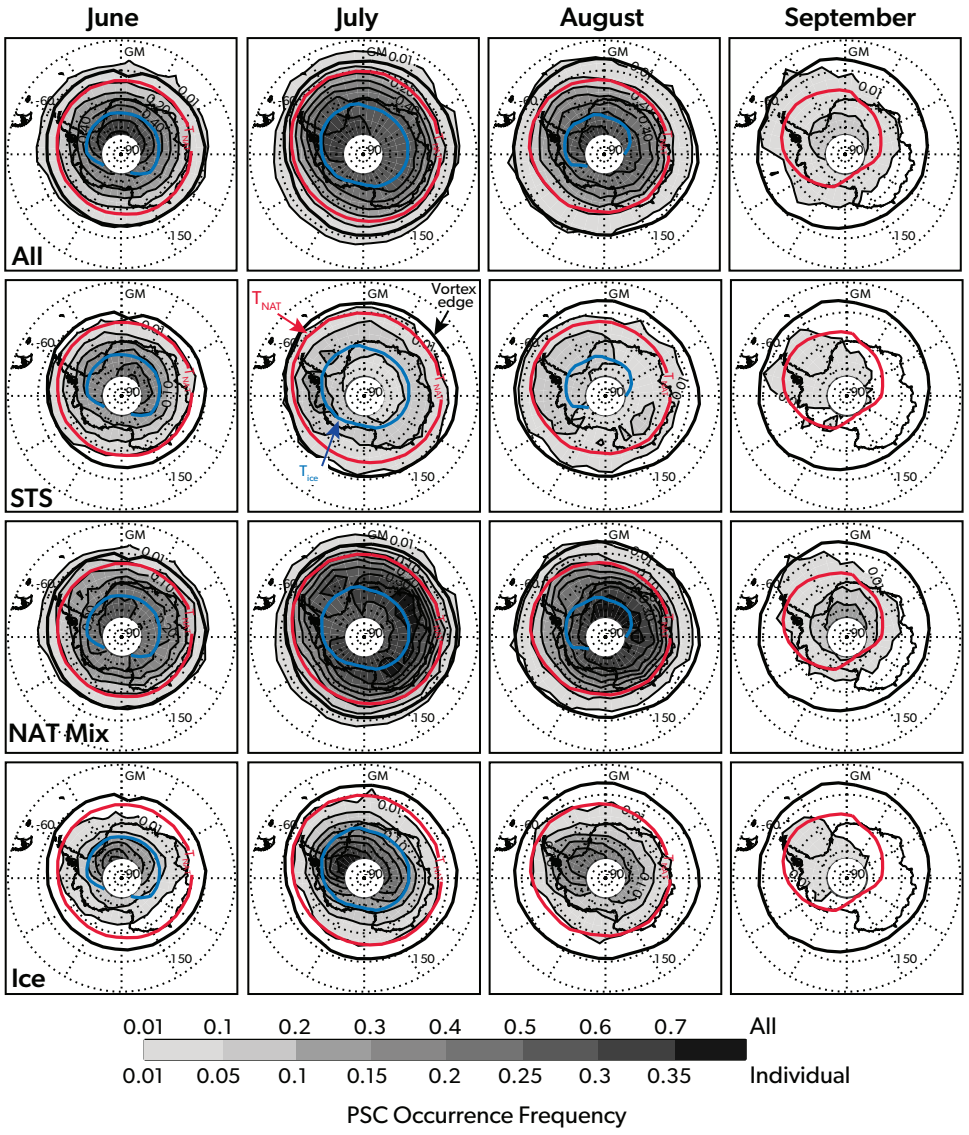

Figure 4-12. Monthly mean polar maps of CALIOP Antarctic PSC occurrence frequency at 500 K (~20 km), averaged over 2006–2018. *(row 1)* All PSCs. *(row 2)* Supercooled ternary solution (STS). *(row 3)* NAT mixtures, including enhanced NAT due to mountain waves. *(row 4)* Ice, including wave ice. Black contours show the mean vortex edge. Solid red and blue contours, respectively, enclose regions where mean $T < T_{NAT}$ and $T < T_{ice}$. The white region over the pole is not sampled by CALIOP. Note that different grayscale ranges are used for "all" PSCs and "individual" compositions. [Adapted from Tritscher et al., 2021, updated from Pitts et al., 2018.]

of wildfire emissions, such as those from the severe bushfires in southeastern Australia in late December 2019 and early January 2020, and the possible ozone depletion by the emissions of a fleet of supersonic and hypersonic aircraft, currently under consideration for future civil transportation.

4.3.1 Polar Stratospheric Clouds: Observations and Modeling of PSC Occurrence, Extent, and Composition

The critical role of PSCs in affecting polar ozone and chlorine chemistry is considered to be well understood (see Dameris, Godin-Beekmann et al., 2014, and Langematz, Tully et al., 2018, for a more detailed description). Nevertheless, as discussed in Dameris, Godin-Beekmann et al. (2014), uncertainties still exist in various aspects, for example the nucleation mechanism for nitric acid trihydrate (NAT) particles, including large "NAT-rocks," or the origin and effects of refractory particles (low-volatility particles of terrestrial or extraterrestrial origin that can promote heterogeneous nucleation). This section reviews the progress made in closing the gaps on the extent, composition, and formation mechanisms of PSCs since the last Assessment. A more comprehensive review is provided by Tritscher et al. (2021).

Following Tritscher et al. (2021), the term "composition" as it relates to PSCs includes their chemical components (e.g., stratospheric sulfuric acid aerosols [SSA, H_2SO_4-H_2O], supercooled ternary solution [STS, H_2SO_4-HNO_3-H_2O] droplets, nitric acid trihydrate [NAT, $HNO_3 \bullet 3H_2O$] or other hydrates of HNO_3 or H_2SO_4, or H_2O ice), particle phase states (e.g., droplets or crystals), and states of mixing. Contemporary observations by three spaceborne instruments—MIPAS, MLS, and CALIOP—provide an unprecedented seasonal polar vortex-wide data record of PSC occurrence and composition in both hemispheres from 2002 to present (2021; Pitts et al., 2018; Höpfner et al., 2018; Spang et al., 2018; Tritscher et al., 2021). A detailed comparison of these datasets revealed consistency in the PSC coverage between CALIOP and MIPAS, and in PSC composition for homogeneous cloud scenes between CALIOP, MIPAS, and MLS. Agreement between PSCs observed by the spaceborne instruments and ground-based lidars in Antarctica is also good regarding the general features of the PSC season, such as the occurrence in the different composition classes and its altitude dependence during the season. However, differences were detected on the basis of daily observations, mainly owing to the high geographic variability of PSCs (Snels et al., 2019, 2021). The new PSC climatology allows further analyses of PSC characteristics, such as the seasonal, geographical, and height coverage of the different PSC composition classes and their interannual variability. **Figure 4-12** shows the 2006–2018 average of monthly mean polar maps of CALIOP Antarctic PSC occurrence frequency at about 20 km altitude for different PSC composition classes. PSC occurrence is roughly bounded by the $T < T_{NAT}$ contour and increases poleward, with the highest occurrence frequencies (>60%) generally located within the region of $T < T_{ice}$. The contours of the frequency of PSC occurrence and of the cold pool are pushed slightly off the pole toward the Antarctic Peninsula, in association with frequent mountain wave activity (i.e., wave ice in **Figure 4-12**) in this region, as also found by Spang et al. (2018) in PSC observations from MIPAS.

With the new CALIOP PSC climatology, it became possible to investigate multi-decadal trends in PSC occurrence by comparing the CALIOP dataset from 2006–2017 with the Stratospheric Aerosol Measurement (SAM) solar occultation PSC occurrence record from 1978–1989 (Poole and Pitts, 1994). It was found that in the Antarctic, PSC occurrence is very similar between the two periods, whereas in the Arctic PSC occurrence has significantly increased in early winter (December and January; Pitts et al., 2018). This different development of Arctic versus Antarctic PSC occurrence is consistent with lower-stratospheric temperature trends derived from MSU4 satellite observations, which show a significant Arctic cooling in December and January for the period 1998–2016, while Antarctic temperature changes in this period are small relative to the period 1979–1997 (Figure 5-6a, c in Karpechko, Maycock et al., 2018). The Arctic PSC increase may have had implications for Arctic lower-stratospheric ozone, which decreased between 1998 and 2018 (Hu et al., 2022; see also *Section 4.3.4.3*). Any future cooling of the Arctic lower stratosphere (either by reduced dynamical forcing from the troposphere or induced by climate change) is expected to enhance PSC occurrence and—provided ozone-depleting substances (ODSs) are still present—reduce lower-stratospheric ozone abundances.

In the previous Assessment, two major NAT particle formation mechanisms were discussed: homogeneous nucleation from STS droplets, producing large NAT particles relevant for explaining the observed denitrification, and heterogeneous nucleation of NAT on ice, producing small particles. It was also proposed that refractory particles of meteoritic origin might serve as condensation nuclei of large NAT particles, so-called NAT-rocks (Langematz, Tully et al., 2018, and references therein). As reviewed by Tritscher et al. (2021), the fundamental understanding of PSC formation pathways and particle characteristics has advanced since then. While there are strong indications that homogeneous nucleation of NAT particles from STS droplets seems to be largely suppressed under stratospheric conditions, two heterogeneous NAT nucleation processes exist: NAT nucleation on ice, which has been shown to be efficient in mountain wave ice clouds; and NAT nucleation on foreign nuclei, observed at $T > T_{ice}$. The heterogeneous nuclei may be of meteoritic origin, although other refractory materials or organics have also been identified in stratospheric aerosol particles (James et al., 2018; Schneider et al., 2021).

As reported in Dameris, Godin-Beekmann et al. (2014) and Langematz, Tully et al. (2018), unusually large PSC particles, also called NAT-rocks, had been detected in earlier Arctic aircraft campaigns. They are of interest as sequestering of nitric acid in these particles might lead to efficient denitrification (Tritscher et al., 2021, and references therein). By applying a new method to detect such populations of HNO_3-containing particles using infrared limb observations, populations of aspherical NAT particles with median radii ≥3 μm were detected vortex-wide during Arctic winter 2011/12 (Woiwode et al., 2019). The study emphasizes the key role of the detected particles for the denitrification of the Arctic winter stratosphere. However, the measured extensive gas-phase HNO_3 sequestration and condensed gas-phase equivalent HNO_3 of 10 ppbv or more exceed model simulations for different Arctic winters by up to one order of magnitude. Likewise, models fail to reproduce the long persistence and slow sedimentation of the detected populations, which might be due to the highly aspherical shape of the detected particles and their lower fall speeds (Westbrook, 2008; Woiwode et al., 2019).

4.3.2 Polar Chemistry: Observations and Modeling

4.3.2.1 Observations

Since the last Assessment, various studies have focused on the chlorine and bromine chemistry in the polar lowermost stratosphere during the exceptionally cold Arctic winter of 2015/16. Extreme meteorological conditions early in the 2015/16 winter induced rapid ozone loss, until a sudden stratospheric warming at the beginning of March 2016 curtailed further chemical processing. High-resolution and high-accuracy datasets obtained from instruments onboard the High Altitude and LOng Range Research Aircraft (HALO) allowed the variations in trace gas distributions in the UTLS over the course of this exceptional Arctic winter to be probed in fine detail.

A consistent series of in situ high-resolution mass spectrometric observations of HCl and $ClONO_2$ from the AIMS instrument onboard HALO was analyzed to study the chemistry of the lower-stratospheric outflow region of the 2015/16 Arctic polar vortex, together with total inorganic chlorine (Cl_y) and active chlorine (ClO_x) derived from simultaneous measurements of CFC-12. The new data highlight the altitude dependence of the pathway for chlorine deactivation in the lowermost vortex, with HCl dominating below the 380 K isentropic surface and $ClONO_2$ prevailing above (Marsing et al., 2019).

Chlorine activation and deactivation in the lowermost stratosphere during the 2015/16 Arctic winter were further analyzed utilizing time series of satellite measurements, remote-sensing measurements from the airborne limb imager GLORIA, and simulations with atmospheric models (Johansson et al., 2019). Time series of the satellite measurements reveal unusually low HCl and $ClONO_2$ at 380 K from the beginning of January to the end of February 2016, while ClO was strongly enhanced. In March 2016, unusually rapid chlorine deactivation into HCl was observed instead of deactivation into $ClONO_2$, the more typical pathway for deactivation in the Arctic. This is explained by very low ozone abundances together with low temperatures, conditions that favor HCl reformation. During this exceptional Arctic winter, the high-resolution GLORIA instrument observed strongly enhanced $ClONO_2$ values of up to 1100 pptv in the tropopause region, showing mesoscale structures in the two-dimensional vertical cross sections of $ClONO_2$ that result in part from local chlorine deactivation and in part from transport of previously deactivated air. In addition, GLORIA measurements of $ClONO_2$ and O_3 were used to evaluate simulations from a chemistry transport model and a chemistry climate model; the comparisons showed agreement within the expected performance of both models (Johansson et al., 2019).

GLORIA observations along the flight track of HALO together with tracer-tracer correlations also enabled the quantification of HNO_3 distributions in the lowermost stratosphere with high spatial resolution throughout the Arctic winter 2015/16. Large-scale as well as local fine structures with enhanced absolute HNO_3 volume mixing ratios as high as 11 ppbv were found at altitudes of 13 km in January, with nitrified filaments persisting until the middle of March (Braun et al., 2019). Narrow coherent structures tilted with altitude of enhanced HNO_3, observed in mid-January, were interpreted as regions recently nitrified by sublimating HNO_3-containing particles.

Calculations of Cl_y in the lower stratosphere derived from chlorinated source gas measurements onboard the HALO aircraft during the campaign in the Arctic in 2015/16 were compared with those from a campaign in the Antarctic in austral winter/spring 2019 (Jesswein et al., 2021). A new air mass classification system was used, based on high-resolution in situ measurements during the campaigns, to map measurements to the vortex, vortex boundary region, and mid-latitudes. Although the Antarctic vortex was unusually weak in 2019 in the wake of a minor sudden warming, up to 50% of the total chlorine could be found in inorganic form inside the vortex at about 5 km above the tropopause. In the mid-latitudes, only about 15% of the total chlorine was found in inorganic form. In contrast to the Antarctic polar vortex in 2019, the Arctic polar vortex in 2015/16 was one of the strongest compared to previous years (Matthias et al., 2016). At a comparable altitude inside the vortex, only around 40% of total chlorine was found in inorganic form, whereas roughly 20% was found at mid-latitudes. Inside the respective vortices, the amount of Cl_y was higher during the Southern Hemisphere campaign than during the Northern Hemisphere campaign by up to 540 ppt (at the same altitude).

4.3.2.2 Theoretical Basis and Modeling

In Langematz, Tully et al. (2018), the chemical reactions involved in polar ozone depletion were discussed for specific winters, including the relevant reaction pathways and cycles. Since then, this work has been continued (Zafar et al., 2018), and the known stratospheric chemistry has been evaluated for the Arctic winter and spring 2020/21 (Feng et al., 2021; Grooß and Müller, 2021).

The record ozone depletion in the Arctic spring 2020 is well reproduced by chemical transport models (CTMs) that include state-of-the-art chemistry schemes and that obtain meteorological information from reanalyses, such as the CLaMS and TOMCAT chemistry models. As discussed in detail in *Section 4.2.4.2*, the simulated stratospheric ozone loss in Arctic spring 2020 in both CTMs agrees well with satellite observations and balloon-borne ozone sondes (Grooß and Müller, 2021; Feng et al., 2021; Weber et al., 2021), demonstrating that known stratospheric chemistry in combination with transport can explain the observed severe Arctic ozone depletion for the specific meteorological conditions in winter/spring 2019/20 (i.e., a stable stratospheric polar vortex and low temperatures).

Despite the capability of state-of-the-art CTMs to reproduce the observed polar ozone depletion, one open issue, already noted in the previous Assessment (Langematz, Tully et al., 2018), remains unresolved. Analysis of chlorine chemistry in current CTMs and CCMs (chemistry-climate models) revealed that the simulated HCl depletion in the cold and dark early-winter polar vortex is too weak and occurs too late compared to that observed (Wohltmann et al., 2017; Grooß et al., 2018). This discrepancy, which is more prominent in the Antarctic but has also been seen in cold Arctic winters (Grooß et al., 2018; Grooß and Müller, 2021), seems to be due to some unknown process. As the HCl discrepancy occurs in early winter, when ozone loss rates are slow, its effect on the ozone column loss throughout the Antarctic winter and spring is minor (~2%; Grooß et al., 2018).

As discussed in Langematz, Tully et al. (2018), high levels of active chlorine are maintained in the core of the Antarctic lower-stratospheric polar vortex during spring, despite rapid

gas-phase production of HCl. Maintenance of active chlorine is achieved through HCl null cycles in which HCl production is balanced by immediate reactivation (Müller et al., 2018). Using box-model simulations representative of vortex core conditions, Zafar et al. (2018) showed that the chemistry of the methyl peroxy radical (CH_3O_2) is essential for these HCl null cycles and thus for Antarctic lower-stratospheric chlorine and ozone loss chemistry.

4.3.3 Very Short-Lived Halogenated Substances

Chemical destruction of ozone in the polar spring occurs through catalytic cycles involving ClO and BrO radicals. These species are part of the inorganic chlorine and bromine families, which are produced in the stratosphere following the degradation of natural and anthropogenic source gases. Because air in the polar lower stratosphere is aged, even ODSs with relatively long lifetimes (decades or more) are largely decomposed to the inorganic families. Therefore, the contribution of different chlorine- and bromine-containing source gases to polar ozone depends on the additional amount of Cl or Br delivered to the stratosphere, which provides a way of comparing the impact of chlorine and bromine VSLSs on polar ozone with longer-lived species.

Natural brominated VSLSs (e.g., $CHBr_3$ [bromoform] and CH_2Br_2 [dibromomethane]) transport around 5 ppt bromine to the stratosphere (see discussion in *Chapter 1*) out of the current total bromine loading of around 20 ppt. This bromine will have a proportionate effect on polar ozone loss that occurs via the BrO + ClO catalytic cycles. Although there are few direct recent observations in the polar region, the contribution of VSLSs to polar bromine is expected to be similar to the mean contributions (sum of product gas and source gas injection) at lower latitudes (Wang et al., 2019; Barrera et al., 2020; Fiehn et al., 2018; Filus et al., 2020; Adcock et al., 2021), for which there is no observational evidence of a long-term trend. In situ aircraft observations of total and speciated bromine from aircraft flights in the late summer and fall UTLS at northern middle and high latitudes confirmed estimates of the current mean bromine loading of 19.2 ± 1.2 ppt and also found evidence for a somewhat variable stratospheric input of short-lived bromine species such that there are regions of higher bromine of 20.9 ± 0.8 ppt (Rotermund et al., 2021). Understanding this variability is important for understanding extra-polar transport pathways, but the impact on polar ozone loss will depend largely on the mean abundance of bromine. As the levels of brominated ODSs decrease, natural bromine, including VSLSs, will make a relatively larger contribution to polar ozone loss.

Chlorinated VSLSs are mainly anthropogenic in origin (e.g., dichloromethane [CH_2Cl_2]) and currently contribute around 130 (100–160) ppt (**Table 1-6**) to the current total chlorine loading of around 3500 ppt. The chlorine from VSLSs is thus expected to make a proportional contribution to polar ozone loss through the main ClO + ClO and ClO + BrO catalytic cycles. An increase in chlorinated VSLSs (Hossaini et al., 2019; Harrison et al., 2019; Claxton et al., 2020) is estimated to have slowed the decline of long-lived HCl in the upper stratosphere in the period 2004–2017 by about 15% (Hossaini et al., 2019).

There is renewed interest but significant uncertainty in the possible role of iodine in stratospheric chemistry. Iodine is present in very small abundances and is largely natural in origin (*Chapter 1*). Previous estimates of the upper limits on the amount of iodine reaching the stratosphere have recently been revised upward, to up to 1 ppt (Koenig et al., 2020). CCM simulations show that stratospheric iodine abundances consistent with those from low-latitude observations (0.77 ppt; Koenig et al., 2020) could contribute 4% of the observed Antarctic springtime column ozone loss, equivalent to the loss induced by 3.1 pptv bromine (Cuevas et al., 2022). Further work is needed to assess the uncertainties in iodine chemistry and elucidate the possible role that iodine trends may play in polar ozone trends.

4.3.4 Dynamical Impacts on Polar Ozone

4.3.4.1 Synthesis of the Role of Dynamics in the Last Four Arctic and Antarctic Springs

As discussed in *Sections 4.2.3* and *4.2.4*, the evolution of total column ozone (TCO) in the four Arctic and Antarctic springs since the last Assessment was characterized by large interannual variability. In the Northern Hemisphere, a series of three springs with weak ozone loss (2018, 2019, 2021) was interrupted in spring 2020, when record-low TCO was measured over the Arctic. In the Antarctic, ozone holes consistent in size and depth with what is expected from the slow decline in ODSs appeared in three of the four spring seasons (2018, 2020, 2021), while in the Southern Hemisphere spring of 2019, an unusually weak ozone hole developed. Also noteworthy was the record persistence of the 2020 and 2021 Antarctic ozone holes well into December. Although the weak Antarctic ozone loss in 2019, the strong Arctic ozone loss in 2020, and the duration of the 2020 and 2021 Antarctic ozone holes were exceptional, they are in line with the current understanding of the chemical and dynamical factors that determine polar ozone loss.

As explained in more detail in previous Assessments (e.g., Dameris, Godin-Beekmann et al., 2014; Langematz, Tully et al., 2018), polar ozone loss is controlled by both chemical and dynamical processes. In most Northern Hemisphere winters, tropospheric planetary waves propagate upward into the stratosphere, where they weaken the stratospheric polar vortex and warm the Arctic stratosphere. These effects lead to reduced chemical ozone depletion and enhanced descent of ozone-rich air into the lower stratosphere by the Brewer-Dobson circulation (BDC) and thus to higher ozone abundances throughout winter and spring. During sudden stratospheric warmings (SSWs), for example, Arctic TCO may increase rapidly by up to about 50 DU due to eddy transport linked to enhanced wave drag (de la Cámara, 2018; Hong and Reichler, 2021). After SSW events, the eddy transport of ozone is reduced in the upper stratosphere, leading to a more rapid decay in ozone toward climatological values than in the lower stratosphere, where isentropic irreversible mixing delays the return to pre-SSW values (de la Cámara, 2018; Hong and Reichler, 2021). In contrast, in winters with weak planetary wave activity, as is common in the Southern Hemisphere, stable and large polar vortices enclosing cold air develop, providing conditions for efficient chemical ozone depletion. In combination with suppressed dynamical replenishment of ozone, strong and occasionally long-lasting ozone loss occurs, as was the case in the austral springs of 2020 and 2021.

Both the weak Antarctic ozone hole in 2019 and the strong Arctic ozone loss in March 2020 resulted from atypical dynamical conditions in the respective winters. In September 2019,

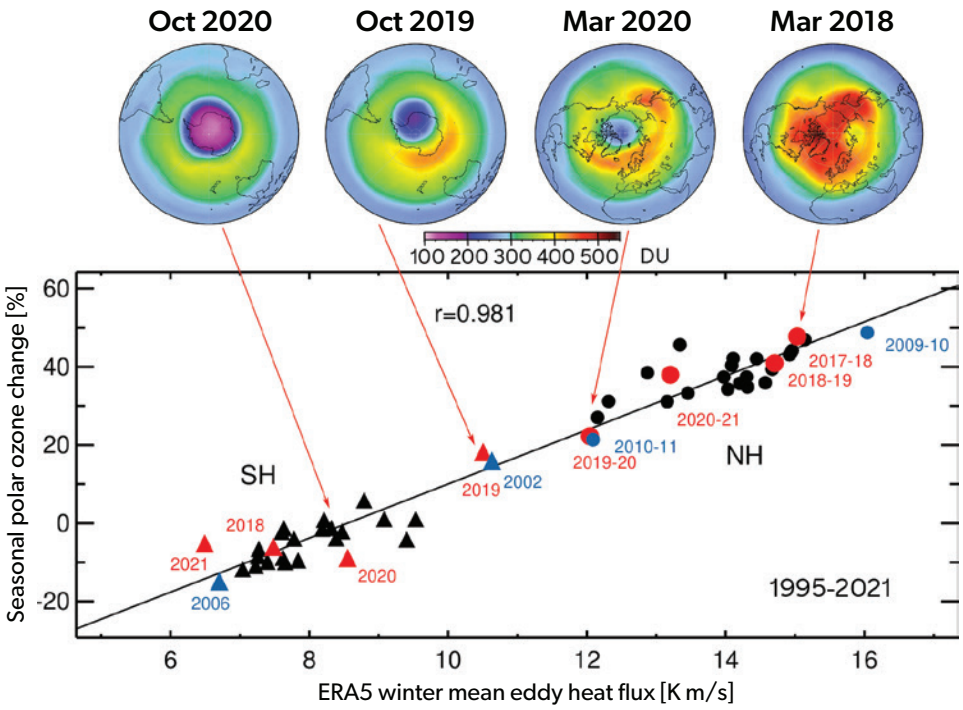

Figure 4-13. Observed polar cap (>50° latitude) total column ozone (TCO) change between spring and the preceding autumn (%) as a function of the extratropical winter-mean eddy heat flux (September to March in the Northern Hemisphere [NH, dots] and March to September in the Southern Hemisphere [SH, triangles]) derived from GOME-SCIAMACHY-GOME-2 ozone (1995–2021) and ECMWF ERA5 meteorological data (1995–2021) separately in each hemisphere. The four recent SH and NH winters are labeled in red. Years with extreme low and high TCO in either hemisphere are labeled in blue. Polar TCO distributions from GOME-2B for two selected recent years in the Antarctic *(left pair)* and Arctic *(right pair)* are shown at the top. [Updated from Weber et al., 2011, and Langematz, Tully et al., 2018.]

chemical ozone depletion was halted by a strong minor SSW that weakened the polar vortex and warmed stratospheric air above PSC formation temperatures (see *Section 4.2.3.2*). In the Arctic winter 2019/20, the stratospheric polar vortex was the strongest and most persistently cold in over 40 years, leading to enhanced chemical ozone depletion and reduced dynamical replenishment of ozone (see *Section 4.2.4.2*). While anomalous, both cases are fully in line with the established linear relationship between the seasonal high-latitude TCO change between autumn and the following spring and the mid-latitude winter-mean eddy heat flux, used as a metric for dynamical activity (Weber et al., 2011; **Figure 4-13**). These two winters are very close to the previous extreme cases in austral spring 2002 and boreal spring 2011 and bridge the two separated Northern and Southern Hemisphere value clusters.

4.3.4.2 Predictability of Arctic Spring Ozone

The dominant role of dynamical variability for Arctic spring ozone gives rise to the question of whether polar spring ozone is predictable based on meteorological forecast systems. The evolution of Arctic ozone in spring is strongly coupled to the evolution of the stratospheric polar vortex throughout the previous winter (e.g., Weber et al., 2011). To predict the stratospheric state in winter, meteorological forecast systems need to capture both stratospheric extremes, i.e., strong polar vortex events, which may last for several weeks, sometimes enhanced by wave reflection, and SSWs, which evolve more rapidly and are driven by tropospheric planetary wave forcing. Both states are additionally affected by the phases of the 11-year solar cycle, the Quasi-Biennial Oscillation (QBO), and the El Niño-Southern Oscillation (ENSO). Forecasts from six seasonal prediction systems consistently predicted the extreme Northern Hemisphere stratospheric polar vortex in winter 2019/20, with the ensemble mean forecasts for January/February/March 2020 from two models exceeding any equivalent in their hindcast periods (Lee et al., 2020). This study showed that seasonal prediction systems are able to produce exceptional signals for a strong stratospheric polar vortex. The prediction skill of Arctic ozone in the three Arctic springs with strongest ozone loss (1997, 2011, 2020) was assessed by Rao and Garfinkel (2020, 2021). They found predictive skill for low March 2011 Arctic ozone when initializing the seasonal forecast systems in early March and then applying empirical models using different forecasted metrics of the stratospheric polar vortex as predictors. The predictive skill from these empirical models, however, was lower than the ozone prediction from the chemical scheme of the forecast system that provided the meteorological input fields to the empirical models. March ozone loss in 2011 was more predictable than the 1997 and 2020 ozone losses, possibly due to more favorable meteorological background conditions (Rao and Garfinkel, 2020).

4.3.4.3 Arctic Winter Variability Under Climate Change

As discussed in recent Assessments (e.g., Langematz, Tully et al., 2018, and references therein), year-to-year variability and trends in Arctic ozone in winter and spring are strongly influenced by dynamical processes. Upward propagating and dissipating planetary waves, often associated with SSWs, lead to weaker stratospheric polar vortices with higher temperatures, thus reducing the number of days cold enough for heterogeneous chemical ozone depletion. In addition, the BDC is enhanced in years with high planetary wave activity, which leads to a stronger poleward-downward transport and increased meridional mixing of ozone-rich air into the Arctic stratosphere. Simulations with climate and chemistry-climate models consistently project an increase of the BDC in a future climate with enhanced greenhouse gas (GHG) abundances (Karpechko, Maycock et al., 2018; see also *Section 5.2.4*). Hence, more ozone would be transported to Northern Hemisphere high latitudes in winter and spring, and Arctic ozone recovery would be accelerated. On the other hand, no robust evidence of future changes in major SSWs was found in a multi-model assessment of CCMI projections of the 21st century (Ayarzagüena et al., 2018). An analysis of CMIP6 climate model projections for quadrupled carbon dioxide (CO_2) concentrations revealed that the SSW frequency is sensitive to an increase in CO_2 forcing; however, there was no consensus among the models on the sign of these changes in SSW frequency (Ayarzagüena et al., 2020).

Changes in SSW occurrence in a future climate—in either direction—will likely be driven by changes in the dynamical forcing from tropospheric planetary waves in combination with a changed stratospheric background climatology. For example, Langematz, Tully et al. (2018) discussed in detail the impact of the dynamical forcing of the polar stratosphere by sea surface temperature anomalies (SSTAs) in the tropical Pacific Ocean during ENSO. Likewise, SSTAs over the North Pacific were suggested to have significant effects on the stratospheric Arctic vortex via dynamical processes (e.g., Hurwitz et al., 2012; Hu et al., 2018; Li et al., 2018). A link between North Pacific SSTAs and ozone was suggested by Hu et al. (2022), who show that about 30% of the observed negative ozone trend in the Arctic lower stratosphere in March, derived from MERRA-2 reanalyses for the period 1998–2018, can be explained by North Pacific SSTAs in February, associated with the second leading mode (PC2), the so-called Victoria mode, of North Pacific SST variability (Bond et al., 2003). Arctic ozone concentrations decrease with the warm phases of Victoria mode–related North Pacific SSTAs and increase with its cold phases. The decrease in Arctic lower-stratospheric ozone during 1998–2018 is consistent with an increase in the PC2 of the North Pacific SSTAs. The Victoria mode–related SSTAs tend to weaken the Aleutian low, thus impeding the upward propagation of wavenumber-1 waves into the subpolar lower stratosphere. As a result, the BDC is weakened and less ozone is transported from the ozone-rich middle stratosphere to the ozone-poor lower stratosphere. The derived Arctic lower-stratospheric ozone decrease in 1998–2018 was thus to a large degree the result of natural decadal SST variability rather than evidence for continuous chemical ozone depletion by ODSs.

In recent years, a further potential source of dynamical forcing of the stratosphere has attracted increasing attention. This forcing is driven by the observed seasonal decline in Arctic sea ice concentration over the last decades, particularly in the Barents and Kara (BK) Seas. A stratospheric pathway has been proposed that links Arctic sea ice decline and mid-latitude weather anomalies. The hypothesis is that decreased sea ice cover during early winter, especially over the BK Seas, enhances the upward propagation of planetary waves with wavenumbers 1 and 2, subsequently weakening the stratospheric polar vortex in mid-winter (Kim et al., 2014; Nakamura et al., 2016). So far, no consensus has been reached on the influence of the Arctic sea ice decline and the associated Arctic warming (Arctic amplification) on European mid-latitude winter weather (see Cohen et al., 2020, for a review). However, modeling studies with regional sea ice melt confined to the BK Seas and a well-resolved stratosphere do simulate a weakened stratospheric polar vortex and a cooling of the mid-latitudes in winter, consistent with the observations (Screen, 2017; Zhang et al., 2018; Mori et al., 2019; Hoshi et al., 2019). In an analysis of CMIP5 simulations forced with the high RCP8.5 GHG emissions scenario, Kretschmer et al. (2020) found a nonlinear response of the stratospheric polar vortex to a future global mean warming that includes a weakening of the vortex caused by sea ice loss in the BK Seas and an opposite vortex response once the BK Seas are ice free. The identified polar vortex weakening is accompanied by an increase of the eddy heat flux at 100 hPa, indicating enhanced dynamical forcing from the troposphere. The results of Kretschmer et al. (2020) are consistent with those of Manzini et al. (2018), who analyzed the stratospheric winter response in two consecutive global warming periods of 2 K each in a large ensemble of experiments from a single climate model. They found a shift from an easterly wind change (i.e., a vortex weakening) in the first warming period to a westerly wind change (i.e., a vortex strengthening) in the second warming period and concluded that Arctic sea ice changes can act to trigger a nonlinear atmospheric response. Studies thus suggest an increase in stratospheric dynamical activity in the Northern Hemisphere late winter throughout the remainder of the 21st century, i.e., the period of Arctic sea ice decline. However, the role of the stratospheric pathway for the Arctic/mid-latitude linkage, and in particular the dynamical forcing of the Northern Hemisphere winter stratosphere by Arctic sea ice loss, remains an open question (Kretschmer et al., 2020) and is intensely debated.

A recent analysis of simulations from CMIP5 and CMIP6 models highlights that in an extreme GHG scenario, the potential for the formation of PSCs in individual cold winters that experience little or no dynamical forcing from the troposphere will rise toward the end of the 21st century, providing favorable conditions for episodic large seasonal loss of Arctic TCO (von der Gathen et al., 2021; see discussion in *Section 4.5.3.3*). Similar episodes with future high PSC formation potential are found in models with interactive ozone chemistry. However, in these models, the impact of increasing dynamical forcing becomes the dominant factor for Arctic ozone in the second half of the 21st century (Langematz et al., 2014; Bednarz et al., 2016). This is consistent with projections from CCMI models (Dhomse et al., 2018) and four CMIP6 models with interactive ozone (Keeble et al., 2021; see *Section 4.5.3.4* and **Figure 4-24**) of an accelerated Arctic ozone recovery and a super-recovery (higher TCO than in 1980) by the end of the 21st century for the more severe GHG scenarios.

In general, the quantification of Arctic polar ozone is complicated by uncertainties in the applied methods and models. These uncertainties include limitations in the ability of models to

reproduce observed polar temperatures, as well as the fact that most CMIP6 models lack the chemical modules necessary to properly account for ozone feedbacks.

4.3.5 Other Factors Affecting Polar Ozone

4.3.5.1 Solar Variability

Langematz, Tully et al. (2018) reported in detail on the impact of energetic particle precipitation (EPP) on polar ozone and on the progress in deriving EPP effects on atmospheric composition and ozone from satellite data and chemistry-climate models (CCMs). Since then, a number of studies have contributed to better quantification and understanding of the solar forcing amplitude in both solar electromagnetic radiation and EPP.

Motivated by the construction of new solar input datasets for the CMIP6 model intercomparison study, Kunze et al. (2020) compared the implications of the prescribed spectral and total solar irradiance (SSI/TSI) dataset for the simulated 11-year solar ozone response in simulations with two CCMs. Both sets of CCM simulations used five different solar forcing datasets, including the most recent CMIP6 dataset (Matthes et al., 2017). They found that at polar latitudes, the magnitude of the solar TCO signal is only marginally affected by the solar irradiance dataset used (Kunze et al., 2020).

Polar ozone can be destroyed by EPP either through sporadic large fluxes of solar protons (solar proton events [SPEs]) after solar coronal mass ejections (CMEs) or by the continuous impact of the solar wind on Earth's magnetosphere, leading to energetic electron precipitation (EEP) associated with geomagnetic storms. Both types of EPP induce enhanced ionization levels in the middle and upper polar atmosphere, leading to the production of NO_x. The NO_x is long lived during winter and destroys ozone either locally in the upper stratosphere and mesosphere (EPP direct effect) or in the lower stratosphere after being transported downward by the BDC in the winter polar vortex (EPP indirect effect; see, e.g., the reviews of Sinnhuber et al., 2012, and Mironova et al., 2015).

EPP is closely linked to the phase of the 11-year solar cycle and is thus characterized by quasi-regular oscillations with sporadic enhancements after SPEs. It mainly affects polar ozone in the upper stratosphere and mesosphere. Nevertheless, EPP effects on polar ozone are non-negligible. Sinnhuber et al. (2018) find an average EPP-induced decrease in Antarctic TCO of about 4% in each winter/spring. The timing of the strongest ozone response to SPEs in the winter/spring season coincides with the maximum signal of upper-stratospheric polar ozone recovery from ODSs, with trends maximizing in the autumn/winter seasons in both hemispheres (Stone et al., 2018). Thus, accounting for SPEs is important for the detection of ozone recovery in the upper stratosphere. Moreover, EPP has the potential to affect lower-stratospheric polar ozone by interfering with catalytic ozone depletion in Antarctic spring, as originally suggested by Jackman et al. (2000) and Funke et al. (2014). Observational evidence from different satellite datasets suggests that Antarctic springtime ozone increases in the lower stratosphere are associated with higher-than-average EPP during the preceding winter (Gordon et al., 2020, 2021). Due to the EPP indirect effect, NO_x is transported from the upper mesosphere into the lower stratosphere, where it remains at least until late spring (Gordon et al., 2020). Through reaction with chlorine monoxide (ClO), chlorine nitrate ($ClONO_2$) is formed, preventing some of the NO_x- and Cl_x-driven catalytic ozone destruction. This buffering mechanism will be less effective when the atmospheric chlorine loading decreases in the future.

Toward the second half of the 21st century, polar EPP-NO_x is expected to increase in the stratosphere due to circulation changes associated with rising GHG concentrations. The projected increase in downward transport from the mesosphere in a stronger BDC leads to an enhanced EPP indirect effect. With declining ODSs, NO_x catalytic ozone destruction, and thus the contribution of EPP-NO_x, will become more prominent (Maliniemi et al., 2020; see also *Section 4.5.3.4*).

To investigate the impacts of EPP on polar ozone, models including either high-top ionization/chemistry schemes or employing parameterizations of EPP effects are applied. Simulations with CCMs forced with EPP-induced NO_y anomalies from satellite data or including simple parameterizations of NO_x and HO_x production by SPEs qualitatively reproduce the observed decrease of polar ozone following SPEs in the upper stratosphere (see also Langematz, Tully et al., 2018). However, recent studies suggest that the impact of both SPEs and EEP might be underestimated in current models. Kalakoski et al. (2020) show that the polar ozone response to SPEs in the upper stratosphere is enhanced when detailed ion chemistry reactions in the lower ionosphere are included, as they lead to increased conversion of HCl to reactive Cl_x species. New observational evidence has also emerged that the current CMIP6 parameterizations of EEP from Earth's radiation belt (van de Kamp et al., 2016) underestimate the effects of EEP on polar ozone. Nesse Tyssøy et al. (2019) found that the CMIP6 model fails to reproduce the electron flux level and variability associated with the strongest CMEs as well as the duration of EEP events during solar maximum. As a result, the modeled NO_x enhancements by EEP in the mesosphere and upper stratosphere are too low, and the associated ozone loss is too weak (Nesse Tyssøy et al., 2019). This result is consistent with CCM simulations that showed better agreement with observations of the descent of NO_x when—in contrast to the CMIP6 parameterization—improved electron flux information was used (Pettit et al., 2019). Similar conclusions were also drawn based on calculated ionization rates from balloon observations of 500 EEP events (Mironova et al., 2019). The authors found differences from the CMIP6 recommended ionization rates that lead to an underestimation of the NO_x enhancement by more than 100% and of the associated ozone loss by up to 25% in the mesosphere. However, with an average EPP-induced decrease in Antarctic TCO of about 4% in each winter/spring (Sinnhuber et al., 2018), the effect of such an underestimation of mesospheric ozone loss by EPP on TCO is likely to be small.

The above findings are supported by Duderstadt et al. (2021), who estimated electron precipitation by scaling observations from the Van Allen Probes instruments, which measure trapped electrons directly in the radiation belts, to observations from the FIREBIRD II CubeSats, which measure precipitating electrons from polar low-Earth orbit. The derived flux ratios from 35 conjunctions of the satellites between 2015 and 2017 were statistically analyzed in terms of 50th, 75th, and 100th percentiles, indicating the NO_x and ozone changes from the median (50% percentile) to the highest (100% percentile) values of the distribution. **Figure 4-14** shows the modeled enhancement of NO_x and reduction of O_3 averaged over the stratospheric polar vortex during the weeks following the March 2013 electron precipitation event. Enhancements of NO_x descending into the upper

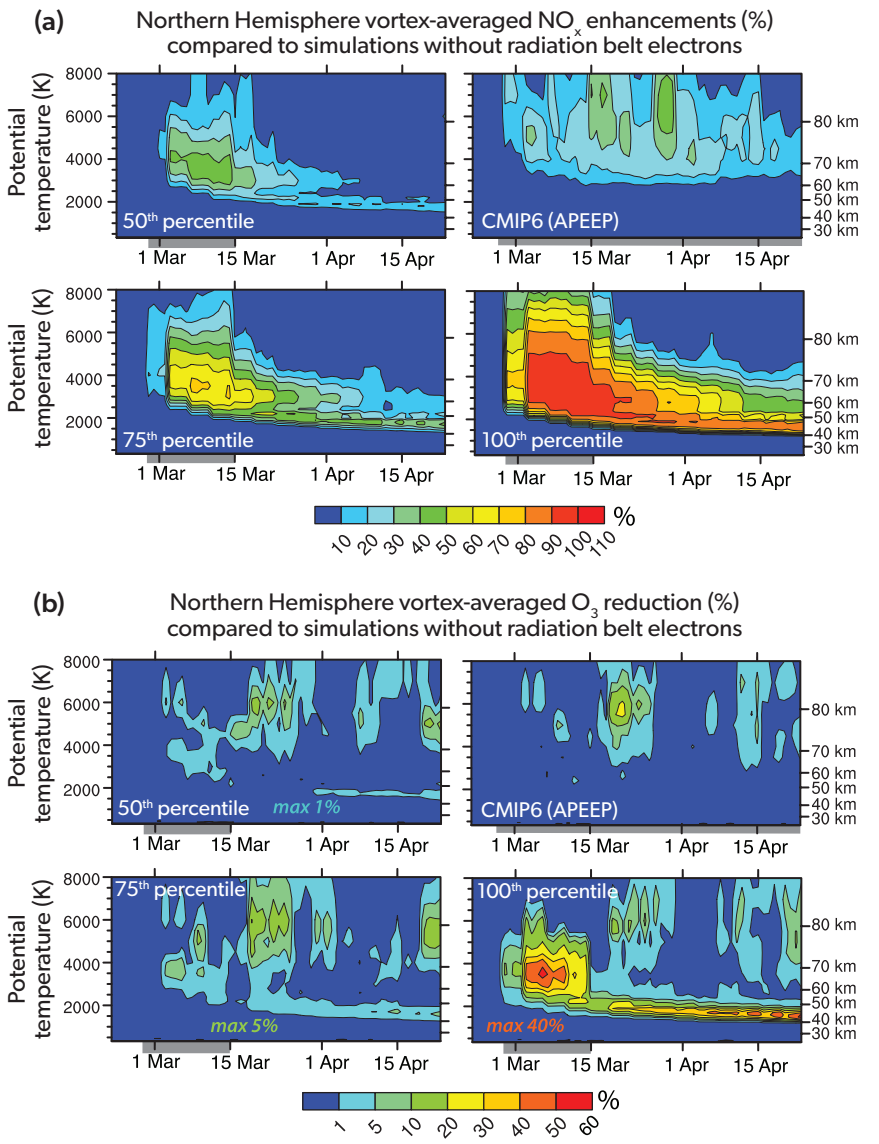

Figure 4-14. WACCM simulations for the March 2013 electron precipitation event showing longer-term (a) enhancements of NO_x and (b) reductions of O_3 averaged over the Northern Hemisphere polar vortex from radiation belt electrons. Gray bars along the x-axis represent times when medium energy electron ionization is included in the simulations. Percentiles refer to the flux ratios of the two instruments. [From Duderstadt et al., 2021.]

stratosphere (40–50 km) reach 20–30% for the 50th percentile flux ratios and 80–90% for the 100th percentile case, and the enhancements persist through April. In situ reductions of ozone at 40–50 km altitude are only 1% for the 50th percentile case but up to 40% for the 100th percentile case (Duderstadt et al., 2021).

4.3.5.2 Volcanic Eruptions

In Langematz, Tully et al. (2018), the impact of large volcanic eruptions, which increase the amount of sulfate aerosols in the stratosphere, was highlighted. Observations from ozonesondes and Aura MLS, as well as CCM simulations, suggested that the eruption of the Chilean volcano Calbuco contributed to the record-large Antarctic ozone hole in spring 2015.

Comparisons of coupled chemistry-climate-aerosol model simulations with satellite and balloon observations (Stone et al., 2017; Zhu et al., 2018) show that volcanic sulfate aerosols from the Calbuco eruption were transported from mid-latitudes toward the Antarctic and slowly descended during transport. The modeled aerosol number density indicates that Calbuco sulfate aerosols penetrated into the Antarctic polar vortex starting in May and led to ozone depletion in September 2015, particularly at around 100 hPa and 70°S, up to 35% higher than if there had been no eruption. The simulated aerosol surface area density, earlier ozone loss, and larger area of the ozone hole are consistent with the presence of volcanic sulfate layers observed at 16 km, as well as with previous model studies (e.g., Solomon et al., 2016).

As discussed in the previous Assessment (Langematz, Tully et al., 2018), the injection of halogens from large volcanic eruptions into the stratosphere is expected to become more relevant in a future atmosphere with declining anthropogenic halogens. Simulations with 2-D CTMs have suggested substantial ozone reductions in the polar regions from the injection of volcanic halogens, and they also highlighted the increasing role of short-lived brominated substances in determining whether future volcanic eruptions will cause ozone depletion (Klobas et al., 2017). Combining for the first time a complex 3-D CCM with

a measurement-based dataset of sulfur, chlorine, and bromine releases from tropical volcanic eruptions, Brenna et al. (2019) investigated the effects of halogen emissions by large, explosive volcanic eruptions under preindustrial atmospheric conditions. A volatile mass representative of large sulfur- and halogen-rich eruptions was deduced from an average of 28 eruptions of variable composition along the Central American Volcanic Arc (CAVA) over a time interval of 200 ka. Assuming an injection of 10% of the erupted halogen mass into the stratosphere, their simulations reveal a decade-long depletion of the ozone layer by about 20% globally. In the Arctic, a maximum TCO decline of more than 200 DU (45%) takes place in the first spring after the eruption, followed by ozone decreases of more than 120 DU (20%) in the post-eruption years 2 and 3. In the Antarctic, ozone depletions comparable to present-day ozone holes occur in springs 3–6 after the eruption, with minimum TCO below 100 DU and maximum ozone hole area extent in October of year 4. These results are, however, sensitive to the halogen injection efficiency, with a reduced ozone response for a halogen injection efficiency smaller than 10%.

4.3.5.3 Wildfire Emissions

Severe bushfires in southeastern Australia in late December 2019 and early January 2020 (the Australian New Year's event [ANY]) injected large amounts of smoke and tropospheric air into the Southern Hemisphere stratosphere (Kablick et al., 2020; Khaykin et al., 2020; Allen et al., 2020; Schwartz et al., 2020). Satellite observations show that heterogeneous chlorine activation occurred on the smoke particles at Southern Hemisphere mid-latitudes, leading to strong and persistent depletion in stratospheric HCl and enhancement of ClO that peaked in mid-2020 (Santee et al., 2022; Bernath et al., 2022). However, although such strong and sustained mid-latitude chlorine activation was unprecedented, it was still an order of magnitude or more weaker than that in a typical winter polar vortex (Santee et al., 2022). Southern Hemisphere mid-latitude ozone was anomalously low during that period, but there is currently no consensus about the relative roles of transport and chemistry in inducing the mid-latitude ozone anomaly (see related discussion in *Section 3.2.1.3*) or the potential contribution of ANY to polar ozone depletion in 2020. Some studies suggest non-negligible chemical depletion of polar ozone caused by the ANY smoke, with the contribution to ozone loss comparable to that of the sulfate aerosols from the Calbuco eruption in 2015 (Yu et al., 2021; Rieger et al., 2021). One model simulation yielded 10–20 DU of additional ozone loss due to heterogeneous reactions on sulfuric acid–coated smoke particles between August and September, resulting in a 12% increase in the ozone hole area compared to a control simulation with no smoke (Yu et al., 2021). However, an analysis of the ANY plumes using satellite observations and meteorological fields from a reanalysis that succeeded in tracking several of the largest plumes found no evidence that any of them penetrated or altered the chemistry of the then-developing Antarctic vortex (Schwartz et al., 2020). Thus, the impact of the ANY smoke on Antarctic ozone remains highly uncertain.

4.3.5.4 Supersonic and Hypersonic Aircraft Emissions

Different organizations and companies are once again reconsidering the development of a supersonic transport (SST) aircraft fleet designed for the commercial and business jet airline markets. SST aircraft would fly at supersonic speeds (Mach 2–2.5) at cruise altitudes between 13 and 23 km in the lower stratosphere. In parallel, new technologies are being explored with the aim of developing a hypersonic transport (HST) aircraft fleet flying at a speed of Mach 5–8 and cruise altitudes between 30 and 40 km (Yanes, 2020). Both types of aircraft will potentially release substantial amounts of water vapor (H_2O) and nitrogen oxides (NO_x) into the stratosphere, with concomitant strong effects on stratospheric ozone. Updated estimates of the expected ozone change were recently presented for a range of H_2O and NO_x emissions scenarios based on WACCM simulations.

Zhang et al. (2021) investigated the potential effects on stratospheric ozone of a hypothetical fleet of 500 or 1000 High Speed Civil Transport (HSCT) aircraft, based on projections made in NASA's 1999 Atmospheric Effects of Aviation Project (AEAP) Report (Kawa et al., 1999). The HSCT aircraft had been designed for long-range flights at Mach 2.4. Different levels of NO_x emissions with either constant or zero H_2O emissions from the AEAP report were prescribed, with atmospheric background conditions of the year 2015 assumed. Due to interactions between different ozone loss cycles, ozone responses of different signs were found in different regions of the atmosphere. For the basic NO_x scenario, the model simulates maximum ozone production of +1.4% in the UTLS at 11 km and ozone reduction above that level, reaching a maximum of −1.2% at 22 km at high latitudes in June. The same ozone change pattern appears for all scenarios with enhanced NO_x. Ozone depletion maximizes in the Northern Hemisphere, where most of the flights take place, at cruise altitudes (between 21 and 25 km), with peak ozone loss at high latitudes. TCO loss is found over most of the globe for the entire year, but maximum TCO loss occurs in the polar regions in springtime (–0.4% in March in the Northern Hemisphere and –1.2% in October in the Southern Hemisphere). While H_2O emissions generally have a much smaller effect on ozone depletion than NO_x emissions, they become more important in the Southern Hemisphere polar winter because they increase the surface area density of ice and thus promote heterogeneous ozone depletion.

In addition to the ongoing development of SSTs, the concept of a civil HST fleet is under consideration for future intercontinental travel. Estimates of the emissions of hypersonic aircraft are much more uncertain than those for SSTs, due to the present-day lack of concrete information on the type of engines to be used, the combustion systems and their emissions, and the size of the future fleet and flight conditions, such as the optimal flight altitudes. To assess the impact on the stratospheric ozone layer of such a hypothetical future HST aircraft fleet, Kinnison et al. (2020) conducted sensitivity studies, using estimated H_2O and NO_x concentrations emitted by aircraft flying at either 30 or 40 km altitude. The emissions and flight routes used to establish these concentrations were identical to the 1999 AEAP scenario, also adopted by Zhang et al. (2021). In summary, the study shows that NO_x emissions of an HST fleet of the assumed size would have the potential to substantially reduce the atmospheric ozone column. At high northern latitudes, the reduction in the ozone column is of the order of 8–10% (25 DU) for a 30 km injection, near the ozone maximum, and close to 5–8% (20 DU) for a 40 km injection (**Figure 4-15**). The emissions prescribed in the simulations of the HSCT (Zhang et al., 2021) and HST (Kinnison et al., 2020) aircraft fleets are the same. However, as they are emitted at different

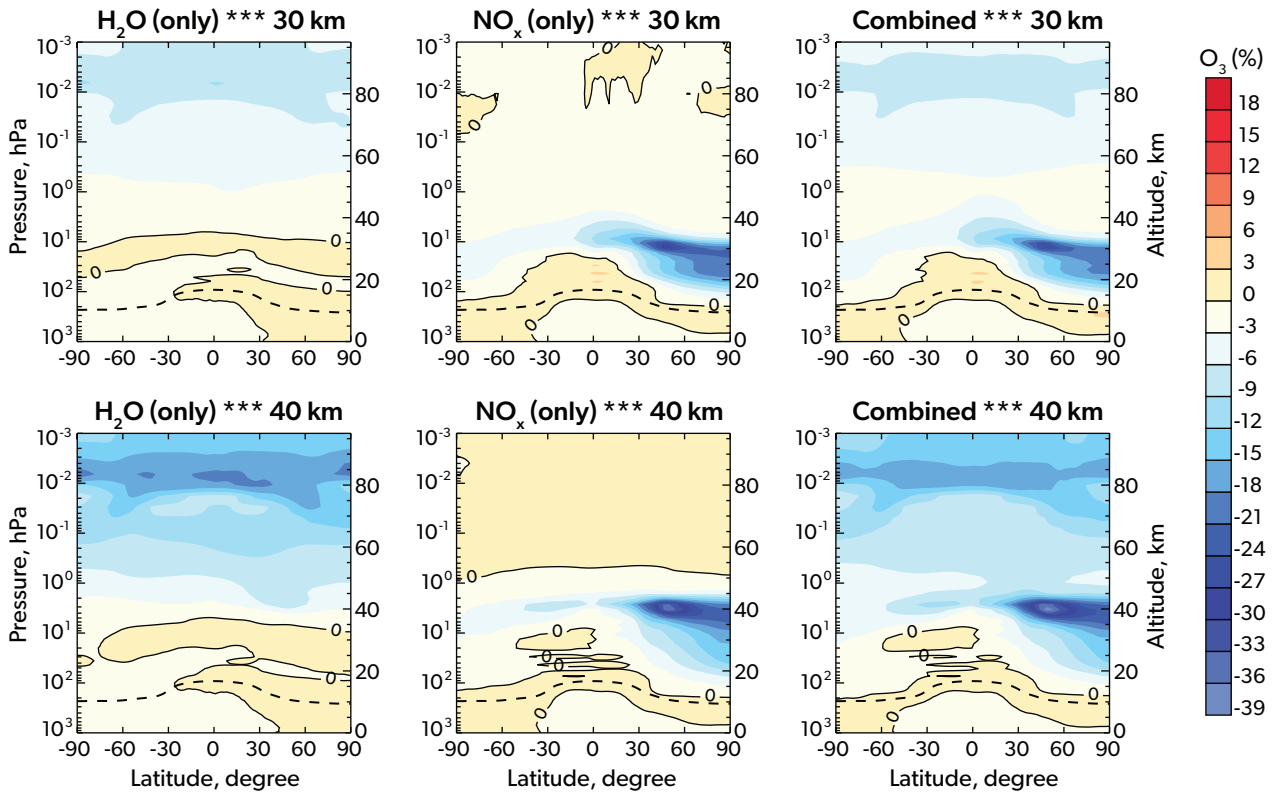

Figure 4-15. Percent change in the atmospheric concentration of ozone for an injection of H_2O *(left panels)*, NO_x *(middle panels)*, and combined NO_x + H_2O *(right panels)* by a fleet of HST operating at 30 km *(upper panels)* and 40 km *(lower panels)*. The black dashed lines denote the tropopause. [From Kinnison et al., 2020.]

heights in the stratosphere, their impact on ozone is larger for the HST fleet. Most of the ozone reduction is due to the release in the atmosphere of NO_x, while H_2O emissions primarily reduce ozone in the upper atmosphere (**Figure 4-15**) and, therefore, have a minor effect on the TCO response. The ozone depletion is largest in the Northern Hemisphere polar region (**Figure 4-15**) and most pronounced in spring and fall. The maximum reduction at high latitudes in the Southern Hemisphere is of the order of 2%.

In contrast, the NO_x emitted by a hypothetical scenario of hydrogen-fueled hypersonic airplanes has been estimated to have a negligible effect on global stratospheric ozone, but with enhanced impact over the poles (Ingenito, 2018).

While Zhang et al. (2021) and Kinnison et al. (2020) should be regarded as sensitivity studies using a specified dynamics setup for the simulations and estimated aircraft emissions, they both show an enhanced risk of a reduction in the stratospheric ozone layer by potential future fleets of SST or HST aircraft, consistent with previous assessments (e.g., Dameris et al., 1998; Kawa et al., 1999).

4.3.5.5 Rocket Emissions

With improving availability of commercial space launches and a growing interest in human settlements in space, the impact of rocket emissions on stratospheric polar ozone is expected to increase substantially in the coming decades. The composition of the rocket emissions products and their potential to deplete ozone strongly depend on the type of propellant used (solid, liquid, or hydrogen). A review of the ongoing research is presented in *Section 7.2.8.1*.

4.4 RECOVERY OF POLAR OZONE

4.4.1 Polar Ozone Recovery in Previous Assessments

The 2006 Ozone Assessment (Bodeker, Waugh et al., 2007) defined three stages of stratospheric ozone recovery: 1) a statistically significant slowing of the rate of ozone decline, 2) the onset of ozone increases above the previous minimum values (so-called turnaround) due to declining equivalent effective stratospheric chlorine (EESC), and 3) full recovery, which, in the absence of factors that alter the sensitivity of ozone to ozone-depleting substances (ODSs; e.g., volcanic eruptions), is likely to occur when EESC returns to 1980 levels. It should be noted, however, that even 1980 EESC levels are well above natural ODS abundances.

The 2014 Ozone Assessment (Dameris, Godin-Beekmann et al., 2014) noted that although Antarctic total column ozone (TCO) appeared to have begun increasing since reaching a minimum at the turn of the 21st century, and that the rate of that increase appeared to be consistent with the decline in ODSs, uncertainties

in measurements and statistical analyses precluded definitive attribution of the increasing Antarctic stratospheric ozone to decreasing ODSs. The most recent Assessment (Langematz, Tully et al., 2018) concluded that evidence had emerged after the 2014 Assessment that the second stage of ozone recovery had started. Trends in ozone over Antarctica during the month of September since the year 2000 were shown to be statistically significant, with an increase in observed total ozone and a decrease in ozone hole size and depth. Furthermore, these changes could be attributed at least partly to decreasing ODSs, particularly to declining stratospheric chlorine. For Arctic springtime stratospheric ozone, in contrast, recovery trends had not yet been reported. This is not unexpected, as Arctic springtime stratospheric ozone is dominated by large year-to-year dynamically induced variability of the polar vortex. The third stage of recovery, with springtime polar TCO returning to 1980 historical levels (see *Section 4.5*), is not expected until around mid-century.

The 2018 Assessment (Langematz, Tully et al., 2018) also reported that many studies since the 2014 Assessment had explored recovery detection. They noted that because of differences in datasets used, time periods over which trends were calculated, and analysis methods, direct comparison between published results was difficult and not very meaningful. However, all reported studies found clear signs of recovery despite these differing approaches, and this was considered to be a sign of the robustness of the finding of detectable ozone recovery. Updating trend values from those particular studies in this Assessment by extending the length of their analysis periods—even if practicable—would not resolve the complexities of their intercomparison. Hence, we focus on new publications since the previous Assessment, as well as recent Antarctic ozone holes and whether they have challenged the 2018 Assessment findings.

4.4.2 Long-Term Antarctic Ozone Trend and Onset of Antarctic Ozone Recovery

4.4.2.1 New Research into Antarctic Ozone Recovery

Since the last Assessment (Langematz, Tully et al., 2018), several studies have been published on trend detection in Antarctic stratospheric ozone and attribution of trends to ODSs.

One metric that has been explored is the frequency of occurrence of (extremely) low ozone concentrations and episodes of near-complete Antarctic stratospheric ozone destruction at selected altitudes due to ozone loss saturation. Ozone loss saturation refers to the concept that once near-complete ozone loss occurs, adding more ODSs will not result in more ozone depletion. As a consequence, with currently decreasing ODSs, expectations are that at some point in the future ozone loss saturation will no longer occur. Thus, the occurrence of loss saturation and/or extremely low ozone concentrations provides an alternative metric for monitoring ozone layer recovery. Although Antarctic ozone loss saturation is predicted to occur until at least mid-century, its frequency is expected to decline. Detection of such a decline would be an important milestone in stratospheric ozone layer recovery. A wide range of ozone data for the period 1979–2017, including profile measurements from balloon soundings and satellites, as well as TCO observations from Antarctic ground-based stations and satellites, show that extremely small ozone concentrations and ozone loss saturation started to occur after 1987 and peaked near the year 2000, after which a marked decrease was observed (Kuttippurath et al., 2018). The reduction in the frequency of occurrence of ozone loss saturation over the period 2001–2017 is consistent throughout the datasets.

Langematz, Tully et al. (2018) reported the first detection of post-year-2000 statistically significant trends in Antarctic stratospheric ozone based on different methods specifically for the month of September (Solomon et al., 2016; de Laat et al., 2017; Pazmiño et al., 2018; Weber et al., 2018). Building on those findings, Strahan et al. (2019) analyzed chemical transport model (CTM) simulations of past, present, and future Antarctic stratospheric ozone to identify which commonly used Antarctic ozone hole metrics best track declining ODS levels. The largest sensitivity of vortex-average column ozone was found for the period 1–20 September. Stronger dynamical variability during Antarctic spring increasingly obscures the ODS signal in post-September long-term ozone trends. In addition, the ozone mass deficit (OMD) best tracks trends in ODSs. The OMD relative to the 250 DU level was found to be a slightly better metric compared to the commonly used OMD relative to the 220 DU level. The former better samples the vortex edge region, which is where model simulations show that the largest decreases in ozone loss occur. In addition, approximately 25% of the increase in Antarctic springtime ozone levels can be attributed to seasonal pre-ozone hole Antarctic stratospheric ozone conditions (e.g., in the month of June).

Changes in the strength of the Brewer-Dobson circulation (BDC) have also been analyzed recently for their links to polar ozone trends (Fu et al., 2019). Satellite observations of stratospheric temperatures and meteorological reanalysis data show that the global annual mean BDC accelerated over the period 1980–1999 compared to 2000–2018. These decadal differences are attributed almost exclusively to the Southern Hemisphere BDC cell and stratospheric ozone depletion and healing in the ozone hole (see also Polvani et al., 2017). They are accompanied by a trend in post-year-2000 Antarctic stratospheric radiative warming during the month of September. An analysis of regional patterns of past Antarctic stratospheric warming in September and October similarly attributed at least part of an observed 2007–2017 warming to ozone recovery (Xia et al., 2020). Prior warming trends, between 1979 and 2006, in the Southern Hemisphere high-latitude stratosphere were mainly attributed to changes in the BDC and phase shifts of the stratospheric stationary waves.

Linear trends in a number of standard Antarctic ozone hole metrics for the period 1979–2017 have also been analyzed (Tully et al., 2019). These metrics include the minimum in 15-day average total ozone, maximum in 15-day average 220 DU ozone hole area, minimum in 15-day average OMD, and the duration of the ozone hole. Trends for the periods before and after the year 2000 are calculated for both unadjusted raw data and data that have been adjusted to account for the impact of stratospheric dynamics. The analysis uses TOMS, OMI, and OMPS TCO data, as well as temperature data from MERRA-2 for the adjustment. Trends towards reduced ozone depletion since 2001 are found to be statistically insignificant in the unadjusted data; statistically significant trends of a similar magnitude are found in the adjusted data (Tully et al., 2019).

Significant trends in September-average Antarctic ozone hole area (defined by the 220 DU contour) were found if only years characterized by similarly cold meteorological conditions

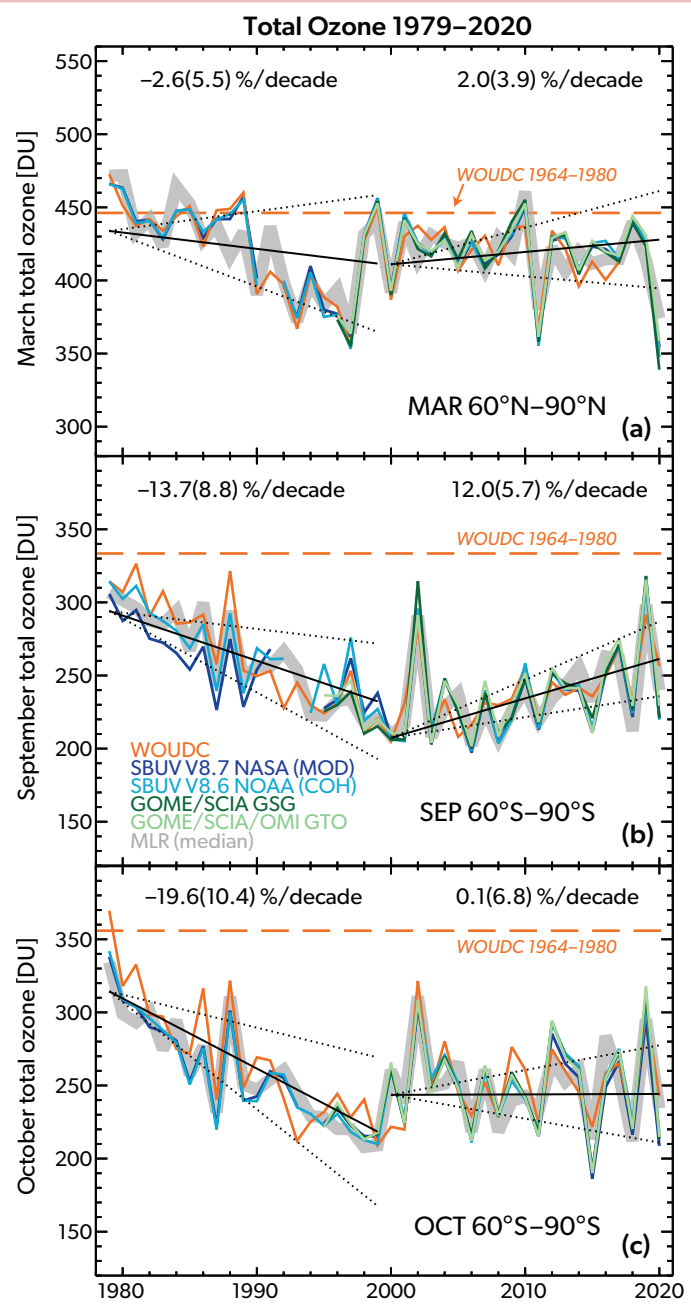

Figure 4-16. Total ozone time series for (a) the Arctic (60–90°N) in the month of March and (b, c) the Antarctic (60–90°S) in the months of September and October, derived from five long-term observational datasets: WOUDC (based on the GAW network of ground-based Dobson and Brewer instruments; orange line), SBUV 8.7 processed by NASA (blue line), SBUV 8.6 processed by NOAA (cyan line), GOME-SCIAMACHY-GOME-2 (GSG; dark green line), and GOME-type Total Ozone (GTO; light green line). The dashed orange lines show the 1964–1980 mean ozone levels from the WOUDC data. In each panel, the median of the datasets has been used to show the results of applying a multiple linear regression (MLR) with independent linear trends analysis (thick gray line). Regressor terms include the solar cycle, QBO, ENSO, volcanic aerosol, and the strength of the Brewer-Dobson circulation. The black solid lines indicate the linear trends before and after the year 2000, the ODS peak in the polar regions. The black dotted lines indicate the 2σ uncertainty of the MLR trend estimates. Trend numbers are indicated for the pre- and post-ODS peak period in the top part of the plots. Numbers in parentheses are the 2σ trend uncertainty. [Adapted from Weber et al., 2022, updated from Langematz, Tully et al., 2018.]

were considered (Kramarova et al., 2021). Using years identified (based on MERRA-2) as having 50 hPa September 60–90°S mean temperature at least one standard deviation below the 1980–2020 mean (33rd percentile), a significant downward trend in post-year-2000 September-average ozone hole area was calculated, in good agreement with expectations based on trends in ODSs.

Bodeker and Kremser (2021) reported a trend reversal in Antarctic ozone hole metrics around the turn of the century using the National Institute of Water and Atmospheric Research/Bodeker Scientific (NIWA-BS) TCO database covering the period 1979–2019. The trend reversal was attributed to the turn-of-the-century peak in stratospheric chlorine and bromine concentrations. Note that a robust attribution analysis of the drivers of long-term variability in Antarctic ozone hole metrics has not been conducted using the NIWA-BS record.

A recent study explored changes in the onset of early spring ozone depletion by comparing an ensemble of chemistry-climate model multi-member simulations for 1980–2024 with observed September Antarctic ozone hole area through 2021 (Stone et al., 2021). Agreement between the model simulations and observations was generally good. Significantly later start dates for the onset of rapid ozone depletion were found after the year 2000. In addition, a substantial reduction over the past decade was found in both measured and modeled ozone hole depth during September but not October. The significant September

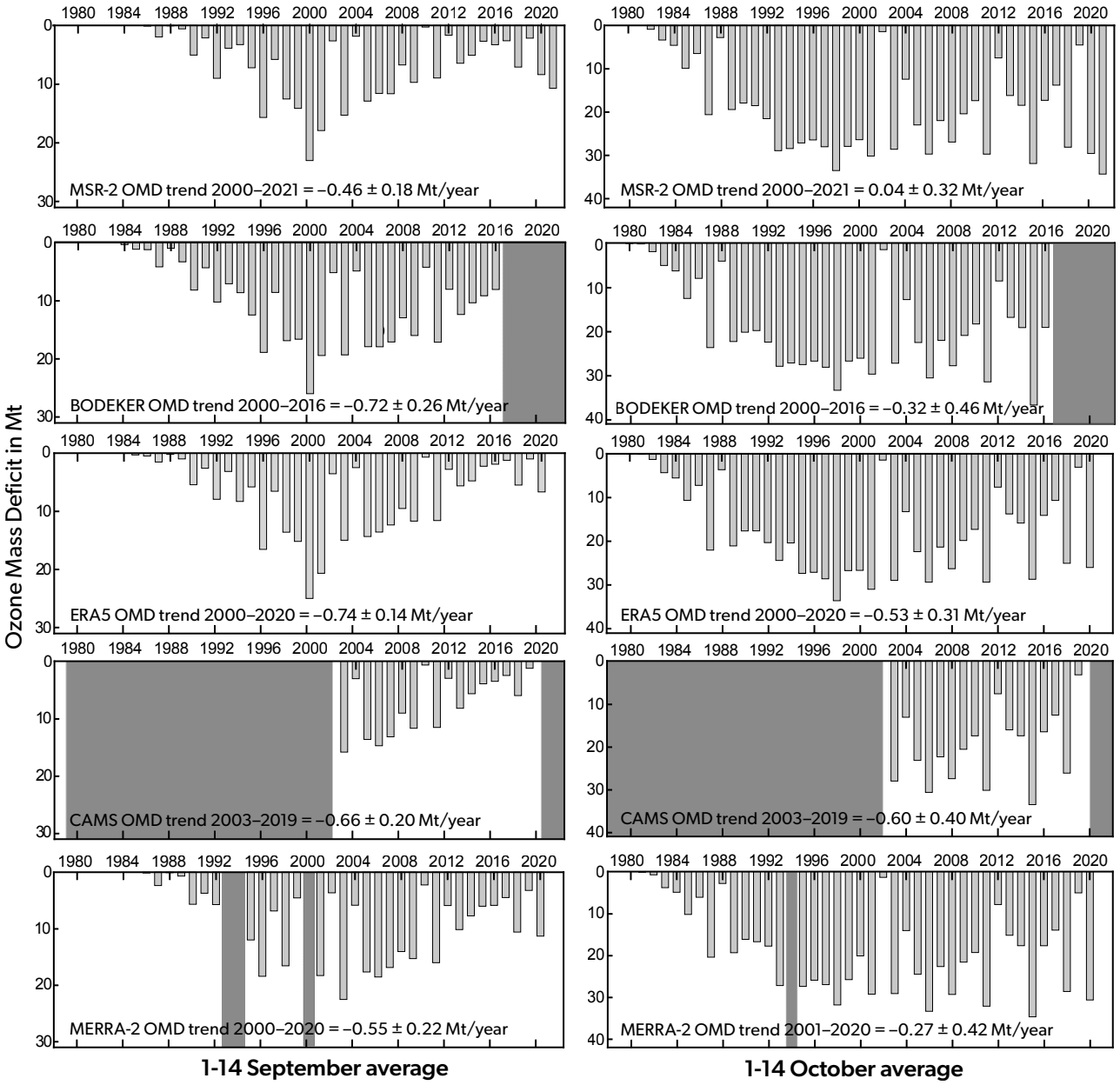

Figure 4-17. Antarctic 220 DU ozone mass deficit (in megatons) averages for 1–14 September *(left column)* and 1–14 October *(right column)* for different daily total column ozone reanalysis datasets. Dark grey bars indicate unavailable or unreliable years in the datasets. For MERRA-2, unreliable years (September 1993, 1994, 2000; October 2000) are related to orbital drifts in various SBUV-carrying satellites (Davis et al., 2017; Wargan et al., 2017). Linear trends are based on a standard ordinary linear regression. MERRA-2: Gelaro et al. (2017); MSR-2: van der A et al. (2015); ECMWF/ERA5: Hersbach et al. (2020); ECMWF/CAMS: Inness et al. (2019); BODEKER v3.51: Bodeker et al. (2021). MSR-2 and BODEKER datasets accessed December 2021; all other datasets accessed December 2020.

results were derived even without accounting for dynamical variability via, for example, a multivariate regression. For the years 2015, 2018, 2020, and 2021, dynamical processes were found to be the main cause of large (late) spring Antarctic ozone holes, possibly exacerbated by volcanic eruptions (2015) and bushfire smoke (2020). The differences in results between September and October point to chemical processes dominating the early part of the ozone hole season from August through September, while dynamical processes play a leading role in determining ozone hole size and depth from October through December. As a consequence, it is more complicated to derive recovery information from October–December data than from September data. The later start date for the onset of rapid ozone depletion is considered a robust sign of ozone recovery post-2000, despite the occurrence of large Antarctic ozone holes later during austral spring.

4.4.2.2 Recent Antarctic Winters in the Context of Stratospheric Ozone Recovery

As noted in *Section 4.2.3*, since the last Assessment three remarkable Antarctic springtime stratospheric ozone seasons have been observed. The evolution of the Antarctic ozone hole in these three years—2019, 2020, and 2021—was discussed in detail in *Sections 4.2.3.2* and *4.2.3.3*. In short, in 2019, strong wave driving resulted in enhanced early springtime stratospheric warming and a strong September minor sudden warming. Hence, springtime Antarctic ozone depletion was substantially reduced in 2019. In contrast, a lack of strong tropospheric wave driving in 2020 and 2021—especially from October onwards—resulted in an anomalously cold Antarctic stratosphere in both years. In 2020, the time period with temperatures below the chlorine activation threshold was prolonged by approximately one month, with chlorine remaining activated through October; depletion also persisted for several weeks longer than typical in 2021. The unusually quiescent dynamical state resulted in ozone holes persisting into late December in 2020 and mid-December in 2021. Overall, the average TCO south of 60°S since 2018 continued to follow the pattern of past years in September and October, with statistically significant post-year-2000 trends in September but not in October (**Figure 4-16**).

In 2019, the ozone destruction rate in September prior to the occurrence of the strong minor sudden stratospheric warming was similar to rates observed during previous years (Wargan et al., 2020; Kramarova et al., 2020; Saffiedine et al., 2020). In 2020 and 2021, the early September OMDs were larger than those during the decade 2010–2019 but still significantly smaller than those during the decade 2000–2010, while the OMDs reached during the first half of October were comparable to those in the 1990s and 2000s (**Figure 4-17**). It is not unexpected that, under favorable atmospheric conditions, very large ozone depletion can be reached despite decreased levels of ODSs. Müller et al. (2018), for example, noted that even with the expected continued decline in ODSs, years with extremely low Antarctic stratospheric ozone concentrations may continue to occur until the middle of the 21st century. Model simulations also show that large and long-lasting ozone holes are likely to occur occasionally during the period of ozone recovery (Stone et al., 2021).

Post-year-2000 trends for the average 1–14 September Antarctic 220 DU OMD for a range of TCO reanalysis datasets are indistinguishable in magnitude within statistical uncertainties (**Figure 4-17**). This agreement indicates that trends in Antarctic early to mid-September total ozone are robust with regard to the choice of total ozone reanalysis dataset. The average 1–14 October 220 DU OMD trend values do not show signs of the start of recovery, consistent with the emerging consensus that the month of September—especially the first half of that month—is more appropriate for recovery detection (Solomon et al., 2016; de Laat et al., 2017; Strahan et al., 2019; Stone et al., 2021).

In summary, recently published studies provide additional support for the conclusion of the previous Assessment (Langematz, Tully et al., 2018) that evidence has emerged for statistically significant trends in stratospheric ozone since the year 2000 over Antarctica, particularly in the month of September. Results from alternative trend analysis approaches and metrics such as ozone loss saturation and ozone hole start dates are also consistent with recovery detection. Indications are also emerging of recent Antarctic stratospheric warming consistent with increasing ozone. Of the plethora of Antarctic ozone recovery metrics and approaches, early September OMD appears to best track trends in ODSs (with the 250 DU OMD providing slightly better results than the 220 DU OMD). However, while decreasing post-year-2000 early springtime Antarctic stratospheric ozone depletion can be largely explained by declining ODSs, whether other processes have contributed—and by how much—remains an outstanding question. Finally, reported detection of recovery is not challenged by the remarkable recent Antarctic ozone holes in 2019, 2020, and 2021, including the record-breaking duration of the 2020 and 2021 ozone holes and their near-record ozone depletion in the month of October.

4.4.3 Long-Term Arctic Ozone Trend

As stated in previous Assessments, detection of stratospheric ozone recovery in the Arctic is much more difficult than in the Antarctic. Persistence of the springtime vortex facilitates strong ozone destruction; however, in a typical year, stratospheric dynamical activity leads to vortex breakup before the end of March (see **Figure 4-3**). In rare instances when the Arctic vortex has remained intact well into April, substantial stratospheric ozone depletion has been observed, most recently in 2020 (see *Section 4.2.4* and references therein; other years were 1997 and 2011). Increasing greenhouse gas concentrations will affect stratospheric ozone loss during future cold Arctic winters by lowering stratospheric temperatures (see *Section 4.5.3.3* for further discussion). Some recent Arctic winters have been characterized by particularly low stratospheric temperatures (**Figure 4-2**). However, the low frequency of occurrence of cold Arctic winters with large ozone loss precludes definitive assessment of decadal Arctic stratospheric ozone trends, which remain statistically not significant (see **Figure 4-16a**). The lack of robust decadal ozone trends, in turn, precludes attribution to decadal changes in ODSs, temperature, water vapor, and possibly even Arctic stratospheric vortex stability. Thus, confident conclusions cannot be drawn about Arctic stratospheric ozone recovery at this time.

4.4.4 Benefits Achieved by the Montreal Protocol and Its Amendments and Adjustments

Langematz, Tully et al. (2018) reported that model simulations assuming continuous growth of ODSs indicated that in the absence of Montreal Protocol controls, by 2013 the Antarctic ozone hole would have been significantly larger and longer-lived than observed, and ozone loss at subpolar southern latitudes would also have been larger. For example, a continuous 3% yr^{-1} increase in ODSs after 1987 would have yielded a 40% deeper Antarctic ozone hole in 2011 (Chipperfield et al., 2015). In addition, in Arctic winters favoring catalytic ozone loss, much more extensive ozone loss would have occurred, resulting in conditions previously only observed over Antarctica.

Feng et al. (2021) and Wilka et al. (2021) further explored what Arctic polar stratospheric ozone conditions would have been in 2020 under unabated emissions of ODSs, assuming a 3–3.5% yr^{-1} increase since 1985. This represents another decade of emissions compared to the case discussed in Langematz, Tully et al. (2018) and results in ODS levels approximately 2.5 times the actual 2020 levels and approximately twice the peak late-20th-century levels. Under such a scenario, minimum Antarctic TCO values

of 50 DU would have occurred by 2020. This is approximately half the minimum TCO values of about 100 DU that occasionally have been observed for the past three decades over Antarctica. It represents approximately a 75% reduction in minimum TCO values compared to those in 1980, and an 85–90% reduction in minimum TCO values compared to the level of 1960 (1960 and 1980 estimates from Dhomse et al., 2018). In addition, springtime Arctic ozone depletion would have begun earlier and lasted longer. In the Arctic for the unusually cold spring of 2020, minimum column values of about 100 DU were modeled. However, given the large interannual variability in the stability of the Arctic polar stratospheric vortex, the occurrence of large Arctic stratospheric ozone depletion would have remained rare. Nevertheless, under such a scenario, Arctic conditions similar to those currently occurring over Antarctica would have become reality for years with an unusually stable and long-lived stratospheric vortex, such as those in 2011 or 2020. Furthermore, for typical Arctic springtime conditions, TCO would also have been significantly smaller by up to several tens of percent, and even in summertime, TCO would have been smaller due to gas-phase depletion.

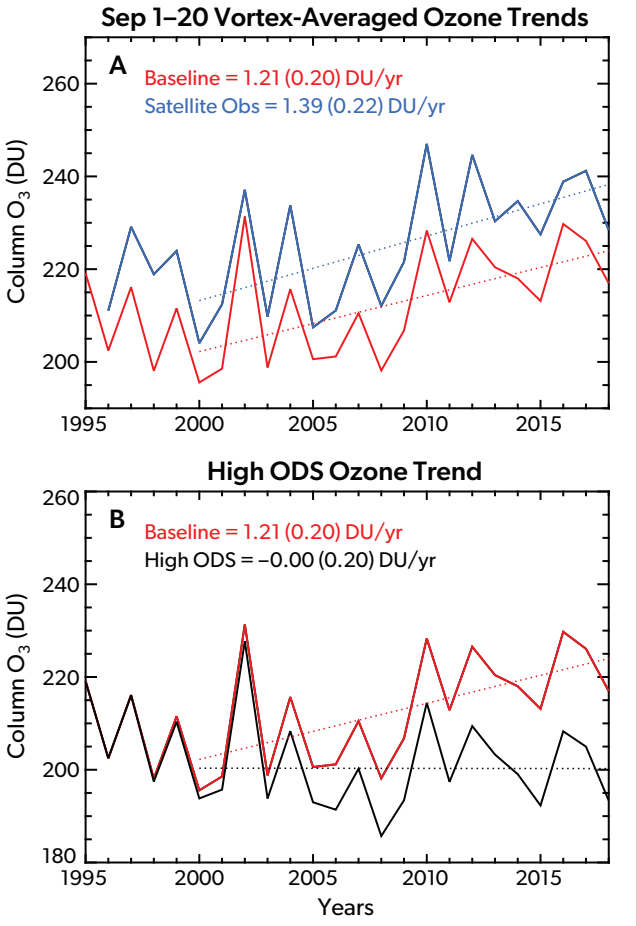

Figure 4-18. The 1–20 September Antarctic vortex-mean column ozone and 2000–2018 trends (with 95% confidence intervals in parentheses) for (a) TOMS/OMI/OMPS (blue) and model simulations using realistically varying ODS levels (baseline; red), and (b) simulations using baseline (red) and high (black) ODSs. [From Strahan et al., 2019.]

The benefits of the Montreal Protocol can also be assessed by estimating the recovery signal in ozone, i.e., how much more severe ozone depletion would have been under certain conditions with the "peak halogen" loadings observed in the late 1990s. A simulation using the TOMCAT CTM with halogenated ODSs fixed at 1995 levels produced Arctic polar cap-averaged TCO 20 DU lower than that observed in the cold winter of 2019/20 (Feng et al., 2021). Strahan et al. (2019) also explored scenarios in which ODS levels remained similar to the maximum observed levels of the late 1990s. They used CTM simulations (GMI integrated with MERRA-2 meteorology) with ODSs resembling observed ODS trends, resulting in Antarctic vortex-average post-peak-ODS ozone trends consistent with observations, apart from a small offset (CTM simulations were biased low compared to observations). The "fixed 1995 ODS" simulation showed no post-peak positive trend in TCO (**Figure 4-18**). Furthermore, with maximum halogen loading, recent Antarctic ozone holes would have been deeper by approximately 20 DU. This indicates that the observed positive trend in 1–20 September Antarctic vortex average total ozone can be attributed to decreasing ODSs rather than to interannual variability in Antarctic vortex dynamics. Given a post-1960 decline of approximately 100 DU (models) or 150 DU (observations) of Antarctic springtime ozone (Langematz et al., 2016; Amos et al., 2020), an increase of 20 DU corresponds approximately to a 15–20% recovery.

Overall, these findings reinforce that the Montreal Protocol and its Amendments and adjustments averted more extreme polar stratospheric ozone depletion and the development of an Arctic ozone hole. Furthermore, these findings bolster the conclusion that the occurrence of record-breaking (or nearly so) ozone depletion in 2020 over both the Arctic and the Antarctic was caused by rare but not unexpected atmospheric conditions and is not cause for concern about the effectiveness of the implementation of the Montreal Protocol.

4.5 FUTURE CHANGES IN POLAR OZONE

This section examines the projected future changes in polar ozone from chemistry-climate model (CCM) simulations from three model intercomparison exercises:

- **CCMVal-2**: Based on the second phase of the SPARC Chemistry-Climate Model Validation (CCMVal; Morgenstern et al., 2010; WMO, 2010; WMO, 2014). The ODS mixing ratios that drive EESC projections originate from WMO (2007).
- **CCMI-1**: Based on phase one of the SPARC Chemistry-Climate Model Initiative (CCMI; Eyring et al., 2013; Morgenstern et al., 2017; WMO, 2018). The ODS mixing ratios that drive EESC projections originate from WMO (2010).
- **CMIP6**: Based on the Coupled Model Intercomparison Project Phase 6 (O'Neill et al., 2014; Meinshausen et al., 2017). The ODS mixing ratios that drive EESC projections originate from Meinshausen et al. (2020).

The recent CMIP6 results have not been part of any previous WMO Scientific Assessment of Ozone Depletion. The CCMVal-2 and CCMI-1 results are shown in this Assessment for continuity with the two previous Assessments (WMO, 2014, 2018). Results from the currently ongoing CCMI-2022 intercomparison (Plummer et al., 2021; ODS projections from WMO, 2018) are not included in this Assessment. At present, only a few models have

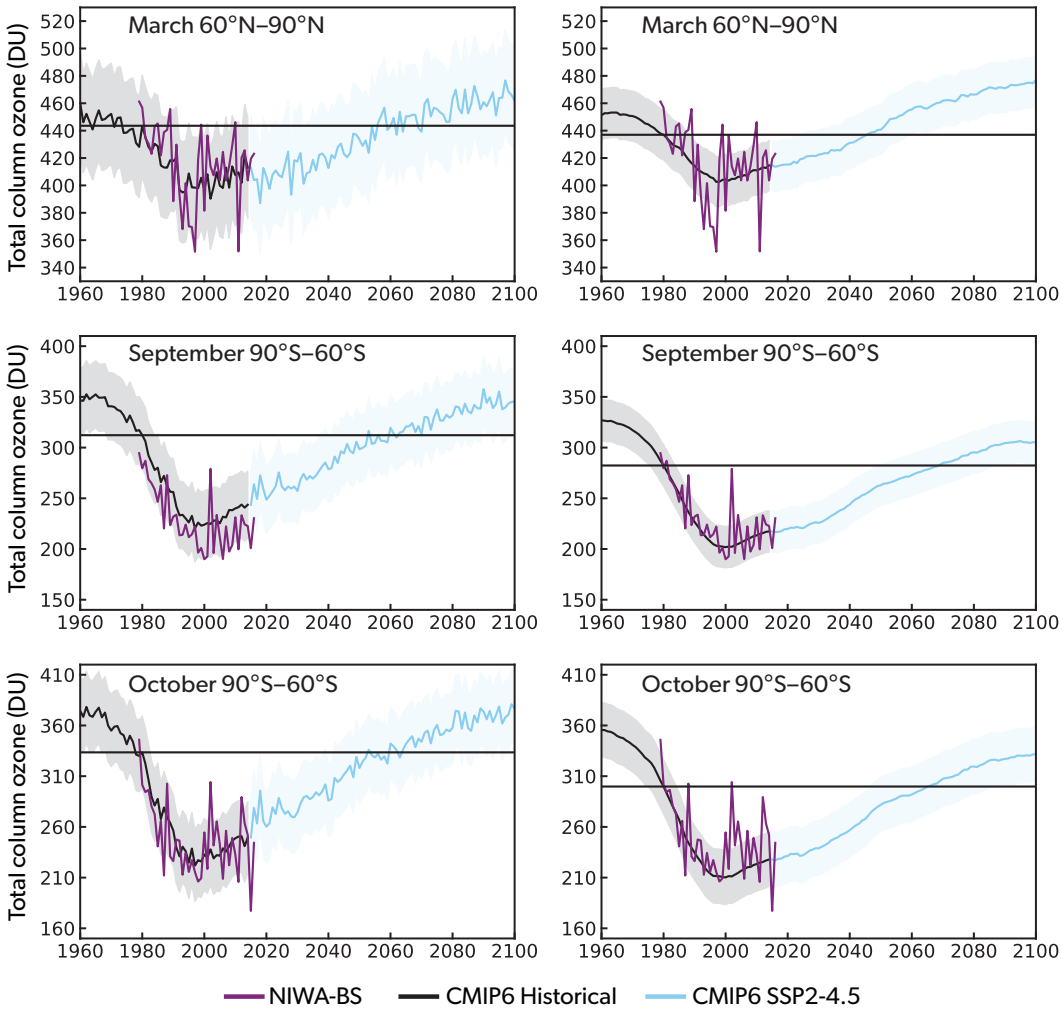

Figure 4-19. Time series of the multi-model mean (MMM) polar total column ozone (TCO, in Dobson units) from CMIP6 simulations for the Northern Hemisphere in March *(top row)*, Southern Hemisphere in September *(middle row)*, and Southern Hemisphere in October *(bottom row)*. In all cases, mean TCO is calculated as an average across 60–90° latitude. The CMIP6 results (Keeble et al., 2021) are for SSP2-4.5 (see **Figure 4-21** for other emissions scenarios) and include data from five participating CCMs for the Antarctic (CESM2-WACCM, CNRM-ESM2-1, GFDL-ESM4, MRI-ESM2-0, and UKESM1-0-LL); for the Arctic, MRI-ESM2-0 was excluded from the MMM (see text). The solid black horizontal lines show the 1980 reference values for each latitude band. The left column shows the unadjusted model values. The right column follows the approach discussed in Dhomse et al. (2018), where the mean biases between the observational data (the NIWA-BS dataset) and the reference simulation are derived for the 1980–1984 period and subtracted from all years over the 1960–2100 period. The right column also has an 11-year boxcar filter applied. Also shown are the observations based on NIWA-BS data (purple lines; Bodeker et al., 2021). The shaded region is the 1σ deviation.

completed the future simulations, and no analysis has been performed. This paucity of information precludes robust conclusions and the inclusion of CCMI-2022 results here.

4.5.1 New Ozone Projections from Chemistry-Climate Models

The CCMs that participated in CCMVal-2 (WMO, 2010, 2014) and CCMI-1 (WMO, 2018) were developed circa 2013 or before. The CCMI-1 projections are discussed in detail in Dhomse et al. (2018) and Langematz, Tully et al. (2018). Many CCMs that performed simulations used in prior WMO Assessments have been updated for participation in the CMIP6 (Keeble et al., 2021) activities. This includes updates to chemistry schemes (updated rate constant representation and enhanced tropospheric chemistry in all models) and interactive coupling of atmosphere-only CCMs to deep-ocean models. Many of the CCMs have also increased horizontal resolution. The scenarios for CMIP6 include a hindcast period (1960–2014) and a forecast period (2015–2100) that follows the CMIP6 shared socioeconomic pathway (SSP) scenarios. In this Assessment, we show forecast scenarios based on the SSP1-2.6, SSP2-4.5, SSP3-7.0, and SSP5-8.5 scenarios (O'Neill et al., 2014). (The number after the hyphen in the SSP name defines the Representative Concentration Pathway [RCP] used. For example,

for SSP2-4.5, the mean global radiative forcing will be 4.5 W m^{-2} by the year 2100.) The relevant simulations and forcing for this Assessment are summarized in Braesicke, Neu et al. (2018, Box 3-2; CCMVal-2, CCMI-1) and **Box 3-4** (CMIP6).

4.5.2 Projections of Polar Ozone: Long and Near Term

This section focuses on the future evolution of Antarctic and Arctic polar ozone by CCMs that have participated in the CCMI-1 and CMIP6 assessments. Comparison of the results from these two sets of simulations builds on the discussion in *Section 3.4* and the associated discussion regarding ozone return dates; refer to that section for a discussion of uncertainties in model internal variability, structural uncertainty, and scenario uncertainty (see also Box 3-3 in Braesicke, Neu et al., 2018).

The baseline GHG scenario for CCMI-1 is based on the RCP6.0 scenario (Dhomse et al., 2018), while for CMIP6 it is based on the SSP2-4.5 (i.e., RCP4.5) scenario. More information on how uncertainties affect return dates is given in *Section 4.5.4.2*. The ozone recovery metric in the following two sections is the commonly used date of return of the ozone layer to values in 1980, the year when the ozone hole started appearing and polar observations became routinely available.

4.5.2.1 Future Antarctic Spring Total Column Ozone

Figure 4-19 shows the modeled evolution of total column ozone (TCO) in the Antarctic (60–90°S) in September and October (middle and bottom rows, respectively) for the multi-model mean (MMM) from the CMIP6 simulations of all five models, along with past observations. The shaded regions around the MMM TCO represent the 1σ standard deviation across the models. September is shown since many recent studies focusing on the detectability of Antarctic ozone recovery (Solomon et al., 2016; Pazmiño et al., 2018; Strahan et al., 2019; see related discussion in *Section 4.4.2.1*) have shown that this is a key month with a relatively dynamically stable vortex and that this month includes the initial onset and growth of the chemical ozone loss. October is also shown for continuity with previous Assessments. The CMIP6 MMM is divided into two periods: 1) the hindcast period (1950–2014, black lines) and 2) the forecast period (2015–2100, light blue lines). The CMIP6 ensemble has only five CCMs with interactive chemistry, whereas CCMI-1, used in the WMO (2018) projections, has 19 models with interactive chemistry.

The left column in **Figure 4-19** shows unadjusted results. In order to make a robust estimate of ozone return dates, biases between each model's simulation and the observations need to be accounted for. The right column follows the approach discussed in Dhomse et al. (2018), where the mean biases between the observational data (the NIWA-BS dataset) and the reference simulation are derived for the 1980–1984 period. Here an adjusted time series (in DU) for each model is then calculated by subtracting the respective observational bias. An 11-year boxcar filter is also applied to the adjusted model results to remove the effects of natural cycles in the data, particularly the 11-year solar cycle in TCO. This smoothing is applied to the bias-adjusted model results because these are used to determine return dates and the interannual and decadal variability seen in model projections can mask the long-term recovery trends. In contrast, the observed data reflect real-world variability in TCO resulting from dynamical variability and therefore are expected to be more variable. Despite these differences in variability represented by the modeled and observed time series shown in **Figure 4-19**, over the full hindcast period the bias-adjusted MMM TCO shows good agreement with observations, including during the strong decrease of Antarctic ozone in the 1980s and early 1990s. In both, a broad TCO minimum occurs around the year 2000.

A large spread in potential return dates in the model simulations arises partly because the bias-corrected model time series start to diverge as they proceed through the 21st century (**Figure 4-19**), but principally because the model time series approach the return threshold at very shallow angles, so even a few-DU difference between simulations translates into many years for the return dates. Smaller variability in return dates from previous Assessments was possibly due to the larger number of models available from the CCMI-1 and CCMVal-2 intercomparison projects (see discussion of the variance in the TCO projections in **Figure 3-24a**).

Simulated Antarctic September TCO is projected in the CMIP6 MMM (using SSP2-4.5) to return to the 1980 abundance shortly after mid-century (year 2066). The shaded region in **Figure 4-19** shows the 1σ uncertainty error bars about the MMM.

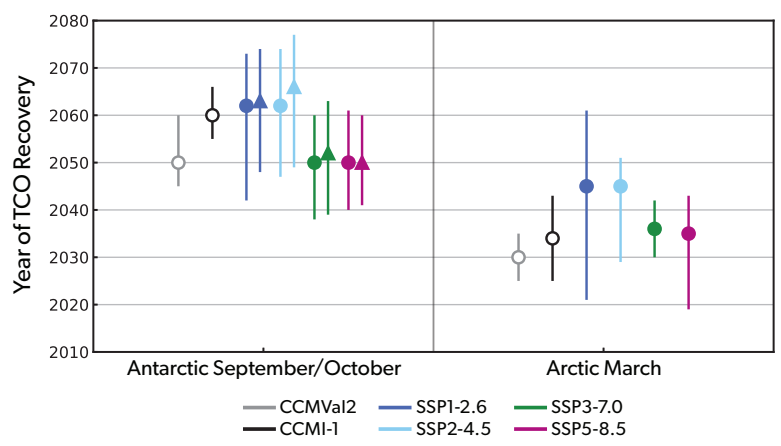

Figure 4-20. Total column ozone 1980 return dates for different CCM experiments. The left panel shows the Antarctic (90–60°S) mean for September (triangles) and October (circles), along with the estimated 1σ uncertainties (whiskers). The error bars are calculated as the first and last time the 1σ envelope around the projection in **Figure 4-19** crosses the return threshold. The right panel shows the Arctic (60–90°N) mean for March (circles) with estimated 1σ uncertainties (whiskers). [Update of Figure 4-22 from Langematz, Tully et al. (2018) now including CMIP6 projections using various SSPs (filled symbols), in addition to CCMVal2 and CCMI-1 projections (open circles).]

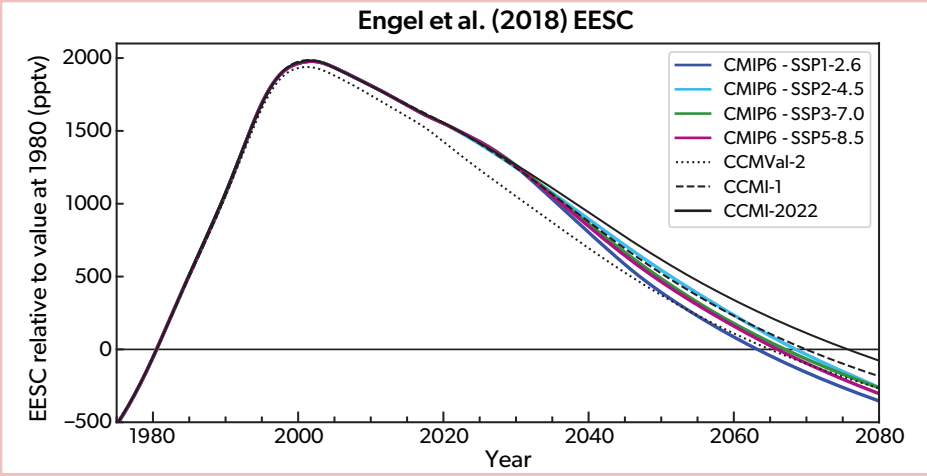

Figure 4-21. Equivalent effective stratospheric chlorine (EESC; pptv) for a mean age-of-air of 5.5 years (representative of the polar lower stratosphere) with an alpha factor for bromine reactivity equal to 60 (Engel et al., 2018). Seven different halogen recovery scenarios used as input to CCM experiments are shown.

The first and last time the 1σ envelope around the projection crosses the return threshold is shown as whisker lines in **Figure 4-20**. The October TCO MMM returns 4 years earlier (year 2062) with a similar range. Compared to results in Langematz, Tully et al. (2018), the current October TCO CMIP6 MMM estimate is later by ~2 years. The equivalent effective stratospheric chlorine (EESC) evolution is similar between the two intercomparisons (see **Figure 4-21**); however, CCMI-1 (used in the WMO, 2018, projection) was based on the RCP6.0 GHG scenario, which differs from the CMIP6 SSP2-4.5 (i.e., RCP4.5) such that the MMM in the CCMI-1 assessment would tend to recover earlier (see *Section 4.5.3.4*). The return date and its uncertainty are discussed in more detail in *Section 4.5.4*.

4.5.2.2 Future Arctic Spring Total Column Ozone

The temporal evolution of the Arctic March TCO MMM (60–90°N) derived from the CMIP6 SSP2-4.5 simulations is presented in **Figure 4-19** (top row). The Arctic MMM includes all participating CCMs except MRI-ESM2-0, which was removed from the MMM because of its lack of hindcast TCO depletion. As in the Antarctic, the bias-adjusted MMM TCO shows good agreement with observations (purple lines). In the forecast period, a TCO return date to 1980 conditions is expected near mid-century for CMIP6 SSP2-4.5 (year 2045), with a range between 2029 and 2051 (**Figure 4-20**). These new CMIP6 TCO projections suggest an MMM return date for Arctic spring that is later by ~11 years compared to the CCMI-1 estimate (Langematz, Tully et al., 2018). In the Arctic, the influence from the differences in the GHG scenario will play more of a role; all things being equal, the CCMI-1 MMM would be expected to recover earlier than the CMIP6 MMM (see *Section 4.5.3.1*). The return date and its uncertainty are discussed in more detail in *Section 4.5.4*.

4.5.3 Factors Controlling Future Polar Ozone

4.5.3.1 Changing Role of ODSs and GHGs

Ozone-depleting substances (ODSs) are expected to decrease in the future, and greenhouse gases (GHGs) are on a trajectory to increase (**Box 3-4**). Therefore, the relative radiative and chemical effects of ODSs and GHGs on polar ozone will change with time. CCMI-1 simulations using separate forcing assumptions addressed the sensitivity of TCO to ODSs and GHGs. The CCMI-1 reference simulation (i.e., REF-C2; RCP6.0) and two separate forcing simulations (i.e., SEN-C2-fODS and SEN-C2-fGHG; Morgenstern et al., 2017) are shown in Langematz, Tully et al. (2018, Figure 4-19). The REF-C2 included the RCP6.0 GHG forcing scenario, while the SEN-C2-fODS (also using the RCP6.0 GHG scenario) and SEN-C2-fGHG scenarios set the abundance of ODSs and GHGs, respectively, to a constant 1960 value between 1960 and 2100. In the Antarctic (October mean), the SEN-C2-fODS shows no ozone depletion from 1960 through 2100, with only a slight ozone increase (<5 DU) by the end of the 21st century. The same region and period for the SEN-C2-fGHG simulation has a temporal evolution in TCO similar to that of the REF-C2 reference simulation, which includes a hindcast period of large ozone depletion consistent with observations. However, after the middle of the century, the GHG forcing contained within the REF-C2 shows an increase in the TCO recovery (~10 DU) relative to the SEN-C2-fODS. In the Arctic (March mean), the ODS and GHG sensitivity is different. Here, the SEN-C2-fODS shows a stronger influence of GHGs from 1960 to 2100, and the SEN-C2-fGHG deviates more from the REF-C2 than modeled in the Antarctic (October mean). This ozone increase is caused by increasing GHG abundances, which both cool the stratosphere, thereby reducing gas-phase chemical ozone loss, and strengthen the Brewer-Dobson circulation (BDC), leading to increased poleward and downward transport of ozone in Arctic spring (e.g., Oman et al., 2010; Oberländer et al., 2013). Note that the multi-model study of Polvani et al. (2019) showed that ODSs are responsible for more than half of the modeled increasing BDC trend in the 1980–2000 period. In the future, decreasing ODSs as a consequence of the Montreal Protocol and its Amendments and adjustments are projected to strongly decelerate the BDC until year 2080, reducing the mean age-of-air trends by more than one half and thus substantially mitigating the impact of carbon dioxide (CO_2) strengthening the BDC. Polvani et al. (2019) also found that the depletion/recovery of stratospheric ozone over Antarctica contributes to seasonal and hemispheric asymmetries in the BDC trends, and they suggest that this impact could be a method for detection of a BDC trend in the coming decades. However, it should be noted that there is still a discrepancy between age-of-air trends derived from models and those derived from observations (Strahan et al., 2020; Prignon et al., 2021).

4.5.3.2 Impact of Noncompliant CFC-11 Production

The global emissions of CFC-11 were expected to decrease after 2010 based on full phaseout of production and consumption. However, Montzka et al. (2018) showed that emissions started to increase in 2013 and remained elevated through 2018 (*Chapter 1*), in violation of the Montreal Protocol. The mean emissions enhancement during the period 2014–2017 relative to 2008–2012 is estimated to be 13.7 Gg yr^{-1} (Montzka et al., 2021), and the cumulative unexpected emissions of CFC-11 during 2012–2019 are estimated to be 120–440 Gg (WMO, 2021). See *Chapter 1* for more discussion on the observed changes in chlorofluorocarbons (CFCs).

Subsequent modeling studies have examined the effects of these and hypothetical other additional CFC-11 emissions on TCO recovery (Dhomse et al., 2019; Dameris et al., 2019; Fleming et al., 2020; Keeble et al., 2020; Lickley et al., 2020; WMO, 2021). Due to the large fractional release of CFC-11 abundance in the polar region (Newman et al., 2007), the delay in TCO recovery is linearly dependent on the resultant inorganic chlorine increase. Simulations using the GSFC2D model show, for example, that sustained emissions at the large level of 72 Gg yr^{-1} would shift the 1980 return date for Antarctic ozone by 25 years (Fleming et al., 2020). This example of sustained CFC-11 emissions is probably not realistic but was included as a sensitivity study by Carpenter, Daniel et al. (2018). Using the UKCA CCM, Keeble et al. (2020) also note that the largest delay in ozone recovery due to enhanced CFC-11 concentrations occurs in the Antarctic spring.

Figure 4-22 shows the Antarctic TCO return date to 1980 levels for various cumulative additional CFC-11 emissions compared to baseline halogen simulations (Carpenter, Daniel et al., 2018, A1 scenario) for two CCMs (UKCA and GEOSCCM), one two-dimensional model (GSFC2D), and one three-dimensional CTM (TOMCAT). Atmospheric CFC-11 abundances in the baseline halogen scenario are based on compliance with the Montreal Protocol over the full timeline. Three models (UKCA, GSFC2D, and TOMCAT) performed perturbation simulations with different assumptions of additional CFC-11 (and in some cases CFC-12 converted to equivalent CFC-11) emissions based on noncompliant production. Model sensitivities in return date to additional noncompliant CFC-11 emissions are shown (i.e., return date versus cumulative additional CFC-11 emissions in Gg). This was done for September mean ozone in the Antarctic, since that is the month with the largest ozone loss rates. The linear fits to the model scenarios in **Figure 4-22** suggest that they can be scaled to other emissions scenarios. The TOMCAT CTM, which does not include climate feedbacks, gives the largest slope of 7.1 years per 1000 Gg. The GSFC2D gives the smallest slope of 4.0 years per 1000 Gg, but, as a 2-D model, it cannot capture the full 3-D behavior of the Antarctic polar vortex. The UKCA results are in between, with a slope of 6.4 years per 1000 Gg. The suggested range is most likely 4–7 years per 1000 Gg of cumulative noncompliant CFC-11 emissions. Therefore, the observed cumulative additional emissions of 120–440 Gg in the 2012–2019 period would add an additional 0.5–3.1 years to the September date of return to 1980 conditions (WMO, 2021).

4.5.3.3 Dynamical Variability in Arctic Spring

There is uncertainty about the role of dynamical variability in modulating future stratospheric Arctic ozone. Observations and model studies have shown that chemical loss of Arctic ozone from halogens is strongly controlled by low temperatures that promote the formation of polar stratospheric clouds (PSCs). In the future, as ODSs decrease and GHGs increase, large Arctic ozone depletion events may still occur. That is, with the persistence into springtime of a cold and dynamically isolated Arctic vortex, ozone loss could be comparable to that in the cold Northern Hemisphere springs of 2011, 2016, and 2020 (see discussion in *Section 4.3.4*). CCM studies have shown that enhanced GHG abundances will cause cooling in the Arctic winter upper and middle stratosphere (Langematz, Tully et al., 2018, and references therein). This cooling will accelerate ozone recovery from ODSs in the upper stratosphere by slowing down the rates of gas-phase ozone loss

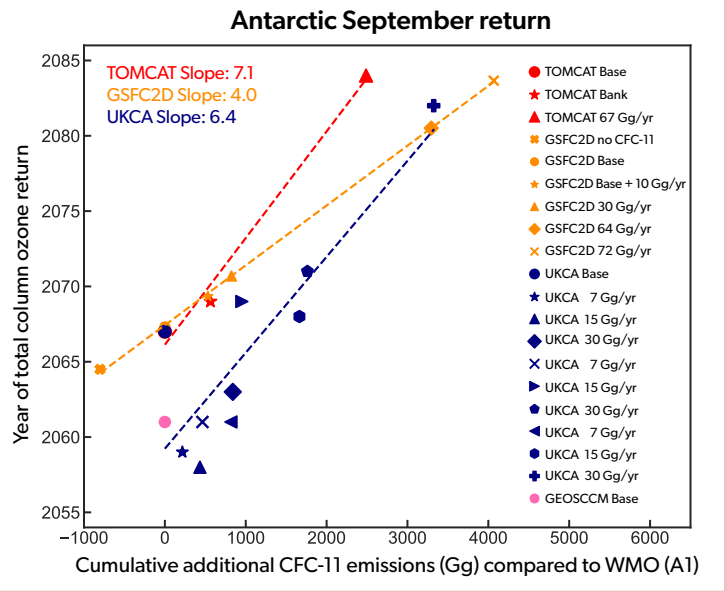

Figure 4-22. Dependence of September mean Antarctic (90–65°S) column ozone 1980 return dates on cumulative additional (compared to WMO, 2018, A1 baseline scenario) equivalent CFC-11 emissions (Gg), as in **Figure 3-28** for global ozone. The colors indicate the model, and the symbols correspond to different simulations with that model. Each model performed a base simulation using the WMO (2018) A1 baseline scenario. The models also performed perturbation simulations with different assumptions of additional CFC-11 emissions (and in some cases CFC-12 emissions converted to equivalent CFC-11 emissions), quantified as Gg equivalent CFC-11 emissions along the x-axis. The dashed lines (with numerical values giving the slope in years per 1000 Gg) show the best linear fits to the simulations for each model.

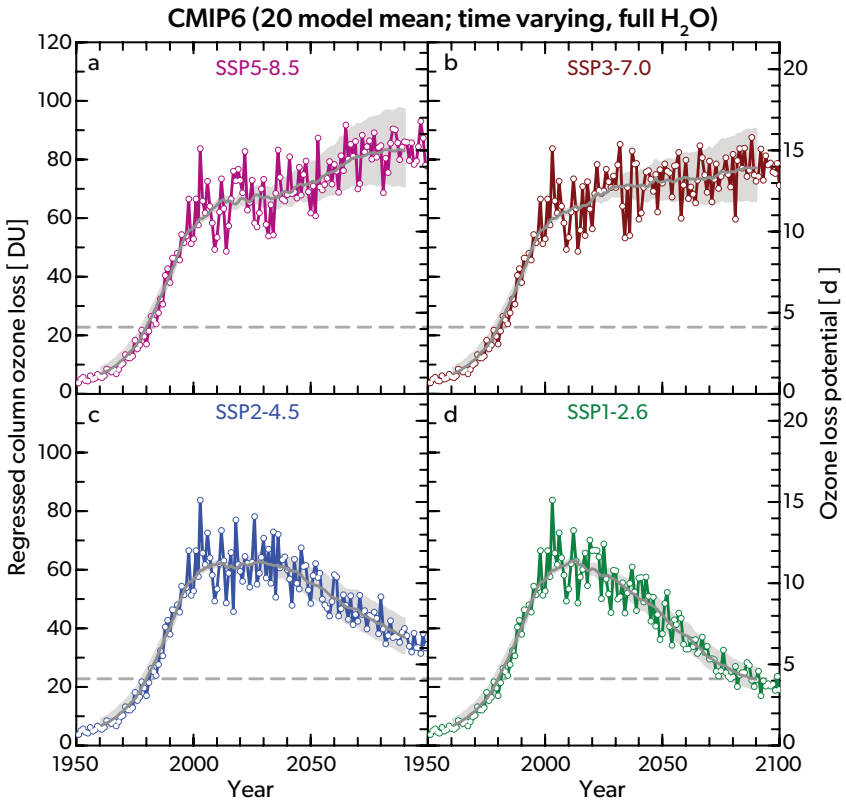

Figure 4-23. Ensemble-mean regressed Arctic column ozone loss (ΔO_3^{REG}, DU; left ordinate) and Ozone Loss Potential (OLP, days; right ordinate) as a function of year. ΔO_3^{REG} represents the chemical ozone loss in the lower-stratospheric portion of the Arctic vortex, and OLP represents the number of days a volume of air equal to that of the Arctic vortex is exposed to PSC conditions over the course of an ozone loss season. The OLP derivation uses the model polar stratospheric H_2O, which accounts for increasing stratospheric humidity due to both increasing CH_4 oxidation and warming of the tropical tropopause; the HNO_3 abundance is taken from present-day observations. The regressed column ozone loss is computed from each of the model OLPs. The gray solid line shows a 21-year running mean (±10 years) of the ensemble mean of the regressed column ozone loss (ΔO_3^{REG}) for each SSP, the gray shaded area represents a 21-year running mean of the range in ΔO_3^{REG} for exponents of 1 (upper boundary) and 1.4 (lower boundary) of the expression for OLP, and the gray dashed horizontal lines denote the 1980 value of ΔO_3^{REG}. (a) SSP5-8.5, (b) SSP3-7.0, (c) SSP2-4.5, and (d) SSP1-2.6 scenarios. [From von der Gathen et al., 2021.]

reactions. A recent study examining PSC formation potential (PFP, the seasonal integral of the ratio of the volume of the region containing PSCs [V_{PSC}] to the volume of the Arctic vortex) from four reanalysis datasets suggests that cold Arctic stratospheric winters have become colder over the past 40 years (von der Gathen et al., 2021; see also Vargin et al., 2022, and related discussion in *Section 4.2.2.2*). For future projections, von der Gathen et al. (2021) used a simple relationship between PFP and EESC to derive an ozone loss potential (OLP). The derived OLP and regressed column loss (from the OLP based on present-day observations of ozone loss) from 16 general circulation models (GCMs) and four CCMs (with interactive chemistry) for four different GHG scenarios (SSP5-8.5, SSP3-7.0, SSP2-4.5, and SSP1-2.6) are shown in **Figure 4-23**. The seasonal chemical ozone loss diagnostic shown here represents the amount of ozone chemically removed in the lower-stratospheric portion of the Arctic vortex, rather than the resulting TCO depletion over the polar cap. This figure uses the GCM- and CCM-derived time series of polar stratospheric water vapor (H_2O), which reflect increases in stratospheric humidity arising from both increasing methane (CH_4) oxidation and warming of the tropical tropopause. Moister conditions in the lower stratosphere are more conducive to PSC formation. Therefore, the net effect of strong GHG increases on polar chemical loss in the future is the combination of stratospheric cooling and enhanced supply of H_2O and CH_4 from the troposphere.

Von der Gathen et al. (2021) concluded that if stratospheric humidity rises as projected and GHGs follow either the SSP5-8.5 or the SSP3-7.0 trajectories, then there is an increased potential for Arctic column ozone depletion to occur until the end of the century, despite the expected decline in halogen loading. That is, cooling and moistening of the Arctic stratosphere could act in concert to prolong the period over which significant seasonal chemical ozone losses are expected to occur in the future and could even lead to losses larger than those currently seen in severe Arctic winters (von der Gathen et al., 2021). However, it should be noted that the four CCMs, which have a better representation of stratospheric dynamics (e.g., planetary wave activity influence on the BDC, etc.), showed 20–25% lower OLP at the end of the century than that found for the 16 GCMs. The potential for increased chemical ozone depletion later in the century will be affected by many dynamical processes that may not be adequately represented in current models, especially those lacking interactive ozone chemistry. See further discussion of dynamical control of polar ozone under climate change in *Section 4.3.4.3*.

4.5.3.4 The Role of GHG Scenarios

Future ozone recovery is influenced by carbon dioxide (CO_2), methane (CH_4), and nitrous oxide (N_2O) through radiative processes that cool the stratosphere (*Chapter 5*). CH_4 and N_2O also have chemical effects that can impact future ozone abundances. Many studies have investigated the impact of the assumed CH_4 and N_2O future scenarios on ozone abundance and recovery (see

Section 4.5.3.3 of Langematz, Tully et al., 2018, and references therein). It is well known that increases in CH_4 and N_2O will generate larger amounts of hydrogen oxides (HO_x) and nitrogen oxides (NO_x), respectively, and also that increased NO_x will enhance catalytic middle-stratospheric ozone loss. Therefore, in general, the ozone return date is expected to be later if there are increases in N_2O or earlier if there are decreases in N_2O. However, the effect of future increases in N_2O varies with altitude and also depends on the temporal evolution of other GHGs.

For changes in CH_4, the situation is more complicated. In a similar manner to NO_x, increased HO_x from CH_4 oxidation will decrease upper-stratospheric ozone. However, CH_4 can also affect the partitioning of reactive chlorine through the reaction of $CH_4 + Cl \rightarrow HCl + CH_3$, with more CH_4 generally leading to an increase in stratospheric ozone via a decrease in the abundance of reactive chlorine. Thus, future increases in CH_4 are expected to lead to increases in stratospheric column ozone, notwithstanding the impact on Arctic H_2O discussed in *Section 4.5.3.3*. Recently, experiments with $2\times CH_4$ and $5\times CH_4$ present-day mixing ratios were conducted using a CCM (Winterstein et al., 2019). Twenty-year time-slice simulations were conducted consistent with year-2010 halogen conditions. These very large quasi-instantaneous increases in CH_4 strongly affected tropospheric chemistry by reducing the hydroxyl radical (OH) abundance, which resulted in extending the lifetime of CH_4 and many other chemical substances. In the stratosphere, there were substantial increases in stratospheric water vapor (SWV) of 50% and 250% for the $2\times CH_4$ and $5\times CH_4$ simulations, respectively, which cooled the stratosphere by several degrees. This cooling caused an increase in the TCO globally, except in the Antarctic spring due to enhanced PSC chemistry. Ozone in the tropical lowermost stratosphere decreased due to enhanced upwelling. This work did not specifically examine Arctic PSC chemistry, although both the $2\times CH_4$ and the $5\times CH_4$ simulations did show lower-stratospheric ozone decreases of a few percent in the wintertime Arctic. Prescribed sea surface temperatures were used, so tropospheric warming feedbacks were not included. A follow-up study (Stecher et al., 2020) incorporated a mixed-layer ocean model into the CCM to account for additional tropospheric warming. As in the previous study, they found that strong increases in CH_4 reduced OH in the troposphere and extended the CH_4 lifetime. However, a slow climate feedback also arose and counteracted this reduction in OH through increases in tropospheric water vapor and ozone, thereby damping the quasi-instantaneous response found by Winterstein et al. (2019).

Future scenarios with larger GHG abundances lead to an overall higher level of simulated stratospheric ozone (Langematz, Tully et al., 2018). Increased GHG levels result in lower temperatures in the middle atmosphere. These cooler conditions will decrease ozone loss reactions and result in an ozone increase in the upper stratosphere. The choice of GHG scenario can also affect the modeled amount of polar NO_x that is transported from the upper mesosphere and thermosphere into the upper stratosphere. Using a CCM, Maliniemi et al. (2021) showed that NO_x produced by energetic electron precipitation (EEP) and partly by solar ultraviolet above the stratopause is transported down into the polar upper stratosphere. This study used four different GHG scenarios. They showed that the larger the GHG forcing scenario, the greater the amount of NO_x transported into the upper stratosphere (see *Section 4.5.3.1*). This additional NO_x depletes more

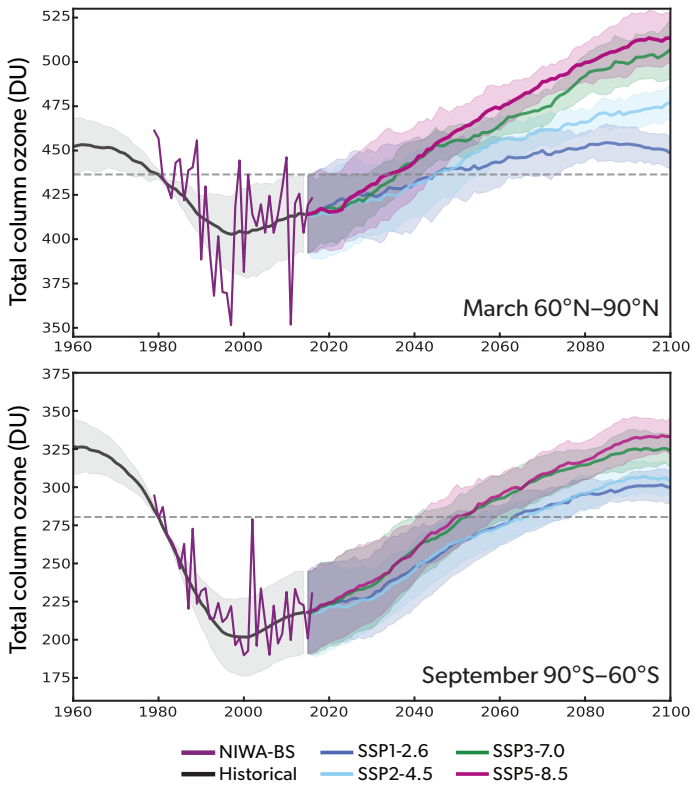

Figure 4-24. Impact of GHG scenarios (SSP1-2.6, SSP2-4.5, SSP3-7.0, SSP5-8.6) on polar total column ozone in the CMIP6 model ensemble; for the list of models included in each hemisphere, see the caption of **Figure 4-19**. Historical and projected polar cap average TCO is shown for March in the Arctic *(top)* and September in the Antarctic *(bottom)*. Observations (purple lines) are from the NIWA-BS dataset. The dashed gray lines show the 1980 reference values for each latitude band.

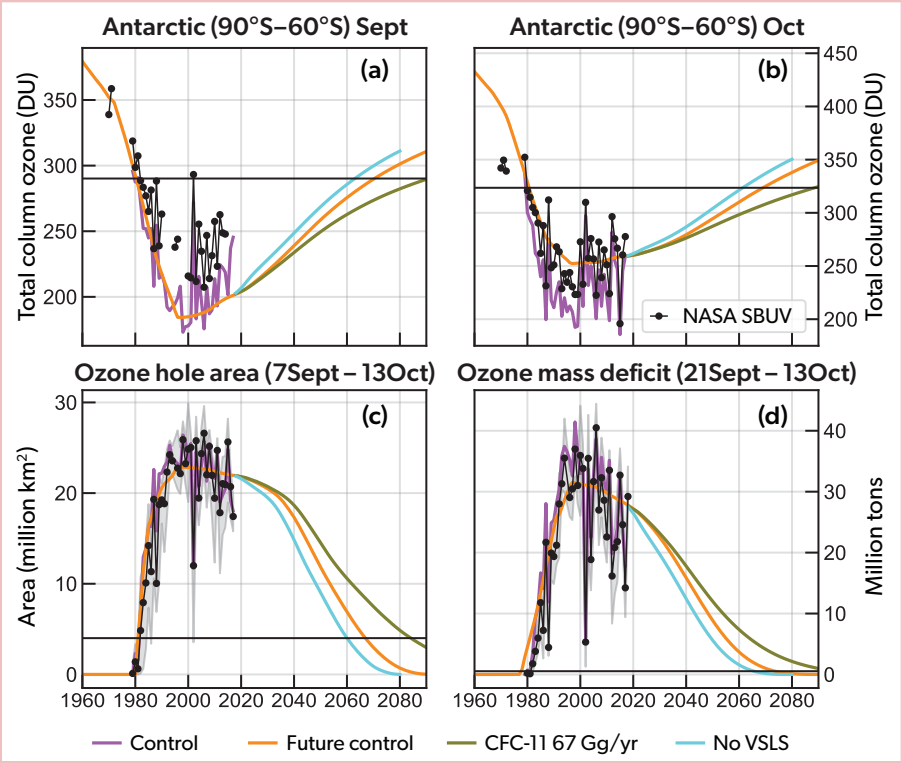

Figure 4-25. Antarctic ozone and metrics quantifying ozone loss as a function of additional CFC-11 and VSLS emissions. Mean column ozone (DU) averaged from 90–60°S for (a) September and (b) October from four TOMCAT 3-D model simulations: control (varying meteorology), future control (2000 meteorology), with constant 67 Gg yr^{-1} emissions of CFC-11, and with no chlorinated very short-lived substances (VSLSs), as well as SBUV observations from 1960 to 2019 (black lines with dots). The horizontal black lines indicate the modeled 1980 values. (c) Estimates of the size of the Antarctic ozone hole under control, future control, 67 Gg yr^{-1} CFC-11 emissions, no VSLSs, and as observed (based on ozonewatch.gsfc.nasa.gov) using the area contained within the 220 DU contour (10^6 km^2; averaged over the period 7 September–13 October). (d) As in (c) but for ozone mass deficit (10^6 metric tons; averaged over the period 21 September–13 October). The gray shading in panels (c) and (d) gives the maximum and minimum values for each year in the period analyzed. Additional emissions of CFC-11 at the level assumed would delay recovery of the Antarctic ozone hole, meaning a delay in the date of return to 1980 values, by around 17.5 years. Similarly, elimination of chlorinated VSLS emissions is projected to speed up the ozone return by around 7 years (for both September and October). [Adapted from Chipperfield et al., 2020, and Dhomse et al., 2019.]

ozone, offsetting the ozone increases driven by climate cooling acting to decrease the rate of the NO_x catalytic ozone loss cycle. This result indicates that NO_x production in the upper mesosphere and thermosphere will be an important factor for the future upper-stratospheric Antarctic ozone evolution and could potentially prevent a super-recovery (i.e., where ozone abundance is greater than the 1980 values) in that altitude region.

Therefore, the TCO recovery to a historical baseline (e.g., 1980 conditions) will depend strongly on the GHG scenario (**Box 3-4**), particularly in the Arctic. This is shown in **Figure 4-24** using projections from the CCMs used in the CMIP6 model ensemble. This figure shows results from five CCMs for the Antarctic and four CCMs for the Arctic (Keeble et al., 2021), as well as four different SSPs (SSP1-2.6, SSP2-4.5, SSP3-7.0, and SSP5-8.5). The TCO return date and range for each SSP is shown in **Figure 4-20**. As discussed in *Section 4.5.3.1*, the Arctic is more sensitive to GHG evolution than the Antarctic. The March MMM TCO recovery to 1980 conditions occurs around the year 2045 for the SSP1-2.6 (range of −24 and +16 DU in the 1σ deviation at that time) and SSP2-4.5 (range of −16 and +6 DU) simulations, with SSP2-4.5 having more of a super-recovery by the end of the 21st century (~35 DU above the 1980 baseline). The 1980 return dates for the SSP3-7.0 and SSP5-8.5 MMM simulations are earlier (~2035) than for the SSP1.2-6 and SSP2-4.5 scenarios, and they show a larger super-recovery by the end of the 21st century, with an increase in TCO above the baseline of ~70 DU. This is consistent with the results for the CCMI-1 assessment (Langematz, Tully et al., 2018).

In the Antarctic spring, there is less spread in the temporal evolution of the TCO across SSPs. The September return date to 1980 conditions is around the years 2063 and 2066 for SSP1-2.6 and SSP2-4.5, respectively. The 1980 return date is around 2052 and 2050 for SSP3-7.0 and SSP5-8.5, respectively. This is approximately 16 years earlier for SSP5-8.5 relative to the baseline SSP2-4.5 scenario. This new CMIP6 assessment result of a strong dependence of Antarctic ozone recovery on GHG scenario is not consistent with the CCMI-1 results discussed in Dhomse et al. (2018) and Langematz, Tully et al. (2018). This sensitivity of Antarctic recovery to climate change scenario may be due to the use of a smaller number of updated models (and model realizations) contained in the CMIP6 assessment (Keeble et al., 2021) relative to the larger CCMI-1 study. In addition, the evolution of GHGs could be different in these CMIP6 models (see discussion of uncertainty in polar ozone projections in *Section 4.5.4*).

4.5.3.5 The Role of VSLSs (Bromine and Chlorine)

Results from simulations examining the effects of VSLS bromine emissions (e.g., bromoform [$CHBr_3$] and dibromomethane [CH_2Br_2]) on future polar ozone remain mixed, with no new information since the last Assessment (Langematz, Tully et al., 2018). Yang et al. (2014) and Oman et al. (2016) suggest that including VSLS bromine will extend the return date to 1980 conditions by

~10 years and 6–8 years, respectively, while Fernandez et al. (2017) do not see a change in the return date from inclusion of VSLS brominated species within the variability of the ensemble members. Thus, the magnitude of any potential impacts of VSLS bromine emissions on ozone recovery remains uncertain.

Total VSLS chlorine (e.g., chloroform [$CHCl_3$] and dichloromethane [CH_2Cl_2]) has a contribution of around 130 (100–160) ppt in the present-day stratosphere (*Chapter 1*; Hossaini et al., 2018; Fang et al., 2019). **Figure 4-25** shows the impact of keeping the VSLS chlorine flux constant at current conditions (Dhomse et al., 2019; Chipperfield et al., 2020). This contrasts with what was shown in Langematz, Tully et al. (2018), where a positive trend in VSLS chlorine abundance was assumed. **Figure 4-25** shows the 1980 return dates for both the Antarctic September and October polar cap TCO, along with two additional diagnostics, i.e., ozone hole area and ozone mass deficit. The "future" control case simulation includes present-day emissions of VSLS chlorine. The "no VSLS" case zeroes these emissions. Including VSLS chlorine emissions delays the TCO return date to 1980 conditions by approximately 7 years. For comparison, the more extreme noncompliant CFC-11 emissions scenario of 67 Gg yr^{-1} (WMO, 2018) delays the TCO return date to 1980 conditions by ~17.5 years, although the impact will scale for smaller perturbations (see *Section 4.5.3.2*). The ozone hole area and ozone mass deficit diagnostics give the same return dates (within ±1 year) as the TCO for both the VSLS chlorine and 67 Gg yr^{-1} noncompliant emissions scenarios.

4.5.4 Uncertainty in Polar Ozone Projections

Current CCMs, developed over the past 20 years, have similar representations of dynamical, transport, and chemical processes (e.g., SPARC, 2010; Morgenstern et al., 2017). Nevertheless, there are three types of uncertainties that still need to be considered (Box 3-3 of Braesicke, Neu et al., 2018). The first is internal variability, which arises from chaotic processes and can be minimized by running multiple realizations with different starting conditions and forming an ensemble average. The second is structural uncertainty, which arises from different representations of resolution (e.g., high-top models that include a well-resolved stratosphere versus low-top models that have an upper lid below the stratopause), including or not an interactive QBO, and/or representing a deep ocean. The choice of chemical mechanism and/or the choice of laboratory rate constant recommendations can also add to the overall uncertainty (e.g., Fleming et al., 2015). The third is scenario uncertainty, whereby the specification of ODS and GHG time series can have large impacts on a given ozone recovery diagnostic. The assumed ODS scenario, in particular, has a direct impact on the polar TCO return date, especially in the Antarctic, where changes in GHGs and climate have comparatively smaller impacts on ozone (Klobas et al., 2020).

4.5.4.1 Model Uncertainty

Ideally, the multi-model mean (MMM) ozone return date would be calculated using an ensemble of models that are fully independent. However, model components are shared amongst families of models, so they are not strictly independent. Amos et al. (2020) developed a procedure to use observations to assess and account for both model performance and model independence (**Figure 4-26**). Model performance was derived from comparison to observations and used to weight the CCMI-1 ensemble simulations to derive weighted-mean estimates of Antarctic ozone depletion and subsequent ozone recovery. The return to 1980 date from this weighted MMM was the year 2056 (95% confidence interval 2052–2060). While the ozone return date found in this work (2056) is different from that (2062) found by Dhomse et al. (2018), these two dates are not easily comparable, as they are created from different subsets of the same ensemble. For the subset of models in Amos et al. (2020), the simple MMM return date was three years earlier (2053) than the weighted mean. Amos et al. (2020) also argued that the weighted MMM showed a greater projective skill than the simple MMM. The construction of a weighted mean also provided insight into model performance and dependence between the models.

4.5.4.2 Uncertainty in Ozone Return Dates

Although ozone recovery is underway (see *Section 4.4*), uncertainty remains about how it will progress in the future and what metric is best to diagnose it. The date for the atmosphere to return to a specified state does not take account of variability in

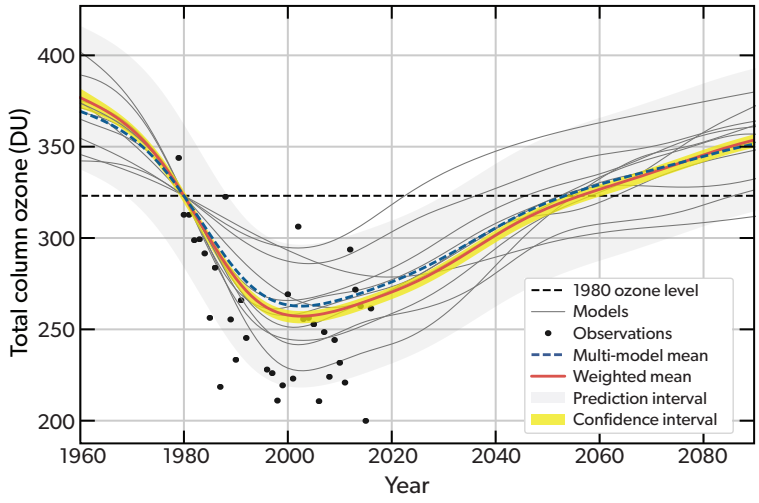

Figure 4-26. Simulated and observed Antarctic (60–90°S) October TCO. The weighted model mean is shown in red, the multi-model mean in blue, and individual model trends in gray lines. Observed TCO (black dots) are from NIWA-BS data. All model projections and ensemble projections are normalized to the observational 1979–1981 mean, shown as the black dashed line, and so they converge in the year 1980. The 95% confidence and prediction intervals for the weighted mean are also shown with yellow and light gray shading, respectively. [From Amos et al., 2020.]

that pathway or in the impact of other transient factors before the final return date. Pyle et al. (2022) discuss the use of integrated ozone depletion as a metric for ozone recovery both globally and in specific regions. This metric integrates the additional ozone depletion, based on model simulations, due to any emissions scenario over the full (possibly multi-decadal) duration of the impact, taking account of short-term perturbations and avoiding sensitivity to the date of a single return event. For this metric, a simple empirical expression exists for perturbations due to long-lived ODSs. For the Antarctic ozone hole in particular, other established measures of its size (e.g., ozone mass deficit, ozone hole area) may give a more robust perspective on recovery, especially when considered together and when applied to periods of greatest sensitivity to halogen-induced chemical loss (**Figure 4-25**; Dhomse et al., 2019).

Sensitivity to ODS and GHG Scenarios. A direct influence on the ozone return date is the choice of the halogen recovery scenario. In **Figure 4-21**, the EESC based on Engel et al. (2018) is shown for a specific polar condition (i.e., mean age of 5.5 years). The evolution of EESC is shown for CCMI-1 and CMIP6 (different EESC for each SSP; SSP2-4.5 is the baseline scenario). Comparison of the CCMI-1 EESC (RCP6.0) to the CMIP6 EESC (SSP2-4.5) suggests that very little difference is expected in the return date, which is borne out in the return dates in **Figure 4-20**. However, the EESC for the currently ongoing CCMI-2022, based on Carpenter, Daniel et al. (2018), shows a five-to-seven-year extension in the halogen recovery relative to CCMI-1 and CMIP6 SSP2-4.5 (**Figure 4-21**). This change in EESC alone would translate to an extension of the Antarctic TCO return date as implied in **Figure 4-22**, but simulations based on this halogen scenario are not included in this Assessment.

Sensitivity to VSLSs. Langematz, Tully et al. (2018) discussed the uncertainty in both bromine and chlorine future VSLS emissions and found that the uncertainty in the delay of the return date of Antarctic TCO to historical values was somewhere between several years and up to three decades. This uncertainty includes the unknown influence of climate change on the emissions of bromine-containing VSLSs, predominantly from oceanic emissions (e.g., Tegtmeier et al., 2015; Ziska et al., 2018). The chlorine-containing VSLSs (e.g., $CHCl_3$, CH_2Cl_2) are mainly produced by industry (*Chapter 1*). Hossaini et al. (2017) assumed a future impact on the return date to 1980 conditions from a continuous increase in CH_2Cl_2 with a mean emission rate observed for the 2004–2014 period. This increasing CH_2Cl_2 emissions rate delayed the ozone return date by approximately 20 years. In *Section 4.5.3.5*, this study was updated with a constant flux based on present-day conditions (**Figure 4-25**). The delay in the ozone return to 1980 values was approximately 7 years. There have not been any additional studies since the 2018 Assessment that have reduced projected VSLS return date uncertainty.

REFERENCES

Adcock, K.E., P.J. Fraser, B.D. Hall, R.L. Langenfelds, G. Lee, S.A. Montzka, D.E. Oram, T. Röckmann, F. Stroh, W.T. Sturges, B. Vogel, and J.C. Laube, Aircraft based observations of ozone-depleting substances in the upper troposphere and lower stratosphere in and above the Asian summer monsoon, ***J. Geophys. Res. Atmos.***, ***126*** (1), e2020JD033137, doi:10.1029/2020JD033137, 2021.

Albers, J.R., J. Perlwitz, A.H. Butler, T. Birner, G.N. Kiladis, Z.D. Lawrence, G.L. Manney, A.O. Langford, and J. Dias, Mechanisms governing interannual variability of stratosphere-to-troposphere ozone transport, ***J. Geophys. Res. Atmos.***, ***123*** (1), 234–260, doi:10.1002/2017JD026890, 2018.

Allen, D.R., M.D. Fromm, G.P. Kablick III, and G.E. Nedoluha, Smoke with induced rotation and lofting (SWIRL) in the stratosphere, ***J. Atmos. Sci.***, ***77*** (12), 4297–4316, doi:10.1175/JAS-D-20-0131.1, 2020.

Amos, M., P.J. Young, J.S. Hosking, J.-F. Lamarque, N.L. Abraham, H. Akiyoshi, A.T. Archibald, S. Bekki, M. Deushi, P. Jöckel, D. Kinnison, O. Kirner, M. Kunze, M. Marchand, D.A. Plummer, D. Saint-Martin, K. Sudo, S. Tilmes, and Y. Yamashita, Projecting ozone hole recovery using an ensemble of chemistry-climate models weighted by model performance and independence, ***Atmos. Chem. Phys.***, ***20***, 9961–9977, doi:10.5194/acp-20-9961-2020, 2020.

Ayarzagüena, B., A.J. Charlton-Perez, A.H. Butler, P. Hitchcock, I.R. Simpson, L.M. Polvani, N. Butchart, E.P. Gerber, L. Gray, B. Hassler, P. Lin, F. Lott, E. Manzini, R. Mizuta, C. Orbe, S. Osprey, D. Saint-Martin, M. Sigmond, M. Taguchi, E.M. Volodin, and S. Watanabe, Uncertainty in the response of sudden stratospheric warmings and stratosphere-troposphere coupling to quadrupled CO_2 concentrations in CMIP6 models, ***J. Geophys. Res. Atmos.***, ***125*** (6), e2019JD032345, doi:10.1029/2019JD032345, 2020.

Ayarzagüena, B., L.M. Polvani, U. Langematz, H. Akiyoshi, S. Bekki, N. Butchart, M. Dameris, M. Deushi, S.C. Hardiman, P. Jöckel, A. Klekociuk, M. Marchand, M. Michou, O. Morgenstern, F.M. O'Connor, L.D. Oman, D.A. Plummer, L. Revell, E. Rozanov, D. Saint-Martin, J. Scinocca, A. Stenke, K. Stone, Y. Yamashita, K. Yoshida, and G. Zeng, No robust evidence of future changes in major stratospheric sudden warmings: a multi-model assessment from CCMI, ***Atmos. Chem. Phys.***, ***18***, 11277–11287. doi:10.5194/acp-18-11277-2018, 2018.

Bahramvash Shams, S., V.P. Walden, J.W. Hannigan, W.J. Randel, I.V. Petropavlovskikh, A.H. Butler, and A. de la Cámara, Analyzing ozone variations and uncertainties at high latitudes during sudden stratospheric warming events using MERRA-2, ***Atmos. Chem. Phys.***, ***22*** (8), 5435–5458, doi:10.5194/acp-22-5435-2022, 2022.

Baldwin, M.P., B. Ayarzagüena, T. Birner, N. Butchart, A.H. Butler, A.J. Charlton-Perez, D.I.V. Domeisen, C.I. Garfinkel, H. Garny, E.P. Gerber, M.I. Hegglin, U. Langematz, and N.M. Pedatella, Sudden stratospheric warmings, ***Rev. Geophys.***, ***59*** (1), e2020RG000708, doi:10.1029/2020RG000708, 2021.

Barrera, J.A., R.P. Fernandez, F. Iglesias-Suarez, C.A. Cuevas, J.-F. Lamarque, and A. Saiz-Lopez, Seasonal impact of biogenic very short-lived bromocarbons on lowermost stratospheric ozone between 60°N and 60°S during the 21st century, ***Atmos. Chem. Phys.***, ***20***, 8083–8102, doi:10.5194/acp-20-8083-2020, 2020.

Bednarz, E.M., A.C. Maycock, N.L. Abraham, P. Braesicke, O. Dessens, and J.A. Pyle, Future Arctic ozone recovery: The importance of chemistry and dynamics, ***Atmos. Chem. Phys.***, ***16***, 12,159–12,176, doi:10.5194/acp-16-12159-2016, 2016.

Bernath, P., C. Boone, and J. Crouse, Wildfire smoke destroys stratospheric ozone, ***Science***, ***375***, 1292–1295, doi:10.1126/science.abm5611, 2022.

Bernhard, G.H., V.E. Fioletov, J.-U. Grooß, I. Ialongo, B. Johnsen, K. Lakkala, G.L. Manney, and R. Müller, Ozone and UV radiation [in "State of the Climate in 2018"], ***Bull. Amer. Meteor. Soc.***, ***100,*** S274–S277, doi:10.1175/2019BAMSStateoftheClimate.1, 2019.

Bernhard, G.H., V.E. Fioletov, J.-U. Grooß, I. Ialongo, B. Johnsen, K. Lakkala, G.L. Manney, R. Müller, and T. Svendby, Record-breaking increases in Arctic solar ultraviolet radiation caused by exceptionally large ozone depletion in 2020, ***Geophys. Res. Lett.***, ***47*** (24), e2020GL090844, doi:10.1029/2020GL090844, 2020.

Bodeker, G.E., and D.W. Waugh (Lead Authors), H. Akiyoshi, P. Braesicke, V. Eyring, D.W. Fahey, E. Manzini, M.J. Newchurch, R.W. Portmann, A. Robock, K.P. Shine, W. Steinbrecht, and E.C. Weatherhead, The Ozone Layer in the 21st Century, Chapter 6 in ***Scientific Assessment of Ozone Depletion: 2007***, Global Ozone Research and Monitoring Project–Report No. 50, World Meteorological Organization, Geneva, Switzerland, 2007.

Bodeker, G.E., and S. Kremser, Indicators of Antarctic ozone depletion: 1979 to 2019, ***Atmos. Chem. Phys.***, ***21***, 5289–5300, doi:10.5194/acp-21-5289-2021, 2021.

Bodeker, G.E., J. Nitzbon, J.S. Tradowsky, S. Kremser, A. Schwertheim, and J. Lewis, A global total column ozone climate data record, ***Earth Syst. Sci. Data***, ***13*** (8), 3885–3906, doi:10.5194/essd-13-3885-2021, 2021.

Bognar, K., R. Alwarda, K. Strong, M.P. Chipperfield, S.S. Dhomse, J.R. Drummond, W. Feng, V. Fioletov, F. Goutail, B. Herrera, G.L. Manney, E.M. McCullough, L.F. Millán, A. Pazmino, K.A. Walker, T. Wizenberg, and X. Zhao, Unprecedented spring 2020 ozone depletion in the context of 20 years of measurements at Eureka, Canada, ***J. Geophys. Res. Atmos.***, ***126*** (8), e2020JD034365, doi:10.1029/2020JD034365, 2021.

Bond, N.A., J.E. Overland, M. Spillane, and P. Stabeno, Recent shifts in the state of the North Pacific, ***Geophys. Res. Lett.***, ***30*** (23), doi:10.1029/2003GL018597, 2003.

Braesicke, P., and J. Neu et al. (Lead Authors), V. Fioletov, S. Godin-Beekmann, D. Hubert, I. Petropavlovskikh, M. Shiotani, and B.-M Sinnhuber, Update on Global Ozone: Past, Present, and Future, Chapter 3 in ***Scientific Assessment of Ozone Depletion: 2018***, Global Ozone Research and Monitoring Project–Report No. 58, World Meteorological Organization, Geneva, Switzerland, 2018.

Braun, M., J.-U. Grooß, W. Woiwode, S. Johansson, M. Höpfner, F. Friedl-Vallon, H. Oelhaf, P. Preusse, J. Ungermann, B.-M. Sinnhuber, H. Ziereis, and P. Braesicke, Nitrification of the lowermost stratosphere during the exceptionally cold Arctic winter 2015–2016, ***Atmos. Chem. Phys.***, ***19***, 13681–13699, doi:10.5194/acp-19-13681-2019, 2019.

Breeden, M.L., A.H. Butler, J.R. Albers, M. Sprenger, and A.O. Langford, The spring transition of the North Pacific jet and its relation to deep stratosphere-to-troposphere mass transport over western North America, ***Atmos. Chem. Phys.***, ***21***, 2781–2794, doi:10.5194/acp-21-2781-2021, 2021.

Brenna, H., S. Kutterolf, and K. Krüger, Global ozone depletion and increase of UV radiation caused by pre-industrial tropical volcanic eruptions, ***Sci. Rep.,*** ***9*** (1), 9435, doi:10.1038/s41598-019-45630-0, 2019.

Bushra, N., and R.V. Rohli, Relationship between atmospheric teleconnections and the northern hemisphere's circumpolar vortex, ***Earth Space Sci.***, ***8*** (9), e2021EA001802, doi:10.1029/2021EA001802, 2021.

Butchart, N., and E.E. Remsberg, The area of the stratospheric polar vortex as a diagnostic for tracer transport on an isentropic surface, ***J. Atmos. Sci.***, ***43***, 1319–1339, doi:10.1175/1520-0469(1986)043<1319:TAOTSP>2.0.CO;2, 1986.

Butler, A.H., J.P. Sjoberg, D.J. Seidel, and K.H. Rosenlof, A sudden stratospheric warming compendium, ***Earth Syst. Sci. Data***, ***9*** (1), 63–76, doi:10.5194/essd-9-63-2017, 2017.

Butler, A.H., A. Charlton-Perez, D.I.V. Domeisen, I.R. Simpson, and J. Sjoberg, Predictability of northern hemisphere final stratospheric warmings and their surface impacts, ***Geophys. Res. Lett.***, ***46*** (17-18), 10578–10588, doi:10.1029/2019GL083346, 2019.

Butler, A.H., Z.D. Lawrence, S.H. Lee, S.P. Lillo, and C.S. Long, Differences between the 2018 and 2019 stratospheric polar vortex split events, ***Q. J. R. Meteorol. Soc.***, ***146***, 3503–3521, doi:10.1002/qj.3858, 2020.

Butler, A.H., and D.I.V. Domeisen, The wave geometry of final stratospheric warming events, ***Weather Clim. Dynam.***, ***2,*** 453–474, doi:10.5194/wcd-2-453-2021, 2021.

Carpenter, L.J., and J.S. Daniel (Lead Authors), E.L. Fleming, T. Hanaoka, J. Hu, A.R. Ravishankara, M.N. Ross, S. Tilmes, T.J. Wallington, and D.J. Wuebbles, Scenarios and Information for Policymakers, Chapter 6 in ***Scientific Assessment of Ozone Depletion: 2018***, Global Ozone Research and Monitoring Project–Report No. 58, World Meteorological Organization, Geneva, Switzerland, 2018.

Cellitti, M.P., J.E. Walsh, R.M. Rauber, and D.H. Portis, Extreme cold air outbreaks over the United States, the polar vortex, and the large-scale circulation, ***J. Geophys. Res. Atmos.***, ***111*** (D2), doi:10.1029/2005JD006273, 2006.

Charlton, A.J., and L.M. Polvani, A new look at stratospheric sudden warmings: Part I: Climatology and modeling benchmarks, ***J. Clim.***, ***20*** (3), 449–469, doi:10.1175/JCLI3996.1, 2007.

Chipperfield, M.P., S.S. Dhomse, W. Feng, R.L. McKenzie, G. Velders, and J.A. Pyle, Quantifying the ozone and UV benefits already achieved by the Montreal Protocol, ***Nat. Commun.***, ***6***, 7233, doi:10.1038/ncomms8233, 2015.

Chipperfield, M.P., R. Hossaini, S.A. Montzka, S. Reimann, D. Sherry, and S. Tegtmeier, Renewed and emerging concerns over the production and emission of ozone-depleting substances, ***Nat. Rev. Earth Environ.***, ***1*** (5), 251–263, doi:10.1038/s43017-020-0048-8, 2020.

Claxton, T., R. Hossaini, C. Wilson, S.A. Montzka, M.P. Chipperfield, O. Wild, E.M. Bednarz, L.J. Carpenter, S.J. Andrews, S.C. Hackenberg, J. Mühle, D. Oram, S. Park, M.-K. Park, E. Atlas, M. Navarro, S. Schauffler, D. Sherry, M. Vollmer, T. Schuck, A. Engel, P.B. Krummel, M. Maione, J. Arduini, T. Saito, Y. Yokouchi, S. O'Doherty, D. Young, and C. Lunder, A synthesis inversion to constrain global emissions of two very short lived chlorocarbons: dichloromethane, and perchloroethylene, ***J. Geophys. Res. Atmos.***, ***125*** (12), e2019JD031818, doi:10.1029/2019JD031818, 2020.

Cohen, J., X. Zhang, J. Francis, T. Jung, R. Kwok, J. Overland, T.J. Ballinger, U.S. Bhatt, H.W. Chen, D. Coumou, S. Feldstein, H. Gu, D. Handorf, G. Henderson, M. Ionita, M. Kretschmer, F. Laliberte, S. Lee, H.W. Linderholm, W. Maslowski, Y. Peings, K. Pfeiffer, I. Rigor, T. Semmler, J. Stroeve, P.C. Taylor, S. Vavrus, T. Vihma, S. Wang, M. Wendisch, Y. Wu, and J. Yoon, Divergent consensuses on Arctic amplification influence on midlatitude severe winter weather, ***Nat. Clim. Change***, ***10*** (1), 20–29, doi:10.1038/s41558-019-0662-y, 2020.

Cohen, J.L., L. Agel, M. Barlow, C.I. Garfinkel, and I. White, Linking Arctic variability and change with extreme winter weather in the United States, ***Science***, ***373*** (6559), 1116–1121, doi:10.1126/science.abi9167, 2021.

Cuevas, C.A., R.P. Fernandez, D.E. Kinnison, Q. Li., J.-F. Lamarque, T. Trabelsi, J.S. Francisco, S. Solomon, and A. Saiz-Lopez, The influence of iodine on the Antarctic stratospheric ozone hole, ***Proc. Natl. Acad. Sci.***, ***119*** (7), e2110864119, doi:10.1073/pnas.e2110864119, 2022.

Dai, G., C. Li, Z. Han, D. Luo, and Y. Yao, The nature and predictability of the East Asian extreme cold events of 2020/21, ***Adv. Atmos. Sci.***, doi:10.1007/s00376-021-1057-3, 2021.

Dameris, D., V. Grewe, I. Köhler, R. Sausen, C. Brühl, J.-U. Grooß, and B. Steil, Impact of aircraft NO_x emissions on tropospheric and stratospheric ozone, part II: 3-D model results, ***Atmos. Environ.***, ***32***, 3185–3199, doi:10.1016/S1352-2310(97)00505-0, 1998.

Dameris, M., and S. Godin-Beekmann (Lead Authors), S. Alexander, P. Braesicke, M. Chipperfield, A.T.J. de Laat, Y. Orsolini, M. Rex, and M.L. Santee, Polar Stratospheric Ozone: Past, Present, and Future, Chapter 3 in ***Scientific Assessment of Ozone Depletion: 2014***, Global Ozone Research and Monitoring Project–Report No. 55, World Meteorological Organization, Geneva, Switzerland, 2014.

Dameris, M., P. Jöckel, and M. Nützel, Possible implications of enhanced chlorofluorocarbon-11 concentrations on ozone, ***Atmos. Chem. Phys.***, ***19*** (22), 13759–13771, doi:10.5194/acp-19-13759-2019, 2019.

Dameris, M., D.G. Loyola, M. Nützel, M. Coldewey-Egbers, C. Lerot, F. Romahn, and M. van Roozendael, Record low ozone values over the Arctic in boreal spring 2020, ***Atmos. Chem. Phys.***, ***21***, 617–633, doi:10.5194/acp-21-617-2021, 2021.

Davis, S.M., M.I. Hegglin, M. Fujiwara, R. Dragani, Y. Harada, C. Kobayashi, C. Long, G.L. Manney, E.R. Nash, G.L. Potter, S. Tegtmeier, T. Wang, K. Wargan, and J.S. Wright, Assessment of upper tropospheric and stratospheric water vapor and ozone in reanalyses as part of S-RIP, ***Atmos. Chem. Phys.***, ***17***, 12743–12778, doi:10.5194/acp-17-12743-2017, 2017.

de la Cámara, A., M. Abalos, P. Hitchcock, N. Calvo, and R.R. Garcia, Response of Arctic ozone to sudden stratospheric warmings, ***Atmos. Chem. Phys.***, ***18***, 16499–16513, doi:10.5194/acp-18-16499-2018, 2018.

de Laat, A.T.J., M. van Weele, and R.J. van der A, Onset of stratospheric ozone recovery in the Antarctic ozone hole in assimilated daily total ozone columns, ***J. Geophys. Res. Atmos.***, ***122***, 11,880–11,899, doi:10.1002/2016JD025723, 2017.

DeLand, M.T., P.K. Bhartia, N. Kramarova, and Z. Chen, OMPS LP observations of PSC variability during the NH 2019–2020 season, ***Geophys. Res. Lett.***, ***47*** (20), e2020GL090216, doi:10.1029/2020GL090216, 2020.

Dhomse, S.S., D. Kinnison, M.P. Chipperfield, R.J. Salawitch, I. Cionni, M.I. Hegglin, N.L. Abraham, H. Akiyoshi, A.T. Archibald, E.M. Bednarz, S. Bekki, P. Braesicke, N. Butchart, M. Dameris, M. Deushi, S. Frith, S.C. Hardiman, B. Hassler, L.W. Horowitz, R.-M. Hu, P. Jöckel, B. Josse, O. Kirner, S. Kremser, U. Langematz, J. Lewis, M. Marchand, M. Lin, E. Mancini, V. Marécal, M. Michou, O. Morgenstern, F.M. O'Connor, L. Oman, G. Pitari, D.A. Plummer, J.A. Pyle, L.E. Revell, E. Rozanov, R. Schofield, A. Stenke, K. Stone, K. Sudo, S. Tilmes, D. Visioni, Y. Yamashita, and G. Zeng, Estimates of ozone return dates from Chemistry-Climate Model Initiative simulations, ***Atmos. Chem. Phys.***, ***18*** (11), 8409–8438, doi:10.5194/acp-18-8409-2018, 2018.

Dhomse, S.S., W. Feng, S.A. Montzka, R. Hossaini, J. Keeble, J.A. Pyle, J.S. Daniel, and M.P. Chipperfield, Delay in recovery of the Antarctic ozone hole from unexpected CFC-11 emissions, ***Nat. Commun.***, ***10*** (1), ***5781***, doi:10.1038/s41467-019-13717-x, 2019.

Domeisen, D.I.V., and A.H. Butler, Stratospheric drivers of extreme events at the Earth's surface, ***Comm. Earth Environ.***, ***1*** (1), 59, doi:10.1038/s43247-020-00060-z, 2020.

Douglass, A., and V. Fioletov (Coordinating Lead Authors), S. Godin-Beekmann, R. Müller, R.S. Stolarski, A. Webb, A. Arola, J.B. Burkholder, J.P. Burrows, M.P. Chipperfield, R. Cordero, C. David, P.N. den Outer, S.B. Diaz, L.E. Flynn, M. Hegglin, J.R. Herman, P. Huck, S. Janjai, I.M. Jánosi, J.W. Krzyścin, Y. Liu, J. Logan, K. Matthes, R.L. McKenzie, N.J. Muthama, I. Petropavlovskikh, M. Pitts, S. Ramachandran, M. Rex, R.J. Salawitch, B.-M. Sinnhuber, J. Staehelin, S. Strahan, K. Tourpali, J. Valverde-Canossa, and C. Vigouroux, Stratospheric Ozone and Surface Ultraviolet Radiation, Chapter 2 in ***Scientific Assessment of Ozone Depletion: 2010***, Global Ozone Research and Monitoring Project–Report No. 52, World Meteorological Organization, Geneva, Switzerland, 2011.

Duderstadt, K.A., C.-L. Huang, H.E. Spence, S. Smith, J.B. Blake, A.B. Crew, A.T. Johnson, D.M. Klumpar, D.R. Marsh, J.G. Sample, M. Shumko, and F.M. Vitt, Estimating the impacts of radiation belt electrons on atmospheric chemistry using FIREBIRD II and Van Allen Probes observations, ***J. Geophys. Res. Atmos.***, ***126*** (7), e2020JD033098, doi:10.1029/2020JD033098, 2021.

Engel, A., H. Bönisch, J. Ostermöller, M.P. Chipperfield, S. Dhomse, and P. Jöckel, A refined method for calculating equivalent effective stratospheric chlorine, ***Atmos. Chem. Phys.***, ***18***, 601–619, doi:10.5194/acp-18-601-2018, 2018.

Eyring, V., J.M. Arblaster, I. Cionni, J. Sedláček, J. Perlwitz, P.J. Young, S. Bekki, D. Bergmann, P. Cameron-Smith, W.J. Collins, G. Faluvegi, K.-D. Gottschaldt, L.W. Horowitz, D.E. Kinnison, J.-F. Lamarque, D.R. Marsh, D. Saint-Martin, D.T. Shindell, K. Sudo, S. Szopa, and S. Watanabe, Long-term ozone changes and associated climate impacts in CMIP5 simulations, ***J. Geophys. Res. Atmos.***, ***118***, 5029–5060, doi:10.1002/jgrd.50316, 2013.

Fang, X., S. Park, T. Saito, R. Tunnicliffe, A.L. Ganesan, M. Rigby, S. Li, Y. Yokouchi, P.J. Fraser, C.M. Harth, P.B. Krummel, J. Mühle, S. O'Doherty, P.K. Salameh, P.G. Simmonds, R.F. Weiss, D. Young, M.F. Lunt, A.J. Manning, A. Gressent, and R.G. Prinn, Rapid increase in ozone-depleting chloroform emissions from China, ***Nat. Geosci.***, ***12*** (2), 89–93, doi:10.1038/s41561-018-0278-2, 2019.

Fernandez, R.P., D.E. Kinnison, J-F. Lamarque, S. Times, and A. Saiz-Lopez, Impact of biogenic very short-lived bromine on the Antarctic ozone hole during the 21st century, ***Atmos. Chem. Phys.***, ***17***, 1673–1688, doi:10.5194/acp-17-1673-2017.

Feng, W., S.S. Dhomse, C. Arosio, M. Weber, J.P. Burrows, M.L. Santee, and M.P. Chipperfield, Arctic ozone depletion in 2019/20: Roles of chemistry, dynamics and the Montreal Protocol, ***Geophys. Res. Lett.***, ***48*** (4), e2020GL091911, doi:10.1029/2020GL091911, 2021.

Fiehn, A., B. Quack, C.A. Marandino, and K. Krüger, Transport variability of very short lived substances from the West Indian Ocean to the stratosphere, ***J. Geophys. Res. Atmos.***, ***123*** (10), 5720–5738, doi:10.1029/2017JD027563, 2018.

Filus, M.T., E.L. Atlas, M.A. Navarro, E. Meneguz, D. Thomson, M.J. Ashfold, L.J. Carpenter, S.J. Andrews, and N.R.P. Harris, Transport of short-lived halocarbons to the stratosphere over the Pacific Ocean, ***Atmos. Chem. Phys.***, ***20***, 1163–1181, doi:10.5194/acp-20-1163-2020, 2020.

Fleming, E.L., C. George, D.E. Heard, C.H. Jackman, M.J. Kurylo, W. Mellouki, V.L. Orkin, W.H. Swartz, T.J. Wallington, P.H. Wine, and J.B. Burkholder, The impact of current CH_4 and N_2O atmospheric loss process uncertainties on calculated ozone abundances and trends, ***J. Geophys. Res.***, ***120***, 5267–5293, doi:10.1002/2014JD022067, 2015.

Fleming, E.L., P.A. Newman, Q. Liang, and J.S. Daniel, The impact of continuing CFC-11 emissions on stratospheric ozone, ***J. Geophys. Res.***, ***125*** (3), e2019JD031849, doi:10.1029/2019JD031849, 2020.

Fu, Q., S. Solomon, H.A. Pahlavan, and P. Lin, Observed changes in Brewer–Dobson circulation for 1980–2018, ***Environ. Res. Lett., 14*** (11), 114026, doi:10.1088/1748-9326/ab4de7, 2019.

Fujiwara, M., J.S. Wright, G.L. Manney, L.J. Gray, J. Anstey, T. Birner, S. Davis, E.P. Gerber, V.L. Harvey, M.I. Hegglin, C.R. Homeyer, J.A. Knox, K. Krüger, A. Lambert, C.S. Long, P. Martineau, A. Molod, B.M. Monge-Sanz, M.L. Santee, S. Tegtmeier, S. Chabrillat, D.G.H. Tan, D.R. Jackson, S. Polavarapu, G.P. Compo, R. Dragani, W. Ebisuzaki, Y. Harada, C. Kobayashi, W. McCarty, K. Onogi, S. Pawson, A. Simmons, K. Wargan, J.S. Whitaker, and C-Z. Zou, Introduction to the SPARC Reanalysis Intercomparison Project (S-RIP) and overview of the reanalysis systems, ***Atmos. Chem. Phys.***, ***17***, 1417–1452, doi:10.5194/acp-17-1417-2017, 2017.

Funke, B., M. López-Puertas, G.P. Stiller, and T. von Clarmann, Mesospheric and stratospheric NO_y produced by energetic particle precipitation during 2002–2012, ***J. Geophys. Res.***, ***119***, 4429–4446, doi:10.1002/2013JD021404, 2014.

Gelaro, R., W. McCarty, M.J. Suárez, R. Todling, A. Molod, L. Takacs, C.A. Randles, A. Darmenov, M.G. Bosilovich, R. Reichle, K. Wargan, L. Coy, R. Cullather, C. Draper, S. Akella, V. Buchard, A. Conaty, A.M. da Silva, W. Gu, G.-K. Kim, R. Koster, R. Lucchesi, D. Merkova, J.E. Nielsen, G. Partyka, S. Pawson, W. Putman, M. Rienecker, S.D. Schubert, M. Sienkiewicz, and B. Zhao, The modern-era retrospective analysis for research and applications, version 2 (MERRA-2), ***J. Clim.***, ***30***, 5419–5454, doi:10.1175/JCLI-D-16-0758.1, 2017.

Gordon, E.M., A. Seppälä, and J. Tamminen, Evidence for energetic particle precipitation and quasi-biennial oscillation modulations of the Antarctic NO_2 springtime stratospheric column from OMI observations, ***Atmos. Chem. Phys.***, ***20***, 6259–6271, doi:10.5194/acp-20-6259-2020, 2020.

Gordon, E.M., A. Seppälä, B. Funke, J. Tamminen, and K.A. Walker, Observational evidence of energetic particle precipitation NO_x (EPP-NO_x) interaction with chlorine curbing Antarctic ozone loss, ***Atmos. Chem. Phys.***, ***21***, 2819–2836, doi:10.5194/acp-21-2819-2021, 2021.

Griffin, D., K.A. Walker, I. Wohltmann, S.S. Dhomse, M. Rex, M.P. Chipperfield, W. Feng, G.L. Manney, J. Liu, and D. Tarasick, Stratospheric ozone loss in the Arctic winters between 2005 and 2013 derived with ACE-FTS measurements, ***Atmos. Chem. Phys.***, ***19***, 577–601, doi:10.5194/acp-19-577-2019, 2019.

Grooß, J.-U., R. Müller, R. Spang, I. Tritscher, T. Wegner, M.P. Chipperfield, W. Feng, D.E. Kinnison, and S. Madronich, On the discrepancy of HCl processing in the core of the wintertime polar vortices, ***Atmos. Chem. Phys.***, ***18***, 8647–8666, doi:10.5194/acp-18-8647-2018, 2018.

Grooß, J.-U., and R. Müller, Simulation of record Arctic stratospheric ozone depletion in 2020, ***J. Geophys. Res. Atmos.***, ***126*** (12), e2020JD033339, doi:10.1029/2020JD033339, 2021.

Haigh, J.D., and H.K. Roscoe, The final warming date of the Antarctic polar vortex and influences on its interannual variability, ***J. Clim.***, ***22***, 5809–5819, doi:10.1175/2009JCLI2865.1, 2009.

Harrison, J.J., M.P. Chipperfield, R. Hossaini, C.D. Boone, S. Dhomse, W. Feng, and P.F. Bernath, Phosgene in the upper troposphere and lower stratosphere: A marker for product gas injection due to chlorine-containing very short-lived substances, ***Geophys. Res. Lett.***, ***46***, 1032–1039, doi:10.1029/2018GL079784, 2019.

Hauchecorne, A., C. Claud, P. Keckhut, and A. Mariaccia, Stratospheric Final Warmings fall into two categories with different evolution over the course of the year, ***Commun. Earth Environ.***, ***3*** (1), doi:10.1038/s43247-021-00335-z, 2022.

Hendon, H.H., D.W. Thompson, E.-P. Lim, A.H. Butler, P.A. Newman, L. Coy, and A. Scaife, Rare forecasted climate event under way in the Southern Hemisphere, ***Nature***, ***573*** (7775), 495–495, doi:10.1038/d41586-019-02858-0, 2019.

Hersbach, H., B. Bell, P. Berrisford, S. Hirahara, A. Horányi, J. Muñoz-Sabater, J. Nicolas, C. Peubey, R. Radu, D. Schepers, A. Simmons, C. Soci, S. Abdalla, X. Abellan, G. Balsamo, P. Bechtold, G. Biavati, J. Bidlot, M. Bonavita, G. De Chiara, P. Dahlgren, D. Dee, M. Diamantakis, R. Dragani, J. Flemming, R. Forbes, M. Fuentes, A. Geer, L. Haimberger, S. Healy, R.J. Hogan, E. Hólm, M. Janisková, S. Keeley, P. Laloyaux, P. Lopez, C. Lupu, G. Radnoti, P. de Rosnay, I. Rozum, F. Vamborg, S. Villaume, and J.-N. Thépaut, The ERA5 global reanalysis, ***Q. J. R. Meteorol. Soc.***, ***146***, 1999–2049, doi:10.1002/qj.3803, 2020.

Hong, H.-J., and T. Reichler, Local and remote response of ozone to Arctic stratospheric circulation extremes, ***Atmos. Chem. Phys.***, ***21***, 1159–1171, doi:10.5194/acp-21-1159-2021, 2021.

Höpfner, M., T. Deshler, M. Pitts, L. Poole, R. Spang, G. Stiller, and T. von Clarmann, The MIPAS/Envisat climatology (2002–2012) of polar stratospheric cloud volume density profiles, ***Atmos. Meas. Tech.***, ***11***, 5901–5923, doi:10.5194/amt-11-5901-2018, 2018.

Hoshi, K., J. Ukita, M. Honda, T. Nakamura, K. Yamazaki, Y. Miyoshi, and R. Jaiser, Weak stratospheric polar vortex events modulated by the Arctic sea ice loss, ***J. Geophys. Res. Atmos***, ***124***, 858–869, doi:10.1029/2018JD029222, 2019.

Hossaini, R., M.P. Chipperfield, S.A. Montzka, A.A. Leeson, S.S. Dhomse, and J.A. Pyle, The increasing threat to stratospheric ozone from dichloromethane, ***Nat. Commun.***, ***8***, 186–190, doi:10.1038/ncomms15962, 2017.

Hossaini, R., E. Atlas, S.S. Dhomse, M.P. Chipperfield, P.F. Bernath, A.M. Fernando, J. Mühle, A.A. Leeson, S.A. Montzka, W. Feng, J.J. Harrison, P. Krummel, M.K. Vollmer, S. Reimann, S. O'Doherty, D. Young, M. Maione, J. Arduini, and C.R. Lunder, Recent trends in stratospheric chlorine from very short-lived substances, ***J. Geophys. Res. Atmos***, ***124*** (4), 2318–2335, doi:10.1029/2018JD029400, 2019.

Hu, D., Z. Guan, W. Tian, and R. Ren, Recent strengthening of the stratospheric Arctic vortex response to warming in the central North Pacific, ***Nat. Commun.***, ***9*** (1), 1697, doi:10.1038/s41467-018-04138-3, 2018.

Hu, D., Z. Guan, M. Liu, and W. Feng, Dynamical mechanisms for the recent ozone depletion in the Arctic stratosphere linked to North Pacific sea surface temperatures, ***Clim. Dyn.***, ***58*** (9), 2663–2679, doi:10.1007/s00382-021-06026-x, 2022.

Hu, J.G., R.C. Ren, and H.M. Xu, Occurrence of winter stratospheric sudden warming events and the seasonal timing of spring stratospheric final warming, ***J. Atmos. Sci.***, ***71***, 2319–2334, doi:10.1175/JAS-D-13-0349.1, 2014.

Huang, J., P. Hitchcock, A.C. Maycock, C.M. McKenna, and W. Tian, Northern Hemisphere cold air outbreaks are more likely to be severe during weak polar vortex conditions, ***Comm. Earth Env.***, ***2*** (1), 147, doi:10.1038/s43247-021-00215-6, 2021.

Hurwitz, M.M., P.A. Newman, and C.I. Garfinkel, On the influence of North Pacific sea surface temperature on the Arctic winter climate, ***J. Geophys. Res.***, ***117*** (D19), doi:10.1029/2012JD017819, 2012.

Ingenito, A., Impact of hydrogen fueled hypersonic airliners on the O_3 layer depletion, ***Int. J. Hydrog. Energy***, ***43***, 22694–22704, doi:10.1016/j.ijhydene.2018.09.208, 2018.

Inness, A., M. Ades, A. Agustí-Panareda, J. Barré, A. Benedictow, A.-M. Blechschmidt, J.J. Dominguez, R. Engelen, H. Eskes, J. Flemming, V. Huijnen, L. Jones, Z. Kipling, S. Massart, M. Parrington, V.-H. Peuch, M. Razinger, S. Remy, M. Schulz, and M. Suttie, The CAMS reanalysis of atmospheric composition, ***Atmos. Chem. Phys.***, ***19***, 3515–3556, doi:10.5194/acp-19-3515-2019, 2019.

Inness, A., S. Chabrillat, J. Flemming, V. Huijnen, B. Langenrock, J. Nicolas, I. Polichtchouk, and M. Razinger, Exceptionally low Arctic stratospheric ozone in spring 2020 as seen in the CAMS reanalysis, ***J. Geophys. Res. Atmos.***, ***125*** (23), e2020JD033563, doi:10.1029/2020JD033563, 2020.

IPCC (Intergovenmental Panel on Climate Change), ***Climate Change 2021: The Physical Science Basis. Contribution of Working Group I to the Sixth Assessment Report of the Intergovernmental Panel on Climate Change***, edited by V. Masson-Delmotte, P. Zhai, A. Pirani, S.L. Connors, C. Péan, S. Berger, N. Caud, Y. Chen, L. Goldfarb, M.I. Gomis, M. Huang, K. Leitzell, E. Lonnoy, J.B.R. Matthews, T.K. Maycock, T. Waterfield, O. Yelekçi, R. Yu, and B. Zhou, Cambridge University Press, Cambridge, United Kingdom, 2021.

Jackman, C.H., E.L. Fleming, and F.M. Vitt, Influence of extremely large solar proton events in a changing stratosphere, ***J. Geophys. Res.***, ***105***, 11659–11670, doi:10.1029/2000JD900010, 2000.

James, A.D., J.S.A. Brooke, T.P. Mangan, T.F. Whale, J.M.C. Plane, and B.J. Murray, Nucleation of nitric acid hydrates in polar stratospheric clouds by meteoric material, ***Atmos. Chem. Phys.***, ***18***, 4519–4531, doi:10.5194/acp-18-4519-2018, 2018.

Jesswein, M., H. Bozem, H.-C. Lachnitt, P. Hoor, T. Wagenhäuser, T. Keber, T. Schuck, and A. Engel, Comparison of inorganic chlorine in the Antarctic and Arctic lowermost stratosphere by separate late winter aircraft measurements, ***Atmos. Chem. Phys.***, ***21*** (23), 17225–17241, doi:10.5194/acp-21-17225-2021, 2021.

Johansson, S., M.L. Santee, J.-U. Grooß, M. Höpfner, M. Braun, F. Friedl-Vallon, F. Khosrawi, O. Kirner, E. Kretschmer, H. Oelhaf, J. Orphal, B.-M. Sinnhuber, I. Tritscher, J. Ungermann, K.A. Walker, and W. Woiwode, Unusual chlorine partitioning in the 2015/16 Arctic winter lowermost stratosphere: observations and simulations, ***Atmos. Chem. Phys.***, ***19***, 8311–8338, doi:10.5194/acp-19-8311-2019, 2019.

Kablick, G.P., D.R. Allen, M.D. Fromm, and G.E. Nedoluha, Australian PyroCb smoke generates synoptic-scale stratospheric anticyclones, ***Geophys. Res. Lett.***, ***47*** (13), e2020GL088101, doi:10.1029/2020GL088101, 2020.

Kalakoski, N., P.T. Verronen, A. Seppälä, M.E. Szeląg, A. Kero, and D.R. Marsh, Statistical response of middle atmosphere composition to solar proton events in WACCM-D simulations: the importance of lower ionospheric chemistry, ***Atmos. Chem. Phys.***, ***20***, 8923–8938, doi:10.5194/acp-20-8923-2020, 2020.

Karpechko, A.Y., and A.C. Maycock (Lead Authors), M. Abalos, H. Akiyoshi, J.M. Arblaster, C.I. Garfinkel, K.H. Rosenlof, and M. Sigmond, Stratospheric Ozone Changes and Climate, Chapter 5 in ***Scientific Assessment of Ozone Depletion: 2018***, Global Ozone Research and Monitoring Project–Report No. 58, World Meteorological Organization, Geneva, Switzerland, 2018.

Kawa, S.R., J.G. Anderson, S.L. Baughcum, C.A. Brock, W.H. Brune, R.C. Cohen, D.E. Kinnison, P.A. Newman, J.M. Rodriguez, R.S. Stolarski, D. Waugh, and S.C. Wofsy, ***Assessment of the Effects of High-Speed Aircraft in the Stratosphere: 1998***, NASA Technical Paper TP-1999-209237, Washington, DC: National Aeronautics and Space Administration, 1999.

Keeble, J., N.L. Abraham, A.T. Archibald, M.P. Chipperfield, S. Dhomse, P.T. Griffiths, and J.A. Pyle, Modelling the potential impacts of the recent, unexpected increase in CFC-11 emissions on total column ozone recovery, ***Atmos. Chem. Phys., 20***, 7153–7166, doi:10.5194/acp-20-7153-2020, 2020.

Keeble, J., B. Hassler, A. Banerjee, R. Checa-Garcia, G. Chiodo, S. Davis, V. Eyring, P.T. Griffiths, O. Morgenstern, P. Nowack, G. Zeng, J. Zhang, G. Bodeker, S. Burrows, P. Cameron-Smith, D. Cugnet, C. Danek, M. Deushi, L.W. Horowitz, A. Kubin, L. Li, G. Lohmann, M. Michou, M.J. Mills, P. Nabat, D. Olivié, S. Park, Ø. Seland, J. Stoll, K.-H. Wieners, and T. Wu, Evaluating stratospheric ozone and water vapor changes in CMIP6 models from 1850 to 2100, ***Atmos. Chem. Phys.***, ***21***, 5015–5061, doi:10.5194/acp-21-5015-2021, 2021.

Khaykin, S., B. Legras, S. Bucci, P. Sellitto, L. Isaksen, F. Tencé, S. Bekki, A. Bourassa, L. Rieger, D. Zawada, J. Jumelet, and S. Godin-Beekmann, The 2019/20 Australian wildfires generated a persistent smoke-charged vortex rising up to 35 km altitude, ***Commun. Earth Environ., 1*** (1), 22, doi:10.1038/s43247-020-00022-5, 2020.

Kim, B.-M., S.-W. Son, S.-K. Min, J.-H. Jeong, S.-J. Kim, X. Zhang, T. Shim, and J.-H. Yoon, Weakening of the stratospheric polar vortex by Arctic sea-ice loss, ***Nat. Commun.***, ***5***, 4646, doi:10.1038/ncomms5646, 2014.

Kinnison, D., G.P. Brasseur, S.L. Baughcum, J. Zhang, and D. Wuebbles, The impact on the ozone layer of a potential fleet of civil hypersonic aircraft, ***Earth's Future***, ***8*** (10), e2020EF001626, doi:10.1029/2020EF001626, 2020.

Klekociuk A.R., M.B. Tully, P.B. Krummel, S.I. Henderson, D. Smale, R. Querel, S. Nichol, S.P. Alexander, P.J. Fraser, and G. Nedoluha, The Antarctic ozone hole during 2018 and 2019, ***J. South. Hemisphere Earth Syst. Sci.***, ***71***, 66–91, doi:10.1071/ES20010, 2021.

Klekociuk, A.R., M. Tully, P. Krummel, S. Henderson, D. Smale, R. Querel, S. Nichol, S.P. Alexander, P. Fraser, and G. Nedoluha, The Antarctic Ozone Hole during 2020, ***J. South. Hemisphere Earth Syst. Sci., 72***, doi:10.1071/ES21015, 2022.

Klobas, J.E., D.M. Wilmouth, D.K. Weisenstein, J.G. Anderson, and R.J. Salawitch, Ozone depletion following future volcanic eruptions, ***Geophys. Res. Lett.***, ***44*** (14), 7490–7499, doi:10.1002/2017GL073972, 2017.

Klobas, J.E., D.K. Weisenstein, R.J. Salawitch, and D.M. Wilmouth, Reformulating the bromine alpha factor and equivalent effective stratospheric chlorine (EESC): evolution of ozone destruction rates of bromine and chlorine in future climate scenarios, ***Atmos. Chem. Phys.***, ***20***, 9459–9471, doi:10.5194/acp-20-9459-2020, 2020.

Koenig, T.K., S. Baidar, P. Campuzano-Jost, C.A. Cuevas, B. Dix, R.P. Fernandez, H. Guo, S.R. Hall, D. Kinnison, B.A. Nault, K. Ullmann, J.L. Jimenez, A. Saiz-Lopez, and R. Volkamer, Quantitative detection of iodine in the stratosphere, ***Proc. Natl. Acad. Sci.***, ***117*** (4), 1860–1866; doi:10.1073/pnas.1916828117, 2020.

Kömüşcü, A.Ü., and K. Oğuz, Analysis of cold anomalies observed over Turkey during the 2018/2019 winter in relation to polar vortex and other atmospheric patterns, ***Meteorol. Atmos. Phys.***, ***133***, 1327–1354, doi:10.1007/s00703-021-00806-0, 2021.

Kramarova, N., P.A. Newman, E.R. Nash, S.E. Strahan, C.S. Long, B. Johnson, M. Pitts, M.L. Santee, I. Petropavlovskikh, G.O. Braathen, L. Coy, and J. de Laat, 2018 Antarctic ozone hole [in ''State of the Climate in 2018''], ***Bull. Amer. Meteor. Soc.***, ***100***, S185–S187, doi:10.1175/2019BAMSStateoftheClimate.1, 2019.

Kramarova, N., P.A. Newman, E.R. Nash, S.E. Strahan, C.S. Long, B. Johnson, M. Pitts, M.L. Santee, I. Petropavlovskikh, L. Coy, and J. de Laat, 2019 Antarctic ozone hole [in "State of the Climate in 2019"], ***Bull. Amer. Meteor. Soc.***, ***101***, S310–S312, doi:10.1175/BAMS-D-20-0090.1, 2020.

Kramarova, N., P.A. Newman, E.R. Nash, S.E. Strahan, C.S. Long, B. Johnson, M. Pitts, M.L. Santee, I. Petropavlovskikh, L. Coy, J. de Laat, G.H. Bernhard, S. Stierle, and K. Lakkala, 2020 Antarctic ozone hole [in "State of the Climate in 2020"], ***Bull. Amer. Meteor. Soc.***, ***102***, S345–S349, doi:10.1175/BAMS-D-21-0081.1, 2021.

Kretschmer, M., J. Cohen, V. Mattias, J. Runge, and D. Coumou, The different stratospheric influence on cold-extremes in Eurasia and North America, ***npj Clim. Atmos. Sci.***, ***1*** (1), doi:10.1038/s41612-018-0054-4, 2018.

Kretschmer, M., G. Zappa, and T.G. Shepherd, The role of Barents–Kara sea ice loss in projected polar vortex changes, ***Weather Clim. Dynam.***, ***1***, 715–730, doi:10.5194/wcd-1-715-2020, 2020.

Kunze, M., T. Kruschke, U. Langematz, M. Sinnhuber, T. Reddmann, and K. Matthes, Quantifying uncertainties of climate signals in chemistry climate models related to the 11-year solar cycle – Part 1: Annual mean response in heating rates, temperature, and ozone, ***Atmos. Chem. Phys.***, ***20***, 6991–7019, doi:10.5194/acp-20-6991-2020, 2020.

Kuttippurath, J., P. Kumar, P.J. Nair, and P.C. Pandey, Emergence of ozone recovery evidenced by reduction in the occurrence of Antarctic ozone loss saturation, ***npj Clim. Atmos. Sci., 1*** (1), 42, doi:10.1038/s41612-018-0052-6, 2018.

Kuttippurath, J., W. Feng, R. Müller, P. Kumar, S. Raj, G.P. Gopikrishnan, and R. Roy, Exceptional loss in ozone in the Arctic winter/spring of 2019/2020, ***Atmos. Chem. Phys.***, ***21***, 14019–14037, doi:10.5194/acp-21-14019-2021, 2021.

Langematz, U., S. Meul, K. Grunow, E. Romanowsky, S. Oberländer, J. Abalichin, and A. Kubin, Future Arctic temperature and ozone, The role of stratospheric composition changes, ***J. Geophys. Res. Atmos.***, ***119***, 2092–2112, doi:10.1002/2013JD021100, 2014.

Langematz, U., F. Schmidt, M. Kunze, G.E. Bodeker, and P. Braesicke, Antarctic ozone depletion between 1960 and 1980 in observations and chemistry–climate model simulations, ***Atmos. Chem. Phys.***, ***16***, 15619–15627, doi:10.5194/acp-16-15619-2016, 2016.

Langematz, U., and M. Tully (Lead Authors), N. Calvo, M. Dameris, A.T.J. de Laat, A. Klekociuk, R. Müller, and P. Young, Polar Stratospheric Ozone: Past, Present, and Future, Chapter 4 in ***Scientific Assessment of Ozone Depletion: 2018***, Global Ozone Research and Monitoring Project–Report No. 58, World Meteorological Organization, Geneva, Switzerland, 2018.

Lawrence, Z.D., and G.L. Manney, Characterizing stratospheric polar vortex variability with computer vision techniques, ***J. Geophys. Res. Atmos.***, ***123***, 1510–1535, doi:10.1002/2017JD027556, 2018.

Lawrence, Z.D., G.L. Manney, and K. Wargan, Reanalysis intercomparisons of stratospheric polar processing diagnostics, ***Atmos. Chem. Phys.***, ***18***, 13547–13579, doi:10.5194/acp-18-13547-2018, 2018.

Lawrence, Z.D., J. Perlwitz, A.H. Butler, G.L. Manney, P.A. Newman, S.H. Lee, and E.R. Nash, The remarkably strong Arctic stratospheric polar vortex of winter 2020: Links to record-breaking Arctic Oscillation and ozone loss, ***J. Geophys. Res.***, ***125*** (22), e2020JD033271, doi:10.1029/2020JD033271, 2020.

Lecouffe, A., S. Godin-Beekmann, A. Pazmiño, and A. Hauchecorne, Evolution of the intensity and duration of the Southern Hemisphere stratospheric polar vortex edge for the period 1979–2020, ***Atmos. Chem. Phys.***, 22, 4187–4200, doi:10.5194/acp-22-4187-2022, 2022.

Lee, S.H., J.C. Furtado, and A.J. Charlton-Perez, Wintertime North American weather regimes and the Arctic stratospheric polar vortex, ***Geophys. Res. Lett.***, ***46***, 14,892–14,900, doi:10.1029/2019GL085592, 2019.

Lee, S.H., and A.H. Butler, The 2018–2019 Arctic stratospheric polar vortex, ***Weather***, ***75*** (2), 52–57, doi:10.1002/wea.3643, 2020.

Lee, S.H., Z.D. Lawrence, A.H. Butler, and A.Y. Karpechko, Seasonal forecasts of the exceptional Northern Hemisphere winter of 2020, ***Geophys. Res. Lett.***, ***47*** (21), e2020GL090328, doi:10.1029/2020GL090328, 2020.

Lee, S.H., The January 2021 sudden stratospheric warming, ***Weather***, ***76***, 135–136, doi:10.1002/wea.3966, 2021.

Li, Y., W. Tian, F. Xie, Z. Wen, J. Zhang, D. Hu, and Y. Han, The connection between the second leading mode of the winter North Pacific sea surface temperature anomalies and stratospheric sudden warming events, ***Clim. Dyn. 51***, 581–595, doi:10.1007/s00382-017-3942-0, 2018.

Lickley M., S. Solomon, S. Fletcher, G.J.M. Velders, J. Daniel, M. Rigby, S.A. Montzka, L.J.M. Kuijpers, and K. Stone, Quantifying contributions of chlorofluorocarbon banks to emissions and impact on the ozone layer and climate, ***Nat. Commun.***, ***11*** (1), doi:10.1038/s41467-020-15162-7, 2020.

Lillo, S.P., S.M. Cavallo, D.B. Parsons, and C. Riedel, The role of a tropopause polar vortex in the generation of the January 2019 extreme Arctic outbreak, ***J. Atmos. Sci.***, ***78***, 2801–2821, doi:10.1175/JAS-D-20-0285.1, 2021.

Lim, E.P., H.H. Hendon, G. Boschat, D. Hudson, D.W.J. Thompson, A.J. Dowdy, and J.M. Arblaster, Australian hot and dry extremes induced by weakenings of the stratospheric polar vortex, ***Nat. Geosci.***, ***12***, 896–901, doi:10.1038/s41561-019-0456-x, 2019.

Lim, E., H.H. Hendon, A.H. Butler, D.W.J. Thompson, Z.D. Lawrence, A.A. Scaife, T.G. Shepherd, I. Polichtchouk, H. Nakamura, C. Kobayashi, R. Comer, L. Coy, A. Dowdy, R.D. Garreaud, P.A. Newman, and G. Wang, The 2019 Southern Hemisphere stratospheric polar vortex weakening and its impacts, ***Bull. Amer. Meteor. Soc***, ***102*** (6), E1150–E1171, doi:10.1175/BAMS-D-20-0112.1, 2021.

Liu, G., T. Hirooka, N. Eguchi, and K. Krüger, Dynamical evolution of a minor sudden stratospheric warming in the Southern Hemisphere in 2019, ***Atmos. Chem. Phys.***, ***22***, 3493–3505, doi:10.5194/acp-22-3493-2022, 2022.

Livesey, N.J., M.L. Santee, and G.L. Manney, A Match-based approach to the estimation of polar stratospheric ozone loss using Aura Microwave Limb Sounder observations, ***Atmos. Chem. Phys.***, ***15***, 9945–9963, doi:10.5194/acp-15-9945-2015, 2015.

Lyons, B.A., A. Hasell, and N.J. Stroud, Enduring extremes? Polar vortex, drought, and climate change beliefs, ***Environ. Commun.***, ***12*** (7), 876–894, doi:10.1080/17524032.2018.1520735, 2018.

Maliniemi, V., D.R. Marsh, H.N. Tyssøy, and C. Smith-Johnsen, Will climate change impact polar NO_x produced by energetic particle precipitation?, ***Geophys. Res. Lett.***, ***47*** (9), e2020GL087041, doi:10.1029/2020GL087041, 2020.

Maliniemi, V., H.N. Tyssøy, C. Smith-Johnsen, P. Arsenovic, and D.R. Marsh, Effects of enhanced downwelling of NOx on Antarctic upper-stratospheric ozone in the 21st century, ***Atmos. Chem. Phys.***, ***21***, 11,041–11,052, 2021, doi:10.5194/acp-21-11041-2021, 2021.

Manney, G.L., M.L. Santee, M. Rex, N.J. Livesey, M.C. Pitts, P. Veefkind, E.R. Nash, I. Wohltmann, R. Lehmann, L. Froidevaux, L.R. Poole, M.R. Schoeberl, D.P. Haffner, J. Davies, V. Dorokhov, H. Gernandt, B. Johnson, R. Kivi, E. Kyrö, N. Larsen, P.F. Levelt, A. Makshtas, C.T. McElroy, H. Nakajima, M.C. Parrondo, D.W. Tarasick, P. von der Gathen, K.A. Walker, and N.S. Zinoviev, Unprecedented Arctic ozone loss in 2011, ***Nature***, ***478*** (7370), 469–475, doi:10.1038/nature10556, 2011a.

Manney, G.L., M.I. Hegglin, W.H. Daffer, M.L. Santee, E.A. Ray, S. Pawson, M.J. Schwartz, C.D. Boone, L. Froidevaux, N.J. Livesey, W.G. Read, and K.A. Walker, Jet characterization in the upper troposphere/lower stratosphere (UTLS): Applications to climatology and transport studies, ***Atmos. Chem. Phys.***, ***11*** (12), 6115–6137, doi:10.5194/acp-11-6115-2011, 2011b.

Manney, G.L., M.I. Hegglin, W.H. Daffer, M.J. Schwartz, M.L. Santee, and S. Pawson, Climatology of upper tropospheric-lower stratospheric (UTLS) jets and tropopauses in MERRA, ***J. Clim.***, ***27***, 3248–3271, doi:10.1175/JCLI-D-13-00243.1, 2014.

Manney, G.L., Z.D. Lawrence, M.L. Santee, W.G. Read, N.J. Livesey, A. Lambert, L. Froidevaux, H.C. Pumphrey, and M.J. Schwartz, A minor sudden stratospheric warming with a major impact: Transport and polar processing in the 2014/2015 Arctic winter, ***Geophys. Res. Lett.***, ***42***, 7808–7816, doi:10.1002/2015GL065864, 2015.

Manney, G.L., N.J. Livesey, M.L. Santee, L. Froidevaux, A. Lambert, Z.D. Lawrence, L.F. Millán, J.L. Neu, W.G. Read, M.J. Schwartz, and R.A. Fuller, Record low Arctic stratospheric ozone in 2020: MLS observations of chemical processes and comparisons with previous extreme winters, ***Geophys. Res. Lett.***, ***47*** (16), e2020GL089063, doi:10.1029/2020GL089063, 2020.

Manney, G.L., A.H. Butler, Z.D. Lawrence, K. Wargan, and M.L. Santee, What's in a name? On the use and significance of the term "polar vortex", ***Geophys. Res. Lett.***, e2021GL097617, doi:10.1029/2021GL097617, 2022.

Manzini, E., A.Y. Karpechko, and L. Kornblueh, Nonlinear response of the stratosphere and the North Atlantic-European climate to global warming, ***Geophys. Res. Lett.***, ***45***, 4255–4263, doi:10.1029/2018GL077826, 2018.

Marsing, A., T. Jurkat-Witschas, J.-U. Grooß, S. Kaufmann, R. Heller, A. Engel, P. Hoor, J. Krause, and C. Voigt, Chlorine partitioning in the lowermost Arctic vortex during the cold winter 2015/2016, ***Atmos. Chem. Phys.***, ***19***, 10757–10772, doi:10.5194/acp-19-10757-2019, 2019.

Matthes, K., B. Funke, M.E. Andersson, L. Barnard, J. Beer, P. Charbonneau, M.A. Clilverd, T. Dudok de Wit, M. Haberreiter, A. Hendry, C.H. Jackman, M. Kretzschmar, T. Kruschke, M. Kunze, U. Langematz, D.R. Marsh, A.C. Maycock, S. Misios, C.J. Rodger, A.A. Scaife, A. Seppälä, M. Shangguan, M. Sinnhuber, K. Tourpali, I. Usoskin, M. van de Kamp, P.T. Verronen, and S. Versick, Solar forcing for CMIP6 (v3.2), ***Geosci. Model Dev.***, ***10***, 2247–2302, doi:10.5194/gmd-10-2247-2017, 2017.

Matthias, V., A. Dörnbrack, and G. Stober, The extraordinarily strong and cold polar vortex in the early northern winter 2015/2016, ***Geophys. Res. Lett.***, ***43***, 287–294, doi:10.1002/2016GL071676, 2016.

McPeters, R., M. Kroon, G. Labow, E. Brinksma, D. Balis, I. Petropavlovskikh, J.P. Veefkind, P.K. Bhartia, and P.F. Levelt, Validation of the Aura Ozone Monitoring Instrument total column ozone product, ***J. Geophys. Res.***, ***113***, D15S14, doi:10.1029/2007JD008802, 2008.

McPeters, R.D., S. Frith, and G.J. Labow, OMI total column ozone: extending the long-term data record, ***Atmos. Meas. Tech.***, ***8***, 4845–4850, doi:10.5194/amt-8-4845-2015, 2015.

Meinshausen, M., E. Vogel, A. Nauels, K. Lorbacher, N. Meinshausen, D.M. Etheridge, P.J. Fraser, S.A. Montzka, P.J. Rayner, C.M. Trudinger, P.B. Krummel, U. Beyerle, J.G. Canadell, J.S. Daniel, I.G. Enting, R.M. Law, C.R. Lunder, S. O'Doherty, R.G. Prinn, S. Reimann, M. Rubino, G.J.M. Velders, M.K. Vollmer, R.H.J. Wang, and R. Weiss, Historical greenhouse gas concentrations for climate modelling (CMIP6), ***Geosci. Model Dev.***, ***10***, 2057–2116, doi:10.5194/gmd-10-2057-2017, 2017.

Meinshausen, M., Z.R.J. Nicholls, J. Lewis, M.J. Gidden, E. Vogel, M. Freund, U. Beyerle, C. Gessner, A. Nauels, N. Bauer, J.G. Canadell, J.S. Daniel, A. John, P.B. Krummel, G. Luderer, N. Meinshausen, S.A. Montzka, P.J. Rayner, S. Reimann, S.J. Smith, M. van den Berg, G.J.M. Velders, M.K. Vollmer, and R.H.J. Wang, The shared socioeconomic pathway (SSP) greenhouse gas concentrations and their extensions to 2500, ***Geosci. Model Dev.***, ***13***, 3571–3605, doi:10.5194/gmd-13-3571-2020, 2020.

Mironova, I.A., K.L. Aplin, F. Arnold, G.A. Bazilevskaya, R.G. Harrison, A.A. Krivolutsky, K.A. Nicoll, E.V. Rozanov, E. Turunen, and I.G. Usoskin, Energetic particle influence on the Earth's atmosphere, ***Space Sci. Rev.***, ***194***, 1–96, doi:10.1007/s11214-015-018-4, 2015.

Mironova, I.A., A.A. Artamonov, G. Bazilevskaya, E. Rozanov, G.A. Kovaltsov, V.S. Makhmutov, L. Mishev, and A.V. Karagodin, Ionization of the polar atmosphere by energetic electron precipitation retrieved from balloon measurements, ***Geophys. Res. Lett.***, ***46*** (2), 990–996, doi:10.1029/2018GL079421, 2019.

Montzka, S., G. Dutton, P. Yu, E. Ray, R. Portmann, J. Daniel, L. Kuijpers, B. Hall, D. Mondeel, C. Siso, J. Nance, M. Rigby, A. Manning, L. Hu, F. Moore, B. Miller, and J. Elkins, An unexpected and persistent increase in global emissions of ozone-depleting CFC-11, ***Nature, 557***, 413–417, doi:10.1038/s41586-018-0106-2, 2018.

Montzka, S.A., G.S. Dutton, R.W. Portmann, M.P. Chipperfield, S. Davis, W. Feng, A.J. Manning, E. Ray, M. Rigby, B.D. Hall, C. Siso, J.D. Nance, P.B. Krummel, J. Mühle, D. Young, S. O'Doherty, P.K. Salameh, C.M. Harth, R.G. Prinn, R.F. Weiss, J.W. Elkins, H. Walter-Terrinoni, and C. Theodoridi, A decline in global CFC-11 emissions during 2018–2019, ***Nature, 590***, 428–432, doi:10.1038/s41586-021-03260-5, 2021.

Morgenstern, O., M. Giorgetta, K. Shibata, V. Eyring, D. Waugh, T. Shepherd, H. Akiyoshi, J. Austin, A.J.G. Baumgaertner, S. Bekki, P. Braesicke, C. Brühl, M.P. Chipperfield, D. Cugnet, M. Dameris, S. Dhomse, S.M. Frith, H. Garny, A. Gettelman, S.C. Hardiman, M.I. Hegglin, P. Jöckel, D.E. Kinnison, J.-F. Lamarque, E. Mancini, E. Manzini, M. Marchand, M. Michou, T. Nakamura, J.E. Nielsen, D. Olivié, G. Pitari, D.A. Plummer, E. Rozanov, J.F. Scinocca, D. Smale, H. Teyssèdre, M. Toohey, W. Tian, and Y. Yamashita, Review of the formulation of present-generation stratospheric chemistry-climate models and associated external forcings, ***J. Geophys. Res.***, ***115*** (D3), doi:10.1029/2009JD013728, 2010.

Morgenstern, O., M.I. Hegglin, E. Rozanov, F.M. O'Connor, N.L. Abraham, H. Akiyoshi, A.T. Archibald, S. Bekki, N. Butchart, M.P. Chipperfield, M. Deushi, S.S. Dhomse, R.R. Garcia, S.C. Hardiman, L.W. Horowitz, P. Jöckel, B. Josse, D. Kinnison, M. Lin, E. Mancini, M.E. Manyin, M. Marchand, V. Marécal, M. Michou, L.D. Oman, G. Pitari, D.A. Plummer, L.E. Revell, D. Saint-Martin, R. Schofield, A. Stenke, K. Stone, K. Sudo, T.Y. Tanaka, S. Tilmes, Y. Yamashita, K. Yoshida, and G. Zeng, Review of the global models used within phase 1 of the Chemistry–Climate Model Initiative (CCMI), ***Geosci. Model Dev.***, ***10***, 639–671, doi:10.5194/gmd-10-639-2017, 2017.

Mori, M., Y. Kosaka, M. Watanabe, H. Nakamura, and M. Kimoto, A reconciled estimate of the influence of Arctic sea-ice loss on recent Eurasian cooling, ***Nat. Clim. Change***, ***9***, 123–129, doi:10.1038/s41558-018-0379-3, 2019.

Müller, R., J.-U. Grooß, C. Lemmen, D. Heinze, M. Dameris, and G. Bodeker, Simple measures of ozone depletion in the polar stratosphere, ***Atmos. Chem. Phys.***, ***8***, 251–264, doi:10.5194/acp-8-251-2008, 2008.

Müller, R., J.-U. Grooß, A.M. Zafar, S. Robrecht, and R. Lehmann, The maintenance of elevated active chlorine levels in the Antarctic lower stratosphere through HCl null cycles, ***Atmos. Chem. Phys.***, ***18***, 2985–2997, doi:10.5194/acp-18-2985-2018, 2018.

Nakamura, T., K. Yamazaki, K. Iwamoto, M. Honda, Y. Miyoshi, Y. Ogawa, Y. Tomikawa, and J. Ukita, The stratospheric pathway for Arctic impacts on midlatitude climate, ***Geophys. Res. Lett.***, ***43***, 494–3501, doi:10.1002/2016GL068330, 2016.

Nash, E.R., P.A. Newman, J.E. Rosenfeld, and M.R. Schoeberl, An objective determination of the polar vortex using Ertel's potential vorticity, ***J. Geophys. Res., 101***, 9471–9478, doi:10.1029/96JD00066, 1996.

Nesse Tyssøy, H., A. Haderlein, M.I. Sandanger, and J. Stadsnes, Intercomparison of the POES/MEPED loss cone electron fluxes with the CMIP6 parametrization, ***J. Geophys. Res. Space Phys.***, ***124***, 628–642, doi:10.1029/2018JA025745, 2019.

Newman, P.A., S.R. Kawa, and E.R. Nash, On the size of the Antarctic ozone hole, ***Geophys. Res. Lett.***, ***31***, L21104, doi:10.1029/2004GL020596, 2004.

Newman, P.A., J.S. Daniel, D.W. Waugh, and E.R. Nash, A new formulation of equivalent effective stratospheric chlorine (EESC), ***Atmos. Chem. Phys.***, ***7***, 4537–4552, doi:10.5194/acp-7-4537-2007, 2007.

Newman, P.A. and M. Rex (Lead Authors), P.O. Canziani, K.S. Carslaw, K. Drdla, S. Godin-Beekmann, C.H. Jackman, K. Kreher, U. Langematz, R. Müller, H. Nakane, Y.J. Orsolini, R.J. Salawitch, M.L. Santee, M. von Hobe, and S. Yoden, Polar Ozone: Past and Present, Chapter 4 in ***Scientific Assessment of Ozone Depletion: 2007***, Global Ozone Research and Monitoring Project–Report No. 50, World Meteorological Organization, Geneva, Switzerland, 2007.

Newman, P.A., E.R. Nash, N. Kramarova, and A. Butler, The 2019 southern stratospheric warming [in ''State of the Climate in 2019''], ***Bull. Amer. Meteor. Soc.***, ***101***, S297–S298, doi: 0.1175/BAMS-D-20-0090.1, 2020.

Oberländer, S., U. Langematz, and S. Meul, Unraveling impact factors for future changes in the Brewer-Dobson circulation, ***J. Geophys. Res. Atmos.***, ***118***, 10,296–10,312, doi:10.1002/jgrd.50775, 2013.

Olsen, M.A., G.L. Manney, and J. Liu, The ENSO and QBO impact on ozone variability and stratosphere-troposphere exchange relative to the subtropical jets, ***J. Geophys. Res.***, ***124***, doi:10.1029/2019JD030435, 2019.

Oman, L.D., D.A. Plummer, D.W. Waugh, J. Austin, J.F. Scinocca, A.R. Douglass, R.J. Salawitch, T. Canty, H. Akiyoshi, S. Bekki, P. Braesicke, N. Butchart, M.P. Chipperfield, D. Cugnet, S. Dhomse, V. Eyring, S. Frith, S.C. Hardiman, D.E. Kinnison, J.-F. Lamarque, E. Mancini, M. Marchand, M. Michou, O. Morgenstern, T. Nakamura, J.E. Nielsen, D. Olivié, G. Pitari, J. Pyle, E. Rozanov, T.G. Shepherd, K. Shibata, R.S. Stolarski, H. Teyssèdre, W. Tian, Y. Yamashita, and J.R. Ziemke, Multimodel assessment of the factors driving stratospheric ozone evolution over the 21st century, ***J. Geophys. Res. Atmos.***, ***115*** (D24), doi:10.1029/2010JD014362, 2010.

Oman, L.D., A.R. Douglass, R.J. Salawitch, T.P. Canty, J.R. Ziemke, and M. Manyin, The effect of representing bromine from VSLS on the simulation and evolution of Antarctic ozone, ***Geophys. Res. Lett.***, ***43***, 9869–9876, doi:10.1002/2016GL070471, 2016.

O'Neill, B.C., E. Kriegler, K. Riahi, K.L. Ebi, S. Hallegatte, T.R. Carter, R. Mathur, and D.P. van Vuuren, A new scenario framework for climate change research: the concept of shared socioeconomic pathways, ***Clim. Change, 122*** (3)**,** 387–400, doi:10.1007/s10584-013-0905, 2014.

Pazmiño, A., S. Godin-Beekmann, A. Hauchecorne, C. Claud, S. Khaykin, F. Goutail, E. Wolfram, J. Salvador, and E. Quel, Multiple symptoms of total ozone recovery inside the Antarctic vortex during austral spring, ***Atmos. Chem. Phys.***, ***18***, 7557–7572, doi:10.5194/acp-18-7557-2018, 2018.

Pérot, K., and Y. Orsolini, Impact of the major SSWs of February 2018 and January 2019 on the middle atmospheric nitric oxide abundance, ***J. Atmos. Sol. Terr. Phys.***, ***218***, 105586, doi:10.1016/j.jastp.2021.105586, 2021.

Pettit, J.M., C.E. Randall, E.D. Peck, D.R. Marsh, M. van de Kamp, X. Fang, V.L. Harvey, C.J. Rodger, and B. Funke, Atmospheric effects of >30-keV energetic electron precipitation in the southern hemisphere winter during 2003, ***J. Geophys. Res. Space Phys.***, ***124*** (10), 8138–8153, doi:10.1029/2019JA026868, 2019.

Pitts, M.C., L.R. Poole, and R. Gonzalez, Polar stratospheric cloud climatology based on CALIPSO spaceborne lidar measurements from 2006 to 2017, ***Atmos. Chem. Phys.***, ***18***, 10881–10913, doi:10.5194/acp-18-10881-2018, 2018.

Plummer D., T. Nagashima, S. Tilmes, A. Archibald, G. Chiodo, S. Fadnavis, H. Garny, B. Josse, J. Kim, J.-F. Lamarque, O. Morgenstern, L. Murray, C. Orbe, A. Tai, M. Chipperfield, B. Funke, M. Juckes, D. Kinnison, M. Kunze, B. Luo, K, Matthes, P.A. Newman, C. Pascoe, and T. Peter, CCMI-2022: A new set of Chemistry-Climate Model Initiative (CCMI) community simulations to update the assessment of models and support upcoming Ozone Assessment activities, ***SPARC newsletter***, (57), [available at: https://www.sparc-climate.org/wp-content/uploads/sites/5/2021/07/SPARCnewsletter_Jul2021_web.pdf#page=22], 2021.

Polvani, L.M., M. Abalos, R. Garcia, D. Kinnison, and W.J. Randel, Significant weakening of Brewer-Dobson circulation trends over the 21st century as a consequence of the Montreal Protocol, ***Geophys. Res. Lett.***, ***45***, 401–409, doi:10.1002/2017GL075345, 2017.

Polvani, L.M., L. Wang, M. Abalos, N. Butchart, M.P. Chipperfield, M. Dameris, M. Deushi, S.S. Dhomse, P. Jöckel, D. Kinnison, M. Michou, O. Morgenstern, L.D. Oman, D.A. Plummer, and K.A. Stone, Large impacts, past and future, of ozone-depleting substances on Brewer-Dobson circulation trends: A multimodel assessment, ***J. Geophys. Res. Atmos.***, ***124*** (13), 6669–6680, doi:10.1029/2018JD029516, 2019.

Poole, L.R., and M.C. Pitts, Polar stratospheric cloud climatology based on Stratospheric Aerosol Measurement II observations from 1978 to 1989, ***J. Geophys. Res. Atmos.***, ***99***, 13,083–13,089, doi:10.1029/94JD00411, 1994.

Prignon, M., S. Chabrillat, M. Friedrich, D. Smale, S.E. Strahan, P.F. Bernath, M.P. Chipperfield, S.S. Dhomse, W. Feng, D. Minganti, C. Servais, and E. Mahieu, Stratospheric fluorine as a tracer of circulation changes: Comparison between infrared remote-sensing observations and simulations with five modern reanalyses, ***J. Geophys. Res.***, ***126*** (19), e2021JD034995, doi:10.1029/2021JD034995, 2021.

Pyle, J.A., J. Keeble, N.L. Abraham, M.P. Chipperfield, and P.T. Griffiths, Integrated ozone depletion as a metric for ozone recovery, ***Nature***, ***608***, 719–723, doi:10.1038/s41586-022-04968-8, 2022.

Rao, J., R. Ren, H. Chen, Y. Yu, and Y. Zhou, The stratospheric sudden warming event in February 2018 and its prediction by a climate system model, ***J. Geophys. Res. Atmos.***, ***123***, 13,332–13,345, doi:10.1029/2018JD028908, 2018.

Rao, J., C.I. Garfinkel, H. Chen, and I.P. White, The 2019 New Year stratospheric sudden warming and its real-time predictions in multiple S2S models, ***J. Geophys. Res. Atmos.***, ***124***, 11155–11174, doi:10.1029/2019JD030826, 2019.

Rao, J., and C.I. Garfinkel, Arctic ozone loss in March 2020 and its seasonal prediction in CFSv2: A comparative study with the 1997 and 2011 cases, ***J. Geophys. Res. Atmos.***, ***125*** (21), e2020JD033524, doi:10.1029/2020JD033524, 2020.

Rao, J., C.I. Garfinkel, I.P. White, and C. Schwartz, The Southern Hemisphere minor sudden stratospheric warming in September 2019 and its predictions in S2S models, ***J. Geophys. Res. Atmos.***, ***125*** (14), e2020JD032723, doi:10.1029/2020JD032723, 2020.

Rao, J., and C.I. Garfinkel, The strong stratospheric polar vortex in March 2020 in sub-seasonal to seasonal models: Implications for empirical prediction of the low Arctic total ozone extreme, ***J. Geophys. Res. Atmos.***, ***126*** (9), e2020JD034190, doi:10.1029/2020JD034190, 2021.

Rex, M., R.J. Salawitch, H. Deckelmann, P. von der Gathen, N.R.P. Harris, M.P. Chipperfield, B. Nau- jokat, E. Reimer, M. Allaart, S.B. Andersen, R. Bevilacqua, G.O. Braathen, H. Claude, J. Davies, H. De Backer, H. Dier, V. Dorokhov, H. Fast, M. Gerding, S. Godin-Beekmann, K. Hoppel, B. Johnson, E. Kyrö, Z. Litynska, D. Moore, H. Nakane, M.C. Parrondo, A.D. Risley Jr., P. Skrivankova, R. Stübi, P. Viatte, V. Yushkov, and C. Zerefos, Arctic winter 2005: Implications for stratospheric ozone loss and climate change, ***Geophys. Res. Lett.***, ***33***, L23808, doi:10.1029/2006GL026731, 2006.

Rieger, L.A., W.J. Randel, A.E. Bourassa, and S. Solomon, Stratospheric temperature and ozone anomalies associated with the 2020 Australian New Year fires, ***Geophys. Res. Lett.***, ***48*** (24), e2021GL095898, doi:10.1029/2021GL095898, 2021.

Rotermund, M.K., V. Bense, M.P. Chipperfield, A. Engel, J.-U. Grooß, P. Hoor, T. Hüneke, T. Keber, F. Kluge, B. Schreiner, T. Schuck, B. Vogel, A. Zahn, and K. Pfeilsticker, Organic and inorganic bromine measurements around the extratropical tropopause and lowermost stratosphere: Insights into the transport pathways and total bromine, ***Atmos. Chem. Phys.***, ***21*** (20), 15,375–15,407, doi:10.5194/acp-21-15375-2021, 2021.

Safieddine, S., M. Bouillon, A.-C. Paracho, J. Jumelet, F. Tencé, A. Pazmiño, F. Goutail, C. Wespes, S. Bekki, A. Boynard, J. Hadji Lazaro, P.-F. Coheur, D. Hurtmans, and C. Clerbaux, Antarctic ozone enhancement during the 2019 sudden stratospheric warming event, ***Geophys. Res. Lett.***, ***47*** (14), e2020GL087810, doi:10.1029/2020GL087810, 2020.

Saha, S., S. Moorthi, H. Pan, X. Wu, J. Wang, S. Nadiga, P. Tripp, R. Kistler, J. Woollen, D. Behringer, H. Liu, D. Stokes, R. Grumbine, G. Gayno, J. Wang, Y. Hou, H. Chuang, H.H. Juang, J. Sela, M. Iredell, R. Treadon, D. Kleist, P. van Delst, D. Keyser, J. Derber, M. Ek, J. Meng, H. Wei, R. Yang, S. Lord, H. van den Dool, A. Kumar, W. Wang, C. Long, M. Chelliah, Y. Xue, B. Huang, J. Schemm, W. Ebisuzaki, R. Lin, P. Xie, M. Chen, S. Zhou, W. Higgins, C. Zou, Q. Liu, Y. Chen, Y. Han, L. Cucurull, R.W. Reynolds, G. Rutledge, and M. Goldberg, The NCEP climate forecast system reanalysis, ***Bull. Am. Meteorol. Soc.***, ***91***, 1015–1058, doi:10.1175/2010BAMS3001.1, 2010.

Santee, M.L., A. Lambert, G.L. Manney, N.J. Livesey, L. Froidevaux, J.L. Neu, M.J. Schwartz, L.F. Millán, F. Werner, W.G. Read, M. Park, R.A. Fuller, and B.M. Ward, Prolonged and pervasive perturbations in the composition of the Southern Hemisphere midlatitude lower stratosphere from the Australian New Year's fires, ***Geophys. Res. Lett.***, ***49*** (4), e2021GL096270, doi:10.1029/2021GL096270, 2022.

Schneider, J., R. Weigel, T. Klimach, A. Dragoneas, O. Appel, A. Hünig, S. Molleker, F. Köllner, H.-C. Clemen, O. Eppers, P. Hoppe, P. Hoor, C. Mahnke, M. Krämer, C. Rolf, J.-U. Grooß, A. Zahn, F. Obersteiner, F. Ravegnani, A. Ulanovsky, H. Schlager, M. Scheibe, G.S. Diskin, J.P. DiGangi, J.B. Nowak, M. Zöger, and S. Borrmann, Aircraft-based observation of meteoric material in lower-stratospheric aerosol particles between 15 and 68°N, ***Atmos. Chem. Phys.***, ***21***, 989–1013, doi:10.5194/acp-21-989-2021, 2021.

Schwartz, M.J., M.L. Santee, H.C. Pumphrey, G.L. Manney, A. Lambert, N.J. Livesey, L. Millán, J.L. Neu, W.G. Read, and F. Werner, Australian New Year's pyroCb impact on stratospheric composition, ***Geophy. Res. Lett.***, ***47*** (24), e2020GL090831, doi:10.1029/2020GL090831, 2020.

Screen, J.A., Simulated atmospheric response to regional and Pan-Arctic sea-ice loss, ***J. Clim.***, ***30*** (11), 3945–3962, doi:10.1175/JCLI-D-16-0197.1, 2017.

Screen, J.A., C. Deser, and L. Sun, Reduced risk of North American cold extremes due to continued Arctic sea ice loss, ***Bull. Amer. Meteor. Soc.***, ***96*** (9), 1489–1503, doi:10.1175/BAMS-D-14-00185.1, 2015.

Shen, X., L. Wang, and S. Osprey, Tropospheric forcing of the 2019 Antarctic sudden stratospheric warming, ***Geophys. Res. Lett.***, ***47*** (20), e2020GL089343, doi:10.1029/2020GL089343, 2020.

Shepherd, M., 12 weather and climate concepts that confuse the public, ***Forbes,*** [available at: https://www.forbes.com/sites/marshallshepherd/2016/12/13/12-weather-and-climate-concepts-that-confuse-the-public/?sh=2943e192350b], 2016.

Sinnhuber, M., H. Nieder, and N. Wieters, Energetic particle precipitation and the chemistry of the mesosphere/lower thermosphere, ***Surv. Geophys.***, ***33*** (6), 1281–1334, doi:10.1007/s10712-012-9201-3, 2012.

Sinnhuber, M., U. Berger, B. Funke, H. Nieder, T. Reddmann, G. Stiller, S. Versick, T. von Clarmann, and J.M. Wissing, NO_y production, ozone loss and changes in net radiative heating due to energetic particle precipitation in 2002–2010, ***Atmos. Chem. Phys.***, ***18*** (2), 1115–1147, doi:10.5194/acp-18-1115-2018, 2018.

Smale, D., S.E. Strahan, R. Querel, U. Frieß, G.E. Nedoluha, S.E. Nichol, J. Robinson, I. Boyd, M. Kotkamp, R.M. Gomez, M. Murphy, H. Tran, and J. McGaw, Evolution of observed ozone, trace gases, and meteorological variables over Arrival Heights, Antarctica (77.8°S, 166.7°E) during the 2019 Antarctic stratospheric sudden warming, ***Tellus B: Chem. Phys. Meteorol.***, ***73*** (1), 1–18, doi:10.1080/16000889.2021.1933783, 2021.

Snels, M., A. Scoccione, L. Di Liberto, F. Colao, M. Pitts, L. Poole, T. Deshler, F. Cairo, C. Cagnazzo, and F. Fierli, Comparison of Antarctic polar stratospheric cloud observations by ground-based and space-borne lidar and relevance for chemistry–climate models, ***Atmos. Chem. Phys.***, ***19***, 955–972, doi:10.5194/acp-19-955-2019, 2019.

Snels, M., F. Colao, F. Cairo, I. Shuli, A. Scoccione, M. De Muro, M. Pitts, L. Poole, and L. Di Liberto, Quasi-coincident observations of polar stratospheric clouds by ground-based lidar and CALIOP at Concordia (Dome C, Antarctica) from 2014 to 2018, ***Atmos. Chem. Phys.***, ***21***, 2165–2178, doi:10.5194/acp-21-2165-2021, 2021.

Solomon, S., J. Haskins, D.J. Ivy, and F. Min, Fundamental differences between Arctic and Antarctic ozone depletion, ***Proc. Natl. Acad. Sci.***, ***111*** (17), 6220–6225, doi:10.1073/pnas.1319307111, 2014.

Solomon, S., D.J. Ivy, D. Kinnison, M.J. Mills, R.R. Neely III, and A. Schmidt, Emergence of healing in the Antarctic ozone layer, ***Science***, ***353*** (6296), 269–274, doi:10.1126/science.aae0061, 2016.

Spang, R., L. Hoffmann, R. Müller, J.-U. Grooß, I. Tritscher, M. Höpfner, M. Pitts, A. Orr, and M. Riese, A climatology of polar stratospheric cloud composition between 2002 and 2012 based on MIPAS/Envisat observations, ***Atmos. Chem. Phys.***, ***18***, 5089–5113, doi:10.5194/acp-18-5089-2018, 2018.

SPARC CCMVal (Stratosphere-troposphere Processes And their Role in Climate), ***SPARC Report on the Evaluation of Chemistry-Climate Models***, edited by V. Eyring, T.G. Shepherd, and D.W. Waugh, SPARC Report No. 5, WCRP-132, WMO/TD-No. 1526, 478 pp., [available at: http://www.atmosp.physics.utoronto.ca/SPARC/ccmval_final/index.php], 2010.

SPARC (Stratosphere-troposphere Processes And their Role in Climate), ***SPARC Reanalysis Intercomparison Project (S-RIP) Final Report***, edited by M. Fujiwara, G.L. Manney, L.J. Gray, and J.S. Wright, SPARC Report No. 10, WCRP-17/2020, doi:10.17874/800dee57d13, 2022.

Stecher, L., F. Winterstein, M. Dameris, P. Jockel, M. Ponater, and M. Kunze, Slow feedbacks resulting from strongly enhanced atmospheric methane mixing ratios in a chemistry–climate model with mixed-layer ocean, ***Atmos. Chem. Phys.***, ***21***, 731–754, doi:10.5194/acp-21-731-2021, 2021.

Stone, K.A., S. Solomon, D.E. Kinnison, M.C. Pitts, L.R. Poole, M.J. Mills, A. Schmidt, R.R. Neely III, D. Ivy, M.J. Schwartz, J.-P. Vernier, B.J. Johnson, M.B. Tully, A.R. Klekociuk,G. König-Langlo, and S. Hagiya, Observing the impact of Calbuco volcanic aerosols on South Polar ozone depletion in 2015, ***J. Geophys. Res. Atmos.***, ***122***, 11862–11879, doi:10.1002/2017JD026987, 2017.

Stone, K.A., S. Solomon, and D.E. Kinnison, On the identification of ozone recovery, ***Geophys. Res. Lett.***, ***45***, 5158–5165, doi:10.1029/2018GL077955, 2018.

Stone, K.A., S. Solomon, D.E. Kinnison, and M.J. Mills, On recent large Antarctic ozone holes and ozone recovery metrics, ***Geophys. Res. Lett.***, ***48*** (22), e2021GL095232, doi:10.1029/2021GL095232, 2021.

Strahan, S.E., A.R. Douglass, and S.D. Steenrod, Chemical and dynamical impacts of stratospheric sudden warmings on Arctic ozone variability, ***J. Geophys. Res. Atmos.***, ***121***, 11,836–11,851, doi:10.1002/2016JD025128, 2016.

Strahan, S.E., A.R. Douglass, and M.R. Damon, Why do Antarctic ozone recovery trends vary?, ***J. Geophys. Res. Atmos., 124***, 8837–8850, doi:10.1029/2019JD030996, 2019.

Strahan, S.E., D. Smale, A.R. Douglass, T. Blumenstock, J.W. Hannigan, F. Hase, N.B. Jones, E. Mahieu, J. Notholt, L.D. Oman, I. Ortega, M. Palm, M. Prignon, J. Robinson, M. Schneider, R. Sussmann, and V.A. Velazco, Observed hemispheric asymmetry in stratospheric transport trends from 1994 to 2018, ***Geophys. Res. Lett.***, ***47*** (17), e2020GL088567, doi:10.1029/2020GL088567, 2020.

Tegtmeier, S., M. Rex, I. Wohltmann, and K. Krüger, Relative importance of dynamical and chemical contributions to Arctic wintertime ozone, ***Geophys. Res. Lett.***, ***35***, L17801, doi:10.1029/2008GL034250, 2008.

Tegtmeier, S., F. Ziska, I. Pisso, B. Quack, G.J.M. Velders, X. Yang, and K. Krüger, Oceanic bromoform emissions weighted by their ozone depletion potential, ***Atmos. Chem. Phys.***, ***15***, 13,647–13,663, doi:10.5194/acp-15-13647-2015, 2015.

Tritscher, I., M.C. Pitts, L.R. Poole, S.P. Alexander, F. Cairo, M.P. Chipperfield, J.-U. Grooß, M. Höpfner, A. Lambert, B. Luo, S. Molleker, A. Orr, R. Salawitch, M. Snels, R. Spang, W. Woiwode, and T. Peter, Polar stratospheric clouds: Satellite observations, processes, and role in ozone depletion, ***Rev. Geophys.***, ***59*** (2), e2020RG000702, doi:10.1029/2020RG000702, 2021.

Tully, M.B., P.B. Krummel, and A.R. Klekociuk, Trends in Antarctic ozone hole metrics 2001–17, ***J. South. Hemisph. Earth Syst. Sci., 69*** (1), 52–56, doi:10.1071/ES19020, 2019.

UCAR, Why the polar vortex keeps breaking out of the Arctic, ***University Corporation for Atmospheric Research***, [available at: https://scied.ucar.edu/learning-zone/climate-change-impacts/why-polar-vortex-keeps-breaking-out-arctic], 2021.

UC Davis, What is the polar vortex?, ***University of California, Davis,*** [available at: https://climatechange.ucdavis.edu/climate-change-definitions/what-is-the-polar-vortex], 2019.

Vargin, P.N., S.V. Kostrykin, E.M. Volodin, A.I. Pogoreltsev, and K. Wei, Arctic stratosphere circulation changes in the 21st century in simulations of INM CM5, ***Atmosphere***, ***13*** (1), 25, doi:10.3390/atmos13010025, 2022.

van de Kamp, M., A. Seppälä, M.A. Clilverd, C.J. Rodger, P.T. Verronen, and I.C. Whittaker, A model providing long-term data sets of energetic electron precipitation during geomagnetic storms, ***J. Geophys. Res. Atmos.***, ***121*** (20), 12,520–12,540, doi:10.1002/2015jd024212, 2016.

van der A, R.J., M.A.F. Allaart, and H.J. Eskes, Multi-Sensor Reanalysis (MSR) of total ozone, version 2. Dataset, ***Royal Netherlands Meteorological Institute (KNMI)***, doi:10.21944/temis-ozone-msr2, 2015.

von der Gathen, P., R. Kivi, I. Wohltmann, R.J. Salawitch, and M. Rex, Climate change favours large seasonal loss of Arctic ozone, ***Nat. Commun., 12*** (1)**,** 3886, doi:10.1038/s41467-021-24089-6, 2021.

Wallace, J.M., I.M. Held, D.W.J. Thompson, K.E. Trenberth, and J.E. Walsh, Global warming and winter weather, ***Science***, ***343*** (6172), 729–730, doi:10.1126/science.343.6172.729, 2014.

Wang, S., D. Kinnison, S.A. Montzka, E.C. Apel, R.S. Hornbrook, A.J. Hills, D.R. Blake, B. Barletta, S. Meinardi, C. Sweeney, F. Moore, M. Long, A. Saiz-Lopez, R.P. Fernandez, S. Tilmes, L.K. Emmons, and J.-F. Lamarque, Ocean biogeochemistry control on the marine emissions of brominated very short-lived ozone-depleting

substances: a machine-learning approach, ***J. Geophys. Res. Atmos.***, ***124*** (22), 12319–12339, doi:10.1029/2019JD031288, 2019.

Wang, S.-Y., L. Hipps, R.R. Gillies, and J.-H. Yoon, Probable causes of the abnormal ridge accompanying the 2013–2014 California drought: ENSO precursor and anthropogenic warming footprint, ***Geophys. Res. Lett.***, ***41***, 3220–3226, doi:10.1002/2014GL059748, 2014.

Wargan, K., G. Labow, S. Frith, S. Pawson, N. Livesey, and G. Partyka, Evaluation of the ozone fields in NASA's MERRA-2 reanalysis, ***J. Clim.***, ***30*** (8), 2961–2988, doi:10.1175/JCLI-D-16-0699.1, 2017.

Wargan, K., B. Weir, G.L. Manney, S.E. Cohn, and N.J., Livesey, The anomalous 2019 Antarctic ozone hole in the GEOS Constituent Data Assimilation System with MLS observations, ***J. Geophys. Res. Atmos., 125*** (18), e2020JD033335, doi:10.1029/2020JD033335, 2020.

Waugh, D.W., A.H. Sobel, and L.M. Polvani, What is the polar vortex and how does it influence weather?, ***Bull. Am. Meteor. Soc.***, ***98*** (1), 37–44, doi:10.1175/BAMS-D-15-00212.1, 2017.

Weber, M., S. Dikty, J.P Burrows, H. Garny, M. Dameris, A. Kubin, J. Abalichin, and U. Langematz, The Brewer-Dobson circulation and total ozone from seasonal to decadal time scales, ***Atmos. Chem. Phys.***, ***11***, 11221–11235, doi:10.5194/acp-11-11221-2011, 2011.

Weber, M., M. Coldewey-Egbers, V.E. Fioletov, S.M. Frith, J.D. Wild, J.P. Burrows, C.S. Long, and D. Loyola, Total ozone trends from 1979 to 2016 derived from five merged observational datasets – the emergence into ozone recovery, ***Atmos. Chem. Phys.***, ***18*** (3), 2097–2117, doi:10.5194/acp-18-2097-2018, 2018.

Weber, M., C. Arosio, W. Feng, S.S. Dhomse, M.P. Chipperfield, A. Meier, J.P. Burrows, K.-U. Eichmann, A. Richter, and A. Rozanov, The unusual stratospheric Arctic winter 2019/20: Chemical ozone loss from satellite observations and TOMCAT chemical transport model, ***J. Geophys. Res. Atmos.***, ***126*** (6), e2020JD034386, doi:10.1029/2020JD034386, 2021.

Weber, M., C. Arosio, M. Coldewey-Egbers, V. Fioletov, S.M. Frith, J.D. Wild, K. Tourpali, J.P. Burrows, and D. Loyola, Global total ozone recovery trends attributed to ODS changes derived from five merged ozone datasets, ***Atmos. Chem. Phys.***, ***22*** (10), 6843–6859, doi:10.5194/acp-22-6843-2022, 2022.

Westbrook, C.D., The fall speeds of sub-100 µm ice crystals, ***Q. J. Roy. Meteor. Soc.***, ***134***, 1243–1251, doi:10.1002/qj.290, 2008.

Wilka, C., S. Solomon, D. Kinnison, and D. Tarasick, An Arctic ozone hole in 2020 if not for the Montreal Protocol, ***Atmos. Chem. Phys., 21,*** 15771–15781, doi:10.5194/acp-21-15771, 2021.

Winterstein, F., F. Tanalski, P. Jockel, M. Dameris, and M. Ponater, Implication of strongly increased atmospheric methane concentrations for chemistry-climate connections, ***Atmos. Chem. Phys.***, ***19***, 7151–7163, doi:10.5194/acp-19-7151-2019, 2019.

WMO (World Meteorological Organization), ***Scientific Assessment of Ozone Depletion: 2006***, Global Ozone Research and Monitoring Project–Report No. 50, 572 pp., Geneva, Switzerland, 2007.

WMO (World Meteorological Organization), ***Scientific Assessment of Ozone Depletion: 2010***, Global Ozone Research and Monitoring Project–Report No. 52, 516 pp., Geneva, Switzerland, 2010.

WMO (World Meteorological Organization), ***Scientific Assessment of Ozone Depletion: 2014***, Global Ozone Research and Monitoring Project–Report No. 55, 416 pp., Geneva, Switzerland, 2014.

WMO (World Meteorological Organization***), Scientific Assessment of Ozone Depletion: 2018***, Global Ozone Research and Monitoring Project–Report No. 58, 588 pp., Geneva, Switzerland, 2018.

WMO (World Meteorological Organization), ***Report on Unexpected Emissions of CFC-11***, Ozone Research and Monitoring, A Report of the Scientific Assessment Panel of the Montreal Protocol on Substance that Deplete the Ozone Layer–No. 1268, Geneva, Switzerland, 2021.

Wohltmann, I., P. von der Gathen, R. Lehmann, M. Maturilli, H. Deckelmann, G.L. Manney, J. Davis, D. Tarasick, N. Jepsen, R. Kivi, N. Lyall, and M. Rex, Near complete local reduction of Arctic stratospheric ozone by severe chemical loss in spring 2020, ***Geophys. Res. Lett.***, ***47***, e2020GL089547, doi:10.1029/2020GL089547, 2020.

Wohltmann, I., P. von der Gathen, R. Lehmann, H. Deckelmann, G.L. Manney, J. Davies, D. Tarasick, N. Jepsen, R. Kivi, N. Lyall, and M. Rex, Chemical evolution of the exceptional Arctic stratospheric winter 2019/2020 compared to previous Arctic and Antarctic winters, ***J. Geophys. Res. Atmos.***, ***126*** (18), e2020JD034356, doi:10.1029/2020JD034356, 2021.

Woiwode, W., M. Höpfner, L. Bi, F. Khosrawi, and M.L. Santee, Vortex-wide detection of large aspherical NAT particles in the Arctic winter 2011/12 stratosphere, ***Geophys. Res. Lett.***, ***46***, 13420–13429, doi:10.1029/2019GL084145, 2019.

Wright, C.J., R.J. Hall, T.P. Banyard, N.P. Hindley, I. Krisch, D.M. Mitchell, and W.J.M. Seviour, Dynamical and surface impacts of the January 2021 sudden stratospheric warming in novel Aeolus wind observations, MLS and ERA5, ***Weather Clim. Dynam.***, ***2,*** 1283–1301, doi:10.5194/wcd-2-1283-2021, 2021.

Xia, Y., W. Xu, Y. Hu, and F. Xi, Southern-Hemisphere high-latitude stratospheric warming revisit, ***Clim. Dyn., 54,*** 1671–1682, doi:10.1007/s00382-019-05083-7, 2020.

Yamazaki, Y., V. Matthias, Y. Miyoshi, C. Stolle, T. Siddiqui, G. Kervalishvili, J. Laštovička, M. Kozubek, W. Ward, D.R. Themens, S. Kristoffersen, and P. Alken, September 2019 Antarctic sudden stratospheric warming: Quasi-6-day wave burst and ionospheric effects, ***Geophys. Res. Lett.***, ***47*** (1), e2019GL086577, doi:10.1029/2019GL086577, 2020.

Yanes, J., Hypersonic: The future of aviation, ***OpenMind BBVA***, [available at: https://www.bbvaopenmind.com/en/technology/future/hypersonic-the-future-of-aviation], 2020.

Yang, X., N.L. Abraham, A.T. Archibald, P. Braesicke, J. Keeble, P.J. Telford, N.J. Warwick, and J.A. Pyle, How sensitive is the recovery of stratospheric ozone to changes in concentrations of very shortlived bromocarbons?, ***Atmos. Chem. Phys.***, ***14***, 10,431–10,438, doi:10.5194/acp-14- 10431-2014, 2014.

Yook, S., D.W.J. Thompson, and S. Solomon, Climate impacts and potential drivers of the unprecedented Antarctic ozone holes of 2020 and 2021, ***Geophys. Res. Lett.***, ***49*** (10), e2022GL098064, doi:10.1029/2022GL098064, 2022.

Yu, B., and X. Zhang, A physical analysis of the severe 2013/2014 cold winter in North America, ***J. Geophys. Res. Atmos.***, ***120***, 10,149–10,165, doi:10.1002/2015JD023116, 2015.

Yu, P., S.M. Davis, O.B. Toon, R.W. Portmann, C.G. Bardeen, J.E. Barnes, H. Telg, C. Maloney, and K.H. Rosenlof, Persistent stratospheric warming due to 2019–2020 Australian wildfire smoke, ***Geophys. Res. Lett.***, ***48*** (7), e2021GL092609, doi:10.1029/2021GL092609, 2021.

Zafar, A.M., R. Müller, J.-U. Grooß, S. Robrecht, B. Vogel, and R. Lehmann, The relevance of reactions of the methyl peroxy radical (CH_3O_2) and methylhypochlorite (CH_3OCl) for Antarctic chlorine activation and ozone loss, ***Tellus B: Chem. Phys. Meteorol.***, ***70*** (1), 1–18, doi:10.1080/16000889.2018.1507391, 2018.

Zhang, P., Y. Wu, I.R. Simpson, K.L. Smith, X. Zhang, B. De, and P. Callaghan, A stratospheric pathway linking a colder Siberia to Barents–Kara sea ice loss, ***Sci. Adv.,*** ***4*** (7), doi:10.1126/sciadv.aat6025, 2018.

Zhang, J., D. Wuebbles, D. Kinnison, and S.L. Baughcum, Potential impacts of supersonic aircraft emissions on ozone and resulting forcing on climate: An update on historical analysis, ***J. Geophys. Res. Atmos.***, ***126*** (6), e2020JD034130, doi:10.1029/2020JD034130, 2021.

Ziska, F., B. Quack, I. Stemmler, S. Tegtmeier, and K. Krüger, Future emissions of marine halogenated very short-lived substances under climate change, ***J. Atmos. Chem.***, ***74*** (2), 245–260, doi:10.1007/s10874-016-9355-3, 2017.

Zhu, Y., O.B. Toon, D. Kinnison, V.L. Harvey, M.J. Mills, C.G. Bardeen, M. Pitts, N. Bègue, J.-B. Renard, G. Berthet, and F. Jégou, Stratospheric aerosols, polar stratospheric clouds, and polar ozone depletion after the Mount Calbuco eruption in 2015, ***J. Geophys. Res. Atmos.***, ***123*** (21), 12,308–12,331, doi:10.1029/2018JD028974, 2018.

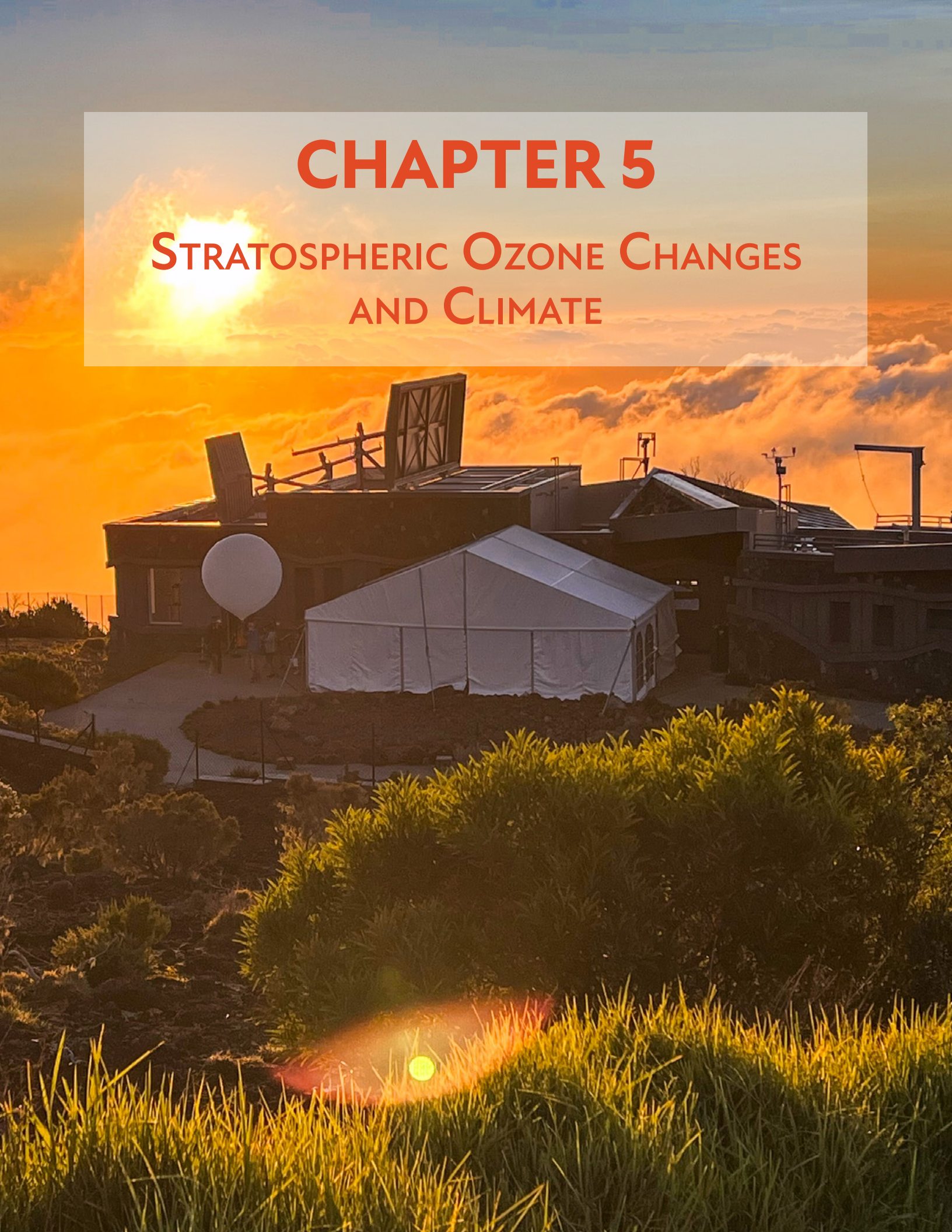

CHAPTER 5

Stratospheric Ozone Changes and Climate

About the cover image:
The Hunga Tonga-Hunga Ha'apai volcanic eruption in January 2022 lofted water vapor and other emissions well into the stratosphere in the southern hemisphere. Downwind, sunsets changed color as seen from the Maïdo Observatory on Réunion Island.

Photo credit: Elizabeth Asher, NOAA CSL / CIRES

CHAPTER 5

Stratospheric Ozone Changes and Climate

Lead Authors : Hella Garny
Harry Hendon

Coauthors : Marta Abalos
Gabriel Chiodo
Ariaan Purich
William J. Randel
Karen Smith
David Thompson

Contributing Authors : James A. Anstey
Blanca Ayarzagüena
Antara Banerjee
Ramiro Checa Garcia
Martyn P. Chipperfield
Martin Dameris
Rishav Goyal
Paul A. Newman
Felix Plöger
Lorenzo Polvani
Karen H. Rosenlof
Anja Schmidt
William Seviour
Keith Shine
Neil Swart
Paul J. Young

Review Editors : Amy H. Butler
Amanda Maycock

CONTENTS

Chapter 5: Stratospheric Ozone Changes and Climate

SCIENTIFIC SUMMARY

Since the last Assessment, new research has continued to quantify, attribute and improve the understanding of long-term changes in stratospheric climate. New studies are assessed that quantify the effects of ozone-depleting substances and ozone changes on the climate system, including atmospheric temperatures and circulation, the ocean and the cryosphere. The new results support the main conclusions from the previous Assessment.

Changes in stratospheric climate

- **Stratospheric Temperature: The global middle and upper stratosphere continues to cool at a rate of ~–0.6 K decade^{-1} because of growing levels of well-mixed greenhouse gases (GHGs; primarily carbon dioxide [CO_2]) and evolving stratospheric ozone in response to changing ozone-depleting substances (ODSs).** Lower-stratospheric temperatures have been near constant since the late 1990s. The overall evolution is consistent with the well-understood effects of ozone, ODSs, GHGs, stratospheric aerosols, and solar variability. This is in agreement with previous Assessments.
- **Stratospheric Water Vapor: Since the last Assessment, the understanding of processes that influence water vapor entry into the stratosphere has strengthened.** Interannual variations in lower-stratospheric water vapor are quantitatively consistent with observed tropical tropopause temperatures, with small contributions from monsoon circulations and overshooting convection. Models predict small multi-decadal increases in tropopause temperature and lower-stratospheric water vapor as a response to GHG increases, but these changes are still not evident within the variability of the observational records.
- **Brewer-Dobson Circulation[7] (BDC):**
  - **The BDC in the lower stratosphere has accelerated in recent decades and is predicted to continue to accelerate in the future given continued increases in GHG abundances.** This result is confirmed by models, observations, and reanalyses. New studies since the last Assessment confirm the attribution of the BDC acceleration by models to increases in GHGs and ODS-induced ozone depletion over the last decades of the 20th century. Model simulations indicate that the decline of ODSs and subsequent recovery of ozone should have acted to reduce the rate of BDC acceleration after the year 2000, but there is not yet sufficient analysis to determine whether this change has been detectable outside of the natural variability in the BDC.
  - **Estimates of past BDC trends in the middle and upper stratosphere based on observations continue to be opposite in sign from modeled trends.** However, new observationally based estimates since the last Assessment bring observed trends closer to modeled trends.
- **Polar Vortex Trends and Variability: Recent extreme polar vortex events in both hemispheres caused strong variations of polar ozone. However, currently there is no evidence for a systematic trend toward more frequent polar vortex disruptions in either hemisphere.**
  - Two sudden stratospheric warming (SSW)[8] events have been observed in the Southern Hemisphere (SH) since the start of comprehensive satellite records in 1979. New model studies show that this is consistent with model simulations, and no change in SSW frequency is necessary to explain this occurrence rate. The delay of the austral polar vortex breakup date, which in the past was driven by ozone depletion, is not expected to fully reverse by the end of the 21st century, due to the opposing effect of GHG increases under moderate and high emission scenarios.
  - In the Northern Hemisphere (NH), new studies confirm that changes in SSW frequency and in polar vortex strength are not robustly detected in the historical record, and future changes are not robust across models.
- **Quasi-Biennial Oscillation (QBO)[9]: Since the last Assessment, there is more confidence that the amplitude of the QBO will weaken in the future as a result of acceleration of the BDC**, but there is still large uncertainty about any change in its periodicity and the associated ozone variability.
  - New model studies infer that further disruptions of the QBO, such as occurred in 2016 and 2019, might become more likely as a result of increasing GHGs.

Ozone and ODS effects on climate

- **Ozone and ODS Radiative Forcing (RF): New estimates confirm previous Assessments in that the RF from ODSs, including the indirect effect on ozone abundances, has been positive over the second half of the 20th century, contributing to anthropogenic GHG forcing.** The newest best estimate of stratosphere-adjusted RF over the period 1850–2011 from stratospheric ozone changes is –0.02 W m^{-2}, with an uncertainty of ± 0.13 W m^{-2}. The range in this RF remains smaller than the RF from ODSs (0.337 W m^{-2}). However, new studies reveal uncertainties in the estimation of radiative forcing, due to 1) rapid adjustments arising from tropospheric circulation changes and 2) uncertainties in modeled ozone

[7] The global zonal mean circulation that transports mass, heat, and tracers in the stratosphere.

[8] Based on an adapted SSW definition in the Southern Hemisphere; see *Chapter 5, Section 5.2.6.1.*

[9] Quasi-periodic (period ~28 months) oscillation of stratospheric equatorial winds from easterly to westerly.

trends. Since the late 1990s, the RF from ODSs and changes in stratospheric ozone abundances has remained approximately constant as a consequence of the Montreal Protocol.

- **ODS Effects on Climate:** There is new evidence since the last Assessment that suggests that the direct radiative effects of ODSs on climate not only contributed to global warming but also enhanced Arctic amplification[10] in the late 20th century.
- **Role of Stratospheric Ozone in the Climate Response to GHG Forcing:** Evidence suggests that GHG-induced ozone changes act to dampen the GHG-induced surface temperature warming. New estimates since the last Assessment confirm that this climate feedback by stratospheric ozone is negative but smaller than previously estimated. In addition, there is new evidence for an influence of stratospheric ozone on the tropospheric and stratospheric circulation response to GHGs via ozone-circulation coupling.
- **Relevance of Stratospheric Ozone-Circulation Coupling for Trends and Interannual Variability:**
  - Two-way ozone-circulation coupling modulates the effects of ozone depletion and recovery on SH stratospheric circulation trends, as well as stratospheric interannual variability in the tropics and extratropics in both hemispheres.
  - There have been no detectable effects of long-term ODS-driven ozone trends in the Arctic on tropospheric and surface climate. Yet, new evidence shows that for individual years low springtime Arctic ozone can amplify existing stratospheric circulation anomalies and their subsequent influence on tropospheric circulation and surface climate.
- **Signature of Ozone Recovery in the Southern Hemisphere Circulation:**
  - **Antarctic ozone depletion led to pronounced changes in the SH atmospheric circulation, as summarized in the previous Assessments.** New evidence suggests that the recovery of Antarctic ozone is now evident as changes in SH atmospheric circulation trends between the ozone depletion and recovery eras (the eras before and after roughly the year 2000, respectively). The observed changes in circulation trends are significant at stratospheric altitudes but on the fringe of significance in the troposphere; model simulations support the hypothesis that the changes in atmospheric circulation trends are driven by the onset of ozone recovery.
  - Climate simulations suggest that in the future the effects of ozone recovery will compete with the effects of GHG increases on SH tropospheric circulation changes, resulting in a poleward shift of the mid-latitude jet in all seasons under high GHG emissions scenarios but little change or even an equatorward shift of the jet in austral summer under low GHG emissions scenarios.
- **Ozone-Induced Impacts on the SH Ocean and Cryosphere:**
  - **Ocean and Sea Ice**: Observed upper Southern Ocean warming and freshening since the 1950s is driven primarily by increasing GHGs. Stratospheric ozone depletion plays a secondary role in the warming. In agreement with previous Assessments, ozone trends are unlikely to have driven the observed high-latitude sea surface temperature cooling and weak sea ice changes since 1979. Ocean eddies continue to remain a source of uncertainty in the ocean's response to wind changes.
  - **Carbon Uptake**: The Southern Ocean carbon uptake exhibits strong decadal variations. Ozone changes are unlikely to have substantially contributed to the observed net change in Southern Ocean carbon uptake, consistent with the conclusion from the previous Assessment.
  - **Antarctic Ice Sheet**: New modeling evidence suggests that stratospheric ozone depletion could potentially have influenced the surface mass balance of the Antarctic ice sheet by enhancing precipitation over the continent in the latter part of the 20th century. However, the underlying processes whereby stratospheric ozone depletion influences continentwide precipitation are poorly constrained; further, observed Antarctic surface mass balance shows large variability.

Climate impacts of the Montreal Protocol

- New evidence since the last Assessment shows that the decline in ODS emissions due to the implementation of the Montreal Protocol has already had an influence on SH circulation trends due to the stabilization and slow recovery of the Antarctic ozone hole, leading to a change in trends in the austral summer tropospheric circulation.
- Recent modeling studies estimate that the Montreal Protocol has already resulted in the avoidance of 0.17 ± 0.06 K global surface warming and 0.45 ± 0.23 K of Arctic surface warming in 2020, and will likely avoid about 0.5–1 K (0.79 ± 0.24 K) of global surface warming by the mid-21st century compared to a scenario with uncontrolled ODS emissions.
- New evidence since the last Assessment suggests that the Montreal Protocol has also potentially avoided an additional 0.5–1.0 K globally averaged surface warming by the end of the 21st century by protecting the terrestrial carbon sink from ultraviolet (UV) radiation damage, which would cause additional CO_2 to remain in the atmosphere.

[10] Arctic amplification refers to the ratio of Arctic warming (60–90°N) to global warming over a given time period.

5.1 INTRODUCTION

A dedicated chapter on ozone-climate interactions has been part of the Ozone Assessment reports since 2006. While the main focus was initially on how anthropogenic climate change affects stratospheric ozone, since 2010 the focus has broadened on two-way interactions between stratospheric ozone and climate. The chapter is similar in scope to Chapter 5 of the 2018 Assessment (Karpechko, Maycock et al., 2018), assessing past and projected future changes in stratospheric climate and the role of stratospheric ozone and ozone-depleting substances (ODSs) for the climate system. The chapter builds on the chapters of previous Assessments with similar scope, as summarized below.

5.1.1 Summary from the Previous Assessment

Chapter 5 of the previous Assessment (Karpechko, Maycock et al., 2018) provided a detailed assessment of our knowledge of stratospheric temperature evolution. It was concluded that global average temperature in the lower stratosphere (13–22 km) cooled by about 1 K between 1979 and the late 1990s but has not changed significantly since then. In the lower stratosphere, ozone trends were the major cause of the observed cooling between the late 1970s and the mid-1990s. In the middle and upper stratosphere, long-lived greenhouse gases (GHGs) played a larger role in the cooling trends over this period. For the upper stratosphere (40–50 km), one-third of the observed cooling over the period 1979–2005 was due to ODSs and associated ozone changes, while two-thirds was due to well-mixed GHGs. Chemistry-climate model projections showed that the magnitude of future stratospheric temperature trends is dependent on the assumed future GHG concentrations, with higher GHG scenarios showing more cooling in the middle and upper stratosphere over the 21st century. The projected increase in global stratospheric ozone during this period (due to both decreasing ODSs and increasing GHGs) would offset part of the stratospheric cooling due to increasing GHGs.

The last Assessment concluded that there are indications for the acceleration of the stratospheric overturning circulation, the Brewer-Dobson circulation (BDC), in the lower stratosphere. In particular, observed changes in temperature and constituents indicate that tropical upwelling in the lower stratosphere has strengthened over the last ~30 years, in qualitative agreement with model simulations and reanalysis datasets. It is well understood that enhanced abundances of well-mixed GHGs lead to increased tropical upwelling in the lower stratosphere via changes in atmospheric wave dissipation. Moreover, changes in ODSs (and associated changes in ozone) were concluded to be a main driver of past and future changes of the BDC. In particular, increases in ODS concentrations between about 1980 and 2000 induced a notable increase in downwelling over the Antarctic, with an associated increase of tropical upwelling. The reduction of ODS concentrations after 2000 were simulated to reduce the GHG-induced acceleration of the BDC in the future. However, observational evidence for externally forced long-term changes in the BDC remain uncertain. The last Assessment concluded that as a consequence of a strengthening of the stratospheric overturning circulation and stratospheric ozone recovery, a future increase in stratosphere-troposphere exchange of ozone is projected to occur, increasing the future global tropospheric ozone burden.

Antarctic ozone depletion was concluded to be the dominant driver of the changes in Southern Hemisphere tropospheric circulation in austral summer during the late 20th century, with associated weather impacts including a trend toward the positive polarity of the Southern Annular Mode (SAM) index and a wider Hadley cell. The trend toward the positive phase of the SAM index is associated with a southward shift of the mid-latitude westerly jet and storm track, resulting in drier conditions at higher latitudes of New Zealand and, as a result of the associated expansion of the Hadley cell, wetter conditions over subtropical latitudes of eastern Australia. Surface cooling occurs over Antarctica and warming on the peninsula. During other seasons, the contribution from increasing well-mixed GHGs played a more dominant role. In contrast, no robust links between stratospheric ozone depletion and long-term changes in Northern Hemisphere surface climate were established.

The changes in tropospheric weather patterns driven by ozone depletion were concluded to have played a role in the observed recent temperature, salinity, and circulation trends in the Southern Ocean, but the impact on Antarctic sea ice remained unclear. Modeling studies indicated that ozone depletion should have contributed to a decrease in Antarctic sea ice extent; hence, it cannot explain the observed sea ice increase between 1979 and 2015. The unprecedented rapid decline of Antarctic sea ice in 2016 was linked with the strong negative SAM (i.e., an equatorward shift of the extratropical surface westerlies) and extratropical sea surface temperature (SST) anomalies forced by the tropics. It was concluded that the inability of climate models to reproduce the observed Antarctic sea ice trends since 1979 limits confidence in the modeled sea ice response to ozone depletion. No robust evidence was found for a hypothesized causal link between the strength of the Southern Ocean carbon sink and ozone depletion. A remarkable reinvigoration of the Southern Ocean carbon sink was reported to have occurred since the early 2000s, following the previously reported slowdown of the carbon sink between the 1980s and early 2000s. Those results indicate that atmospheric circulation changes (whether driven by ozone depletion or not) have not had a considerable impact on the net strength of the Southern Ocean carbon sink.

The last Assessment concluded that as a result of the Montreal Protocol, global sea level rise of at least several centimeters has been avoided. This sea level rise would have occurred due to thermal expansion of the oceans stemming from the additional global warming from unregulated ODS emissions.

5.1.2 Scope of Chapter

The overall scope of this chapter is similar to that of Chapter 5 of the 2018 Assessment (Karpechko, Maycock et al., 2018) and Chapter 4 of the 2014 Assessment (Arblaster, Gillett et al., 2014). It provides an update to our knowledge of changes in stratospheric climate and assesses the role of stratospheric ozone changes for the climate system. Changes in stratospheric climate including temperature, circulation, and water vapor are assessed in *Section 5.2*; the changes are attributed to natural and anthropogenic forcing agents. The evolution of most relevant forcing agents is discussed elsewhere in the Assessment (*Chapters 1* and *2*) and therefore is only briefly summarized here (in *Section 5.2.1*). *Section 5.3* discusses the effects of stratospheric ozone changes on the whole climate system, from the stratosphere to the ocean, including the effect of ODS changes on surface climate through their direct radiative effects, for which new evidence has

been found since the last Assessment. Since the last Assessment, the role of two-way coupling between ozone and circulation received much attention, motivating a section on ozone-dynamical coupling. The last section of this chapter (*Section 5.4*) updates our knowledge of the climate impacts of the Montreal Protocol. Since we are by now well into the period of declining ODS concentrations, we can report on already-realized climate impacts of the Montreal Protocol in this section.

5.2 OBSERVED AND SIMULATED CHANGES IN STRATOSPHERIC CLIMATE

5.2.1 Overview of Relevant Anthropogenic and Natural Forcing Agents

Stratospheric climate change is influenced by a number of anthropogenic and natural external forcings. The evolution of most of those forcing agents is described elsewhere in the Assessment, so we provide only a brief summary below.

The evolution of ODS concentrations to date is described in detail in *Chapter 1* and hydrofluorocarbons (HFCs) in *Chapter 2*. Overall, ODS concentrations and the related total chlorine and bromine loading of the atmosphere have continued to decline since the last Assessment. ODSs impact the climate system through their important role in stratospheric ozone chemistry and because they are potent GHGs (see *Section 5.3.1*).

Anthropogenic GHGs, defined here as the three most important well-mixed GHGs (carbon dioxide [CO_2], methane [CH_4], and nitrous oxide [N_2O]), affect stratospheric temperatures directly, leading to cooling (see Box 5-1 in Karpechko, Maycock et al., 2018). Further, GHG-induced tropospheric warming plays an important role in stratospheric climate through its effect on large-scale circulation. An update on the evolution of global abundances and growth rates of CH_4 and N_2O is given in *Section 1.5.1* and the development of CO_2 abundances are covered in great detail in the recent Intergovernmental Panel on Climate Change (IPCC) report (IPCC, 2021). Briefly, the atmospheric abundance of all three GHGs continued to increase at rates similar to or higher than in previous years, and CO_2 reached a global average annual mean mixing ratio of 412.45 ppm in 2020. The CH_4 annual mean mixing ratio reached about 1874 ppt in 2020, and N_2O reached about 333 ppt in 2020 (see *Section 1.5.1*). The effects of the COVID-19 pandemic on the world economy resulted in a notable reduction of CO_2 emissions of about 7% compared to 2019 (Le Quéré et al., 2021; Szopa et al., 2021). But since atmospheric CO_2 concentrations are the result of the balance of a number of source and sink processes, the effect of those reduced emissions was not detected in global abundances or in the atmospheric concentration growth rate (Szopa et al., 2021).

The evolution of the global stratospheric ozone layer is determined by atmospheric chemistry and dynamics (described in detail in *Chapter 3*), but stratospheric ozone also acts as a forcing agent on the atmosphere and the climate system. The global ozone layer is beginning to recover from the effects of ODSs, with the near-global mean (60°S–60°N) total ozone column increasing by about 0.3% decade^{-1} since the late 1990s. Therefore, the impacts of stratospheric ozone changes on the climate system (*Section 5.3*) are generally expected to reverse with ozone recovery, which started to appear in the late 1990s to early 2000s. However, ozone changes over the past two decades are regionally dependent, and they are strongly influenced by interannual variability (see *Chapters 3* and *4*), complicating the detection of reversals of ozone-induced trends in stratospheric temperature

Box 5-1. The Hunga Tonga-Hunga Ha'apai Volcanic Eruption of January 2022

Some past major volcanic eruptions have impacted the ozone layer, the stratospheric circulation, and surface climate (see *Sections 5.2* and *6.6*, and the *Chapter 6 Appendix*). The observed stratospheric changes from these events are particularly valuable for understanding the Earth's response to volcanic eruptions, but also for testing, and improving the representation of stratospheric aerosol microphysics, chemistry and dynamics in Earth system models. A very recent major eruption that injected a large amount of material into the stratosphere was the Hunga Tonga-Hunga Ha'apai (20.5°S, 175.4°W; hereafter referred to as HTHH) eruption in January 2022. HTHH produced two major phreatomagmatic (magma and seawater) eruptions on 13 and 15 January 2022. The second eruption initially injected material to altitudes greater than 55 km, which is higher than the stratopause and into the lower mesosphere (Carr et al., 2022). Satellite observations showed westward transport and diffusion of the HTHH plume in the stratosphere throughout the SH low latitudes and into the tropics in the months following the eruption.

The HTHH eruption led to significant perturbations in the stratosphere. Observations from satellite remote-sensing and balloon-borne instruments show the eruption injected SO_2 and HCl into the stratosphere, along with large amounts of H_2O. The H_2O injection was far beyond anything previously observed (Millán et al., 2022), while SO_2 and HCl amounts were within the emissions range from past observed eruptions. The total SO_2 amount emitted into the stratosphere (eventually converted into sulfate aerosol particles) was estimated to be 0.4–0.5 Tg. In comparison, the SO_2 amount injected into the stratosphere by the 1991 Mt. Pinatubo eruption was 15–20 Tg. Measurements from the Microwave Limb Sounder on the Aura satellite and balloon profiles show perturbations of stratospheric water that are unprecedented in the observational record in terms of both magnitude and altitude range. Initial estimates indicate that HTHH added about 10% to the total stratospheric water vapor burden.

Over the next few years, the eruption impact on ozone will be determined from observations and analyzed using model simulations. The injected H_2O and sulfate aerosol are expected to continue to perturb the stratosphere globally and, in particular, in the polar regions over the next years. A more complete understanding of this major and unique event will be available in the 2026 ozone assessment.

and circulation. In the future, stratospheric ozone is projected to recover from the effects of ODSs and to be influenced by increasing GHG concentrations, leading to considerable dependency of the future evolution of stratospheric ozone on the GHG scenario (see *Chapter 3*).

Perturbations to stratospheric aerosol concentrations can have a substantial impact on stratospheric temperatures (see *Section 5.2.2* and *Chapter 6*). Sources of stratospheric aerosols are primarily volcanic eruptions, but pyrocumulonimbus events associated with wildfires can also inject substantial amounts of aerosols into the stratosphere. In particular, the recent devastating bushfires that occurred in austral spring to summer 2019/20 in Australia (often referred to as Australian New Year fires) injected an unprecedented amount of aerosols from wildfire sources into the stratosphere, estimated to be comparable to a smaller-magnitude volcanic eruption (see *Section 6A.4*). While there has been no major volcanic eruption since Mt Pinatubo in 1991, smaller eruptions led to enhanced aerosol levels between 2005 and 2014, approximately doubling stratospheric aerosol optical depth compared to volcanic quiescent periods (see *Section 6.6*). The explosive eruption of Hunga Tonga-Hunga Ha'apai in January 2022 is expected to impact stratospheric ozone, circulation, and potentially surface climate (see **Box 5-1**). The origins and impacts of stratospheric aerosol injection are further detailed in *Chapter 6*.

Another external natural forcing on stratospheric climate is variability in the amount of total solar irradiance reaching the top of Earth's atmosphere. Particularly relevant for the understanding of stratospheric climate trends over recent decades is the 11-year solar cycle. While the total solar irradiance varies by less than 0.1% (or about 1 W m^{-2}; Haigh, 2007) across the 11-year solar cycle, it has a notable influence on stratospheric ozone and temperature, as detailed in *Chapter 3*.

5.2.2 Stratospheric Temperatures

Stratospheric temperature variability and trends are key aspects of the climate system related to stratospheric ozone. Ozone and temperature changes are coupled in the stratosphere, where ozone influences temperature via radiative effects and temperatures impact both ozone-photochemical reaction rates and, in the polar regions, the frequency of occurrence of polar stratospheric clouds (PSCs) and associated impacts on heterogeneous chemical reaction rates (*Section 4.2.2.2*, see also **Box 5-2**). Quantifying and modeling past temperature changes are key goals for attribution and a requisite for confidently projecting future changes.

The 2018 Assessment highlighted improved estimates of observed stratospheric temperature trends from reprocessed datasets and attributed past and future temperature variability based on chemistry-climate model simulations (see *Section 5.1.1*). The major updates since 2018 involve lengthening and further analyses of the observational record, including use of radio occultation measurements beginning in 2002 and further modeling studies of past and future temperature evolution.

5.2.2.1 Observed Temperature Changes

Observations of stratospheric temperature come from operational and research satellite measurements, radiosondes, and long-term lidar measurements at a limited number of stations. Radiosonde observations extend from the surface to the lower stratosphere (~25 km) and span the longest period (since the late 1950s) but are influenced by discontinuities due to instrumentation changes and limited global sampling. Homogenized radiosonde datasets, such as RAOBCORE and RICH (Haimberger et al., 2012), have been constructed to address the instrumentation changes and derived trend results show reasonable agreement with temperature trends across broad layers in the lower stratosphere from satellite data (e.g., Steiner et al., 2020).

Global satellite measurements of tropospheric and stratospheric temperatures are available from the series of operational MSU and SSU instruments from late 1978 to 2005. These data represent broad-layer ~10 km and ~20 km averages atmospheric temperatures for the MSU and SSU measurements, respectively. The MSU time series have been updated using measurements from the series of AMSU instruments, which began in 1998. Merged time series of MSU/AMSU have been produced by several teams, including at the University of Alabama in Huntsville (UAH; Spencer et al., 2017), Remote Sensing Systems (RSS; Mears et al., 2011), and the NOAA Center for Satellite Applications and Research (STAR; Zou and Wang, 2011), with all three taking into account instrument calibration, satellite orbit changes, and other influences. These different merged datasets produce reasonably consistent time series and trend results, especially for the lower stratosphere (Steiner et al., 2020). The SSU time series from 1978 to 2005 were separately merged by Zou et al. (2014) and Nash and Saunders (2015), producing similar results within data uncertainties (Seidel et al., 2016; Maycock et al., 2018); the Zou et al. (2014) data exhibited more consistent vertical structure among the different SSU channels (Seidel et al., 2016). Zou and Qian (2016) extended the Zou et al. (2014) SSU data record beyond 2005 using AMSU measurements, and time series were independently updated by Randel et al. (2016) using research satellite data from Aura MLS (Livesey et al., 2022) and SABER (Remsberg et al., 2008). The updated SSU/AMSU and SSU/MLS time series show excellent agreement through 2018 (Steiner et al., 2020).

Time series of global average temperatures in the troposphere and stratosphere continue to develop as expected (see **Figure 5-1**, providing an update of the data in Steiner et al., 2020), with a warming troposphere and a cooling stratosphere. The stratospheric cooling increases with height, with a net cooling over the period 1979–2020 of approximately 0.8, 2.2, 2.6, and 3.1 K for the lower to upper stratosphere, respectively. As noted in the 2018 Assessment and in the recent IPCC report (Gulev et al., 2021), the rate of decadal-scale stratospheric cooling is larger prior to the late 1990s, with very small long-term changes in the lower stratosphere (TLS) after this time. The long-term trends are modulated by the well-known transient warming events in the lower to middle stratosphere following the El Chichón (1982) and Pinatubo (1991) volcanic eruptions, and the upper stratosphere is further modulated by the 11-year solar cycle. The lower stratospheric temperature (TLS) shows a short-term (~4 months) transient warming in early 2020 following enhanced stratospheric aerosols from the Australian New Year fires (Yu et al., 2021; Rieger et al., 2021).

Recent stratospheric temperature trend analyses include results from high-quality radio occultation measurements, covering an altitude range of ~10–30 km with a vertical resolution of ~1 km, with global observations after 2002 (Shangguan et al., 2019; Steiner et al., 2020). While the data record is still relatively short for climate variability and trends, these measurements will become increasingly important as the data record lengthens in time.

In addition to satellite and radiosonde stratospheric temperature measurements, there are several meteorological reanalysis datasets covering the stratosphere provided by meteorological services. Reanalysis products are widely used in the research community for process studies, but developers have cautioned against their use for long-term trend studies because of discontinuities introduced by the integration of different satellite data records (see also **Box 3-2**). There continue to be refinements in reanalysis systems that improve representation of trends in the relatively data-rich lower stratosphere (e.g., for ERA5.1; Simmons et

Box 5-2. Impact of GHG-Induced Stratospheric Cooling on Ozone Chemistry

The observed cooling of the stratosphere is driven by changes in ozone, ODSs, GHGs, stratospheric aerosols, and solar variability. Increasing concentrations of CO_2 are a major contributor to this cooling (see Box 5-1 in Karpechko and Maycock et al., 2018 and *Section 5.2.2*). Other GHGs modestly enhance this cooling in the middle and upper stratosphere, while in the lower stratosphere, some GHGs (in particular halocarbons) oppose it to some extent (Ramaswamy et al., 2001). This radiatively driven decrease in stratospheric temperatures can be modified by dynamical processes. Climatologically, the stratospheric global overturning circulation leads to adiabatic cooling of the tropics, and adiabatic warming in the extratropics; the projected strengthening of the overturning circulation in response to GHG increases (see *Section 5.2.4*) can increase this dynamical cooling/heating. However, any forced modifications of the circulation at polar latitudes (i.e., changes in the polar vortex and associated polar descending motion) have been obscured by strong interannual variability in the past, and are largely model dependent for future projections, in particular in the Arctic (*Section 5.2.6.1*). This masks any clear trend in winter/spring Arctic lower stratospheric temperatures (*Chapter 4*).

The GHG-induced changes in stratospheric temperatures alter ozone chemistry. The abundance of ozone at a particular location in the stratosphere is governed by three processes: photochemical production, destruction by catalytic cycles, and transport processes. The catalytic destruction cycles occur through homogeneous gas-phase chemistry. In the polar lower stratosphere, heterogeneous chemical processes are also essential for creating the conditions that allow gas-phase ozone loss to occur. The efficiencies of both homogeneous as well as heterogeneous chemical processes depend on temperature, but in different ways. Therefore, stratospheric cooling from GHGs can have contrasting impacts on chemical ozone changes in different regions of the atmosphere, as detailed in the following.

Homogeneous Chemistry

In the stratosphere, ozone is produced by the photolysis of molecular oxygen in a process that is independent of temperature and maximizes in the tropical upper stratosphere. Globally this production is balanced by ozone loss through catalytic cycles involving homogeneous (gas-phase) chemical reactions. The stratospheric circulation transports ozone from regions of net production to regions of net loss. Globally, the most important ozone loss cycles involve reactive nitrogen and hydrogen, although chlorine and bromine play important roles in certain regions such as the polar lower stratosphere (*Chapter 4*) and upper stratosphere (*Chapter 3*). The reaction rates of these loss cycles are temperature dependent, and generally slow down with lower temperatures, causing a net increase in ozone. This inverse relationship between ozone and temperature changes was discovered for the upper stratosphere in the 1970s (Barnett et al., 1975) and the mechanisms have been explored in model simulations since the early 1980s (Haigh and Pyle, 1982). Overall, the slowdown in gas-phase ozone destruction leads to an increase in ozone due to GHG-induced cooling, particularly evident in the middle and upper stratosphere (see *Chapter 3*).

Heterogeneous Chemistry in the Polar Stratosphere

In the polar lower stratosphere, heterogeneous reactions that occur on the surface of polar stratospheric clouds (PSCs; frozen particles and supercooled liquid aerosols) become important. These reactions are responsible for converting chlorine (and to a lesser extent bromine) species into active, ozone-destroying forms. This leads to rapid gas-phase ozone loss once sunlit after the end of the polar night. PSCs form at temperatures below about 195 K. The Antarctic stratosphere reaches temperatures low enough for PSC formation for several weeks in winter and spring every year, but PSC occurrence is much less common and extensive in the Arctic except during very cold winters and springs. Under these specific conditions, significant springtime Arctic ozone destruction is observed (*Chapter 4*). While GHG-induced cooling is generally weak in the lower stratosphere (see *Section 5.2.2*), it could potentially lead to favorable conditions for PSC formation in the Arctic lower stratosphere, and therefore increase ozone depletion. Therefore, if GHG-induced cooling dominates Arctic lower stratosphere temperature changes in the future, we could expect enhanced springtime ozone depletion (*Chapter 4* and *Section 4.5.3.3*), especially while chlorine and bromine levels remain elevated.

In summary, it is well understood that global ozone, especially in the middle and upper stratosphere, increases with decreasing temperatures as the key gas-phase ozone destruction reactions slow down. The GHG-induced cooling has contributed to the observed increase in upper stratospheric ozone over the past two decades (since about year 2000), and will continue to do so in future projections that include rising GHG abundances (see *Chapter 3*). At polar latitudes, there is potential for enhanced ozone depletion due to an increased occurrence of PSCs with lower temperatures. However, it is still under debate whether GHG-forced changes in Arctic lower stratospheric temperatures have already affected PSC formation. Since the Arctic stratosphere is highly dynamically variable, it is also difficult to assess whether future GHG increases will lead to more favorable conditions for PSC formation (see discussion in *Chapter 4*).

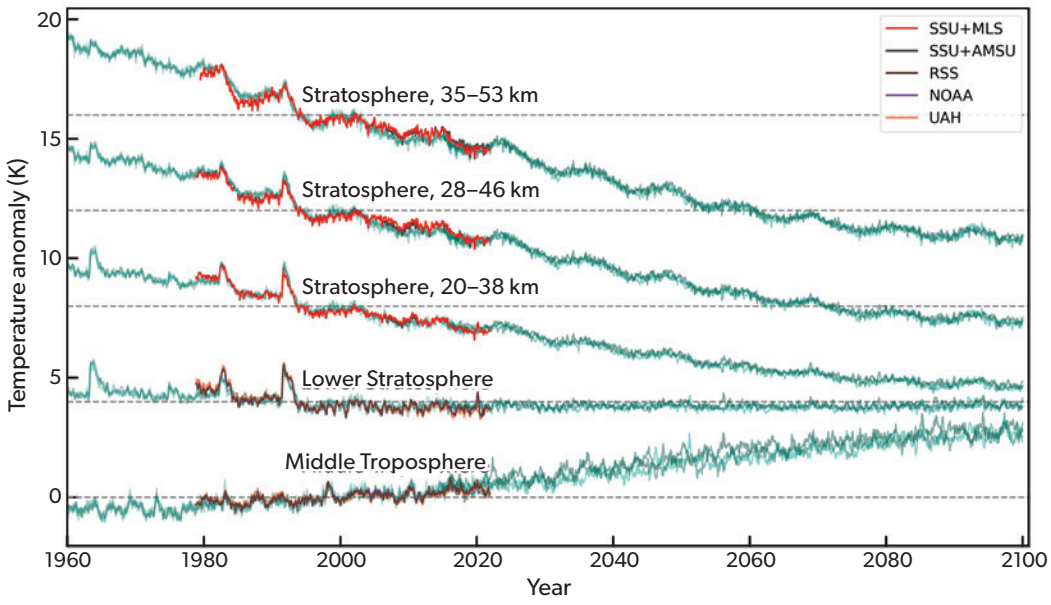

Figure 5-1. Time series of global average temperature anomalies for broad-layer averages from the middle troposphere to the upper stratosphere (bottom to top). Satellite observations are shown for 1979–2020 (see legend), updated from data described in Steiner et al (2020). Note that results from the different observational data sets often overlap, highlighting broad-scale agreement. Temperature anomalies are also shown for WACCM model simulations (green colors) for the recent past (1960–2018), from the so-called Ref-D1 CCMI-2022 simulations incorporating known historical forcings, and including 4 separate realizations. Simulations for 2015–2100 follow the Ref-D2 CCMI-2022 specifications, using SSP2-4.5 forcing and WMO2018 A1 halogens; the runs include an interactive ocean, and 3 realizations are shown. Anomalies from the two sets of model runs are merged for the overlap period 2015–2018.

al., 2020; Santer et al., 2021). However, significant differences in temperature variability and trends are evident among the current generation of reanalyses in the middle and upper stratosphere, where they rely primarily on satellite data (e.g., Long et al., 2017; SPARC, 2022).

5.2.2.2 Simulation and Attribution of Past and Future Stratospheric Temperature Changes

The 2018 Assessment included a review of chemistry-climate model simulations compared to observations, concluding that the model-simulated temperatures were in agreement with observations from the lower to the upper stratosphere for the period 1979–2016. GHG increases are the dominant mechanism for cooling in the middle and upper stratosphere, modulated by ozone changes linked with evolving ODSs and temperature-dependent photochemistry (Aquila et al., 2016; Maycock et al., 2018). Ozone changes that occurred between the start of the observational record in 1979 and the mid-1990s are the dominant influence on temperature in the global lower stratosphere. Stability of lower stratospheric ozone after the late 1990s accounts for the relatively constant TLS temperatures after that time, extending to 2020. **Figure 5-1** includes an updated comparison of observations with simulations of the recent past from one model, showing quantitative agreement for a model forced by observed SSTs, GHGs, and ODSs, along with volcanic and solar cycle effects. Comparisons of lower stratosphere temperature trends across the suite of CMIP6 models using historical forcings highlights significant variability among models but consistent agreement (within uncertainties) with homogenized radiosonde data and ERA5.1 (Mitchell et al., 2020).

Model projections of future atmospheric temperature changes over the 21st century show continued cooling in the middle and upper stratosphere (**Figure 5-1**). Updated evaluations of past and future temperature changes quantify the relative roles of GHGs and ODSs in these trends (Garcia et al., 2019). Ozone decreases lead to relatively strong contributions to middle-to-upper stratosphere cooling during the period of strongest ozone losses (1975–1995); smaller stratospheric temperature trends have occurred prior to and after this period. Modeled future middle-atmosphere temperature trends are dominated by GHG changes, with simulated cooling directly related to the GHG scenario, e.g., stronger cooling for RCP8.5 versus RCP6.0 (**Figure 5-2**) and reduced cooling trends after about 2060 for SSP2-4.5 (**Figure 5-1**). Stratospheric cooling is modulated by corresponding ozone changes, with weaker cooling over the first half of the 21st century, driven by increases in ozone in the upper stratosphere due to decreasing ODSs under the Montreal Protocol.

Overall, our assessment is in agreement with the IPCC (Gulev et al., 2021; Eyring et al., 2021; Lee et al., 2021) in all aspects regarding the evolution of stratospheric temperature. In summary, observational records show continued cooling of the global middle and upper stratosphere (at a rate of about –0.6 K decade^{-1}), while lower-stratospheric temperatures have shown no significant trends since the late 1990s. Model projections of future

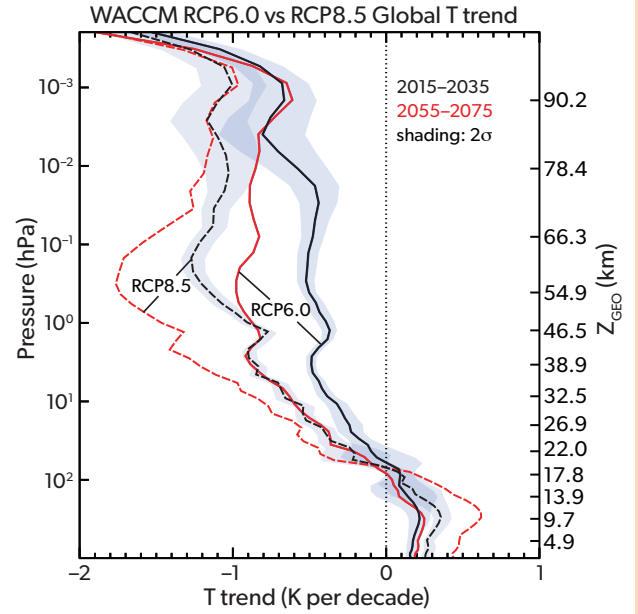

Figure 5-2. Projected global mean temperature trend profiles for periods in the early (2015–2035) and late (2055–2075) 21st century calculated from the WACCM chemistry–climate model for the RCP6.0 (solid) and RCP8.5 (dashed) emissions scenarios. The uncertainty ranges (2 standard deviations) are shown for 2015–2035 trends in both scenarios and are also representative of the uncertainties for the 2055–2075 profile. [From Garcia et al., 2019.]

atmospheric temperature changes over the 21st century show continued cooling in the middle and upper stratosphere, with the magnitude depending on the GHG emissions scenario. This evolution is consistent with the expected effects of changes in ozone, ODSs, and GHGs, as well as variability induced by stratospheric aerosols and solar variability.

5.2.3 Stratospheric Water Vapor

Stratospheric water vapor directly influences the climate system through longwave radiative processes, wherein increased water vapor cools the lower stratosphere and warms the troposphere (Forster and Shine, 1999; Solomon et al., 2010; Li and Newman, 2020). Stratospheric water vapor also influences ozone abundances through its role as a source of reactive hydrogen (HO_x) and via the formation of PSCs. The 2018 Assessment highlighted continuing measurements of water vapor from satellites and balloons and their general agreement in terms of variability and changes. The observational satellite data record of stratospheric water vapor, which is based on merged datasets from the early 1990s to the present, is characterized by large decadal-scale variability, including well-known decreases around the year 2000 (e.g., Solomon et al., 2010) and increases thereafter (Yue et al., 2019). However, there are no significant long-term trends in the observations over the period 1993–2020 (Yu et al., 2022). Recent work has strengthened the observational understanding of processes influencing water vapor entry across the tropical tropopause, along with improving the evaluation of updated model simulations and improving theoretical knowledge on water vapor radiative effects, as discussed below.

5.2.3.1 Processes Controlling Water Vapor Entry Across the Tropical Tropopause

Stratospheric water vapor is primarily controlled by the freeze-drying of air passing through the cold tropical tropopause, under the influence of the mean upward tropical Brewer-Dobson circulation (BDC). Transport through monsoon circulations and overshooting deep convection can also contribute, but these are likely small effects (Nuetzel et al., 2019; Jensen et al., 2020; O'Neill et al., 2021). Water vapor increases with height in the stratosphere due to the slow oxidation of methane (CH_4), and this contribution becomes relatively important in the tropics above ~25 km, or at higher latitudes where stratospheric air is relatively "aged" (Waugh and Hall, 2002). Observed increases in tropospheric CH_4 (see *Section 5.2.1*) are estimated to contribute ~0.1 ppmv decade^{-1} to the water vapor trend above the middle stratosphere, accounting for a substantial fraction of the 2002–2018 observed trends in this region from the SABER satellite (Yue et al., 2019). High-quality satellite measurements of stratospheric water vapor since the early 1990s (from the HALOE, SABER, and Aura MLS satellites) provide improved understanding of processes influencing variability and trends. Comparisons of satellite data with stratospheric balloon measurements at several locations (Hurst et al., 2016) suggested a possible drift in MLS v4.2 water vapor retrievals after 2010, which has been partially corrected in updated MLS v5.1 retrievals (Livesey et al., 2021).

Satellite observations demonstrate strong control of tropical tropopause temperatures on interannual water vapor changes throughout the near-global (60°S–60°N) stratosphere (Randel and Park, 2019). Tropical lower stratosphere water vapor variations are strongly correlated with the cold point tropopause (**Figure 5-3**, left panel). The associated near-equatorial water vapor anomalies subsequently propagate vertically in the tropics and poleward in the lower stratosphere, following the BDC. Reconstruction based on lagged regressions with tropopause temperatures capture a majority of water vapor variability in these regions (**Figure 5-3**, right panel). Water vapor variations in the extratropical lowermost stratosphere (below the 380 K isentrope), which are key for radiative effects, are less strongly coupled to the tropical tropopause. The close relationship of tropical stratospheric water vapor and tropopause temperature also occurs for zonal asymmetries (Suneeth and Das, 2020). Boreal summer monsoon circulations contribute to water vapor transport into the deep tropics (Nuetzel et al., 2019), contributing up to 14% to the moist phase of the annual cycle (i.e., the tropical tape recorder). This results in somewhat weaker coupling of water vapor with tropical tropopause temperatures in this season (Randel and Park, 2019). While convective ice lofting associated with extreme convection has been discussed as a possible contribution to the stratospheric water vapor budget, enhancements above background concentrations occur infrequently in the deep tropics and have a limited impact (Jensen et al., 2020; Plaza et al., 2020; Feng and Huang, 2021). Observations suggest direct hydration is more important over North America during boreal summer, with the influence of direct water injection reaching up to approximately 1 km above the local cold point tropopause (Yu et al., 2019; Wang et al., 2019a; Jensen et al., 2020). Over the coming years, we expect to see perturbations in stratospheric water vapor from

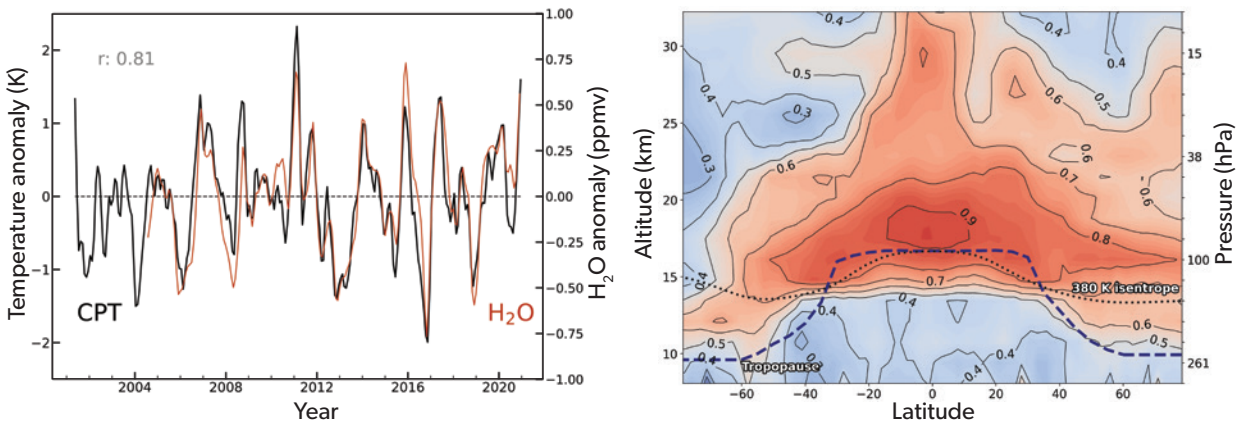

Figure 5-3. Temperature control of water vapor entry at the tropical tropopause. *(left)* Time series of deseasonalized anomalies in tropical cold point tropopause (CPT) temperature from GPS radio occultation (10°S–10°N) and equatorial (5°N–5°S) 83 hPa water vapor from Aura MLS. *(right)* Correlation of deseasonalized anomalies in Aura MLS water vapor over 2004–2020 versus water vapor reconstructed from lagged regressions onto the tropical CPT. [Updated from Randel and Park (2019) using MLS v5.1 H_2O retrievals (Lambert et al., 2020).]

the unprecedented eruption of the Hunga Tonga-Hunga Ha'apai volcano (see **Box 5-1**).

5.2.3.2 Updates on Modeling and Understanding of Radiative Effects of Stratospheric Water Vapor

Stratospheric water vapor has been analyzed in CCMI and CMIP6 models, showing overall consistent behavior compared to observations and close coupling to tropical tropopause temperatures within each model. However, there is a large diversity among models in cold point temperatures and water vapor amounts (Keeble et al., 2021; Garfinkel et al., 2021). Climate change projections consistently show decadal-scale increases in tropopause temperatures and stratospheric water vapor. Detailed calculations demonstrate that water vapor exhibits a similar response to diverse climate forcing agents (including CO_2, CH_4, solar variability, and sulfate aerosol) through slow feedbacks involving equilibration of SSTs. For forcings that directly warm the tropical tropopause region, such as black carbon aerosols, water vapor changes mostly represent a fast (non-SST-mediated) rather than a slow response (Wang and Dessler, 2020).

There is improved understanding of the climate feedback through stratospheric water vapor changes from analyses of large perturbations in idealized CO_2 quadrupling experiments within the multi-model CMIP5 effort (Banerjee et al., 2019) and analyses from experiments in individual model studies (Li and Newman, 2020; Huang et al., 2020). Stratospheric water vapor increases produce a positive net climate feedback, contributing up to ~10% of the global mean surface warming under CO_2 quadrupling. However, there is considerable intermodel variability in these results, possibly due to both intermodel differences (e.g., in radiative transfer codes) and differences in calculation of the feedback (e.g., offline radiative feedback calculations versus fixed water vapor experiments). Results from one model suggest that associated feedbacks from upper-tropospheric temperatures and clouds can reduce the surface warming feedback to a few percent (Huang et al., 2020). These differences call for improved understanding of the complex feedback mechanisms, and for quantifying the differences in methodologies used to calculate the feedbacks. Calculations highlight the important role of water vapor in the extratropical lowermost stratosphere for radiative feedback. Water vapor also impacts stratospheric temperatures and circulation, including contributing ~30% of the simulated acceleration of the BDC in one model (Li and Newman, 2020).

In summary, new studies since the last Assessment led to improved process understanding of water vapor entry to the stratosphere by showing that interannual changes in lower-stratospheric water vapor are quantitatively consistent with observed tropical tropopause temperatures. Monsoon circulations and overshooting convection have relatively small contributions. Models predict small decadal-scale increases in tropopause temperature and lower-stratospheric water vapor as a response to GHG increases, but these changes are not evident within the year-to-year variability of the observational records. Lastly, radiative effects of stratospheric water vapor under climate change are sizable but exhibit considerable model uncertainty.

5.2.4 Brewer-Dobson Circulation

Chapter 5 of the previous Assessment (Karpechko, Maycock et al., 2018) showed that the discrepancy in trends in the strength of the BDC between observations and models, first pointed out in the 2000s (Engel et al., 2009; Waugh et al., 2009), can be reconciled in the lower stratosphere but persists in the mid-to-upper stratosphere. Specifically, models project a robust strengthening of the BDC throughout the stratosphere in response to increasing GHGs. The 2018 Assessment shows that while there is observational evidence to support the strengthening of the BDC in the lower stratosphere, observations from tracer measurements show weakening trends (albeit not significant) at upper levels (above ~24 km).

Since the 2018 Assessment, a number of studies have advanced knowledge on this open question by providing new estimates of the uncertainty in stratospheric mean age of air (AoA) derived from tracer observations. Mean AoA is a measure of the average transport time from a reference surface (e.g., the tropopause or ground) to a certain point in the stratosphere and thus quantifies the integrated strength of the BDC. A negative trend in AoA would therefore be consistent with a strengthened BDC. AoA can be estimated from long-lived tracers and compared to models (see Box 5-2 in Karpechko, Maycock et al., 2018). However, deriving AoA values from observations that are comparable with models is not trivial, and understanding how different factors influence the trends is key, given the small trend values relative to the large internal variability. Uncertainties are due to the nonlinearity of tracer time series (Garcia et al., 2011; Fritsch et al., 2020), as well as to chemical sinks, in particular of SF_6 (sulfur hexafluoride; Kouznetsov et al., 2020; Kovacs et al., 2017; Leedham-Elvige et al., 2018; Adcock et al., 2021; Loeffel et al., 2022).

Similar to the 2018 Assessment, the best estimates of the observed and modeled trends are of opposite sign in the northern middle stratosphere. This is illustrated in **Figure 5-4**, which shows the most recent estimates of mean AoA trends at northern mid-latitudes in the middle stratosphere in observations and models. The model output has been subsampled to mimic the limited sampling of the observations (following Abalos et al., 2021). A new result is that the large observational uncertainties in the latest estimates result in a partial overlap with the model trends (over 50% of the simulation error bars have some overlap with the lower bound in the latest observational estimate). This modest step toward convergence of the modeled and observed ranges partly results from the larger uncertainties in the model trends when accounting for the limited spatial and temporal sampling in the observations (as pointed out in Garcia et al., 2011) and partly from updated parameters in the derivation of AoA from observed tracer abundances (Fritsch et al., 2020). Additional uncertainty that is not fully taken into account arises from the model results being based on idealized AoA tracers and therefore not exactly comparable with the observational estimates, which are based on real tracers. While acknowledging these uncertainties is a key advance since the 2018 Assessment, there remains a clear disagreement in the sign of BDC trends between models and observations in the middle and upper stratosphere.

New evaluation of the BDC in reanalyses since the last Assessment provides evidence that the spread in the climatology and the trends is too large among different reanalysis products to help constrain their values (Chabrillat et al., 2018; Ploeger et al., 2019; Diallo et al., 2021; Chapter 5 of SPARC, 2022). Most reanalyses feature an acceleration of the BDC (i.e., a negative AoA trend) over the last ~30 years, consistent with models but inconsistent with observations, as shown in **Figure 5-5**. However, this figure also reveals the important differences in the magnitude and spatial structure of the trends across different reanalysis datasets. ERA-Interim is the only reanalysis showing positive AoA trends in the NH mid-to-upper stratosphere over the period considered. These positive trends are consistent with observations but inconsistent with other reanalyses, including the new-generation ECMWF reanalysis, ERA5 (**Figure 5-5**; for further details, see Chapter 5 of SPARC, 2022).

Decadal changes in AoA over the most recent period (since approximately 2002) obtained from satellite tracer measurements reveal an inter-hemispheric asymmetry, with BDC strengthening (AoA decrease) in the Southern Hemisphere and weakening (AoA increase) in the Northern (Stiller et al., 2012; Mahieu et al., 2014; Stiller et al., 2017; Strahan et al., 2020; Han et al., 2019). Such asymmetry in recent decadal AoA changes is captured by all modern reanalyses (Ploeger et al., 2019; 2021; Ploeger and

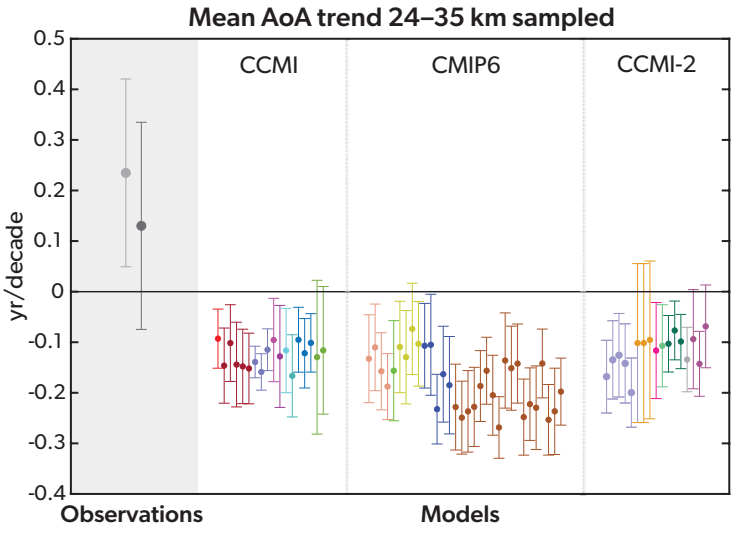

Figure 5-4. Mean AoA trends for the period 1975–2005 from observations and model simulations, with model data sampled at times and locations corresponding to the observations (Engel et al., 2009; Fritsch et al., 2020). Specifically, AoA is averaged over 24–35 km log-pressure altitudes and sampled at the same latitudes and months as the observations. Three families of model simulations are shown: CCMI REF-C1, CMIP6 historical, and CCMI2 REF-D1. Each model is represented in a different color, and multiple ensemble simulations are included for some models, to account for the influence of internal variability on the trends. The mean AoA trend derived from observations is shown on the left (inside the gray shaded area): the original value from Engel et al. (2009) (light gray), and that obtained from the same data but using an updated method to derive AoA from tracer concentrations, as described in Fritsch et al. (2020) (dark gray). Error bars represent least square regression slope uncertainty at the 95% confidence level for the models, while for the observations they include additional measurement error estimates. [Adapted from Abalos et al., 2021.]

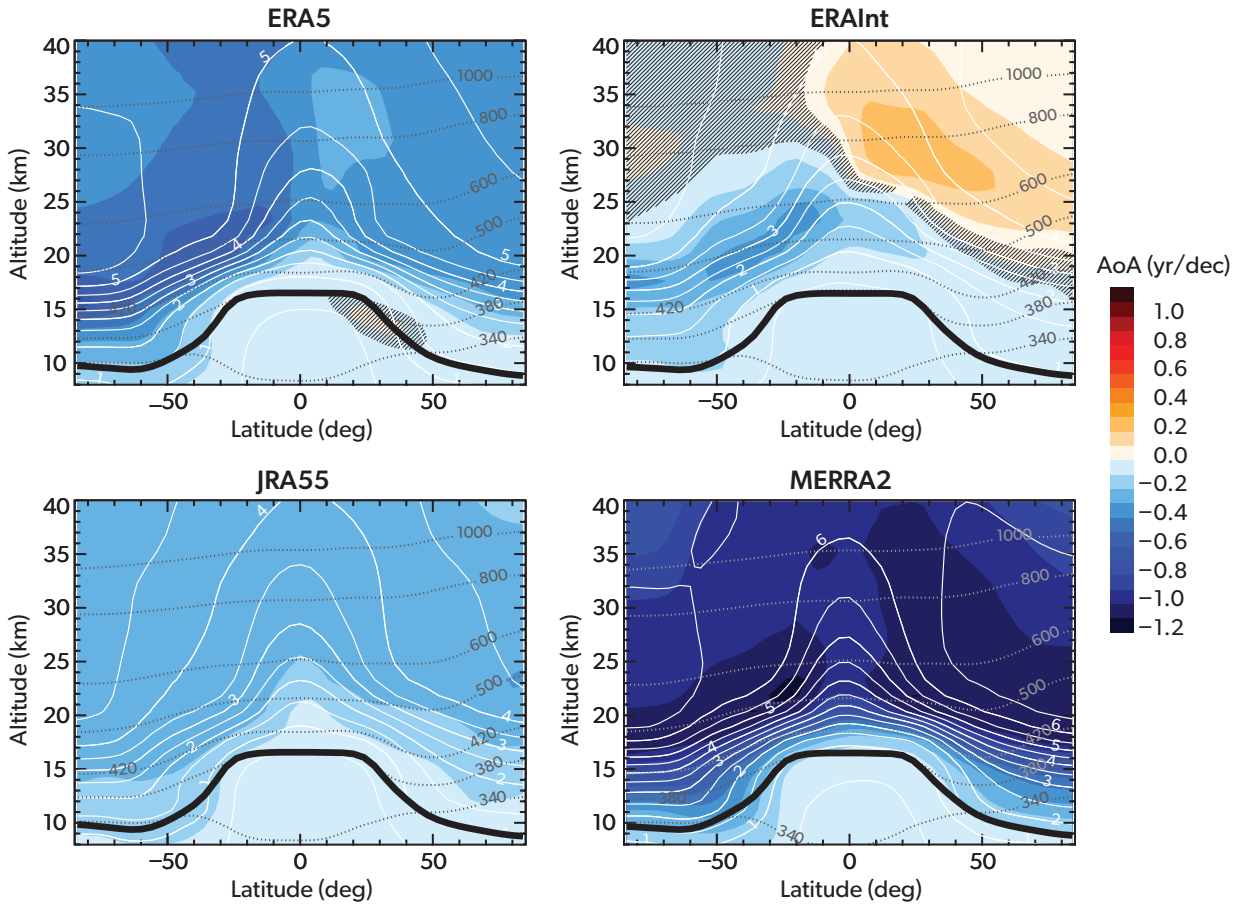

Figure 5-5. Trends in mean AoA in four modern reanalyses over the period 1989–2015 (shading), computed using the Lagrangian transport model CLaMS. Thin solid contours show the mean AoA climatology, with contour spacing of six months. The solid thick contour shows the lapse-rate WMO tropopause. Thin dashed contours show selected isentropes with labeled values in K. Note that the updated ERA5.1 is used for the 2000–2006 period in the ERA5 panel, as in Ploeger et al. (2021). [Adapted from Ploeger et al., 2019, 2021.]

Garny, 2022). The mechanism proposed to explain these changes consists of a southward displacement of the region of tropical upwelling and associated changes in mixing, which in turn has been linked to decadal variability associated with the Quasi-Biennial Oscillation (QBO; Strahan et al., 2020). Differences in changes in the deep and shallow residual circulation branches have also been proposed to affect the inter-hemispheric asymmetry (Han et al., 2019, Ploeger and Garny, 2022). These recent studies highlight the crucial role of internal climate variability in limiting the detection of externally forced long-term trends over the observational period. In particular, it is important to account for this decadal internal variability in transport in order to interpret recent trends in lower-stratospheric ozone (see *Chapter 3*).

In model simulations, two main external forcings dominate the long-term BDC trends: trends in GHGs and trends in ODSs. The proposed mechanism for the former is that as well-mixed GHGs warm the troposphere, the associated changes in thermal wind balance in the subtropical lower stratosphere modify wave propagation and dissipation conditions, which in turn accelerate the residual circulation (Shepherd and McLandress, 2011). A robust strengthening of the BDC with GHG increases has been projected by models for decades, and new multi-model studies provide updated confirmation of this result (Eichinger et al., 2019; Polvani et al., 2019; Abalos et al., 2021). The global stratospheric mean AoA is projected to decrease about −0.05 years decade^{-1} over the 21st century under the RCP6.0 scenario (Eichinger et al., 2019). In general, trends emerge faster in the integrated measure of mean AoA compared to the residual circulation strength and emerge faster in the lower stratosphere (shallow branch) than in the middle stratosphere (deep branch) (Abalos et al., 2021). While ODSs are also well-mixed GHGs, their main impact on the BDC occurs through the dynamical coupling with Antarctic ozone depletion (Abalos et al., 2019). Specifically, the polar lower-stratospheric cooling due to ozone depletion delays the polar vortex breakdown (see *Section 5.2.6.1*) and leads to enhanced wave propagation in austral summer. The key role of ODSs on the BDC trends highlighted in the previous Assessment has been confirmed by further studies over the last few years. Specifically, ozone depletion was the main driver of the acceleration in austral summer polar downwelling over the

last decades of the 20th century. Moreover, its effect extends to the annual mean global circulation, such that more than half of the modeled mean BDC acceleration over the last few decades of the 20th century was driven by ozone depletion (Oman et al., 2009, Polvani et al., 2018; Li et al., 2018, Abalos et al., 2019; Polvani et al., 2019). Simulations using RCP6.0 and A1 WMO scenarios for well-mixed GHGs and ODSs, respectively, consistently predict a future (2000–2080) global mean AoA trend that is about 50% weaker than the simulated trends for the past (1980–2000) due to ozone recovery (Polvani et al., 2019). A weakening of the tropical upwelling trends after the year 2000 derived from satellite temperature observations (Fu et al., 2019) is consistent with the timing of ozone stabilization and recovery. However, the observationally derived trends of tropical upwelling in Fu et al. (2019) do not feature the expected seasonality of ozone depletion and recovery effects on the BDC, which maximizes in the December–January–February period for SH downwelling in models.

As reviewed in Chapter 5 of the last Assessment (Karpechko, Mayock et al., 2018), the mean transport time along the BDC, quantified by AoA, is the space- and time-integrated effect of two main processes: the residual circulation and two-way mixing (Plumb, 2002). Since the last Assessment, a number of studies highlighted the importance of those processes for the simulation of stratospheric transport and its trends. AoA trends are driven by a combination of an enhanced residual circulation and mixing changes, and intermodel differences in the trend magnitude relate to differences in mixing changes (Eichinger et al., 2019). Moreover, recent studies have shown that differences in mixing (independent of the residual circulation) are the main cause of the large intermodel differences in the AoA climatology (Dietmüller et al., 2018). These results highlight the importance of both resolved and sub-grid-scale mixing for constraining stratospheric transport in global models. Another important result from new studies is that nudging the model's meteorology to reanalysis fields does not help constrain the BDC. On the contrary, it increases the intermodel spread (Chrysanthou et al., 2019; Orbe et al., 2020; Davis et al., 2020; Davis et al., 2022). This result cautions against the use of nudged simulations for studies of the BDC and underlines the need to improve nudging techniques, as nudged simulations are often used to compare with observations.

In summary, new studies on BDC changes confirm the long-known robust result that models simulate a BDC strengthening, caused by both GHG increases and by ozone depletion that was driven by ODS increases over the last four decades of the 20th century. Future strengthening of the BDC due to increasing GHG concentrations outweighs the effects of ozone recovery in the RCP6.0 scenario; as a result, an acceleration (though weaker by about 50%) is expected in the future. The longstanding discrepancy between models and observational evidence of past BDC trends in the mid-stratosphere is not yet resolved. Nevertheless, updated calculations of observational AoA estimates marginally overlap with the simulated strengthening of the BDC. Overall, recent studies highlight the crucial role of observational uncertainties and internal decadal variability in limiting the detection of externally forced BDC trends.

5.2.5 Stratosphere-to-Troposphere Transport

Variations in stratosphere-troposphere exchange are important contributors to the variability of ozone concentrations, particularly in the troposphere, where the background concentrations are small compared to those of the stratosphere. The last Assessment stated that both greenhouse gas increase and stratospheric ozone recovery will tend to increase the future stratosphere-to-troposphere transport (STT) of ozone. This result has recently been shown to be robust across CCMI models. This is due to the stronger STT associated with the strengthening of the BDC in response to increasing greenhouse gas abundances (see *Section 5.2.4*), as well as to an increased ozone reservoir in the lowermost stratosphere with ozone recovery (Abalos et al., 2020). Consistent with the latter mechanism, stratospheric ozone depletion has had a large impact on tropospheric ozone trends over the period 1979–1994 in some regions (Griffiths et al., 2020). The strong coupling between ozone STT and the acceleration of the residual circulation in models is illustrated in **Figure 5-6**; models with a stronger acceleration of the BDC feature larger increases of stratospheric-origin ozone concentrations in the troposphere. The stratospheric ozone tracer is the same as ozone in the stratosphere and has chemical and depositional loss (but no production) in the troposphere. In addition to this large-scale mechanism, an increase in tropopause fold frequency with climate change could contribute to local enhancements of ozone STT in the future (Akritidis et al., 2019).

In addition to the importance of ozone STT, the evolution of the global tropospheric ozone burden depends to a large extent

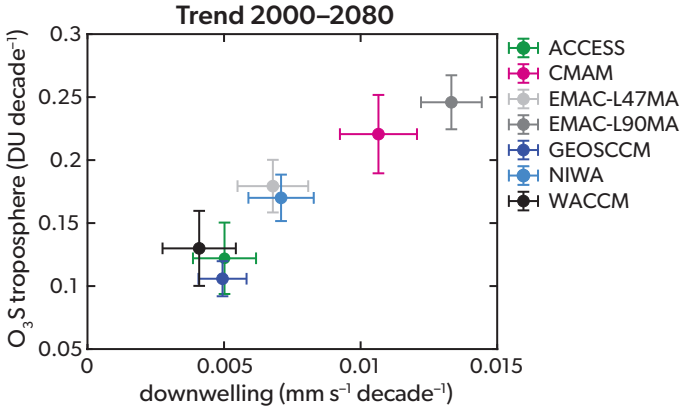

Figure 5-6. Relationship between downwelling changes and stratosphere-to-troposphere ozone transport, shown as a scatter plot of trends in a stratospheric ozone tracer integrated over the troposphere versus extratropical downwelling acceleration in the lower stratosphere (averaged 30°N/30°S and the poles at 70 hPa) for seven models, based on CCMI-1 REF-C2 simulations. The stratospheric ozone tracer is the ozone that originated in the stratosphere and has chemical and depositional loss (but no production) in the troposphere. [Adapted from Abalos et al., 2020.]

on the evolution of tropospheric ozone precursor emissions. This is reflected in the different evolution of tropospheric ozone in the various SSP scenarios, with methane emissions playing a particularly important role (Morgenstern et al., 2018; Abalos et al., 2020). More details on the future evolution of tropospheric ozone and the different factors affecting it can be found in *Section 3.4.5* and **Box 3-4**.

In order to best understand and model the externally forced long-term trends in ozone STT, it is important to quantify the internal interannual variability. New studies since the last Assessment find a significant increase in ozone STT during the positive El Niño-Southern Oscillation (ENSO) phase near the Pacific subtropical jet, in agreement with previous results, while the QBO effects on STT remain more uncertain (Olsen et al., 2019). The influence of stratospheric ozone on interannual variability in tropospheric concentrations is particularly strong in North America (Liu et al., 2020), due to enhanced STT mainly in spring (Breeden et al., 2021). Nevertheless, the effects of ENSO and the QBO on the globally integrated ozone STT are small (Olsen et al., 2019).

In summary, consistent with the previous Assessment, increased ozone transport from the stratosphere to the troposphere is expected in a future climate, due to both strengthened BDC and stratospheric ozone recovery.

5.2.6 Stratospheric Winds

5.2.6.1 Polar Vortices

The state of the stratospheric polar vortex in both the Southern and Northern Hemispheres is a crucial factor in determining the possibility for heterogeneous ozone depletion (see *Chapter 4*, including the definition of polar vortex in **Box 4-1**). Conversely, the strength of the polar vortex can be modified by strong polar ozone depletion through an increase of the meridional temperature gradient. The following section assesses dynamical variability of the polar vortex and its long-term changes, while *Chapter 4* discusses its role for polar ozone.

In previous Assessments, it was reported that the strong SH polar ozone depletion had led to an increase in vortex strength in austral spring and summer, resulting in a delay of the SH polar vortex breakdown. This trend attenuated over more recent years, consistent with the lack of trend in polar ozone (see *Chapter 4*). Ozone recovery is expected to lead to earlier vortex breakup dates. Models project that increasing GHG concentrations will delay recovery of the SH vortex breakup date, although the mechanism for this delay is not entirely understood (Ceppi and Shepherd, 2019; Mindlin et al., 2020). As a result of the two opposing effects of ozone recovery and GHG increase on the SH vortex, the delay caused by ozone depletion is projected to not be fully reversed by the end of the 21st century (Wilcox and Charlton-Perez, 2013; Rao and Garfinkel, 2021a). The vortex breakup date will rather remain constant or become delayed even further (Mindlin et al., 2021) in both moderate- and high-emissions scenarios (Rao and Garfinkel, 2021a). As further detailed in *Section 5.3.2*, recent studies indicate that two-way coupling between ozone and polar vortex dynamics enhanced past ozone-induced trends in the polar vortex.

As stated in the last Assessment and in the IPCC Sixth Assessment Report (IPCC AR6; see Section 2.3.1.4.5 of Gulev et al., 2021), large interannual and decadal variability hinders the detection of long-term changes in the NH polar vortex, and it was assessed that the vortex weakening over the last decades is likely a result of internal variability. There are no indications for a past influence of NH polar ozone depletion on long-term polar vortex trends, due both to the far weaker ozone depletion in the Northern compared to the Southern Hemisphere and to the strong interannual variability in the NH polar vortex.

Future changes in the NH polar vortex strength are uncertain, and the mechanisms for changes in the polar vortex, as well as reasons for the large intermodel spread, are still under discussion (Wu et al., 2019; Ayarzagüena et al., 2018, 2020; Rao and Garfinkel, 2021b). The nonlinearity of the response of the polar vortex strength to surface warming reported by Manzini et al. (2018) has been further supported by analysis of a multi-model dataset (Kretschmer et al., 2020). Arctic sea ice loss trends continue to be explored as potential drivers for a future decrease of the NH polar vortex strength (Kretschmer et al., 2020; Kim and Kim, 2020), although some studies question this connection (e.g., Seviour, 2017). Another suggested driver of the future trends in the NH polar vortex are changes in vertical planetary wave propagation conditions, driven by the warming trend in the tropical troposphere (Karpechko and Manzini, 2017). In addition to changes in its mean strength, studies report a possible future shift of the position of the vortex (Matsumara et al., 2021). Under high-emissions scenarios, it was projected that the occurrence of low temperatures within the polar vortex will increase in the future (von der Gathen, 2021), with potentially important impacts for polar ozone (see *Chapter 4* and **Box 5-2**). However, the robustness and mechanism for such increases in the occurrence of low temperatures, and how they are linked to dynamical changes of the polar vortex or to radiative effects, remain to be understood.

Recent winters have exhibited strong anomalies in both the Arctic and Antarctic polar vortices, resulting in strong ozone anomalies (see *Chapter 4*). In early 2020, the NH polar vortex was anomalously strong, leading to a record-low ozone (Lawrence et al., 2020; *Section 4.2.4.2*). In other years (e.g., 2018 and 2019), the Arctic polar vortex experienced sudden breakdowns, so-called sudden stratospheric warmings (SSWs; Baldwin et al., 2021; *Section 4.2.2.1*). Although there is not a unique definition, a frequently used criterion is that SSWs are classified as major if the zonal wind at 10 hPa and around 60° latitude reverses to easterlies (Charlton and Polvani, 2007; Baldwin et al., 2021; Butler et al., 2015 and references therein). SSWs occur about every other year in the Northern Hemisphere (with an average of about 6 major SSWs every 10 years). Polar ozone abundances are strongly modulated by SSWs, both due to transport anomalies associated with SSWs (de la Cámara et al., 2018; Hong and Reichler, 2021) and to the prevention of necessary conditions for polar ozone depletion (see *Chapter 4*). Strong natural, internal variability, including low-frequency decadal variability (Dimdore-Miles et al., 2021), prevents the detection of potential small-amplitude changes in SSW frequency, so that no consistent long-term change in SSW frequency has been detected in the Northern Hemisphere over the past decades. No robust future changes in the NH SSW frequency are projected in long model integrations from state-of-the-art multi-model studies (see **Figure 5-7**), irrespective of the climate change forcing scenario (Ayarzagüena et al., 2018; Rao and Garfinkel, 2021b). Moreover, in most recent model simulations with extreme CO_2 concentrations imposed, several individual models show statistically significant changes in the SSW

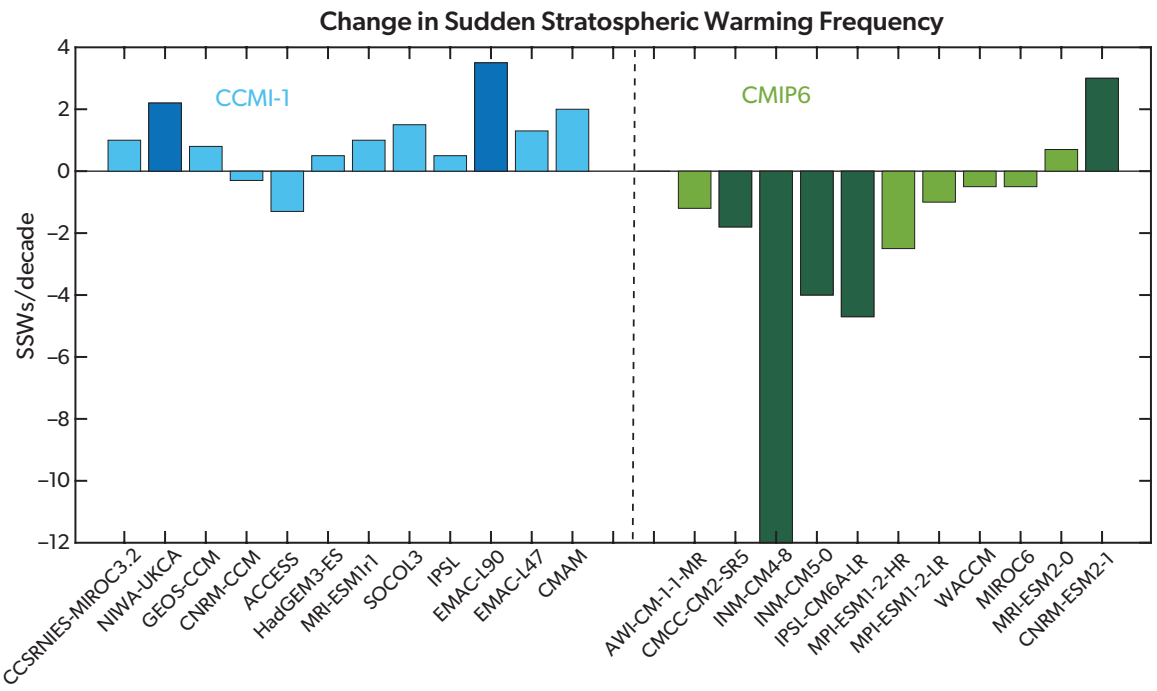

Figure 5-7. Simulated change in the frequency of NH Sudden Stratospheric Warming (SSW) events in the future (2061–2100) relative to the 1960–1999 average in CCMI-1 model simulations (REF-C2; blue bars) and in CMIP6 model simulations under scenario SSP3-7.0 (green bars). The SSW definition is based on the reversal of the zonal-mean zonal wind at 60°N and 10 hPa to easterlies (see Charlton and Polvani, 2007, for the exact definition). Darker colored bars in both indicate statistically significant future-minus-past differences at the 95% confidence level. [Updated from Ayarzagüena et al., 2018.]

frequency, but there is no consensus on the sign of this change (Ayarzagüena et al., 2020). Overall, in agreement with IPCC AR6 (Eyring et al., 2021), we assess that there is no evidence for forced changes in NH SSW frequency. On the other hand, recent studies have highlighted the importance of non-SSW influences of the polar vortex on both ozone and surface climate. In particular, shifts or stretching of the vortex may influence climate and weather differently (Kretschmer et al., 2018; Lee et al., 2019; Butler and Domeisen, 2021; Cohen et al., 2021).

In the Southern Hemisphere, only one major SSW has been observed so far (in 2002). In September 2019, the Antarctic polar vortex experienced its second-strongest disruption ever observed (*Section 4.2.3.2*; Lim et al.; 2021). While the 2019 disruption did not meet the criterion of a major SSW, it is widely considered a SSW in terms of its dynamical characteristics. Therefore, it was suggested that the definition of SSW be adapted for the Southern Hemisphere based on the anomalies of the zonal wind at 60°S and 10 hPa passing below −40 m s^{-1} (Jucker et al., 2021), which is met by the two events in 2002 and 2019. In contrast to the strong disruption in 2019, the two following Antarctic spring seasons (2020 and 2021) both featured a strong and long-lasting polar vortex that led to a large and exceptionally persistent ozone hole (*Section 4.2.3.3*). This prompts the question of whether we can expect a future change in polar vortex variability. Given that SSWs are very rare events in the Southern Hemisphere, their frequency can be estimated only from long model integrations. Two recent studies were the first to attempt this task, and while based on different models, they both report a similar SSW frequency of about one event in 25 years (Wang et al., 2020; Jucker et al., 2021). The observed rate of major SSWs is one event (i.e., the 2002 event) since the start of the comprehensive satellite record in 1979 and thus lies below the rate estimated from models. When using the adapted definition for the Southern Hemisphere, which includes the observed 2019 event, the observed rate of two events in 42 years is well within the range expected from the model studies. Therefore, current evidence suggests that the rate of occurrence over the past decades is within expectations, and there is no evidence for changes in SH SSW frequency.

Future changes in the SH SSW rate are addressed in a single study, which projects a strong decrease in the yearly occurrence probability of SSWs in the Southern Hemisphere (from 4.6% in the present day to 0.3% in a future 4xCO_2 climate based on the adapted SSW definition), linked to a general increase in polar vortex strength under increased GHG abundances (Jucker et al., 2021). This result by a single model is backed up by analysis of CMIP6 models in the same study (Jucker et al., 2021), but these results are very uncertain due to the limited simulation length (Ayarzagüena et al., 2020) and model biases in the SH polar vortex strength.

In summary, current evidence suggests that, in both moderate- and high-emissions climate scenarios, a delay in the vortex breakup date of the SH polar vortex that was driven by ozone depletion in the past will not reverse in the future due to the opposing effect of increasing GHGs. Trends in the strength of the

NH polar vortex remain insignificant in the observational period, and future trends are uncertain in sign. While recent years exhibited strong polar vortex variability in both hemispheres, there is currently no evidence for changes in the frequency of SSWs in either hemisphere up to the present day. For the future, climate models project inconsistent changes in NH SSW frequency, and one recent study suggests a possible decrease in the occurrence rate of SH SSWs in response to strong CO_2 forcing.

5.2.6.2 Quasi-Biennial Oscillation

The Quasi-Biennial Oscillation (QBO) refers to the alternating westerly and easterly zonal winds that descend in the tropical stratosphere with a period of about 28 months. The QBO affects stratospheric ozone (see also *Section 3.2.1.1*) both in the tropics and extratropics by modulating vertical and meridional transport and by modulating temperature that affects ozone chemistry (primarily in the mid-to-upper equatorial stratosphere). The descending easterly phase of the QBO is associated with enhanced tropical upwelling and so results in reduced ozone in the lower tropical stratosphere that lags the QBO-temperature anomaly by a quarter cycle. The compensating downwelling in the extratropics, primarily in the NH winter, results in enhanced extratropical stratospheric ozone. The opposite occurs during the descent of the westerly phase of the QBO. In the upper stratosphere, the induced ozone variation is controlled by temperature-dependent photochemistry and is out of phase with the QBO-temperature anomaly. Due to the decadal variation of the QBO (both intensity and period; Shibata and Naoe, 2022), the QBO-induced ozone variability has obscured detection of secular changes in ozone, such as those expected as a result of ozone recovery (Ball et al., 2019), and therefore effects of the QBO need to be carefully accounted for in assessing future secular changes in ozone. Nonetheless, the overall impact of the QBO on hemispheric or global mean ozone is small (Olsen et al., 2019). However, the disruption of the descending easterly phase of the QBO in 2016, which was unprecedented in the observational record at that time, resulted in a sustained increase of tropical ozone and decrease in extratropical ozone (Diallo et al., 2018). Another disruption of the QBO occurred in 2019 (Anstey et al., 2021), raising the possibility that the QBO and its impact on ozone may change in the future (Anstey at al., 2021; see also *Section 3.2.1.1*).

Since the last Assessment, there has been considerable progress in simulating the QBO in global climate models, with 15 out of the 30 models contributing to CMIP6 able to simulate a realistic QBO (Richter et al., 2020a). There is a consensus across the CMIP6 models that are able to depict the QBO, the QBOi models (Butchart et al., 2018), and other models (Naoe et al., 2017; DallaSanta et al., 2021) that the QBO will weaken in the mid-to-lower stratosphere in a warming climate. This occurs in the $2xCO_2$ and $4xCO_2$ time slice simulations with the QBOi models (Richter et al., 2020b) and for the CMIP6 simulations using the Shared Socioeconomic Pathways (SSP) SSP3-7.0 and SSP5-8.5 scenarios (Richter et al., 2020a). This is usually attributed to enhanced equatorial upwelling associated with an acceleration of the BDC in response to increasing GHGs (Kawatani and Hamilton, 2013), which acts to oppose the descent of the QBO wind variations.

Progress in simulating and projecting the changes in the QBO has been achieved by widespread adoption of non-orographic gravity-wave parameterizations that are able to drive the alternating equatorial descending easterly and westerly QBO winds. A drawback of relying on non-orographic gravity-wave parameterizations is that the projected changes in the QBO as a result of climate change (and possibly ozone recovery) exhibit dependencies on these parameterizations (Anstey et al., 2022). Although the periodicity and latitudinal extent of the QBO in circulation and temperature are well simulated in these models, there remains a persistent underestimation of the amplitude of the QBO that extends from the lower stratosphere down to the tropopause (Bushell et al., 2020; Richter et al., 2019; Richter et al., 2020a; Anstey et al., 2022). This lower stratospheric bias in QBO amplitude means that processes that are strongly modulated by the QBO, such as troposphere-stratosphere exchange, are unlikely to be well captured, and therefore adds uncertainty in projections of how these processes might change in the future. The models also commonly underestimate the remote impact of the QBO on the NH winter vortex (Rao et al., 2020; Anstey et al., 2022), which partly results from a misrepresentation of the seasonal phase locking of the QBO (i.e., the tendency for phase transition at 50 hPa to occur during April–June and for the downward phase propagation to be slowest during the winter). For both the $2xCO_2$ and $4xCO_2$ time slice runs with the QBOi models (Richter et al., 2020b) and the various SSP projections with the CMIP6 models for the end of the century (Anstey et al., 2021), the subtropical westerlies in the lower-to-mid- stratosphere increase, acting to shift the critical line for wave dissipation closer to the equator. This equatorward shift of the critical line will result in an increase in equatorward penetration of extratropical wave driving that acts to decelerate the stratospheric zonal flow. Together with a weakening of the QBO as a result of a strengthened BDC (see *Section 5.2.4*), this enhanced equatorward penetration of extratropical wave driving in a warming climate implies that future disruptions of the QBO, such as occurred during 2016 and 2019, could become more common in the future (Anstey et al., 2021). No evidence of an increased frequency of disruptions was found in one model with interactive ozone (DallaSanta et al., 2021), but it is difficult to draw conclusions from any single model because the details of the projected changes in the QBO vary widely across the models (e.g., Richter et al., 2020b).

The QBO-induced ozone variations in the lower equatorial stratosphere are primarily governed by transport variations, while temperature-dependent photochemical ozone variations are dominant higher in the stratosphere (Zhang et al., 2021). This indicates that inclusion of interactive ozone chemistry is required in order to infer future changes in QBO-induced ozone variations, but the vast majority of the models examined in CMIP6 and the QBOi did not use interactive ozone. Furthermore, there is growing evidence that the observed QBO-induced ozone variations are of sufficient magnitude to potentially provide feedback onto the QBO (Kataoka et al., 2020; Pohlmann et al., 2019; Shibata, 2021). This possible feedback was inferred to be positive in two different chemistry-climate models (Naoe et al., 2017; DallaSanta et al., 2021), with the amplitude of the QBO-induced ozone variation also increasing. On the other hand, Shibata (2021) artificially increased the magnitude of the ozone variation passed to the radiation code in a CCM and found little impact on the amplitude of the QBO but a lengthening of the QBO period. However, because there has so far been little focus on the simulation of the QBO with interactive ozone, there is still low confidence in the simulated impacts and especially in the positive feedback on amplitude.

Strengthening of the QBO-induced ozone variation despite a projected weakening of the QBO partly derives from the expected recovery of ozone (Naoe et al., 2017; DallaSanta et al., 2021). The simulated ozone-dynamical feedback can also act to offset the decline in amplitude of the QBO as a result of increasing greenhouse gases (DallaSanta et al., 2021), indicating that increasing confidence in projected changes of the QBO and its impacts on ozone variations will require the inclusion of explicit ozone-dynamical coupling (see also **Box 5-4** and *Section 5.3.2.1.3*).

In summary, since the last Assessment, there is more confidence that the QBO will weaken in the future as a result of acceleration of the BDC in a warming climate. However, there remains large uncertainty about any change in its periodicity and about the associated impact on ozone variability. New evidence infers that disruptions of the QBO may become more likely in a warming climate.

5.3 EFFECTS OF CHANGES IN STRATOSPHERIC OZONE AND ODSs ON CLIMATE

The climate impacts of stratospheric ozone changes on tropospheric and surface climate are well established and widely documented. Ozone depletion has been deemed the key driver of late–20th century austral summer atmospheric circulation changes in the Southern Hemisphere, as well as one of the drivers of changes in the SH cryosphere and ocean. Here, we focus on new findings since the last Assessment. This includes new quantifications of the radiative forcing from ODSs and ozone (*Section 5.3.1*). We also highlight an emerging body of evidence pointing at the direct climate impacts of ODSs, independent of ozone depletion, and the importance of stratospheric ozone-climate feedbacks and ozone-circulation coupling on a range of timescales. In particular, we highlight new evidence concerning the climate effects of the Montreal Protocol and reveal that some of these effects may have already begun to be realized (*Sections 5.3.2* and *5.4*).

5.3.1 Radiative Impacts of Ozone and ODSs on Tropospheric Climate and Ozone-Climate Feedbacks

Changes in stratospheric ozone can affect climate in a number of ways. Aside from inducing stratospheric cooling (*Section 5.2.2*) and changes in the stratospheric (*Sections 5.2.4* and *5.2.5*) and tropospheric (*Section 5.3.2*) circulation, trends in stratospheric ozone and ODS abundances introduce a radiative forcing perturbation that is a substantial fraction of the total anthropogenic radiative forcing over the second half of the 20th century (Forster et al., 2021). This section focuses on what has been learned about radiative forcing since the last Ozone Assessment (*Section 5.3.1.1*). The climate effects of stratospheric ozone and ODSs are traditionally studied in conjunction, as they are closely coupled via heterogeneous and homogeneous chemistry. Here, we review new evidence on their effects in isolation, such as the direct effects of ODSs on climate (*Section 5.3.1.2*) and those of GHG-induced stratospheric ozone changes on climate (*Section 5.3.1.3*).

5.3.1.1 Ozone Radiative Forcing

Radiative forcing is one of the key metrics for quantifying the potential climate effects of historical ODS emissions and the resulting ozone changes. Traditionally, the standard definition adopted to quantify the radiative forcing of historical ozone and ODS changes is the stratosphere-adjusted radiative forcing. In the following, the term "radiative forcing" (RF) refers to this stratosphere-adjusted radiative forcing definition. Some studies have adopted the "effective radiative forcing" (ERF) definition that was mandated by IPCC AR5. However, as detailed below, given the

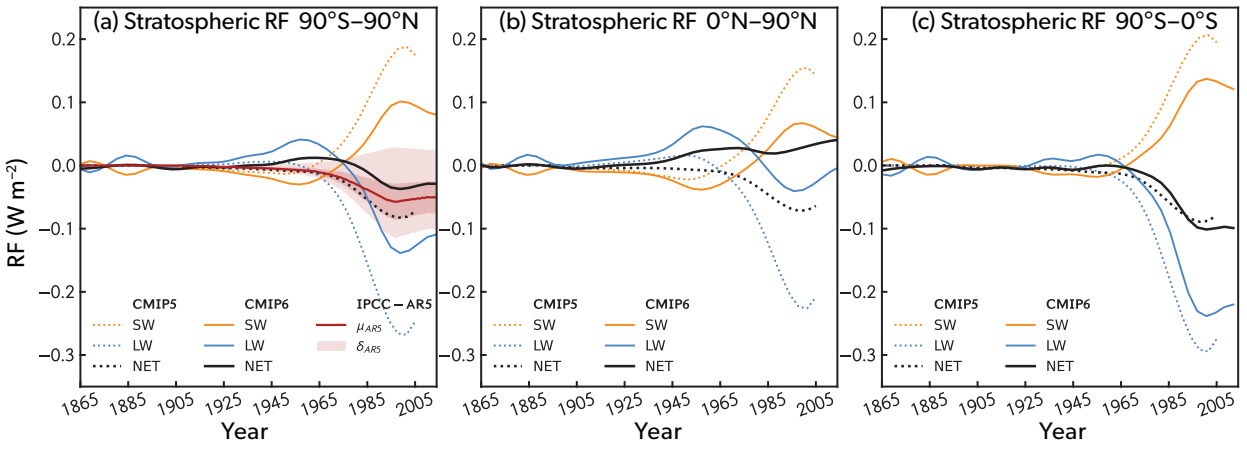

Figure 5-8. Radiative forcing from stratospheric ozone relative to 1850 and its evolution over the 20th century, from the ozone datasets compiled for CMIP6 (solid lines) and CMIP5 (Cionni et al., 2011; dotted lines), as well as the IPCC AR5 estimate (red line) and its uncertainty (shading), for the global mean (*left panel*), Northern Hemisphere (*center panel*), and Southern Hemisphere (*right panel*). The stratosphere-adjusted RF in this figure is evaluated at the tropopause. Yellow lines denote the SW forcing, while blue lines show the LW component in the CMIP5 and CMIP6 estimates. [Adapted from Checa-Garcia et al., 2018.]

larger uncertainty in the ERF quantification, the stratosphere-adjusted RF is the focus of our Assessment (see also **Box 5-3** on radiative forcing).

Since the last Assessment, updated RF values (relative to 1850) for whole-atmosphere ozone have been derived (Checa-Garcia et al., 2018; Skeie et al., 2020) and have recently been assessed in IPCC AR6 (*Section 7.3.2.1* of Forster et al., 2021). These values are listed in **Table 5-1**, along with several previously reported values for reference. The 3-D ozone forcing dataset compiled for CMIP6 models without interactive chemistry ("CMIP6 ozone" in **Table 5-1**) produces a whole-atmosphere (stratospheric + tropospheric) ozone RF over the period 1850–2010 of 0.3 W m^{-2}, in agreement with the value reported in IPCC AR5 (0.35 W m^{-2}), and this RF is almost entirely due to tropospheric ozone (0.33 W m^{-2}). The whole-atmosphere ozone RF in the new CMIP6 dataset is double (0.30 versus 0.15 W m^{-2}) that in its predecessor, the CMIP5 ozone dataset (Cionni et al., 2011). Even larger values are obtained in Skeie et al. (2020) (0.41 W m^{-2}) and in IPCC AR6 (0.47 W m^{-2}; Forster et al., 2021), which is likely due to the larger emissions of tropospheric ozone precursors used in CMIP6 models than in the two CCMI models employed in the production of the CMIP6 ozone forcing dataset. In addition, the forcing in Forster et al., 2021 is relative to 1750 rather than 1850.

The RF arising from stratospheric ozone changes over the historical period has been estimated by a number of studies since the last Assessment, based on different reanalysis or model datasets (as summarized in **Table 5-1**). Consistent with previous Assessments, the RF due to stratospheric ozone is much smaller than that due to tropospheric ozone, since it is the result of competing effects in the longwave (LW) and shortwave (SW) radiation (**Figure 5-8**; see also **Box 5-3**). The global mean RF is dominated by the Southern Hemisphere. Since stratospheric ozone trends are larger and more consistent across models in the Southern than in the Northern Hemisphere, the RF estimates there are more robust across the ozone datasets than in the Northern Hemisphere (**Figure 5-8**). New estimates of the net global mean stratospheric ozone RF in the historical period based on multiple CCMs generally range from a small (<0.1 W m^{-2}) net positive to a small net negative RF (see **Table 5-1**), likely caused by the compensation of LW and SW effects, as seen in forcing datasets depicted in **Figure 5-8**. The reanalysis-based RF estimate over the period 1750–2010 is near zero (+0.003 ± 0.20 W m^{-2}) in the global mean (Bellouin et al., 2020; based on CAMS reanalysis data), which is well within the range of the model-based estimates.

Compared to previous model-based estimates of global mean stratospheric RF, newer estimates from CMIP6 are generally slightly smaller but also span a wider range (see **Table 5-1** and **Figure 5-8**). The ozone forcing dataset produced for CMIP6 results in a slightly smaller global mean stratospheric ozone RF over the period 1850–2010 compared to its CMIP5 predecessor (–0.03 ± 0.06 W m^{-2} versus –0.08 W m^{-2}; Checa-Garcia et al., 2018; Cionni et al., 2011; see also **Figure 5-8**). In Chapter 7 of the Working Group I contribution to IPCC AR6 (Forster et al., 2021), the 1850–2010 stratospheric ozone RF was suggested to be 0.02

Table 5-1. Radiative forcing from stratospheric, tropospheric, and total ozone from the studies assessed in this chapter, along with the definition of RF method (following the forcing definitions used by IPCC AR6), the time period of the forcing, and the input dataset for the calculations. The CMIP6 ozone dataset is constructed by averaging the output of two CCMI models (WACCM and CMAM) driven with precursor and ODS emissions and all historical forcings over the period 1850–2014 (Checa-Garcia et al., 2018). In CMIP5, the ozone dataset is derived from simulated tropospheric ozone, while ozone in the stratosphere it is based on satellite observations since 1979 and statistical extrapolations before that date (Cionni et al., 2011). In studies using model simulations as the input dataset, the RF has been calculated from each individual CCM output. In Skeie et al. (2020), a different stratospheric ozone RF range of –0.02 ± 0.14 W m^{-2} is obtained when excluding one outlier model (UKESM) but including all other models with comprehensive stratospheric chemistry. The uncertainty range represents the 5–95% range, unless otherwise noted. Some sensitivity of the RF to the tropopause definition arises when separating stratospheric and tropospheric ozone, but this effect is only marginal (Stevenson et al., 2013).

Study	RF definition	Time period	Input dataset	Stratospheric Ozone	Tropospheric Ozone	Total
Checa-Garcia et al., 2018	SARF	1850–2010	CMIP6 ozone	–0.03 ± 0.06 (a)	0.33 ± 0.16 (a)	0.30 ± 0.15 (a)
Skeie et al., 2020	SARF	1850–2010	CMIP6 models (b)	0.02 ± 0.07	0.39 ± 0.07	0.41 ± 0.12
Skeie et al., 2020*	SARF	1850–2010	CMIP6 models (c)	–0.02 ± 0.14		
Bellouin et al., 2020	SARF	1750–2010 (d)	Re-analysis (e)	0.00 ± 0.20 (f)	0.33 ± 0.27 (f)	0.32 ± 0.32 (f)
Thornhill et al., 2021	ERF	1850–2014	CMIP6 models			0.33 ± 0.11 (g)
Michou et al., 2020	ERF	1850–2010	Single CMIP6 model	–0.04		
IPCC-AR6	ERF (h)	1750–2019 (i)	assessed			0.47 ± 0.23
Cionni et al., 2011	SARF	1850–2011	CMIP5 ozone	–0.08	0.23	0.15
Stevenson et al., 2013	SARF	1750–2010 (i)	ACCMIP models		0.41 ± 0.14	
IPCC-AR5	SARF	1750–2011 (i)	assessed	–0.05 ± 0.10 (a)	0.40 ± 0.20 (a)	0.35 ± 0.20 (a)

(*) differs from published range (see c)
(a) 5-95% interval using parametric formula (Myhre et al., 2013)
(b) excluding models without trop chem and model with excessive depletion (5 out of 11)
(c) including all models with strat chem, excluding model with excessive depletion (9 out of 11)
(d) end year is average 2003–2017
(e) reanalysis is based on modeling (CAMS)
(f) 5–95% interval calculated from combined structural uncertainties
(g) emission-based ERF (linear sum of individual GHGs)
(h) ERF is taken to be equal the SARF
(i) extrapolations to extended period made adding offsets

± 0.07 W m^{-2}, based on CCMs participating in CMIP6 (Skeie et al., 2020), compared to a range of –0.05 ± 0.10 W m^{-2} assessed by IPCC AR5. The CMIP6 range was obtained by excluding models without tropospheric chemistry (but which do simulate stratospheric chemistry) and one model with excessive ozone depletion (UKESM). Taking all CMIP6 models with interactive stratospheric chemistry except UKESM into account yields a range of –0.02 ± 0.14 W m^{-2}, which is closer to previous estimates (see **Table 5-1**; Skeie et al., personal communication). In general, these different estimates agree on a flattening of the global stratospheric ozone RF since the late 1990s (Dhomse et al., 2018; **Figure 5-8**), consistent with the emergence of healing of the ozone layer (*Chapter 3*).

In the future, the stratospheric ozone RF is expected to remain

Box 5-3. Radiative Forcing from Ozone and ODSs: Methods and Uncertainties

The radiative forcing (RF) metric quantifies the radiative energy flux perturbation exerted by natural and anthropogenic forcings into the climate system. A positive forcing introduces a net radiative gain, ultimately leading to surface warming, until increased thermal emissions to space restore the balance; a negative forcing operates in the opposite way, causing cooling (Ramaswamy et al., 2019). Historically, RF has been defined by the change in the energy balance in the climate system when a forcing is introduced with respect to a preindustrial climate. However, this instantaneous evaluation of the energy imbalance (termed "instantaneous radiative forcing") does not represent the actual climate impact of the forcing introduced, in particular regarding the surface warming, as rapid adjustments of the temperature in the stratosphere can mute the RF, making it substantially different from the instantaneous RF (Pincus et al., 2020). These adjustments in the stratospheric temperature are commonly estimated by the fixed dynamical heating (FDH) method (Forster and Shine, 1997). This method involves adjusting stratospheric temperatures until a new equilibrium is reached, assuming that the dynamical heating remains unchanged, and keeping tropospheric temperatures fixed. This is the standard method to estimate the RF of historical ozone changes and is commonly referred to as the stratosphere-adjusted radiative forcing (see IPCC AR5). An example of the implementation of this method in modern CCMs is given by Conley et al. (2013), and this method is used to calculate the ozone RF here in *Chapter 5*. Other Chapters (*Chapter 1, 2, 7*) infer the RF of individual source gases by using Tabulated Radiative Efficiency values (see the *Annex*), which include or neglect certain adjustments (e.g. lifetime, tropospheric adjustments), but these adjustments only have a small (<10%) effect on the total RF of major ODS species, making their RF sufficiently close to the SARF (e.g., Thornhill et al., 2021).

The stratosphere-adjusted RF definition reduces the sensitivity to the details of the tropopause definition. However, forcing agents such as ozone and ODSs can also produce rapid adjustments in the troposphere, such as adjustments in temperature and clouds, which can themselves be quantified as forcings; these are not captured by the stratosphere-adjusted RF. Incorporation of these responses in the forcing makes it more representative of the actual climate impacts of the forcing; this is achieved using the effective radiative forcing (ERF; Forster et al., 2016) definition. ODSs induce temperature changes in the upper troposphere / lower stratosphere (UTLS; Forster and Joshi, 2005; McLandress et al., 2014; Chiodo and Polvani, 2022), a large portion of which would be missed using the FDH; this raises the question whether the stratosphere-adjusted RF is an appropriate measure of the ERF for ODSs. However, given the considerable uncertainties associated with ERF estimates (see *Section 5.3.1.1*), most studies on ozone RF so far have focused only on the stratosphere-adjusted RF.

The RF originating from stratospheric ozone trends over the 20th century is primarily due to the modulation of ozone by ODSs. However, the division of ozone RF forcing into its components of stratospheric and tropospheric ozone does not directly attribute ozone RF forcing to ODSs. This is because tropospheric ozone can be influenced by ODS-driven stratospheric ozone decreases, a component deemed important in certain models (e.g., Shindell et al., 2013) but which strongly depends on stratosphere-troposphere exchange processes (Banerjee et al., 2018; see also *Section 5.2.5*). Existing estimates of ODS-attributed ozone RF are substantially stronger (more negative) than the stratospheric ozone RF arising from historical trends (see *Section 5.3.1.1*), but the net forcing by ODSs, including associated ozone changes, is still found to be positive in current estimates (Thornhill et al., 2021).

The radiative effects of ODSs and ozone are determined by their intrinsic properties. ODSs, among which CFCs contribute more than 85% of the RF, have a long lifetime and are relatively well mixed in the troposphere. ODSs have strong absorption bands in the LW part of the spectrum. As such, they reduce the outgoing LW flux, and an increase in ODS atmospheric abundance leads to a positive RF (see *Chapter 1*). Uncertainty in these properties has a small impact on their RF (Chiodo and Polvani, 2022). Their RF is partly balanced by the negative RF from the associated stratospheric ozone losses (Myhre et al., 2013; see *Section 5.3.1.1*). Ozone molecules have a more complex spectrum, with absorption bands in the solar shortwave (SW) and in the longwave (LW) (Goody and Yung, 1989). The radiative effect of ozone is strongly altitude dependent, with ozone changes near the tropopause being most effective at absorbing LW and thus contributing to climate change, due to the large temperature difference between this region (where the absorption takes place) and the Earth's surface (the emissions source; Lacis et al., 1990). Ozone changes at upper-stratospheric levels have a much smaller or even slightly opposite effect on the net forcing. Further, the LW and SW effects of stratospheric ozone changes strongly compensate each other. Depletion of stratospheric ozone leads to reduced SW absorption and thus an increase in the incident SW flux at the tropopause (i.e., a positive forcing). Reduced SW absorption cools the stratosphere, which in turn reduces the LW flux at the tropopause, a negative forcing. The balance between the SW and LW terms crucially depends on the season, location, and magnitude of the ozone perturbation (Ramanathan and Dickinson, 1979). Taken together, the offsetting contributions of LW and SW explain the small net value of stratospheric ozone RF, leading to uncertainty even in its sign.

at a similar value as estimated for present-day or trend to slightly more negative values by the end of the 21st century, depending on the scenario (see **Table 5-2**, based on CMIP6 ozone forcing datasets and calculated consistent with the approach of Checa-Garcia et al., 2018). The small changes in future stratospheric ozone RF are due to the opposite effects of climate change in low and high latitudes. GHG increases lead to a decrease in ozone in the tropical lower stratosphere due to increasing tropical upwelling, driving a negative ozone RF in the tropics. In mid- and high latitudes, decreased stratospheric halogen loading and an enhanced BDC lead to an increase in ozone abundances, driving a positive ozone RF. Low and mid-range scenarios (SSP1-2.6 and SSP2-4.5) show small changes in stratospheric ozone RF values, likely because RF changes due to ODS-driven ozone recovery are compensated by RF changes due to GHG-driven tropical ozone decreases. For high-end scenarios (SSP5-8.5), future stratospheric ozone RF values decrease, likely because the RF effects of GHG-driven tropical ozone decreases dominate.

The RF by ODSs is assessed in *Chapters 1* and *2*, which report RFs in 2020 of 0.337 W m^{-2} for ODSs (defined as chlorofluorocarbons [CFCs] + hydrochlorofluorocarbons [HCFCs] + halons + solvents) and 0.04 W m^{-2} for HFCs. The combined effects of ODS and stratospheric ozone trends result in a net positive RF when taken as the sum of the two individual forcings and thus contribute to surface warming over the 20th century (see *Section 5.3.1.2*). A different approach to summing up the direct ODS RF and stratospheric ozone RF is to explicitly attribute (whole atmosphere) ozone changes to ODS emissions; this emissions-based RF of ODSs, including induced ozone changes, is likewise found to be positive by current model studies (Thornhill et al., 2021).

Studies that used the stratosphere-adjusted RF definition are discussed above. A few other studies have adopted ERF, the RF definition mandated by IPCC AR5 (Forster et al., 2016; see also **Box 5-3**). The ERF of ODSs inferred from observations, including the indirect effects via ozone and other rapid tropospheric adjustments, is estimated to lie between 0.03 and 0.14 W m^{-2} (Morgenstern et al., 2021, revising Morgenstern et al., 2020 ; see also *Chapter 7*). Taken at face value, the lower bound of this estimate would imply that ODS-driven changes in stratospheric ozone and rapid adjustments effectively cancel the direct RF of ODSs (0.337 W m^{-2} by 2020; see *Chapter 1*), resulting in a smaller warming influence of ODSs than considered likely in AR5 and most climate models (see *Section 5.3.1.2*). However, there is considerable uncertainty in those estimates arising from the methods (e.g., uncertainty in the linear regression), the limited number of models included in the assessment, and biases in the simulated ozone trends. An important but highly uncertain component of the ERF due to ODSs are cloud changes arising from positive (ozone-induced) trends in the Southern Annular Mode (SAM) in the Southern Hemisphere (O'Connor et al., 2021); rapid adjustments of this type introduce uncertainty in ERF estimates. Other analyses of CMIP6 models suggest that in the global mean, rapid adjustments to ozone and ODSs are weak (Skeie et al., 2020; Hodnebrog et al., 2020). In line with this, the ERF of stratospheric ozone from one model study (Michou et al., 2020, reporting a value of –0.04 W m^{-2}) is well within the range of the stratospheric ozone stratosphere-adjusted RF from the aforementioned studies. We thus conclude, similar to IPCC AR6 (Forster et al., 2021), that confidence in rapid adjustments is still limited, and therefore our assessment is based on the stratosphere-adjusted RF.

Overall, we assess that the RF due to long-term stratospheric ozone trends over the historical period (1850–2010) is near zero due to the cancellation of LW and SW effects, with a large uncertainty range, at –0.02 ± 0.13 W m^{-2}, based on the uncertainties provided among all studies assessed here (see **Table 5-1**). The best estimate of –0.02 W m^{-2} is the average from three estimates—the CMIP6 ozone forcing (Checa-Garcia et al., 2018; –0.03 W m^{-2}), the reanalysis study of Bellouin et al. (2020; 0.003 W m^{-2}), and the average over all CMIP6 models with stratospheric chemistry (Skeie et al., 2020; –0.02 W m^{-2})—while the uncertainty range (0.13 W m^{-2}) encompasses all CMIP6 models with stratospheric chemistry (Skeie et al., personal communication), as well as methodological uncertainties (e.g., tropopause definition and the preindustrial ozone climatology). For the extended period 1850–2019, the stratospheric ozone RF is in the same range as for 1850–2010, as uncertainty outweighs any changes arising from ozone trends over 2010–2019. Hence, the net RF by ODSs (+0.337 W m^{-2}; see *Chapter 1*), including its impacts on long-term stratospheric ozone trends, is positive and contributes to global warming, as assessed in *Section 5.3.1.2*. It has become clear since the last Assessment that rapid adjustments arising from tropospheric circulation changes might play a role in determining the climate response to ODSs at regional scales, but the magnitude of these adjustments is highly uncertain and model dependent, although it is unlikely to offset the global direct forcing by ODSs.

5.3.1.2 ODS Direct Effects on Climate

Several studies have highlighted the important role that ODSs alone have had on climate, in addition to their impact on climate through affecting stratospheric ozone abundances. As outlined in the previous section, *Chapter 1* of this Assessment, as well as in IPCC AR6 (see Figure 6.12a in Szopa et al., 2021, and

Table 5-2. Radiative forcing from future stratospheric ozone, calculated at the tropopause as in Checa-Garcia et al. (2018) using the future CMIP6 ozone datasets compiled for IPCC AR6 (Checa-Garcia 2022, personal communication).

Scenario	RF definition	Time period	Input dataset	Stratospheric ozone
SSP126	SARF	1850–2099	CMIP6 ozone	–0.03 ± 0.06
SSP245	SARF	1850–2099	CMIP6 ozone	–0.04 ± 0.08
SSP370	SARF	1850–2099	CMIP6 ozone	–0.02 ± 0.04
SSP460	SARF	1850–2099	CMIP6 ozone	–0.03 ± 0.06
SSP585	SARF	1850–2099	CMIP6 ozone	–0.09 ± 0.18

Uncertainty is taken using parametric formula (Myhre et al., 2013)

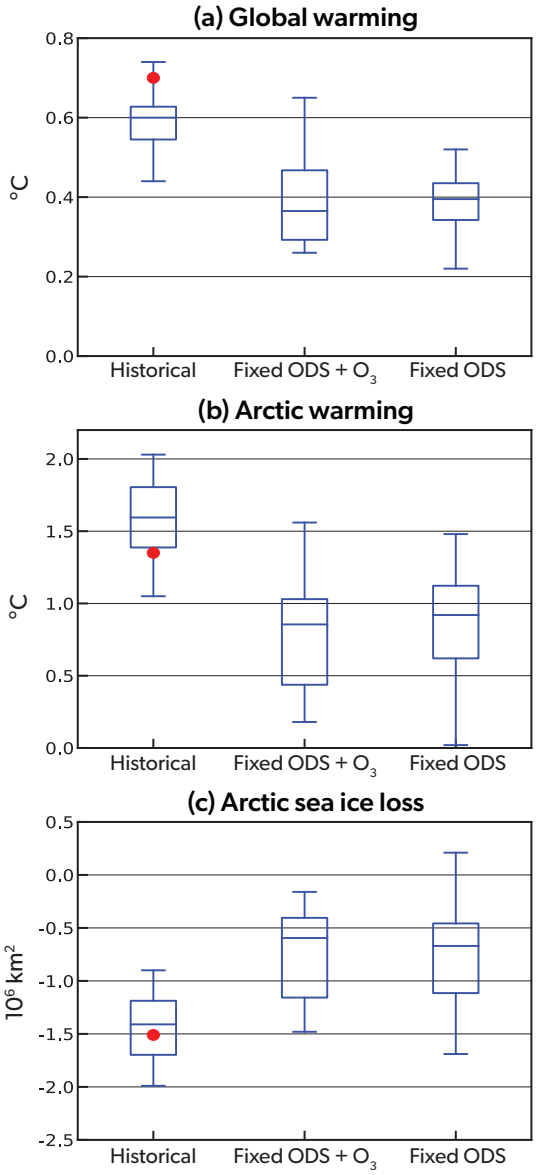

Figure 5-9. Climate impact of ODSs for the period 1955–2005. (a) Annual mean global surface-temperature change over the period 1955–2005 for each ten-member Community Earth System Model Version 1 (CESM-CAM5) ensemble, as labelled on the abscissa. The boxes extend from the lower to upper quartile of the data, with a line at the median and whiskers showing the entire range across each ensemble (b) As in (a) but for Arctic temperatures, averaged (60–90°N). (c) As in (a) but for September Arctic sea ice extent. Red circles denote the observed values obtained from GISTEMP27 v.3 for surface temperature and HadISST28v.2.2.0 for sea ice. The change over the period 1955–2005 is computed as the linear trend multiplied by the number of years (51). In each panel, the means of the Fixed ODS and ozone (Fixed ODS+O_3) (ODSs and stratospheric ozone fixed at year 1955 levels) and Fixed ODS (ODSs fixed at year 1955 levels) ensembles are significantly different from that of the Historical ensemble at the 99% confidence level by two-tailed t-test. [Adapted from Polvani et al., 2020.]

Section 7.3.2.4 and Table 7.5 of Forster et al., 2021), both the stratosphere-adjusted RF and the ERF (i.e., even when accounting for the RF via stratospheric ozone loss) of ODSs are likely to be positive. Over the second half of the 20th century (1955–2005), the RF by ODSs is second only to CO_2, making ODSs an important anthropogenic influence on climate in recent decades (Velders et al., 2007; Polvani et al., 2020). Since the last Assessment, new evidence from independent chemistry-climate and Earth-system model studies have shown the important role that ODSs have played in enhancing Arctic warming (Goyal et al., 2019; Polvani et al., 2020; Liang et al., 2022). **Figure 5-9** shows the large contribution of ODSs to global and Arctic warming and sea ice loss over the 1955–2005 period (Polvani et al., 2020). Excluding the trend in ODSs reduces annual mean historical global warming by approximately one-third (**Figure 5-9a**), and Arctic warming (and September sea ice loss) by approximately half. This indicates that ODSs appear to enhance Arctic amplification (**Figure 5-9b** and **c**); i.e. the Arctic warmed 2.7 times more than the global mean in the historical ensemble compared to only 2 times more in the ensemble with fixed ODS and ozone (comparing **Figure 5-9a** and **b**). This result is supported by another study (Liang et al., 2022), which reports that Arctic amplification caused by ODSs is 1.44 times stronger than that caused by CO_2 over the same time period. The impact of stratospheric ozone loss on global and Arctic temperature change appears negligible (comparing the Fixed ODS+O_3 and Fixed ODS ensembles in **Figure 5-9**). Although the specific mechanism responsible for enhanced Arctic amplification due to ODSs is not yet clear, radiative feedback analysis suggests a key contribution from local Arctic feedbacks (Polvani et al., 2020; Liang et al., 2022). However, the robustness of the effects of ODSs on Arctic warming is still questionable as these studies were all based on related models.

There is also evidence that ODSs have contributed to a weakening of the Walker circulation (a zonal overturning cell in the equatorial Pacific) over the 1955–2005 period due to a rapid warming of the Eastern Tropical Pacific SSTs (Polvani and Bellomo, 2019). However, there is no consensus as to whether the observed Walker circulation has indeed weakened since the middle of the last century, and questions have been raised about the fidelity of using climate models to simulate the response of Eastern Tropical Pacific SSTs to increasing greenhouse gases (Clement et al., 1996; Cane et al., 1997; Seager et al., 2019). Overall, evidence of the direct ODS effects on climate continue to emerge but are not yet robust.

5.3.1.3 Role of Stratospheric Ozone in the Climate Response to CO_2 Forcing

The effects of stratospheric ozone changes induced by ODS emissions on the climate system have been widely documented across many Ozone Assessments (WMO, 2010, 2014, 2018). Conversely, the role of stratospheric ozone in modifying the climate system's response to GHG increases has received less attention. The response of the stratospheric ozone layer to GHG forcing can impact the global mean surface temperature response to GHG forcing, thus acting as a true climate feedback (termed "ozone-climate feedback" in the following discussion). Furthermore, the stratospheric ozone response to GHG forcing can modify the stratospheric and tropospheric circulation response to GHGs via ozone-circulation coupling. The relevant processes involved in the ozone-climate feedback and ozone-circulation coupling are

Box 5-4. Ozone-Climate Feedbacks and Ozone-Circulation Coupling

Stratospheric ozone plays an important role in the radiative budget of the atmosphere. It not only reduces the incidence of UV radiation at the surface but also plays a key role in determining the thermal structure of the stratosphere by heating the upper stratosphere by more than 20 K. Ozone heating also substantially influences the temperature near the tropical tropopause layer (TTL), thereby also influencing global stratospheric water vapor amounts (e.g., Ming et al., 2017). Ozone also acts as a greenhouse gas, due to its absorption band near 10 μm wavelength.

Previously, most research on the effects of stratospheric ozone on climate has focused on the impacts of chemical ozone depletion due to ODSs (WMO, 2010, 2014, 2018), considering ozone as a "forcing". Recently, attention has focused on the quantification of the two-way coupling between stratospheric ozone and the climate system via radiation, dynamical, and chemical processes. This coupling is initiated by stratospheric ozone variations that are either externally forced (e.g., due to changes in CO_2) or internally produced by climate variability on a range of timescales from sub-seasonal to multi-decadal.

Stratospheric ozone is strongly coupled with temperature via radiation and chemistry; this coupling is at the core of the mechanism behind stratospheric ozone-circulation coupling, shown in **Box 5-4 Figure 1**. On sub-seasonal to interannual timescales, circulation and temperature anomalies, such as those associated with variations in the polar vortex strength, induce ozone anomalies. This is due not only to transport but also to temperature-dependent chemistry. Aside from homogeneous chemistry in the polar stratosphere, heterogeneous chemistry plays a key role when temperatures are low enough for PSC formation and sufficient abundances of ODSs are available (Calvo et al., 2015; *Chapter 4*). Ozone in turn affects temperature via radiation, feeding back on the initial temperature and circulation anomaly (see the light blue circle in **Box 5-4 Figure 1**). Thus, ozone modifies the initial stratospheric circulation anomalies, and this can further influence the tropospheric circulation via stratosphere-troposphere dynamical coupling. There is evidence that this coupling may influence the stratosphere-troposphere circulation in individual years and can influence sub-seasonal prediction in both the Southern (*Section 5.3.2.1.1*) and Northern Hemispheres (*Section 5.3.2.1.2*).

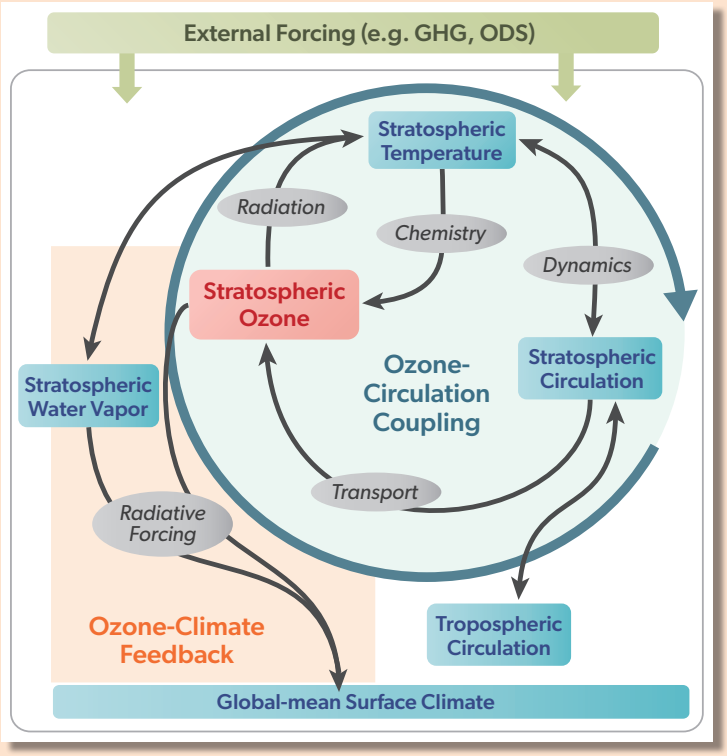

Box 5-4 Figure 1. Schematic of stratospheric ozone-circulation coupling and ozone-climate feedbacks. The stratospheric ozone-climate feedback modifies the response of global surface climate to an external forcing such as increasing GHGs. Ozone-circulation coupling can be induced by changes due to external forcings (e.g., CO_2-driven stratospheric temperature and circulation changes), and subsequent ozone changes modify the circulation response to the forcing. Ozone-circulation coupling is also induced by internal variability (e.g., an anomalous strong and cold polar vortex), and can modify the stratosphere-troposphere circulation in individual years.

The two-way coupling between ozone and the circulation also contributes to the response to forced changes to the climate system. For example, when atmospheric CO_2 concentrations increase, the stratosphere cools (as explained in Box 5-1 of Karpechko, Maycock et al., 2018) and the troposphere and surface warm. Globally, stratospheric cooling from CO_2 leads to an increase in ozone abundances due to the temperature dependence of ozone chemistry (see **Box 5-2**). Tropospheric warming leads to an acceleration of the BDC, driving an ozone decrease in the lower tropical stratosphere. These ozone changes radiatively warm the upper stratosphere and the polar regions and cool the TTL, leading to a decrease in stratospheric water vapor. These heating and cooling effects driven by ozone changes affects temperature gradients, inducing an ozone-circulation coupling that modulates the response of the stratospheric circulation to CO_2 forcing, as well as the tropospheric circulation response (see *Section 5.3.1.3*). These processes apply not only to increases in CO_2 but also to any external forcing, including ODSs (see *Section 5.3.2.2.1*), and also CH_4 or N_2O, although this is less well studied.

Furthermore, the CO_2-driven stratospheric ozone changes, as well as subsequent stratospheric water vapor changes, induce an indirect RF, potentially impacting the global mean surface temperature response to CO_2 forcing. The relationship of the global mean surface temperature change to a change in the net energy budget at the top of the atmosphere (e.g., resulting from CO_2 forcing) is commonly defined as a climate feedback (see Box 7.1 in Forster et al., 2021). In the recent IPCC report (IPCC, 2021), climate feedbacks were grouped into physical feedbacks (for

example, those associated with water vapor and surface albedo), biogeophysical and biogeochemical feedbacks, and long-term feedbacks associated with ice sheets. Stratospheric ozone contributes to the group of biogeochemical climate feedbacks (Szopa et al., 2021). Recent studies on quantifying this stratospheric ozone climate feedback are assessed in *Section 5.3.1.3*.

Models without interactive stratospheric ozone chemistry do not simulate the coupling between ozone and the circulation and thus miss the modulation of temperature and circulation anomalies and trends, as well as the resulting climate feedback through stratospheric ozone. The quantification of the role of those processes is the subject of ongoing research, including their impact on the climate response to CO_2 (*Section 5.3.1.3*) and to ODSs (*Section 5.3.2.2.1*), as well as their role for stratospheric and tropospheric variability on interannual timescales (*Section 5.3.2.1*).

detailed in **Box 5-4**, and new research into the climate impacts of stratospheric ozone changes under GHG forcing (mainly CO_2) is assessed in the following.

In the last Assessment, it was stated that stratospheric ozone-climate feedbacks are more likely to reduce rather than increase the equilibrium climate sensitivity (ECS), quantified as the near-equilibrium global warming response to an abrupt quadrupling of atmospheric CO_2 concentrations. However, the uncertainty in the feedback across models is large (0–20% in the ECS, or –0.01 to –0.13 W m^{-2} K^{-1} in the climate feedback), contributing to a substantial fraction (~30%) of the uncertainty in the net non-CO_2 biogeochemical feedbacks under climate change (Section 6.4.5 of Szopa et al., 2021). Since the last Assessment, new insights have been gained into possible reasons for the model uncertainty in the ozone-climate feedback. These include inconsistencies between the chemical and thermal tropopause when ozone abundances are prescribed (Nowack et al., 2018, 2015), leading to biases such as a too-warm cold point temperature and excessive moistening of the stratosphere (Hardiman et al., 2019; Nowack et al., 2018). It has been shown that this effect can lead to an overestimation of the ECS by about 10% (Hardiman et al., 2019) in one model that previously reported a very strong ozone feedback (20%) on ECS (e.g., Nowack et al., 2017, 2015), and this bias can generally be expected to be large in models with sufficiently high vertical resolution and high climate sensitivity.

Aside from specifications near the tropopause, the other possible source of uncertainty in the ozone-climate feedback is how ozone itself is affected by increasing GHGs, as it changes quite differently across climate models (Chiodo et al., 2018). In a simple 1-D radiative convective equilibrium model (Dacie et al., 2019), imposing a 4xCO_2 forcing while keeping ozone at preindustrial levels leads to cooling of the stratosphere and warming of the troposphere (**Figure 5-10**). Imposing ozone changes under 4xCO_2 (which are prescribed from CCMs) leads to 5–10 K less cooling in the upper stratosphere and enhanced cooling (of 2–3 K) of the lower stratosphere (compare solid blue and pink lines in right panel of **Figure 5-10**), consistent with the sign of the prescribed ozone change. Further, surface warming is slightly reduced (from 6.6 to 6.3 K), consistent with the negative feedback on ECS reported in other studies (Dietmüller et al., 2014; Muthers et al., 2014; Nowack et al., 2015). The reduction in ECS when imposing different ozone perturbations in this 1-D model ranges between 0 and 10%, whereas in a more complex CCM, imposing a range of ozone perturbations does not affect ECS at all (Chiodo and Polvani, 2019). This suggests that the magnitude of the stratospheric ozone feedback on ECS is likely to be model-dependent but unlikely to affect ECS by more than 10%, with most of the uncertainty originating in the interactions between ozone and physical feedbacks, such as with clouds or the lapse rate. Ozone might also modulate the climate response to forcing agents other than CO_2, such as methane (Stecher et al., 2021), but this has not yet received much attention.

In addition, there is new evidence that stratospheric ozone-circulation coupling modifies the atmospheric circulation response to CO_2. Stratospheric ozone modulates the stratospheric cooling due to CO_2 (Chiodo and Polvani, 2019; Dietmüller et al., 2014; Nowack et al., 2018, 2015; Kuilman et al., 2020) and can subsequently affect dynamics through changes in the meridional temperature gradient. In the stratosphere, model simulations with interactive ozone show a dampening of GHG-induced tropical upwelling increases, reducing the QBO amplitude (DallaSanta et al., 2021). In the troposphere, interactive stratospheric ozone reduces the poleward shift of the eddy-driven jet in response to GHG increases (Chiodo and Polvani, 2017; Nowack et al., 2018; Chiodo and Polvani, 2019) and damps the ENSO response (Nowack et al., 2017). While these are individual model findings and have not yet been tested for consistency across multiple models, they consistently suggest that stratospheric ozone may affect several aspects of tropospheric and surface climate beyond the global mean surface temperature, inducing a negative feedback on a variety of circulation metrics and thereby counteracting the effects of GHGs.

Taken together, we assess that stratospheric ozone–climate feedbacks are still uncertain but more likely to reduce than increase ECS, consistent with the conclusions of the previous Assessment (WMO, 2018) and IPCC AR6 (Szopa et al., 2021). Based on new evidence since the last Assessment, we revise the range of ECS reduction due to the stratospheric ozone-climate feedback to 0–10%, with reductions beyond 10% deemed unlikely. While not yet quantified with high certainty, there is robust evidence that stratospheric ozone affects other aspects beyond ECS, such as the atmospheric circulation response to GHGs in both the stratosphere and troposphere.

5.3.2 Ozone/Dynamical Coupling

Stratospheric ozone is strongly coupled to the stratospheric circulation, as its abundances are largely determined by transport, especially in the lower stratosphere. In turn, stratospheric ozone itself affects the circulation via changes in radiative heating and temperature gradients (see **Box 5-4**). In previous Assessments, the effects of stratospheric ozone on circulation have been studied in the context of long-term depletion and recovery trends. Updates on the impact of ozone trends on circulation, with particular emphasis on the emerging signal from the Montreal Protocol since the early 2000s, are provided in *Section 5.3.2.2*.

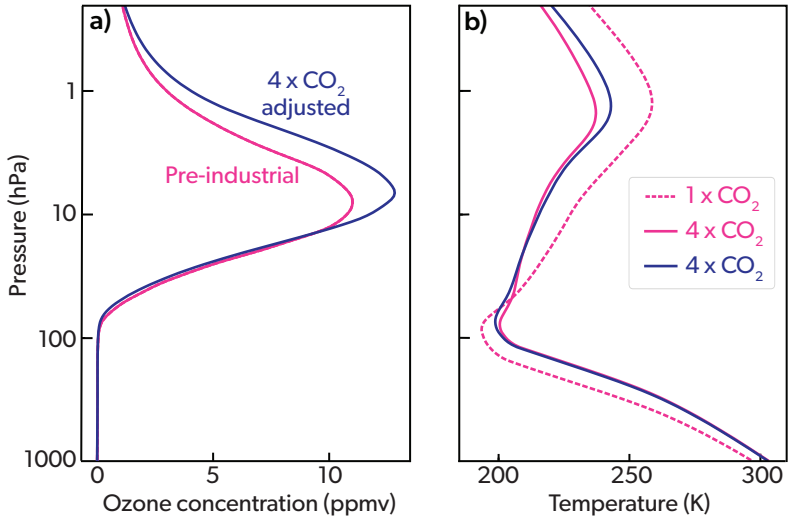

Figure 5-10. Stratospheric ozone feedback on temperature changes simulated by a simple 1-D radiative convective equilibrium model. Vertical profile of *(left)* tropical mean zonal mean ozone for preindustrial climate (pink) and for 4xCO_2 (blue), and *(right)* resulting temperature profiles from the model for preindustrial climate (pink dashed), and for 4xCO_2 forcing when prescribing the preindustrial ozone profile (pink) or the 4xCO_2 ozone profile (blue). [Adapted from Dacie et al., 2019.]

Since the last Assessment, new work has provided evidence that interannual variations in ozone may affect stratospheric circulation and its coupling to the troposphere, in much the same way as long-term trends. While interannual variations in ozone are largely driven by circulation variability, they are also affected by chemistry, in particular for polar ozone when ODS abundances are high (see *Chapter 4*). This radiative-dynamical-chemical coupling between ozone and circulation (see **Box 5-4**) can lead to ozone-induced surface impacts on sub-seasonal to interannual timescales, as assessed in *Section 5.3.2.1*. When integrated over longer timescales, the two-way ozone-circulation coupling also alters the circulation and climate response to long-term ozone trends, as discussed in *Section 5.3.2.2.1*.

5.3.2.1 Ozone-Circulation Coupling on Seasonal to Interannual Timescales

Stratospheric ozone has large variations on sub-seasonal to interannual timescales, particularly in springtime in the polar stratosphere (*Chapter 4*). Recent dramatic examples of this are the weakened springtime polar cap ozone depletion in the Antarctic in 2019 (Wargan et al., 2020) and the large depletion in the Arctic in 2020 (Lawrence et al., 2020). These interannual variations in polar cap ozone may further amplify stratospheric temperature variations and thus provide a coupling to the circulation, as described in **Box 5-4**. Given the relatively long timescales (i.e., 1–2 months) associated with stratosphere-troposphere coupling (Lim et al., 2018, 2019), ozone information could provide a source of sub-seasonal to seasonal predictability for surface climate (Son et al., 2013; Bandoro et al., 2014). However, the causality in the link between ozone extremes and surface climate to date is unclear and subject to debate, as downward coupling may come from stratospheric dynamics rather than ozone itself. In the 2018 Assessment, it was noted that interannual variations in Arctic and Antarctic ozone may be important for surface climate, but work remains to better quantify this connection. Here, we discuss the newest evidence in this field for the Antarctic (*Section 5.3.2.1.1*), the Arctic (*Section 5.3.2.1.2*), and the tropics (*Section 5.3.2.1.3*).

5.3.2.1.1 Antarctic

In previous Assessments, it was noted that there is a statistical link between Antarctic polar cap ozone in springtime and spring-to-summer surface climate, including widespread variations in precipitation and surface air temperature across the Southern Hemisphere (Son et al., 2013; Bandoro et al., 2014). However, interannual variations in springtime ozone are strongly coupled with the polar vortex through ozone transport and polar ozone depletion (see **Box 5-4, Figure 1**). Variations in the polar vortex are associated with changes in surface climate (Byrne and Shepherd, 2018; Lim et al., 2018; Thompson et al., 2005), making it difficult to tease apart the effect of ozone on the circulation from that of downward coupling from the polar vortex without such ozone effects (Karpechko, Maycock et al., 2018).

Since the last Assessment, the link between vortex variability, ozone, and surface climate on interannual timescales has been revisited using climate and sub-seasonal to seasonal (S2S) prediction models. The polar vortex weakening in spring 2019, which may have contributed to Australian New Year fires in the following summer (Lim et al., 2021), was also linked with the smallest ozone hole since the early 1980s (*Chapter 4*), but the role of ozone in these events is unclear. The observed surface signals following years with extreme ozone perturbations have been reproduced in CCMs but with mixed success. For example, one model reproduces the link between November ozone and Australian summer temperatures only when observed SSTs are prescribed, but it fails to capture the link when the ocean is coupled (Gillett et al., 2019). This hints at the role of observed SSTs, rather than ozone, in driving the ozone/SAM and ozone/surface temperature relationship in this model. Other CCMs reproduce the observed surface signals, even in ocean-coupled simulations (Damiani et al., 2020). Model biases, such as the too-long-lived SH polar vortex and/or excessive ENSO amplitudes, may hinder models' ability to simulate the interannual relationship reliably. Moreover, the observed correlation between November ozone and SH surface climate in summer is strong over the 1979–2012 period but becomes weak if a shorter period (1979–2004) is analyzed (Gillett et al., 2019), raising questions about the possible role of natural variability.

Lastly, the relative roles of ozone and dynamical downward coupling from the stratosphere are unclear, as none of these studies quantified the impact of interactive ozone on the ozone/surface climate link.

The causal impact of stratospheric ozone variations on surface climate has been quantified only for some extreme events in the SH stratosphere (Hendon et al., 2020). The major SSW of September 2002 was a unique event, with one of the largest disruptions of the stratospheric vortex on record, resulting in a strongly negative SAM (Thompson et al., 2005), and hot, dry conditions over Australia in October (**Figure 5-11**). In 2002, Antarctic ozone abundances in September were exceptionally high, thus offering a unique opportunity for a case study on the ozone/surface climate connection. Seasonal model forecasts using climatological ozone underpredict the SAM anomaly in October and, as a consequence, the regional signals over Australia (CTRL in **Figure 5-11**). Conversely, prescribing the observed ozone anomalies of 2002 in the ACCESS forecasting model leads to enhanced regional signals, which come closer to observations (difference between EXPR and CTRL in **Figure 5-11**). The signature originates from enhanced persistence of the stratospheric signal of the SSW event due to ozone-circulation coupling, which drives an enhanced negative SAM. This provides evidence for ozone effects on SH surface climate but only for a specific event (2002) and in one model. A similar sub-seasonal model prediction study is consistent with these results for the entire 2004–2020 period (Oh et al., 2022). Recently, it was suggested that high ozone abundances occurring during SSWs may initially lead to a positive tropospheric SAM in spring (a "fast response") and subsequently drive a negative SAM in early summer (a "slow response"; Jucker et al., 2022). While this hypothesis explains the observed behavior following the 2019 SSW event, it is inconsistent with observations for the 2002 SSW and remains to be tested for other cases and with more realistic configurations and other models.

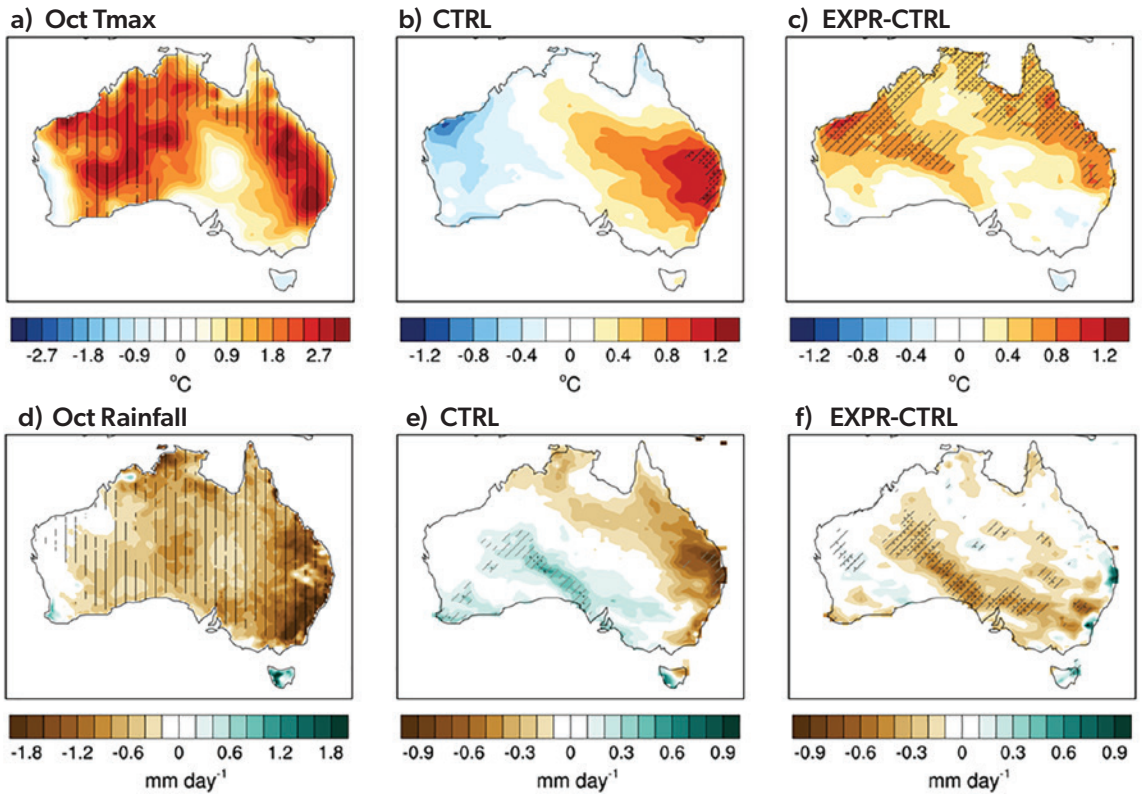

Figure 5-11. Effect of stratospheric ozone anomalies on surface climate in October 2002. Panels (a) and (d) show the observed anomaly in (a) maximum temperature (units: K) and (d) precipitation (units: mm/day) for October 2002. Panels (b) and (e) show the simulated temperature (b) and precipitation (d) anomalies, averaged across and 11 members ensemble of model simulations using the ACCESS forecasting model when fixed climatological ozone concentrations are used (CTRL). Panels (c) and (f) show the ensemble-mean difference in temperature (c) and precipitation (f) between model simulations where the observed 2002 ozone anomalies were used (EXPR) and the CTRL simulations (shown in panels b and d) using a fixed climatological ozone (CTRL). Hatching in (a) and (d) indicates where the October 2002 anomaly falls in the upper 20% and lower 20% tails, respectively, of the observed distribution for the period 1990–2012 (excluding 2002). Stippling and hatching in (b) and (e) indicate where the predicted values fall within the 5% and 10% tails, respectively, of the distribution based on the hindcast control simulations spanning the period 1990–2012 (excluding 2002). Stippling and hatching in (c) and (f) indicate where the null hypothesis of no difference between EXPR and CTRL is rejected at the 5% (10%) level based on resampling of the 11 ensemble members from the CTRL and EXPR for 2002. [Adapted from Hendon et al., 2020.]

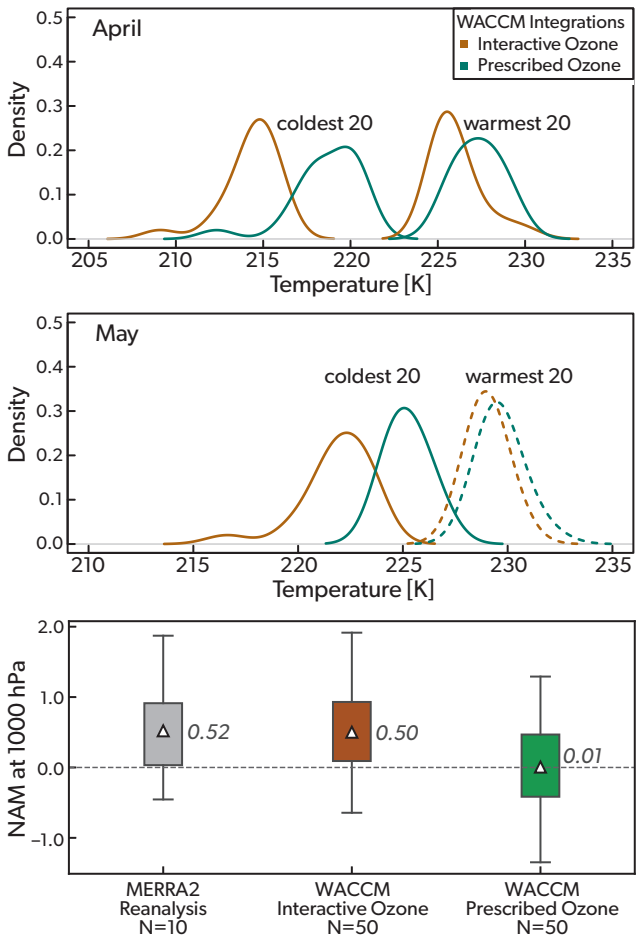

Figure 5-12. Impact of interannual Arctic ozone variations on stratospheric temperatures and tropospheric circulation. Probability distribution functions for (*top*) April and (*middle*) May monthly mean Arctic lower stratospheric (50 hPa) polar cap temperature for the coldest and warmest 20 years in perpetual year-2000 Whole Atmosphere Community Climate Model (WACCM) integrations with interactive chemistry (brown) and with prescribed climatological zonal mean ozone (green). Solid curves indicate a significant difference between the two integrations at the 95% level, while dashed curves indicate no significant difference. (*bottom*) Box plots of the Northern Annular Mode (NAM) index at 1000 hPa following winters with extreme ozone loss. The box plot shows the distribution of the mean NAM Index (20 - 90°N) at 1000 hPa in the month following the ozone minimum for the MERRA2 reanalysis (gray), WACCM integrations with interactive middle atmosphere chemistry (brown) and the WACCM integrations in which ozone chemistry is decoupled from the radiation scheme, i.e. the radiation scheme uses a prescribed climatological year-2000 zonal mean ozone field (green). In the bottom panel, in the WACCM integrations with prescribed ozone, chemistry is still calculated in the background so that ozone depletion events can be identified following the methodology in Friedel et al. (2022). Triangles and numbers indicate the mean NAM index in the month after the ozone minima, averaged over the 25% most extreme winters. The upper and lower edges of the boxes show the upper and lower quartile, the whiskers represent the maximum and minimum values of the respective distribution. [Top and middle panels adapted from Rieder et al., 2019, and bottom panel adapted from Friedel et al., 2022.]

Taken together, we assess that interannual variations in the severity of the Antarctic ozone hole likely affect SH surface climate by inducing variations in the tropospheric SAM (e.g., a weaker ozone hole and attendant weaker polar vortex result in a swing to the negative polarity of the SAM in the summertime, reflected by an equatorward shift of the mid-latitude westerlies). However, the robustness and causality of the ozone-SAM-surface link on interannual timescales, and thus the added value for predictability, is still unclear, especially on regional scales (Australia), where other modes of variability (e.g., the Indian Ocean Dipole and ENSO) can have a more direct impact. Climate models show only limited skill in reproducing the observed relationship, and the role of natural variability and/or model bias remains unclear.

5.3.2.1.2 Arctic

The previous Assessment noted that studies examining the influence of interannual variability in springtime Arctic stratospheric ozone on NH tropospheric and surface climate yielded mixed results. Some studies find no or limited influence (Cheung et al., 2014; Karpechko et al., 2014; Smith and Polvani, 2014) and others find a significant influence of springtime low Arctic ozone that resembles the positive phase of the North Atlantic Oscillation/Northern Annular Mode (NAO/NAM), but only in the presence of high ODS concentrations and/or sufficient chemical ozone loss (Smith and Polvani, 2014; Calvo et al., 2015; Ivy et al., 2017). The positive phase of the NAM is associated with a stronger and poleward-shifted jet stream, anomalous surface warming over Eurasia, anomalous surface cooling over Greenland and northeastern Canada, and anomalously high precipitation over northern Europe. Since the previous Assessment, a number of studies linking late–20th century Arctic springtime ozone variability and NH surface climate have been published (Xie et al., 2018; Ma et al., 2019; Stone et al., 2019; Ma and Xie, 2020; Maleska et al., 2020; Stone et al., 2020; Xia et al., 2021). Yet isolating any direct influence of ozone anomalies from that of stratospheric circulation anomalies and stratosphere-troposphere coupling remains a challenge as ozone and circulation are inherently coupled via both transport and chemistry (see **Box 5-4**; Fusco and Salby, 1999; Randel et al., 2002; Tegtmeier et al., 2008; Rieder et al., 2014; de la Cámara et al., 2018; Haase and Matthes, 2019; Harari et al., 2019; Oehrlein et al., 2020; Hong and Reichler, 2021).

New modeling evidence supports a significant correlation between Arctic springtime ozone anomalies and polar cap surface air pressure, but this correlation becomes insignificant when adjusted for stratospheric circulation anomalies (Harari et al., 2019). Consistent with this result, another modeling study found that the composite difference in sea level pressure between low and high Arctic springtime ozone years during the 1985–2005 period projected almost entirely onto the NAM, underscoring the dominant role of large-scale circulation in linking ozone extremes to surface climate (Maleska et al., 2020).

The above studies (Harari et al., 2019; Maleska et al., 2020), however, do not directly isolate the contribution of potential coupling between ozone and large-scale dynamics, and recent work comparing simulations with and without interactive middle-atmosphere chemistry in the presence of late–20th century ODS concentrations has highlighted the importance of this coupling for both NH stratospheric and tropospheric climate (Rae et al., 2019; Haase and Matthes, 2019; Rieder et al., 2019; Romanowsky et al., 2019; Oehrlein et al., 2020; Friedel et al., 2022; see also **Box 5-4**). For example, cold extremes in Arctic polar lower-stratospheric temperature are significantly colder in a model simulation with interactive chemistry than in a simulation with prescribed ozone (**Figure 5-12** top and middle panel; Rieder et al., 2019). This suggests that ozone-circulation coupling is important for NH stratospheric climate. Recent modeling work in which the radiative effects of ozone are decoupled from ozone itself provides evidence that ozone-circulation coupling in the stratosphere can have a significant impact on tropospheric and surface climate via stratosphere-troposphere coupling (**Figure 5-12** bottom panel; Friedel et al., 2022; see also **Box 5-4**): under year-2000 ODS concentrations, ozone-circulation coupling leads to a significantly more positive NAM at the surface (1000 hPa) for years with low ozone in spring. Although there is clear evidence of this coupling, the magnitude and significance of its contribution may be sensitive to statistical sampling and the configuration of the CCM (Haase and Matthes, 2019; Oehrlein et al., 2020; Friedel et al., 2022). Finally, analysis of model output during the 1985–2005 period suggests that rapid adjustments in high clouds associated with localized extreme chemical ozone loss and a decrease in upper-tropospheric stability may also contribute to the link between springtime ozone and surface climate (Maleska et al., 2020; Xia et al., 2021).

The extent to which the representation of ozone variability in forecast models leads to improved skill is mixed. One study found that when a new prognostic ozone scheme is interactive with radiation, there is improved skill in the North Atlantic region for both medium- and long-range hindcasts due to an improvement in the representation of stratosphere-troposphere coupling (Monge-Sanz et al., 2022). In contrast, another study examining forecasts of individual extreme ozone loss years (1997, 2011, and 2020) found that the forecasts do not consistently capture the observed link between low ozone extremes and near-surface temperatures in the Northern Hemisphere (Rao and Garfinkel, 2020). The 2020 extreme ozone depletion event (Lawrence et al., 2020) was an exception, however, and the subsequent Eurasian surface warming was reasonably well predicted 2–3 weeks in advance (Rao and Garfinkel, 2020; Rao and Garfinkel, 2021c; Xia et al., 2021).

In summary, based on substantial new research since the previous Assessment, our determination is that although the influence of interannual variability in Arctic springtime ozone on NH surface climate is primarily driven by the large-scale circulation, there is evidence for a non-negligible contribution from ozone-circulation coupling during the late 20th century when high ODS concentrations contribute to chemical ozone loss (Calvo et al., 2015; Maleska et al., 2020; Friedel et al., 2022; **Box 5-4**). Uncertainty remains in the quantification of the contribution of this coupling to NH surface climate.

5.3.2.1.3 Tropics

Since the last Assessment, a few studies have shown that ozone-circulation coupling may affect the variability in the tropical stratosphere under steady-state preindustrial conditions. One study (Yook et al., 2020) simulated that interactive ozone chemistry increases the variability in tropical stratospheric temperatures in one global model by a factor of two (**Figure 5-13a**). The increased variability is primarily driven by tropical upwelling and its effects on ozone at interannual timescales; ozone in turn feeds back onto temperature via LW and SW heating, with the latter dominating near the TTL region. Due to the long radiative timescales in this region, ozone not only affects the variance but also imparts additional memory from one month to the next (**Figure 5-13b**). Most remarkably, this study shows that models

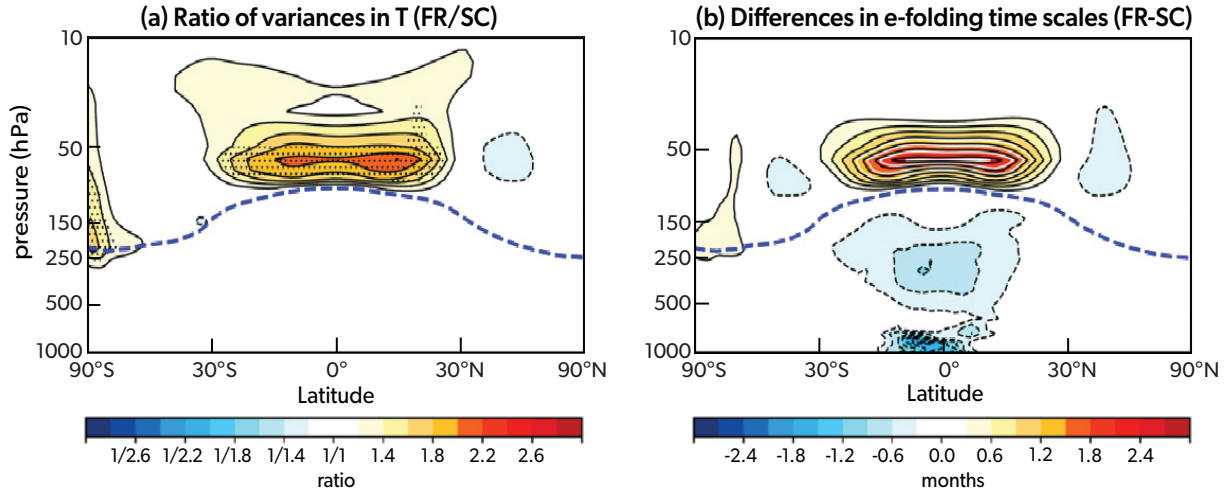

Figure 5-13. Impact of ozone variations on temperature variability. (a) Ratio of zonal mean temperature variance between a WACCM simulation with interactive ozone (FR) and one with specified ozone (SC), and (b) the difference in the e-folding timescale of temperature (in months) between the two simulations (FR-SC). [Adapted from Yook et al., 2020.]

with prescribed ozone systematically underestimate the temperature variance in this region. One caveat about this study is that an artificial QBO is nudged in this model. This may dampen the impact of ozone coupling on the tropical upwelling and thus interfere with the effects of ozone on temperature variance. In a model with an internally generated QBO, interactive ozone leads to a slight prolongation in the QBO period (from 29 to 31 months) and an intensification of the QBO amplitude (DallaSanta et al., 2021; see *Section 5.2.6.2*). These results are consistent with the notion of ozone-induced enhanced temperature variance in the tropical stratosphere and are also consistent with previous work using other models with an internally generated QBO and interactive ozone (Shibata and Deushi, 2005), as well as with simulations with prescribed ozone (Bushell et al., 2010), although the differences in the temperature variance are much smaller and only marginally significant.

Overall, there is new evidence since the last Assessment for effects of interannual variability in ozone, not only at high latitudes but also in the tropical regions. However, these results remain limited to a few individual model studies and are a subject of ongoing analysis.

5.3.2.2 Impact of Ozone Trends on the Tropospheric Circulation and Surface Climate

The linkages between SH ozone depletion and tropospheric circulation trends were first noted in observations in 2002 (Thompson and Solomon, 2002). The effects of stratospheric ozone losses on surface climate were simulated in fixed sea surface temperature experiments in the early 2000s (Sexton, 2001; Kindem and Christianson, 2001), and in a coupled climate model a few years later (Gillett and Thompson, 2003). The anticipated linkages between ozone recovery and the surface flow were explored in coupled chemistry-climate models in 2008 (Son et al., 2008). Since that time, the role of stratospheric ozone depletion and recovery in tropospheric climate has been reproduced in a large number of numerical experiments (e.g., Son et al., 2010; Thompson et al., 2011; Seviour et al., 2017, and references therein). Recently produced historical reconstructions of the SAM suggest that the positive trend in the SAM during the decades prior to 2000, which is attributed to ozone depletion, is unprecedented in the last millennia and thus falls well outside the range of natural climate variability (Fogt and Marshall, 2020).

The 2010, 2014, and 2018 Assessments provided extensive reviews of the signatures of ozone depletion and recovery in the tropospheric circulation. As of the 2018 Assessment, the state of our understanding was the following:

1. Observations indicate that the SH tropospheric jets shifted poleward and the SAM shifted toward its positive polarity over the period of large SH stratospheric ozone depletion, from roughly 1980 to 2000.
2. The largest trends in the SH tropospheric climate occurred during the austral summer months.
3. Climate simulations indicate that the bulk of the observed SH trends were due to Antarctic ozone depletion.
4. Climate simulations suggest that ozone recovery will lead to a reversal of the SH trends that arose from Antarctic ozone depletion.
5. Antarctic ozone depletion and recovery-related trends in the tropospheric circulation have widespread impacts on SH surface climate.
6. There is little evidence for similarly robust linkages between stratospheric ozone depletion and surface climate in the Northern Hemisphere.

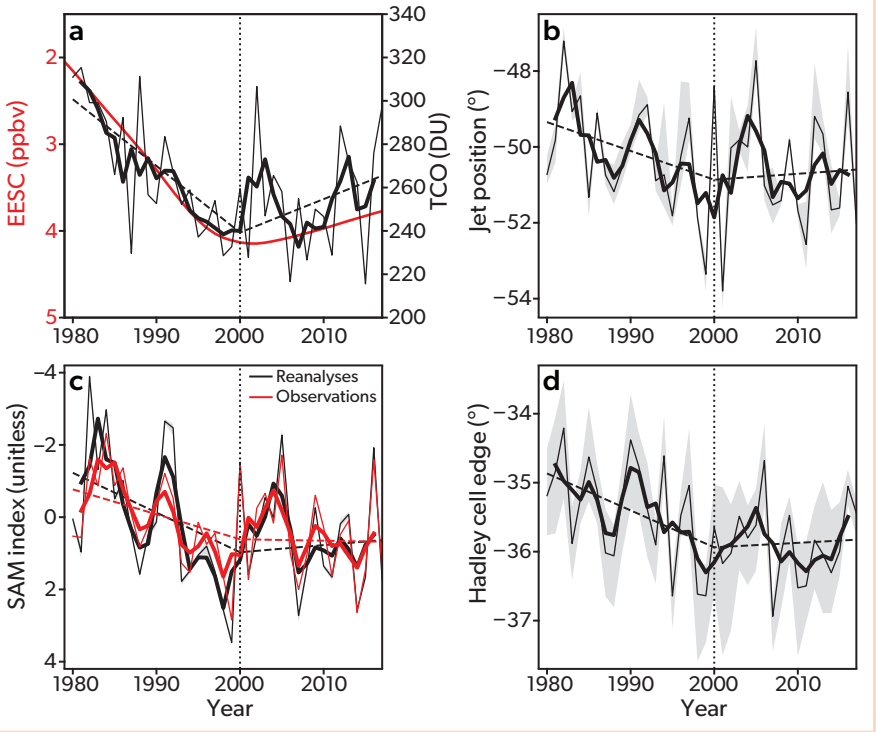

Figure 5-14. Observed total ozone and Southern Hemisphere tropospheric circulation. Time series of (a) EESC (note the inverted left y axis) for polar winter conditions and Antarctic total column ozone (TCO; right axis) averaged over September through November, with the latter measured by SBUV (in DU). (b) position of the SH mid-latitude jet in reanalysis data in DJF, (c) the SAM index (note the inverted y axis) as derived from reanalysis data and from station observations in DJF, (d) position of the edge of the Hadley cell in reanalysis data in DJF. Renalysis data are averages across four products (ERA-I, JRA-55, MERRA2-ana and MERRA2-asm). The thin lines are unsmoothed quantities, and thick lines represent centered three-year smoothed values. Two piecewise continuous linear trend lines for the unsmoothed data (dashed lines) are drawn for the periods 1980–2000 and 2000–2017. [From Banerjee et al., 2020.]

Since the 2018 Assessment, the availability of longer data records has permitted identification of the signature of ozone recovery in tropospheric circulation trends. **Figure 5-14a** (from Banerjee et al., 2020) summarizes the long-term behavior of SH stratospheric ozone during the period of large ozone losses and the onset of recovery. Antarctic stratospheric ozone concentrations indicate signs of recovery since roughly 2000 (Solomon et al., 2016; Stone et al., 2018; *Chapter 4*). However, from **Figure 5-14a** it is also clear that identifying the trend in ozone since 2000 (dashed line) is complicated by the large interannual variability during this period (thin black line). The SAM index exhibits trends similar to those found in total column ozone (**Figure 5-14c**): 1) the large decreases in ozone concentrations prior to year 2000 are accompanied by increases in the SAM index and 2) the onset of recovery following year 2000 is accompanied by no clear trend in the SAM index. The changes in the SAM index are accompanied by consistent changes in the position of the mid-latitude jet and the edge of the Hadley cell (**Figure 5-14 b** and **d**).

The signature of ozone recovery in circulation trends is clearest in the changes in circulation trends between the period of large ozone depletion and the onset of recovery (Banerjee et al., 2020; Zambri et al., 2021). For example, **Figure 5-15** shows that the period prior to 2001 was marked by significant decreases in polar ozone during November (panel a), polar stratospheric temperatures during November and December (panel b), and polar geopotential height during November and December (panel c; see the caption for data sources). It was also marked by changes in the upper-tropospheric circulation in December and January, consistent with a trend toward the positive polarity of the SAM (panel d). As noted in both Banerjee et al. (2020) and Zambri et al. (2021), the period following 2001 (i.e., the onset of recovery) was not marked by significant trends in any of those fields. The differences in trends between the periods prior to and after 2001 are significant at stratospheric levels and on the fringe of significance at upper-tropospheric levels (**Figure 5-15**; Zambri et al., 2021).

Thus, observations to date indicate that:

1. consistent with the anticipated effects of ozone recovery, the observed SH springtime ***stratospheric*** circulation trends since ~2001 are not statistically significant, but the changes in the circulation trends between the pre- and post-2001 periods are statistically significant (Banerjee et al., 2020; Zambri et al., 2021); and
2. the attendant changes in SH summertime ***tropospheric*** circulation trends are consistent with the changes found in the stratosphere (Banerjee et al., 2020; Zambri et al., 2021) but are on the fringe of significance (Zambri et al., 2021).

It is worth emphasizing that the results shown in **Figures 5-14** and **5-15** extend only through 2018 and thus do not include the strong polar vortex and large ozone losses of SH spring 2020 and spring 2021.

The inferred influence of changes in ozone trends on changes in tropospheric circulation trends is supported by experiments run on coupled chemistry-climate simulations and prescribed-ozone climate model simulations (Banerjee et al., 2020; Zambri et al., 2021; see *Section 5.4*). As noted in previous Assessments, the influence of increasing greenhouse gases on the SAM will likely oppose the effects of ozone recovery on the SAM during austral summer (e.g., Arblaster and Meehl, 2006; Thompson et al., 2011, Figure 3). The experiments in Banerjee et al. (2020) provide further numerical support for this hypothesis.

Various dynamical and radiative mechanisms have been proposed to explain how ozone-induced changes in the stratospheric flow are communicated to the surface. These are summarized in the 2018 Assessment. As of this writing, the relative importance of the various proposed forcing mechanisms remains unclear and is a key focus of current research.

There is novel evidence that ozone-induced trends in the SAM exhibit longitudinal variations that have potentially important implications for the surface impacts of ozone depletion (Waugh et al., 2020). However, as concluded in Chapter 10 of IPCC AR6 (Doblas-Reyes et al., 2021), internal climate variability and uncertainty is too strong at the regional scale to robustly attribute past regional surface climate change to specific anthropogenic forcings such as stratospheric ozone depletion. Likewise, Mindlin et al. (2021) highlight the large uncertainties in future regional climate change that arise from the uncertainties in the circulation response.

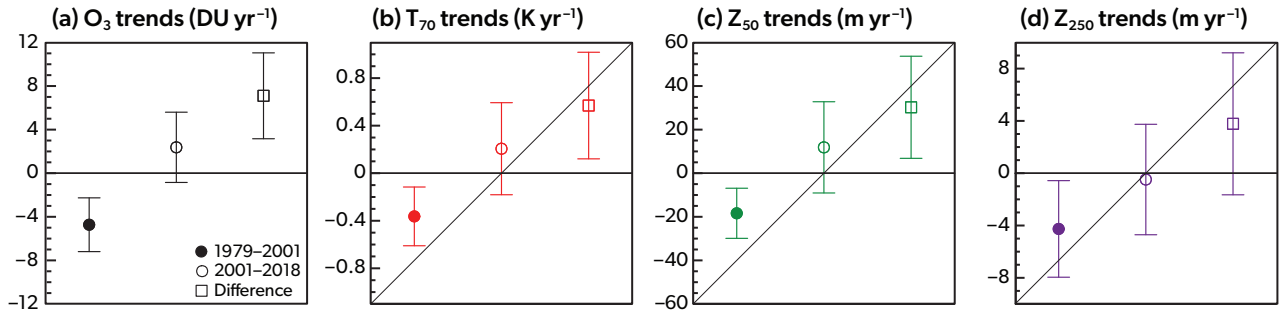

Figure 5-15. Trends in Southern Hemisphere high-latitude (65–90°S) ozone and circulation. (a) November ozone (DU yr^{-1}), (b) November–December 70 hPa temperature (K yr^{-1}), (c) November–December 50 hPa geopotential height (m yr^{-1}), and (d) December–January 250 hPa geopotential height (m yr^{-1}) for 1979–2001 (filled circles), 2001–2018 (open circles), and the difference (squares). Error bars represent the adjusted 95% confidence intervals of the trends. Ozone data are from the TOMS/OMI merged ozone dataset; temperature and geopotential height are from ERA5. [From Zambri et al., 2021.]

As was the case in the 2018 Assessment, there are no detectable NH surface impacts of long-term Arctic ozone changes over the past ~4 decades. However, for individual years with low springtime Arctic ozone, new model evidence indicates that the ozone anomalies induce changes to the stratospheric circulation, with subsequent surface impacts (as discussed in *Section 5.3.2.1.2*).

Comparison with the IPCC AR6. Since the 2018 Assessment, the relative roles of ozone depletion and greenhouse gases in future climate change have been quantified in CMIP6 climate change simulations (Mindlin et al., 2021; Lee et al., 2021). Simulations from the CMIP6 archive support conclusions from earlier analyses (e.g., Arblaster and Meehl, 2006; McLandress et al., 2010; Thompson et al., 2011, Figure 3); namely, that the anticipated influence of ozone recovery on the SH circulation during austral summer is opposed by the anticipated influence of increasing GHGs on the SH circulation. This opposing influence on SH summer circulation changes is consistent with their scenario dependency by the end of the century, as reported in Chapter 4 of the Working Group I contribution to IPCC AR6 (Lee et al., 2021), which stated, "there is *high confidence* that in high-emissions scenarios (SSP3-7.0 and SSP5-8.5) the SAM becomes more positive in all seasons, while in the lowest scenario (SSP1-1.9) there is a robust decrease in austral summer." This finding is further supported by recent work (Revell et al., 2022), which in addition highlights the dependency of changes in the summer circulation jets on the evolution of stratospheric ozone in the models, in particular emphasizing the important role of consistency of stratospheric ozone with the underlying GHG scenario.

However, the IPCC AR6 report also notes that the "contribution [to the SAM] from ozone forcing evaluated with the four available models is not significant (Fig. 3.34b)" (Figure 3.34 and associated text in Eyring et al., 2021). Taken at face value, the above statement appears to contradict two decades of numerical evidence that reaches the opposite conclusion, including evidence derived from CMIP5 (Barnes and Polvani, 2013) and summarized in the past three Ozone Assessments (WMO, 2010, 2014, 2018).

There are two aspects of the evidence presented in Chapter 3 of the Working Group I contribution to IPCC AR6 (Eyring et al., 2021) that contribute to the discrepancies between their results (see Figure 3.34 of Eyring et al., 2021) and results reported here and in the last three Assessments (WMO, 2010, 2014, 2018):

1. The SAM index used in Eyring et al. (2021) is based on the algebraic difference between sea level pressure (SLP) at two discrete latitudes (40°S and 65°S) that lie very close to the nodes—not the centers of action—of the SAM in the SLP field. Variations in the SAM are better captured by indices that account for the hemispheric-scale structure of the pattern.
2. Eyring et al. (2021) summarizes simulated trends in the SAM from two periods: 1979–2019 and 2000–2019. Neither period is well positioned to isolate the signature of ozone depletion on surface climate. The former period samples not only the era of large stratospheric ozone depletion but also the era of the onset of recovery. The latter period does not sample the era of large stratospheric ozone depletion.

The summary remarks in Chapter 3 of the Working Group I contribution to IPCC AR6 (Eyring et al., 2021) align more closely with the conclusions reported here. In this case, AR6 states "While ozone depletion contributed to the trend from the 1970s to the 1990s (*medium confidence*), its influence has been small since 2000, leading to a weaker summertime SAM trend over 2000–2019 (*medium confidence*)". Our assessment agrees with the general conclusions in the above statement but would assign higher confidences given the evidence reviewed here and in past WMO reports (WMO, 2010, 2014, 2018).

5.3.2.2.1 Impact of Two-Way Ozone-Circulation Coupling on Antarctic/Southern Hemisphere Trends

As discussed in *Section 5.3.2.1.2* and **Box 5-4**, the nature of how ozone and, consequently, coupling between ozone and circulation are represented in climate models has been an ongoing area of research. In many climate models, ozone concentrations are prescribed as a monthly and zonal mean forcing, such as the recommended IGAC/SPARC ozone fields used in the CMIP5 model runs (Eyring et al., 2013; Cionni et al., 2011). Prescribing monthly and zonal mean ozone rather than interactively computing it neglects important aspects of ozone variability and trends, including zonal asymmetries in ozone and high temporal frequency events, specifically the evolution of the seasonal ozone hole in the Southern Hemisphere (Crook et al., 2008; Gillett et al., 2009; Waugh et al., 2009; Neely et al., 2014; Haase et al., 2020), as well as ozone-circulation couplings (Rae et al., 2019; Haase et al., 2020; Ivanciu et al., 2021; Lin and Ming, 2021; see also *Section 5.3.2.1.2*). As such, the recommended ozone forcing for CMIP6 now includes zonal asymmetries (Checa-Garcia et al., 2018), although many models continue to use a zonal mean ozone forcing (Keeble et al., 2021).

In the previous Assessment, calculations comparing the CCMI and CMIP5 multi-model ensembles suggested that the representation of ozone (interactive in the CCMI ensemble but largely prescribed in the CMIP5 ensemble) did not affect the simulation of SH tropospheric circulation trends in December–January–February (DJF, i.e., austral summer; Son et al., 2018). In contrast, a recent analysis of CMIP6 historical DJF SAM trends noted a greater influence of ozone depletion relative to greenhouse gases in simulations with interactive ozone chemistry than those without (Morgenstern, 2021). Large systematic model differences, varying ensemble sizes, and differences in which ozone forcing is used and how it is prescribed within such multi-model ensembles contribute to the ambiguity of these results (Keeble et al., 2021). Previous single-model studies have shown that the representation of ozone can have a significant effect on SH circulation variability and trends, particularly in the stratosphere, and some studies also show an effect in the troposphere (Crook et al., 2008; Gillett et al., 2009; Waugh et al., 2009; Neely et al., 2014).

Since the last Assessment, several single-model studies have reexamined the effect of ozone-circulation coupling on summertime SH circulation trends. The studies compared ensembles of CCM integrations with either fully interactive ozone or prescribed ozone and found that both zonally asymmetric ozone and ozone-circulation coupling in the interactive integrations contribute to significantly colder and stronger SH polar cap stratospheric temperature and zonal wind trends, respectively (Haase et al., 2020; Ivanciu et al., 2021; Lin and Ming, 2021). It was suggested that zonal wind-induced wave dissipation and/or wave dissipation via ozone radiative damping may be playing an important role when ozone chemistry is interactive and may be amplified

in the presence of high concentrations of ODSs (Lin and Ming, 2021). The effect of interactive ozone on tropospheric trends, however, was ambiguous, with one study showing no effect over the 1969–1998 period (Haase et al., 2020) and the other using a different climate model showing significantly larger trends in tropospheric zonal wind over the 1958–2013 period (Ivanciu et al., 2021).

In summary, our assessment is that two-way ozone-circulation coupling has a robust influence on SH stratospheric circulation trends and amplifies the circulation response to ODS-forced ozone changes. Thus, model studies using prescribed ozone fields might underestimate those effects. Whether the amplified stratospheric circulation response also influences the tropospheric circulation trends has not yet been robustly shown.

5.3.3 Impacts of Ozone Changes on the Oceans and the Cryosphere

5.3.3.1 Ocean Impacts

Winds over the Southern Ocean play a fundamental role in driving the ocean circulation. Over the period ~1980–2000, summer trends in the SAM and in westerly winds have been mainly attributed to ozone depletion; since 2000, summer trends in the SAM have not been significant (*Section 5.3.2.2*). Westerly wind stress over the Southern Ocean drives equatorward Ekman transport, resulting in mixed-layer divergence and upwelling at high latitudes (on the poleward side of the westerly wind jet) and convergence and downwelling at mid-latitudes (on the equatorward side of the westerly wind jet; Hall and Visbeck, 2002; Sen Gupta and England, 2006). A positive SAM trend implies a poleward shift and/or strengthening of the surface westerly wind stress and thus a poleward shift and/or strengthening in the regions of mixed-layer divergence and convergence. Observations of the upper 2000 m of the Southern Ocean have shown a broadscale warming and freshening (Karpechko, Maycock et al., 2018; Rintoul, 2018). The last Assessment reported a substantial role for ozone depletion, through its influence on surface wind stress, in recent trends of the Southern Ocean circulation during austral summer. The warming of the upper ocean at 30–60°S is, however, mainly driven by an increasing abundance of greenhouse gases, with ozone depletion playing a secondary role (Karpechko, Maycock et al., 2018).

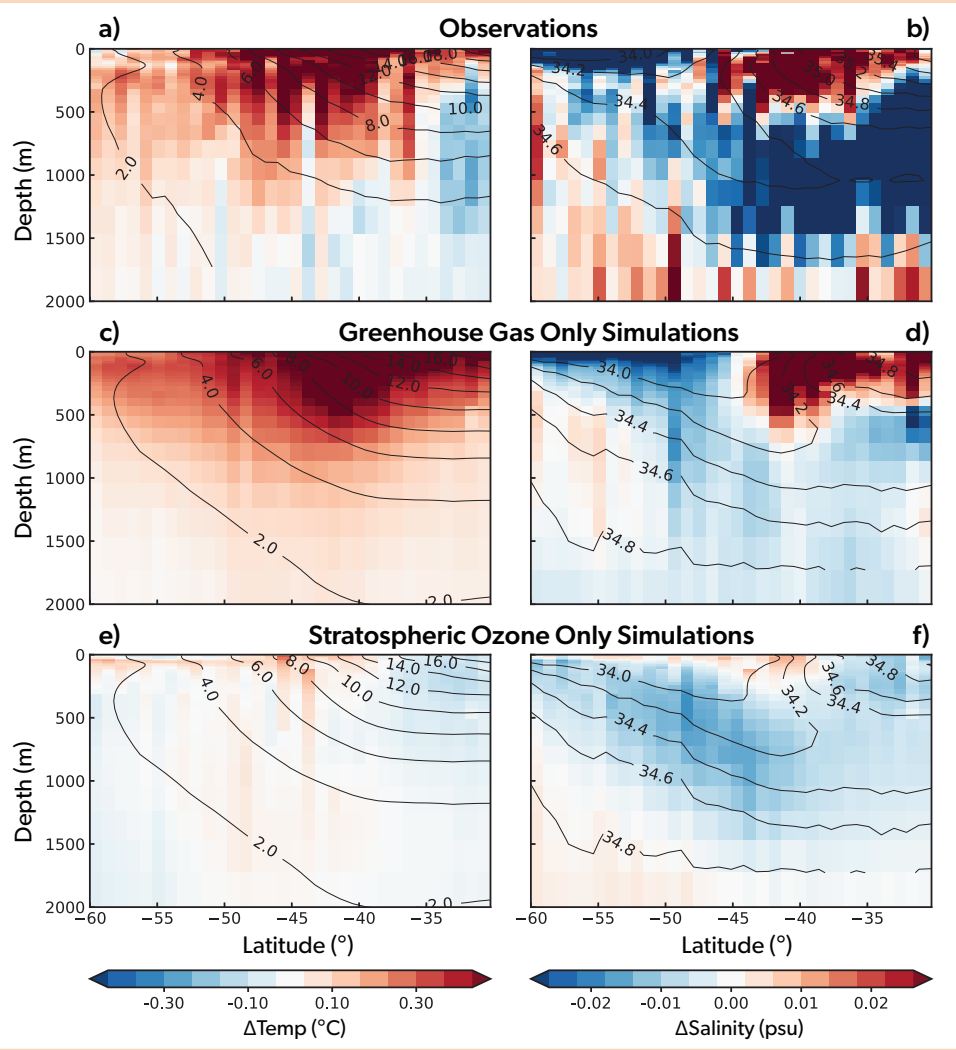

Figure 5-16. Observed and simulated changes in Southern Ocean temperature and salinity. Zonal mean (a, c, e) temperature, and (b, d, f) salinity, from (a, b) observations, (c, d) ensemble means of the CanESM2 greenhouse-gas-only simulations, and (e, f) stratospheric-ozone-only simulations. Anomalies represent the difference between the 2006–2015 mean and the mean over a 1950–1980 base period. Black contours show the climatological temperature and salinity. The CanESM2 fields (c, d, e, f) are subsampled to match observational coverage and scaled to best match the observations using scaling factors of (c) 0.70, (d) 0.74, (e) 1.77, and (f) 0.70. [Adapted from Swart et al., 2018.]

Recent studies continue to show long-term broadscale warming and freshening in the upper 2000 m of the Southern Ocean south of 35°S since the 1950s (**Figure 5-16**; Rintoul, 2018; Swart et al., 2018), since the 1980s (Bronselaer et al., 2020), and since the 1990s (Auger et al., 2021). Recent modeling evidence suggests that poleward-intensifying winds contribute to the broadscale warming and freshening (Bronselaer et al., 2020). A period of rapid warming in the upper 2000 m of the Southern Ocean was observed over the period 2003–2012, but the pace of warming has slowed down since, with decadal variations in warming rates related to variations in the SAM and the Interdecadal Pacific Oscillation (Wang et al., 2021). Despite the broadscale warming of the upper 2000 m of the ocean south of ~35°S, SSTs have cooled at higher latitudes (south of ~50°S) since the 1980s (Armour et al., 2016; Haumann et al., 2020) and the 1990s (Auger et al., 2021; see **Figure 5-17a**). The high-latitude surface cooling has been accompanied by a freshening and linked to increased sea ice (Morrow and Kestenare, 2017; Fan et al., 2014).

Since the last Assessment, further evidence suggests that increasing greenhouse gases are the primary driver of Southern Ocean subsurface warming and freshening (**Figure 5-16**; Swart et al., 2018; Hobbs et al., 2021), with stratospheric ozone depletion playing a secondary or lesser role in driving warming (Swart et al., 2018; Li et al., 2021; Liu et al., 2022). Physically, surface fluxes of heat and freshwater are found to be the primary driver of changes, with wind-driven changes in ocean transport playing a secondary role (Swart et al., 2018; Armour et al., 2016). The proportion of Southern Ocean changes that are attributed to stratospheric ozone depletion varies across modeling studies (Sigmond et al., 2011; Solomon et al., 2015; Swart et al., 2018; Hobbs et al., 2021; Li et al., 2021; Liu et al., 2022). While previous work found 30% of both temperature and salinity changes across the Southern Ocean to be due to increasing ODSs and the resulting ozone depletion (Solomon et al., 2015), an ozone contribution to salinity changes was not formally detected in recent studies (Swart et al., 2018; Hobbs et al., 2021). This is possibly because of the different study periods considered, because greenhouse gas and ozone fingerprints are similar for salinity and thus difficult to separate (Swart et al., 2018), because the salinity response to anthropogenic forcings across the Southern Ocean is model dependent (Hobbs et al., 2021), and/or because of different ozone forcing configurations across the studies. A recent modeling study separating the combined influences of stratospheric ozone depletion and increased tropospheric ozone from the influence of stratospheric ozone depletion only reports that both contribute to the interior Southern Ocean warming over the period 1955–2000, with increased tropospheric ozone making a larger contribution to the overall Southern Ocean heat content change (Liu et al., 2022). Based on the dominance of greenhouse gas forcing over the historical period (Solomon et al., 2015; Swart et al., 2018; Hobbs et al., 2021) and despite the projected mitigating effects of ozone recovery on wind-driven ocean changes (Sigmond et al., 2011; Wang et al., 2014; Ivanciu et al., 2022), it is expected that greenhouse gases will continue to dominate and the Southern Ocean will continue to warm and freshen over coming decades (Swart et al., 2018; Ivanciu et al., 2022).

In a variety of model simulations, the high-latitude Southern Ocean exhibits a two-timescale SST response to a hypothetical step change in the SAM such as occurs in abrupt ozone-hole experiments (when ozone is abruptly changed from pre-ozone

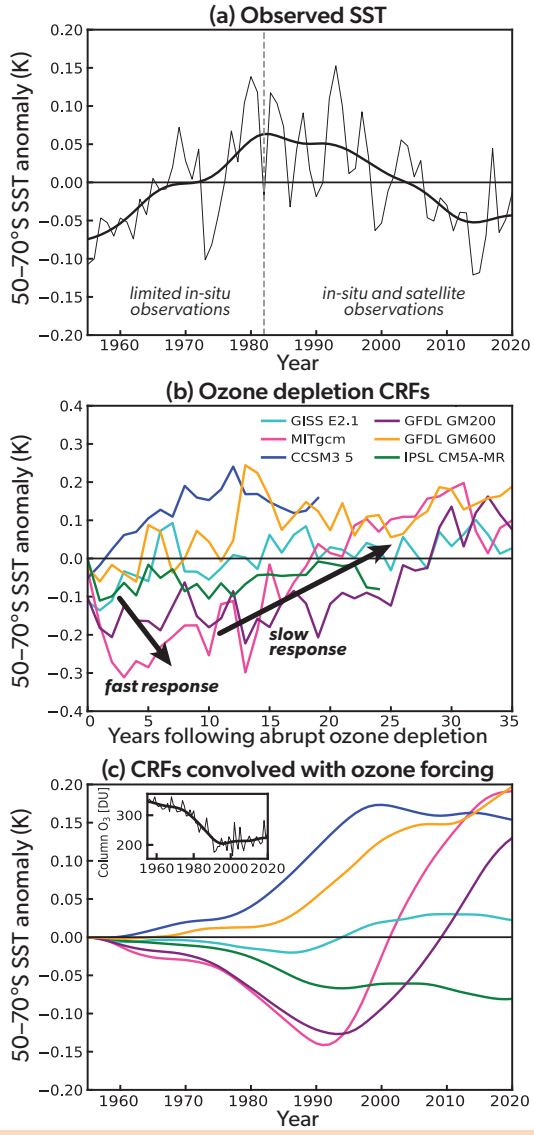

Figure 5-17. Observed and simulated evolution of high-latitude SST. (a) Observed 50–70°S average SST anomaly time series from the HadISST dataset. Anomalies are calculated relative to the 1955–2020 mean, and the bold line shows the 20-year running mean smoothed with a Hanning window. (b) Ensemble-mean time series of annual-mean SST anomaly averaged over 50–70°S from six different climate models simulating the climate response functions (CRFs) to abrupt ozone-hole conditions. The idealized ozone forcing reveals two timescales to the SST response—an initial cooling (the fast response) followed by an eventual warming (the slow response)—as indicated by large arrows; however, there is a large spread in responses across models. (c) Convolution of the anomalous SST response to abrupt ozone-hole conditions in (b) with time-evolving ozone forcing, as shown in the insert (October-mean 60–90°S column ozone from the WACCM chemistry-climate model). The convolved SST time series in (c) differ from the observed SST time series in (a), suggesting ozone depletion is unlikely to have been the primary driver of the observed high-latitude SST cooling since ~1980. [Adapted from Seviour et al., 2019.]

depletion levels to ozone-hole levels; **Figure 5-17b**; Ferreira et al., 2015; Seviour et al., 2019). The two-timescale SST response was described in detail in the last Assessment (Karpechko, Maycock et al., 2018). The fast SST response to strengthened and/or poleward-shifted westerly winds occurs over months to years and is characterized by increased northward Ekman transport, causing SST cooling (negative SST anomalies in **Figure 5-17b**); the slow response occurring over years to decades is characterized by upwelling of relatively warm water from below the mixed layer, causing an SST warming (positive SST anomalies in **Figure 5-17b**; Marshall et al., 2014). Despite additional abrupt ozone-hole simulations since the last Assessment, the timescale of transition from initial cooling to subsequent warming remains poorly constrained (Seviour et al., 2019), leading to continued uncertainty in the SST response to time-evolving ozone depletion (**Figure 5-17c**). Furthermore, since the last Assessment high-resolution modeling has found that mesoscale eddies oppose anomalous wind-driven upwelling, preventing long-term warming (Doddridge et al., 2019). Thus, the spread in model behavior in the fast and slow responses to the SAM are likely related to the parameterization and/or resolution of eddies in the different models (Seviour et al., 2019; Doddridge et al., 2019). Even when biases in model climatology are taken into account, the current model evidence for the expected SST response to observed ozone depletion (initial cooling followed by longer-term warming) suggests that ozone depletion is unlikely to have been the primary driver of the observed high-latitude surface cooling since the late 1970s (see **Figure 5-17a**; Seviour et al., 2019).

In summary, since the last Assessment, the Southern Ocean (35–60°S, 0–2000 m depth) overall has continued to warm and freshen (Rintoul, 2018; Swart et al., 2018). Two formal detection and attribution studies have identified increasing greenhouse gases as the primary driver of the Southern Ocean warming and freshening (Swart et al., 2018; Hobbs et al., 2021), with the role of ozone depletion in driving ocean warming identified as secondary (Swart et al., 2018). Further modeling evidence suggests that ozone depletion has not been the primary driver of the observed high-latitude surface cooling (Seviour et al., 2019). However, this conclusion is based on coarse-resolution models; high-resolution modeling suggests that mesoscale eddies could influence the long-term temperature response to wind changes (Doddridge et al., 2019). Overall, our confidence in the understanding and attribution of the observed high-latitude surface cooling is low. Simulations with eddy-resolving ocean models to examine the response of the Southern Ocean to increased westerly winds would be necessary to reduce this uncertainty in the response in high-latitude ocean circulation to ozone depletion.

5.3.3.2 Sea Ice Impacts

A number of studies summarized in previous Assessments have investigated the influence of the ozone hole on Antarctic sea ice trends. Over the satellite period, total Antarctic sea ice coverage has shown a modest increasing trend; however, this total increase masks both regional (Hobbs et al., 2015) and temporal (Meehl et al., 2016; Eayrs et al., 2021) variations, and lacks statistical significance (Gulev et al., 2021). The 2014 and 2018 Assessments reported that a variety of climate model simulations that isolated the impact of stratospheric ozone depletion from that of increasing greenhouse gases all simulated decreasing Antarctic sea ice in response to ozone depletion, in contrast to the observed increasing trend in sea ice.

Since the last Assessment, there is further modeling evidence that ozone depletion has not driven the observed long-term changes in Antarctic sea ice. CMIP5 models capture the observed relationship between the SAM and sea ice extent during austral summer, but the SAM explains only 15% of interannual variability in sea ice extent during austral fall—and thus that SAM trends and ozone depletion are not the primary drivers of the observed sea ice increase over the satellite era (Polvani et al., 2021). In an assessment of the two-timescale response, Antarctic sea ice extent is shown to decline monotonically in response to abrupt ozone-hole conditions in five out of six models (Seviour et al., 2019), consistent with previous modeling studies (Holland et al., 2017), but contrasting with the weak observed sea ice changes (Handcock and Raphael, 2020).

Confidence in modeling studies involving Antarctic sea ice remains low because coupled models run under full historical forcings (CMIP5 and CMIP6) simulate a decline in Antarctic sea ice that contrasts with observed changes (as assessed in Eyring et al., 2021). Over the period 1979–2018, Antarctic sea ice area trends in CMIP6 models are marginally consistent with observed trends (Roach et al., 2020). Some recent modeling evidence suggests that internal variability alone could lead to a multi-decadal increase in Antarctic sea ice similar to observed trends (Zhang et al., 2019; Singh et al., 2019), but other lines of evidence suggest that internal variability cannot account for the modeled/observed discrepancy (Hobbs et al., 2015; Chemke and Polvani, 2020). Evidence suggests that the stronger-than-observed decline in Antarctic sea ice in coupled climate models is influenced by biased surface heat flux trends (Chemke and Polvani, 2020) and biased thermodynamics (Blanchard-Wrigglesworth et al., 2021). The Southern Ocean warm bias in CMIP models (Beadling et al., 2020) has been linked to a cloud-based shortwave radiation bias in CMIP5 models (Hyder et al., 2018). Overall, confidence in attributing changes in Antarctic sea ice is limited because of climate model deficiencies in capturing the observed Antarctic sea ice trends over the satellite era (Eyring et al., 2021).

A retreat of Antarctic sea ice unprecedented in the historical satellite record was observed during austral spring and early summer of 2016 and was discussed in the last Ozone Assessment. This sudden retreat of sea ice has been linked to changes in the SAM, which became strongly negative in November (Turner et al., 2017; Schlosser et al., 2018), with easterly wind anomalies contributing to the record low sea ice (Wang et al., 2019b; Eayrs et al., 2021). The near-record negative SAM during November has been linked to stratospheric polar vortex weakening and associated higher ozone (Wang et al., 2019b), tropical convective conditions (Meehl et al., 2019), and internal variability (Stuecker et al., 2017; Purich and England, 2019).

The last Assessment concluded that ozone-hole changes cannot explain recent trends in Antarctic sea ice, and new studies support this conclusion. As in the last Assessment, confidence in the role of the ozone hole on Antarctic sea ice trends remains low, because of the limited number of ozone-only simulations available for analysis and because the majority of climate models still do not reproduce observed Antarctic sea ice trends since 1979 due to Southern Ocean thermal and sea ice model biases. This lack of ability to simulate past sea ice trends inhibits the assessment of the role of future ozone recovery in future sea ice trends.

5.3.3.3 Ocean Carbon

The Southern Ocean accounts for about 40% of the global oceanic uptake of anthropogenic CO_2 (Khatiwala et al., 2009; Frölicher et al., 2015). As described in *Section 5.3.3.1*, the westerly winds over the Southern Ocean influence the meridional overturning circulation and thus the outgassing and uptake of carbon from and to the ocean. The westerly wind strengthening implied by a positive SAM trend enhances both the high-latitude upwelling, increasing outgassing, and the mid-latitude downwelling, increasing uptake (Le Quéré et al., 2007; Lovenduski et al., 2007). In the last Assessment, the availability of longer observational datasets and improved analysis techniques confirmed earlier studies showing a carbon sink slowdown between the 1980s and early 2000s (Le Quéré et al., 2007), and also revealed a reinvigoration of the carbon sink between 2002 and 2012 (Landschützer et al., 2015; Munro et al., 2015).

Since the last Assessment, further observation-based evidence suggests that the Southern Ocean carbon sink varies substantially on decadal timescales (Gruber et al., 2019; Keppler and Landschützer, 2019). A weakening of the carbon uptake during the 1990s, initially attributed to the ozone hole (Le Quéré et al., 2007; Forster, Thompson et al., 2011), has been linked to the positive SAM that enhanced the high-latitude upwelling of CO_2 during this period (DeVries et al., 2017; Gruber et al., 2019). After ~2000, the carbon uptake rebounded, increasing the global ocean carbon sink strength back to that expected based on atmospheric CO_2 levels (DeVries et al., 2017; Gruber et al., 2019). A subsequent weakening of the carbon sink since ~2011 has been observed (Gruber et al., 2019; Keppler and Landschützer, 2019).

In agreement with the last Assessment, there is little new evidence suggesting that long-term changes in ozone are affecting the Southern Ocean carbon sink. Evidence suggests that decadal atmospheric circulation changes impact the net strength of the Southern Ocean carbon sink. While the positive SAM during the 1990s has been linked with a short-term slowdown of the carbon sink (DeVries et al., 2017; Gruber et al., 2019), suggesting a possible ozone influence during this decade, evidence based on upscaled observations suggests that the total Southern Ocean carbon uptake south of 35°S over 1982–2016 has not been altered considerably by the positive SAM trend (Keppler and Landschützer, 2019). The observed decadal variations in the Southern Ocean carbon sink may be due to natural variability (Gruber et al., 2019).

5.3.3.4 Ice Sheet and Shelf Impacts

The influence of the ozone hole on Antarctic ice sheets and shelves has not been covered in detail in previous Assessments. Observational evidence suggests that the Antarctic ice sheet has only recently started responding to climate change (Noble et al., 2020). Antarctic surface mass balance shows no clear trends over the satellite era but exhibits large variability (Rignot et al., 2019), with extreme precipitation events making a large contribution to annual precipitation accumulation over the continent and determining the interannual variability (Turner et al., 2019). Trends in total mass balance since 1979 have been driven by ice discharge (Rignot et al., 2019), with recent observations over 2003–2019 showing the West Antarctic ice sheet losing mass while the East Antarctic ice sheet exhibits large variability (Smith et al., 2020). Overall, the Antarctic ice sheet lost mass between 1992 and 2017 (Gulev et al., 2021).

New evidence suggests that stratospheric ozone depletion could potentially have influenced the net balance of the Antarctic ice sheet, but this is highly uncertain. First, modeling evidence suggests that stratospheric ozone depletion and/or ODSs drove increased snow accumulation over Antarctica over the late 20th century, leading to an increase in the surface mass balance (Previdi and Polvani, 2017; Lenaerts et al., 2018; Chemke et al., 2020). However, observations show large variability and no clear trends in Antarctic surface mass balance (Rignot et al., 2019). Second, and conversely, various lines of evidence suggest that a positive SAM (i.e., a poleward shift of the mid-latitude westerlies) could be associated with increased transport of warm off-shelf waters onto the Antarctic shelf at certain locations (Spence et al., 2014; Jenkins et al., 2016), providing heat for basal melting and increasing ice sheet mass loss (Shepherd et al., 2004; The IMBIE Team, 2018). One study utilizing a regional ocean-ice model forced with anthropogenic forcings and tropical Pacific variability simulated on-shelf ocean warming and increased basal melt in the Amundsen Sea, likely due to the westerly wind trend over the shelf break (Naughten et al., 2022). However, there is a lack of evidence directly linking stratospheric ozone changes to ice shelf changes, and attributing ocean-mediated changes is highly challenging due to both observational and modeling limitations around the Antarctic margins. Our assessment concludes that there is much uncertainty over the influence of stratospheric ozone changes on ice sheets and shelves.

5.4 CLIMATE IMPACTS OF THE MONTREAL PROTOCOL

5.4.1 Realized Climate Impacts of the Montreal Protocol

The length of the observational time series over the period of relative stabilization of global ozone concentrations (see *Chapter 3*) allows, for the first time, an assessment of the realized impacts of the Montreal Protocol on climate based on observations and an attribution of these impacts to the Montreal Protocol using targeted model integrations. As discussed in *Section 5.3.2.2*, recent studies of spring and summertime SH circulation trends have detected a pause or change in sign of the trends between the late 20th century and the early 21st century (Banerjee et al., 2020, Zambri et al., 2021; Mindlin et al., 2021). Specifically, a pause in the summertime trends in SH tropospheric circulation, such as the SAM, zonal-mean zonal winds, jet position, and Hadley cell edge, have been detected in reanalyses for the 2000–2017 period (**Figure 5-14**; Banerjee et al., 2020). In the zonal-mean zonal wind, the pause is attributed to a "tug-of-war" between two climate forcings: a stabilization and recovery of Antarctic stratospheric ozone due to the Montreal Protocol and global warming due to greenhouse gases. This attribution is made by comparing reanalyses (**Figure 5-18a–c**) to model integrations where the ODS and stratospheric ozone signal is extracted in a multi-model ensemble of chemistry-climate models (**Figure 5-18d–f**) for two time periods, an ozone depletion period of 1980–2000 and an ozone recovery period of 2000–2017. The role of greenhouse gases is diagnosed using other single-forcing integrations (**Figure 5-18g–i**). A pause in the summer SAM index trend is also evident in the CMIP6 models for the historical time period, and the attribution of this pause to the reduction in ozone-depleting substances in recent decades is supported by

multiple linear regression models (Morgenstern, 2021; Mindlin et al., 2021). As highlighted in *Section 5.3.2.2* and in previous Assessments, the impact of ozone depletion on the summertime SAM and SH surface climate trends has been significant, and a pause in these trends may have implications for near- and long-term future SH climate change (Mindlin et al., 2021). The duration of the pause in the SH tropospheric circulation trends will depend on the tug-of-war described above, i.e., the pace and magnitude of future global warming (Barnes et al., 2014; Mindlin et al., 2021; Sections 4.3.3.1 and 4.5.1.6 in Lee et al., 2021) and the pace of ozone recovery, which has the potential to be delayed by unexpected CFC-11 emissions (Dhomse et al., 2019; Fleming et al., 2021), ODS emissions from natural sources (Fang et al., 2019), nitrous oxide emissions (Fang et al., 2019), and enhanced wildfire smoke injection in a warming climate (Solomon et al., 2022; Bernath et al., 2022).

As noted in previous Assessments, "world-avoided" integrations have been used to evaluate the impact of the Montreal Protocol on climate. The world-avoided scenario is an idealized counterfactual scenario and typically assumes that uncontrolled ODSs would have increased at a rate of 3–3.5% per year in the absence of the Montreal Protocol based on expected growth in gross domestic product (GDP) and market analysis (e.g., Prather et al., 1996; Velders et al., 2007; Newman et al., 2009; Garcia et al., 2012). While ODS emissions were growing faster than this before the Montreal Protocol was signed (Table 2.5-1 in WMO, 1989), a sustained rate of emissions of ODSs of 3–3.5% per year should be viewed as only one of many possible world-avoided scenarios, which could also include scenarios with varying assumptions about future GDP growth. For the purposes of this Assessment, the world-avoided scenario allows for the examination of the sensitivity of climate to increasing ODS emissions and the accompanying ozone loss. Comparing world-avoided integrations to those including controls on ODS emissions, previous Assessments have reported that a steady increase in ODS emissions would have led to approximately double the amount of global warming by the end of the 21st century (Velders et al., 2007; Garcia et al., 2012). Here, world-avoided integrations are used to assess new evidence of the impact of the Montreal Protocol on present-day climate change.

The comparison of historical and RCP scenario integrations to world-avoided integrations provides an estimate of the impact of the Montreal Protocol on surface climate over the past several decades. Based on model simulations from three studies (Young et al., 2021; Goyal et al., 2019; Virgin and Smith, 2019), we assess that controls on ODS emissions under the Montreal Protocol have avoided at present-day (average over years 2015–2024) approximately 0.1–0.2°C global surface warming (with an ensemble weighted mean of 0.17°C ± 0.06°C[2]) and 0.2–0.6°C Arctic surface warming (ensemble weighted mean of 0.45°C ± 0.23°C). Using additional integrations with only world-avoided changes in stratospheric ozone included, the avoided warming is attributed primarily to the stabilization and slight decrease in ODS concentrations and is offset somewhat by cooling due to stratospheric ozone loss (Goyal et al., 2019; consistent with *Section 5.3.1.1* and **Box 5-3**).

In summary, our assessment is that the implementation of the Montreal Protocol has had a significant effect on the climate over the past several decades in two notable ways: the stabilization of the Antarctic ozone hole has led to a pause in SH circulation trends, and the rapid decline in ODS emissions has mitigated GHG-driven global warming.

5.4.2 Future Climate Impacts of the Montreal Protocol

As in previous Assessments, world-avoided integrations are also used to quantify avoided future climate change. While there has been limited new literature on the topic since the previous Assessment, based on three new studies (Goyal et al., 2019; Virgin and Smith, 2019; Young et al., 2021) we assess that by the mid-21st century (average over years 2041–2060) the Montreal Protocol controls would result in the avoidance of approximately 0.5–1.0°C global surface warming (ensemble weighted mean of 0.79°C ± 0.24°C). The globally averaged RF from the years 2005–2065 is approximately double in world-avoided scenarios due to uncontrolled emissions of ODSs compared to the RCP4.5 scenario (Virgin and Smith, 2019). This work supports findings of previous studies that compared the world-avoided scenario to the A1B and B2 SRES scenarios (Velders et al., 2007) or the RCP4.5 scenario (Garcia et al., 2012). Avoided Arctic warming is primarily due to reductions in ODS emissions rather than the mitigation of stratospheric ozone loss (Goyal et al., 2019; see also *Section 5.3.1.2*); however, recent work suggests that the relationship between Arctic warming and polar cap-averaged radiative forcing in the world-avoided scenario appears to be complex due to the unique combination of high ODS concentrations and substantial stratospheric ozone loss (Virgin and Smith, 2019). Arctic polar cap-averaged positive radiative feedbacks (i.e., long-wave cloud feedbacks) and atmospheric heat flux convergence rather than polar cap-averaged radiative forcing alone play a key role in contributing to world-avoided Arctic warming (Virgin and Smith, 2019).

Recent work also confirms that in the absence of the Montreal Protocol, by the mid-21st century a warmer planet would have resulted in an enhanced hydrological cycle, with substantial increases in precipitation in the polar regions and a further decline in Arctic sea ice extent relative to the RCP8.5 scenario (Goyal et al., 2019; Wu et al., 2013).

As reported in Chapter 5 of the previous Assessment (Karpechko, Maycock et al., 2018), the phasedown of HFCs under the Kigali Amendment to the Montreal Protocol will also have an impact on global climate, as HFCs are potent GHGs. In *Chapter 2* of this Assessment, it is shown that this phasedown is already underway due to national and regional regulations, with HFC emissions over the 2017–2019 period being 20% lower than the WMO (2018) HFC baseline scenario (*Section 2.4.1*). Under the WMO (2018) baseline scenario, it was estimated that HFCs would contribute 0.3–0.5 K to global mean surface warming by 2100 (Section 2.3.1 of Montzka, Velders et al. 2018). New estimates based on current policies project that HFCs would contribute 0.14–0.31 K by 2100, and with the additional provisions of the Kigali Amendment this is reduced to approximately 0.04 K (*Sections 2.4.2* and *2.4.3*; Velders et al., 2022). Independent modeling analysis confirms that HFCs have a significant climate

1 The uncertainty bounds include uncertainty due to natural variability and model uncertainty, based on three independent model studies with 5, 3, and 1 ensemble member, respectively.

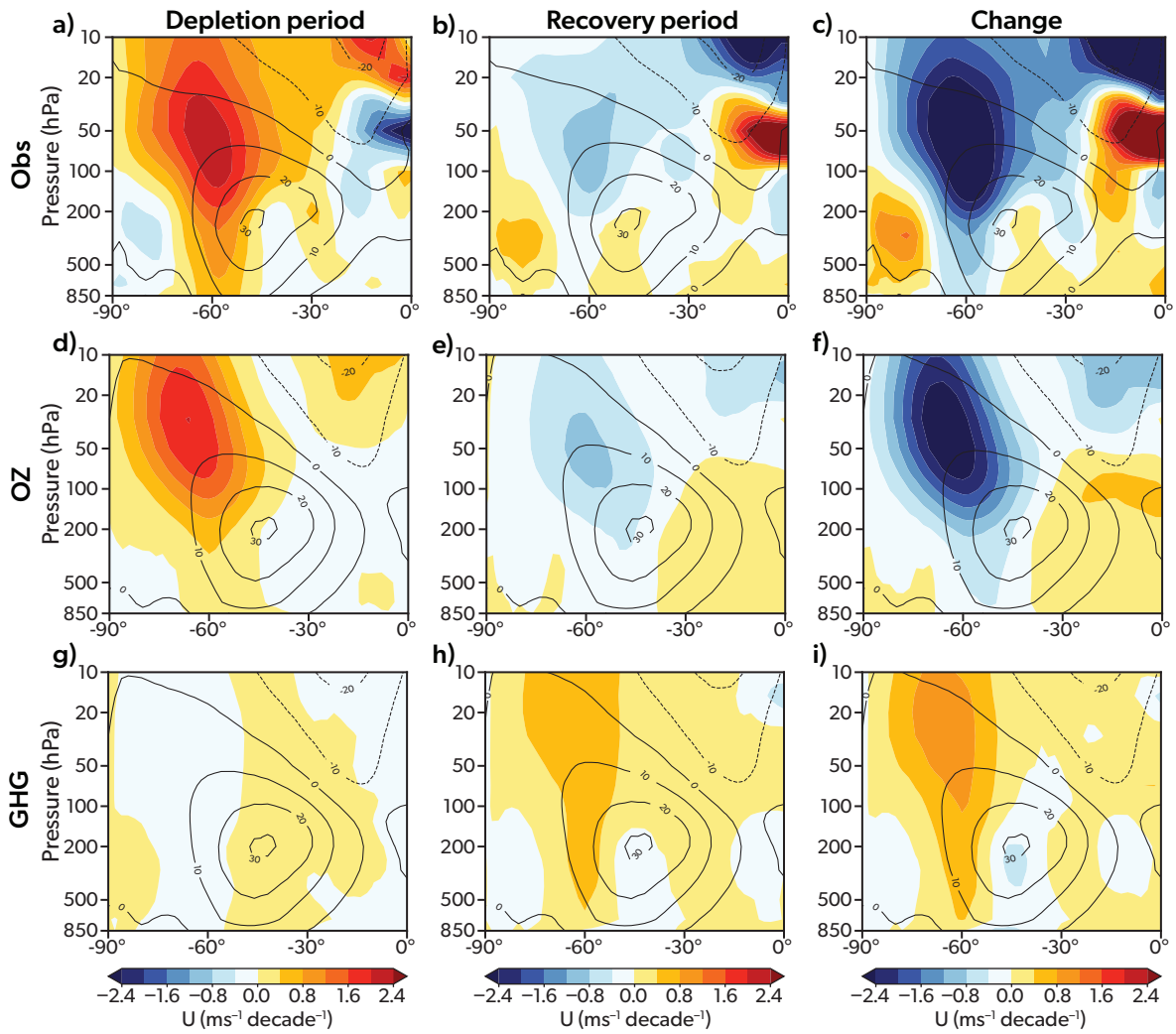

Figure 5-18. Observed and simulated Southern Hemisphere zonal average zonal wind trends. The top row shows an average of four reanalysis data products (ERA-Interim, JRA-55, MERRA2-ana, MERRA2-asm), and the middle and bottom rows show an ensemble mean of CCMVal-2 and CCMI chemistry-climate model integrations. Latitude-altitude cross sections of zonal average zonal wind trends (color shading) for DJF are shown for the depletion period *(left column)*, recovery period (*middle column*), and the difference between the two *(right column)*. Fingerprints are shown for the simulations with single forcings by (d–f) ozone (OZ) and (g–i) GHGs. For illustrative purposes, the contours show the climatologies (in m s^{-1}; for d–i, the climatologies are for the ALL-forcing integrations; for f and i, the climatology is over the entire change period). [Adapted from Banerjee et al., 2020.]

impact. Earth system model integrations following the RCP8.5 scenario with uncontrolled HFC emissions compared with a world-avoided scenario in which HFCs were not introduced indicate that HFC emissions contribute approximately 0.1 K to global warming from the 1970s to the 2050s (Goyal et al., 2019), in agreement with the previous Assessment. In addition, consistent with a previous analysis using a 2-D (latitude-pressure) interactive chemistry, radiation, and dynamics model (Hurwitz et al., 2015), a new 3-D chemistry-climate model study with prescribed SSTs shows that by the end of the century, uncontrolled HFC emissions following both the lower and upper limit of the previous scenarios of Velders et al. (2014) lead to warming of the tropical upper troposphere and lower stratosphere and a strengthening of the Brewer-Dobson circulation (BDC) but a weakening of the Hadley cell relative to a zero HFC concentrations scenario (Dupuy et al., 2021).

Moving beyond the surface climate, a recent study found that the Montreal Protocol has significantly protected the terrestrial carbon sink by preventing a decrease in net primary production associated with UV damage of plants (Young et al., 2021). Using output from world-avoided simulations, it is estimated that atmospheric carbon dioxide concentrations may have been 18–37% higher by 2100 (**Figure 5-19a**) if controls on ODS emissions under the Montreal Protocol had not protected the terrestrial biosphere from UV damage, contributing to an additional 0.5–1.0 K to globally averaged surface warming by 2100 (**Figure 5-19b**). The large range of estimates reflects the uncertainty in the plant response to UV. Protection of the terrestrial carbon sink is a

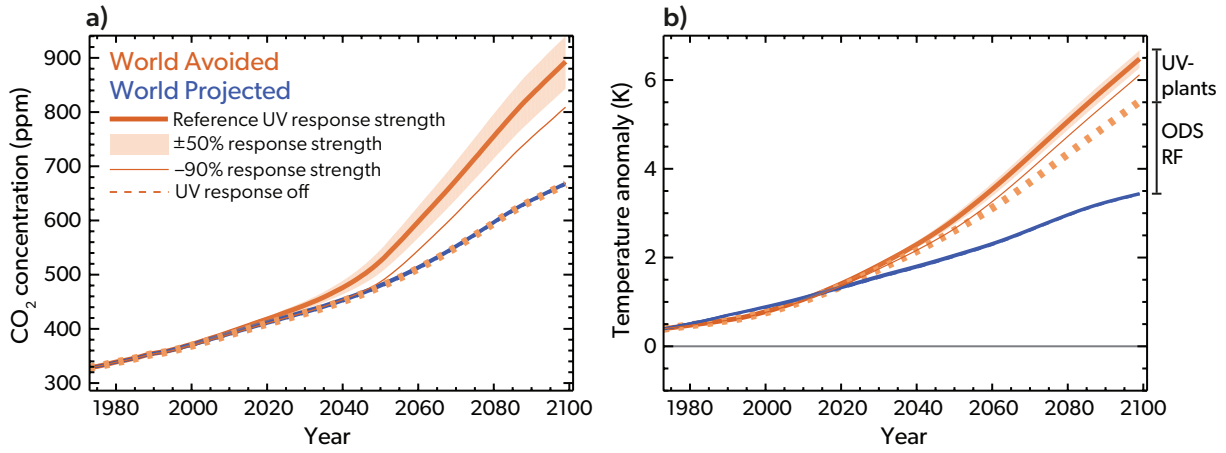

Figure 5-19. The effect of UV-driven changes in vegetation (UV-plants) on atmospheric CO_2 and surface temperature. (a) Time series of atmospheric CO_2 concentrations and (b) anomalies in global-mean surface air temperature for a regular future projection (World Projected, blue; approximately RCP6.0) and a World Avoided projection (World Avoided, orange), estimated using a carbon cycle model. The dashed orange lines are results from a World Avoided projection with the 'UV response off', the shading around the thick orange lines indicates the range of the responses from the simulations with 50% and 150% UV response strength (with respect to the reference UV case) and the thin orange lines show the effect of reducing the UV response strength to –90%. The labelled ranges in (b) indicate the World Avoided warming above the World Projected that results from direct radiative forcing of the additional CFCs and the additional CO_2 from the UV-driven damage to plants and their ability to act as a carbon store. [Adapted from Young et al., 2021.]

previously unexamined climate benefit of the Montreal Protocol.

With respect to projected ozone recovery and its impact on climate, earlier sections of this chapter have assessed recent literature, including *Section 5.2.4* on the BDC, *Section 5.2.6* on stratospheric winds, *Section 5.3.2.2* on SH tropospheric circulation and surface climate, and *Section 5.3.3* on the Southern Ocean and Antarctic sea ice.

Since the previous Assessment, a number of studies have examined the impact of the recent unexpected emissions of CFC-11 from 2012 to 2018 (*Section 1.2.1*) on ozone recovery, and these are assessed in *Section 3.4.4* (for global ozone) and *Section 4.5.3.2* (for polar ozone). With respect to the climate impacts of these emissions, simulations with a chemistry-climate model with prescribed sea surface temperatures show that continued CFC-11 emissions at a rate of 72.5 Gg $year^{-1}$ from 2017 to 2100 lead to a significant delay in global and Antarctic ozone recovery of 1 and 33 years, respectively, compared to the WMO (2018) baseline scenario (Fleming et al., 2021). In addition, a significant dynamical response in the SH stratosphere was identified, including a cooling of the polar lower stratosphere of 1.5 K and a corresponding acceleration of the polar vortex, with a delay in the vortex breakdown by four days and a decrease in the age of air by 0.1 year averaged over the 2080–2100 period (Fleming et al., 2021).

Overall, our assessment confirms that the Montreal Protocol has significantly contributed to the mitigation of anthropogenic global warming through the controls on ODS emissions. New evidence suggests an additional effect through the protection of the terrestrial carbon sink from harmful UV radiation. Potential future unexpected emissions of controlled ODSs and the associated ozone loss will have a small but significant impact on stratospheric temperature and circulation trends in the Southern Hemisphere.

REFERENCES

Abalos, M., L. Polvani, N. Calvo, D.E. Kinnison, F. Ploeger, W.J. Randel, S. Solomon, New insights on the impact of ozone-depleting substances on the Brewer-Dobson circulation, ***J. Geophys. Res. Atmos.***, ***124***, 2435–2451, doi:10.1029/2018JD029301, 2019.

Abalos, M., C. Orbe, D.E. Kinnison, D. Plummer, L.D. Oman, P. Jöckel., O. Morgenstern, R.R. Garcia, G. Zeng, K.A. Stone, and M. Dameris, Future trends in stratosphere-to-troposphere transport in CCMI models, ***Atmos. Chem. Phys.***, ***20***, 6883–6901, doi:10.5194/acp-20-6883-2020, 2020.

Abalos, M., N. Calvo, S. Benito-Barca, H. Garny, S.C. Hardiman, P. Lin, M.B. Andrews, N. Butchart, R.R. Garcia, C. Orbe, D. Saint-Martin, S. Watanabe, and K. Yoshida, The Brewer-Dobson circulation in CMIP6, ***Atmos. Chem. Phys.***, ***21*** (17), 13,571–13,591, doi:10.5194/acp-21-13571-2021, 2021.

Adcock, K.E., P.J. Fraser, B.D. Hall, R.L. Langenfelds, G. Lee, S.A. Montzka, D.E. Oram, T. Röckmann, F. Stroh, W.T. Sturges, B. Vogel, and J.C. Laube, Aircraft-based observations of ozone-depleting substances in the upper troposphere and lower stratosphere in and above the Asian summer monsoon, ***J. Geophys. Res. Atmos.***, ***126*** (1), e2020JD033137, doi:10.1029/2020JD033137, 2021.

Akritidis, D., A. Pozzer, and P. Zanis, On the impact of future climate change on tropopause folds and tropospheric ozone, ***Atmos. Chem. Phys.***, ***19***, 14,387–14,401, doi:10.5194/acp-19-14387-2019, 2019.

Anstey, J.A., T.P. Banyard, N. Butchart, L. Coy, P.A. Newman, S. Osprey, and C. Wright, Prospect of increased disruption to the QBO in a changing climate, ***Geophys. Res. Lett.***, ***48*** (15), e2021GL093058, doi:10.1029/2021GL093058, 2021.

Anstey, J.A., S.M. Osprey, J. Alexander, M.P. Baldwin, N. Butchart, L. Gray, Y. Kawatani, P.A. Newman, and J.H. Richter, Impacts, processes and projections of the quasi-biennial oscillation. ***Nat Rev Earth Environ 3,*** 588–603, doi.org/10.1038/s43017-022-00323-7, 2022.

Aquila, V., W.H. Swartz, D.W. Waugh, P.R. Colarco, S. Pawson, L.M. Polvani, and R.S. Stolarski, Isolating the roles of different forcing agents in global stratospheric temperature changes using model integrations with incrementally added single forcings, ***J. Geophys. Res. Atmos.,121***, 8067–8082, doi:10.1002/2015JD02384, 2016.

Arblaster, J.M., and G.A. Meehl, Contributions of external forcings to Southern Annular Mode trends, ***J. Clim.***, ***19*** (12), 2896–2905, doi:10.1175/JCLI3774.1, 2006.

Arblaster, J.M., N.P Gillett (Lead Authors), N. Calvo, P.M. Forster, L.M. Polvani, S.-W. Son, D.W. Waugh, and P.J. Young, Stratospheric ozone changes and climate, Chapter 4 in ***Scientific Assessment of Ozone Depletion: 2014***, Global Ozone Research and Monitoring Project–Report No. 55, World Meteorological Organization, 416 pp., Geneva, Switzerland, 2014.

Armour, K.C., J. Marshall, J.R. Scott, A. Donohoe, and E.R. Newsom, Southern Ocean warming delayed by circumpolar upwelling and equatorward transport, ***Nat. Geosci.***, ***9***, 549–554, doi:10.1038/ngeo2731, 2016.

Auger, M., R. Morrow, E. Kestenare, J.B. Sallee, and R. Cowley, Southern Ocean in-situ temperature trends over 25 years emerge from interannual variability, ***Nat. Commun.***, ***12***, 514, doi:10.1038/s41467-020-20781-1, 2021.

Ayarzagüena, B., L.M. Polvani, U. Langematz, H. Akiyoshi, S. Bekki, N. Butchart, M. Dameris, M. Deushi, S.C. Hardiman, P. Jöckel, A. Klekociuk, M. Marchand, M. Michou, O. Morgenstern, F.M. O'Connor, L.D. Oman, D. Plummer, L. Revell, E. Rozanov, D. Saint-Martin, J. Scinocca, A. Stenke, K. Stone, Y. Yamashita, K. Yoshida, and G. Zeng, No robust evidence of future changes in major stratospheric sudden warmings: a multi-model assessment from CCMI, ***Atmos. Chem. Phys.***, ***18***, 11,277–11,287, doi:10.5194/acp-18-11277-2018, 2018.

Ayarzagüena, B., A.J. Charlton-Perez, A.H. Butler, P. Hitchcock, I. Simpson, L.M. Polvani, N. Butchart, E.P. Gerber, L. Gray, B. Hassler, P. Lin, F. Lott, E. Manzini, R. Mizuta, C. Orbe, S. Osprey, D. Saint-Martin, M. Sigmond, M. Taguchi, E.M. Volodin, and S. Watanabe, Uncertainty in the response of sudden stratospheric warmings and stratosphere-troposphere coupling to quadrupled CO2 concentrations in CMIP6 models, ***J. Geophys. Res. Atmos.***, ***125*** (6), e2019JD032345, doi:10.1029/2019JD032345, 2020.

Baldwin, M.P., B. Ayarzagüena, T. Birner, N. Butchart, A.H. Butler, A.J. Charlton-Perez, D.I.V. Domeisen, C.I. Garfinkel, H. Garny, E.P. Gerber, M.I. Hegglin, U. Langematz, and N.M. Pedatella, Sudden stratospheric warmings, ***Rev. Geophys.***, ***59*** (1), e2020RG000708, doi:10.1029/2020RG000708, 2021.

Ball, W.T., J. Alsing, J. Staehelin, S.M. Davis, L. Froidevaux, and T. Peter, Stratospheric ozone trends for 1985–2018: sensitivity to recent large variability, ***Atmos. Chem. Phys.***, ***19*** (19), 12,731–12,748, doi:10.5194/acp-19-12731-2019, 2019.

Bandoro, J., S. Solomon, A. Donohoe, D.W.J. Thompson, and B.D. Santer, Influences of the Antarctic ozone hole on Southern Hemispheric summer climate change, ***J. Clim.***, ***27*** (16), 6245–6264, doi:10.1175/JCLI-D-13-00698.1, 2014.

Banerjee, A., A.C. Maycock, and J.A. Pyle, Chemical and climatic drivers of radiative forcing due to changes in stratospheric and tropospheric ozone over the 21st century, ***Atmos. Chem. Phys.***, ***18***, 2899–2911, doi:10.5194/acp-18-2899-2018, 2018.

Banerjee, A., G. Chiodo, M. Previdi, M. Ponater, A.J. Conley, and L.M. Polvani, Stratospheric water vapor: An important climate feedback, ***Clim. Dyn.***, ***53***, 1697–1710, doi:10.1007/s00382-019-04721-4, 2019.

Banerjee, A., J.C. Fyfe, L.M. Polvani, D. Waugh, and K.-L. Chang, A pause in Southern Hemisphere circulation trends due to the Montreal Protocol, ***Nature***, ***579***, 544–548, doi:10.1038/s41586-020-2120-4, 2020.

Barnes, E. A. and Polvani, L. M.: Response of the Midlatitude Jets, and of Their Variability, to Increased GreenhouseGases in the CMIP5 Models. ***J. Clim., 26***, 7117–7135. https://doi.org/10.1175/JCLI-D-12-00536.1, 2013.

Barnes, E.A., N.W. Barnes, and L.M. Polvani, Delayed Southern Hemisphere climate change induced by stratospheric ozone recovery, as projected by the CMIP5 models, ***J. Clim.***, ***27***, 852–867, doi:10.1175/JCLI-D-13-00246.1, 2014.

Barnett, J.J., J.T. Houghton and J.A. Pyle, The temperature dependence of the ozone concentration near the stratopause, ***Q. J. Roy. Meteorol. Soc.***, 101, 245-257, doi:10.1002/qj.49710142808, 1975.

Beadling, R.L., J.L. Russell, R.J. Stouffer, M. Mazloff, L.D. Talley, P.J. Goodman, J.B. Sallée, H.T. Hewitt, P. Hyder and A. Pandde, Representation of Southern Ocean properties across coupled model intercomparison project generations: CMIP3 to CMIP6, ***J. Clim.***, 33, 6555–6581, doi:10.1175/JCLI-D-19-0970.1, 2020.

Bellouin, N., W. Davies, K.P. Shine, J. Quaas, J. Mülmenstädt, P.M. Forster, C. Smith, L. Lee, L. Regayre, G. Brasseur, N. Sudarchikova, I. Bouarar, O. Boucher, and G. Myhre, Radiative forcing of climate change from the Copernicus reanalysis of atmospheric composition, ***Earth Syst. Sci. Data***, ***12*** (3), 1649–1677, doi:10.5194/essd-12-1649-2020, 2020.

Bernath, P., C. Boone, and J. Crouse, Wildfire smoke destroys stratospheric ozone, ***Science***, ***375*** (6586), 1292–1295, doi:10.1126/science.abm5611, 2022.

Blanchard-Wrigglesworth, E., L.A. Roach, A. Donohoe, and Q. Ding, Impact of winds and Southern Ocean SSTs on Antarctic sea ice trends and variability, ***J. Clim.***, ***34***, 949–965, doi:10.1175/jcli-d-20-0386.1, 2021.

Breeden, M. L., Butler, A. H., Albers, J. R., Sprenger, M., and Langford, A. O., The spring transition of the North Pacific jet and its relation to deep stratosphere-to-troposphere mass transport over western North America, ***Atmos. Chem. Phys., 21***, 2781–2794, https://doi.org/10.5194/acp-21-2781-2021, 2021.

Bronselaer, B., J.L. Russell, M. Winton, N.L. Williams, R.M. Key, J.P. Dunne, R.A. Feely, K.S. Johnson, and J.L. Sarmiento, Importance of wind and meltwater for observed chemical and physical changes in the Southern Ocean, ***Nat. Geosci.***, ***13***, 35–42, doi:10.1038/s41561-019-0502-8, 2020.

Bushell, A.C., D.R. Jackson, N. Butchart, S.C. Hardiman, T.J. Hinton, S.M. Osprey, and L.J. Gray, Sensitivity of GCM tropical middle atmosphere variability and climate to ozone and parameterized gravity wave changes, ***J. Geophys. Res. Atmos.***, ***115*** (D15), doi:10.1029/2009JD013340, 2010.

Bushell, A.C., J.A. Anstey, N. Butchart, Y. Kawatani, S.M. Osprey, J.H. Richter, F. Serva, P. Braesicke, C. Cagnazzo, C.-C. Chen, H.-Y. Chun, R.R. Garcia, L.J. Gray, K.

Hamilton, T. Kerzenmacher, Y.-H. Kim, F. Lott, C. McLandress, H. Naoe, J. Scinocca, A.K. Smith, T.N. Stockdale, S. Versick, S. Watanabe, K. Yoshida, and S. Yukimoto, Evaluation of the Quasi-Biennial Oscillation in global climate models for the SPARC QBO-initiative, ***Q. J. R. Meteorol. Soc., 148*** (744), 1459–1489, doi:10.1002/qj.3765, 2020.

Butchart, N., J.A. Anstey, K. Hamilton, S. Osprey, C. McLandress, A.C. Bushell, Y. Kawatani, Y.-H. Kim, F. Lott, J. Scinocca, T.N. Stockdale, M. Andrews, O. Bellprat, P. Braesicke, C. Cagnazzo, C.-C. Chen, H.-Y. Chun, M. Dobrynin, R.R. Garcia, J. Garcia-Serrano, L.J. Gray, L. Holt, T. Kerzenmacher, H. Naoe, H. Pohlmann, J.H. Richter, A.A. Scaife, V. Schenzinger, F. Serva, S. Versick, S. Watanabe, K. Yoshida, and S. Yukimoto, Overview of experiment design and comparison of models participating in phase 1 of the SPARC Quasi-Biennial Oscillation initiative (QBOi), ***Geosci. Model Dev.***, *11*, 1009–1032, doi:10.5194/gmd-11-1009-2018, 2018.

Butler, A.H., D.J. Seidel, S.C. Hardiman, N. Butchart, T. Birner, and A. Match, Defining sudden stratospheric warmings, ***Bull. Amer. Meteor. Soc.***, *96* (11), 1913–1928, doi:10.1175/BAMS-D-13-00173.1, 2015.

Butler, A.H., and D.I.V. Domeisen, The wave geometry of final stratospheric warming events, ***Weather Clim. Dynam.***, *2* (2), 453–474, doi: 10.5194/wcd-2-453-2021, 2021.

Byrne, N.J., and T.G. Shepherd, Seasonal persistence of circulation anomalies in the Southern Hemisphere stratosphere and its implications for the troposphere, ***J. Clim.***, *31* (9), 3467–3483, doi:10.1175/JCLI-D-17-0557.1, 2018.

Calvo, N., L.M. Polvani, and S. Solomon, On the surface impact of Arctic stratospheric ozone extremes, ***Environ. Res. Lett.***, *10* (9), 094003, doi:10.1088/1748-9326/10/9/094003, 2015.

Cane, M.A., A.C. Clement, A. Kaplan, Y. Kushnir, D. Pozdnyakov, R. Seager, S.E. Zebiak, and R. Murtugudde, Twentieth-century sea surface temperature trends, ***Science***, *275* (5302), 957–960, doi:10.1126/science.275.5302.957, 1997.

Carr, J. L., Á. Horváth, D.L. Wu, and M.D. Friberg, Stereo plume height and motion retrievals for the record-setting Hunga Tonga-Hunga Ha'apai eruption of 15 January 2022, ***Geophys. Res. Lett.***, *49*, e2022GL098131. https://doi.org/10.1029/2022GL098131, 2022.

Ceppi, P., and T.G. Shepherd, The role of the stratospheric polar vortex for the austral jet response to greenhouse gas forcing, ***Geophys. Res. Lett.***, *46*, 6972– 6979, doi:10.1029/2019GL082883, 2019.

Chabrillat, S., C. Vigouroux, Y. Christophe, A. Engel, Q. Errera, D. Minganti, B. Monge-Sanz, A. Segers, and E. Mahieu, Comparison of mean age of air in five reanalyses using the BASCOE transport model, ***Atmos. Chem. Phys.***, *18*, 14,715–14,735, doi:10.5194/acp-18-14715-2018, 2018.

Charlton, A.J., and L.M. Polvani, A new look at stratospheric sudden warmings. Part I: Climatology and modeling benchmarks, ***J. Clim.***, *20* (3), 449–469, doi:10.1175/JCLI3996.1, 2007.

Checa-Garcia, R., M.I. Hegglin, D. Kinnison, D.A. Plummer, and K.P. Shine, Historical tropospheric and stratospheric ozone radiative forcing using the CMIP6 database, ***Geophys. Res. Lett.***, *45* (7), 3264–3273, doi:10.1002/2017GL076770, 2018.

Chemke, R., and L.M. Polvani, Using multiple large ensembles to elucidate the discrepancy between the 1979–2019 modeled and observed Antarctic sea ice trends, ***Geophys. Res. Lett.***, *47* (15), doi:10.1029/2020gl088339, 2020.

Chemke, R., M. Previdi, M.R. England, and L.M. Polvani, Distinguishing the impacts of ozone and ozone-depleting substances on the recent increase in Antarctic surface mass balance, ***Cryosphere***, *14*, 4135–4144, doi:10.5194/tc-14-4135-2020, 2020.

Cheung, J.C.H., J.D. Haigh, and D.R. Jackson, Impact of EOS MLS ozone data on medium-extended range ensemble weather forecasts, ***J. Geophys. Res. Atmos.***, *119*, 9253–9266, doi:10.1002/ 2014JD021823, 2014.

Chiodo, G., and L.M. Polvani, Reduced Southern Hemispheric circulation response to quadrupled CO2 due to stratospheric ozone feedback, ***Geophys. Res. Lett.*** *44*, 465–474, doi:10.1002/2016GL071011, 2017.

Chiodo, G., L.M. Polvani, D.R. Marsh, A. Stenke, W. Ball, E. Rozanov, S. Muthers, and K. Tsigaridis, The response of the ozone layer to quadrupled CO2 concentrations, ***J. Clim.***, *31*, 3893–3907, doi:10.1175/JCLI-D-17-0492.1, 2018.

Chiodo, G., and L.M. Polvani, The response of the ozone layer to quadrupled CO2 concentrations: Implications for climate, ***J. Clim.***, *32*, 7629–7642, doi:10.1175/JCLI-D-19-0086.1, 2019.

Chiodo, G., and L.M. Polvani, New insights on the radiative impacts of ozone depleting substances, ***Geophys. Res. Lett.***, *49* (10), doi:10.1029/2021GL096783, 2022.

Chrysanthou, A., A.C. Maycock, M.P. Chipperfield, S. Dhomse, H. Garny, D.E. Kinnison, H. Akiyoshi, M. Deushi, R.R. Garcia, P. Jöckel, O. Kirner, G. Pitari, D.A. Plummer, L. Revell, E. Rozanov, A. Stenke, R.Y. Tanaka, D. Visioni, and Y. Yamashita, The effect of atmospheric nudging on the stratospheric residual circulation in chemistry–climate models, ***Atmos. Chem. Phys.***, *19*, 11,559–11,586, doi:10.5194/acp-19-11559-2019, 2019.

Cionni, I., V. Eyring, J.F. Lamarque, W.J. Randel, D.S. Stevenson, F. Wu, G.E. Bodeker, T.G. Shepherd, D.T. Shindell, and D.W. Waugh, Ozone database in support of CMIP5 simulations: results and corresponding radiative forcing, ***Atmos. Chem. Phys.***, *11*, 11,267–11,292, doi:10.5194/acp-11-11267-2011, 2011.

Clement, A.C., R. Seager, M.A. Cane, and S.E. Zebiak, An ocean dynamical thermostat, ***J. Clim.***, *9* (9) 2190–2196, doi:10.1175/1520-0442(1996)009<2190:AODT>2.0.CO;2, 1996.

Cohen, J., L. Agel, M. Barlow, C. I. Garfinkel, and I. White, Linking Arctic variability and change with extreme winter weather in the United States, Science, 373, no. 6559, Art. no. 6559, doi: 10.1126/science.abi9167, 2021.

Conley, A.J., J.-F. Lamarque, F. Vitt, W.D. Collins, and J. Kiehl, PORT, a CESM tool for the diagnosis of radiative forcing, ***Geosci. Model Dev.***, *6*, 469–476, doi:10.5194/gmd-6-469-2013, 2013.

Crook, J.A., N.P. Gillett, and S.P. Keeley, Sensitivity of Southern Hemisphere climate to zonal asymmetry in ozone, ***Geophys. Res. Lett.***, *35* (7), doi:10.1029/2007GL032698, 2008.

Dacie, S., L. Kluft, H. Schmidt, B. Stevens, S.A. Buehler, P.J. Nowack, S. Dietmüller, N.L. Abraham, and T. Birner, A 1D RCE study of factors affecting the tropical tropopause layer and surface climate, ***J. Clim.***, *32*, 6769–6782, doi:10.1175/JCLI-D-18-0778.1, 2019.

DallaSanta, K., C. Orbe, D. Rind, D.L. Nazarenko, and J. Jonas, Dynamical and trace gas responses of the quasi-biennial oscillation to increased CO2, ***J. Geophys. Res. Atmos***, *126* (6), e2020JD034151, doi:10.1029/2020JD034151, 2021.

Damiani, A., R.R. Cordero, P.J. Llanillo, S. Feron, J.P. Boisier, R. Garreaud, R. Rondanelli, H. Irie, and S. Watanabe, Connection between Antarctic ozone and climate: Interannual precipitation changes in the Southern Hemisphere, ***Atmosphere***, *11* (6), 579, doi:10.3390/atmos11060579, 2020.

Davis, N.A., S.M. Davis, R.W. Portmann, E. Ray, K.H. Rosenlof, and P. Yu, A comprehensive assessment of tropical stratospheric upwelling in the specified dynamics Community Earth System Model 1.2. 2–Whole Atmosphere Community Climate Model (CESM (WACCM)), ***Geosci. Model Dev.***, *13*, 717–734, doi:10.5194/gmd-13-717-2020, 2020.

Davis, N.A., P. Callaghan, I.R. Simpson, and S. Tilmes, Specified dynamics scheme impacts on wave-mean flow dynamics, convection, and tracer transport in CESM2 (WACCM6), ***Atmos. Chem. Phys.***, *22*, 197–214, doi:10.5194/acp-22-197-2022, 2022.

de la Cámara, A., M. Abalos, P. Hitchcock, N. Calvo, and R.R. Garcia, Response of Arctic ozone to sudden stratospheric warmings, ***Atmos. Chem. Phys.***, *18*, 16,499–16,513, doi:10.5194/acp-18-16499-2018, 2018.

DeVries, T., M. Holzer, and F. Primeau, Recent increase in oceanic carbon uptake driven by weaker upper-ocean overturning, ***Nature***, *542*, 215–218, doi:10.1038/nature21068, 2017.

Dhomse, S.S., D. Kinnison, M.P. Chipperfield, R.J. Salawitch, I. Cionni, M.I. Hegglin, N.L. Abraham, H. Akiyoshi, A.T. Archibald, E.M. Bednarz, S. Bekki, P. Braesicke, N. Butchart, M. Dameris, M. Deushi, S. Frith, S.C. Hardiman, B. Hassler, L.W. Horowitz, R.-M. Hu, P. Jöckel, B. Josse, O. Kirner, S. Kremser, U. Langematz, J. Lewis, M. Marchand, M. Lin, E. Mancini, V. Marécal, M. Michou, O. Morgenstern, F.M. O'Connor, L. Oman, G. Pitari, D.A. Plummer, J.A. Pyle, L.E. Revell, E. Rozanov, R. Schofield, A. Stenke, K. Stone, K. Sudo, S. Tilmes, D. Visioni, Y. Yamashita, and G. Zeng, Estimates of ozone return dates from Chemistry-Climate Model Initiative simulations, ***Atmos. Chem. Phys.***, *18*, 8409–8438, doi:10.5194/acp-18-8409-2018, 2018.

Dhomse, S.S., W. Feng, S.A. Montzka, R. Hossaini, J. Keeble, J.A. Pyle, J. Daniel, and M.P. Chipperfield, Delay in recovery of the Antarctic ozone hole from unexpected CFC-11 emissions, ***Nat. Commun.***, *10* (1), 5781, doi:10.1038/s41467-019-13717-x, 2019.

Diallo, M., M. Riese, T. Birner, P. Konopka, R. Müller, M.I. Hegglin, M.L. Santee, M. Baldwin, B. Legras, and F. Ploeger, Response of stratospheric water vapor and ozone to the unusual timing of El Niño and the QBO disruption in 2015–2016, ***Atmos. Chem. Phys.***, *18*, 13,055–13,073, doi:10.5194/acp-18-13055-2018, 2018.

Diallo, M., M. Ern, and F. Ploeger, The advective Brewer–Dobson circulation in the

ERA5 reanalysis: climatology, variability, and trends, ***Atmos. Chem. Phys.***, ***21***, 7515–7544, doi:10.5194/acp-21-7515-2021, 2021.

Dietmüller, S., M. Ponater, and R. Sausen, Interactive ozone induces a negative feedback in CO2-driven climate change simulations, ***J. Geophys. Res. Atmos., 119***, 1796–1805, doi:10.1002/2013JD020575, 2014.

Dietmüller, S., R. Eichinger, H. Garny, T. Birner, H. Boenisch, G. Pitari, E. Mancini, D. Visioni, A. Stenke, L. Revell, E. Rozanov, D.A. Plummer, J. Scinocca, P. Jöckel, L. Oman, M. Deushi, S. Kiyotaka, D.E. Kinnison, R. Garcia, O. Morgenstern, G. Zeng, K.A. Stone, and R. Schofield, Quantifying the effect of mixing on the mean age of air in CCMVal-2 and CCMI-1 models, ***Atmos. Chem. Phys.***, ***18***, 6699–6720, doi:10.5194/acp-18-6699-2018, 2018.

Dimdore-Miles, O., L. Gray, and S. Osprey, Origins of multi-decadal variability in sudden stratospheric warmings, ***Weather Clim. Dynam.***, ***2*** (1), 205–231, doi:10.5194/wcd-2-205-2021, 2021.

Doblas-Reyes, F.J., A.A. Sörensson, M. Almazroui, A. Dosio, W.J. Gutowski, R. Haarsma, R. Hamdi, B. Hewitson, W.-T. Kwon, B.L. Lamptey, D. Maraun, T.S. Stephenson, I. Takayabu, L. Terray, A. Turner, and Z. Zuo, Linking Global to Regional Climate Change, Chapter 10 in ***Climate Change 2021: The Physical Science Basis. Contribution of Working Group I to the Sixth Assessment Report of the Intergovernmental Panel on Climate Change***, edited by V. Masson-Delmotte, P. Zhai, A. Pirani, S.L. Connors, C. Péan, S. Berger, N. Caud, Y. Chen, L. Goldfarb, M.I. Gomis, M. Huang, K. Leitzell, E. Lonnoy, J.B.R. Matthews, T.K. Maycock, T. Waterfield, O. Yelekçi, R. Yu, and B. Zhou, Cambridge University Press, Cambridge, United Kingdom and New York, NY, USA, 149 pp., doi:10.1017/9781009157896.012, 2021.

Doddridge, E.W., J. Marshall, H. Song, J.-M. Campin, M. Kelley, and L. Nazarenko, Eddy compensation dampens Southern Ocean sea surface temperature response to westerly wind trends, ***Geophys. Res. Lett.***, ***46***, 4365–4377, doi:10.1029/2019gl082758, 2019.

Dupuy, E., H. Akiyoshi, and Y. Yamashita, Impact of unmitigated HFC emissions on stratospheric ozone at the end of the 21st century as simulated by chemistry-climate models, ***J. Geophys. Res. Atmos.***, ***126*** (21), e2021JD035307, doi:10.1029/2021JD035307, 2021.

Eayrs, C., X. Li, M.N. Raphael, and D.M. Holland, Rapid decline in Antarctic sea ice in recent years hints at future change, ***Nat. Geosci.***, ***14***, 460–464, doi:10.1038/s41561-021-00768-3, 2021.

Eichinger, R., S. Dietmüller, H. Garny, P. Šácha, T. Birner, H. Bönisch, G. Pitari, D. Visioni, A. Stenke, E. Rozanov, L. Revell, D.A. Plummer, P. Jöckel, L. Oman, M. Deushi, D.E. Kinnison, R.R. Garcia, O. Morgenstern, G. Zeng, K.A. Stone, and R. Schofield, The influence of mixing on the stratospheric age of air changes in the 21st century, ***Atmos. Chem. Phys.***, ***19***, 921–940, doi:10.5194/acp-19-921-2019, 2019.

Engel, A., T. Möbius, H. Bönisch, U. Schmidt, R. Heinz, I. Levin, E. Atlas, S. Aoki, T. Nakazawa, S. Sugawara, F. Moore, D. Hurst, J. Elkins, S. Schauffler, A. Andrews, and K. Berine, Age of stratospheric air unchanged within uncertainties over the past 30 years, ***Nat. Geosci.***, ***2***, 28–31, doi:10.1038/GEO388, 2009.

Eyring, V., J.M. Arblaster, I. Cionni, J. Sedlacek, J. Perlwitz, P.J. Young, S. Bekki, D. Bergmann, P. Cameron-Smith, W. Collins, G. Faluvegi, K.-D. Gottschaldt, L. Horowitz, D. Kinnison, J.-F. Lamarque, D.R. Marsh, D. Saint-Martin, D. Shindell, K. Sudo, S. Szopa, and S. Watanabe, Long-term ozone changes and associated climate impacts in CMIP5 simulations, ***J. Geophys. Res. Atmos.***, ***118*** (10), 5029–5060, doi:10.1002/jgrd.50316, 2013.

Eyring, V., N.P. Gillett, K.M. Achuta Rao, R. Barimalala, M. Barreiro Parrillo, N. Bellouin, C. Cassou, P.J. Durack, Y. Kosaka, S. McGregor, S. Min, O. Morgenstern, and Y. Sun, Human Influence on the Climate System, Chapter 3 in ***Climate Change 2021: The Physical Science Basis. Contribution of Working Group I to the Sixth Assessment Report of the Intergovernmental Panel on Climate Change***, edited by V. Masson-Delmotte, P. Zhai, A. Pirani, S. L. Connors, C. Péan, S. Berger, N. Caud, Y. Chen, L. Goldfarb, M. I. Gomis, M. Huang, K. Leitzell, E. Lonnoy, J. B. R. Matthews, T. K. Maycock, T. Waterfield, O. Yelekçi, R. Yu, and B. Zhou, Cambridge University Press, Cambridge, United Kingdom and New York, NY, USA, 129 pp., doi:10.1017/9781009157896.005, 2021.

Fan, T., C. Deser, and D.P. Schneider, Recent Antarctic sea ice trends in the context of Southern Ocean surface climate variations since 1950, ***Geophys. Res. Lett.***, ***41***, 2419–2426, doi:10.1002/2014gl059239, 2014.

Fang, X., J.A. Pyle, M.P. Chipperfield, J.S. Daniel, S. Park, and R.G. Prinn, Challenges for the recovery of the ozone layer, ***Nat. Geosci.***, ***12***, 592–596, doi:10.1038/s41561-019-0422-7, 2019.

Feng, J., and Y. Huang, Impacts of tropical cyclones on the thermodynamic conditions in the tropical tropopause layer observed by A-Train satellites, ***Atmos. Chem. Phys.***, ***21***, 15,493–15,518, doi:10.5194/acp-21-15493-2021, 2021.

Ferreira, D., J. Marshall, C.M. Bitz, S. Solomon, and A. Plumb, Antarctic Ocean and sea ice response to ozone depletion: A two-time-scale problem, ***J. Clim.***, ***28***, 1206–1226, doi:10.1175/jcli-d-14-00313.1, 2015.

Fleming, E.L., Q. Liang, L.D. Oman, P.A. Newman, F. Li, and M.M. Hurwitz, Stratospheric impacts of continuing CFC-11 emissions simulated in a chemistry-climate model, ***J. Geophys. Res. Atmos.***, ***126*** (9), doi:10.1029/2020JD033656, 2021.

Fogt, R.L., and G.J. Marshall, The Southern Annular Mode: Variability, trends, and climate impacts across the Southern Hemisphere, ***WIREs Clim. Change***, ***11*** (4), doi:10.1002/wcc.652, 2020.

Forster, P., T. Storelvmo, K. Armour, W. Collins, J.-L. Dufresne, D. Frame, D.J. Lunt, T. Mauritsen, M.D. Palmer, M. Watanabe, M. Wild, and H. Zhang, The Earth's Energy Budget, Climate Feedbacks, and Climate Sensitivity, Chapter 7 in ***Climate Change 2021: The Physical Science Basis, Contribution of Working Group I to the Sixth Assessment Report of the Intergovernmental Panel on Climate Change***, edited by V. Masson-Delmotte, P. Zhai, A. Pirani, S.L. Connors, C. Péan, S. Berger, N. Caud, Y. Chen, L. Goldfarb, M.I. Gomis, M. Huang, K. Leitzell, E. Lonnoy, J.B.R. Matthews, T.K. Maycock, T. Waterfield, O. Yelekçi, R. Yu, and B. Zhou, Cambridge University Press, Cambridge, United Kingdom and New York, NY, USA, 131 pp., doi:10.1017/9781009157896.009, 2021.

Forster, P.M., and D.W.J. Thompson (Coordinating Lead Authors), M.P. Baldwin, M.P. Chipperfield, M. Dameris, J.D. Haigh, D.J. Karoly, P.J. Kushner, W.J. Randel, K.H. Rosenlof, D.J. Seidel, S. Solomon, G. Beig, P. Braesicke, N. Butchart, N.P. Gillett, K.M. Grise, D.R. Marsh, C. McLandress, T.N. Rao, S.-W. Son, G.L. Stenchikov, and S. Yoden, Stratospheric Changes and Climate, Chapter 4 in ***Scientific Assessment of Ozone Depletion: 2010***, Global Ozone Research and Monitoring Project–Report No. 52, World Meteorological Organization, Geneva, Switzerland, 2011.

Forster, P.M., T. Richardson, A.C. Maycock, C.J. Smith, B.H. Samset, G. Myhre, T. Andrews, R. Pincus, and M. Schulz, Recommendations for diagnosing effective radiative forcing from climate models for CMIP6, ***J. Geophys. Res. Atmos., 121***, 12,460–12,475, doi:10.1002/2016JD025320, 2016.

Forster, P.M.D.F., and K.P. Shine, Radiative forcing and temperature trends from stratospheric ozone changes, ***J. Geophys. Res. Atmos., 102***, 10,841–10,855, doi:10.1029/96JD03510, 1997.

Forster, P.M.D.F., and K.P. Shine, Stratospheric water vapor changes as a possible contributor to observed stratospheric cooling, ***Geophys. Res. Lett.***, ***26***, 3309–3312, doi:10.1029/1999GL010487, 1999.

Forster, P.M.D.F., and M. Joshi, The role of halocarbons in the climate change of the troposphere and stratosphere, ***Clim. Change***, ***71***, 249–266, doi:10.1007/s10584-005-5955-7, 2005.

Friedel, M., G. Chiodo, A. Stenke, D. Domeisen, S. Fueglistaler, J. Anet, and T. Peter, Springtime arctic ozone depletion forces northern hemisphere climate anomalies, ***Nat. Geosci.***, ***15,*** 541–547, doi:10.1038/s41561-022-00974-7, 2022.

Fritsch, F., H. Garny, A. Engel, H. Bönisch, and R. Eichinger, Sensitivity of age of air trends to the derivation method for non-linear increasing inert SF6, ***Atmos. Chem. Phys.***, ***20***, 8709–8725, doi:10.5194/acp-20-8709-2020, 2020.

Frölicher, T.L., J.L. Sarmiento, D.J. Paynter, J.P. Dunne, J.P. Krasting, and M. Winton, Dominance of the Southern Ocean in anthropogenic carbon and heat uptake in CMIP5 models, ***J. Clim.***, ***28*** (2), 862–886, doi:10.1175/jcli-d-14-00117.1, 2015.

Fu, Q., S. Solomon, H.A. Pahlavan, and P. Lin, Observed changes in Brewer–Dobson circulation for 1980–2018, ***Environ. Res. Lett.***, ***14*** (11), 114026, doi:10.1088/1748-9326/ab4de7, 2019.

Fusco, A.C., and M.L. Salby, Interannual variations of total ozone and their relationship to variations of planetary wave activity, ***J. Clim.***, ***12*** (6), 1619–1629, doi:10.1175/1520-0442(1999)012<1619:IVOTOA>2.0.CO;2, 1999.

Garcia, R.R., W.J. Randel, and D.E. Kinnison, On the determination of age of air trends from atmospheric trace species, ***J. Atmos. Sci.***, ***68***, 139–154, doi:10.1175/2010JAS3527, 2011.

Garcia, R.R., D.E. Kinnison, and D.R. Marsh, "World avoided" simulations with the whole atmosphere community climate model, ***J. Geophys. Res. Atmos., 117*** (D23), D23303, doi:10.1029/2012JD018430, 2012.

Garcia, R.R., J. Yue, and J.M. Russell III, Middle atmosphere temperature trends in the twentieth and twenty-first centuries simulated with the Whole Atmosphere Community Climate Model (WACCM), ***J. Geophys. Res. Space Phys.***, ***124*** (10), 7984–7993, doi:10.1029/2019JA026909, 2019.

Garfinkel, C.I., O. Harari, S. Ziskin Ziv, J. Rao, O. Morgenstern, G. Zeng, S. Tilmes, D. Kinnison, F.M. O'Connor, N. Butchart, M. Deushi, P. Jöckel, A. Pozzer, and S. Davis, Influence of the El Niño–Southern Oscillation on entry stratospheric water vapor in coupled chemistry–ocean CCMI and CMIP6 models, ***Atmos. Chem. Phys.***, ***21***, 3725–3740, doi:10.5194/acp-21-3725-2021, 2021.

Gillett, N.P., and D.W.J. Thompson, Simulation of recent Southern Hemisphere climate change, ***Science***, ***302*** (5643), 273–275, doi:10.1126/science.1087440, 2003.

Gillett, N.P., J.F. Scinocca, D.A. Plummer, and M.C. Reader, Sensitivity of climate to dynamically consistent zonal asymmetries in ozone, ***Geophys. Res. Lett.***, ***36*** (10), doi:10.1029/2009GL037246, 2009.

Gillett, Z.E., J.M. Arblaster, A.J. Dittus, M. Deushi, P. Jöckel, D.E. Kinnison, O. Morgenstern, D.A. Plummer, L.E. Revell, E. Rozanov, R. Schofield, A. Stenke, K.A. Stone, and S. Tilmes, Evaluating the relationship between interannual variations in the Antarctic ozone hole and Southern Hemisphere surface climate in chemistry–climate models, ***J. Clim.***, ***32*** (11), 3131–3151, doi:10.1175/JCLI-D-18-0273.1, 2019.

Goody, R.M., and Y.L. Yung, Atmospheric Radiation: Theoretical Basis, Oxford University Press, 2nd Edition, doi:10.1093/oso/9780195051346.001.0001, 1989.

Goyal, R., M.H. England, A. Sen Gupta, and M. Jucker, Reduction in surface climate change achieved by the 1987 Montreal Protocol, ***Environ. Res. Lett.***, ***14*** (12), doi:10.1088/1748-9326/ab4874, 2019.

Griffiths, P.T., J. Keeble, Y.M. Shin, N.L. Abraham, A.T. Archibald, and J.A. Pyle, On the changing role of the stratosphere on the tropospheric ozone budget: 1979–2010, ***Geophys. Res. Lett.***, ***47*** (10), e2019GL086901, doi:10.1029/2019GL086901, 2020.

Gruber, N., P. Landschutzer, and N.S. Lovenduski, The variable Southern Ocean carbon sink, ***Annu. Rev. Mar. Sci.***, ***11*** (1), doi:10.1146/annurev-marine-121916-063407, 2019.

GVP (Global Volcanism Program), Report on Hunga Tonga-Hunga Ha'apai (Tonga), In: Sennert, S.K (ed.), ***Weekly Volcanic Activity Report, 12 January-18 January 2022***, Smithsonian Institution and US Geological Survey, 2022.

Gulev, S.K., P.W. Thorne, J. Ahn, F.J. Dentener, C.M. Domingues, S. Gerland, D. Gong, D.S. Kaufman, H.C. Nnamchi, J. Quaas, J.A. Rivera, S. Sathyendranath, S.L. Smith, B. Trewin, K. von Shuckmann, and R.S. Vose, Changing State of the Climate System, Chapter 2 in ***Climate Change 2021: The Physical Science Basis. Contribution of Working Group I to the Sixth Assessment Report of the Intergovernmental Panel on Climate Change***, edited by V. Masson-Delmotte, P. Zhai, A. Pirani, S.L. Connors, C. Péan, S. Berger, N. Caud, Y. Chen, L. Goldfarb, M.I. Gomis, M. Huang, K. Leitzell, E. Lonnoy, J.B.R. Matthews, T.K. Maycock, T. Waterfield, O. Yelekçi, R. Yu, and B. Zhou, Cambridge University Press, Cambridge, United Kingdom and New York, NY, USA, 135 pp., doi:10.1017/9781009157896.004, 2021.

Haase, S., and K. Matthes, The importance of interactive chemistry for stratosphere troposphere coupling, ***Atmos. Chem. Phys.***, ***19*** (5), 3417–3432, doi:10.5194/acp 19 3417 2019, 2019.

Haase, S., J. Fricke, T. Kruschke, S. Wahl, and K. Matthes, Sensitivity of the Southern Hemisphere circumpolar jet response to Antarctic ozone depletion: prescribed versus interactive chemistry, ***Atmos. Chem. Phys.***, ***20***, 14,043–14,061, doi:10.5194/acp-20-14043-2020, 2020.

Haigh, J.D., The Sun and the Earth's climate, ***Living Rev. Sol. Phys.***, ***4*** (1), 2, doi:10.12942/lrsp-2007-2, 2007.

Haigh, J.D. and J.A. Pyle, Ozone perturbation experiments in a two-dimensional circulation model, ***Q. J. Roy. Meteorol. Soc.***, 108, 551–574, doi:10.1002/qj.49710845705, 1982.

Haimberger, L., C. Tavolato, and S. Sperka, Homogenization of the global radiosonde temperature dataset through combined comparison with reanalysis background series and neighboring stations, ***J. Clim.***, ***25***, 8108–8131, doi:10.1175/JCLI-D-11-00668.1, 2012.

Hall, A., and M. Visbeck, Synchronous variability in the Southern Hemisphere atmosphere, sea ice, and ocean resulting from the annular mode, ***J. Clim.***, ***15*** (21), 3043–3057, doi:10.1175/1520-0442(2002)015<3043:SVITSH>2.0.CO;2, 2002.

Han, Y., W. Tian, M.P. Chipperfield, J. Zhang, F. Wang, W. Sang, J. Luo, W. Feng, A. Chrysanthou, and H. Tian, Attribution of the hemispheric asymmetries in trends of stratospheric trace gases inferred from Microwave Limb Sounder (MLS) measurements, ***J. Geophys. Res. Atmos.***, ***124***, 6283–6293, doi:10.1029/2018JD029723, 2019.

Handcock, M.S., and M.N. Raphael, Modeling the annual cycle of daily Antarctic sea ice extent, ***Cryosphere***, ***14***, 2159–2172, doi:10.5194/tc-14-2159-2020, 2020.

Harari, O., C.I. Garfinkel, S. Ziskin Ziv, O. Morgenstern, G. Zeng, S. Tilmes, D. Kinnison, M. Deushi, P. Jöckel, A. Pozzer, F.M. O'Connor, and S. Davis, Influence of Arctic stratospheric ozone on surface climate in CCMI models, ***Atmos. Chem. Phys.***, ***19*** (14), 9253–9268, doi:10.5194/acp-19-9253-2019, 2019.

Hardiman, S.C., M.B. Andrews, T. Andrews, A.C. Bushell, N.J. Dunstone, H. Dyson, G.S. Jones, J.R. Knight, E. Neininger, F.M. O'Connor, J.K. Ridley, M.A. Ringer, A.A. Scaife, C.A. Senior, and R.A. Wood, The impact of prescribed ozone in climate projections run with HadGEM3-GC3. 1, ***J. Adv. Model. Earth Syst.***, ***11***, 3443–3453, doi:10.1029/2019MS001714, 2019.

Haumann, F.A., N. Gruber, and M. Münnich, Sea-ice induced Southern Ocean subsurface warming and surface cooling in a warming climate, ***AGU Adv.***, ***1*** (2), doi:10.1029/2019AV000132, 2020.

Hendon, H.H., E.-P. Lim, and S. Abhik, Impact of interannual ozone variations on the downward coupling of the 2002 Southern Hemisphere stratospheric warming, ***J. Geophys. Res. Atmos.***, ***125*** (16), doi:10.1029/2020JD032952, 2020.

Hobbs, W.R., N.L. Bindoff, and M.N. Raphael, New perspectives on observed and simulated Antarctic sea ice extent trends using optimal fingerprinting techniques, ***J. Clim.***, ***28*** (4), 1543–1560, doi:10.1175/jcli-d-14-00367.1, 2015.

Hobbs, W.R., C. Roach, T. Roy, J.-B. Sallée, and N. Bindoff, Anthropogenic temperature and salinity changes in the Southern Ocean, ***J. Clim.***, ***34***, 215–228, doi:10.1175/jcli-d-20-0454.1, 2021.

Hodnebrog, Ø., G. Myhre, R.J. Kramer, K.P. Shine, T. Andrews, G. Faluvegi, M. Kasoar, A. Kirkevåg, J.-F. Lamarque, J. Mülmenstädt, D. Olivié, B.H. Samset, D. Shindell, C.J. Smith, T. Takemura, and A. Voulgarakis, The effect of rapid adjustments to halocarbons and N2O on radiative forcing, ***npj Clim. Atmos. Sci.***, ***3*** (1), 43, doi:10.1038/s41612-020-00150-x, 2020.

Holland, M.M., L. Landrum, Y. Kostov, and J. Marshall, Sensitivity of Antarctic sea ice to the Southern Annular Mode in coupled climate models, ***Clim. Dyn.***, ***49*** (5), 1813–1831, doi:10.1007/s00382-016-3424-9, 2017.

Hong, H.-J., and T. Reichler, Local and remote response of ozone to Arctic stratospheric circulation extremes, ***Atmos. Chem. Phys.***, ***21***, 1159–1171, doi:10.5194/acp-21-1159-2021, 2021.

Huang, Y., Wang, Y. and H. Huang, Stratospheric water vapor feedback disclosed by a locking experiment. Geophys. Res. Lett., 47(12), p.e2020GL087987, 2020.

Hurst, D.F., W.G. Read, H. Vomel, H.B. Selkirk, K.H. Rosenlof, S.M. Davis, E.G. Hall, A.F. Jordan, and S.J. Oltmans, Recent divergences in stratospheric water vapor measurements by frost point hygrometers and the Aura Microwave Limb Sounder, ***Atmos. Meas. Tech.***, ***9*** (9), 4447–4457, doi:10.5194/amt-9-4447-2016, 2016.

Hurwitz M.M., E.L. Fleming, P.A. Newman, F. Li, E. Mlawer, K. Cady-Pereira and R. Bailey, Ozone depletion by hydrofluorocarbons, Geophys. Res. Lett. 42 8686–92, 2015.

Hyder, P., J. Edwards, R.P. Allan, H.T. Hewitt, T.J. Bracegirdle, J.M. Gregory, R.A. Wood, A.J.S. Meijers, J. Mulcahy, P. Field, K. Furtado, A. Bodas-Salcedo, K.D. Williams, D. Copsey, S.A. Josey, C. Liu, C.D. Roberts, C. Sanchez, J. Ridley, L. Thorpe, S.C. Hardiman, M. Mayer, D.I. Berry, and S.E. Belcher, Critical Southern Ocean climate model biases traced to atmospheric model cloud errors, ***Nat. Commun.***, ***9***, 3625, doi:10.1038/s41467-018-05634-2, 2018.

The IMBIE team, Mass balance of the Antarctic Ice Sheet from 1992 to 2017, ***Nature***, ***558***, 219–222, doi:10.1038/s41586-018-0179-y, 2018.

IPCC (Intergovenmental Panel on Climate Change), Climate Change 2021: The Physical Science Basis. Contribution of Working Group I to the Sixth Assessment Report of the Intergovernmental Panel on Climate Change, edited by V. Masson-Delmotte, P. Zhai, A. Pirani, S.L. Connors, C. Péan, S. Berger, N. Caud, Y. Chen, L. Goldfarb, M.I. Gomis, M. Huang, K. Leitzell, E. Lonnoy, J.B.R. Matthews, T.K. Maycock, T. Waterfield, O. Yelekçi, R. Yu, and B. Zhou, Cambridge University Press, Cambridge, United Kingdom and New York, NY, USA, In press, doi:10.1017/9781009157896, 2021.

Ivanciu, I., K. Matthes, S. Wahl, J. Harlaß, and A. Biastoch, Effects of prescribed CMIP6 ozone on simulating the Southern Hemisphere atmospheric circulation response to ozone depletion, ***Atmos. Chem. Phys.***, ***21***, 5777–5806, doi:10.5194/acp-21-5777-2021, 2021.

Ivanciu, I., K. Matthes, A. Biastoch, S. Wahl, and J. Harlaß, Twenty-first century Southern Hemisphere impacts of ozone recovery and climate change from the stratosphere to the ocean, ***Weather Clim. Dynam.***, ***3***, 139–171, doi:10.5194/wcd-3-139-2022, 2022.

Ivy, D.J., S. Solomon, N. Calvo, and D.W.J. Thompson, Observed connections of Arctic stratospheric ozone extremes to Northern Hemisphere surface climate, ***Environ. Res. Lett.***, ***12*** (2), 024004, doi:10.1088/1748-9326/aa57a4, 2017.

Jenkins, A., P. Dutrieux, S. Jacobs, E.J. Steig, G.H. Gudmundsson, J. Smith, and K.J. Heywood, Decadal ocean forcing and Antarctic ice sheet response: Lessons from the Amundsen Sea, ***Oceanography***, ***29*** (4), 106–117, doi:10.5670/oceanog.2016.103, 2016.

Jensen, E.J., L.L. Pan, S. Honomichl, G.S. Diskin, M. Kramer, N. Spelten, G. Günther, D.F. Hurst, M. Fujiwara, H. Vömel, H.B. Selkirk, J. Suzuki, M.J. Schwartz, and J.B. Smith, Assessment of observational evidence for direct convective hydration of the lower stratosphere, ***J. Geophys. Res. Atmos.***, ***125*** (15), e2020JD032793, doi:10.1029/2020jd032793, 2020.

Jucker, M., T. Reichler, and D.W. Waugh, How frequent are Antarctic sudden stratospheric warmings in present and future climate?, ***Geophys. Res. Lett.***, ***48*** (11), e2021GL093215, doi:10.1029/2021GL093215, 2021.

Jucker, M., and R. Goyal, Ozone-forced Southern Annular Mode during Antarctic stratospheric warming events, ***Geophys. Res. Lett.***, ***49*** (4), doi:10.1029/2021GL095270, 2022.

Karpechko, A.Y., J. Perlwitz, and E. Manzini, A model study of tropospheric impacts of the Arctic ozone depletion 2011, ***J. Geophys. Res. Atmos.***, ***119*** (13), 7999–8014, doi:10.1002/2013JD021350, 2014.

Karpechko, A. Y., and Manzini, E., Arctic Stratosphere Dynamical Response to Global Warming, ***Journal of Climate***, ***30***(17), 7071-7086, doi.org/10.1175/JCLI-D-16-0781.1, 2017.

Karpechko, A.Y., and A.C. Maycock (Lead Authors), M. Abalos, H. Akiyoshi, J.M. Arblaster, C.I. Garfinkel, K.H. Rosenlof, and M. Sigmond, Stratospheric Ozone Changes and Climate, Chapter 5 in ***Scientific Assessment of Ozone Depletion: 2018***, Global Ozone Research and Monitoring Project–Report No. 58, 73 pp., World Meteorological Organization, Geneva, Switzerland, 2018.

Kataoka T., H. Tatebe, H. Koyama, T. Mochizuki, K. Ogochi, H. Naoe, Y. Imada, H. Shiogama, M. Kimoto, and M. Watanabe, Seasonal to decadal predictions with MIROC6: description and basic evaluation, ***J. Adv. Model. Earth Syst.***, ***12*** (12), doi:10.1029/2019MS002035, 2020.

Kawatani, Y., and K. Hamilton, Weakened stratospheric quasibiennial oscillation driven by increased tropical mean upwelling, ***Nature***, ***497***, 478–481, doi:10.1038/nature12140, 2013.

Keeble, J., B. Hassler, A. Banerjee, R. Checa-Garcia, G. Chiodo, S. Davis, V. Eyring, P.T. Griffiths, O. Morgenstern, P. Nowack, G. Zeng, J. Zhang, G. Bodeker, S. Burrows, P. Cameron-Smith, D. Cugnet, C. Danek, M. Deushi, L.W. Horowitz, A. Kubin, L. Li, G. Lohmann, M. Michou, M.J. Mills, P. Nabat, D. Olivié, S. Park, Ø. Seland, J. Stoll, K.-H. Wieners, and T. Wu, Evaluating stratospheric ozone and water vapour changes in CMIP6 models from 1850 to 2100, ***Atmos. Chem. Phys.***, ***21***, 5015–5061, doi:10.5194/acp-21-5015-2021, 2021.

Keppler, L., and P. Landschutzer, Regional wind variability modulates the Southern Ocean carbon sink, ***Sci. Rep.***, ***9***, 7384, doi:10.1038/s41598-019-43826-y, 2019.

Khatiwala, S., F. Primeau, and T. Hall, Reconstruction of the history of anthropogenic CO2 concentrations in the ocean, ***Nature***, ***462***, 346–349, doi:10.1038/nature08526, 2009.

Kim, J., and K.Y. Kim, Characteristics of stratospheric polar vortex fluctuations associated with sea ice variability in the Arctic winter, ***Clim. Dyn.***, ***54***, 3599–3611, doi:10.1007/s00382-020-05191-9, 2020.

Kindem, I., and B. Christiansen, Tropospheric response to stratospheric ozone loss, ***Geophys. Res. Lett.***, ***28***, 1547–1550, doi:10.1029/2000GL012552, 2001.

Kouznetsov, R., M. Sofiev, J. Vira, and G. Stiller, Simulating age of air and the distribution of SF_6 in the stratosphere with the SILAM model, ***Atmos. Chem. Phys.***, ***20***, 5837–5859, doi:10.5194/acp-20-5837-2020, 2020.

Kovács, T., W. Feng, A. Totterdill, J.M.C. Plane, S. Dhomse, J.C. Gómez-Martín, G. Stiller, F. Haenel, C. Smith, P. Forster, R.R. Garcia, D. Marsh, and M.P. Chipperfield, Determination of the atmospheric lifetime and global warming potential of sulfur hexafluoride using a three-dimensional model, ***Atmos. Chem. Phys.***, ***17***, 883–898, doi:10.5194/acp-17-883-2017, 2017.

Kretschmer, M., J. Cohen, V. Matthias, J. Runge, and D. Coumou, The different stratospheric influence on cold-extremes in Eurasia and North America, ***npj Clim. Atmos. Sci.***, ***1***, 44, doi:10.1038/s41612-018-0054-4, 2018.

Kretschmer, M., G. Zappa, and T.G. Shepherd, The role of Barents–Kara sea ice loss in projected polar vortex changes, ***Weather Clim. Dynam.***, ***1***, 715–730, doi:10.5194/wcd-1-715-2020, 2020.

Kuilman, M.S., Q. Zhang, M. Cai, and Q. Wen, Using the climate feedback response analysis method to quantify climate feedbacks in the middle atmosphere, ***Atmos. Chem. Phys.***, ***20***, 12,409–12,430, doi:10.5194/acp-20-12409-2020, 2020.

Lacis, A.A., D.J. Wuebbles, and J.A. Logan, Radiative forcing of climate by changes in the vertical distribution of ozone, ***J. Geophys. Res. Atmos.***, ***95***, 9971–9981, doi:10.1029/JD095iD07p09971, 1990.

Lambert, A., W. Read, and N. Livesey, ***MLS/Aura level 2 water vapor (H2O) mixing ratio V005***, Goddard Earth Sciences Data and Information Services Center (GES DISC), Greenbelt, Maryland, USA, 2020.

Landschützer, P., N. Gruber, F.A. Haumann, C. Rödenbeck, D.C.E. Bakker, S. Van Heuven, M. Hoppema, N. Metzl, C. Sweeney, T. Takahashi, B. Tilbrook, and R. Wanninkhof, The reinvigoration of the Southern Ocean carbon sink, ***Science***, ***349***, 1221–1224, doi:10.1126/science.aab2620, 2015.

Lawrence, Z.D., J. Perlwitz, A.H. Butler, G.L. Manney, P.A. Newman, S.H. Lee, and E.R. Nash, The remarkably strong Arctic stratospheric polar vortex of winter 2020: Links to record-breaking Arctic oscillation and ozone loss, ***J. Geophys. Res. Atmos.***, ***125*** (22), doi:10.1029/2020JD033271, 2020.

Le Quéré, C., C. Rödenbeck, E.T. Buitenhuis, T.J. Conway, R. Langenfelds, A. Gomez, C. Labuschagne, M. Ramonet, T. Nakazawa, N. Gillett, and M. Heimann, Saturation of the Southern Ocean CO2 sink due to recent climate change, ***Science***, ***316*** (5832), 1735–1738, doi:10.1126/science.1136188, 2007.

Le Quéré, C., G.P. Peters, P. Friedlingstein, R.M. Andrew, J.G. Canadell, S.J. Davis, R.B. Jackson, and M.W. Jones, Fossil CO2 emissions in the post-COVID-19 era, ***Nat. Clim. Change***, ***11***, 197–199, doi:10.1038/s41558-021-01001-0, 2021.

Lee, J.-Y., J. Marotzke, G. Bala, L. Cao, S. Corti, J.P. Dunne, F. Engelbrecht, E. Fischer, J.C. Fyfe, C. Jones, A. Maycock, J. Mutemi, O. Ndiaye, S. Panickal, and T. Zhou, Future Global Climate: Scenario-Based Projections and Near-Term Information, Chapter 4 in ***Climate Change 2021: The Physical Science Basis, Contribution of Working Group I to the Sixth Assessment Report of the Intergovernmental Panel on Climate Change***, edited by V. Masson-Delmotte, P. Zhai, A. Pirani, S.L. Connors, C. Péan, S. Berger, N. Caud, Y. Chen, L. Goldfarb, M.I. Gomis, M. Huang, K. Leitzell, E. Lonnoy, J.B.R. Matthews, T.K. Maycock, T. Waterfield, O. Yelekçi, R. Yu, and B. Zhou, Cambridge University Press, Cambridge, United Kingdom and New York, NY, USA, 119 pp., doi:10.1017/9781009157896.006, 2021.

Lee, S.H., J.C. Furtado, and A.J. Charlton-Perez, Wintertime North American weather regimes and the Arctic stratospheric polar vortex, ***Geophys. Res. Lett.***, ***46***, 14,892–14,900, doi:10.1029/2019GL085592, 2019.

Leedham Elvidge, E., H. Bönisch, C.A.M. Brenninkmeijer, A. Engel, P.J. Fraser, E. Gallacher, R. Langenfelds, J. Mühle, D.E. Oram, E.A. Ray, A.R. Ridley, T. Röckmann, W.T. Sturges, R.F. Weiss, and J.C. Laube, Evaluation of stratospheric age of air from CF_4, C_2F_6, C_3F_8, CHF_3, HFC-125, HFC-227ea and SF_6; implications for the calculations of halocarbon lifetimes, fractional release factors and ozone depletion potentials, ***Atmos. Chem. Phys.***, ***18***, 3369–3385, doi:10.5194/acp-18-3369-2018, 2018.

Lenaerts, J.T.M., J. Fyke, and B. Medley, The signature of ozone depletion in recent Antarctic precipitation change: A study with the Community Earth System Model, ***Geophys. Res. Lett.***, ***45*** (23), 12,931–12,939, doi:10.1029/2018gl078608, 2018.

Li, F., P. Newman, S. Pawson, and J. Perlwitz, Effects of greenhouse gas increase and stratospheric ozone depletion on stratospheric mean age of air in 1960–2010, ***J. Geophys. Res. Atmos.***, ***123*** (4), 2098–2110, doi:10.1002/2017JD027562, 2018.

Li, F., and P. Newman, Stratospheric water vapor feedback and its climate impacts in the coupled atmosphere–ocean Goddard Earth Observing System Chemistry-Climate Model, ***Clim. Dynam.***, ***55*** (5), 1585–1595, doi:10.1007/s00382-020-05348-6, 2020.

Li, S., W. Liu, K. Lyu, and X. Zhang, The effects of historical ozone changes on Southern Ocean heat uptake and storage, ***Clim. Dyn.***, ***57***, 2269–2285, doi:10.1007/s00382-021-05803-y, 2021.

Liang, Y.-C., L.M. Polvani, M. Previdi, K.L. Smith, M.R. England, and G. Chiodo, Stronger Arctic amplification from ozone-depleting substances than from carbon dioxide, ***Environ. Res. Lett.***, ***17*** (2), doi:10.1088/1748-9326/ac4a31, 2022.

Lim, E.-P., H.H. Hendon, and D.W.J. Thompson, Seasonal evolution of stratosphere-troposphere coupling in the Southern Hemisphere and implications for the predictability of surface climate, ***J. Geophys. Res. Atmos.***, ***123***, 12,002–12,016, doi:10.1029/2018JD029321, 2018.

Lim, E.-P., H.H. Hendon, G. Boschat, D. Hudson, D.W.J. Thompson, A.J. Dowdy, and J.M. Arblaster, Australian hot and dry extremes induced by weakenings of the stratospheric polar vortex, ***Nat. Geosci.***, ***12***, 896–901, doi:10.1038/s41561-019-0456-x, 2019.

Lim, E.-P., H.H. Hendon, A.H. Butler, D.W.J. Thompson, Z.D. Lawrence, A.A. Scaife, T.G. Shepherd, I. Polichtchouk, H. Nakamura, C. Kobayashi, R. Comer, L. Coy, A. Dowdy, R.D. Garreaud, P.A. Newman, and G. Wang, The 2019 Southern Hemisphere stratospheric polar vortex weakening and its impacts, ***Bull. Am. Meteorol. Soc.***, ***102*** (6), E1150–E1171, doi:10.1175/BAMS-D-20-0112.1, 2021.

Lin, P., and Y. Ming, Enhanced climate response to ozone depletion from ozone–circulation coupling, ***J. Geophys. Res. Atmos***, ***126*** (7), doi:10.1029/2020JD034286, 2021.

Liu, J., J.M. Rodriguez, L.D. Oman, A.R. Douglass, M.A. Olsen, and L. Hu, Stratospheric impact on the Northern Hemisphere winter and spring ozone interannual variability in the troposphere, ***Atmos. Chem. Phys.***, ***20***, 6417–6433, doi:10.5194/acp-20-6417-2020, 2020.

Liu, W., M.I. Hegglin, R. Checa-Garcia, S. Li, N.P. Gillett, K. Lyu, X. Zhang, and N.C. Swart, Stratospheric ozone depletion and tropospheric ozone increases drive Southern Ocean interior warming, ***Nat. Clim. Change***, ***12***, 365–372, doi:10.1038/s41558-022-01320-w, 2022.

Livesey, N.J., W.G. Read, L. Froidevaux, A. Lambert, M.L. Santee, M.J. Schwartz, L.F. Millán, R.F. Jarnot, P.A. Wagner, D.F. Hurst, K.A. Walker, P.E. Sheese, and G.E. Nedoluha, Investigation and amelioration of long-term instrumental drifts in water vapor and nitrous oxide measurements from the Aura Microwave Limb Sounder (MLS) and their implications for studies of variability and trends, ***Atmos. Chem. Phys.***, ***21***, 15,409–15,430, doi:10.5194/acp-21-15409-2021, 2021.

Livesey, N.J., W.G. Read, P.A. Wagner, L. Froidevaux, M.L. Santee, M.J. Schwartz, A. Lambert, L.F. Millán Valle, H.C. Pumphrey, G.L. Manney, R.A. Fuller, R.F. Jarnot, B.W. Knosp, R.R. Lay, Version 5.0x Level 2 and 3 data quality and description document, Tech. Rep. No. JPL D-105336 Rev. B, Jet Propulsion Laboratory, California Institute of Technology Pasadena, CaliforniaJet Propulsion Lab, 2022.

Loeffel, S., R. Eichinger, H. Garny, T. Reddmann, F. Fritsch, S. Versick, G. Stiller, and F. Haenel, The impact of sulfur hexafluoride (SF6) sinks on age of air climatologies and trends, ***Atmos. Chem. Phys.***, ***22***, 1175–1193, doi:10.5194/acp-22-1175-2022, 2022.

Long, C.S., M. Fujiwara, S. Davis, D.M. Mitchell, and C.J. Wright, Climatology and interannual variability of dynamic variables in multiple reanalyses evaluated by the SPARC Reanalysis Intercomparison Project (S-RIP), ***Atmos. Chem. Phys.***, ***17***, 14,593–14,629, doi:10.5194/acp-17-14593-2017, 2017.

Lovenduski, N.S., N. Gruber, S.C. Doney, and I.D. Lima, Enhanced CO2 outgassing in the Southern Ocean from a positive phase of the Southern Annular Mode, ***Glob. Biogeochem. Cycles***, ***21*** (2), doi:10.1029/2006gb002900, 2007.

Ma, X., F. Xie, J. Li, X. Zheng, W. Tian, R. Ding, C. Sun, and J. Zhang, Effects of Arctic stratospheric ozone changes on spring precipitation in the northwestern United States, ***Atmos. Chem. Phys.***, ***19***, 861–875, doi:10.5194/acp-19-861-2019, 2019.

Ma, X., and F. Xie, Predicting April precipitation in the Northwestern United States based on Arctic stratospheric ozone and local circulation, ***Front. Earth Sci.***, ***8***, 56, doi:10.3389/feart.2020.00056, 2020.

Mahieu, E., M.P. Chipperfield, J. Notholt, T. Reddmann, J. Anderson, P.F. Bernath, T. Blumenstock, M.T. Coffey, S.S. Dhomse, W. Feng, B. Franco, L. Froidevaux, D.W.T. Griffith, J.W. Hannigan, F. Hase, R. Hossaini, N.B. Jones, I. Morino, I. Murata, H. Nakajima, M. Palm, C. Paton-Walsh, J.M. RussellII III, M. Schneider, C. Servais, D. Smale, and K.A. Walker, Recent Northern Hemisphere stratospheric HCl increase due to atmospheric circulation changes, ***Nature***, ***515***, 104–107, doi:10.1038/nature13857, 2014.

Maleska, S., K.L. Smith, and J. Virgin, Impacts of stratospheric ozone extremes on Arctic high cloud, ***J. Clim.***, ***33***, 8869–8884, doi:10.1175/JCLI-D-19-0867.1, 2020.

Manzini, E., A. Karpechko, and L. Kornblueh, Nonlinear response of the stratosphere and the North Atlantic-European climate to global warming, ***Geophys. Res. Lett.***, ***45***, 4255–4263, doi:10.1029/ 2018GL077826, 2018.

Marshall, J., K.C. Armour, J.R. Scott, Y. Kostov, U. Hausmann, D. Ferreira, T.G. Shepherd, and C.M. Bitz, The ocean's role in polar climate change: asymmetric Arctic and Antarctic responses to greenhouse gas and ozone forcing, ***Philos. Trans. R. Soc. A***, ***372*** (2019), 20130040, doi:10.1098/rsta.2013.0040, 2014.

Matsumura, S., K. Yamazaki, and T. Horinouchi, Robust asymmetry of the future Arctic polar vortex is driven by tropical Pacific warming, ***Geophys. Res. Lett.***, ***48*** (11), e2021GL093440, doi:10.1029/2021GL093440, 2021.

Maycock, A.C., W.J. Randel, A.K. Steiner, A.Y. Karpechko, J. Christy, R. Saunders, D.W.J. Thompson, C.-Z. Zou, A. Chrysanthou, N. Luke Abraham, H. Akiyoshi, A.T. Archibald, N. Butchart, M. Chipperfield, M. Dameris, M. Deushi, S. Dhomse, G. Di Genova, P. Jöckel, D.E. Kinnison, O. Kirner, F. Ladstädter, M. Michou, O. Morgenstern, F. O'Connor, L. Oman, G. Pitari, D.A. Plummer, L.E. Revell, E. Rozanov, A. Stenke, D. Visioni, Y. Yamashita, and G. Zeng, Revisiting the mystery of recent stratospheric temperature trends, ***Geophys. Res. Lett.***, ***45***, 9919–9933, doi:10.1029/2018GL078035, 2018.

McLandress, C., A.I. Jonsson, D.A. Plummer, M.C. Reader, J.F. Scinocca, and T.G. Shepherd, Separating the dynamical effects of climate change and ozone depletion. Part I: Southern Hemisphere stratosphere, ***J. Clim.***, ***23*** (18), 5002–5020, doi:10.1175/2010JCLI3586.1, 2010.

McLandress, C., T.G. Shepherd, M.C. Reader, D.A. Plummer, and K.P. Shine, The climate impact of past changes in halocarbons and CO2 in the tropical UTLS region, ***J. Clim.***, ***27***, 8646–8660, doi:10.1175/JCLI-D-14-00232.1, 2014.

Mears, C.A., F.J. Wentz, P. Thorne, and D. Bernie, Assessing uncertainty in estimates of atmospheric temperature changes from MSU and AMSU using a Monte-Carlo estimation technique, ***J. Geophys. Res. Atmos.***, ***116*** (D8), D08112, doi:10.1029/2010JD014954, 2011.

Meehl, G.A., J.M. Arblaster, C.M. Bitz, C.T.Y. Chung, and H. Teng, Antarctic sea-ice expansion between 2000 and 2014 driven by tropical Pacific decadal climate variability, ***Nat. Geosci.***, ***9***, 590–595, doi:10.1038/ngeo2751, 2016.

Meehl, G.A., J.M. Arblaster, C.T.Y. Chung, M.M. Holland, A. DuVivier, L. Thompson, D. Yang, and C.M. Bitz, Sustained ocean changes contributed to sudden Antarctic sea ice retreat in late 2016, ***Nat. Commun.***, ***10*** (1), 14, doi:10.1038/s41467-018-07865-9, 2019.

Michou, M., P. Nabat, D. Saint-Martin, J. Bock, B. Decharme, M. Mallet, R. Roehrig, R. Séférian, S. Sénési, and A. Voldoire, Present-day and historical aerosol and ozone characteristics in CNRM CMIP6 simulations, ***J. Adv. Model. Earth Syst.***, ***12*** (1), doi:10.1029/2019MS001816, 2020.

Millán, L., M.L. Santee, A. Lambert, N.J. Livesey, F. Werner, M. Schwartz, H.C. Pumphrey, G.L. Manney, Y. Wang, H. Su, W. Longtau, W.G. Read, L. Froidevaux, Hunga Tonga-Hunga Ha'apai Hydration of the Stratosphere, ***Geophys. Res. Lett.***, ***49***, e2022GL099381. https://doi.org/10.1029/2022GL099381, 2022.

Mindlin, J., T.G. Shepherd, C.S. Vera, M. Osman, G. Zappa, R.W. Lee, and K.I. Hodges, Storyline description of Southern Hemisphere midlatitude circulation and precipitation response to greenhouse gas forcing, ***Clim., Dyn.***, ***54***, 4399–4421, doi:10.1007/s00382-020-05234-1, 2020.

Mindlin, J., T.G. Shepherd, C. Vera, and M. Osman, Combined effects of global warming and ozone depletion/recovery on Southern Hemisphere atmospheric circulation and regional precipitation, ***Geophys. Res. Lett.***, ***48***, e2021GL092568, doi:10.1029/2021GL092568, 2021.

Ming, A., A.C. Maycock, P. Hitchcock, and P. Haynes, The radiative role of ozone and water vapour in the annual temperature cycle in the tropical tropopause layer, ***Atmos. Chem. Phys.***, ***17***, 5677–5701, doi:10.5194/acp-17-5677-2017, 2017.

Mitchell, D.M., Y.T. E. Lo, W. J. M. Seviour, L. Haimberger and L.M. Polvani, The vertical profile of recent tropical temperature trends: Persistent model biases in the context of internal variability, ***Environ. Res. Lett.,*** 15, 1040b4, 2020

Montzka, S. A., Velders, G. J. M. (lead authors), Krummel, P. B., Mühle, J., Orkin, V. L., Park, S., Shah, N., and Walter-Terrinoni, H.: Hydrofluorocarbons (HFCs), Chapter 2 in: ***Scientific Assessment of Ozone Depletion***: 2018, Global Ozone Research and Monitoring, World Meteorological Organization, Geneva, Switzerland, 2018.

Monge-Sanz, B.M., A. Bozzo, N. Byrne, M.P. Chipperfield, M. Diamantakis, J. Flemming, L.J. Gray, R.J. Hogan, L. Jones, L. Magnusson, I. Polichtchouk, T.G. Shepherd, N. Wedi, and A. Weisheimer, A stratospheric prognostic ozone for seamless Earth system models: performance, impacts and future, ***Atmos. Chem. Phys.***, ***22***, 4277–4302, doi:10.5194/acp-22-4277-2022, 2022.

Morgenstern, O., H. Akiyoshi, Y. Yamashita, D.E. Kinnison, R.R. Garcia, D.A. Plummer, J. Scinocca, G. Zeng, E. Rozanov, A. Stenke, L.E. Revell, G. Pitari, E. Mancini, E., G. Di Genova, S.S. Dhomse, and M.P. Chipperfield, Ozone sensitivity to varying greenhouse gases and ozone-depleting substances in CCMI-1 simulations, ***Atmos. Chem. Phys.***, ***18***, 1091–1114, doi:10.5194/acp-18-1091-2018, 2018.

Morgenstern, O., The Southern Annular Mode in 6th coupled model intercomparison project models, ***J. Geophys. Res. Atmos***, ***126*** (5), doi:10.1029/2020JD034161, 2021.

Morgenstern, O., S.M. Frith, G.E. Bodeker, V. Fioletov, and R.J. van der A, Reevaluation of total-column ozone trends and of the Effective Radiative Forcing of ozone-depleting substances, ***Geophys. Res. Lett.***, ***48*** (21), doi:10.1029/2021GL095376, 2021.

Morrow, R., and E. Kestenare, 22-year surface salinity changes in the Seasonal Ice Zone near 140°E off Antarctica, ***J. Mar. Syst.***, 175, 46–62, doi:10.1016/j.jmarsys.2017.07.003, 2017.

Munro, D.R., N.S. Lovenduski, T. Takahashi, B.B. Stephens, T. Newberger, and C. Sweeney, Recent evidence for a strengthening CO2 sink in the Southern Ocean from carbonate system measurements in the Drake Passage (2002–2015), ***Geophys. Res. Lett.***, ***42*** (18), 7623–7630, doi:10.1002/2015gl065194, 2015.

Muthers, S., Anet, J.G., Stenke, A., Raible, C.C., Rozanov, E., Brönnimann, S., Peter, T., Arfeuille, F.X., Shapiro, A.I., Beer, J. and F. Steinhilber, The coupled atmosphere–chemistry–ocean model SOCOL-MPIOM. Geosci. Model Dev., 7(5), pp.2157-2179, doi:10.5194/gmd-7-2157-2014, 2014.

Myhre, G., D. Shindell, F.-M. Bréon, W. Collins, J. Fuglestvedt, J. Huang, D. Koch, J.-F. Lamarque, D. Lee, B. Mendoza, T. Nakajima, A. Robock, G. Stephens, T. Takemura, and H. Zhang, Anthropogenic and Natural Radiative Forcing, Chapter 8 in ***Climate Change 2013: The Physical Science Basis, Contribution of Working Group I to the Fifth Assessment Report of the Intergovernmental Panel on Climate Change***, edited by T.F. Stocker, D. Qin, G.-K. Plattner, M. Tignor, S.K. Allen, J. Boschung, A. Nauels, Y. Xia, V. Bex, and P.M. Midgley, Cambridge University Press, Cambridge, United Kingdom and New York, NY, USA, [available at: https://www.ipcc.ch/site/assets/uploads/2018/02/WG1AR5_Chapter08_FINAL.pdf], 2013.

Naoe, H., M. Deushi, K. Yoshida, and K. Shibata, Future changes in the ozone quasi-biennial oscillation with increasing GHGs and ozone recovery in CCMI simulations, ***J. Clim.***, ***30*** (17), 6977–6997, doi:10.1175/JCLI-D-16-0464, 2017.

Nash, J., and R. Saunders, A review of Stratospheric Sounding Unit radiance observations for climate trends and reanalyses, ***Q. J. R. Meteorol. Soc.***, ***141***, 2103–2113, doi:10.1002/qj.2505, 2015.

Naughten, K.A., P.R. Holland, P. Dutrieux, S. Kimura, D.T. Bett, and A. Jenkins, Simulated twentieth- century ocean warming in the Amundsen Sea, West Antarctica, ***Geophys. Res. Lett.***, ***49*** (5), e2021GL094566, doi:10.1029/2021GL094566, 2022.

Neely III, R.R., D.R. Marsh, K.L. Smith, S.M. Davis, and L.M. Polvani, Biases in Southern Hemisphere climate trends induced by coarsely specifying the temporal resolution of stratospheric ozone, ***Geophys. Res. Lett.***, ***41*** (23), 8602–8610, doi:10.1002/2014GL061627, 2014.

Newman, P.A., L.D. Oman, A.R. Douglass, E.L. Fleming, S.M. Frith, M.M. Hurwitz, S.R. Kawa, C.H. Jackman, N.A. Krotkov, E.R. Nash, J.E. Nielsen, S. Pawson, R.S. Stolarski, and G.J.M. Velders, What would have happened to the ozone layer if chlorofluorocarbons (CFCs) had not been regulated?, ***Atmos. Chem. Phys.***, ***9***, 2113–2128, doi:10.5194/ acp-9-2113-2009, 2009.

Noble, T.L., E.J. Rohling, A.R.A. Aitken, H.C. Bostock, Z. Chase, N. Gomez, L.M. Jong, M.A. King, A.N. Mackintosh, F.S. McCormack, R.M. McKay, L. Menviel, S.J. Phipps, M.E. Weber, C.J. Fogwill, B. Gayen, N.R. Golledge, D.E. Gwyther, A. McC. Hogg, Y.M. Martos, B. Pena-Molino, J. Roberts, T. van de Flierdt, and T. Williams, The sensitivity of the Antarctic ice sheet to a changing climate: past, present, and future, ***Rev. Geophys.***, ***58*** (4), doi:10.1029/2019rg000663, 2020.

Nowack, P.J., N.L. Abraham, A.C. Maycock, P. Braesicke, J.M. Gregory, M.M. Joshi, A. Osprey, and J.A. Pyle, A large ozone–circulation feedback and its implications for global warming assessments, ***Nat. Clim. Change***, ***5***, 41–45, doi:10.1038/nclimate2451, 2015.

Nowack, P.J., P. Braesicke, N.L. Abraham, and J.A. Pyle, On the role of ozone feedback in the ENSO amplitude response under global warming, ***Geophys. Res. Lett.***, ***44***, 3858–3866, doi:10.1002/2016GL072418, 2017.

Nowack, P.J., N.L. Abraham, P. Braesicke, and J.A. Pyle, The impact of stratospheric ozone feedbacks on climate sensitivity estimates, ***J. Geophys. Res. Atmos.***, ***123***, 4630–4641, doi:10.1002/2017JD027943, 2018.

Nuetzel, M., A. Podglajen, H. Garny, and F. Ploeger, Quantification of water vapour transport from the Asian monsoon to the stratosphere, ***Atmos. Chem. Phys.***, ***19***, 8947–8966, doi:10.5194/acp-19-8947-2019, 2019.

O'Connor, F.M., N.L. Abraham, M. Dalvi, G.A. Folberth, P.T. Griffiths, C. Hardacre, B.T. Johnson, R. Kahana, J. Keeble, B. Kim, O. Morgenstern, J.P. Mulcahy, M. Richardson, E. Robertson, J. Seo, S. Shim, J.C. Teixeira, S.T. Turnock, J. Williams, A.J. Wiltshire, S. Woodward, and G. Zeng, Assessment of preindustrial to present-day anthropogenic climate forcing in UKESM1, ***Atmos. Chem. Phys.***, ***21***, 1211–1243, doi:10.5194/acp-21-1211-2021, 2021.

Oehrlein, J., G. Chiodo, and L.M. Polvani, The effect of interactive ozone chemistry on weak and strong stratospheric polar vortex events, ***Atmos. Chem. Phys.***, ***20*** (17), 10,531–10,544, doi:10.5194/acp-20-10531-2020, 2020.

Oh, J., S.W. Son, J. Choi E.P. Lim, C. Garfinkel, H. Hendon, Y. Kim, and H.S. Kang, Impact of stratospheric ozone on the subseasonal prediction in the southern hemisphere spring, ***Prog. Earth Planet. Sci.***, ***9*** (1), doi:10.1186/s40645-022-00485-4, 2022.

Olsen, M.A., G.L. Manney, and J. Liu, The ENSO and QBO impact on ozone variability and stratosphere troposphere exchange relative to the subtropical jets, ***J. Geophys. Res. Atmos.***, ***124***, 7379–7392, doi:10.1029/2019JD030435, 2019.

Oman, L., D.W. Waugh, S. Pawson, R.S. Stolarski, and P.A. Newman, On the influence of anthropogenic forcings on changes in the stratospheric mean age, ***J. Geophys. Res. Atmos.***, ***114*** (D3), D03105, doi:10.1029/2008JD010378, 2009.

O'Neill, M.E., L. Orf, G.M. Heymsfield, and K. Halbert, Hydraulic jump dynamics above supercell thunderstorms, ***Science***, ***373*** (6560), 1248–1251, doi:10.1126/science.abh3857, 2021.

Orbe, C., D.A. Plummer, D.W. Waugh, H. Yang, P. Jöckel, D.E. Kinnison, B. Josse. V. Marecal, M. Deushi, N.L. Abraham, A.T. Archibald, M.P. Chipperfield, S. Dhomse, W. Feng, and S. Bekki, Description and Evaluation of the specified-dynamics experiment in the Chemistry-Climate Model Initiative, ***Atmos. Chem. Phys.***, ***20***, 3809–3840, doi:10.5194/acp-20-3809-2020, 2020.

Pincus, R., S.A. Buehler, M. Brath, C. Crevoisier, O. Jamil, K.F. Evans, J. Manners, R.L. Menzel, E.J. Mlawer, D. Paynter, R.L. Pernak, and Y. Tellier, Benchmark calculations of radiative forcing by greenhouse gases, ***J. Geophys. Res. Atmos.***, ***125*** (23), e2020JD033483, doi:10.1029/2020JD033483, 2020.

Plaza, N.P., A. Podglajen, C. Pena-Ortiz, and F. Ploeger, Processes influencing lower stratospheric water vapor in monsoon anticyclones: insights from Lagragian modelling, ***Atmos. Chem. Phys.***, ***21*** (12), 9585–9607, doi:105194/acp-21-9585-2021, 2021.

Ploeger, F., B. Legras, E. Charlesworth, X. Yan, M. Diallo, P. Konopka, T. Birner, M. Tao, A. Engel, and M. Riese, How robust are stratospheric age of air trends from different reanalyses?, ***Atmos. Chem. Phys.***, ***19***, 6085–6105, doi:10.5194/acp-19-6085-2019, 2019.

Ploeger, F., M. Diallo, E. Charlesworth, P. Konopka, B. Legras, J. C. Laube, J.-U. Grooß, G. Günther, A. Engel, and M. Riese, The stratospheric Brewer–Dobson circulation inferred from age of air in the ERA5 reanalysis, ***Atmos. Chem. Phys.***, ***21***, 8393–8412, doi:10.5194/acp-21-8393-2021, 2021.

Ploeger, F. and Garny, H., Hemispheric asymmetries in recent changes in the stratospheric circulation, ***Atmos. Chem. Phys.***, ***22***, 5559–5576, https://doi.org/10.5194/acp-22-5559-2022, 2022.

Plumb, R.A., Stratospheric transport, ***J. Meteorol. Soc. Japan***, ***80***, 793–809, doi:10.2151/jmsj.80.793, 2002.

Pohlmann, H., W.A. Müller, M. Bittner, S. Hettrich, K. Modali, K. Pankatz, and J. Marotzke, Realistic quasi-biennial oscillation variability in historical and decadal hindcast simulations using CMIP6 forcing, ***Geophys. Res. Lett.***, ***46***, 14,118–14,125, doi:10.1029/2019GL084878, 2019.

Polvani, L.M., M. Abalos, R. Garcia, D. Kinnison, and W.J. Randel, Significant weakening of Brewer-Dobson circulation trends over the 21st century as a consequence of the Montreal Protocol, ***Geophys. Res. Lett.***, ***45***, doi:10.1002/2017GL075345, 2018.

Polvani, L.M., and K. Bellomo, The key role of ozone-depleting substances in weakening the walker circulation in the second half of the twentieth century, ***J. Clim.***, ***32*** (5), 1411–1418, doi:10.1175/JCLI-D-17-0906.1, 2019.

Polvani, L.M., L. Wang, M. Abalos, N. Butchart, M.P. Chipperfield, M. Dameris, M. Deushi, S.S. Dhomse, P. Jöckel, D. Kinnison, M. Michou, O. Morgenstern, L.D. Oman, D.A. Plummer, and K.A. Stone, Large impacts, past and future, of ozone-depleting substances on Brewer-Dobson circulation trends: A multimodal assessment, ***J. Geophys. Res. Atmos.***, ***124***, 6669–6680, doi:10.1029/2018JD029516, 2019.

Polvani, L.M., M. Previdi, M.R. England, G. Chiodo, and K.L. Smith, Substantial twentieth-century Arctic warming caused by ozone-depleting substances, ***Nat. Clim. Change***, ***10***, 130–133, doi:10.1038/s41558-019-0677-4, 2020.

Polvani, L.M., A. Banerjee, R. Chemke, E.W. Doddridge, D. Ferreira, A. Gnanadesikan, M.A. Holland, Y. Kostov, J. Marshall, W.J.M. Seviour, S. Solomon, and D.W. Waugh, Interannual SAM modulation of Antarctic sea ice extent does not account for its long-term trends, pointing to a limited role for ozone depletion, ***Geophys. Res. Lett.***, ***48*** (21), e2021GL094871, doi:10.1029/2021GL094871, 2021.

Prather, M., P. Midgley, F.S. Rowland, and R. Stolarski, The ozone layer: The road not taken, ***Nature***, ***381***, 551–554, doi:10.1038/381551a0, 1996.

Previdi, M., and L.M. Polvani, Impact of the Montreal Protocol on Antarctic surface mass balance and implications for global sea level rise, ***J. Clim.***, ***30***, 7247–7253, doi:10.1175/jcli-d-17-0027.1, 2017.

Purich, A., and M.H. England, Tropical teleconnections to Antarctic sea ice during

austral spring 2016 in coupled pacemaker experiments, ***Geophys. Res. Lett.***, ***46***, 6848–6858, doi:10.1029/2019gl082671, 2019.

Rae, C.D., J. Keeble, P. Hitchcock, and P.A. Pyle, Prescribing zonally asymmetric ozone climatologies in climate models: Performance compared to a chemistry-climate model, ***J. Adv. Model. Earth Syst.***, ***11***, 918–933, doi:10.1029/2018ms001478, 2019.

Ramanathan, V., and R.E. Dickinson, The role of stratospheric ozone in the zonal and seasonal radiative energy balance of the earth-troposphere system, ***J. Atmos. Sci.***, ***36*** (6), 1084–1104, doi:10.1175/1520-0469(1979)036<1084:TROSOI>2.0.CO;2, 1979.

Ramaswamy, V., M.-L. Chanin, J. Angell, J. Barnett, D. Gaffen, M. Gelman, P. Keckhut, Y. Koshelkov, K. Labitzke, J.-J.R. Lin, A. O'Neill, J. Nash, W. Randel, R. Rood, K. Shine, M. Shiotani, and R. Swinbank, Stratospheric temperature trends: Observations and model simulations, ***Rev. Geophys.***, 39(1), 71– 122, doi:10.1029/1999RG000065, 2002.

Ramaswamy, V., W. Collins, J. Haywood, J. Lean, N. Mahowald, G. Myhre, V. Naik, K.P. Shine, B. Soden, G. Stenchikov, and T. Storelvmo, Radiative forcing of climate: the historical evolution of the radiative forcing concept, the forcing agents and their quantification, and applications, ***Meteorol. Monogr.***, ***59*** (1), doi:10.1175/AMSMONOGRAPHS-D-19-0001.1, 2019.

Randel, W., and M. Park, Diagnosing observed stratospheric water vapor relationships to the cold point tropical tropopause, ***J. Geophys. Res. Atmos.***, ***124***, 7018–7033, doi:10.1029/2019JD030648, 2019.

Randel, W.J., F. Wu, and R. Stolarski, Changes in column ozone correlated with the stratospheric EP flux, ***J. Meteorol. Soc. Japan***, ***80***, 849–862, doi:10.2151/jmsj.80.849, 2002.

Randel, W.J., A.K. Smith, F. Wu, C.-Z. Zou, and H. Qian, Stratospheric temperature trends over 1979-2015 derived from combined SSU, MLS and SABER satellite observations, ***J. Clim.***, ***29*** (13), 4843–4859, doi:10.1175/JCLI-D-15-0629.1, 2016.

Rao, J., and C.I. Garfinkel, Arctic ozone loss in March 2020 and its seasonal prediction in CFSv2: A comparative study with the 1997 and 2011 cases, ***J. Geophys. Res. Atmos.***, ***125*** (21), e2020JD033524, doi:10.1029/2020JD033524, 2020.

Rao, J., C.I. Garfinkel, and I.P. White, How does the Quasi-Biennial Oscillation affect the boreal winter tropospheric circulation in CMIP5/6 models?, ***J. Clim.***, ***33***, 8975–8996, doi:10.1175/JCLI-D-20-0024.1, 2020.

Rao, J., and C.I. Garfinkel, Projected changes of stratospheric final warmings in the Northern and Southern Hemispheres by CMIP5/6 models, ***Clim. Dyn.***, ***56***, 3353–3371, doi:10.1007/s00382-021-05647-6, 2021a.

Rao, J., and C.I. Garfinkel, CMIP5/6 models project little change in the statistical characteristics of sudden stratospheric warmings in the 21st century, ***Environ. Res. Lett.***, ***16*** (3), 034024, doi:10.1088/1748-9326/abd4fe, 2021b.

Rao, J., and C.I. Garfinkel, The strong stratospheric polar vortex in March 2020 in sub-seasonal to seasonal models: Implications for empirical prediction of the low Arctic total ozone extreme, ***J. Geophys. Res. Atmos.***, ***126*** (9), doi:10.1029/2020JD034190, 2021c.

Remsberg, E.E., B.T. Marshall, M. Garcia-Comas, D. Krueger, G.S. Lingenfelser, J. Martin-Torres, M.G. Mlynczak, J.M. Russell III, A.K. Smith, Y. Zhao, C. Brown, L.L. Gordley, M.J. Lopez-Gonzalez, M. Lopez-Puertas, C.-Y. She, M.J. Taylor, and R.E. Thompson, Assessment of the quality of the Version 1.07 temperature-versus-pressure profiles of the middle atmosphere from TIMED/SABER, ***J. Geophys. Res. Atmos.***, ***113*** (D17), doi:10.1029/2008JD010013, 2008.

Revell, L.E., F. Robertson, H. Douglas, O. Morgenstern, and D. Frame, Influence of ozone forcing on 21st century Southern Hemisphere surface westerlies in CMIP6 models, ***Geophys. Res. Lett.***, ***49***, e2022GL098252, doi:10.1029/2022GL098252, 2022.

Richter, J.H., C.C. Chen, Q. Tang, Q., S. Xie, and P.J. Rasch, Improved simulation of the QBO in E3SMv1, ***J. Adv. Model. Earth Syst.***, ***11***, 3403–3418, doi:10.1029/2019MS001763, 2019.

Richter, J.H., J.A. Anstey, N. Butchart, Y. Kawatani, G.A. Meehl, S. Osprey, and I.R. Simpson, Progress in simulating the quasi-biennial oscillation in CMIP models, ***J. Geophys. Res. Atmos.***, ***125*** (8), e2019JD032362, doi:10.1029/2019JD032362, 2020a.

Richter, J.H., N. Butchart, Y. Kawatani, A.C. Bushell, L. Holt, F. Serva, J. Anstey, I.R. Simpson, S. Osprey, K. Hamilton, P. Braesicke, C. Cagnazzo, C.-C. Chen, R.R. Rolando, L.J. Gray, T. Kerzenmacher, F. Lott, C. McLandress, H. Naoe, J. Scinocca, T N. Stockdale, S. Versick, S. Watanabe, K. Yoshida, and S. Yukimoto, Response of the quasi-biennial oscillation to a warming climate in global climate models, ***Q. J. R. Meteorol. Soc.***, ***148*** (744), 1490–1518, doi:10.1002/qj.3749, 2020b.

Rieder, H.E., L.M. Polvani, and S. Solomon, Distinguishing the impacts of ozone-depleting substances and well-mixed greenhouse gases on Arctic stratospheric ozone and temperature trends, ***Geophys. Res. Lett.***, ***41*** (7), 2652–2660, doi:10.1002/2014GL059367, 2014.

Rieder, H.E., G. Chiodo, J. Fritzer, C. Wienerroither, and L.M. Polvani, Is interactive ozone chemistry important to represent polar cap stratospheric temperature variability in Earth-System Models?, ***Environ. Res. Lett.***, ***14*** (4), 044026, doi:10.1088/1748-9326/ab07ff, 2019.

Rieger, L., W.J. Randel, A.E. Bourassa, and S. Solomon, Stratospheric temperature and ozone anomalies associated with the 2020 Australian New Year fires, ***Geophys. Res. Lett.***, ***48*** (24), e2021GL095898, doi:10.1029/2021GL095898, 2021.

Rignot, E., J. Mouginot, B. Scheuchl, M. van den Broeke, M.J. van Wessem, and M. Morlighem, Four decades of Antarctic Ice Sheet mass balance from 1979-2017, ***Proc. Natl. Acad. Sci.***, ***116***, 1095–1103, doi:10.1073/pnas.1812883116, 2019.

Rintoul, S.R., The global influence of localized dynamics in the Southern Ocean, ***Nature***, ***558***, 209–218, doi:10.1038/s41586-018-0182-3, 2018.

Roach, L.A., J. Dörr, C.R. Holmes, F. Massonnet, E.W. Blockley, D. Notz, T. Rackow, M.N. Raphael, S.P. O'Farrell, D.A. Bailey, and C.M. Bitz, Antarctic sea ice area in CMIP6, ***Geophys. Res. Lett.***, ***47*** (9), doi:10.1029/2019gl086729, 2020.

Romanowsky, E., D. Handorf, R. Jaiser, I. Wohltmann, W. Dorn, J. Ukita, J. Cohen, K. Dethloff, and M. Rex, The role of stratospheric ozone for Arctic-midlatitude linkages, ***Sci. Rep.***, ***9*** (1), 7962, doi:10.1038/s41598-019-43823-1, 2019.

Santer, B.D., S. Po-Chedley, C. Mears, J.C. Fyfe, N. Gillett, Q. Fu, J.F. Painter, S. Solomon, A.K. Steiner, F.J. Wentz, M.D. Zelinka, and C.-Z. Zou, Using climate model simulations to constrain observations, ***J. Clim.***, ***34*** (15), 6281–6301, doi:10.1175/JCLI-D-20-0768.1, 2021.

Schlosser, E., F.A. Haumann, and M.N. Raphael, Atmospheric influences on the anomalous 2016 Antarctic sea ice decay, ***Cryosphere***, ***12***, 1103–1119, doi:10.5194/tc-12-1103-2018, 2018.

Seager, R., M.A. Cane, N. Henderson, D.E. Lee, R. Abernathey, and H. Zhang, Strengthening of the tropical Pacific zonal SST gradient is a consistent response to rising greenhouse gases, ***Nature Clim. Change***, ***9***, 517–522, doi:10.1038/s41558-019-0505-x, 2019.

Seidel, D.J., J. Li, C. Mears, I. Moradi, J. Nash, W.J. Randel, R. Saunders, D.W.J. Thompson, and C.-Z. Zou, Stratospheric temperature changes during the satellite era, ***J. Geophys. Res. Atmos.***, ***121*** (2), 664–681, doi:10.1002/2015JD024039, 2016.

Sen Gupta, A., and M.H. England, Coupled ocean–atmosphere–ice response to variations in the Southern Annular Mode, ***J. Clim.***, ***19***, 4457–4486, doi:10.1175/JCLI3843.1, 2006.

Seviour, W.J.M., Weakening and shift of the Arctic stratospheric polar vortex: Internal variability or forced response?, ***Geophys. Res. Lett.***, ***44***, 3365–3373, doi:10.1002/2017GL073071, 2017.

Seviour, W.J.M., D.W. Waugh, L.M. Polvani, G.J.P. Correa, and C.I. Garfinkel, Robustness of the simulated tropospheric response to ozone depletion, ***J. Clim.***, ***30***, 2577–2585, doi:10.1175/JCLI-D-16-0817.1, 2017.

Seviour, W.J.M., F. Codron, E.W. Doddridge, D. Ferreira, A. Gnanadesikan, M. Kelley, Y. Kostov, J. Marshall, L.M. Polvani, J.L. Thomas, and D.W. Waugh, The Southern Ocean sea surface temperature response to ozone depletion: a multimodel comparison, ***J. Clim.***, ***32***, 5107–5121, doi:10.1175/jcli-d-19-0109.1, 2019.

Sexton, D., The effect of stratospheric ozone depletion on the phase of the Antarctic Oscillation, ***Geophys. Res. Lett.***, ***28*** (19), 3697–3700, doi:10.1029/2001GL013376, 2001.

Shangguan, M., W. Wang, and S. Jin, Variability of temperature and ozone in the upper troposphere and lower stratosphere from multi-satellite observations and reanalysis data, ***Atmos. Chem. Phys.***, ***19***, 6659–6679, doi:10.5194/acp-19-6659-2019, 2019.

Shepherd, A., D. Wingham, and E. Rignot, Warm ocean is eroding West Antarctic ice sheet, ***Geophys. Res. Lett.***, ***31*** (23), doi:10.1029/2004gl021106, 2004.

Shepherd, T.G., and C. McLandress, A robust mechanism for strengthening of the Brewer-Dobson Circulation in response to climate change: Critical-layer control of subtropical wave breaking, ***J. Atmos. Sci.***, ***68*** (4), 784–797, doi:10.1175/2010JAS3608.1, 2011.

Shibata, K., and M. Deushi, Radiative effect of ozone on the

quasi-biennial oscillation in the equatorial stratosphere, ***Geophys. Res. Lett.***, ***32*** (24), doi:10.1029/2005GL023433, 2005.

Shibata, K., Simulations of ozone feedback effects on the equatorial quasi-biennial oscillation with a chemistry–climate model, ***Climate***, ***9*** (8), 123, doi:10.3390/cli9080123, 2021.

Shibata, K., and H. Naoe, Decadal amplitude modulations of the stratospheric quasi-biennial oscillation, ***J. Meteorol. Soc. Japan***, ***100***, 29–44, doi:10.2151/jmsj.2022-001, 2022.

Shindell, D., G. Faluvegi, L. Nazarenko, K. Bowman, J.-F. Lamarque, A. Voulgarakis, G.A. Schmidt, O. Pechony, and R. Ruedy, Attribution of historical ozone forcing to anthropogenic emissions, ***Nat. Clim. Change***, ***3***, 567–570, doi:10.1038/nclimate1835, 2013.

Sigmond, M., M.C. Reader, J.C. Fyfe, and N.P. Gillett, Drivers of past and future Southern Ocean change: Stratospheric ozone versus greenhouse gas impacts, ***Geophys. Res. Lett.***, ***38*** (12), L12601, doi:10.1029/2011GL047120, 2011.

Simmons, A., C. Soci, J. Nicolas, B. Bell, P. Berrisford, R. Dragani, J. Flemming, L. Haimberger, S. Healy, H. Hersbach, and A. Horányi, ***Global stratospheric temperature bias and other stratospheric aspects of ERA5 and ERA5.1***, ECMWF Technical Memoranda No. 859, European Centre for Medium-Range Weather Forecasts, 40 pp., doi:10.21957/rcxqfmg0, 2020.

Singh, H.A., L.M. Polvani, and P.J. Rasch, Antarctic sea ice expansion, driven by internal variability, in the presence of increasing atmospheric CO2, ***Geophys. Res. Lett.***, ***46*** (24), 14,762–14,771, doi:10.1029/2019GL083758, 2019.

Skeie, R.B., G. Myhre, Ø. Hodnebrog, P.J. Cameron-Smith, M. Deushi, M.I. Hegglin, L.W. Horowitz, R.J. Kramer, M. Michou, M.J. Mills, D.J.L. Olivié, F.M.O. Connor, D. Paynter, B.H. Samset, A. Sellar, D. Shindell, T. Takemura, S. Tilmes, and T. Wu, Historical total ozone radiative forcing derived from CMIP6 simulations, ***npj Clim. Atmos. Sci.***, ***3*** (1), 32, doi:10.1038/s41612-020-00131-0, 2020.

Smith, B., B. Smith, H.A. Fricker, A.S Gardner, B. Medley, J. Nilsson, F.S Paolo, N. Holschuh, S. Adusumilli, K. Brunt, B. Csatho, K. Harbeck, T. Markus, T. Neumann, M.R. Siegfried, and H.J. Zwally, Pervasive ice sheet mass loss reflects competing ocean and atmosphere processes, ***Science***, ***368*** (6496), 1239–1242, doi:10.1126/science.aaz5845, 2020.

Smith, K.L., and L.M. Polvani, The surface impacts of Arctic stratospheric ozone anomalies, ***Environ. Res. Lett.***, ***9*** (7), doi:10.1088/1748- 9326/9/7/074015, 2014.

Solomon, A., L.M. Polvani, K.L. Smith, and R.P. Abernathey, The impact of ozone depleting substances on the circulation, temperature, and salinity of the Southern Ocean: An attribution study with CESM1(WACCM), ***Geophys. Res. Lett.***, ***42***, 5547–5555, doi:10.1002/2015gl064744, 2015.

Solomon, S., K.H. Rosenlof, R.W. Portmann, J.S. Daniel, S.M. Davis, T.J. Sanford, and G.-K. Plattner, Contributions of stratospheric water vapor to decadal changes in the rate of global warming, ***Science***, ***327*** (5970), 1219–1223, doi:10.1126/science.1182488, 2010.

Solomon, S., D.J. Ivy, D. Kinnison, M.J. Mills, R.R. Neely, and A. Schmidt, Emergence of healing in the Antarctic ozone layer, ***Science***, ***353***, 269–274, doi:10.1126/science.aae0061, 2016.

Solomon, S., K. Dube, K. Stone, P. Yu, D. Kinnison, O.B. Toon, S.E. Strahan, K.H. Rosenlof, R. Portmann, S. Davis, W. Randel, P. Bernath, C. Boone, C.G. Bardeen, A. Bourassa, D. Zawada, and D. Degenstein, On the stratospheric chemistry of midlatitude wildfire smoke, ***Proc. Natl. Acad. Sci.***, ***119*** (10), doi:10.1073/pnas.2117325119, 2022.

Son, S.-W., L.M. Polvani, D.W. Waugh, H. Akiyoshi, R.R. Garcia, D. Kinnison, S. Pawson, E. Rozanov, T.G. Shepherd, and K. Shibata, The impact of stratospheric ozone recovery on the Southern Hemisphere westerly jet, ***Science***, ***320*** (5882), 1486–1489, doi:10.1126/science.1155939, 2008.

Son, S.-W., E.P. Gerber, J. Perlwitz, L.M. Polvani, N. P. Gillett, K.-H. Seo, V. Eyring, T.G. Shepherd, D. Waugh, H. Akiyoshi, J. Austin, A. Baumgaertner, S. Bekki, P. Braesicke, C. Brühl, N. Butchart, M.P. Chipperfield, D. Cugnet, M. Dameris, S. Dhomse, S. Frith, H. Garny, R. Garcia, S.C. Hardiman, P. Jöckel, J.F. Lamarque, E. Mancini, M. Marchand, M. Michou, T. Nakamura, O. Morgenstern, G. Pitari, D.A. Plummer, J. Pyle, E. Rozanov, J.F. Scinocca, K. Shibata, D. Smale, H. Teyssèdre, W. Tian, and Y. Yamashita, Impact of stratospheric ozone on Southern Hemisphere circulation change: A multimodel assessment, ***J. Geophys. Res. Atmos.***, ***115*** (D3), doi:10.1029/ 2010JD014271, 2010.

Son, S.-W., A. Purich, H.H. Hendon, B.-M. Kim, and L.M. Polvani, Improved seasonal forecast using ozone hole variability?, ***Geophys. Res. Lett.***, ***40***, 6231–6235, doi:10.1002/2013GL057731, 2013.

Son, S.-W., B-R Han, C.I. Garfinkel, S.-Y. Kim, P. Rokjin, N.L. Abraham, H. Akiyoshi, A.T. Archibald, N. Butchart, M.P. Chipperfield, M. Dameris, M. Deushi, S.S. Dhomse, S.C. Hardiman, P. Jöckel, D. Kinnison, M. Michou, O. Morgenstern, F.M. O'Connor, L.D. Oman, D.A. Plummer, A. Pozzer, L.E. Revell, E. Rozanov, A. Stenke, K. Stone, S. Tilmes, Y. Yamashita, and G. Zeng, Tropospheric jet response to Antarctic ozone depletion: An update with Chemistry-Climate Model Initiative (CCMI) models, ***Environ. Res. Lett.***, ***13*** (5), doi:10.1088/1748-9326/aabf21, 2018.

SPARC (Stratosphere-troposphere Processes And their Role in Climate), ***SPARC Reanalysis Intercomparison Project (S-RIP) Final Report***, edited by M. Fujiwara, G.L. Manney, L.J. Gray, and J.S. Wright, SPARC Report No. 10, WCRP-6/2021, doi:10.17874/800dee57d13, 2022.

Spence, P., S.M. Griffies, M.H. England, A. McC. Hogg, O.A. Saenko, and N.C. Jourdain, Rapid subsurface warming and circulation changes of Antarctic coastal waters by poleward shifting winds, ***Geophys. Res. Lett.***, ***41*** (13), 4601–4610, doi:10.1002/2014gl060613, 2014.

Spencer, R.W., J.R. Christy, and W.D. Braswell, UAH Version 6 global satellite temperature products: Methodology and results, ***Asia Pac. J. Atmos. Sci.***, ***53***, 121–130, doi:10.1007/s13143-017-0010-y, 2017.

Stecher, L., F. Winterstein, M. Dameris, P. Joeckel, M. Ponater, and M. Kunze, Slow feedbacks resulting from strongly enhanced atmospheric methane mixing ratios in a chemistry–climate model with mixed-layer ocean, ***Atmos. Chem. Phys.***, ***21***, 731–754, doi:10.5194/acp-21-731-2021, 2021.

Steiner, A.K., F. Ladstädter, W.J. Randel, A.C. Maycock, Q. Fu, C. Claud, H. Gleisner, L. Haimberger, S.-P. Ho, P. Keckhut, T. Leblanc, C. Mears, L.M. Polvani, B.D. Santer, T. Schmidt, V. Sofieva, R. Wing, and C.-Z. Zou, Observed temperature changes in the troposphere and stratosphere from 1979 to 2018, ***J. Clim.***, ***33***, 8165–8194, doi:10.1175/JCLI-D-19-0998.1, 2020.

Stevenson, D.S., P.J. Young, V. Naik, J.-F. Lamarque, D.T. Shindell, A. Voulgarakis, R.B. Skeie, S.B. Dalsoren, G. Myhre, T.K. Berntsen, G.A. Folberth, S.T. Rumbold, W.J. Collins, I.A. MacKenzie, R.M. Doherty, G. Zeng, T.P.C. van Noije, A. Strunk, D. Bergmann, P. Cameron-Smith, D.A. Plummer, S.A. Strode, L. Horowitz, Y.H. Lee, S. Szopa, K. Sudo, T. Nagashima, B. Josse, I. Cionni, M. Righi, V. Eyring, A. Conley, K.W. Bowman, O. Wild, and A. Archibald, Tropospheric ozone changes, radiative forcing and attribution to emissions in the Atmospheric Chemistry and Climate Model Intercomparison Project (ACCMIP), ***Atmos. Chem. Phys.***, ***13***, 3063–3085, doi:10.5194/acp-13-3063-2013, 2013.

Stiller, G.P., T. von Clarmann, F. Haenel, B. Funke, N. Glatthor, U. Grabowski, S. Kellmann, M. Kiefer, A. Linden, S. Lossow, and M. López-Puertas, Observed temporal evolution of global mean age of stratospheric air for the 2002 to 2010 period, ***Atmos. Chem. Phys.***, ***12***, 3311–3331, doi:10.5194/acp-12-3311-2012, 2012.

Stiller, G.P., F. Fierli, F. Ploeger, C. Cagnazzo, B. Funke, F.J. Haenel, T. Reddmann, M. Riese, and T. von Clarmann, Shift of subtropical transport barriers explains observed hemispheric asymmetry of decadal trends of age of air, ***Atmos. Chem. Phys.***, ***17***, 11,177–11,192, doi:10.5194/acp-17-11177-2017, 2017.

Stone, K.A., S. Solomon, and D.E. Kinnison, On the identification of ozone recovery, ***Geophys. Res. Lett.***, ***45*** (10), 5158–5165, doi:10.1029/2018GL077955, 2018.

Stone, K.A., S. Solomon, D.E. Kinnison, C.F. Baggett, and E.A. Barnes, Prediction of Northern Hemisphere regional surface temperatures using stratospheric ozone information, ***J. Geophys. Res. Atmos.***, ***124***, 5922–5933, doi:10.1029/2018JD029626, 2019.

Stone, K.A., S. Solomon, and D.E. Kinnison, Prediction of Northern Hemisphere regional sea ice extent and snow depth using stratospheric ozone information, ***J. Geophys. Res. Atmos.***, ***125*** (22), e2019JD031770, doi:10.1029/2019JD031770, 2020.

Strahan, S.E., D. Smale, A.R. Douglass, T. Blumenstock, J.W. Hannigan, F. Hase, N.B. Jones, E. Mahieu, J. Notholt, L.D. Oman, I. Ortega, M. Palm, M. Prignon, J. Robinson, M. Schneider, R. Sussmann, and V.A. Velazco, Observed hemispheric asymmetry in stratospheric transport trends from 1994 to 2018, ***Geophys. Res. Letters***, ***47***, e2020GL088567, doi:10.1029/2020GL088567, 2020.

Stuecker, M.F., C.M. Bitz, and K.C. Armour, Conditions leading to the unprecedented low Antarctic sea ice extent during the 2016 austral spring season, ***Geophys. Res. Lett.***, ***44***, 9008–9019, doi:10.1002/2017gl074691, 2017.

Suneeth, K.V., and S.S. Das, Zonally resolved water vapour coupling with tropical tropopause temperature: Seasonal and interannual variability, and influence of the Walker circulation, ***Clim. Dyn.***, ***54***, 4657–4673, doi:10.1007/s00382-020-05255-w, 2020.

Swart, N.C., S.T. Gille, J.C. Fyfe, and N.P. Gillett, Recent Southern Ocean warming

and freshening driven by greenhouse gas emissions and ozone depletion, ***Nat. Geosci.***, ***11***, 836–841, doi:10.1038/s41561-018-0226-1, 2018.

Szopa, S., V. Naik, B. Adhikary, P. Artaxo, T. Berntsen, W.D. Collins, S. Fuzzi, L. Gallardo, A. Kiendler-Scharr, Z. Klimont, H. Liao, N. Unger, and P. Zanis, Short-Lived Climate Forcers, Chapter 6 in ***Climate Change 2021: The Physical Science Basis. Contribution of Working Group I to the Sixth Assessment Report of the Intergovernmental Panel on Climate Change*** edited by V. Masson-Delmotte, P. Zhai, A. Pirani, S.L. Connors, C. Péan, S. Berger, N. Caud, Y. Chen, L. Goldfarb, M.I. Gomis, M. Huang, K. Leitzell, E. Lonnoy, J.B.R. Matthews, T.K. Maycock, T. Waterfield, O. Yelekçi, R. Yu, and B. Zhou, Cambridge University Press, Cambridge, United Kingdom and New York, NY, USA, 105 pp., doi:10.1017/9781009157896.008, 2021.

Tegtmeier, S., M. Rex, I. Wohltmann, and K. Krüger, Relative importance of dynamical and chemical contributions to Arctic wintertime ozone, ***Geophys. Res. Lett.***, ***35*** (17), L17801, doi:10.1029/2008GL034250, 2008.

Thompson, D.W.J., and S. Solomon, Interpretation of recent Southern Hemisphere climate change, ***Science***, ***296*** (5569), 895–899, doi:10.1126/science.1069270, 2002.

Thompson, D.W.J., M.P. Baldwin, and S. Solomon, Stratosphere–troposphere coupling in the Southern Hemisphere, ***J. Atmos. Sci.***, ***62*** (3), 708–715, doi:10.1175/JAS-3321.1, 2005.

Thompson, D.W.J., S. Solomon, P.J. Kushner, M.H. England, K.M. Grise, and D.J. Karoly, Signatures of the Antarctic ozone hole in Southern Hemisphere surface climate change, ***Nat. Geosci.***, ***4*** (11), 741–749, doi:10.1038/ngeo1296, 2011.

Thornhill, G.D., W.J. Collins, R.J. Kramer, D. Olivié, R.B. Skeie, F.M. O'Connor, N.L. Abraham, R. Checa-Garcia, S.E. Bauer, M. Deushi, L.K. Emmons, P.M. Forster, L.W. Horowitz, B. Johnson, J. Keeble, J.-F. Lamarque, M. Michou, M.J. Mills, J.P. Mulcahy, G. Myhre, P. Nabat, V. Naik, N. Oshima, M. Schulz, C.J. Smith, T. Takemura, S. Tilmes, T. Wu, G. Zeng, and J. Zhang, Effective radiative forcing from emissions of reactive gases and aerosols–a multi-model comparison, ***Atmos. Chem. Phys.***, ***21*** (2), 853–874, doi:10.5194/acp-21-853-2021, 2021.

Turner, J., T. Phillips, G.J. Marshall, J.S. Hosking, J.O. Pope, T.J. Bracegirdle, and P. Deb, Unprecedented springtime retreat of Antarctic sea ice in 2016, ***Geophys. Res. Lett.***, ***44***, 6868–6875, doi:10.1002/2017gl073656, 2017.

Turner, J., T. Phillips, M. Thamban, W. Rahaman, G.J. Marshall, J.D. Wille, V. Favier, V.H.L. Winton, E. Thomas, Z. Wang, M. van den Broeke, J.S. Hosking, and T. Lachlan-Cope, The dominant role of extreme precipitation events in Antarctic snowfall variability, ***Geophys. Res. Lett.***, ***46***, 3502–3511, doi:10.1029/2018gl081517, 2019.

Velders, G.J.M., S.O. Andersen, J.S. Daniel, D.W. Fahey, and M. McFarland, The Importance of the Montreal Protocol in protecting climate, ***Proc. Natl. Acad. Sci.***, ***104*** (12), 4814–4819, doi:10.1073/ pnas.0610328104, 2007.

Velders, G.J.M., J.S. Daniel, S.A. Montzka, I. Vimont, M. Rigby, P.B. Krummel, J. Muhle, S. O'Doherty, R.G. Prinn, R.F. Weiss, and D. Young, Projections of hydrofluorocarbon (HFC) emissions and the resulting global warming based on recent trends in observed abundances and current policies, ***Atmos. Chem. Phys.***, ***22*** (9), 6087–6101, doi:10.5194/acp-2021-1070, 2022.

Virgin, J.G., and K.L. Smith, Is Arctic amplification dominated by regional radiative forcing and feedbacks: Perspectives from the World-Avoided scenario, ***Geophys. Res. Lett.***, ***46***, 7708–7717, doi:10.1029/2019GL082320, 2019.

von der Gathen, P., R. Kivi, I. Wohltmann, R.J. Salawitch, and M. Rex, Climate change favours large seasonal loss of Arctic ozone, ***Nat. Commun.***, ***12***, 3886, doi:10.1038/s41467-021-24089-6, 2021.

Wang, G., W. Cai, and A. Purich, Trends in Southern Hemisphere wind-driven circulation in CMIP5 models over the 21st century: Ozone recovery versus greenhouse forcing, ***J. Geophys. Res. Ocean***, ***119***, 2974–2984, doi:10.1002/2013JC009589, 2014.

Wang, G., H.H. Hendon, J.M. Arblaster, E.-P. Lim, S. Abhik, and P. van Rensch, Compounding tropical and stratospheric forcing of the record low Antarctic dseaice in 2016, ***Nat. Commun.***, ***10***, 13, doi:10.1038/s41467-018-07689-7, 2019b.

Wang L., S.C. Hardiman, P.E. Bett, R.E. Comer, C. Kent, and A.A. Scaife, What chance of a sudden stratospheric warming in the southern hemisphere?, ***Environ. Res. Lett.***, ***15*** (10), 104038, doi:10.1088/1748-9326/aba8c1, 2020.

Wang, L., K. Lyu, W. Zhuang, W. Zhang, S. Makarim, and X.-H. Yan, Recent shift in the warming of the Southern Oceans Modulated by decadal climate variability, ***Geophys. Res. Lett.***, ***48*** (3), doi:10.1029/2020gl090889, 2021.

Wang, X., A.E. Dessler, M.R. Schoeberl, W. Yu, and T. Wang, Impact of convectively lofted ice on the seasonal cycle of water vapor in the tropical tropopause layer, ***Atmos. Chem. Phys.***, ***19***, 14,621–14,636, doi:10.5194/acp-19-14621-2019, 2019a.

Wang, X., and A.E. Dessler, The response of stratospheric water vapor to climate change driven by different forcing agents, ***Atmos. Chem. Phys.***, ***20***, 13,267–13,282, doi:10.5194/acp-20-13267-2020, 2020.

Wargan, K., B. Weir, G.L. Manney, S.E. Cohn, and N.J. Livesey, The anomalous 2019 Antarctic ozone hole in the GEOS Constituent Data Assimilation System with MLS observations, ***J. Geophys. Res. Atmos.***, ***125*** (18), e2020JD033335, doi:10.1029/2020JD033335, 2020.

Waugh, D.W., and T.M. Hall, Age of stratospheric air: Theory, observations, and models, ***Rev. Geophys.***, ***40*** (4), doi:10.1029/2000RG000101, 2002.

Waugh, D.W., Age of stratospheric air, ***Nat. Geosci.***, ***2*** (1), 14–16, doi:10.1038/ngeo397, 2009.

Waugh, D.W., L. Oman, P.A. Newman, R.S. Stolarski, S. Pawson, J.E. Nielsen, and J. Perlwitz, Effect of zonal asymmetries in stratospheric ozone on simulated Southern Hemisphere climate trends, ***Geophys. Res. Lett.***, ***36*** (18), doi:10.1029/2009GL040419, 2009.

Waugh, D.W., A. Banerjee, J.C. Fyfe, and L.M. Polvani, Contrasting recent trends in Southern Hemisphere westerlies across different ocean basin, ***Geophys. Res. Lett.***, ***47*** (18), doi:10.1029/2020GL088890, 2020.

Wilcox, L.J., and A.J. Charlton-Perez, Final warming of the Southern Hemisphere polar vortex in high- and low-top CMIP5 models, ***J. Geophys. Res. Atmos.***, ***118***, 2535–2546, doi:10.1002/jgrd.50254, 2013.

WMO (World Meteorological Organization), Scientific Assessment of Ozone Depletion: 1989, Volume I, Global Ozone Research and Monitoring Project–Report No. 20, 532 pp., Geneva, Switzerland, 1989.

WMO (World Meteorological Organization), ***Scientific Assessment of Ozone Depletion: 2010***, Global Ozone Research and Monitoring Project–Report No. 52, 516 pp., Geneva, Switzerland, 2010.

WMO (World Meteorological Organization), ***Scientific Assessment of Ozone Depletion: 2014***, Global Ozone Research and Monitoring Project–Report No. 55, 416 pp., Geneva, Switzerland, 2014.

WMO (World Meteorological Organization), ***Scientific Assessment of Ozone Depletion: 2018***, Global Ozone Research and Monitoring Project–Report No. 58, 588 pp., Geneva, Switzerland, 2018.

Wu, Y., L.M. Polvani, and R. Seager: The Importance of the Montreal Protocol in Protecting Earth's Hydroclimate, Journal of Climate, 26(12), 4049-4068, 2013.

Wu, Y., I.R. Simpson, and R. Seager, Intermodel spread in the Northern Hemisphere stratospheric polar vortex response to climate change in the CMIP5 models, ***Geophys. Res. Lett.***, ***46***, 13,290–13,298, doi:10.1029/2019GL085545, 2019.

Xia, Y., Y. Hu, Y. Huang, C. Zhao, F. Xie, and Y. Yang, Significant contribution of severe ozone loss to the Siberian-Arctic surface warming in spring 2020, ***Geophys. Res. Lett.***, ***48***, e2021GL092509, doi:10.1029/2021GL092509, 2021.

Xie, F., X. Ma, J. Li, J. Huang, W. Tian, J. Zhang, Y. Hu, C. Sun, X. Zhou, J. Feng, and Y. Yang, An advanced impact of Arctic stratospheric ozone changes on spring precipitation in China, ***Clim. Dyn.***, ***51***, 4029–4041, doi:10.1007/s00382-018-4402-1, 2018.

Yook, S., D.W.J. Thompson, S. Solomon, and S.-Y. Kim, The key role of coupled chemistry–climate interactions in tropical stratospheric temperature variability, ***J. Clim.***, ***33***, 7619–7629, doi:10.1175/JCLI-D-20-0071.1, 2020.

Young, P.J., A.B. Harper, C. Huntingford, N.D. Paul, O. Morgenstern, P.A. Newman, L.D. Oman, S. Madronich, and R.R. Garcia, The Montreal Protocol protects the terrestrial carbon sink, ***Nature***, ***596***, 384–388, doi:10.1038/s41586-021-03737-3, 2021.

Yu, P., S.M. Davis, O.B. Toon, R.W. Portmann, C.G. Bardeen, J.E. Barnes, H. Telg, C. Maloney, and K.H. Rosenlof, Persistent stratospheric warming due to 2019–2020 Australian wildfire smoke, ***Geophys. Res. Lett.***, ***48*** (7), doi:10.1029/2021GL092609, 2021.

Yu, W., R. Garcia, J. Yue, J. Russell III, and M. Mlynczak, Variability of water vapor in the tropical middle atmosphere observed from satellites and interpreted using SD WACCM simulations, ***J. Geophys. Res. Atmos.***, ***127*** (13), doi:10.1029/2022JD036714, 2022.

Yue, J., J. Russell, Q. Gan, T. Wang, P. Rong, R. Garcia, and M. Mlynczak, Increasing

water vapor in the stratosphere and mesosphere after 2002, ***Geophys. Res. Lett.***, ***46***, 13,452–13,460, doi:10.1029/2019gl084973, 2019.

Zambri, B., S. Solomon, D.W.J. Thompson, and Q. Fu, Emergence of Southern Hemisphere stratospheric circulation changes in response to ozone recovery, ***Nat. Geosci.***, ***14***, 638–644, doi:10.1038/s41561-021-00803-3, 2021.

Zhang, J., C. Zhang, K. Zhang, M. Xu, J. Duan, M.P. Chipperfield, W. Feng, S. Zhao, and F. Xie, The role of chemical processes in the quasi-biennial oscillation (QBO) signal in stratospheric ozone, ***Atmos. Environ.***, ***244***, 117906, doi:10.1016/j.atmosenv.2020.117906, 2021.

Zhang, L., T.L. Delworth, W. Cooke, and X. Yang, Natural variability of Southern Ocean convection as a driver of observed climate trends, ***Nat. Clim. Change***, ***9***, 59–65, doi:10.1038/s41558-018-0350-3, 2019.

Zou, C.-Z., and W. Wang, Intersatellite calibration of AMSU-A observations for weather and climate applications, ***J. Geophys. Res. Atmos.***, ***116*** (D23), D23113, doi:10.1029/2011JD016205, 2011.

Zou, C.-Z., H. Qian, W. Wang, L. Wang, and C. Long, Recalibration and merging of SSU observations for stratospheric temperature trend studies, ***J. Geophys. Res. Atmos.***, ***119*** (23), 13,180–13,205, doi:10.1002/2014JD021603, 2014.

Zou, C.-Z., and H. Qian, Stratospheric temperature climate data record from merged SSU and AMSU-A observations, ***J. Atmos. Ocean. Technol.***, ***33*** (9), 1967–1984, doi:10.1175/JTECH-D-16-0018.1, 2016.

CHAPTER 6

Stratospheric Aerosol Injection and Its Potential Effect on the Stratospheric Ozone Layer

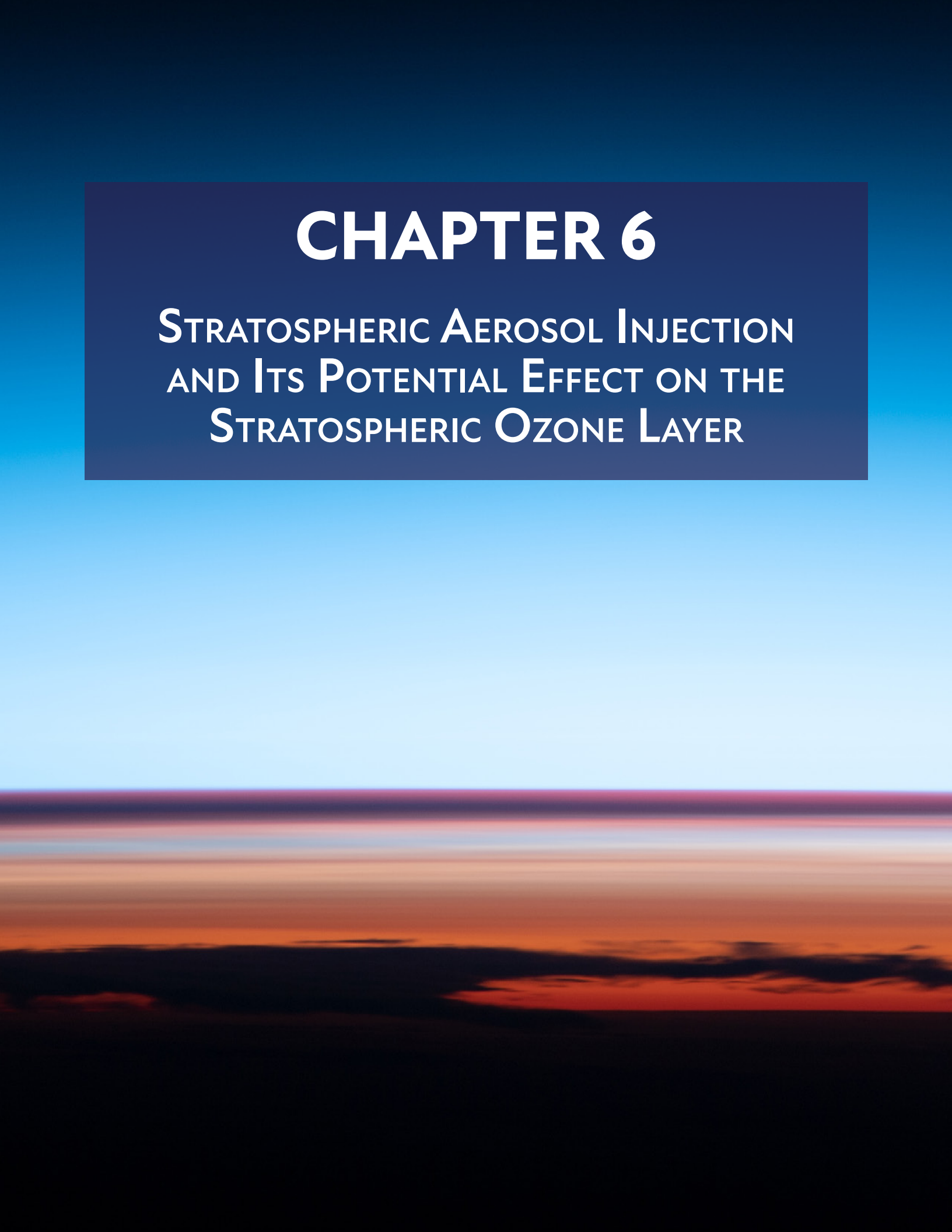

About the cover image:
The topmost, reddish-colored band is an aerosol layer between 23 and 30 km altitude as observed from the International Space Station on 12 February 2020. The layer resulted when the plume of unusually intense wildfires in Australia reached the lower stratosphere.

Photo credit: Provided by the ISS Crew Earth Observations Facility and the Earth Science and Remote Sensing Unit, Johnson Space Center, NASA

CHAPTER 6

Stratospheric Aerosol Injection and its Potential Effect on the Stratospheric Ozone Layer

Lead Authors : James Haywood
Simone Tilmes

Coauthors : Frank Keutsch
Ulrike Niemeier
Anja Schmidt
Daniele Visioni
Pengfei Yu

Contributing Authors : John Dykema
Anthony Crawford Jones
Anton Laasko
Catherine A. Wilka

Review Editors : Valentina Aquila
Karen H. Rosenlof

CONTENTS

Chapter 6: Stratospheric Aerosol Injection and Its Potential Effect on the Stratospheric Ozone Layer

SCIENTIFIC SUMMARY

Since the 2018 Ozone Assessment global warming has continued, having now reached approximately 1.2 °C above preindustrial levels. All climate model scenarios considered by IPCC (2021) indicate continued future warming beyond 1.5 °C above the preindustrial level, a limit that has been proposed to prevent further detrimental impacts. Ambitious mitigation and decarbonization efforts are required to minimize the likely overshoot of temperatures above this limit and to stabilize global surface temperatures in the future. However, with a temperature overshoot, irreversible impacts on the climate system may still occur. Stratospheric aerosol injection (SAI) has been suggested as a potential mechanism for reflecting sunlight back to space, thereby offsetting some of the surface warming. Evidence from explosive volcanic eruptions and various model simulations has shown that increasing stratospheric sulfate aerosols can substantially cool the planet. SAI and other solar radiation modification (SRM) approaches may therefore be the only option to keep the global surface temperature below the limit of 1.5 °C. The amount and duration of SAI required would depend on how fast atmospheric greenhouse gas (GHG) concentrations are lowered through mitigation and decarbonization efforts.

While SAI could reduce some of the impacts of global warming, it cannot restore past climatic conditions and would very likely cause unintended consequences, including changes in stratospheric ozone concentrations. To date, Earth system models (ESMs) have performed simulations to provide information on the climate impacts, benefits, and risks of SAI. Little research has been done to quantify the effects of SAI on the stratospheric composition and total column ozone (TCO) in a multi-model setting, and even fewer studies have examined the effects of aerosol types other than sulfate. While existing studies do not suggest a deepening of the ozone hole beyond that already experienced, current shortcomings in model representation of required processes limit confidence in the results.

This new chapter of the Ozone Assessment assesses the impacts of SAI on stratospheric ozone through SAI-related changes in stratospheric chemistry and transport. The dependence of SAI effects on future climate change scenarios and injection strategies, as well as uncertainties in our current understanding and model shortcomings, are assessed. Side effects and risks beyond the effects on stratospheric ozone are only briefly covered. It is well recognized that any potential future deployment of SAI is fundamentally linked to complex moral, ethical, and governance issues. These aspects are of critical importance but beyond the scope of this chapter, which will focus solely on physical science.

Framing SAI scenarios and strategies

- **Based on the observed cooling after large volcanic eruptions and various model studies, stratospheric aerosol injection (SAI) has the potential to reduce global mean temperatures. However, SAI cannot fully offset the widespread effects of global warming and produces unintended consequences, including effects on ozone.**

Details of these effects depend on the specifics of the SAI scenario and injection strategies. SAI uses stratospheric aerosols to reflect sunlight back to space, thereby cooling the planet. A straightforward offsetting of global warming from greenhouse gases (GHGs) cannot be achieved because SAI reduces a fraction of the incoming sunlight, which is seasonally and latitudinally dependent, while GHGs interact with terrestrial radiation and warm the planet more uniformly across latitudes and seasons. In addition, aerosol heating of the lowermost stratosphere by SAI using sulfate would result in further residual impacts, including changes in regional temperatures, precipitation, and stratospheric ozone. Details of the future climate scenario, the SAI scenario (i.e., the degree of SAI cooling applied), and applied SAI strategy (i.e., the specifics of injection location, timing, and material for achieving predefined climate goals) determine the specifics of the resulting impacts and risks.

- **Changes in future ozone using SAI depend on details of future climate change and the degree of SAI cooling applied. The three different SAI scenarios considered in this report (Figure 6-2, reproduced here) result in significantly different future ozone.** The "peakshaving" scenario (Panel A in Fig. 6-2) assumes delayed and then aggressive mitigation and carbon dioxide removal (CDR). SAI offsets the overshoot of the surface temperature target until greenhouse gases have been sufficiently reduced. The "strong SAI" scenario (Panel B) assumes a limited or no-mitigation high-warming future scenario, requiring continuously increasing SAI to keep surface temperatures from exceeding the climate target (dashed line). The "medium SAI" scenario (Panel C) assumes a limited or no-mitigation high-warming future scenario in which global warming is reduced to that of a moderate mitigation scenario (red line) by the deployment of SAI. A qualitative illustration of the required injection amounts for each scenario is shown in Panel D. The impacts on ozone of many other possible SAI scenarios have not been comprehensively studied to date. These scenarios currently do not include any socioeconomic feedbacks related to SAI.
- **In model simulations, different injection strategies have been developed to mitigate some of the unintended climate impacts of SAI.** For the same scenario, the specifics of the injection strategy, including location, timing, and material, can be adjusted to better achieve desired global and regional climate targets and minimize regional changes. Some models include a feedback control algorithm to modulate annual stratospheric sulfur injections in order to reach predefined climate temperature goals and other impact-relevant targets. Adjustments of sulfur injection to account for climate feedbacks help in managing uncertainties and limiting some of the side effects of SAI. Different strategies change the effectiveness of SAI and its effects on stratospheric ozone.

SAI effects on radiation and temperature

- **Multi-model comparisons reveal large uncertainties in forcing and surface cooling per unit of sulfur injected, which are attributed to differences in model complexity in representing key processes and details of SAI strategies.** Using sulfate aerosol, the efficacy of the radiative forcing ranges between −0.04 and −0.1 W m^{-2} per Tg SO_2 yr^{-1}, and the resulting surface cooling ranges from 0.04 to 0.14 °C per Tg SO_2 yr^{-1} based on a multi-model analysis. Continuous annual injection rates vary between 8 and 16 Tg of SO_2 yr^{-1} to cool the Earth by 1 °C; this range is approximately equivalent to the estimated injection amount from Mount Pinatubo in 1991, which resulted in less than 0.5 °C global surface cooling. The significant uncertainties associated with these values are attributed to differences in model representations of stratospheric chemistry, transport, radiation, and aerosol microphysical processes, including differences in model resolution. The choices of SAI injection location, timing, and material influence the resulting stratospheric aerosol mass, optical depth, and surface area density (SAD), which determine both cooling efficacy and impacts on stratospheric ozone.

Mechanisms for SAI impacts on ozone

- **Despite the limited number of model studies, some robust impacts of SAI on ozone have been identified. The combined effects of large-scale, long-term SAI on ozone are driven by 1) an increase in aerosol surface area, 2) stratospheric halogen concentrations, and 3) aerosol-induced heating of the stratosphere, which changes both stratospheric ozone chemistry and stratospheric dynamics.** SAI impacts on total column ozone (TCO) are regionally and seasonally dependent and result in ozone reduction in spring over Antarctica due to the increase in chemical ozone depletion. In contrast, an increase in TCO is possible (with increasing SAI amount) in the tropics, as well as in the winter Northern Hemisphere (NH) in mid- and high latitudes, due to increased tropical chemical ozone production rates and increased poleward transport.
  - **Enhanced stratospheric sulfate aerosol increases stratospheric heterogeneous chemical reaction rates and can enhance or deplete ozone depending on the altitude, latitude, and season.** Net chemical ozone production rates decrease in the lower polar stratosphere in winter and spring where halogen and hydrogen catalytic cycles are most important but increase in the tropical mid-stratosphere where the nitrogen cycle is most important. The magnitude and sign of ozone changes depend on the details of the SAI aerosol distribution and the current stratospheric halogen and nitrous oxide concentrations, as well as on any changes

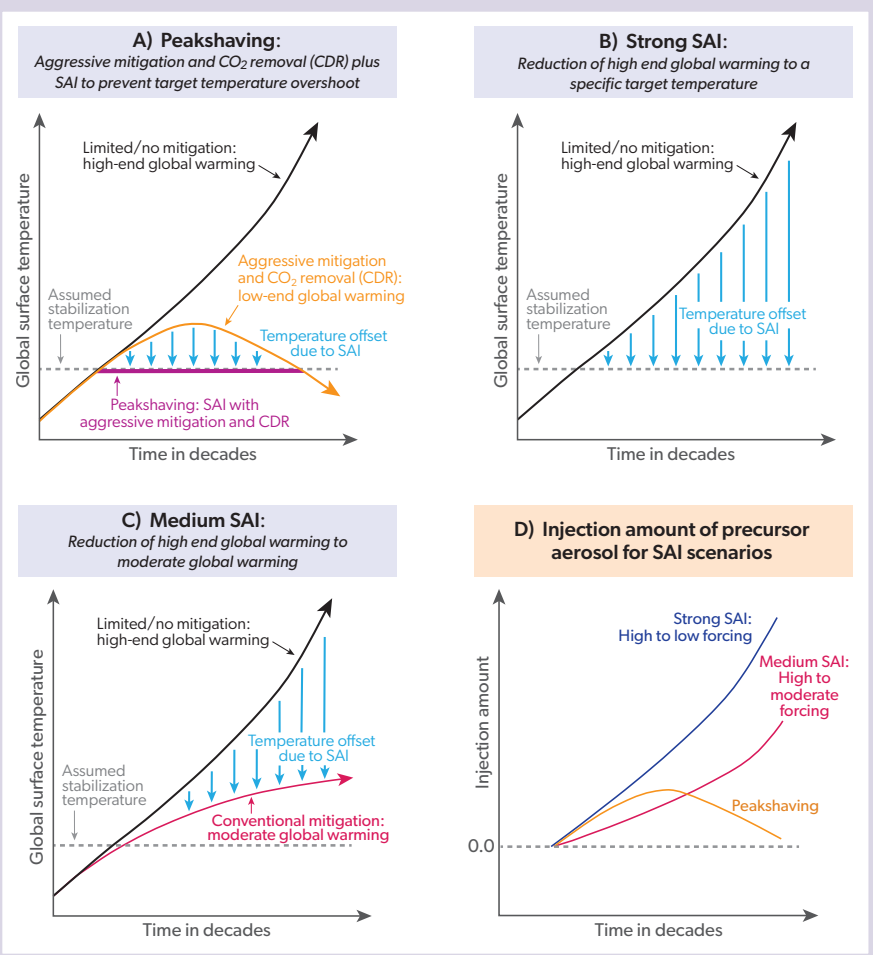

Figure 6-2. Schematic diagram representing the concept of three policy-relevant SAI scenarios: peakshaving scenario, strong SAI scenario, and medium SAI scenario. Different lines illustrate global mean surface temperatures for future scenarios: a limited or no mitigation scenario leading to strong future global warming (black line); a so-called "overshoot scenario" that assumes strong mitigation and Carbon Dioxide Removal (CDR), and leads to a temporary overshoot of global mean temperatures above sustainable limits for some time (orange); a peakshaving scenario that applies temporary SAI to the overshoot scenario in order to prevent the increase in global mean temperature from exceeding these sustainable limits (purple line); and a moderate warming scenario (red). The blue arrows represent the approximate relative magnitude of the temperature impact of the applied SAI. The bottom right panel shows the stratospheric injection that is applied under each of these three scenarios.

in stratospheric water vapor due to changes in transport and temperature that occur in response to SAI.

- **Enhanced stratospheric sulfate aerosol also impacts stratospheric temperature, transport, and chemistry, causing a general increase of ozone concentrations in the tropics and mid- to high latitudes through enhanced transport from the tropics to high latitudes.** Increased sulfate aerosols in SAI scenarios heat the lower tropical stratosphere by 4.6 ± 2.7 °C per 1 °C surface cooling, with variation across models and injection strategy. The heating induced by aerosols changes the vertical and horizontal transport in the stratosphere and polar vortex dynamics and leads to an acceleration of the lower branch of Brewer-Dobson Circulation (BDC). The stronger transport of ozone to high latitudes with SAI can overcompensate for the effects of ozone depletion, especially in the Northern Hemisphere winter in the strong SAI scenario. Heating of the tropopause results in increases in stratospheric water vapor. For any given scenario, the impacts of SAI on stratospheric temperature, transport, and dynamics are strongly model dependent.

SAI impacts on ozone in the future

- **Future changes in TCO resulting from SAI would be in addition to changes driven by future climate conditions and stratospheric halogen burden, as described in *Chapters 3*, *4*, and *5*. The SAI-related TCO changes depend on the required SAI injection rate, which is different for the three defined SAI scenarios (Figure 6-2). Compared to conditions without SAI, significant TCO reductions are expected in October over Antarctica for any SAI applications within the 21st century that are sufficient to appreciably impact climate warming.**
  - **In October over Antarctica, aerosol injection rates sufficient to achieve a 0.5 °C global cooling over the period 2020–2040 result in a reduction of TCO of around 58 ± 20 DU compared to no SAI. Smaller initial injection rates to achieve cooling of 0.2 °C between 2020 and 2040 result in a modeled reduction in TCO of 17 ± 9 DU.** Large injection rates based on the peakshaving and strong SAI scenarios starting in 2020 bring TCO close to the minimum values observed between 1990 and 2000, while smaller injection rates in the medium SAI scenario lead to less TCO reduction. The initial phase-in of SAI leads to relatively larger reductions in TCO over Antarctica in spring compared to a case without SAI because of nonlinearities in microphysical processes.
  - **In October over Antarctica, the magnitude of TCO changes in the second half of the 21st century increase with increasing injection rates. Injection rates and the resulting TCO reductions are scenario, strategy, and model dependent.** Under the strong SAI scenario, with injections starting in 2020, model simulations suggest that Antarctic TCO is reduced by around 55 ± 20 DU in October throughout the 21st century and the ozone hole recovery is delayed between 25 and 50 years. In this case, the effect of continually increasing injections is offset by the simultaneously declining chlorine burden in response to Montreal Protocol provisions. SAI, therefore, counters some of the super recovery of TCO above 1980 values driven by increasing greenhouse gases. The medium SAI scenario results in a smaller TCO reduction of between 9 and 29 DU (based on three models), and the peakshaving scenario results in no significant ozone loss by 2100 due to SAI (based on one model).
  - **In the Arctic in spring, SAI starting in 2020 to achieve global cooling of 0.5 °C by 2040 results in TCO reductions between 13 DU ± 10 DU and 22 ± 21 DU compared to no SAI, with no significant changes after 2040, based on results from two different models. The change in TCO for smaller initial injection rates is not significant.** In the Arctic, chemical changes are in part offset by changes in dynamics, resulting in smaller SAI-induced changes of TCO compared to Antarctica. As a result, SAI only slightly offsets the super recovery of TCO in a high-GHG scenario. Modeled impacts on TCO in the Arctic under the medium SAI scenario are smaller and not significant. These results, which are based on ensemble means of zonal and monthly mean TCO comparisons, do not reflect possible larger regional ozone changes that may occur within the Arctic polar vortex for years with warm and cold vortex conditions.
  - **In NH mid-latitudes in winter, increasing SAI toward the end of the century in both the strong and medium SAI scenarios can lead to a significant TCO increase relative to that in a scenario with no GHG mitigation and without SAI.** In both SAI scenarios, the increased heating in the tropical lower stratosphere causes increased transport of ozone from the tropics to mid- and high latitudes, resulting in a greater increase in TCO with injection amount. SAI, therefore, enhances the super recovery of TCO for a high-GHG scenario. No significant TCO changes occur in NH mid-latitudes in the peakshaving scenario.

Other side effects, risks, and limitations of SAI

- **Limited aerosol injections in a peakshaving scenario minimize SAI-induced side effects and climate risks, including reductions in global precipitation, while climate impacts and risks increase in scenarios with less mitigation and more SAI.** A portfolio of climate responses, including effective mitigation and decarbonization, limits the amount of SAI needed to maintain the global surface temperature below specific targets. Since SAI offsets the warming from atmospheric GHGs, limiting SAI would reduce the risks associated with a potential abrupt termination of SAI. Such an abrupt termination would result in a rapid (within 10 years) return of climate to the non-SAI climate base state if SAI was not restarted. Other side effects induced by SAI, such as Eurasian winter warming and associated precipitation impacts and a significant weakening of the Asian monsoon, depend on the amount of SAI. Ocean acidification depends mostly on atmospheric carbon dioxide (CO_2) concentrations and is impacted only to a small extent by SAI.

SAI using aerosols other than sulfates

- **The use of aerosols other than sulfate is expected to change the effects on ozone via changes in**

heterogeneous chemistry and dynamics and transport. Comprehensive climate model simulations to quantify these effects have yet to be performed. Other aerosol types that absorb less solar radiation would heat the tropical lower stratosphere much less than sulfate. They are also potentially more chemically inert and less impactful on stratospheric ozone. Materials that have been considered include calcium carbonate, titanium dioxide, aluminum oxide, and diamond. The effects on ozone are less certain for these alternate materials owing to the paucity of laboratory and modeling studies investigating them and the lack of natural analogs.

Evaluation of models

- **The study of SAI is aided by natural analogs. Volcanic eruptions and pyrocumulonimbus events are useful, albeit imperfect, natural analogs for assessing SAI.** Present-day Earth system models may not accurately simulate the effects of stratospheric aerosol perturbations on ozone and other side effects. Remote sensing and in situ observations of volcanic eruptions and pyrocumulonimbus (pyroCb) formation provide essential information on the stratospheric evolution of injected sulfur dioxide and resultant sulfate aerosol, which can be used to assess and improve SAI models. However, remote and in situ observations valuable for evaluating the effects of injected aerosols on the ozone layer are generally lacking. SAI scenarios with continuous aerosol (precursor) injections will produce different stratospheric aerosol distributions than pulse injections that occur with natural analogs; therefore, accurately simulating these natural events is a necessary but not sufficient constraint on model fidelity in representing SAI.

6.1 INTRODUCTION

There is growing recognition that the 21st Conference of the Parties (COP21) to the United Nations Framework Convention on Climate Change limits of 1.5 °C (IPCC, 2018) or 2 °C above preindustrial levels are going to be extremely difficult to achieve under even the strongest mitigation scenarios (e.g., Rogelj et al., 2016; Millar et al., 2017; IPCC, 2018; Tollefson, 2018). Reaching these temperature limits to avoid further climate impacts may require considering additional interventions, including solar radiation modification (SRM) and carbon dioxide removal (CDR). While CDR may be effective in the long run, this approach very likely does not prevent an overshoot of these surface temperatures limits for some time. Even a temporary overshoot of surface temperatures can lead to irreversible climate impacts (IPCC, 2021, 2022), and SRM may be the only option to prevent this.

Various SRM approaches have been discussed to deliberately cool the planet by reflecting more sunlight back to space (NAS, 2021). One such approach is injecting aerosols (or their gaseous precursors) to enhance the stratospheric aerosol layer and reflect additional sunlight back to space, thereby cooling the planet. This approach is referred to as stratospheric aerosol injection (SAI; NAS, 2021) and has been motivated by the observed temporary surface cooling after large explosive volcanic eruptions. Such eruptions periodically inject millions of tonnes of sulfur dioxide (SO_2) into the stratosphere, where it forms reflective sulfate aerosols (Robock, 2000). Since Earth system models (ESMs) have been used to study the effects of SO_2 injections from volcanic eruptions for decades, they have been adopted to also study the effects of SAI using SO_2 injections. Furthermore, the availability of extensive observations subsequent to these eruptions allows evaluation of the impacts of SO_2 injections in models. Besides the intended benefits of SAI to counter the effects of global warming, SAI produces unintended consequences and risks, including impacts on stratospheric ozone (e.g., Crutzen, 2006).

This chapter provides the first comprehensive stratospheric ozone-focused assessment of the state of SAI research. *Section 6.1* covers motivations and a brief history and defines specific terminology used in this assessment. *Section 6.2* provides background on important processes required for simulating SAI, sensitivities to the assumed injections on radiative forcing and aerosol surface area density, and model uncertainties in simulating these processes. *Section 6.3* assesses the general effects of SAI on ozone concentrations and sensitivities on ozone to the injection details. *Section 6.4* quantifies changes in total column ozone (TCO) for three specified future scenarios and briefly addresses additional side effects and climate impacts of SAI in the context of different future scenarios to place the impact on TCO in the context of the larger arena of this developing research field. The chapter abstains from addressing complex moral, ethical, and governance issues (e.g., Robock, 2008a; Preston, 2013; Lawrence et al., 2018). *Section 6.5* assesses the potential effects of using materials other than sulfate for SAI, and *Section 6.6* assesses the importance of natural analogues of aerosol injections for reducing uncertainties in process understanding and model representation for SAI projections.

6.1.1 Motivation for Assessing the Effects of SAI on Stratospheric Ozone

Global warming has continued over the last decade and currently (in 2021) stands at approximately 1.2 °C above preindustrial levels (IPCC, 2021). Each of the observed global annual mean temperatures over the last seven years has been among the warmest on record, and the global mean temperature in 2020 tied with 2016 as the warmest year on record (IPCC, 2021). All climate model simulations suggest continued global warming throughout the next two decades (IPCC, 2021; **Figure 6-1**). Future global modeling scenarios known as Shared Socioeconomic Pathways (SSPs) range from a very strong mitigation scenario that includes negative carbon emissions (SSP1-1.9) to a limited or no-mitigation pathway (SSP5-8.5), which leads to an acceleration of global warming to around 5.5 °C above preindustrial conditions by 2100 (**Figure 6-1**). The range of surface temperature changes per scenario is indicated by the colored shaded area in **Figure 6-1**.

The multi-model mean from even the strongest mitigation pathway (SSP1-1.9) overshoots the 1.5 °C target, peaking around 2050 before falling below 1.5 °C above preindustrial levels by 2100. A growing body of evidence shows that climate-induced damages frequently scale exponentially rather than linearly in key variables such as the frequency of extreme precipitation (e.g., Myhre et al., 2019), heatwaves (e.g., Christidis et al., 2015), and droughts (e.g., Samaniego et al., 2018) and that the accelerated warming of the high latitudes causes thawing of permafrost, melting of glaciers, and reductions of sea ice leading to sea level rise. Tipping points might also be reached whereby key elements of the climate system such as the Amazon rainforest or the West Antarctic ice sheet could irreversibly collapse (e.g., Lenton et al., 2019). The application of climate intervention methods may be the only option to prevent the future climate from reaching critical temperatures and potential tipping points (e.g., NAS, 2021).

Climate intervention (CI) is defined in this report as "the deliberate large-scale manipulation of an environmental process that affects the Earth's climate, in an attempt to counteract the effects of global warming." We adopt the terminology "climate intervention" (NRC, 2015), although we recognize that "climate engineering" (Hamilton, 2013; Keith, 2013), "climate geoengineering" (Lawrence et al., 2018), and "geoengineering" (Shepherd, 2009; NAS, 2021) are also commonly used throughout the scientific literature. Two very different CI strategies have been proposed: carbon dioxide removal (CDR) and solar radiation modification (SRM) (**Box 6-1 Figure 1**). CDR methods seek to actively remove carbon dioxide from the atmosphere, while SRM seeks to reduce global warming by increasing the reflectivity of the planet.

CDR methods include afforestation, ocean alkalinization, and iron fertilization to promote marine carbon uptake, as well as technologies such as bioenergy with carbon capture and storage (BECCS), capturing carbon from biofuels in the form of charcoal to use as a fertilizer (biochar), and direct air capture (Shepherd, 2009; Lawrence et al., 2018; NRC, 2015 Lee et al., 2021; Josep et al., 2021). These methods have not yet been developed at a scale large enough to reduce carbon dioxide concentrations significantly within the next one to two decades (Keller et al., 2018; Fuss et al., 2020), but they have the potential to contribute significantly to global warming abatement in the second half of the 21st century. Some CDR approaches have their own side effects that may limit their large-scale deployment, including substantial costs or implications for, e.g., water availability or food production (Smith et al., 2016). Such concerns further strengthen the motivation to understand the implications of SRM.

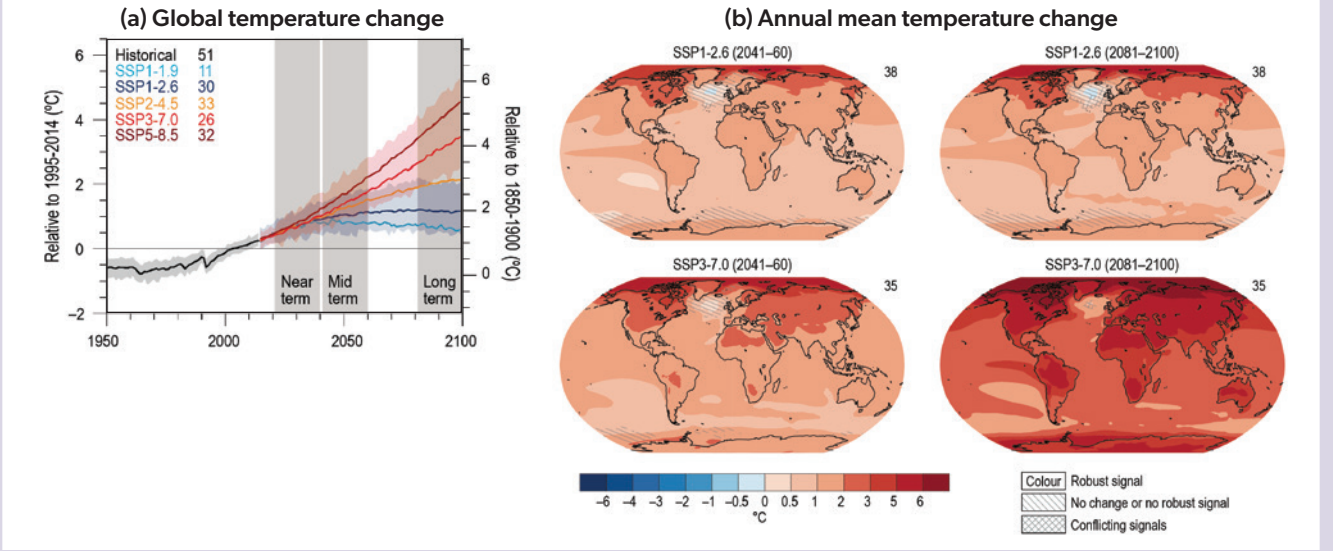

Figure 6-1. (a) Multi-model simulated time series from 1950 to 2100 for global annual average surface air temperature changes relative to the 1995–2014 average (left axis) and the 1850–1900 average (right axis). The curves show averages over the CMIP6 simulations, the shadings around the SSP1-2.6 and SSP3-7.0 curves show 5–95% ranges, and the numbers in the legend after each experiment show the number of model simulations used. (b) The global mean distribution of mid-term (2041–2060) and long-term (2081–2100) changes in annual mean surface temperature. The number of model simulations used is indicated in the top right of the maps. No overlay indicates regions where the change is robust and emerges from internal variability (i.e., 66% of the models show a change greater than the internal-variability threshold, and at least 80% of the models agree on the sign of change). Diagonal lines indicate regions with no change or no robust significant change. Crossed lines indicate areas of conflicting signals. [Both panels reproduced from Lee et al., 2021.]

SRM methods include utilizing mirrors in space; increasing the reflectivity of land or ocean surfaces (surface albedo); increasing the reflectivity of marine clouds (marine cloud brightening, MCB); and increasing the reflectivity of the stratospheric aerosol layer via stratospheric aerosol injection, SAI. We adopt the term "stratospheric aerosol injection" throughout this report but recognize that "stratospheric aerosol intervention" and "stratospheric aerosol geoengineering" are also frequently used in the scientific literature. Cirrus cloud thinning (CCT) is also frequently considered under SRM, although this method is based more on reducing cirrus cloud impact on outgoing terrestrial radiation rather than on reflecting sunlight (e.g., Lohmann and Gasparini, 2017). Based on assessments of the potential cooling impact, readiness, cost-effectiveness, and risks (e.g., Shepherd, 2009; NAS, 2021), SAI is potentially one of the most effective global methods. SAI involves the long-term injection of aerosols, or their precursors, into the stratosphere, where their atmospheric lifetime can reach one to two years. The resulting enhanced aerosol layer reflects sunlight back to space, thereby cooling the planet (Shepherd, 2009; Lawrence et al., 2018; NAS, 2021). While the technology for SAI does not yet exist, it has become the most discussed SRM technique in the scientific literature. A portfolio of CI strategies has been suggested in addition to mitigation and adaptation, which could include a temporary application of SAI to avoid the worst impacts of global warming until emissions reductions and CDR reduce and stabilize atmospheric GHG concentrations (e.g., Long and Shepherd, 2014; Sugiyama et al., 2018).

In many studies, SO_2 has been considered as the injection material for SAI because volcanic eruptions serve as natural analogs to SAI (see *Section 6.6* for more details). Observations after large explosive volcanic eruptions that injected large amounts of SO_2 into the stratosphere have conclusively demonstrated a measurable reduction in global surface temperatures within a year or two (e.g., Angell and Korshover, 1984; Hansen et al., 1992; Soden et al., 2002). Multiple smaller eruptions during the early 21st century are also thought to have contributed to the observed masking of some of the global warming at that time (e.g., Santer et al., 2014; Haywood et al., 2014). Explosive volcanic eruptions that emit sulfur species into the stratosphere allow benchmarking of current-generation aerosol and climate models against a wealth of observations of the impacts of volcanic emissions on ozone concentrations and sulfate aerosol properties, including their temporal and spatial evolution. However, in most cases, volcanic eruptions also inject other materials, including dust, halogens, and water, which result in different effects compared to those from sulfur injections alone (e.g., Zhu et al., 2020). There are also clear limits to this analogy, because explosive eruptions are pulsed injections of material into a relatively small area of the stratosphere, which contrasts with continuous or repeated injections (or a slow ramp-up) of SO_2 in strategically selected locations under SAI scenarios (e.g., Duan et al., 2019). These differences can make it difficult to project SAI impacts on ozone and climate response based on volcanic eruptions.

Another analog of SAI is the injection of aerosols into the stratosphere in vigorous wildfire events that result in the formation of pyrocumulonimbus clouds (pyroCbs). A number of satellite observations have recently shown that biomass-burning aerosols embedded in pyroCbs can reach the stratosphere. Enhanced

Box 6-1. Overview of Climate Intervention Methods

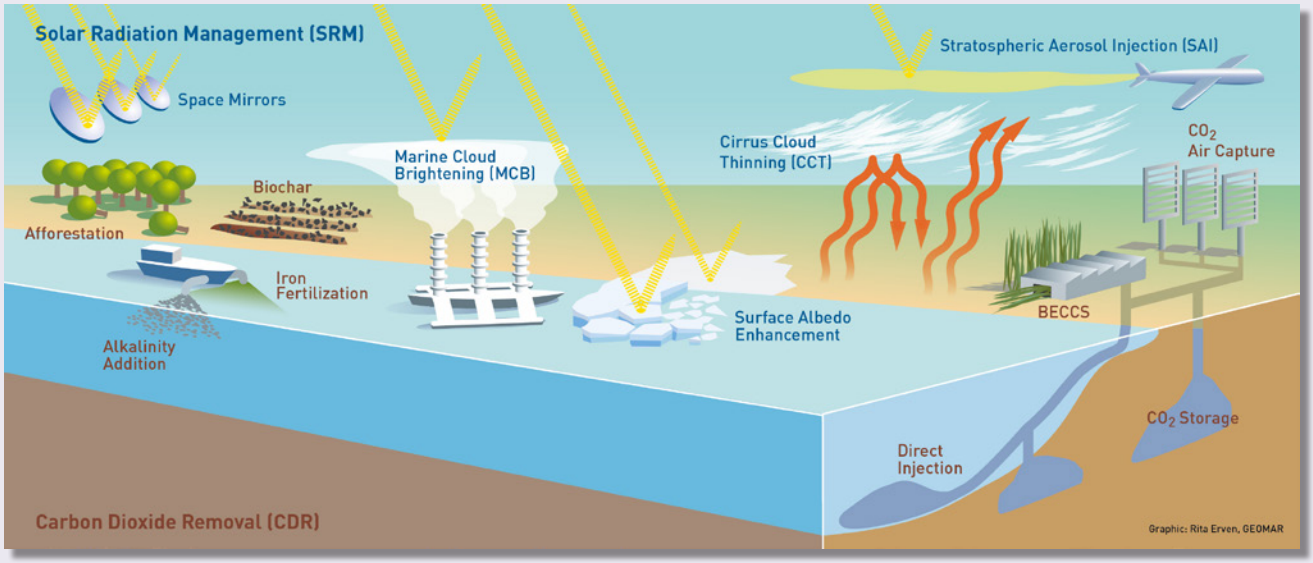

Box 6-1 Figure 1. Schematic diagram showing some prominent proposed climate intervention methods. CDR methods include afforestation, biochar, BECCS, iron fertilization, and alkalinity addition to the ocean. SRM methods represented are SAI, MCB, space mirrors, CCT, and surface albedo enhancement technologies. *Courtesy of Rita Erven, GEOMAR.*

Glossary of Climate Intervention Terminology

BECCS*: bioenergy with carbon capture and storage. A CDR technique using energy derived from any form of biomass or its metabolic by-products whereby a relatively pure stream of carbon dioxide (CO_2) from industrial and energy-related sources is separated (captured), conditioned, compressed, and transported to a storage location for long-term isolation from the atmosphere.

Biochar*. A CDR technique producing a stable carbon-rich material produced by heating biomass in an oxygen-limited environment. Biochar may be added to soils to improve soil functions and to reduce greenhouse gas emissions from biomass and soils, as well as for carbon sequestration.

CCT: cirrus cloud thinning. A proposed climate intervention technique often classified under SRM, although it relies on increasing emissions of terrestrial radiation to space.

CI: climate intervention. Defined in this report as the deliberate large-scale manipulation of an environmental process that affects the Earth's climate, in an attempt to counteract the effects of global warming. This includes both SRM and CDR.

CDR*: carbon dioxide removal. Anthropogenic activities that remove CO_2 from the atmosphere and durably store it in geological, terrestrial, or ocean reservoirs, or in products. This includes existing and potential anthropogenic enhancement of biological or geochemical sinks and direct air capture and storage but excludes natural CO_2 uptake not directly caused by human activities.

MCB: marine cloud brightening. An SRM climate intervention strategy aimed at brightening low marine clouds through the injection of aerosol particles, thereby increasing the planetary albedo.

Planetary albedo. The ratio of the amount of solar radiation reflected by the planet to that incident upon it. The global broadband planetary albedo is approximately 0.3.

SAI: stratospheric aerosol injection. A proposed SRM technique to enhance the stratospheric aerosol layer to increase the reflectivity of the planet and hence reduce global mean surface temperatures.

Space mirrors. A proposed SRM technique to block some sunlight by placing mirrors at the Lagrangian point between Earth and the sun to decrease the global surface temperature.

SRM*: solar radiation modification. The intentional modification of the Earth's shortwave radiative budget with the aim of reducing warming. Stratospheric aerosol injection, marine cloud brightening, and land surface albedo modification are examples of proposed SRM methods.

Surface albedo. The ratio of the solar radiation reflected by Earth's surface to that incident upon it. The broadband mean surface albedo is approximately 0.15.

**Adopted from IPCC (2018).*

solar absorption by black carbon and the organics-dominated chemical composition of these smoke particles can impact ozone and climate differently from sulfate aerosols (e.g., Rieger et al., 2021).

6.1.2 A Brief History of SAI Research

The earliest suggestion of injecting sulfur into the stratosphere to combat global warming was proposed by Budyko (1974). This topic was then only occasionally discussed in the scientific literature for the next three decades (e.g., Rasch et al., 2008a, and references therein). Crutzen et al. (2006) was one of the first to suggest possible impacts of SAI on stratospheric ozone. He used simple scaling arguments derived from the Pinatubo eruption to estimate that stratospheric injections of around 10 Tg SO_2 yr^{-1} (1 Tg = 1 million tonnes) would be needed to balance the warming impact of doubled atmospheric concentrations of carbon dioxide. Wigley (2006) used a simple energy balance model and derived a similar estimate, suggesting a combined mitigation and SAI approach for stabilizing climate. These and other early simple model approaches were improved upon by introducing models that represent the sulfur cycle more explicitly using single-moment aerosol models and that include the representation of oceans either through slab-ocean (Rasch et al., 2008b) or fully coupled ocean models (Robock et al., 2008b). The first studies that quantitatively assessed the impact of deliberate SAI upon the ozone layer also appeared, finding a considerable delay in the Antarctic ozone hole recovery (Tilmes et al., 2008; Heckendorn et al., 2009).

Thereafter, more and more SAI modeling studies began to appear using fully coupled global atmospheric-ocean models. These models often did not include interactive stratospheric chemistry (e.g., Kravitz et al., 2009; Jones et al., 2010; 2011; Niemeier et al., 2011; English et al., 2012). A few studies attempted to compare the impacts of similar SAI simulations performed across different climate models (e.g., Jones et al., 2011; Rasch et al., 2008b; Schmidt et al., 2012), but comprehensive attribution of differences in results from climate models proved to be hampered by the lack of standardization of the objectives of the SAI approaches and the related emission scenarios. These problems led to the first comprehensive attempts to standardize model scenarios by the Geoengineering Model Intercomparison Project (GeoMIP; Kravitz et al., 2011).

GeoMIP formulated idealized model experiments to aid understanding of the effects of SAI on the Earth system (Kravitz et al., 2011) and provides the most comprehensive multi-model assessment of the effects of SRM to date (e.g., Kravitz et al., 2015). Different GeoMIP experiments have evolved over time, from solar dimming experiments where the solar constant was turned down to offset instantaneous quadrupling or steadily increasing carbon dioxide concentrations (referred to as the G1 and G2 scenarios, respectively; Kravitz et al., 2015) to more complicated and policy-relevant SAI experiments (the G3, G4, and G6 scenarios; Kravitz et al., 2015). Simulations were run using fully coupled global climate models (CMIP5 and CMIP6 generations), with most models performing the relatively simple solar dimming experiments (e.g., Kravitz et al., 2011; 2021; Niemeier et al., 2013). Fewer models were able to directly simulate sulfur injections, which requires comprehensive stratospheric aerosol microphysical modeling. The first GeoMIP-coordinated multi-model assessments of impacts on stratospheric ozone and surface ultraviolet radiation were documented by Pitari et al. (2014). Two model experiments, G3 and G6, include both SAI and solar dimming versions (G3, G3S, G6solar, and G6sulfur; Kravitz et al., 2015), allowing comparisons of the impacts of the two methods (Niemeier et al., 2013; Xia et al., 2017; Visioni et al., 2021a; Jones et al., 2021). These studies have shown that solar dimming is an imperfect analog for modeling the climate impacts of SAI and assessing its effects on stratospheric ozone (see *Section 6.3*). Other multi-model comparisons are in progress, based on the Chemistry-Climate Model Initiative (CCMI; Morgenstern et al., 2017; Plummer et al., 2021); these use a prescribed aerosol distribution to examine the effects of SAI on stratospheric ozone.

Besides additional single-model studies that use simple equatorial injection strategies, more complex SAI deployment strategies to minimize residual climate impacts have been developed and applied (Kravitz et al., 2017) and used as the basis for other studies, including the Geoengineering Large ENSemble project (GLENS; Tilmes et al., 2018a; 2020; see **Box 6-2**). A new large-ensemble model study using a similar strategy to GLENS, the Assessing Responses and Impacts of Solar climate intervention on the Earth system with stratospheric aerosols project (ARISE; Richter et al., 2022), has recently been documented.

In parallel with the development of individual and coordinated modeling studies, there has been limited research into potential delivery mechanisms. SAI would require the long-term delivery of millions of tonnes of SO_2 or other suitable materials into the stratosphere for any substantive global cooling (e.g., Smith et al., 2020; Robock, 2020); currently, no scalable delivery system exists. A fleet of specially designed high-altitude aircraft has been suggested as a feasible delivery system (McClellan et al., 2012; Smith and Wagner, 2018), although tethered balloons, rockets, artillery, and rigid towers have also been suggested (Robock et al., 2009; Davidson et al., 2012). Each of these is hampered by technological constraints, in particular when it comes to delivery of significant payloads above 20 km altitude. There have also been suggestions for enhancing stratospheric aerosol concentrations through lower-altitude tropospheric injections, both using photophoretic levitation (Keith, 2010) and absorption of sunlight to loft the particles into the stratosphere (Gao et al., 2021). Other suggestions include injecting carbonyl sulfide in the upper troposphere where it is transported to the stratosphere and slowly forms sulfate (Quaglia et al., 2022). However, the technical logistics of practical deployment through such means have not been sufficiently explored. No outdoor field experiments have been conducted up to this point, and detailed discussions about requirements and issues regarding field experiments are presented in the recent NAS (2021) report.

6.1.3 SAI Scenarios and Strategies

Just as the impacts of future global warming (including the evolution of stratospheric ozone) strongly depend on future emissions pathways, the impacts of SAI are strongly dependent on the details of the SAI scenario and the underlying future greenhouse gas emissions pathway (the baseline scenario; e.g., Niemeier et al., 2011; Tilmes et al., 2017; Richter et al., 2017, Jones et al., 2018; Irvine et al., 2020, Tilmes, 2020). Multiple hypothetical SAI scenarios and strategies have been developed for modeling studies, based on the goals of the specific project or the purpose of the research; some were designed for understanding specific processes in the climate system and others for impact relevance.

In this section, we define the terms "scenario" and "strategy".

6.1.3.1 SAI Scenarios

We define "SAI scenario" as the desired global mean outcome. While IPCC (2021) defines its scenarios in terms of the global mean radiative forcing by 2100, SAI scenarios are most frequently defined in terms of the global mean temperature or degree of cooling. Current SAI scenarios do not include socioeconomic feedbacks of the implementation of SAI. Examples of SAI scenarios include maintaining global mean temperatures at 1.5 °C or 2 °C above preindustrial conditions or reducing the global mean temperature from a high-end global warming scenario to a more moderate global warming scenario. Three different SAI scenarios are assessed with regard to effects on total column ozone in *Section 6.4*.

Without SAI, only very drastic and immediate mitigation and significant CDR can prevent overshoot of an assumed stabilization surface temperature (**Figure 6-2**, grey, dashed lines). The global mean surface temperature from most projected future scenarios exceeds the 1.5 °C and 2 °C COP21 limits (**Figure 6-1**; IPCC, 2021). Here, we assess modeling studies that investigate the effects of SAI on ozone based on three SAI scenarios. Each of these scenarios considers different baseline GHG scenarios and temperature targets and therefore has different impacts on total column ozone (TCO). While many possible SAI scenarios have been studied, the most comprehensive large-ensemble or multi-model studies relevant for TCO impacts can be summarized in the three scenarios analyzed here. The first two scenarios are based on ensemble simulations from one modeling framework, while the results of the last scenario are based on a multi-model study using three different ESMs. All scenarios discussed here inject SO_2 into the stratosphere to form sulfate aerosols; comprehensive ESM studies using other injection materials currently do not exist. Schematic diagrams of the three scenarios, together with the temporal evolution of the quantity of SO_2 injected, are provided in **Figure 6-2**, and each of the injection strategies is discussed in detail in the subsections that follow. Note that the resulting temperature change from specific baseline scenarios are themselves very uncertain owing to differences in climate sensitivity of the various models. In addition, there is significant uncertainty about how much cooling can be achieved with a specific amount of SAI (*Section 6.2.2.*). Consequently, the amount of injection needed to reach specific temperature targets is very uncertain.

Peakshaving Scenario. The peakshaving scenario prevents overshoot of global mean surface temperature above assumed temperature limits by applying a limited amount of SAI to avoid the worst impacts of global warming during the period it takes for strong mitigation and decarbonization efforts to reduce and stabilize greenhouse gas concentrations (e.g., Wigley, 2006; Long

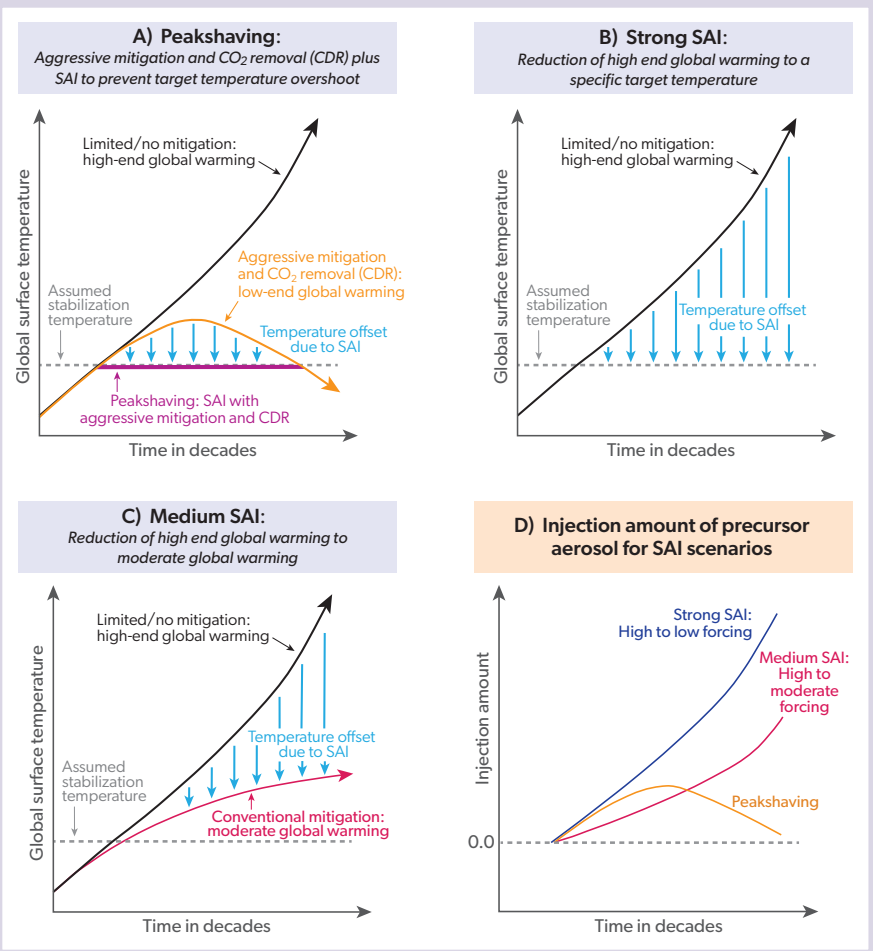

Figure 6-2. Schematic diagram representing the concept of three policy-relevant SAI scenarios: peakshaving scenario, strong SAI scenario, and medium SAI scenario. Different lines illustrate global mean surface temperatures for future scenarios: a limited or no mitigation scenario leading to strong future global warming (black line); a so-called "overshoot scenario" that assumes strong mitigation and Carbon Dioxide Removal (CDR), and leads to a temporary overshoot of global mean temperatures above sustainable limits for some time (orange); a peakshaving scenario that applies temporary SAI to the overshoot scenario in order to prevent the increase in global mean temperature from exceeding these sustainable limits (purple line); and a moderate warming scenario (red). The blue arrows represent the approximate relative magnitude of the temperature impact of the applied SAI. The bottom right panel shows the stratospheric injection that is applied under each of these three scenarios.

and Shepherd, 2014; Sugiyama et al., 2018). For this scenario, SAI is slowly phased in and later phased out to keep temperatures from rising above the target temperature (**Figure 6-2**, top left panel). Depending on the effectiveness of mitigation and decarbonization efforts, SAI application may be required for several decades or even centuries before atmospheric greenhouse gases have been sufficiently reduced to stabilize surface temperatures (e.g., Tilmes et al., 2016, 2020; Jones et al., 2018). A peakshaving scenario that requires strong mitigation and CDR may pose the least risk to the climate system among the scenarios analyzed in this assessment, since the relatively limited deployment time and injection rate reduce potential side effects and any termination effect (see *Section 6.4.2*). Currently, the impacts on ozone for this scenario can be assessed based only on a single model (Tilmes et al., 2020), using a baseline scenario SSP5-3.4-OS (**Box 3-4 Figure 1**) that follows the SSP5-8.5 high-forcing scenario until 2040 and after that deploys large-scale CDR and strong reductions in methane. SAI is applied to keep surface temperatures at 1.5 °C above preindustrial levels while minimizing inter-hemispheric and pole-to-equator gradients. This scenario requires maximum injections of up to ~15 Tg SO_2 yr^{-1} around 2060; 15 Tg SO_2 is approximately the amount injected by the explosive 1991 Mount Pinatubo eruption. An additional scenario to keep surface temperatures at 2.0 °C above preindustrial levels, which would reduce injections of sulfur by approximately 50% relative to stabilizing temperatures at 1.5 °C above preindustrial levels, has also been performed (Tilmes et al., 2020).

Strong SAI Scenario. The strong SAI scenario prevents high-end global warming under a scenario with high projected greenhouse gas emissions (Representative Concentration Pathway [RCP] 8.5 / SSP5-8.5, **Box 3-4 Figure 1**), with the objective of meeting the COP21 targets. Large ensembles of this scenario have so far been performed using only CESM (WACCM) within the GLENS simulations (Kravitz et al., 2017, Richter et al., 2017, Tilmes et al., 2018a; *Section 6.1.*) and CESM2 (WACCM6) (Tilmes et al., 2020), although a more limited number of ensembles have been performed with other models (Jones et al., 2018). To prevent surface temperature from increasing under this greenhouse gas scenario using SAI, steadily increasing sulfur injections between 2020 and 2100 are required (**Figure 6-2**, top right panel). Injections were simulated to reach between 30 Tg SO_2 yr^{-1} (Jones et al., 2018) and 55 Tg SO_2 yr^{-1} (Tilmes et al., 2018a) by 2100. This is between three and five times the mass of sulfur injected per year by the Mount Pinatubo eruption in 1991 (assuming Pinatubo injected 10 Tg SO_2; Mills et al., 2017). Different SAI strategies (*Section 6.1.3.2*) have been applied to this SAI scenario, using a feedback controller (**Box 6-2**) and varying the altitude of injections or injecting only at the equator. These different strategies lead to different impacts on stratospheric ozone (Jones et al., 2018; Kravitz et al., 2019; Tilmes et al., 2021). As the SO_2 injection increases with time, the risks of side effects and any termination effect (see *Section 6.4.2*) also increase with time.

Medium SAI Scenario. As in the strong SAI scenario, the medium scenario also prevents the high-end global warming projected under a scenario with high greenhouse gas emissions, but its target surface temperature is that of a more moderate greenhouse gas emissions scenario (RCP4.5 / SSP2-4.5). This scenario leads to moderate global warming that is significantly above COP21 targets. Six GeoMIP models have performed this type of modeling experiment using SSP5-8.5 as the baseline scenario and temperatures under the SSP2-4.5 greenhouse gas scenario as the target; this is known as the GeoMIP G6 scenario (e.g., Jones et al., 2021; Visioni et al., 2021a; Tilmes et al., 2022). Only three of the participating six models (CNRM-ESM2-I, UKESM1-0-LL, and CESM2(WACCM)) include interactive chemistry and calculate the effect of SAI on TCO (*Section 6.4.2*). The SAI strategy for achieving these scenarios was defined by injections in a region around the equator. Progressively larger SO_2 emissions are required between 2020 and 2100, ranging from 3 to 7 Tg SO_2 yr^{-1} in 2050 and reaching between 20 and 30 Tg SO_2 yr^{-1} by 2100 (see **Figure 6-2**, bottom left panel). This scenario is similar to halving future global warming (e.g., Irvine et al., 2019, 2020). Analysis based on GLENS simulations show that for this scenario only, 1.3% of land areas would see a significant change in water availability compared to present day, and those regions would experience wetting, not drying, contradicting the assumption that solar climate intervention leads to a general drying (Irvine et al., 2020).

6.1.3.2 SAI Strategies

The underpinning deployment assumptions for achieving specific climate goals are defined here as "SAI strategies". Strategies are understood here as the specifics of SAI applications, injection locations (including latitude, longitude, and altitude), injection timing (continuous or pulse injections), and injection material. Model simulations have revealed several robust side effects if global solar dimming or injections at the equator are applied, which include overcooling of tropical regions, continued residual warming in polar regions, and overcompensation of global mean and regional precipitation reductions (Bala, 2008; Robock et al., 2008b; Schmidt et al., 2012; Niemeier et al., 2013; Kravitz et al., 2013; Tilmes et al., 2013; Huneeus et al., 2014; Kravitz et al., 2021). Additional side effects on the climate system may include a shift in the intertropical convergence zone (ITCZ) and hurricane frequency and intensity in simulations that apply SAI to a single hemisphere (Haywood et al., 2013; Jones et al., 2017; see *Section 6.4.2*). Model experiments have therefore applied specifically designed strategies to minimize some of these deleterious side effects. These strategies include injections at multiple locations and seasons in order to reduce impacts on, e.g., inter-hemispheric and pole-to-equator surface temperature gradients, using a feedback control algorithm (see **Box 6-2**). Other examples of SAI strategies include the use of sulfate or chemically inert materials instead of SO_2 (*Section 6.5*). Thus, different SAI strategies could deliver the same SAI scenario but result in different impacts on climate and stratospheric ozone.

6.2 IMPACTS OF SAI ON RADIATIVE FORCING, TEMPERATURES, AND AEROSOL SURFACE AREA DENSITY

To cool the Earth's surface using stratospheric aerosol injection (SAI), sulfate aerosols or their gaseous precursors (e.g., SO_2) would be deliberately injected into the stratosphere. Transport by stratospheric winds associated with the Brewer–Dobson circulation (BDC) can result in near-global coverage of the resulting sulfate aerosol layer. Transport processes are coupled to microphysical processes, as they determine sulfur concentrations, sulfate particle numbers, and size distributions. These nonlinear processes make the impact of SAI very dependent on the injection strategy. For example, model simulations show that stratospheric

Box 6-2. Reaching Climate Targets Using Feedback Control

Earlier SAI studies often modeled injection of SO_2 or sulfate aerosols within a region around the equatorial stratosphere, resulting in a nonuniform global distribution of stratospheric sulfate with a maximum concentration at the equator (*Section 6.2*). This results in an overcooling of the tropics and an undercooling at high latitudes compared to a scenario without SAI. In a new approach, changes in surface temperature are modulated through injections of sulfur at four predefined locations, 15°N, 15°S, 30°N, and 30°S. The resulting stratospheric sulfate distribution is more evenly spread across latitudes (**Box 6-2 Figure 1**, top panels). Multiple stratospheric injection latitudes coupled with a feedback control algorithm has been used to maintain 2020 surface temperatures while following the high-GHG emissions RCP8.5 baseline scenario (Kravitz et al., 2017). The so-called feedback loop successfully responds to changes in climate feedbacks by adjusting the injection amounts for each of the predefined injection locations. Model simulations that use this approach are able to keep global mean surface temperatures at predefined levels with regional surface temperatures more similar to present day compared to using equatorial injections (**Box 6-2 Figure 1**, middle and bottom panels).

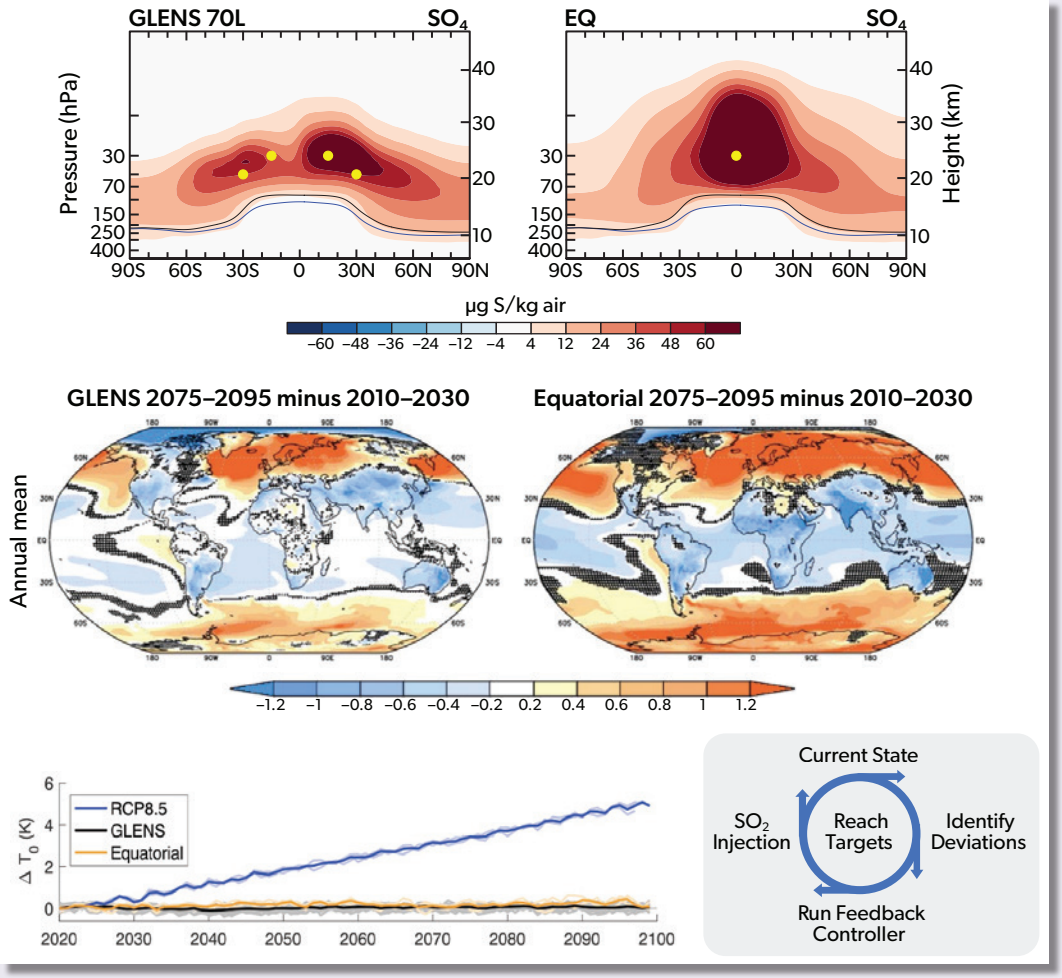

Box 6-2 Figure 1. *(top)* Zonal mean changes in sulfate concentrations between simulations with and without SAI over the period 2070–2089 using GLENS four-point injections *(left)* and equator injections *(right)*. Both simulations use a feedback controller *(bottom right)* that iteratively adjusts the injected sulfur amount in each location in order to stabilize the global, annual average surface temperature (for the equatorial injection) and in addition the inter-hemispheric and pole-to-equator surface temperature gradients for the four-point injections *(bottom left)*. The tropopause location in the control (no injection) run is shown in black and for the SAI experiment in blue; injection locations are indicated as yellow dots. *(middle)* Maps of surface temperature change (K) for the GLENS four-point injections *(left)* and for equatorial injections *(right)*, where the change refers to the difference in the mean over the periods 2075–2095 and 2010–2030. Stippling indicates regions that are not statistically significant at the 95% confidence level, as calculated using Welch's t-test. *(bottom left)* Change in annual mean surface temperature from the 2010–2030 average following the RCP8.5 (blue) scenario and with SAI following the GLENS four-point injection strategy (black) and equatorial injection strategy (orange). Faint lines indicate individual model run ensemble members, and thick lines indicate ensemble means. *(bottom right)* Illustration of the feedback control loop. [Adapted from Tilmes et al., 2020, and Kravitz et al., 2019.]

A feedback control algorithm in climate models was first applied to maintain global mean surface temperatures by reducing the solar constant (MacMartin et al., 2014a, 2014b; Kravitz et al., 2014). Later, this method was applied to meet three climate objectives at the same time: the targeted global mean surface temperature, inter-hemispheric temperature gradient, and pole-to-equator temperature gradient (Kravitz et al., 2016). This method was then integrated into a more complicated framework using the Whole Atmosphere Community Climate Model (WACCM; Mills et al., 2017, MacMartin et al., 2017). Such an approach requires precalculated response functions for each injection latitude. Emissions adjustments have been tested for different time periods. For example, injections were adjusted annually for the GLENS model runs, while seasonal injection adjustments were performed in later studies (Visioni et al., 2019, 2020a). Different climate targets have also been suggested, including precipitation-based climate metrics and targets for sea ice extent, although these strategies are still in their infancy (Lee et al., 2021).

injection at the equator or at four points at 30°N, 15°N, 15°S, and 30°S, will result in very different spatial and size distributions of the aerosols (see **Box 6-2**) and cause different impacts on ozone. In addition, model-specific differences in physics and simulated tracer transport add to simulated nonlinearities, and both are responsible for large differences between model results. It is therefore still uncertain how much surface temperature reduction would be obtained for 1 Tg yr^{-1} of SO_2 injection. This section provides the foundation for understanding related microphysical and transport processes, as well as SAI interactions with radiation (*Section 6.2.1*). *Section 6.2.2* summarizes model differences and shortcomings in representing processes important for SAI and assesses the effects of SAI on radiation and surface temperatures, based on multiple model comparisons. *Section 6.2.3* assesses uncertainties in the radiation and temperature effects as a result of using different injection strategies. A summary of the important SAI processes and uncertainties based on existing model studies is then given in *Section 6.2.4*.

6.2.1 Aerosol Processes Relevant for SAI Efficacy

The life cycle of sulfate in the stratosphere is governed by chemistry, aerosol microphysics, transport, and interaction with radiation. All of these nonlinear interactions, together with details of the injection strategies, determine the final aerosol spatial distribution, burden, aerosol optical depth, and aerosol surface area density (SAD). A brief summary of processes and interactions important for SAI is included in the following section, mainly based on Kremser et al. (2016).

6.2.1.1 Sulfate Aerosol Chemistry and Microphysical Processes

Six major processes are important for the formation and the life cycle of stratospheric sulfate aerosols: oxidation, nucleation, coagulation, condensation, evaporation, and sedimentation (**Figure 6-3**). These processes impact the total aerosol number concentration and size distribution, as well as the aerosol lifetime and radiative properties. Natural sources of stratospheric sulfuric acid (H_2SO_4) include oceanic and terrestrial emissions of carbonyl sulfide (COS) and dimethyl sulfide (DMS). COS is stable in the troposphere and is oxidized to form gaseous precursors of sulfate aerosols in the stratosphere. The main natural sources for the other stratospheric gaseous precursor, SO_2, are large explosive volcanic eruptions and large forest fires. SO_2 can be oxidized to H_2SO_4 and then condenses to form sulfate aerosols, which have a lifetime of 1–1.5 years in the stratosphere both under unperturbed conditions (Weisenstein et al., 2006; Mills et al., 2016) and with SAI (Heckendorn et al., 2009; Niemeier et al., 2011; English et al., 2012; Visioni et al., 2017a). In the stratosphere, new aerosols are mainly formed by the co-condensation of H_2SO_4 and water via binary homogeneous nucleation (e.g., Vehkamäki et al., 2002). Low temperature, high relative humidity, and low particle SADs provide optimal conditions for homogeneous nucleation (Kremser et al., 2016). The primary nucleation regions within the stratosphere are the tropical tropopause layer (TTL) region and the polar middle stratosphere. The location and amount of any SAI application impacts the speed of the nucleation processes. Particle growth of newly formed aerosols occurs mainly through coagulation, particle collision, and condensation. The growth due to condensation of H_2SO_4 vapor on particles is mainly controlled by H_2SO_4 concentrations and occurs throughout the life cycle of the stratospheric aerosol particles. Coagulation is most effective between fine (aerosol radius $r < 0.01$ µm) and coarse ($r > 1$ µm) particles (Seinfeld and Pandis, 2007), as large particles have a large surface and are a good target for smaller particles. This behavior has consequences for SAI. In contrast to sporadically erupting large volcanoes, SAI requires continuous injections to sustain an aerosol layer over many years. The consequent formation of new fine particles occurs in regions populated by particles from previous injections. In such conditions, coagulation becomes the dominant microphysical process affecting aerosol size, especially for continuous injections (Heckendorn et al., 2009). Injections over short time periods and small areas (e.g., one grid box) confine small freshly nucleated particles to a smaller region (in time and space). This reduces the relevance of coagulation, resulting in smaller particles (Niemeier and Timmreck, 2015). In any case, the particle size becomes larger with increasing injection rate as freshly formed particles coagulate and sulfur condenses on larger existing particles (Weisenstein et al., 2022).

The main removal processes for stratospheric aerosols are sedimentation of large particles and evaporation in warmer regions of the stratosphere above 32 to 35 km (Kremser et al., 2016). The evaporated gases may later re-nucleate and re-condense in cold stratospheric areas, mostly at high latitudes and high altitudes, after being transported within the BDC (see *Section 6.2.1.2*). Sedimentation or gravitational settling through the tropopause depends strongly on particle size, as well as the local vertical updraft velocity, which counters sedimentation. In regions with strong vertical advection, such as the tropical pipe, both vertical advection and sedimentation play important roles in the resulting particle number and size. Thus, Earth system models (ESMs) have to accurately model the transport processes, as well as growth processes, of aerosols. The resulting aerosol particle size distribution influences the aerosol optical properties (for

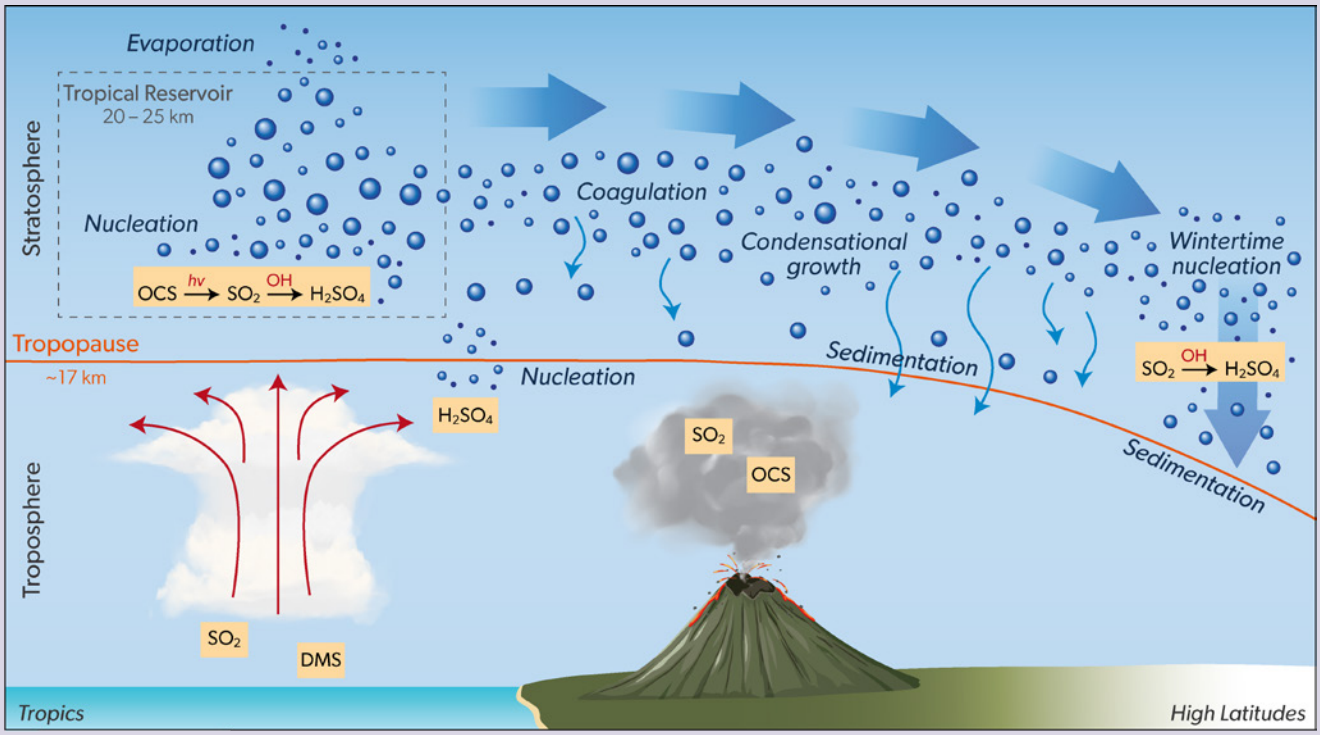

Figure 6-3. Life cycle of stratospheric sulfate, relevant aerosol microphysical processes, and stratospheric transport processes. [Adapted from Kremser et al., 2016.]

both solar and terrestrial radiation), the residence time, and the dispersion and transport of the aerosols.

6.2.1.2 Transport

Sulfur injected into the lower stratosphere is transported zonally with strong stratospheric winds and vertically and meridionally by the BDC, which is a large hemispheric circulation with an ascendant branch in the tropics and subsidence over the poles at high latitudes (**Figure 6-3**). In the extratropics, poleward motion dominates, with fast meridional mixing in the "surf zone" in the lower stratosphere (15 to 30 km altitude) and a slower meridional motion above. The surf zone is bounded by transport barriers around the winter polar vortex and in the subtropics (Butchart, 2014). Equatorial injections into the lower part of the tropical stratosphere result in the transport of aerosols towards the poles and mixing in the surf zone leads to a globally distributed aerosol layer. The main descending branch at high latitudes in the winter hemisphere (and the related transport out of the stratosphere), is a sink for the sulfate aerosols. In the wintertime, the air in the polar vortex is isolated, so sulfate aerosols reach the poles in spring and summer only after the breakdown of the polar vortex.

The resulting aerosol distribution differs with the location of the injection and the injection strategy (Heckendorn et al., 2009; Pierce et al., 2010; Niemeier et al., 2011; English et al., 2012; Tilmes et al., 2017). The injection of sulfur into the ascending branch of the BDC in the tropics results in the longest sulfate lifetime and global coverage. Injections at high latitudes result in a much shorter lifetime, and the aerosol is mostly confined to the hemisphere of injection (Robock et al., 2008a, Jones et al., 2017). The subtropical transport barriers hinder exchange between the hemispheres. Therefore, continuous injections poleward of ~30° latitude in one hemisphere will result in the transport of only a small amount of aerosol into the other hemisphere (e.g., Tilmes et al., 2017). Within the equatorial tropics, wind patterns are determined by the Quasi-Biennial Oscillation (QBO), a pattern of strong easterly or westerly jets, which change direction with a phase of roughly two years. The heating of the stratosphere from aerosols can alter the QBO and with that other transport patterns (see *Section 6.3*). It is impossible to create a persistent regional stratospheric sulfate layer over only a small region or a single country because of the nature of stratospheric transport.

6.2.1.3 Interaction with Radiation

Sulfate aerosols scatter solar (shortwave [SW]) radiation and absorb at terrestrial (i.e., infrared [IR] and near-IR) wavelengths. The addition of sulfate aerosols in the stratosphere therefore causes an intentional cooling of the troposphere as a result of reduced incoming SW radiation and an unintentional warming in the lower stratosphere through the absorption of IR and near-IR radiation (Timmreck and Graf, 2006; Aquila et al., 2014). This results in a change in the temperature gradient within the stratosphere and troposphere. For a realistic size distribution of stratospheric aerosols, as determined from observations following volcanic eruptions, scattering of sunlight is most efficient for aerosols with effective radii between 0.3 and 0.4 µm; aerosols below 0.1 µm and above 1 µm are inefficient at interacting with radiation at solar wavelengths (Mie, 1908; Dykema et al., 2016). Absorption of terrestrial radiation increases strongly for sulfate aerosols larger than 1 µm owing to increases in the imaginary part of the refractive indices at these wavelengths (Laakso et al., 2022).

For reference, stratospheric aerosol effective radii, observed at Laramie, Wyoming (USA), were in the range of 0.1 to 0.15 μm before the Mount Pinatubo eruption and around 0.4 to 0.5 μm one year after the eruption (Kleinschmitt et al., 2017; Deshler et al., 2019). For SAI, the resulting effective radii of aerosols depend on the injection strategy, varying between 0.2 and 0.6 μm for injection rates between 2 and 100 Tg SO_2 yr^{-1} (Kleinschmitt et al., 2018; Laakso et al., 2022).

Radiative forcing provides a useful metric for assessing the magnitude of the climatic response from a particular perturbation, as the temperature response to a perturbation is approximately proportional to its forcing (IPCC, 2021). Following the IPCC definition, the effective radiative forcing (ERF) is the change in net (solar plus terrestrial) irradiance at the top of the atmosphere (TOA) caused by the stratospheric aerosol as measured in W m^{-2} after the stratosphere has adjusted to radiative equilibrium. General circulation models (GCMs) using prescribed sea surface temperatures (SSTs) calculate ERF as an estimate of the TOA radiative imbalance. For simply comparing the effects of different sulfate distributions, models are able to internally calculate the radiative forcing of the sulfate for each model time step: the radiation module performs a second calculation without considering stratospheric aerosols. In this way, the instantaneous radiative forcing (IRF) of the aerosol can be determined without considering the impacts of adjustments on climate. IRF is not directly comparable to the radiative forcing changes derived from ESMs that are coupled to an ocean module, as they include adjustments of stratospheric and surface temperatures.

The effectiveness of SAI varies with season and latitude because it depends on the amount of incoming solar radiation. Therefore, very little SW reduction is expected from SAI at high and mid-latitudes in winter, while more continuous radiative changes occur in the tropics. In contrast, the radiative forcing of greenhouse gases (GHGs) varies only a little with latitude as it is mostly caused by absorption of terrestrial radiation, which is less dependent on the season (Govindasamy and Caldeira, 2000; Kravitz et al., 2011). GHG temperature impacts also have a different vertical profile compared to that from SAI due to the heating of the sulfate aerosols in the lower stratosphere (Ferraro et al., 2014; Henry and Merlis, 2020). Therefore, uniformly applied SAI across the globe does not completely offset the warming of GHGs, and residual warming still occurs, particularly at high latitudes.

Secondary feedbacks, such as modifications in the concentration of stratospheric water vapor and ozone due to SAI, may also affect the overall radiative forcing. A stratospheric water vapor increase, produced by the warming of the lower stratosphere and the tropopause, would have a positive radiative effect (Richter et al., 2017; Krishnamohan et al., 2019; Huang et al., 2020; Visioni et al., 2021b). The stratospheric lifetime of methane (CH_4) and its concentration may also be affected by tropospheric and stratospheric hydroxyl radical (OH) changes. Both contributions would result in a minor positive forcing that would offset only a fraction of the large negative forcing produced by the aerosols (Visioni et al., 2017a).

6.2.2 Model Uncertainties and Simulated Global Radiative Forcing and Surface Temperature Response to SAI

Variations in modeled radiative forcing and surface temperature response to SAI arise from differences in the simulated

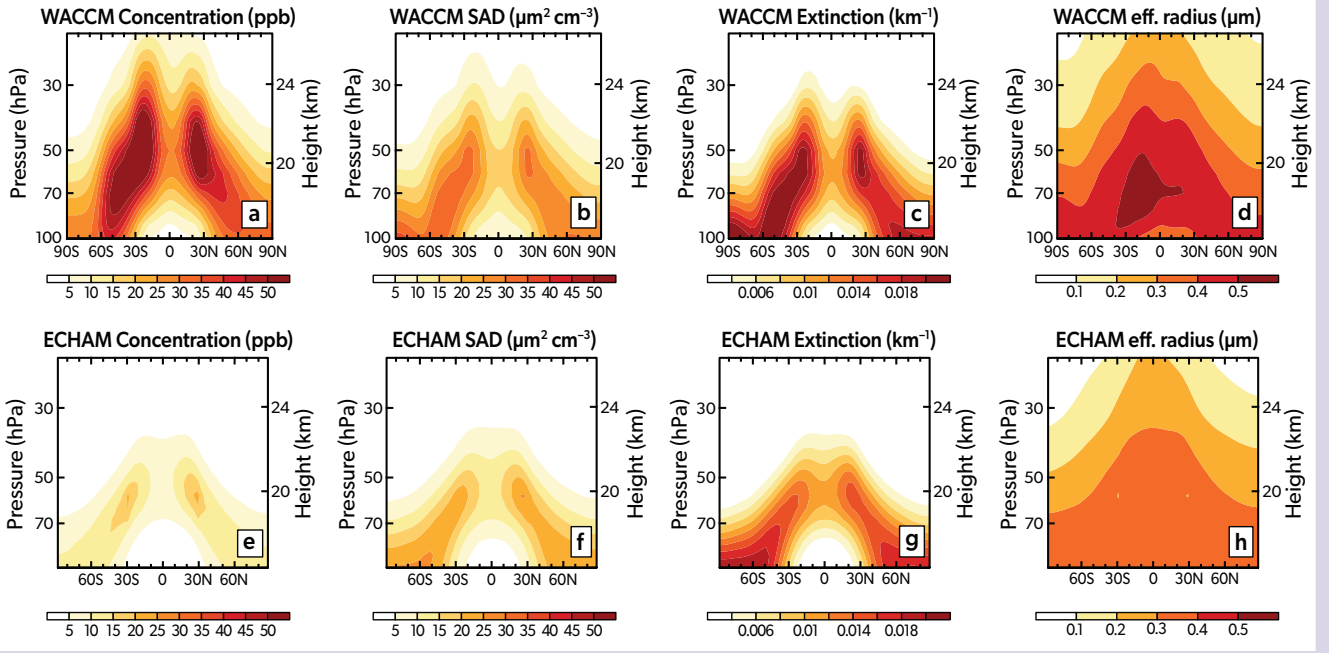

Figure 6-4. (a, e) The concentration of total sulfur (gas and aerosols), (b, f) surface area density (SAD), (c, g) light extinction, and (d, h) effective radius, averaged zonally and over time, as simulated with the CESM (WACCM) (a–d) and MAECHAM5-HAM (e–h) models. In both models, 10 Tg SO_2 yr^{-1} is continuously injected into two single grid boxes at 30°N and 30°S at an altitude of 18–21 km. [Adapted from Weisenstein et al., 2022.]

sulfate aerosol geographic distribution and particle size, which result from details of the injection strategy and the complex and nonlinear interplay between transport, oxidation chemistry, and microphysical processes (*Section 6.2.1*). Most existing climate models neglect at least some of the couplings between these processes, and variations across models in what processes are accounted for may also feed back onto impacts on chemistry and ozone. First, we outline the range of existing stratospheric aerosol descriptions in models and the differences in their complexity that contribute to the uncertainty in our understanding of the effects of SAI on stratospheric ozone. After that, an assessment of the range of changes in radiative forcing and surface temperature from different GCMs is given.

6.2.2.1 Aerosol Representation in Models, Complexity, and Uncertainties

The simplest way to approximate the effects of SAI in models is to turn down the solar constant. However, the impacts of these global solar dimming experiments differ substantially from SAI applications using sulfate aerosols. Besides resulting in very different climate outcomes, these experiments do not consider the increase in stratospheric SAD and do not simulate the associated chemical effects. Furthermore, in contrast to SAI, solar dimming does not heat the lower tropical stratosphere (Niemeier et al., 2013; Kalidini et al., 2015; Irvine et al., 2017; Jones et al., 2021); hence, the effect on stratospheric ozone is quite different from simulations where aerosols are added to the stratosphere (see *Section 6.3*). Slightly more complicated approaches prescribe a thin stratospheric aerosol layer at a constant geopotential height (Krishnamohan et al., 2019) or scale aerosol microphysical and optical properties via imposed aerosol optical depth (AODs), taken from aerosol microphysical simulations or observations after the Mount Pinatubo eruption. In this case, the models simulate aerosol radiative interactions and climate impacts but no feedback on particle transport and chemistry (e.g., Niemeier et al., 2013; Ferraro et al., 2015). The next step up in complexity is an online representation of bulk aerosol properties via single-moment schemes: this accounts for the transport of aerosol mass but not for the evolution of the aerosol size distribution, which is prescribed (e.g., Jones et al., 2017). Much more complex aerosol parameterizations describe processes such as nucleation, condensation, and coagulation and include explicit treatment of both aerosol mass and number distributions assuming lognormal distributions (e.g., Mills et al., 2016; Niemeier and Timmreck, 2015). The most general, but computationally expensive, representations of aerosol properties are size-resolving sectional aerosol schemes, which often use a high number of size bins with fixed widths (Kokkola et al., 2009; English et al., 2012; Kleinschmitt et al., 2018; Laakso et al., 2022).

Different aerosol microphysical parameterizations can result in significantly different aerosol distributions and radiative forcing. Comparisons of two different aerosol microphysical schemes within one GCM (Laakso et al, 2022), a modal scheme with four sulfate modes and a sectional scheme with ten bins, indicate that the modal scheme requires a roughly five-times-larger sulfur injection than the sectional scheme to reduce the radiative forcing to preindustrial levels by the end of the century (see *Section 6.2.3*).

Differences in simulated transport also have an impact on the resulting sulfate concentrations. **Figure 6-4** shows results from two GCMs that apply the same SAI strategy (Niemeier et al., 2020). Both models are coupled to modal aerosol schemes. The model with the strongest vertical uplift results in an aerosol concentration twice as large as in the model with weaker vertical uplift (compare **Figure 6-4a** and **e**). The stronger vertical uplift also results in larger SAD and light extinction and larger effective radii (**Figure 6-4b–d**, **f–h**), with consequences for aerosol light scattering efficiency and heterogeneous chemistry.

The interaction between the injected sulfur and other stratospheric chemical components can also impact the simulated

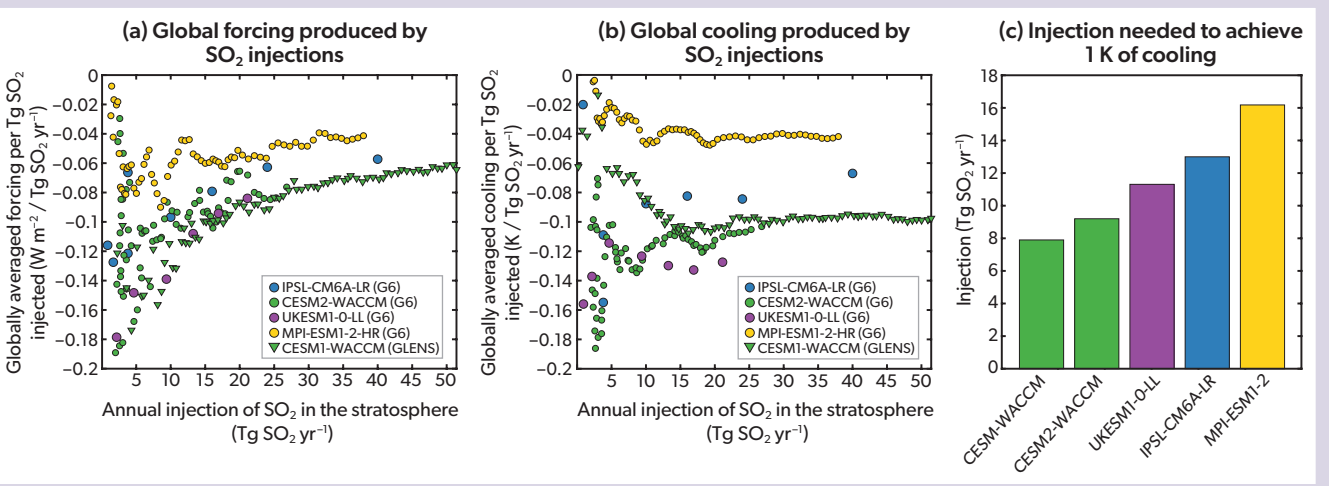

Figure 6-5. Radiation and temperature response from different Earth system model simulations of the GeoMIP scenario G6sulfur (medium SAI) and of CESM1 (WACCM) simulations in the GLENS (strong SAI) scenario. The injection rate is in Tg SO_2 yr^{-1} (after Visioni et al., 2021a). (a) Globally averaged top-of-the-atmosphere all-sky radiative forcing (which includes the response of all ESM components) normalized by the SO_2 injection rates. (b) Annual mean global surface temperature anomaly normalized by the SO_2 injection rates. A five-year running mean has been applied to the results. (c) Injection rate of SO_2 needed to cool the globally averaged surface temperature by 1 K.

results of SAI (Richter et al., 2017). For example, a decrease in stratospheric ozone and the associated relative cooling owing to reduced absorption of UV radiation partially counters the warming due to the aerosols. This influences stratospheric dynamics and causes a different dynamical response, including in the QBO, compared to a model with prescribed ozone concentrations (Brenna et al., 2021; Franke et al., 2021), and this can also affect the ozone concentration (*Section 6.3.2.2*). The understanding of these interactions is still limited. Also, the complexity and treatment of chemical processes in different models affect the simulated impacts on other chemical species such as OH and CH_4 (Visioni et al., 2017b), which in turn affect ozone. The omission of very-short-lived halogen species in models may lead to an underestimation of the impacts of SAI on ozone (Tilmes et al., 2012). Other model shortcomings include missing processes or interactions, such as how aerosols from SAI might affect cirrus clouds as they settle out of the stratosphere (Visioni et al., 2022). An overview of model improvements needed to narrow uncertainties in SAI is summarized in Eastham et al. (2021).

6.2.2.2 Simulated Surface Temperature and Radiative Forcing

The aim of SAI is to reduce temperatures at the Earth's surface to reduce the risk of climate change through a small reduction in the amount of solar radiation reaching the surface. **Figure 6-5** shows the cooling per mass of SO_2 injected in SAI simulations in six different Earth System models (ESMs) under the medium and strong SAI scenarios (**Figure 6-2**). For the medium SAI scenario, not all models used the same injection strategy; some models injected sulfur between 10°N and 10°S and between 18 and 20 km, while CESM2-WACCM injected at the equator at around 25 km altitude. Some models simulated the sulfate evolution with interactive stratospheric aerosol microphysics, while other models used an imposed sulfate distribution that had been calculated using a GCM coupled with a microphysical aerosol module (see Visioni et al., 2021a, for details). Some models included interactive stratospheric chemistry, while others did not. Differences across the models in radiative forcing efficiency (forcing per injected unit mass) and efficiency of temperature reduction are largest for smaller simulated injection amounts (<20 Tg SO_2 yr^{-1}; **Figure 6-5a**, **b**) and somewhat smaller for larger injections. The forcing efficiency ranges from –0.04 to –0.1 W m^{-2} per Tg SO_2 yr^{-1} and the temperature efficiency from –0.04 to –0.14 K per Tg SO_2 yr^{-1} for an injection of 20 Tg SO_2 yr^{-1}. This implies that sustained injection rates of 8–16 Tg of SO_2 yr^{-1} would be needed in order to cool the Earth by 1 K (**Figure 6-5c**; Visioni et al., 2021a). This range in the amount of sulfur that would be injected annually in this SAI scenario is approximately equal to the observationally-based estimate of the mass of sulfur injected into the stratosphere by Mount Pinatubo in a single event in 1991.

6.2.3 Sensitivities of Aerosol Distribution to Injection Strategy and Consequences for Radiation

Various SAI strategies have been studied with models that include aerosol microphysical processes. Different injection

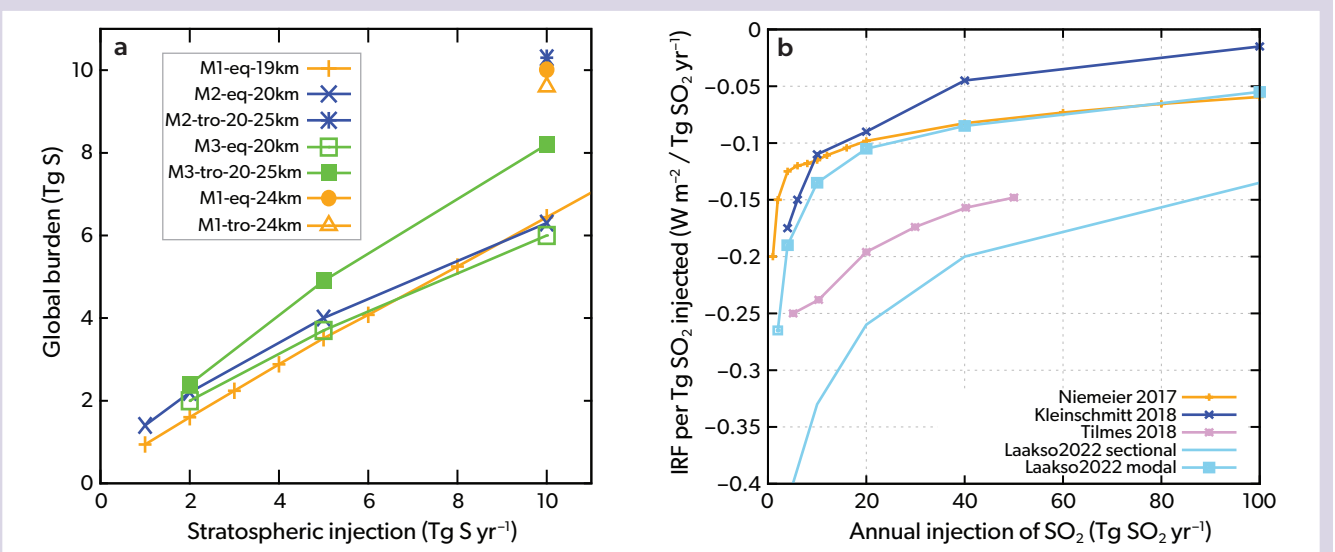

Figure 6-6. (a) Globally averaged sulfur burden for varying injection rates based on simulations in different models (after Niemeier and Timmreck, 2015). M1: results of Niemeier and Timmreck (2015) for injections of SO_2 at the equator (5°N, 120°E) at altitudes of 19 km and 24 km. M2: injections of SO_2 between 5°N and 5°S at an altitude of 20 km and between 30°N and 30°S between altitudes of 20 and 25 km (English et al., 2012). M3: same injection method as M2, but results after Pierce et al. (2010). (b) Internally derived stratospheric instantaneous aerosol radiative forcing (IRF) at the top of the atmosphere scaled per mass of injected SO_2, based on three GCMs (Niemeier and Schmidt, 2017; Kleinschmitt et al., 2018; Laakso et al., 2022) and one ESM (Tilmes et al., 2018a). All models include aerosol microphysical processes. IRF is calculated as the difference between two calls to the model radiation scheme, one including and one excluding sulfate aerosols, and does not allow the stratosphere to equilibrate to the new radiative equilibrium. While IRF is a measure of the change in radiative balance caused by the aerosols, it cannot be directly translated into surface temperature changes because it does not include the additional longwave radiation that is retained by a warmer stratosphere, which negates part of the cooling produced by aerosol scattering.

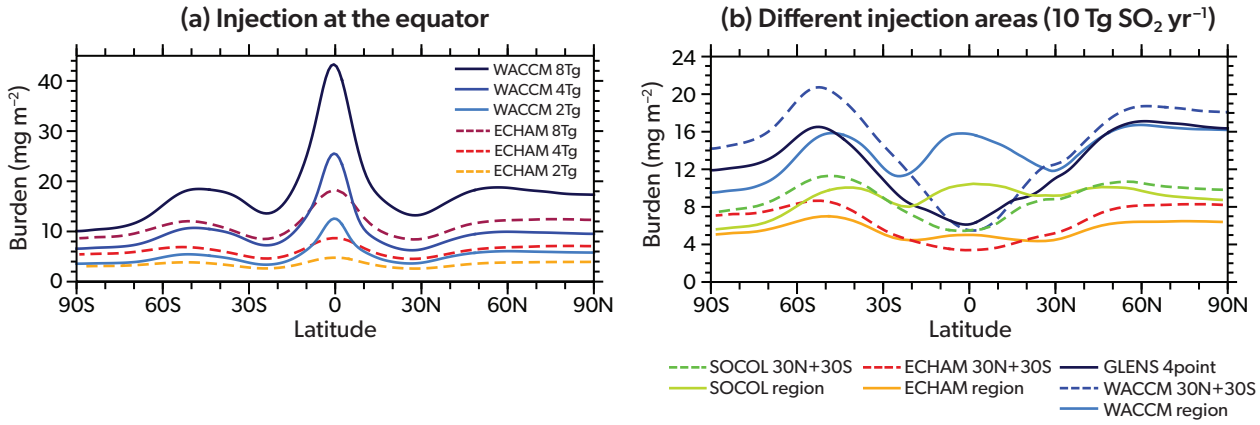

Figure 6-7. (a) Zonally averaged sulfur burden in two different models for three different injection rates, for runs where SO_2 was injected continuously into one grid box at the equator (after Niemeier et al., 2020). (b) Zonally averaged sulfate burden in three different models with 10 Tg SO_2 yr^{-1} injections employing three different strategies: 2 grid boxes at 30°N and 30°S, a belt between 30°N and 30°S along the equator (region; after Weisenstein et al., 2022), and at four different grid points: 30°N, 15°N, 15°S, 30°S (GLENS four-point; after Tilmes et al., 2018a).

strategies result in different spatial aerosol distributions and particle sizes and consequently cause different impacts on climate and ozone. The following subsections give an overview of the sensitivity of the aerosol distribution to SAI injection strategy using GCMs coupled to aerosol microphysical modules and using fixed sea surface temperatures (SST). These studies used continuous or pulsed injections of a constant mass rate (Tg yr^{-1}) at different altitudes and locations. Consequences for the impact on ozone are given in *Section 6.3.2* and **Table 6-2**.

6.2.3.1 Sensitivity to Increasing Injection Rates

Increasing injection rates result in a sublinear increase of the globally averaged sulfate aerosol burden (i.e., diminishing returns), as shown in **Figure 6-6a**. The four models agree quite well on the factor of increase (times ~1.8 for a doubling of the injection rate). Comparing the instantaneous radiative forcing (IRF) of four different studies shows a much wider spread in the model results (**Figure 6-6b**). The IRF efficiency (forcing gain per injected mass unit) ranges between –0.09 and –0.26 W m^{-2} per Tg SO_2 yr^{-1} for an injection of 20 Tg SO_2 yr^{-1}. The resulting forcing of 20 Tg SO_2 yr^{-1} would therefore be between –1.8 and –5.2 W m^{-2}, which shows that the forcing produced by a given injected mass of sulfur is currently very uncertain.

The models consistently show that the forcing efficiency decreases exponentially with increasing injection rate (Niemeier and Timmreck, 2015); e.g., quadrupling the injection of the most efficient model from 10 to 40 Tg SO_2 yr^{-1} decreases the forcing per unit mass from 0.33 to 0.2 W m^{-2} per Tg SO_2 yr^{-1}. This behavior results from the increase in particle size with increasing injection rate (*Section 6.2.1.1*), producing aerosols with a less optimal size for scattering sunlight, increased absorption of terrestrial radiation, and a greater sedimentation rate through the tropopause and therefore reduced effectiveness (Heckendorn et al., 2009; Pierce et al., 2010; English et al., 2012; Niemeier and Timmreck, 2015). One main reason for the larger differences between aerosol forcing and mass is the difference in simulated particle sizes in models, as shown by the light blue curves in **Figure 6-6a** and **b**, simulated with the same GCM, but different microphysical parameterizations. Diminishing returns may have important consequences that influence the efficacy of any SAI strategy: to offset more forcing, relatively more injected mass is needed, producing more heating in the tropical stratosphere with larger impacts on stratospheric ozone and climate.

6.2.3.2 Sensitivity to Injection Altitude

Several studies have shown that the cooling efficiency of stratospheric aerosols is larger for injections into tropical regions at altitudes well above the tropopause (around 25 km or 30 hPa in tropical regions) than at lower altitudes closer to the tropopause (around 20 km or 75 hPa; e.g., Jones et al., 2017; Niemeier and Timmreck, 2015; Tilmes et al., 2017, 2018b). This is because injection at higher altitudes prevents the fast removal of aerosols and their precursors, and it allow aerosols to reach even higher altitudes through the vertical updraft of the BDC. For tropical injections, the global sulfate burden increases by 30–50% when the injection altitude is increased by 5 km (**Figure 6-6a**). However, this is not true for all SAI injection strategies such as injections outside the tropics (Niemeier and Schmidt, 2017; Laakso et al., 2022; see **Table 6-1** for altitude dependency), because the injection location influences the simulated meridional distribution of the aerosols, which also depends on the injection amount. Injections at higher altitudes may be more efficient in terms of radiative forcing but are not necessarily more desirable for ozone. High-altitude injections have a larger impact on ozone via the catalytic nitrogen cycle, which dominates in the middle stratosphere. With lower altitude injections, a more concentrated aerosol distribution closer to the tropopause results in stronger heating in the tropical stratosphere, with consequences for transport and stratospheric water vapor changes (Tilmes et al., 2018b).

6.2.3.3 Dependency on Injection Latitude for Point Injections

The globally averaged sulfur burden is maximized for aerosol injections in the inner tropics (i.e. in the vicinity of the equator)

Table 6-1. Estimates of globally averaged top-of-the-atmosphere sulfate radiative forcing from different studies. The results are grouped based on whether the studies focused on responses to injection at specific altitudes, longitudinal areas, or a zonal area, the use of regional and point injections, pulsed injections, and the use of stable injections versus a feedback control strategy. Injection rates refer to the total stratospheric injections per year.

Study	Injection rate (Tg S yr^{-1})		W m^{-2}	W m^{-2}	W m^{-2}	Net (SW+LW) or SW only
Altitude			**Low (<20km)**	**Middle (~20km)**	**High (>20km)**	
Kleinschmitt et al., 2018	10	one-lon, 2° N – 0° S	–1.5	–1.8	–1.5	Net (SW+LW)
Laakso et al., 2022	5	band, 10° N – 10° S, sectional aer. model	–3.26	–3.29	–3.79	Net (SW+LW)
Laakso et al., 2022	5	band, 10° N – 10° S, modal aer. model	–1.75	–1.33	–1.59	Net (SW+LW)
Niemeier and Timmreck, 2015	10	one-lon, 2.8° N to Eq	–2.03		–3.02	Net (SW+LW)
Niemeier and Timmreck, 2015	10	one-lon, 30° N to 30° S	–1.81		–2.76	Net (SW+LW)
Niemeier and Schmidt, 2017	10	one-lon, 2.8° N to Eq	–1.78		–1.92	Net (SW+LW)
Vattioni et al., 2019	1.87	band, 15° N – 15° S, 20 km	–0.96		–1.22	SW
Longitudinal area			Narrow (<10°)	Middle	Broad (>50°)	
Kleinschmitt et al., 2018	10	one-lon	–1.5		–1.5	Net (SW+LW)
Laakso et al., 2022	5	band, sectional model	–3.81	–3.29	–3.09	Net (SW+LW)
Laakso et al., 2022	5	band, modal model	–1.21	–1.33	–1.53	Net (SW+LW)
Niemeier and Timmreck, 2015	10	one-lon	–2.03	–2.06	–1.81	Net (SW+LW)
Vattioni et al., 2019	1.87	band	–0.96	–0.93	–1.00	SW
Zonal area			**One-lon**	**Band over longitudes**		
Laakso et al., 2022	5	2° N – 2° S, 21 km, sectional aer. model	–4.13	–3.81		Net (SW+LW)
Laakso et al., 2022	5	2° N – 2° S, 21 km, modal aer. model	–1.96	–1.21		Net (SW+LW)
Niemeier and Timmreck, 2015	10	2.8° N to 0°, 19 km	–2.03	–1.79		Net (SW+LW)
Vattioni et al., 2019	1.87	3.75° N – 3.75° S, 20 km	–1.51	–0.96		SW
Regional / point injections		**(30° S – 30° N, band) / (30° S and 30° N one-lon)**	**Region**	**2-model grid points**		
Weisenstein et al., 2022	5	Model: CESM2(WACCM)	–2.4	–2.2		Net (SW+LW)
Weisenstein et al., 2022	5	Model: MAECHAM5-HAM	–0.8	–1.1		Net (SW+LW)
Weisenstein et al., 2022	5	Model: SOCOL-AER	–1.6	–1.7		Net (SW+LW)
Pulsed			**Low rate (2 yr^{-1})**	**High rate (≥6 yr^{-1})**	**Continuous**	
Kleinschmitt et al., 2018	10	one-lon, 2° N – 0° S, 17 km	–1.6		–1.5	Net (SW+LW)
Laakso et al., 2022	5	band, 10° N – 10° S, sectional model	–4.36	–3.58	–3.29	Net (SW+LW)
Laakso et al., 2022	5	band, 10° N – 10° S, modal model	–2.08	–1.36	–1.33	Net (SW+LW)
Heckendorn et al., 2009	5	band, 5° N – 5° S, 20 km	–1.64	–1.29	–1.06	SW
Vattioni et al., 2019	1.87	10° N – 10° S, 20 km	–1.51		–0.96	SW
Stable injections / Feedback-control strategy (GLENS)			**Region**	**GLENS**		
(Weisenstein et al., 2022 /	5	30° S – 30° N, band / Feedback-control	–2.4	–2.16		Net (SW+LW)
Tilmes et al., 2018b (GLENS))	25	30° S – 30° N, band / Feedback-control	–7.1	–7.21		Net (SW+LW)

(Jones et al., 2017; Niemeier and Schmidt, 2017; Tilmes et al., 2018b; Franke et al., 2021). However, this might not be the optimal injection strategy because the tropical confinement of the aerosols causes a local burden maximum in the tropics (**Figure 6-7a**). Injections outside the inner tropics have been simulated in recent studies targeting changes beyond global mean surface temperature, including pole-to-equator and inter-hemispheric temperature gradients (e.g., Kravitz et al., 2017). **Figure 6-7b** shows results of simultaneous two point-like injections at 30°N and 30°S of a total of 10 Tg SO_2 yr^{-1} (Franke et al., 2021; Weisenstein et al., 2022). The injection outside of the subtropical transport barrier reduces the sulfate aerosol transport into the tropics and therefore results in a minimum aerosol burden in the tropics (**Figure 6-7b**). The global coverage of the aerosols is more homogenous for injections in the outer tropics, and this reduces tropical heating of the sulfate aerosols due to less equatorial confinement (Kravitz et al., 2019). Consequently, surface cooling is spatially more even, and the increase of stratospheric water vapor, as well as the impact on the QBO, are reduced (Aquila et al., 2014; Niemeier and Schmidt, 2017; Richter et al., 2017; Franke et al., 2021).

6.2.3.4 Dependency on Single Points / Regional Injections (Area)

Whether the injection of sulfur is concentrated in one area or distributed across different locations plays a crucial role for the simulated burden and radiative forcing. Injections into a larger region, between 30°S and 30°N and over all longitudes (solid lines in **Figure 6-7b**), still produce a peak in the aerosol column burden over the equator, but the peak is smaller than for injections at one grid point at the equator (**Figure 6-7a**). Many models (Heckendorn et al., 2009; Niemeier and Timmreck, 2015; Vattioni et al., 2019; Laakso et al., 2022) agree that injections into one grid point in the inner tropics result in less coagulation and therefore smaller particles than injections into multiple grid points, either along the equator (see "zonal area" group of studies in **Table 6-1**) or over multiple latitudes toward the extratropics ("longitudinal area" group of studies in **Table 6-1**). This results in slower removal (i.e., larger burden) and larger radiative forcing. However, the impact of widening the injection area latitudinally is not consistent across models, with disagreements on what is the most effective approach. This is because of inconsistencies in the injection locations among simulations or differences in representing stratospheric dynamical processes (e.g., the QBO) across models.

6.2.3.5 Dependency of Injection Timing

Studies agree that pulsed injections into the tropics, e.g., injections over one month twice a year, result in stronger radiative forcing per injected mass than continuous injections (see "pulsed" group of model runs in **Table 6-1**). Continuous sulfur injections lead to a continuous formation of sulfuric acid (H_2SO_4) and a continuous supply of freshly nucleated small particles (Heckendorn et al., 2009). These coagulate with larger particles, leading to the quicker formation of large particles and a shift of the aerosol size distribution to larger effective radii. Aerosols that grow to larger than the optimal optical size (*Section 6.2.1.3*) scatter sunlight less efficiently and are removed faster from the stratosphere owing to higher sedimentation rates. Pulsed injections reduce the formation of freshly nucleated small particles to a short period in time, consequently forming an aerosol size distribution with smaller effective radii. These processes also explain the higher efficiency in terms of radiative forcing per injected mass for single grid point injections compared to injections along several longitudes.

SAI aims to reduce incoming solar radiation, which is the largest for overhead sun and is dependent on the length of day. Injecting into the region where the sun reaches the zenith can lead to stronger radiative forcing at mid-latitudes and weaker radiative forcing in the tropics. This may result in a 5–60% stronger global mean forcing per emitted mass (Laakso et al., 2017, 2022). Visioni et al. (2019) found that injections at 15° latitude in the spring of the corresponding hemisphere result in the largest reductions in incoming solar radiation per mass injected.

6.2.3.6 Gaseous Versus Particulate Injection

Aerosol mass and size distributions with SAI are also dependent on whether the SAI strategy prescribes the injection of accumulation-mode H_2SO_4 aerosol or gas-phase SO_2 (Vattioni et al., 2019; Franke et al., 2021; Weisenstein et al., 2022). Increasing the rate of SO_2 injections increases particle size, which, as noted above, decreases stratospheric aerosol lifetime and radiative forcing efficiency (*Section 6.2.3.1*). This problem could be combated by directly injecting optimally sized accumulation-mode particles. It has been suggested that if H_2SO_4 or SO_3 (sulfur trioxide) vapor are were released into an aircraft wake, nucleation and coagulation in the confined plume would result in a distribution of sulfate particles in the accumulation size range (0.05–0.2 μm radius; Pierce et al., 2010; Benduhn et al., 2016; Vattioni et al., 2019). Due to their coarse horizontal resolution, GCMs are not able to simulate the rapid initial formation of accumulation-mode sulfate particles after the injection of H_2SO_4 vapor. Therefore, in these simulations the injection of H_2SO_4 is modeled as direct injection of SO_4 (sulfate) aerosol into the accumulation mode (Vattioni et al., 2019). Results from three GCMs consistently show a higher aerosol burden and smaller particle sizes for injections of accumulation-mode SO_4 compared to SO_2 considering different injection strategies and models (Weisenstein et al., 2022). The higher aerosol concentration causes a stronger impact on stratospheric dynamics, but less H_2SO_4 injection would be necessary to achieve the same climate impact. All three models show a reduced increase in particle size with increased injection rate if using accumulation-mode SO_4 injections.

6.2.4 Summary of SAI Processes and Model Uncertainties

Many processes that determine the effects of SAI on both the climate and ozone are often simplified or missing from climate models. This includes the coupling of chemistry, aerosols, and radiation, as well as aerosol microphysical processes. Simplified, and therefore computationally cheaper, aerosol schemes are used for centennial simulations in ESMs. A more detailed representation of the life cycle of sulfate would require computationally expensive sectional microphysical modules. In addition, the grid resolution of current global models is far too coarse to simulate processes that take place right after an injection from a small pipe of an aircraft or other delivery system; instead, injections are assumed to occur uniformly into one model grid box. An additional shortcoming is the representation of aerosol-cloud interactions, in particular the impact of the injected material on cirrus clouds.

Besides differences in physical processes, another major reason for the disagreement across models in simulated aerosol burden and radiative forcing is the different representation of large-scale dynamic processes in the stratosphere. For example, different horizontal and vertical grid resolutions result in different grid-box mean vertical velocities within the models, even without SAI. Those differences, in addition to specifics of the aerosol microphysics schemes in the model, result in different aerosol size distributions, which induce different amounts of heating, vertical lifting, and sedimentation. Consequently, the models react differently to the varying injection strategies.

Despite these uncertainties, the models consistently show that increasing injection rates result in diminishing returns for both aerosol burden and radiative forcing, as well as an exponential decrease in radiative forcing efficiency. There is also general agreement that the global coverage of the aerosols is more homogenous for injections outside of the immediate equatorial band than for injections close to the equator. Nevertheless, there is poor agreement between the models on the amount of sulfur needed to achieve cooling of the Earth's global mean temperature by 1 °C. This relates both to the SAI-induced radiative forcing response in models and to differences in the climate sensitivity of

ECMs, which strongly influence the simulated global mean temperature change under climate scenarios without SAI (see also **Figure 6-1**).

6.3 IMPACTS OF SAI USING SULFATE ON STRATOSPHERIC OZONE, CHEMISTRY, TRANSPORT

In this section, we assess the relevant processes driving SAI impacts on ozone. We identify differences in the impacts of SAI (using sulfate, or its precursors) on stratospheric ozone under specific SAI strategies (*Section 6.1.3*) as projected in recent climate modeling studies. Here, the effects of SAI on stratospheric ozone are mostly based on comparisons of simulations with and without SAI.

6.3.1 Effects of SAI on Stratospheric Chemistry

As evidenced from explosive volcanic eruptions (e.g., Solomon, 1999), enhancements of the stratospheric sulfate aerosol layer from continuous SAI would result in elevated aerosol surface area density (SAD), which directly influences chemical production and loss of stratospheric ozone through heterogeneous reactions and their impact on catalytic ozone cycles (**Figure 6-8**, middle row). The SAD amounts and geographic distributions depend on the details of the injection strategy, including altitude above the tropopause, latitudinal injection location, and the seasonality of injections (*Section 6.2*).

One effect of enhanced stratospheric SAD is increased nitrogen pentoxide (N_2O_5) hydrolysis at the interface of the liquid acidic sulfate particles, resulting in the production of nitric acid (HNO_3): ($N_2O_5 + H_2O_{(aq)} \longrightarrow 2\ HNO_3$). HNO_3 is a low-reactive nitrogen reservoir; therefore, the increase of HNO_3 at the expense of nitrogen oxides reduces the catalytic ozone loss cycles (Fahey et al., 1993). The reactive nitrogen cycle is most important in the mid- and upper stratosphere (altitudes above 30 hPa; **Figure 6-8**, top row). The strongest reductions in ozone loss rates based on this cycle are therefore simulated for the upper part of the aerosol layer (with a peak around 15 hPa in the tropics; e.g., Tilmes et al., 2017). These effects are present at all latitudes, with the largest importance in the tropical and mid-latitude stratosphere. Ozone loss rates from the reactive nitrogen cycle are reduced the most for high-altitude injection (**Figure 6-8**, green dashed versus solid lines).

In the lower stratosphere, ozone loss cycles involving the reactive chlorine (ClO_x), bromine (BrO_x), and hydrogen (HO_x) families are most important. An enhanced stratospheric SAD results in the activation of halogens from reservoir species such as chlorine nitrate ($ClONO_2$) and hydrogen chloride (HCl) to chlorinated species such as chlorine (Cl_2) and hypochlorous acid (HOCl) via reactions such as $ClONO_2 + H_2O \longrightarrow HOCl + HNO_3$, $ClONO_2 + HCl \longrightarrow Cl_2 + HNO_3$, and $HOCl + HCl \longrightarrow Cl_2 + H_2O$. In the presence of sunlight, Cl_2 and HOCl photolyze rapidly to form reactive halogen species that drive catalytic ozone-destroying reactions. Reactions with nitrogen dioxide (NO_2) convert halogen and hydrogen radicals back into reservoir species. Thus, the combined effect of activating halogens and reducing NO_2 results in increased ozone loss via the halogen and HO_x catalytic ozone loss cycles as a result of increased stratospheric SAD (Drdla and Mueller, 2012). These processes are most effective at temperatures lower than 200 K and are thus most efficient in the polar regions.

The ozone loss cycles described above are strongly dependent on the halogen and nitrogen loading in the atmosphere. Chlorine and bromine cycles are expected to be reduced with the projected future decline in halocarbon atmospheric abundances, and hence the role of these cycles in stratospheric ozone loss is expected to decrease. On the other hand, nitrous oxide (N_2O) may become the dominant ozone-depleting substance in the future (Ravishankara et al., 2009). The net effect of increased stratospheric SAD on the ozone column will depend on the balance of decreased net chemical production from hydrogen and halogen catalytic cycles versus the increased net chemical production from nitrogen oxide catalytic cycles (e.g., Xia et al., 2017). The altitude dependence of the importance of these cycles could result in changes in the vertical distribution of ozone even with small overall changes in the ozone column (Heckendorn et al., 2009 Tilmes et al., 2017).

Ozone loss cycles involving hydrogen oxide radicals (HO_x) are important in both the lower and the upper stratosphere. Changes in the hydrogen cycles would be influenced not only by changes in NO_x but also by SAI-induced changes to stratospheric water vapor (Richter et al., 2018; Tilmes et al., 2018b; Visioni et al., 2021b). This increase occurs due to the warming of the lower stratosphere and tropical tropopause layer (TTL) by the aerosols (see *Section 6.2.2.1*) and leads to an increase of HO_x ozone loss cycles through the reaction $H_2O + O(^1D) \longrightarrow 2OH$. A secondary pathway for SAI to increase water vapor in the stratosphere is through an increase of the stratospheric methane lifetime and concentrations due to an increase in the transport of methane in the mid-stratosphere due to enhanced upwelling (Visioni et al., 2017b). Water vapor increases are greater with injections at low altitudes than at high altitudes because the former lead to more concentrated sulfate mass closer to the tropopause and therefore enhanced heating of the tropopause, which leads to reduced dehydration in the TTL (Tilmes et al., 2017). Finally, the reactive oxygen cycles would also be perturbed in the tropical region due to changes in the air temperature from SAI, but this would produce a minor loss in ozone compared to other cycles. Combined net chemical ozone production rates show an increase most pronounced in the mid-stratosphere tropics, and a decrease in the lower stratosphere, particularly at high latitudes, as well as in the upper stratosphere (**Figure 6-8**, right middle panel).

At mid-latitudes, Robrecht et al. (2021) explored the importance of a possible pathway through which increasing water vapor in the lowermost stratosphere during the North American summer monsoon season may increase ozone loss if conditions are cold and moist enough. As SAI would both warm and add water vapor to the layer where chlorine activation may happen, they found that less than 0.3% of ozone may be depleted through that pathway.

6.3.2 Effects of SAI on Ozone Via Changes in Stratospheric Dynamics and Transport

6.3.2.1 Large-Scale Impacts

In addition to the direct chemical effects produced by the increased SAD, an enhanced sulfate layer would also affect ozone through transport changes. These changes are predominantly

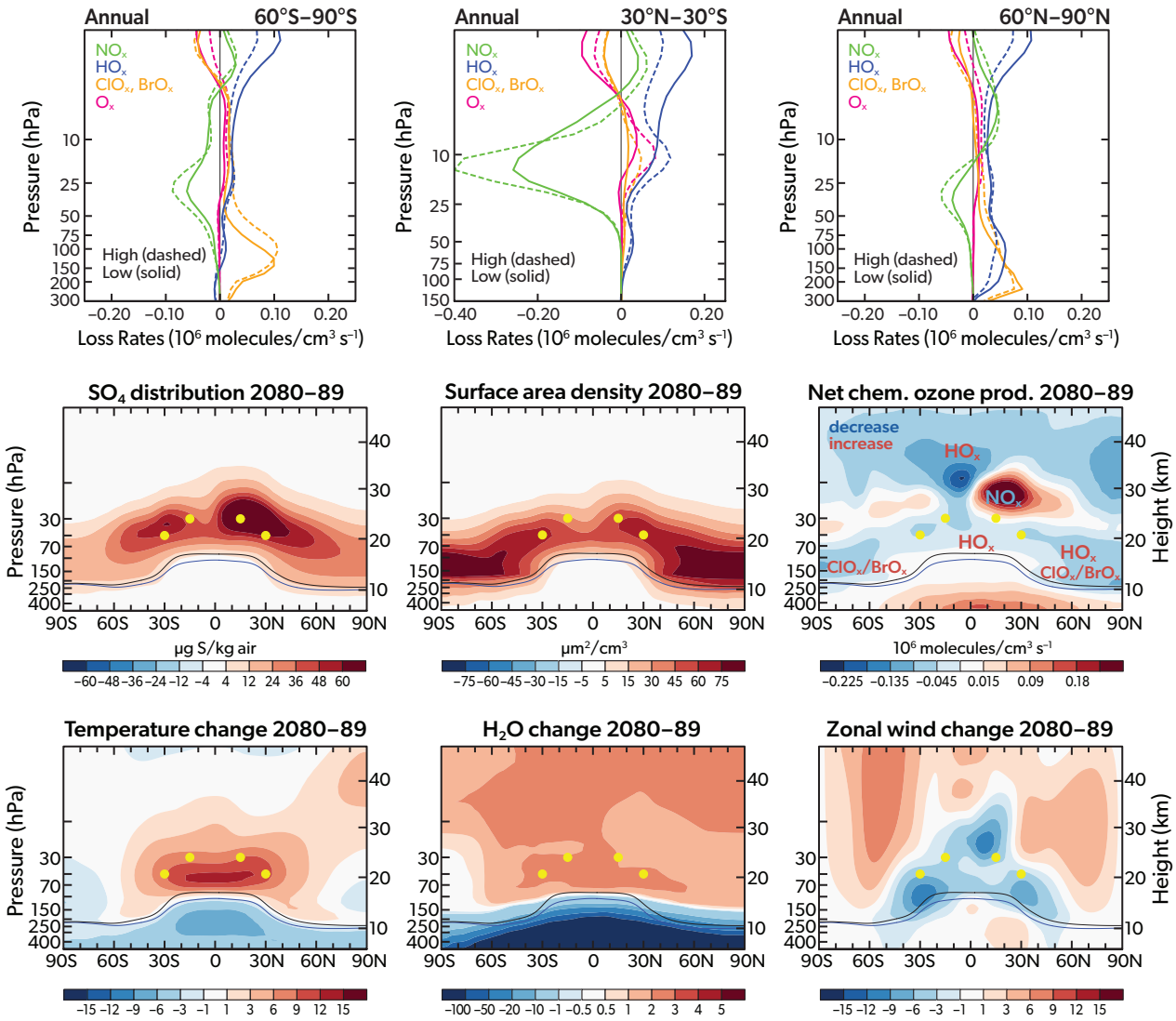

Figure 6-8. *(top row)* Chemical loss rates through different ozone loss cycles in two different SO_2 injection simulations relative to a baseline simulation without SO_2 injection. Values are annual averages of values between 30°N and 30°S and for the period 2042–2049 for a high-altitude injection case—"High (dashed)"—injecting 24 Tg SO_2 yr^{-1} at 30 hPa (~25 km altitude) and a low-altitude injection case—"Low (solid)"—injecting 32 Tg SO_2 yr^{-1} at 70 hPa (between 19 and 20 km altitude), with annual injections divided equally between 15°N and 15°S. The three panels show, from left to right, the latitudinal bands 60–90°S, 30°N–30°S, and 60–90°N. *(middle and bottom rows)* Differences between the ensemble average of an SAI scenario in the GLENS modeling study for the period 2080–2089 and the control (RCP8.5) for the same period for zonally and annually averaged quantities: sulfate burden *(middle left)*, aerosol surface area density *(middle center)*, net chemical ozone production rate *(middle right)*, temperature *(bottom left)*, water vapor *(bottom center)*, and zonal wind *(bottom right)*. The lapse rate tropopause is indicated as a black line for the control and a blue line for the SO_2 injection cases. Yellow dots indicate injection locations. [From Tilmes et al., 2021.]

induced by two processes: the heating of the tropical lower stratosphere and the cooling of the surface caused by the reduced incoming shortwave radiation. The magnitude of this lower-stratospheric heating depends on the sulfate mass and therefore the amount of sulfate injected. It is somewhat dependent on the latitudinal aerosol distribution, which is determined by the injection strategy (e.g., Richter et al., 2017). For example, in simulations using CESM1 (WACCM), equatorial injections have been shown to result in larger tropical stratospheric heating compared to injections outside the equator (Kravitz et al., 2019), and low-altitude injections have been shown to heat the tropopause more than high-altitude injections (Tilmes et al., 2017). The effect of SAI on stratospheric temperature anomalies in the tropical lower stratosphere shows a quasi-linear relationship to aerosol optical depth (AOD; **Figure 6-9**). Models show a large spread in the stratospheric warming produced by aerosols: an increased optical depth of 0.1 results in a warming of 2.8 ± 1.6 °C (range between 0.8 and 4.9 °C for the G6sulfur runs done with GeoMIP

models and in runs with CESM1(WACCM) in the GLENS simulations. This translates into an approximate tropical lower-stratospheric temperature increase of 4.6 ± 2.7 °C per degree of surface cooling achieved through SAI. This range in stratospheric warming may arise not only from differences in the simulated size distributions but also from different radiative approaches across models, as well as from differences in the radiative effects of affected chemical species such as ozone and water vapor (Visioni et al., 2021b).

Several robust effects have been identified to result from SAI-induced stratospheric heating (**Figure 6-9**). The updraft in the tropics is reduced below the injection locations and increased above the injection locations (Pitari et al., 2014; Tilmes et al., 2017; Franke et al., 2021). The reduced updraft of ozone-poor air from the troposphere below the injection location drives an increase in ozone in the lower tropical stratosphere (Tilmes et al., 2009). The resulting decrease in the temperature gradient between the tropics and mid-latitudes above the subtropical jet produces a weakening in the subtropical jets and a weakening of the Eliassen-Palm (EP) flux divergence (which is caused by changes in large-scale planetary waves) at the top the subtropical jets (Tilmes et al., 2017; Franke et al., 2021). These changes are expected consequences of a weakening of the Hadley cell and a reduction in residual vertical velocity (w*) below the injection altitude. The simulated increase in momentum deposition in the middle and high latitudes is in accordance with the acceleration of the BDC and the strengthening of the polar jet streams in winter and spring of each hemisphere. A cooler polar vortex is expected to increase heterogeneous reactions and therefore ozone depletion.

The stratospheric heating perturbation and resulting effects depend on the horizontal and vertical extent of the aerosol layer and on details of the aerosol distribution (e.g., Richter et al., 2017; Tilmes et al., 2017). For example, injections at higher altitudes result in a stronger and cooler polar vortex than injections at lower altitudes, but there is a greater increase in horizontal transport

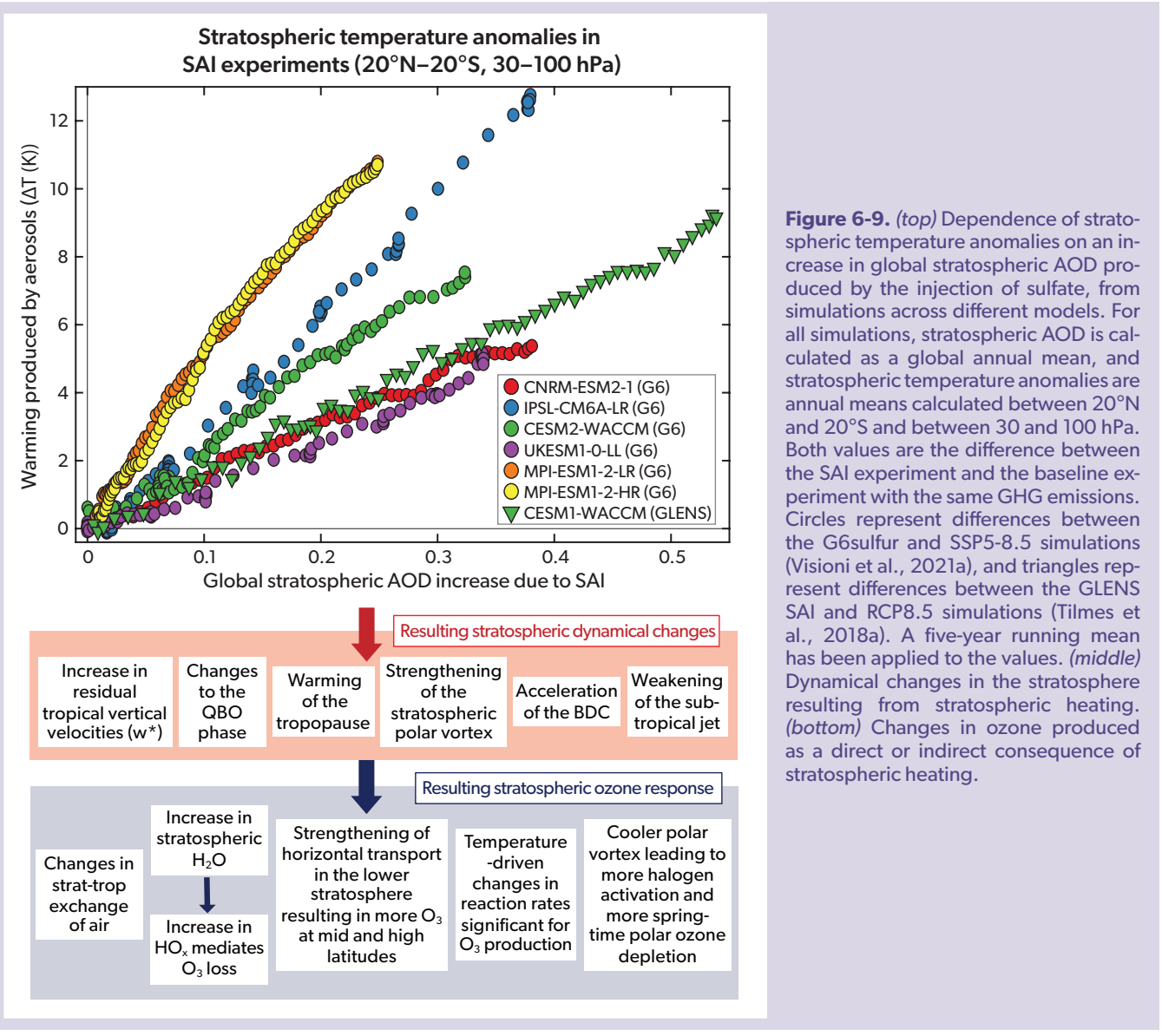

Figure 6-9. *(top)* Dependence of stratospheric temperature anomalies on an increase in global stratospheric AOD produced by the injection of sulfate, from simulations across different models. For all simulations, stratospheric AOD is calculated as a global annual mean, and stratospheric temperature anomalies are annual means calculated between 20°N and 20°S and between 30 and 100 hPa. Both values are the difference between the SAI experiment and the baseline experiment with the same GHG emissions. Circles represent differences between the G6sulfur and SSP5-8.5 simulations (Visioni et al., 2021a), and triangles represent differences between the GLENS SAI and RCP8.5 simulations (Tilmes et al., 2018a). A five-year running mean has been applied to the values. *(middle)* Dynamical changes in the stratosphere resulting from stratospheric heating. *(bottom)* Changes in ozone produced as a direct or indirect consequence of stratospheric heating.

from the tropics to the high latitudes in the low-altitude injection case. Furthermore, equatorial injections have been shown to result in larger tropical stratospheric heating than extra-equatorial injections (Kravitz et al., 2019).

6.3.2.2 Effects on the Quasi-Biennial Oscillation

The heating of the lower stratosphere caused by SAI would modify the thermal heat balance and produce a stronger residual vertical advection of zonal momentum. The changes in stratospheric temperature consequently modify zonal winds, and this effect weakens the downwelling propagation of winds in the Quasi-Biennial Oscillation (QBO) and ultimately lead to a prolonged westerly phase of the QBO (Franke et al., 2021). This effect would be relevant for ozone, as the QBO phase influences the stratospheric transport of chemical species (Niemeier and Schmidt, 2017). This mechanism, first theorized by Aquila et al. (2014), has been further confirmed in successive studies (Jones et al., 2016a; Niemeier et al., 2020; Franke et al., 2021; Jones et al., 2021, 2022) for equatorial injections. However, the simulated magnitude of the changes to the QBO period depends on the amount of injection, with notable inter-model differences: for instance, simulations with CESM1(WACCM) required only 4 Tg S yr^{-1} to lock the QBO in a permanent westerly phase, whereas twice as much was needed in simulations with the ECHAM model (Niemeier et al., 2020).

A recent assessment of six of the models participating in the GeoMIP G6sulfur experiment shows significant variability in the fidelity of the representation of the QBO even without SAI perturbations. It also shows a large model range in the amount of SO_2 injection at which the QBO phase becomes locked in a permanent westerly phase (Jones et al., 2022). The impact of equatorial injections of stratospheric aerosols is strongly dependent on the degree of aerosol absorption and hence stratospheric heating rates (Jones et al., 2016a; Haywood et al., 2022). However, for injections poleward of the inner tropics, which results in less localized tropical stratospheric heating, multiple models have simulated minor or no disruption of the QBO phase (Richter et al., 2017, 2018; Kravitz et al., 2019; Franke et al., 2021). Inter-model differences in the projections of the QBO behavior therefore strongly depend on model specifics: increasing the model vertical and horizontal resolution results in stronger tropical confinement of air masses, which impacts the simulated QBO phase (Niemeier et al., 2020). In addition, differences in the description of chemistry matters. SAI simulations with interactive ozone result in reduced stratospheric ozone production compared to simulations with fixed ozone. The resulting differences in the longwave and shortwave heating impact the QBO differently, which is assumed to be the reason for mainly westerly jets in a simulation with fixed ozone, and easterly jets in a simulation with interactive ozone (Richter et al., 2017; Franke et al., 2021). Changes in the QBO can also impact the transport of ozone, as a westerly phase of the QBO is associated with increased tropical confinement of air in the stratosphere (Niemeier and Schmidt, 2017). The importance

Table 6-2. Summary of different injection parameters that affect ozone changes in the stratosphere. All rows except the first discuss differences based on the injection of the same quantity of material.

Injection Details	Summary of Findings	Implications for Ozone
Sensitivity to increasing injection rates	Increasing sulfur dioxide (SO_2) injection rates lead to a sublinear increase of the aerosol burden due to the microphysical growth of the resulting aerosol particles. Dynamical changes from differences in stratospheric heating also contribute to nonlinear changes in transport (Kravitz et al., 2019).	Small injections are more efficient at increasing SAD than larger ones and therefore have a relatively stronger impact on ozone. The start of SAI can lead to an abrupt decrease in Southern Hemisphere (SH) polar ozone (Tilmes et al., 2021). Larger injections increase aerosol size and the heating of the tropical lower stratosphere and induce stronger effects on dynamics.
Sensitivity to injection altitudes	Injections at higher altitudes in general result in a higher aerosol burden and are therefore more efficient in terms of producing surface cooling. Lower-altitude applications may require significantly more mass to be injected. However, in some cases additional factors may cause the opposite result (see **Table 6-1**).	Injections at lower altitudes within the stratosphere result in stronger stratospheric heating and a greater water vapor increase than high-altitude injections. Transport changes from the equator to the poles are stronger for low-altitude injection cases, resulting in an increase of ozone in high latitudes in winter (Tilmes et al., 2017, 2021).
Sensitivity to single versus multiple injection points	Longitudinal band injections result in larger particles and reduce the aerosol burden and therefore the efficiency of SAI compared to point injections (*Section 6.2.3.4*). Effects on aerosol burden of distributing the injection across a broader latitudinal area are mixed across models.	Smaller particles with point injections result in larger SAD with stronger ozone depletion compared to regional or longitudinal band injections. However, other factors, including changes in aerosol mass and resulting dynamical changes, can result in an increase in ozone, which is model dependent and can also depend on the injection material (**Figure 6-11**).
Sensitivity to the injection latitude	Injections in the tropics, but away from the equator (i.e., 15°N/S) have higher forcing efficiency than injections at the equator and can result in more spatially uniform surface cooling and fewer side effects.	Equatorial injections lead to enhanced stratospheric heating and therefore a greater water vapor increase and a stronger SH polar vortex (Visioni et al., 2020b). This results in larger polar ozone depletion than for injections away from the equator (Tilmes et al., 2021).
Gaseous versus particulate injection	Sulfuric acid (H_2SO_4) injections increase the radiative efficacy, defined as the radiative forcing per unit of sulfur injection, relative to SO_2 injection. This is due to the production of smaller particles that scatter light more efficiently and have a longer lifetime.	H_2SO_4 injections lead to a very similar pattern of ozone impact as SO_2 injections. However, ozone depletion is 10–20% greater using H_2SO_4 due to larger sulfate aerosol burdens, smaller mean particle size, and consequently larger SAD throughout the stratosphere (Weisenstein et al., 2022). The need for a smaller injection mass to obtain a similar amount of radiative forcing may offset this, which means that for a given forcing, the two may have similar ozone impacts.
Sensitivity to injection timing	Pulse injections or selected seasonal injections improve the efficiency of SO_2 injections.	An increased SAD burden during spring would result in larger ozone depletion at high latitudes. On the other hand, the need for a smaller injected mass to obtain a similar amount of radiative forcing results in fewer changes to ozone (Visioni et al., 2019; Visioni et al., 2020a). The start date of SAI matters for ozone, due to the projected changes in the halogen and nitrogen content in the future, which influence ozone loss.

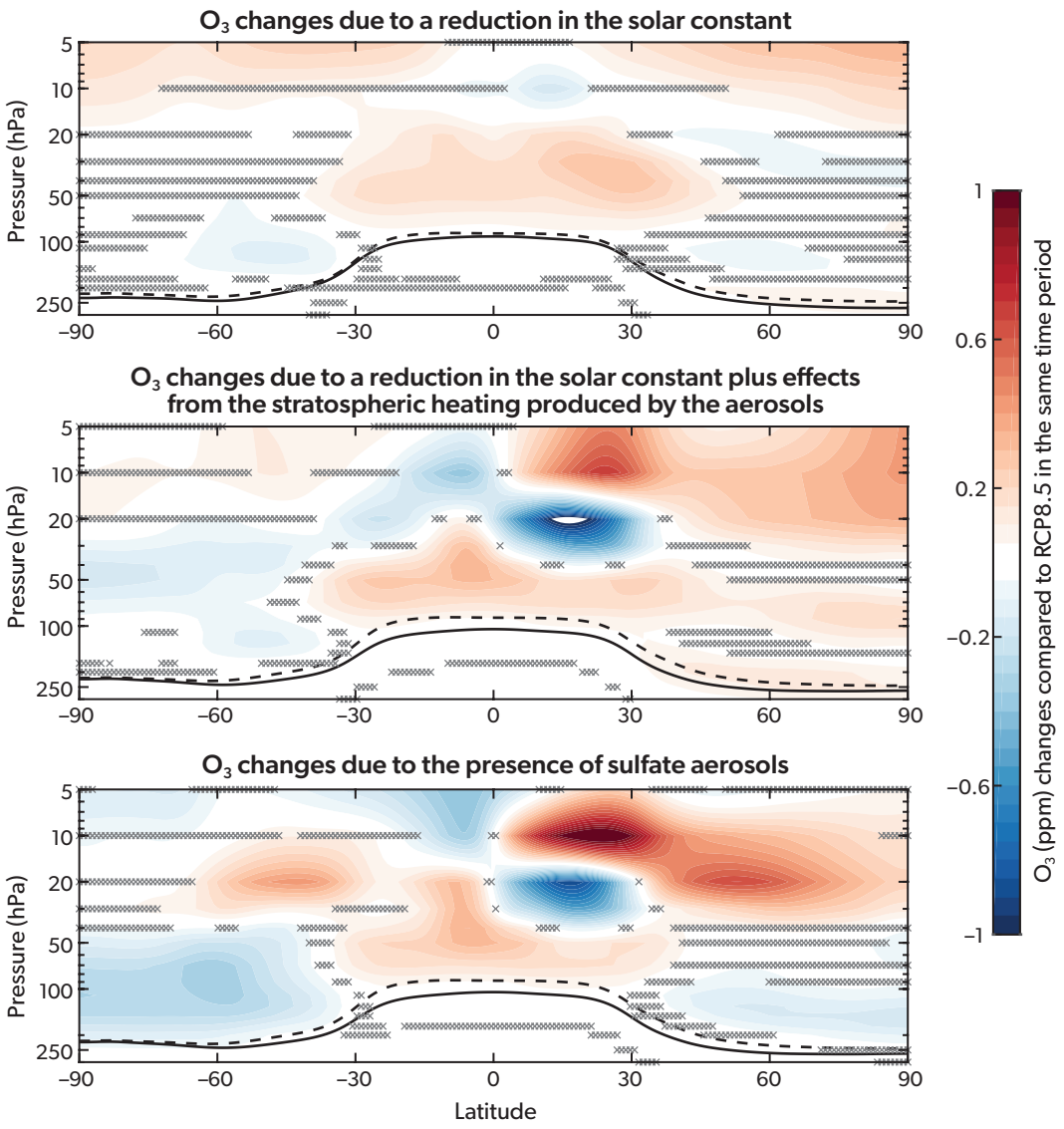

Figure 6-10. *(top)* Ozone concentration changes due to a reduction of the solar constant required to reduce the global, annual average surface temperature from that in the RCP8.5 scenario in the 2070–2090 period to that in the 2010–2030 period. *(middle)* Ozone concentration changes due to a reduction of the solar constant and an imposed stratospheric heating equivalent to that which would be produced by the aerosols in the simulations shown in the bottom panel. *(bottom)* Ozone concentration changes due to an increase in stratospheric sulfate aerosols at a concentration required to reduce the global, annual average surface temperature from that under the RCP8.5 scenario in the 2070–2090 period to that in the 2010–2030 period. The dashed black lines represent the tropopause height in RCP8.5 (2070–2090), and the continuous black lines represent the tropopause height in the geoengineering experiment. Hatched areas indicate regions where the differences are not statistically different from zero. [Adapted from Visioni et al., 2021b.]

of these effects depends on specifics of the injection locations and the potential breakdown of the QBO (Jones et al., 2022).

6.3.3 Combined Effects of Chemistry and Dynamical Changes with SAI on Stratospheric Ozone

Combined changes in chemical production rates, vertical and horizontal transport, and circulation influence the overall changes of stratospheric ozone concentration and therefore total column ozone (TCO). As outlined above and in *Sections 6.2.1* and *6.2.2*, changes in transport are more strongly influenced by the spatial distribution of sulfate mass, while chemical changes are more strongly influenced by the distribution of aerosol surface area density. Both depend on the details of the injection strategy and may scale differently (for instance, depending on latitude) with the injection amount (*Section 6.2*). In general, in the SH polar regions, ozone is largely controlled by chemical changes, particularly during winter and spring, resulting in reductions in ozone. Chemical changes are also important in the upper tropical

stratosphere and mid-latitudes as a result of the reduced reactive nitrogen cycle.

Contrasting ozone changes across simulations that include different processes reveal the importance of the effects of sulfate aerosols on chemistry and transport. In **Figure 6-10**, changes in ozone are contrasted in three different model experiments. The first experiment is a simulation with solar dimming only (top panel), the second includes solar dimming and an imposed stratospheric heating effect by sulfate aerosols but does not include other effects of the aerosols (middle panel), and the third simulates the addition of sulfate aerosols and therefore includes both the heating and chemical effects of the aerosols (bottom panel; Visioni et al., 2021b). These experiments are compared to control simulations without perturbation. Simulations of solar dimming show a limited effect on annually averaged ozone concentrations, with some increase in ozone due to the cooling produced by the reduced solar constant. In the simulations representing aerosol effects, shifts in the aerosol distribution to one hemisphere (e.g., in the Northern Hemisphere, in the example in **Figure 6-10**) result in an uneven interhemispheric change in ozone. Heating-induced transport changes are most important in the tropics and the lowermost stratosphere outside the polar vortex. An increase in ozone in the lower tropical stratosphere is the result of reduced upwelling below the injections and is due to cooler temperatures in the troposphere. A decrease in ozone in the middle stratosphere is a result of stronger upwelling above the injection locations. Furthermore, increases in ozone at mid- to high latitudes are the result of stronger horizontal exchange toward the poles. In summary, the changes in ozone concentration depend strongly on the region (latitude) and season and result from both chemical and dynamical influences of increased stratospheric aerosols with SAI.

6.3.4 Response of Ozone to Different SAI Injection Strategies

Ozone concentration changes discussed in *Section 6.3.3* are shown for one specific injection strategy. However, details of the magnitude of the changes in chemistry and transport depend also on the specifics of the injection strategy and therefore the details of the simulated aerosol distribution (*Section 6.2.3*). A summary of the relationship between specifics of the injection strategy and responses to ozone concentrations based on single model studies is presented in **Table 6-2**.

Simulated ozone responses to SAI can vary with both injection strategy and model (Weisenstein et al., 2022). Responses to SAI are isolated by using fixed sea surface temperatures (averaged over 1988–2007) and fixed greenhouse gases and chlorofluorocarbons (from 2040) in all model experiments shown in **Figure 6-11**. Here, the same injection strategies are applied in two models, including simulations that injected sulfur at two grid points (30°N and 30°S) and at 20 km altitude, simulations that injected in a region (multiple grid points) between 30°N and 30°S and between 19 and 21 km altitude, and simulations that injected sulfur in the form of SO_2 or as accumulation-mode H_2SO_4 aerosols. All the simulations indicate a consistent response of TCO to SAI, with less TCO reduction in the tropics and more TCO reduction in mid- to high latitudes for two-point injections versus regional injections. A stronger TCO reduction occurs if using H_2SO_4 versus SO_2 injections due to a larger resulting sulfate aerosol burden. However, some differences between the SAI response on TCO occur, with the largest disagreement at high latitudes.

6.4 SCENARIO DEPENDENCIES OF SAI ON TOTAL COLUMN OZONE AND OTHER SIDE EFFECTS AND RISKS

The impact of stratospheric aerosol injection (SAI) on total column ozone (TCO) in an SAI scenario is the result of changes in both heterogeneous chemistry (through changes in surface area density [SAD]) and dynamics (including transport, temperature, and water vapor changes; *Section 6.3*). A strong dependency of reductions in TCO and SAD exists during the Antarctic ozone hole season, which is strongly chemically controlled (Tilmes et al., 2020). However, changes in SAD are nonlinearly dependent

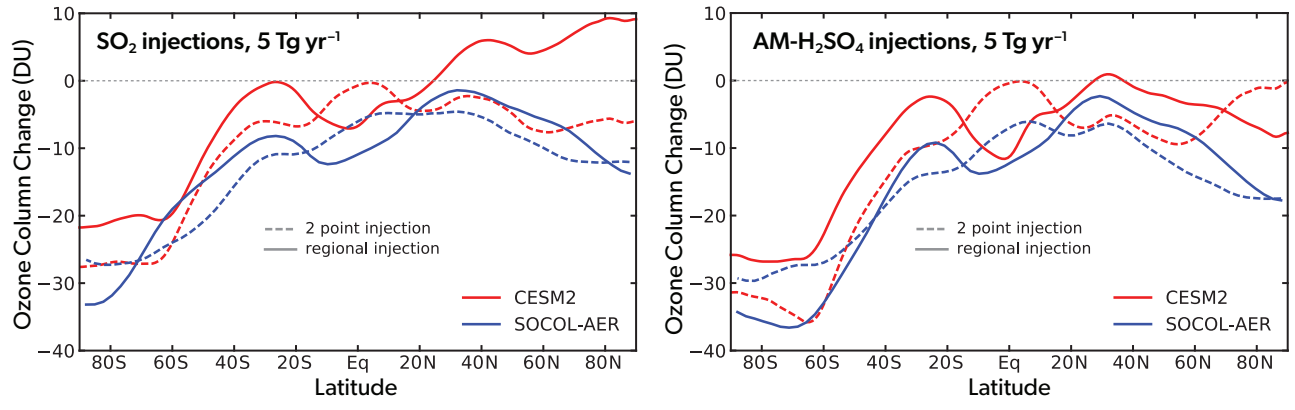

Figure 6-11. Simulated changes in stratospheric total column ozone from simulations in two models (CESM2(WACCM) and SOCOL-AER) with different aerosol microphysics and horizontal and vertical resolutions. Results are shown for different injection materials (gaseous SO_2 *[left]* and accumulation mode AM-H_2SO_4 *[right]*) and injection locations (two-point, 30°N and 30°S, 20 km altitude; regional, from 30°N to 30°S, 19–21 km altitude). [From Weisenstein et al., 2022.]

on the sulfur injection amount. The initial commencement of injections produces smaller aerosol diameters and thus relatively larger SAD per unit of mass than those from continued and larger injections (*Section 6.2*). The impact of changes in SAD on TCO also differs with region and season and is dependent on the associated emissions scenarios, because their effects depend on the concentrations of halogens, nitrous oxide, methane, and other constituents (*Chapter 7*). For example, declining stratospheric halogens in a model simulation with fixed annual amounts of sulfur injected between 2020 and 2070 lead to a decline in global TCO depletion during the 50 years of the experiment (Pitari et al., 2014; Xia et al., 2017).

While global and annually averaged changes in TCO per SAI injection amount for simulated future scenarios have been reported (e.g., Pitari et al., 2014; Weisenstein et al., 2015; Xia et al., 2017), simple measures do not reflect large seasonal and latitudinal ozone changes that can cancel each other out if averaged annually and globally. It is therefore more meaningful to report TCO changes with SAI as a function of season and for different regions, as done here.

Finally, conclusions on whether side effects may outweigh benefits under future SAI scenarios cannot be drawn by isolating any one aspect of the impacts of SAI (e.g., on stratospheric ozone). A more holistic assessment of the major benefits, impacts, and risks of different SAI implementation scenarios and strategies beyond their impact on stratospheric ozone is therefore required and assessed in *Section 6.4.2*.

6.4.1 SAI Response of Total Column Ozone in Different 21st-Century Scenarios

We assess the impacts of SAI on TCO using three SAI scenarios (peakshaving, strong SAI, and medium SAI; *Section 6.1.3.1*) based on recent modeling studies that include interactive aerosols and chemistry in the stratosphere. Simulations following the peakshaving and strong SAI scenarios (Tilmes et al., 2020) are

Table 6-3. Change in total column ozone between future scenarios with SAI and without SAI between the periods 2030–2039 and 2080–2099 for different sets of model experiments (see text for more information). Ranges given are the standard deviation of the ensemble/multi-model mean annual value for the selected 10 years and for different regions and seasons: tropics (20°N–20°S), January averages for NH mid-latitudes (40–60°N), and polar latitudes over the NH (60–90°N) in March and over the SH (60–90°S) in October. "EQ" represents equatorial injections and "Four Point" refers to four-point injections. Bold numbers indicate significant changes in TCO.

	Peakshaving (Four-Point) Minus Baseline (DU)	Strong SAI (Four-Point) Minus Baseline (DU)	Medium SAI (EQ) Minus Baseline (DU)	Peakshaving (Four-Point) Minus Baseline (DU)	Strong SAI (Four-Point) Minus Baseline (DU)	Medium SAI (EQ) Minus Baseline (DU)
	2030–2039 0.5 °C cooling	2030–2039 0.5 °C cooling	2030–2039 0.2 °C cooling	2080–2099 1.5 °C cooling	2080–2099 ~4 °C cooling	2080–2099 1.8 °C cooling
SH Pole (October)						
WACCM (RCP)		**–64 ± 10**			**–61 ± 10**	
WACCM6 (SSP)	**–52 ± 13**	**–52 ± 13**	**–17 ± 9**	–7 ± 13	**–48 ± 10**	**–31 ± 4**
CNRM-ESM2-1			–1 ± 8			**–17 ± 10**
UKESM1-0-LL			1 ± 4			**–8 ± 4**
NH Pole (March)						
WACCM (RCP)		**–22 ± 21**			4 ± 20	
WACCM6 (SSP)	**–13 ± 10**	**–13 ± 10**	2 ± 9	3 ± 20	–8 ± 21	6 ± 7
CNRM-ESM2-1			(–22 ± 14)*			7 ± 21
UKESM1-0-LL			–5 ± 18			7 ± 9
Mid-latitudes (NH January)						
WACCM (RCP)		**–7 ± 4**			**14 ± 8**	
WACCM6 (SSP)	1 ± 7	1 ± 7	4 ± 2	0 ± 7	6 ± 11	**16 ± 6**
CNRM-ESM2-1			0 ± 1			**18 ± 3**
UKESM1-0-LLI			–1 ± 2			**14 ± 4**
Tropics						
WACCM (RCP)		–1 ± 2			**9 ± 2**	
WACCM6 (SSP)	–1 ± 2	–1 ± 2	1 ± 1	**4 ± 1**	**8 ± 2**	**4 ± 1**
CNRM-ESM2-1			0 ± 1			**2 ± 1**
UKESM1-0-LL			–1 ± 2			**–3 ± 1**

*This value is not shown in **Figure 6-12** because changes in TCO in this simulation are not due to injections of sulfur, which started around 2040 in this model (for more details, see Tilmes et al., 2022).

performed with CESM2(WACCM6) using four-point injections at ~5 km above the tropopause with SSP5-8.5 and SSP5-3.4OS as the baseline scenarios. The strong SAI scenario has also been performed with CESM1(WACCM) as part of GLENS using the RCP8.5 baseline scenario. In both cases, injection rates per location were determined using a feedback control algorithm (**Box 6-2**). For the medium SAI scenario, we assess multi-model results based on three Earth system models (ESMs). The different ESMs used a similar injection strategy in a region around the equator, with one model (CESM2(WACCM6)) injecting at 5 km above the tropopause and the other two models (CNRM-ESM2-1, UKESM1-0-LL) at 1 km above the tropopause (Visioni et al., 2021a; Tilmes et al., 2022) but only two (CESM2(WACCM6) and UKESM1-0-LL) included interactive stratosphere aerosols, and one (CNRM-ESM2-1) used prescribed aerosol radiative properties. While there are additional differences in the specifics of the models, including chemistry and physics, some robust conclusions on the effects of SAI on TCO can be drawn, as summarized in **Table 6-3** and **Figure 6-12**.

For comparisons of the different experiments (and models), four selected cases (regions and seasons) of interest are defined: the tropics (20°N–20°S), January averages for Northern Hemisphere (NH) mid-latitudes (40–60°N), and polar latitudes over the NH (60–90°N) in March and over the Southern Hemisphere (SH) (60–90°S) in October. **Table 6-3** and **Figure 6-12** show differences in TCO for these cases in comparison to their respective baseline scenarios during the same period. Since changes are not linear with time, we illustrate different time periods: one in the near future (2030–2039 average) and one toward the end of the 21st century (2080–2099 average). To contrast differences in TCO evolution for the peakshaving and the strong SAI scenarios, we illustrate the TCO evolution (**Figure 6-13**) and differences with and without SAI (**Figure 6-14**) for the same model version CESM2(WACCM6) and the same injection strategy. Differences between three models for the medium SAI scenario are illustrated in **Figure 6-15**.

6.4.1.1 Changes in SH Spring Polar TCO

In the polar regions, particularly during austral winter and spring, chemical ozone depletion is the dominant process, while transport is important for ozone impacts in other seasons. In addition, changes in the strength of the polar vortex and resulting cooler temperatures can play an important role in the effects of SAI on column ozone (*Section 6.3*). The magnitude of ozone

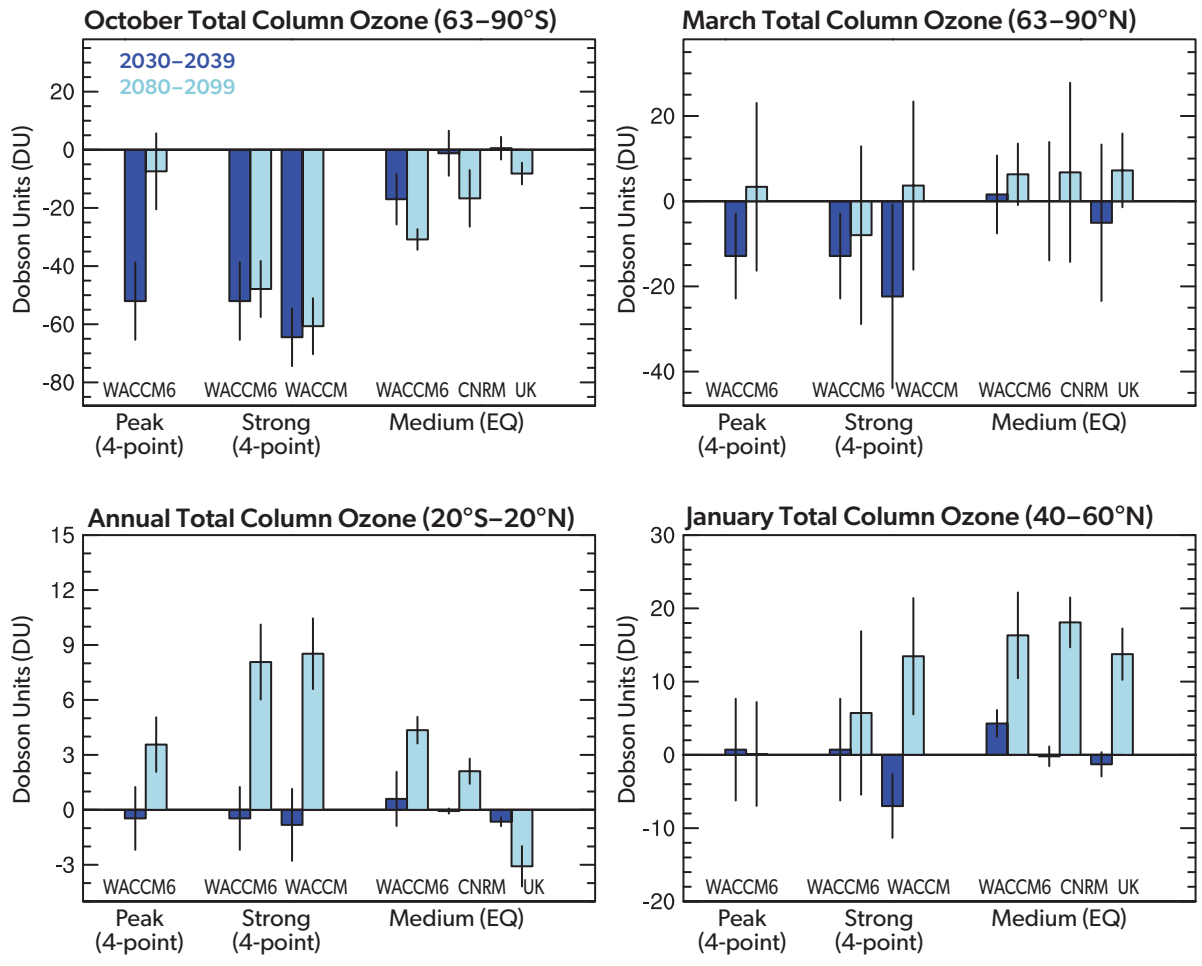

Figure 6-12. Bar chart of the TCO changes given in **Table 6-3**.

depletion is therefore strongly driven by the abundance of halogens in the stratosphere and changes in SAD. This can be seen in two features of past ozone trends: After 1980, Antarctic TCO exhibited a strong decline of over 80 DU (consistent with **Figure 4-4**), driven by increasing halogen concentrations. After the Mount Pinatubo eruption in 1991, and the associated increase in aerosol SAD, ozone decreased by a further 40–60 DU within the next five years (**Figure 6-13**, left top).

The reduction of the stratospheric halogen burden and changes in SAD also play a role in the projected future impacts under the peakshaving, medium and strong SAI scenarios. The gradual phasing in of sulfur injections in all three scenarios increases SAD quickly during the first 10 years, then moderately thereafter. This leads to a rather abrupt initial deepening of the Antarctic ozone hole, which is stronger under the peakshaving and strong SAI scenarios (following the same scenario until 2040) than under

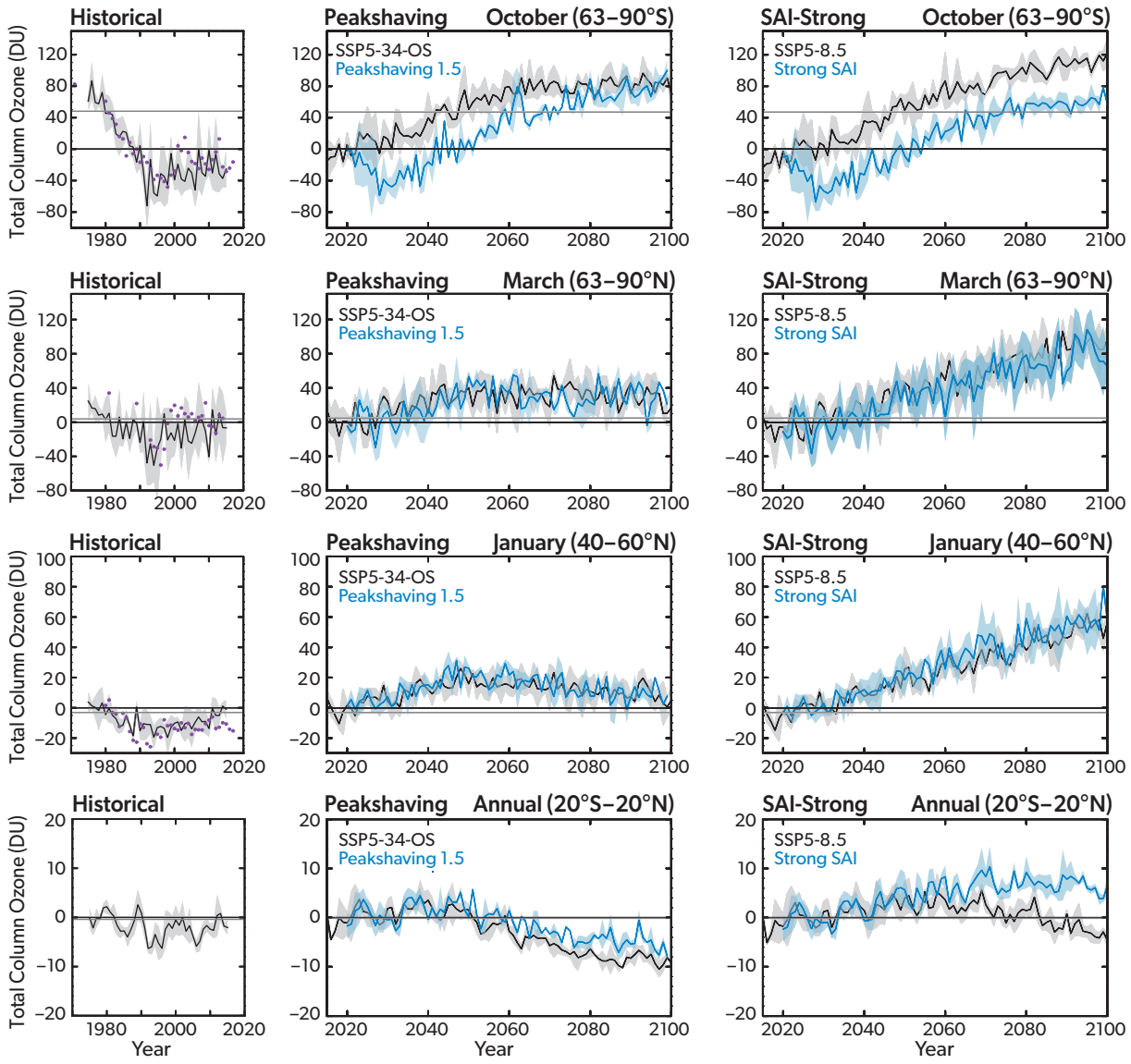

Figure 6-13. Simulated impacts on TCO in different latitude bands and seasons (*rows*), relative to the 2015–2025 TCO average, for the past (historical; *left column*) and projected for the peakshaving (*middle column*) and strong (*right column*) SAI scenarios. The ensemble means are shown for the baseline scenario (black) with standard deviation (gray shading) and for the SAI experiments (blue) with the standard deviation (light blue shading) based on simulations with CESM2(WACCM6) using SSP5-3.4-OS and SSP5-8.5 for the baseline scenarios, against which the peakshaving and strong SAI scenarios are compared, respectively. Black horizontal lines indicate the 2020 values and gray lines the 1980 values, based on the model simulations. In the historical TCO panels, a three-year running mean has been applied to the TCO observations from the Solar Backscatter Ultraviolet (SBUV) Merged Ozone Data Set (Frith et al., 2017; purple symbols) to facilitate comparison with the ensemble mean of the control simulation.

the medium SAI scenario (**Figures 6-14** and **6-15**). In the SH austral spring, for the peakshaving and strong SAI scenarios the initial ramp-up of the injections to cool 0.5 °C in 20 years leads to ozone depletion in 2030–2039 of 52 ± 13 DU in the CESM2(WACCM6) simulations and 64 ± 10 DU in the CESM1(WACCM) simulations. This results in an average depletion of 58 ± 20 DU, when accounting for additional uncertainties driven by the injection strategy (see below). Here, SAI is simulated to start in 2020, and the resulting TCO depletion in this early period is nearly as strong as was observed during the historic period with the deepest ozone holes. Injections in later years are likely to have a smaller effect because of the expected decline in the stratospheric halogen burden with time (see *Chapter 7* and **Figure 7-7**).

Reductions in TCO in SH austral spring are less strong for the medium SAI scenario because of a smaller required cooling in this experiment of about 0.2 °C for the first 20 years and smaller required SAI injections compared to the peakshaving and strong scenarios (**Figure 6-15**). The decline in TCO over SH Antarctic spring between 2030 and 2039 is only present in the CESM2(WACCM6) simulations (17 ± 9 DU ozone loss). The other two models did not require significant sulfur injection during the period 2030–2039 in this scenario and therefore did not show any ozone loss (see Tilmes et al., 2022, for more details).

Toward the end of the 21st century (2080–2099), the SH Antarctic spring TCO changes differ significantly between the three scenarios. For the peakshaving scenario, simulated SH polar TCO is reduced by only 7 ± 13 DU compared to the baseline. For this scenario, the recovery of the ozone hole is therefore expected to happen before the end of the 21st century. The strong SAI scenario assumes continuously increasing annual sulfur injection rates toward the end of the 21st century and decreasing stratospheric halogen content; the net result is that reductions in SH polar TCO are essentially the same in 2080–2099 for the two model versions (61 ± 10 DU and 48 ± 10) as they are in 2030–2039 (64 ± 10 DU and 52 ± 13 DU; **Table 6.3** and **Figure 6-12**). This results in a delay of the ozone recovery, which can vary from 25 to over 55 years depending on the injection strategy (latitude and altitude of injections, as discussed in Tilmes et al., 2021). For the medium SAI scenario, the stronger increase in injected mass toward the end of the century leads to increasing SH Antarctic spring ozone loss of up to 31 ± 4 DU in 2080–2099 in the CESM2(WACCM6) simulations and between 8 and 17 DU for simulations with the other models.

The results presented in this section are specific to the injection strategy used. Larger ozone loss up to 20 DU has been simulated for equatorial injections (Tilmes et al., 2021). This is because equatorial injections result in a more pronounced strengthening of the polar vortex and cooler vortex temperatures, as well as strongly enhanced stratospheric water vapor compared to four-point injections outside the equator. Furthermore, the smallest reductions in TCO during Antarctic spring (up to 20 DU) are expected for low-altitude injections, at around 20 km (Tilmes et al., 2021). Injections of sulfur at lower altitudes result in a shallower aerosol distribution than high-altitude injections, and aerosol that is more concentrated towards the tropopause. This results in changes in the importance of different ozone loss cycles, while the resulting increase in stratospheric water vapor increases HO_x-driven ozone loss cycles. Furthermore, the more-confined

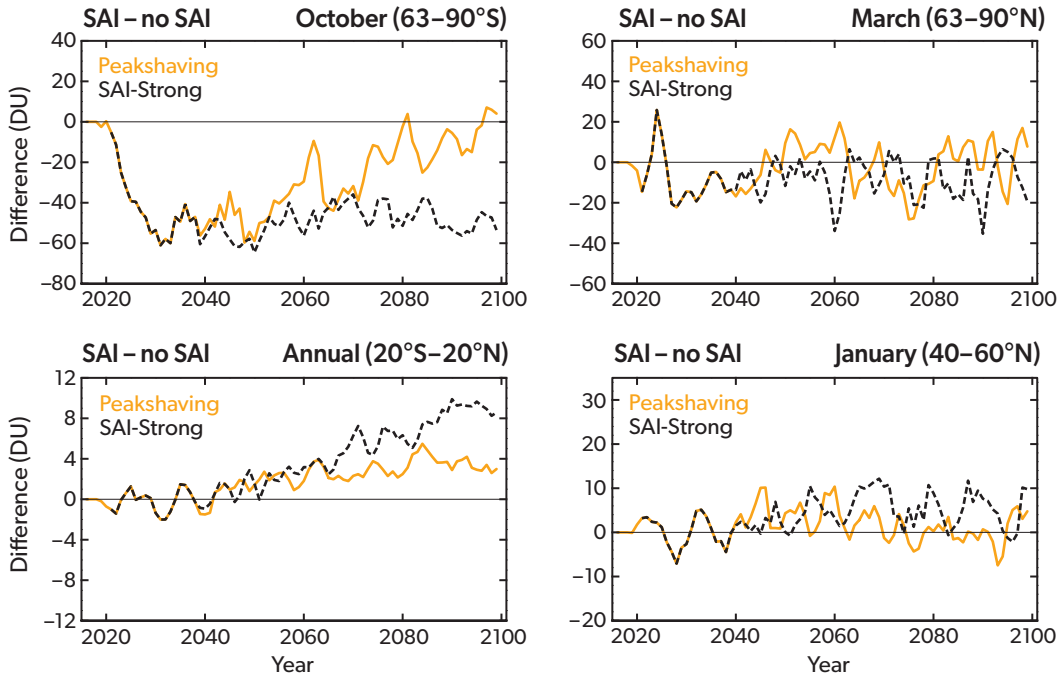

Figure 6-14. Ensemble mean differences in TCO between simulations that include SAI (in the peakshaving [orange] and strong [black] SAI scenarios) and TCO in the baseline simulation (no SAI), for different regions and seasons (different panels), as shown in **Figure 6-13**. A running mean of three years has been applied to the differences.

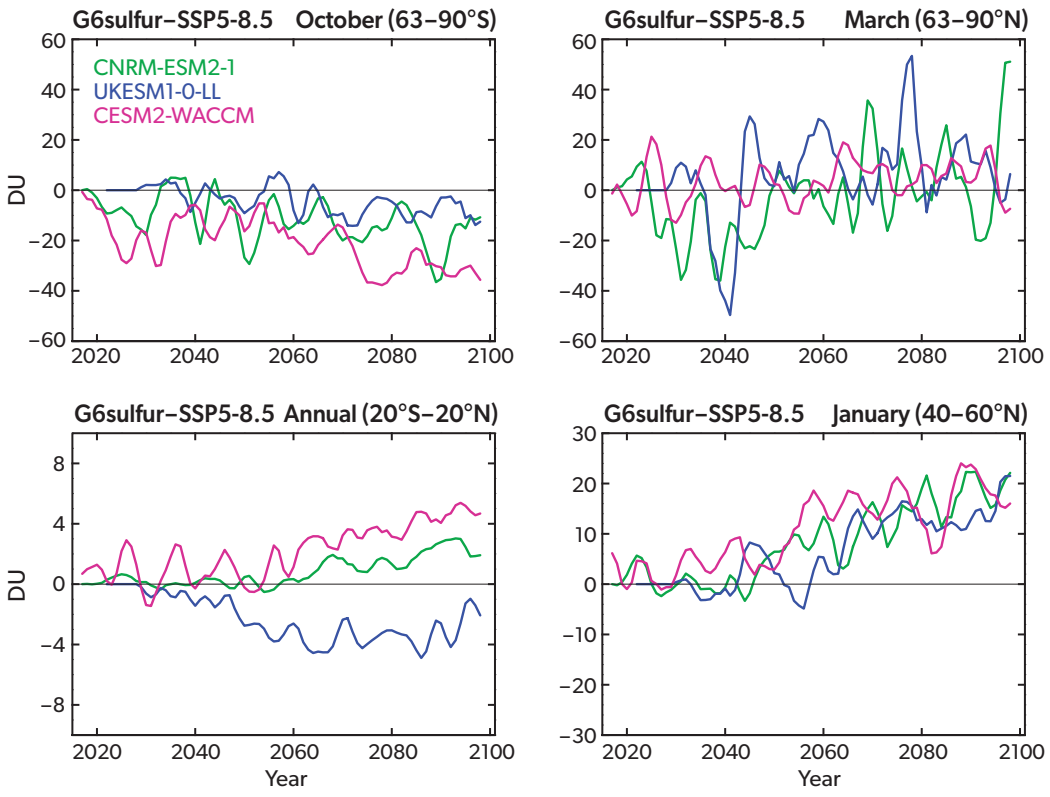

Figure 6-15. Differences between the ensemble mean of simulated total column ozone between 2020 and 2100 in the medium SAI scenario and in the baseline simulation (SSP5-8.5 with no SAI), for runs using the three different models (colored lines) and for four different seasons and regions (different panels). [From Tilmes et al., 2022.]

heating at the tropical tropopause in the low-altitude injection simulation induces a stronger transport of ozone toward mid- and high latitudes, which counters the larger reduction of net chemical ozone production rates.

6.4.1.2 Changes in NH Spring Polar Total Column Ozone

The strength and temperature of the Arctic polar vortex varies strongly from year to year. For the NH polar region in March, cooler winters can result in a stronger reduction in TCO in the polar vortex with increased SAD, relative to that in warmer winters (Tilmes et al., 2008). Changes in TCO in the NH polar region are therefore more strongly driven by transport changes than are changes in TCO at SH high latitudes. NH polar spring TCO reductions reached 50 DU between 1990 and 2000 based on observations using a three-year running mean. This is comparable to the ensemble mean of the model simulations (**Figure 6-13**). The large variability of Arctic ozone loss depending on the meteorological situation is not reflected in the monthly-mean zonal-average analyses. Much smaller reductions in NH polar spring TCO are projected for 2030–2039 in the three SAI scenarios considered here, with reductions of 13 ± 10 DU and 22 ± 21 DU in the peakshaving and strong SAI scenarios (where ranges reflect differences across model versions), for both the peakshaving and strong SAI scenarios (**Table 6-3** and **Figure 6-12**). TCO changes in the medium SAI scenario relative to the baseline scenario vary in the sign and so are not significant (Tilmes et al., 2022). Toward the end of the century, changes in TCO are not statistically significant for any of the three SAI scenarios. As for the historical period, ensemble means of monthly and zonally averaged TCO values over 63–90°N, as are shown here, do not reflect chemical changes during very cold or warm Arctic winters and therefore may lead to an underestimation of regional TCO changes. A more detailed investigation of TCO within the polar vortex over the Arctic on an annual basis has not been performed at this point.

6.4.1.3 Changes in Total Column Ozone at NH Winter Mid-latitudes

NH mid-latitude winter TCO declined by around 10–20 DU between 1980 and the 1990–2000 period in both the observations and in the model simulations (**Figure 6-13**). After the year 2000, the model simulates an increase in TCO, reaching amounts close to 1980 values around 2020. Later in the 21st century, with a strong future warming scenario the model simulates a super-recovery of ozone at mid- to high latitudes during NH winter due to stratospheric cooling and GHG-induced increases in downwelling of the Brewer-Dobson circulation (BDC; Butler et al., 2016). With SAI, simulations indicate that the lower-stratospheric heating and the resulting acceleration of the BDC can result in an additional increase in stratospheric ozone and other stratospheric trace species, such as nitrous oxide (N_2O), chlorofluorocarbons (CFCs), and methane (CH_4), particularly in the winter and spring of

the corresponding hemisphere (Visioni et al., 2017b; Tilmes et al., 2017). These changes produce a mixed chemical response, with a reduction in the net chemical production of ozone in the lowermost stratosphere and the upper stratosphere and an increase in the mid-stratosphere due to the reduced reactive nitrogen cycle. Depending on the injection location, the largest change in mid-latitude ozone with SAI was simulated to occur between 40°N and 60°N in January (Tilmes et al., 2018b).

Changes in the first 20 years of the SAI applications in NH winter mid-latitudes in January are, for the most part, not significant. Toward the end of the 21st century, 2080–2099, the strong SAI scenario simulated using CESM2(WACCM6) and the medium SAI scenario simulated using all three models produce a significant increase in TCO, of between 14 and 18 DU (Tilmes et al., 2022). Considering different strategies for the strong SAI scenario, the largest and earliest simulated increase in TCO compared to baseline conditions was found for the equatorial injections (Tilmes et al., 2021).

6.4.1.4 Changes in Total Column Ozone in the Tropics

In the tropics, TCO declined from 1980 values between 1990 and 2000, with a maximum reduction of around 5 DU, and increased again thereafter to reach 1980 values around 2020. Future scenarios without SAI show either a decline or an increase in tropical TCO depending on the scenario (Keeble et al., 2021). Changes in TCO in the tropics with SAI result from a combination of increases and decreases in ozone concentration at different altitudes, depending on the chemical and dynamical changes (*Section 6.3*). In the earlier years of simulated SAI implementation (2030–2039), none of the three selected SAI scenarios indicate significant changes in tropical TCO. However, toward the end of the 21st century, significant increases in TCO are simulated for the peakshaving (4 ± 1 DU) and strong (9 ± 2 DU) SAI scenarios. The three different models used for the medium SAI scenario show a mixed signal, leading to no changes in the multi-model mean tropical TCO. Increases in ozone in the tropical mid-stratosphere are more pronounced with increasing injection amounts, while chemical reductions due to the HO_x and ClO_x cycles are more pronounced during the beginning of the injections. The largest increase in TCO is projected for a high-altitude injection case, consistent with an aerosol distribution that reaches higher in altitude and therefore has a larger chemical production of ozone through the nitrogen cycle (Tilmes et al., 2021).

6.4.2 Other Impacts and Risks Based on Different SAI Scenarios

The intended benefits expected from SAI are the reduction or stabilization of global and regional surface temperatures and, consequently, a reduction in climate change impacts. Model simulations uniformly demonstrate that solar dimming reduces global mean temperatures and therefore can counter surface warming under a range of different future scenarios (**Figure 6-16**; e.g., Govindasamy and Caldeira, 2000; Kravitz et al., 2013, 2021). Depending on the strategies used to reach specific surface temperature targets (**Box 6-2**), the benefits of SAI-induced cooling include reducing changes in extreme heat and rainfall events (Curry et al., 2014; Muthyala et al., 2018a, 2018b; Bhowmick et al., 2021). The reduction in extreme precipitation with SAI (Ji et al., 2018) has been shown to result in reductions in flood risks in most of the regions of the globe (Wei et al., 2018). Other benefits include the recovery of sea ice (Jones et al., 2018; Kravitz, 2020), and land ice area (by maintaining the ice sheet surface mass balance; Tilmes et al., 2020); an increase in ocean net primary productivity (Tilmes et al., 2020); and a decrease in the frequency of extreme storms in the North Atlantic and heatwaves in Europe (Jones et al., 2018).

In addition to these benefits, there are various unintended side effects (e.g., Robock et al., 2008a; Robock et al., 2020) beyond changes in ozone (*Sections 6.3* and *6.4.1*). Some of these side effects increase with SAI amount, including an overcompensating reduction in global precipitation compared to the baseline scenarios with increasing greenhouse gas warming. We note that global precipitation is only one measure for changes in the hydrological cycle, and other measures including evaporation and soil moisture should also be considered for detailed climate impact assessments. **Figure 6-16** shows the effects of applying SAI to different future scenarios with the objective of maintaining temperatures at or below 1.5 °C above preindustrial conditions, based on GHG scenarios ranging from strong mitigation to moderate mitigation, delayed mitigation, and no mitigation (Jones et al., 2018; Tilmes et al., 2020). The strongest reductions in global mean precipitation were simulated for the no-mitigation scenario coupled with strong SAI, while no significant precipitation changes occurred in the simulations where there is strong mitigation of GHG emissions and only a small amount of SAI is needed to keep temperatures from rising above the 1.5 °C limit (**Figure 6-16**). There are also various other plausible future SAI scenarios that have been discussed in the literature but are not discussed here. Other risks, including the termination effect (see below), also strongly increase with injection amount and therefore the cooling amount imposed with SAI. Other side effects, such as ocean acidification and impacts on land primary productivity, strongly depend on the GHG emissions scenario, while the selected SAI scenario affects these measures only to a small degree.

In the following, we give a brief overview of other side effects and risks beyond the effects on ozone. The list below is not intended to be comprehensive or exhaustive, as there are other risks and consequences besides those detailed here that are beyond the scope of this assessment.

The following are side effects of significant (climate changing) solar radiation modification (SRM) that are independent of the SRM strategy or approach that would be used (e.g., stratospheric aerosol injection, marine cloud brightening, or cirrus cloud thinning). These risks scale with the amount of SRM applied and hence depend on the specifics of the SRM scenario.

- **Termination risk:** If any significant SRM application was suddenly terminated, the Earth's climate would rebound to the baseline climate within a matter of years, and this could result in unprecedented rates of climate change (e.g., Jones et al., 2013). This could have severe consequences, such as warming rates beyond the adaptive capacity of vulnerable ecosystems (Trisos et al., 2018). However, a slower ramp-down or a continuation of SRM shortly after a sudden termination could potentially prevent these effects (Parker and Irvine, 2018).
- **Risks of uneven inter-hemispheric SRM applications:** SRM, if applied largely unevenly to the two hemispheres or applied in only one hemisphere, would introduce an inter-hemispheric cooling gradient across the equator. The resulting

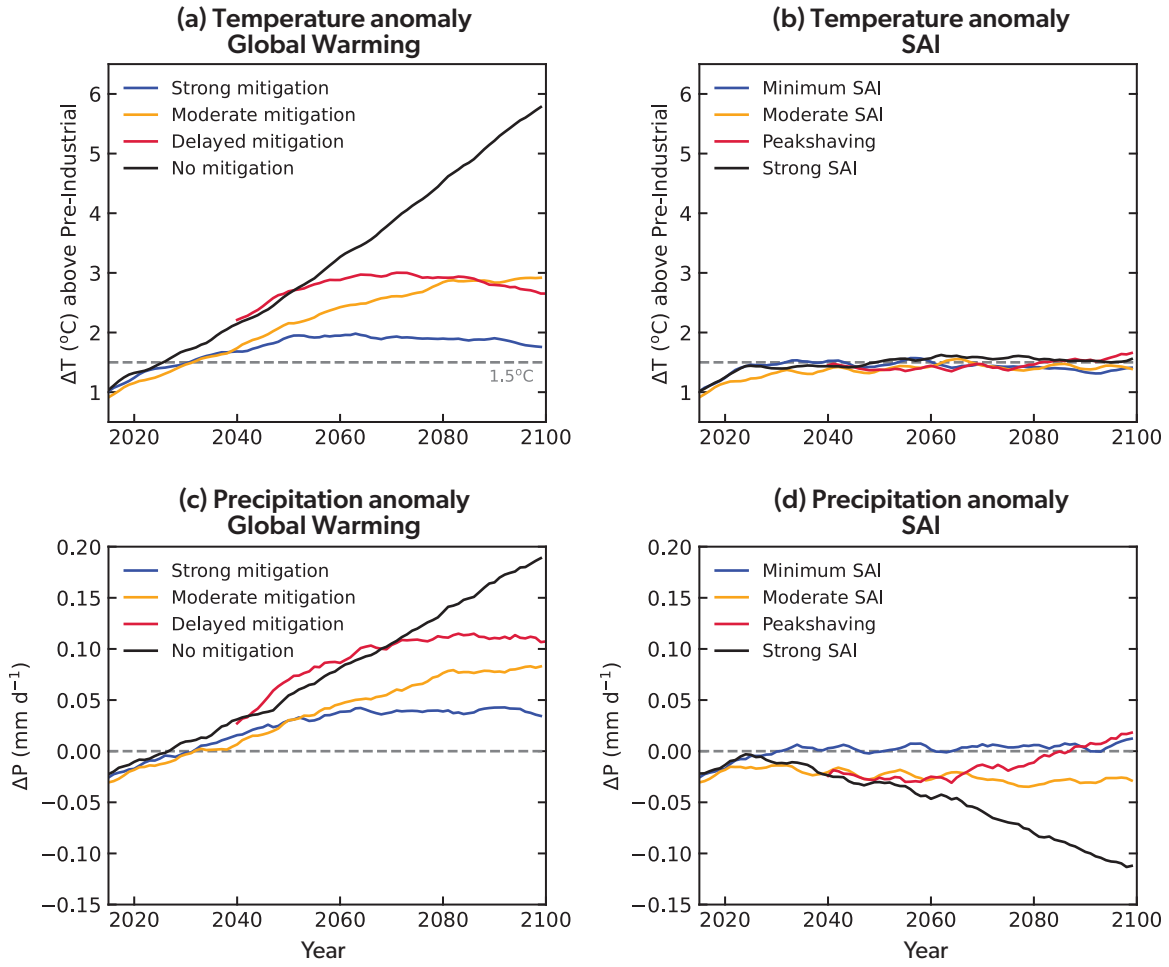

Figure 6-16. Global mean surface temperature anomaly in (a) global warming simulations and (b) corresponding simulations in which SAI is applied to maintain temperature at 1.5 °C above preindustrial levels, and (c, d) the equivalent global mean precipitation time series. "No mitigation / strong SAI" refers to the average of the RCP8.5 / GEO-8.5 simulations of Jones et al. (2018) and the SSP5-8.5 / SSP5-8.5 1.5 simulations of Tilmes et al. (2020). "Delayed mitigation / peakshaving" refers to the SSP-3.4-OS / SSP-3.4-OS 1.5 simulations of Tilmes et al. (2020). "Moderate mitigation / moderate SAI" and "strong mitigation / minimum SAI" refer to the RCP4.5 / GEO-4.5 and RCP2.6 / GEO-2.6 simulations of Jones et al. (2018), respectively. The baseline periods are RCP8.5 2020–2030 for Jones et al. (2018) and SSP5-8.5 2015–2025 for Tilmes et al. (2020), or approximately the decade in which the Paris threshold of preindustrial temperature +1.5 °C is exceeded in the respective climate model. All time series are smoothed by five-year running means.

cross-equatorial energy and moisture transport (Hwang and Frierson, 2013; Stephens et al., 2016; Hawcroft et al., 2017) would shift the intertropical convergence zone (ITCZ) toward the (relatively) warmer hemisphere and therefore change the rainfall pattern (e.g., Caldeira and Wood, 2008; Robock et al., 2008b; Haywood et al., 2013; Jones et al., 2017). Such impacts have been observed after high-latitude explosive volcanic eruptions that preferentially load the stratosphere in one hemisphere (e.g., Oman et al., 2006; Jones et al., 2017).

- **Ocean acidification:** Ocean acidification, which is induced by high CO_2 concentrations, cannot be mitigated significantly by SRM (Matthews and Turner, 2009). Coral bleaching, which is more strongly dependent on ocean temperatures than on ocean acidity, does appear to be somewhat mitigated by SRM (Kwiatkowski et al., 2015).
- **Sea level rise:** Stabilizing global mean temperature through SRM would substantially reduce sea level rise in the future (Irvine et al., 2017). However, keeping sea surface temperatures from rising does not completely offset the deep ocean heat uptake, which causes the net downwelling radiative flux at the top of the atmosphere to remain positive (Jones et al., 2018; Fasullo et al., 2018); thus, stabilizing global sea level rise would require overcooling the Earth system (Irvine et al., 2018).

The following are side effects and risks that are specific to global solar dimming or SAI, although some similar changes may also apply to other SRM methods:

- **Impacts on the hydrological cycle:** Solar dimming weakens the hydrological cycle (Tilmes et al., 2013; Niemeier et

al., 2013; Fyfe et al., 2013; Ferraro et al., 2014), consistent with observations after volcanic eruptions (Trenberth and Dai, 2007). Using SAI may amplify this effect, especially if strongly absorbing aerosols are used (Ferraro et al., 2014; Visioni et al., 2021b; Haywood et al., 2022). Following a strong SAI scenario, an increase in global precipitation in the baseline scenario would be increasingly overcompensated by the growing amount of aerosol injection needed to compensate for GHG warming, as demonstrated in two independent model studies (**Figure 6-16**; Jones et al., 2018; Tilmes et al., 2020). This can result in reductions in rainfall and a weakening of monsoonal precipitation in some regions (Simpson et al., 2019). On the other hand, the precipitation increases in a low-forcing GHG scenario without SAI would be reversed to close to present-day conditions if a peakshaving SAI scenario were applied.

- **Tropospheric circulation and regional climate:** SAI using sulfate aerosols weakens storm tracks due to induced changes in the latitudinal temperature and humidity gradients, forcing a poleward shift of the storm tracks. This effect predominantly impacts the Northern Hemisphere (Gertler et al., 2020). Stratospheric heating using sulfate SAI can induce a positive anomaly of the North Atlantic Oscillation (NAO) during the Northern Hemisphere winter season and a winter warming over Eurasia, with associated increased rainfall in northern Europe and decreased rainfall in southern Europe (Banerjee et al., 2021; Jones et al., 2022). In addition, surface winds imposed by changes in stratospheric dynamics can change the upwelling of warm waters around Antarctica, thereby impacting the surface climate (McCusker et al., 2015).
- **Impacts on acid rain:** Aerosols (and precursors) injected into the stratosphere inevitably deposit back to the surface. Depending on the material injected (e.g., SO_2) this could contribute to acidification of precipitation. Even for the strong SAI scenario using sulfate, SAI would not significantly increase the amount of sulfate deposited over polluted regions on a decadal scale compared to current anthropogenic emissions of SO_2. However, more pristine areas at high latitudes may see significant increases in sulfate deposition (Kravitz et al., 2009; Visioni et al., 2020c). The effects of other aerosols (*Section 6.5*) that could potentially be used for SAI have not been investigated.
- **Impacts on tropospheric ozone:** Solar dimming applied to offset the effects of increasing GHG concentrations can lead to an increase in surface ozone due to the increase in stratospheric ozone from both the increasing GHGs, reductions in sunlight, and reductions in stratospheric water vapor (Nowack et al., 2016). On the other hand, SAI can lead to a reduction in global tropospheric and surface ozone, due to the decrease in stratosphere-troposphere exchange of ozone (if stratospheric ozone depletion has increased) and reduced tropospheric ozone production based on the ozone-destroying hydrogen cycle. The decrease in surface ozone may lead to a reduction in associated mortality (Nowack et al., 2016; Xia et al., 2017; Eastham et al., 2018).
- **Impacts on vegetation and crops:** Solar dimming experiments have shown that reduced surface heat stress from SRM-induced cooling can combine with the fertilization effect of increased CO_2 concentrations to lead to a reduction in some negative impacts of climate change on crops and vegetation (Xia et al., 2014; Glienke et al., 2015; Fan et al., 2021). In addition to the beneficial impact on crops from enhanced photosynthesis from higher CO_2 concentrations, SAI may enhance the terrestrial photosynthesis rate by increasing the ratio of direct to diffuse radiation at the surface (Xia et al., 2016, 2017; Cao, 2018), although the magnitude of this positive climate response is contested (Proctor et al., 2018).
- **Impact on surface ultraviolet (UV) and visible radiation:** Studies that have investigated the impact of SAI on UV irradiance at the surface have found little change in UV in the tropics and mid-latitudes and an increase in UV in polar regions (e.g., Tilmes et al., 2012, Pitari et al., 2014; Visioni et al., 2017). These impacts are due to the combined impacts of increases in ozone concentrations and the strong scattering of UV radiation back to space from the aerosol at tropical and mid-latitudes and ozone depletion at polar latitudes. The substantial increase of stratospheric aerosol for a strong SAI scenario towards the end of the 21st century has been simulated to result in a significant reduction of UV (around 20–30%) in the subtropics and higher latitudes compared to present day (Madronich et al., 2019). A simultaneous decrease in the biologically active irradiances for DNA damage by 25–33% was modelled, with comparable contributions from the effects of the aerosol scattering of UV radiation and of ozone recovery. On the other hand, the photosynthetically active radiation (PAR), which is mainly affected by the changes in diffuse-direct ratio of radiation, shows an increase of up 35–40% in high northern latitudes.

6.5 ALTERNATIVE SAI MATERIALS

The impact of sulfuric acid aerosol on stratospheric ozone results from its physical and chemical properties, i.e., its bulk complex refractive index, aerosol size distribution, and the chemical composition of the aerosol surface. Alternative materials with different properties could reduce ozone loss resulting from heterogeneous chemistry or from the dynamical response due to heating from absorption of solar and terrestrial radiation. The heating and resulting dynamical response depend on material bulk properties that can be observationally constrained with reasonable confidence. The heterogeneous chemistry responsible for activating halogen species and converting nitrogen oxides (NO_x) to nitric acid (HNO_3) depends on details of the surface composition and associated chemical mechanisms. Laboratory studies of these properties are challenging, and the large uncertainty is due to an imperfect understanding of the evolution of the surfaces of alternative materials over stratospheric lifetimes. Coatings of candidate aerosol particles by sulfuric acid and reactions with sulfuric acid, nitric acid, or hydrogen chloride may significantly impact the aerosol chemical and optical properties (e.g., Tang et al., 2014; Dai et al., 2020).

Alternative materials can potentially reduce impacts on stratospheric ozone, but uncertainty in their net radiative and chemical properties (or impacts) is currently considerable compared to that for sulfate (*Section 6.3*). The properties of sulfates and their impacts are comparatively well studied, and processes are more or less comprehensively included as a key stratospheric aerosol component in climate models, owing to the necessity of quantifying the periodic cooling from explosive volcanic eruptions (*Section 6.2.2.1*). Simulations of the impacts of stratospheric

sulfate perturbations have been benchmarked against a relatively large set of observations and measurements (*Section 6.6*), providing more confidence in their representation than in any alternative materials. This section provides an assessment of the limited number of studies that have investigated alternative particles and how they might impact stratospheric heating rates, dynamics, and heterogeneous chemistry.

6.5.1 Motivation

Many materials, especially solid ones, do not have acidic or water-containing surfaces and thus do not have the same ozone-depleting surface heterogeneous chemical reactions as sulfate. The impacts of these particles on ozone will differ owing to different surface properties (e.g., their catalytic activity, hygroscopicity, pH, surface roughness, and the degree to which they become coated with naturally occurring sulfate) and how these vary over stratospheric lifetimes. There is little information on these properties for alternative materials. The bulk optical properties of numerous materials exhibit negligible absorption of solar or terrestrial radiation. Many, such as silicon carbide, alumina, and calcite, have other promising qualities, e.g., non-toxicity or ease of production at low costs. Few materials are truly transparent to terrestrial radiation in the atmospheric window; diamond is a notable exception. Some absorb only in the longwave infrared or in the terrestrial radiation spectral regions that coincide with absorption bands of other atmospheric constituents, which reduces their impact on stratospheric heating. These include alumina, calcite, zirconia, and titania (both rutile and anatase polymorphs), but titania is a well-known photocatalyst with strong ultraviolet absorption in the visible (UV-VIS). There is consensus that using pure materials with well-characterized optical properties and little absorption would reduce the dynamical response caused by the heating in the lowermost tropical stratosphere with sulfate aerosols, and with that the effects on stratospheric ozone would be reduced. However, additional complications of these materials can include toxicity; formation of coatings, as these aerosols mix with stratospheric aerosols from natural sources; and potential impacts on cirrus clouds. Such complexities have not yet been adequately addressed in the scientific literature.

While there are few studies on the impacts of alternative materials on ozone and certainly no complete treatment within climate models, an increasing number of studies are focusing on some aspect of alternative materials within the context of stratospheric climate intervention (Ferraro et al., 2011, 2012; Pope et al., 2012; Weisenstein et al., 2015; Jones et al., 2016a; Keith et al., 2016; Dykema et al., 2016; Moon et al., 2018 Cziczo et al., 2019; Dai et al., 2020; Huynh and McNeill, 2021).

6.5.2 Effects of Different Aerosols on Heating, Radiation, and Dynamic Response

The optical properties of alternative materials determine the radiative forcing they produce, which is central to their efficacy for stratospheric climate intervention, as well as how they would affect stratospheric heating rates and the resulting dynamical responses. Even for alternative particles with no absorption of radiation, minor stratospheric heating at altitudes above the aerosol results from the increased backscatter of solar UV-Vis radiation, which is then absorbed by ozone and other trace gases. This effect is more than an order of magnitude smaller than the direct heating from absorption by sulfuric acid aerosols (Dykema et al., 2016). Stratospheric heating and the associated dynamical responses result from materials with non-zero imaginary refractive indices in the solar UV-Vis (titania) or the atmospheric window in the terrestrial IR (sulfuric acid).

Standalone radiative transfer calculations have been used to investigate a range of materials (e.g., Ferraro et al., 2011, 2012; Dykema et al., 2016). **Figure 6-17** shows the stratospheric temperature change for loadings of some candidate alternative particles that produce a radiative forcing of –1 Wm^{-2}. The imaginary part of the refractive index for sulfate increases significantly at wavelengths larger than 1.2 μm, where the incident radiation is many orders of magnitude less than at the peak of the solar spectrum. However, it still causes significant stratospheric heating. Other materials, in particular diamond, have a much smaller effect on stratospheric temperature (Dykema et al., 2016).

Few studies have used general circulation models (GCMs) to study the impacts of using alternative materials for SAI. Jones et al. (2016a) imposed fixed size distributions for stratospheric aerosols within the HadGEM2-CCS climate model and compared the impacts of black carbon and titania to those of sulfate. Both of these materials have strong absorption bands in the solar UV-VIS range. Black carbon has a very large heating effect in the stratosphere. This absorption results in strong stratospheric heating, which is shown to result in a rapid collapse of the QBO (Jones et al., 2016a, Haywood et al., 2022). Ferraro et al. (2015) performed simulations similar to the G1 GeoMIP simulations, using stratospheric aerosol burdens sufficient to offset quadrupled carbon dioxide. Their simulations showed that the use of titania and sulfate both resulted in a strong intensification of the Northern Hemisphere polar vortex and a northward shift of the storm tracks. The heating of the tropical tropopause with titania was larger than with sulfate, due to the strong UV-VIS absorption of titania compared with sulfate (**Figure 6-18**). Ferraro's study, however, was highly idealized, with a very concentrated tropical aerosol layer. Dykema et al. (2016) demonstrated that diamond, moissanite (SiC), alumina

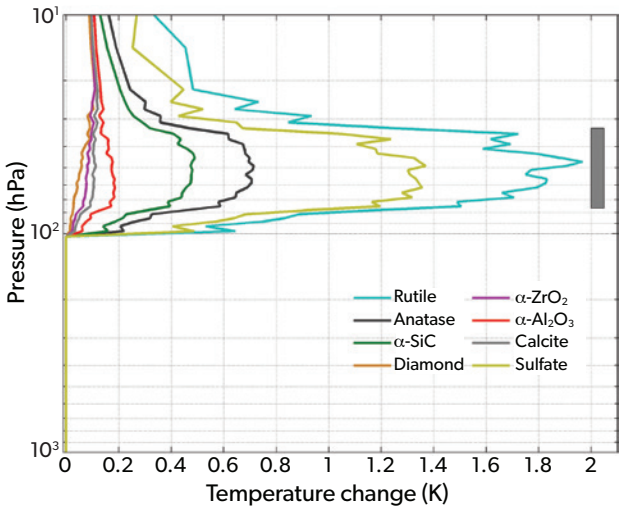

Figure 6-17. Equilibrium stratospheric heating produced by a mass of monodisperse solid aerosols of optimized radii sufficient to achieve –1 Wm^{-2} shortwave radiative forcing. The gray bar on the right shows the approximate location of the aerosol layer. [Adapted from Dykema et al., 2016.]

(Al_2O_3), and calcium carbonate ($CaCO_3$) as calcite should have greatly reduced dynamical impacts due to less radiative heating and thus may be favorable in the trade-off between radiative forcing and dynamical response when compared to sulfate aerosols. However, this assumes that the complex refractive indices of the aerosols remain unchanged over the stratospheric lifetime of the particles, which is not proven, especially for reactive materials such as calcium carbonate. Idealized climate model simulations, where the absorption from sulfate aerosols is increased in the solar spectrum, reveal significantly greater impacts on stratospheric heating with resultant strong impacts on the QBO, a strongly enhanced positive phase of the North Atlantic Oscillation and the associated rainfall patterns, enhanced stratospheric water vapor, and a delay in the recovery of the Antarctic ozone hole (Haywood et al., 2022).

In summary, compared to sulfate, the use of non-absorbing materials should effectively reduce stratospheric heating and associated dynamical responses, which should therefore reduce dynamically induced ozone changes. Large uncertainties result from 1) lack of confidence in the optical properties of materials over stratospheric lifetimes relative to their baseline and/or potentially idealized literature values, 2) limitations in quantitative knowledge of absorption coefficients (Dykema et al. 2016), 3) the small number of studies investigating dynamical responses with alternative materials, and 4) uncertainties in the potential impacts of different materials on other aspects of the climate system such as on cirrus clouds (Cziczo et al., 2019).

6.5.3 Chemical Effects on Ozone Using Alternative Materials

Sensitivity studies using a chemical-transport model indicate that non-absorbing materials such as diamond and alumina may greatly reduce stratospheric ozone loss compared to sulfate (Weisenstein et al., 2015; **Figure 6-18**).

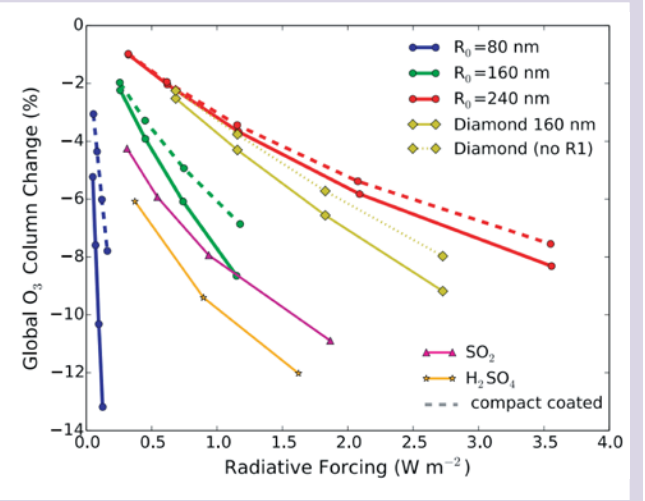

Figure 6-18. The trade-off between ozone depletion and radiative forcing for some alternative geoengineering materials and for sulfuric acid, based on simulations using the AER-2D chemical-transport model. Sulfuric acid is injected either as gas-phase SO_2 (pink) or 95 nm diameter sulfuric acid particles (orange). The blue, green, and red lines correspond to alumina particles with different radii, and the dashed lines assume that the fractal aggregates from coagulation become compact. For diamond (light green), the dotted line assumes that the $ClONO_2$ + HCl reaction does not occur (referred to as "no R1"). Generally, smaller particles result in greater ozone destruction, as their surface area for a specific radiative forcing is higher than for larger particles. The higher real part of the refractive index of diamond compared to alumina explains the smaller ozone change per radiative forcing compared to the case with the same size alumina particles. For both diamond and alumina, scenarios exist with lower ozone loss than for SO_2 or H_2SO_4. [From Weisenstein et al., 2015.]

Laboratory studies have found high uptake coefficients for the HCl + $ClONO_2$ reaction, together with reduced hydrolysis of nitrogen pentoxide (N_2O_5) for alumina compared to sulfuric acid (H_2SO_4) (e.g., Molina et al. (1997). Chlorine nitrate ($ClONO_2$) reactivity has been studied on titania at room temperature but without the addition of hydrogen chloride (HCl) or hypochlorous acid (HOCl) (which would both be present in the stratosphere), so the utility of the studies is limited (Tang et al., 2016). Similarly, N_2O_5 and hydroperoxy radical (HO_2) uptake on titania have been studied only at room temperature (Tang et al., 2014; Moon et al., 2018), with the latter study concluding that the uptake of HO_2 radicals on titania likely is too slow to impact ozone chemistry. The implications of the difference in heterogeneous chemistry of alumina compared to sulfuric acid remain uncertain.

Hypothetically, calcium carbonate stratospheric aerosol could increase ozone concentrations based on the potential rapid uptake of HCl and HNO_3 by calcium carbonate particles, changing the sign of the trade-off between radiative forcing and ozone present for sulfate (Keith et al., 2016). However, HNO_3 and HCl chemistry on calcium carbonate at room temperature suggest only moderate uptake rates. In addition, initial uptake rates of HCl and HNO_3 on calcium carbonate are low and decrease further via passivation under stratospheric conditions; i.e., there is rapid formation of a non-reactive surface layer that greatly slows down further reaction (Dai et al., 2020). Observed uptake coefficients orders of magnitude higher than those determined by Dai et al. (2020) were found at stratospheric temperatures (Huynh and McNeill, 2021), but the degree of passivation after HCl exposure, which determines the actual stratospheric reactivity, could not be determined.

The AER-2D model that includes the calcium carbonate chemistry of Dai et al. (2020) shows a small amount of ozone depletion (**Figure 6-19**, solid green line), in contrast to an enhancement in ozone at most latitudes when passivation is not accounted for (**Figure 6-19**, solid magenta line). In addition to the reactions studied in the lab by Dai et al. (2020; included in the solid lines in **Figure 6-19**), reactions involving $ClONO_2$ + HCl and $ClONO_2$ + HOCl would also affect ozone (green and magenta dashed lines in **Figure 6-19**). There is very limited understanding of this material under stratospheric conditions, so the rates of these unmeasured chlorine reactions, and additional currently unknown reactions, could have other potentially significant impacts on ozone, especially over the Antarctic regions (**Figure 6-19**). There are few experiments for how alternative materials could affect chemistry under more extreme polar vortex conditions. This complexity and the large number of heterogeneous surface reactions that are possible and the reactivity of materials such as calcium carbonate, whose surfaces will age and change composition over their

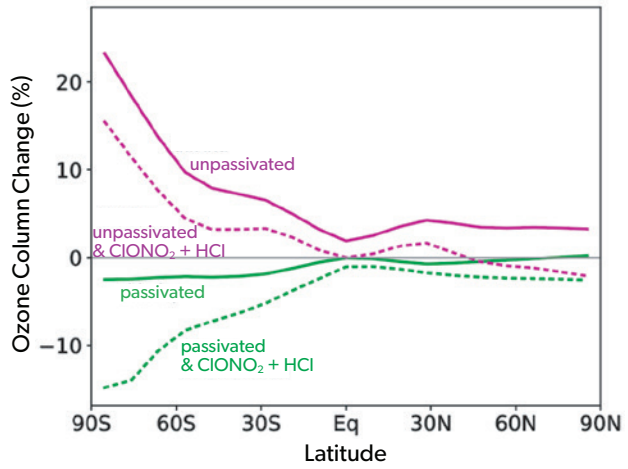

Figure 6-19. The impact on TCO of using calcium carbonate for SAI when considering the laboratory-observed passivation (green lines) or unpassivated assumption (magenta lines). Dashed lines show the relationship when accounting for the additional $ClONO_2$ + HCl reaction based on the Molina et al. (1997) alumina rates. [From Dai et al., 2020, Supplementary Material.]

stratospheric lifetimes, result in a high degree of uncertainty in the direct chemical impact of alternative materials on stratospheric ozone.

6.5.4 Paucity of Observations and Limited Model Capabilities

Overall, the state of knowledge of the impacts of alternative materials on stratospheric ozone is severely limited by a paucity of laboratory and field observations, particularly under stratospheric conditions. This limitation also has resulted in a very small number of modeling studies of alternative materials. Although it is likely that materials exist that result in decreased chemical and dynamical impacts on stratospheric ozone, any potential risks and tradeoffs are far from understood.

The impacts of SAI with the injection of alternative materials on ozone will depend on a number of additional uncertainties and higher-order effects. The coupling of chemistry and dynamics is just as important for alternative materials as it is for sulfate. Uncertainties are larger for alternative materials than for sulfate due to the much smaller number of studies; in addition, there is increased complexity resulting from the addition of a new component to the stratospheric composition. Interactions of alternative materials with background sulfate have not been quantified and could be significant. Unreactive materials such as diamond would become coated with sulfuric acid from coagulation and condensation, making them more reactive. Reactive species such as calcium carbonate would interact with sulfuric acid, nitric acid, and other constituents, affecting their properties. It is possible that coagulation of sulfuric acid particles with unreactive solid particles results in incomplete coatings. As with tropospheric aerosol mixtures, varying degrees of internal and external mixtures of composite aerosol particles are likely to be created. This increases the uncertainties in both optical and chemical properties of such particles and directly impacts the chemical and dynamical response of the perturbation. Thus, despite the potential for greatly reducing impacts on stratospheric ozone compared to sulfate, confidence in how alternative particles would affect the stratosphere and ozone, and therefore whether they are preferable to sulfate, is hindered by significant research gaps.

6.6 VOLCANOES AND PYROCUMULONIMBUS AS NATURAL ANALOGS TO SAI

As described in previous sections, ESM simulations show large uncertainties with regard to the effects of SAI on radiation, surface temperature, and other impacts, including ozone. Reducing these uncertainties would increase confidence in the projected impacts under different SAI scenarios and strategies. Natural analogs provide a unique opportunity for identifying shortcomings in models; these models are the only tools available to project future changes under SAI. The majority of coordinated ESM modeling experiments for studying the effects of SAI on the climate system use stratospheric SO_2 injections, thereby paralleling the periodic injections of SO_2 by explosive volcanic eruptions and their impacts on climate. Satellite measurements of radiative fluxes after the 1991 Mount Pinatubo eruption show a peak monthly-mean net top-of-atmosphere radiative flux anomaly between 60°S and 60°N of around −3 W m^{-2}. For context, by design the medium SAI GeoMIP G6sulfur simulations exert a continuous radiative forcing of approximately −4 W m^{-2} at the end of the 21st century (Kravitz et al., 2015).

Another natural analog of periodic aerosol injections into the stratosphere is when biomass burning creates pyrocumulonimbus (pyroCb) events. Such events occur when convection generated by the fire produces a cumulonimbus cloud that is sufficiently vigorous to transport both smoke and moisture into the lower stratosphere.

Both explosive volcanic eruptions and pyroCb events provide opportunities for benchmarking the current generation of aerosol and climate models against a wealth of observations (*Appendix 6A*). This includes testing the modeled spatial and temporal evolution of the aerosol distribution, microphysical properties, effects on radiation, and their impacts on stratospheric ozone. We restrict our assessment to the utility of analogies on aerosol microphysical and spatial distributions and their impacts on ozone. An assessment of how well the models represent the observed impacts of volcanic eruptions on climate impacts—such as surface cooling, a spin-down of the hydrological cycle, shifts in monsoon precipitation, and influences on key modes of climate variability—is provided in *Appendix 6A*, where the utility of pyroCb events in assessing models is also discussed.

6.6.1 Volcanic Eruptions as Analogs for SAI: Limitations and Opportunities

Measurements clearly show that large explosive volcanic eruptions, such as that of Mount Pinatubo in 1991, can perturb stratospheric ozone by increasing aerosol SAD for heterogeneous chemistry and catalytic ozone loss cycles, affecting ozone photolysis rates (e.g., Solomon, 1999, and references therein). In addition, there are indirect effects on ozone resulting from radiative heating of the stratosphere and subsequent circulation changes caused by the volcanic sulfate aerosol, similar to those described

in *Sections 6.2* and *6.3*. Measurements after volcanic eruptions provide an opportunity to benchmark model performance and to understand the likely impact of SAI on ozone, because the same chemical and radiative heating processes are valid for volcanic eruptions and for SAI using SO_2 or other sulfate aerosol precursors (*Section 6.2*).

Detailed observations of SO_2 and resulting sulfate aerosols from small-magnitude eruptions between 2008 and 2019 using satellites, surface-based sun photometers, and surface-based lidars have provided insights into the microphysical evolution of stratospheric volcanic aerosols and their impacts on stratospheric transport (e.g., Muser et al., 2020; de Leeuw et al., 2021). These data have been used to assess and improve the representation of sulfur chemistry and microphysics in global climate models (e.g., Mills et al., 2016, 2017; Schmidt et al., 2018).

Measurements and model simulations of volcanic eruptions also provide a means for quantifying the expected stratospheric ozone changes resulting from SO_2 injections (*Section 6.2*). There are, however, clear limits to the analogy of volcanic aerosols with SAI, mainly because explosive eruptions produce pulsed injections of SO_2 into a relatively small area in the stratosphere, which contrasts with the continuous, decadal-long injection of SO_2 in strategically selected locations under most SAI scenarios. Continuous SAI applications contrast with the observations of a sudden increase in SAD, followed by a slow decline after a volcanic eruption. No large-magnitude volcanic eruptions during the satellite area have taken place during a very cold Arctic winter; as a result, current observations may underestimate the magnitude of polar ozone loss that could occur during long-term SAI applications (Tilmes et al., 2008). A continuously enhanced aerosol layer with SAI would have a longer-term impact on the stratospheric circulation than that from volcanic eruptions (see *Appendix 6A*). Other differences include the type of material injected under volcanic eruptions—which frequently inject volcanic ash, water vapor, and halogens, together with sulfur—and different climate response times to pulsed and continuous injections; these factors lead to differences in the ozone and climate response between volcanic eruptions and SAI (e.g., MacMynowski, et al., 2011; Duan et al., 2019).

In models, the availability of key oxidants such as OH becomes limited following volcanic eruptions (Bekki, 1996; Mills et al., 2017) due to the injection of large amounts of SO_2 into one or only a few model grid boxes. This affects the concentration and lifetime of SO_2, the rate of sulfate aerosol formation, and the growth of sulfate aerosol particles. Clyne et al. (2021) show that for pulsed SO_2 emissions, the injection strategy (i.e., single model grid box or along a band of longitudes) and the details of the OH chemistry representation (i.e., interactive or prescribed) lead to large differences in aerosol lifetime and stratospheric aerosol optical depth (AOD), similar to those across different SAI strategies (see *Section 6.3*). Many of the simulated differences between pulsed injections of SO_2 from volcanoes and continuous injections under SAI are caused by nonlinearities in sulfur oxidation chemistry and aerosol microphysics; SAI injections would occur in an already aerosol-laden atmosphere, which favors condensation and coagulation over nucleation (e.g., Laakso et al., 2017). Model simulations and observations reveal that aerosol dispersion during the initial stages of an eruption is strongly influenced by injection height and thus local meteorology (e.g., Bourassa et al., 2012; Jones et al., 2016b; de Leeuw et al., 2021). On the other hand, for continuous SAI, which takes place over several years, the interannual differences in the aerosol distribution are small and less dependent on initial meteorological conditions (e.g., Tilmes et al., 2017; Visioni et al., 2019).

With volcanic eruptions, there are commonly co-emissions of species other than sulfur (such as volcanic ash, halogens, and water vapor), whereas under SAI this would generally not be the case. Many co-emitted species can affect the aerosol lifetime, oxidation rates, and radiative heating rates and can cause lofting of sulfur species to higher altitudes (Zhu et al., 2020; Muser et al., 2020; Niemeier et al., 2020; Kloss et al., 2021; Stenchikov et al., 2021). Disentangling and quantifying the effects of co-emitted species on sulfate aerosol lifetimes and dispersion in observations is difficult. Modeling studies provide indications of the relative rate at which different co-emitted species affect heating rates and lofting (Muser et al., 2020; Kloss et al., 2021; Stenchikov et al., 2021). Some volcanic co-emissions such as halogens can also directly affect stratospheric ozone under present-day ozone-depleting substance levels, as well as indirectly affect stratospheric heating rates and thus water vapor concentrations (e.g., Staunton-Sykes et al., 2021, and references therein). In addition, future research may suggest that the optimum SAI strategy is to inject H_2SO_4 instead of SO_2 (*Section 6.2*) or to use a completely different substance (*Section 6.5*), further limiting the analogy between volcanic eruptions and SAI.

6.6.2 Model Simulations of Volcanic Effects on Ozone

Following the June 1991 Mount Pinatubo eruption, satellite and ozonesonde data show a loss of ozone in the lower stratosphere, particularly in winter and spring in polar regions between 1991 and 1993 (e.g., Grant et al., 1992; Randel et al., 1995; *Chapters 3* and *4*). Total column ozone was reduced by up to 8% in the first month after the eruption in the tropics and by up to 10% in the Northern Hemisphere. Ozone depletion in the aerosol plume was much higher, reaching around 20% at altitudes between 24 km and 25 km (McCormick et al., 1995). In the mid-latitudes of the Southern Hemisphere, increases in total column ozone of up to 10 DU were observed in the middle stratosphere between July and December 1991, likely caused by both chemical and dynamical changes (e.g., Koike et al., 1994; Van Roozendael et al., 1997). Recent modeling studies suggest that the volcanically induced dynamical perturbation played a key role in transporting ozone from the tropics to the extratropics of the Southern Hemisphere, thus explaining the lack of ozone depletion there (Pitari and Mancini, 2002; Poberaj et al., 2011; Aquila et al., 2013; Dhomse et al., 2014). The same modeling studies suggest that after about six months heterogeneous chemical ozone loss dominates, with additive effects of the initial dynamical perturbation and the chemical perturbation due to the volcanic aerosols. Following the eruption of Mount Pinatubo, a maximum decrease in total column nitrogen dioxide (NO_2) of about 35% in both the Arctic and at mid-latitudes in January 1992 is evident, with a recovery to background values by August 1995 (Van Roozendael et al. 1997). Maximum reductions in local NO_2 concentrations of up to 60% were measured in the lower stratosphere at around 22 km altitude in summer 1992 (Johnston et al., 1992; Van Roozendael et al., 1997; Danilin et al., 1999) and correlated well with the 40-fold (or more) increase in the aerosol SAD (Thomason et al., 1997). Similar measurements exist for

nitric oxide (NO), suggesting a role for nitrogen pentoxide (N_2O_5) hydrolysis with increasing SAD, which has been found in various model studies applying SAI.

Studies that isolate the effect of increased volcanic aerosol find good correlation between modeled SAD and observed ozone depletion (Wilka et al., 2018); these increases in SAD are associated with large- and small-magnitude volcanic eruptions, suggesting that heterogeneous chemistry was the primary driver of increased ozone loss between 1980 and 2014 (when halogen stratospheric concentrations were high). The 1991 Mount Pinatubo eruption, which caused the largest observed polar ozone perturbation to date, did not emit significant amounts of chlorine or other halogen compounds that could have catalyzed ozone loss. Measurements after the 1982 El Chichón eruption support the same mechanisms for ozone loss, with increases in aerosol SAD of up to 50 μm^2 cm^{-3} at mid-latitudes between 18 km and 20 km in early 1983 (Hofmann and Solomon, 1989). In this case, the eruption might have injected HCl into the stratosphere, with observed column HCl enhancements above 12 km altitude between 22°N and 35°N on the order of 40% in the first six months post-eruption (Mankin and Coffey, 1984). This would have amplified the catalytic depletion of total column ozone, which reached more than 10% after the eruption (Hofmann and Solomon, 1989). The difference in **Figure 6-20** between the blue and the orange curves, which show the evolution of ozone in a model simulation with and without volcanic aerosols, respectively, supports this view. The aerosol-free simulation shows no increase in the rate of ozone depletion above the overall trend in the years affected by the 1991 Mount Pinatubo eruption and a significantly decreased effect in the years affected by the 1982 El Chichón eruption.

Measurements and modeling studies show that since the 1991 Mount Pinatubo eruption, a series of small-magnitude eruptions have contributed to polar ozone depletion in Antarctica (**Figure 6-21**; Solomon et al., 2016; Wilka et al., 2018; Stone et al., 2017; Zhu et al., 2018). Measurements show that in 2015, the Antarctic ozone hole was particularly large and long-lasting, which in models and observations has been attributed to the existence of a very cold and undisrupted stratospheric polar vortex combined with the impacts of the April 2015 Calbuco eruption

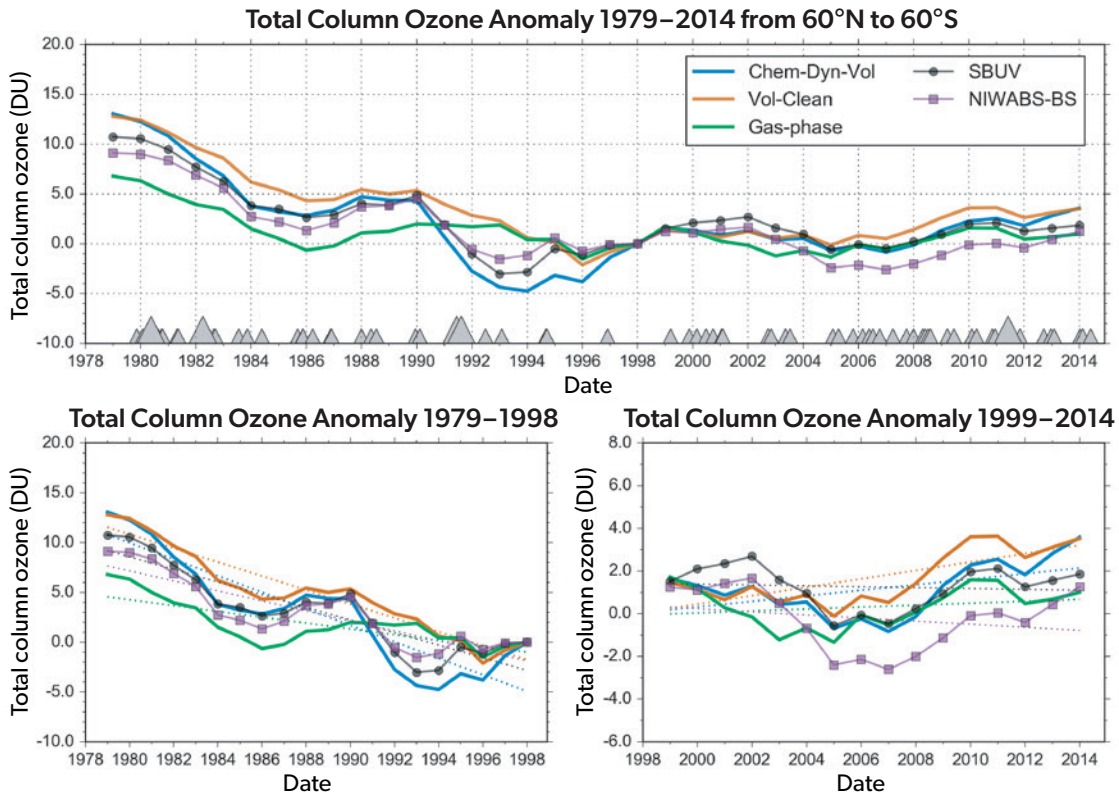

Figure 6-20. *(top)* Time series of model-simulated three-year running mean of 60°N–60°S total column ozone anomalies with respect to 1998 values from 1979 to 2014 with gas-phase, Vol-Clean, and Chem-Dyn-Vol runs shown as green, orange, and blue solid lines, respectively. The Chem-Dyn-Vol run includes full chemistry, specified dynamics, and volcanic aerosols taken from the Neely and Schmidt (2016) database; the Vol-Clean run has no volcanic aerosols but all other processes; and the gas-phase run turns off all heterogeneous chemistry. Solar Backscatter Ultraviolet and National Institute of Water and Atmospheric Research-Bodeker Scientific total column ozone data are shown by the black line with circles and the purple line with squares, respectively. Grey triangles at the bottom indicate volcanic eruptions, with the larger triangles indicating eruptions of Volcanic Explosivity Index 5 and 6. *(bottom)* Time series of anomalies in global mean total column ozone and their respective linear fits for the periods 1979–1998 *(left)* and 1999–2014 *(right)*. [From Wilka et al., 2018, with fit parameters given in Table 1 of that publication.]

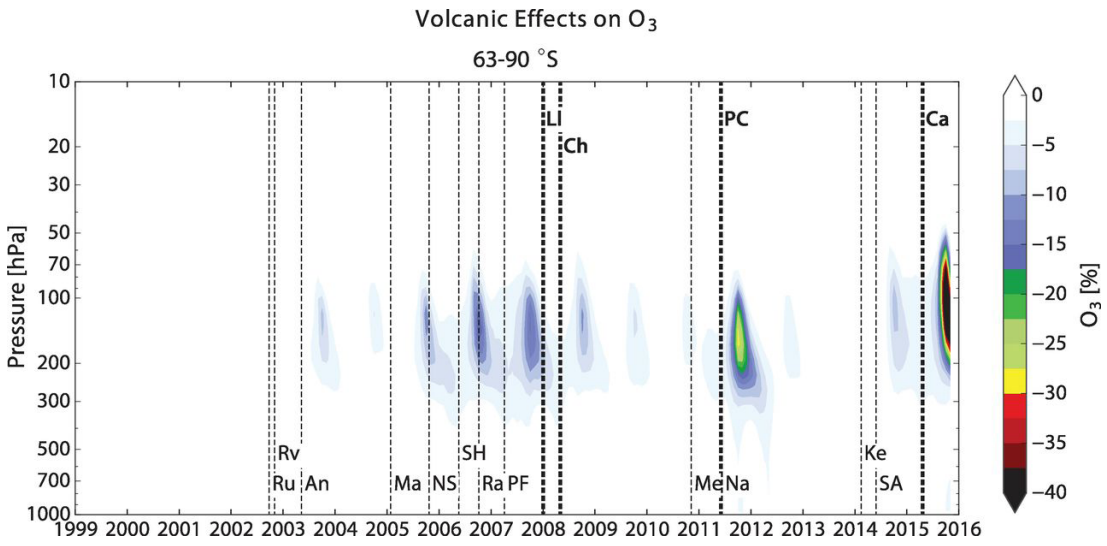

Figure 6-21. Model-calculated percentage changes in ozone concentrations in Antarctica (63–90°S) due to a series of small-magnitude volcanic eruptions. Tropical eruptions are shown at the bottom and higher-latitude eruptions at the top. Abbreviations: An, Anatahan; Ca, Calbuco; Ch, Chaitén; Ke, Kelut; Ll, Llaima; Ma, Manam; Me, Merapi; Na, Nabro; NS, Negra Sierra; PC, Puyehue-Cordón Caulle; PF, Piton de la Fournaise; Ra, Rabaul (also referred to as Tavurvur); Ru, Ruang; Rv, Reventador; SA, Sangeang Api; SH, Soufrière Hills. [From Solomon et al., 2016.]

in Chile (*Chapter 4*; Solomon et al., 2016; Wilka et al., 2018; Stone et al., 2017; Zhu et al., 2018; Rieger et al., 2021). Based on observations and model simulations, Berthet et al. (2017) show that after the 2009 Sarychev eruption, NO_2 was depleted to a similar degree as following the 1991 Mount Pinatubo eruption, but ozone loss was relatively limited at 16 km and smaller in magnitude than during Pinatubo by at least a factor of 10. These observations and model simulations provide useful guidance on the expected effects of SAI on ozone and indicate that even small aerosol injections, as during the onset period of SAI, can have a significant impact on ozone.

6.6.3 Model Simulations of Volcanic Aerosol Properties

Most Earth system models participating in the CMIP6 model intercomparison used in the latest IPCC assessment (Lee et al., 2021) use prescribed stratospheric volcanic aerosol datasets derived either from observations (e.g., Thomason et al., 2018; Kovilakam et al., 2020) or a blend of observations and models (Arfeuille et al., 2014). Model intercomparisons conducted under CMIP6 and dedicated to volcanic eruptions, such as the Volcanic Forcings Model Intercomparison Project (VolMIP), stipulate a

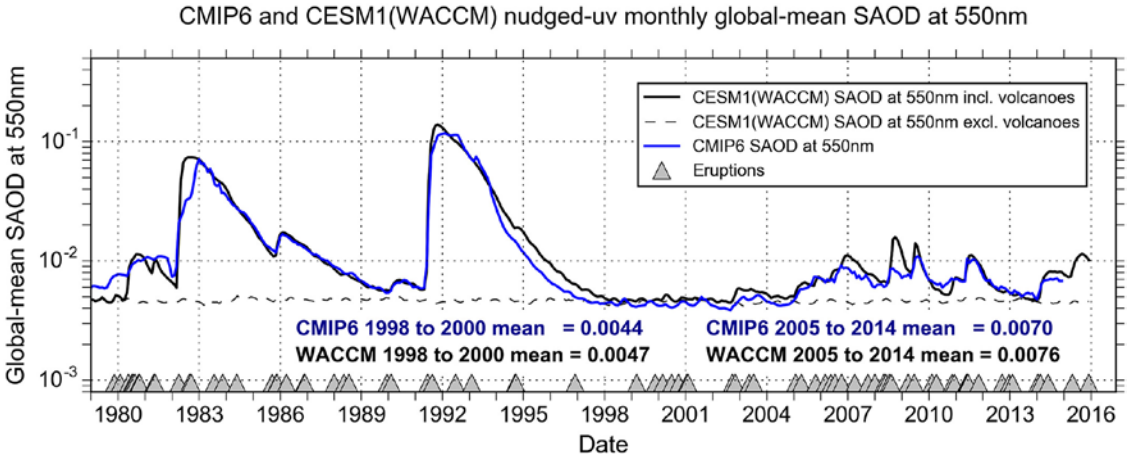

Figure 6-22. Comparison of satellite-based (blue line) and model-simulated (solid black line: including volcanic SO_2 emissions; dashed black line: omitting volcanic SO_2 emissions) monthly global mean stratospheric aerosol optical depth (SAOD) at 550 nm. [From Schmidt et al., 2018.]

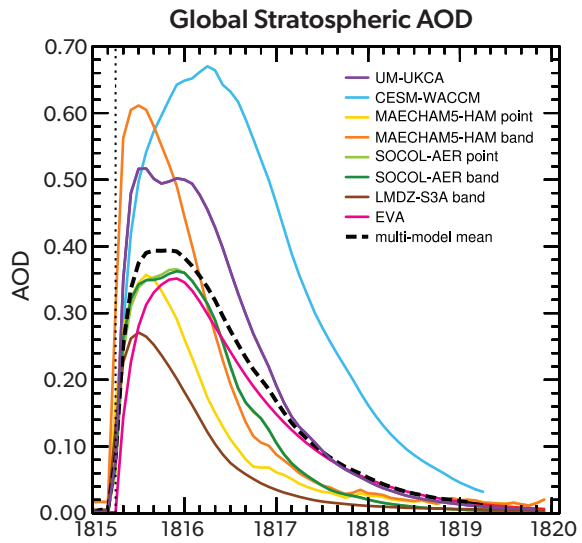

Figure 6-23. Ensemble averaged, global mean stratospheric AOD (at 550 nm) as simulated for an 1815 Mount Tambora–type eruption emitting 60 Tg of SO_2, using different models. The black line is the mean of the CESM-WACCM (blue), UM-UKCA (purple), SOCOL-AER point (light green), MAECHAM5-HAM point (gold), LMDZ-S3A band (dark brown), and EVA (red) models. Results for the SOCOL-AER band and MAECHAM5-HAM band models using different injection approaches are shown in dark green and orange, respectively. The vertical dotted line marks the date of injection of SO_2, which is slightly offset from the zero AOD in the models due to the temporal resolution of the model output and curve smoothing. [From Clyne et al., 2021.]

standardized protocol whereby prescribed aerosol datasets are used to ensure that the spatial distribution of aerosols is consistent. This allows quantification of model uncertainty in the response of ozone and climate to a volcanic forcing (Zanchettin et al., 2016) without confounding issues arising from, for example, differences in the implementation of volcanic emissions (Clyne et al., 2021).

Models with interactive aerosol and chemistry schemes use volcanic SO_2 emissions as input. **Figure 6-21** shows that climate models with detailed aerosol and sulfur chemistry schemes nudged to meteorological reanalyses can simulate stratospheric AOD under volcanically quiescent and perturbed conditions and are in good agreement with satellite-based measurements (Mills et al., 2016; Schmidt et al., 2018). After the two recent large volcanic eruptions of El Chichón in 1982 and Mount Pinatubo in 1991, models reveal that between 2005 and 2014, a series of small-magnitude eruptions doubled the total stratospheric AOD compared to volcanically quite periods (**Figure 6-22**; Kovilakam et al., 2020; Schmidt et al., 2018; Thomason et al., 2018; Mills et al., 2016).

No direct measurements exist for larger SO_2 perturbations, and confidence in interactive sulfate aerosol and sulfur chemistry schemes is much lower for SO_2 injections greater than 10–20 Tg of SO_2. For example, for very-large-magnitude eruptions emitting 60 Tg of SO_2 (which is representative of the 1815 Mount Tambora eruption), a model intercomparison reveals large inter-model differences in the simulated magnitude of the volcanic forcing and surface temperature response, despite the models using the same eruption source parameters (Zanchettin et al., 2016). Clyne et al. (2021) show that for eruptions emitting 60 Tg of SO_2, the magnitude and timing of the peak in global mean stratospheric aerosol optical depth and effective radius differ substantially across simulations (**Figure 6-23**). Such emissions levels are extremely large compared to those under the peakshaving and medium SAI scenarios and are at the extreme end of strong SAI scenario.

Recent studies also suggest that there is uncertainty in the effective radiative forcing diagnosed in models for large explosive eruptions such as Mount Pinatubo in 1991. Rapid adjustments and the cloud response to a volcanic forcing are particularly large sources of this uncertainty (e.g., Gregory et al., 2016; Marshall et al., 2020; Schmidt et al., 2018). There is also substantial uncertainty in the stratospheric heating rates and the subsequent dynamical response simulated in models following explosive eruptions (e.g., Driscoll et al., 2012; Zambri et al., 2017), as also reflected in SAI simulations (**Figure 6-9**). Uncertainties in heating rates and dynamical responses have implications for the hemispheric distribution of the sulfate aerosols, which in turn affects ozone chemistry (e.g., as discussed in Aquila et al., 2013, for Mount Pinatubo).

Model configuration and model specifics such as the vertical resolution in the stratosphere and the details of the radiative transfer scheme affect the magnitude of the diagnosed volcanic forcing, which is also the case for SAI studies (*Section 6.2.2*). Although no systematic uncertainty assessment has been carried out to date, Hansen et al. (2002) estimate that these model uncertainties equate to uncertainties in radiative forcing of between 15% and 50%, depending on the eruption specifics. Many of the discrepancies have common causes and can largely be explained either by missing first-order model physics, chemistry, or other processes (Clyne et al., 2021). As in SAI simulations, the use of sectional versus modal aerosol schemes can have a very large effect on the results (e.g., English et al., 2013; Laakso et al., 2021).

Overall and despite limitations, volcanic eruptions offer an opportunity to benchmark current-generation aerosol and climate models against a wealth of observations. In particular, small-magnitude volcanic eruptions that have occurred over the satellite era have the benefit of a greater number of higher-quality observations and can be used for refining emissions estimates and injection altitudes (e.g., de Leeuw et al., 2021) and for detailed assessment of the performance of models with respect to their predicted effects on ozone, as well as the temporal and spatial evolution of both SO_2 and the resulting sulfate aerosol plume (e.g., Haywood et al., 2010; Muser et al., 2020). These observations can help improve our understanding of the underlying physical and chemical processes, as well as the uncertainties involved in SAI proposals.

APPENDIX 6A : OBSERVATIONS AND VOLCANIC IMPACTS ON CLIMATE

6A.1 OBSERVATIONS

Observational constraints for model simulations of the evolution of stratospheric plumes of SO_2 and the resulting sulfate, as well as biomass-burning aerosol plumes from pyrocumulonimbus, are available from a number of sources. Satellite retrievals include estimates of the SO_2 injection amounts and altitudes from instruments operating in the UV (e.g., TROPOMI) and IR (IASI) spectral regions (e.g., Karagulian et al., 2010; Clarisse et al., 2012; Theys et al., 2017; de Leeuw et al., 2021).

Once SO_2 is oxidized and processed to optically active sulfate aerosol, limb-sounding instruments (e.g., SAGE I–III, Baumann et al., 2003; OSIRIS, Bourassa et al., 2012; OMPS, Kloss et al., 2021) and lidar instruments (e.g., CALIPSO, Vernier et al., 2011; CATS, Christian et al., 2019) are able to measure the spatial distribution and the altitude of the resulting aerosol plume. Detecting sulfate aerosols from traditional nadir-viewing instruments operating at visible wavelengths is difficult owing to the presence of underlying clouds. Absorbing aerosols can be detected using UV wavelengths, as is done for absorbing smoke aerosols (e.g., TROPOMI; Torres et al., 2020). Ground-based remote sensing instrumentation also provides essential validation for models in the form of lidar systems (e.g., Barnes and Hoffman, 1997; Chazette et al., 1995) and high-altitude sun-photometer sites such as Mauna Loa that are at a sufficiently remote location and at a sufficient altitude to be largely uninfluenced by tropospheric aerosols (e.g., Haywood et al., 2010). There are also a limited number of recent aerosol observations from routine long-haul flights of the IAGOS/CARIBIC network that are providing new insights into stratospheric aerosol evolution and modeling capabilities for both volcanic sulfate and biomass-burning smoke in the upper troposphere and lower stratosphere (e.g., Osborne et al., 2022). Balloon-borne measurements with optical particle counters yield additional high-quality stratospheric aerosol data that provide essential information on the microphysical evolution of aerosol size distributions (e.g., Deshler et al., 2003).

6A.2 VOLCANIC EFFECTS ON RADIATIVE FORCING AND TEMPERATURE

Since 1978, satellite remote sensing has provided measurements of volcanic SO_2 emissions from over 1000 volcanic eruptions, yielding an average SO_2 emissions rate from explosive and effusive eruptions of 3 Tg SO_2 yr^{-1} between 1978 and 2021, of which an average of about 1 Tg SO_2 yr^{-1} is injected into the stratosphere (Carn et al., 2016, 2017). However, there is significant interannual variability in the emissions into the stratosphere, with some years receiving negligible SO_2 from explosive volcanic eruptions and others having many times the longer-term mean annual injection rate. Between 2008 and 2019, small-magnitude eruptions such as those of Kasatochi in 2008 (Kravitz et al., 2010), Sarychev in 2009 (Haywood et al., 2010), and Raikoke in 2019 (Kloss et al., 2021; de Leeuw et al., 2021) have each injected around 1.5 Mt of SO_2 into the stratosphere.

The sudden increase in stratospheric sulfate aerosol mass and number concentration from volcanic SO_2 injections changes the size distribution of stratospheric aerosols and increases the aerosol SAD compared to volcanically quiescent periods. The latter largely explains heterogeneous chemistry-induced ozone changes, and the nature of the change in the aerosol bulk properties. In particular, the injected mass and particle size dictate the strength of the climate perturbations following eruptions (Pinto et al., 1989; Lacis et al., 1992; Timmreck et al., 2010). Compared to the volcanically quiescent period prior to the eruption, the eruption of Mount Pinatubo in 1991 caused a 60-fold increase in the stratospheric sulfate burden (McCormick et al., 1995), an increase in particle number concentrations of 2 orders of magnitude (Deshler et al., 2003), and a 40-fold increase in the SAD (Thomason et al., 1997). Satellite measurements of radiative fluxes after the 1991 Mount Pinatubo eruption show a peak monthly mean net top-of-atmosphere radiative flux anomaly between 60°S and 60°N of around –3 W m^{-2}. For context, by design the medium SAI GeoMIP G6sulfur simulations exert a continuous radiative forcing of approximately –4 W m^{-2} at the end of the 21st century (Kravitz et al., 2015). Measurements from the period of the Mount Pinatubo eruption have been used to test global model simulations, revealing reasonable model performance (Minnis et al., 1993; Mills et al., 2017; Schmidt et al., 2018). The relationship between the mass of SO_2 emitted and the resulting climate effect are nonlinear (Pinto et al., 1989; Timmreck et al., 2009) because of a combination of OH radical oxidation chemistry limiting H_2SO_4 vapor production (and thus sulfate aerosol burden) and an enhanced coagulation of numerous small particles leading to rapid shifts in the particle size distribution toward very large sizes. These findings predated similar findings from SAI climate intervention strategies (e.g., *Section 6.2.3.1*) and have been key to adjusting modeled emissions scenarios and strategies to minimize such impacts (e.g., *Section 6.2.3.2*).

Analysis of instrumental temperature records, for which low-frequency climate variations and the influence of El Niño-Southern Oscillation (ENSO) have been removed, suggest a maximum post-eruption global mean surface cooling of 0.2–0.3 K when averaged for the eruptions of Krakatau (1883), Santa Maria (1902), Katmai (1912), Agung (1963), El Chichón (1982), and Pinatubo (1991; Robock and Mao, 1995; Robock, 2000). The 1991 Mount Pinatubo and Cerro Hudson eruptions emitted approximately 10–15 Tg of SO_2 into the stratosphere, which resulted in a peak global mean near-surface cooling of ~0.3–0.5 K in mid-1992 (e.g., McCormick et al., 1995; Soden et al., 2002; Thompson and Solomon, 2009) and a warming of up to 3.5 K in the tropical stratosphere (Labitzke, 1994, Labitzke and McCormick, 1992). Note that the surface temperature response

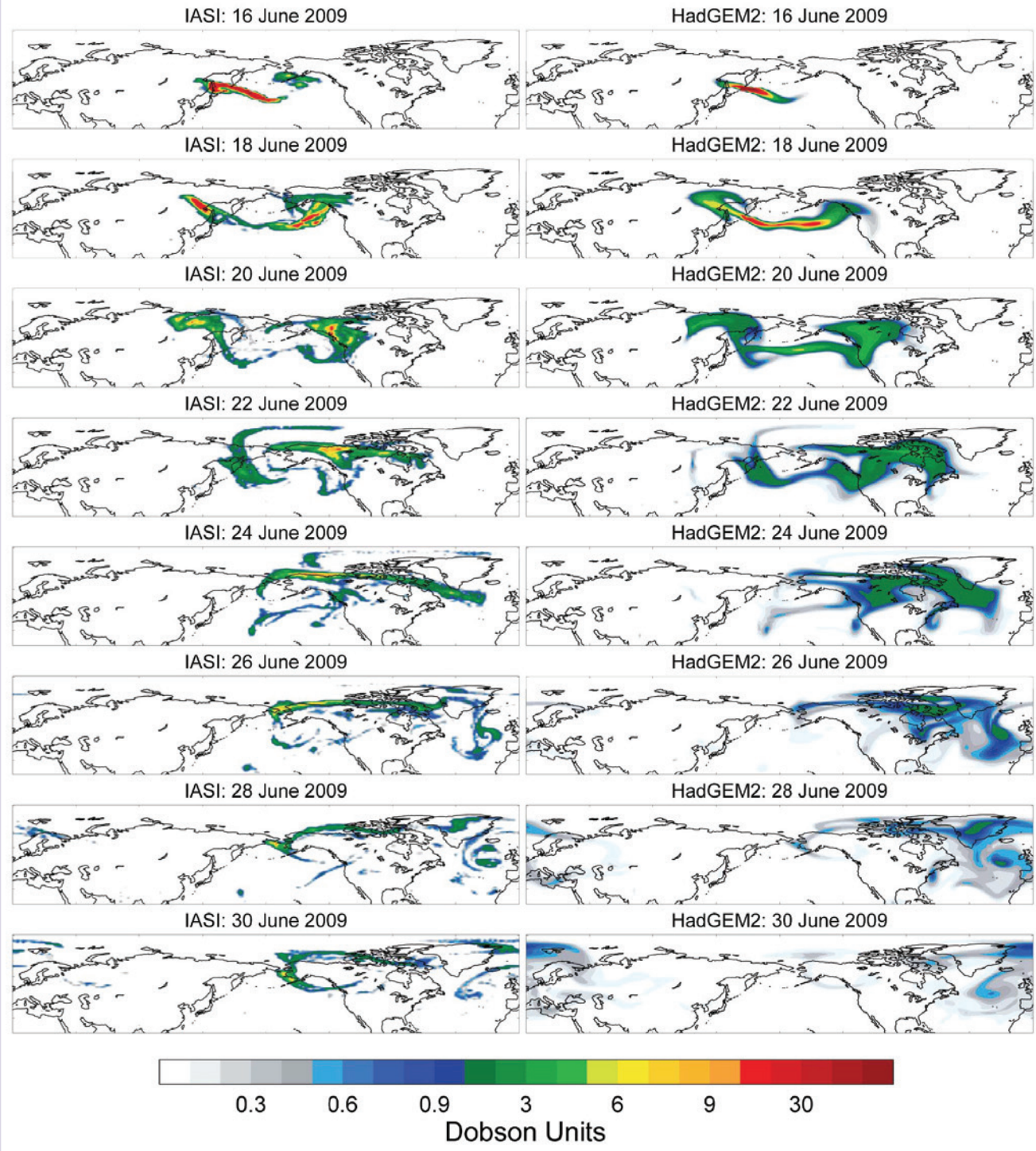

Figure 6A-1. Panels show the evolution of the plume of SO_2 from the Sarychev eruption. The column on the left represents observations from the IASI sensor, while that on the right represents model simulations from the HadGEM2 climate model. [From Haywood et al., 2010.]

was influenced by the strong El Niño event in 1991–1994 (e.g., Lehner et al., 2016) and other dynamical feedbacks (Soden et al., 2002). Typically, the surface temperature response over land is detectable for two to three years. Using SAI, continuous emissions of 8–16 Tg of SO_2 yr^{-1} would be required to cool the Earth by 1 K (*Section 6.2*); it is acknowledged that there are many differences in the atmospheric and climatic responses between pulse and continuous injections (e.g., Duan et al., 2019). The duration, magnitude, and spatial pattern of the surface temperature response following volcanic eruptions depends on eruption characteristics such as the mass of SO_2 emitted, eruption season and latitude (e.g., Marshall et al., 2020), and local meteorology (Jones et al., 2016b) and climatological conditions prior to the eruption (e.g., Robock and Mao, 1995). Instrumental records also show a warming of the North American and Eurasian continents by 2 K or more during the first or second winter after large explosive eruptions (Robock and Mao, 1992), which is consistent with a forced positive North Atlantic Oscillation (NAO) response, but the magnitude of any causal link and the driving mechanism is still debated (Polvani et al., 2019).

6A.3 VOLCANIC EFFECTS ON CLIMATE DYNAMICS

Radiative heating of the lowermost tropical stratosphere following tropical explosive eruptions leads to an increased meridional temperature gradient and enhanced upwelling in the tropical stratosphere, similar to what has been described for SAI applications. This leads to enhanced transport of ozone from the tropical stratosphere toward higher latitudes (Kinne et al., 1992; Tilmes et al., 2004) and a strengthening of the polar vortex (e.g., Bittner et al., 2016), which further enhances polar ozone loss.

Dynamical processes affecting ozone concentrations are intertwined with chemical processes in the same regions, and they thus potentially mask or enhance some of the chemical loss of ozone following an eruption. The QBO and ENSO phase contribute to year-to-year variability in stratospheric ozone concentrations and further complicate the attribution of individual processes to ozone loss (e.g., Telford et al., 2009). Changes in stratospheric ozone concentrations at mid-latitudes are closely linked to dynamical and radiative perturbations induced by volcanic eruptions in modeling studies (e.g., Telford et al., 2009; Aquila et al., 2013; Dhomse et al., 2014); this is similar to what has been found in SAI modeling studies. In addition, there are feedbacks between stratospheric ozone loss and stratospheric temperature variability in that stratospheric ozone loss results in less UV absorption, which in turn affects the aerosol heating rate (Kinne et al., 1992; Rosenfeld et al., 1997).

Volcanic eruptions can also provide guidance on the specific SAI deployment strategies and the expected impacts. Observations and climate models reveal that volcanic eruptions can cause reductions in global precipitation, with complex regional precipitation responses (e.g., Iles et al., 2013; Trenberth and Dai, 2007). Such a spin-down of the hydrological cycle is also observed in many SAI simulations (e.g., Kravitz et al., 2013). After the high-latitude eruption of Katmai (1912), where stratospheric AODs were enhanced in the Northern Hemisphere, models simulate a significant shift of rain-bearing clouds associated with the intertropical convergence zone (ITCZ) toward the south. Two consequences of this shift were observed historic minimum river flows in both the Nile and Niger Rivers (e.g., Oman et al., 2006) and the lack of any Atlantic hurricanes (Evan, 2012). Such features appear to be due to the asymmetry of hemispheric stratospheric AODs, and this appears to be well represented in model simulations of both volcanic eruptions and SAI (Haywood et al., 2013; Jones et al., 2017). Recognition of these features has contributed to efforts to minimize inter-hemispheric temperature gradients in SAI strategies (e.g., MacMartin et al., 2014a; **Box 6-2**).

SAI-induced heating in the lower tropical stratosphere will have a long-term effect on stratospheric dynamics (Aquila et al., 2014) that does not recover after a few years, as it does for volcanic eruptions (Brenna et al., 2021). Effects on the QBO, stratospheric water vapor concentrations, and ozone will therefore differ in magnitude and longevity between SAI and volcanic eruptions. For example, Aquila et al. (2014) and Jones et al. (2022) suggest that the QBO phase could be severely disrupted and potentially locked into the westerly phase by SAI under medium SAI scenarios, although specific SAI strategies outside of the immediate equatorial region have been developed to mitigate that effect (Richter et al., 2017, 2018; Kravitz et al., 2019; Franke et al., 2021). In models, a positive phase of the NAO and associated continental winter warming and increased precipitation over northern Europe is a robust signal in simulations of SAI (Banerjee et al., 2021; Jones et al., 2021, 2022) but not in simulations of volcanic eruptions (e.g., Polvani et al., 2019). Continuous decadal-scale injections of sulfur will lead to a continuous reduction in surface warming (or to surface cooling, depending on the SAI application), albeit smaller in magnitude than for pulsed volcanic SO_2 emissions (Duan et al., 2019), while the effects of volcanic eruptions are shorter lived.

6A.4 PYROCONVECTION EVENTS AS NATURAL ANALOGUES FOR SAI

Extreme wildfires can generate deep thunderstorms (or pyroCbs), which can inject large amounts of particles, water vapor, and other biomass-burning emissions into the stratosphere (Fromm et al., 2010). The pyroCb biomass-burning particles, which consist of organic carbon, inorganic components, and a significant fraction of black carbon (e.g., Wu et al., 2021), are transported within the stratosphere and have a residence time of months. For example, the stratospheric e-folding residence time of the 2017 Pacific Northwest (wildfire) Event (PNE) was about five months (Yu et al., 2019). The resulting particles can scatter sunlight back to space, absorb solar and terrestrial radiation, and impact the chemical and radiative equilibrium in the stratosphere. While biomass-burning aerosols have not been suggested as candidate SAI particles because of their strong radiative heating (Kravitz et al., 2012; Haywood et al., 2022), observations of pyroCb aerosols are useful for model evaluation purposes. However, the strong radiative heating could potentially be used to loft aerosols from the mid-troposphere to the stratosphere. Gao et al. (2021) estimate that black carbon with a concentration of 10 microgram per cubic meter could be sufficient to loft SAI material from 13.5 km to ~20 km, utilizing solar absorption and the resulting lofting to reach the needed altitudes.

A number of pyroCb events have been identified and analyzed using satellite measurements since the year 2000 (Fromm et al., 2010). Among them, the 2017 PNE (Peterson et al., 2018; Khaykin et al., 2018; Yu et al., 2019; Torres et al., 2020) and the

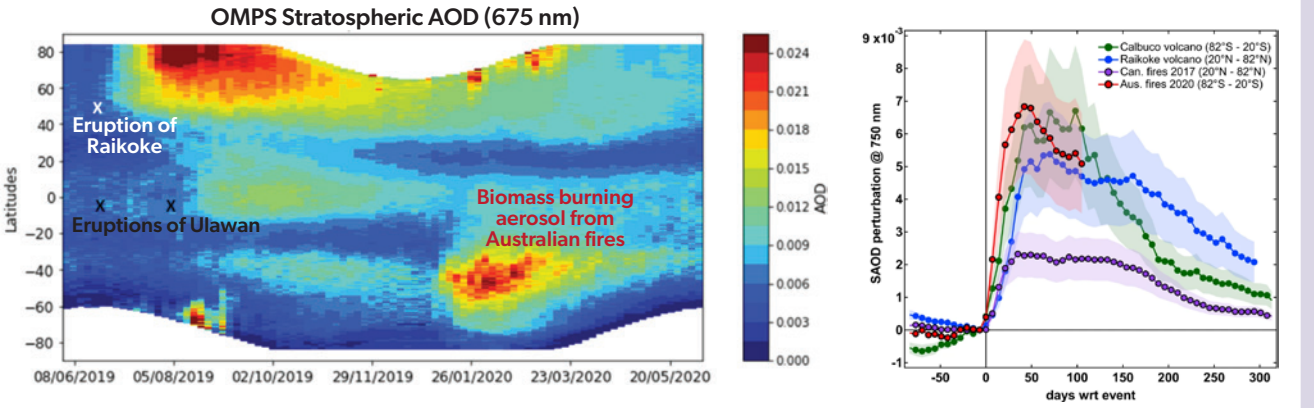

Figure 6A-2. *(left)* Stratospheric AODs from the Southeast Australia fires, compared to those from Raikoke and Ulawan eruptions (adapted from Kloss et al., 2021). *(right)* Stratospheric AOD from the 2017 PNE and 2019–2020 Australian fires, compared to that from the 2015 Calbuco and 2019 Raikoke volcanoes. [Adapted from Khaykin et al., 2020.]

2019–2020 Southeast Australia New Year (SEANY; Khaykin et al., 2020; Kablick et al., 2020; Kloss et al., 2021; Schwartz et al., 2020; Yu et al., 2021; Peterson et al., 2021; Rieger et al., 2021; Damany-Pearce et al., 2022) events injected the largest amounts of biomass-burning aerosols into the stratosphere. The estimated mass injected into the stratosphere by the PNE was 0.1–0.3 Tg (Peterson et al., 2018). Estimates of the injected mass for the SEANY event range from 0.2 to 3.1 Tg (Khaykin et al., 2020; Yu et al., 2021; Hirsch and Koren, 2020), which is comparable to the ~1.5 Tg SO_2 emissions from the Kasatochi volcano (2008) in the Aleutian Islands and the emissions from the Sarychev (2009) and Raikoke (2019) volcanic eruptions in the Kuril Islands. The perturbation of the global mean SAOD at mid-visible wavelengths by the SEANY biomass-burning particles is close to that from the Calbuco (2015) and Raikoke volcano eruptions (**Figure 6A-2**). In each of these cases, the stratospheric AOD perturbation takes over one year to return to background values (Khaykin et al., 2020; Damany-Pearce et al., 2022).

The number and scope of pyroCb modeling studies are relatively limited compared to those for volcanic eruptions. Modeling studies (Christan et al., 2019; Yu et al., 2019; Das et al., 2021; Yu et al., 2021; Osborne et al., 2022) show that the spatial-temporal distributions of the pyroCb biomass-burning particles can generally be well simulated by operational atmospheric dispersion and climate models. These model simulations assume emissions rates and use profiles derived from satellite retrievals as constraints and have been validated using downstream satellite retrievals, surface-based lidar observations, and in situ aircraft observations (e.g., Osborne et al., 2022). However, the present pyroCb modeling is far from sufficient for a comprehensive understanding of key processes and impacts, based on the following shortcomings.

Remote sensing measurements show that significant amounts of water vapor, carbon monoxide, and acetonitrile were also lofted into the stratosphere during the SEANY pyroCb biomass-burning plumes (Schwartz et al., 2020; Khaykin et al., 2020). Airborne and balloon-borne in situ measurements of the pyroCb biomass-burning plume composition are necessary to quantify the emissions, but these measurements are extremely rare at present. As a result, the composition and chemical and physical properties of the plume and the biomass-burning aerosol remain unclear, which prevents a comprehensive understanding of the climate implications of the pyroCb biomass-burning particles.

Wildfire-generated pyroconvection transports large amounts of aerosols and other biomass-burning emissions into the upper troposphere in hours (Peterson et al., 2018). In models, this process occurs at the sub-grid scale; convection and thunderstorms are usually too small to be fully captured by climate models, which typically have a spatial resolution of about 100 kilometers and a temporal resolution of about 1 hour. For this reason, in climate models (Christan et al., 2019; Yu et al., 2019; Das et al., 2021; Yu et al., 2021) pyroCb biomass-burning particles are injected directly into the upper troposphere, and the injection height and area are approximated using observations from remote sensing a day or so after the fire starts.

Measurements and modeling studies suggest that the pyroCb smoke may significantly affect stratospheric ozone through similar heterogeneous reactions on the surface of the volcanic or SAI sulfate aerosols (*Sections 3.2.1.3* and *4.2.3.2*). Recent studies have implicated the SEANY fires and the resulting biomass-burning aerosol particles as a potential contributor to the anomalously deep and long-lived ozone hole that occurred in 2020 (e.g., Rieger et al., 2021; Solomon et al., 2022; Yook et al., 2022; Damany-Pearce et al., 2022). Due to insufficient knowledge on the heterogeneous reaction rate on the surface of organic aerosols, especially those (partly) coated with sulfuric acid, the estimated ozone loss caused by the pyroCb biomass-burning particles is highly uncertain.

To reproduce these pyroCb events, climate models would need to include interactive aerosol-radiation feedbacks, sufficient stratospheric chemistry (e.g., heterogeneous chemistry, halogen chemistry, etc., which have not been studied for stratospheric biomass-burning aerosols), and accurate representation of the stratospheric background and volcanic aerosols. The injected particles can coagulate and grow in the stratosphere for months, and the effective size of the particles can evolve. Consequently, the size-evolving related aerosol microphysics needs to be well represented in climate models.

REFERENCES

Angell, J.K., and J. Korshover, Comparison of tropospheric temperatures following Agung and El Chichón volcanic eruptions, ***Mon. Weather Rev.***, ***112*** (7), 1457–1463, doi:10.1175/1520-0493(1984)112<1457:COTTFA>2.0.CO;2, 1984.

Aquila, V., L.D. Oman, R. Stolarski, A.R. Douglass, and P.A. Newman, The response of ozone and nitrogen dioxide to the eruption of Mount Pinatubo at southern and northern midlatitudes, ***J. Atmos. Sci.***, ***70*** (3), 894–900, doi:10.1175/JAS-D-12-0143.1, 2013.

Aquila, V., C.I. Garfinkel, P.A. Newman, L.D. Oman, and D.W. Waugh, Modifications of the quasi-biennial oscillation by a geoengineering perturbation of the stratospheric aerosol layer, ***Geophys. Res. Lett.***, ***41*** (5), 1738–1744, doi:10.1002/2013GL058818, 2014.

Arfeuille, F., D. Weisenstein, H. Mack, E. Rozanov, T. Peter, and S. Brönnimann, Volcanic forcing for climate modeling: a new microphysics-based data set covering years 1600–present, ***Clim. Past***, ***10*** (1), 359–375, doi:10.5194/cp-10-359-2014, 2014.

Bala, G., P.B. Duffy, and K.E. Taylor, Impact of geoengineering schemes on the global hydrological cycle, ***Proc. Natl. Acad. Sci.***, ***105*** (22), 7664–7669, doi:10.1073/pnas.0711648105, 2008.

Bamber, J.L., M. Oppenheimer, R.E. Kopp, W.P. Aspinall, and R.M. Cooke, Ice sheet contributions to future sea-level rise from structured expert judgment, ***Proc. Natl. Acad. Sci.***, ***116*** (23), 11195, doi:10.1073/pnas.1817205116, 2019.

Banerjee, A., A.H. Butler, L.M. Polvani, A. Robock, I.R. Simpson, and L. Sun, Robust winter warming over Eurasia under stratospheric sulfate geoengineering–the role of stratospheric dynamics, ***Atmos. Chem. Phys.***, ***21*** (9), 6985–6997, doi:10.5194/acp-21-6985-2021, 2021.

Barnes, J.E., and D.J. Hofmann, Lidar measurements of stratospheric aerosol over Mauna Loa Observatory, ***Geophys. Res. Lett.***, ***24*** (15), 1923–1926, doi:10.1029/97GL01943, 1997.

Bauman, J.J., P.B. Russell, M.A. Geller, and P. Hamill, A stratospheric aerosol climatology from SAGE II and CLAES measurements: 2. Results and comparisons, 1984–1999, ***J. Geophys. Res. Atmos.***, ***108*** (D13), doi:10.1029/2002JD002993, 2003.

Bekki, S., J.A. Pyle, W. Zhong, R. Toumi, J.D. Haigh, and D.M. Pyle, The role of microphysical and chemical processes in prolonging the climate forcing of the Toba eruption, ***Geophys. Res. Lett.***, ***23*** (19), 2669–2672, doi:10.1029/96GL02088, 1996.

Benduhn, F., J. Schallock, and M.G. Lawrence, Early growth dynamical implications for the steerability of stratospheric solar radiation management via sulfur aerosol particles, ***Geophys. Res. Lett.***, ***43***, 9956–9963, doi:10.1002/2016GL070701, 2016.

Berthet, G., F. Jégou, V. Catoire, G. Krysztofiak, J.B. Renard, A.E. Bourassa, D.A. Degenstein, C. Brogniez, M. Dorf, S. Kreycy, and K. Pfeilsticker, Impact of a moderate volcanic eruption on chemistry in the lower stratosphere: balloon-borne observations and model calculations. ***Atmos Chem and Phys***, ***17***(3), pp.2229-2253, 2017.

Bhowmick, M., S.K. Mishra, B. Kravitz, S. Sahany, and P. Salunke, Response of the Indian summer monsoon to global warming, solar geoengineering and its termination, ***Sci. Rep.***, ***11*** (1), 9791, doi:10.1038/s41598-021-89249-6, 2021.

Bittner, M., H. Schmidt, C. Timmreck, and F. Sienz, Using a large ensemble of simulations to assess the Northern Hemisphere stratospheric dynamical response to tropical volcanic eruptions and its uncertainty, ***Geophys. Res. Lett.***, ***43*** (17), 9324–9332, doi:10.1002/2016GL070587, 2016.

Bourassa, A.E., L.A. Rieger, N.D. Lloyd, and D.A. Degenstein, Odin-OSIRIS stratospheric aerosol data product and SAGE III intercomparison, ***Atmos. Chem. Phys.***, ***12*** (1), 605–614, doi:10.5194/acp-12-605-2012, 2012.

Brenna, H., S. Kutterolf, M.J. Mills, U. Niemeier, C. Timmreck, and K. Krüger, Decadal disruption of the QBO by tropical volcanic supereruptions, ***Geophys. Res. Lett.***, ***48*** (5), e2020GL089687, doi:10.1029/2020GL089687, 2021.

Budyko, M.I., Izmeniya Klimata. Gidrometeoizdat, also published as: Budyko, M.I. 1977 Climatic changes (transl. Izmeniia Klimata Leningrad: Gidrometeoizdat, 1974), ***American Geophysical Union***, Washington, DC, 1974.

Butchart, N., The Brewer-Dobson circulation, ***Rev. Geophys.***, ***52*** (2),157–184, doi:10.1002/2013RG000448, 2014.

Butler, A.H., J.S. Daniel, R.W. Portmann, A.R. Ravishankara, P.J. Young, D.W. Fahey, and K.H. Rosenlof, Diverse policy implications for future ozone and surface UV in a changing climate, ***Environ. Res. Lett.***, ***11*** (6), 064017, doi:10.1088/1748-9326/11/6/064017, 2016.

Caldeira, K., and L. Wood, Global and Arctic climate engineering: numerical model studies, ***Philos. Trans. Royal Soc. A: Math. Phys. Eng. Sci.***, ***366*** (1882), 4039–4056, doi:10.1098/rsta.2008.0132, 2008.

Canadell, J.G., P.M.S. Monteiro, M.H. Costa, L. Cotrim da Cunha, P.M. Cox, A.V. Eliseev, S., Henson, M. Ishii, S. Jaccard, C. Koven, A. Lohila, P.K. Patra, S. Piao, J. Rogelj, S. Syampungani, S. Zaehle, and K. Zickfeld, Global Carbon and other Biogeochemical Cycles and Feedbacks, Chapter 5, in ***Climate Change 2021: The Physical Science Basis. Contribution of Working Group I to the Sixth Assessment Report of the Intergovernmental Panel on Climate Change***, edited by V. Masson-Delmotte, P. Zhai, A. Pirani, S. L. Connors, C. Péan, S. Berger, N. Caud, Y. Chen, L. Goldfarb, M. I. Gomis, M. Huang, K. Leitzell, E. Lonnoy, J.B.R. Matthews, T. K. Maycock, T. Waterfield, O. Yelekçi, R. Yu and B. Zhou, 144 pp., Cambridge University Press, Cambridge, United Kingdom, doi:10.1017/9781009157896.007, 2021.

Cao, L., L. Duan, G. Bala, and K. Caldeira, Simulated climate and terrestrial biosphere response to three radiation geoengineering schemes, in ***AGU Fall Meeting Abstracts***, Vol. 2018, GC31H-1351 pp., 2018.

Carn, S.A., L. Clarisse, and A.J. Prata, A.J., Multi-decadal satellite measurements of global volcanic degassing. ***Journal of Volcanology and Geothermal Research***, ***311***, pp.99-134, 2016.

Carn, S.A., V.E. Fioletov, C.A. McLinden, C. Li, and N.A. Krotkov, A decade of global volcanic SO2 emissions measured from space. ***Scientific reports***, ***7***(1), pp.1-12, 2017.

Chazette, P., C. David, J. Lefrère, S. Godin, J. Pelon, and G. Mégie, Comparative lidar study of the optical, geometrical, and dynamical properties of stratospheric post-volcanic aerosols, following the eruptions of El Chichon and Mount Pinatubo, ***J. Geophys. Res. Atmos.***, ***100*** (D11), 23,195–23,207, doi:10.1029/95JD02268, 1995.

Christian, K., J. Wang, C. Ge, D. Peterson, E. Hyer, J. Yorks, and M. McGill, Radiative forcing and stratospheric warming of pyrocumulonimbus smoke aerosols: First modeling results with multisensor (EPIC, CALIPSO, and CATS) views from space, ***Geophys. Res. Lett.***, ***46*** (16), 10,061–10,071, doi:10.1029/2019GL082360, 2019.

Christidis, N., G.S. Jones, and P.A. Stott, Dramatically increasing chance of extremely hot summers since the 2003 European heatwave, ***Nat. Clim. Change***, ***5*** (1), 46–50, doi:10.1038/nclimate2468, 2015.

Clarisse, L., D. Hurtmans, C. Clerbaux, J. Hadji-Lazaro, Y. Ngadi, and P.-F. Coheur, Retrieval of sulphur dioxide from the infrared atmospheric sounding interferometer (IASI), ***Atmos. Meas. Tech.***, ***5*** (3), 581–594, doi:10.5194/amt-5-581-2012, 2012.

Clyne M, Lamarque JF, Mills MJ, Khodri M, Ball W, Bekki S, Dhomse SS, Lebas N, Mann G, Marshall L, Niemeier U. Model physics and chemistry causing intermodel disagreement within the VolMIP-Tambora Interactive Stratospheric Aerosol ensemble. Atmos. Chem. Phys., 21, 3317–3343, https://doi.org/10.5194/acp-21-3317-2021, 2021.

Crutzen, P.J., Upper limits on atmospheric ozone reductions following increased application of fixed nitrogen to the soil, ***Geophys. Res. Lett.***, ***3*** (3), 169–172, doi:10.1029/GL003i003p00169, 1976.

Crutzen, P.J., Albedo enhancement by stratospheric sulfur injections: a contribution to resolve a policy dilemma?, ***Clim. Change***, ***77*** (3-4), 211, doi:10.1007/s10584-006-9101-y, 2006.

Curry, C.L., J. Sillmann, D. Bronaugh, K. Alterskjær, J.N.S. Cole, B. Kravitz., J.E. Kristjánsson, H. Muri, U. Niemeier, A. Robock, and S. Tilmes, A multi-model examination of climate extremes in an idealized geoengineering experiment, ***J. Geophys. Res. Atmos.***, ***119*** (7), 3900–3923, doi:10.1002/2013JD020648, 2014.

Cziczo, D.J., M.J. Wolf, B. Gasparini, S. Münch, and U. Lohmann, Unanticipated side

effects of stratospheric albedo modification proposals due to aerosol composition and phase, ***Sci. Rep.***, ***9*** (1), 1–7, doi:10.1038/s41598-019-53595-3, 2019.

Dai, Z., D.K. Weisenstein, F.N. Keutsch, and D.W. Keith, Experimental reaction rates constrain estimates of ozone response to calcium carbonate geoengineering, ***Commun. Earth. Environ.***, ***1*** (1), 1–9, doi:10.1038/s43247-020-00058-7, 2020.

Danilin, M.Y., J.M. Rodriguez, W. Hu, M.K. Ko, D.K. Weisenstein, J.B. Kumer, J.L. Mergenthaler, J.M. Russell III, M. Koike, G.K. Yue, and N.B. Jones, Nitrogen species in the post-Pinatubo stratosphere: Model analysis utilizing UARS measurements, ***J. Geophys. Res. Atmos.***, ***104*** (D7), 8247–8262, doi:10.1029/1999JD900024, 1999.

Damany-Pearce, L., B.T. Johnson, A.F. Wells, M.J. Osborne, J. Allan, C. Belcher, J.M. Haywood, Australian wildfires cause the largest stratospheric warming since Pinatubo and extends the lifetime of the Antarctic ozone hole, Scientific Reports, DOI: 10.1038/s41598-022-15794-3, 2022.

Das, S., P.R. Colarco, L.D. Oman, G. Taha, and O. Torres, The long-term transport and radiative impacts of the 2017 British Columbia pyrocumulonimbus smoke aerosols in the stratosphere, ***Atmos. Chem. Phys.***, ***21***, 12,069–12,090, doi:10.5194/acp-21-12069-2021, 2021.

Davidson, P., C. Burgoyne, H. Hunt, and M. Causier, Lifting options for stratospheric aerosol geoengineering: advantages of tethered balloon systems, ***Philos. Trans. Royal Soc. A: Math. Phys. Eng. Sci.***, ***370*** (1974), 4263–4300, doi:10.1098/rsta.2011.0639, 2012.

de Leeuw, J., A. Schmidt, C.S. Witham, N. Theys, I.A. Taylor, R.G. Grainger, R.J. Pope, J. Haywood, M. Osborne, and N.I. Kristiansen, The 2019 Raikoke volcanic eruption: Part 1 Dispersion model simulations and satellite retrievals of volcanic sulfur dioxide, ***Atmos. Chem. Phys.***, ***21*** (14), 10,851–10,879, doi:10.5194/acp-2020-889, 2021.

Deshler, T., M.E. Hervig, D.J. Hofmann, J.M. Rosen, and J.B. Liley, Thirty years of in situ stratospheric aerosol size distribution measurements from Laramie, Wyoming (41 N), using balloon-borne instruments, ***J. Geophys. Res. Atmos.***, ***108*** (D5), doi:10.1029/2002JD002514, 2003.

Deshler, T., B. Luo, M. Kovilakam, T. Peter, and L.E. Kalnajs, Retrieval of aerosol size distributions from in situ particle counter measurements: Instrument counting efficiency and comparisons with satellite measurements, ***J. Geophys. Res. Atmos.***, ***124*** (9), 5058–5087, doi:1029/2018JD029558, 2019.

Dhomse, S.S., K.M. Emmerson, G.W. Mann, N. Bellouin, K.S. Carslaw, M.P. Chipperfield, R. Hommel, N.L. Abraham, P. Telford, P. Braesicke, M. Dalvi, C.E. Johnson, F. O'Connor, O. Morgenstern, J.A. Pyle, T. Deshler, J.M. Zawodny, and L.W. Thomason., Aerosol microphysics simulations of the Mt. Pinatubo eruption with the UM-UKCA composition-climate model, ***Atmos. Chem. Phys.***, ***14*** (20), 11,221–11,246, doi:10.5194/acp-14-11221-2014, 2014.

Doiron, S.D., G.J. Bluth, C.C. Schnetzler, A.J. Krueger, and L.S. Walter, Transport of Cerro Hudson SO_2 clouds, ***Eos***, ***72*** (45), 489–498, doi:10.1029/90EO00354, 1991.

Drdla, K., and R. Müller, Temperature thresholds for chlorine activation and ozone loss in the polar stratosphere, ***Ann. Geophys.***, ***30*** (7), 1055–1073, doi:10.5194/angeo-30-1055-2012, 2012.

Driscoll, S., A. Bozzo, L.J. Gray, A. Robock, and G. Stenchikov, Coupled Model Intercomparison Project 5 (CMIP5) simulations of climate following volcanic eruptions, ***J. Geophys. Res. Atmos.***, ***117*** (D17), doi:10.1029/2012JD017607, 2012.

Duan, L., L. Cao, G. Bala, and K. Caldeira, Climate response to pulse versus sustained stratospheric aerosol forcing, ***Geophys. Res. Lett.***, ***46***, 8976–8984, doi:10.1029/2019GL083701, 2019.

Dykema, J.D., D.W. Keith, and F.N. Keutch, Improved aerosol radiative properties as a foundation for solar geoengineering risk assessment, ***Geophys. Res. Lett.***, ***43***, 7758–7766, doi:10.1002/2016GL069258, 2016.

Eastham, S.D., D.K. Weisenstein, D.W. Keith, and S.R. Barrett, Quantifying the impact of sulfate geoengineering on mortality from air quality and UV-B exposure, ***Atmos. Environ.***, ***187***, 424–434, doi:10.1016/j.atmosenv.2018.05.047, 2018.

Eastham, S., S. Doherty, D. Keith, J.H. Richter, and L. Xia, Improving models for solar climate intervention research, ***Eos***, ***102***, doi:10.1029/2021EO156087, 2021.

English, J.M., O.B. Toon, and M.J. Mills, Microphysical simulations of sulfur burdens from stratospheric sulfur geoengineering, ***Atmos. Chem. Phys.***, ***12*** (10), 4775–4793, doi:10.5194/acp-12-4775-2012, 2012.

English, J.M., O.B. Toon, and M.J. Mills, Microphysical simulations of large volcanic eruptions: Pinatubo and Toba, ***J. Geophys. Res. Atmos.***, ***118*** (4), 1880–1895, doi:10.1002/jgrd.50196, 2013.

Evan, A.T., Atlantic hurricane activity following two major volcanic eruptions. ***Journal of Geophysical Research: Atmospheres***, ***117***(D6), 2012.

Fahey, D.H., S.R. Kawa, E.L. Woodbridge, P. Tin, J.C. Wilson, H.H. Jonsson, J.E. Dye, D. Baumgardner, S. Borrmann, D.W. Toohey, L.M. Avallone, M.H. Proffitt, J. Margitan, M. Loewenstein, J.R. Podolske, R.J. Salawitch, S.C. Wofsy, M.K.W. Ko, D.E. Anderson, M.R. Schoeber, and K.R. Chan, ***In situ*** measurements constraining the role of sulphate aerosols in mid-latitude ozone depletion, ***Nature***, ***363*** (6429), 509–514, doi:10.1038/363509a0, 1993.

Fan, Y., J. Tjiputra, H. Muri, D. Lombardozzi, C.E. Park, S. Wu, and D. Keith, Solar geoengineering can alleviate climate change pressures on crop yields, ***Nat. Food***, ***2*** (5), 373–381, doi:10.1038/s43016-021-00278-w, 2021.

Fasullo, J.T., S. Tilmes, J.H. Richter, B. Kravitz, D.G. MacMartin, M.J. Mills, and I.R. Simpson, Persistent polar ocean warming in a strategically geoengineered climate, ***Nature Geosci.***, ***11*** (12), 910–914, doi:10.1038/s41561-018-0249-7, 2018.

Ferraro, A.J., E.J. Highwood, and A.J. Charlton-Perez, Stratospheric heating by potential geoengineering aerosols, ***Geophys. Res. Lett.***, ***38*** (24), doi:10.1029/2011GL049761, 2011.

Ferraro, A. J., E.J. Highwood, and A. J. Charlton-Perez, Correction to "Stratospheric heating by potential geoengineering aerosols," Geophys. Res. Lett.,39, L10808, doi:10.1029/2012GL052175, 2012.

Ferraro, A.J., E.J. Highwood, and A.J. Charlton-Perez, Weakened tropical circulation and reduced precipitation in response to geoengineering, ***Environ. Res. Lett.***, ***9*** (1), 014001, doi:10.1088/1748-9326/9/1/014001, 2014.

Ferraro, A.J., A.J. Charlton-Perez, and E.J. Highwood, Stratospheric dynamics and midlatitude jets under geoengineering with space mirrors and sulfate and titania aerosols, ***J. Geophys. Res. Atmos.***, ***120*** (2), 414–429, doi:10.1002/2014JD022734, 2015.

Franke, H., U. Niemeier, and D. Visioni, Differences in the QBO response to stratospheric aerosol modification depending on injection strategy and species, ***Atmos. Chem. Phys.***, ***21*** (11), 8615–8635, doi:10.5194/acp-21-8615-2021, 2021.

Frith, S.M., R.S. Stolarski, N.A. Kramarova, and R.D. McPeters, Estimating uncertainties in the SBUV Version 8.6 merged profile ozone data set, ***Atmos. Chem. Phys.***, ***17*** (23), 14,695–14,707, doi:10.5194/acp-17-14695-2017, 2017.

Fromm, M.D., D.T. Lindsey, R. Servranckx, G. Yue, T. Trickl, R. Sica, P. Doucet, and S. Godin-Beekmann, The untold story of pyrocumulonimbus, ***Bull. Amer. Meteor. Soc.***, ***91*** (9), 1193–1210, doi:10.1175/2010BAMS3004.1, 2010.

Fuss, S., J.G. Canadell, P. Ciais, R.B. Jackson, C.D. Jones, A. Lyngfelt, G.P. Peters, and D.P. Van Vuuren, Moving toward net-zero emissions requires new alliances for carbon dioxide removal, ***One Earth***, ***3*** (2), 145–149, doi:10.1016/j.oneear.2020.08.002, 2020.

Fyfe, J.C., J.N.S. Cole, V.K. Arora, and J.F. Scinocca, Biogeochemical carbon coupling influences global precipitation in geoengineering experiments, ***Geophys. Res. Lett.***, ***40*** (3), 651–655, doi:10.1002/grl.50166, 2013.

Gao, R.S., K.H. Rosenlof, B. Kärcher, S. Tilmes, O.B. Toon, C. Maloney, and P. Yu, Toward practical stratospheric aerosol albedo modification: Solar-powered lofting, ***Sci. Adv.***, ***7*** (20), doi:10.1126/sciadv.abe3416, 2021.

Gertler, C.G., P.A. O'Gorman, B. Kravitz, J.C. Moore, S.J. Phipps, and S. Watanabe, Weakening of the extratropical storm tracks in solar geoengineering scenarios, ***Geophys. Res. Lett.***, ***47*** (11), e2020GL087348, doi:10.1029/2020GL087348, 2020.

Glienke, S., P.J. Irvine, and M.G. Lawrence, The impact of geoengineering on vegetation in experiment G1 of the GeoMIP, ***J. Geophys. Res. Atmos.***, ***120*** (19), 10,196–10,213, doi:10.1002/2015JD024202, 2015.

Govindasamy, B., and K. Caldeira, Geoengineering Earth's radiation balance to mitigate CO2-induced climate change, ***Geophys. Res. Lett.***, ***27*** (14), 2141–2144, doi:10.1029/1999GL006086, 2000.

Grant, W.B., J. Fishman, E.V. Browell, V.G. Brackett, D. Nganga, A. Minga, B. Cros, R.E. Veiga, C.F. Butler, M.A. Fenn, and G.D. Nowicki, Observations of reduced ozone concentrations in the tropical stratosphere after the eruption of Mount Pinatubo, ***Geophys. Res. Lett.***, ***19*** (11), 1109–1112, doi:10.1029/92GL01153, 1992.

Gregory, J.M., and T. Andrews, Variation in climate sensitivity and feedback parameters during the historical period, ***Geophys. Res. Lett.***, ***43*** (8), 3911–3920, doi:10.1002/2016GL068406, 2016.

Hamilton, C., ***Earthmasters: the dawn of the age of climate engineering***, Yale University Press, 2013.

Hansen, J., A. Lacis, R. Ruedy, and M. Sato, Potential climate impact of Mount Pinatubo eruption, ***Geophys. Res. Lett.***, ***19*** (2), 215–218, doi:10.1029/91GL02788, 1992.

Hansen, J., M. Sato, L. Nazarenko, R. Ruedy, A. Lacis, D. Koch, I. Tegen, T. Hall, D. Shindell, B. Santer, and P.Stone, Climate forcings in Goddard Institute for space studies SI2000 simulations. ***Journal of Geophysical Research: Atmospheres***, ***107***(D18), pp.ACL-2, 2002.

Hawcroft, M., J.M. Haywood, M. Collins, A. Jones, A.C. Jones, and G. Stephens, Southern Ocean albedo, inter-hemispheric energy transports and the double ITCZ: Global impacts of biases in a coupled model, ***Clim Dyn.***, ***48*** (7), 2279–2295, doi:10.1007/s00382-016-3205-5, 2017.

Haywood, J.M., A. Jones, L. Clarisse, A. Bourassa, J. Barnes, P. Telford, N. Bellouin, O. Boucher, P. Agnew, C. Clerbaux, and P. Coheur, Observations of the eruption of the Sarychev volcano and simulations using the HadGEM2 climate model, ***J. Geophys. Res. Atmos.***, ***115*** (D21), doi:10.1029/2010JD014447, 2010.

Haywood, J.M., A. Jones, N. Bellouin, and D. Stephenson, Asymmetric forcing from stratospheric aerosols impacts Sahelian rainfall, ***Nat. Clim. Change***, ***3*** (7), 660–665, doi:10.1038/nclimate1857, 2013.

Haywood, J.M., A. Jones, and G.S. Jones, The impact of volcanic eruptions in the period 2000–2013 on global mean temperature trends evaluated in the HadGEM2-ES climate model, ***Atmos. Sci. Lett.***, ***15*** (2), 92–96, doi:10.1002/asl2.471, 2014.

Haywood, J.M., A. Jones, B. Johnson, and W.M. Smith, Assessing the consequences of including aerosol absorption in potential stratospheric aerosol injection climate intervention strategies, ***Atmos. Chem. Phys.***, ***22*** (9), 6135–6150, doi:10.5194/acp-22-6135-2022, 2022.

Heckendorn, P., D. Weisenstein, S. Fueglistaler, B.P. Luo, E. Rozanov, M. Schraner, L.W. Thomason, and T. Peter, The impact of geoengineering aerosols on stratospheric temperature and ozone, ***Environ. Res. Lett., 4*** (4), 045108, doi:10.1088/1748-9326/4/4/045108, 2009.

Hendricks, J., E. Lippert, H. Petry, and A. Ebel, Heterogeneous reactions on and in sulfate aerosols: Implications for the chemistry of the midlatitude tropopause region, ***J. Geophys. Res. Atmos.***, ***104*** (D5), 5531–5550, doi:10.1029/1998JD100098, 1999.

Henry, M., and T.M. Merlis, Forcing dependence of atmospheric lapse rate changes dominates residual polar warming in solar radiation management climate scenarios, ***Geophys. Res. Lett.***, ***47*** (15), e2020GL087929, doi:10.1029/2020GL087929, 2020.

Hirsch, E., and I. Koren, Record-breaking aerosol levels explained by smoke injection into the stratosphere, ***Science, 371***, 1269–1274, doi:10.1126/science.abe1415, 2021.

Hofmann, D.J., and S. Solomon, Ozone destruction through heterogeneous chemistry following the eruption of El Chichon, ***J. Geophys. Res. Atmos.***, ***94*** (D4), 5029–5041, doi:10.1029/JD094iD04p05029, 1989.

Huang, Y., Y. Wang, and H. Huang, Stratospheric water vapor feedback disclosed by a locking experiment, ***Geophys. Res. Lett.***, ***47*** (12), e2020GL087987, doi:10.1029/2020GL087987, 2020.

Huneeus, N., O. Boucher, K. Alterskjaer, J.N. Cole, C.L. Curry, D. Ji, A. Jones, B. Kravitz, J.E. Kristjánsson, J.C. Moore, and H. Muri, Forcings and feedbacks in the GeoMIP ensemble for a reduction in solar irradiance and increase in CO2, ***J. Geophys. Res. Atmos.***, ***119*** (9), 5226–5239, doi:10.1002/2013JD021110, 2014.

Huynh, H.N., and V.F. McNeill, Heterogeneous reactivity of HCl on CaCO3 aerosols at stratospheric temperature, ***ACS Earth Space Chem.***, ***5*** (8), 1896–1901, doi:10.1021/acsearthspacechem.1c00151, 2021.

Hwang, Y.T., and D.M. Frierson, Link between the double-Intertropical Convergence Zone problem and cloud biases over the Southern Ocean, ***Proc. Natl. Acad. Sci.***, ***110*** (13), 4935–4940, doi:10.1073/pnas.1213302110, 2013.

Iles, C.E., G.C. Hegerl, A.P. Schurer, and X. Zhang, The effect of volcanic eruptions on global precipitation. ***Journal of Geophysical Research: Atmospheres***, ***118***(16), pp.8770-8786, 2013.

IPCC (Intergovenmental Panel on Climate Change), ***Global warming of 1.5°C. An IPCC Special Report on the impacts of global warming of 1.5°C above preindustrial levels and related global greenhouse gas emission pathways, in the context of strengthening the global response to the threat of climate change, sustainable development, and efforts to eradicate poverty***, edited by V. Masson-Delmotte, P. Zhai, H. O. Pörtner, D. Roberts, J. Skea, P.R. Shukla, A. Pirani, W. Moufouma-Okia, C. Péan, R. Pidcock, S. Connors, J. B. R. Matthews, Y. Chen, X. Zhou, M. I. Gomis, E. Lonnoy, T. Maycock, M. Tignor, and T. Waterfield, 630 pp., Cambridge University Press, Cambridge, United Kingdom, 2018.

IPCC (Intergovenmental Panel on Climate Change), ***Climate Change 2021: The Physical Science Basis. Contribution of Working Group I to the Sixth Assessment Report of the Intergovernmental Panel on Climate Change***, edited by V. Masson-Delmotte, P. Zhai, A. Pirani, S.L. Connors, C. Péan, S. Berger, N. Caud, Y. Chen, L. Goldfarb, M.I. Gomis, M. Huang, K. Leitzell, E. Lonnoy, J.B.R. Matthews, T.K. Maycock, T. Waterfield, O. Yelekçi, R. Yu, and B. Zhou, Cambridge University Press, Cambridge, United Kingdom, 2021.

IPCC (Intergovenmental Panel on Climate Change), ***Climate Change 2022: Mitigation of Climate Change. Contribution of Working Group III to the Sixth Assessment Report of the Intergovernmental Panel on Climate Change***, edited by P.R. Shukla, J. Skea, R. Slade, A. Al Khourdajie, R. van Diemen, D. McCollum, M. Pathak, S. Some, P. Vyas, R. Fradera, M. Belkacemi, A. Hasija, G. Lisboa, S. Luz, J. Malley, Cambridge University Press, Cambridge, United Kingdom and New York, NY, USA, doi:10.1017/9781009157926, 2022.

Irvine, P.J., B. Kravitz, M.G. Lawrence, D. Gerten, C. Caminade, S.N. Gosling, E.J. Hendy, B.T. Kassie, W.D. Kissling, H. Muri, A. Oschlies, and S.J. Smith, Towards a comprehensive climate impacts assessment of solar geoengineering, ***Earth's Future***, ***5*** (1), 93–106, doi:10.1002/2016EF000389, 2017.

Irvine, P.J., D.W. Keith, and J. Moore, Brief communication: Understanding solar geoengineering's potential to limit sea level rise requires attention from cryosphere experts, ***The Cryosphere***, ***12*** (7), 2501–2513, doi:10.5194/tc-12-2501-2018, 2018.

Irvine, P., K. Emanuel, J. He, L.W. Horowitz, G. Vecchi, and D. Keith, Halving warming with idealized solar geoengineering moderates key climate hazards, ***Nat. Clim. Change***, ***9*** (4), 295–299, doi:10.1038/s41558-019-0398-8, 2019.

Irvine, P.J., and D.W. Keith, Halving warming with stratospheric aerosol geoengineering moderates policy-relevant climate hazards, ***Environ. Res. Lett.***, ***15*** (4), 044011, doi:10.1088/1748-9326/ab76de, 2020.

Ji, D., S. Fang, C.L. Curry, H. Kashimura, S. Watanabe, J.N. Cole, A. Lenton, H. Muri, B. Kravitz, and J.C. Moore, Extreme temperature and precipitation response to solar dimming and stratospheric aerosol geoengineering, ***Atmos. Chem. Phys.***, ***18*** (14), 10,133–10,156, doi:10.5194/acp-18-10133-2018, 2018.

Jiang, J., L. Cao, D.G. MacMartin, I.R. Simpson, B. Kravitz, W. Cheng, D. Visioni, S. Tilmes, J.H. Richter, and M.J. Mills, Stratospheric sulfate aerosol geoengineering could alter the high-latitude seasonal cycle, ***Geophys. Res. Lett.***, ***46*** (23), 14,153–14,163, doi:10.1029/2019GL085758, 2019.

Johnston, P.V., R.L. McKenzie, J.G. Keys, and W.A. Matthews, Observations of depleted stratospheric NO2 following the Pinatubo volcanic eruption. ***Geophysical research letters***, ***19***(2), pp.211-213, 1992.

Jones, A., J.M. Haywood, O. Boucher, B. Kravitz, and A. Robock, Geoengineering by stratospheric SO2 injection: results from the Met Office HadGEM2 climate model and comparison with the Goddard Institute for Space Studies ModelE, ***Atmos. Chem. Phys.***, ***10*** (13), 5999–6006, doi:10.5194/acp-10-5999-201010, 74217434, 2010.

Jones, A., J.M. Haywood, and O. Boucher, A comparison of the climate impacts of geoengineering by stratospheric SO2 injection and by brightening of marine stratocumulus cloud, ***Atmos. Sci. Lett.***, ***12*** (2), 176–183, doi:10.1002/asl.291, 2011.

Jones, A., J.M. Haywood, K. Alterskjær, O. Boucher, J.N.S. Cole, C.L. Curry, P.J. Irvine, D. Ji, B. Kravitz, J.E. Kristjánsson, J.C. Moore, U. Niemeier, A. Robock, H. Schmidt, B. Singh, S. Tilmes, S. Watanabe, and J.-H. Yoon, The impact of abrupt suspension of solar radiation management (termination effect) in experiment G2 of the Geoengineering Model Intercomparison Project (GeoMIP), ***J. Geophys. Res. Atmos.***, ***118*** (17), 9743–9752, doi:10.1002/jgrd.50762, 2013.

Jones, A.C., J.M. Haywood, and A. Jones, Climatic impacts of stratospheric geoengineering with sulfate, black carbon and titania injection, ***Atmos. Chem. Phys.***, ***16*** (5), 2843–2862, doi:10.5194/acp-16-2843-2016, 2016a.

Jones, A.C., J.M. Haywood, A. Jones, and V. Aquila, Sensitivity of volcanic aerosol dispersion to meteorological conditions: A Pinatubo case study, ***J. Geophys. Res. Atmos.***, ***121*** (12), 6892–6908, doi:10.1002/2016JD025001, 2016b.

Jones, A.C., J.M. Haywood, N. Dunstone, K. Emanuel, M.K. Hawcroft, K.I. Hodges, and A. Jones, Impacts of hemispheric solar geoengineering on tropical cyclone frequency, ***Nat. Commun.***, ***8*** (1), 1–10, doi:10.1038/s41467-017-01606-0, 2017.

Jones, A.C., M.K. Hawcroft, J.M. Haywood, A. Jones, X. Guo, and J.C. Moore, Regional climate impacts of stabilizing global warming at 1.5 K using solar geoengineering, ***Earth's Future***, ***6*** (2), 230–251, doi:10.1002/2017EF000720, 2018.

Jones, A., J.M. Haywood, A.C. Jones, S. Tilmes, B. Kravitz, and A. Robock, North Atlantic Oscillation response in GeoMIP experiments G6solar and G6sulfur: why detailed modelling is needed for understanding regional implications of solar radiation management, ***Atmos. Chem. Phys.***, ***21*** (2), 1287–1304, doi:10.5194/acp-21-1287-2021, 2021.

Jones, A., J.M. Haywood, A.A. Scaife, O. Boucher, M. Henry, B. Kravitz, P. Nabat, U. Niemeier, R. Séférian, and D. Visioni, The impact of stratospheric aerosol intervention on the North Atlantic and Quasi-Biennial Oscillations in the Geoengineering Model Intercomparison Project (GeoMIP) G6sulfur experiment, ***Atmos Chem Phys***, https://doi.org/10.5194/acp-22-2999-2022, 2022.

Kablick, G.P., D.R. Allen, M.D. Fromm, and G.E. Nedoluha, Australian pyroCb smoke generates synoptic-scale stratospheric anticyclones, ***Geophys. Res. Lett.***, 47, e2020GL088101, doi:10.1029/2020GL088101, 2020.

Kalidindi S., G. Bala, A. Modak, and K. Caldeira, Modeling of solar radiation management: a comparison of simulations using reduced solar constant and stratospheric sulphate aerosols, ***Clim. Dyn.***, *44* (9), 2909–2925, doi:10.1007/s00382-014-2240-3, 2015.

Karagulian, F., L. Clarisse, C. Clerbaux, A.J. Prata, D. Hurtmans, and P.F. Coheur, Detection of volcanic SO2, ash, and H2SO4 using the Infrared Atmospheric Sounding Interferometer (IASI), ***J. Geophys. Res. Atmos.***, *115* (D2), doi:10.1029/2009JD012786, 2010.

Keeble, J., B. Hassler, A. Banerjee, R. Checa-Garcia, G. Chiodo, S. Davis, V. Eyring, P.T. Griffiths, O. Morgenstern, P. Nowack, G. Zeng, J. Zhang, G. Bodeker, S. Burrows, P. Cameron-Smith, D. Cugnet, C. Danek, M. Deushi, L.W. Horowitz, A. Kubin, L. Li, G. Lohmann, M. Michou, M.J. Mills, P. Nabat, D. Olivié, S. Park, Ø. Seland, J. Stoll, K.-H. Wieners, and T. Wu, Evaluating stratospheric ozone and water vapour changes in CMIP6 models from 1850 to 2100, ***Atmos. Chem. Phys.***, *21* (6), 5015–5061, doi:10.5194/acp-21-5015-2021, 2021.

Keith, D., ***A case for climate engineering***, MIT Press, 224 pp., 2013.

Keith, D.W., Photophoretic levitation of engineered aerosols for geoengineering, ***Proc. Natl. Acad. Sci.***, *107* (38), 16,428–16,431, doi:10.1073/pnas.1009519107, 2010.

Keith, D.W., D.K. Weisenstein, J.A. Dykema, and F.N. Keutsch, Stratospheric solar geoengineering without ozone loss, ***Proc. Natl. Acad. Sci.***, *113* (52), 14,910–14,914, doi:10.1073/pnas.1615572113, 2016.

Keller, D.P., A. Lenton, V. Scott, N.E. Vaughan, N. Bauer, D. Ji, C.D. Jones, B. Kravitz, H. Muri, and K. Zickfeld, The carbon dioxide removal model intercomparison project (CDRMIP): rationale and experimental protocol for CMIP6, ***Geosci. Model Dev.***, *11* (3), 1133–1160, doi:10.5194/gmd-11-1133-2018, 2018.

Khaykin, S.M., S. Godin-Beekmann, A. Hauchecorne, J. Pelon, F. Ravetta, and P. Keckhut, Stratospheric smoke with unprecedentedly high backscatter observed by lidars above southern France, ***Geophys. Res. Lett***, 45, 1639–1646, doi:10.1002/2017GL076763, 2018.

Khaykin, S., B. Legras, S. Bucci, P. Sellitto, L. Isaksen, F. Tencé, S. Bekki, A. Bourassa, L. Rieger, D. Zawada, J. Jumelet, and S. Godin-Beekmann, The 2019/20 Australian wildfires generated a persistent smoke-charged vortex rising up to 35 km altitude, ***Commun. Earth Environ.***, *1* (1), 22, doi:10.1038/s43247-020-00022-5, 2020.

Kinne, S., O.B. Toon, and M.J. Prather, Buffering of stratospheric circulation by changing amounts of tropical ozone a Pinatubo Case Study, ***Geophys. Res. Lett.***, *19* (19), 1927–1930, doi:10.1029/92GL01937, 1992.

Kleinschmitt, C., O. Boucher, S. Bekki, F. Lott, and U. Platt, The Sectional Stratospheric Sulfate Aerosol module (S3A-v1) within the LMDZ general circulation model: description and evaluation against stratospheric aerosol observations, ***Geosci. Model Dev.***, *10* (9), 3359–3378, doi:10.5194/gmd-10-3359-2017, 2017.

Kleinschmitt, C., O. Boucher, and U. Platt, Sensitivity of the radiative forcing by stratospheric sulfur geoengineering to the amount and strategy of the SO2 injection studied with the LMDZ-S3A model, ***Atmos. Chem. Phys.***, *18* (4), 2769-2786, doi:10.5194/acp-18-2769-2018, 2018.

Kloss, C., G. Berthet, P. Sellitto, F. Ploeger, G. Taha, M. Tidiga, M. Eremenko, A. Bossolasco, F. Jégou, J.-B. Renard, and B. Legras, Stratospheric aerosol layer perturbation caused by the 2019 Raikoke and Ulawun eruptions and their radiative forcing, ***Atmos. Chem. Phys.***, *21* (1), 535–560, doi:10.5194/acp-21-535-2021, 2021.

Koike, M., N.B. Jones, W.A. Matthews, P.V. Johnston, R.L. McKenzie, D. Kinnison, and J. Rodriguez, Impact of Pinatubo aerosols on the partitioning between NO2 and HNO3, ***Geophys. Res. Lett.***, *21* (7), 597–600, doi:10.1029/94GL00303, 1994.

Kokkola H., R. Hommel, J. Kazil, U. Niemeier, A.-I. Partanen, J. Feichter, and C. Timmreck, Aerosol microphysics modules in the framework of the ECHAM5 climate model – intercomparison under stratospheric conditions, ***Geosci. Model Dev.***, *2* (2), 97–112, doi:10.5194/gmd-2-97-2009, 2009.

Kovilakam, M., L.W. Thomason, N. Ernest, L. Rieger, A. Bourassa, and L. Millán, The global space-based stratospheric aerosol climatology (version 2.0): 1979–2018, ***Earth Syst. Sci. Data***, *12* (4), 2607–2634, doi:10.5194/essd-12-2607-2020, 2020.

Kravitz, B., A. Robock, L. Oman, G. Stenchikov, and A.B. Marquardt, Sulfuric acid deposition from stratospheric geoengineering with sulfate aerosols, ***J. Geophys. Res. Atmos.***, *114* (D14), doi:10.1029/2009JD011918, 2009.

Kravitz, B., A. Robock, and A. Bourassa, Negligible climatic effects from the 2008 Okmok and Kasatochi volcanic eruptions, ***J. Geophys. Res.***, *115* (D2), doi:10.1029/2009JD013525, 2010.

Kravitz, B., A. Robock, O. Boucher, H. Schmidt, K.E. Taylor, G. Stenchikov, and M. Schulz, The geoengineering model intercomparison project (GeoMIP), ***Atmos. Sci. Lett.***, *12* (2), 162–167, doi:10.1002/asl.316, 2011.

Kravitz, B., A. Robock, D.T. Shindell, and M.A. Miller, Sensitivity of stratospheric geoengineering with black carbon to aerosol size and altitude of injection, ***J. Geophys. Res.***, *117* (D9), doi:10.1029/2011JD017341, 2012.

Kravitz, B., K. Caldeira, O. Boucher, A. Robock, P.J. Rasch, K. Alterskjær, D.B. Karam, J.N. Cole, C.L. Curry, J.M. Haywood, and P.J. Irvine, Climate model response from the geoengineering model intercomparison project (GeoMIP), ***J. Geophys. Res. Atmos.***, *118* (15), 8320–8332, doi:10.1002/jgrd.50646, 2013.

Kravitz, B., D.G. MacMartin, D.T. Leedal, P.J. Rasch, and A.J. Jarvis, Explicit feedback and the management of uncertainty in meeting climate objectives with solar geoengineering, ***Environ. Res. Lett.***, *9* (4), 044006, doi:10.1088/1748-9326/9/4/044006, 2014.

Kravitz, B., A. Robock, S. Tilmes, O. Boucher, J.M. English, P.J. Irvine, A. Jones, M.G. Lawrence, M. MacCracken, H. Muri, and J.C. Moore, The geoengineering model intercomparison project phase 6 (GeoMIP6): simulation design and preliminary results, ***Geosci. Model Dev.***, *8* (10), 3379–3392, doi:10.5194/gmd-8-3379-2015, 2015.

Kravitz, B., D.G. MacMartin, H. Wang, and P.J. Rasch, Geoengineering as a design problem, ***Earth Syst. Dynam.***, *7*, 469–497, doi:10.5194/esd-7-469-2016, 2016.

Kravitz, B., D.G. MacMartin, M.J. Mills, J.H. Richter, S. Tilmes, J.F. Lamarque, J.J. Tribbia, and F. Vitt, First simulations of designing stratospheric sulfate aerosol geoengineering to meet multiple simultaneous climate objectives, ***J. Geophys. Res. Atmos.***, *122* (23), 12,616–12,634, doi:10.1002/2017JD026874, 2017.

Kravitz, B., D.G. MacMartin, S. Tilmes, J.H. Richter, M.J. Mills, W. Cheng, K. Dagon, A.S. Glanville, J.F. Lamarque, I.R. Simpson, and J. Tribbia, Comparing surface and stratospheric impacts of geoengineering with different SO2 injection strategies, ***J. Geophys. Res. Atmos.***, *124* (14), 7900–7918, doi:10.1029/2019JD030329, 2019.

Kravitz, B., D.G. MacMartin, D. Visioni, O. Boucher, J.N. Cole, J. Haywood, A. Jones, T. Lurton, P. Nabat, U. Niemeier, and A. Robock, Comparing different generations of idealized solar geoengineering simulations in the Geoengineering Model Intercomparison Project (GeoMIP), ***Atmos. Chem. Phys., 21*** (6), 4231–4247, doi:10.5194/acp-21-4231-2021, 2021.

Kremser, S., L.W. Thomason, M. von Hobe, M. Hermann, T. Deshler, C. Timmreck, M. Toohey, A. Stenke, J.P. Schwarz, R. Weigel, and S. Fueglistaler, Stratospheric aerosol—Observations, processes, and impact on climate, ***Rev. Geophys.***, *54* (2), 278–335, doi:10.1002/2015RG000511, 2016.

Krishnamohan, K.P.S.P., G. Bala, L. Cao, L. Duan, and K. Caldeira, Climate system response to stratospheric sulfate aerosols: sensitivity to altitude of aerosol layer, ***Earth Syst. Dynam.***, *10*, 885–900, doi:10.5194/esd-10-885-2019, 2019.

Kwiatkowski, L., P. Cox, P.R. Halloran, P.J. Mumby, and A.J. Wiltshire, Coral bleaching under unconventional scenarios of climate warming and ocean acidification, ***Nat. Clim. Change***, *5* (8), 777–781, doi:10.1038/nclimate2655, 2015.

Laakso, A., H. Korhonen, S. Romakkaniemi, and H. Kokkola, Radiative and climate effects of stratospheric sulfur geoengineering using seasonally varying injection areas, ***Atmos. Chem. Phys.***, *17* (11), 6957–6974, doi:10.5194/acp-17-6957-2017, 2017.

Laakso, A., U. Niemeier, D. Visioni, S. Tilmes, and H. Kokkola, Dependency of the impacts of geoengineering on the stratospheric sulfur injection strategy part 1: Intercomparison of modal and sectional aerosol module, ***Atmos. Chem. Phys.***, *22*, 93–118, doi:10.5194/acp-22-93-2022, 2022.

Labitzke, K. and M.P. McCormick, Stratospheric temperature increases due to Pinatubo aerosols. ***Geophysical Research Letters***, *19*(2), pp.207-210, 1992.

Labitzke, K., Stratospheric temperature changes after the Pinatubo eruption. ***Journal of Atmospheric and Terrestrial Physics***, *56*(9), pp.1027-1034, 1994.

Lacis, A., J. Hansen, and M. Sato, Climate forcing by stratospheric aerosols, ***Geophys. Res. Lett.***, *19* (15), 1607–1610, doi:10.1029/92GL01620, 1992.

Lawrence, M.G., S. Schäfer, H. Muri, V. Scott, A. Oschlies, N.E. Vaughan, O. Boucher, H. Schmidt, J. Haywood, and J. Scheffran, Evaluating climate geoengineering proposals in the context of the Paris Agreement temperature goals, ***Nat. Commun.***, ***9*** (1), 1–19, doi:10.1038/s41467-018-05938-3, 2018.

Lee, J.-Y., J. Marotzke, G. Bala, L. Cao, S. Corti, J.P. Dunne, F. Engelbrecht, E. Fischer, J.C. Fyfe, C. Jones, A. Maycock, J. Mutemi, O. Ndiaye, S. Panickal, and T. Zhou, Future Global Climate: Scenario-Based Projections and Near-Term Information, Chapter 4, in ***Climate Change 2021: The Physical Science Basis. Contribution of Working Group I to the Sixth Assessment Report of the Intergovernmental Panel on Climate Change***, edited by V. Masson-Delmotte, P. Zhai, A. Pirani, S.L. Connors, C. Péan, S. Berger, N. Caud, Y. Chen, L. Goldfarb, M.I. Gomis, M. Huang, K. Leitzell, E. Lonnoy, J.B.R. Matthews, T.K. Maycock, T. Waterfield, O. Yelekçi, R. Yu, and B. Zhou, 120 pp., Cambridge University Press, Cambridge, United Kingdom, doi:10.1017/9781009157896.006, 2021.

Lee, W.R., D.G. MacMartin, D. Visioni, and B. Kravitz, High latitude stratospheric aerosol geoengineering can be more effective if injection is limited to spring, ***Geophys. Res. Lett.***, ***48*** (9), e2021GL092696, doi:10.1029/2021GL092696, 2021.

Lehner, F., A.P. Schurer, G.C. Hegerl, C. Deser, and T.L. Frölicher, The importance of ENSO phase during volcanic eruptions for detection and attribution. ***Geophysical Research Letters***, ***43***(6), pp.2851-2858, 2016.

Lenton, T.M., J. Rockström, O. Gaffney, S. Rahmstorf, K. Richardson, W. Steffen, and H.J. Schellnhuber, Climate tipping points—too risky to bet against, ***Nature***, 592–595, doi:10.1038/d41586-019-03595-0, 2019.

Lohmann, U., and B. Gasparini, A cirrus cloud climate dial?, ***Science***, ***357*** (6348), 248–249, doi:10.1126/science.aan3325, 2017.

Long J.C.S., and J.G. Shepherd, The strategic value of geoengineering research, in ***Global Environmental Change***, edited by B. Freedman, 13 pp., Springer, Dordrecht, Netherlands, doi:10.1007/978-94-007-5784-4_24, 2014.

Madronich, S., S. Tilmes, B. Kravitz, D.G. MacMartin, and J.H. Richter, Response of surface ultraviolet and visible radiation to stratospheric SO2 injections. ***Atmosphere***, ***9***(11), p.432, 2018.

MacMartin, D.G., D.W. Keith, B. Kravitz, and K. Caldeira, Management of trade-offs in geoengineering through optimal choice of non-uniform radiative forcing, ***Nat. Clim. Change***, ***3*** (4), 365–368, doi:10.1038/nclimate1722, 2013.

MacMartin, D.G., B. Kravitz, D.W. Keith, and A. Jarvis, Dynamics of the coupled human–climate system resulting from closed-loop control of solar geoengineering, ***Clim. Dyn.***, ***43*** (1), 243–258, doi:10.1007/s00382-013-1822-9, 2014a.

MacMartin, D.G., K. Caldeira, and D.W. Keith, Solar geoengineering to limit the rate of temperature change, ***Philos. Trans. Royal Soc. A: Math. Phys. Eng. Sci.***, ***372*** (2031), 20140134, doi:10.1098/rsta.2014.0134, 2014b.

MacMartin, D.G., B. Kravitz, S. Tilmes, J.H. Richter, M.J. Mills, J.F. Lamarque, J.J. Tribbia, and F. Vitt, The climate response to stratospheric aerosol geoengineering can be tailored using multiple injection locations, ***J. Geophys. Res. Atmos.***, ***122*** (23), 12,574–12,590, doi:10.1002/2017JD026868, 2017.

MacMynowski, D.G., D.W. Keith, K. Caldeira, and H.J. Shin, Can we test geoengineering?, ***Energy Environ. Sci.***, ***4*** (12), 5044–5052, doi:10.1039/C1EE01256H, 2011.

Mankin, W.G., and M.T. Coffey, Increased stratospheric hydrogen chloride in the El Chichon cloud, ***Science***, ***226*** (4671), 170–172, doi:10.1126/science.226.4671.170, 1984.

Marshall, L.R., C.J. Smith, P.M. Forster, T.J. Aubry, T. Andrews, and A. Schmidt, Large variations in volcanic aerosol forcing efficiency due to eruption source parameters and rapid adjustments, ***Geophys. Res. Lett.***, ***47*** (19), e2020GL090241, doi:10.1029/2020GL090241, 2020.

Matthews, H.D., and S.E. Turner, Of mongooses and mitigation: ecological analogues to geoengineering, ***Environ. Res. Lett.***, ***4*** (4), 045105, doi:10.1088/1748-9326/4/4/045105, 2009.

McClellan, J., D.W. Keith, and J. Apt, Cost analysis of stratospheric albedo modification delivery systems, ***Environ. Res. Lett.***, ***7*** (3), 034019, doi:10.1088/1748-9326/7/3/034019, 2012.

McCormick, M.P., L.W. Thomason, and C.R. Trepte, Atmospheric effects of the Mt Pinatubo eruption, ***Nature***, ***373*** (6513), 399–404, doi:10.1038/373399a0, 1995.

McCusker, K.E., D.S. Battisti, and C.M. Bitz, Inability of stratospheric sulfate aerosol injections to preserve the West Antarctic Ice Sheet, ***Geophys. Res. Lett.***, ***42*** (12), 4989–4997, doi:10.1002/2015GL064314, 2015.

Mie, G., Sättigungsstrom und Stromkurve einer schlecht leitenden Flüssigkeit, ***Ann. Phys.***, ***331*** (8), 597–614, doi:10.1002/andp.19083310810, 1908.

Millar, R.J., J.S. Fuglestvedt, P. Friedlingstein, J. Rogelj, M.J. Grubb, H.D. Matthews, R.B. Skeie, P.M. Forster, D.J. Frame, and M.R. Allen, Emission budgets and pathways consistent with limiting warming to 1.5 °C, ***Nat. Geosci.***, ***10*** (10), 741–747, doi:10.1038/ngeo3031, 2017.

Mills, M.J., A. Schmidt, R. Easter, S. Solomon, D.E. Kinnison, S.J. Ghan, R.R. Neely III, D.R. Marsh, A. Conley, C.G. Bardeen, and A. Gettelman, Global volcanic aerosol properties derived from emissions, 1990–2014, using CESM1 (WACCM), ***J. Geophys. Res. Atmos.***, ***121*** (5), 2332–2348, doi:10.1002/2015JD024290, 2016.

Mills, M.J., J.H. Richter, S. Tilmes, B. Kravitz, D.G. MacMartin, A.A. Glanville, J.J. Tribbia, J.F. Lamarque, F. Vitt, A. Schmidt, and A. Gettelman, Radiative and chemical response to interactive stratospheric sulfate aerosols in fully coupled CESM1 (WACCM), ***J. Geophys. Res. Atmos.***, ***122*** (23), 13,061–13,078, doi:10.1002/2017JD027006, 2017.

Minnis, P., E.F. Harrison, L.L. Stowe, G.G. Gibson, F.M. Denn, D.R. Doelling, and W.L. Smith Jr, Radiative climate forcing by the Mount Pinatubo eruption, ***Science***, ***259*** (5100), 1411–1415, doi:10.1126/science.259.5100.1411, 1993.

Molina, M.J., L.T. Molina, R. Zhang, R.F. Meads, and D.D. Spencer, The reaction of ClONO2 with HCl on aluminum oxide, ***Geophys. Res. Lett.***, ***24*** (13), 1619–1622, doi:10.1029/97GL01560, 1997.

Moon, D.R., G.S. Taverna, C. Anduix-Canto, T. Ingham, M.P. Chipperfield, P.W. Seakins, M.T. Baeza-Romero, and D.E. Heard, Heterogeneous reaction of HO 2 with airborne TiO 2 particles and its implication for climate change mitigation strategies, ***Atmos. Chem. Phys.***, ***18*** (1), 327–338, doi:10.5194/acp-18-327-2018, 2018.

Morgenstern, O., M.I. Hegglin, E. Rozanov, F.M. O'Connor, N.L. Abraham, H. Akiyoshi, A.T. Archibald, S. Bekki, N. Butchart, M.P. Chipperfield, M. Deushi, S.S. Dhoms, R.R. Garcia, S.C. Hardiman, L.W. Horowitz, P. Jöckel, B. Josse, D. Kinnison, M. Lin, E. Mancini, M.E. Manyin, M. Marchand, V. Marécal, M. Michou, L.D. Oman, G. Pitari, D.A. Plummer, L.E. Revell, D, Saint-Martin, R. Schofield, A. Stenke, K. Stone, K. Sudo, T.Y. Tanaka, S. Tilmes, Y. Yamashita, K. Yoshida, and G. Zeng, Review of the global models used within phase 1 of the Chemistry–Climate Model Initiative (CCMI), ***Geosci. Model Dev.***, ***10*** (2), 639–671, doi:10.5194/gmd-10-639-2017, 2017.

Muser, L.O., G.A. Hoshyaripour, J. Bruckert, Á. Horváth, E. Malinina, S. Wallis, F.J. Prata, A. Rozanov, C. von Savigny, H. Vogel, and B. Vogel, Particle aging and aerosol–radiation interaction affect volcanic plume dispersion: evidence from the Raikoke 2019 eruption, ***Atmos. Chem. Phys.***, ***20*** (23), 15,015–15,036, doi:10.5194/acp-20-15015-2020, 2020.

Muthyala, R., G. Bala, and A. Nalam, Regional scale analysis of climate extremes in an SRM geoengineering simulation, Part 1: Precipitation Extremes, ***Curr. Sci.***, ***114*** (5), 1024–1035, doi:10.18520/cs/v114/i05/1024-1035, 2018a.

Muthyala, R., G. Bala, and A. Nalam, Regional scale analysis of climate extremes in an SRM geoengineering simulation, Part 2: Temperature Extremes, ***Curr. Sci.***, ***114*** (5), 1036–1045, doi:10.18520/cs/v114/i05/1036-1045, 2018b.

Myhre, G., K. Alterskjær, C.W. Stjern, Ø. Hodnebrog, L. Marelle, B.H. Samset, J. Sillmann, N. Schaller, E. Fischer, M. Schulz, and A. Stohl, Frequency of extreme precipitation increases extensively with event rareness under global warming, ***Sci. Rep.***, ***9*** (1), 1–10, doi:10.1038/s41598-019-52277-4, 2019.

NAS (U.S. National Academy of Sciences), ***Reflecting Sunlight: Recommendations for Solar Geoengineering Research and Research Governance***, 328 pp., The National Academies Press, Washington, DC, doi:10.17226/25762, 2021.

NRC (National Research Council), ***Climate Intervention: Carbon Dioxide Removal and Reliable Sequestration***, 154 pp., The National Academies Press, Washington, DC, doi:10.17226/18805, 2015.

Neely III, R.R and A. Schmidt, VolcanEESM: Global volcanic sulphur dioxide (SO2) emissions database from 1850 to present. ***Centre for Environmental Data Analysis***. https://doi.org/10.5285/76ebdc0b-0eed-4f70-b89e-55e606bcd568, 2016.

Niemeier, U., H. Schmidt, and C. Timmreck, The dependency of geoengineered sulfate aerosol on the emission strategy, ***Atmos. Sci. Lett.***, ***12*** (2), 189–194, doi:10.1002/asl.304, 2011.

Niemeier, U., H. Schmidt, K. Alterskjær, and J.E. Kristjánsson, Solar irradiance reduction via climate engineering: Impact of different techniques on the energy balance and the hydrological cycle, ***J. Geophys. Res. Atmos.***, ***118***, 11,905–11,917, doi:10.1002/2013JD020445, 2013.

Niemeier, U., and C. Timmreck, What is the limit of climate engineering by

stratospheric injection of SO2?, ***Atmos. Chem. Phys.***, ***15*** (16), 9129–9141, doi:10.5194/acp-15-9129-2015, 2015.

Niemeier, U., and H. Schmidt, Changing transport processes in the stratosphere by radiative heating of sulfate aerosols, ***Atmos. Chem. Phys.***, ***17***, 14,871–14,886, doi:10.5194/acp-17-14871-2017, 2017.

Niemeier, U., J.H. Richter, and S. Tilmes, Differing responses of the quasi-biennial oscillation to artificial SO2 injections in two global models, ***Atmos. Chem. Phys.***, ***20***, 8975–8987, doi:10.5194/acp-20-8975-2020, 2020.

Nowack, P.J., N.L. Abraham, P. Braesicke, and J.A. Pyle, Stratospheric ozone changes under solar geoengineering: implications for UV exposure and air quality, ***Atmos. Chem. Phys.***, ***16*** (6), 4191–4203, doi:10.5194/acp-16-4191-2016, 2016.

Oman, L., A. Robock, G.L. Stenchikov, and T. Thordarson, High-latitude eruptions cast shadow over the African monsoon and the flow of the Nile, ***Geophys. Res. Lett.***, ***33*** (18), doi:10.1029/2006GL027665, 2006.

Osborne, M.J., J. de Leeuw, C. Witham, A. Schmidt, F. Beckett, N. Kristiansen, J. Buxmann, C. Saint, E.J. Welton, J. Fochesatto, A.R. Gomes, U. Bundke, A. Petzold, F. Marenco, and J. Haywood, The 2019 Raikoke volcanic eruption part 2: Particle phase dispersion and concurrent wildfire smoke emissions, ***Atmos. Chem. Phys.***, ***22*** (5), 2975–2997, doi:10.5194/acp-2021-448, 2022.

Parker, A. and P.J. Irvine, P.J., The risk of termination shock from solar geoengineering. ***Earth's Future***, ***6***(3), pp.456-467, 2018.

Peterson, D.A., J.R. Campbell, E.J. Hyer, M.D. Fromm, G.P. Kablick III, J.H. Cossuth, and M.T. DeLand, Wildfire-driven thunderstorms cause a volcano-like stratospheric injection of smoke, ***npj Clim. Atmos. Sci.***, ***1*** (1), doi:10.1038/s41612-018-0039-3, 2018.

Peterson, D.A., M.D. Fromm, R.H.D. McRae, J.R. Campbell, E.J. Hyer, G. Taha, C.P. Camacho, G.P. Kablick III, C.C. Schmidt, and M.T. DeLand, Australia's Black Summer pyrocumulonimbus super outbreak reveals potential for increasingly extreme stratospheric smoke events, ***npj Clim. Atmos. Sci., 4*** (1), doi:10.1038/s41612-021-00192-9, 2021.

Pierce, J.R., D.K. Weisenstein, P. Heckendorn, T. Peter, and D.W. Keith, Efficient formation of stratospheric aerosol for climate engineering by emission of condensible vapor from aircraft, ***Geophys. Res. Lett.***, ***37*** (18), doi:10.1029/2010GL043975, 2010.

Pinto, J.P., R.P. Turco, and O.B. Toon, Self-limiting physical and chemical effects in volcanic eruption clouds, ***J. Geophys. Res. Atmos.***, ***94*** (D8), 11,165–11,174, doi:10.1029/JD094iD08p11165, 1989.

Pitari, G., and E. Mancini, Short-term climatic impact of the 1991 volcanic eruption of Mount Pinatubo and effects on atmospheric tracers, ***Nat. Hazards Earth Syst. Sci.***, ***2*** (1/2), 91–108, doi:10.5194/nhess-2-91-2002, 2002.

Pitari, G., V. Aquila, B. Kravitz, A. Robock, S. Watanabe, I. Cionni, N.D. Luca, G.D. Genova, E. Mancini, and S. Tilmes, Stratospheric ozone response to sulfate geoengineering: Results from the Geoengineering Model Intercomparison Project (GeoMIP), ***J. Geophys. Res. Atmos.***, ***119*** (5), 2629–2653, doi:10.1002/2013JD020566, 2014.

Plummer, D., T. Nagashima, S. Tilmes, A. Archibald, G. Chiodo, S. Fadnavis, H. Garny, B. Josse, J. Kim, J.-F. Lamarque, O. Morgenstern, L. Murray, C. Orbe, A. Tai, M. Chipperfield, B. Funke, M. Juckes, D. Kinnison, M. Kunze, B. Luo, K. Matthes, P.A. Newman, C. Pascoe, and T. Peter, CCMI-2022: A new set of Chemistry-Climate Model Initiative (CCMI) Community Simulations to Update the Assessment of Models and Support Upcoming Ozone Assessment Activities, SPARC newsletter, [available at: https://www.sparc-climate.org/wp-content/uploads/sites/5/2021/07/SPARCnewsletter_Jul2021_web.pdf#page=22], 2021.

Poberaj, C.S., J. Staehelin, and D. Brunner, Missing stratospheric ozone decrease at Southern Hemisphere middle latitudes after Mount Pinatubo: a dynamical perspective, ***J Atmos Sci.***, ***68*** (9), 1922–1945, doi:10.1175/JAS-D-10-05004.1, 2011.

Polvani, L.M., A. Banerjee, and A. Schmidt, Northern Hemisphere continental winter warming following the 1991 Mount Pinatubo eruption: reconciling models and observations, ***Atmos. Chem. Phys.***, ***19*** (9), 6351–6366, doi:10.5194/acp-19-6351-2019, 2019.

Pope, F.D., P. Braesicke, R.G. Grainger, M. Kalberer, I.M. Watson, P.J. Davidson, and R.A. Cox, Stratospheric aerosol particles and solar-radiation management, ***Nat. Clim. Change***, ***2*** (10), 713–719, doi:10.1038/nclimate1528, 2012.

Portmann, R.W., S. Solomon, R.R. Garcia, L.W. Thomason, L.R. Poole, and M.P. McCormick, Role of aerosol variations in anthropogenic ozone depletion in the polar regions, ***J. Geophys. Res. Atmos.***, ***101*** (D17), 22,991–23,006, doi:10.1029/96JD02608, 1996.

Preston, C.J., Ethics and geoengineering: reviewing the moral issues raised by solar radiation management and carbon dioxide removal, ***Wiley Interdiscip. Rev. Clim. Change***, ***4*** (1), 23–37, doi:10.1002/wcc.198, 2013.

Proctor, J., S. Hsiang, J. Burney, M. Burke, and W. Schlenker, Estimating global agricultural effects of geoengineering using volcanic eruptions, ***Nature***, ***560*** (7719), 480–483, doi:10.1038/s41586-018-0417-3, 2018.

Quaglia, I., D. Visioni, G. Pitari, and B. Kravitz, An approach to sulfate geoengineering with surface emissions of carbonyl sulfide. ***Atmos. Chem. Phys***, ***22***(9), pp.5757-5773, 2022.

Randel, W.J., F. Wu, J.M. Russell III, J.W. Waters, and L. Froidevaux, Ozone and temperature changes in the stratosphere following the eruption of Mount Pinatubo, ***J. Geophys. Res. Atmos.***, ***100*** (D8), 16,753–16,764, doi:10.1029/95JD01001, 1995.

Rasch, P.J., S. Tilmes, R.P. Turco, A. Robock, L. Oman, C.C. Chen, G.L. Stenchikov, and R.R. Garcia, An overview of geoengineering of climate using stratospheric sulphate aerosols, ***Philos. Trans. Royal Soc. A: Math. Phys. Eng. Sci.***, ***366*** (1882), 4007–4037, doi:10.1098/rsta.2008.0131, 2008a.

Rasch, P.J., P.J. Crutzen, and D.B. Coleman, Exploring the geoengineering of climate using stratospheric sulfate aerosols: the role of particle size, ***Geophys. Res. Lett.***, ***35*** (2), L02809, doi:10.1029/2007GL032179, 2008b.

Ravishankara, A.R., J.S. Daniel, and R.W. Portmann, R.W., Nitrous oxide (N2O): the dominant ozone-depleting substance emitted in the 21st century. ***science***, ***326***(5949), pp.123-125, 2009.

Richter, J. H., S. Tilmes ,M.J. Mills, J.J. Tribbia, B. Kravitz, D.G. MacMartin, F. Vitt, and J.-F. Lamarque, Stratospheric dynamical response and ozone feedbacks in the presence of SO_2 injections, ***J. Geophys. Res. Atmos.***, ***122***, 12,557–12,573, doi:10.1002/2017JD026912, 2017.

Richter, J. H., S. Tilmes, A. Glanville, B. Kravitz, D.G. MacMartin, M.J. Mills, I.R. Simpson, F. Vitt, J.J. Tribbia, and J.-F. Lamarque, Stratospheric response in the first geoengineering simulation meeting multiple surface climate objectives, ***J. Geophys. Res. Atmos.***, ***123*** (11), 5762–5782, doi:10.1029/2018JD028285, 2018.

Richter, J.H., D. Visioni, D. MacMartin, D.A. Bailey, W. Lee, S. Woodhouse, N.A. Rosenbloom, M.R. Tye, and J.F. Lamarque, Assessing Responses and Impacts of Solar climate intervention on the Earth system with stratospheric aerosol injection (ARISE-SAI): protocol and initial results from the first simulations, ***Geosci. Model Dev.***, 15, 8221–8243, https://doi.org/10.5194/gmd-15-8221-2022, 2022.

Rieger, L.A., W.J. Randel, A.E. Bourassa, and S. Solomon,. Stratospheric temperature and ozone anomalies associated with the 2020 Australian New Year fires, ***Geophys. Res. Lett.***, ***48***, e2021GL095898, doi:10.1029/2021GL095898, 2021.

Robock, A. and J. Mao, Winter warming from large volcanic eruptions. ***Geophysical Research Letters***, ***19***(24), pp.2405-2408, 1992.

Robock, A., and J. Mao, The volcanic signal in surface temperature observations, ***J. Clim.***, ***8*** (5), 1086–1103, doi:10.1175/1520-0442(1995)008<1086:TVSIST>2.0.CO;2, 1995.

Robock, A., Volcanic eruptions and climate, ***Rev. Geophys.***, ***38*** (2), 191–219, doi:10.1029/1998RG000054, 2000.

Robock, A., 20 reasons why geoengineering may be a bad idea, ***Bull. At. Sci.***, ***64*** (2), 14–18, doi:10.2968/064002006, 2008a.

Robock, A., L. Oman, and G.L. Stenchikov, Regional climate responses to geoengineering with tropical and Arctic SO2 injections, ***J. Geophys. Res.***, ***113*** (D16), D16101, doi:10.1029/2008JD010050, 2008b.

Robock, A., A. Marquardt, B. Kravitz, and G. Stenchikov, Benefits, risks, and costs of stratospheric geoengineering, ***Geophys. Res. Lett.***, ***36*** (19), doi:10.1029/2009GL039209, 2009.

Robock, A., Benefits and risks of stratospheric solar radiation management for climate intervention (geoengineering), ***Bridge***, ***50*** (1), 59–67, [available at: http://climate.envsci.rutgers.edu/pdf/RobockBridge.pdf], 2020.

Robrecht, S., B. Vogel, S. Tilmes, and R. Müller, Potential of future stratospheric ozone loss in the midlatitudes under global warming and sulfate geoengineering, ***Atmos. Chem. Phys.***, ***21*** (4), 2427–2455, doi:10.5194/acp-21-2427-2021, 2021.

Rogelj, J., M. den Elzen, N. Höhne, T. Fransen, H. Fekete, H. Winkler, R. Schaeffer, F. Sha, K. Riahi, and M. Meinshausen, Paris Agreement climate proposals need a boost to keep warming well below 2 °C, ***Nature***, ***534*** (7609), 631–639, doi:10.1038/nature18307, 2016.

Rogelj, J., O. Geden, A. Cowie, and A. Reisinger, Net-zero emissions targets are

vague: three ways to fix, ***Nature***, ***591***, 365–368, doi:10.1038/d41586-021-00662-3, 2021.

Rosenfeld, J.E., D.B. Considine, P.E. Meade, J.T. Bacmeister, C.H. Jackman, and M.R. Schoeberl, Stratospheric effects of Mount Pinatubo aerosol studied with a coupled two-dimensional model, ***J. Geophys. Res. Atmos.***, ***102*** (D3), 3649–3670, doi:10.1029/96JD03820, 1997.

Samaniego, L., S. Thober, R. Kumar, N. Wanders, O. Rakovec, M. Pan, M. Zink, J. Sheffield, E.F. Wood, and A. Marx, Anthropogenic warming exacerbates European soil moisture droughts, ***Nat. Clim. Change***, ***8*** (5), 421–426, doi:10.1038/s41558-018-0138-5, 2018.

Santer, B.D., C. Bonfils, J.F. Painter, M.D. Zelinka, C. Mears, S. Solomon, G.A. Schmidt, J.C. Fyfe, J.N. Cole, L. Nazarenko, and K.E. Taylor, Volcanic contribution to decadal changes in tropospheric temperature, ***Nat. Geosci.***, ***7*** (3), 185–189, doi:10.1038/ngeo2098, 2014.

Schmidt, A., M.J. Mills, S. Ghan, J.M. Gregory, R.P. Allan, T. Andrews, C.G. Bardeen, A. Conley, P.M. Forster, A. Gettelman, and R.W. Portmann, Volcanic radiative forcing from 1979 to 2015, ***J. Geophys. Res. Atmos.***, ***123*** (22), 12,491–12,508, doi:10.1029/2018JD028776, 2018.

Schmidt, H., K. Alterskjær, D. Bou Karam, O. Boucher, A. Jones, J.E. Kristjánsson, U. Niemeier, M. Schulz, A. Aaheim, F. Benduhn, and M. Lawrence, Solar irradiance reduction to counteract radiative forcing from a quadrupling of CO2: climate responses simulated by four earth system models, ***Earth Syst. Dyn.***, ***3*** (1), 63–78, doi:10.5194/esd-3-63-2012, 2012.

Schwartz, M.J., M.L. Santee, H.C. Pumphrey, G.L. Manney, A. Lambert, N.J. Livesey, L. Millán, J.L. Neu, W.G. Read, and F. Werner, Australian new year's pyroCb impact on stratospheric composition, ***Geophys. Res. Lett.***, ***47*** (24), e2020GL090831, doi:10.1029/2020GL090831, 2020.

Seinfeld, J.H., and S.N. Pandis, ***Atmospheric Chemistry and Physics: From Air Pollution to Climate Change***, 2nd Edition, John Wiley & Sons, New York, NY, 2007.

Shepherd, J.G., ***Geoengineering the climate: science, governance and uncertainty***, 99 pp., Royal Society, London, United Kingdom, 2009.

Shi, Q., J.T. Jayne, C.E. Kolb, D.R. Worsnop, and P. Davidovits, Kinetic model for reaction of ClONO2 with H2O and HCl and HOCl with HCl in sulfuric acid solutions, ***J. Geophys. Res. Atmos.***, ***106*** (D20), 24,259–24,274, doi:10.1029/2000JD000181, 2001.

Simpson, I.R., S. Tilmes, J.H. Richter, B. Kravitz, D.G. MacMartin, M.J. Mills, J.T. Fasullo, and A.G. Pendergrass, The regional hydroclimate response to stratospheric sulfate geoengineering and the role of stratospheric heating, ***J. Geophys. Res. Atmos.***, ***124*** (23), 12,587–12,616, doi:10.1029/2019JD031093, 2019.

Smith, P., S.J. Davis, F. Creutzig, S. Fuss, J. Minx, B. Gabrielle, E. Kato, R.B. Jackson, A. Cowie, E. Kriegler, D.P. van Vuuren, J. Rogelj, P. Ciais, J. Milne, J.G. Canadell, D. McCollum, G. Peters, R. Andrew, V. Krey, G. Shrestha, P. Friedlingstein, T. Gasser, A. Grübler, W.K. Heidug, M. Jonas, C.D. Jones, F. Kraxner, E. Littleton, J. Lowe, J.R. Moreira, N. Nakicenovic, M. Obersteiner, A. Patwardhan, M. Rogner, E. Rubin, A. Sharifi, A. Torvanger, Y. Yamagata, J. Edmonds, and C. Yongsung, Biophysical and economic limits to negative CO2 emissions, ***Nat. Clim. Change***, ***6*** (1), 42–50, doi:10.1038/nclimate2870, 2016.

Smith, W., and Wagner, G., Stratospheric aerosol injection tactics and costs in the first 15 years of deployment, ***Environ. Res. Lett.***, ***13*** (12), 124001, doi:10.1088/1748-9326/aae98d, 2018.

Smith, W., The cost of stratospheric aerosol injection through 2100, ***Environ. Res. Lett.***, ***15*** (11), 114004, doi:10.1088/1748-9326/aba7e7, 2020.

Soden, B.J., R.T. Wetherald, G.L. Stenchikov, and A. Robock, Global cooling after the eruption of Mount Pinatubo: A test of climate feedback by water vapor, ***Science***, ***296*** (5568), 727–730, 10.1126/science.296.5568.727, 2002.

Solomon, S., R.W. Portmann, R.R. Garcia, L.W. Thomason, L.R. Poole, and M.P. McCormick, The role of aerosol variations in anthropogenic ozone depletion at northern midlatitudes, ***J. Geophys. Res. Atmos.***, ***101*** (D3), 6713–6727, doi:10.1029/95JD03353, 1996.

Solomon, S., R.W. Portmann, R.R. Garcia, W. Randel, F. Wu, R. Nagatani, J. Gleason, L. Thomason, L.R. Poole, and M.P. McCormick, Ozone depletion at mid-latitudes: Coupling of volcanic aerosols and temperature variability to anthropogenic chlorine, ***Geophys. Res. Lett.***, ***25*** (11), 1871–1874, doi:10.1029/98GL01293, 1998.

Solomon, S., Stratospheric ozone depletion: A review of concepts and history, ***Rev. Geophys.***, ***37*** (3), 275–316, doi:10.1029/1999RG900008, 1999.

Solomon, S., D.J. Ivy, D. Kinnison, M.J. Mills, R.R. Neely III, and A. Schmidt, Emergence of healing in the Antarctic ozone layer, ***Science***, ***353*** (6296), 269–274, doi:10.1126/science.aae0061, 2016.

Solomon, S., K. Dube, K. Stone, K., P. Yu, D. Kinnison, O.B. Toon, S.E. Strahan, K.H. Rosenlof, R. Portmann, S. Davis, and W. Randel, 2022. On the stratospheric chemistry of midlatitude wildfire smoke. ***Proceedings of the National Academy of Sciences***, ***119***(10), p.e2117325119, 2022.

SPARC (Stratospheric Processes And their Role in Climate), ***SPARC Assessment of Stratospheric Aerosol Properties (ASAP)***, edited by L. Thomason and T. Peter, SPARC Report No. 4, WCRP-124, WMO/TD No. 1295, [available at: www.sparc-climate.org/publications/sparc-reports/], 2006.

Staunton-Sykes, J., T.J. Aubry, Y.M. Shin, J. Weber, L.R. Marshall, N. Luke Abraham, A. Archibald, and A. Schmidt, Co-emission of volcanic sulfur and halogens amplifies volcanic effective radiative forcing, ***Atmos. Chem. Phys.***, ***21*** (11), 9009–9029, doi:10.5194/acp-21-9009-2021, 2021.

Stenchikov, G., A. Ukhov, S. Osipov, R. Ahmadov, G. Grell, K. Cady-Pereira, E. Mlawer, and M. Iacono, How does a Pinatubo-size volcanic cloud reach the middle stratosphere?, ***J. Geophys. Res. Atmos.***, ***126*** (10), e2020JD033829, doi:10.1029/2020JD033829, 2021.

Stephens, G.L., M.Z. Hakuba, M. Hawcroft, J.M. Haywood, A. Behrangi, J.E. Kay, and P.J Webster, The curious nature of the hemispheric symmetry of the Earth's water and energy balances, ***Curr. Clim. Change Rep.***, ***2*** (4), 135–147, doi:10.1007/s40641-016-0043-9, 2016.

Stone, K.A., S. Solomon, D.E. Kinnison, M.C. Pitts, L.R. Poole, M.J. Mills, A. Schmidt, R.R. Neely III, D. Ivy, M.J. Schwartz, J.P. Vernier, B.J. Johnson, M.B. Tully, A.R. Klekociuk, G. König-Langlo, and S. Hagiya, Observing the impact of Calbuco volcanic aerosols on South Polar ozone depletion in 2015, ***J. Geophys. Res. Atmos.***, ***122*** (21), 11,862–11,879, doi:10.1002/2017JD026987, 2017.

Sugiyama, M., Y. Arino, T. Kosugi, A. Kurosawa, and S. Watanabe, Next steps in geoengineering scenario research: Limited deployment scenarios and beyond, ***Clim. Policy***, ***18*** (6), 681–689, doi:10.1080/14693062.2017.1323721, 2018.

Tang, M., J. Keeble, P.J. Telford, F.D. Pope, P. Braesicke, P.T. Griffiths, N.L. Abraham, J. McGregor, I.M. Watson, R.A. Cox, and J.A. Pyle, Heterogeneous reaction of $ClONO_2$ with TiO_2 and SiO_2 aerosol particles: implications for stratospheric particle injection for climate engineering, ***Atmos. Chem. Phys.***, ***16*** (23), 15,397–15,412, doi:10.5194/acp-16-15397-2016, 2016.

Tang, M.J., P.J. Telford, F.D. Pope, L. Rkiouak, N.L. Abraham, A.T. Archibald, P. Braesicke, J.A. Pyle, J. McGregor, I.M. Watson, and R.A. Cox, Heterogeneous reaction of N_2O_5 with airborne TiO_2 particles and its implication for stratospheric particle injection, ***Atmos. Chem. Phys.***, ***14*** (12), 6035–6048, doi:10.5194/acp-14-6035-2014, 2014.

Telford, P., P. Braesicke, O. Morgenstern, and J. Pyle, Reassessment of causes of ozone column variability following the eruption of Mount Pinatubo using a nudged CCM, ***Atmos. Chem. Phys.***, ***9*** (13), 4251–4260, doi:10.5194/acp-9-4251-2009, 2009.

Theys, N., I.D. Smedt, H. Yu, T. Danckaert, J.V. Gent, C. Hörmann, T. Wagner, P. Hedelt, H. Bauer, F. Romahn, and M. Pedergnana, Sulfur dioxide retrievals from TROPOMI onboard Sentinel-5 Precursor: algorithm theoretical basis, ***Atmos. Meas. Tech.***, ***10*** (1), 119–153, doi:10.5194/amt-10-119-2017, 2017.

Thomason, L.W., G.S. Kent, C.R. Trepte, and L.R. Poole, A comparison of the stratospheric aerosol background periods of 1979 and 1989–1991, ***J. Geophys. Res. Atmos.***, ***102*** (D3), 3611–3616, doi:10.1029/96JD02960, 1997.

Thomason, L.W., N. Ernest, L. Millán, L. Rieger, A. Bourassa, J.P. Vernier, G. Manney, B. Luo, F. Arfeuille, and T. Peter, A global space-based stratospheric aerosol climatology: 1979–2016, ***Earth Syst. Sci. Data***, ***10*** (1), 469–492, doi:10.5194/essd-10-469-2018, 2018.

Tie, X., and G. Brasseur, The response of stratospheric ozone to volcanic eruptions: Sensitivity to atmospheric chlorine loading, ***Geophys. Res. Lett.***, ***22*** (22), 3035–3038, doi:10.1029/95GL03057, 1995.

Tie, X., G.P. Brassuer, C. Granier, A. De Rudder, and N. Larsen, Model study of polar stratospheric clouds and their effect on stratospheric ozone: 2. Model results, ***J. Geophys. Res. Atmos.***, ***101*** (D7), 12,575–12,584, doi:10.1029/96JD00403, 1996.

Tilmes, S., R. Müller, J.U. Grooß, and J.M. Russell III, Ozone loss and chlorine activation in the Arctic winters 1991-2003 derived with the tracer-tracer correlations. ***Atmospheric Chemistry and Physics***, ***4***(8), pp.2181-2213, 2004.

Tilmes, S., R. Müller, and R. Salawitch, The sensitivity of polar ozone depletion to proposed geo-engineering schemes, ***Science***, ***320*** (5880), 1201–1204, doi:10.1126/science.1153966, 2008.

Tilmes, S., R.R. Garcia, D.E. Kinnison, A. Gettelman, and P.J. Rasch, Impact of geoengineered aerosols on the troposphere and stratosphere, ***J. Geophys. Res. Atmos.***, ***114*** (D12), doi:10.1029/2008JD011420, 2009.

Tilmes, S., Kinnison, D. E., Garcia, R. R., Salawitch, R., Canty, T., Lee-Taylor, J., Madronich, S., and Chance, K.: Impact of very short-lived halogens on stratospheric ozone abundance and UV radiation in a geo-engineered atmosphere, Atmos. Chem. Phys., 12, 10945–10955, https://doi.org/10.5194/acp-12-10945-2012, 2012.

Tilmes, S., J. Fasullo, J.F. Lamarque, D.R. Marsh, M. Mills, K. Alterskjær, H. Muri, J.E. Kristjánsson, O. Boucher, M. Schulz, and J.N. Cole, The hydrological impact of geoengineering in the Geoengineering Model Intercomparison Project (GeoMIP), ***J. Geophys. Res. Atmos.***, ***118*** (19), 11,036–11,058, doi:10.1002/jgrd.50868, 2013.

Tilmes, S., B.M. Sanderson, and B.C. O'Neill, Climate impacts of geoengineering in a delayed mitigation scenario, ***Geophys. Res. Lett.***, ***43*** (15), 8222–8229, doi:10.1002/2016GL070122, 2016.

Tilmes, S., J.H. Richter, M.J. Mills, B. Kravitz, D.G. MacMartin, F. Vitt, J.J. Tribbia, and J.-F. Lamarque, Sensitivity of aerosol distribution and climate response to stratospheric SO2 injection locations, ***J. Geophys. Res. Atmos.***, ***122*** (23), 12,591–12,615, doi:10.1002/2017JD026888, 2017.

Tilmes, S., J.H. Richter, B. Kravitz, D.G. MacMartin, M.J. Mills, I.R. Simpson, A.S. Glanville, J.T. Fasullo, A.S. Phillips, J.-F. Lamarque, J. Tribbia, J. Edwards, J., S. Mickelson, and S. Ghosh, CESM1 (WACCM) stratospheric aerosol geoengineering large ensemble project, ***Bull. Am. Meteorol. Soc., 99*** (11), 2361–2371, doi:10.1175/BAMS-D-17-0267.1, 2018a.

Tilmes, S., J.H. Richter, M.J. Mills, B. Kravitz, D.G. MacMartin, R.R. Garcia, D.E. Kinnison, J.-F. Lamarque, J. Tribbia, and F. Vitt, Effects of different stratospheric SO_2 injection altitudes on stratospheric chemistry and dynamics, ***J. Geophys. Res. Atmos.***, ***123***, 4654–4673, doi:10.1002/2017JD028146, 2018b.

Tilmes, S., D.G. MacMartin, J. Lenaerts, L.V. Kampenhout, L. Muntjewerf, L. Xia, C.S. Harrison, K.M. Krumhardt, M.J. Mills, B. Kravitz, and A. Robock, Reaching 1.5 and 2.0 °C global surface temperature targets using stratospheric aerosol geoengineering, ***Earth Syst. Dyn.***, ***11*** (3), 579–601, doi:10.5194/esd-11-579-2020, 2020.

Tilmes, S., J.H. Richter, B. Kravitz, D.G. MacMartin, A.S. Glanville, D. Visioni, D.E. Kinnison, and R. Müller, Sensitivity of total column ozone to stratospheric sulfur injection strategies, ***Geophys. Res. Lett.***, ***48*** (19), e2021GL094058, doi:10.1029/2021GL094058, 2021.

Tilmes, S., D. Visioni, A. Jones, J. Haywood, R. Séférian, P. Nabat, O. Boucher, E.M. Bednarz, and U. Niemeier, Stratospheric ozone response to sulfate aerosol and solar dimming climate interventions based on the G6 Geoengineering Model Intercomparison Project (GeoMIP) simulations, ***Atmos. Chem. Phys.***, ***22*** (7), 4557–4579, doi:10.5194/acp-2021-1003, 2022.

Timmreck, C., and H.-F. Graf, The initial dispersal and radiative forcing of a Northern Hemisphere mid-latitude super volcano: a model study, ***Atmos. Chem. Phys.***, ***6***, 35–49, doi:10.5194/acp-6-35-2006, 2006.

Timmreck, C., S.J. Lorenz, T.J. Crowley, S. Kinne, T.J. Raddatz, M.A. Thomas, and J.H. Jungclaus, Limited temperature response to the very large AD 1258 volcanic eruption, ***Geophys. Res. Lett.***, ***36*** (21), doi:10.1029/2009GL040083, 2009.

Timmreck, C., H.F. Graf, S.J. Lorenz, U. Niemeier, D. Zanchettin, D. Matei, J.H. Jungclaus, and T.J. Crowley, Aerosol size confines climate response to volcanic super-eruptions, ***Geophys. Res. Lett.***, ***37*** (24), doi:10.1029/2010GL045464, 2010.

Tollefson, J., IPCC says limiting global warming to 1.5 °C will require drastic action, ***Nature***, ***562*** (7726), 172–173, doi:10.1038/d41586-018-06876-2, 2018.

Thompson, D.W. and S. Solomon,Understanding recent stratospheric climate change. ***Journal of Climate***, ***22***(8), pp.1934-1943, 2009.

Torres, O., H. Jethva, C. Ahn, G. Jaross, and D.G. Loyola, TROPOMI aerosol products: evaluation and observations of synoptic-scale carbonaceous aerosol plumes during 2018–2020, ***Atmos. Meas. Tech.***, ***13*** (12), 6789–6806, doi:10.5194/amt-13-6789-2020, 2020.

Trenberth, K.E., and A. Dai, Effects of Mount Pinatubo volcanic eruption on the hydrological cycle as an analog of geoengineering, ***Geophys. Res. Lett.***, ***34*** (15), doi:10.1029/2007GL030524, 2007.

Trisos, C.H., G. Amatulli, J. Gurevitch, A. Robock, L. Xia, and B. Zambri, Potentially dangerous consequences for biodiversity of solar geoengineering implementation and termination, ***Nat. Ecol. Evol.***, ***2*** (3), 475–482, doi:10.1038/s41559-017-0431-0, 2018.

Van Roozendael, M., M. De Maziere, C. Hermans, P.C. Simon, J.P. Pommereau, F. Goutail, X.X. Tie, G. Brasseur, and C. Granier, Ground-based observations of stratospheric NO2 at high and midlatitudes in Europe after the Mount Pinatubo eruption, ***J. Geophys. Res. Atmos.***, ***102*** (D15), 19,171–19,176, doi:10.1029/97JD01098, 1997.

Vattioni, S., D. Weisenstein, D. Keith, A. Feinberg, T. Peter, and A. Stenke, Exploring accumulation-mode H_2SO_4 versus SO_2 stratospheric sulfate geoengineering in a sectional aerosol–chemistry–climate model, ***Atmos. Chem. Phys.***, ***19***, 4877–4897, doi:10.5194/acp-19-4877-2019, 2019.

Vehkamäki, H., M. Kulmala, I. Napari, K.E.J. Lehtinen, C. Timmreck, M. Noppel, and A. Laaksonen, An improved parameterization for sulfuric acid water nucleation rates for tropospheric and stratospheric conditions, ***J. Geophys. Res.***, ***107*** (D22), 4622, doi:10.1029/2002JD002184, 2002.

Vernier, J.P., L.W. Thomason, J.P. Pommereau, A. Bourassa, J. Pelon, A. Garnier, A. Hauchecorne, L. Blanot, C. Trepte, D. Degenstein, and F. Vargas, Major influence of tropical volcanic eruptions on the stratospheric aerosol layer during the last decade, ***Geophys. Res. Lett.***, ***38*** (12), doi:10.1029/2011GL047563, 2011.

Visioni, D., G. Pitari, and V. Aquila, Sulfate geoengineering: a review of the factors controlling the needed injection of sulfur dioxide, ***Atmos. Chem. Phys.***, ***17***, 3879–3889, doi:10.5194/acp-17-3879-2017, 2017a.

Visioni, D., G. Pitari, V. Aquila, S. Tilmes, I. Cionni, G. Di Genova, and E. Mancini, Sulfate geoengineering impact on methane transport and lifetime: results from the Geoengineering Model Intercomparison Project (GeoMIP), ***Atmos. Chem. Phys.***, ***17***, 11,209–11,226, doi:10.5194/acp-17-11209-2017, 2017b.

Visioni, D., G. Pitari, G. di Genova, S. Tilmes, and I. Cionni, Upper tropospheric ice sensitivity to sulfate geoengineering, ***Atmos. Chem. Phys.***, ***18***, 14,867–14,887, doi:10.5194/acp-18-14867-2018, 2018.

Visioni, D., D.G. MacMartin, B. Kravitz, S. Tilmes, M.J. Mills, J.H. Richter, and M.P. Boudreau, Seasonal injection strategies for stratospheric aerosol geoengineering, ***Geophys. Res. Lett.***, ***46*** (13), 7790-7799, doi:10.1029/2019GL083680, 2019.

Visioni, D., D.G. MacMartin, B. Kravitz, J.H. Richter, S. Tilmes, and M.J. Mills, Seasonally modulated stratospheric aerosol geoengineering alters the climate outcomes, ***Geophys. Res. Lett.***, ***47*** (12), e2020GL088337, doi:10.1029/2020GL088337, 2020a.

Visioni, D., D.G. MacMartin, B. Kravitz, W. Lee, I.R. Simpson, and J.H. Richter, Reduced poleward transport due to stratospheric heating under stratospheric aerosols geoengineering, ***Geophys. Res. Lett.***, ***47*** (17), e2020GL089470, doi:10.1029/2020GL089470, 2020b.

Visioni, D., E. Slessarev, D.G. MacMartin, N.M. Mahowald, C.L. Goodale, and L. Xia, What goes up must come down: impacts of deposition in a sulfate geoengineering scenario, ***Environ. Res. Lett.***, ***15*** (9), 094063, doi:10.1088/1748-9326/ab94eb, 2020c.

Visioni, D., D.G. MacMartin, B. Kravitz, O. Boucher, A. Jones, T. Lurton, M. Martine, M.J. Mills, P. Nabat, U. Niemeier, R. Séférian, and S. Tilmes, Identifying the sources of uncertainty in climate model simulations of solar radiation modification with the G6sulfur and G6solar Geoengineering Model Intercomparison Project (GeoMIP) simulations, ***Atmos. Chem. Phys.***, ***21***, 10,039–10,063, doi:10.5194/acp-21-10039-2021, 2021a.

Visioni, D., D.G. MacMartin, and B. Kravitz, Is turning down the sun a good proxy for stratospheric sulfate geoengineering?, ***J. Geophys. Res. Atmos.***, ***126*** (5), e2020JD033952, doi:10.1029/2020JD033952, 2021b.

Visioni, D., S. Tilmes, C. Bardeen, M. Mills, D.G. MacMartin, B. Kravitz, and Richter, J.H., 2022, Limitations of assuming internal mixing between different aerosol species: a case study with sulfate geoengineering simulations. ***Atmospheric Chemistry and Physics***, ***22***(3), pp.1739-1756, 2022.

Wei, L., D. Ji, C. Miao, H. Muri, and J.C. Moore, Global streamflow and flood response to stratospheric aerosol geoengineering, ***Atmos. Chem. Phys.***, ***18*** (21), 16,033–16,050, doi:10.5194/acp-18-16033-2018, 2018.

Weisenstein, D., S. Bekki, G. Pitari, C. Timmreck, and M. Mills, Modeling of Stratospheric Aerosols, Chapter 6, in ***SPARC Assessment of Stratospheric Aerosol Properties (ASAP)***, edited by L. Thomason and Th. Peter, SPARC Report No. 4, WCRP-124, WMO/TD–No. 1295, 54 pp., Stratosphere-troposphere Processes And their Role in Climate, [available at: https://www.sparc-climate.org/publications/sparc-reports/sparc-report-no-4/], 2006.

Weisenstein, D.K., D.W. Keith, and J.A. Dykema, Solar geoengineering using solid aerosol in the stratosphere, ***Atmos. Chem. Phys.***, ***15*** (20), 11,835–11,859, doi:10.5194/acp-15-11835-2015, 2015.

Weisenstein, D.K., D. Visioni, H. Franke, U. Niemeier, S. Vattioni, G. Chiodo, T. Peter, and D.W. Keith, An interactive stratospheric aerosol model intercomparison of solar geoengineering by stratospheric injection of SO2 or accumulation-mode sulfuric acid aerosols, ***Atmos. Chem. Phys.***, ***22***, 2955–2973, doi:10.5194/acp-22-2955-2022, 2022.

Wigley, T.M.L., A combined mitigation/geoengineering approach to climate stabilization, ***Science***, ***314***, 452–454, doi:10.1126/science.1131728, 2006.

Wilka, C., K. Shah, K. Stone, S. Solomon, D. Kinnison, M. Mills, A. Schmidt, and R.R. Neely III, On the role of heterogeneous chemistry in ozone depletion and recovery. ***Geophysical Research Letters***, ***45***(15), pp.7835-7842, 2018.

Wu, H., J.W. Taylor, J.M. Langridge, C. Yu, J.D. Allan, K. Szpek, M.I. Cotterell, P.I. Williams, M. Flynn, P. Barker, C. Fox, G. Allen, J. Lee, and H. Coe, Rapid transformation of ambient absorbing aerosols from West African biomass burning, ***Atmos. Chem. Phys.***, ***21***, 9417–9440, doi:10.5194/acp-21-9417-2021, 2021.

Xia, L., A. Robock. J.N.S. Cole, C.L. Curry, D. Ji, A. Jones, B. Kravitz, J.C. Moore, H. Muri, U. Niemeier, B. Singh, S. Tilmes, S. Watanabe, and J.-H. Yoon, Solar Radiation Management impacts on agriculture in China: A case study in the Geoengineering Model Intercomparison Project (GeoMIP), ***J. Geophys. Res. Atmos.***, ***119*** (14), 8695–8711, doi:10.1002/2013JD020630, 2014.

Xia, L., A. Robock, S. Tilmes, and R.R. Neely, Stratospheric sulfate geoengineering could enhance the terrestrial photosynthesis rate, ***Atmos. Chem. Phys.***, ***16*** (3), 1479–1489, doi:10.5194/acp-16-1479-2016, 2016.

Xia, L., P.J. Nowack, S. Tilmes, and A. Robock, Impacts of stratospheric sulfate geoengineering on tropospheric ozone, ***Atmos. Chem. Phys.***, ***17***, 11,913–11,928, doi:10.5194/acp-17-11913-2017, 2017.

Yook, S., D.W. Thompson, and S. Solomon, Climate impacts and potential drivers of the unprecedented Antarctic ozone holes of 2020 and 2021. ***Geophysical Research Letters***, p.e2022GL098064, 2022.

Young, R.E., H. Houben, and O.B. Toon, Radiatively forced dispersion of the Mount Pinatubo volcanic cloud and induced temperature perturbations in the stratosphere during the first few months following the eruption, ***Geophys. Res. Lett.***, ***21*** (5), 369–372, doi:10.1029/93GL03302, 1994.

Yu, P., O.B. Toon, C.G. Bardeen, Y. Zhu, K.H. Rosenlof, R.W. Portmann, T.D. Thornberry, R.S. Gao, S.M. Davis, E.T. Wolf, and J. de Gouw, Black carbon lofts wildfire smoke high into the stratosphere to form a persistent plume, ***Science***, ***365*** (6453), 587–590, doi:10.1126/science.aax1748, 2019.

Yu, P., S.M. Davis, O.B. Toon, R.W. Portmann, C.G. Bardeen, J.E. Barnes, H. Telg, C. Maloney, and K.H. Rosenlof, Persistent stratospheric warming due to 2019–2020 Australian wildfire smoke, ***Geophys. Res. Lett.***, ***48*** (7), e2021GL092609, doi:10.1029/2021GL092609, 2021.

Zambri, B., A.N. LeGrande, A. Robock, and J. Slawinska, Northern Hemisphere winter warming and summer monsoon reduction after volcanic eruptions over the last millennium, ***J. Geophys. Res. Atmos.***, ***122*** (15), 7971–7989, doi:10.1002/2017JD026728, 2017.

Zanchettin, D., M. Khodri, C. Timmreck, M. Toohey, A. Schmidt, E.P. Gerber, G. Hegerl, A. Robock, F.S.R. Pausata, W.T. Ball, S.E. Bauer, S. Bekki, S.S. Dhomse, A.N. LeGrande, G.W. Mann, L. Marshall, M. Mills, M. Marchand, U. Niemeier, V. Poulain, E. Rozanov, A. Rubino, A. Stenke, K. Tsigaridis, and F. Tummon, The Model Intercomparison Project on the climatic response to Volcanic forcing (VolMIP): experimental design and forcing input data for CMIP6, ***Geosci. Model Dev.***, ***9*** (8), 2701–2719, doi:10.5194/gmd-9-2701-2016, 2016.

Zhu, Y., O.B. Toon, D. Kinnison, V.L. Harvey, M.J. Mills, C.G. Bardeen, M. Pitts, N. Bègue, J.B. Renard, G. Berthet, and F. Jégou, Stratospheric aerosols, polar stratospheric clouds, and polar ozone depletion after the Mount Calbuco eruption in 2015, ***J. Geophys. Res. Atmos.***, ***123*** (21), 12,308–12,331, doi:10.1029/2018JD028974, 2018.

Zhu, Y., O.B. Toon, E.J. Jensen, C.G. Bardeen, M.J. Mills, M.A. Tolbert, P. Yu, and S. Woods, Persisting volcanic ash particles impact stratospheric SO2 lifetime and aerosol optical properties, ***Nat. Commun.***, ***11*** (1), 1–11, doi:10.1038/s41467-020-18352-5, 2020.

CHAPTER 7

Scenarios and Information for Policymakers

About the cover image:
The Montreal Protocol on Substances that Deplete the Ozone Layer has been ratified by every country on Earth – all 198 United Nations Member States.

Photo credit: MyCreative via Adobe Stock

CHAPTER 7

Scenarios and Information for Policymakers

Lead Authors : John S. Daniel
Stefan Reimann

Coauthors : Paul Ashford
Eric L. Fleming
Ryan Hossaini
Megan J. Lickley
Robyn Schofield
Helen Walter-Terrinoni

Contributing Authors : Laura McBride
Sunyoung Park
Martin N. Ross
Ross J. Salawitch
David Sherry
Susann Tegtmeier
Guus J. M. Velders

Review Editors : Lambert J. M. Kuijpers
Donald J. Wuebbles

CONTENTS

Chapter 7: Scenarios and Information for Policymakers

SCIENTIFIC SUMMARY

In its evaluation of future scenarios, this chapter uses reduced complexity models to calculate future impacts on ozone and climate. These models supplement the results from more complex models discussed in Chapters 3–6, with the added advantage that the simpler framework allows exploration of a greater number of scenarios and sensitivity experiments.

Post-Kigali Information of Interest

- **The Kigali Amendment to the Montreal Protocol, along with regional and national regulatory and voluntary actions taken before Kigali entered into force, is expected to substantially limit future climate forcing by HFCs.** Assuming global compliance with the Kigali Amendment, it is expected that HFCs will cause a peak radiative forcing of about 100 mW m^{-2} by mid-century. This may be compared to some past projections of forcing absent the Kigali Amendment or regulation under another convention, the highest being in excess of 400 mW m^{-2} in 2050, with substantial increases after that. Given the regional and national regulatory and voluntary actions taken before Kigali entered into force, and assuming global adherence to the Kigali Amendment to the Montreal Protocol, the contribution of HFCs to global annual average warming is projected to be 0.04 °C in 2100 (*Chapter 2*), with a continued decline after that time.
- **The elimination of all long-lived HFC emissions (including HFC-23) from 2023 onward represents an extreme example of the potential opportunities for future HFC reductions and would reduce the average radiative forcing over 2023–2100 by 79 mW m^{-2}**, with additional benefits continuing after 2100. This is more than twice the benefit of eliminating all controlled ODS emissions from the baseline scenario and would reduce the warming attributable to all HFCs to less than 0.01 °C by 2100. Of the 79 mW m^{-2}, 51 mW m^{-2} arises from future production and usage of long-lived HFCs (excluding HFC-23), 16 mW m^{-2} comes from future emissions from current banks, and 11 mW m^{-2} comes from emissions of HFC-23.
- **If emissions of HFC-23, a potent greenhouse gas, remain at the current relative level compared with HCFC-22 production, HFC-23 has the potential to cause about half of the climate forcing (30 mW m^{-2}) of all the other HFCs, combined, by 2100.** HFC-23 is emitted into the atmosphere mainly as a by-product from the production of HCFC-22. Its emissions relative to the amounts of HCFC-22 produced have not changed much in recent years and are higher than would be expected if state-of-the-art destruction had been performed during the HCFC-22 production process. While the Kigali Amendment to the Montreal Protocol requires that HFC-23 be "destroyed to the extent practicable," this requirement and the connected reporting of emissions went into effect only on 1 January 2020, and thus reporting is still incomplete and the global response is unclear. Through 2019, the emissions of HFC-23 as a fraction of HCFC-22 production indicate that a considerable part of the produced HFC-23 was still being released unabated into the atmosphere.
- **Other sources of HFC-23 emissions to the atmosphere may exist and could contribute to its atmospheric burden.** There could be contributions to HFC-23 abundances through formation and loss during the production of tetrafluoroethene (TFE) and from the incineration of HCFC-22. Furthermore, direct emissions could grow from the use of HFC-23 in low-temperature refrigeration, although it is not the only refrigerant used in this application.
- **The Kigali Amendment's control of high-GWP HFCs is expected to lead to overwhelmingly positive climate benefits. Nevertheless, there is a potential for certain negative side effects.** Hydrofluoroolefins (HFOs) are increasingly used for replacing high-global warming potential (GWP) HFCs in refrigeration, foam blowing, and various other applications. This replacement leads to less climate change. However, high-volume usage of CCl_4 (carbon tetrachloride) as a feedstock in the production of HFOs, a usage and production not controlled by the Montreal Protocol, could lead to sustained elevated abundances of CCl_4 if current techniques are continued and some fraction of feedstock production continues to be emitted. A second side effect is that HFO-1234yf emitted into the atmosphere will be fully converted to the stable trifluoroacetic acid (TFA; see below).
- **Trifluoroacetic acid (TFA), which is produced in the atmosphere from the degradation of HFCs, HCFCs, HFOs, and HCFOs, is not expected to harm the environment over the next few decades, although some regional concerns have been raised; periodic evaluation of this assessment is suggested, as important gaps in our understanding remain.** This assessment is based on updated estimates of the TFA formation from current atmospheric concentrations of HFCs and HCFCs (hydrochlorofluorocarbons) and their projected decline, as well as the expected increasing abundance of HFOs as HFC and HCFC replacements within the next years. With long-lived HFCs being replaced with high-TFA-producing, short-lived HFOs, more TFA will be formed in the atmosphere. Because of the shorter lifetime of HFOs, this TFA is expected to be deposited nearer to the location of emissions. Other anthropogenic sources of TFA, such as the incineration of polytetrafluoroethene (PTFE), could also contribute. In view of changing and potential unknown sources, concentrations of TFA should be monitored for changes in different parts of the environment, with a special focus on highly populated regions and on the remote ocean.

Updates on the Climate Impact of Gases Controlled by the Montreal Protocol

- **In the baseline scenario, future emissions of HFCs (excluding HFC-23), HFC-23, HCFCs, and CFCs contribute**

approximately 68, 11, 9, and 9 mW m^{-2} to radiative forcing, respectively, averaged over the 2023–2100 period. Of the 68 mW m^{-2} from HFCs, 51 mW m^{-2} arise from future production. For reference, CO_2 (carbon dioxide) emissions from fossil fuel usage over this time period are projected to contribute an average of about 3250 mW m^{-2} in the SSP2-4.5 scenario. The total radiative forcing from CFCs, HCFCs, and their HFC replacements is projected to continue to remain roughly constant for the next decade or two. After about 2040, the ODS and HFC restrictions of the Montreal Protocol, if adhered to, are expected to ensure a continued decline in the total RF from ODSs and their replacements. Previous expected increases in RF driven by projected HFC increases throughout the century are now mitigated by assumed compliance with the Kigali Amendment.

- **The effective radiative forcing of the halocarbons has been revised to encompass lower values due to a larger range of estimated negative forcing from the ozone depletion they cause.** This offset of the halocarbon direct radiative forcing remains highly uncertain.

Ozone-Depleting Substances (ODSs) and Their Replacements: Impacts on Ozone and Climate

Below, we discuss potential trajectories of equivalent effective stratospheric chlorine (EESC; a proxy for ozone depletion) and radiative forcing (a proxy for climate change) that result from our current understanding of the emissions of individual gases or groups of gases and the processes that lead to these emissions. We reference these potential changes to the so-called baseline scenario, which should be considered a plausible future pathway for these gases that is consistent with the controls of the Montreal Protocol. The specific assumptions made in the baseline scenario can be extremely important to the results. Note that the combined impact of changing assumptions is not always simply the addition of each of the changes. It is also important to recognize that the return date of EESC to 1980 levels is quite sensitive to any change in the EESC concentration because of the relatively small rate at which the EESC is projected to decline around the middle of this century. While a change in the return date to 1980 EESC levels measured in tenths of years or even a few years cannot be discerned in the atmosphere, primarily due to natural variability, this metric can be useful for comparing various alternative ODS scenarios.

It should also be noted that the EESC formalism adopted here is the same one that was applied in Appendix 6C of the 2018 Assessment and reflects our improved scientific understanding of EESC (see Section 7.3*). This alters the time evolution of EESC and dates when EESC returns to 1980 levels when compared with the older approach used in the main part of Chapter 6 of the 2018 Assessment, but it has little effect on the relative impacts of the various alternative future scenarios. If EESC comparisons are made with the 2018 Assessment, it is most appropriate to compare to those found in Appendix 6C rather than in Table 6-5 of that Assessment.*

- **Changes in the current baseline scenario lead to a delay in the return of mid-latitude and polar EESC to 1980 levels by 4 years and 7 years, respectively, compared with the baseline scenario in the previous Assessment. This is due mainly to a larger assessed CFC-11 bank, and to a lesser degree, to a larger assessed CFC-12 bank.** The larger bank for CFC-11 does not include any explicit increase due to unreported production over the past decade, as that amount is highly uncertain.
- **The unexpected emissions of CFC-11 declined after 2018. The continued elimination of this emission and the production that has caused it will prevent a substantial impact on ozone and climate.** Cumulative unexpected emissions over 2012–2019 have been estimated at 120–440 Gg. Since then, these annual emissions have diminished substantially from their peak amount. The integrated emissions over this period are calculated to lead to a delay in the return of mid-latitude EESC to 1980 levels by about one year and to cause an additional radiative forcing of 2 mW m^{-2} averaged over 2023–2100. It is unclear how much of the production that led to these emissions has gone into banks, as opposed to having already been emitted. If the unexpected emissions over 2012–2019 were associated with the production of insulating foams, it is estimated that they would have accounted for 25% to 45% of the unreported production, with the rest (146–1320 Gg) going into the CFC-11 bank. The impact of any increase in the bank can be estimated from knowing that a hypothetical 1000 Gg added to the 2020 bank delays the return of mid-latitude EESC to 1980 levels by almost four years and leads to an additional averaged radiative forcing over 2023–2100 of about 6 mW m^{-2}.
- **The hypothetical elimination of all future ODS emissions would bring forward the return of mid-latitude and polar EESC to 1980 levels by 16 years and 19 years, respectively, and increase the average of global stratospheric ozone levels in the period 2020–2070 by about 2 DU.** It would also reduce average radiative forcing by 31 mW m^{-2} averaged over 2023–2100. These emissions are dominated by the release from current banks, with a smaller contribution from future production of ODSs that is controlled by the Montreal Protocol and emissions associated with production intended for feedstock purposes. Estimates of bank sizes are highly uncertain though; the bank approach used in the scenarios here has resulted in substantially larger 2020 banks than estimated in the previous Assessment.
- **In the baseline scenario, future emissions from current CFC banks contribute more to EESC than do emissions from either HCFC banks or halon banks.** However, given the uncertainty in estimates of current bank sizes, these differences are likely not statistically significant. An elimination of the emissions from the CFC banks are calculated to bring forward the return of mid-latitude EESC to 1980 levels by about 5 years. In this chapter, there is no evaluation made regarding the accessibility of various banks in terms of recapture and destruction.
- **In the baseline scenario, future emissions from current HCFC banks contribute more to climate change than do future emissions from either CFC banks or halon banks.** However, the differences in the climate impacts between the banks of HCFCs and CFCs are likely not statistically significant. Again, there is no evaluation made regarding the accessibility of various banks in terms of recapture and destruction.

- **Elimination of future emissions of methyl bromide (CH_3Br) from quarantine and preshipment (QPS) applications, not controlled by the Montreal Protocol, would accelerate the return of mid-latitude and polar EESC to 1980 levels by about two years and would increase globally averaged total ozone by 0.2 DU when averaged over 2020–2070.** Production for QPS use has remained relatively stable over the last two decades and now constitutes almost 99% of reported production of CH_3Br, since emissions from other uses have declined dramatically. Non-QPS applications of CH_3Br were completely phased out in 2015, except for approved critical use exemptions (CUEs). These CUEs have declined by a factor of ~200 since 2005 and make up the remaining ~1% of reported production. CH_3Br has little direct impact on climate.
- **Otherwise controlled ODSs have increasingly been used as feedstocks. With estimated emission rates of 2–4% (4.3% for CCl_4) from the produced ODSs, this has resulted in estimated emissions associated with ODS feedstock applications of 37–59 Gg (15–19 ODP-Gg) in 2019. The influence on ozone of these emissions was dominated by emissions from the feedstock use of CCl_4. When compared to the baseline scenario, in which these emissions continue at current levels, an elimination of emissions associated with feedstock use would bring forward the return of mid-latitude and polar EESC to 1980 levels by about 4 and 5 years, respectively.** Between 2009 and 2019, the mass of ODSs used as feedstocks, which is not controlled under the Protocol, increased by 75%. When expressed in units of Gg ODP (Gg multiplied by the ozone depletion potential), the increase in feedstock-linked production was only 41% over the same period, as HCFC-22, with a relatively low ODP, was responsible for the highest growth. Eliminating all these emissions in the future would reduce averaged radiative forcing by 6 mW m^{-2} compared with the baseline scenario.
- **Of the feedstock production reported, estimated emissions from CCl_4 and HCFC production dominate the impact on climate over the coming decades. These two groups lead to an increased average radiative forcing over 2023–2100 of 5 mW m^{-2} in the baseline scenario.** The size of this climate effect is dependent on the assumptions made in the baseline scenario regarding feedstock production growth.
- **CCl_4 feedstock production and usage increased by a factor of about two within the last decade. If CCl_4 emissions associated with these allowed uses continue to grow through 2030 as they have been growing over the past decade, future CCl_4 atmospheric concentrations will decline more slowly and will be about twice as high (+20 ppt) in 2100 than in the baseline scenario, in which feedstock-related emissions remain constant.** As reported in the 2018 Assessment, CCl_4 emissions inferred from atmospheric observations continue to be considerably higher than those estimated from feedstock uses, as reported to the United Nations Environment Programme (UNEP), and other known sources. CCl_4 emissions related to its feedstock production and usage have been assessed to be 4.3% of the produced amount of CCl_4, with a relatively large associated uncertainty. Calculated as ODP-weighted emissions, the emissions from feedstock use of CCl_4 in 2019 was 11.2 ODP-Gg yr^{-1}, or 60–74% of all feedstock-related emissions. This is important, as the usage of CCl_4 is projected to continue to increase because of its application in the growing production of HFOs in the replacement of the long-lived HFCs. An elimination of all future CCl_4 emissions associated with feedstock usage would reduce radiative forcing by about 2 mW m^{-2} compared with the baseline scenario when averaged over 2023–2100.
- **In addition to CCl_4, the most important contributions to ODP-weighted emissions from other ODSs used as feedstock are from CFC-113 and CFC-114 (2.3–4.6 ODP-Gg), from HCFC-22 (0.5–1.1 ODP-Gg), and from the sum of other HCFCs (0.1–0.3 ODP-Gg), with the highest contribution from HCFC-142b.** These values are based on estimated emissions of 2–4% relative to the production amount. The increased use of HCFC-22 and other HCFCs as feedstocks for fluoropolymer production within the last decades is expected to continue into the future. On the other hand, the usage of feedstock chemicals for the production of HFCs will likely decline because of the Kigali Amendment.
- **The production and usage of short-lived chlorinated solvents is not controlled by the Montreal Protocol, and some are used in large amounts. Their impact on stratospheric ozone, and their ODPs, vary depending on the season and location of emissions and could grow in the future even as emissions from long-lived ODSs decline.** More than 1600 Gg of $CHCl_3$ (chloroform) are used as feedstock in the production of HCFC-22. Emissions from $CHCl_3$ used as a feedstock are comparable to its solvent emissions. CH_2Cl_2 (dichloromethane), TCE (trichloroethene), and PCE (perchloroethene) are also used as feedstock chemicals, although their emissions are dominated by emissive uses (e.g., from solvents).
- **Sustained increases in anthropogenic chlorinated very short-lived substance (VSLS) emissions, as seen for CH_2Cl_2 over the last two decades, would lead to more stratospheric ozone depletion in the future.** While observed growth rates of CH_2Cl_2 have been highly variable and future projections are believed to be highly uncertain, emissions have continued to increase since the last Assessment. If emission rates remain constant at their present level into the future, CH_2Cl_2 is projected to deplete 0.8–1.7 DU averaged over 2020 to 2070 compared to a case of zero future emissions. Any reduction in the production and consumption of CH_2Cl_2 would have a rapid impact on ozone, since this VSLS is both emitted soon after production and is cleansed out of the stratosphere within a few years.
- **A reduction in future N_2O emissions from that in the baseline scenario (SSP2-4.5) to that in the SSP scenario with the strongest N_2O mitigation (SSP1-1.9) results in a 0.5 DU increase in ozone averaged over 2020 to 2070, or about one-quarter of the impact of eliminating all emissions from controlled ODSs beginning in 2023.** This emission reduction also leads to a radiative forcing reduction of 43 mW m^{-2} averaged over 2023–2100. The magnitude of this N_2O reduction represents a decrease in anthropogenic N_2O emissions of 3% compared with the baseline scenario when averaged over 2020–2070.

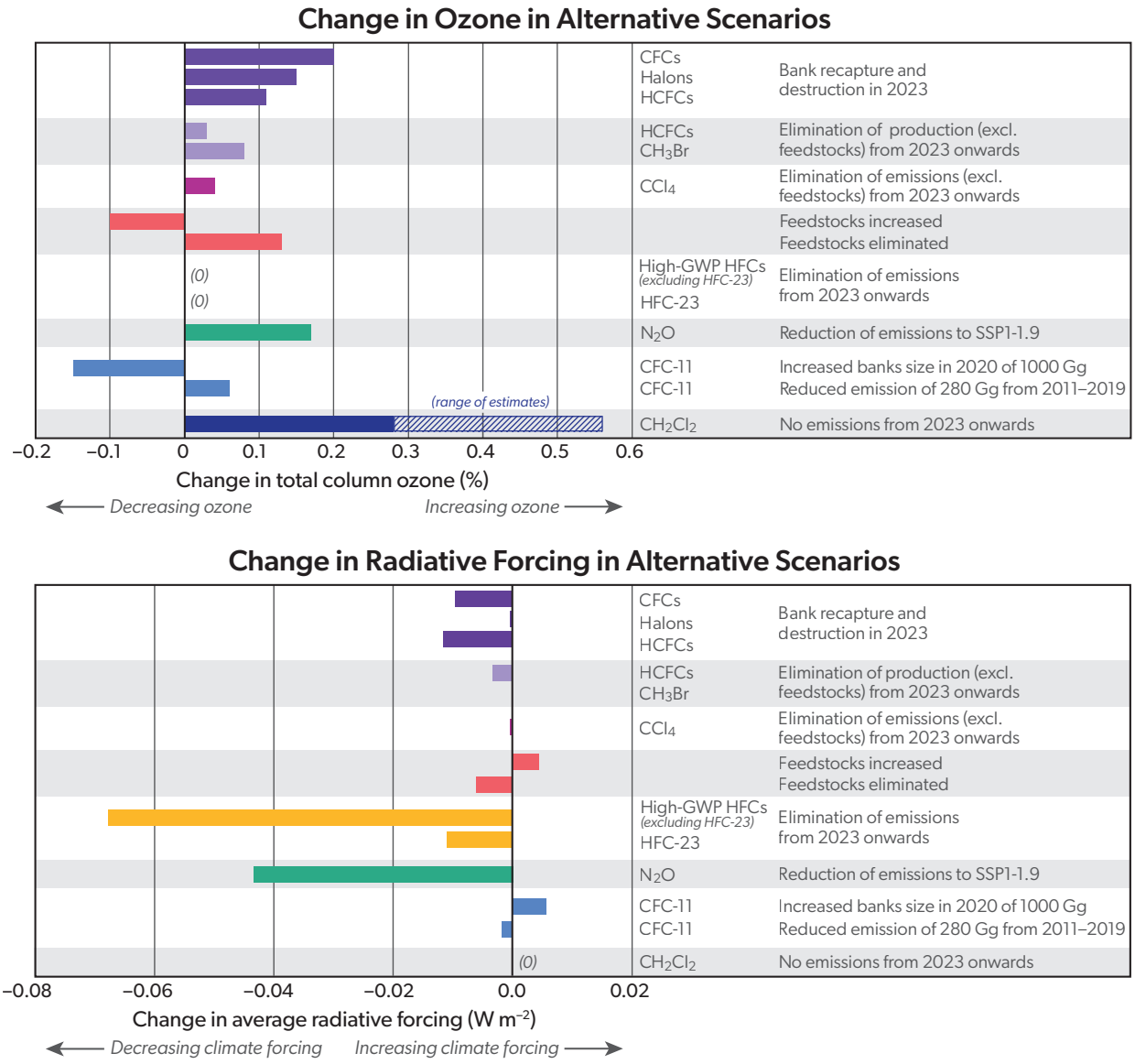

Figure 7-1. Impacts of various alternative scenarios and test cases on total column ozone (averaged over 2020 through 2070) and radiative forcing of climate (averaged over 2023 through 2100) compared with the baseline scenario. The scenarios and cases include reduced N_2O emissions (SSP1-1.9 scenario), elimination of emissions for HFCs, HFC-23, CH_2Cl_2, and CCl_4 (excluding emissions from feedstock production and usage) starting in 2023, elimination of future production of CH_3Br and HCFCs starting in 2023 (excluding feedstock production and usage), and elimination and destruction of banks of halons, HCFCs and CFCs in 2023. Also considered are the unexpected CFC-11 emissions over 2012–2019 (assumed to be 280 Gg in total), an additional 1000 Gg in the 2020 CFC-11 bank, elimination of all feedstock-related emissions starting in 2023, and a case in which feedstock-related emissions are allowed to grow at their current growth rates through 2030 and are then held constant. Potential climate benefits from improved energy efficiency in the refrigeration and air conditioning sector are not included here, and are thought to have the potential to have an impact much larger than that of any of the scenarios and cases considered here. For reference, current total column ozone depletion is about 2% when averaged over 60°S–60°N, and the current radiative forcing from CO_2 is about 2 W m^{-2}.

Impacts of Mitigation Options and Particular Scenarios

Figure 7.1 (also shown as Figure ES-8 in this document) shows the ozone and climate-relevant changes that would occur if various actions were to be taken. These changes are shown as the differences in global total column ozone averaged over 2020–2070 and in radiative forcing averaged over 2023–2100, both relative to the baseline scenario, which includes the Kigali Amendment controls for HFCs in Annex F, Group 1. The options available to hasten the recovery of the ozone layer are somewhat limited, mostly because past actions have already been very successful at reducing emissions of ODSs and their replacements.

- For the ODSs, the single most effective ozone depletion and climate change mitigation option, not considering technical feasibility, is bank recapture and destruction of the CFC banks; however, large uncertainties in the CFC-11 and CFC-12 banks have been reported in the literature, with the recent production associated with the unexpected emissions of CFC-11 further adding to uncertainties in the bank sizes. Furthermore, no assessment has been made here regarding the fraction of the banks that are accessible for capture or the fraction that are active.
- For CH_3Br, elimination of production for currently uncontrolled QPS applications is shown.
- For CCl_4, the impact of eliminating emissions from controlled production starting in 2023 is shown.
- For CH_2Cl_2, an uncontrolled ozone-depleting gas with an atmospheric lifetime of ~180 days, future emissions continue to have the potential to lead to more ozone depletion than emissions from many of the other alternative scenarios explored here. CH_2Cl_2 is emitted mainly from Asia, and emissions and concentrations have been growing steadily in recent years.
- For N_2O, the impacts of a strong mitigation scenario (SSP1-1.9) are compared to the base-line scenario (SSP2-4.5).
- For HFCs, the impact of a hypothetical complete global phaseout of production (excluding HFC-23) starting in 2023 is shown. An additional scenario is included in which HFC-23 emissions are reduced to virtually zero, consistent with the current best practice of incineration, rather than the assumed emissions rate of 1.6% of HCFC-22 production included in the baseline scenario, in order to show the effect of nearly eliminating by-product emissions.

Updates on Impacts of Greenhouse Gases and Other Processes on Future Stratospheric Ozone

In this section, we summarize potentially important impacts on the future of the ozone layer that could result from anthropogenic activity not associated with ODS or replacement production and consumption and that is not controlled by the Montreal Protocol. Net stratospheric cooling, which is projected in many scenarios due to increases in greenhouse gas concentrations, is predicted to lead to increases in upper-stratospheric ozone at all latitudes, with a more complex pattern of ozone changes in the lower stratosphere, including a decrease at tropical latitudes driven by changes in dynamics and transport; these processes are discussed in detail in Chapters 3 *and* 4. *Potential climate intervention activities that may affect ozone are discussed in* Chapter 6.

- **Our ability to accurately predict future changes in the ozone layer continues to be limited more by uncertainties in the future levels of CO_2, CH_4 (methane), and N_2O than by uncertainties in the levels of ODSs.** Global mean tropospheric warming, as well as stratospheric cooling, will drive ozone changes through both atmospheric circulation and chemistry, while changing CH_4 and N_2O will lead to further changes in the chemistry associated with stratospheric ozone. Future ozone levels depend on the path of greenhouse gas emissions and aerosol abundances, as well as the sensitivity of the climate system to these emissions.
- **Rocket launches presently have a small effect on total stratospheric ozone (much less than 0.1%). However, rocket systems using new propellants (e.g., hydrogen and methane) could exert a substantial influence in the future.** The future scenarios of space industry emissions consider the potential for a significant increase in launch rates, the adoption of new launch-vehicle propellants, and an increase in middle-atmosphere aerosol and the production of NO (nitrogen monoxide) by reentering space debris. Many of the impacts of rocket activity involve chemistry and radiative interactions that are poorly understood and, in some cases, not yet studied. Furthermore, the planned development of massive low-Earth orbit satellite constellations (megaconstellations) could cause particulates resulting from space debris reentry to become comparable to that from launch emissions; little is known about the impacts of reentry particles, and their accumulation in the stratosphere has not been modeled. The uncertainties in these processes and in any potential new emission sources limit the confidence level of predictions of present and future impacts of space industry emissions on stratospheric ozone. Periodic assessment and critical knowledge gap identification are warranted.
- **The influence of hydrogen as an energy carrier on stratospheric ozone remains uncertain.** Hydrogen-based energy will likely play a role in a future non- or reduced-fossil economy. However, if it is not a dominant energy carrier, it is unlikely that it will significantly affect ozone. This statement should be reevaluated periodically.
- **The impacts of supersonic aircraft on stratospheric ozone are discussed in *Chapter 4*.**
- **Climate intervention approaches that affect the stratospheric ozone layer are discussed in *Chapter 6*.**

7.1 INTRODUCTION

As documented by many prior WMO Ozone Assessments, control measures introduced under the Montreal Protocol and its Amendments have been resoundingly successful, as evidenced by the 99% reduction in the reported production of ODSs since the peak in the late 1980s. As the ozone-depleting substances (ODSs) have been successfully replaced by hydrofluorocarbons (HFCs) and through other measures (*Chapters 1* and *2*), indications of reduced ozone depletion are emerging (*Chapters 3* and *4*). While HFCs do not contribute to ozone depletion, they do contribute to climate change and were recently included in the Montreal Protocol through the Kigali Amendment.

This chapter provides an update to Chapter 6 of the 2018 Assessment. It focuses on possible options and sensitivity scenarios to support policymakers in decisions related to further protecting stratospheric ozone and minimizing effects on climate from ODSs and their replacements. As production and consumption of controlled ODSs have continued to decline, policy options for reducing their future emissions have become somewhat more limited; however, some options remain that have notable potential for ozone and climate protection. Some of these are related to ODSs and their replacements, and some are not.

Policy-relevant issues discussed in this chapter include: 1) climate and ozone depletion impacts of future ODS and HFC emissions from multiple sources, including continued production for use as feedstocks; 2) future climate and/or ozone depletion impacts from continued production and use of other short- and long-lived compounds not currently controlled; 3) other future environmental effects of ODSs, HFCs, and short-lived replacement compounds; and 4) potential impacts of future high-altitude transportation and satellite activities.

In the rest of this section, key points from WMO (2018) are summarized, followed by a description of the objectives and the contents of this chapter.

7.1.1 Summary of Findings from the Previous Assessment

The Kigali Amendment to the Montreal Protocol went into force on 1 January 2019, around the time the 2018 Ozone Assessment was published. Some of the key findings from that Assessment involved the Kigali Amendment. Specifically, the large expected climate benefit of that Amendment was assessed, and the benefits of faster and deeper controls on HFC production and consumption were explored. Other key findings in Chapter 6 of the previous Assessment (Carpenter, Daniel et al., 2018) included the following:

- A proposed N_2O mitigation option was highlighted as having a larger impact on CO_2-equivalent emissions over 2020–2060 than even the elimination of all emissions of controlled ODSs.
- Emissions of ODSs from the estimated banks were assessed to be slightly more important than future production for ozone depletion over the next four decades.
- CCl_4 emissions, as projected, continued to have the largest influence on future stratospheric ozone of all controlled ODSs.
- The importance of destroying HFC-23 (a by-product of the production of HCFC-22) to limit its future climate impact was underscored.
- The role of climate change, and specifically the influence of future CO_2 levels, on stratospheric ozone was highlighted.
- The existence of large gaps in our understanding of how future rocket activity might affect stratospheric ozone levels was raised.
- The continuing gaps in our understanding of the trifluoroacetic acid (TFA) budget were pointed out, along with the expectation that TFA would not rise to levels that would harm the environment over the next few decades.

7.1.2 Key Issues to Be Addressed in This Chapter

In this chapter, we describe updates to our understanding of actions related to the Montreal Protocol and its Amendments that could alter the recovery of the ozone layer and impact Earth's climate or other parts of the natural environment. In addition, other potential threats to and influences on the ozone layer are discussed. As in previous Assessments, we use equivalent effective stratospheric chlorine (EESC) as a proxy for the amount of stratospheric ozone depletion caused by ODSs that contain chlorine and/or bromine and reside in the atmosphere for more than a few months. The return of EESC to 1980 values is used as a metric to compare different future scenarios related to altered production, emissions, and banks of ozone-depleting ODSs on ozone layer recovery. The EESC formulation used here is based on Engel et al. (2017) and was described in Section 6.4.1 in Carpenter, Daniel et al. (2018), with scenario results shown in Appendix 6C of that chapter. This represents a different approach to calculating EESC than used in Ozone Assessments before 2018.

In addition to EESC, we use 2-D model simulations to estimate changes in future ozone depletion for various scenarios. The 2-D model is needed to quantify the effect of the various scenarios on ozone itself and to evaluate compounds that cannot be easily quantified with EESC or do not affect ozone through halogen chemistry (e.g., CO_2, CH_4, and N_2O). The 2-D model is used here in scenario evaluation rather than a 3-D model since it has been shown to capture the key necessary processes for emissions of long-lived source gases, including long-term changes in EESC, the Brewer-Dobson circulation (as reflected by the stratospheric age of air), and projections of future ozone (see, e.g., Appendix 6B of WMO, 2018). Thus, the substantially increased computational cost of running a 3-D model is deemed too great for the added benefit. The exception to this is when considering the short-lived CH_2Cl_2, for which we use published 3-D model calculations of ozone depletion potential (ODPs) to estimate the impact of future emissions scenarios on ozone depletion. Note that 3-D model projections of global and polar ozone and analyses of expected recovery dates are presented in *Chapters 3* and *4*. These 3-D model calculations and the 2-D model include changes in greenhouse gas levels and in atmospheric transport, and thus their recovery dates are not expected to be the same as the recovery dates determined from EESC alone.

Our ability to reasonably constrain future changes in the ozone layer continues to be limited more by uncertainties in the future levels of CO_2, CH_4, and N_2O than by uncertainties in the levels of ODSs, owing to the fact that the Montreal Protocol has highly constrained future ODS trajectories. Importantly, ozone levels in some regions of the atmosphere could exceed historic natural levels if CO_2 and CH_4 mixing ratios, in particular, continue

to increase in the future, with possible consequences to humans and natural ecosystems, assuming natural levels represent a desired balance. The influence of CO_2 on stratospheric ozone occurs primarily through its role in the climate system as a driver of change in stratospheric temperatures and atmospheric circulation. The influences of CH_4 and N_2O occur primarily through their roles as chemical reagents in the atmosphere. ODSs themselves are greenhouse gases, and their influence on climate and ozone layer depletion are intricately intertwined. We discuss these influences separately for clarity of presentation.

A foundational aspect of this chapter is the choice of scenarios used to assess future possible impacts on ozone depletion and climate change. These scenarios begin with a baseline scenario, against which others are compared. The baseline scenario is not a "most likely" scenario, nor is it a prediction. It consists of a plausible set of well-defined production or emissions assumptions, depending on the gas. The primary purpose of the baseline and alternative scenarios is to assess the impacts of various sources of future production and emissions on ozone depletion and climate change. Notice that the various actions associated with the alternative scenarios discussed later in this chapter affect future ozone to a much smaller degree than what has already been accomplished by the Montreal Protocol. Some of the specific activities that could be important to future ozone depletion and climate change are explored in this chapter through simulations and include the following:

- Using the latest atmospheric observations of ODS mixing ratios, latest current bank estimates, and latest global lifetimes to develop new ODS scenarios; these scenarios are used to explore the impacts of future emissions from banks and production on the return of EESC to 1980 levels, on ozone depletion itself, as well as on climate forcing. In addition to scenarios in the previous Assessment, emissions from feedstock production and use are explicitly included for several ODSs.
- Generating future scenarios for the emissions of HFC-23, which is closely associated with the production of HCFC-22.
- Incorporating future emissions scenarios for the other key HFCs, developed in *Chapter 2*, into the analysis of future climate impacts from anthropogenic activities.
- Developing an analysis for assessing the future contribution of HFOs and HFCs to TFA in precipitation and in sea water.
- Providing an updated assessment of the potential impact of very short-lived substances (VSLSs) on future ozone depletion.
- Assessing plausible impacts of the recent unexpected emission and associated production of CFC-11 on future ozone depletion and discussing the current status and remaining key uncertainties associated with this issue.
- Using the latest generation of climate scenarios, which include greenhouse gas emissions and mixing ratios, to reassess the potential future impact of CO_2, CH_4, and N_2O on ozone abundances.
- Including an expanded modeling capability to explore the future impact of revised CFC-11 and CFC-12 bank estimates (unrelated to the unexpected emissions issue).
- Briefly summarizing the potential gains that can be achieved through a focus on energy efficiency in air-conditioning and refrigeration applications as the world transitions away from long-lived HFCs. This is discussed in more detail in *Chapter 2*.
- Assessing the potential impact of a foreseeable large increase in future rocket launches, including possible changes in their propellants, as well as estimating the effect of a planned fleet of new supersonic airplanes on the ozone layer.

7.2 ISSUES OF POTENTIAL IMPORTANCE TO STRATOSPHERIC OZONE AND CLIMATE

7.2.1 ODSs Controlled Under the Montreal Protocol and VSLSs

In this section, current and future emissions of ODSs and VSLSs are discussed. As emissive uses of ODSs are increasingly controlled by the Montreal Protocol, emissions from the direct application of these substances are now largely restricted to hydrochlorofluorocarbons (HCFCs) mostly from Article 5 countries, and to exempted applications of methyl bromide (CH_3Br). However, emissions are ongoing from built-in ODSs (i.e., banks) and from the usage of ODSs and VSLSs as building blocks in the synthesis of other chemicals (i.e., feedstocks). Additionally, some unintended emissions of halogenated intermediates and undesired by-products, which arise during the production of halogenated compounds, are occurring.

7.2.1.1 Emissions from Usage

Production and consumption of CFCs, CCl_4 (carbon tetrachloride), and CH_3CCl_3 (trichloroethane, methyl chloroform) have been banned for emissive uses under the Montreal Protocol. Nevertheless, because of the perceived use of CFC-11 in foam blowing in eastern China and potentially other parts of the world, emissions of CFC-11 increased between 2012 and 2018, when compared with the preceding years. After Montzka et al. (2018) and Rigby et al. (2019) highlighted this increase, emissions dropped considerably in 2019 (*Chapter 1*). WMO (2021) estimates that cumulative emissions that originated from this associated production were 120–440 Gg over 2012–2019. There are still large ongoing emissions of CCl_4 and, to a minor degree, of several CFCs and CH_3CCl_3. Large-scale unreported production seems to be an unlikely source for these compounds, but emissions from banks (*Section 7.2.1.2*) and fugitive emissions from losses during production and usage of feedstocks (*Section 7.2.1.3*) could be playing an important role.

For HCFCs, the overall demand for emissive uses has been declining for several years due to increasingly stringent controls by the Montreal Protocol and adequate financial support by the Multilateral Fund for conversions. The significant remaining applications in Article 5 countries are in the refrigeration, air-conditioning, and foam sectors. For refrigeration and air-conditioning, there is still demand for HCFC-22 for the servicing of existing equipment, as a substantial part of the charged amount is emitted over time. In non-Article 5 countries, where the infrastructure exists, the remaining HCFC-22 demand in the air-conditioning sector is now met from recovered and reclaimed HCFC-22 or from recycled materials. In the USA, there is no specified end-date for the use of reclaimed or recycled HCFC-22 in air-conditioning equipment, so emissions will continue at some level until all HCFC-22-based equipment has reached the end of its

operational life. In Article 5 countries, recovery is less likely, as newly produced chemical material continues to be available and reclamation infrastructure is less well established.

For the foam sector, HCFC-141b remains the primary ozone-depleting blowing agent still in use in Article 5 countries, albeit with some HCFC-22 and HCFC-142b used as gaseous blowing agents in extruded polystyrene. However, most, if not all, of this use is limited to those Article 5 countries where HCFC Phaseout Management Plans (HPMPs) are still ongoing. For foams, there is no economical recovery route for recycling the HCFC-141b that is already incorporated into products. Hence, any remaining demand in Article 5 countries will have to be met from new supplies. The Montreal Protocol has set the phaseout date for all newly produced HCFCs in Article 5 countries as 2030, but most HPMPs at the country level foresee phaseouts of use ahead of that date. The remaining uses of HCFC-141b as a blowing agent tend to be in smaller enterprises where the investment to use alternative blowing agents is prohibitive. For example, in the case of polyurethane spray foam applications, the use of hydrocarbon blowing agents has not been adopted for safety reasons. At the point of in situ applications of these spray foams, emissions of around 15–20% of the blowing agents in question occur.

CH_3Br is globally banned from use in agriculture with only critical-use exemptions (CUEs) allowed. However, quarantine and pre-shipment (QPS) uses are not restricted, albeit production for these uses has to be reported. CUEs declined from nearly 20,000 t in 2005 to currently <30 t (TEAP, 2021a). This amount is insignificant in comparison with the usage in QPS of about 9000 t in 2019 (*Chapter 1*).

Halons are completely banned except for critical uses, such as in civil aircraft. Fire extinguisher refilling uses recycled halons, for which a global market exists, and emissions are restricted to maintenance and to usage during fire events.

7.2.1.2 Emissions from Banks

When equipment is produced that contains halocarbons, a part of the quantity used is emitted during the production, while the rest is contained within the equipment for its intended use and is subject to later release. This reservoir of stored halocarbons within equipment is referred to as halocarbon banks. Quantifying existing banks and their contribution to future emissions is key to interpreting the sources of ongoing halocarbon emissions and estimating future potential emissions. **Box 7-1** explains the characteristics of banks and their long-term behavior, as well as the ways that have been used to calculate the amounts of ODSs and replacement compounds stored in banks at a given time. As discussed in *Section 7.4*, accurate knowledge of the sizes of current banks is a key aspect in projecting future ODS mixing ratios and the resulting ozone depletion as well as climate forcing.

Box 7-1. Banks

In the context of ODSs, "banks" refers to equipment and applications that contain ODSs. These ODSs will eventually be released to the atmosphere if pre-emptive action of capturing and destroying them is not taken. Bank characteristics, such as magnitude and release rates, differ by compound and their respective uses. For example, compounds used in foam have long residence times within their banks (~2% yr^{-1} release rates), uses such as refrigeration and air-conditioning have moderate residence times (~10% yr^{-1} release rates), and compounds in applications such as for aerosol generation and use as solvents are emitted quickly (~50–100% yr^{-1} release rates) (Ashford et al., 2004). Release rates also vary depending on the life cycle phase. The technological ease of bank capture depends on the type of application and life cycle phase. Banks existing in products still in use are referred to as active banks, and once products have been decommissioned and reside in a landfill or in some other waste stream (TEAP, 2021b), these banks are referred to as inactive and are generally more difficult to capture and are likely to have different release rates.

Previously published bank estimates have varied widely due to the widespread use of ODSs and the associated difficulty in assessing the total amount of equipment and applications containing ODSs, as well as different modeling approaches and assumptions. International assessments prior to 2006 primarily relied on top-down analyses, where banks were estimated as the cumulative difference between production and emissions. Bank estimates in this approach are very sensitive to small biases in annual emissions and production estimates, with the resulting biases in bank estimates increasing over time (Velders, Daniel et al., 2014). Biases in emissions can be caused by biases in atmospheric mixing ratio observations and in ODS lifetime estimates. Biases in production can result from biases in production figures reported to the Ozone Secretariat, for example.

In bottom-up estimates (e.g. Ashford et al., 2004; IPCC/TEAP, 2005), the inventory of sales, by-product, or equipment type are carefully tallied along with estimated release rates by application use. While there are reasonable estimates for production and leakage rates of various equipment types, these estimates are also subject to uncertainties. Bottom-up methods are generally independent of observed atmospheric mixing ratios and the estimated lifetimes of the various ODSs.

Since 2006 and the publication of bottom-up bank estimates (IPCC/TEAP, 2005), international assessments have used a hybrid approach that starts with bottom-up bank estimates in a given year and uses the top-down method to propagate banks forward in time, using yearly reported production and observationally derived emissions. In the present Assessment, we adopt a Bayesian analysis of banks (Lickley et al., 2020, 2021, 2022). In the Bayesian method, banks are estimated by developing initial (prior) bank estimates where production is associated with the application and equipment type following the bottom-up method, relying on reported and published data, accounting for large uncertainties in production and leakage rates, and then finding the best (in a Bayesian sense) parameters that are statistically consistent with atmospheric mixing ratios. The result is a final (posterior) distribution of banks by equipment type, along with an updated estimate of release rates for each equipment type (Lickley et al. 2020, 2021, 2022).

7.2.1.3 Emissions from Feedstock Production and Usage

Although the produced quantities of ODSs used as feedstocks must be reported by the Parties to the Montreal Protocol, they are exempted from controls. This exemption was granted under the assumption that emissions during production and usage of feedstocks are small. In this section, the fugitive emissions of ODSs, HFCs, and VSLSs from production and uses of feedstock are evaluated. Many feedstock chemicals contain chlorine, some or all of which is displaced by fluorine by using HF (hydrofluoric acid) in the process of manufacturing the final halogenated product. **Table 7-1** and **Figure 7-2** summarize the most important chlorinated feedstocks, intermediates, by-products, and their halogenated products, which are most relevant for the Montreal Protocol and the Kigali Amendment. Whereas intermediates are substances that can be used further to produce the final product, undesired by-products are also produced in the process but cannot usefully react further and are therefore removed from the final product for destruction or potential release into the atmosphere. Feedstock-related emissions can occur during the production of the feedstock chemical, from its storage, and/or during transport (**Box 7-2**). Finally, emissions occur during the conversion to the final product, which may require several intermediate stages, consisting of fugitive leaks in the storage and/or transport processes, and possible trace residual levels in the ultimate products. In addition, the charging and discharging of cylinders or road/rail containers may also contribute to emissions.

Figure 7-2 provides an overview of the feedstocks used in the production of some key synthetic, fluorinated greenhouse gases. In the course of their production, different chlorinated substances (ODSs and uncontrolled chemicals) are fluorinated, which can result in their emissions and the formation of several ODSs as intermediates and by-products. Annual production rates of the most important ODS feedstock chemicals between 2000

Table 7-1. Regulated ODSs used as feedstocks, with their uses and annual production for feedstock applications in 2019 (UNEP, 2021). Calculated emissions are given in Gg and ODP-Gg (in parentheses). The relative contribution of feedstock emissions to global emissions is calculated against global emissions figures from *Chapter 1*.

Feedstock	Industrial Products[1]	Global Feedstock Production[2] [Gg]	Feedstock Emissions[3] [Gg] (ODP Emissions[4] [CFC-11-eq Gg])	Percentage of Feedstock Emissions Versus Global Emissions (2019)[5]
CCl_4	HFC-245fa HFC-365mfc HFC-236fa HFO-1234yf HFO-1234ze(E) HCFO-1233zd Tetrachloroethene	318	13.6 (11.2)	32%
1,1,1-trichloroethane	HCFC-142b HCFC-141b HFC-143a	84	1.7 (0.2)	78%
CFC-113 CFC-113a	CTFE (HFO-1113) HFC-134a HFO-1336mzz	108	2.2–4.3 (1.8–3.6)	43–87%
CFC-114 CFC-114a	HFC-134a	45	0.9–1.8 (0.5–1.0)	33–66%
HCFC-22	TFE, a monomer to PTFE, HFP, and other fluoropolymers. Isoflurane/desflurane anesthetics	713	14.3–28.5 (0.5–1.1)	4–8%
HCFC-124 HCFC-124a	HFC-125 HFC-134a	25	0.5–1.0 (0.01–0.02)	19-37%
HCFC-141b	HFC-143a	13	0.3–0.5 (0.03–0.05)	0.5–0.9%
HCFC-142b	HFO-1132a (VDF) monomer, HFC-143a	174	3.5–7.0 (0.2–0.4)	17–33%
Halon-1301	Fipronil	1.3	0.03–0.05 (0.5–1.0)	2–4%
Minor Chemicals[6]		11	0.2–0.4 (0.04–0.09)	
Total Gg of Regulated ODSs		1492	37.2–58.9	
Total ODP-Gg		558	15.0-18.7	

Notes:
[1] Feedstock usage from Montzka, Reimann et al. (2011), TEAP progress report (TEAP, 2020), Sherry et al. (2018), Table S2 of Chipperfield et al. (2020), and Andersen et al. (2021).
[2] Global feedstock production from UNEP (2021).
[3] Relative emissions from feedstock usage are estimated to be 2% for 1,1,1-trichloroethane, 4.3% for CCl_4, and 2–4% for all the other chemicals (**Box 7-2**).
[4] ODP values from **Table 7-4**.
[5] Global emissions in 2019: Average between 2018-2020 and NOAA/AGAGE from *Chapter 1*.
[6] Minor chemicals: HCFC-123, HCFC-133/133a, HCFC-225, methyl bromide, bromochloromethane (UNEP, 2021), characterized by an average ODP of 0.22, when weighted by production mass.

Box 7-2. Feedstock-Related Emissions

Emissions from the production and use of feedstock chemicals relative to their production volumes are summarized in **Table 7-1**. Feedstock emissions estimated in this section are used as input for the scenarios in *Section 7.4*. For 1,1,1-trichloroethane, relative emissions are assessed at 2%, related to the 2019 ratio of global emissions against reported global production (**Table 7-1**). 1,1,1-trichloroethane is an excellent tracer for generally estimating feedstock losses, because emissions from banks can be neglected, as it was historically used only as a solvent. For all other feedstock chemicals (except CCl_4; see below), emissions of 2–4% relative to their production were estimated, which covers the range between the 2% above and the Tier 1 default emissions factor of 4% for fluorochemical production (IPCC, 2019). Further evidence of real-world emissions from feedstocks comes from industry-based estimates of 1.5–3.3% of fugitive emissions during production of CFCs and HCFCs (Gamlen et al., 1986; Midgley and Fisher, 1993; Ashford et al., 2004) and additional emissions of 1% during the usage of feedstocks (as estimated for HCFC-22 by Midgley and Fisher (1993)). An additional rationalization of the upper margin of 4% is substantiated from estimated emissions of 4–6% during the historic production of CFC-11 (TEAP, 2021b), which, however, could have been as high as 15% in the case of small and poorly operated enterprises, as assessed during the recent surge in CFC-11 production in eastern China.

Feedstock-related emissions of CCl_4 are treated separately, as they have been specifically assessed in the past by SPARC (2016) and Sherry et al. (2018), by estimating that 0.4% of the global production of chloromethanes is emitted as CCl_4 and by adding process-specific emissions from the usage of CCl_4 as feedstock. In 2014, this resulted in estimated emissions of 15 Gg (i.e., 7.4% of the 203 Gg of CCl_4 produced that year). In this chapter, this number has been revised for 2019 by estimating that 2% (0.9–4.0%), or 6.4 Gg (2.9–12.7 Gg), of the produced amount of CCl_4 (318 Gg) is emitted during the production process and an additional fraction of 7.2 Gg (2.2–9.8 Gg) from its usage (**Figure 7-4**; update of Sherry et al., 2018). This results in a best estimate of 4.3% (13.6 Gg, 5.1–22.5 Gg) of feedstock-related emissions of CCl_4 in 2019 (i.e., combination of pathways C and D in **Figure 7-4**).

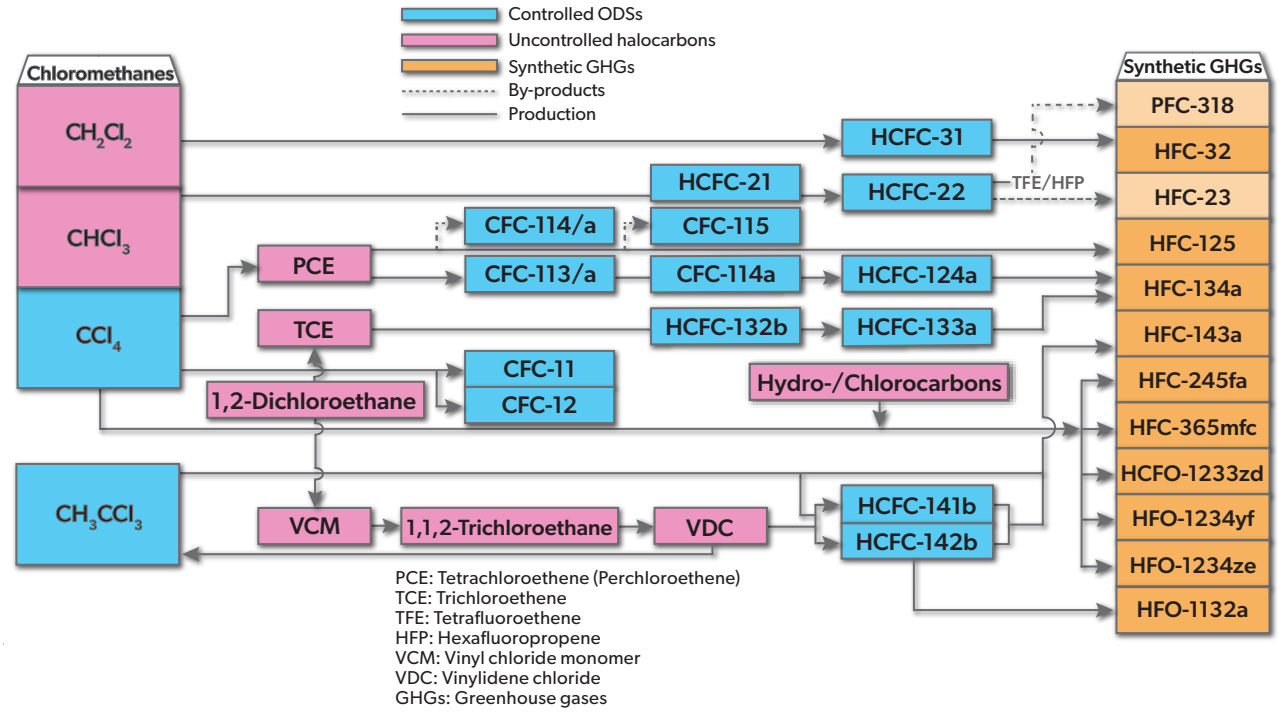

Figure 7-2. Controlled ODSs and uncontrolled halocarbons used as feedstocks for the production of controlled ODSs and synthetic greenhouse gases (GHGs). Uncontrolled halocarbons are shown in purple, controlled ODSs in light blue. Synthetic greenhouse gases, as the final products, are shown in orange. Intermediates are drawn in-line from the feedstock chemical to the final product; by-products are connected by a dotted line. HCFC-22 is mostly used for the synthesis of PTFE, (polytetrafluoroethene) with TFE (tetrafluoroethene) and HFP (hexafluoropropene) as intermediates. PFC-318 and HFC-23 are by-products but are also used to a smaller extent as final products, which are indicated by lighter orange.

and 2019 (UNEP, 2020) are shown in **Figure 7-3**. In addition, **Table 7-1** summarizes the amounts of ODSs that were used as feedstocks in 2019 and shows their estimated fugitive emissions, as well as the ratio of ODS emissions from this use to their global total, as an average between 2018–2020 (*Chapter 1*).

In 2019, a greater mass of HCFC-22 was produced in a single year than any other fluorocarbon in history, with a global production close to 1000 Gg. More than 700 Gg (>70%) of this is reported to be used as feedstock in the production of PTFE (polytetrafluoroethene), HFP (hexafluoropropene), and other fluorinated monomers. Production related to feedstock usage has increased by more than a factor of five from 2000 to 2019. More recently, HCFC-22 has also started to be used for the synthesis of HFO-1234yf. The usage of HCFC-22 as a feedstock chemical is expected to grow until market saturation of the produced fluoro-derivatives is reached or environmentally based restrictions are imposed. Current estimated feedstock-related emissions of 14–29 Gg yr^{-1} (**Table 7-1**) are less than 10% of the current global HCFC-22 emissions (*Chapter 1*), but this fraction is projected to increase, as emissions from refrigerants and foam-blowing agents are expected to decline.

At more than 300 Gg yr^{-1}, CCl_4 was the chemical with the second-highest mass production rate for feedstock usage in 2019. In recent decades, inexplicably high and ongoing global emissions have been calculated for CCl_4 using observationally-based methods. This issue has been highlighted in three previous Ozone Assessments (2006, 2010, 2014). The studies of SPARC (2016) and Sherry et al. (2018) show that emissions of CCl_4 from feedstock production and its use were higher than previously estimated. This finding significantly reduced the gap between top-down and bottom-up estimates of CCl_4 emissions. Historically, CCl_4 was used for producing CFC-11 and CFC-12, which, according to the Montreal Protocol, was due to cease for both production and consumption by 2010. However, with the renewed production of CFC-11 in eastern China and potentially elsewhere (WMO, 2021), a minimum of an additional 360 Gg of CCl_4 was estimated to have been produced (TEAP, 2021b) between 2012 and 2018 as feedstock for this application. These values are not included in the global sum of reported feedstock usages of CCl_4 in **Figure 7-3** and **Table 7-1**.

Production for allowed uses of CCl_4 increased by a factor of two in the last decade. Currently, CCl_4 is used in the production of tetrachlorethene and other base chemicals, as well as for the synthesis of HFC-245fa, HFC-365mfc, and the newly introduced HFO-1234yf, HFO-1234ze(E), and HCFO-1233zd. The specific hydrocarbons or chlorocarbons used to react with CCl_4 in the products, illustrated in **Figure 7-2**, determine the specific end product. For instance, the reaction of CCl_4 with ethene provides the chlorocarbon base for HFO-1234yf, whereas the selection of vinyl chloride monomer (VCM) as a reactant with CCl_4 provides the base for HFC-245fa. In the future, it is expected that the amounts of CCl_4 used for HFCs will decline due to the Kigali Amendment, whereas those for the production of HFOs are currently expected to increase steadily until economic saturation is reached.

In **Figure 7-4** the pathways of emissions of CCl_4 are compiled as an update of Sherry et al. (2018) (see explanation in **Box 7-2**). In 2019, emissions of feedstock production and fugitive emissions from usage are estimated at 13.6 Gg (5.1–22.5 Gg), or 4.3% (1.6–7.1%) of the produced CCl_4 (pathways C and D in **Figure 7-4**). In addition, another 5 Gg (2.5–7.5 Gg) are estimated to arise from inadvertent sources (i.e., the production of chlorine and base chemicals such as the production of VCM from 1,2-dichloroethane; pathway B) and around 5–10 Gg from legacy emissions (e.g., from landfills and contaminated soils; pathway A). In total, the best estimate of the sum of the contributions from these different sources, 26.1 Gg (12.6–40.0 Gg) in 2019, still leaves a considerable gap to the estimated global emissions of 43 Gg in 2019 from *Chapter 1*.

The third most produced feedstock is HCFC-142b, which is used for manufacturing fluoropolymers. In parallel to HCFC-22, its usage has increased continuously and reached around 170 Gg yr^{-1} in 2019. Emissions of HCFC-142b related to feedstock usage are estimated to have contributed 17–33% to its global emissions in 2019 (**Table 7-1**), with the remaining fraction from declining emissive uses from foam production and banks.

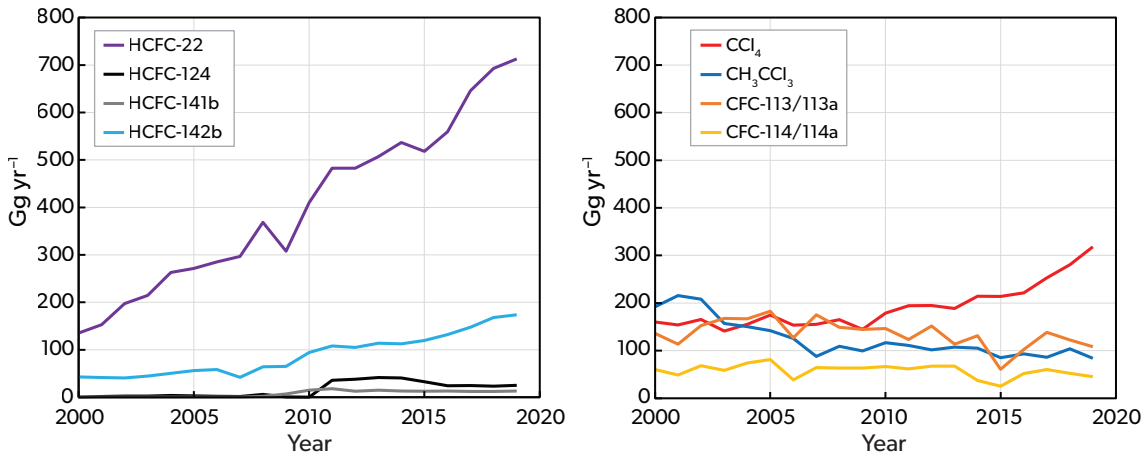

Figure 7-3. Global production of ozone-depleting substances for feedstock usage, which is exempted from the Montreal Protocol controls (UNEP, 2021).

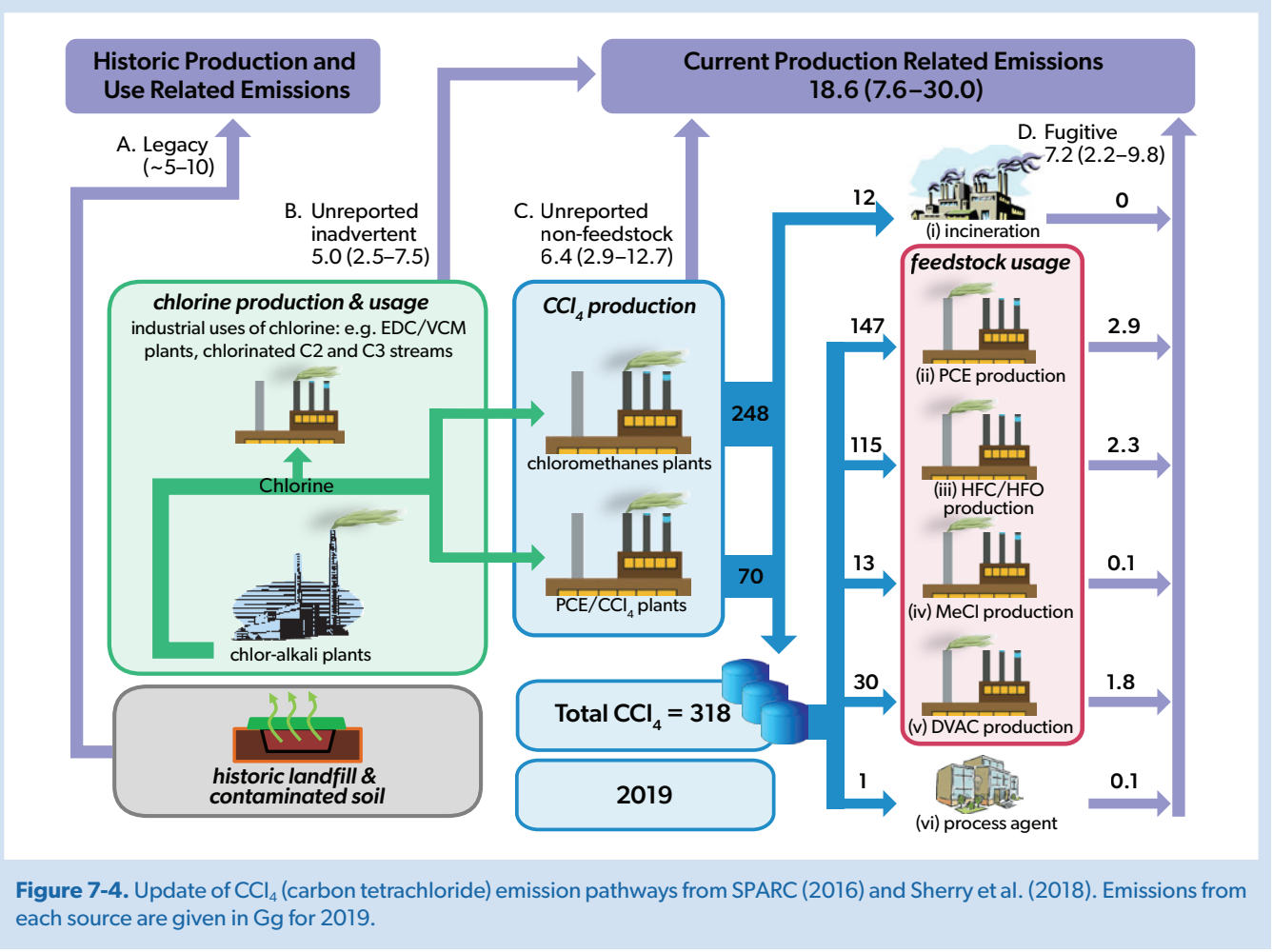

Figure 7-4. Update of CCl_4 (carbon tetrachloride) emission pathways from SPARC (2016) and Sherry et al. (2018). Emissions from each source are given in Gg for 2019.

Currently 1,1,1-trichloroethane (CH_3CCl_3), CFC-113/113a, and CFC-114/114a are nearly exclusively used as feedstock chemicals in the synthesis of widely used HFCs, HCFCs, and fluoropolymers (Table 7-1 and Figure 7-2). While the amounts used for the production of HFCs and HCFCs are still considerable, they are decreasing steadily, and, with the Kigali Amendment restrictions, the importance of these product compounds for emissive uses is projected to progressively decline. This tendency could be partly compensated for by an increased demand in the production of fluoropolymers, which would lead to a stabilization in emissions, albeit at potentially lower amounts than at present. Interestingly, the estimated feedstock emissions rate of 2–4% for CFC-113/CFC-113a and CFC-114/CFC-114a yields emissions that are lower than the measurement-based estimate of global emissions (*Chapter 1*). For CFC-114/CFC-114a, this could be explained by potential emissions as an undesired by-product in the production of HFC-125.

Declared feedstock usages of HCFC-124/124a and HCFC-141b are in principle related to their production as intermediates, but in some instances, they are also reported as feedstocks (see Box 7-2). As they are mainly used for the production of HFCs, their importance is also projected to decline.

In total, the recent usage of ODSs as feedstocks has been rising substantially. Between 2009 and 2019 the mass of ODSs used as feedstocks, which is not controlled under the Protocol, increased by 75% (Figure 7-3). When expressed as emissions in units of Gg ODP (Table 7-2), this increase in feedstock-linked production was 41%. This difference between absolute mass emissions and ODP-based emissions is due to the fact that HCFC-22, with a relatively low ODP, was responsible for the highest growth. If the original ODPs from the Montreal Protocol were used instead of the ODPs recommended in this Assessment (Table 7-2), the ODP-weighted increase would be 46% instead of 41%.

In addition to the ODSs and HFCs regulated by the Montreal Protocol, the nonregulated chlorinated VSLSs dichloromethane (CH_2Cl_2), chloroform ($CHCl_3$), trichloroethene (C_2HCl_3), and tetrachloroethene (C_2Cl_4) are also used in large amounts as feedstock chemicals (Chipperfield et al., 2020). In fact, Figure 7-2 shows that the usage of these VSLSs and 1,2-dichloroethane as feedstock is the starting point for the synthesis of either the ODS feedstock chemicals discussed above or provides an ODS-free feedstock route for the production of halogenated compounds. Because of their much lower ozone depletion potentials (ODPs), emissions during feedstock usage are generally of minor importance to the ozone layer. Nevertheless, a short discussion of their uses is included here.

About 96% of the nearly 1500 Gg of chloroform ($CHCl_3$) produced in 2016 was used as feedstock in the production

Table 7-2. Atmospheric lifetimes, fractional release factors (FRFs), and ODPs for long-lived halocarbons. FRFs are for mid-latitude conditions and are from Engel et al. (2017). Lifetime uncertainties are based on (SPARC, 2013) lifetimes as evaluated by Daniel, Velders et al. (2014). See *Chapter 1* for further discussion on atmospheric lifetimes and FRFs.

Halocarbon	Global Lifetime (yrs)	Lifetime Uncertainty (1σ)	Fractional Release Factors	ODPs	
				This Assessment's Recommendation	In Montreal Protocol
Annex A-I					
CFC-11	52	±22%	0.47	1.0	1.0
CFC-12	102	±15%	0.24	0.75	1.0
CFC-113	93	±17%	0.30	0.82	0.8
CFC-114	189	±12%	0.13	0.53	1.0
CFC-115	540	±17%	0.07	0.45	0.6
Annex A-II					
Halon-1301	72	±13%	0.32	17.0	10.0
Halon-1211	16	±29%	0.65	7.1	3.0
Halon-2402	28	±19%	0.66	15.6	6.0
Annex B-II					
CCl_4	30		0.56	0.82	1.1
Annex B-III					
CH_3CCl_3	5.0	±3%	0.61	0.12	0.1
Annex C-I					
HCFC-22	11.6	±16%	0.15	0.037	0.055
HCFC-123	1.4			0.02	0.02
HCFC-124	5.9			0.022	0.022
HCFC-141b	8.8	±15%	0.34	0.095	0.11
HCFC-142b	17.1	±14%	0.17	0.054	0.065
HCFC-225ca	1.9			0.025	0.025
HCFC-225cb	5.8			0.033	0.033
Annex E					
CH_3Br	0.8	±17%	0.60	0.57	0.6
Others					
Halon-1202	2.5	±33%	0.67	1.8	
CH_3Cl	0.9	±18%	0.44	0.015	

of HCFC-22 (Chipperfield et al., 2020). HCFC-22 production increased by 17% between 2016 and 2019 (UNEP, 2021), so the feedstock-related production of $CHCl_3$ is estimated to be around 1700 Gg in 2019. Assuming a loss rate of 2–4%, as for the other feedstock chemicals, implies emissions of 32–68 Gg yr^{-1}, which is comparable to the emissions from its use as a solvent (Chipperfield et al., 2020). This could partly explain the large increase in $CHCl_3$ emissions over the last decade (*Chapter 1*). In contrast, only around 15% of the ~1200 Gg of dichloromethane (CH_2Cl_2) produced was used as feedstock—mainly in the production of HFC-32, with the remainder being used and emitted as a solvent (Chipperfield et al., 2020). Next are trichloroethene (TCE) and tetrachloroethene (also named PCE, perchloroethene), whose usage as feedstocks in the production of HFCs is higher than the amounts used as solvents. Finally, 1,2-dichloroethane is used as a feedstock for the production of TCE and, via chloroethene (VCM, vinyl chloride) and 1,1,2-trichloroethane, for the production of 1,1-dichloroethene (VDC), which is then used to produce 1,1,1-trichloroethane, HCFC-141b, and HCFC-142b (**Figure 7-2**).

7.2.1.4 Emissions of Intermediates and Undesired By-Products

In addition to emissions from banks and feedstock usages, controlled substances (ODSs and HFCs) can also be lost to the atmosphere as chemical intermediates and undesired by-products during the production of a final product.

Generally, for intermediates and undesired by-products, relative emissions of 1% or smaller are estimated, relative to the produced final products. For HFC-23 as a by-product of HCFC-22 production, relative emissions of 1.6% are estimated, which is the average of the global HFC-23 emissions relative to the HCFC-22 production between 2014–18 (Stanley et al., 2020).

Emissions of intermediates can occur during their production and use on-site. The production and then consumption

of intermediates are not reported as feedstock use under the Montreal Protocol. It is only if intermediates are transported off-site that their usage has to be reported as feedstocks. A number of these intermediates have been detected recently in the atmosphere that are likely due to fugitive emissions during the synthesis of chemical products; these are summarized in *Chapter 1*. The most prominent examples are HCFC-31 from the production of HFC-32 (Schoenenberger et al., 2015), as well as HCFC-132b and HCFC-133a from the production of HFC-134a (Vollmer et al., 2021). In addition, CFC-114, CFC-114a, and CFC-115 are by-products in the production of HFC-125 (**Figure 7-2**). As the origin of these intermediates and by-products in the atmosphere is related to the production of HFCs, their importance is projected to decline in the future.

Further examples of undesired by-product formation are HFC-23 from the production of HCFC-22 (*Section 7.2.2.1*) and the formation of c-C_4F_8 (PFC-318) from the pyrolysis of HCFC-22 to manufacture TFE (tetrafluoroethene) and HFP (Mühle et al., 2022). In addition, atmospheric CFC-13 is potentially at least partly released as a by-product from the production of other fluorochemicals (Vollmer et al., 2018). Finally, CCl_4 is potentially emitted as a by-product during the use of chlorine in the production of several chlorinated chemicals, such as ethylene dichloride (EDC), vinyl chloride monomer (VCM), and other organic operations (**Figure 7-4**).

7.2.2 HFCs Controlled Under the Kigali Amendment of the Montreal Protocol

This section covers issues related to HFCs, which have recently become controlled under the Kigali Amendment. First, the future implications of the gap between reported emissions of HFC-23 from its by-product formation in the production of HCFC-22 and its actual measurement-based emissions are discussed. Then, the reported HFC feedstock uses are assessed, followed by a short discussion of the potential for energy efficiency improvements when equipment filled with HFCs is replaced. Decisions on which kind of foam-blowing agent or refrigerant should be used are policy relevant, and these issues are discussed in *Chapter 2* in conjunction with existing HFC usages; only a short summary on this topic is given in this section.

7.2.2.1 HFC-23

HFC-23 is predominantly released into the atmosphere as an undesired by-product from the production of HCFC-22 and from the subsequent production of tetrafluoroethene. Additional minor emissions occur from the electronics industry, from aluminum smelters, and from its usage in ultra-low refrigeration (e.g. Simmonds et al., 2018). The recent surge in demand for ultra-low-temperature cooling devices for storing vaccines could potentially increase emissions from this source, although other refrigerants are also used for these devices, and current emissions are estimated to be small in comparison with those related to the production of HCFC-22 (TEAP, 2021c). This potential new source is not included in the projections, as no information is yet available of this emerging market.

Technical solutions for destroying HFC-23, which is emitted in the production of HCFC-22, are available and economically viable (TEAP, 2018a). However, in contrast to the basket of other HFCs with an agreed phasedown schedule, restrictions on HFC-23 are prescribed only qualitatively in the Kigali Amendment as follows: "Each country manufacturing HCFC-22 or HFCs shall ensure that starting in 2020 the emissions of HFC-23 generated in production facilities are destroyed to the extent practicable using technology approved by the Montreal Protocol" (UNEP, 2016). The reporting of related emissions went into effect on 1 January 2020, so current reporting is still potentially incomplete.

As outlined in *Chapter 2* and related to the discussions by Stanley et al. (2020), abatement capacities seem to have been used only partially in recent years. If this continues to be true in the long term, compliance with the Kigali Agreement will not be met. In view of the uncertainty of the future development and the currently fragmentary documentation of HFC-23 destruction, two different scenarios have been developed to project future HFC-23 emissions within this Assessment. For both scenarios, production of HCFC-22 is assumed to increase by 5.8% yr^{-1} until 2030 (representing the average increase from 2014–2019) and to stabilize thereafter, with increasing feedstock usage compensating for a decrease in emissive applications. One scenario assumes full compliance with the Protocol, with emissions of only 0.08% relative to the produced HCFC-22. This scenario estimates an effective destruction capacity of 97% of the 2.8% (1.5–4.0%) of undesired HFC-23 produced per mass of HCFC-22 without incineration (McCulloch and Lindley, 2007). Remaining small emissions are related to failures and to maintenance work at the destruction systems. The other scenario, which is used as our baseline scenario, assumes a business-as-usual behavior, with an emissions rate of 1.6% relative to the HCFC-22 production (*Section 7.2.1.4*) and where destruction capacities are only partly exploited.

An additional contribution to the ongoing emissions could also be from the formation of HFC-23 in the pyrolysis reaction from HCFC-22 to TFE and HFP, used in fluoroplastics production, when fluorinated catalysts are used (Sung et al., 2006; Ebnesajjad, 2015). Furthermore, Ha et al. (2011) detected HFC-23 as the main product of the thermal treatment of HCFC-22, which could be important, as HCFC-22 from dismantled old air-conditioner systems is potentially incinerated. None of these additional potential sources has been included in the future scenarios related to the by-product formation from HCFC-22 production, but they could be key elements in closing the gap between known sources and measurement-based emissions, as discussed in *Chapter 2*.

7.2.2.2 Feedstock Usage of HFCs

To date, the amounts of HFCs used as feedstocks are much lower than those of ODSs. The submission of production and consumption data to the United Nations Environment Programme (UNEP), which is prescribed for feedstock usages of HFCs within the Kigali Amendment, is still incomplete, as not all countries with potential HFC feedstock usages have signed the treaty yet. Known applications are the use of HFC-152a and HFC-23 (TEAP, 2020). The dehydrofluorination of HFC-152a is the most broadly used chemical process for the production of vinyl fluoride, which means a considerable part of the produced HFC-152a is used as feedstock. HFC-23 is used as a minor feedstock (e.g., <1 Gg yr^{-1}) in the production of halon-1301, which is then used as feedstock in the production of fipronil (**Table 7-1**).

7.2.2.3 Energy Efficiency

An in-depth discussion on the potential for energy efficiency gains in connection with the future phasedown of HFCs used as

refrigerants in air-conditioning and refrigeration can be found in *Section 2.4.6*. In short, the replacement of old equipment containing HFCs with high Global Warming Potentials (GWPs) by new installations and low-GWP alternatives, as well as not-in-kind solutions, has the potential for multiple positive effects on climate change. For example, the emissions of low-GWP alternatives will directly reduce projected radiative forcing of climate. Also, and thought to have greater potential climate benefit, the transition to new refrigerants is an opportunity to implement design changes for achieving higher energy efficiency and therefore lowering greenhouse gas emissions from energy use.

7.2.3 Replacement Compounds of Controlled Halocarbons (HFOs and Others)

With the adoption of the Kigali Amendment, high-GWP HFCs as replacement compounds for ODSs are, themselves, supposed to be phased down. In **Figure 7-5**, historic and projected emissions of ODSs, high-GWP HFCs, and low-GWP alternatives are shown in Tg yr^{-1} and Pg CO_2-equivalents yr^{-1}, together with their influence on climate, expressed as radiative forcing (update of Figure 2-21 of Montzka, Velders et al. (2018), using data from Velders et al. (2022)). Whereas emissions of high-GWP HFCs are not projected to decline until after around 2025, ODS emissions are projected to continue their current steady decline. For both groups of compounds, emissions are expected to still occur in 2100, albeit at much lower levels than today. Due to the long lifetime of these compounds, their effect on climate, as measured by their radiative forcing (**Figure 7-5c**), will only slowly decrease after 2040 and is expected to still be around 50% of their maximum by 2100. Low-GWP alternatives to long-lived HFCs include both fluorinated alkenes (HFOs, HCFOs, HBFOs) and non-halogenated compounds, such as hydrocarbons, CO_2, and NH_3. These two groups are expected to constitute an important fraction of the low-GWP compounds in the future. Given the dynamics in the application markets, however, it is very difficult to estimate the future ratio of these halogenated alkenes relative to non-halogenated substitutes (*Section 7.2.3.3*). It can be expected that non-halogenated substitutes will comprise a substantial share of the low-GWP compounds. This assumption is substantiated, as historically after adoption of the Montreal Protocol, ODSs with large ODPs were also only partly replaced by HCFCs and HFCs. Therefore, it is estimated in this report that only 50% of the future low-GWP emissions (**Figure 7-5**) will be due to HFOs; this same assumption is also applied in the assessment of future trifluoroacetic acid (TFA) formation in *Section 7.2.5.1*.

7.2.3.1 Fluorinated Low-GWP Alkenes (HFOs, HCFOs, HBFOs)

HFOs (hydrofluoroolefins), HCFOs, (hydrochlorofluoroolefins), and HBFOs (hydrobromofluoroolefins) are fluorinated alkenes that are being introduced as low-GWP substitutes during the phasedown of HFCs (**Table 7-3**). Depending on their chemical and physical properties, they can be used in a similar way as the HFCs they replace. Their atmospheric lifetimes are small, and, therefore, their emissions do not contribute perceptibly to climate change. However, some of these compounds can

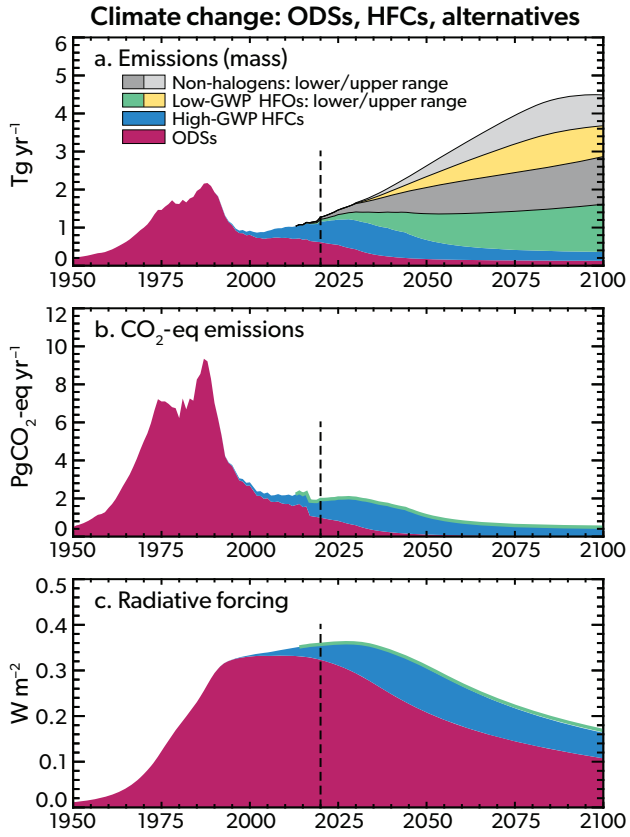

Figure 7-5. Historical and projected contributions to climate change from ODSs, high-GWP HFCs, low-GWP HFOs and non-halogenated alternatives, assuming full compliance with the provisions of the Montreal Protocol, including the Kigali Amendment [update of Figure 2-21 from Montzka, Velders et al., 2018]. Shown are (a) emissions by mass, (b) CO_2-eq emissions, and (c) direct radiative forcing. Only the direct GWP-weighted emissions and radiative forcing of the ODSs and HFCs are shown. The ODS emissions from around 1980 through 2020 are derived from atmospheric observations and after 2020 are from this scenario (distinction indicated by dashed vertical lines). The contributions of the low-GWP HFOs in panels b and c, are smaller than the thickness of the green curves. Not included here are contributions from HFC-23, indirect radiative effects from ozone depletion, and indirect effects associated with the energy used by equipment and the associated CO_2 emissions.

contribute to the formation of the stable compound TFA, as discussed in *Section 7.2.5.1*. An additional issue is the prevailing process for producing these compounds, some of which use CCl_4 as a feedstock, (*Section 7.2.1*) and therefore leads to ODS emissions (*Section 7.2.1.3*).

7.2.3.2 Non-halogenated Substitutes and Not-In-Kind Solutions

Several non-halogenated ODS substitutes have been used for decades in various applications. Hydrocarbons are the compounds of choice when considering alternatives, and in some countries are even mandatory (e.g., for use in domestic refrigeration and foam blowing). In addition, NH_3 and CO_2 are valid alternatives for large-scale cooling facilities. While CO_2 was also discussed as a replacement for HFC-134a in mobile air conditioners, HFO-1234yf was ultimately chosen, although CO_2 is still used in small quantities. Finally, so-called not-in-kind solutions are gaining increased attention, especially for cooling applications. Techniques such as solid-state cooling materials and Stirling coolers are discussed in, for example, Qian et al. (2016) and TEAP (2018b). All of these compounds and techniques have to be evaluated for their energy efficiency and integrative effects on climate (see *Section 7.2.2.3* and *Section 2.4.6* on energy efficiency).

7.2.3.3 Trifluoroiodomethane (CF_3I)

CF_3I, with an ODP of 0.008–0.016 (Youn et al., 2010), has been evaluated since the late 1990s as a replacement compound for halons in fire extinguishers, but it was never marketed as such (TEAP, 2018c). Recently, however, it has been proposed as an ingredient of low-GWP refrigerant blends in order to lower their flammability. Related to its ODP, Zhang et al. (2020) proposed using a new metric, called SODP (stratospheric ozone depletion potential), which includes only the fraction of ozone loss that takes place in the stratosphere. The SODP for CF_3I was determined to be essentially zero (within statistical error), as large fractions of CF_3I are destroyed in the troposphere, where the actual iodine-catalyzed ozone destruction occurs. It is too early to evaluate the general implications and acceptance of using SODP or ODP for assessing the ozone-depletion abilities for other VSLSs; historically, ODPs of these compounds have been calculated using a range of different methods (Zhang et al., 2020). If CF_3I were adopted in suggested blends and uses, the overall quantities of CF_3I potentially released could become significant.

7.2.4 Anthropogenic and Biogenic Very Short-Lived Substances (VSLSs)

VSLSs are not controlled under the Montreal Protocol. However, there is now strong evidence from observations and models that VSLSs contribute to stratospheric chlorine and bromine and therefore also to the ozone loss in this part of the atmosphere (see *Chapter 1*).

7.2.4.1 Chlorinated VSLSs

Currently, the most important chlorinated VSLSs in terms of their potential to deplete ozone are dichloromethane (CH_2Cl_2), chloroform ($CHCl_3$), 1,2-dichloroethane (CH_2ClCH_2Cl), trichloroethene (C_2HCl_3), and tetrachloroethene (C_2Cl_4). With the exception of chloroform, which also has significant natural sources, chlorinated VSLSs are largely of anthropogenic origin. They are emitted from their use as solvents and as feedstock chemicals in the production of HFCs and other chemicals (**Figure 7-2** and Chipperfield et al., 2020). As a group, chlorinated VSLSs contributed 3.5% to total tropospheric chlorine in 2020 (Chapter 1). While this contribution is still small, the relevance of VSLSs for stratospheric ozone depletion has increased over time (*Chapter 1* and Hossaini et al., 2017; Fang et al., 2019; Hossaini et al., 2019). Since the last Assessment, new studies have reported substantial increases in chlorinated VSLS emissions from Asia (Fang et al., 2019; Say et al., 2019; Claxton et al., 2020), and new information on the ODPs of chlorinated VSLSs has become available.

Dichloromethane (CH_2Cl_2) is a widely used VSLS whose atmospheric abundance and global emissions have both increased

Table 7-3. HFOs, HCFOs, and an HFBO currently in use and foreseen for future use, with their chemical formula, GWP, atmospheric lifetime, and main applications.

	Formula	GWP[1]	Atmospheric Lifetime[1]	Main Applications
HFO-1234yf	$CF_3CF=CH_2$	<1	12 days	Refrigerant Component of HFC-HFO blends
HFO-1234ze(E)	trans- $CF_3CH=CFH$	1	19 days	Refrigerant Component of HFC-HFO blends Aerosol propellant Insulation foam-blowing agent
HFO-1336mzz(Z)	cis-$CF_3CH=CHCF_3$	2	27 days	Refrigerant Fire extinguisher Insulation foam-blowing agent
HFO- 1336mzz(E)	trans-$CF_3CH=CHCF_3$	26	121 days	Refrigerant
HCFO-1233zd(E)	trans-$CHCl=CHCF_3$	4	42 days	Refrigerant Insulation foam-blowing agent Precision solvent
HCFO-1224yd(Z)	CF_3-$CF=CHCl$	<1	12 days	Refrigerant Polyurethane foam-blowing agent
HBFO-1233xfB	$CF_3CBr=CH_2$	<1	3.5 days	Fire extinguisher

Note:
[1] Atmospheric lifetimes and GWPs from *Annex*.

by more than a factor of two since the mid-2000s (*Chapter 1*). The issue of the growth of CH_2Cl_2 emissions was raised by Hossaini et al. (2017), who concluded that elimination of future CH_2Cl_2 emissions would have a substantial positive impact on total column ozone (see also Figure 6-1 of Carpenter, Daniel et al., 2018). CH_2Cl_2 is used in a wide range of solvent applications, notably as a process solvent in pharmaceutical processing, as a blowing agent in polyurethane foam production, and as an essential feedstock in HFC-32 production (Feng et al., 2018; Chipperfield et al., 2020; An et al., 2021). Around 90% of global CH_2Cl_2 emissions have been estimated to emanate from Asia (Claxton et al., 2020). Chloroform ($CHCl_3$), another prominent chlorinated VSLS, is used primarily (>95% of that produced) as a feedstock in HCFC-22 production and is also a by-product from water chlorination and from bleaching processes in the pulp and paper industry (e.g. McCulloch, 2003). Global $CHCl_3$ emissions have increased considerably within the last decade (*Chapter 1*), with regional inverse modeling showing that enhanced emissions from China are likely responsible (Fang et al., 2019).

A detailed examination of possible future industrial production of chlorinated VSLSs has yet to be performed. Hence, predictions of future VSLS emissions and ozone impacts are highly uncertain. Once HCFC-22 emissive applications are nearly phased out, which must occur by 2030 per the Montreal Protocol, $CHCl_3$ demand will likely be tied to the demand for HCFC-22 produced for feedstock usage, such as in the production of PTFE (*Section 7.2.1.3*). As $CHCl_3$ and CH_2Cl_2 are co-produced in chloromethane plants, supply and demand issues affecting one compound should invariably impact the other, although chloromethane plants have some flexibility to determine the extent to which one or the other compound is produced. By extrapolating recent trends, it is anticipated that Asian emissions will exert a dominant influence on the trajectory of global chlorinated VSLS emissions in the next decade. A bottom-up analysis (Feng et al., 2018) predicts that Chinese emissions will increase monotonically to the year 2030 under a business-as-usual scenario. This is substantiated by An et al. (2021), who estimated that CH_2Cl_2 emissions from China increased from 232 Gg in 2012 to 627 Gg in 2019, which practically covers the total global CH_2Cl_2 emissions increase in this period. Given the large uncertainties, we examine three scenarios to span a range of possibilities in *Section 7.4*: one in which the growth of CH_2Cl_2 emissions continues until 2022 and then stabilizes, one with the elimination of CH_2Cl_2 emissions beginning in 2023, and one in which emissions continue the increase as they have exhibited over the past five years through 2030, after which year they remain constant.

It has been well established that the ODP of a VSLS is dependent on the location and season of its emissions (e.g. Brioude et al., 2010; Pisso et al., 2010). However, to date, very few studies have considered the ODPs of the above chlorinated VSLSs. One recent analysis (Claxton et al., 2019) revealed that the ODPs of chlorinated VSLSs vary only slightly with the season of emissions but could differ by a factor of two to three depending on the source location. The highest ODP values were assessed for emissions from Tropical Asia and industrialized East Asia, which, in view of 1) the currently large regional emissions (e.g., Fang et al., 2019; Claxton et al., 2020) and 2) the existence of efficient regional transport pathways to the tropical upper troposphere (e.g. Oram et al., 2017), make it a significant finding.

7.2.4.2 Brominated and Iodinated VSLSs

In contrast to chlorinated VSLSs, brominated and iodinated VSLSs are predominantly produced naturally in the ocean. The most abundant brominated VSLSs are bromoform ($CHBr_3$) and dibromomethane (CH_2Br_2), with important source regions in coastal and shelf waters (e.g. Quack and Wallace, 2003). Natural production of $CHBr_3$ and CH_2Br_2 involves marine organisms such as macroalgae and phytoplankton, while the sea-air flux is driven by their oceanic abundance, temperature, and surface winds. The spatiotemporal variability of emissions and tropospheric transport processes are key factors controlling the contribution of brominated VSLSs to stratospheric bromine (Hossaini et al., 2013; Hossaini et al., 2016).

Atmospheric abundances of brominated VSLSs have not shown any trends (*Chapter 1*). However, oceanic production, sea-air fluxes, atmospheric lifetimes, and transport pathways of VSLSs are all sensitive to changing environmental conditions. Changes in VSLS emissions could occur due to changing irradiance and temperature affecting the production of halocarbons by macroalgae (e.g., Keng et al., 2020). In addition, climate change and ocean acidification will affect the distribution, abundance, and diversity of macroalgae itself, with further consequences for VSLS production. Thus, very large uncertainties exist in the prediction of future VSLS sources, as the responses of macroalgae toward environmental changes are highly species- and compound-specific. Sea-air fluxes of natural VSLSs have been predicted to increase throughout the 21st century due to changing physical forcings such as sea surface temperature and wind speed, assuming constant VSLS mixing ratios (Ziska et al., 2017). Recently quantified anthropogenic sources of $CHBr_3$ from power plants also have the potential to increase their total emissions over time (Maas et al., 2021). Finally, climate-driven changes to the troposphere's oxidizing power and to the troposphere-stratosphere transport may alter the contribution of VSLSs to the stratospheric halogen budget (Dessens et al., 2009; Hossaini et al., 2012; Falk et al., 2017). Overall, there is no clear picture of how brominated VSLS emissions and their contribution to stratospheric bromine will change in the future due to the large uncertainties associated with all these individual factors.

Iodinated VSLSs are present in the troposphere (*Chapter 1*), including methyl iodide (CH_3I). Like brominated VSLSs, organic iodine emissions from the ocean can be impacted by climate parameters (Keng et al., 2020). However, very little long-term data on tropospheric CH_3I trends exist, impeding future predictions of natural production and potential anthropogenic sources (Yokouchi et al., 2012; Zeng et al., 2020). Inorganic iodine emissions of hypoiodous acid (HOI) and iodine (I_2) from the ocean are driven by the reaction of ozone with iodide (I^-) at the ocean surface. Atmospheric iodine mixing ratios have tripled since 1950 (Cuevas et al., 2018), most likely because increased surface ozone leads to growing oceanic iodine emissions (Legrand et al., 2018).

Future inorganic iodine emissions will depend strongly on socioeconomic development and associated changes in anthropogenic ozone deposition and oceanographic changes impacting the sea-surface iodide abundance, among other factors (Iglesias-Suarez et al., 2020).

7.2.5 Breakdown Products from Anthropogenic Halocarbons

The atmospheric degradation of HCFCs, HFCs, and HFOs is initiated by their reaction with the hydroxyl radical (OH) leading to the formation of halogenated carbonyl compounds, which can further react to secondary products. Discussions in this section are related to trifluoroacetic acid (TFA) and carbon tetrafluoride (CF_4), which are both more stable in the environment than the primarily emitted halocarbons. Whereas TFA has some herbicidal properties, CF_4 is a strong greenhouse gas. In addition, degradation of halocarbons also contributes to the formation of tropospheric ozone, but mixing ratios of halocarbons are too small in comparison with other volatile organic compounds to make a considerable contribution.

7.2.5.1 Trifluoroacetic Acid (TFA)

TFA is a very strong acid with low to moderate toxicity for a range of organisms (Neale et al., 2021). It is found in many environmental compartments in varying concentrations, and its origin in these different parts of the environment is still an area of active research (*Chapter 2*; Joudan et al. (2021)). Here, the ranges of future TFA concentrations in precipitation and in ocean water are projected between 2020 and 2100. The model is restricted to the formation of TFA from the degradation of HFC-134a and HFO-1234yf, which, according to current knowledge, are expected to have the most significant influence on future TFA concentrations among those gases controlled by the Montreal Protocol or used as substitutes. Other fluorocarbons containing a CF_3 group also have the potential of being degraded to TFA in the atmosphere, albeit with a lower influence, as they currently have very small atmospheric mixing ratios and lower conversion rates to TFA (see also *Chapter 2*). Thus, the resulting TFA concentrations in different parts of the environment should be treated as lower-range projections. The contribution of HFC-134a is calculated by using its projected future mixing ratios, taken from Velders et al. (2022), with a lifetime of 14 years and a conversion rate to TFA of 7–20% (Wallington et al., 1994). For the short-lived HFO-1234yf, with a conversion rate to TFA of 100%, projected emissions are taken from the low and high scenarios of low-GWP alternatives shown in **Figure 7-5**. Thereby, it is assumed that 50% of the future emissions of the low-GWP alternatives (**Figure 7-5**) are related to HFOs, of which 50% is HFO-1234yf. The resulting projected annual TFA formation rates related to HFC-134a and HFO-1234yf are shown in **Table 7-4** for the years 2020, 2050, and 2100. In addition, the mass of deposited TFA from each and for the two together is given for the periods 2020–2050 and 2020–2100.

With an estimated total atmospheric formation and deposition of 31.5–51.9 Tg of TFA between 2020 and 2100 (**Table 7-3**), and subsequent transfer to the ocean, average TFA concentrations in sea water are projected to increase by 23–38 ng/L between 2020 and 2100, assuming a total ocean volume of 1.37×10^9 km^3. This would signify a substantial increase compared with the total ocean content of 61–205 Tg of TFA around the year 2000 reported in Scott et al. (2005), based on measuring varying concentrations in different ocean parts, or the 274 Tg of TFA reported in Frank et al. (2002), based on a measured constant concentration of 200 ng/L. The additional contribution of TFA related to the degradation of HFC-134a alone is estimated to be 1.0–2.9 Tg between 2020 and 2100.

With a total global precipitation volume of 5.5×10^{17} liters, and assuming that TFA will be deposited through wet deposition only, the degradation from HFC-134a and HFO-1234yf is projected to result in a global average TFA concentration in precipitation of 660–970 ng/L in 2050 and 1150–1910 ng/L in 2100. This would represent an increase of a factor of around two to three in 2050 and of around three to six in 2100, when compared to the precipitation-weighted average of 340 ng/L of TFA found in Germany in 2018–19 (Freeling et al., 2020).

The global average deposition rate of TFA from the combined degradation of HFC-134a and HFO-1234yf is projected to be 0.7–1.0 kg km^{-2} yr^{-1} and 1.2–2.1 kg km^{-2} yr^{-1} in 2050 and 2100, respectively. In the first period, these numbers are comparable to those in the regional projections for 2030 (Wang et al., 2018) and 2040 (David et al., 2021). While all these global averages in concentration and depositions are still far below the toxic values for aquatic organisms, as summarized by Solomon et al. (2016) and Neale et al. (2021), regional studies focused in highly populated and industrialized areas have projected regions of higher impact and high concentrations in precipitation and in the atmosphere (e.g. Henne et al., 2012; Wang et al., 2018; David et al., 2021; Holland et al., 2021). Understanding the TFA budget in the different environmental compartments is key for evaluating the future

Table 7-4. Projected annual TFA production rate due to atmospheric conversion of HFC-134a and HFO-1234yf in 2020, 2050, and 2100, as well as cumulative projected totals of deposited TFA mass between 2020 and 2050 and between 2020 and 2100, in Tg (1012 g).

	HFC-134a	HFO-1234yf	Sum
Annual TFA Formation			
2020	0.01–0.03 Tg yr^{-1}	0.03–0.03 Tg yr^{-1}	0.04–0.06 Tg yr^{-1}
2050	0.02–0.05 Tg yr^{-1}	0.34–0.49 Tg yr^{-1}	0.36–0.54 Tg yr^{-1}
2100	0.01–0.02 Tg yr^{-1}	0.63–1.03 Tg yr^{-1}	0.64–1.05 Tg yr^{-1}
Sums of Deposited TFA			
2020–2050	0.5–1.5 Tg	5.3–6.6 Tg	5.8–8.1 Tg
2020–2100	1.0–2.9 Tg	30.5–49.0 Tg	31.5–51.9 Tg

Note:
The calculation of the formation of TFA from HFC-134a is based on its expected mixing ratio of HFC-134a (Velders et al., 2022) and its lifetime of 14 years. Conversion rates from the destroyed HFC-134a amounts to TFA were 7–20%. For HFOs, it is assumed that 50% of the future emissions of low-GWP alternatives (**Figure 7-5**; Velders et al., 2022) are related to HFOs, from which it is assumed that 50% is HFO-1234yf, with a conversion rate of 100% to TFA.

environmental impacts of anthropogenic TFA. Of specific interest in this respect is the uncertainty in the natural background of TFA found in the ocean (Frank et al., 2002; Scott et al., 2005; Joudan et al., 2021).

In addition, other sources of TFA in the atmosphere could also gain in importance. An increasing bank of fluoropolymers raises the possibility of TFA formation from the thermic destruction of fluoropolymers (Ellis et al., 2001; Cui et al., 2019), such as in waste incinerators or from uncontrolled burning.

7.2.5.2 Carbon Tetrafluoride (CF_4)

CF_4 is a very strong greenhouse gas that is emitted by various industrial sources (*Chapter 1*). In addition, Jubb et al. (2015) found that CF_4 is formed from the UV photolysis of trifluoroacetylfluoride ($CF_3C(O)F$), which itself is an atmospheric degradation product of several halocarbons (e.g., 13% of HFC-134a and 100% of HFO-1234yf; see *Section 7.2.5.1*). However, the relative production of CF_4 from $CF_3C(O)F$ is extremely small, as formation of CF_4 from $CF_3C(O)F$ is only possible in the presence of UV wavelengths found in the stratosphere and above. For 2100, Jubb et al. (2015) estimated a contribution of 9 t for HFC-134a. For the very short-lived HFO-1234yf the contribution is expected to be even smaller. This is insignificant relative to the global CF_4 emissions, currently around 15 Gg yr^{-1} (*Chapter 1*).

7.2.6 The Key Climate Gases: Carbon Dioxide, Methane, and Nitrous Oxide

The most important drivers of climate change over the last century are the well-mixed greenhouse gases (GHGs) carbon dioxide (CO_2), methane (CH_4), and nitrous oxide (N_2O). The atmospheric abundances and associated radiative forcings of climate from these gases have increased substantially in the industrial era (see *Chapters 1*, *3*, and *5*). Their future increase will depend on policy actions related to curbing climate change. Future changes in halogen mixing ratios will take place against the backdrop of the changing chemical, radiative, and climatic conditions caused by these GHGs, and future stratospheric ozone levels will be strongly dependent on their future emissions and mixing ratios. The continuing increase of these GHGs has important effects on stratospheric ozone through cooling of the stratosphere, which slows the ozone chemical loss rates. The resulting climate change from increasing GHGs also strengthens the stratospheric Brewer-Dobson circulation, which will redistribute ozone (see *Chapter 5*). In addition, CH_4 and N_2O are also key chemical gases affecting the ozone layer directly. The breakdown of N_2O in the stratosphere enhances nitrogen oxides (NO_x) and depletes ozone, while increases in CH_4 lead to ozone changes that vary with altitude, with net production in total column ozone.

For this Assessment, the new Shared Socioeconomic Pathway (SSP) scenarios are used for future projections of the major GHGs. These replace the previous Representative Concentration Pathway (RCP) scenarios used in the last Assessment. The SSPs are designed based on socioeconomic and technological development and adapt the future climate radiative forcing outcomes used for the RCPs, while providing more detail in the variety of climate outcomes that can be obtained (Gidden et al., 2019; Meinshausen et al., 2020; Chen, Rojas, Samset et al., 2021).

Section 7.4.3.1 examines how the changing mixing ratios of CO_2, CH_4, and N_2O under selected SSPs could affect future changes in stratospheric ozone relative to the changing emissions and mixing ratios of halogenated compounds. The nine selected scenarios include updates of the four RCPs having the same radiative forcing levels of 2.6, 4.5, 6.0, and 8.5 W m^{-2}, as well as five scenarios that fill gaps not covered in the RCPs (Gidden et al., 2019). These SSPs include five high-priority scenarios from the Sixth Assessment Report of the Intergovernmental Panel on Climate Change, including a lower-bound 1.9 W m^{-2} scenario (Rogelj et al., 2018), which corresponds to the most optimistic interpretation of Article 2 of the Paris Agreement and comes closest to holding the global temperature increase to below 1.5 °C.

7.2.7 Deliberate Climate Intervention

Chapter 6 provides a comprehensive analysis of the influence of deliberate climate interventions on the stratospheric ozone layer.

7.2.8 Other Potential Influences on Stratospheric Ozone

In this section, the potential impact of future anthropogenic emissions from a large-scale rocket economy, potential new supersonic airplanes, and a hydrogen-based energy system is discussed. In addition, the current knowledge of the impact of volcanoes and wildfires is summarized.

7.2.8.1 Influence of a Growing Spaceflight Industry

Emissions from rockets and their effect on stratospheric ozone have been the subject of research since the 1970s. Since the previous Assessment, significant launch growth has occurred and more satellites have been launched into low-Earth orbit than during the previous 60 years, an increase entailing larger rockets and greater launch rates.

The greatest part of this growth has come from kerosene-fueled rockets, from which black carbon (BC) emissions have doubled in the past four years (Miraux, 2022). Emissions from solid-fuel rockets have increased only slightly, and this trend is likely to continue. On the other hand, hydrazine-fueled rocket launches have decreased during this period because of propellant toxicity concerns. The number of hydrogen-fueled launches has been approximately constant, representing only a small fraction of all launches. Methane-fueled rockets, in advanced testing, are expected to play a significant role in the future, although the rate at which methane replaces existing rocket fuel is uncertain.

Rocket propulsion systems typically combine the exhaust from several of the four primary propellant types during a single launch (by fuel: kerosene, ammonium perchlorate, hydrazine, and hydrogen). Mixed rocket emissions into the stratosphere are mostly (>90% of about 8 Gg yr^{-1}) a combination of CO_2, CO, H_2O, NO, and OH with the exact amounts depending on propellant and altitude. None of these gas-phase emission components have a significant effect on stratospheric ozone, except at implausibly larger launch rates (Larson et al., 2017; Ryan et al., 2022). NO_x emissions (<1%) from some rocket types can affect ozone (Ross et al., 2004), although to a lesser degree than solid fuel chlorine emission.

Direct ozone loss caused by chlorine emissions (0.2 Gg yr^{-1}) from solid fuel rockets into the stratosphere is well understood.

Models generally agree on the amount and distribution of ozone loss (Voigt et al., 2013; Ryan et al., 2022). Alumina emissions from solid fueled rockets (0.4 Gg yr^{-1}) cause ozone loss by heterogeneous Cl_y (inorganic chlorine) activation reactions; this is less well bounded because of uncertainties in the alumina surface area density, extent of sulfate coating, and reaction coefficients (Danilin et al., 2003). In situ plume data suggest that ozone loss from alumina could be larger than the loss from chlorine (Danilin et al., 2001), and this question remains unresolved.

Indirect ozone loss caused by the absorption and scattering of solar radiation by rocket BC and alumina particles in the stratosphere have not yet been comprehensively investigated. General principals of stratospheric processes suggest that rocket BC and alumina increase heating rates and temperature in the stratosphere and cause ozone loss (Lee et al., 2021). This is confirmed by new models of rocket BC emissions (Maloney et al., 2022; Ryan et al., 2022), which show ozone loss from rocket BC is comparable to ozone loss from rocket chlorine emissions (per propellant mass), consistent with models of climate change mitigation using stratospheric BC (Weisenstein et al., 2015).

With a very large number of 100,000 projected hydrogen-fueled reusable small rocket launches per year, H_2O emissions from space travel has been estimated to enhance stratospheric water by up to 9%, leading to a 20% increase in polar stratospheric clouds (PSCs) in both hemispheres (Larson et al., 2017). An even larger effect of hydrogen-based space travel is through anticipated increases in stratospheric NO_x, which, combined with HO_x cycle perturbations, leads to 0.5% loss of the globally averaged ozone column, with column losses in the polar regions exceeding 2%.

The effect on ozone of stratospheric aerosols generated by destruction of space debris during reentry is a new area of research (Boley and Byers, 2021; Ryan et al., 2022). It is expected that spaceflight architectures that assume disposal of space debris into the mesosphere via destructive reentry will take on greater importance in coming years (Ross and Jones, 2022). Reentry vaporization and lower mesosphere particle production and sedimentation presents a source of stratospheric particles that could exceed those from present-day launches by 2030 (Boley and Byers, 2021). Very little is known about the composition, sizes, and steady state distribution of reentry particles or their possible impact on stratospheric ozone. Nitrogen oxide (NO) produced during heating of the atmosphere during reentry reduces mesospheric ozone (Ryan et al., 2022), though reentry NO production rates are poorly quantified.

In view of the rapid growth of rocket launches, rocket fuels, spacecraft in orbit, and the anticipated increase in space debris reentries these knowledge gaps suggest further assessments are warranted.

7.2.8.2 Influence of a New Fleet of Supersonic Airplanes

Early research on the environmental effect of supersonic airplanes warned of potential adverse effects on stratospheric ozone, mainly through their emissions of NO_x into the stratosphere (e.g., Crutzen, 1972). This concern was reinforced by later studies (e.g., Johnston et al., 1989). To date, this potential source of ozone loss has not been realized, since the first generation of supersonic passenger planes was decommissioned in 2003. However, hypothetical concepts for a new generation of supersonic airplanes are now again being developed. The potential influence of supersonic and hypersonic aircrafts on stratospheric ozone are discussed in *Section 4.2.5.3*.

7.2.8.3 Influence of a Potential Future Hydrogen Economy

Hydrogen fuel cells could play a role in future clean energy supply systems if produced using renewable energy sources. If their use is widespread, it will potentially lead to elevated atmospheric hydrogen mixing ratios because of leakages during storage and usage. With an atmospheric lifetime of two years (Paulot et al., 2021), surface emissions of hydrogen can at least partly reach the stratosphere. Further, direct emissions into the upper troposphere and lowermost stratosphere are expected if planned hydrogen-fueled airplanes and rockets are realized (*Section 7.2.8.1*).

In both the troposphere and stratosphere, hydrogen is oxidized to water vapor. The influence will be small in the troposphere because the water vapor perturbation is minimal compared with the background. In the stratosphere, additional hydrogen increases H_2O concentrations. However, it is generally concluded that the effect of future surface emissions from an economy that is only partly reliant on hydrogen as an energy carrier will be too small to have a substantial effect on stratospheric ozone (e.g. Warwick et al., 2004; van Ruijven et al., 2011; Vogel et al., 2011; Wang et al., 2013). If hydrogen were to play a major role in future energy policy, a potential influence, e.g., via the enhanced production of PSCs, has been modeled (Tromp et al., 2003).

7.2.8.4 Impact of Volcanoes and Wildfires

Volcanoes are well known to have an intermittent effect on stratospheric ozone through their input of aerosols and sulfur dioxide (SO_2) into the stratosphere (e.g., Langematz, Tully et al., 2018). Recently, the effect of wildfires has also been discussed (*Sections 3.2.1.3* and *4.3.5.3*). Strong Siberian wildfires (2019–2020) were responsible for a layer of dust in the lower stratosphere and could have contributed to very low stratospheric ozone concentrations over the Arctic during the same period of time (Ohneiser et al., 2021). In addition, strong Australian bushfires may also have contributed to very low ozone levels in the Antarctic in the spring of 2020 (Rieger et al., 2021) and have an at least sporadic negative effect also on mid-latitude ozone (Solomon et al., 2022). If intense fires in the temperate to subpolar regions increase, then these fires could have a potential long-term influence on stratospheric ozone.

7.3 METRICS FOR CHANGES IN OZONE AND CLIMATE

7.3.1 Metrics for Changes in Ozone

As in past Ozone Assessments, one key metric used to evaluate the ability of various ozone-depleting substances to destroy stratospheric ozone is their contribution to equivalent effective stratospheric chlorine (EESC; for a detailed description of this metric, see Box 5-2 of Harris, Wuebbles et al. (2014)). The other primary metric used in *Section 7.4* is the globally averaged ozone

depletion as calculated by a two-dimensional model. Semi-empirical ODPs are updated but are no longer used to evaluate the relative differences among the various presented scenarios. In calculating EESC, there have been minor changes in the adopted fractional release factors (FRFs), which represent the fractions of ODSs that have been broken down from their organic forms into inorganic molecules that can then be converted to molecules that can deplete ozone. These FRFs are consistent with the adopted EESC approach, which is used in *Chapter 1* of this document and was discussed in Section 6.4.3.1 and Appendix 6C of Carpenter, Daniel et al. (2018). The adopted FRF values are shown in **Table 7-2** along with the resulting semi-empirical ODPs, which are almost identical to those given in Carpenter, Daniel et al. (2018). For comparison, the ODPs used in the Montreal Protocol are also shown in the table. In evaluating the various scenarios discussed in *Section 7.4*, we use the integrated EESC differences over the time period from the year 2023 through the year when EESC returns to the 1980 level for each particular scenario. Consistent with no longer using GWP-weighted emissions as a metric to evaluate the climate impact (see *Section 7.3.2*), we do not compare scenarios using cumulative ODP-weighted emissions as was done in the previous Assessment. As discussed in *Chapter 1*, there have been some updates to the ODS lifetimes used in this Assessment. These lifetime updates are included in the *Annex*.

A more substantial change to the analysis of the ODSs in this chapter relative to the main section of Carpenter, Daniel et al. (2018) arises from using the revised EESC approach of Engel et al. (2017). The new approach used to calculate EESC leads to a larger effective stratospheric age of air compared with the previously assumed 3 years at mid-latitudes and 5.5 years in polar regions and was discussed in detail in Section 6.4.1 of Carpenter, Daniel et al. (2018). The effective increase in the age of air, combined with the fact that the EESC slope is steeper with time around 1980 than the projected slope when EESC returns to 1980 levels, leads to a delay of more than a decade in the projected time for mid-latitude EESC to return to 1980 levels with the Engel et al. (2017) EESC approach relative to that used in the main chapter of Carpenter, Daniel et al. (2018). The advantages of this newer approach were recognized in the 2018 Assessment, which is why both were discussed in Carpenter, Daniel et al. (2018) and scenario results of the Engel et al. (2017) approach were shown in Appendix 6C. If the scenario results of this chapter are to be fairly compared with those of Carpenter, Daniel et al. (2018), the results here should be compared with those of Table 6C-1 in Appendix 6C of Carpenter, Daniel et al. (2018) and not the results shown in their Table 6-5. Unfortunately, the change in EESC approach also inhibits straightforward comparisons with scenario results (using EESC) from Ozone Assessments before 2018. It should be noted that because nearly all of the source gases have almost fully dissociated by the time they make it to the polar vortexes, the difference between the two EESC approaches is substantially smaller in polar regions than it is at mid-latitudes. It should also be noted that in regions where full dissociation has not occurred, the move to the approach of Engel et al. (2017) introduces another potentially significant model sensitivity relating to atmospheric transport. Given this, when future comparisons of EESC are made with different models, it would be important to indicate which differences are due to model differences and which are due to ODS scenario differences.

7.3.2 Metrics for Changes in Climate

The climate metrics used in Carpenter, Daniel et al. (2018) were global warming potentials (GWPs), global temperature change potentials (GTPs), and radiative forcing (RF). A description of these metrics can be found in Box 5-3 of Harris, Wuebbles et al. (2014), and a discussion of radiative forcing can be found in **Box 5-3** of this Assessment. A search for better metrics continues in the scientific and policy community, with the most appropriate metric dependent on the particular purpose. Recently, Forster, Storelvmo et al. (2021) have discussed two new metrics that are demonstrably better when the goal is to have similar temperature change outcomes from similar metric-weighted emissions trajectories; these are GWP* and combined global temperature change potential (CGTP). Both approaches require that gases be divided into long-lived ones, which behave like CO_2 in that the amount of warming depends on the cumulative emissions, and short-lived ones, whose warming depends on changes in emissions. The GWP* approach, for example, has frequently been used to compare warming from CO_2 (long-lived) with that from CH_4 (short-lived). However, when there are important gases with intermediate lifetimes, this categorization is ambiguous and imperfect. In this chapter, for example, the way in which CCl_4 and CFC-11 are categorized have significant effects on the relative comparisons of the scenarios. Because of this and the shortcomings identified in using the traditional GWP-weighting to equate the climate impact of GHG emissions with substantially different lifetimes (see, e.g., Chapter 7 of the Working Group I contribution to IPCC AR6: Forster, Storelvmo et al., 2021), in this chapter, we compare the climate impact of various scenarios by using the averaged radiative forcing over the period 2023–2100.

In calculating the radiative forcing of the scenarios discussed in *Section 7.4*, the radiative efficiency (RE) factor estimates that have changed the most significantly since the previous Assessment are for CFC-11 and CFC-12. Hodnebrog et al. (2020b) have estimated that tropospheric feedbacks of these compounds imply their REs should be increased by 13% and 12%, respectively, and they have been changed accordingly.

Additional terminology that is relevant to the calculation of indirect GWPs in this section is effective radiative forcing (ERF). A detailed discussion of ERF and how it compares with RF is found in **Box 5-3**. The ERF of the halocarbons includes the offsetting radiative forcing due to the ozone depletion they cause, which is the dominant response, as well as to other adjustments such as tropospheric responses including cloudiness and circulation changes. In a case where the various atmospheric responses to an increase of a specific ODS mixing ratio completely offsets its direct radiative forcing, the ERF of that ODS would be zero. Three studies have been published since the previous Assessment that estimated the ERF of the combined ODSs (Morgenstern et al., 2020; O'Connor et al., 2021; Thornhill et al., 2021), and another has updated radiative efficiency estimates of the halocarbons as well as the resulting GWPs (Hodnebrog et al., 2020a). One of the ERF studies (Morgenstern et al., 2020) has attempted to remove the effect of the large variation among models in their calculated ozone depletion by constraining their modeled ERF estimate using observed depletion amounts. In their assessment of these studies, Forster, Storelvmo et al. (2021) suggest an ERF for all ODSs plus the HFCs in 2019 (relative to 1850) of 0.01 to 0.40 W m^{-2}, when including the responses in ozone depletion as well as in stratospheric water vapor and atmospheric methane mixing ratios. While the

radiative efficiencies for the key ODSs have changed little over the last four years (see, e.g., *Annex*), the uncertainty range for the ERF of the ODSs now encompasses smaller values; i.e., the offset through responses could be larger than previous Ozone and IPCC Assessments have suggested. Despite modeling improvements and a new approach constraining the ERF estimates with observations, the uncertainty in the ERFs remains substantial, as discussed in *Section 5.3.1.1*. The uncertainty range implies that the forcing offsets range between approximately no offset to a complete offset of the ODS direct radiative forcing. These ERFs, which include the radiative impact of ozone depletion resulting from ODSs, are used only in the calculation of indirect GWPs in this chapter. The comparison of the various scenarios presented in **Table 7-6** and the figures that show radiative forcing do not consider the radiative impact of ozone depletion.

The direct and indirect GWPs are shown in **Table 7-5**. The direct GWPs capture only the direct radiative effect of the ODSs themselves, including stratospheric temperature adjustment and, for CFC-11 and CFC-12, tropospheric adjustments. The offsetting radiative effects of ozone responses, as well as the smaller effects of methane and water vapor responses, to changes in ODS mixing ratios are given by the indirect GWPs (**Table 7-5**). The sum of the direct and indirect GWPs therefore approximately capture the full radiative effect of an ODS's emissions. The indirect GWPs given in **Table 7-5** incorporate the midrange of the new ERF in their calculation, using the same EESC-scaling approach described Daniel et al. (1995) and in previous Assessments (e.g., Carpenter, Daniel et al., 2018). The full uncertainty range varies between roughly 0 and twice the indirect GWP quoted. When compared with the equivalent Table 6-3 of the WMO (2018) Assessment, the slightly more negative indirect GWPs are apparent. As in previous Assessments, the relative magnitudes of the direct and indirect GWPs vary widely across the different ODSs, with key factors including whether the compound has a bromine atom instead of chlorine (since bromine is roughly 60 times more effective than chlorine at depleting ozone), the number of halogen atoms, and the radiative efficiency of the ODS. While HFCs do not cause chemical ozone depletion, they do alter stratospheric temperatures, which in turn leads to stratospheric ozone changes (Hurwitz et al., 2015; Dupuy et al., 2021). These changes are, however, minimal and are not considered in our indirect GWP calculations.

This ERF revision to the ozone forcing in response to the ODSs is also important for understanding the climate forcing role of the ODSs collectively. We do not include the offset of the ozone response in evaluating the scenarios later in this chapter but do point out that if the lower ERF estimates prove to be accurate, this would imply that the phasedown of the ODSs by the Montreal Protocol would have a smaller globally averaged climate impact than previously estimated, at least from a strictly global radiative point of view. Again, however, it is important to note the large uncertainty in determining this offsetting radiative

Table 7-5. Indirect GWPs from ozone depletion compared with direct GWPs for select ODSs. We calculate the "indirect" GWP using the radiative effect of the responses in ozone, methane, and stratospheric water vapor to the ODS. This indirect GWP calculation approach follows Daniel et al. (1995) and assumes that, as with ozone, all three indirect responses track EESC. The radiative forcing due to ozone depletion from 1979 to 2000 is updated to –0.17 W m^{-2}; this is 50% of the direct forcing from the ODSs and HFCs and is in approximately the middle of the range of this same ratio in Szopa, Naik et al. (2021). The relative uncertainty in this radiative forcing offset response (IPCC, 2021) translates directly to the same relative uncertainty in indirect GWPs. Notice that the number of significant figures shown for both indirect and direct GWPs are not meant to represent the level of uncertainty; instead, they are shown so changes relative to past studies and future studies can be more easily tracked.

Gas	Direct GWP 100-yr	Indirect GWP 100-yr
CFC-11	6410	–4390
CFC-12	12,500	–3490
CFC-113	6530	–3600
CFC-114	9450	–1490
CFC-115	9630	–355
HCFC-22	1910	–133
HCFC-123	91	–43
HCFC-124	596	–55
HCFC-141b	808	–302
HCFC-142b	2190	–219
HCFC-225ca	137	–45
HCFC-225cb	557	–69
CH_3CCl_3	164	–366
CCl_4	2150	–3460
CH_3Br	2	–1400
Halon 1211	1990	–25,400
Halon 1301	7430	–75,800
Halon 2402	2260	–64,400

forcing from ozone depletion (see *Section 5.3.1.1*) and to note that this remains an active area of research. We also reiterate that the issue of a potential ozone forcing offset does not apply to HFCs and thus will not alter estimates of the radiative forcing benefit of the Kigali Amendment.

7.4 SCENARIOS AND SENSITIVITY ANALYSES

7.4.1 Tools Used in Analyses of Ozone and Climate Effects

As in recent Ozone Assessments, the foundation for the ODS scenarios generated in this chapter are observed atmospheric mixing ratios of the ODSs and their replacements, as well as their global lifetimes, reported production to UNEP, and estimates of ODS banks (**Box 7-1**). The historical mixing ratios to which all the scenarios are tied, and from which annual emissions are estimated, are taken from a combination of the Advance Global Atmospheric Gases Experiment (AGAGE) and National Oceanic and Atmospheric Administration (NOAA) observational networks (*Chapter 1*). The production data are taken from what the Parties have reported to the Ozone Secretariat, aggregated into Article 5 and non-Article 5 country groups. The lifetimes for the ODSs considered in this chapter have been updated from those in the 2018 Assessment and are presented in the *Annex* of this Assessment as well as in **Table 7-2**.

We continue to use the 1-box model that has been used in the past several Ozone Assessments. In this model, banks are prescribed for a given starting year, chosen here to be 2020, and from these are calculated going forward from that year by adding projected annual production and subtracting projected annual emissions. It is important to recognize that the temporal evolution of these banks is performed in a relatively simplistic manner, with only a single bank for each compound. Thus, that bank can contain a mix of accessible and inaccessible banks as well as active and inactive banks, for example. In the previous three Assessments (WMO 2011, 2014, 2018), 2008 bank values were projected forward from estimates from UNEP (2009). Here, bank starting values are taken using a Bayesian approach described in Lickley et al. (2020, 2021, 2022). These banks represent the most recent comprehensive estimate of banks that has been peer-reviewed. Nonetheless, there are substantial uncertainties associated with these estimates. One contributing factor to uncertainties in both the Lickley approach and the previously used approach is uncertainties in global lifetimes, which lead to a bias in the emissions estimated from atmospheric concentration observations. Any biases in either production or emissions can have a significant impact on the bank size estimated for the present and moving into the future. A discussion of the potential impacts of these alternative bank estimates for ozone and climate is found in *Section 7.4.3*.

The Technology and Economic Assessment Panel (TEAP) has also performed a model analysis of CFC-11 banks. In their approach, they use estimates of release rates that vary over the bank's life cycle (WMO, 2021). These bank size estimates are consistent with the values calculated by Lickley et al. (2020), giving further credibility to their use in this chapter.

As in the previous Assessment, the GSFC 2-D model, described in Appendix 6B of Carpenter, Daniel et al. (2018) and in Fleming et al. (2020), is used to evaluate the ozone response for the scenarios developed here. The use of this 2-D model will again allow us to evaluate the impact of future projections of CO_2, CH_4, and N_2O.

7.4.2 Baseline Scenario

Future scenarios are derived in this chapter for the long-lived ODSs, CH_2Cl_2 (dichloromethane), and HFC-23. Projections for the other HFCs are described in *Chapter 2* and are incorporated here. HFC-23 scenarios are developed in this chapter because of the close association of HFC-23 emissions with HCFC-22 production. Beyond the ODSs, various scenarios of future mixing ratios of CO_2, CH_4, and N_2O are also examined with the 2-D model to show their influence on future ozone levels.

The scenario chosen to be the baseline scenario for non-ODS GHGs is SSP2-4.5. Of the five SSP narratives, this comes closest to representing a middle-of-the-road pathway, with social, economic, and technological trends projected to be not substantially different from what has occurred in the past. In addition, this is the baseline scenario used in the Chemistry-Climate Model Initiative (CCMI) model calculations, which are used elsewhere in this Assessment.

In general, the key assumptions that determine future ODS mixing ratios are 1) their global lifetimes, 2) projections of future production, 3) current banks, and 4) release rates from production, including production intended for feedstock use and from banks. For production intended for emissive uses (i.e., non-feedstock uses), it is assumed that all halon and CFC production has ceased globally, along with HCFC production in non-Article 5 countries. In Article 5 countries, future HCFC production is held constant at 2020 levels until 2025, after which it phases down in steps according to the Protocol controls. An important difference between the baseline scenario used here and the baseline scenarios in previous Assessments is that we include some emissions from feedstock production for the compounds CFC-113/CFC-113a, CFC-114/CFC114a, HCFC-22, HCFC-141b, HCFC-142b, CH_3CCl_3, CH_3Br, and CCl_4 and allow these emissions to continue into the future. The emissions from feedstocks are uncertain, and we conservatively make the assumption that 2% of production associated with feedstock usage is emitted in the year of production (see **Box 7-2** for a discussion of feedstock-related emissions) for all compounds except CCl_4, for which it is assumed to be 4.3% (see *Section 7.2.1.3* and **Figure 7-4**). These CCl_4 emissions arise from a combination of emissions from its production (i.e., unreported, non-feedstock emissions in **Figure 7-4**) and from the feedstock usage. Note that this 4.3% has been revised downward from that given in the SPARC CCl_4 report (SPARC, 2016). There are substantial increasing feedstock production trends over at least the past few years for HCFC-22 and CCl_4 (**Figure 7-3**). Nevertheless, in our baseline scenario, we assume that future production for feedstock use remains fixed at the 2020 levels. As discussed in **Box 7-2**, CCl_4 projections are calculated differently than the projections for other ODSs due to the large uncertainty in the sources of recent and current emissions. We assume that the current emissions are made up of a feedstock-related emissions component, an inadvertent component related to other industrial sources, and emissions related to historic production (e.g., from landfills; see **Figure 7-4**). It is assumed that emissions from this historic production are linearly phased out between 2021 and 2030, after which they remain zero, and the only continuing

emissions are associated with feedstock production and use as well as inadvertent production losses.

For the banks considered, including CFC-11, CFC-12, HCFC-22, HCFC-141b, HCFC-142b, halon-1211, and halon-1301, the Lickley approach (Lickley et al., 2022) is used to estimate banks at the beginning of 2020. These 2020 banks, along with historical emissions and reported production values are used to estimate banks back to 2015. Then, over the 2015–2020 time period, a single average annual percentage release rate from the bank is calculated for each compound and assumed to remain constant into the future. This uniquely determines future emission scenarios for each of the banked compounds, with annual production added to and annual emissions subtracted from the bank each year.

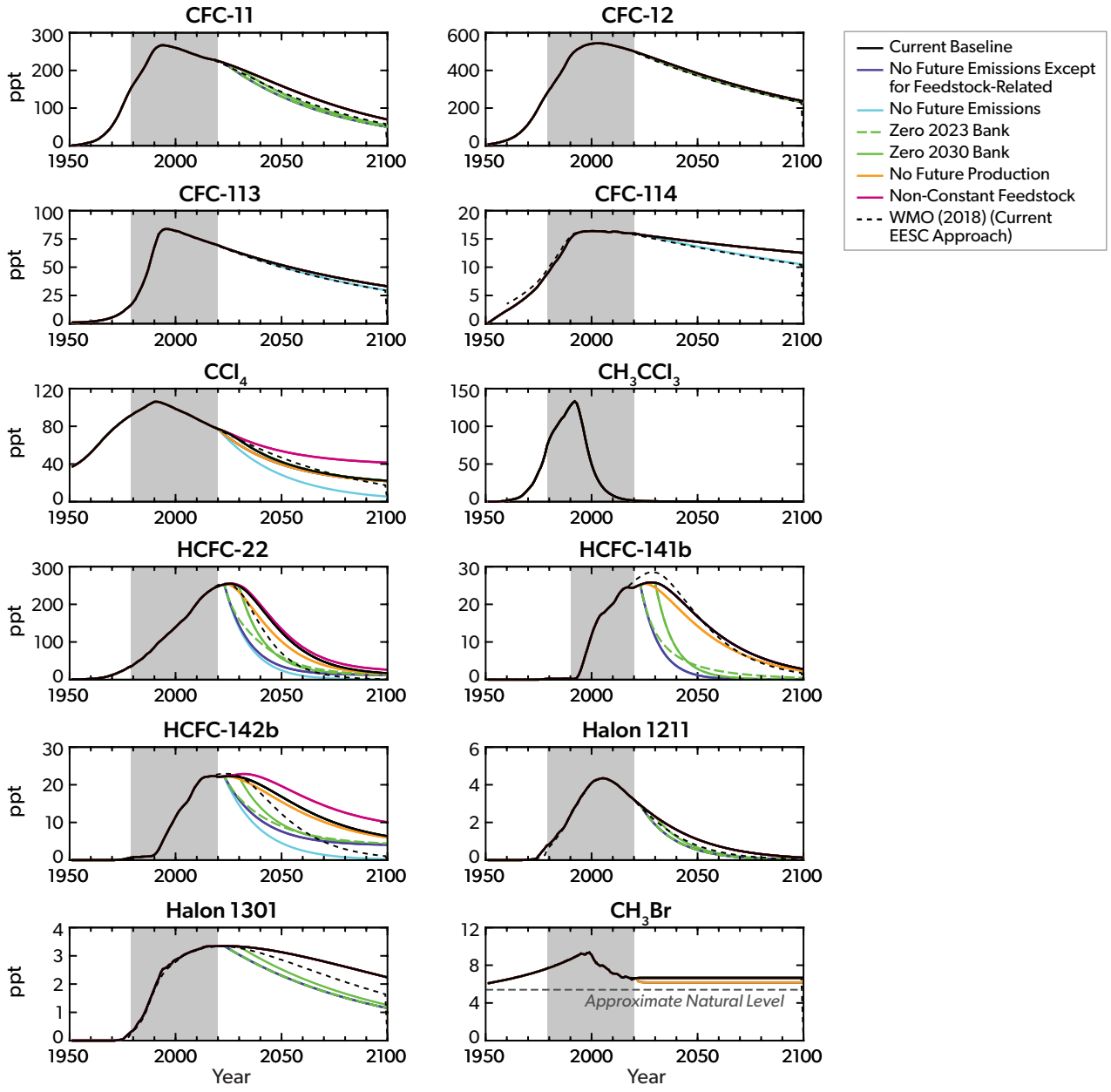

Figure 7-6. Comparison of mixing ratios from the current baseline scenario (solid black curves) with those of the alternative scenarios described in *Section 7.4.3* and those of the baseline scenario from the 2018 Assessment (dashed black curves). Alternative scenarios shown include the elimination of the banks in 2023 and 2030 (dashed and solid green curves, respectively), elimination of production from 2023 onward (orange curves), elimination of emissions from 2023 onward except for emissions associated with feedstock production (dark blue curves), elimination of all emissions from 2023 onward (light blue curves), and a "non-constant" feedstock production scenario in which feedstock production continues to increase or decrease in the future at the rate experienced over the past decade (described in the text; magenta curves).

CH_3Br is assumed to have no further controlled production globally, and continuing emissions arise from assumed constant ongoing production for critical use exemptions (CUEs) and quarantine and pre-shipment (QPS) uses consistent with what has been reported for 2020. Halon-1202 and halon-2402 are assumed to have no future emissions, and the mixing ratio of CH_3Cl remains at 539.5 ppt, a level assumed to be consistent with no further anthropogenic activity; while some anthropogenic emissions are likely to continue (see *Section 7.2*), these are not expected to significantly affect the conclusions of this chapter and thus are not considered here.

We also include in the discussion below the impact of CH_2Cl_2 on ozone, as calculated from 3-D model studies. We do not include this compound in our 2-D model calculations because of the dependence on the time of year and location of emissions (both latitude and longitude) in determining how much reaches the stratosphere. It is accepted that 3-D models are required to accurately calculate the transport of short-lived compounds from the surface to the stratosphere.

Finally, we develop a baseline scenario for HFC-23, including only its relationship to production of HCFC-22. HFC-23 is considered only in the climate forcing calculation since it has no chlorine, bromine, or iodine in it, and the change in ozone from its temperature impact would be minimal in our scenarios. While the HCFC-22 production intended for emissive uses is controlled by the Montreal Protocol, future feedstock production is uncontrolled. We assume that the emissions of HFC-23 are equal to 1.6% of the HCFC-22 production, where destruction capacities are only partly employed (*Section 7.2.1.4*). For the HFC-23 scenario, we assume that the HCFC-22 feedstock production increases through 2030 at the recently reported rate and remains constant thereafter. The baseline scenario for the other HFCs is developed and described in *Chapter 2*.

The ODS mixing ratios for the baseline scenario are shown in **Figure 7-6** and are tabulated in **Appendix Table 7A-1**. HFC-23 mixing ratios are also included in **Appendix Table 7A-1** starting in 2018. Many of the ODS projections are very similar to those of the baseline scenario from the 2018 Assessment. The biggest differences arise from the upward revision of bank estimates and, for some compounds, from including future emissions associated with feedstock production. HCFC-22 mixing ratios show the largest increases in the coming decades when compared with the previous Assessment, with values from 2042 to 2056 more than 50 ppt larger in the present projections. CFC-11 and CFC-12 both are larger by more than 10 ppt compared with the 2018 Assessment for periods in the future.

7.4.3 Alternative Future Scenarios

The primary alternative ODS scenarios are designed to assess the relative contributions of various sources of emissions to future ozone depletion and climate change. Specifically, we develop some scenarios that include the elimination of all emissions or production of certain compounds beginning in 2023 and some that eliminate banks that are projected to exist in 2023 or 2030. The purpose of examining two separate years for the elimination of banks is to provide some estimate of the benefit of quick action; however, this comparison depends on how quickly the ODSs are released from the banks and thus likely has more uncertainty associated with it than some of the other scenario comparisons. As stated earlier, there is also no differentiation of bank type in this chapter, which would be useful information if one wished to determine the practicality of capturing a bank. By grouping all banks into a single bank, we do not differentiate between active and inactive banks or the type of equipment in which the banked compound resides, nor can we comment on the accessibility of any bank. HFCs are also evaluated for their impact on climate under future scenarios in which all emissions, production, or banks are eliminated from 2023 onward.

Other alternative ODS scenarios performed are meant to estimate the impact of the unreported production and associated emissions of CFC-11 over the past decade, as well as the potential impacts of future emissions associated with uncontrolled production intended for feedstock applications. To quantify the impact of feedstock usage, we include a scenario in which all emissions associated with feedstock applications are eliminated beginning in 2023. We include an additional scenario that is identical to the baseline scenario except that through 2030, feedstock production for each compound considered is allowed to continue increasing or decreasing at the same rate as exhibited over the 2010–2020 period. Of course, changes after 2030 would further affect any conclusion, but we hold production constant after 2030 due to the speculative nature such projections would entail. It is important to recognize that the feedstock results presented in this chapter are specifically dependent on the ODS emissions that are assumed to be associated with feedstock activity in the baseline scenario.

Future ODS projections for selected alternative scenarios are included in **Figure 7-6** for comparison with the baseline scenario of this chapter and the baseline scenario of WMO (2018).

For CH_2Cl_2, we estimate the impact of future emissions if they are allowed to grow through 2030 at the rate exhibited over the past five years, after which emissions are held constant. Furthermore, we also estimate the effect of the elimination of all CH_2Cl_2 emissions after 2023.

For CO_2, CH_4, and N_2O, we examine eight alternative SSP scenarios that range from substantially lower (SSP1-1.9) to substantially higher (SSP5-8.5) greenhouse gas radiative forcing by the end of the century. We examine the impact of these different concentrations collectively and individually to show the specific effect that each compound has on future ozone levels.

The specific scenarios discussed above are evaluated for their impacts on stratospheric ozone and climate in **Table 7-6**.

7.4.3.1 Stratospheric Ozone Implications

The mid-latitude EESC evolution for selected key ODS scenarios is shown in **Figure 7-7**. This shows that in the baseline scenario, mid-latitude EESC returns to its 1980 levels at the beginning of 2066, about six years later than in the baseline scenario of the 2018 Assessment (cf. Appendix 6C of Carpenter, Daniel et al. (2018)). This is primarily due to the higher concentrations of CFC-11 and CFC-12 that result from the larger bank estimates used here compared with the previous Assessment. Polar EESC returns to 1980 levels in 2087, about nine years later than in Carpenter, Daniel et al. (2018). Slight changes in the age spectrum function used in the EESC calculation also contribute about one and two years to these mid-latitude and polar delays, respectively. In Carpenter, Daniel et al. (2018), the function describing the age spectrum for use in the Engel et al. (2017) approach, assumed a width to mean age ratio of 0.5 as suggested in Newman et al.

Table 7-6. *See caption on facing page.*

Scenario	Change in Integrated EESC[1] Relative to Baseline Scenario for the Mid-latitude Case		Year When EESC is Expected to Drop Below 1980 Value *(year x)*		Change in Average Radiative Forcing 2023–2100 (mW m^{-2})	Change in Integrated O_3 Depletion: 2020–2070 (%)
	$\int_{1980}^{year\ x} EESC\ dt$	$\int_{2023}^{year\ x} EESC\ dt$	Mid-latitude	Antarctic Vortex		
A1: Baseline scenario	0.0	0.0	2066.0	2086.6	0.0	0.0
Elimination of production for emissive uses[2]:						
All ODSs	–3.2	–9.6	2063.2	2084.1	–3.7	–0.15
HCFCs	–0.5	–1.5	2065.6	2086.3	–3.3	–0.03
CCl_4	–0.9	–2.6	2065.5	2086.3	–0.4	–0.04
CH_3Br for QPS and CUE	–1.9	–5.6	2064.1	2084.7	–0.0	–0.08
HFCs (except HFC-23)					–51.4	
Elimination of emission for emissive uses[3]:						
All Controlled ODSs	–10.1	–30.1	2052.9	2072.1	–25.1	–0.60
CFCs	–3.3	–10.0	2061.2	2080.7	–9.5	–0.20
Halons	–3.1	–9.3	2062.1	2082.0	–0.4	–0.12
HCFCs	–2.6	–7.7	2063.9	2085.1	–14.8	–0.14
CCl_4	–0.9	–2.6	2065.5	2086.3	–0.4	–0.04
CH_3CCl_3	0.0	0.0	2066.0	2086.6	0.0	–0.00
CH_3Br for QPS	–1.9	–5.6	2064.1	2084.7	0.0	–0.08
All ODS emissions, including related to feedstock use	–11.3	–33.8	2050.5	2068.1	–31.1	–0.71
HFCs (except HFC-23)					–67.7	
HFC-23					–10.9	
Entire 2023 bank captured and destroyed:						
All ODSs	–7.7	–22.9	2055.6	2074.7	–21.5	–0.46
All CFCs	–3.3	–10.0	2061.2	2080.7	–9.5	–0.20
All halons	–3.1	–9.3	2062.1	2082.0	–0.4	–0.15
All HCFCs	–2.1	–6.3	2064.4	2085.4	–11.6	–0.11
HFCs (except HFC-23)					–16.2	
Entire 2030 bank captured and destroyed:						
All ODSs	–4.7	–13.9	2057.7	2076.6	–15.7	–0.29
All CFCs	–1.8	–5.5	2062.5	2082.1	–6.1	–0.11
All halons	–1.9	–5.6	2062.8	2082.6	–0.3	–0.10
All HCFCs	–1.5	–4.6	2064.2	2085.2	–9.3	–0.09
Other scenarios:						
Continuing feedstock trend through 2030	2.3	6.8	2070.3	2092.1	+4.4	+0.10
Additional 1000 Gg bank of CFC-11 in 2021	3.0	9.0	2069.7	2090.3	+5.6	+0.15
Reduced CFC-11 of 280 Gg over 2012–2019	–1.2	–3.7	2065.2	2085.9	–1.7	-0.06
N_2O mitigation (uses SSP1-1.9 for N_2O)					–43.4	–0.17
No future CH_2Cl_2 anthropogenic emissions						–0.28 to –0.56
CH_2Cl_2 emissions increasing through 2030, then constant						+0.06 to +0.12

Note:
[1]EESC is calculated according to the approach described in Engel et al. (2017); this change accounts for a delay in the return of mid-latitude EESC to 1980 levels of more than a decade when compared with Table 6-5 of WMO (2018).
[2]Production scenarios all allow for non-emissive uses, such as those associated with feedstock usage.
[3]Emission scenarios allow for continued emission associated with non-emissive uses.

Table 7-6. Comparison of scenarios and test cases, showing the year when EESC[1] drops below the 1980 value for both mid-latitudes and in the Antarctic vortex, as well as integrated mid-latitude EESC differences relative to the baseline scenario; the integral is performed from 1980 or 2023 through the time when mid-latitude EESC returns to 1980 levels (denoted as "year x"). Also shown are changes in average radiative forcing over 2023–2100 and average global ozone depletion over 2020–2070. Future changes in CH_4 and CO_2 may also significantly alter ozone levels and radiative forcing, likely by amounts larger than any of the cases considered in this table (see, e.g., text in *Section 7.4.3.1*). Average radiative forcing from the ODSs in the baseline scenario, against which other scenarios are compared, is 0.22 W m^{-2} (220 mW m^{-2}); for HFC-23 it is 0.02 W m^{-2}, and for the other HFCs it is 0.08 W m^{-2}. For comparison, the current radiative forcing of CO_2 is about 2 W m^{-2}.

(2007); here we assume the ratio of the square of the width to the age is 0.7 yr, taken form Engel et al. (2017).

Figure 7-8 and **Figure 7-9** compare the impact of selected scenarios on globally averaged total column ozone, respectively, as calculated with the 2-D model. As expected, the ozone response exhibits a roughly inverse relationship with the EESC curves. While the subsequent discussion specifically refers to ozone and ozone depletion, EESC generally responds in a consistent manner with ozone depletion across the various scenarios shown in these figures as well as in **Table 7-6**.

Elimination of all halogenated ODS emissions starting in 2023 increases future global ozone above the baseline, with a 0.71%[11] increase in globally averaged column ozone averaged over 2020–2070 (**Table 7-6**), and it moves the date when EESC returns to 1980 levels forward by 16 years for mid-latitudes and 19 years for polar regions. Elimination of all ODS emissions represents the lowest future EESC that can be achieved with the lifetimes assumed here; these global lifetimes determine how quickly the various ODS atmospheric mixing ratios decline. CFCs, halons, HCFCs, CH_3Br, and CCl_4 (including emissions from production and use in feedstock applications) all contribute notably to future ODS emissions in the baseline scenario.

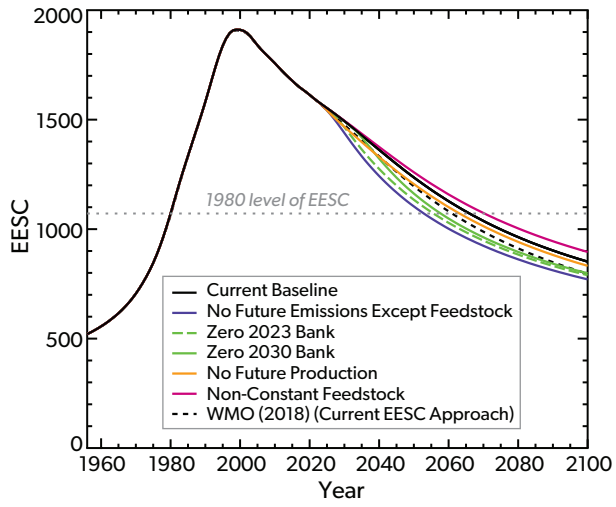

Figure 7-7. Mid-latitude EESC time series for the scenarios shown in **Figure 7-6**. The 2018 Assessment EESC values have been calculated using the approach adopted in this chapter and applied to the mixing ratios of that baseline scenario to obtain a consistent comparison.

In the baseline scenario, future feedstock-related emissions lead to a 0.11% decrease in globally averaged total ozone averaged over 2020 through 2070 and an increase in radiative forcing of 6 mW m^{-2} when averaged over 2023–2100. If feedstock emissions continue to change through 2030 at the same rate as over the past decade and are held constant thereafter, this would decrease total ozone averaged over 2020 through 2070 by an additional 0.10% and increase averaged radiative forcing by an additional 4 mW m^{-2} when averaged over 2023 through 2100.

The scenarios that assume hypothetical full capture and destruction of ODS banks in 2023 or 2030 (**Figure 7-9**) have a much larger effect on reducing future ozone depletion than does the scenario in which production of all ODSs is eliminated starting in 2023. As stated above, however, it should be recognized that there are substantial uncertainties in the current bank size estimates. The Lickley et al. (2022) bank values are generally higher than those projected for 2020 when starting with the 2008 values of IPCC/TEAP (2005); this is also the case for projections from the IPCC/TEAP (2005) banks estimated for 2002. It is our assessment that the uncertainties in bank values remain large at this time, with commensurate uncertainties in the extent to which capture and destruction of the banks could benefit climate and ozone.

Using the results from WMO (2021), we can put the potential impacts of the unreported production of CFC-11 over the past decade into context with the results above. We evaluate the impact of the unexpected emissions over the 2012–2019 period by assuming emissions associated with unreported production of 280 Gg, the middle of the range (120–440 Gg) given in WMO (2021). We also examine the impact of an additional 1000 Gg in the CFC-11 bank in 2020. While the increase in the CFC-11 bank from the unreported production is uncertain, this value of 1000 Gg can be used to approximately scale other potential bank increases if more certainty is eventually gained as to how much of the recent unreported production went into applications relative to how much has already been emitted. A CFC-11 bank increase of this size (1000 Gg) is projected to lead to about a 0.15% decrease to global column ozone averaged through 2070. This can be compared with the emissions through 2019 (280 Gg) associated with the unreported production causing an additional 0.06% depletion averaged over 2020–2070. It is thought likely that the observed

[11] Ozone change percentages modeled in this chapter are calculated with the simplifying assumption of a background globally averaged column ozone level of 300 DU. Thus, a 1% change represents a 3 DU change

emissions over this time period were associate with foam production, and historically it is found that about 25%–45% of the production is emitted through the foam production process. This would imply an increase in the CFC-11 bank of 146–1320 Gg. This range is comparable to another recent estimate of the increase in CFC-11 banks of 90 to 725 Gg due to this unreported production (Montzka et al., 2021).

To explore further how future emissions of other climate-relevant gases could affect ozone, **Figure 7-10** shows the range in future global total ozone associated with nine selected SSP scenarios (1-1.9, 1-2.6, 2-4.5, 3-7.0, 3-7.0-low NTCF [near-term climate forcer], 4-3.4, 4-6.0, 5-3.4 overshoot (OS), and 5-8.5). The influences of CO_2, CH_4, and N_2O are shown in combination (top panel), as well as individually (lower three panels), where the latter are calculated by varying each gas individually while using the baseline SSP2-4.5 scenario for the other two gases. The baseline ODS scenario is used in all runs. The processes responsible for the ozone impacts of these greenhouse gases (GHGs) are discussed in *Chapter 3* and in past Assessments. When compared with **Figures 7-8** and **7-9**, it is apparent that the variations of each of these three GHGs across the SSP scenarios lead to a substantially wider range of possible future ozone levels than from the ODS scenarios alone. For example, the difference in global ozone in 2100 between the baseline ODS scenario and a scenario with no ODS emissions from 2023 is 0.6% (**Figure 7-8**). This contrasts with a range of 6% across the SSP scenarios due to the combined impact of the three GHGs, and ranges of 3%, 4%, and 1.5% due to the individual ranges of CO_2, CH_4, and N_2O concentrations, respectively. Thus, policies that affect the future evolution of these three GHGs in particular will be important for predicting how ozone will change. The impacts of N_2O and ODS mitigation through the 21st century are also directly compared in **Figure 7-8**.

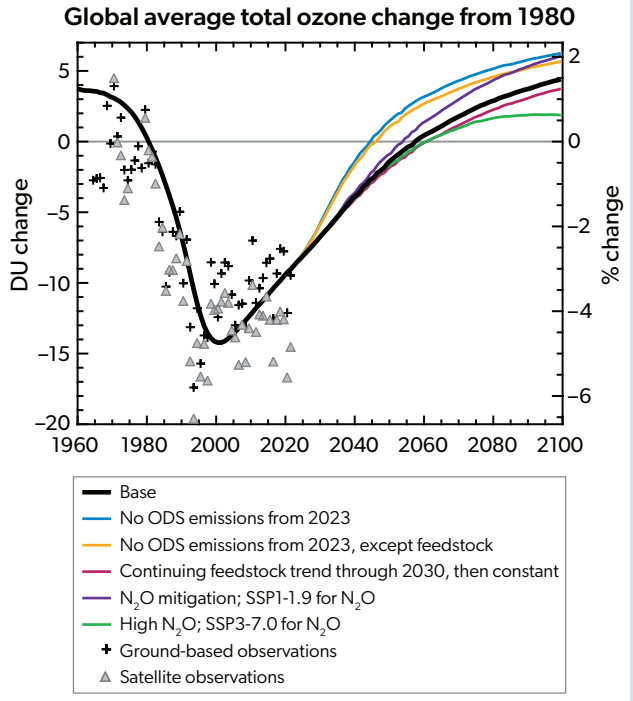

Figure 7-8. Influence of selected scenarios on globally averaged (90°S–90°N) total ozone relative to that in 1980. The scenarios include the baseline scenario; no long-lived ODS emissions from 2023 onward; no long-lived ODS emissions from 2023 onward except for feedstock uses; feedstock emission changes continuing at the same rate experienced over the past decade through 2030, then held constant; an N_2O mitigation scenario in which the low SSP1-1.9 projection is used for future N_2O mixing ratios; and a high N_2O scenario in which the high SSP3-7.0 projection is used for future N_2O mixing ratios, with all other assumptions following the baseline scenario. Calculations are from the GSFC 2-D model. The figure also shows observed global and annually averaged total ozone relative to the 1979–1981 average, from ground-based (black plus signs) and satellite (grey triangles) observations.

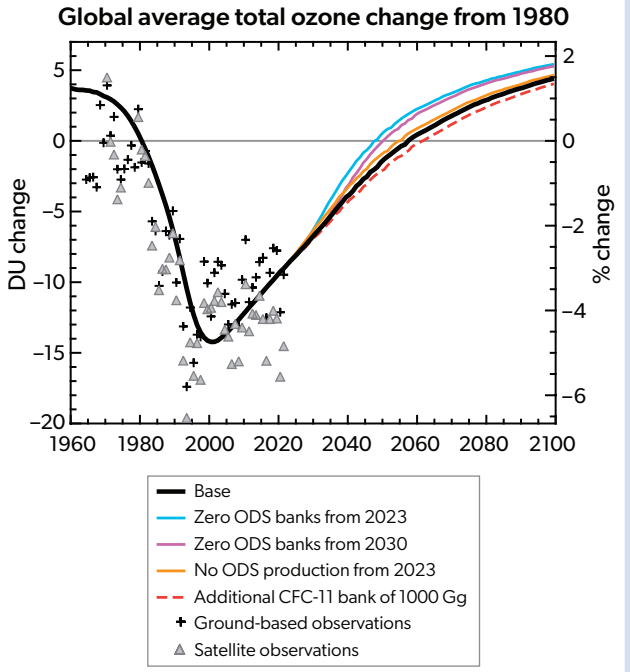

Figure 7-9. Same as in **Figure 7-8** but for additional scenarios. These scenarios include the baseline scenario; full capture and destruction of the ODS banks in 2023 but allowing continued production; full capture and destruction of the ODS banks in 2030 but allowing continued production; no ODS production from 2023 onward; and an additional 1000 Gg in the CFC-11 bank in 2020, with all other assumptions following the baseline scenario. Calculations are from the GSFC 2-D model. The figure also shows observed global and annually averaged total ozone relative to the 1979–1981 average, from ground-based (black plus signs) and satellite (grey triangles) observations.

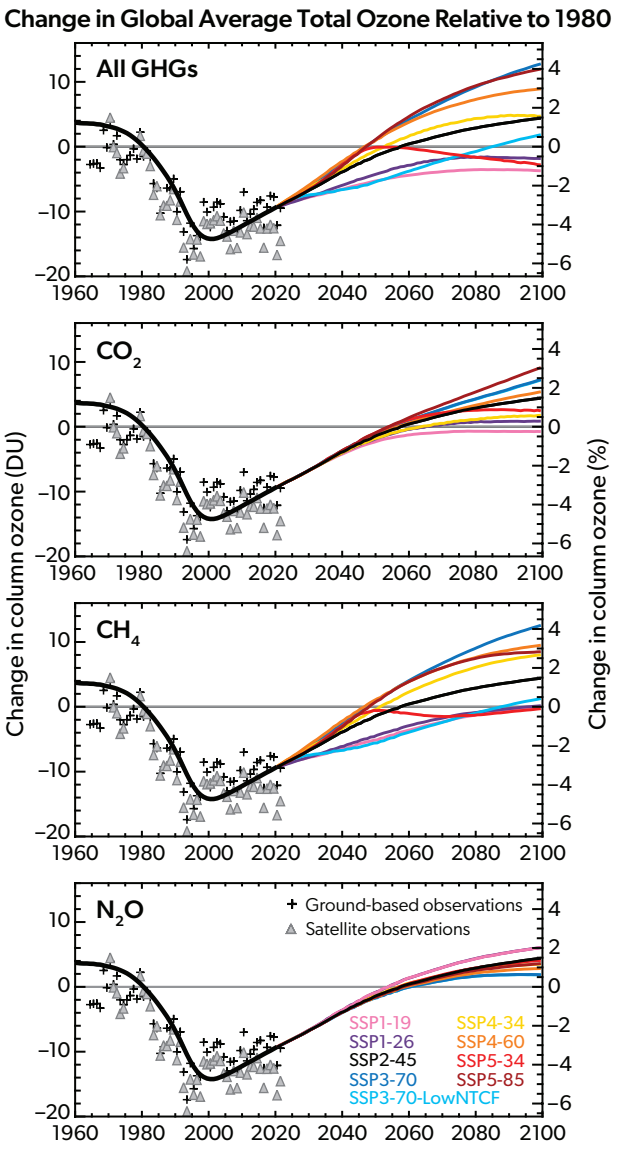

Figure 7-10. As in **Figure 7-9**, but showing global total column ozone responses to a range of future CO_2, CH_4, and N_2O emissions scenarios in the presence of decreasing ODSs. The colored lines depict the range in projected ozone for the nine SSP scenarios listed in the bottom panel, due to future changes in all three GHGs combined (*top panel*), and individually by varying each gas while using the baseline SSP2-4.5 scenario for the other two gases. For CO_2 and CH_4, the highest and lowest assumed emissions correspond to the highest and lowest ozone curves, respectively, while the opposite is true for N_2O. All simulations use the baseline ODS scenario. Calculations are from the GSFC 2-D model, which compares well with 3-D models, including for the CH_4 and N_2O perturbations (see WMO-2018, Appendix 6B).

Finally, two alternative scenarios are examined for CH_2Cl_2, namely (1) continued strong growth in emissions until 2030, with constant emissions thereafter, and (2) immediate cessation of emissions. Ozone impacts of these scenarios are shown in **Table 7-6**. Unlike the CFCs, CH_2Cl_2 has a short lifetime and thus responds rapidly to changes in emissions. If emissions quickly decrease in the future, the delivery of CH_2Cl_2 to stratospheric chlorine will also fall rapidly. Under scenario (1), a range of 3-D model ODP values (Claxton et al. 2019) implies that integrated global ozone depletion over 2020–2070 (shown in the final column of **Table 7-6**) would increase by a rather small amount (0.06%–0.12%). However, the continuing large variability in its surface abundances makes estimates of future concentrations highly uncertain and hinders evaluation of the plausibility of this scenario. If, on the other hand, all anthropogenic emissions of CH_2Cl_2 were to cease in 2023, the reduction in average ozone depletion from 2020–2070 relative to the baseline scenario would be more significant (0.28–0.56%). The amount of reduction in ozone depletion would be dependent on the regional variation of emissions sources, with the largest depletion reduction being for emissions sources in tropical Asia. The effect on average ozone depletion from 2020–2070 would be about 40–80% of the effect of eliminating all ODS emissions in 2023.

7.4.3.2 Climate Implications

The radiative forcing time series for ODSs in the baseline scenario and selected alternative scenarios are shown in **Figure 7-11**. As mentioned previously (*Section 7.3.2*), the forcing from these compounds due to ozone destruction is not included in this figure, in **Table 7-6**, or in our discussion below. Even with the extreme scenario that assumes no additional emissions of ODSs

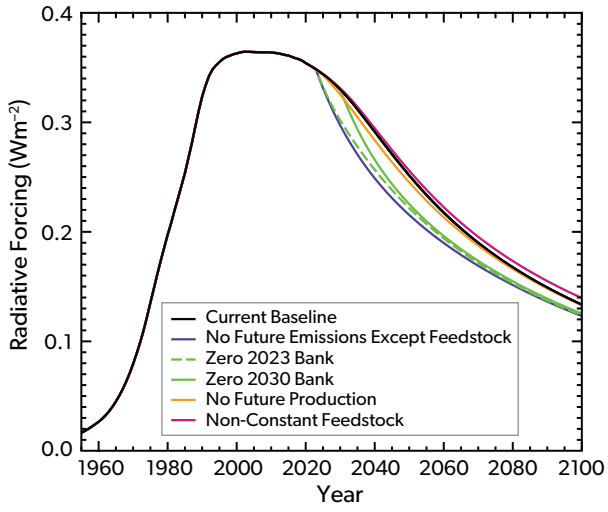

Figure 7-11. Direct radiative forcing (RF) from the combination of compounds and scenarios shown in **Figure 7-6**. The climate impacts of ozone depletion, resulting from the presence of these ODSs, is not included in this forcing. As indicated by the negative Indirect GWPs in **Table 7-5**, inclusion of the ODS impact on ozone would result in lower effective radiative forcing (ERF), although the extent to which it would be lower remains highly uncertain.

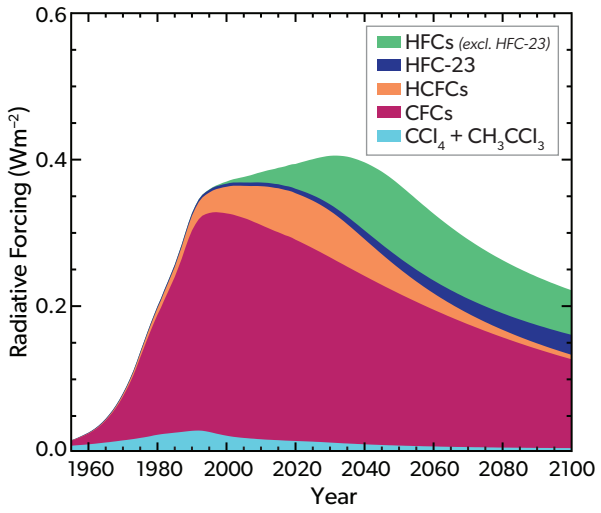

Figure 7-12. Contributions of various groups of ODSs and HFCs to direct radiative forcing for the baseline scenario. The light blue area represents forcing from CCl_4 and CH_3CCl_3, combined. CFC, HCFC, HFC-23, and other HFC (excluding HFC-23) contributions are then progressively stacked on top.

from 2023 onward, climate benefits are limited when compared with the forcing due to compounds already in the atmosphere. Compared to the baseline scenario, the average radiative forcing reduction arising from the elimination of all ODS emissions from 2023 onward (excluding feedstocks), from the capture and destruction of the 2023 ODS banks, and from the elimination of ODS production from 2023 onward is 25.1, 21.5, and 3.7 mW m^{-2}, respectively, when averaged over 2023–2100 (**Table 7-6**). If emissions associated with feedstocks were also assumed to be eliminated from 2023 onward, the average radiative forcing reduction would be 31.1 mW m^{-2} rather than 25.1 mW m^{-2}. A breakdown of the contribution from individual compounds or compound groups to the radiative forcing values is shown in **Figure 7-12** for the baseline scenario.

Using the assumptions described earlier in this section for the magnitude of emissions arising from unreported production of CFC-11 over the past decade, we estimate an average radiative forcing impact of 1.7 mW m^{-2} over 2023–2100 from these emissions. As stated in *Section 7.4.3.1*, it is unclear how much recent unreported production has contributed to the global CFC-11 bank. Thus, any additional contribution from any augmentation to the CFC-11 bank from unreported production remains highly uncertain and is not included in this estimate. As in *Section 7.4.3.1*, we can calculate the potential impact of an additional 1000 Gg added to the 2020 CFC-11 bank. This would lead to an additional 5.6 mW m^{-2} averaged over 2023–2100 and can be scaled to other CFC-11 bank sizes. These radiative forcing estimates also do not include any impact from potential co-emissions of CFC-12 or, to a lesser extent, CCl_4, that might have been associated with the recent, unreported CFC-11 production.

Figure 7-12 includes additional radiative forcing contributions of HFC-23 and the other HFCs calculated for the baseline scenario. The impact of potentially reducing future HFC emissions is strongly dependent on the assumption underlying the baseline scenario. For example, if the baseline scenario overestimates the future radiative forcing compared with what will happen under existing controls, the benefit of a hypothetical elimination of future emissions or production would also be overestimated. As was seen in Figure 6-7 of the 2018 Assessment, HFC forcing remains relatively constrained and does not increase sharply in the future because global adherence to the Kigali Amendment is assumed in the baseline scenario. **Figure 7-12** also shows that if HFC-23 emissions progress as assumed in the baseline scenario, its forcing continues to increase through the end of the century, even as the forcing from other HFCs will have begun to decline. Because of its long lifetime, any potential future declines in HFC-23 mixing ratios after 2100, or even before, could only happen slowly. In the baseline scenario, in which it is assumed that the destruction rate of HFC-23 relative to HCFC-22 production is not increased, its radiative forcing in 2100 is projected to be about half of all the other HFCs together (**Figure 7-12**). If destruction were maximized, consistent with current technical abilities, forcing from HFC-23 would remain minor. As shown in **Table 7-6**, elimination of HFC-23 emissions beginning in 2023 would reduce average radiative forcing over 2023–2100 by 11 mW m^{-2}. Elimination of the other HFC emissions in 2023 would reduce average radiative forcing by 68 mW m^{-2}, with future production accounting for about three-quarters of this total.

Not shown in the previous figures, but noted in **Table 7-6**, is that the reduction of N_2O emissions from our baseline scenario (SSP2-4.5) to the SSP1-1.9 scenario reduces average radiative forcing by 43 mW m^{-2}. SSP1-1.9 is the scenario considered with the greatest N_2O emissions mitigation; this anthropogenic reduction in emissions is about 3% when compared with the baseline scenario and averaged over 2020–2070.

To provide some context for the previous forcing values, the average radiative forcing by CO_2 over the 2023–2100 period in our baseline scenario (SSP2-4.5) is about 3250 mW m^{-2}.

Appendix Table 7A-1. Atmospheric mixing ratios (in ppt) of the ODSs considered in the baseline scenario. Values are for the beginning of the corresponding year. Values represent a combination of AGAGE and NOAA networks for years when those observations are available (see *Chapter 1*). Projection assumptions are discussed in *Sections 7.4.1* and *7.4.2*.

Year	CFC-11	CFC-12	CFC-113	CFC-114	CFC-115	CCl_4	CH_3CCl_3	HCFC-22
1955	3.3	14.3	1.3	1.1	0.0	42.3	0.1	1.0
1956	4.3	16.7	1.3	1.4	0.0	44.0	0.2	1.1
1957	5.6	19.4	1.4	1.6	0.0	45.9	0.4	1.3
1958	6.9	22.6	1.6	1.9	0.0	47.8	0.7	1.5
1959	8.2	25.9	1.7	2.1	0.0	49.9	1.0	1.7
1960	9.5	29.5	1.9	2.3	0.0	52.1	1.5	2.1
1961	11.1	33.9	2.0	2.6	0.0	54.4	2.0	2.4
1962	13.3	38.8	2.3	2.8	0.0	56.8	2.4	2.9
1963	16.1	44.4	2.5	3.0	0.0	59.3	3.2	3.4
1964	19.5	51.1	2.8	3.3	0.0	61.8	3.9	4.1
1965	23.5	58.8	3.1	3.5	0.0	64.4	4.7	4.9
1966	28.1	67.5	3.5	3.8	0.0	66.9	5.8	5.9
1967	33.1	77.3	3.9	4.1	0.1	69.3	7.6	7.1
1968	38.8	88.3	4.4	4.4	0.1	71.6	10.1	8.5
1969	45.3	100.6	4.9	4.7	0.1	73.8	13.0	10.3
1970	52.8	114.3	5.5	5.0	0.2	75.9	16.3	12.1
1971	61.3	129.3	6.3	5.3	0.2	78.0	19.1	14.1
1972	70.6	145.3	7.1	5.6	0.3	80.0	22.7	16.2
1973	81.1	162.8	8.1	6.0	0.4	81.9	27.4	18.6
1974	93.0	182.2	9.1	6.3	0.5	83.7	33.5	21.3
1975	106.1	203.1	10.4	6.8	0.7	85.5	40.0	23.8
1976	118.5	223.2	11.9	7.3	0.9	87.2	45.5	26.6
1977	130.9	242.6	13.5	7.8	1.1	88.8	53.1	29.8
1978	142.5	261.2	15.0	8.3	1.3	90.4	62.5	33.2
1979	153.2	279.0	16.6	8.8	1.5	91.6	74.7	34.8
1980	162.3	296.7	19.0	9.3	1.8	93.2	82.2	38.9
1981	170.7	311.4	21.5	9.9	1.9	94.8	88.8	43.1
1982	179.3	329.4	25.3	10.5	2.1	96.0	93.8	47.1
1983	187.6	345.3	28.9	11.0	2.4	97.1	97.9	50.9
1984	196.3	362.5	32.6	11.4	2.7	98.4	102.2	54.8
1985	205.5	378.0	37.3	11.9	3.1	99.6	106.8	59.1
1986	215.5	397.2	42.1	12.6	3.5	101.0	110.5	65.0
1987	226.6	416.0	47.5	13.2	4.0	102.6	113.3	70.1
1988	237.7	437.6	54.5	13.8	4.4	103.7	118.5	73.8
1989	247.4	458.7	61.3	14.5	4.8	104.9	123.2	79.6
1990	255.1	476.2	67.8	15.1	5.3	106.1	127.3	86.3
1991	260.5	489.6	73.5	15.5	5.7	106.2	131.0	92.8
1992	263.9	500.8	79.2	15.8	6.1	105.8	133.1	98.9
1993	266.4	510.1	81.4	16.0	6.5	105.3	130.5	103.5
1994	266.9	516.1	83.0	16.1	6.8	104.4	122.2	108.6
1995	266.3	522.2	83.7	16.2	7.2	103.7	110.6	113.5
1996	265.2	528.5	83.8	16.3	7.5	102.8	98.2	119.2
1997	264.3	533.2	83.6	16.3	7.7	101.8	84.0	124.1
1998	262.9	536.3	83.2	16.3	7.9	100.8	71.1	128.9
1999	261.5	539.1	82.7	16.4	8.0	99.7	59.5	134.3

HCFC-141b	HCFC-142b	Halon-1211	Halon-1202	Halon-1301	Halon-2402	CH_3Br	CH_3Cl	HFC-23
0.0	0.0	0.00	0.00	0.00	0.00	6.3	491.3	
0.0	0.0	0.00	0.00	0.00	0.00	6.3	495.1	
0.0	0.0	0.00	0.00	0.00	0.00	6.3	498.8	
0.0	0.0	0.00	0.00	0.00	0.00	6.4	502.6	
0.0	0.0	0.00	0.00	0.00	0.00	6.4	506.4	
0.0	0.0	0.00	0.00	0.00	0.00	6.5	510.3	
0.0	0.0	0.00	0.00	0.00	0.00	6.5	514.2	
0.0	0.0	0.00	0.00	0.00	0.00	6.6	517.9	
0.0	0.0	0.00	0.00	0.00	0.00	6.6	521.5	
0.0	0.0	0.00	0.00	0.00	0.00	6.7	524.9	
0.0	0.0	0.00	0.00	0.00	0.00	6.7	528.1	
0.0	0.0	0.00	0.00	0.00	0.00	6.8	531.0	
0.0	0.0	0.00	0.00	0.00	0.00	6.9	533.6	
0.0	0.0	0.01	0.00	0.00	0.01	6.9	536.0	
0.0	0.0	0.01	0.00	0.00	0.01	7.0	538.0	
0.0	0.0	0.02	0.00	0.00	0.02	7.0	539.9	
0.0	0.0	0.03	0.00	0.00	0.02	7.1	541.4	
0.0	0.1	0.04	0.00	0.01	0.03	7.2	542.8	
0.0	0.1	0.06	0.00	0.02	0.04	7.2	544.0	
0.0	0.1	0.09	0.00	0.03	0.05	7.3	544.9	
0.0	0.2	0.23	0.01	0.04	0.06	7.4	545.8	
0.1	0.3	0.37	0.01	0.11	0.08	7.4	546.5	
0.1	0.4	0.50	0.01	0.18	0.09	7.5	547.1	
0.2	0.6	0.64	0.01	0.24	0.11	7.6	547.6	
0.2	0.7	0.78	0.01	0.31	0.14	7.7	548.0	
0.2	0.8	0.84	0.01	0.36	0.15	7.7	548.4	
0.2	0.8	0.96	0.01	0.46	0.17	7.8	548.6	
0.3	0.8	1.07	0.01	0.59	0.19	7.9	548.9	
0.2	0.8	1.21	0.01	0.69	0.20	8.0	549.1	
0.2	0.9	1.39	0.01	0.78	0.22	8.1	549.3	
0.3	1.0	1.51	0.01	0.92	0.25	8.2	549.4	
0.3	1.0	1.61	0.01	1.09	0.27	8.3	549.5	
0.3	1.0	1.74	0.02	1.28	0.29	8.3	549.6	
0.3	1.0	1.94	0.02	1.47	0.32	8.4	549.7	
0.3	1.1	2.17	0.02	1.65	0.35	8.5	549.8	
0.3	1.4	2.38	0.02	1.84	0.38	8.6	549.8	
0.2	2.0	2.63	0.02	2.04	0.41	8.8	549.9	
0.2	2.8	2.80	0.02	2.19	0.43	8.9	549.9	
0.4	3.9	2.96	0.03	2.41	0.44	9.0	549.9	
1.3	5.1	3.16	0.03	2.53	0.46	9.1	550.0	
2.7	6.2	3.36	0.03	2.56	0.47	9.3	562.5	
4.5	7.3	3.52	0.04	2.60	0.47	9.2	546.4	
6.5	8.4	3.67	0.04	2.68	0.48	9.1	536.5	
8.2	9.4	3.84	0.04	2.71	0.49	9.3	556.9	
10.1	10.4	3.98	0.04	2.82	0.49	9.3	566.4	

Year	CFC-11	CFC-12	CFC-113	CFC-114	CFC-115	CCl_4	CH_3CCl_3	HCFC-22
2000	259.9	541.2	82.1	16.4	8.1	98.6	49.7	139.3
2001	258.4	542.9	81.8	16.4	8.2	97.6	41.5	144.9
2002	256.7	543.6	81.2	16.4	8.2	96.6	34.5	150.7
2003	254.5	543.6	80.4	16.4	8.3	95.6	28.8	155.7
2004	252.6	543.4	79.6	16.4	8.3	94.6	24.0	160.6
2005	250.4	542.7	78.9	16.4	8.4	93.7	20.0	165.9
2006	248.3	541.8	78.4	16.4	8.4	92.7	16.7	172.0
2007	246.1	539.8	77.7	16.3	8.4	91.5	14.0	179.1
2008	244.1	537.4	76.9	16.2	8.4	90.4	11.7	187.4
2009	242.2	535.3	76.1	16.2	8.4	89.1	9.9	195.2
2010	240.4	532.3	75.7	16.3	8.4	87.9	8.3	202.5
2011	238.3	529.5	75.0	16.3	8.4	86.8	6.9	210.0
2012	236.3	526.9	74.4	16.3	8.4	85.6	5.8	216.0
2013	234.4	523.9	73.7	16.2	8.4	84.6	4.8	221.5
2014	232.8	520.9	73.0	16.1	8.4	83.5	4.0	226.5
2015	231.6	518.3	72.5	16.1	8.5	82.4	3.3	231.6
2016	230.2	514.9	71.8	16.1	8.5	81.2	2.8	235.3
2017	229.1	511.4	71.2	16.0	8.5	80.1	2.4	239.3
2018	228.3	508.6	70.7	16.0	8.6	79.2	2.1	242.6
2019	227.2	505.1	70.1	16.0	8.7	78.4	1.8	245.5
2020	225.0	500.8	69.4	16.0	8.7	77.3	1.5	247.5
2021	223.3	497.1	68.7	15.9	8.7	76.5	1.3	249.7
2022	221.5	493.4	67.9	15.8	8.7	75.6	1.1	251.4
2023	219.7	489.6	67.2	15.8	8.6	74.6	1.0	252.6
2024	217.8	485.8	66.6	15.7	8.6	73.6	0.9	253.5
2025	215.8	481.9	65.9	15.7	8.6	72.5	0.8	254.1
2026	213.8	478.0	65.3	15.6	8.6	71.2	0.7	254.4
2027	211.7	474.0	64.7	15.6	8.6	69.9	0.7	253.8
2028	209.6	470.1	64.0	15.5	8.6	68.6	0.6	252.5
2029	207.4	466.1	63.4	15.5	8.6	67.1	0.6	250.6
2030	205.3	462.1	62.8	15.4	8.5	65.6	0.5	248.1
2031	203.1	458.1	62.2	15.4	8.5	64.1	0.5	245.2
2032	200.8	454.1	61.6	15.3	8.5	62.5	0.5	241.3
2033	198.5	450.2	61.0	15.3	8.5	61.1	0.5	236.7
2034	196.3	446.2	60.5	15.2	8.5	59.6	0.4	231.4
2035	194.0	442.2	59.9	15.2	8.5	58.3	0.4	225.6
2036	191.6	438.2	59.3	15.1	8.4	56.9	0.4	219.4
2037	189.3	434.2	58.7	15.1	8.4	55.6	0.4	212.9
2038	187.0	430.3	58.2	15.0	8.4	54.4	0.4	206.2
2039	184.6	426.4	57.6	15.0	8.4	53.2	0.4	199.3
2040	182.3	422.4	57.1	14.9	8.4	52.0	0.4	192.4
2041	179.9	418.5	56.5	14.9	8.4	50.9	0.4	185.5
2042	177.6	414.7	56.0	14.8	8.4	49.8	0.4	178.5
2043	175.2	410.8	55.5	14.8	8.3	48.7	0.4	171.5
2044	172.9	407.0	55.0	14.7	8.3	47.7	0.4	164.6
2045	170.5	403.2	54.4	14.7	8.3	46.7	0.4	157.8
2046	168.2	399.4	53.9	14.7	8.3	45.8	0.4	151.2
2047	165.9	395.6	53.4	14.6	8.3	44.8	0.4	144.7

HCFC-141b	HCFC-142b	Halon-1211	Halon-1202	Halon-1301	Halon-2402	CH_3Br	CH_3Cl	HFC-23
11.8	11.4	4.10	0.05	2.86	0.49	9.1	554.2	
13.5	12.5	4.20	0.05	2.90	0.49	8.6	541.2	
14.8	13.3	4.25	0.04	2.93	0.49	8.3	537.0	
16.1	13.9	4.29	0.04	2.98	0.49	8.1	542.5	
17.0	14.6	4.32	0.04	3.04	0.49	7.9	539.6	
17.5	15.2	4.34	0.04	3.08	0.48	8.0	541.6	
17.9	15.9	4.34	0.03	3.10	0.48	7.9	538.5	
18.5	16.9	4.32	0.03	3.14	0.47	7.7	542.1	
19.1	18.1	4.27	0.03	3.17	0.47	7.5	544.8	
19.6	19.3	4.22	0.03	3.19	0.46	7.3	543.2	
20.1	20.0	4.16	0.02	3.21	0.46	7.1	541.1	
20.9	20.8	4.08	0.02	3.24	0.45	7.1	534.8	
21.9	21.5	4.01	0.02	3.26	0.44	7.1	535.8	
22.8	21.8	3.91	0.02	3.30	0.44	6.9	542.6	
23.5	22.1	3.81	0.02	3.33	0.43	6.7	538.9	
24.1	22.1	3.71	0.02	3.34	0.42	6.7	546.0	
24.4	22.2	3.60	0.01	3.34	0.42	6.8	555.4	
24.6	22.3	3.50	0.01	3.34	0.41	6.7	549.3	
24.4	22.3	3.40	0.01	3.34	0.41	6.6	539.5	30.0
24.4	22.3	3.31	0.01	3.35	0.40	6.5	539.5	31.2
24.4	22.1	3.21	0.01	3.34	0.40	6.6	539.5	32.4
24.7	22.1	3.11	0.01	3.35	0.38	6.6	539.5	33.7
25.0	22.2	3.02	0.00	3.35	0.37	6.7	539.5	35.0
25.2	22.2	2.92	0.00	3.35	0.36	6.7	539.5	36.3
25.4	22.2	2.83	0.00	3.35	0.34	6.7	539.5	37.7
25.6	22.2	2.74	0.00	3.35	0.33	6.7	539.5	39.2
25.7	22.3	2.65	0.00	3.34	0.32	6.7	539.5	40.6
25.8	22.2	2.56	0.00	3.34	0.31	6.7	539.5	42.0
25.8	22.2	2.48	0.00	3.34	0.30	6.7	539.5	43.5
25.8	22.1	2.40	0.00	3.33	0.29	6.7	539.5	45.1
25.7	22.0	2.32	0.00	3.33	0.28	6.7	539.5	46.8
25.6	21.9	2.24	0.00	3.32	0.27	6.7	539.5	48.4
25.4	21.8	2.16	0.00	3.32	0.26	6.7	539.5	50.0
25.1	21.7	2.08	0.00	3.31	0.25	6.7	539.5	51.6
24.8	21.5	2.01	0.00	3.31	0.24	6.7	539.5	53.2
24.4	21.3	1.94	0.00	3.30	0.23	6.7	539.5	54.8
24.0	21.0	1.87	0.00	3.29	0.22	6.7	539.5	56.4
23.6	20.8	1.80	0.00	3.28	0.22	6.7	539.5	58.0
23.1	20.5	1.74	0.00	3.27	0.21	6.7	539.5	59.5
22.6	20.3	1.68	0.00	3.26	0.20	6.7	539.5	61.1
22.1	20.0	1.61	0.00	3.25	0.19	6.7	539.5	62.6
21.6	19.7	1.56	0.00	3.24	0.19	6.7	539.5	64.2
21.1	19.4	1.50	0.00	3.23	0.18	6.7	539.5	65.7
20.5	19.1	1.44	0.00	3.22	0.17	6.7	539.5	67.2
20.0	18.8	1.39	0.00	3.21	0.17	6.7	539.5	68.7
19.4	18.5	1.34	0.00	3.19	0.16	6.7	539.5	70.2
18.9	18.1	1.29	0.00	3.18	0.16	6.7	539.5	71.7
18.3	17.8	1.24	0.00	3.17	0.15	6.7	539.5	73.2

Year	CFC-11	CFC-12	CFC-113	CFC-114	CFC-115	CCl_4	CH_3CCl_3	HCFC-22
2048	163.5	391.9	52.9	14.6	8.3	43.9	0.4	138.3
2049	161.2	388.2	52.4	14.5	8.2	43.1	0.4	132.1
2050	158.9	384.5	51.9	14.5	8.2	42.2	0.4	126.1
2051	156.6	380.8	51.4	14.4	8.2	41.4	0.4	120.4
2052	154.4	377.2	51.0	14.4	8.2	40.6	0.4	114.8
2053	152.1	373.6	50.5	14.3	8.2	39.9	0.4	109.4
2054	149.8	370.0	50.0	14.3	8.2	39.2	0.4	104.2
2055	147.6	366.5	49.6	14.3	8.2	38.4	0.4	99.3
2056	145.4	363.0	49.1	14.2	8.1	37.8	0.4	94.5
2057	143.2	359.5	48.6	14.2	8.1	37.1	0.4	90.0
2058	141.0	356.0	48.2	14.1	8.1	36.5	0.4	85.7
2059	138.9	352.6	47.7	14.1	8.1	35.8	0.4	81.5
2060	136.7	349.2	47.3	14.0	8.1	35.2	0.4	77.6
2061	134.6	345.9	46.9	14.0	8.1	34.7	0.4	73.9
2062	132.5	342.5	46.4	14.0	8.0	34.1	0.4	70.3
2063	130.4	339.2	46.0	13.9	8.0	33.6	0.4	66.9
2064	128.4	335.9	45.6	13.9	8.0	33.0	0.4	63.7
2065	126.4	332.7	45.2	13.8	8.0	32.5	0.4	60.7
2066	124.3	329.5	44.8	13.8	8.0	32.0	0.4	57.8
2067	122.4	326.3	44.4	13.8	8.0	31.6	0.4	55.1
2068	120.4	323.1	43.9	13.7	8.0	31.1	0.4	52.5
2069	118.4	320.0	43.5	13.7	7.9	30.7	0.4	50.0
2070	116.5	316.9	43.2	13.6	7.9	30.2	0.4	47.7
2071	114.6	313.8	42.8	13.6	7.9	29.8	0.4	45.6
2072	112.8	310.8	42.4	13.6	7.9	29.4	0.4	43.5
2073	110.9	307.7	42.0	13.5	7.9	29.0	0.4	41.6
2074	109.1	304.8	41.6	13.5	7.9	28.6	0.4	39.8
2075	107.3	301.8	41.2	13.4	7.9	28.3	0.4	38.0
2076	105.5	298.9	40.9	13.4	7.8	27.9	0.4	36.4
2077	103.7	296.0	40.5	13.4	7.8	27.6	0.4	34.9
2078	102.0	293.1	40.1	13.3	7.8	27.3	0.4	33.5
2079	100.3	290.2	39.8	13.3	7.8	26.9	0.4	32.1
2080	98.6	287.4	39.4	13.2	7.8	26.6	0.4	30.9
2081	96.9	284.6	39.1	13.2	7.8	26.3	0.4	29.7
2082	95.3	281.8	38.7	13.2	7.8	26.0	0.4	28.5
2083	93.7	279.1	38.4	13.1	7.7	25.8	0.4	27.5
2084	92.1	276.4	38.0	13.1	7.7	25.5	0.4	26.5
2085	90.5	273.7	37.7	13.1	7.7	25.2	0.4	25.6
2086	88.9	271.0	37.4	13.0	7.7	25.0	0.4	24.7
2087	87.4	268.4	37.0	13.0	7.7	24.7	0.4	23.9
2088	85.9	265.8	36.7	12.9	7.7	24.5	0.4	23.2
2089	84.4	263.2	36.4	12.9	7.7	24.3	0.4	22.4
2090	83.0	260.6	36.1	12.9	7.6	24.1	0.4	21.8
2091	81.5	258.1	35.8	12.8	7.6	23.8	0.4	21.1
2092	80.1	255.6	35.4	12.8	7.6	23.6	0.4	20.6
2093	78.7	253.1	35.1	12.8	7.6	23.4	0.4	20.0
2094	77.3	250.6	34.8	12.7	7.6	23.2	0.4	19.5
2095	76.0	248.2	34.5	12.7	7.6	23.1	0.4	19.0

HCFC-141b	HCFC-142b	Halon-1211	Halon-1202	Halon-1301	Halon-2402	CH_3Br	CH_3Cl	HFC-23
17.8	17.5	1.19	0.00	3.16	0.15	6.7	539.5	74.7
17.3	17.2	1.14	0.00	3.14	0.14	6.7	539.5	76.2
16.7	16.8	1.10	0.00	3.13	0.14	6.7	539.5	77.7
16.2	16.5	1.06	0.00	3.11	0.13	6.7	539.5	79.1
15.7	16.2	1.02	0.00	3.10	0.13	6.7	539.5	80.6
15.2	15.9	0.98	0.00	3.08	0.12	6.7	539.5	82.1
14.7	15.6	0.94	0.00	3.07	0.12	6.7	539.5	83.5
14.2	15.2	0.90	0.00	3.05	0.11	6.7	539.5	84.9
13.7	14.9	0.87	0.00	3.04	0.11	6.7	539.5	86.4
13.3	14.6	0.83	0.00	3.02	0.11	6.7	539.5	87.8
12.8	14.3	0.80	0.00	3.01	0.10	6.7	539.5	89.2
12.4	14.0	0.77	0.00	2.99	0.10	6.7	539.5	90.6
12.0	13.7	0.74	0.00	2.97	0.09	6.7	539.5	92.1
11.6	13.4	0.71	0.00	2.96	0.09	6.7	539.5	93.5
11.2	13.1	0.68	0.00	2.94	0.09	6.7	539.5	94.9
10.8	12.9	0.65	0.00	2.92	0.09	6.7	539.5	96.2
10.4	12.6	0.63	0.00	2.91	0.08	6.7	539.5	97.6
10.1	12.3	0.60	0.00	2.89	0.08	6.7	539.5	99.0
9.7	12.1	0.58	0.00	2.87	0.08	6.7	539.5	100.4
9.4	11.8	0.55	0.00	2.85	0.07	6.7	539.5	101.8
9.0	11.6	0.53	0.00	2.84	0.07	6.7	539.5	103.1
8.7	11.3	0.51	0.00	2.82	0.07	6.7	539.5	104.5
8.4	11.1	0.49	0.00	2.80	0.07	6.7	539.5	105.8
8.1	10.8	0.47	0.00	2.78	0.06	6.7	539.5	107.2
7.8	10.6	0.45	0.00	2.76	0.06	6.7	539.5	108.5
7.5	10.4	0.43	0.00	2.75	0.06	6.7	539.5	109.8
7.3	10.2	0.41	0.00	2.73	0.06	6.7	539.5	111.2
7.0	10.0	0.39	0.00	2.71	0.06	6.7	539.5	112.5
6.8	9.8	0.38	0.00	2.69	0.05	6.7	539.5	113.8
6.5	9.6	0.36	0.00	2.67	0.05	6.7	539.5	115.1
6.3	9.4	0.35	0.00	2.65	0.05	6.7	539.5	116.4
6.1	9.2	0.33	0.00	2.63	0.05	6.7	539.5	117.7
5.8	9.0	0.32	0.00	2.61	0.05	6.7	539.5	119.0
5.6	8.8	0.31	0.00	2.60	0.04	6.7	539.5	120.3
5.4	8.7	0.29	0.00	2.58	0.04	6.7	539.5	121.6
5.2	8.5	0.28	0.00	2.56	0.04	6.7	539.5	122.8
5.0	8.3	0.27	0.00	2.54	0.04	6.7	539.5	124.1
4.8	8.2	0.26	0.00	2.52	0.04	6.7	539.5	125.4
4.7	8.0	0.25	0.00	2.50	0.04	6.7	539.5	126.6
4.5	7.9	0.24	0.00	2.48	0.04	6.7	539.5	127.9
4.3	7.7	0.23	0.00	2.46	0.03	6.7	539.5	129.1
4.2	7.6	0.22	0.00	2.44	0.03	6.7	539.5	130.4
4.0	7.5	0.21	0.00	2.43	0.03	6.7	539.5	131.6
3.9	7.3	0.20	0.00	2.41	0.03	6.7	539.5	132.8
3.7	7.2	0.19	0.00	2.39	0.03	6.7	539.5	134.1
3.6	7.1	0.18	0.00	2.37	0.03	6.7	539.5	135.3
3.5	7.0	0.17	0.00	2.35	0.03	6.7	539.5	136.5
3.3	6.9	0.17	0.00	2.33	0.03	6.7	539.5	137.7

Year	CFC-11	CFC-12	CFC-113	CFC-114	CFC-115	CCl_4	CH_3CCl_3	HCFC-22
2096	74.6	245.7	34.2	12.7	7.6	22.9	0.4	18.6
2097	73.3	243.4	33.9	12.6	7.5	22.7	0.4	18.2
2098	72.0	241.0	33.6	12.6	7.5	22.5	0.4	17.8
2099	70.8	238.6	33.3	12.6	7.5	22.4	0.4	17.4
2100	69.5	236.3	33.1	12.5	7.5	22.2	0.4	17.0

HCFC-141b	HCFC-142b	Halon-1211	Halon-1202	Halon-1301	Halon-2402	CH_3Br	CH_3Cl	HFC-23
3.2	6.8	0.16	0.00	2.31	0.03	6.7	539.5	138.9
3.1	6.7	0.15	0.00	2.29	0.03	6.7	539.5	140.1
3.0	6.6	0.15	0.00	2.28	0.02	6.7	539.5	141.3
2.9	6.5	0.14	0.00	2.26	0.02	6.7	539.5	142.5
2.8	6.4	0.13	0.00	2.24	0.02	6.7	539.5	143.7

REFERENCES

An, M., L.M. Western, D. Say, L. Chen, T. Claxton, A.L. Ganesan, R. Hossaini, P.B. Krummel, A.J. Manning, J. Mühle, S. O'Doherty, R.G. Prinn, R.F. Weiss, D. Young, J. Hu, B. Yao, and M. Rigby, Rapid increase in dichloromethane emissions from China inferred through atmospheric observations, ***Nat. Commun.***, *12*(1), 7279, doi:10.1038/s41467-021-27592-y, 2021.

Andersen, S.O., S. Gao, S. Carvalho, T. Ferris, M. Gonzalez, N.J. Sherman, Y. Wei, and D. Zaelke, Narrowing feedstock exemptions under the Montreal Protocol has multiple environmental benefits, ***Proc. Natl. Acad. Sci.***, *118*(49), e2022668118, doi:10.1073/pnas.2022668118, 2021.

Ashford, P., D. Clodic, A. McCulloch, and L. Kuijpers, Emission profiles from the foam and refrigeration sectors comparison with atmospheric concentrations. Part 1: Methodology and data, ***Int. J. Refrig.***, *27*(7), 687-700, doi:10.1016/j.ijrefrig.2004.07.025, 2004.

Boley, A.C., and M. Byers, Satellite mega-constellations create risks in Low Earth Orbit, the atmosphere and on Earth, ***Sci. Rep.***, *11*(1), 10642, doi:10.1038/s41598-021-89909-7, 2021.

Brioude, J., R.W. Portmann, J.S. Daniel, O.R. Cooper, G.J. Frost, K.H. Rosenlof, C. Granier, A.R. Ravishankara, S.A. Montzka, and A. Stohl, Variations in ozone depletion potentials of very short-lived substances with season and emission region, ***Geophys. Res. Lett.***, *37*(19), doi:10.1029/2010GL044856, 2010.

Burkholder, J.B., Ø. Hodnebrog, and V.L. Orkin, Summary of Abundances, Lifetimes, Ozone Depletion Potentials (ODPs), Radiative Efficiencies (REs), Global Warming Potentials (GWPs), and Global Temperature change Potentials (GTPs), Appendix A in ***Scientific Assessment of Ozone Depletion: 2018***, Global Ozone Research and Monitoring Project–Report No. 58, World Meteorological Organization, Geneva, Switzerland, 2018.

Carpenter, L.J., and J.S. Daniel (Lead Authors), E.L. Fleming, T. Hanaoka, J. Hu, A.R. Ravishankara, M.N. Ross, S. Tilmes, T.J. Wallington, and D.J. Wuebbles, Scenarios and Information for Policymakers, Chapter 6 in ***Scientific Assessment of Ozone Depletion: 2018***, Global Ozone Research and Monitoring Project–Report No. 58, World Meteorological Organization, Geneva, Switzerland, 2018.

Chen, D., M. Rojas, B.H. Samset, K. Cobb, A. Diongue Niang, P. Edwards, S. Emori, S.H. Faria, E. Hawkins, P. Hope, P. Huybrechts, M. Meinshausen, S.K. Mustafa, G.-K. Plattner, and A.-M. Tréguier, Framing, Context, and Methods, Chapter 1 in ***Climate Change 2021: The Physical Science Basis. Contribution of Working Group I to the Sixth Assessment Report of the Intergovernmental Panel on Climate Change***, edited by V. Masson-Delmotte, P. Zhai, A. Pirani, S.L. Connors, C. Péan, S. Berger, N. Caud, Y. Chen, L. Goldfarb, M.I. Gomis, M. Huang, K. Leitzell, E. Lonnoy, J.B.R. Matthews, T.K. Maycock, T. Waterfield, O. Yelekçi, R. Yu, and B. Zhou, Cambridge University Press, Cambridge, United Kingdom and New York, NY, USA, 139 pp., doi:10.1017/9781009157896.003, 2021.

Chipperfield, M.P., R. Hossaini, S.A. Montzka, S. Reimann, D. Sherry, and S. Tegtmeier, Renewed and emerging concerns over the production and emission of ozone-depleting substances, ***Nat. Rev. Earth Environ.***, *1*(5), 251-263, doi:10.1038/s43017-020-0048-8, 2020.

Claxton, T., R. Hossaini, O. Wild, M.P. Chipperfield, and C. Wilson, On the Regional and Seasonal Ozone Depletion Potential of Chlorinated Very Short-Lived Substances, ***Geophys. Res. Lett.***, *46*(10), 5489-5498, doi:10.1029/2018GL081455, 2019.

Claxton, T., R. Hossaini, C. Wilson, S.A. Montzka, M.P. Chipperfield, O. Wild, E.M. Bednarz, L.J. Carpenter, S.J. Andrews, S.C. Hackenberg, J. Mühle, D. Oram, S. Park, M.-K. Park, E. Atlas, M. Navarro, S. Schauffler, D. Sherry, M. Vollmer, T. Schuck, A. Engel, P.B. Krummel, M. Maione, J. Arduini, T. Saito, Y. Yokouchi, S. O'Doherty, D. Young, and C. Lunder, A Synthesis Inversion to Constrain Global Emissions of Two Very Short Lived Chlorocarbons: Dichloromethane, and Perchloroethylene, ***J. Geophys. Res.***, *125*(12), e2019JD031818, doi:10.1029/2019JD031818, 2020.

Crutzen, P.J., SST's: A Threat to the Earth's Ozone Shield, ***Ambio***, *1*(2), 41-51, 1972.

Cuevas, C.A., N. Maffezzoli, J.P. Corella, A. Spolaor, P. Vallelonga, H.A. Kjær, M. Simonsen, M. Winstrup, B. Vinther, C. Horvat, R.P. Fernandez, D. Kinnison, J.-F. Lamarque, C. Barbante, and A. Saiz-Lopez, Rapid increase in atmospheric iodine levels in the North Atlantic since the mid-20th century, ***Nat. Comm.***, *9*(1), 1452, doi:10.1038/s41467-018-03756-1, 2018.

Cui, J., J. Guo, Z. Zhai, and J. Zhang, The contribution of fluoropolymer thermolysis to trifluoroacetic acid (TFA) in environmental media, ***Chemosphere***, *222*, 637-644, doi:10.1016/j.chemosphere.2019.01.174, 2019.

Daniel, J.S., S. Solomon, and D.L. Albritton, On the evaluation of halocarbon radiative forcing and global warming potentials, ***J. Geophys. Res.***, *100*(D1), 1271-1285, doi:10.1029/94JD02516, 1995.

Danilin, M.Y., P.J. Popp, R.L. Herman, M.K.W. Ko, M.N. Ross, C.E. Kolb, D.W. Fahey, L.M. Avallone, D.W. Toohey, B.A. Ridley, O. Schmid, J.C. Wilson, D.G. Baumgardner, R.R. Friedl, T.L. Thompson, and J.M. Reeves, Quantifying uptake of HNO_3 and H_2O by alumina particles in Athena-2 rocket plume, ***J. Geophys. Res.***, *108*(D4), doi:10.1029/2002JD002601, 2003.

Danilin, M.Y., R.-L. Shia, M.K.W. Ko, D.K. Weisenstein, N.D. Sze, J.J. Lamb, T.W. Smith, P.D. Lohn, and M.J. Prather, Global stratospheric effects of the alumina emissions by solid-fueled rocket motors, ***J. Geophys. Res.***, *106*(D12), 12727-12738, doi:10.1029/2001JD900022, 2001.

David, L.M., M. Barth, L. Höglund-Isaksson, P. Purohit, G.J.M. Velders, S. Glaser, and A.R. Ravishankara, Trifluoroacetic acid deposition from emissions of HFO-1234yf in India, China and the Middle East, ***Atmos. Chem. Phys.***, *21*, 14833–14849, doi:10.5194/acp-21-14833-2021, 2021.

Dessens, O., G. Zeng, N. Warwick, and J. Pyle, Short-lived bromine compounds in the lower stratosphere; impact of climate change on ozone, ***Atmos. Sci. Lett.***, *10*(3), 201-206, doi:10.1002/asl.236, 2009.

Dupuy, E., H. Akiyoshi, and Y. Yamashita, Impact of Unmitigated HFC Emissions on Stratospheric Ozone at the End of the 21st Century as Simulated by Chemistry-Climate Models, ***J. Geophys. Res.***, *126*(21), e2021JD035307, doi:10.1029/2021JD035307, 2021.

Ebnesajjad, S., Preparation of Tetrafluoroethylene and Other Monomers, In: ***Fluoroplastics (2nd Edition)***, William Andrew Publishing, Oxford, 48–75 pp., 2015.

Ellis, D.A., S.A. Mabury, J.W. Martin, and D.C.G. Muir, Thermolysis of fluoropolymers as a potential source of halogenated organic acids in the environment, ***Nature***, *412*(6844), 321-324, doi:10.1038/35085548, 2001.

Engel, A., H. Bonisch, J. Ostermoller, M.P. Chipperfield, S. Dhomse, and P. Jöckel, A refined method for calculating equivalent effective stratospheric chlorine, ***Atmos. Chem. Phys.***, *18*(2), 601-619, doi:10.5194/acp-18-601-2018, 2017.

Falk, S., B.-M. Sinnhuber, G. Krysztofiak, P. Jocket, P. Graf, and S.T. Lennartz, Brominated VSLS and their influence on ozone under a changing climate, ***Atmos. Chem. Phys.***, *17*(18), 11313-11329, doi:10.5194/acp-2017-11313-2017, 2017.

Fang, X., S. Park, T. Saito, R. Tunnicliffe, A.L. Ganesan, M. Rigby, S. Li, Y. Yokouchi, P.J. Fraser, C.M. Harth, P.B. Krummel, J. Mühle, S. O'Doherty, P.K. Salameh, P.G. Simmonds, R.F. Weiss, D. Young, M.F. Lunt, A.J. Manning, A. Gressent, and R.G. Prinn, Rapid increase in ozone-depleting chloroform emissions from China, ***Nat. Geosci.***, *12*(2), 89-93, doi:10.1038/s41561-018-0278-2, 2019.

Feng, Y., P. Bie, Z. Wang, L. Wang, and J. Zhang, Bottom-up anthropogenic dichloromethane emission estimates from China for the period 2005–2016 and predictions of future emissions, ***Atmos. Environ.***, *186*, 241-247, doi:10.1016/j.atmosenv.2018.05.039, 2018.

Fleming, E.L., P.A. Newman, Q. Liang, J.S. Daniel, The impact of continuing CFC-11 emissions on stratospheric ozone, ***J. Geophys. Res.***, 125(3), e2019JD031849, doi:10.1029/2019JD031849, 2020.

Forster, P., T. Storelvmo, K. Armour, W. Collins, J.-L. Dufresne, D. Frame, D.J. Lunt, T. Mauritsen, M.D. Palmer, M. Watanabe, M. Wild, and H. Zhang, The Earth's Energy Budget, Climate Feedbacks, and Climate Sensitivity, Chapter 7 in ***Climate Change 2021: The Physical Science Basis, Contribution of Working Group I to the Sixth Assessment Report of the Intergovernmental Panel on Climate Change***, edited by V. Masson-Delmotte, P. Zhai, A. Pirani, S.L. Connors, C. Péan, S. Berger, N. Caud, Y. Chen, L. Goldfarb, M.I. Gomis, M. Huang, K. Leitzell, E. Lonnoy, J.B.R.

Matthews, T.K. Maycock, T. Waterfield, O. Yelekçi, R. Yu, and B. Zhou, Cambridge University Press, Cambridge, United Kingdom and New York, NY, USA, 131 pp., doi:10.1017/9781009157896.009, 2021.

Frank, H., E.H. Christoph, O. Holm-Hansen, and J.L. Bullister, Trifluoroacetate in ocean waters, ***Environ. Sci. Technol.***, ***36***(1), 12-15, doi:10.1021/es0101532, 2002.

Freeling, F., D. Behringer, F. Heydel, M. Scheurer, T.A. Ternes, and K. Nödler, Trifluoroacetate in Precipitation: Deriving a Benchmark Data Set, ***Environ. Sci. Technol.***, ***54***(18), 11210-11219, doi:10.1021/acs.est.0c02910, 2020.

Gamlen, P.H., B.C. Lane, P.M. Midgley, and J.M. Steed, The production and release to the atmosphere of CCl_3F and CCl_2F_2 (chlorofluorocarbons CFC 11 and CFC 12), ***Atmos. Environ.***, ***20***(6), 1077-1085, doi:10.1016/0004-6981(86)90139-3, 1986.

Gidden, M.J., K. Riahi, S.J. Smith, S. Fujimori, G. Luderer, E. Kriegler, D.P. van Vuuren, M. van den Berg, L. Feng, D. Klein, K. Calvin, J.C. Doelman, S. Frank, O. Fricko, M. Harmsen, T. Hasegawa, P. Havlik, J. Hilaire, R. Hoesly, J. Horing, A. Popp, E. Stehfest, and K. Takahashi, Global emissions pathways under different socioeconomic scenarios for use in CMIP6: a dataset of harmonized emissions trajectories through the end of the century, ***Geosci. Model Dev.***, ***12***(4), 1443-1475, doi:10.5194/gmd-12-1443-2019, 2019.

Ha, J.-M., D. Kim, J. Kim, B.S. Ahn, Y. Kim, and J.W. Kang, High-temperature hydrodechlorination of ozone-depleting chlorodifluoromethane (HCFC-22) on supported Pd and Ni catalysts, ***J. Environ. Sci. Health A***, ***46***(9), 989-996, doi:10.1080/10934529.2011.586262, 2011.

Harris, N.R.P., and D.J. Wuebbles (Lead Authors), J.S. Daniel, J. Hu, L.J.M. Kuijpers, K.S. Law, M.J. Prather, and R. Schofield, Scenarios and Information for Policymakers, Chapter 5 in ***Scientific Assessment of Ozone Depletion: 2014***, Global Ozone research and Monitoring Project–Report No. 55, World Meteorological Organization, Geneva, Switzerland, 2014.

Henne, S., D.E. Shallcross, S. Reimann, P. Xiao, D. Brunner, S. O'Doherty, and B. Buchmann, Future Emissions and Atmospheric Fate of HFC-1234yf from Mobile Air Conditioners in Europe, ***Environ. Sci. Technol.***, ***46***(3), 1650-1658, doi:10.1021/es2034608, 2012.

Hodnebrog, Ø., B. Aamaas, J.S. Fuglestvedt, G. Marston, G. Myhre, C.J. Nielsen, M. Sandstad, K.P. Shine, and T.J. Wallington, Updated Global Warming Potentials and Radiative Efficiencies of Halocarbons and Other Weak Atmospheric Absorbers, ***Rev. Geophys.***, ***58***(3), e2019RG000691, doi:10.1029/2019RG000691, 2020a.

Hodnebrog, Ø., G. Myhre, R.J. Kramer, K.P. Shine, T. Andrews, G. Faluvegi, M. Kasoar, A. Kirkevåg, J.-F. Lamarque, J. Mülmenstädt, D. Olivié, B.H. Samset, D. Shindell, C.J. Smith, T. Takemura, and A. Voulgarakis, The effect of rapid adjustments to halocarbons and N_2O on radiative forcing, ***NPJ Clim. Atmos. Sci.***, ***3***(1), 43, doi:10.1038/s41612-020-00150-x, 2020b.

Holland, R., M.A.H. Khan, I. Driscoll, R. Chhantyal-Pun, R.G. Derwent, C.A. Taatjes, A.J. Orr-Ewing, C.J. Percival, and D.E. Shallcross, Investigation of the Production of Trifluoroacetic Acid from Two Halocarbons, HFC-134a and HFO-1234yf and Its Fates Using a Global Three-Dimensional Chemical Transport Model, ***ACS Earth Space Chem.***, ***5***(4), 849-857, doi:10.1021/acsearthspacechem.0c00355, 2021.

Hossaini, R., E. Atlas, S.S. Dhomse, M.P. Chipperfield, P.F. Bernath, A.M. Fernando, J. Mühle, A.A. Leeson, S.A. Montzka, W. Feng, J.J. Harrison, P. Krummel, M.K. Vollmer, S. Reimann, S. O'Doherty, D. Young, M. Maione, J. Arduini, and C.R. Lunder, Recent Trends in Stratospheric Chlorine From Very Short-Lived Substances, ***J. Geophys. Res.***, ***124***(4), 2318-2335, doi:10.1029/2018JD029400, 2019.

Hossaini, R., M.P. Chipperfield, S. Dhomse, C. Ordóñez, A. Saiz-Lopez, N.L. Abraham, A. Archibald, P. Braesicke, P. Telford, N. Warwick, X. Yang, and J. Pyle, Modelling future changes to the stratospheric source gas injection of biogenic bromocarbons, ***Geophys. Res. Lett.***, ***39***(20), doi:10.1029/2012GL053401, 2012.

Hossaini, R., M.P. Chipperfield, S.A. Montzka, A.A. Leeson, S.S. Dhomse, and J.A. Pyle, The increasing threat to stratospheric ozone from dichloromethane, ***Nat. Comm.***, ***8***(15962), doi:10.1038/ncomms15962, 2017.

Hossaini, R., H. Mantle, M.P. Chipperfield, S.A. Montzka, P. Hamer, F. Ziska, B. Quack, K. Krüger, S. Tegtmeier, E. Atlas, S. Sala, A. Engel, H. Bönisch, T. Keber, D. Oram, G. Mills, C. Ordóñez, A. Saiz-Lopez, N. Warwick, Q. Liang, W. Feng, F. Moore, B.R. Miller, V. Marécal, N.A.D. Richards, M. Dorf, and K. Pfeilsticker, Evaluating global emission inventories of biogenic bromocarbons, ***Atmos. Chem. Phys.***, ***13***(23), 11819-11838, doi:10.5194/acp-13-11819-2013, 2013.

Hossaini, R., P.K. Patra, A.A. Leeson, G. Krysztofiak, N.L. Abraham, S.J. Andrews, A.T. Archibald, J. Aschmann, E.L. Atlas, D.A. Belikov, H. Bönisch, L.J. Carpenter, S. Dhomse, M. Dorf, A. Engel, W. Feng, S. Fuhlbrügge, P.T. Griffiths, N.R.P. Harris, R. Hommel, T. Keber, K. Krüger, S.T. Lennartz, S. Maksyutov, H. Mantle, G.P. Mills, B. Miller, S.A. Montzka, F. Moore, M.A. Navarro, D.E. Oram, K. Pfeilsticker, J.A. Pyle, B. Quack, A.D. Robinson, E. Saikawa, A. Saiz-Lopez, S. Sala, B.M. Sinnhuber, S. Taguchi, S. Tegtmeier, R.T. Lidster, C. Wilson, and F. Ziska, A multi-model intercomparison of halogenated very short-lived substances (TransCom-VSLS): linking oceanic emissions and tropospheric transport for a reconciled estimate of the stratospheric source gas injection of bromine, ***Atmos. Chem. Phys.***, ***16***(14), 9163-9187, doi:10.5194/acp-16-9163-2016, 2016.

Hurwitz, M.M., E.L. Fleming, P.A. Newman, F. Li, E. Mlawer, K. Cady-Pereira, and R. Bailey, Ozone depletion by hydrofluorocarbons, ***Geophys. Res. Lett.***, ***42***(20), 8686-8692, doi:10.1002/2015GL065856, 2015.

Iglesias-Suarez, F., A. Badia, R.P. Fernandez, C.A. Cuevas, D.E. Kinnison, S. Tilmes, J.-F. Lamarque, M.C. Long, R. Hossaini, and A. Saiz-Lopez, Natural halogens buffer tropospheric ozone in a changing climate, ***Nat. Clim. Change***, ***10***(2), 147-154, doi:10.1038/s41558-019-0675-6, 2020.

IPCC, (Intergovernmental Panel on Climate Change), Chemical Industry Emissions, Chapter 3 in, ***2019 Refinement to the 2006 IPCC Guidelines for National Greenhouse Gas Inventories***, 49th Session of the IPCC, Kyoto, Japan, 2019.

IPCC/TEAP (Intergovernmental Panel on Climate Change, Technology and Economic Assessment Panel), ***Special Report on Safeguarding the Ozone Layer and the Global Climate System: Issues Related to Hydrofluorocarbons and Perfluorocarbons***, 478 pp., Cambridge University Press, Cambridge, United Kingdom, doi:10.13140/2.1.4337.2161, 2005.

Johnston, H.S., D.E. Kinnison, and D.J. Wuebbles, Nitrogen oxides from high-altitude aircraft: An update of potential effects on ozone, ***J. Geophys. Res.***, ***94***(D13), 16351-16363, doi:10.1029/JD094iD13p16351, 1989.

Joudan, S., A.O. De Silva, and C.J. Young, Insufficient evidence for the existence of natural trifluoroacetic acid, ***Environ Sci Process Impacts***, ***23***(11), 1641-1649, doi:10.1039/D1EM00306B, 2021.

Jubb, A.M., M.R. McGillen, R.W. Portmann, J.S. Daniel, and J.B. Burkholder, An atmospheric photochemical source of the persistent greenhouse gas CF_4, ***Geophys. Res. Lett.***, ***42***(21), 9505-9511, doi:10.1002/2015GL06619, 2015.

Keng, F.S.-L., S.-M. Phang, N. Abd Rahman, E.C. Leedham Elvidge, G. Malin, and W.T. Sturges, The emission of volatile halocarbons by seaweeds and their response towards environmental changes, ***J. Appl. Phycol.***, ***32***(2), 1377-1394, doi:10.1007/s10811-019-02026-x, 2020.

Langematz, U., M. Tully, N. Calvo, M. Dameris, A.T.J. de Laat, A. Klekociuk, R. Müller, and P. Young, Polar Stratospheric Ozone: Past, Present, and Future, Chapter 4 in Scientific Assessment of Ozone Depletion: 2018, In Global Ozone Research and Monitoring Project–Report No. 58. Geneva, Switzerland, World Meteorological Organization, 2018.

Larson, E.J.L., R.W. Portmann, K.H. Rosenlof, D.W. Fahey, J.S. Daniel, and M.N. Ross, Global atmospheric response to emissions from a proposed reusable space launch system, ***Earths Future***, ***5***(1), 37-48, doi:10.1002/2016EF000399, 2017.

Lee, W.R., D.G. MacMartin, D. Visioni, and B. Kravitz, High-Latitude Stratospheric Aerosol Geoengineering Can Be More Effective if Injection Is Limited to Spring, ***Geophys. Res. Lett.***, ***48***(9), e2021GL092696, doi:10.1029/2021GL092696, 2021.

Legrand, M., J.R. McConnell, S. Preunkert, M. Arienzo, N. Chellman, K. Gleason, T. Sherwen, M.J. Evans, and L.J. Carpenter, Alpine ice evidence of a three-fold increase in atmospheric iodine deposition since 1950 in Europe due to increasing oceanic emissions, ***Proc. Natl. Acad. Sci.***, ***115***(48), 12136-12141, doi:10.1073/pnas.1809867115, 2018.

Lickley, M., S. Fletcher, M. Rigby, and S. Solomon, Joint inference of CFC lifetimes and banks suggests previously unidentified emissions, ***Nat. Comm.***, ***12***(1), 2920, doi:10.1038/s41467-021-23229-2, 2021.

Lickley, M., S. Solomon, S. Fletcher, G.J.M. Velders, J. Daniel, M. Rigby, S.A. Montzka, L.J.M. Kuijpers, and K. Stone, Quantifying contributions of chlorofluorocarbon banks to emissions and impacts on the ozone layer and climate, ***Nat. Comm.***, ***11***(1), 1380, doi:10.1038/s41467-020-15162-7, 2020.

Lickley, M., J.S. Daniel, E.L. Fleming, S. Reimann, and S. Solomon, Bayesian assessment of chlorofluorocarbon (CFC), hydrochlorofluorocarbon (HCFC) and halon banks suggest large reservoirs still present in old equipment, ***Atmos. Chem. Phys.***, ***22***, 11125–11136, doi: 10.5194/acp-22-11125-2022, 2022.

Maas, J., S. Tegtmeier, Y. Jia, B. Quack, J.V. Durgadoo, and A. Biastoch, Simulations of anthropogenic bromoform indicate high emissions at the coast of East Asia, ***Atmos. Chem. Phys.***, ***21***(5), 4103–4121, doi:10.5194/acp-21-4103-2021, 2021.

Maloney, C.M., R.W. Portmann, M.N. Ross, and K.H. Rosenlof, The Climate and

Ozone Impacts of Black Carbon Emissions From Global Rocket Launches, *J. Geophys. Res., 127*(12), e2021JD036373, doi:10.1029/2021JD036373, 2022.

McCulloch, A., Chloroform in the environment: occurrence, sources, sinks and effects, *Chemosphere*, *50*(10), 1291-1308, doi: 10.1016/S0045-6535(02)00697-5, 2003.

McCulloch, A., and A.A. Lindley, Global emissions of HFC-23 estimated to year 2015, *Atmos. Environ., 41*(7), 1560-1566, doi:10.1016/j.atmosenv.2006.02.021, 2007.

Meinshausen, M., Z.R.J. Nicholls, J. Lewis, M.J. Gidden, E. Vogel, M. Freund, U. Beyerle, C. Gessner, A. Nauels, N. Bauer, J.G. Canadell, J.S. Daniel, A. John, P.B. Krummel, G. Luderer, N. Meinshausen, S.A. Montzka, P.J. Rayner, S. Reimann, S.J. Smith, M. van den Berg, G.J.M. Velders, M.K. Vollmer, and R.H.J. Wang, The shared socio-economic pathway (SSP) greenhouse gas concentrations and their extensions to 2500, *Geosci. Model Dev.*, *13*(8), 3571-3605, doi:10.5194/gmd-13-3571-2020, 2020.

Midgley, P.M., and D.A. Fisher, The production and release to the atmosphere of chlorodifluoromethane (HCFC 22), *Atmos. Environ.*, *27*(14), 2215-2223, doi:10.1016/0960-1686(93)90051-Y, 1993.

Miraux, L., Environmental limits to the space sector's growth, *Sci. Tot. Environ.*, *806*, 150862, doi:10.1016/j.scitotenv.2021.150862, 2022.

Montzka, S.A., G.S. Dutton, R.W. Portmann, M.P. Chipperfield, S. Davis, W. Feng, A.J. Manning, E. Ray, M. Rigby, B.D. Hall, C. Siso, J.D. Nance, P.B. Krummel, J. Mühle, D. Young, S. O'Doherty, P.K. Salameh, C.M. Harth, R.G. Prinn, R.F. Weiss, J.W. Elkins, H. Walter-Terrinoni, and C. Theodoridi, A decline in global CFC-11 emissions during 2018–2019, *Nature*, *590*(7846), 428-432, doi:10.1038/s41586-021-03260-5, 2021.

Montzka, S.A., G.S. Dutton, P. Yu, E. Ray, R.W. Portmann, J.S. Daniel, L. Kuijpers, B.D. Hall, D. Mondeel, C. Siso, J.D. Nance, M. Rigby, A.J. Manning, L. Hu, F. Moore, B.R. Miller, and J.W. Elkins, An unexpected and persistent increase in global emissions of ozone-depleting CFC-11, *Nature*, *557*(7705), 413-417, doi:10.1038/s41586-018-0106-2, 2018.

Montzka, S.A., S. Reimann, (Coordinating Lead Authors) A. Engel, K. Krüger, S. O`Doherty, W.T. Sturges, D. Blake, M. Dorf, P. Fraser, L. Froidevaux, K. Jucks, K. Kreher, M.J. Kurylo, A. Mellouki, J. Miller, O.-J. Nielsen, V.L. Orkin, R.G. Prinn, R. Rhew, M.L. Santee, A. Stohl, and D. Verdonik, Ozone-Depleting Substances (ODSs) and Related Chemicals, Chapter 1 in *Scientific Assessment of Ozone Depletion: 2010*, Global Ozone Research and Monitoring Project–Report No. 52, World Meteorological Organization, Geneva, Switzerland, 2011.

Montzka, S.A., and G.J.M. Velders (Lead Authors), P.B. Krummel, J. Mühle, V.L. Orkin, S. Park, N. Shah, H. Walter-Terrinoni, P. Bernath, C. Boone, L. Hu, M.J. Kurylo, E.L. Elvidge, M. Maione, B.R. Miller, S. O'Doherty, M. Rigby, I.J. Simpson, M.K. Vollmer, R.F. Weiss, L.J.M. Kuijpers, and W.T. Sturges, Hydrofluorocarbons (HFCs), Chapter 2 in *Scientific Assessment of Ozone Depletion: 2018*, Global Ozone Research and Monitoring Project–Report No. 58, World Meteorological Organization, Geneva, Switzerland, 2018.

Morgenstern, O., F.M. O'Connor, B.T. Johnson, G. Zeng, J.P. Mulcahy, J. Williams, J. Teixeira, M. Michou, P. Nabat, L.W. Horowitz, V. Naik, L.T. Sentman, M. Deushi, S.E. Bauer, K. Tsigaridis, D.T. Shindell, and D.E. Kinnison, Reappraisal of the Climate Impacts of Ozone-Depleting Substances, *Geophys. Res. Lett.*, *47*(20), e2020GL088295, doi:10.1029/2020GL088295, 2020.

Mühle, J., L.J.M. Kuijpers, K.M. Stanley, M. Rigby, L.M. Western, J. Kim, S. Park, C.M. Harth, P.B. Krummel, P.J. Fraser, S. O'Doherty, P.K. Salameh, R. Schmidt, D. Young, R.G. Prinn, R.H.J. Wang, and R.F. Weiss, Global emissions of perfluorocyclobutane (PFC-318, c-C4F8) resulting from the use of hydrochlorofluorocarbon-22 (HCFC-22) feedstock to produce polytetrafluoroethylene (PTFE) and related fluorochemicals, *Atmos. Chem. Phys., 22*(5), 3371-3378, doi:10.5194/acp-22-3371-2022, 2022.

Neale, R.E., P.W. Barnes, T.M. Robson, P.J. Neale, C.E. Williamson, R.G. Zepp, S.R. Wilson, S. Madronich, A.L. Andrady, A.M. Heikkilä, G.H. Bernhard, A.F. Bais, P.J. Aucamp, A.T. Banaszak, J.F. Bornman, L.S. Bruckman, S.N. Byrne, B. Foereid, D.P. Häder, L.M. Hollestein, W.C. Hou, S. Hylander, M.A.K. Jansen, A.R. Klekociuk, J.B. Liley, J. Longstreth, R.M. Lucas, J. Martinez-Abaigar, K. McNeill, C.M. Olsen, K.K. Pandey, L.E. Rhodes, S.A. Robinson, K.C. Rose, T. Schikowski, K.R. Solomon, B. Sulzberger, J.E. Ukpebor, Q.W. Wang, S.Å. Wängberg, C.C. White, S. Yazar, A.R. Young, P.J. Young, L. Zhu, and M. Zhu, Environmental effects of stratospheric ozone depletion, UV radiation, and interactions with climate change: UNEP Environmental Effects Assessment Panel, Update 2020, *Photochem. Photobiol. Sci.*, *20*(1), 1-67, doi:10.1007/s43630-020-00001-x, 2021.

Newman, P.A., J.S. Daniel, D.W. Waugh, and E.R. Nash, A new formulation of equivalent effective stratospheric chlorine (EESC), *Atmos. Chem. Phys., 7*(17), 4537-4552, doi:10.5194/acp-7-4537-2007, 2007.

O'Connor, F.M., N.L. Abraham, M. Dalvi, G.A. Folberth, P.T. Griffiths, C. Hardacre, B.T. Johnson, R. Kahana, J. Keeble, B. Kim, O. Morgenstern, J.P. Mulcahy, M. Richardson, E. Robertson, J. Seo, S. Shim, J.C. Teixeira, S.T. Turnock, J. Williams, A.J. Wiltshire, S. Woodward, and G. Zeng, Assessment of pre-industrial to present-day anthropogenic climate forcing in UKESM1, *Atmos. Chem. Phys.*, *21*(2), 12111243, doi:10.5194/acp-21-1211-2021, 2021.

Ohneiser, K., A. Ansmann, A. Chudnovsky, R. Engelmann, C. Ritter, I. Veselovskii, H. Baars, H. Gebauer, H. Griesche, M. Radenz, J. Hofer, D. Althausen, S. Dahlke, and M. Maturilli, The unexpected smoke layer in the High Arctic winter stratosphere during MOSAiC 2019–2020, *Atmos. Chem. Phys.*, *21*(20), 15783-15808, doi:10.5194/acp-21-15783-2021, 2021.

Oram, D.E., M.J. Ashfold, J.C. Laube, L.J. Gooch, S. Humphrey, W.T. Sturges, E. Leedham-Elvidge, G.L. Forster, N.R.P. Harris, M.I. Mead, A.A. Samah, S.M. Phang, C.F. Ou-Yang, N.H. Lin, J.L. Wang, A.K. Baker, C.A.M. Brenninkmeijer, and D. Sherry, A growing threat to the ozone layer from short-lived anthropogenic chlorocarbons, *Atmos. Chem. Phys., 17*(19), 11929-11941, doi:10.5194/acp-17-11929-2017, 2017.

Paulot, F., D. Paynter, V. Naik, S. Malyshev, R. Menzel, and L.W. Horowitz, Global modeling of hydrogen using GFDL-AM4.1: Sensitivity of soil removal and radiative forcing, *Int. J. Hydrog. Energy*, *46*(24), 13446-13460, doi:10.1016/j.ijhydene.2021.01.088, 2021.

Pisso, I., P.H. Haynes, and K.S. Law, Emission location dependent ozone depletion potentials for very short-lived halogenated species, *Atmos. Chem. Phys., 10*(24), 12025-12036, doi:10.5194/acp-10-12025-2010, 2010.

Qian, S., D. Nasuta, A. Rhoads, Y. Wang, Y. Geng, Y. Hwang, R. Radermacher, and I. Takeuchi, Not-in-kind cooling technologies: A quantitative comparison of refrigerants and system performance, *Int. J. Refrig., 62*, 177-192, doi:10.1016/j.ijrefrig.2015.10.019, 2016.

Quack, B., and D.W.R. Wallace, Air-sea flux of bromoform: Controls, rates, and implications, *Global Biogeochem. Cycles*, *17*(1), doi:10.1029/2002GB001890, 2003.

Rieger, L.A., W.J. Randel, A.E. Bourassa, and S. Solomon, Stratospheric Temperature and Ozone Anomalies Associated With the 2020 Australian New Year Fires, *Geophys. Res. Lett., 48*(24), e2021GL095898, doi:10.1029/2021GL095898, 2021.

Rigby, M., S. Park, T. Saito, L.M. Western, A.L. Redington, X. Fang, S. Henne, A.J. Manning, R.G. Prinn, G.S. Dutton, P.J. Fraser, A.L. Ganesan, B.D. Hall, C.M. Harth, J. Kim, K.R. Kim, P.B. Krummel, T. Lee, S. Li, Q. Liang, M.F. Lunt, S.A. Montzka, J. Mühle, S. O'Doherty, M.K. Park, S. Reimann, P.K. Salameh, P. Simmonds, R.L. Tunnicliffe, R.F. Weiss, Y. Yokouchi, and D. Young, Increase in CFC-11 emissions from eastern China based on atmospheric observations, *Nature*, *569*(7757), 546-550, doi:10.1038/s41586-019-1193-4, 2019.

Rogelj, J., A. Popp, K.V. Calvin, G. Luderer, J. Emmerling, D. Gernaat, S. Fujimori, J. Strefler, T. Hasegawa, G. Marangoni, V. Krey, E. Kriegler, K. Riahi, D.P. van Vuuren, J. Doelman, L. Drouet, J. Edmonds, O. Fricko, M. Harmsen, P. Havlík, F. Humpenöder, E. Stehfest, and M. Tavoni, Scenarios towards limiting global mean temperature increase below 1.5 °C, *Nat. Clim. Change*, *8*(4), 325-332, doi:10.1038/s41558-018-0091-3, 2018.

Ross, M.N., M.Y. Danilin, D.K. Weisenstein, and M.K.W. Ko, Ozone depletion caused by NO and H2O emissions from hydrazine-fueled rockets, *J. Geophys. Res., 109*(D21), doi:10.1029/2003JD004370, 2004.

Ross, M.N., and K.L. Jones, Implications of a growing spaceflight industry: Climate change, *J. Space Saf. Eng.*, doi:10.1016/j.jsse.2022.04.004, 2022.

Ryan, R.G., E.A. Marais, C.J. Balhatchet, and S.D. Eastham, Impact of Rocket Launch and Space Debris Air Pollutant Emissions on Stratospheric Ozone and Global Climate, *Earths Future*, *10*(6), e2021EF002612, doi:https://doi.org/10.1029/2021EF002612, 2022.

Say, D., A.L. Ganesan, M.F. Lunt, M. Rigby, S. O'Doherty, C. Harth, A.J. Manning, P.B. Krummel, and S. Bauguitte, Emissions of halocarbons from India inferred through atmospheric measurements, *Atmos. Chem. Phys.*, *19*(15), 9865-9885, doi:10.5194/acp-19-9865-2019, 2019.

Schoenenberger, F., M.K. Vollmer, M. Rigby, M. Hill, P.J. Fraser, P.B. Krummel, R.L. Langenfelds, T.S. Rhee, T. Peter, and S. Reimann, First observations, trends, and emissions of HCFC-31 (CH2ClF) in the global atmosphere, *Geophys. Res. Lett., 42*(18), 7817-7824, doi:10.1002/2015GL064709, 2015.

Scott, B.F., R.W. Macdonald, K. Kannan, A. Fisk, A. Witter, N. Yamashita, L. Durham, C. Spencer, and D.C.G. Muir, Trifluoroacetate Profiles in the Arctic, Atlantic,

and Pacific Oceans, ***Environ. Sci. Technol.***, ***39***(17), 6555-6560, doi:10.1021/es047975u, 2005.

Sherry, D., A. McCulloch, Q. Liang, S. Reimann, and P.A. Newman, Current sources of carbon tetrachloride (CCl_4) in our atmosphere, ***Environ. Res. Lett.***, ***13***(2), 024004, doi:10.1088/1748-9326/aa9c87, 2018.

Simmonds, P.G., M. Rigby, A. McCulloch, M.K. Vollmer, S. Henne, J. Mühle, S. O'Doherty, A.J. Manning, P.B. Krummel, P.J. Fraser, D. Young, R.F. Weiss, P.K. Salameh, C.M. Harth, S. Reimann, C.M. Trudinger, L.P. Steele, R.H.J. Wang, D.J. Ivy, R.G. Prinn, B. Mitrevski, and D.M. Etheridge, Recent increases in the atmospheric growth rate and emissions of HFC-23 (CHF_3) and the link to HCFC-22 ($CHClF_2$) production, ***Atmos. Chem. Phys.***, ***18***(6), 4153-4169, doi:10.5194/acp-18-4153-2018, 2018.

Solomon, K.R., G.J.M. Velders, S.R. Wilson, S. Madronich, J. Longstreth, P.J. Aucamp, and J.F. Bornman, Sources, fates, toxicity, and risks of trifluoroacetic acid and its salts: Relevance to substances regulated under the Montreal and Kyoto Protocols, ***J. Toxicol. Environ. Health B***, ***19***(7), 289-304, doi:10.1080/10937404.2016.1175981, 2016.

Solomon, S., K. Dube, K. Stone, P. Yu, D. Kinnison, O.B. Toon, S.E. Strahan, K.H. Rosenlof, R. Portmann, S. Davis, W. Randel, P. Bernath, C. Boone, C.G. Bardeen, A. Bourassa, D. Zawada, and D. Degenstein, On the stratospheric chemistry of midlatitude wildfire smoke, ***Proc. Natl. Acad. Sci.***, ***119***(10), e2117325119, doi:10.1073/pnas.2117325119, 2022.

SPARC (Stratosphere-troposphere Processes And their Role in Climate), ***SPARC Report on the Lifetimes of Stratospheric Ozone-Depleting Substances, Their Replacements, and Related Species***, edited by M.K.W. Ko, P.A. Newman, S. Reimann, and S.E. Strahan, SPARC Report No. 6, WCRP-15/2013, [available at: https://www.sparc-climate.org/fileadmin/customer/6_Publications/SPARC_reports_PDF/6_SPARC_LifetimeReport_Web.pdf], 2013.

SPARC (Stratosphere-troposphere Processes And their Role in Climate), ***SPARC Report on the Mystery of Carbon Tetrachloride***, edited by Q. Liang, P.A. Newman, and S. Reimann, SPARC Report No. 7, WCRP-13/2016, [available at: https://www.wcrp-climate.org/WCRP-publications/2016/SPARC_Report7_2016.pdf], 2016.

Stanley, K.M., D. Say, J. Mühle, C.M. Harth, P.B. Krummel, D. Young, S.J. O'Doherty, P.K. Salameh, P.G. Simmonds, R.F. Weiss, R.G. Prinn, P.J. Fraser, and M. Rigby, Increase in global emissions of HFC-23 despite near-total expected reductions, ***Nat. Comm.***, ***11***(1), 397, doi:10.1038/s41467-019-13899-4, 2020.

Sung, D.J., D.J. Moon, J. Kim, S. Moon, and S.-I. Hong, Production of TFE by catalytic pyrolysis of chloro-difluoromethane (CHC1F2), ***Stud. Surf. Sci. Catal.***, ***159***, 233–236, doi:10.1016/S0167-2991(06)81576-4, 2006.

Szopa, S., V. Naik, B. Adhikary, P. Artaxo, T. Berntsen, W.D. Collins, S. Fuzzi, L. Gallardo, A. Kiendler-Scharr, Z. Klimont, H. Liao, N. Unger, and P. Zanis, Short-Lived Climate Forcers. In Climate Change 2021: The Physical Science Basis. Contribution of Working Group I to the Sixth Assessment Report of the Intergovernmental Panel on Climate Change [Masson-Delmotte, V., P. Zhai, A. Pirani, S.L. Connors, C. Péan, S. Berger, N. Caud, Y. Chen, L. Goldfarb, M.I. Gomis, M. Huang, K. Leitzell, E. Lonnoy, J.B.R. Matthews, T.K. Maycock, T. Waterfield, O. Yelekçi, R. Yu, and B. Zhou (eds.)]. Cambridge University Press, Cambridge, United Kingdom and New York, NY, USA, pp. 817–922, doi:10.1017/9781009157896.008, 2021.

TEAP (Technology and Economic Assessment Panel), ***Decision XXIX/4 TEAP Task Force Report on destruction technologies for controlled substances - Addendum to the May 2018 Supplemental Report,*** United Nations Environment Programme, Vol. 1, ISBN: 978-9966-076-44-1, Nairobi, Kenya, [available at: https://ozone.unep.org/science/assessment/teap], 2018a.

TEAP (Technology and Economic Assessment Panel), ***2018 Report of the Refrigeration, Air Conditioning and Heat Pumps Technical Options Committee***, United Nations Environment Programme, ISBN: 978-9966-076-58-8, Nairobi, Kenya, [available at: https://ozone.unep.org/sites/default/files/2019-04/RTOC-assessment-report-2018_0.pdf], 2018b.

TEAP (Technology and Economic Assessment Panel), ***Report of the Halons Technical Options Committee December 2018***, United Nations Environment Programme, Vol. 1, ISBN: 978-9966-076-48-9, Nairobi, Kenya, [available at: https://ozone.unep.org/sites/default/files/assessment_panels/HTOC_assessment_2018.pdf], 2018c.

TEAP (Technology and Economic Assessment Panel), ***Report of the Technology and Economic Assessment Panel: Progress Report***, United Nations Environment Programme, Vol. 1, ISBN: 978-9966-076-83-0, Nairobi, Kenya, [available at: https://ozone.unep.org/sites/default/files/2020-06/TEAP-Progress-report-and-response-decXXXI-8-may2020_0.pdf], 2020.

TEAP (Technology and Economic Assessment Panel), ***Evaluation of 2021 Critical Use Nominations for Methyl Bromide and Related Issues: Final Report***, United Nations Environment Programme, Vol. 5, ISBN: 978-9966-076-92-2, Nairobi, Kenya, [available at: https://ozone.unep.org/system/files/documents/TEAP-CUN-final-report-september-2021.pdf], 2021a.

TEAP (Technology and Economic Assessment Panel), ***Decision XXXI/3 TEAP Task Force Report on Unexpected Emissions of Trichlorofluoromethane (CFC-11)***, United Nations Environment Programme, Vol. 3, ISBN: 978-9966-076-89-2, Nairobi, Kenya, [available at: https://ozone.unep.org/system/files/documents/Final_TEAP-DecisionXXXI-3-TF-Unexpected-Emissions-of-CFC-11-may2021.pdf], 2021b.

TEAP (Technology and Economic Assessment Panel), ***Report of the Refrigeration Technical Options Committee Vaccines Cold Chain Subcommittee***, Addendum to the TEAP 2021 Progress Report, United Nations Environment Programme, ISBN: 978-9966-076-90-8, Nairobi, Kenya, [available at: https://ozone.unep.org/system/files/documents/TEAP-RTOC-technical-note-vaccines-cold-chain.pdf], 2021c.

Thornhill, G.D., W.J. Collins, R.J. Kramer, D. Olivié, R.B. Skeie, F.M. O'Connor, N.L. Abraham, R. Checa-Garcia, S.E. Bauer, M. Deushi, L.K. Emmons, P.M. Forster, L.W. Horowitz, B. Johnson, J. Keeble, J.F. Lamarque, M. Michou, M.J. Mills, J.P. Mulcahy, G. Myhre, P. Nabat, V. Naik, N. Oshima, M. Schulz, C.J. Smith, T. Takemura, S. Tilmes, T. Wu, G. Zeng, and J. Zhang, Effective radiative forcing from emissions of reactive gases and aerosols – a multi-model comparison, ***Atmos. Chem. Phys.***, ***21***(2), 853-874, doi:10.5194/acp-21-853-2021, 2021.

Tromp, T.K., R.-L. Shia, M. Allen, J.M. Eiler, and Y.L. Yung, Potential Environmental Impact of a Hydrogen Economy on the Stratosphere, ***Science***, ***300***(5626), 1740-1742, doi:10.1126/science.1085169, 2003.

UNEP (United Nations Environment Programme), ***Assessment of Alternatives to HCFCs and HFCs and Update of the TEAP 2005 Supplement Report Data***, Report of the UNEP Technology and Economic Assessment Panel, Task Force Decision XX/8 Report, 129 pp, Nairobi, Kenya, [available at: https://ozone.unep.org/system/files/documents/teap-may-2009-decisionXX-8-task-force-report.pdf], 2009.

UNEP (United Nations Environment Programme), ***Amendment to the Montreal Protocol on Substances that Deplete the Ozone Layer***, United Nations Environment Programme, Kigali, Rwanda, [available at: https://treaties.un.org/Pages/ViewDetails.aspx?src=IND&mtdsg_no=XXVII-2-f&chapter=27&clang=_en], 2016.

UNEP, Production and consumption of ozone depleting substances under the Montreal Protocol, Nairobi, Kenya, http://ozone.unep.org/en/data-reporting/data-centre, (United Nations Environment Programme), 2020.

UNEP (United Nations Environment Programme), ***Report of the Technology and Economic Assessment Panel: Progress Report***, United Nations Environment Programme, Vol. 1, 127 pp., ISBN: 978-9966-076-91-5, Nairobi, Kenya, [available at: https://ozone.unep.org/system/files/documents/TEAP-2021-Progress-report.pdf], 2021.

van Ruijven, B., J.-F. Lamarque, D.P. van Vuuren, T. Kram, and H. Eerens, Emission scenarios for a global hydrogen economy and the consequences for global air pollution, ***Glob. Environ. Change***, ***21***(3), 983-994, doi:10.1016/j.gloenvcha.2011.03.013, 2011.

Velders, G.J.M., and J.S. Daniel, Uncertainty analysis of projections of ozone-depleting substances: Mixing ratios, EESC, ODPs, and GWPs, ***Atmos. Chem. Phys.***, ***14***(6), 2757-2776, doi:10.5194/acp-14-2757-2014, 2014.

Velders, G.J.M., J.S. Daniel, S.A. Montzka, I. Vimont, M. Rigby, P.B. Krummel, J. Muhle, S. O'Doherty, R.G. Prinn, R.F. Weiss, and D. Young, Projections of hydrofluorocarbon (HFC) emissions and the resulting global warming based on recent trends in observed abundances and current policies, ***Atmos. Chem. Phys.***, ***22***(9), 6087-6101, doi:10.5194/acp-22-6087-2022, 2022.

Vogel, B., T. Feck, and J.-U. Grooß, Impact of stratospheric water vapor enhancements caused by CH_4 and H_2O increase on polar ozone loss, ***J. Geophys. Res.***, ***116***(D5), doi:10.1029/2010JD014234, 2011.

Voigt, C., U. Schumann, K. Graf, and K.-D. Gottschaldt, Impact of rocket exhaust plumes on atmospheric composition and climate, Progres in Propulsion Physics, ***4***, 657-670, doi:10.1051/eucass/201304657, 2013.

Vollmer, M.K., J. Mühle, S. Henne, D. Young, M. Rigby, B. Mitrevski, S. Park, C.R. Lunder, T.S. Rhee, C.M. Harth, M. Hill, R.L. Langenfelds, M. Guillevic, P.M. Schlauri, O. Hermansen, J. Arduini, R.H.J. Wang, P.K. Salameh, M. Maione, P.B. Krummel, S. Reimann, S. O'Doherty, P.G. Simmonds, P.J. Fraser, R.G. Prinn, R.F. Weiss, and L.P. Steele, Unexpected nascent atmospheric emissions of three ozone-depleting hydrochlorofluorocarbons, ***Proc. Natl. Acad. Sci.***, ***118***(5), e2010914118, doi:10.1073/pnas.2010914118, 2021.

Vollmer, M.K., D. Young, C.M. Trudinger, J. Mühle, S. Henne, M. Rigby, S. Park, S.

Li, M. Guillevic, B. Mitrevski, C.M. Harth, B.R. Miller, S. Reimann, B. Yao, L.P. Steele, S.A. Wyss, C.R. Lunder, J. Arduini, A. McCulloch, S. Wu, T.S. Rhee, R.H.J. Wang, P.K. Salameh, O. Hermansen, M. Hill, R.L. Langenfelds, D. Ivy, S. O'Doherty, P.B. Krummel, M. Maione, D.M. Etheridge, L. Zhou, P.J. Fraser, R.G. Prinn, R.F. Weiss, and P.G. Simmonds, Atmospheric histories and emissions of chlorofluorocarbons CFC-13 ($CClF_3$), ΣCFC-114 (C_2Cl2F_4), and CFC-115 (C_2ClF_5), ***Atmos. Chem. Phys.***, ***18***(2), 979-1002, doi:10.5194/acp-18-979-2018, 2018.

Wallington, T.J., W.F. Schneider, D.R. Worsnop, O.J. Nielsen, J. Sehested, W. DeBruyn, and J.A. Shorter, Atmospheric chemistry and environmental impact of CFC replacements: HFCs and HCFCs, ***Environ. Sci. Technol.***, ***28***(7), 320A-326A, doi:10.1021/es00056a002, 1994.

Wang, D., W. Jia, S.C. Olsen, D.J. Wuebbles, M.K. Dubey, and A.A. Rockett, Impact of a future H_2 based road transportation sector on the composition and chemistry of the atmosphere; Part 2: Stratospheric ozone, ***Atmos. Chem. Phys., 13***(13), 6139-6150, doi:10.5194/acp-13-6139-2013, 2013.

Wang, Z., Y. Wang, J. Li, S. Henne, B. Zhang, J. Hu, and J. Zhang, Impacts of the Degradation of 2,3,3,3-Tetrafluoropropene into Trifluoroacetic Acid from Its Application in Automobile Air Conditioners in China, the United States, and Europe, ***Environ. Sci. Technol., 52***(5), 2819-2826, doi:10.1021/acs.est.7b05960, 2018.

Warwick, N.J., S. Bekki, E.G. Nisbet, and J.A. Pyle, Impact of a hydrogen economy on the stratosphere and troposphere studied in a 2-D model, ***Geophys. Res. Lett., 31***(5), doi:10.1029/2003GL019224, 2004.

Weisenstein, D.K., D.W. Keith, and J.A. Dykema, Solar geoengineering using solid aerosol in the stratosphere, ***Atmos. Chem. Phys.***, ***15***(20), 11835-11859, doi:10.5194/acp-15-11835-2015, 2015.

WMO (World Meteorological Organization), Scientific Assessment of Ozone Depletion: 2010, Global Ozone Research and Monitoring Project–Report No. 52, 516 pp., Geneva, Switzerland, 2011.

WMO (World Meteorological Organization), Scientific Assessment of Ozone Depletion: 2014, Global Ozone Research and Monitoring Project–Report No. 55, 416 pp., Geneva, Switzerland, 2014.

WMO (World Meteorological Organization), Scientific Assessment of Ozone Depletion: 2018, Global Ozone Research and Monitoring Project–Report No. 58, 588 pp., Geneva, Switzerland, 2018.

WMO (World Meteorological Organization), Report on the Unexpected Emissions of CFC-11, Ozone Re-search and Monitoring, WMO-No. 1268, 84 pp., Geneva, Switzerland, 2021.

Yokouchi, Y., Y. Nojiri, D. Toom-Sauntry, P. Fraser, Y. Inuzuka, H. Tanimoto, H. Nara, R. Murakami, and H. Mukai, Long-term variation of atmospheric methyl iodide and its link to global environmental change, ***Geophys. Res. Lett., 39***(23), doi:10.1029/2012GL053695, 2012.

Youn, D., K.O. Patten, D.J. Wuebbles, H. Lee, and C.W. So, Potential impact of iodinated replacement compounds CF_3I and CH_3I on atmospheric ozone: a three-dimensional modeling study, ***Atmos. Chem. Phys.***, ***10***(20), 10129-10144, doi:10.5194/acp-10-10129-2010, 2010.

Zeng, L., J. Dang, H. Guo, X. Lyu, I.J. Simpson, S. Meinardi, Y. Wang, L. Zhang, and D.R. Blake, Long-term temporal variations and source changes of halocarbons in the Greater Pearl River Delta region, China, ***Atmos. Environ.***, ***234***, 117550, doi:10.1016/j.atmosenv.2020.117550, 2020.

Zhang, J., D.J. Wuebbles, D.E. Kinnison, and A. Saiz-Lopez, Revising the Ozone Depletion Potentials Metric for Short-Lived Chemicals Such as CF_3I and CH_3I, ***J. Geophys. Res.***, ***125***(9), e2020JD032414, doi:10.1029/2020JD032414, 2020.

Ziska, F., B. Quack, S. Tegtmeier, I. Stemmler, and K. Krüger, Future emissions of marine halogenated very-short lived substances under climate change, ***J. of Atmos. Chem., 74***(2), 245-260, doi:10.1007/s10874-016-9355-3, 2017.

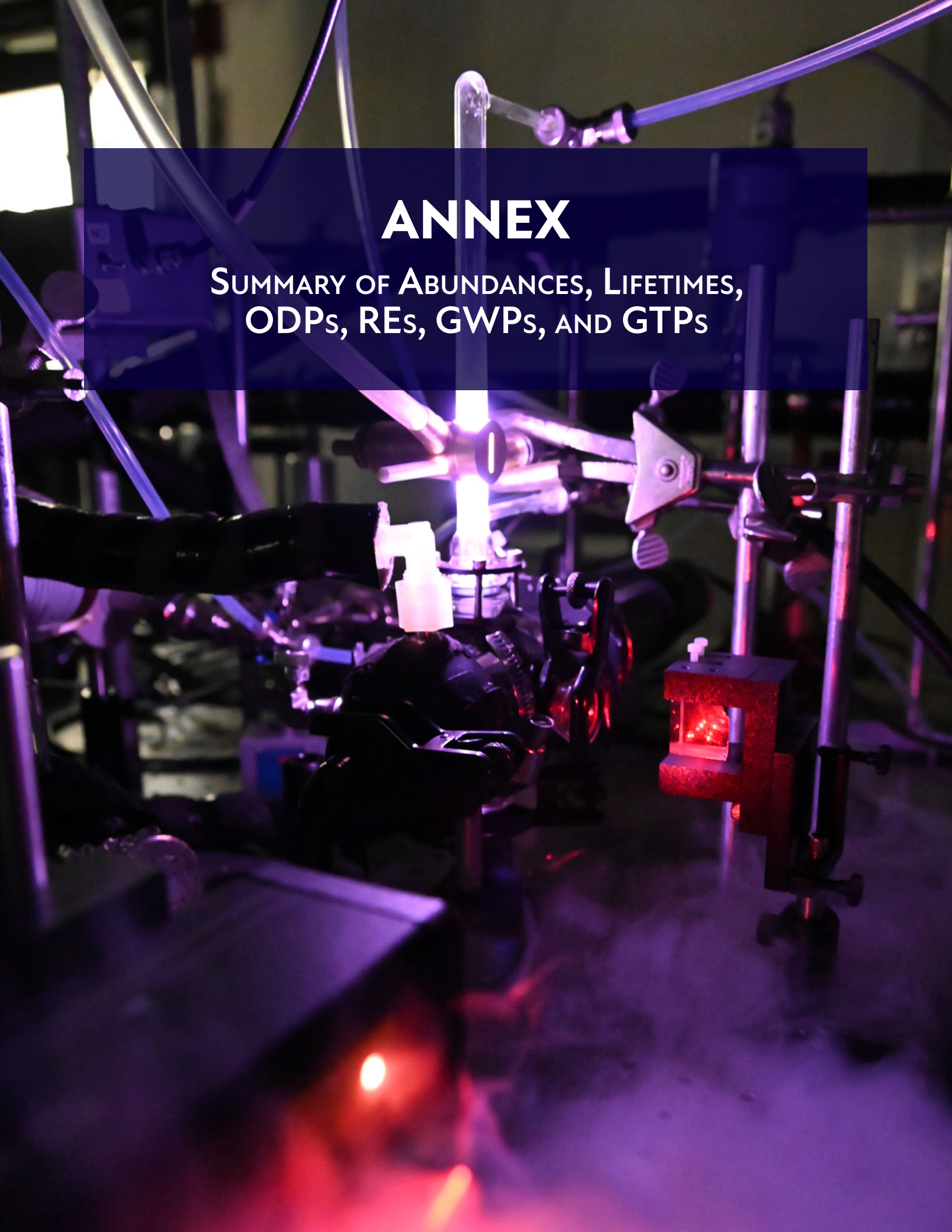

ANNEX

Summary of Abundances, Lifetimes, ODPs, REs, GWPs, and GTPs

About the cover image:
Laboratory studies of the chemical and physical properties of atmospheric trace species are essential to understand the fundamental processes that affect stratospheric ozone and climate.

Photo credit: Daniel Van Hoomissen, NOAA CSL / CIRES

ANNEX

Summary of Abundances, Lifetimes, ODPs, REs, GWPs, and GTPs

Lead Authors : James B. Burkholder
Øivind Hodnebrog

Contributors : Brian C. McDonald
Vladimir Orkin
Vassilis C. Papadimitriou
Daniel Van Hoomissen

CONTENTS

Annex: Summary of Abundances, Lifetimes, ODPs, REs, GWPs, and GTPs

SCIENTIFIC SUMMARY

- The present analysis has updated climate metrics that reflect 2019 CO_2 forcing.
- The hydrocarbon, hydrofluorocarbon (HFC), and chlorinated molecule sections were expanded.
- A new halogenated aldehyde section has been included.
- Climate metric values have been updated using a recently improved method for calculating radiative efficiencies with stratospheric temperature adjustment included. For carbon dioxide (CO_2), methane (CH_4), nitrous oxide (N_2O), CFC-11, and CFC-12, the reported radiative efficiencies also include tropospheric adjustments.
- Climate-carbon feedbacks have been included for all compounds, consistent with the methods of the Intergovernmental Panel on Climate Change Sixth Assessment Report (AR6, 2022). Differences between climate metrics reported here and those in AR6 are due to total lifetime and radiative efficiency updates included here.
- The low wavenumber, usually <500 cm^{-1}, contribution to radiative efficiencies is usually not determined by experimental infrared absorption spectra. The low wavenumber contribution was evaluated using theoretically calculated spectra for all molecules. The contributions are typically a small positive adjustment, 0–5%, but need to be evaluated on a molecule basis.
- Theoretically calculated infrared absorption spectra have been added for molecules previously lacking experimental and theoretical values.

A.1 INTRODUCTION

The *Annex* contains a compilation of atmospheric abundance, lifetime, ozone depletion potential (ODP), and radiative metrics for ozone depleting substances (ODSs), replacement compounds, and related species covered under the umbrella of the Ozone Assessment. The table builds upon the metrics reported in previous assessments from the Intergovernmental Panel on Climate Change (2013; 2022) and the World Meteorological Organization (WMO) (2014; 2018) and United Nations Environment Programme (UNEP). The *Annex* provides updates based on new studies and refined methods for evaluating climate metrics. The *Annex* content has been expanded from Appendix A of the previous Ozone Assessment (WMO, 2018) to include an expanded coverage of potential replacement compounds, e.g. hydrofluorocarbons (HFCs), as well as several prominent hydrocarbons observed in urban environments and commercially used chlorinated compounds. A summary is provided below that is broken into the following categories and/or classes of molecules.

The ozone depletion potentials (ODPs) and global warming potentials (GWPs) given in **Table A-5** may differ in some cases from the metrics for controlled substances reported in the Montreal Protocol and subsequent Amendments due to consideration of recent experimental data, methods of analysis, and/or assessment recommendations, e.g. recommendation given in Burkholder et al. (2019), SPARC (2013), and WMO (2014; 2018).

The following subsections describe the methods applied to derive the recommendations provided in **Table A-5**. An extensive set of table footnotes provide the literature source, parameters, or method used to derive the reported metric. The table contains both long- and short-lived (lifetimes <~0.5 years) compounds. Metrics given for short-lived molecules are dependent on the time and location of their emissions, as they are not expected to be well-mixed in the atmosphere. Hence, the abundances and metrics reported are to be considered representative values but are most likely not valid for all spatial and temporal emissions scenarios.

Index	Category	Number of Compounds
1	CO_2, CH_4, and N_2O	
2	Hydrocarbons	13
3	Oxygenated Hydrocarbons	7
4	Chlorofluorocarbons (CFCs)	13
5	Hydrochlorofluorocarbons (HCFCs)	274
6	Hydrofluorocarbons (HFCs)	162
7	Unsaturated Hydrofluorocarbons	32
8	Chlorocarbons and Hydrochlorocarbons	20
9	Unsaturated Hydrochlorocarbons and Chlorocarbons	23
10	Unsaturated Chlorofluorocarbons and Hydrochlorofluorocarbons	19

Index	Category	Number of Compounds
11	Bromocarbons, Hydrobromocarbons, and Halons	18
12	Unsaturated Bromocarbons	9
13	Unsaturated Bromochlorofluorocarbons	1
14	Fully Fluorinated Species	34
15	Halogenated Ethers	74
16	Fluoroesters	25
17	Halogenated Alcohols	15
18	Halogenated Ketones	9
19	Halogenated Aldehydes	10
20	Iodocarbons	11
21	Special Compounds	10

A.2 EVALUATION METHODOLOGY

A.2.1 Compound Name, Chemical Formula, and CAS RN

Table A-5 has a row for each compound that contains the compound name and/or abbreviation, the chemical formula, and the compound's Chemical Abstracts Service registry number (CAS RN), which provides for effective searching of the table. Some compounds, however, do not have assigned CAS RNs.

A.2.2 Atmospheric Abundance

The data provided for atmospheric abundances were taken from *Chapters 1* and *2* of this report for the year 2020, where possible, or from the last WMO Ozone Assessment, as noted in the footnotes. A compound's abundance typically falls into one of the following categories: 1) compounds with known emissions sources for which global observations are available, 2) compounds with known sources but with only local or regional observations, and 3) compounds with no known sources or observations. The abundances provided in the table are only intended to provide a snapshot of a molecule's atmospheric abundance, in particular for short-lived compounds. *Chapters 1* and *2* in this report and in the previous Assessment provide an analysis of reported abundances and trends, as well as the most relevant citations.

A.2.3 Total and Atmospheric Lifetimes

Total lifetime (τ_{Total}) includes tropospheric OH reactive and photolysis loss, stratospheric loss due to reaction (OH and $O(^1D)$) and photolysis, and ocean, soil, aerosol, and cloud uptake. Atmospheric lifetimes do not include heterogeneous loss processes such as ocean uptake.

$$\frac{1}{\tau_{Total}} = \frac{1}{\tau_{Trop}} + \frac{1}{\tau_{Strat}} + \frac{1}{\tau_{Meso}}$$

$$\frac{1}{\tau_{Trop}} = \frac{1}{\tau_{OH}^{Trop}} + \frac{1}{\tau_{h\nu}^{Trop}} + \frac{1}{\tau_{het}^{Trop}}$$

$$\frac{1}{\tau_{Strat}} = \frac{1}{\tau_{OH}^{Strat}} + \frac{1}{\tau_{O(^1D)}} + \frac{1}{\tau_{h\nu}^{Strat}}$$

Note that loss due to Cl-atom reaction is not included here but may represent a significant loss process for some molecules under certain spatial and temporal conditions, e.g. urban coastal regions. Mesospheric loss processes are negligible except for very long-lived compounds, as noted in the **Table A-5** footnotes. Total lifetimes reported in the last Assessment are included for comparison with the 2022 updates.

The tropospheric partial lifetime due to reaction with the OH radical, τ_{OH}^{Trop}, was calculated relative to the lifetime for methyl chloroform (CH_3CCl_3; 6.1 years) using a temperature of 272 K. OH reaction rate coefficients are taken from Burkholder et al. (2019) unless stated otherwise in the footnote. Lifetimes for very short-lived substances (VSLSs) are reported using the same method and are considered representative lifetimes, because their local lifetimes will depend on the time and location of their emissions. A representative range of local lifetimes taken from WMO (2014) Chapter 1 (Tables 1-5, 1-11) are given in parenthesis where available. The tropospheric OH partial lifetime for CH_3CCl_3 (6.1 years) was calculated from an overall lifetime of 5.0 years derived from the Advanced Global Atmospheric Gases Experiment (AGAGE) and National Oceanic and Atmospheric Administration (NOAA) monitoring networks using a stratospheric partial lifetime of 38

Table A-1. Tropospheric photolysis lifetimes for key ozone depleting substances (ODSs) reported in the literature.

Molecule	Formula	Lifetime (years)	Reference
Nitrous oxide	N_2O	14,600	SPARC (2013)*
Carbon tetrachloride	CCl_4	1230	SPARC (2013)*
CFC-11	CCl_3F	1770	SPARC (2013)*
CFC-12	CCl_2F_2	12,500	SPARC (2013)*
CFC-112	CCl_2FCCl_2F	2280	Davis et al. (2016)
CFC-112a	CCl_3CClF_2	1190	Davis et al. (2016)
CFC-113	CCl_2FCClF_2	8120	SPARC (2013)*
CFC-113a	CCl_3CF_3	1480	Davis et al. (2016)
CFC-114	$CClF_2CClF_2$	19,600	SPARC (2013)*
CFC-114a	CCl_2FCF_3	8300	Davis et al. (2016)
(*E*)-R316c	(*E*)-1,2-c-$C_4F_6Cl_2$	3600	Papadimitriou et al. (2013b)
(*Z*)-R316c	(*Z*)-1,2-c-$C_4F_6Cl_2$	10,570	Papadimitriou et al. (2013b)
Bromodichloromethane	$CHBrCl_2$	222 days	WMO Table 1-5 (2014)
Dibromochloromethane	$CHBr_2Cl$	160 days	WMO Table 1-5 (2014)
Methylene bromide	CH_2Br_2	13.7	WMO Table 1-5 (2014)
Bromoform	$CHBr_3$	~23 days	Papanastasiou et al. (2014)
Halon-1202	CBr_2F_2	2.74	Papanastasiou et al. (2013)
Halon-1211	$CBrClF_2$	27.2	Papanastasiou et al. (2013)
Halon-1301	$CBrF_3$	4050	SPARC (2013)**
Halon-2402	$CBrF_2CBrF_2$	85.5	Papanastasiou et al. (2013)

* Model mean given in SPARC (2013) Table 5.6, scaled to recommended lifetime.
** Model mean given in SPARC (2013) Table 5.6, scaled to $CBrF_3$ UV cross section reported by Bernard et al. (2015)

years and an ocean partial lifetime of 94 years, see Prinn et al. (2005).

Ultraviolet (UV) photolysis loss has been included as a molecule loss process in the total lifetime analysis. The evaluation of photolysis lifetimes typically requires atmospheric model calculations to derive global annually averaged lifetimes. Photolysis lifetimes in the troposphere and stratosphere are taken from the literature whenever possible. Tropospheric photolysis lifetimes for key ODSs are given in **Table A-1**. In the absence of literature values, molecular properties and the similarity with other molecules were used to estimate photolysis lifetimes.

The stratospheric partial lifetime is not a directly observable molecular property and was estimated based on atmospheric model calculations, where available, and empirical relationships for the OH, O(^{1}D), and photolysis partial lifetimes. Stratospheric lifetimes are not reported for VSLSs. The minimum transport limited stratospheric partial lifetime was taken to be 20 years. Stratospheric OH reactive loss partial lifetimes were estimated based on the empirical correlation derived using 2-D model results reported in SPARC (2013): $\log_{10}(\tau_{Strat})=1.528+0.901 \times \log_{10}(\tau_{OH}^{Trop})$. The O(^{1}D) lifetime was based on the measured or estimated reaction rate coefficient, i.e., reactant loss ($k_{reactive}$, cm^3 molecule^{-1} s^{-1}), and the empirical lifetime relationship reported in Bernard et al. (2018): $\tau_{O(^1D)}(\text{years}) = 3.7 \times 10^{-8}/k_{reactive}$. Where experimental data were not available, the O(^{1}D) reactivity was estimated using the activity relationship for H atom and Cl atom abstraction given in Baasandorj et al. (2013). Stratospheric photolysis partial lifetimes were taken from model calculations or based on the empirical estimates given in Orkin et al. (2013) or for the hydrochlorofluorocarbons (HCFCs) from Papanastasiou et al. (2018).

Heterogeneous losses include uptake to the ocean, soil, aerosol, and cloud droplets. Partial lifetimes for these processes are included in the evaluation of a molecule's total lifetime where possible. The available literature and recommended lifetimes for soil and ocean loss are given in **Table A-2**. Aerosol and cloud uptake is an important loss process for certain highly soluble molecules, e.g. halogenated aldehydes, which may also hydrolyze or form hydrates in solution. In these cases, an uptake lifetime of ~1 week was assumed representative of this loss process and is noted in the footnote for each of those molecules.

A.2.4 Ozone Depletion Potential (ODP)

The ODPs reported here are obtained from atmospheric model simulations or via a semiempirical relationship, e.g. for a chlorinated ODS:

$$ODP_i = \frac{n_{Cl}}{3} \times \frac{f_i}{f_{CFC\text{-}11}} + \frac{\tau_i}{\tau_{CFC\text{-}11}} + \frac{m_{CFC\text{-}11}}{m_i}$$

where n_{Cl} is the number of chlorine atoms in the molecule, f_i is the fractional release factor for the molecule (see *Chapter 7*), τ_i is the total lifetime, and m_i is the molecular mass of the molecule. For brominated and iodine molecules, the number of halogen atoms is adjusted, and enhancement factors of 60 (see *Chapter 7*) and ~250, respectively, are included as multiplicative factors.

A.2.5 Radiative Efficiency (RE)

A.2.5.1 Spectral Radiative Efficiency Curve

Radiative efficiency (RE) values were calculated using the empirical approach given in Shine and Myhre (2020) and based on the same experimental absorption cross sections as in Hodnebrog et al. (2020a), unless noted otherwise. This approach involves a spectral RE curve, also known as the "Pinnock curve," where the instantaneous radiative forcing for a weak absorber is given per unit cross section as a function of wavenumber. The RE, in units of W m^{-2} ppb^{-1}, is obtained by multiplying the curve with the absorption spectrum of a compound and integrating over all wavenumbers. The Pinnock curve was first established by Pinnock et al. (1995) using a narrow-band radiative transfer model with 10 cm^{-1} spectral resolution. Hodnebrog et al. (2013) provided an updated curve, that was used in WMO (2018), by using a

Table A-2. Ocean and soil loss partial lifetimes reported in the literature.*

Molecule	Formula	Soil Lifetime (years)	Reference	Ocean Lifetime (years)	Reference
Methyl chloride	CH_3Cl	4.2	Hu (2012)	12	Hu et al. (2013)
Methyl bromide	CH_3Br	3.35	Montzka and Reimann (2011)	3.1	Hu et al. (2012)
Carbon tetrachloride	CCl_4	375 (288–536)	Rhew and Happel (2016), SPARC (2016)	124 (110–150)	Suntharalingam et al. (2019)
HCFC-21	$CHCl_2F$	–		673	Yvon-Lewis and Butler (2002)
HCFC-22	$CHClF_2$	–		1174	Yvon-Lewis and Butler (2002)
HCFC-124	$CHClFCF_3$	–		1855	Yvon-Lewis and Butler (2002)
HCFC-141b	CH_3CCl_2F	–		9190	Yvon-Lewis and Butler (2002)
HCFC-142b	CH_3CClF_2	–		122,200	Yvon-Lewis and Butler (2002)
HFC-41	CH_3F	–		1340	Yvon-Lewis and Butler (2002)
HFC-125	CHF_2CF_3	–		10,650	Yvon-Lewis and Butler (2002)
HFC-134a	CH_2FCF_3	–		5909	Yvon-Lewis and Butler (2002)
HFC-152a	CH_3CHF_2	–		1958	Yvon-Lewis and Butler (2002)
Methyl chloroform	CH_3CCl_3	–		94	Yvon-Lewis and Butler (2002)
Sulfuryl fluoride	SO_2F_2	–		40	Mühle et al. (2009)

* Possible range of lifetime given in parenthesis.

line-by-line (LBL) model run at 0.02 cm^{-1} spectral resolution and with more refined atmospheric profiles of temperature, clouds, and greenhouse gas abundances. Shine and Myhre (2020) generated a new curve (see also *Section A.2.5.2*) based on the same LBL model but with changes in the representation of clouds and the water vapor continuum.

A.2.5.2 Infrared Absorption Spectra

REs were calculated using a compound's room temperature infrared absorption spectrum. Absorption spectra were taken from the literature where possible. The Hodnebrog et al. (2020a) database of RE values, based on experimental literature infrared spectra, provides the reference for many of the RE values presented here.

In the absence of experimentally measured infrared absorption spectra, REs were determined based on theoretically calculated spectra, e.g. for HCFCs by Papanastasiou et al. (2018), HFCs by Burkholder et al. (2020), and fluoroesters by Bravo et al. (2011a). Theoretical methods have been applied to provide spectra for the compounds lacking RE values listed in Appendix A of the previous Assessment.

A.2.5.3 Stratospheric Temperature Adjustment

In the last Assessment, a generic 10% increase of the instantaneous radiative forcing was assumed for all compounds to account for stratospheric temperature adjustment, as in Hodnebrog et al. (2013). Here, the improved method of Shine and Myhre (2020) has been used. In contrast to the previous spectral RE curves, which yield instantaneous REs, Shine and Myhre (2020) included stratospheric temperature adjustment in the spectral RE curve by calculating the adjustment using a narrow-band model and applying this adjustment to the instantaneous RE curve derived using the LBL model. The magnitude of the stratospheric temperature adjustment is dependent on the infrared absorption spectrum of the compound and, in general, is in the 10 ± 5% range.

A.2.5.4 Lifetime Adjustment

The RE value calculations assume the compound is well mixed in the atmosphere. However, most compounds have a nonuniform vertical and horizontal distribution in the atmosphere. As in the last Assessment, the adjusted RE values reported in the summary table are lifetime adjusted using the approximate fractional correction (f) factors derived in Hodnebrog et al. (2013).

For compounds primarily removed by UV photolysis in the stratosphere, $f(\tau)=1-0.1826\tau^{-0.3339}$ (applicable for lifetimes of $10 < \tau < 10^4$ years). For compounds primarily removed by reaction with the OH radical, $f(\tau)=\frac{a\tau^b}{1+c\tau^d}$, where a = 2.962, b = 0.9312, c = 2.994, d = 0.9302 (applicable for $10^{-4} < \tau < 10^4$ years). Different factors were used for CFC-11 (0.927), CFC-12 (0.970), and halon-1211 (0.937) because explicit radiative transfer calculations are available for these compounds, for details see Hodnebrog et al. (2013). Note that OH radical fractional correction factors are particularly approximate for very short-lived compounds (VSLCs) due to the spatial and temporal dependence on their emissions.

A.2.5.5 Low-Frequency Infrared Absorption Adjustment

The vast majority of experimentally measured infrared absorption spectra do not provide data below ~500 cm^{-1}. There is, however, a component of the radiative forcing profile in this region. The larger molecules in particular that are included in **Table A-5** have low-frequency vibrations or torsions that would contribute a positive adjustment to their REs. We have performed a theoretically based survey of the molecules in the summary table to evaluate the low-frequency contribution. The adjustment needs to be considered on a molecule-by-molecule basis but is relatively small (0–5%) for the majority of the molecules in the table. The adjustment is generally larger for the larger (more carbon atoms) and heavier (higher molecular weight) molecules. The adjustments have been applied to the molecules in **Tables A-3** and **A-5**.

A.2.5.6 Tropospheric Adjustments and Effective Radiative Efficiency

In the last Assessment, stratospheric temperature adjustment was included in the radiative efficiencies while tropospheric adjustments were not. However, radiative efficiencies that also include tropospheric adjustments better represent the climate change response, e.g. the temperature response due to a perturbation in halocarbon concentrations. REs with tropospheric adjustments are denoted here as effective radiative efficiencies and are based on the concept of effective radiative forcing (ERF). IPCC AR6 defines ERF as the change in net downward radiative flux at the top of the atmosphere (TOA) following adjustments in both tropospheric and stratospheric temperature, water vapor, clouds, and some surface properties that are uncoupled to changes in global surface air temperature, see Forster et al. (2021). While REs without tropospheric adjustments can be calculated in offline radiation codes with high spectral resolution, calculations of effective REs typically rely on computationally expensive simulations with global climate models (GCMs), and this is currently not feasible for a large number of compounds. However, recent studies have quantified tropospheric adjustments: for CO_2, see Vial et al. (2013), Zhang and Huang (2014), and Smith et al. (2020; 2018); for CH_4 see Smith et al. (2018) and Modak et al. (2018), and for

Table A-3. Comparison between radiative efficiencies (RE) and effective radiative efficiencies, which include tropospheric adjustments. Here, stratospheric temperature adjustment, lifetime adjustment, and low-frequency infrared absorption adjustment are included for both RE and effective RE. Uncertainties are given as 5–95% confidence intervals.

	CO_2	CH_4	N_2O	CFC-11	CFC-12
RE (W m^{-2} ppb^{-1})	$(1.27 \pm 0.13) \times 10^{-5}$	$(4.52 \pm 0.63) \times 10^{-4}$	$(2.98 \pm 0.30) \times 10^{-3}$	0.267 ± 0.037	0.320 ± 0.045
Effective RE (W m^{-2} ppb^{-1})	$(1.33 \pm 0.16) \times 10^{-5}$	$(3.89 \pm 0.78) \times 10^{-4}$	$(3.19 \pm 0.51) \times 10^{-3}$	0.299 ± 0.057	0.358 ± 0.068

N_2O, CFC-11, and CFC-12 see Hodnebrog et al.(2020b), and effective REs for these compounds have been assessed in Forster et al. (2021). Specifically, tropospheric adjustments were estimated as +5 ± 5%, –14 ± 15%, +7 ± 13%, +13 ± 10%, and +12 ± 14%, respectively, of the REs (uncertainties are given as 5–95% confidence intervals), but an adjustment of 12% was used for both CFC-11 and CFC-12. For other halogenated compounds, tropospheric adjustments are assumed to be 0 ± 13% due to lack of calculations. The assessed tropospheric adjustments from AR6 are adopted here to calculate effective REs in **Tables A-3** and **A-5**.

Table A-3 shows a comparison of REs and effective REs for compounds where estimates of tropospheric adjustments are available. It is important to note that uncertainties associated with effective RE are larger than for RE, and magnitudes of tropospheric adjustments are generally associated with low confidence in AR6 (Forster et al., 2021). GCMs have less sophisticated radiation schemes than offline radiative transfer models, and unrealistically strong perturbations in concentrations are often needed to avoid noise caused by natural variability dominating the climate change signal, thus not accounting for possible nonlinear effects. The magnitudes of tropospheric adjustments, particularly for clouds, vary between different GCMs and between the different radiative kernel methods needed to separate individual adjustments from the instantaneous radiative forcing, see Smith et al. (2018) and Hodnebrog et al. (2020b). Another source of uncertainty arises because tropospheric adjustments are based on GCM simulations with fixed sea surface temperatures while, ideally, temperatures over land should also have been held fixed, see Andrews et al. (2021). In the effective RE estimates here, the radiative response to land surface temperature change is only partially accounted for, see Section 7.3.1 in Forster et al. (2021) for further discussion.

The total radiative forcing uncertainty for halogenated compounds is estimated to be ~14% for compounds with lifetimes >~5 years and ~24% for compounds with lifetimes <~5 years, see Hodnebrog et al. (2020a). These numbers increase to 19% and 26%, respectively, for effective RE uncertainty. For CO_2, CH_4, and N_2O, the effective RE uncertainty is 12%, 20%, and 16%, respectively, from Forster et al. (2021).

A.2.6 Global Warming Potential (GWP)

Absolute Global Warming Potentials (AGWPs). Radiative metrics reported here (GWPs and global temperature change potentials [GTPs]) are calculated relative to CO_2 and based on a 2019 CO_2 abundance of 409.9 ppm. The response of the carbon cycle to an instantaneous pulse of CO_2 emissions, known as the impulse response function, is unchanged from the last Assessment and taken from Joos et al. (2013). The CO_2 AGWPs for the 20-, 100-, and 500-year time horizons are 2.434×10^{-14}, 8.947×10^{-14}, and 3.138×10^{-13} W m^{-2} yr kg^{-1}, respectively, and are consistent with the values reported in IPCC AR6 (Forster et al., 2021).

A.2.7 Global Temperature Change Potential (GTP)

Absolute Global Temperature Change Potentials (AGTPs). The CO_2 AGTPs for the 50- and 100-year time horizons are 4.277×10^{-16} and 3.946×10^{-16} K kg^{-1}, respectively, and are consistent with the values reported in IPCC AR6 (Forster et al., 2021). These values are approximately 30% smaller than those used in the last Assessment, and this is mainly because of updates to

Table A-4. Comparison of GWP and GTP values for a selection of compounds when climate-carbon feedback is: included for CO_2 only as in WMO (2018), excluded for all compounds as in Hodnebrog et al. (2020a), and included for both CO_2 and non-CO_2 compounds. The impulse response function is from Gasser et al. (2017) instead of Joos et al. (2013), to be able to exclude the climate-carbon feedback for CO_2, and the contribution from low-frequency wavenumbers to the RE is not included here. Thus, the GWP and GTP values with climate-carbon feedback included for all compounds are slightly different from the recommended values in **Table A-5**.

	Climate-Carbon Feedback						
	CO_2	Compound	GWP (20)	GWP (100)	GWP (500)	GTP (50)	GTP (100)
CFC-11							
	✓	–	8110	5910	1980	5950	3270
	–	–	8370	6360	2230	6450	3620
	✓	✓	8290	6210	2100	6340	3520
CFC-12							
	✓	–	12,400	11,900	5400	12,500	9700
	–	–	12,800	12,800	6080	13,600	10,800
	✓	✓	12,700	12,500	5720	13,200	10,300
HCFC-22							
	✓	–	5440	1800	516	633	334
	–	–	5610	1940	581	687	370
	✓	✓	5580	1900	546	742	366
CH_3CCl_3							
	✓	–	549	152	44	30	27
	–	–	566	164	49	33	30
	✓	✓	565	161	46	37	30

the global surface temperature response function, see Section 7.6.1.2 in Forster et al. (2021) for details, affecting both the AGTP for CO_2 and the AGTPs for the non-CO_2 compounds.

A.3 CLIMATE-CARBON FEEDBACK

Compounds that warm the surface due to their direct radiative forcing also influence climate indirectly through perturbations of carbon fluxes. When the surface warms, a net flux of CO_2 goes into the atmosphere and leads to further warming, known as the climate-carbon feedback, for example see Gasser et al. (2017). In the previous Assessment, climate-carbon feedbacks were included for CO_2, while no climate feedbacks were included for the other compounds. Here, climate-carbon feedbacks are included for all components, consistent with IPCC AR6 Section 7.6.1.3 (Forster et al., 2021). **Table A-4** shows metric values for different combinations of climate-carbon feedback and illustrates the bias introduced when this feedback is included only for CO_2 and not for the non-CO_2 compounds. Excluding the climate-carbon feedback completely generally leads to smaller differences against values with the feedback included for both CO_2 and non-CO_2 compounds.

A.4 INDIRECT EFFECTS

The climate metric values presented in **Table A-5** are due to the direct radiative effect only. This means that the negative radiative forcing resulting from stratospheric ozone depletion by ODSs is not included in these estimates. In some cases, these can be large and potentially offset the direct effect, see *Section 7.3.2* and **Table 7A-1** for further information. Indirect effects of methane (e.g., through production of ozone and stratospheric water vapor) and nitrous oxide (through methane lifetime reduction and stratospheric ozone depletion) are also not included here. Non-methane hydrocarbons generally have small direct radiative effects, and it is important to note that their indirect effects, mainly through tropospheric ozone production and changes in methane lifetime, can be significant as reported by Collins et al. (2002) and Hodnebrog et al. (2018). There are also indirect effects caused by degradation of halogenated compounds, see Burkholder et al. (2015), where some breakdown products have high GWP values as reported in Jubb et al. (2015) and Bravo et al. (2011a) and discussed in *Section 7.2.5*.

A.5 METRIC UNCERTAINTIES

Uncertainties in GWP and GTP values for halogenated compounds depend on several factors: lifetime, radiative efficiency, global surface temperature response function (for GTP), and the radiative efficiency and impulse response function for CO_2. Contributions from these factors to the radiative metrics were explored for four halogenated compounds (CFC-11, PFC-14, HFC-134a, and HFC-32) in IPCC AR6, and the total uncertainty in GWP and GTP values typically range from 30% to 60% (5–95% confidence interval) for the metrics and time horizons considered here, see Supplementary Tables 7.SM.10–7.SM.13 in Smith et al. (2021) for details. Note that metrics based solely on theoretically calculated infrared absorption spectra will, in general, have even greater uncertainties.

Table A-5. Atmospheric abundances; lifetimes; radiative efficiencies (REs); direct effect Global Warming Potentials (GWPs) for 20-, 100-, and 500-year time horizons; and Global Temperature Change Potentials (GTPs) for 50- and 100-year time horizons

Industrial Designation or Chemical Name	Chemical Formula	CAS RN	Atmospheric Abundance[a]	WMO (2018) Total Lifetime (years)	WMO (2022) Total Lifetime (years)	Tropospheric (OH Reactive Loss) Lifetime 2022 (years)
Carbon dioxide	CO_2	124-38-9	412.5 ppm			
Methane, non-fossil	CH_4	74-82-8	1879 ppb	12.4	11.8	
Methane, fossil	CH_4	74-82-8		12.4	11.8	
Nitrous oxide	N_2O	10024-97-2	333.0 ppb	123	109	
Hydrocarbons						
Ethane	CH_3CH_3	74-84-0			76 days	76 days
Ethene	$CH_2=CH_2$	74-85-1			1.7 days	1.7 days
Acetylene	HCCH	74-86-2			0.1 days	0.1 days
Propene	$CH_2=CHCH_3$	115-07-1		0.4 days (0.27–0.50 days)	0.4 days (0.27–0.50 days)	0.4 days
Propane, R-290	$CH_3CH_2CH_3$	74-98-6		15 days (9.9–27 days)	15 days (9.9–27 days)	15 days
n-butane	$CH_3CH_2CH_2CH_3$	106-97-8			6.5 days	6.5 days
Isobutane, R-600a	$(CH_3)_2CHCH_3$	75-28-5		7 days (5.2–10.7 days)	7.0 days (5.2–10.7 days)	7.0 days
Isobutene	$(CH_3)_2C=CH_2$	115-11-7		0.2 days (0.15–0.29 days)	0.2 days (0.15–0.29 days)	0.2 days
n-pentane	$CH_3CH_2CH_2CH_2CH_3$	109-66-0		3 days (2.7–6.5 days)	4.0 days (2.7–6.5 days)	4.0 days
Isopentane	$(CH_3)_2CHCH_2CH_3$	78-78-4		4 days (2.9–6.0 days)	3.9 days (2.9–6.0 days)	3.9 days
Cyclopentane	$c\text{-}CH_2CH_2CH_2CH_2CH_2$	287-92-3		3 days (2.2–5.3 days)	3.2 days (2.2–5.3 days)	3.2 days
Benzene	C_6H_6	71-43-2			~10.0 days	10.0 days
Toluene	C_7H_8	108-88-3			~29 days	29 days
Oxygenated Hydrocarbons						
Formaldehyde	CH_2O	50-00-0		–	0.08 days	1.6 days
Ethanol	CH_3CH_2OH	64-17-5		–	4.1 days	4.1 days
Acetaldehyde	CH_3CHO	75-07-0		–	0.7 days	0.8 days
Methyl formate	CH_3OCHO	107-31-3		87 days (60–143 days)	86 days	87 days
Acetone	$CH_3C(O)CH_3$	67-64-1		–	26 days	87 days
Isopropanol	$(CH_3)_2CHOH$	67-63-0		2 days (1.5–2.9 days)	2.4 days (1.5–2.9 days)	2.4 days
Methylal	$CH_3OCH_2OCH_3$	109-87-5		2 days (1.5–2.8 days)	2.6 days (1.5–2.8 days)	2.6 days
Chlorofluorocarbons						
CFC-11	CCl_3F	75-69-4	224 ppt	52	52	–
CFC-12	CCl_2F_2	75-71-8	497.2 ppt	102	102	–
CFC-13	$CClF_3$	75-72-9	3.32 ppt	640	640	–
CFC-112	CCl_2FCCl_2F	76-12-0	0.39 ppt	63.6	63.6	–
CFC-112a	$CClF_2CCl_3$	76-11-9	0.08 ppt	52	52	–
CFC-113	CCl_2FCClF_2	76-13-1	68.9 ppt	93	93	–
CFC-113a	CCl_3CF_3	354-58-5	0.95 ppt	55	55	–
CFC-114	$CClF_2CClF_2$	76-14-2	16.3 ppt	189	189	–
CFC-114a	CCl_2FCF_3	374-07-2	1.11 ppt	105	105	–
CFC-115	$CClF_2CF_3$	76-15-3	8.7 ppt	540	540	–
CFC-216ba	$CClF_2CClFCF_3$	–	38 ppq	135	135	–
CFC-216ca	$CClF_2CF_2CClF_2$	–	20 ppq	~135	~135	–
(E)-R316c ((E)-1,2-dichlorohexafluoro-cyclobutane)	$(E)\text{-}1,2\text{-}c\text{-}C_4F_6Cl_2$	3832-15-3		75	75	–
(Z)-R316c ((Z)-1,2-dichlorohexafluoro-cyclobutane)	$(Z)\text{-}1,2\text{-}c\text{-}C_4F_6Cl_2$	3934-26-7		114	114	–
1,2,3,4-Tetrachlorohexafluorobutane (TCHFB)	$C_4Cl_4F_6$	375-45-1			>50	–
Hydrochlorofluorocarbons						
HCFC-21	$CHFCl_2$	75-43-4		1.7	1.71	1.82

Stratospheric Lifetime 2022 (years)	ODP	Radiative Efficiency (well mixed) ($W\ m^{-2}\ ppb^{-1}$) [b]	Recommended Adjusted Effective Radiative Efficiency ($W\ m^{-2}\ ppb^{-1}$) [c]	GWP 20-yr	GWP 100-yr	GWP 500-yr	GTP 50-yr	GTP 100-yr	Footnotes *A: Atmospheric Abundance L: Lifetime O: Ozone Depletion Potential R: Radiative Metrics*
	0		1.33E-05	1	1	1	1	1	A1, O1, R1
	0		3.89E-04	79.7	27	7.25	10.4	4.72	A1, L1, O1, R1
	0		3.89E-04	82.5	29.8	9.99	13.2	7.46	O1, R1
	0.017		3.20E-03	273	273	130	290	233	A1, L1, O2, R1
–	0	0.004	1.61E-03	3	<1	<1	<1	<1	L2, R2
–	0	0.039	7.75E-04	<<1	<<1	<<1	<<1	<<1	L2, R2
–	0	0.041	5.91E-05	<<1	<<1	<<1	<<1	<<1	L2, R2
–	0	0.031	1.65E-04	<<1	<<1	<<1	<<1	<<1	L2, O1, R3
–	0	0.003	3.96E-04	<<1	<<1	<<1	<<1	<<1	L2, O1, R2
–	0	0.004	2.60E-04	<<1	<<1	<<1	<<1	<<1	L2
–	0	0.004	2.87E-04	<<1	<<1	<<1	<<1	<<1	L2, O1, R2
–	0	0.023	7.38E-05	<<1	<<1	<<1	<<1	<<1	L2, O1, R2
–	0	0.023	2.11E-04	<<1	<<1	<<1	<<1	<<1	L2, O1, R2
–	0	0.006	2.57E-04	<<1	<<1	<<1	<<1	<<1	L2, O1, R2
–	0	0.006	1.41E-04	<<1	<<1	<<1	<<1	<<1	L2, O1, R2
–	0	0.003	2.82E-04	<<1	<<1	<<1	<<1	<<1	L3, O1, R2
–	0	0.014	1.54E-03	<1	<<1	<<1	<<1	<<1	L3, O1, R2
–	0	0.004	4.60E-06	<<1	<<1	<<1	<<1	<<1	L2, O1, R3
–	0	0.044	2.20E-03	<1	<<1	<<1	<<1	<<1	L2, O1, R2
–	0	0.017	1.80E-04	<<1	<<1	<<1	<<1	<<1	L2, O1, R2
–	0	0.108	4.90E-02	46	13	4	3	2	L2, O1, R2
–		0.027	6.10E-03	2	<1	<1	<1	<<1	L2, R2
–	0	0.06	1.80E-03	<<1	<<1	<<1	<<1	<<1	L2, O1, R3
–	0	0.169	6.40E-03	<1	<<1	<<1	<<1	<<1	L2, O1, R2
55	1	0.28	0.299	8560	6410	2150	6540	3640	A2, L4, L5, R4
103	0.75	0.33	0.358	12,700	12,500	5710	13,200	10,400	A2, L4, L5, O3, O4, R4
–	0.3	0.284	0.279	12,400	16,300	17,600	17,100	18,900	A2, L6, O5, R2
65.4	0.98	0.295	0.281	5600	4600	1670	4800	3010	A2, L4, L7, O6, R5
53.8	0.86	0.258	0.246	4750	3550	1190	3620	2020	A2, L4, L7, O6, R5
94.5	0.82	0.314	0.302	6870	6530	2840	6920	5220	A2, L4, L5, O3, O4, R2
57.5	0.73	0.253	0.241	5110	3930	1350	4030	2320	A2, L4, L7, O6, R5
191	0.53	0.325	0.315	8280	9450	6160	10,000	9430	A2, L4, L5, O3, O4, R2
106.7	0.72	0.309	0.297	7490	7410	3440	7870	6230	A2, L4, L7, O6, R5
664	0.45	0.252	0.247	7430	9630	9910	10,100	11,000	A2, L5, L8, O3, R2
135	0.35	0.42	0.406	8090	8580	4610	9110	7860	A2, L9, O7, R6
~135	~0.35	0.37	0.357	7110	7540	4050	8010	6910	A2, L9, O7, R6
76	0.46	0.282	0.273	4870	4290	1670	4510	3080	L10, O8, R7
115	0.54	0.311	0.302	5630	5710	2780	6060	4940	L10, O8, R7
–	–	0.46	0.439	5640	4140	1370	4200	2280	L3, R6
29.8	0.036	0.176	0.145	578	161	46	36	29	L2, L11, O9, R2

Industrial Designation or Chemical Name	Chemical Formula	CAS RN	Atmospheric Abundance[a]	WMO (2018) Total Lifetime (years)	WMO (2022) Total Lifetime (years)	Tropospheric (OH Reactive Loss) Lifetime 2022 (years)
HCFC-22	CHF_2Cl	75-45-6	247.8 ppt	11.9	11.6	13
HCFC-31	CH_2FCl	593-70-4	0.11 ppt	1.2	1.29	1.33
HCFC-121	$CHCl_2CCl_2F$	354-14-3		1.11	1.1	1.17
HCFC-121a	$CHClFCCl_3$	354-11-0		2.67	2.67	2.96
HCFC-122	$CHCl_2CClF_2$	354-21-2		0.9	0.912	0.955
HCFC-122a	$CHClFCCl_2F$	354-15-4		3.1	3.11	3.43
HCFC-122b	CHF_2CCl_3	354-12-1		9.31	9.3	12.6
HCFC-123	$CHCl_2CF_3$	306-83-2		1.3	1.31	1.38
HCFC-123a	$CHClFCClF_2$	354-23-4		4	4.03	4.31
HCFC-123b	CHF_2CCl_2F	812-04-4		11.8	11.8	15.1
HCFC-124	$CHClFCF_3$	2837-89-0	1.1 ppt	5.9	5.9	6.28
HCFC-124a	CHF_2CClF_2	354-25-6		17	17	19
HCFC-131	$CHCl_2CHClF$	359-28-4		0.76	0.756	0.786
HCFC-131a	CH_2ClCCl_2F	811-95-0		2.57	2.57	2.8
HCFC-131b	CH_2FCCl_3	2366-36-1		2.33	2.324	2.55
HCFC-132	$CHClFCHClF$	25915-78-0		1.73	1.73	1.81
HCFC-132a	$CHCl_2CHF_2$	471-43-2		1.12	1.12	1.18
HCFC-132b	$CH_2ClCClF_2$	1649-08-7	0.14 ppt	3.5	3.5	3.73
HCFC-132c	CH_2FCCl_2F	1842-05-3		4.1	4.08	4.52
HCFC-133	$CHClFCHF_2$	431-07-2		3.1	3.06	3.21
HCFC-133a	CH_2ClCF_3	75-88-7	0.45 ppt	4.6	4.48	4.74
HCFC-133b	CH_2FCClF_2	421-04-5		7.2	7.2	7.71
HCFC-141	$CH_2ClCHClF$	430-57-9		1.14	1.14	1.19
HCFC-141a	CH_2FCHCl_2	430-53-5		0.5	0.497	0.51
HCFC-141b	CH_3CCl_2F	1717-00-6	24.5 ppt	9.4	8.81	10.7
HCFC-142	CH_2ClCHF_2	338-65-8		2.6	2.61	2.73
HCFC-142a	$CH_2FCHClF$	338-64-7		1.58	1.58	1.64
HCFC-142b	CH_3CClF_2	75-68-3	21.7 ppt	18	17.1	19.3
HCFC-151	CH_2ClCH_2F	762-50-5		0.49	0.488	0.5
HCFC-151a	CH_3CHClF	1615-75-4		1.16	1.16	1.2
HCFC-221aa	$CHCl_2CCl_2CCl_2F$	422-28-6		0.93	0.933	0.979
HCFC-221ab	$CHClFCCl_2CCl_3$	422-26-4		2.67	2.67	2.96
HCFC-221ba	$CHCl_2CClFCCl_3$	422-40-2		1.11	1.1	1.17
HCFC-221da	$CCl_3CHClCCl_2F$	431-79-8		3.29	3.29	3.71
HCFC-221ea	$CCl_3CHFCCl_3$	–		3.52	3.51	3.99
HCFC-222aa	$CHCl_2CCl_2CClF_2$	422-30-0		1.11	1.1	1.17
HCFC-222ab	$CHClFCCl_2CCl_2F$	147728-31-2		2.67	2.67	2.96
HCFC-222ac	$CHF_2CCl_2CCl_3$	422-27-5		9.29	9.28	12.6
HCFC-222ba	$CHCl_2CClFCCl_2F$	146254-26-4		1.11	1.1	1.17
HCFC-222bb	$CHClFCClFCCl_3$	147728-30-1		3.15	3.15	3.54
HCFC-222ca	$CHCl_2CF_2CCl_3$	422-49-1		1.38	1.38	1.47
HCFC-222da	$CCl_2FCHClCCl_2F$	431-82-3		4.48	4.48	5.23
HCFC-222db	$CCl_3CHClCClF_2$	431-80-1		4.62	4.62	5.42
HCFC-222ea	$CCl_3CHFCCl_2F$	146254-25-3		4.68	4.67	5.49
HCFC-223aa	$CHCl_2CCl_2CF_3$	422-35-5		1.11	1.1	1.17
HCFC-223ab	$CHClFCCl_2CClF_2$	144909-54-6		3.18	3.18	3.54
HCFC-223ac	$CHF_2CCl_2CCl_2F$	422-29-7		9.29	9.28	12.6
HCFC-223ba	$CHCl_2CClFCClF_2$	422-41-3		1.39	1.38	1.47
HCFC-223bb	$CHClFCClFCCl_2F$	145599-91-3		3.18	3.18	3.54

Stratospheric Lifetime 2022 (years)	ODP	Radiative Efficiency (well mixed) ($W\ m^{-2}\ ppb^{-1}$) [b]	Recommended Adjusted Effective Radiative Efficiency ($W\ m^{-2}\ ppb^{-1}$) [c]	GWP 20-yr	GWP 100-yr	GWP 500-yr	GTP 50-yr	GTP 100-yr	Footnotes *A: Atmospheric Abundance L: Lifetime O: Ozone Depletion Potential R: Radiative Metrics*
120	0.038	0.223	0.214	5610	1910	546	744	368	A2, L5, L11, O3, R2
36.7	0.019	0.088	0.068	307	85	24	19	15	A2, L2, O9, R8
20	0.03	0.193	0.147	209	58	17	13	10	L12, O10, R2
27.4	0.066	0.197	0.172	592	165	47	37	30	L12, O10, R9
20	0.022	0.22	0.16	207	57	16	13	10	L12, O9, R2
33.8	0.067	0.227	0.203	891	248	71	56	45	L12, O9, R2
35.5	0.17	0.221	0.211	2440	772	220	239	145	L12, O10, R9
25.7	0.02	0.203	0.16	329	91	26	20	17	L2, O3, R2
62.9	0.039	0.25	0.228	1430	400	114	91	73	L2, O9, R2
53.8	0.124	0.248	0.238	3570	1220	349	485	236	L12, O10, R9
105	0.022	0.222	0.207	2060	596	170	143	110	A3, L2, O3, R2
161	0.026	0.258	0.251	5140	2080	595	1220	450	L12, O10, R2
20	0.019	0.14	0.097	116	32	9	7	6	L12, O10, R9
31.4	0.056	0.184	0.16	650	181	52	41	33	L12, O10, R9
26.2	0.054	0.145	0.125	460	128	36	29	23	L12, O10, R9
39.1	0.025	0.174	0.147	452	126	36	28	23	L12, O10, R2
23.9	0.02	0.167	0.129	257	71	20	16	13	L12, O10, R2
57.5	0.038	0.214	0.192	1190	332	95	75	61	A2, L2, O10, R9
41.8	0.062	0.186	0.171	1230	345	98	79	63	L2, O9, R2
67.8	0.017	0.195	0.173	1070	298	85	67	54	L12, O10, R9
82.6	0.019	0.164	0.15	1340	378	108	87	69	A2, L13, O9, R10
110	0.024	0.218	0.206	2800	834	238	215	155	L12, O10, R9
29.5	0.022	0.094	0.0745	174	48	14	11	9	L12, O10, R2
20	0.011	0.095	0.0573	58	16	5	4	3	L12, O10, R9
49.4	0.102	0.168	0.161	2590	808	231	239	152	A2, L5, L11, O3, R2
60.1	0.019	0.125	0.109	678	189	54	42	34	L12, O10, R9
42.3	0.015	0.136	0.111	419	116	33	26	21	L12, O10, R9
148	0.057	0.199	0.194	5400	2190	628	1300	477	A2, L5, L11, O3, R2
20	0.008	0.049	0.0295	42	12	3	3	2	L12, O10, R9
33.2	0.015	0.08	0.0617	208	58	16	13	10	L12, O10, R9
20	0.027	0.24	0.175	146	41	12	9	7	L12, O10, R9
27.4	0.069	0.197	0.172	409	114	32	26	21	L12, O10, R9
20	0.032	0.221	0.168	165	46	13	10	8	L12, O10, R9
29	0.083	0.259	0.231	675	189	54	43	34	L12, O10, R9
29.5	0.088	0.238	0.214	666	186	53	42	34	L12, O10, R9
20	0.028	0.285	0.216	226	63	18	14	11	L12, O10, R9
27.4	0.061	0.257	0.224	567	158	45	35	29	L12, O10, R9
35.2	0.191	0.224	0.214	1660	525	150	162	99	L12, O10, R9
20	0.028	0.268	0.204	213	59	17	13	11	L12, O10, R9
28.6	0.071	0.217	0.193	576	161	46	36	29	L12, O10, R9
21.6	0.034	0.253	0.201	264	73	21	16	13	L12, O10, R9
31.2	0.097	0.292	0.267	1120	316	90	73	58	L12, O10, R9
31.4	0.1	0.273	0.251	1080	306	87	71	56	L12, O10, R9
31.4	0.101	0.26	0.239	1040	295	84	68	54	L12, O10, R9
20	0.024	0.256	0.194	217	60	17	13	11	L12, O10, R9
31.4	0.059	0.308	0.274	883	246	70	56	45	L12, O10, R9
35.2	0.164	0.297	0.282	2340	739	211	229	139	L12, O10, R9
23.1	0.029	0.316	0.251	352	98	28	22	18	L12, O10, R9
31.4	0.059	0.258	0.23	741	207	59	47	38	L12, O10, R9

Industrial Designation or Chemical Name	Chemical Formula	CAS RN	Atmospheric Abundance[a]	WMO (2018) Total Lifetime (years)	WMO (2022) Total Lifetime (years)	Tropospheric (OH Reactive Loss) Lifetime 2022 (years)
HCFC-223bc	$CHF_2CClFCCl_3$	147728-32-3		10.6	10.6	15.1
HCFC-223ca	$CHCl_2CF_2CCl_2F$	422-52-6		1.38	1.38	1.47
HCFC-223cb	$CHClFCF_2CCl_3$	422-50-4		3.88	3.88	4.45
HCFC-223da	$CCl_2FCHClCClF_2$	431-83-4		6.48	6.48	7.86
HCFC-223db	$CCl_3CHClCF_3$	431-81-2		6.47	6.47	8.02
HCFC-223ea	$CCl_2FCHFCCl_2F$	–		6.28	6.28	7.74
HCFC-223eb	$CCl_3CHFCClF_2$	54002-59-4		6.46	6.47	8.02
HCFC-224aa	$CHClFCCl_2CF_3$	139754-75-9		3.15	3.15	3.54
HCFC-224ab	$CHF_2CCl_2CClF_2$	422-32-2		11.3	11.3	15.1
HCFC-224ba	$CHCl_2CClFCF_3$	422-47-9		1.39	1.39	1.47
HCFC-224bb	$CHClFCClFCClF_2$	422-42-4		4.1	4.09	4.45
HCFC-224bc	$CHF_2CClFCCl_2F$	139754-76-0		11.3	11.3	15.1
HCFC-224ca	$CHCl_2CF_2CClF_2$	422-54-8		1.79	1.8	1.92
HCFC-224cb	$CHClFCF_2CCl_2F$	422-53-7		1.57	1.57	1.64
HCFC-224cc	$CHF_2CF_2CCl_3$	422-51-5		12.5	12.5	19
HCFC-224da	$CClF_2CHClCClF_2$	431-85-6		10.4	10.4	12.3
HCFC-224db	$CCl_2FCHClCF_3$	431-84-5		9.39	9.4	12
HCFC-224ea	$CCl_2FCHFCClF_2$	53063-53-9		9.16	9.15	11.6
HCFC-224eb	CCl_3CHFCF_3	53063-52-8		8.88	8.9	11.9
HCFC-225aa	$CHF_2CCl_2CF_3$	128903-21-9		11.8	11.8	15.1
HCFC-225ba	$CHClFCClFCF_3$	422-48-0		4.2	4.2	4.45
HCFC-225bb	$CHF_2CClFCClF_2$	422-44-6		15.9	16	19
HCFC-225ca	$CHCl_2CF_2CF_3$	422-56-0		1.9	1.9	2.03
HCFC-225cb	$CHClFCF_2CClF_2$	507-55-1		5.9	5.77	6.26
HCFC-225cc	$CHF_2CF_2CCl_2F$	13474-88-9		14.1	14.1	19
HCFC-225da	$CClF_2CHClCF_3$	431-86-7		16.3	16.3	19.5
HCFC-225ea	$CClF_2CHFCClF_2$	136013-79-1		15.3	15.3	18.1
HCFC-225eb	$CCl_2FCHFCF_3$	51346-64-6		13.4	13.4	17.7
HCFC-226ba	$CHF_2CClFCF_3$	422-57-1		17	17	19
HCFC-226ca	$CHClFCF_2CF_3$	422-55-9		5.47	5.48	5.8
HCFC-226cb	$CHF_2CF_2CClF_2$	431-87-8		21.6	21.6	24.7
HCFC-226da	$CF_3CHClCF_3$	359-58-0		27.7	27.7	32.6
HCFC-226ea	$CClF_2CHFCF_3$	51346-64-6		24.9	24.8	28.8
HCFC-231aa	$CHCl_2CCl_2CHClF$	–		0.799	0.805	0.839
HCFC-231ab	$CH_2ClCCl_2CCl_2F$	1538604-29-3		1.61	1.61	1.73
HCFC-231ac	$CH_2FCCl_2CCl_3$	–		2.33	2.32	2.55
HCFC-231ba	$CHCl_2CClFCHCl_2$	–		0.56	0.569	0.586
HCFC-231bb	$CH_2ClCClFCCl_3$	421-94-3		2.54	2.54	2.8
HCFC-231da	$CHCl_2CHClCCl_2F$	1538604-31-7		0.54	0.542	0.557
HCFC-231db	$CHClFCHClCCl_3$	1943659-45-7		1.34	1.34	1.43
HCFC-231ea	$CHCl_2CHFCCl_3$	–		0.76	0.768	0.799
HCFC-231fa	$CCl_2FCH_2CCl_3$	313696-58-1		6.26	6.26	7.71
HCFC-232aa	$CHClFCCl_2CHClF$	–		1.65	1.65	1.77
HCFC-232ab	$CHCl_2CCl_2CHF_2$	872817-81-7		1.01	1.02	1.07
HCFC-232ac	$CH_2ClCCl_2CClF_2$	1538604-30-6		2.56	2.56	2.8
HCFC-232ad	$CH_2FCCl_2CCl_2F$	–		2.33	2.32	2.55
HCFC-232ba	$CHCl_2CClFCHClF$	–		0.99	0.989	1.04
HCFC-232bb	$CH_2ClCClFCCl_2F$	1943659-44-6		2.56	2.56	2.8
HCFC-232bc	$CH_2FCClFCCl_3$	–		3.64	3.63	4.14

Stratospheric Lifetime 2022 (years)	ODP	Radiative Efficiency (well mixed) ($W\ m^{-2}\ ppb^{-1}$) [b]	Recommended Adjusted Effective Radiative Efficiency ($W\ m^{-2}\ ppb^{-1}$) [c]	GWP 20-yr	GWP 100-yr	GWP 500-yr	GTP 50-yr	GTP 100-yr	Footnotes *A: Atmospheric Abundance L: Lifetime O: Ozone Depletion Potential R: Radiative Metrics*
35.7	0.185	0.254	0.242	2200	725	207	256	138	L12, O10, R9
21.6	0.029	0.29	0.23	323	90	26	20	16	L12, O10, R9
30.2	0.073	0.259	0.235	919	258	73	59	47	L12, O10, R9
37.1	0.111	0.321	0.301	1880	551	157	136	102	L12, O10, R9
33.4	0.117	0.245	0.229	1430	419	119	103	78	L12, O10, R9
33.2	0.114	0.292	0.273	1660	485	138	118	90	L12, O10, R9
33.4	0.117	0.271	0.254	1590	464	132	114	86	L12, O10, R9
28.9	0.049	0.278	0.247	847	236	67	53	43	L12, O10, R9
44.6	0.141	0.314	0.301	3060	1030	295	390	198	L12, O10, R9
24.5	0.023	0.268	0.213	324	90	26	20	16	L12, O10, R9
51.2	0.047	0.304	0.277	1230	344	98	79	63	L12, O10, R9
44.6	0.141	0.318	0.305	3100	1050	299	396	201	L12, O10, R9
27.5	0.028	0.312	0.259	509	142	40	32	26	L12, O10, R9
35	0.022	0.301	0.244	419	116	33	26	21	L12, O10, R9
36.7	0.174	0.322	0.31	3350	1180	336	498	229	L12, O10, R9
67.1	0.096	0.36	0.344	3310	1090	310	376	206	L12, O10, R9
43.4	0.119	0.298	0.284	2550	811	231	254	153	L12, O10, R9
43.3	0.117	0.324	0.308	2710	856	244	261	161	L12, O10, R9
35.3	0.126	0.247	0.234	2020	633	180	189	119	L12, O10, R9
53.8	0.094	0.279	0.268	3030	1040	296	412	200	L12, O10, R9
74.3	0.025	0.279	0.254	1250	350	100	80	64	L12, O10, R9
99.5	0.069	0.326	0.315	4210	1650	472	915	347	L12, O10, R9
31.5	0.025	0.262	0.22	494	137	39	31	25	L5, O3, R2
73.3	0.033	0.314	0.294	1930	557	159	133	103	L5, O3, R2
55.2	0.11	0.355	0.342	4280	1580	452	766	318	L12, O10, R9
100	0.071	0.313	0.303	4090	1620	463	914	343	L12, O10, R9
98.7	0.068	0.35	0.339	4430	1700	486	900	351	L12, O10, R9
54.8	0.105	0.299	0.288	3500	1270	362	579	251	L12, O10, R9
161	0.019	0.278	0.27	4040	1630	468	963	354	L12, O10, R9
98	0.013	0.28	0.26	1780	509	145	120	94	L12, O10, R9
174	0.022	0.351	0.342	5680	2610	753	1890	665	L12, O10, R9
185	0.025	0.28	0.274	4960	2630	774	2230	842	L12, O10, R9
180	0.023	0.317	0.309	5400	2680	782	2140	773	L12, O10, R9
20	0.022	0.173	0.122	101	28	8	6	5	L12, O10, R9
23	0.042	0.212	0.173	285	79	23	18	14	L12, O10, R9
26.2	0.058	0.173	0.148	351	98	28	22	18	L12, O10, R9
20	0.015	0.174	0.11	64	18	5	4	3	L12, O10, R9
26.9	0.063	0.18	0.156	405	113	32	25	21	L12, O10, R9
20	0.015	0.209	0.13	72	20	6	4	4	L12, O10, R9
21.3	0.036	0.172	0.136	187	52	15	11	9	L12, O10, R9
20	0.021	0.184	0.127	100	28	8	6	5	L12, O10, R9
33.2	0.143	0.206	0.193	1180	344	98	84	64	L12, O10, R9
245	0.036	0.208	0.17	309	86	24	19	16	L12, O10, R9
20	0.024	0.188	0.14	157	44	12	10	8	L12, O10, R9
29.4	0.053	0.248	0.216	608	169	48	38	31	L12, O10, R9
26.2	0.05	0.24	0.206	526	146	42	33	27	L12, O10, R9
20	0.023	0.213	0.157	171	48	14	10	9	L12, O10, R9
29.4	0.053	0.247	0.215	605	168	48	38	31	L12, O10, R9
29.7	0.075	0.219	0.197	782	219	62	50	40	L12, O10, R9

Industrial Designation or Chemical Name	Chemical Formula	CAS RN	Atmospheric Abundance[a]	WMO (2018) Total Lifetime (years)	WMO (2022) Total Lifetime (years)	Tropospheric (OH Reactive Loss) Lifetime 2022 (years)
HCFC-232ca	$CHCl_2CF_2CHCl_2$	1112-14-7		0.7	0.711	0.737
HCFC-232cb	$CH_2ClCF_2CCl_3$	677-54-3		4.47	4.46	5.21
HCFC-232da	$CHCl_2CHClCClF_2$	67879-59-8		0.82	0.824	0.859
HCFC-232db	$CHClFCHClCCl_2F$	1943659-46-8		1.51	1.51	1.61
HCFC-232dc	$CHF_2CHClCCl_3$	–		2.83	2.83	3.15
HCFC-232ea	$CHCl_2CHFCCl_2F$	–		0.83	0.836	0.872
HCFC-232eb	$CHClFCHFCCl_3$	–		2.04	2.04	2.22
HCFC-232fa	$CCl_2FCH_2CCl_2F$	313696-57-0		9.23	9.22	12.5
HCFC-232fb	$CCl_3CH_2CClF_2$	460-89-9		10.2	10.2	14.4
HCFC-233aa	$CHClFCCl_2CHF_2$	–		2.63	2.63	2.87
HCFC-233ab	$CH_2ClCCl_2CF_3$	7125-83-9		2.57	2.57	2.8
HCFC-233ac	$CH_2FCCl_2CClF_2$	–		3.71	3.7	4.14
HCFC-233ba	$CHClFCClFCHClF$	–		2.1	2.11	2.23
HCFC-233bb	$CHCl_2CClFCHF_2$	13058-99-6		1.27	1.27	1.34
HCFC-233bc	$CH_2ClCClFCClF_2$	421-95-4		4.75	4.75	5.21
HCFC-233bd	$CH_2FCClFCCl_2F$	–		3.71	3.7	4.14
HCFC-233ca	$CHCl_2CF_2CHClF$	131221-36-8		1.27	1.27	1.34
HCFC-233cb	$CH_2ClCF_2CCl_2F$	421-99-8		4.57	4.57	5.21
HCFC-233cc	$CH_2FCF_2CCl_3$	131211-71-7		6.26	6.26	7.71
HCFC-233da	$CHCl_2CHClCF_3$	431-51-6		0.896	0.897	0.939
HCFC-233db	$CHClFCHClCClF_2$	1943659-38-8		2.37	2.37	2.52
HCFC-233dc	$CHF_2CHClCCl_2F$	–		3.55	3.56	3.96
HCFC-233ea	$CHCl_2CHFCClF_2$	–		0.982	0.981	1.03
HCFC-233eb	$CHClFCHFCCl_2F$	54377-32-1		2.32	2.32	2.51
HCFC-233ec	$CHF_2CHFCCl_3$	54306-56-8		4.13	4.13	4.77
HCFC-233fa	$CCl_2FCH_2CClF_2$	333-26-6		15.4	15.4	23.3
HCFC-233fb	$CCl_3CH_2CF_3$	7125-84-0		16.4	16.4	29.3
HCFC-234aa	$CHF_2CCl_2CHF_2$	17705-30-5		6.51	6.51	7.54
HCFC-234ab	$CH_2FCCl_2CF_3$	149329-24-8		3.76	3.76	4.14
HCFC-234ba	$CHClFCClFCHF_2$	425-94-5		3.39	3.4	3.61
HCFC-234bb	$CH_2ClCClFCF_3$	149329-25-9		4.84	4.83	5.21
HCFC-234bc	$CH_2FCClFCClF_2$	149329-26-0		7.01	7.01	7.71
HCFC-234ca	$CHClFCF_2CHClF$	70341-81-0		2.74	2.74	2.9
HCFC-234cb	$CHCl_2CF_2CHF_2$	4071-01-6		1.65	1.64	1.74
HCFC-234cc	$CH_2ClCF_2CClF_2$	422-00-5		9.46	9.43	10.6
HCFC-234cd	$CH_2FCF_2CCl_2F$	70192-63-1		6.64	6.64	7.71
HCFC-234da	$CHClFCHClCF_3$	146916-90-7		2.67	2.67	2.82
HCFC-234db	$CHF_2CHClCClF_2$	1945188-10-2		5.69	5.69	6.18
HCFC-234ea	$CHCl_2CHFCF_3$	53063-54-0		1.06	1.06	1.11
HCFC-234eb	$CHClFCHFCClF_2$	139754-77-1		2.88	2.87	3.04
HCFC-234ec	$CHF_2CHFCCl_2F$	–		5.32	5.33	6.04
HCFC-234fa	$CClF_2CH_2CClF_2$	76140-39-1		31	31	43.4
HCFC-234fb	$CCl_2FCH_2CF_3$	64712-27-2		45	37	97.8
HCFC-235ba	$CHF_2CClFCHF_2$	144429-90-3		8.8	8.81	9.5
HCFC-235bb	$CH_2FCClFCF_3$	230956-35-1		7.21	7.2	7.71
HCFC-235ca	$CH_2ClCF_2CF_3$	28103-66-4		9.82	9.78	10.6
HCFC-235cb	$CHClFCF_2CHF_2$	422-02-6		4.45	4.45	4.7
HCFC-235cc	$CH_2FCF_2CClF_2$	679-99-2		14.2	14.2	15.7
HCFC-235da	$CHF_2CHClCF_3$	134251-06-2		7.55	7.55	8.09

Stratospheric Lifetime 2022 (years)	ODP	Radiative Efficiency (well mixed) ($W\ m^{-2}\ ppb^{-1}$) [b]	Recommended Adjusted Effective Radiative Efficiency ($W\ m^{-2}\ ppb^{-1}$) [c]	GWP 20-yr	GWP 100-yr	GWP 500-yr	GTP 50-yr	GTP 100-yr	Footnotes *A: Atmospheric Abundance L: Lifetime O: Ozone Depletion Potential R: Radiative Metrics*
20	0.017	0.185	0.125	98	27	8	6	5	L12, O10, R9
31.2	0.09	0.223	0.204	987	278	79	64	51	L12, O10, R9
20	0.019	0.244	0.172	156	43	12	10	8	L12, O10, R9
24	0.033	0.24	0.193	321	89	25	20	16	L12, O10, R9
27.8	0.06	0.204	0.179	556	155	44	35	28	L12, O10, R9
20	0.019	0.224	0.159	146	41	12	9	7	L12, O10, R9
25.1	0.045	0.209	0.176	395	110	31	25	20	L12, O10, R9
35.2	0.176	0.269	0.256	2280	722	206	222	136	L12, O10, R9
35.6	0.194	0.247	0.236	2260	736	210	250	140	L12, O10, R9
31.6	0.043	0.208	0.182	569	158	45	36	29	L12, O10, R9
31.4	0.042	0.221	0.192	587	163	47	37	30	L12, O10, R9
35.2	0.057	0.277	0.25	1090	306	87	69	56	L12, O10, R9
37.8	0.031	0.233	0.198	497	138	39	31	25	L12, O10, R9
23.3	0.023	0.216	0.168	254	71	20	16	13	L12, O10, R9
53.3	0.057	0.276	0.254	1410	399	114	92	73	L12, O10, R9
35.2	0.057	0.278	0.251	1100	307	88	70	56	L12, O10, R9
23.3	0.023	0.218	0.17	257	71	20	16	13	L12, O10, R9
37.3	0.069	0.268	0.246	1320	372	106	86	68	L12, O10, R9
33.2	0.1	0.258	0.242	1720	501	143	122	93	L12, O10, R9
20	0.017	0.196	0.142	152	42	12	9	8	L12, O10, R9
40.1	0.034	0.269	0.232	654	182	52	41	33	L12, O10, R9
34.8	0.055	0.266	0.239	1010	282	80	64	51	L12, O10, R9
20.4	0.019	0.239	0.177	207	57	16	13	10	L12, O10, R9
30.2	0.038	0.25	0.215	593	165	47	37	30	L12, O10, R9
30.6	0.068	0.254	0.23	1120	314	90	72	58	L12, O10, R9
45.7	0.207	0.327	0.316	4170	1610	459	856	333	L12, O10, R9
37.3	0.247	0.21	0.204	2780	1100	316	628	235	L12, O10, R9
47.4	0.062	0.211	0.198	1590	464	132	115	86	L12, O10, R9
40.8	0.039	0.238	0.215	1040	291	83	66	53	L12, O10, R9
56.9	0.028	0.237	0.212	930	260	74	59	47	L12, O10, R9
67	0.035	0.234	0.216	1330	376	107	87	69	L12, O10, R9
77.3	0.045	0.292	0.275	2340	695	198	177	129	L12, O10, R9
51	0.025	0.23	0.202	716	199	57	45	36	L12, O10, R9
29.2	0.02	0.24	0.196	417	116	33	26	21	L12, O10, R9
85.1	0.054	0.278	0.265	2830	900	257	283	170	L12, O10, R9
47.6	0.063	0.297	0.278	2260	665	190	166	123	L12, O10, R9
50.3	0.024	0.234	0.204	705	196	56	44	36	L12, O10, R9
71.6	0.039	0.289	0.268	1910	550	157	131	101	L12, O10, R9
23.1	0.014	0.213	0.16	220	61	17	14	11	L12, O10, R9
52.4	0.026	0.268	0.236	876	244	70	55	44	L12, O10, R9
45.1	0.052	0.293	0.272	1830	522	149	123	96	L12, O10, R9
108	0.132	0.353	0.346	6540	3700	1100	3300	1320	L12, O10, R9
59.7	0.35	0.272	0.267	5290	3310	1020	3140	1400	L2, O9, R9
121	0.018	0.235	0.223	2490	777	222	230	146	L12, O10, R9
110	0.017	0.254	0.239	2280	681	194	176	127	L12, O10, R9
126	0.018	0.223	0.212	2550	820	234	266	155	L12, O10, R9
85.2	0.014	0.255	0.2331	1450	410	117	94	75	L12, O10, R9
146	0.021	0.289	0.279	4220	1560	447	764	315	L12, O10, R9
112	0.017	0.244	0.23	2280	687	196	182	128	L12, O10, R9

Industrial Designation or Chemical Name	Chemical Formula	CAS RN	Atmospheric Abundance[a]	WMO (2018) Total Lifetime (years)	WMO (2022) Total Lifetime (years)	Tropospheric (OH Reactive Loss) Lifetime 2022 (years)
HCFC-235ea	$CHClFCHFCF_3$	134251-06-2		7.36	7.36	7.88
HCFC-235eb	$CHF_2CHFCClF_2$	162102-07-0		3.18	3.18	3.33
HCFC-235fa	$CClF_2CH_2CF_3$	677-55-4		61.7	61.8	88.6
HCFC-241aa	CH_2ClCCl_2CHClF	–		1.43	1.43	1.52
HCFC-241ab	$CH_2FCCl_2CHCl_2$	–		0.77	0.772	0.803
HCFC-241ac	$CH_3CCl_2CCl_2F$	7126-06-9		5.18	5.18	6.18
HCFC-241ba	$CH_2ClCClFCHCl_2$	3175-26-6		0.79	0.793	0.826
HCFC-241bb	$CH_3CClFCCl_3$	3175-25-5		7.76	7.74	10
HCFC-241da	$CHCl_2CHClCHClF$	21981-25-9		0.56	0.565	0.581
HCFC-241db	$CH_2ClCHClCCl_2F$	666-27-3		0.53	0.534	0.549
HCFC-241dc	$CH_2FCHClCCl_3$	84816-05-7		0.75	0.756	0.786
HCFC-241ea	$CHCl_2CHFCHCl_2$	–		0.42	0.42	0.429
HCFC-241eb	$CH_2ClCHFCCl_3$	–		1.05	1.05	1.11
HCFC-241fa	$CHCl_2CH_2CCl_2F$	175897-94-6		0.53	0.54	0.555
HCFC-241fb	$CHClFCH_2CCl_3$	23153-22-2		1.48	1.48	1.59
HCFC-242aa	$CHF_2CCl_2CH_2Cl$	–		2.13	2.12	2.29
HCFC-242ab	CH_2FCCl_2CHClF	–		1.78	1.78	1.91
HCFC-242ac	$CH_3CCl_2CClF_2$	7126-05-8		8.09	8.08	10
HCFC-242ba	$CHClFCClFCH_2Cl$	7164-14-9		1.99	2	2.11
HCFC-242bb	$CHCl_2CClFCH_2F$	–		1.03	1.04	1.09
HCFC-242bc	$CH_3CClFCCl_2F$	7126-04-7		8.09	8.08	10
HCFC-242ca	$CHCl_2CF_2CH_2Cl$	–		1.09	1.09	1.15
HCFC-242cb	$CH_3CF_2CCl_3$	1112-05-6		12.3	12.3	18.7
HCFC-242da	$CHClFCHClCHClF$	–		1.32	1.32	1.38
HCFC-242db	$CHCl_2CHClCHF_2$	1980063-50-0		0.73	0.733	0.761
HCFC-242dc	$CH_2ClCHClCClF_2$	431-24-3		1.2	1.2	1.25
HCFC-242dd	$CH_2FCHClCCl_2F$	–		0.83	0.835	0.871
HCFC-242ea	$CHCl_2CHFCHClF$	2106760-91-0		0.72	0.728	0.756
HCFC-242eb	$CH_2ClCHFCCl_2F$	–		1.24	1.24	1.31
HCFC-242ec	$CH_2FCHFCCl_3$	–		1.7	1.71	1.84
HCFC-242fa	$CHCl_2CH_2CClF_2$	460-63-9		0.74	0.74	0.768
HCFC-242fb	$CHClFCH_2CCl_2F$	175897-95-7		1.61	1.6	1.71
HCFC-242fc	$CHF_2CH_2CCl_3$	213248-60-3		4.14	4.14	4.78
HCFC-243aa	$CHF_2CCl_2CH_2F$	155329-34-3		2.99	2.99	3.25
HCFC-243ab	$CH_3CCl_2CF_3$	7126-01-4		8.33	8.32	10
HCFC-243ba	$CHF_2CClFCH_2Cl$	–		3.63	3.64	3.88
HCFC-243bb	$CHFClCClFCH_2F$	1379241-46-9		2.67	2.67	2.82
HCFC-243bc	$CH_3CClFCF_2Cl$	7126-00-3		15.6	15.6	18.7
HCFC-243ca	CH_2ClCF_2CHClF	67406-68-2		2.89	2.96	3.14
HCFC-243cb	$CHCl_2CF_2CH_2F$	70192-70-0		1.46	1.46	1.54
HCFC-243cc	$CH_3CF_2CFCl_2$	7125-99-7		18	18.2	27.1
HCFC-243da	$CHF_2CHClCHFCl$	338-75-0		1.97	1.97	2.07
HCFC-243db	$CH_2ClCHClCF_3$	338-75-0		1.44	1.45	1.51
HCFC-243dc	$CH_2FCHClCF_2Cl$	199171-49-8		2.03	2.03	2.13
HCFC-243ea	$CHFClCHFCHFCl$	151771-08-3		1.57	1.57	1.64
HCFC-243eb	$CHCl_2CHFCHF_2$	1081835-90-6		0.9	0.898	0.938
HCFC-243ec	$CH_2ClCHFCF_2Cl$	149329-27-1		1.7	1.7	1.78
HCFC-243ed	$CH_2FCHFCFCl_2$	–		2.03	2.03	2.17
HCFC-243fa	$CHCl_2CH_2CF_3$	460-69-5		0.78	0.781	0.813

Stratospheric Lifetime 2022 (years)	ODP	Radiative Efficiency (well mixed) ($W\ m^{-2}\ ppb^{-1}$) [b]	Recommended Adjusted Effective Radiative Efficiency ($W\ m^{-2}\ ppb^{-1}$) [c]	GWP 20-yr	GWP 100-yr	GWP 500-yr	GTP 50-yr	GTP 100-yr	Footnotes *A: Atmospheric Abundance L: Lifetime O: Ozone Depletion Potential R: Radiative Metrics*
111	0.017	0.244	0.229	2230	667	190	174	124	L12, O10, R9
69.4	0.012	0.305	0.272	1230	342	98	77	62	L12, O10, R9
204	0.051	0.306	0.302	7250	5880	2110	6120	3770	L12, O10, R9
23.5	0.035	0.139	0.111	190	53	15	12	10	L12, O10, R9
20	0.02	0.13	0.0902	84	23	7	5	4	L12, O10, R9
32.1	0.112	0.201	0.186	1130	321	92	75	59	L12, O10, R9
20	0.02	0.168	0.118	112	31	9	7	6	L12, O10, R9
34.3	0.163	0.197	0.186	1590	480	137	129	90	L12, O10, R9
20	0.014	0.151	0.0952	65	18	5	4	3	L12, O10, R9
20	0.014	0.184	0.114	73	20	6	4	4	L12, O10, R9
20	0.019	0.159	0.11	100	28	8	6	5	L12, O10, R9
20	0.011	0.138	0.0778	39	11	3	2	2	L12, O10, R9
20	0.027	0.159	0.119	150	42	12	9	8	L12, O10, R9
20	0.014	0.173	0.107	69	19	5	4	3	L12, O10, R9
22.2	0.037	0.176	0.1417	252	70	20	16	13	L12, O10, R9
29.3	0.039	0.151	0.128	355	99	28	22	18	L12, O10, R9
27.2	0.034	0.153	0.127	296	82	23	18	15	L12, O10, R9
41.9	0.125	0.236	0.224	2150	658	188	182	123	L12, O10, R9
36.7	0.033	0.176	0.148	387	108	31	24	20	L12, O10, R9
21	0.021	0.174	0.13	177	49	14	11	9	L12, O10, R9
41.9	0.125	0.252	0.239	2300	702	200	194	131	L12, O10, R9
21.6	0.022	0.185	0.14	200	55	16	12	10	L12, O10, R9
36.3	0.206	0.258	0.248	3180	1110	316	460	215	L12, O10, R9
29.2	0.024	0.179	0.141	243	68	19	15	12	L12, O10, R9
20	0.015	0.169	0.116	111	31	9	7	6	L12, O10, R9
27.6	0.023	0.214	0.165	259	72	21	16	13	L12, O10, R9
20	0.017	0.217	0.154	168	47	13	10	8	L12, O10, R9
20	0.015	0.17	0.116	111	31	9	7	6	L12, O10, R9
23	0.025	0.207	0.161	261	73	21	16	13	L12, O10, R9
23.5	0.034	0.205	0.169	378	105	30	23	19	L12, O10, R9
20	0.015	0.214	0.147	142	40	11	9	7	L12, O10, R9
26.1	0.031	0.239	0.195	408	113	32	25	21	L12, O10, R9
30.6	0.075	0.21	0.191	1020	287	82	66	53	L12, O10, R9
37.3	0.036	0.171	0.151	647	180	51	41	33	L12, O10, R9
49.3	0.085	0.216	0.204	2200	677	193	191	127	L12, O10, R9
58	0.033	0.161	0.145	753	211	60	48	39	L12, O10, R9
49.7	0.027	0.179	0.156	597	166	47	37	30	L12, O10, R9
94.2	0.088	0.269	0.26	4170	1620	462	873	336	L12, O10, R9
52.4	0.035	0.204	0.18	763	213	61	48	39	L12, O10, R9
27.3	0.02	0.181	0.145	304	85	24	19	15	L12, O10, R9
55.3	0.19	0.293	0.285	4920	2060	591	1300	464	L2, O9, R9
41.9	0.022	0.189	0.159	450	125	36	28	23	L12, O10, R9
34.5	0.018	0.174	0.139	290	80	23	18	15	L12, O10, R9
42.6	0.023	0.236	0.199	580	161	46	36	29	L12, O10, R9
36.3	0.019	0.207	0.168	379	105	30	23	19	L12, O10, R9
20.8	0.014	0.192	0.139	179	50	14	11	9	L12, O10, R9
38.3	0.02	0.214	0.176	430	119	34	27	22	L12, O10, R9
31.9	0.026	0.248	0.209	609	169	48	38	31	L12, O10, R9
20	0.012	0.174	0.122	137	38	11	8	7	L12, O10, R9

Industrial Designation or Chemical Name	Chemical Formula	CAS RN	Atmospheric Abundance[a]	WMO (2018) Total Lifetime (years)	WMO (2022) Total Lifetime (years)	Tropospheric (OH Reactive Loss) Lifetime 2022 (years)
HCFC-243fb	$CHFClCH_2CF_2Cl$	139754-78-2		2.24	2.24	2.36
HCFC-243fc	$CHF_2CH_2CFCl_2$	213248-61-4		5.07	5.07	5.73
HCFC-244ba	$CH_2FCClFCHF_2$	149329-28-2		5.17	5.18	5.49
HCFC-244bb	$CH_3CClFCF_3$	421-73-8		16.6	16.6	18.7
HCFC-244ca	$CH_2ClCF_2CHF_2$	679-85-6		6.39	6.39	6.82
HCFC-244cb	CH_2FCF_2CHFCl	67406-66-0		4.02	4.02	4.24
HCFC-244cc	$CH_3CF_2CF_2Cl$	421-75-0		31.2	31.2	38.1
HCFC-244da	$CHF_2CHClCHF_2$	19041-02-2		3.88	3.88	4.09
HCFC-244db	$CH_2FCHClCF_3$	117970-90-8		2.44	2.43	2.54
HCFC-244ea	$CHF_2CHFCHFCl$	149447-91-6		2.39	2.39	2.5
HCFC-244eb	$CH_2ClCHFCF_3$	151771-09-4		2.04	2.04	2.12
HCFC-244ec	$CH_2FCHFCF_2Cl$	149448-09-9		2.88	2.88	3.01
HCFC-244fa	$CHFClCH_2CF_3$	149329-29-3		2.37	2.38	2.48
HCFC-244fb	$CHF_2CH_2CF_2Cl$	2730-64-5		7.76	7.76	8.35
HCFC-251aa	$CH_2FCCl_2CH_2Cl$	70192-89-1		1.26	1.27	1.34
HCFC-251ab	CH_3CCl_2CHFCl	–		1.73	1.73	1.85
HCFC-251ba	$CH_2ClCClFCH_2Cl$	7126-16-1		1.34	1.34	1.4
HCFC-251bb	$CH_3CClFCHCl_2$	3175-24-4		1.02	1.02	1.07
HCFC-251da	$CH_2ClCHClCHFCl$	339202-89-0		0.69	0.694	0.719
HCFC-251db	$CH_2FCHClCHCl_2$	–		0.4	0.408	0.416
HCFC-251dc	$CH_3CHClCFCl_2$	421-41-0		0.52	0.521	0.535
HCFC-251ea	$CH_2ClCHFCHCl_2$	76937-36-5		0.47	0.477	0.489
HCFC-251eb	$CH_3CHFCCl_3$	1448144-70-4		0.68	0.685	0.709
HCFC-251fa	$CHClFCH_2CCl_2H$	2106760-90-9		0.33	0.333	0.339
HCFC-251fb	$CH_2ClCH_2CCl_2F$	818-99-5		0.45	0.456	0.467
HCFC-251fc	$CH_2FCH_2CCl_3$	2035078-31-8		0.65	0.654	0.676
HCFC-252aa	$CH_2FCCl_2CH_2F$	154193-88-1		1.94	1.94	2.07
HCFC-252ab	$CH_3CCl_2CHF_2$	–		4.41	4.41	4.93
HCFC-252ba	$CH_2ClCClFCH_2F$	70192-74-4		2.19	2.2	2.31
HCFC-252bb	$CH_3CClFCHClF$	362631-58-1		2.87	2.87	3.04
HCFC-252ca	$CH_2ClCF_2CH_2Cl$	1112-36-3		2.47	2.47	2.61
HCFC-252cb	$CH_3CF_2CHCl_2$	1112-01-2		1.19	1.19	1.25
HCFC-252da	$CH_2ClCHClCHF_2$	82578-00-5		1	1	1.04
HCFC-252db	$CH_2FCHClCHClF$	–		1.15	1.15	1.2
HCFC-252dc	$CH_3CHClCClF_2$	7126-15-0		0.77	0.771	0.799
HCFC-252ea	$CH_2ClCHFCHClF$	111483-26-2		1.02	1.02	1.06
HCFC-252eb	$CH_2FCHFCHCl_2$	–		0.65	0.648	0.67
HCFC-252ec	$CH_3CHFCCl_2F$	151771-10-7		0.84	0.845	0.882
HCFC-252fa	$CHClFCH_2CHClF$	1378824-14-6		1.15	1.14	1.19
HCFC-252fb	$CHCl_2CH_2CHF_2$	131404-17-6		0.66	0.661	0.684
HCFC-252fc	$CH_2ClCH_2CClF_2$	819-00-1		0.94	0.936	0.972
HCFC-252fd	$CH_2FCH_2CCl_2F$	121612-64-4		0.7	0.706	0.732
HCFC-253ba	$CH_2FCClFCH_2F$	151771-11-8		3.66	3.67	3.86
HCFC-253bb	$CH_3CClFCHF_2$	69202-10-4		7.85	7.85	8.46
HCFC-253ca	$CH_2ClCF_2CH_2F$	56758-54-4		4.23	4.23	4.47
HCFC-253cb	CH_3CF_2CHClF	70192-76-6		3.48	3.48	3.66
HCFC-253da	$CH_2FCHClCHF_2$	–		1.67	1.67	1.74
HCFC-253db	$CH_3CHClCF_3$	421-47-6		1.02	1.02	1.06
HCFC-253ea	$CH_2ClCHFCHF_2$	121612-65-5		1.44	1.44	1.5

Stratospheric Lifetime 2022 (years)	ODP	Radiative Efficiency (well mixed) ($W\ m^{-2}\ ppb^{-1}$) [b]	Recommended Adjusted Effective Radiative Efficiency ($W\ m^{-2}\ ppb^{-1}$) [c]	GWP 20-yr	GWP 100-yr	GWP 500-yr	GTP 50-yr	GTP 100-yr	Footnotes *A: Atmospheric Abundance L: Lifetime O: Ozone Depletion Potential R: Radiative Metrics*
45.1	0.024	0.266	0.228	733	204	58	46	37	L12, O10, R9
44	0.056	0.281	0.259	1840	524	150	122	96	L12, O10, R9
90.5	0.017	0.183	0.169	1360	388	111	91	71	L12, O10, R9
148	0.027	0.249	0.241	4420	1770	505	1020	378	L12, O10, R9
101	0.018	0.184	0.172	1670	487	139	119	90	L12, O10, R9
78.6	0.015	0.195	0.177	1120	315	90	72	58	L12, O10, R9
173	0.039	0.28	0.274	6370	3620	1080	3240	1300	L12, O10, R9
77	0.015	0.201	0.182	1120	313	89	71	57	L12, O10, R9
57.4	0.012	0.19	0.164	634	177	50	40	32	L12, O10, R9
56.6	0.012	0.22	0.19	723	201	57	45	37	L12, O10, R9
50.8	0.011	0.18	0.152	494	137	39	31	25	L12, O10, R9
64	0.013	0.254	0.223	1020	284	81	64	52	L12, O10, R9
56.3	0.012	0.217	0.187	708	197	56	44	36	L12, O10, R9
111	0.02	0.301	0.284	3220	976	278	263	182	L12, O10, R9
23.3	0.028	0.091	0.0711	131	36	10	8	7	L12, O10, R9
26.9	0.037	0.129	0.106	266	74	21	16	13	L12, O10, R9
29.4	0.027	0.118	0.0927	180	50	14	11	9	L12, O10, R9
20.8	0.023	0.143	0.107	158	44	13	10	8	L12, O10, R9
20	0.016	0.117	0.079	80	22	6	5	4	L12, O10, R9
20	0.009	0.107	0.0598	35	10	3	2	2	L12, O10, R9
20	0.012	0.192	0.118	89	25	7	5	4	L12, O10, R9
20	0.011	0.125	0.0744	52	14	4	3	3	L12, O10, R9
20	0.016	0.194	0.13	129	36	10	8	6	L12, O10, R9
20	0.008	0.138	0.071	34	10	3	2	2	L12, O10, R9
20	0.011	0.173	0.101	67	19	5	4	3	L12, O10, R9
20	0.015	0.149	0.0985	93	26	7	6	5	L12, O10, R9
31	0.029	0.117	0.0978	305	85	24	19	15	L12, O10, R9
41.9	0.056	0.163	0.149	1040	294	84	67	54	L12, O10, R9
44	0.027	0.112	0.096	340	95	27	21	17	L12, O10, R9
50.9	0.032	0.164	0.145	668	186	53	42	34	L12, O10, R9
47	0.029	0.142	0.123	488	136	39	30	25	L12, O10, R9
24.4	0.019	0.188	0.145	278	77	22	17	14	L12, O10, R9
26.7	0.016	0.119	0.0883	142	40	11	9	7	L12, O10, R9
29.4	0.017	0.127	0.0974	180	50	14	11	9	L12, O10, R9
22.2	0.013	0.211	0.146	181	50	14	11	9	L12, O10, R9
27.2	0.016	0.146	0.109	179	50	14	11	9	L12, O10, R9
20	0.011	0.136	0.0895	93	26	7	6	5	L12, O10, R9
20	0.015	0.24	0.171	233	65	18	14	12	L12, O10, R9
29.4	0.017	0.182	0.139	255	71	20	16	13	L12, O10, R9
20	0.011	0.168	0.111	118	33	9	7	6	L12, O10, R9
25.5	0.015	0.203	0.148	223	62	18	14	11	L12, O10, R9
20	0.012	0.223	0.151	172	48	14	11	9	L12, O10, R9
72.9	0.017	0.139	0.126	831	233	66	53	43	L12, O10, R9
108	0.024	0.194	0.183	2380	722	206	196	135	L12, O10, R9
79.3	0.018	0.147	0.134	1010	285	81	65	52	L12, O10, R9
70.8	0.017	0.204	0.182	1140	319	91	72	58	L12, O10, R9
43.6	0.012	0.14	0.115	348	97	28	21	18	L12, O10, R9
30.2	0.009	0.16	0.12	222	62	18	14	11	L12, O10, R9
39.2	0.011	0.14	0.112	292	81	23	18	15	L12, O10, R9

Industrial Designation or Chemical Name	Chemical Formula	CAS RN	Atmospheric Abundance[a]	WMO (2018) Total Lifetime (years)	WMO (2022) Total Lifetime (years)	Tropospheric (OH Reactive Loss) Lifetime 2022 (years)
HCFC-253eb	$CH_2FCHFCHClF$	151771-12-9		1.5	1.5	1.56
HCFC-253ec	$CH_3CHFCClF_2$	134251-05-1		1.13	1.13	1.17
HCFC-253fa	$CHClFCH_2CHF_2$	149329-30-6		1.83	1.82	1.9
HCFC-253fb	$CH_2ClCH_2CF_3$	460-35-5		1.05	1.05	1.09
HCFC-253fc	$CH_2FCH_2CClF_2$	83124-56-5		1.48	1.48	1.54
HCFC-261aa	$CH_3CCl_2CH_2F$	–		1.06	1.06	1.11
HCFC-261ba	$CH_3CClFCH_2Cl$	420-97-3		2.19	2.19	2.31
HCFC-261da	$CH_2ClCHClCH_2F$	453-01-0		0.45	0.452	0.462
HCFC-261db	$CH_3CHClCHClF$	7799-55-5		0.47	0.467	0.478
HCFC-261ea	$CH_2ClCHFCH_2Cl$	816-38-6		0.54	0.539	0.554
HCFC-261eb	$CH_3CHFCHCl_2$	53074-31-0		0.31	0.31	0.315
HCFC-261fa	CH_2ClCH_2CHClF	83124-60-1		0.57	0.574	0.591
HCFC-261fb	$CH_2FCH_2CHCl_2$	53074-30-9		0.33	0.333	0.339
HCFC-261fc	$CH_3CH_2CCl_2F$	7799-56-6		0.61	0.618	0.638
HCFC-262ba	$CH_3CClFCH_2F$	362631-59-2		3.4	3.41	3.59
HCFC-262ca	$CH_3CF_2CH_2Cl$	420-99-5		3.2	3.17	3.33
HCFC-262da	$CH_2FCHClCH_2F$	102738-79-4		0.92	0.924	0.956
HCFC-262db	$CH_3CHClCHF_2$	430-93-3		0.64	0.642	0.662
HCFC-262ea	$CH_2FCHFCH_2Cl$	37161-81-2		0.83	0.828	0.856
HCFC-262eb	$CH_3CHFCHFCl$	430-96-6		0.66	0.664	0.685
HCFC-262fa	$CH_2ClCH_2CHF_2$	83124-57-6		0.8	0.801	0.828
HCFC-262fb	CH_2FCH_2CHFCl	151771-13-0		0.87	0.872	0.902
HCFC-262fc	$CH_3CH_2CF_2Cl$	421-02-3		1.2	1.2	1.24
HCFC-271ba	$CH_3CClFCH_3$	420-44-0		5	5.04	5.37
HCFC-271da	$CH_3CHClCH_2F$	20372-78-5		0.27	0.274	0.278
HCFC-271ea	CH_3CHFCH_2Cl	430-46-6		0.3	0.298	0.302
HCFC-271fa	$CH_2ClCH_2CH_2F$	462-38-4		0.34	0.339	0.345
HCFC-271fb	CH_3CH_2CHClF	430-55-7		0.49	0.494	0.506
Hydrofluorocarbons						
HFC-23	CHF_3	75-46-7	33.7 ppt	228	228	243
HFC-32	CH_2F_2	75-10-5	23.2 ppt	5.4	5.27	5.47
HFC-41	CH_3F	593-53-3		2.8	2.8	2.92
HFC-125	CHF_2CF_3	354-33-6	32.6 ppt	30	30.7	32.3
HFC-134	CHF_2CHF_2	359-35-3		10	10	10.5
HFC-134a	CH_2FCF_3	811-97-2	113.0 ppt	14	13.5	14.1
HFC-143	CH_2FCHF_2	430-66-0		3.6	3.57	3.7
HFC-143a	CH_3CF_3	420-46-2	25.6 ppt	51	51.8	57.2
HFC-152	CH_2FCH_2F	624-72-6		172 days (114–335 days)	0.473 (114–335 days)	0.485
HFC-152a	CH_3CHF_2	75-37-6	7.1 ppt	1.6	1.5	1.55
HFC-161	CH_3CH_2F	353-36-6		80 days (51–154 days)	0.217 (51–154 days)	0.219
HFC-227ca	$CF_3CF_2CHF_2$	2252-84-8		30	32.2	33.7
HFC-227ea	CF_3CHFCF_3	431-89-0	1.7 ppt	36	35.8	37.5
HFC-236ca	$CHF_2CF_2CHF_2$	680-00-2			11.4	11.8
HFC-236cb	$CH_2FCF_2CF_3$	677-56-5		13.4	13.4	14
HFC-236ea	CHF_2CHFCF_3	431-63-0		11.4	11.4	11.9
HFC-236fa	$CF_3CH_2CF_3$	690-39-1	0.20 ppt	213	213	253
HFC-245ca	$CH_2FCF_2CHF_2$	679-86-7		6.6	6.61	6.88
HFC-245cb	$CF_3CF_2CH_3$	1814-88-6		39.9	39.8	42.9
HFC-245ea	$CHF_2CHFCHF_2$	24270-66-4		3.2	3.26	3.37

Stratospheric Lifetime 2022 (years)	ODP	Radiative Efficiency (well mixed) ($W\ m^{-2}\ ppb^{-1}$) [b]	Recommended Adjusted Effective Radiative Efficiency ($W\ m^{-2}\ ppb^{-1}$) [c]	GWP 20-yr	GWP 100-yr	GWP 500-yr	GTP 50-yr	GTP 100-yr	Footnotes *A: Atmospheric Abundance L: Lifetime O: Ozone Depletion Potential R: Radiative Metrics*
40.4	0.011	0.153	0.123	334	93	26	21	17	L12, O10, R9
32.7	0.009	0.237	0.18	368	102	29	23	19	L12, O10, R9
46.4	0.012	0.207	0.172	566	157	45	35	29	L12, O10, R9
30.8	0.009	0.164	0.123	234	65	19	14	12	L12, O10, R9
39.9	0.011	0.239	0.192	514	143	41	32	26	L12, O10, R9
22.7	0.02	0.092	0.0687	133	37	11	8	7	L12, O10, R9
43.6	0.031	0.095	0.0808	324	90	26	20	16	L12, O10, R9
20	0.009	0.055	0.0319	26	7	2	2	1	L12, O10, R9
20	0.009	0.102	0.06	51	14	4	3	3	L12, O10, R9
20	0.01	0.075	0.0464	46	13	4	3	2	L12, O10, R9
20	0.006	0.121	0.0599	34	9	3	2	2	L12, O10, R9
20	0.011	0.114	0.0726	76	21	6	5	4	L12, O10, R9
20	0.006	0.104	0.0534	33	9	3	2	2	L12, O10, R9
20	0.012	0.206	0.134	152	42	12	9	8	L12, O10, R9
68.6	0.02	0.136	0.122	867	242	69	55	44	L12, O10, R9
65.6	0.019	0.131	0.116	767	214	61	48	39	L12, O10, R9
27.7	0.009	0.074	0.0538	104	29	8	6	5	L12, O10, R9
20.8	0.007	0.12	0.0788	106	29	8	6	5	L12, O10, R9
25.4	0.009	0.09	0.0639	111	31	9	7	6	L12, O10, R9
21.3	0.007	0.144	0.0958	133	37	11	8	7	L12, O10, R9
24.8	0.008	0.121	0.0851	143	40	11	9	7	L12, O10, R9
26.5	0.009	0.134	0.096	175	49	14	11	9	L12, O10, R9
33.7	0.011	0.214	0.165	415	115	33	26	21	L12, O10, R9
83.4	0.028	0.113	0.104	1270	362	103	84	67	L12, O10, R9
20	0.004	0.051	0.0237	16	4	1	<1	<1	L12, O10, R9
20	0.004	0.066	0.032	24	7	2	1	1	L12, O10, R9
20	0.004	0.053	0.0272	23	6	2	1	1	L12, O10, R9
20	0.007	0.105	0.0633	78	22	6	5	4	L12, O10, R9
3,636	0	0.193	0.192	12,400	14,700	10,600	15,500	15,200	A4, L5, O1, R2
146	0	0.12	0.111	2620	749	214	175	138	A4, L5, O1, R2
68.5	0	0.028	0.025	492	137	39	31	25	L2, L11, O1, R2
665	0	0.239	0.234	6790	3820	1140	3400	1350	A4, L5, L11, O1, R2
243	0	0.203	0.204	4110	1330	380	443	252	L2, O1, R2
313	0	0.173	0.167	4060	1470	420	679	292	A4, L5, L11, O1, R2
101	0	0.142	0.129	1310	365	104	83	67	L2, O1, R2
548	0	0.171	0.169	7900	5900	1980	6020	3340	A4, L5, O1, R2
20	0	0.077	0.047	81	22	6	5	4	L2, O1, R2
44.3	0	0.125	0.101	550	153	44	34	28	A4, L5, L11, O1, R2
20	0	0.038	0.016	17	5	1	1	<1	O1, R2
694	0	0.269	0.265	5500	3180	955	2890	1180	L14, O1, R2
754	0	0.278	0.273	5830	3580	1090	3370	1470	A4, L5, L15, O1, R2
268		0.318	0.305	4500	1520	435	581	293	L14, O1, R11
304	0	0.24	0.232	3770	1360	389	623	270	L14, O1, R2
268	0	0.277	0.267	3940	1330	381	509	256	L14, O1, R12
136	0	0.253	0.263	7820	9120	6340	9650	9310	L14, O1, R2
166	0	0.255	0.266	2980	874	249	217	162	L14, O1, RI3
551	0	0.255	0.249	6920	4510	1410	4370	2050	L14, O1, R2
93.2	0	0.18	0.172	999	279	80	63	51	L14, O1, R14

Industrial Designation or Chemical Name	Chemical Formula	CAS RN	Atmospheric Abundance[a]	WMO (2018) Total Lifetime (years)	WMO (2022) Total Lifetime (years)	Tropospheric (OH Reactive Loss) Lifetime 2022 (years)
HFC-245eb	$CH_2FCHFCF_3$	431-31-2		3.2	3.2	3.32
HFC-245fa	$CHF_2CH_2CF_3$	460-73-1	3.2 ppt	7.9	7.74	8.16
HFC-254ca	$CH_2FCF_2CH_2F$	813-75-2			2.56	2.65
HFC-254cb	$CH_3CF_2CHF_2$	40723-63-5			10.8	11.4
HFC-254ea	$CH_2FCHFCHF_2$	24270-68-6			1.94	2.01
HFC-254eb	CH_3CHFCF_3	421-48-7			2.25	2.33
HFC-254fa	$CHF_2CH_2CHF_2$	66794-30-7			3.99	4.14
HFC-254fb	$CH_2FCH_2CF_3$	460-36-6			1.38	1.43
HFC-263ca	$CH_3CF_2CH_2F$	811-94-9			3.67	3.81
HFC-263ea	$CH_2FCHFCH_2F$	66794-36-3			0.533	0.547
HFC-263eb	$CH_3CHFCHF_2$	66794-35-2			1.09	1.12
HFC-263fa	$CH_2FCH_2CHF_2$	24270-67-5			1.07	1.1
HFC-263fb	$CH_3CH_2CF_3$	421-07-8		1.1	1.12	1.16
HFC-272ca	$CH_3CF_2CH_3$	420-45-1		9	9.21	9.7
HFC-272ea	CH_3CHFCH_2F	62126-90-3			0.374	0.381
HFC-272fa	$CH_2FCH_2CH_2F$	462-39-5			0.186	0.188
HFC-272fb	$CH_3CH_2CHF_2$	430-61-5			0.706	0.727
HFC-281ea	CH_3CHFCH_3	420-26-8		27 days (19–46 days)	0.075 (19–46 days)	0.076
HFC-281fa	$CH_3CH_2CH_2F$	460-13-9			0.131	0.132
HFC-329p	$CHF_2CF_2CF_2CF_3$	375-17-7		32	31.5	33
HFC-329me	$CF_3CHFCF_2CF_3$	680-17-1			48.2	50.9
HFC-338q	$CH_2FCF_2CF_2CF_3$	662-35-1			14.6	15.3
HFC-338mce	$CHF_2CHFCF_2CF_3$	119450-58-7			9.27	9.66
HFC-338mec	$CHF_2CF_2CHFCF_3$	35230-11-6			11.7	12.2
HFC-338pcc	$CHF_2CF_2CF_2CHF_2$	377-36-6		13.5	13.5	14
HFC-338mf	$CF_3CH_2CF_2CF_3$	2924-29-0			184	214
HFC-338mee	$CF_3CHFCHFCF_3$	75995-72-1			11.4	11.9
HFC-347mcc	$CH_3CF_2CF_2CF_3$	662-00-0			36.8	39.5
HFC-347mce	$CH_2FCHFCF_2CF_3$	75995-85-6			3.35	3.47
HFC-347mec	$CH_2FCF_2CHFCF_3$	53005-35-9			4.22	4.38
HFC-347pcc	$CH_2FCF_2CF_2CHF_2$	119450-61-2			8.7	9.08
HFC-347mcf	$CHF_2CH_2CF_2CF_3$	161791-36-2			8.64	9.02
HFC-347mee	$CHF_2CHFCHFCF_3$	151868-61-0			5	5.2
HFC-347pce	$CHF_2CHFCF_2CHF_2$	119450-64-5			6.43	6.7
HFC-347mfc	$CHF_2CF_2CH_2CF_3$	119450-65-6			14.6	15.4
HFC-347mef	$CF_3CH_2CHFCF_3$	86884-16-4			8.53	8.9
HFC-356mce	$CH_3CHFCF_2CF_3$	161791-32-8			2.25	2.33
HFC-356mec	$CH_3CF_2CHFCF_3$	76523-97-2			13.8	14.6
HFC-356pcc	$CH_3CF_2CF_2CHF_2$	119450-66-7			10.8	11.4
HFC-356mcf	$CH_2FCH_2CF_2CF_3$	161791-33-9		1.2	1.22	1.26
HFC-356mee	$CH_2FCHFCHFCF_3$	119450-67-8			2.21	2.28
HFC-356pce	$CH_2FCHFCF_2CHF_2$	119450-68-9			2.87	2.98
HFC-356mfc	$CH_2FCF_2CH_2CF_3$	76546-55-9			4.84	5.03
HFC-356pec	$CH_2FCF_2CHFCHF_2$	114810-03-6			2.83	2.93
HFC-356mef	$CHF_2CH_2CHFCF_3$	158421-88-6			2.71	2.81
HFC-356mfe	$CHF_2CHFCH_2CF_3$	76523-98-3			3.05	3.16
HFC-356pcf	$CHF_2CH_2CF_2CHF_2$	119450-69-0			5.43	5.66
HFC-356pee	$CHF_2CHFCHFCHF_2$	392-45-0			3.17	3.29
HFC-356mff	$CF_3CH_2CH_2CF_3$	407-59-0			8.47	8.86

Stratospheric Lifetime 2022 (years)	ODP	Radiative Efficiency (well mixed) ($W\ m^{-2}\ ppb^{-1}$) [b]	Recommended Adjusted Effective Radiative Efficiency ($W\ m^{-2}\ ppb^{-1}$) [c]	GWP 20-yr	GWP 100-yr	GWP 500-yr	GTP 50-yr	GTP 100-yr	Footnotes *A: Atmospheric Abundance L: Lifetime O: Ozone Depletion Potential R: Radiative Metrics*
91.9	0	0.23	0.215	1230	342	98	77	62	L14, O1, R13
153.8	0	0.259	0.251	3190	966	276	260	180	A4, L5, O1, R13
74.5	0	0.17	0.148	782	218	62	49	40	L14, O1, R11
227	0	0.214	0.205	3830	1270	363	457	242	L14, O1, R11
59.2	0	0.201	0.168	673	187	53	42	34	L14, O1, R11
67.1	0	0.211	0.18	836	233	66	52	42	L14, O1, R11
107	0	0.259	0.235	1920	538	154	123	99	L14, O1, R11
44.3	0	0.186	0.148	422	117	33	26	21	L14, O1, R11
97.8	0	0.153	0.138	1230	344	98	78	63	L14, O1, R11
20	0	0.107	0.066	86	24	7	5	4	L14, O1, R11
35.7	0	0.15	0.114	304	84	24	19	15	L14, O1, R11
35.1	0	0.157	0.118	309	86	24	19	16	L14, O1, R11
36.7	0	0.13	0.1	274	76	22	17	14	L14, O1, R14
183	0	0.084	0.085	2060	651	186	200	123	L16, O1, R2
20	0	0.101	0.054	61	17	5	4	3	L14, O1, R11
20	0	0.094	0.036	20	6	2	1	1	L14, O1, R11
24.3	0	0.102	0.069	146	41	12	9	7	L14, O1, R11
20	0	0.054	0.011	3	<1	<1	<1	<1	L14, O1, R11
20	0	0.051	0.016	8	2	<1	<1	<1	L14, O1, R11
714	0	0.319	0.325	5180	2960	885	2660	1080	L17, O1, R2
886	0	0.339	0.334	5890	4240	1390	4280	2270	L14, O1, R11
325	0	0.28	0.271	3470	1300	372	656	265	L14, O1, R11
228	0	0.319	0.303	2930	926	264	286	174	L14, O1, R11
274	0	0.341	0.327	3690	1260	360	495	243	L14, O1, R11
360	0	0.341	0.328	4020	1460	417	673	289	L14, O1, R11
1289	0	0.309	0.306	6790	7720	4950	8180	7650	L14, O1, R11
269	0	0.366	0.351	3900	1320	377	503	253	L14, O1, R11
529	0	0.252	0.247	4910	3060	939	2910	1290	L14, O1, R11
95.4	0	0.257	0.23	999	279	80	63	51	L14, O1, R11
116	0	0.292	0.266	1450	406	116	93	75	L14, O1, R11
205	0	0.304	0.288	2920	907	259	265	170	L14, O1, R11
204	0	0.341	0.323	3250	1010	288	294	189	L14, O1, R11
133	0	0.328	0.303	1930	549	156	127	101	L14, O1, R11
162	0	0.308	0.288	2290	671	191	165	124	L14, O1, R11
300	0	0.322	0.311	4370	1640	469	826	333	L14, O1, R11
202	0	0.344	0.326	3250	1010	287	290	189	L14, O1, R11
67.1	0	0.229	0.196	636	177	50	40	32	L14, O1, R11
268	0	0.262	0.253	3820	1400	400	662	279	L14, O1, R11
227	0	0.276	0.264	3440	1140	326	412	218	L14, O1, R11
39.6	0	0.268	0.208	367	102	29	23	18	L14, O1, R11
65.9	0	0.258	0.22	701	195	56	44	35	L14, O1, R11
82.1	0	0.247	0.218	901	251	72	56	46	L14, O1, R11
125	0	0.272	0.25	1710	486	139	112	89	L14, O1, R11
81	0	0.257	0.226	921	257	73	58	47	L14, O1, R11
78.3	0	0.303	0.265	1030	288	82	65	52	L14, O1, R11
86.4	0	0.298	0.264	1160	323	92	73	59	L14, O1, R11
137	0	0.293	0.271	2060	591	168	139	109	L14, O1, R11
89.1	0	0.28	0.249	1140	317	90	71	58	L14, O1, R11
191	0	0.32	0.303	3330	1030	294	295	193	L14, O1, R11

Industrial Designation or Chemical Name	Chemical Formula	CAS RN	Atmospheric Abundance[a]	WMO (2018) Total Lifetime (years)	WMO (2022) Total Lifetime (years)	Tropospheric (OH Reactive Loss) Lifetime 2022 (years)
HFC-356qcc	$CH_2FCF_2CF_2CH_2F$	114810-02-5			7.03	7.34
HFC-365mcf	$CH_3CH_2CF_2CF_3$	37826-35-0			1.64	1.69
HFC-365mee	$CH_3CHFCHFCF_3$	161791-22-6			1.09	1.12
HFC-365pce	$CH_3CHFCF_2CHF_2$	158421-89-7			4.35	4.52
HFC-365pec	$CH_3CF_2CHFCHF_2$	119450-71-4			5.44	5.67
HFC-365qcc	$CH_3CF_2CF_2CH_2F$	119450-72-5			10.1	10.6
HFC-365mfc	$CH_3CF_2CH_2CF_3$	406-58-6	1.1 ppt	8.9	8.86	9.3
HFC-365mef	$CH_2FCH_2CHFCF_3$	161791-23-7			1.07	1.1
HFC-365pcf	$CH_2FCH_2CF_2CHF_2$	161791-25-9			1.26	1.3
HFC-365mfe	$CH_2FCHFCH_2CF_3$	161791-24-8			0.841	0.867
HFC-365qee	$CH_2FCHFCHFCHF_2$	157016-17-6			1.96	2.03
HFC-365pfc	$CH_2FCF_2CH_2CHF_2$	119450-76-9			3.28	3.4
HFC-365qce	$CH_2FCF_2CHFCH_2F$	119450-75-8			2.07	2.15
HFC-365mff	$CHF_2CH_2CH_2CF_3$	161879-85-2			3.32	3.44
HFC-365pef	$CHF_2CH_2CHFCHF_2$	119450-77-0			2.14	2.22
HFC-374mef	$CF_3CHFCH_2CH_3$	161791-15-7			0.629	0.648
HFC-374mfe	$CF_3CH_2CHFCH_3$	86884-13-1			0.492	0.504
HFC-374mff	$CF_3CH_2CH_2CH_2F$	83234-21-3			0.212	0.214
HFC-374pcf	$CHF_2CF_2CH_2CH_3$	143969-51-1			0.788	0.812
HFC-374pee	$CHF_2CHFCHFCH_3$	161791-16-8			0.908	0.936
HFC-374pef	$CHF_2CHFCH_2CH_2F$	161791-17-9			0.862	0.889
HFC-374pfc	$CHF_2CH_2CF_2CH_3$	625-09-2			3	3.119
HFC-374pfe	$CHF_2CH_2CHFCH_2F$	161791-18-0			0.75	0.772
HFC-374qce	$CH_2FCF_2CHFCH_3$	161791-20-4			1.54	1.59
HFC-374qec	$CH_2FCHFCF_2CH_3$	161791-19-1			2.29	2.37
HFC-374qcf	$CH_2FCF_2CH_2CH_2F$	161791-21-5			1.07	1.11
HFC-374qee	$CH_2FCHFCHFCH_2F$	119382-47-7			1.2	1.24
HFC-374scc	$CH_3CF_2CF_2CH_3$	421-74-9			17.6	18.8
HFC-374pff	$CHF_2CH_2CH_2CHF_2$	161879-84-1			1.38	1.43
HFC-383m	$CH_3CH_2CH_2CF_3$	460-34-4			0.192	0.194
HFC-383pe	$CHF_2CHFCH_2CH_3$	66675-41-0			0.483	0.495
HFC-383pfe	$CHF_2CH_2CHFCH_3$	66675-42-1			0.445	0.455
HFC-383pff	$CHF_2CH_2CH_2CH_2F$	66587-70-0			0.198	0.2
HFC-383qcf	$CH_2FCF_2CH_2CH_3$	66587-71-1			1.22	1.26
HFC-383qee	$CH_2FCHFCHFCH_3$	66587-72-2			0.365	0.372
HFC-383qef	$CH_2FCHFCH_2CH_2F$	66587-73-3			0.491	0.503
HFC-383qfc	$CH_2FCH_2CF_2CH_3$	66587-74-4			1.1	1.14
HFC-383sce	$CH_3CF_2CHFCH_3$	66587-75-5			1.19	1.23
HFC-392pff	$CH_3CH_2CH_2CHF_2$	2358-38-5			0.166	0.167
HFC-392qef	$CH_3CH_2CHFCH_2F$	686-65-7			0.275	0.279
HFC-392qfe	$CH_3CHFCH_2CH_2F$	691-42-9			0.311	0.316
HFC-392qff	$CH_2FCH_2CH_2CH_2F$	372-90-7			0.106	0.106
HFC-392scf	$CH_3CH_2CF_2CH_3$	353-81-1			0.779	0.803
HFC-392see	$CH_3CHFCHFCH_3$	666-21-7			0.279	0.283
HFC-3-10-1q	$CH_3CH_2CH_2CH_2F$	2366-52-1			0.081	0.081
HFC-3-10-1se	$CH_3CH_2CHFCH_3$	359-01-3			0.103	0.104
HFC-b-329my	$CHF_2CF(CF_3)CF_3$	59571-40-3			23.7	24.8
HFC-b-329mz	$CF_3CH(CF_3)CF_3$	382-24-1			589	740
HFC-b-338mz	$CHF_2CH(CF_3)CF_3$	382-20-7			15.2	15.9

Stratospheric Lifetime 2022 (years)	ODP	Radiative Efficiency (well mixed) ($W\ m^{-2}\ ppb^{-1}$) [b]	Recommended Adjusted Effective Radiative Efficiency ($W\ m^{-2}\ ppb^{-1}$) [c]	GWP 20-yr	GWP 100-yr	GWP 500-yr	GTP 50-yr	GTP 100-yr	Footnotes *A: Atmospheric Abundance* *L: Lifetime* *O: Ozone Depletion Potential* *R: Radiative Metrics*
167	0	0.252	0.237	2250	669	191	171	124	L14, O1, R11
50.4	0	0.229	0.187	497	138	39	31	25	L14, O1, R11
35.6	0	0.233	0.176	311	86	25	19	16	L14, O1, R11
112	0	0.22	0.201	1400	394	112	90	72	L14, O1, R11
132	0	0.226	0.209	1790	512	146	120	94	L14, O1, R11
205	0	0.233	0.222	3110	1010	288	339	191	L14, O1, R11
188	0	0.24	0.243	3100	969	276	288	182	A4, L14, O1, R2
35	0	0.244	0.184	319	89	25	20	16	L14, O1, R11
40.3	0	0.231	0.18	367	102	29	23	18	L14, O1, R11
28.5	0	0.232	0.165	225	62	18	14	11	L14, O1, R11
58.8	0	0.206	0.173	549	153	44	34	28	L14, O1, R11
89.4	0	0.232	0.207	1090	306	87	69	56	L14, O1, R11
61.6	0	0.192	0.162	543	151	43	34	27	L14, O1, R11
90.3	0	0.276	0.246	1320	368	105	83	67	L14, O1, R11
63.2	0	0.248	0.211	731	203	58	45	37	L14, O1, R11
22	0	0.209	0.136	158	44	12	10	8	L14, O1, R11
20	0	0.209	0.125	113	32	9	7	6	L14, O1, R11
20	0	0.182	0.075	29	8	2	2	1	L14, O1, R11
26.8	0	0.189	0.132	192	53	15	12	10	L14, O1, R11
30.2	0	0.169	0.122	204	57	16	13	10	L14, O1, R11
28.9	0	0.189	0.135	215	60	17	13	11	L14, O1, R11
81.6	0	0.201	0.177	976	272	78	61	50	L14, O1, R11
25.6	0	0.176	0.121	167	47	13	10	8	L14, O1, R11
47.2	0	0.171	0.139	395	110	31	24	20	L14, O1, R11
65.7	0	0.174	0.149	628	175	50	39	32	L14, O1, R11
34.8	0	0.174	0.131	259	72	20	16	13	L14, O1, R11
38.4	0	0.147	0.114	252	70	20	16	13	L14, O1, R11
268	0	0.221	0.215	4690	1930	553	1180	426	L14, O1, R11
43.3	0	0.21	0.167	425	118	34	26	21	L14, O1, R11
20	0	0.166	0.064	26	7	2	2	1	L14, O1, R11
20	0	0.147	0.088	91	25	7	6	5	L14, O1, R11
20	0	0.16	0.093	89	25	7	5	4	L14, O1, R11
20	0	0.248	0.098	42	12	3	3	2	L14, O1, R11
38.4	0	0.137	0.106	277	77	22	17	14	L14, O1, R11
20	0	0.119	0.064	50	14	4	3	3	L14, O1, R11
20	0	0.115	0.069	73	20	6	4	4	L14, O1, R11
35.3	0	0.14	0.106	250	69	20	15	13	L14, O1, R11
37.8	0	0.151	0.116	295	82	23	18	15	L14, O1, R11
20	0	0.094	0.034	14	4	1	<1	<1	L14, O1, R11
20	0	0.078	0.037	26	7	2	2	1	L14, O1, R11
20	0	0.087	0.043	34	9	3	2	2	L14, O1, R11
20	0	0.098	0.026	7	2	<1	<1	<1	L14, O1, R11
26.1	0	0.114	0.08	159	44	13	10	8	L14, O1, R11
20	0	0.094	0.044	31	9	2	2	2	L14, O1, R11
20	0	0.05	0.011	3	<1	<1	<1	<1	L14, O1, R11
20	0	0.051	0.013	4	1	<1	<1	<1	L14, O1, R11
523	0	0.319	0.311	4530	2200	637	1700	606	L14, O1, R11
2879	0	0.313	0.312	6600	8600	9080	9010	9890	L14, O1, R11
334	0	0.342	0.33	4320	1650	472	868	340	L14, O1, R11

Industrial Designation or Chemical Name	Chemical Formula	CAS RN	Atmospheric Abundance[a]	WMO (2018) Total Lifetime (years)	WMO (2022) Total Lifetime (years)	Tropospheric (OH Reactive Loss) Lifetime 2022 (years)
HFC-b-338py	$CHF_2CF(CF_3)CHF_2$	65781-21-7			11.4	11.8
HFC-b-338mym	$CH_2FCF(CF_3)CF_3$	65781-19-3			14.6	15.3
HFC-b-347mym	$CH_3CF(CF_3)CF_3$	662-00-0			36.8	39.5
HFC-b-347mzm	$CH_2FCH(CF_3)CF_3$	2794-16-3			4.66	4.83
HFC-b-347myp	$CH_2FCF(CF_3)CHF_2$	65781-22-8			8.7	9.08
HFC-b-347mzp	$CHF_2CH(CF_3)CHF_2$	65781-25-1			7.04	7.33
HFC-b-347pyp	$CHF_2CF(CHF_2)CHF_2$	65781-24-0			7.39	7.71
HFC-b-356mzm	$CH_3CH(CF_3)CF_3$	382-09-2			12	12.6
HFC-b-356myp	$CH_3CF(CF_3)CHF_2$	65781-20-6			10.8	11.4
HFC-b-356mzp	$CH_2FCH(CF_3)CHF_2$	32931-17-2			3.52	3.65
HFC-b-356myq	$CH_2FCF(CF_3)CH_2F$	161791-34-0			7.03	7.34
HFC-b-356pzp	$CHF_2CH(CHF_2)CHF_2$	138507-15-0			4.58	4.76
HFC-b-356pyp	$CH_2FCF(CHF_2)CHF_2$	35274-04-5			6.15	6.41
HFC-b-365mzp	$CH_3CH(CF_3)CHF_2$	381-95-3			3.52	3.65
HFC-b-365myq	$CH_3CF(CF_3)CH_2F$	119450-80-5			3.67	3.81
HFC-b-365pyp	$CH_3CF(CHF_2)CHF_2$	65781-23-9			6.25	6.53
HFC-b-365mzq	$CH_2FCH(CF_3)CH_2F$	161791-30-6			0.698	0.718
HFC-b-365pzp	$CH_2FCH(CHF_2)CHF_2$	32864-57-6			2.6	2.69
HFC-b-365pyq	$CHF_2CF(CH_2F)CH_2F$	65781-27-3			4.01	4.17
HFC-b-374my	$CF_3CF(CH_3)CH_3$	154381-59-6			6.42	6.72
HFC-b-374mz	$CF_3CH(CH_3)CFH_2$	161791-27-1			0.969	1
HFC-b-374py	$CHF_2CF(CH_3)CH_2F$	65781-26-2			2.92	3.03
HFC-b-374pzp	$CHF_2CH(CH_3)CHF_2$	161791-28-2			1.93	2
HFC-b-374qyq	$CH_2FCF(CH_2F)CH_2F$	65781-28-4			4.59	4.78
HFC-b-374pzq	$CHF_2CH(CH_2F)CH_2F$	161791-29-3			1.64	1.7
HFC-b-383mz	$CF_3CH(CH_3)CH_3$	1550-49-8			0.988	1.02
HFC-b-383py	$CHF_2CF(CH_3)CH_3$	66587-76-6			3.8	3.96
HFC-b-383pz	$CHF_2CH(CH_3)CH_2F$	66587-77-7			0.678	0.699
HFC-b-383qy	$CH_2FCF(CH_3)CH_2F$	161791-26-0			2.36	2.44
HFC-b-383qzq	$CH_2FCH(CH_2F)CH_2F$	66675-40-9			1.02	1.05
HFC-b-392qy	$CH_2FCF(CH_3)CH_3$	62126-92-5			1.2	1.24
HFC-b-392qz	$CH_2FCH(CH_3)CH_2F$	62126-93-6			0.33	0.336
HFC-b-392pz	$CHF_2CH(CH_3)CH_3$	62126-91-4			0.308	0.313
HFC-b-3-10-1q	$CH_2FCH(CH_3)CH_3$	359-00-2			0.088	0.089
HFC-b-3-10-1sy	$CH_3CF(CH_3)CH_3$	353-61-7			1.2	1.25
HFC-43-10mee	$CF_3CHFCHFCF_2CF_3$	138495-42-8	0.30 ppt	17	17	17.9
HFC-458mfcf	$CF_3CH_2CF_2CH_2CF_3$	–		23.8	23.8	25.4
1,1,2,2,3,3,4-heptafluorocyclo-pentane	cyclo-$CF_2CF_2CF_2CHFCH_2$-	15290-77-4			3.15	3.26
trans-1H,2H-octafluorocyclopen-tane	trans- cyclo-$CF_2CF_2CF_2CHFCHF$-	158389-18-5			3.69	3.82
1-Fluorohexane	n-$C_6H_{13}F$	373-14-8			28.5	33
Fluorobenzene	C_6H_5F	462-06-6			0.059	0.059
HFC-55-10mcff	$CF_3CF_2CH_2CH_2CF_2CF_3$	–		7.7	7.66	8
HFC-52-13p	$CHF_2CF_2CF_2CF_2CF_2CF_3$	355-37-3		35.2	35.1	37
1,1,2,2,3,3-hexafluorocyclopen-tane	cyclo-$CF_2CF_2CF_2CH_2CH_2$-	123768-18-3			1.79	1.85
HFC-72-17p	$CHF_2CF_2CF_2CF_2CF_2CF_2CF_2CF_3$	–		23.8	23.8	24.9
Unsaturated Hydrofluorocarbons						
HFO-1141	CH_2=CHF	75-02-5		2.5 days (1.4–3.1 days)	2.5 days (1.4–3.1 days)	2.5 days

Stratospheric Lifetime 2022 (years)	ODP	Radiative Efficiency (well mixed) ($W\ m^{-2}\ ppb^{-1}$) [b]	Recommended Adjusted Effective Radiative Efficiency ($W\ m^{-2}\ ppb^{-1}$) [c]	GWP 20-yr	GWP 100-yr	GWP 500-yr	GTP 50-yr	GTP 100-yr	Footnotes *A: Atmospheric Abundance* *L: Lifetime* *O: Ozone Depletion Potential* *R: Radiative Metrics*
268	0	0.333	0.319	3540	1200	342	458	230	L14, O1, R11
325	0	0.285	0.275	3520	1320	378	665	268	L14, O1, R11
529	0	0.306	0.3	5960	3720	1140	3530	1570	L14, O1, R11
125	0	0.295	0.271	1620	457	130	105	84	L14, O1, R11
205	0	0.24	0.269	2720	847	242	248	159	L14, O1, R11
174	0	0.356	0.334	2870	851	243	217	158	L14, O1, R11
181	0	0.333	0.314	2800	840	240	220	156	L14, O1, R11
244	0	0.287	0.275	3830	1320	378	535	256	L14, O1, R11
227	0	0.315	0.301	3930	1300	372	469	249	L14, O1, R11
96.9	0	0.291	0.261	1320	369	105	84	67	L14, O1, R11
167	0	0.264	0.248	2360	700	200	178	130	L14, O1, R11
120	0	0.328	0.301	1960	553	158	127	102	L14, O1, R11
151	0	0.281	0.263	2230	649	185	157	120	L14, O1, R11
94.5	0	0.275	0.246	1390	390	111	88	71	L14, O1, R11
97.8	0	0.24	0.216	1270	357	102	81	65	L14, O1, R11
147	0	0.278	0.259	2500	729	208	177	135	L14, O1, R11
24.2	0	0.214	0.144	163	45	13	10	8	L14, O1, R11
74.1	0	0.273	0.238	1000	279	79	62	51	L14, O1, R11
105	0	0.206	0.187	1200	338	96	77	62	L14, O1, R11
144	0	0.224	0.209	2350	687	196	169	127	L14, O1, R11
32	0	0.195	0.144	257	71	20	16	13	L14, O1, R11
79.7	0	0.189	0.167	896	250	71	56	46	L14, O1, R11
57.2	0	0.222	0.186	661	184	52	41	33	L14, O1, R11
13	0	0.152	0.14	1170	329	94	76	60	L14, O1, R11
49.9	0	0.177	0.145	438	122	35	27	22	L14, O1, R11
32.2	0	0.184	0.136	288	80	23	18	14	L14, O1, R11
95.4	0	0.162	0.146	1180	330	94	75	60	L14, O1, R11
23.3	0	0.142	0.095	138	38	11	8	7	L14, O1, R11
66	0	0.127	0.109	550	153	44	34	28	L14, O1, R11
33.1	0	0.105	0.079	172	48	14	11	9	L14, O1, R11
37.5	0	0.093	0.072	220	61	17	14	11	L14, O1, R11
20	0	0.075	0.038	32	9	3	2	2	L14, O1, R11
20	0	0.139	0.069	54	15	4	3	3	L14, O1, R11
20	0	0.039	0.009	2	<1	<1	<1	<1	L14, O1, R11
37.4	0	0.05	0.039	147	41	12	9	7	L14, O1, R11
360	0	0.369	0.359	3980	1610	460	948	348	A4, L2, O1, R2
372	0	0.521	0.508	7550	3670	1060	2850	1020	L2, O1, R6
90.7	0	0.28	0.253	971	271	77	61	49	L18, O1, R15
106	0	0.29	0.266	1090	306	87	69	56	L18, O1, R15
209	0	0.041	0.041	1340	723	213	622	238	L19, O1, R2
20	0	0.065	0.012	2	<1	<1	<1	<<1	L3, O1, R2
178	0	0.59	0.557	3540	1070	305	286	199	L2, O1, R6
659	0	0.593	0.582	6570	3990	1210	3730	1610	L2, O1, R6
55.2	0	0.248	0.21	506	141	40	31	26	L20, O1, R16
525	0	0.765	0.746	5700	2770	804	2150	768	L2, O1, R6
–	0	0.089	2.47E-03	<<1	<<1	<<1	<<1	<<1	L2, O1, R2

Industrial Designation or Chemical Name	Chemical Formula	CAS RN	Atmospheric Abundance[a]	WMO (2018) Total Lifetime (years)	WMO (2022) Total Lifetime (years)	Tropospheric (OH Reactive Loss) Lifetime 2022 (years)
(E)-HFO-1132, (E)-1,2-difluoro-ethene	(E)-CHF=CHF	–			1.3 days	1.3 days
(Z)-HFO-1132, (Z)-1,2-difluoro-ethene	(Z)-CHF=CHF	–			1.6 days	1.6 days
HFO-1132a	$CH_2=CF_2$	75-38-7		4.6 days (3–5.7 days)	4.6 days (3–5.7 days)	4.6 day
HFO-1123	$CHF=CF_2$	359-11-5		1.4 days	1.5 days	1.5 days
HFO-1261yf	$CH_2=CFCH_3$	–			0.7 days	0.7 days
HFO-1261zf, 3-fluoro-1-propene	$CH_2FCH=CH_2$	818-92-8		0.8 days (0.5–1.0 days)	0.9 days (0.5–1.0 days)	0.9 days
HFO-1243zf	$CF_3CH=CH_2$	677-21-4		9 days (5.5–11 days)	9 days (5.5–11 days)	9 days
(E)-HFO-1234ye	$(E)-CHF=CFCHF_2$	–		<5 days	19 days	19 days
(Z)-HFO-1234ye	$(Z)-CHF=CFCHF_2$	–		<5 days	10 days	10 days
(E)-HFO-1234ze	$(E)-CF_3CH=CHF$	29188-24-9	0.023 ppt	19 days (12.8–24 days)	19 days (12.8–24 days)	19 days
(Z)-HFO-1234ze	$(Z)-CF_3CH=CHF$	29118-25-0		10.0 days	9.6 days	9.6 days
HFO-1234zc	$CF_2=CHCHF_2$	–		<5 days	5 days	5 days
HFO-1234yf	$CF_3CF=CH_2$	754-12-1	0.026 ppt	12 days (8.4–16 days)	12 days (8.4–16 days)	12 days
HFO-1234yc	$CF_2=CFCH_2F$	–		~2 days	2 days	2 days
3,3,4,4-tetrafluorocyclobutene	$c-CH=CHCF_2CF_2-$	2714-38-7		84 days	83 days	83 days
2,3,3,4,4-pentafluorocyclo-but-1-ene	$c-CH=CFCF_2CF_2-$	374-31-2		270 days	258 days	268 days
(E)-HFO-1225ye	$(E)-CF_3CF=CHF$	5595-10-8		5.7 days (3.7–6.9 days)	5.7 days (3.7–6.9 days)	5.7 days
(Z)-HFO-1225ye	$(Z)-CF_3CF=CHF$	5528-43-8		10 days (6.2–12 days)	10 days (6.2–12 days)	10 days
HFO-1225yc	$CF_2=CFCHF_2$	–			1.6 days	1.6 days
HFO-1225zc	$CF_2=CHCF_3$	690-27-7		~2 days	2 days	2 days
HFO-1345zfc	$C_2F_5CH=CH_2$	374-27-6		9 days (5.8–11.4 days)	9 days (5.8–11.4 days)	9 days
(E)-HFO-1336mzz	$(E)-CF_3CH=CHCF_3$	–		122 days	121 days	121 days
(Z)-HFO-1336mzz	$(Z)-CF_3CH=CHCF_3$	692-49-9		27 days (16.3–32 days)	27 days (16.3–32 days)	27 days
3,3,3-trifluoro-2-(trifluoromethyl)-1-propene	$(CF_3)_2C=CH_2$	382-10-5			17 days	17 days
HFO-1447fz	$CH_2=CHCF_2CF_2CF_3$	355-08-8		9 days (6–10 days)	33 days	33 days
1,3,3,4,4,5,5-heptafluorocyclo-pentene	$cyclo-CF_2CF_2CF_2CF=CH-$	1892-03-1			254 days	263 days
(E)-HFO-1438mzz	$(E)-CF_3CH=CHCF_2CF_3$	–		122 days	120 days	122 days
(E)-HFO-1438ezy	$(E)-(CF_3)_2CFCH=CHF$	14149-41-8		43 days	43 days	43 days
3,3,4,4,5,5,6,6,6-nonafluoro-hex-1-ene	$C_4F_9CH=CH_2$	19430-93-4		9 days	9 days	9 days
3,3,4,4,5,5,6,6,7,7,8,8,8-trideca-fluorooct-1-ene (HFO-174-13fz)	$C_6F_{13}CH=CH_2$	25291-17-2		9 days	9 days	9 days
3,3,4,4,5,5,6,6,7,7,8, 8,9,9, 10,10,10-heptadecafluoro-dec-1-ene (HFO-194-17fz)	$C_8F_{17}CH=CH_2$	21652-58-4		9 days	9 days	9 days
Chlorocarbons and Hydrochlorocarbons						
Methyl chloroform	CH_3CCl_3	71-55-6	1.4 ppt	5	5	6.1
Carbon tetrachloride	CCl_4	56-23-5	77.6 ppt	32	30	–
Methyl chloride	CH_3Cl	74-87-3	549.4 ppt	0.9	0.9	1.57
Methylene chloride	CH_2Cl_2	75-09-2	45.7 ppt	180 days (95–1070 days)	176 days (95–1070 days)	181 days
Chloroform	$CHCl_3$	67-66-3	8.7 ppt	183 days (97–1145 days)	178 days (97–1145 days)	183 days
1,2-dichloroethane	CH_2ClCH_2Cl	107-06-2	12.8 ppt (10.4–18.3)	82 days (41–555 days)	81.3 days (41–555 days)	82.1 days
Chloroethane	CH_3CH_2Cl	75-00-3		48 days (26–280 days)	47.6 days (26–280 days)	47.8 days
1,1-dichloroethane	CH_3CHCl_2	75-34-3			134 days	134 days
1,1,2-trichloroethane	$CH_2ClCHCl_2$	79-00-5			83 days	84 days
1,1,1,2-tetrachloroethane	CH_2ClCCl_3	630-20-6			3.39	3.85
1,1,2,2-tetrachloroethane	$CHCl_2CHCl_2$	79-34-5			145 days	148 days

Stratospheric Lifetime 2022 (years)	ODP	Radiative Efficiency (well mixed) (W m^{-2} ppb^{-1}) [b]	Recommended Adjusted Effective Radiative Efficiency (W m^{-2} ppb^{-1}) [c]	GWP 20-yr	GWP 100-yr	GWP 500-yr	GTP 50-yr	GTP 100-yr	Footnotes *A: Atmospheric Abundance L: Lifetime O: Ozone Depletion Potential R: Radiative Metrics*
–	0	0.157	2.46E-03	<<1	<<1	<<1	<<1	<<1	L21, O1, R6
–	0	0.115	2.09E-03	<<1	<<1	<<1	<<1	<<1	L21, O1, R6
–	0	0.09	4.32E-03	<1	<<1	<<1	<<1	<<1	L2, O1, R17
–	0	0.117	2.10E-03	<<1	<<1	<<1	<<1	<<1	L2, O1, R18
–	0	0.093	8.32E-04	<<1	<<1	<<1	<<1	<<1	L22, O1, R6
–	0	0.059	6.75E-04	<<1	<<1	<<1	<<1	<<1	L22, O1, R2
–	0	0.177	0.0152	<1	<1	<<1	<<1	<<1	L2, O1, R2
–	0	0.242	0.0399	4	1	<1	<1	<1	L23, O1, R6
–	0	0.204	0.0187	1	<1	<<1	<<1	<<1	L23, O1, R6
–	0	0.284	0.0459	5	1	<1	<1	<1	A4, L2, O1, R2
–	0	0.209	0.0191	1	<1	<<1	<<1	<<1	L2, O1, R2
–	0	0.231	0.0121	<1	<<1	<<1	<<1	<<1	L24, O1, R6
–	0	0.238	0.0268	2	<1	<1	<1	<<1	A4, L2, O1, R2
–	0	0.202	4.61E-03	<<1	<<1	<<1	<<1	<<1	L24, O1, R6
–	0	0.231	0.101	44	12	3	3	2	L2, O1, R19
20	0	0.297	0.205	241	67	19	15	12	L2, O1, R19
–	0	0.259	0.0152	<1	<1	<<1	<<1	<<1	L2, O1, R2
–	0	0.265	2.48E-02	1	<1	<<1	<<1	<<1	L2, O1, R2
–	0	0.207	3.79E-03	<<1	<<1	<<1	<<1	<<1	L25, O1, R6
–	0	0.371	8.47E-03	<<1	<<1	<<1	<<1	<<1	L24, O1, R6
–	0	0.356	0.0168	<1	<1	<<1	<<1	<<1	L2, O1, R6
–	0	0.376	0.193	94	26	7	6	5	L2, O1, R20
–	0	0.393	0.0809	9	2	<1	<1	<1	L2, O1, R21
–	0	0.341	0.0509	3	<1	<1	<1	<1	L26, O1, R2
–	0	0.396	0.0962	11	3	<1	<1	<1	L27, O1, R22
20	0	0.33	0.224	193	54	15	12	10	L28, O1, R23
–	0	0.564	0.289	107	30	8	7	5	L29, O1, R6
–	0	0.325	0.0931	12	3	<1	<1	<1	L30, O1, R24
–	0	0.354	0.0314	<1	<1	<<1	<<1	<<1	L31, O1, R2
–	0	0.396	0.0354	<1	<1	<<1	<<1	<<1	L31, O1, R2
–	0	0.444	0.0397	<1	<1	<<1	<<1	<<1	L31, O1, R2
38	0.12	0.07	0.0655	576	164	47	38	30	A2, L5, L11, O3, R2
44	0.87	0.176	0.172	3870	2150	638	1890	744	A2, L11, L32, O3, O4, R2
30.4	0.015	0.00645	4.66E-03	20	6	2	1	1	A2, L5, L11, O3, R2
–	–	0.048	0.0287	39	11	3	2	2	A2, L2, R2
–	–	0.122	0.0731	72	20	6	4	4	A2, L2, R2
–	–	0.02	8.64E-03	5	1	<1	<1	<1	A3, L2, R2
–	–	0.011	3.43E-03	2	<1	<1	<1	<<1	L2, R2
–	–	0.028	0.0154	14	4	1	<1	<1	L3, R2
–	–	0.05	0.0219	9	2	<1	<1	<1	L33, R2
28	–	0.103	0.0953	459	128	37	29	23	L34, R2
–	–	0.096	0.0543	31	9	2	2	2	L34, R2

Industrial Designation or Chemical Name	Chemical Formula	CAS RN	Atmospheric Abundance[a]	WMO (2018) Total Lifetime (years)	WMO (2022) Total Lifetime (years)	Tropospheric (OH Reactive Loss) Lifetime 2022 (years)
1-chloropropane	$CH_3CH_2CH_2Cl$	540-54-5		16 days (10–80 days)	16.5 days (10–80 days)	16.5 days
2-chloropropane	$CH_3CHClCH_3$	75-29-6		22 days (13–95 days)	22 days (13–95 days)	22 days
1,3-dichloropropane	$CH_2ClCH_2CH_2Cl$	142-28-9			17.5 days	17.5 days
1-chloro-2-methylpropane	$(CH_3)_2CHCH_2Cl$	513-36-0			7.0 days	7.0 days
1-chlorobutane	$CH_3(CH_2)_2CH_2Cl$	109-69-3			5.9 days	5.9 days
1-chloropentane	$CH_3(CH_2)_3CH_2Cl$	543-59-9			0.8 days	0.8 days
Unsaturated Chlorocarbons and Hydrochlorocarbons						
Chloroethene (vinyl chloride)	CH_2=CHCl	75-01-4		1.7 days (0.9–2.2 days)	1.7 days (0.9–2.2 days)	1.7 days
1,1-dichloroethene	CH_2=CCl_2	75-35-4		1 days (0.5–1.3 days)	1 day (0.5–1.3 days)	1 day
(E)-1,2-dichloroethene	(E)-CClH=CClH	156-60-5		5.5 days (3.2–6.7 days)	5.5 days (3.2–6.7 days)	5.5 day
(Z)-1,2-dichloroethene	(Z)-CClH=CClH	156-59-2		5.2 days (3.2–6.7 days)	5.2 days (3.2–6.7 days)	5.2 days
Trichloroethene	CHCl=CCl_2	79-01-6	0.3 ppt	5.6 days (3.3–7.1 days)	5.6 days (3.3–7.1 days)	5.6 days
Perchloroethene	CCl_2=CCl_2	127-18-4	1.13 ppt	110 days (66–245 days)	109 days (66–245 days)	110 days
3-chloro-1-propene	CH_2=$CHCH_2Cl$	107-5-1			1.4 days	1.4 days
3-chloro-1-propyne	CH_2ClC CH	624-65-7			1.4 days	1.4 days
2,3-dichloropropene	CH_2ClCCl=CH_2	78-88-6			1.0 day	1.0 day
1,2-dichloropropene	CHCl=$CClCH_3$	563-54-2			1.4 days	1.4 days
1,3-dichloropropene (E)	(E)-CHCl=$CHCH_2Cl$	10061-02-6			1.6 days	1.6 days
1,3-dichloropropene (Z)	(Z)-CHCl=$CHCH_2Cl$	10061-01-5			0.95 days	0.95 days
3,4-dichloro-1-butene	$CH_2ClCHClCH$=CH_2	760-23-6			0.94 days	0.94 days
Hexachloro-1,3-butadiene	CCl_2=$CClCCl$=CCl_2	87-68-3			1.4 days	1.4 days
Hexachloro-1,3-cyclopentadiene	C_5Cl_6	77-47-4			1.4 days	1.4 days
Chlorobenzene	C_6H_5-Cl	108-90-7			22.8 days	22.8 days
1,4-dichlorobenzene	p-Cl-C_6H_4-Cl	106-46-7			42 days	43 days
1,3-dichlorobenzene	m-Cl-C_6H_4-Cl	541-73-1			18.9 days	19 days
1,2-dichlorobenzene	o-Cl-C_6H_4-Cl	95-50-1			32.4 days	32.5 days
1-chloro-4-methylbenzene	p-Cl-C_6H_4-CH_3	106-43-4			27.2 days	27.3 days
1-chloro-3-methylbenzene	m-Cl-C_6H_4-CH_3	108-41-8			27.2 days	27.3 days
1-chloro-2-methylbenzene	o-Cl-C_6H_4-CH_3	95-49-8			27.2 days	27.3 days
Benzyl chloride	C_6H_5-CH_2Cl	100-44-7			45.2 days	45.6 days
1,2-dichloro-3-(trichloromethyl)-benzene (DCTCB)	$C_7H_3Cl_5$	84613-97-8			134 days	136 days
Unsaturated Chlorofluorocarbons and Hydrochlorofluorocarbons						
CFO-1113 Chlorotrifluoroethene	CF_2=CFCl	79-38-9		1.5 days (0.8–2.1 days)	1.5 days (0.8–2.1 days)	1.5 days
(E)-1,2-fluorochloroethene	(E)-CHCl=CHF	2268-32-8			2.2 days	2.2 days
(Z)-1,2-fluorochloroethene	(Z)-CHCl=CHF	2268-31-7			2.2 days	2.2 days
1,2-dichloro-1,2-difluoroethylene (E)	(E)-CFCl=CFCl	598-88-9			4.9 days	4.9 days
1,2-dichloro-1,2-difluoroethylene (Z)	(Z)-CFCl=CFCl	598-88-9			4.7 days	4.7 days
1,1-dichloro-2,2-difluoro-ethene	CCl_2=CF_2	79-35-6			2.7 days	2.7 days
fluorotrichloroethylene	CCl_2=CClF	359-29-5			2.7 days	2.7 days
3-chloro-1,1,3-trifluoro propene (E)	(E)-CHF_2CF=CHCl	–			5.0 days	5.1 days
3-chloro-1,1,3-trifluoro propene (Z)	(Z)-CHF_2CF=CHCl	–			2.7 days	2.7 days
(E)-HCFO-1233zd	(E)-CF_3CH=CHCl	102687-65-0	0.047 ppt	42.5 days (34–64 days)	41.9 days (34–64 days)	41.9 days
(Z)-HCFO-1233zd	(Z)-CF_3CH=CHCl	99728-16-2		13 days	13 days	13 days
1-chloro-2,3,3,3-tetrafluoropropene (E); (E)-HCFO-1224yd	(E)-CF_3CF=CHCl	3110-38-1			10 days	10 days
1-chloro-2,3,3,3-tetrafluoropropene (Z); (Z)-HCFO-1224yd	(Z)-CF_3CF=CHCl	3110-38-1			12 days	12 days

Stratospheric Lifetime 2022 (years)	ODP	Radiative Efficiency (well mixed) ($W\ m^{-2}\ ppb^{-1}$) [b]	Recommended Adjusted Effective Radiative Efficiency ($W\ m^{-2}\ ppb^{-1}$) [c]	GWP 20-yr	GWP 100-yr	GWP 500-yr	GTP 50-yr	GTP 100-yr	Footnotes *A: Atmospheric Abundance L: Lifetime O: Ozone Depletion Potential R: Radiative Metrics*
–	–	0.0195	2.83E-03	<1	<1	<<1	<<1	<<1	L2, R6
–	–	0.0293	3.67E-03	<1	<1	<<1	<<1	<<1	L2, R6
–	–	0.02	4.40E-03	<1	<1	<<1	<<1	<<1	L35, R2
–	–	0.029	1.42E-03	<<1	<<1	<<1	<<1	<<1	L36, R2
–	–	0.02	9.83E-04	<<1	<<1	<<1	<<1	<<1	L36, R2
–		0.016	1.66E-04	<<1	<<1	<<1	<<1	<<1	L37, R2
–	–	0.041	7.91E-04	<<1	<<1	<<1	<<1	<<1	L2, R2
–	–	0.086	1.17E-03	<<1	<<1	<<1	<<1	<<1	L2, R6
–	<0.0003	0.091	5.15E-03	<1	<<1	<<1	<<1	<<1	L2, O11, R2
–	<0.0003	0.043	2.63E-03	<<1	<<1	<<1	<<1	<<1	L2, O11, R3
–	<0.004	0.099	5.77E-03	<1	<<1	<<1	<<1	<<1	A3, L2, O11, R2
–	–	0.107	0.0522	23	6	2	1	1	A2, L2, R2
–		0.046	7.44E-04	<<1	<<1	<<1	<<1	<<1	L3, R2
–		0.024	4.22E-04	<<1	<<1	<<1	<<1	<<1	L3, R2
–		0.052	6.37E-04	<<1	<<1	<<1	<<1	<<1	L38, R2
–		0.025	4.15E-04	<<1	<<1	<<1	<<1	<<1	L3, R2
–		0.056	1.11E-03	<<1	<<1	<<1	<<1	<<1	L39, R2
–		0.061	7.15E-04	<<1	<<1	<<1	<<1	<<1	L39, R2
–		0.055	6.40E-04	<<1	<<1	<<1	<<1	<<1	L38, R2
–		0.144	2.31E-03	<<1	<<1	<<1	<<1	<<1	L3, R2
–		0.11	1.77E-03	<<1	<<1	<<1	<<1	<<1	L3, R2
–		0.039	7.71E-03	1	<1	<<1	<<1	<<1	L40, R2
–		0.075	0.0226	4	1	<1	<1	<1	L41, R2
–		0.08	0.013	1	<1	<<1	<<1	<<1	L42, R2
–		0.046	0.0115	2	<1	<1	<1	<<1	L42, R2
–		0.05	0.0115	2	<1	<1	<<1	<<1	L3, R2
–		0.054	0.0117	2	<1	<1	<1	<<1	L3, R2
–		0.036	8.02E-03	1	<1	<<1	<<1	<<1	L3, R2
–		0.024	7.32E-03	2	<1	<1	<1	<<1	L3, R2
–		0.134	0.0743	25	7	2	2	1	R6
–	–	0.114	2.03E-03	<<1	<<1	<<1	<<1	<<1	L43, R2
–		0.044	1.08E-03	<<1	<<1	<<1	<<1	<<1	L43, R25
–		0.044	1.11E-03	<<1	<<1	<<1	<<1	<<1	L44, R25
–		0.013	5.99E-03	<1	<<1	<<1	<<1	<<1	L43, L44, R25
–		0.013	5.74E-03	<1	<<1	<<1	<<1	<<1	L44, R25
–		0.007	2.65E-03	<<1	<<1	<<1	<<1	<<1	L43, R25
–		0.13	3.92E-03	<<1	<<1	<<1	<<1	<<1	L3, R2
–		0.232	0.0124	<1	<<1	<<1	<<1	<<1	L45, R6
–		0.174	0.0052	<<1	<<1	<<1	<<1	<<1	L45, R6
–	<0.0004	0.229	0.0651	14	4	1	<1	<1	L2, O11, R26
–	<0.0004	0.213	0.0254	2	<1	<1	<1	<<1	L2, O11, R26
–		0.366	0.0357	2	<1	<1	<<1	<<1	L45, R6
–		0.31	0.0335	2	<1	<1	<1	<<1	L45, R6

Industrial Designation or Chemical Name	Chemical Formula	CAS RN	Atmospheric Abundance[a]	WMO (2018) Total Lifetime (years)	WMO (2022) Total Lifetime (years)	Tropospheric (OH Reactive Loss) Lifetime 2022 (years)
HCFO-1233xf (2-chloro-3,3,3-fluoro-1-propene)	$CF_3CCl=CH_2$	–		42.5 days (34–64 days)	42.3 days (34–64 days)	42.5 days
CFO-1215yc (3-chloro-1,1,2,3,3-fluoro-1-propene)	$CF_2=CFCF_2Cl$	–		~5 days ~(3–7 days)	~5 days ~(3–7 days)	~5 days
3,3-dichloro-1,1,1,2-tetrafluoro-propene	$CCl_2=CFCF_3$	–			14 days	14 days
1,2-dichloro-3,3,3-trifluoro-propene (Z)	(Z)-$CF_3CCl=CHCl$	431-27-6			28.4 days	28.4 days
CFO-1316yff (4,4-dichloro-1,1,2,3,3,4-fluoro-1-butene)	$CF_2=CFCF_2CFCl_2$	–		~5 days ~(3–7 days)	~6 days ~(3–7 days)	~6 days
p-chlorobenzotrifluoride	$ClC_6H_4CF_3$	98-56-6			60 days	60.7 days
Bromocarbons, Hydrobromocarbons, and Halons						
Methyl bromide	CH_3Br	74-83-9	6.68 ppt	0.8	0.8	1.8
Methylene bromide	CH_2Br_2	74-95-3	0.9 ppt (0.6–1.7)	150 days (80–890 days)	147 days (80–890 days)	150 days
Bromoform	$CHBr_3$	75-25-2	1.2 ppt (0.4–4.0)	16 days (8–23 days)	13 days (8–23 days)	57 days (15–88 days)
Halon-1201	$CHBrF_2$	1511-62-2		4.9	4.85	5.68
Halon-1202	CBr_2F_2	75-61-6	0.009 ppt	2.5	2.5	122
Halon-1211	$CBrClF_2$	353-59-3	3.11 ppt	16	16	1.45E+04
Halon-1301	$CBrF_3$	75-63-8	3.32 ppt	72	72	2.10E+04
Bromochloromethane	CH_2BrCl	74-97-5	0.10 ppt (0.07–0.12)	165 days (89–1050 days)	162 days (89–1050 days)	165 days
Bromodichloromethane	$CHBrCl_2$	75-27-4	0.3 ppt (0.1–0.9)	66 days (38–250 days)	66 days (38–250 days)	95 days (56–460 days)
Dibromochloromethane	$CHBr_2Cl$	124-48-1	0.3 ppt (0.1–0.8)	59 days (28–225 days)	49 days (28–225 days)	71 days (45–325 days)
Bromoethane	CH_3CH_2Br	74-96-4		50 days (30–260 days)	50 days (30–260 days)	50 days
1,2-dibromoethane	CH_2BrCH_2Br	106-93-4		89 days (44–590 days)	89 days (44–590 days)	89 days
n-bromopropane	$CH_3CH_2CH_2Br$	106-94-5		15 days (9–65 days)	15 days (9–65 days)	15 days
Iso-bromopropane	$CH_3CHBrCH_3$	75-26-3		20 days (12–88 days)	20 days (12–88 days)	20 days
Halon-2301	CH_2BrCF_3	421-06-7		3.2	2.9	3.25
Halon-2311 / Halothane	$CHBrClCF_3$	151-67-7	0.010 ppt	1	1	1.08
Halon-2401	$CHFBrCF_3$	124-72-1		2.9	2.83	3.15
Halon-2402 isomer	CF_3CFBr_2	–		2.5	28	2.10E+04
Halon-2402	$CBrF_2CBrF_2$	124-73-2	0.40 ppt	28	28	2.10E+04
Unsaturated Bromofluorocarbons						
Bromoethene	$CH_2=CHBr$	593-60-2			34 days	35 days
Bromothrifluoroethene	$CFBr=CF_2$	598-73-2		1.6 days (0.9–2.0 days)	1.6 days (0.9–2.0 days)	1.6 days
1-bromo-2,2-fluoroethene	$CHBr=CF_2$	359-08-0		2.7 days (1.5–3.4 days)	2.7 days (1.5–3.4 days)	2.7 days
3-bromo-1-propene	$CH_2=CHCH_2Br$	106-95-6			20 days	20 days
2-bromo-3,3,3-fluoro-1-propene	$CH_2=CBrCF_3$	1514-82-5		3.2 days (1.8–3.9 days)	3.2 days (1.8–3.9 days)	3.2 days
2-bromo-3,3,4,4,4-fluoro-1-butene	$CH_2=CBrCF_2CF_3$	68318-95-6		3.7 days (2.0–4.6 days)	3.7 days (2.0–4.6 days)	3.7 days
4-bromo-3,3,4,4-fluoro-1-butene	$CH_2=CHCF_2CF_2Br$	18599-22-9		7.5 days (4.7–9.5 days)	7.5 days (4.7–9.5 days)	7.5 days
Benzyl bromide	C_6H_5-CH_2Br	100-39-0			14 days	14 days
Unsaturated Bromochlorofluorocarbons						
4-bromo-3-chloro-3,4,4-trifluoro-1-butene	$CH_2=CHCClFCBrF_2$	374-25-4		4.5 days	4.4 days	4.4 days
Fully Fluorinated Species						
Nitrogen trifluoride	NF_3	7783-54-2	2.3 ppt	569	569	–
Perfluorotriethylamine	$N(C_2F_5)_3$	359-70-6		>1000	>3000	–
Perfluorotripropylamine	$N(C_3F_7)_3$	338-83-0		>1000	>3000	–

Stratospheric Lifetime 2022 (years)	ODP	Radiative Efficiency (well mixed) ($W\ m^{-2}\ ppb^{-1}$) [b]	Recommended Adjusted Effective Radiative Efficiency ($W\ m^{-2}\ ppb^{-1}$) [c]	GWP 20-yr	GWP 100-yr	GWP 500-yr	GTP 50-yr	GTP 100-yr	Footnotes *A: Atmospheric Abundance L: Lifetime O: Ozone Depletion Potential R: Radiative Metrics*
–	–	0.263	0.075	16	4	1	<1	<1	L46, R6
–	–	0.362	0.021	<1	<1	<<1	<<1	<<1	L47, R6
–		0.343	0.0419	2	<1	<1	<1	<1	L3, R6
–		0.318	0.0684	8	2	<1	<1	<1	L48, R6
–	–	0.399	0.0231	<1	<1	<<1	<<1	<<1	L47, R6
–		0.314	0.115	25	7	2	2	1	L49
26.3	0.57	0.006	4.21E-03	9	2	<1	<1	<1	A2, L5, L11, O3, R2
–	3–4	0.017	9.33E-03	5	1	<1	<1	<1	A3, L2, O11, R2
–	1–5	0.018	2.13E-03	<<1	<<1	<<1	<<1	<<1	A3, L2, O11, R2
34		0.165	0.152	1320	375	107	87	69	L2, R2
36	1.8	0.313	0.271	773	215	61	48	39	A2, L2, L5, O3, R2
41	7.1	0.32	0.31	5080	1990	570	1110	420	A2, L2, L5, O3, R4
73.5	17	0.313	0.309	8580	7430	2840	7800	5220	A2, L2, L5, O3, R2
–	–	0.035	0.0202	17	5	1	1	<1	A3, L2, R2
–	–	0.061	0.023	6	2	<1	<1	<1	A3, L2, R6
–	–	0.04	0.0125	2	<1	<1	<1	<<1	A3, L2, R6
–	<0.46	0.018	5.67E-03	2	<1	<1	<1	<<1	L2, O11, R2
–	–	0.027	1.20E-02	4	1	<1	<1	<1	L2, R2
–	<0.17	0.018	2.43E-03	<1	<<1	<<1	<<1	<<1	L2, O11, R2
–	–	0.026	4.32E-03	<1	<1	<<1	<<1	<<1	L2, R2
–	–	0.152	0.135	575	160	46	36	29	L2, R2
–	~1.6	0.18	0.134	163	45	13	10	8	A3, L2, O12, R2
28	–	0.214	0.189	707	197	56	44	36	L2, R2
32	–	0.346	0.339	4420	2360	695	2010	763	L2, L50, R6
41	15.6	0.332	0.325	4240	2260	666	1930	732	A2, L5, L11, O3, R2
–	–	0.041	0.01	2	<1	<1	<1	<1	L51, R2
–	–	0.161	0.003	<<1	<<1	<<1	<<1	<<1	L2, R6
–	–	0.123	0.004	<<1	<<1	<<1	<<1	<<1	L2, R6
–		0.04	0.007	<1	<1	<<1	<<1	<<1	L52, R2
–	<0.05	0.246	0.009	<1	<<1	<<1	<<1	<<1	L2, O11, R6
–	–	0.334	0.013	<1	<<1	<<1	<<1	<<1	L2, R6
–	–	0.348	0.026	<1	<1	<<1	<<1	<<1	L2, R6
–	–	0.032	0.004	<1	<<1	<<1	<<1	<<1	L3, R2
	–	0.329	0.015	<1	<<1	<<1	<<1	<<1	L2, R6
740	0	0.209	0.208	13,600	17,700	18,500	18,600	20,300	A2, L5, L53, O1, R2
>3000	0	0.686	0.69	8770	12,100	16,300	12,500	14,600	L3, O1, R27
>3000	0	0.809	0.816	7390	10,200	13,700	10,600	12,300	L3, O1, R27

Industrial Designation or Chemical Name	Chemical Formula	CAS RN	Atmospheric Abundance[a]	WMO (2018) Total Lifetime (years)	WMO (2022) Total Lifetime (years)	Tropospheric (OH Reactive Loss) Lifetime 2022 (years)
Perfluorotributylamine	$N(C_4F_9)_3$	311-89-7		>1000	>3000	–
Perfluorotripentylamine	$N(C_5F_{11})_3$	338-84-1		>1000	>3000	–
Sulfur hexafluoride	SF_6	2551-62-4	10.3 ppt	3200	850–1280	–
(Trifluoromethyl)sulfur pentafluoride	SF_5CF_3	373-80-8	0.155 ppt	650–950	650–950	–
PFC-14 (Perfluoromethane)	CF_4	75-73-0	86.4 ppt	50,000	50,000	–
PFC-116 (Perfluoroethane)	C_2F_6	76-16-4	4.94 ppt	10,000	10,000	–
PFC-c216 (Perfluorocyclopropane)	c-C_3F_6	931-91-9		3000	3000	–
PFC-218 (Perfluoropropane)	C_3F_8	76-19-7	0.7 ppt	2600	2600	–
PFC-c316 (Perfluorocyclobutene)	c-C_4F_6	697-11-0		1.2	1.2	1.205
PFC-c318 (Perfluorocyclobutane)	c-C_4F_8	115-25-3	1.82 ppt	3200	3200	–
PFC-31-10 (Perfluorobutane)	n-C_4F_{10}	355-25-9		2600	2600	–
PFC-c418 (Perfluorocyclopentene)	c-C_5F_8	559-40-0		1.1	1.06	1.063
PFC-41-12 (Perfluoropentane)	n-C_5F_{12}	678-26-2	0.148 ppt	4100	4100	–
PFC-51-14 (Perfluorohexane)	n-C_6F_{14}	355-42-0	0.22 ppt	3100	3100	–
PFC-61-16 (Perfluoroheptane)	n-C_7F_{16}	335-57-9		3000	3000	–
PFC-71-18 (Perfluorooctane)	n-C_8F_{18}	307-34-6		3000	3000	–
PFC-91-18 (isomer mixture)	$C_{10}F_{18}$	306-94-5		2000	2000	–
PFC-c91-18(Z) (Perfluorodecalin(Z))	(Z)-$C_{10}F_{18}$	60433-12-7		2000	2000	–
PFC-c91-18(E) (Perfluorodecalin(E))	(E)-$C_{10}F_{18}$	60433-11-6		2000	2000	–
PFC-1114	$CF_2=CF_2$	116-14-3		1.2 days (0.7–1.6 days)	1.2 days (0.7–1.6 days)	1.2 days
PFC-1216	$CF_3CF=CF_2$	116-15-4		5.5 days (3.3–7.1 days)	5.5 days (3.3–7.1 days)	5.5 days
Perfluorobuta-1,3-diene	$CF_2=CFCF=CF_2$	685-63-2		1.1 days	1.1 days	1.1 days
Perfluorobut-1-ene	$CF_3CF_2CF=CF_2$	357-26-6		6 days	6.6 days	6.6 days
Perfluoroisobutene	$(CF_3)_2C=CF_2$	382-21-8			14 days	14 days
(E)-Perfluoro-2-butene	(E)-$CF_3CF=CFCF_3$	360-89-4		22 days	22 days	22 days
(Z)-Perfluoro-2-butene	(Z)-$CF_3CF=CFCF_3$	1516-15-9		35 days	35 days	35 days
Perfluoro(2-methyl-2-pentene)	$(CF_3)_2C=CFCF_2CF_3$	1584-03-8		192 days	0.527	0.527
Hexafluorobenzene	C_6F_6	392-56-3			115 days	115 days
PFPHP- Perfluoroperhydrophenanthrene (Vitreon, Flutec PP 11)	$C_{14}F_{24}$	306-91-2			>1000	–
Halogenated Ethers						
HFE-125	CHF_2OCF_3	3822-68-2		135	101.7	147
HFE-134 (HG-00)	CHF_2OCHF_2	1691-17-4		26.9	25.4	28.4
HFE-143a	CH_3OCF_3	421-14-7		4.9	4.82	5.05
HFE-152a	CH_3OCHF_2	359-15-9		1.8	1.78	1.85
HFE-227ea	$CF_3CHFOCF_3$	2356-62-9		54.8	48.4	58.1
1,1,2,2-tetrafluoro-1-(trifluoromethoxy)ethane	$CF_3OCF_2CF_2H$	2356-61-8			15.3	16.6
HCFE-235ca2 (enflurane)	CHF_2OCF_2CHFCl	13838-16-9		4.42	4.38	4.58
HCFE-235da2 (isoflurane)	$CHF_2OCHClCF_3$	26675-46-7	0.11 ppt	3.5	3.48	3.7
HFE-236ca	$CHF_2OCF_2CHF_2$	32778-11-3		22	18.9	23.2
HFE-236ea2 (desflurane)	$CHF_2OCHFCF_3$	57041-67-5	0.37 ppt	14.1	13.7	14.8
HFE-236fa	$CF_3CH_2OCF_3$	20193-67-3		~7.5	7.56	8
HFE-245cb2	$CF_3CF_2OCH_3$	22410-44-2		5	4.99	5.24
HFE-245fa1	$CHF_2CH_2OCF_3$	84011-15-4		~6.7	6.64	7
HFE-245fa2	$CHF_2OCH_2CF_3$	1885-48-9		5.5	5.49	5.77
HFE-254cb1	$CH_3OCF_2CHF_2$	425-88-7		2.5	2.52	2.62
HFE-254eb2	$CH_3OCHFCF_3$	–		110 days (69–200 days)	107 days (69–200 days)	110 days
HFE-263mf	$CF_3CH_2OCH_3$	460-43-5		28 days (19–47 days)	28 days (19–47 days)	29 days

Stratospheric Lifetime 2022 (years)	ODP	Radiative Efficiency (well mixed) ($W\ m^{-2}\ ppb^{-1}$) [b]	Recommended Adjusted Effective Radiative Efficiency ($W\ m^{-2}\ ppb^{-1}$) [c]	GWP 20-yr	GWP 100-yr	GWP 500-yr	GTP 50-yr	GTP 100-yr	Footnotes *A: Atmospheric Abundance L: Lifetime O: Ozone Depletion Potential R: Radiative Metrics*
>3000	0	0.924	0.938	6590	9070	12,200	9430	11,000	L3, O1, R2
>3000	0	1.05	1.06	6090	8370	11,300	8710	10,200	L3, O1, R27
–	0	0.574	0.574	18,400	24,700	29,800	25,800	29,300	A2, L54, O1, R2
650–950	0	0.596	0.594	14,200	18,800	21,400	19,600	22,000	A2, L55, O1, R2
50,000	0	0.099	0.1	5380	7490	10,700	7770	9180	A2, L6, O1, R2
10,000	0	0.263	0.264	9040	12,600	17,700	13,000	15,400	A2, L6, O1, R2
3000	0	0.74	0.747	23,500	32,300	43,600	33,600	39,200	L56, O1, R6
2600	0	0.274	0.276	6920	9500	12,700	9880	11,500	A2, L56, O1, R2
1.2	0	0.33	0.255	453	126	36	28	23	L57, O1, R19
3200	0	0.318	0.328	7740	10,600	14,400	11,100	12,900	A2, L6, O1, R2
2600	0	0.374	0.375	7430	10,200	13,600	10,600	12,300	L56, O1, R2
>1000	0	0.363	0.275	330	92	26	20	17	L58, O1, R28
4100	0	0.412	0.415	6800	9390	12,900	9760	11,400	A3, L6, O1, R2
3100	0	0.455	0.459	6410	8810	11,900	9160	10,700	A2, L6, O1, R2
3000	0	0.51	0.515	6260	8610	11,600	8950	10,400	L56, O1, R2
3000	0	0.565	0.572	6160	8470	11,400	8810	10,300	L56, O1, R2
2000	0	0.545	0.547	5580	7620	9950	7930	9170	L56, O1, R2
2000	0	0.519	0.536	5460	7460	9750	7770	8990	L56, O1, R2
2000	0	0.569	0.583	5940	8120	10,600	8450	9780	L56, O1, R2
–	0	0.126	0.002	<<1	<<1	<<1	<<1	<<1	L2, O1, R2
–	0	0.239	0.014	<1	<<1	<<1	<<1	<<1	L2, O1, R2
–	0	0.244	0.003	<<1	<<1	<<1	<<1	<<1	L2, O1, R2
–	0	0.307	0.021	<1	<1	<<1	<<1	<<1	L2, O1, R2
–	0	0.336	0.041	2	<1	<1	<1	<<1	L3, O1, R2
–	0	0.304	0.055	4	1	<1	<1	<1	L2, O1, R2
–	0	0.304	0.076	9	2	<1	<1	<1	L2, O1, R2
–	0	0.774	0.478	202	56	16	12	10	L2, O1, R6
–	0	0.153	0.077	31	9	2	2	2	L59, O1, R2
>1000	0	0.961	0.984	7390	9900	11,800	10,300	11,700	L3, O1, R6
330	0	0.42	0.416	13,100	12,900	5880	13,700	10,700	L2, O1, R2
241	0	0.459	0.454	12,600	6370	1860	5150	1880	L2, O1, R2
104	0	0.205	0.189	2140	607	173	140	112	L2, O1, R2
50.6	0	0.201	0.168	874	243	69	54	44	L2, O1, R2
288	0	0.466	0.46	9600	6930	2280	7000	3720	L2, O1, R2
197	0	0.687	0.665	9480	3640	1040	1920	751	L60, O1, R6
96.6	0.04	0.448	0.415	2330	657	187	151	120	L2, O12, R2
58.4	0.03	0.475	0.426	1920	536	153	121	98	A2, L2, O12, R2
103	0	0.654	0.638	11,100	4750	1360	3090	1100	L2, O1, R6
188	0	0.482	0.466	6930	2530	722	1190	504	A2, L2, O1, R2
138	0	0.393	0.378	3770	1,30	323	300	211	L3, O1, R2
107	0	0.365	0.34	2650	754	215	175	139	L2, O1, R2
128	0	0.335	0.322	3230	950	271	236	176	L3, O1, R2
113	0	0.388	0.361	3070	880	251	208	162	L2, O1, R2
66	0	0.3	0.262	1200	333	95	75	61	L2, O1, R2
–	0	0.362	0.176	94	26	7	6	5	L2, O1, R6
–	0	0.216	0.046	7	2	<1	<1	<1	L61, O1, R2

Industrial Designation or Chemical Name	Chemical Formula	CAS RN	Atmospheric Abundance[a]	WMO (2018) Total Lifetime (years)	WMO (2022) Total Lifetime (years)	Tropospheric (OH Reactive Loss) Lifetime 2022 (years)
HFE-263m1	$CF_3OCH_2CH_3$	690-22-2		~145 days	143 days	0.4
1,1,2-trifluoro-2-(trifluoromethoxy)-ethane	$CHF_2CHFOCF_3$	84011-06-3		9	8.75	9.3
Perfluoro ethyl vinyl ether	$C_2F_5OCF=CF_2$	–			3.9 days	0.011
HFE-329mcc2	$CHF_2CF_2OCF_2CF_3$	134769-21-4		~25	22.6	25
1,1,1,3,3,3-hexafluoro trifluoro-methoxy	$CF_3OC(CF_3)_2H$	–			84.6	114.8
HFE-338mmz1	$(CF_3)_2CHOCHF_2$	26103-08-2		22.3	21.3	23.5
HFE-338mcf2	$CF_3CH_2OCF_2CF_3$	156053-88-2		~7.5	7.56	8
HFE-338mec3	$CF_3CFHCF_2OCF_2H$	56860-85-6			9.4	10
HFE-347mmz1 (Sevoflurane)	$(CF_3)_2CHOCH_2F$	28523-86-6	0.16 ppt	1.9	1.41	1.46
HFE-347mcc3 (HFE-7000)	$CH_3OCF_2CF_2CF_3$	375-03-1		5.1	5.07	5.32
HFE-347mcf2	$CHF_2CH_2OCF_2CF_3$	171182-95-9		~6.7	6.64	7
HFE-347pcf2	$CHF_2CF_2OCH_2CF_3$	406-78-0		6.1	5.99	6.31
HFE-347mmy1	$(CF_3)_2CFOCH_3$	22052-84-2		3.7	3.66	3.83
HFE-347mcf	$CHF_2OCH_2CF_2CF_3$	56860-81-2		5.8	5.73	6.03
HFE-356mec3	$CH_3OCF_2CHFCF_3$	382-34-3		2.5	2.87	3
HFE-356mff2	$CF_3CH_2OCH_2CF_3$	333-36-8		128 days (79–270 days)	126 days (79–270 days)	128 days
HFE-356pcf2	$CHF_2CH_2OCF_2CHF_2$	50807-77-7		~6	5.7	6
HFE-356pcf3	$CHF_2OCH_2CF_2CHF_2$	35042-99-0		3.5	3.52	3.67
HFE-356pcc3	$CH_3OCF_2CF_2CHF_2$	160620-20-2		2.5	2.87	3
HFE-356mmz1	$(CF_3)_2CHOCH_3$	13171-18-1		65 days (49–128 days)	67 days (49–128 days)	66 days
HFE-365mcf3	$CF_3CF_2CH_2OCH_3$	378-16-5		25 days (17–42 days)	25 days (17–42 days)	26 days
HFE-365mcf2	$CF_3CF_2OCH_2CH_3$	22052-81-9		219 days	0.573	0.59
HFE-374pc2	$CHF_2CF_2OCH_2CH_3$	512-51-6		76 days (49–128 days)	76 days (49–128 days)	77 days
1,1,2,2-tetrafluoro-3-methoxy-propane	$CHF_2CF_2CH_2OCH_3$	60598-17-6		26 days	26 days	26 days
HFE-43-10pccc124 (H-Galden 1040x, HG-11)	$CHF_2OCF_2OC_2F_4OCHF_2$	188690-77-9		14.1	13.7	14.7
HFE-449s1 (HFE-7100)	$C_4F_9OCH_3$	219484-64-7		4.8	5.05	5.3
n-HFE-7100	$n\text{-}C_4F_9OCH_3$	163702-07-6		4.8	5.05	5.3
i-HFE-7100	$i\text{-}C_4F_9OCH_3$	163702-08-7		4.8	5.05	5.3
1-ethoxy-1,1,2,3,3,3-hexafluoro-propane	$CF_3CHFCF_2OCH_2CH_3$	380-34-7		147 days	147 days	150 days
1,1,1,2,2,3,3-Heptafluoro-3-(1,2,2,2-tetrafluoroethoxy)-propane	$CF_3CF_2CF_2OCHFCF_3$	3330-15-2		59.4	51.1	62
HFE-54-11mecf	$CF_3CHFCF_2OCH_2CF_2CF_3$	1000-28-8		9.1	0.95	0.98
HFE-569sf2 (HFE-7200, isomer mix)	$C_4F_9OC_2H_5$	–		0.8	0.784	0.808
n-HFE-7200	$n\text{-}C_4F_9OC_2H_5$	163702-05-4		0.8	0.784	0.808
i-HFE-7200	$i\text{-}C_4F_9OC_2H_5$	163702-06-5		0.63	0.63	0.649
n-HFE-7300	$n\text{-}C_2F_5CF(OCH_3)CF(CF_3)_2$	132182-92-4			4.99	5.23
n-HFE-7500	$n\text{-}C_3F_7CF(OC_2H_5)CF(CF_3)_2$	297730-93-9			0.348	0.354
HFE-236ca12 (HG-10)	$CHF_2OCF_2OCHF_2$	78522-47-1		26.5	25.1	28
HFE-338pcc13 (HG-01)	$CHF_2OCF_2CF_2OCHF_2$	188690-78-0		13.4	13	14
HG-02 (1,1'-oxybis[2-(difluoro-methoxy)-1,1,2,2-tetrafluoro-ethane)	$HF_2C(OCF_2CF_2)_2OCF_2H$	205367-61-9		26.9	25.4	28.4
HG-03 (1,1,3,3,4,4, 6,6,7,7,9,9, 10,10,12,12-hexadecafluoro-2,5,8,11-tetraoxadodecane)	$HF_2C(OCF_2CF_2)_3OCF_2H$	173350-37-3		26.9	25.4	28.4

Stratospheric Lifetime 2022 (years)	ODP	Radiative Efficiency (well mixed) ($W\ m^{-2}\ ppb^{-1}$) [b]	Recommended Adjusted Effective Radiative Efficiency ($W\ m^{-2}\ ppb^{-1}$) [c]	GWP 20-yr	GWP 100-yr	GWP 500-yr	GTP 50-yr	GTP 100-yr	Footnotes *A: Atmospheric Abundance L: Lifetime O: Ozone Depletion Potential R: Radiative Metrics*
–	0	0.227	0.125	103	29	8	6	5	L3, O1, R2
150	0	0.371	0.356	3970	1240	352	363	232	L62, O1, R2
–	0	0.596	0.025	<1	<<1	<<1	<<1	<<1	L63, O1, R6
241	0	0.559	0.555	7410	3490	1010	2620	925	L3, O1, R2
321	0	0.692	0.686	12,300	11,300	4670	11,900	8630	L64, O1, R6
226	0	0.464	0.458	6470	2950	851	2120	743	L2, O1, R2
138	0	0.481	0.461	3540	1070	304	282	198	L65, O1, R2
156	0	0.712	0.682	6170	1960	559	613	369	L3, O1, R6
41.9	0	0.369	0.299	505	140	40	31	25	A2, L2, O1, R2
108	0	0.367	0.343	2040	579	165	135	107	L2, O1, R2
128	0	0.46	0.44	3310	973	278	242	180	L66, O1, R2
120	0	0.516	0.483	3330	964	275	232	178	L2, O1, R13
86.6	0	0.353	0.321	1400	391	112	89	72	L2, O1, R2
116	0	0.55	0.517	3430	987	282	235	182	L2, O1, R6
66	0	0.333	0.297	1120	312	89	70	57	L67, O1, R2
–	0	0.363	0.19	87	24	7	5	4	L2, O1, R2
116	0	0.406	0.388	2810	810	231	192	149	L68, O1, R2
84	0	0.421	0.393	1810	506	144	115	93	L2, O1, R2
66	0	0.349	0.314	1180	330	94	74	60	L67, O1, R2
–	0	0.336	0.127	31	9	2	2	2	L2, O1, R2
–	0	0.294	0.058	6	2	<1	<1	<1	L69, O1, R2
–	0	0.486	0.309	259	72	21	16	13	L2, O1, R6
–	0	0.325	0.132	45	13	4	3	2	L70, O1, R2
–	0	0.256	0.052	6	2	<1	<1	<1	L71, O1, R2
188	0	1.068	1.03	8580	3130	894	1470	624	L2, O1, R2
108	0	0.391	0.362	1710	487	139	113	90	L2, O1, R2
108	0	0.462	0.428	2020	576	164	134	106	L2, O1, R2
108	0	0.371	0.343	1620	462	132	107	85	L2, O1, R2
–	0	0.347	0.195	96	27	8	6	5	L62, O1, R2
292	0	0.6	0.594	8140	6040	2020	6150	3390	L62, O1, R2
30.4	0	0.778	0.575	437	121	35	27	22	L2, O1, R6
25.9	0	0.653	0	<<1	<<1	<<1	<<1	<<1	L72, O1, R6
25.9	0	0.429	0.3	214	59	17	13	11	L72, O1, R2
21.5	0	0.33	0.216	124	34	10	8	6	L72, O1, R2
107	0	0.572	0.536	1790	509	145	118	94	L73, O1, R29
–	0	0.616	0.332	67	19	5	4	3	L73, O1, R29
240	0	0.663	0.669	11,900	5950	1740	4780	1730	L2, O1, R2
183	0	0.904	0.92	9540	3400	972	1500	669	L2, O1, R2
241	0	1.18	1.167	10,900	5520	1610	4460	1630	L74, O1, R30
241	0	1.46	1.451	10,200	5160	1500	4170	1520	L74, O1, R30

Industrial Designation or Chemical Name	Chemical Formula	CAS RN	Atmospheric Abundance[a]	WMO (2018) Total Lifetime (years)	WMO (2022) Total Lifetime (years)	Tropospheric (OH Reactive Loss) Lifetime 2022 (years)
HG-04 (1,1,3,3,4,4,6,6,7,7,9,9,10,10,12,12,13,13,15,15-eicosafluoro-2,5,8,11,14-pentaoxapentadecane)	$HCF_2O(CF_2CF_2O)_4CF_2H$	173350-38-4		26.9	25.4	28.4
HG-20	$HF_2C(OCF_2)_2OCF_2H$	249932-25-0		26.5	25.1	28
HG-21	$HF_2COCF_2CF_2OCF_2OCF_2OCF_2H$	249932-26-1		13.4	13	14
HG-30	$HF_2C(OCF_2)_3OCF_2H$	–		26.5	25.1	28
1-ethoxy-1,1,2,2,3,3,3-heptafluoro-propane	$CF_3CF_2CF_2OCH_2CH_3$	22052-86-4		0.75	0.728	0.75
Fluoroxene	$CF_3CH_2OCH=CH_2$	406-90-6		3.6 days	3.6 days	3.6 days
1,1,2,2-tetrafluoro-1-(fluoromethoxy)ethane	$CH_2FOCF_2CF_2H$	37031-31-5		6.2	5.89	6.2
2-ethoxy-3,3,4,4,5-pentafluoro-tetrahydro-2,5-bis[1,2,2,2-tetrafluoro-1-(trifluoromethyl)ethyl]-furan	$C_{12}H_5F_{19}O_2$	920979-28-8		0.81	0.806	0.83
Fluoro(methoxy)methane	CH_3OCH_2F	460-22-0		73 days	72 days	73 days
Fluoro(fluoromethoxy)methane	CH_2FOCH_2F	462-51-1		0.9	0.872	0.9
Difluoro(fluoromethoxy)methane	CH_2FOCHF_2	461-63-2		3.2	3.17	3.3
Trifluoro(fluoromethoxy)methane	CH_2FOCF_3	2261-01-0		4.2	4.2	4.4
HG'-01	$CH_3OCF_2CF_2OCH_3$	73287-23-7		1.7	1.68	1.74
HG'-02	$CH_3O(CF_2CF_2O)_2CH_3$	485399-46-0		1.7	1.68	1.74
HG'-03	$CH_3O(CF_2CF_2O)_3CH_3$	485399-48-2		1.7	1.68	1.74
HFE-329me3	$CF_3CFHCF_2OCF_3$	428454-68-6		33.6	31	35.3
2-chloro-1,1,2-trifluoro-1-methoxy-ethane	CH_3OCF_2CHFCl	425-87-6		1.43	1.44	1.49
Octafluorooxolane	$c\text{-}C_4F_8O$	773-14-8	0.074 ppt	–	>3000	–
PFPMIE (perfluoropolymethyl-isopropyl ether)	$CF_3OCF(CF_3)CF_2OCF_2OCF_3$	1309353-34-1		800	370	–
HFE-216	$CF_3OCF=CF_2$	1187-93-5		1.6 days	4.7 days	4.7 days
Fluoroesters						
Trifluoromethyl formate	$HC(O)OCF_3$	85358-65-2		<3.5	3.55	3.71
Perfluoroethyl formate	$HC(O)OCF_2CF_3$	313064-40-3		<3.6	3.57	3.73
Perfluoropropyl formate	$HC(O)OCF_2CF_2CF_3$	271257-42-2		<2.6	2.62	2.73
Perfluorobutyl formate	$HC(O)OCF_2CF_2CF_2CF_3$	197218-56-7		<2.6	2.6	2.7
2,2,2-trifluoroethyl formate	$HC(O)OCH_2CF_3$	32042-38-9		200 days	0.54	0.56
3,3,3-trifluoropropyl formate	$HC(O)OCH_2CH_2CF_3$	1344118-09-7		99 days	108 days	110 days
1,2,2,2-tetrafluoroethyl formate	$HC(O)OCHFCF_3$	481631-19-0		3.1	3.12	3.25
1,1,1,3,3,3-hexafluoropropan-2-yl-formate	$HC(O)OCH(CF_3)_2$	856766-70-6		3.1	3.07	3.2
Perfluorobutyl acetate	$CH_3C(O)OCF_2CF_2CF_2CF_3$	209597-28-4		22 days	22 days	22 days
Perfluoropropyl acetate	$CH_3C(O)OCF_2CF_2CF_3$	1344118-10-0		22 days	22 days	22 days
Perfluoroethyl acetate	$CH_3C(O)OCF_2CF_3$	343269-97-6		22 days	22 days	22 days
Trifluoromethyl acetate	$CH_3C(O)OCF_3$	74123-20-9		22 days	22 days	22 days
Methyl carbonofluoridate	$FCOOCH_3$	1538-06-3		1.8	1.74	1.81
1,1-difluoroethyl carbonofluoridate	$FC(O)OCF_2CH_3$	1344118-11-1		110 days	108 days	110 days
1,1-difluoroethyl 2,2,2-trifluoro-acetate	$CF_3C(O)OCF_2CH_3$	–		110 days	119 days	120 days
Ethyl 2,2,2-trifluoroacetate	$CF_3C(O)OCH_2CH_3$	383-63-1		22 days	69 days	70 days
2,2,2-trifluoroethyl 2,2,2-trifluoro-acetate	$CF_3C(O)OCH_2CF_3$	–		180 days	176 days	180 days
Methyl 2,2,2-trifluoroacetate	$CF_3C(O)OCH_3$	431-47-0		1	0.98	1.01
Methyl 2,2-difluoroacetate	$HCF_2C(O)OCH_3$	433-53-4		124 days	122 days	124 days

Stratospheric Lifetime 2022 (years)	ODP	Radiative Efficiency (well mixed) ($W\ m^{-2}\ ppb^{-1}$) [b]	Recommended Adjusted Effective Radiative Efficiency ($W\ m^{-2}\ ppb^{-1}$) [c]	GWP 20-yr	GWP 100-yr	GWP 500-yr	GTP 50-yr	GTP 100-yr	Footnotes *A: Atmospheric Abundance L: Lifetime O: Ozone Depletion Potential R: Radiative Metrics*
241	0	1.5	1.493	8420	4250	1240	3430	1250	L74, O1, R30
240	0	1.181	1.159	15,200	7590	2210	6090	2210	L75, O1, R6
183	0	1.822	1.763	11,700	4170	1190	1840	820	L74, O1, R6
240	0	1.601	1.572	16,300	8150	2370	6540	2370	L75, O1, R6
24.3	0	0.516	0.354	289	80	23	18	14	L70, O1, R6
–	0	0.3	0.012	<1	<<1	<<1	<<1	<<1	L70, O1, R31
119	0	0.468	0.44	3980	1150	328	276	213	L70, O1, R6
26.5	0	0.66	0.467	167	46	13	10	8	L76, O1, R32
–	0	0.191	0.076	56	16	4	3	3	L77, O1, R6
28.3	0	0.191	0.222	566	157	45	35	28	L78, O1, R6
78	0	0.25	0.315	2380	665	190	150	121	L78, O1, R6
95	0	0.308	0.389	3280	923	263	211	169	L78, O1, R6
48	0	0.352	0.291	723	201	57	45	36	L79, O1, R2
48	0	0.683	0.563	816	227	65	50	41	L79, O1, R2
48	0	0.927	0.763	780	217	62	48	39	L79, O1, R2
256	0	0.499	0.5	7400	4190	1250	3740	1500	L80, O1, R2
43	0	0.313	0.251	584	162	46	36	29	L81, O1, R6
>3000	0	0.469	0.469	10,200	14,100	19,000	14,600	17,100	A5, L82, O1, R32
370	0	0.653	0.656	7830	9830	8860	10,300	10,900	L83, O1, R2
–	0	0.491	0.024	<1	<1	<<1	<<1	<<1	L84, O1, R6
110	0	0.347	0.313	2320	650	185	147	119	L85, O1, R34
110	0	0.504	0.456	2370	662	189	150	121	L86, O1, R34
83	0	0.222	0.194	569	158	45	36	29	L86, O1, R34
83	0	0.613	0.54	1270	354	101	79	65	L87, O1, R34
–	0	0.278	0.176	178	49	14	11	9	L88, O1, R34
–	0	0.277	0.138	69	19	5	4	3	L89, O1, R34
77	0	0.396	0.354	1810	504	144	114	92	L90, O1, R34
76	0	0.373	0.335	1250	350	100	79	64	L89, O1, R34
–	0	0.706	0.125	7	2	<1	<1	<1	L91, O1, R34
–	0	0.571	0.101	6	2	<1	<1	<1	L92, O1, R34
–	0	0.572	0.101	8	2	<1	<1	<1	L92, O1, R34
–	0	0.404	0.071	8	2	<1	<1	<1	L92, O1, R34
50	0	0.085	0.071	380	106	30	23	19	L90, O1, R34
–	0	0.352	0.171	95	26	8	6	5	L93, O1, R34
–	0	0.533	0.271	119	33	9	7	6	L89, O1, R34
–	0	0.315	0.122	39	11	3	2	2	L94, O1, R2
–	0	0.428	0.257	152	42	12	9	8	L94, O1, R34
31	0	0.267	0.201	369	103	29	23	19	L94, O1, R35
–	0	0.193	0.101	74	20	6	4	4	L94, O1, R34

Industrial Designation or Chemical Name	Chemical Formula	CAS RN	Atmospheric Abundance[a]	WMO (2018) Total Lifetime (years)	WMO (2022) Total Lifetime (years)	Tropospheric (OH Reactive Loss) Lifetime 2022 (years)
Difluoromethyl 2,2,2-trifluoro-acetate	$CF_3C(O)OCHF_2$	2024-86-4		110 days	108 days	110 days
Vinyl 2,2,2-trifluoroacetate	$CF_3C(O)OCH=CH_2$	433-28-3			1.7 days	1.7 days
Allyl 2,2,2-trifluoroacetate	$CF_3C(O)OCH_2CH=CH_2$	383-67-5			1.5 days	1.5 days
Halogenated Alcohols						
3,3,3-trifluoropropan-1-ol	$CF_3CH_2CH_2OH$	2240-88-2		15 days	16 days	16 days
2,2,3,3,3-pentafluoropropan-1-ol	$CF_3CF_2CH_2OH$	422-05-9		172 days	168 days	172 days
4,4,4-trifluorobutan-1-ol	$CF_3(CH_2)_2CH_2OH$	461-18-7		5.4 days	5.4 days	5.4 days
2,2,3,3,4,4,5,5-octafluorocyclo-pentanol	$-(CF_2)_4CH(OH)-$	16621-87-7		110 days	19.5 days	19.5 days
1,1,1,3,3,3-hexafluoropropan-2-ol	$(CF_3)_2CHOH$	920-66-1		1.9	1.88	1.95
3,3,4,4,5,5,6,6,7,7,7-undeca-fluoroheptan-1-ol	$CF_3(CF_2)_4CH_2CH_2OH$	185689-57-0		17 days	17 days	17.4 days
3,3,4,4,5,5,6,6,7,7,8,8,9,9,9-pentadecafluorononan-1-ol	$CF_3(CF_2)_6CH_2CH_2OH$	755-02-2		17 days	17 days	17.4 days
3,3,4,4,5,5,6,6,7,7,8,8,9,9,10, 10,11,11,11-nonadecafluoro-undecan-1-ol	$CF_3(CF_2)_8CH_2CH_2OH$	87017-97-8		17 days	13 days	12.8 days
2,2,3,3,4,4,4-heptafluoro-butan-1-ol	$CF_3CF_2CF_2CH_2OH$	375-01-9		0.55	0.46	0.472
2,2,3,3-tetrafluoro-1-propanol	$CHF_2CF_2CH_2OH$	76-37-9		93 days	92.4 days	93.6 days
2,2,3,4,4,4-hexafluoro-1-butanol	$CF_3CHFCF_2CH_2OH$	382-31-0		134 days (85–280 days)	132 days (85–280 days)	134 days
2-fluoroethanol	CH_2FCH_2OH	371-62-0		16 days	16.2 days	16.2 days
2,2-difluoroethanol	CHF_2CH_2OH	359-13-7		61 days	60.8 days	61.4 days
2,2,2-trifluoroethanol	CF_3CH_2OH	75-89-8		167 days	163 days	167 days
2,2-3,3,4,4,5,5,5-fluoro-1-pentanol	$CF_3CF_2CF_2CF_2CH_2OH$	–		172 days (111–330 days)	168 days (111–330 days)	172 days
Halogenated Ketones						
1-fluoropropan-2-one	$CH_3C(O)CH_2F$	430-51-3			16 days	136 days
1,1,1-trifluoropropan-2-one	$CF_3C(O)CH_3$	421-50-1			16 days	136 days
1,1,1,3,3,3-hexafluoropropan-2-one	$CF_3C(O)CF_3$	684-16-2			18 days	–
1,1,1-trifluorobutan-2-one	$CF_3C(O)CH_2CH_3$	381-88-4			0.8 days	13.5 days
NOVEC-1230, FK-5-1-12 (Perfluoro -(2-methyl-3-pentanone))	$CF_3CF_2C(O)CF(CF_3)_2$	756-13-8		7 days (7–14 days)	7 days (7–14 days)	–
NOVEC-774 (Tetradecafluoro-2,4-dimethylpentan-3-one)	$(CF_3)_2CFC(O)CF(CF_3)_2$	–		–	7 days	–
Perfluoro(2-methyl-3-hexanone)	$CF_3CF_2CF_2C(O)CF(CF_3)_2$	–		–	7 days	–
Chloroacetone	$CH_3C(O)CH_2Cl$	78-95-5			1 day	32 days
Bromoacetone	$CH_3C(O)CH_2Br$	598-31-2			<2 hours	15 days
Halogenated Aldehydes						
Trifluoroacetaldehyde	CF_3CHO	75-90-1			2.7 days	31 days
Trifluoroacetyl fluoride	CF_3CFO	354-34-7			6.9 days	–
Oxalyl fluoride	$FC(O)C(O)F$	359-40-0			5.1 days	–
3,3,3-trifluoro-propanal	CF_3CH_2CHO	460-40-2		5 days	2.7 days	5.5 days
2,2,3,3,3-pentafluoropropanal	CF_3CF_2CHO	422-06-0			1.4 days	13.5 days
Difluoromalonyl fluoride	$FC(O)CF_2C(O)F$	5930-67-6			6.9 days	–
4,4,4-trifluorobutanal	$CF_3CH_2CH_2CHO$	406-87-1			1.8 days	2.6 days
2,2,3,3,4,4,4-heptafluorobutanal	$CF_3CF_2CF_2CHO$	375-02-0			1.1 days	13.5 days
Tetrafluorosuccinyl fluoride	$FC(O)CF_2CF_2C(O)F$	679-13-0			6.9 days	–
2,2,3,3,4,4,5,5,5-nonafluoro-petanal	$CF_3CF_2CF_2CF_2CHO$	375-53-1			1.1 days	13.5 days

Stratospheric Lifetime 2022 (years)	ODP	Radiative Efficiency (well mixed) ($W\ m^{-2}\ ppb^{-1}$) [b]	Recommended Adjusted Effective Radiative Efficiency ($W\ m^{-2}\ ppb^{-1}$) [c]	GWP 20-yr	GWP 100-yr	GWP 500-yr	GTP 50-yr	GTP 100-yr	Footnotes *A: Atmospheric Abundance L: Lifetime O: Ozone Depletion Potential R: Radiative Metrics*
–	0	0.471	0.23	100	28	8	6	5	L89, O1, R34
–	0	0.261	0.009	<<1	<<1	<<1	<<1	<<1	L95, O1, R2
–	0	0.334	0.008	<<1	<<1	<<1	<<1	<<1	L95, O1, R2
–	0	0.221	0.032	3	<1	<1	<1	<1	L2, O1, R2
–	0	0.289	0.17	125	35	10	8	6	L2, O1, R2
–	0	0.116	0.007	<1	<<1	<<1	<<1	<<1	L96, O1, R2
–	0	0.319	0.054	3	<1	<1	<1	<1	L97, O1, R2
53	0	0.334	0.294	789	219	63	49	40	L97, O1, R2
–	0	0.371	0.058	2	<1	<1	<1	<1	L98, O1, R2
–	0	0.412	0.065	2	<1	<1	<1	<<1	L98, O1, R2
–	0	0.312	0.04	<1	<1	<<1	<<1	<<1	L98, O1, R2
–	0	0.321	0.197	109	30	9	7	5	L99, O1, R2
–	0	0.257	0.122	56	16	4	3	3	L100, O1, R2
–	0	0.424	0.227	108	30	9	7	5	L2, O1, R2
–	0	0.087	0.012	2	<1	<1	<1	<<1	L2, O1, R2
–	0	0.127	0.045	22	6	2	1	1	L2, O1, R2
–	0	0.202	0.1	107	30	8	7	5	L2, O1, R2
–	0	0.529	0.045	20	6	2	1	<1	L2, O1, R6
–	0	0.046	0.026	4	<1	<1	<1	<1	L3, O1, R2
–	0	0.205	0.099	9	3	<1	<1	<1	L3, O1, R2
–	0	0.289	0.147	10	3	<1	<1	<1	L3, O1, R2
–	0	0.205	0.0994	<1	<1	<<1	<<1	<<1	L3, O1, R2
–	0	0.407	0.133	2	<1	<1	<1	<<1	L101, O1, R2
–	0	0.802	0.264	3	<1	<1	<1	<1	L101, L102, O1, R6
–	0	0.768	0.253	3	<1	<1	<1	<1	L101, L102, O1, R6
–		0.038	4.60E-04	<<1	<<1	<<1	<<1	<<1	L103, O1, R2
–		0.045	5.00E-05	<<1	<<1	<<1	<<1	<<1	L104, O1, R6
–	0	0.167	0.00481	<<1	<<1	<<1	<<1	<<1	L105, L106, O1, R2
–	0	0.274	0.0188	<1	<1	<<1	<<1	<<1	L106, O1, R6
–	0	0.188	0.00988	<1	<<1	<<1	<<1	<<1	L106, O1, R6
–	0	0.173	0.00515	<<1	<<1	<<1	<<1	<<1	L106, L107, O1, R2
–	0	0.202	0.00331	<<1	<<1	<<1	<<1	<<1	L3, L106, O1, R2
–	0	0.29	0.0198	<1	<1	<<1	<<1	<<1	L106, O1, R6
–	0	0.163	0.00336	<<1	<<1	<<1	<<1	<<1	L3, L106, O1, R2
–	0	0.25	0.00328	<<1	<<1	<<1	<<1	<<1	L3, L106, O1, R2
–	0	0.375	0.0257	<1	<1	<<1	<<1	<<1	L106, O1, R6
–	0	0.286	0.00376	<<1	<<1	<<1	<<1	<<1	L3, L106, O1, R2

Industrial Designation or Chemical Name	Chemical Formula	CAS RN	Atmospheric Abundance[a]	WMO (2018) Total Lifetime (years)	WMO (2022) Total Lifetime (years)	Tropospheric (OH Reactive Loss) Lifetime 2022 (years)
Iodocarbons						
Methyl iodide	CH_3I	74-88-4	0.8 ppt (0.3–2.1)	<14 days (3.5–14 days)	<14 days (3.5–14 days)	269 days
Bromoiodomethane	CH_2BrI	557-68-6		≤60 mins	≤60 mins	150 days
Chloroiodomethane	CH_2ClI	593-71-5		<100 mins	<100 mins	150 days
Diiodomethane	CH_2I_2	75-11-6		≤5 mins	≤5 mins	3.8 days
Trifluoroiodomethane	CF_3I	2314-97-8		<5 days (0.7–5 days)	<5 days (0.7–5 days)	3
Iodoethane	CH_3CH_2I	75-03-6		<4 days (2.4–13.9 days)	<4 days (2.4–13.9 days)	52 days (13–94 days)
n-iodopropane	$CH_3CH_2CH_2I$	107-08-4		<2 days	<2 days	14.6 days
i-iodopropane	CH_3CHICH_3	75-30-9		<1 day	<1 day	12.7 days
3-iodo-1-propene	$CH_2=CHCH_2I$	556-56-9			<1.2 days	1.4 days
1-iodo-heptafluoropropane	$CF_3CF_2CF_2I$	754-34-7		<2 days	<2 days	3
Tert-butyl iodide	$(CH_3)_3CI$	558-17-8			<5 days	13.6 days
Special Compounds						
Carbonyl fluoride	COF_2	353-50-4		7 days (5–10 days)	7 days (5–10 days)	
Phosphorus tribromide	PBr_3	7789-60-8		<0.01 days	<0.1 day	
Ammonia	NH_3	7664-41-7		(few days)	(few days)	110 days
Carbonyl Sulfide	COS	463-58-1	505 ppt	2	2	–
Sulfuryl fluoride	SO_2F_2	699-79-8	2.6 ppt	36	36	>300
Trifluoroacetic acid (TFA)	$CF_3C(O)OH$	76-05-1			5 days	116 days
3,5-dichloro-2,4,6-trifluoro-pyridine (DCTFP)	$C_5Cl_2F_3N$	1737-93-5			–	–
Heptafluorobutyronitrile	$(CF_3)_2CFCN$	375-00-8			32.7	58.3
Chlorine nitrate	$ClONO_2$	14545-72-3			14 days	–
Bromine nitrate	$BrONO_2$	40423-14-1			~2 hours	–

Table Heading Footnotes:

[a] Atmospheric abundances were taken from *Chapter 1*, *Chapter 2*, and WMO (2018) for the year 2020 or 2016, as noted in the footnotes.

[b] Values in this column include molecule dependent stratospheric temperature adjustment (see *Section A.2.5.2*) and assumes that compounds are well mixed in the atmosphere (note that this assumption leads to overestimation of RE for molecules that have an inhomogeneous atmospheric distribution).

[c] Values in this column include molecule dependent stratospheric temperature adjustment (see *Section A.2.5.2*), lifetime adjustment (*Section A.2.5.3*), low-frequency infrared absorption adjustment (*Section A.2.5.4*), and tropospheric adjustments when relevant (*Section A.2.5.5*).

Abundance Footnotes:

A1 Year 2020 value was taken from the Global Monitoring Laboratory (GML) database (gml.noaa.gov/ccgg/trends).

A2 Taken from Chapter 1 for the year 2020.

A3 Taken from WMO (2018) for the year 2016. Values in parentheses represent a potential range of values.

A4 Taken from Chapter 2 for the year 2020.

A5 Taken from Chapter 1.

Lifetime Footnotes:

L1 Perturbation total lifetime reported in IPCC (2022) used to evaluate climate metrics. The lifetime for CH_4 based on a budget analysis is 9.1 years.

L2 OH rate coefficient was taken from Burkholder et al. (2019).

L3 Estimated OH radical rate coefficient and/or total lifetime.

L4 Tropospheric photolysis partial lifetimes have been included in the total lifetime analysis; see *Section A.1 Introduction*.

L5 Atmospheric lifetimes taken from the recommendations given in the SPARC (2013) lifetime report. Note that in some cases there are slight differences between the combination of the partial lifetimes and the recommended total atmospheric lifetime, which was derived from multi-model results and field observations.

L6 Total lifetime is the best estimate taken from Ravishankara et al. (1993) that includes mesospheric loss due to Lyman-α (121.567 nm) photolysis.

L7 Stratospheric partial lifetime was taken from the 2-D model calculations in Davis et al. (2016). These values are in agreement with the values reported in Laube et al. (2014): 59 (43–95) years for CFC-112, 51 (32–113) years for CFC-112a, and 59 (31–305) years for CFC-113a (scaled to a CFC-11 lifetime of 52 years), but of higher precision.

L8 The total lifetime includes mesospheric loss due to Lyman-α (121.567 nm) photolysis.

L9 Lifetime was taken from Kloss et al. (2014).

Stratospheric Lifetime 2022 (years)	ODP	Radiative Efficiency (well mixed) ($W\ m^{-2}\ ppb^{-1}$) [b]	Recommended Adjusted Effective Radiative Efficiency ($W\ m^{-2}\ ppb^{-1}$) [c]	GWP 20-yr	GWP 100-yr	GWP 500-yr	GTP 50-yr	GTP 100-yr	Footnotes *A: Atmospheric Abundance L: Lifetime O: Ozone Depletion Potential R: Radiative Metrics*
–	<0.42	0.009	0.004	<1	<<1	<<1	<<1	<<1	A3, L2, L108, L109, L110, O11, R2
–	<0.02	0.031	2.00E-05	<<1	<<1	<<1	<<1	<<1	L108, L111, L112, O14, R6
–	<0.07	0.035	4.00E-05	<<1	<<1	<<1	<<1	<<1	L108, L111, L112, O11, R6
–	<0.02	0.038	2.00E-06	<<1	<<1	<<1	<<1	<<1	L108, L111, L113, O14, R2
–	<0.09	0.283	0.067	1	<1	<<1	<<1	<<1	L108, L109, L110, O11, R6
–	<0.02	0.021	0.004	<<1	<<1	<<1	<<1	<<1	L108, L110, L111, L114, O14, R2
–	<0.02	0.0248	5.60E-04	<<1	<<1	<<1	<<1	<<1	L108, L111, L114, O14, R6
–	>0.02	0.043	5.20E-04	<<1	<<1	<<1	<<1	<<1	L108, L114, O14, R2
–	–	0.042	6.00E-04	<<1	<<1	<<1	<<1	<<1	L3, L115, R2
–	<0.09	0.427	9.69E-03	<<1	<<1	<<1	<<1	<<1	L108, L116, O15, R6
–	–	0.032	0.008	<1	<<1	<<1	<<1	<<1	L3, L115, R6
–	–	0.123	0.008	<1	<1	<<1	<<1	<<1	L106, R2
–	–	0.038	<0.001	<<1	<<1	<<1	<<1	<<1	L106, R6
–	–	0.061	0.0014	<1	<<1	<<1	<<1	<<1	L2, L106, R2
60	–	0.016	0.0137	109	30	9	7	6	A3, L117, R2
630	0	0.203	0.2	7130	4390	1340	4140	1820	A2, L2, L118, O1, R2
–	0	0.359	0.019	<1	<1	<<1	<<1	<<1	L106, L119, O1, R2
–	–	0.118	–	–	–	–	–	–	R6
74	0	0.223	0.221	4020	2350	705	2140	884	L120, O1, R37
–	–	0.086	0.0108	1	<1	<<1	<<1	<<1	L121, R2
–	–	0.102	1.09E-04	<<1	<<1	<<1	<<1	<<1	L121, R2

L10 Stratospheric partial lifetime was taken from 2-D model calculations in Papadimitriou et al. (2013b).

L11 Ocean and soil loss partial lifetimes have been included in the total lifetime analysis; see *Section A.1 Introduction*.

L12 Lifetimes were taken from Papanastasiou et al. (2018), where *k*(OH) was calculated using the structure activity relationship (SAR) of DeMore (1996) and stratospheric lifetime estimated as described in the *Section A.1 Introduction*.

L13 Stratospheric lifetime was taken from the 2-D model simulation reported in McGillen et al. (2015).

L14 OH radical rate coefficient was taken from Burkholder et al. (2020).

L15 Stratospheric partial lifetime was calculated using a 2-D model with OH and $O(^1D)$ rate coefficients recommended in SPARC (2013) lifetime report, see *Chapter 3*.

L16 OH radical reactivity was calculated using the structure activity relationships of DeMore (1996) with an assumed E/R of 1700 K.

L17 OH radical reactivity calculated using the room temperature rate coefficient reported by Young et al. (2009) with an assumed E/R of 1700 K.

L18 OH radical rate coefficient was taken from Zhang et al. (2015).

L19 OH radical rate coefficient was assumed to be the same as for HFC-329p.

L20 OH radical rate coefficient was taken from Guo et al. (2019).

L21 OH radical rate coefficient data were taken from Tokuhashi et al. (2018a).

L22 OH radical rate coefficient data were taken from Tokuhashi et al. (2021).

L23 OH radical rate coefficient was assumed to be similar to that of HFO-1234ze.

L24 A lifetime upper limit was estimated based on reactivity trends.

L25 OH radical rate coefficient was taken from Tokuhashi et al. (2021).

L26 OH radical rate coefficient was taken from Papadimitriou et al. (2015).

L27 OH radical rate coefficient was taken from Jiménez et al. (2016).

L28 OH radical rate coefficient was taken from Liu et al. (2016).

L29 The lifetime estimated to be similar to that of (*E*)-$CF_3CH{=}CHCF_3$.

L30 OH radical rate coefficient was taken from Papadimitriou and Burkholder (2016).

L31 OH radical rate coefficient was calculated using the room temperature rate coefficient reported by Sulbaek Andersen et al. (2005a) with an E/R of –170 K.

L32 Partial lifetimes, other than ocean uptake (see *Section A.1 Introduction*), were taken from recommendations in the SPARC (2016) CCl_4 report.

L33 OH radial rate coefficient was taken from Taylor et al. (1992).
L34 OH radial rate coefficient was taken from Jiang et al. (1993).
L35 OH radial rate coefficient was taken from Donaghy et al. (1993).
L36 OH radial rate coefficient was taken from Loison et al. (1998).
L37 OH radial rate coefficient was taken from Markert and Nielsen (1992).
L38 OH radial rate coefficient was taken from Zhang et al. (2017).
L39 OH radial rate coefficient was taken from Tuazon et al. (1988).
L40 OH radial rate coefficient was taken from Bryukov et al. (2009).
L41 OH radial rate coefficient was taken from the studies of Arnts et al. (1989) and Wahner and Zetzsch (1983).
L42 OH radial rate coefficient was taken from Wahner and Zetzsch (1983).
L43 OH radial rate coefficient was taken from Barrera et al. (2015).
L44 OH radial rate coefficient was taken from the studies of Tokuhashi et al. (2019) and Barrera et al. (2015).
L45 OH radial rate coefficient was taken from Tokuhashi et al. (2018b).
L46 Local lifetime was estimated to be similar to that of (*E*)-$CF_3CH=CHCl$.
L47 Local lifetime was estimated to be similar to that of $CF_3CF=CF_2$.
L48 OH radical rate coefficient was taken from Tokuhashi et al. (2021).
L49 OH radical rate coefficient was taken from the studies of Atkinson (1985) and Young et al. (2008).
L50 Lifetime was estimated to be similar to that of CBr_2F_2.
L51 OH radical rate coefficient was taken from Perry et al. (1977).
L52 OH radical rate coefficient was taken from Albaladejo et al. (2003).
L53 Tropospheric (84,150 years) and mesospheric (2531 years) lifetimes were taken from the 2-D model calculations in Papadimitriou et al. (2013a).
L54 Lifetime range derived from the modeling studies of Kovacs et al. (2017), with a reported lifetime of 1278 years, and Ray et al. (2017), with a reported lifetime of 850 years.
L55 Total lifetime range was taken from Takahashi et al. (2002), which included mesospheric loss due to Lyman-α (121.567 nm) photolysis, dissociative electron attachment, and solar proton event loss processes.
L56 Total lifetime was estimate based on the increase in Lyman-α (121.567 nm) absorption cross section (increased photolysis rate) with increasing number of $-CF_2-$ groups in the perfluorocarbon.
L57 OH radical rate coefficient was taken from Jia et al. (2013).
L58 OH radical rate coefficient was taken from Zhang et al. (2017).
L59 OH radical rate coefficient was taken from McIlroy and Tully (1993).
L60 OH radical reaction rate coefficient was taken from Sulbaek Andersen et al. (2005b).
L61 OH radical rate coefficient was taken from the room temperature value from Oyaro et al. (2005) with an assumed E/R of 500 K.
L62 OH radical rate coefficient was taken from the room temperature value from Oyaro et al. (2005) with an assumed E/R of 1500 K.
L63 OH radical reaction rate coefficient was taken from Srinivasulu et al. (2018).
L64 OH radical reaction rate coefficient was taken from Sulbaek Andersen et al. (2005b).
L65 The OH radical reactive loss partial lifetime was estimated to be the same as for $CF_3OCH_2CF_3$.
L66 OH radical reaction rate coefficient was assumed to be the same as $CHF_2CH_2OCF_3$.
L67 The OH radical reactive loss partial lifetime was estimated to be the same as for $CH_3OCF_2CHF_2$.
L68 The OH radical reactive loss partial lifetime was estimated from the sum of the OH partial lifetimes of $CF_3CF_2OCF_2CHF_2$ and $CF_3CF_2OCH_2CHF_2$.
L69 OH radical rate coefficient was taken from the room temperature value from Oyaro et al. (2004) with an assumed E/R of 500 K.
L70 The OH radical partial lifetime was taken from the value in Bravo et al. (2011b).
L71 The OH radical reactive loss partial lifetime was calculated using the room temperature OH rate coefficient from Oyaro et al. (2004) with an assumed E/R of 1000 K.
L72 The OH radical reactive loss partial lifetime was calculated using the room temperature OH rate coefficient from Christensen et al. (1998) with an assumed E/R of 1000 K.
L73 OH radical reaction rate coefficient was taken from Rodriguez et al. (2014).
L74 OH radical reaction rate coefficient was taken from Sulbaek Andersen et al. (2010).
L75 OH radical reaction rate coefficient was assumed to be similar to HG-10.
L76 The OH radical reactive loss partial lifetime was calculated using the room temperature OH rate coefficient from Javadi et al. (2007) with an assumed E/R of 1000 K.
L77 The OH radical reactive loss partial lifetime was calculated using the structure activity relationship estimated OH rate coefficient in Urata et al. (2003).
L78 OH radical rate coefficient was taken from the theoretically calculated value in Blowers et al. (2008).
L79 The OH radical reactive loss partial lifetime was calculated using the room temperature OH rate coefficient from Sulbaek Andersen et al. (2004) with an assumed E/R of 1000 K.
L80 The OH radical reactive loss partial lifetime was calculated using the room temperature OH rate coefficient from Wallington et al. (2004) with an assumed E/R of 1000 K.
L81 The OH radical reactive loss partial lifetime was calculated using the room temperature OH rate coefficient from Tokuhashi et al. (1999).
L82 Total lifetime estimated in Vollmer et al. (2019).
L83 Total lifetime estimated in Young et al. (2006).
L84 The OH radical reactive loss partial lifetime was calculated using the room temperature OH rate coefficient from Mashino et al. (2000) with an assumed E/R of −400 K.

L85 The OH radical reactive loss partial lifetime was calculated using the room temperature OH rate coefficient from Chen et al. (2004b).

L86 The OH radical reactive loss partial lifetime was calculated using the room temperature OH rate coefficient from Chen et al. (2004a).

L87 OH radical rate coefficient was assumed to be similar to that of perfluoropropyl formate ($HC(O)OCF_2CF_2CF_3$).

L88 The OH radical reactive loss partial lifetime was calculated using the room temperature OH rate coefficient from Oyaro et al. (2004) with an assumed E/R of 500 K.

L89 Total lifetime was taken from the estimate in Bravo et al. (2011a).

L90 The OH radical reactive loss partial lifetime was calculated using the room temperature OH rate coefficient from Chen et al. (2006).

L91 The OH radical reactive loss partial lifetime was taken from the estimate in Christensen et al. (1998), which was based on comparison with Cl atom reactivity.

L92 OH radical rate coefficient was assumed to be the same as for perfluorobutyl acetate ($CH_3C(O)OCF_2CF_2CF_2CF_3$).

L93 OH radical rate coefficient was assumed to be the same as for ethyl 2,2,2-trifluoroacetate ($CF_3C(O)OCH_2CH_3$).

L94 The OH radical reactive loss partial lifetime was calculated using the room temperature OH rate coefficient from Blanco and Teruel (2007) with an assumed E/R of 1000 K.

L95 OH radical reaction rate coefficient was taken from Rodriguez et al. (2016).

L96 OH radical reaction rate coefficient was taken from Antiñolo et al. (2011).

L97 OH radical reaction rate coefficient was estimated by comparison with other fluoroalcohols; see Ellis et al. (2003).

L98 The OH radical reactive loss partial lifetime was calculated using the room temperature OH rate coefficient from Ellis et al. (2003) with an assumed E/R of 1000 K.

L99 OH radical rate coefficient was assumed to be the same as $CF_3CF_2CH_2OH$.

L100 OH radical rate coefficient was taken from Antiñolo et al. (2012).

L101 Tropospheric photolysis is the dominant loss process for perfluoroketones; see Taniguchi et al. (2003)and Jackson et al. (2011).

L102 OH radical rate coefficient was assumed to be similar to that of NOVEC-1230.

L103 OH radical reaction rate coefficient was taken from Carr et al. (2003); UV photolysis is the primary loss process, and the lifetime was taken from Burkholder et al. (2002).

L104 UV photolysis is the primary loss process, and the lifetime was taken from Burkholder et al. (2002).

L105 OH radical reaction rate coefficient was taken from Sellevåg et al. (2004).

L106 Heterogeneous uptake is most likely the predominant loss process.

L107 OH radical reaction rate coefficient was taken from Antiñolo et al. (2010).

L108 Total lifetime is primarily determined by UV photolysis with a decreasing local lifetime with increasing altitude.

L109 Lifetime estimates were taken from the 3-D model simulations of Youn et al. (2010).

L110 Lifetime range represents a likely variation in local photolysis partial lifetime with time and location of emissions.

L111 Photolysis lifetimes were taken from Mössinger et al. (1998) for CH_2BrI and Roehl et al. (1997) for CH_2CII, CH_3CH_2I, $CH_3CH_2CH_2I$, and CH_3CHICH_3.

L112 OH radical reaction rate coefficient was assumed to be similar to that of CH_2Br_2.

L113 OH radical reaction rate coefficient was taken from Zhang et al. (2011).

L114 OH radical reaction rate coefficient was taken from Zhang et al. (2012).

L115 UV photolysis rate coefficient was assumed to be the same as for CF_3I.

L116 Photolysis and OH reactivity assumed the same as for CF_3I.

L117 Lifetime was taken from Brühl et al. (2012).

L118 Lifetimes were taken from Papadimitriou et al. (2008) and Mühle et al. (2009).

L119 OH radical reaction rate coefficient was taken from Carr et al. (1994).

L120 OH radical reaction rate coefficient was taken from Blázquez et al. (2017).

L121 Formed in the stratosphere with a predominant UV photolysis loss. UV absorption spectra are recommended in Burkholder et al. (2019).

ODP Footnotes:

O1 Negligible and assigned a value of zero.

O2 Value was taken from Ravishankara et al. (2009).

O3 Value was taken from *Chapter 7*.

O4 A greater ODP value was reported from the 2-D model calculations in Davis et al. (2016): 0.95 (CFC-113), 0.78 (CFC-114), 1.01 (CFC-12), and 1.06 (CCl_4).

O5 Value was taken from the Montreal Protocol.

O6 ODP was taken from the 2-D model calculations in Davis et al. (2016). The semiempirical ODP reported in Laube et al. (2014) is consistent with the Davis et al. (2016) value but has a larger uncertainty range.

O7 ODP was taken from Kloss et al. (2014).

O8 ODP was taken from the 2-D model calculations in Papadimitriou et al. (2013b).

O9 Semiempirical ODP was calculated using an empirical relationship of the fractional release factor with stratospheric lifetime given in Papanastasiou et al. (2018).

O10 ODP was taken from Papanastasiou et al. (2018).

O11 Upper limit of ODPs of short-lived substances reported in the studies of Brioude et al. (2010) for C_2H_5Br, CH_2CBrCF_3, n-C_3H_7Br, C_2HCl_3, CCl_3CHO, CH_3I, CF_3I, C_3F_7I, CH_2CII, and $CHBr_3$; Wuebbles et al. (2009) for C_3H_7Br, C_2HCl_3, and C_2Cl_4; Patten et al. (2010) for HFO-1233zd and *E*-CHCl=CHCl; Youn et al. (2010) for CF_3I and CH_3I; and Tegtmeier et al. (2012) for CH_2Br_2 and $CHBr_3$. The derived ODPs in these studies were shown to be strongly dependent on the region and season of the substance emissions, with the greatest values obtained for emissions in the Indian subcontinent.

O12 ODP was taken from Langbein et al. (1999).

O14 ODP was assumed to be <0.02 for surface emissions.

O15 ODP was assumed to be the same as for CF_3I.

RE, GWP, and GTP Footnotes:

GWP and GTP values that are less then 0.1 are reported as "<<1" in the table. GWP and GTP values that are between 0.1 and 1 are reported as "<1" in the table.

R1 Radiative efficiency and climate metrics were taken from IPCC (2022).

R2 Radiative efficiency was taken from the recommendation given in Hodnebrog et al. (2020a), which was based on a combination of literature review of experimental data and reanalysis. Climate metrics were calculated here.

R3 Radiative efficiency was calculated using the room temperature infrared absorption spectrum reported in the Pacific Northwest National Laboratory (PNNL) database (secure2.pnl.gov/nsd/nsd.nsf). Sharpe et al. (2004).

R4 Radiative efficiency was taken from the recommendation given in Hodnebrog et al. (2020a) with +12% added due to tropospheric adjustments.

R5 Radiative efficiency and climate metrics were calculated using the infrared absorption spectrum reported in Davis et al. (2016) and the lifetime reported here.

R6 Radiative efficiency and climate metrics were calculated using the theoretically calculated infrared absorption spectrum and lifetimes given here.

R7 Radiative efficiency and climate metrics were calculated using the infrared absorption spectrum reported in Papadimitriou et al. (2013b) and the lifetime reported here.

R8 An instantaneous radiative efficiency was reported in Charmet et al. (2013), which was increased by +10% here to approximately account for the stratospheric temperature adjustment.

R9 Radiative efficiency and climate metrics were calculated using the theoretically calculated infrared absorption spectrum in Papanastasiou et al. (2018) and lifetimes given here.

R10 Radiative efficiency metrics were calculated using the infrared spectrum reported in McGillen et al. (2015).

R11 Radiative efficiency and climate metrics were calculated using the theoretically calculated infrared absorption spectrum reported in Burkholder et al. (2020).

R12 Radiative efficiency and climate metrics were calculated using the infrared absorption spectrum reported in Gierczak et al. (1996) and the lifetime reported here.

R13 Radiative efficiency was taken from recommendation given in Hodnebrog et al. (2013), which was based on a combination of literature review of experimental and theoretical data and reanalysis.

R14 Radiative efficiency and climate metrics were calculated using the infrared absorption spectrum reported in Rajakumar et al. (2006) and the lifetime reported here.

R15 Zhang et al. (2015) reported an instantaneous radiative efficiency value, using the Oslo LBL–Pinnock method. In the absence of an experimental spectrum, a +10% stratospheric temperature adjustment was applied here to obtain the radiative efficiency.

R16 Guo et al. (2019) reported an "instantaneous radiative efficiency" value, using the Pinnock method. In the absence of an experimental spectrum, a +10% stratospheric temperature adjustment was applied here to obtain the radiative efficiency.

R17 Radiative efficiency and climate metrics were calculated using the infrared absorption spectrum reported in Baasandorj et al. (2010) and the lifetime reported here.

R18 Radiative efficiency and climate metrics were calculated using the infrared absorption spectrum reported in Baasandorj et al. (2016) and the lifetime reported here.

R19 Radiative efficiency and climate metrics were calculated using the instantaneous radiative efficiency reported in Jai et al. (2013), which was calculated using the Pinnock method, and the lifetimes reported here. In the absence of an experimental spectrum, a +10% stratospheric temperature adjustment was applied to obtain the radiative efficiency here.

R20 Radiative efficiency and climate metrics were based on the infrared spectrum reported in Baasandorj et al. (2018).

R21 Radiative efficiency and climate metrics were based on an average of the instantaneous radiative efficiencies reported in Baasandorj et al. (2011) and Østerstrøm et al. (2017), which were calculated using the Pinnock method, and the lifetimes reported here. In the absence of experimental spectra, a +10% stratospheric temperature adjustment was applied here to obtain the radiative efficiency.

R22 Radiative efficiency and climate metrics were calculated using the instantaneous radiative efficiency reported in Jiménez et al. (2016), which was calculated using the Pinnock method, and the lifetimes reported here. In the absence of an experimental spectrum, a +10% stratospheric temperature adjustment was applied here to obtain the radiative efficiency.

R23 Radiative efficiency and climate metrics were calculated using the instantaneous radiative efficiency reported in Liu et al. (2016), which was calculated using the Pinnock method, and the lifetimes reported here. In the absence of an experimental spectrum, a +10% stratospheric temperature adjustment was applied here to obtain the radiative efficiency.

R24 Radiative efficiency and climate metrics were calculated using the infrared spectrum from Papadimitriou and Burkholder (2016).

R25 Radiative efficiency and climate metrics were calculated using the instantaneous radiative efficiency reported in Barrera et al. (2015), which was calculated using the Pinnock method, and the lifetimes reported here. In the absence of an experimental spectrum, a +10% stratospheric temperature adjustment was applied here to obtain the radiative efficiency.

R26 Radiative efficiency and climate metrics were calculated using the infrared spectrum in Gierczak et al. (2014).

R27 Radiative efficiency and climate metrics were calculated using the infrared spectrum in Bernard et al. (2018).

R28 Radiative efficiency and climate metrics were calculated using the instantaneous radiative efficiency reported in Zhang et al. (2017), which was calculated using the Pinnock method, and the lifetimes reported here. In the absence of an experimental spectrum, a +10% stratospheric temperature adjustment was applied here to obtain the radiative efficiency.

R29 Radiative efficiency and climate metrics were calculated using the instantaneous radiative efficiency reported in Rodríguez et al. (2014), which was calculated using the Pinnock method, and the lifetimes reported here. In the absence of an experimental spectrum, a +10% stratospheric temperature adjustment was applied here to obtain the radiative efficiency.

R30 Radiative efficiency and climate metrics were calculated using the instantaneous radiative efficiency reported in Sulbaek Andersen et al. (2010), which was calculated using the Pinnock method, and the lifetimes reported here. In the absence of an experimental spectrum, a +10% stratospheric temperature adjustment was applied here to obtain the radiative efficiency.

R31 Radiative efficiency and climate metrics were calculated using the instantaneous radiative efficiency reported in Bravo et al. (2013), which was calculated using the Pinnock method, and the lifetimes reported here. In the absence of an experimental spectrum, a +10% stratospheric temperature adjustment was applied here to obtain the radiative efficiency.

R32 Radiative efficiency and climate metrics were calculated using the infrared spectrum in Vollmer et al. (2019).

R33 Radiative efficiency and climate metrics were calculated using the instantaneous radiative efficiency reported in Javadi et al. (2007), which was calculated using the Pinnock method, and the lifetimes reported here. In the absence of an experimental spectrum, a +10% stratospheric temperature adjustment was applied here to obtain the radiative efficiency.

R34 Radiative efficiency and climate metrics were calculated using the recommendation given in Hodnebrog et al. (2013), which was based on the Bravo et al. (2011a) theoretically calculated infrared absorption spectra.

R35 Radiative efficiency and climate metrics were calculated using the instantaneous radiative efficiency reported in Østerstrøm et al. (2015), which was calculated using the Pinnock method, and the lifetimes reported here. In the absence of an experimental spectrum, a +10% stratospheric temperature adjustment was applied here to obtain the radiative efficiency.

R36 An OH radical reaction vertical profile lifetime adjustment was applied for very short-lived compounds lost by UV photolysis.

R37 Radiative efficiency and climate metrics were calculated using the radiative efficiency reported in Sulbaek Andersen (2017), which was calculated using the Pinnock method, with a +10% stratospheric temperature adjustment applied, and the lifetimes reported here.

REFERENCES

Albaladejo, J., B. Ballesteros, E. Jiménez, Y. Díaz de Mera, and E. Martínez, Gas-Phase OH Radical-Initiated Oxidation of the 3-halopropenes studied by PLP-LIF in the temperature range 228-388 K, ***Atmos. Environ.***, ***37***, 2919–2926, doi:10.1016/S1352-2310(03)00297-8, 2003.

Andrews, T., C.J. Smith, G. Myhre, P.M. Forster, R. Chadwick, and D. Ackerley, Effective radiative forcing in a GCM with fixed surface temperatures, ***J. Geophys. Res.***, ***126***, doi:10.1029/2020JD033880, 2021.

Antiñolo, M., S. González, B. Ballesteros, J. Albaladejo, and E. Jiménez, Laboratory studies of $CHF_2CF_2CH_2OH$ and $CF_3CF_2CH_2OH$: UV and IR absorption cross sections and OH rate coefficients between 263 and 358 K, ***J. Phys. Chem. A***, ***116***, 6041–6050, doi:10.1021/jp2111622, 2012.

Antiñolo, M., E. Jiménez, and J. Albaladejo, Temperature effects on the removal of potential HFC replacements, $CF_3CH_2CH_2OH$ and $CF_3(CH_2)_2CH_2OH$, initiated by OH radicals, ***Environ. Sci. Technol.***, ***45***, 4323–4330, doi:10.1021/es103931s, 2011.

Antiñolo, M., E. Jiménez, A. Notario, E. Martínez, and J. Albaladejo, Tropospheric photooxidation of CF_3CH_2CHO and $CF_3(CH_2)_2CHO$ initiated by Cl atoms and OH radicals, ***Atmos. Chem. Phys.***, ***10***, 1911–1922, doi.org/10.5194/acp-10-1911-2010, 2010.

Arnts, R.R., R.L. Seila, and J.J. Bufalini, Determination of room temperature OH rate constants for acetylene, ethylene dichloride, ethylene dibromide, p-dichlorobenzene and carbon disulfide, ***J. Air Pollut. Control Assoc.***, ***39***, 453–460, doi:10.1080/08940630.1989.10466544, 1989.

Atkinson, R., S.M. Aschmann, A.M. Winer, and J.N. Pitts, Atmospheric gas phase loss processes for chlorobenzene, benzotrifluoride, and 4-chlorobenzotrifluoride, and generalization of predictive techniques for atmospheric lifetimes of aromatic compounds, ***Arch. Environ. Contam. Tox.***, ***14***, 417–425, doi:10.1007/BF01055527, 1985.

Baasandorj, M., and J.B. Burkholder, Rate coefficient for the gas-phase OH + $CHF=CF_2$ reaction between 212 and 375 K, ***Int. J. Chem Kinet.***, ***48***, 714–723, doi:10.1002/kin.21027, 2016.

Baasandorj, M., E.L. Fleming, C.H. Jackman, and J.B. Burkholder, $O(^1D)$ kinetic study of key ozone depleting substances and greenhouse gases, ***J. Phys. Chem. A***, ***117***, 2434–2445, doi:10.1021/j312781c, 2013.

Baasandorj, M., G. Knight, V.C. Papadimitriou, R.K. Talukdar, A.R. Ravishankara, and J.B. Burkholder, Rate coefficients for the gas-phase reaction of the hydroxyl radical with $CH_2=CHF$ and $CH_2= CF_2$ ***J. Phys. Chem. A***, ***114***, 4619–4633, doi:10.1021/jp100527z, 2010.

Baasandorj, M., P. Marshall, A.R. Ravishankara, and J.B. Burkholder, Rate coefficient measurements and theoretical analysis of the OH + (***E***)-$CF_3CH=CHCF_3$ reaction, ***J. Phys. Chem. A***, ***122***, 4635–4646, doi:10.1021/acs.jpca.8b02771, 2018.

Baasandorj, M., A.R. Ravishankara, and J.B. Burkholder, Atmospheric chemistry of (***Z***)-$CF_3CH=CHCF_3$: OH radical reaction rate coefficient and global warming potential, ***J. Phys. Chem. A***, ***115***, 10539–10549, doi:10.1021/jp206195g, 2011.

Barrera, J.A., P.R. Dalmasso, J.P.A. Abrate, R.A. Taccone, and S.I. Lane, Kinetic study of the OH and Cl-initiated oxidation, lifetimes and atmospheric acceptability indices of three halogenated ethenes, ***RSC Advances***, ***5***, 73501, doi:10.1039/c5ra13589c, 2015.

Bernard, F., M.R. McGillen, E.L. Fleming, C.H. Jackman, and J.B. Burkholder, $CBrF_3$ (Halon-1301): UV absorption spectrum between 210 and 320 K, atmospheric lifetime, and ozone depletion potential, ***J. Photochem. and Photobio. A: Chem.***, ***306***, 13–20, doi:10.1016/j.jphotochem.2015.03.012, 2015.

Bernard, F., D.K. Papanastasiou, V.C. Papadimitriou, and J.B. Burkholder, Infrared absorption spectra of $N(C_xF_{2x+1})_3$, x = 2-5 perfluoroamines, ***J. Quant. Spectrosc. Rad. Trans.***, ***211***, 166–171, doi:10.1016/j.jqsrt.2018.02.039, 2018.

Blanco, M.B., and M.A. Teruel, Atmospheric degradation of fluoroesters (FESs): Gas-phase reactivity study towards OH radicals at 298 K, ***Atmos. Environ.***, ***41***, 7330–7338, doi:10.1016/j.atmosenv.2007.05.013, 2007.

Blázquez, S., M. Antiñolo, O.J. Nielsen, J. Albaladejo, and E. Jiménez, Reaction kinetics of $(CF_3)_2CFCN$ with OH radicals as a function of temperature (278-358 K): A good replacement for greenhouse SF_6?, ***Chem. Phys. Lett.***, ***687***, 297–302, doi:10.1016/j.cplett.2017.09.039, 2017.

Blowers, P., K.F. Tetrault, and Y. Trujilo-Morehead, Global warming potential predictions for hydrofluoroethers with two carbon atoms, ***Theor. Chem. Account***, ***119***, 369–381, doi:10.1007/s00214-007-0394-3, 2008.

Bravo, I., Y. Diaz-de-Mera, A. Aranda, E. Moreno, D.R. Nutt, and G. Marston, Radiative efficiencies for fluorinated esters: indirect global warming potentials of hydrofluoroethers, ***Phys. Chem. Chem. Phys.***, ***13***, 17185–17193, doi:10.1039/c1cp21874c, 2011a.

Bravo, I., G. Marston, D.R. Nutt, and K.P. Shine, Radiative efficiencies and global warming potentials using theoretically determined absorption cross-sections for several hydrofluoroethers (HFEs) and hydrofluoropolyethers (HFPEs), ***J. Quant. Spectrosc. Rad. Trans.***, ***112***, 1967–1977, doi:10.1016/j.jqsrt.2011.05.001, 2011b.

Bravo, I., A. Rodríguez, D. Rodríguez, Y. Diaz-de-Mera, A. Notario, and A. Aranda, Atmospheric chemistry and environmental assessment of inhalational fluroxene, ***ChemPhysChem***, ***14***, 3834–3842, doi:10.1002/cphc.201300559, 2013.

Brioude, J., R.W. Portmann, J.S. Daniel, O.R. Cooper, G.J. Frost, K.H. Rosenlof, C. Granier, A.R. Ravishankara, S.A. Montzka, and A. Stohl, Variations in ozone depletion potentials of very short-lived substances with season and emission region, ***Geophys. Res. Lett.***, ***37***, L19804, doi:10.1029/2010GL044856, 2010.

Brühl, C., J. Lelieveld, P.J. Crutzen, and H. Tost, The role of carbonyl suphide as a source of stratospheric sulphate aerosol and its impact on climate, ***Atmos. Chem. Phys.***, ***12***, 1239–1253, doi:10.5194/acp-12-1239-2012, 2012.

Bryukov, M.G., V.D. Knyazev, W.M. Gehling, and B. Dellinger, Kinetics of the gas-phase reaction of OH with chlorobenzene, ***J. Phys. Chem. A***, ***113***, 10452–10459, doi:10.1021/jp9049186, 2009.

Burkholder, J.B., R.A. Cox, and A.R. Ravishankara, Atmospheric Degradation of Ozone Depleting Substances, Their Substitutes, and Related Species, ***Chem. Rev.***, ***115***, 3704–3759, doi:10.1021/cr5006759, 2015.

Burkholder, J.B., M.K. Gilles, T. Gierczak, and A.R. Ravishankara, The atmospheric degradation of 1-bromopropane ($CH_3CH_2CH_2Br$): The photochemistry of bromoacetone, ***Geophys. Res. Lett.***, ***29***, doi:10.1029/2002GL014712, 2002.

Burkholder, J.B., P. Marshall, P.P. Bera, J.S. Francisco, and T.J. Lee, Climate metrics for C1-C4 hydrofluorocarbons (HFCs), ***J. Phys. Chem. A***, ***124***, 4793–4800, doi:10.1021/acs.jpca.0c02679, 2020.

Burkholder, J.B., S.P. Sander, J. Abbatt, J.R. Barker, C. Cappa, J.D. Crounse, T.S. Dibble, R.E. Huie, C.E. Kolb, M.J. Kurylo, V.L. Orkin, C.J. Percival, D.M. Wilmouth, and P.H. Wine, "Chemical Kinetics and Photochemical Data for Use in Atmospheric Studies, Evaluation No. 19," JPL Publication 19-5, Jet Propulsion Laboratory, Pasadena, 2020 http://jpldataeval.jpl.nasa.gov., 2019.

Carr, S., D.E. Shallcross, C.E. Canosa-Mas, J.C. Wenger, H.W. Sidebottom, J.J. Treacy, and R.P. Wayne, A kinetic and mechanistic study of the gas-phase reactions of OH radicals and Cl atoms with some halogenated acetones and their atmospheric implications, ***Phys. Chem. Chem. Phys.***, ***5***, 3874–3883, doi:10.1039/b304298g, 2003.

Carr, S., J.J. Treacy, H.W. Sidebottom, R.K. Connell, C.E. Canosa-Mass, R.P. Wayne, and J. Franklin, Kinetics and mechanisms for the reaction of hydroxyl radicals with trifluoroacetic acid under atmospheric conditions, ***Chem. Phys. Lett.***, ***227***, 39–44, doi:10.1016/0009-2614(94)00802-7, 1994.

Charmet, A.P., P. Stoppa, N. Tasinato, S. Giorgianni, V. Barone, M. Biczysko, J. Bloino, C. Cappelli, I. Carnimeo, and C. Puzzarini, An integrated experimental and quantum-chemical investigation on the vibrational spectra of chlorofluoromethane, ***J. Chem. Phys.***, ***139***, 15, doi: 10.1063/1.4825380, 2013.

Chen, L., S. Kutsuna, K. Tokuhashi, and A. Sekiya, Kinetics study of the gas-phase reactions of $C_2F_5OC(O)H$ and ***n***-$C_3F_7OC(O)H$ with OH radicals at 253-328 K, ***Chem. Phys. Lett.***, ***400***, 563–568, doi:10.1016/j.cplett.2004.11.019, 2004a.

Chen, L., S. Kutsuna, K. Tokuhashi, and A. Sekiya, Kinetics of the gas-phase reaction of $CF_3OC(O)H$ with OH radicals at 242-328 K, ***Int. J. Chem. Kinet.***, ***36***, 337–344, doi:10.1002/kin.20004, 2004b.

Chen, L., S. Kutsuna, K. Tokuhashi, and A. Sekiya, Kinetics and mechanisms of $CF_3CHFOCH_3$, $CF_3CHFOC(O)H$, and $FC(O)OCH_3$ reactions with OH radicals, ***J. Phys. Chem. A***, ***110***, 12845–12851, doi:10.1021/jp064917h, 2006.

Christensen, L.K., J. Sehested, O.J. Nielsen, M. Bilde, T.J. Wallington, A. Guschin, L.T. Molina, and M.J. Molina, Atmospheric chemistry of HFE-7200 ($C_4F_9OC_2H_5$): Reaction with OH radicals and fate of $C_4F_9OCH_2CH_2O(\bullet)$ and $C_4F_9OCHO(\bullet)CH_3$ radicals, ***J. Phys. Chem. A***, ***102***, 4839–4845, doi:10.1021/jp981128u, 1998.

Collins, W.J., R.G. Derwent, C.E. Johnson, and D.S. Stevenson, The oxidation of organic compounds in the troposphere and their global warming potentials, ***Climatic Change***, ***52***, 453–479, doi:10.1023/a:1014221225434, 2002.

Davis, M.E., F. Bernard, M.R. McGillen, E.L. Fleming, and J.B. Burkholder, UV and infrared absorption spectra, atmospheric lifetimes, and ozone depletion and global warming potentials for CCl_2FCCl_2F (CFC-112), CCl_3CClF_2 (CFC-112a), CCl_3CF_3 (CFC-113a), and CCl_2FCF_3 (CFC-114a), ***Atmos. Chem. Phys.***, ***16***, 8043–8052, doi:10.5194/acp-16-8043-2016, 2016.

DeMore, W.B., Experimental and estimated rate constants for the reactions of hydroxyl radicals with several halocarbons, ***J. Phys. Chem.***, ***100***, 5813–5820, doi:10.1021/jp953216+, 1996.

Donaghy, T., I. Shanahan, M. Hande, and S. Fitzpatrick, Rate constants and atmospheric lifetimes for the reactions of OH radicals and Cl atoms with haloalkanes, ***Int. J. Chem. Kinet.***, ***25***, 273–284, doi:10.1002/kin.550250407, 1993.

Ellis, D.A., J.W. Martin, S.A. Mabury, M.D. Hurley, M.P. Sulbaek Andersen, and T.J. Wallington, Atmospheric lifetime of fluorotelomer alcohols, ***Environ. Sci. Technol.***, ***37***, 3816–3820, doi:10.1021/es034136j, 2003.

Forster, P., T. Storelvmo, K. Armour, W. Collins, J.-L. Dufresne, D. Frame, D.J. Lunt, T. Mauritsen, M.D. Palmer, M. Watanabe, M. Wild, and H. Zhang, The Earth's Energy Budget, Climate Feedbacks, and Climate Sensitivity, Chapter 7 In Climate Change 2021: ***The Physical Science Basis. Contribution of Working Group I to the Sixth Assessment Report of the Intergovernmental Panel on Climate Change***, edited by Masson-Delmotte, V., P. Zhai, A. Pirani, S.L. Connors, C. Péan, S. Berger, N. Caud, Y. Chen, L. Goldfarb, M.I. Gomis, M. Huang, K. Leitzell, E. Lonnoy, J.B.R. Matthews, T.K. Maycock, T. Waterfield, O. Yelekçi, R. Yu, and B. Zhou, Cambridge University Press, United Kingdom and New York, NY, USA, 131 pp., doi:10.1017/9781009157896.009, 2021.

Gasser, T., G.P. Peters, J.S. Fuglestvedt, W.J. Collins, D.T. Shindell, and P. Ciais, Accounting for the climate–carbon feedback in emission metrics, ***Earth Syst. Dynam.***, ***8***, 235–253, doi:10.5194/esd-8-235-2017, 2017.

Gierczak, T., M. Baasandorj, and J.B. Burkholder, OH + (***E***)- and (***Z***)-1-chloro-3,3,3-trifluoropropene-1 ($CF_3CH=CHCl$) reaction rate coefficients: Stereoisomer-dependent reactivity, ***J. Phys. Chem. A***, ***118***, 11015–11025, doi:10.1021/jp509127h, 2014.

Gierczak, T., R.K. Talukdar, J.B. Burkholder, R.W. Portmann, J.S. Daniel, S. Solomon, and A.R. Ravishankara, Atmospheric fate and greenhouse warming potentials of HFC 236fa and HFC 236ea, ***J. Geophys. Res.***, ***101***, 12905–12911, doi:10.1029/96jd00059, 1996.

Guo, Q., N. Zhang, T. Uchimaru, L. Chen, H. Quan, and J. Mizukado, Atmospheric chemistry for gas-phase reactions of cyc-$CF_2CF_2CF_2CH_XCH_X$- (X = H or F) with OH radicals in the temperature range of 253-328 K, ***Atmos. Environ.***, ***215***, 8, doi:10.1016/j.atmosenv.2019.116895, 2019.

Hodnebrog, Ø., B. Aamaas, J.S. Fuglestvedt, G. Marston, G. Myhre, C.J. Nielsen, M. Sandstad, K.P. Shine, and T.J. Wallington, Updated global warming potentials and radiative efficiencies of halocarbons and other weak atmospheric absorbers, ***Rev. Geophys.***, ***58***, 30, doi:10.1029/2019rg000691, 2020a.

Hodnebrog, Ø., S.B. Dalsoren, and G. Myhre, Lifetimes, direct and indirect radiative forcing, and global warming potentials of ethane (C_2H_6), propane (C_3H_8), and butane (C_4H_{10}), ***Atmos. Sci. Lett.***, ***19***, 7, doi:10.1002/asl.804, 2018.

Hodnebrog, Ø., M. Etminan, J.S. Fuglestvedt, G. Marston, G. Myhre, C.J. Nielsen, K.P. Shine, and T.J. Wallington, Global warming potentials and radiative efficiencies of halocarbons and related compounds: A comprehensive review ***Rev. Geophys.***, ***51***, 300–378, doi:10.1002/rog.20013, 2013.

Hodnebrog, Ø., G. Myhre, R.J. Kramer, K.P. Shine, T. Andrews, G. Faluvegi, M. Kasoar, A. Kirkevåg, J.-F. Lamarque, J. Mülmenstädt, D. Olivié, B.H. Samset, D. Shindell, C.J. Smith, T. Takemura, and A. Voulgarakis, The effect of rapid adjustments to halocarbons and N_2O on radiative forcing, ***Clim. Atmos. Sci.***, ***3***, 43, doi:10.1038/s41612-020-00150-x, 2020b.

Hu, L. The role of the ocean in the atmospheric budgets of methyl bromide, methyl chloride and methane. Doctoral dissertation, Texas A&M University, College Station, TX, U.S.A., 2012.

Hu, L., S.A. Yvon-Lewis, J.H. Butler, J.M. Lobert, and D.B. King, An improved oceanic budget for methyl chloride, ***J. Geophys. Res.***, ***118***, 715–725, doi:10.1029/2012JC008196, 2013.

Hu, L., S.A. Yvon-Lewis, Y. Liu, and T.S. Bianchi, The ocean in near equilibrium with atmospheric methyl bromide, ***Global Biogeochem. Cycles***, ***26***, GB3016, doi:10.1029/2011GB004272, 2012.

IPCC (Intergovernmental Panel on Climate Change), ***Climate Change 2013: The Physical Science Basis, ontribution of Working Group 1 to the Fifth Assessment Report of the Intergovernmental Panel on Climate Change,*** edited by T.F. Stocker, D. Qin, G.-K. Plattner, M. Tignor, S.K. Allen, J. Boschung, A. Nauels, Y. Xia, V. Bex and P.M. Midgley, Cambridge University Press, Cambridge, United Kingdom, 1535 pp., 2013.

IPCC (Intergovenmental Panel on Climate Change), ***Climate Change 2021: The Physical Science Basis, Contribution of Working Group I to the Sixth Assessment Report of the Intergovernmental Panel on Climate Change***, edited by V. Masson-Delmotte, P. Zhai, A. Pirani, S.L. Connors, C. Péan, S. Berger, N. Caud, Y. Chen, L. Goldfarb, M.I. Gomis, M. Huang, K. Leitzell, E. Lonnoy, J.B.R. Matthews, T.K. Maycock, T. Waterfield, O. Yelekçi, R. Yu, and B. Zhou, Cambridge University Press, Cambridge, United Kingdom and New York, NY, USA, In press, doi:10.1017/9781009157896, 2022.

Jackson, D.A., C.J. Young, M.D. Hurley, T.J. Wallington, and S.A. Mabury, Atmospheric degradation of perfluoro-2-methyl-3-pentanone: Photolysis, hydrolysis and hydration, ***Environ. Sci. Technol.***, ***45***, 8030–8036, doi:10.1021/es104362g, 2011.

Javadi, M.S., O.J. Nielsen, T.J. Wallington, M.D. Hurley, and J.G. Owens, Atmospheric chemistry of 2-ethoxy-3,3,4,4,5-pentafluorotetrahydro-2,5-bis[1,2,2,2-tetrafluoro-1-(trifluoromethyl)ethyl]-furan: Kinetics, mechanisms, and products of Cl atom and OH radical initiated oxidation, ***Environ. Sci. Technol.***, ***41***, 7389–7395, doi:10.1021/es071175c, 2007.

Jia, X., L. Chen, J. Mizukado, S. Kutsuna, and K. Tokuhashi, Rate constants for the gas-phase reactions of cyclo-$CX=CXCF_2CF_2$- (X = H, F) with OH radicals at a temperature range of 253-328 K, ***Chem. Phys. Lett.***, ***572***, 21–25, doi:10.1016/j.cplett.2013.04.020, 2013.

Jiang, Z., P.H. Taylor, and B. Dellinger, Laser photolysis/laser-induced fluorescence studies of the reaction of OH with 1,1,1,2- and 1,1,2,2-tetrachloroethane over an extended temperature range, ***J. Phys. Chem.***, ***97***, 5050–5053, doi:10.1021/j100121a033, 1993.

Jiménez, E., S. González, M. Cazaunau, H. Chen, B. Ballesteros, V.r. Daële, J. Albaladejo, and A. Mellouki, Atmospheric degradation initiated by OH radicals of the potential foam expansion agent, $CF_3(CF_2)_2CH=CH_2$ (HFC-1447fz): Kinetics and formation of gaseous products and secondary organic aerosols, ***Environ. Sci. Technol.***, ***50***, 1234–1242, doi:10.1021/acs.est.5b04379, 2016.

Joos, F., R. Roth, J.S. Fuglestvedt, G.P. Peters, I.G. Enting, W. von Bloh, V. Brovkin, E.J. Burke, M. Eby, N.R. Edwards, T. Friedrich, T.L. Frölicher, P.R. Halloran, P.B. Holden, C. Jones, T. Kleinen, F. Mackenzie, K. Matsumoto, M. Meinshausen, G.K. Plattner, A. Reisinger, J. Segschneider, G. Shaffer, M. Steinacher, K. Strassmann, K. Tanaka, A. Timmermann, and A.J. Weaver, Carbon dioxide and climate impulse response functions for the computation of greenhouse gas metrics: a multi-model analysis, ***Atmos. Chem. Phys.***, ***13***, 2793–2825, doi:10.5194/acp-13-2793-2013, 2013.

Jubb, A.M., M.R. McGillen, R.W. Portmann, J.S. Daniel, and J.B. Burkholder, An atmospheric photochemical source of the persistent greenhouse gas CF_4, ***Geophys. Res. Lett.***, ***42***, doi:10.1002/2015GL066193, 2015.

Kloss, C., M.J. Newland, D.E. Oram, P.J. Fraser, C.A.M. Brenninkmeijer, T. Röckmann, and J.C. Laube, Atmospheric abundances, trends and emissions of CFC-216ba, CFC-216ca and HCFC-225ca, ***Atmosphere***, ***5***, 420–434, doi:10.3390/atmos5020420, 2014.

Ko, M.K.W., P.A. Newman, S. Reimann, S.E. Strahan, R.A. Plumb, R.S. Stolarski, J.B. Burkholder, W. Mellouki, A. Engel, E.L. Atlas, M. Chipperfield, and Q. Liang Lifetimes of stratospheric ozone-depleting substances, their replacements, and related species, 2013.

Kovács, T., W. Feng, A. Totterdill, J.M.C. Plane, S. Dhomse, J.C. Gómez-Martín, G.P. Stiller, F.J. Haenel, C. Smith, P.M. Forster, R.R. García, D.R. Marsh, and M.P.

Chipperfield, Determination of the atmospheric lifetime and global warming potential of sulfur hexafluoride using a three-dimensional model, ***Atmos. Chem. Phys.***, ***17***, 883–898, doi:10.5194/acp-17-883-2017, 2017.

Langbein, T., H. Sonntag, D. Trapp, A. Hoffmann, W. Malms, E.-P. Röth, V. Mörs, and R. Zellner, Volatile anaesthetics and the atmosphere: atmospheric lifetimes and atmospheric effects of halothane, enflurane, isoflurane, desflurane and sevoflurane, ***Brit. J. Anaesth***, ***82***, 66–73, doi:10.1093/bja/82.1.66, 1999.

Laube, J.C., M.J. Newland, C. Hogan, C.A.M. Brenninkmeijer, P.J. Fraser, P. Martinerie, D.E. Oram, C.E. Reeves, T. Röckmann, J. Schwander, E. Witrant, and W.T. Sturges, Newly detetecd ozone-depleting substances in the atmosphere, ***Nature Geoscience***, ***7***, 266–269, doi:10.1038/ngeo2109, 2014.

Liu, D., S. Qin, W. Li, D. Zhang, and Z. Guo, Atmospheric chemistry of 1H-Heptafluorocyclopentene (cyc-$CF_2CF_2CF_2CF$=CH−): Rate constant, products, and mechanism of gas-phase reactions with OH radicals, IR absorption spectrum, photochemical ozone creation potential, and global warming potential, ***J. Phys. Chem. A***, ***120***, 9557–9563, doi:10.1021/acs.jpca.6b10348, 2016.

Loison, J.C., L. Ley, and R. Lesclaux, Kinetic study of OH radical reactions with chlorobutane isomers at 298 K, ***Chem. Phys. Lett.***, ***296***, 350–356, doi:10.1016/S0009-2614(98)01058-6, 1998.

Markert, F., and O.J. Nielsen, The reactions of OH radicals with chloralkanes in the temperature range 295-360 K, ***Chem. Phys. Lett.***, ***194***, 123–127, doi:10.1016/0009-2614(92)85753-W, 1992.

Mashino, M., Y. Ninomiya, M. Kawasaki, T.J. Wallington, and M.D. Hurley, Atmospheric chemistry of $CF_3CF=CF_2$: Kinetics and mechanism of its reactions with OH radicals, Cl atoms, and ozone, ***J. Phys. Chem. A***, ***104***, 7255–7260, doi:10.1021/jp000498r, 2000.

McGillen, M.R., F. Bernard, E.L. Fleming, and J.B. Burkholder, HCFC-133a (CF_3CH_2Cl): OH rate coefficient, UV and infrared absorption spectra, and atmospheric implications, ***Geophys. Res. Lett.***, ***42***, 6098–6105, doi:10.1002/2015GL064939, 2015.

McIlroy, A., and F.P. Tully, Kinetic study of OH reactions with perfluoropropene and perfluorobenzene, ***J. Phys. Chem.***, ***97***, 610–614, doi:10.1021/j100105a013, 1993.

Modak, A., G. Bala, K. Caldeira, and L. Cao, Does shortwave absorption by methane influence its effectiveness?, ***Climate Dynamics***, 1–20, doi:10.1007/s00382-018-4102-x, 2018.

Montzka, S.A., S. Reimann, (Coordinating Lead Authors) A. Engel, K. Krüger, S. O`Doherty, and W.T. Sturges, , Ozone-Depleting Substances (ODSs) and Related Chemicals, Chapter 1 in Scientific Assessment of Ozone Depletion: 2010, Global Ozone Research and Monitoring Project–Report No. 52, World Meteorological Organization, Geneva, Switzerland, 2011.

Mössinger, J.C., D.E. Shallcross, and R.A. Cox, UV-VIS absorption cross-sections and atmospheric lifetimes of CH_2Br_2, CH_2I_2 and CH_2BrI, ***J. Chem. Soc., Faraday Trans.***, ***94***, 1391–1396, doi:10.1039/A709160E, 1998.

Mühle, J., J. Huang, R.F. Weiss, R.G. Prinn, B.R. Miller, P.K. Salameh, C.M. Harth, P.J. Fraser, L.W. Porter, B.R. Greally, S. O'Doherty, and P.G. Simonds, Sulfuryl fluoride in the global atmosphere, ***J. Geophys. Res.***, ***114***, D05306, doi:10.1029/2008JD011162, 2009.

Orkin, V.L., V.G. Khamaganov, E.E. Kasimovskaya, and A.G. Guschin, Photochemical properties of some Cl containing halogenated alkanes, ***J. Phys. Chem. A***, ***117***, 5483–5490, doi:10.1021/jp400408y, 2013.

Østerstrøm, F.F., S.T. Andersen, T.I. Solling, O.J. Nielsen, and M.P.S. Andersen, Atmospheric chemistry of ***Z***- and ***E***-$CF_3CH=CHCF_3$, ***Phys. Chem. Chem. Phys.***, ***19***, 735–750, doi:10.1039/C6CP07234H, 2017.

Østerstrøm, F.F., T.J. Wallington, M.P.S. Andersen, and O.J. Nielsen, Atmospheric chemistry of $(CF_3)_2CHOCH_3$, $(CF_3)_2CHOCHO$, and $CF_3C(O)OCH_3$, ***J. Phys. Chem. A***, ***119***, 10540–10552, doi:10.1021/acs.jpca.5b08204, 2015.

Oyaro, N., S.R. Sellevåg, and C.J. Nielsen, Study of the OH and Cl-initiated oxidation, IR absorption cross-section, radiative forcing, and global warming potential of four C_4-hydrofluoroethers, ***Environ. Sci. Technol.***, ***38***, 5567–5576, doi:10.1021/es0497330, 2004.

Oyaro, N., S.R. Sellevåg, and C.J. Nielsen, Atmospheric chemistry of hydrofluoroethers: Reaction of a series of hydrofluoroethers with OH radicals and Cl atoms, atmospheric lifetimes, and global warming potentials, ***J. Phys. Chem. A***, ***109***, 337–346, doi:10.1021/jp047860c, 2005.

Papadimitriou, V.C., and J.B. Burkholder, OH radical reaction rate coefficients, infrared spectrum, and global warming potential of $(CF_3)_2CFCH=CHF$ (HFO-1438ezy(***E***)), ***J. Phys. Chem. A***, ***120***, 6618–6628, doi:10.1021/acs.jpca.6b06096, 2016.

Papadimitriou, V.C., M.R. McGillen, E.L. Fleming, C.H. Jackman, and J.B. Burkholder, NF_3: UV absorption spectrum temperature dependence and the atmospheric and climate forcing implications, ***Geophys. Res. Lett.***, ***40***, 1–6, doi:10.1002/grl.50120, 2013a.

Papadimitriou, V.C., M.R. McGillen, S.C. Smith, A.M. Jubb, R.W. Portmann, B.D. Hall, E.L. Fleming, C.H. Jackman, and J.B. Burkholder, 1,2-Dichlorohexafluorocyclobutane (1,2-c-$C_4F_6Cl_2$, R-316c) a potent ozone depleting substance and greenhous gas: Atmospheric loss processes, lifetimes, and ozone depletion and global warming potentials for the (***E***) and (***Z***) stereoisomers, ***J. Phys. Chem. A***, ***117***, 11049–11065, doi:10.1021/jp407823k, 2013b.

Papadimitriou, V.C., R.W. Portmann, D.W. Fahey, J. Mühle, R.F. Weiss, and J.B. Burkholder, Experimental and theoretical study of the atmospheric chemistry and global warming potential of SO_2F_2, ***J. Phys. Chem. A***, ***112***, 12657–12666, doi:10.1021/jp806368u, 2008.

Papadimitriou, V.C., C.S. Spitieri, P. Papagiannakopoulos, M. Cazaunau, M. Lendar, V. Daëleb, and A. Mellouki, Atmospheric chemistry of $(CF_3)_2C=CH_2$: OH radicals, Cl atoms and O_3 rate coefficients, oxidation end-products and IR spectra, ***Phys. Chem. Chem. Phys.***, ***17***, 25607, doi:10.1039/c5cp03840e, 2015.

Papanastasiou, D.K., A. Beltrone, P. Marshall, and J.B. Burkholder, Global warming potential estimates for C_1-C_3 hydrochlorofluorocarbons (HCFCs) included in the Kigali amendment to the Montreal Protocol, ***Atmos. Chem. Phys.***, ***18***, 6317–6330, doi:10.5194/acp-18-6317-2018, 2018.

Papanastasiou, D.K., S.A. McKeen, and J.B. Burkholder, The very short-lived ozone depleting substance $CHBr_3$ (bromoform): revised UV absorption spectrum, atmospheric lifetime and ozone depletion potential, ***Atmos. Chem. Phys.***, ***14***, 3017–3025, doi: 10.5194/acpd-13-32963-2013, 2014.

Papanastasiou, D.K., N. Rontu Carlon, J.A. Neuman, E.L. Fleming, C.H. Jackman, and J.B. Burkholder, Revised UV absorption spectra, ozone depletion potentials, and global warming potentials for the ozone-depleting substances CF_2Br_2, CF_2ClBr, and CF_2BrCF_2Br, ***Geophys. Res. Lett.***, ***40***, doi:10.1002/GRL.50121, 2013.

Patten, K.O., and D.J. Wuebbles, Atmospheric lifetimes and Ozone Depletion Potentials of trans-1-chloro-3,3,3-trifluoropropylene and trans-1,2-dichloroethylene in a three-dimensional model, ***Atmos. Chem. Phys.***, ***10***, 10867–10874, doi:10.5194/acp-10-10867-2010, 2010.

Perry, R.A., R. Atkinson, and J.N. Pitts, Rate constants for the reaction of OH radicals with CH_2=CHF, CH_2=CHCl, and CH_2=CHBr over the temperature range 299-426 °K, ***J. Chem. Phys.***, ***67***, 458–462, doi:10.1063/1.434889, 1977.

Pinnock, S., M.D. Hurley, K.P. Shine, T.J. Wallington, and T.J. Smyth, Radiative forcing of climate by hydrochlorofluorocarbons and hydrofluorocarbons, ***J. Geophys. Res.***, ***100***, 23227–23238, doi:10.1029/95jd02323, 1995.

Prinn, R.G., J. Huang, R.F. Weiss, D.M. Cunnold, P.J. Fraser, P.G. Simmonds, A. McCulloch, C. Harth, S. Reimann, P. Salameh, S. O'Doherty, R.H.J. Wang, L.W. Porter, B.R. Miller, and P.B. Krummel, Evidence for variability of atmospheric hydroxyl radicals over the past quarter century, ***Geophys. Res. Lett.***, ***32***, L07809, doi:10.1029/2004GL022228, 2005.

Rajakumar, B., R. W. Portmann, J. B. Burkholder, and A. R. Ravishankara, Rate coefficients for the reactions of OH with $CF_3CH_2CH_3$ (HFC-263fb), CF_3CHFCH_2F (HFC-245eb), and $CHF_2CHFCHF_2$ (HFC-245ea) between 238 and 375 K, ***J. Phys. Chem. A***, ***110***, 6724–6731, doi:10.1021/jp056248y, 2006.

Ravishankara, A.R., J.S. Daniel, and R.W. Portmann, Nitrous oxide (N_2O): The dominant ozone-depleting substance emitted in the 21st century, ***Science***, ***326***, 123–125, doi: 10.1126/science.1176985, 2009.

Ravishankara, A.R., S. Solomon, A.A. Turnipseed, and R.F. Warren, Atmospheric lifetimes of long-lived halogenated species, ***Science***, ***259***, 194–199, doi:10.1126/science.259.5092.194, 1993.

Ray, E.A., F.L. Moore, J.W. Elkins, K.H. Rosenlof, J.C. Laube, T. Röckmann, D.R. Marsh, and A.E. Andrews, Quantification of the SF_6 lifetime based on mesospheric loss measured in the stratospheric polar vortex, ***J. Geophys. Res.***, ***122***, doi:10.1002/2016JD026198., 2017.

Rhew, R.C., and J.D. Happell, The atmospheric partial lifetime of carbon tetrachloride with respect to the global soil sink, ***Geophys. Res. Lett.***, ***43***, 2889–2895, doi:10.1002/2016GL067839, 2016.

Rodriguez, A., I. Bravo, D. Rodriguez, M. Tajuelo, Y. Diaz-de-Mera, and A. Aranda, The environmental impact of unsaturated fluoroesters: atmospheric chemistry towards OH radicals and Cl atoms, radiative behavior and cumulative ozone creation, ***RSC Advances***, ***6***, 21833–21843, doi:10.1039/C6RA00630B, 2016.

Rodríguez, A., D. Rodríguez, A. Moraleda, I. Bravo, E. Moreno, and A. Notario, Atmospheric chemistry of HFE-7300 and HFE-7500: Temperature dependent kinetics, atmospheric lifetimes, infrared spectra and global warming potentials, ***Atmos. Environ.***, ***96***, 145–153, doi:10.1016/j.atmosenv.2014.07.033, 2014.

Roehl, C.M., J.B. Burkholder, G.K. Moortgat, A.R. Ravishankara, and P.J. Crutzen, Temperature dependence of UV absorption cross sections and atmospheric implications of several alkyl iodides, ***J. Geophys. Res.***, ***102***, 12819–12829, doi:10.1029/97JD00530, 1997.

Sellevåg, S.R., T. Kelly, H. Sidebottom, and C.J. Nielsen, A study of the IR and UV-Vis absorption cross sections, photolysis and OH-initiated oxidation of CF_3CHO and CF_3CH_2CHO, ***Phys. Chem. Chem. Phys.***, ***6***, 1243–1252, doi:10.1039/b315941h, 2004.

Sharpe, S.W., T.J. Johnson, R.L. Sams, P.M. Chu, G.C. Rhoderick, and P.A. Johnson, Gas-phase databases for quantitative infrared spectroscopy, ***Applied Spectrosc.***, ***58***, 1452–1461, 2004.

Shine, K.P., and G. Myhre, The spectral nature of stratospheric temperature adjustment and its application to halocarbon radiative forcing, ***J. Adv. in Model. Earth Syst.***, ***12***, 16, doi:10.1029/2019ms001951, 2020.

Smith, C.J., R.J. Kramer, G. Myhre, K. Alterskjær, W. Collins, A. Sima, O. Boucher, J.-L. Dufresne, P. Nabat, M. Michou, S. Yukimoto, J. Cole, D. Paynter, H. Shiogama, F.M. O'Connor, E. Robertson, A. Wiltshire, T. Andrews, C. Hannay, R. Miller, L. Nazarenko, A. Kirkevåg, D. Olivié, S. Fiedler, A. Lewinschal, C. Mackallah, M. Dix, R. Pincus, and P.M. Forster, Effective radiative forcing and adjustments in CMIP6 models, ***Atmos. Chem. Phys.***, ***20***, 9591–9618, doi:10.5194/acp-20-9591-2020, 2020.

Smith, C.J., R.J. Kramer, G. Myhre, P.M. Forster, B.J. Soden, T. Andrews, O. Boucher, G. Faluvegi, D. Flaschner, Ø. Hodnebrog, M. Kasoar, V. Kharin, A. Kirkevag, J.F. Lamarque, J. Mulmenstadt, D. Olivié, T. Richardson, B.H. Samset, D. Shindell, P. Stier, T. Takemura, A. Voulgarakis, and D. Watson-Parris, Understanding rapid adjustments to diverse forcing agents, ***Geophys. Res. Lett.***, ***45***, 12023–12031, doi:10.1029/2018gl079826, 2018.

Smith, C., Z.R.J. Nicholls, K. Armour, W. Collins, P. Forster, M. Meinshausen, M.D. Palmer, and M. Watanabe, The Earth's Energy Budget, Climate Feedbacks, and Climate Sensitivity Supplementary Material. In ***Climate Change 2021: The Physical Science Basis. Contribution of Working Group I to the Sixth Assessment Report of the Intergovernmental Panel on Climate Change*** [Masson-Delmotte, V., P. Zhai, A. Pirani, S.L. Connors, C. Péan, S. Berger, N. Caud, Y. Chen, L. Goldfarb, M.I. Gomis, M. Huang, K. Leitzell, E. Lonnoy, J.B.R. Matthews, T.K. Maycock, T. Waterfield, O. Yelekçi, R. Yu, and B. Zhou (eds.)]. Available from https://www.ipcc.ch/, 2021.

SPARC (Stratosphere-troposphere Processes And their Role in Climate), ***SPARC Report on the Lifetimes of Stratospheric Ozone-Depleting Substances, Their Replacements, and Related Species***, edited by M.K.W. Ko, P.A. Newman, S. Reimann, and S.E. Strahan, SPARC Report No. 6, WCRP-15/2013, [available at: https://www.sparc-climate.org/fileadmin/customer/6_Publications/SPARC_reports_PDF/6_SPARC_LifetimeReport_Web.pdf], 2013.

SPARC (Stratosphere-troposphere Processes And their Role in Climate), ***SPARC Report on the Mystery of Carbon Tetrachloride***, edited by Q. Liang, P.A. Newman, and S. Reimann, SPARC Report No. 7, WCRP-13/2016, [available at: https://www.wcrp-climate.org/WCRP-publications/2016/SPARC_Report7_2016.pdf], 2016.

Srinivasulu, G., A.J.C. Bunkan, D. Amedro, and J.N. Crowley, Absolute and relative-rate measurement of the rate coefficient for reaction of perfluoro ethyl vinyl ether ($C_2F_5OCF=CF_2$) with OH, ***Phys. Chem. Chem. Phys.***, ***20***, 3761–3767, doi:10.1039/c7cp08056e, 2018.

Sulbaek Andersen, M.P., V.F. Andersen, O.J. Nielsen, S.P. Sander, and T.J. Wallington, Atmospheric chemistry of $HCF_2O(CF_2CF_2O)_xCF_2H$ (x = 2-4): Kinetics and mechanisms of the chlorine-atom-initiated oxidation, ***ChemPhysChem***, ***11***, 4035–4041, doi:10.1002/cphc.201000438, 2010.

Sulbaek Andersen, M.P., M.D. Hurley, T.J. Wallington, F. Blandini, N.R. Jensen, V. Librando, J. Hjorth, G. Marchionni, M. Avataneo, M. Visca, F.M. Nicolaisen, and O.J. Nielsen, Atmospheric chemistry of $CH_3O(CF_2CF_2O)_nCH_3$ (n=1-3): Kinetics and mechanism of oxidation initiated by Cl atoms and OH radicals, IR spectra, and global warming potentials, ***J. Phys. Chem. A***, ***108***, 1964–1972, doi:10.1021/jp036615a, 2004.

Sulbaek Andersen, M.P., M. Kyte, S.T. Andersen, C.J. Nielsen, and O.J. Nielsen, Atmospheric chemistry of $(CF_3)_2CFCN$: A replacement compound for the most potent industrial greenhouse gas, SF_6, ***Environ. Sci. Technol.***, ***51***, 1321–1329, doi:10.1021/acs.est.6b03758, 2017.

Sulbaek Andersen, M.P., O.J. Nielsen, A. Toft, T. Nakayama, Y. Matsumi, R.L. Waterland, R.C. Buck, M.D. Hurley, and T.J. Wallington, Atmospheric chemistry of $C_xF_{2x+1}CH=CH_2$ (x=1, 2, 4, 6, and 8): Kinetics of gas-phase reactions with Cl atoms, OH radicals, and O_3, ***J. Photochem. and Photobio. A: Chem.***, ***176***, 124–128, doi:10.1016/j.jphotochem.2005.06.015, 2005a.

Sulbaek Andersen, M.P., O.J. Nielsen, T.J. Wallington, M.D. Hurley, and W.B. DeMore, Atmospheric chemistry of $CF_3OCF_2CF_2H$ and $CF_3OC(CF_3)_2H$: Reaction with Cl atoms and OH radicals, degradation mechanism, global warming potentials, and empirical relationship between *k*(OH) and *k*(Cl) for organic compounds, ***J. Phys. Chem. A***, ***109***, 3926–3934, doi:10.1021/jp044635m, 2005b.

Suntharalingam, P., E. Buitenhuis, L.J. Carpenter, J.H. Butler, M.J. Messias, S.J. Andrews, and S.C. Hackenberg, Evaluating oceanic uptake of atmospheric CCl_4: A combined analysis of model simulations and observations, ***Geophys. Res. Lett.***, ***46***, 472–482, doi:10.1029/2018GL080612, 2019.

Takahashi, K., T. Nakayama, Y. Matsumi, S. Solomon, T. Gejo, E. Shigemasa, and T.J. Wallington, Atmospheric lifetime of SF_5CF_3, ***Geophys. Res. Lett.***, ***29***, doi:10.1029/2002GL015356, 2002.

Taniguchi, N., T.J. Wallington, M.D. Hurley, A.G. Guschin, L.T. Molina, and M.J. Molina, Atmospheric chemistry of $C_2F_5C(O)CF(CF_3)_2$: Photolysis and reaction with Cl atoms, OH radicals, and ozone, ***J. Phys. Chem. A***, ***107***, 2674–2679, doi:10.1021/jp0220332, 2003.

Taylor, P.H., Z. Jiang, and B. Dellinger, Laser photolysis/laser-induced fluorescence studies of the reaction of hydroxyl with 1,1,2-trichloroethane over an extended temperature range, ***J. Phys. Chem.***, ***96***, 1293–1296, doi:10.1021/j100182a050, 1992.

Tegtmeier, S., K. Krüger, B. Quack, E.L. Atlas, I. Pisso, A. Stohl, and X. Yang, Emission and transport of bromocarbons: From the West Pacific ocean into the stratosphere, ***Atmos. Chem. Phys.***, ***12***, 10633–10648, doi:10.5194/acp-12-10633-2012, 2012.

Tokuhashi, K., A. Takahashi, M. Kaise, and S. Kondo, Rate constants for the reactions of OH radials with CH_3OCF_2CHFCl, CHF_2OCF_2CHFCl, $CHF_2OCHClCF_3$, and $CH_3CH_2OCF_2CHF_2$, ***J. Geophys. Res.***, ***104***, 18681–18688, doi:10.1029/1999JD900278, 1999.

Tokuhashi, K., K. Takizawa, and S. Kondo, Rate constants for the reactions of OH radicals with fluorinated ethenes: Kinetic measurements and correlation between structure and reactivity, ***J. Phys. Chem. A***, ***122***, 4593–4600, doi:10.1021/acs.jpca.7b11653, 2018a.

Tokuhashi, K., K. Takizawa, and S. Kondo, Rate constants for reactions of OH radials with (*Z*)-$CF_3CCl=CHCl$, $CHF_2CF=CF_2$, (*E*)-$CF_3CH=CHF$, (*Z*)-$CF_3CH=CHF$, $CH_3CF=CH_2$, and $CH_2FCH=CH_2$, ***Atmos. Environ.***, ***255***, 118428, doi:10.1016/j.atmosenv.2021.118428, 2021.

Tokuhashi, K., T. Uchimaru, K. Takizawa, and S. Kondo, Rate constants for the reactions of OH radical with the (*E*)/(*Z*) isomers of $CF_3CF=CHCl$ and $CHF_2CF=CHCl$, ***J. Phys. Chem. A***, ***122***, 3120–3127, doi:10.1021/acs.jpca.7b11923, 2018b.

Tokuhashi, K., T. Uchimaru, K. Takizawa, and S. Kondo, Rate constants for the reactions of OH radicals with the (*E*)/(*Z*) isomers of CFCl=CFCl and (*E*)-CHF=CHF, ***J. Phys. Chem. A***, ***123***, 4834–4843, doi:10.1021/acs.jpca.9b02454, 2019.

Tuazon, E.C., R. Atkinson, S.M. Aschmann, M.A. Goodman, and A.M. Winer, Atmospheric reactions of chloroethenes with the OH radical, ***Int. J. Chem Kinet.***, ***20***, 241–265, doi:10.1002/kin.550200305, 1988.

Urata, S., A. Takada, T. Uchimaru, and A.K. Chandra, Rate constants estimation for the reaction of hydrofluorocarbons and hydrofluoroethers with OH radicals, ***Chem. Phys. Lett.***, ***368***, 215–223, doi:10.1016/S0009-2614(02)01718-9, 2003.

Vial, J., J.-L.L. Dufresne, and S. Bony, On the interpretation of inter-model spread in CMIP5 climate sensitivity estimates, ***Climate Dynamics***, ***41***, 3339–3362, doi:10.1007/s00382-013-1725-9, 2013.

Vollmer, M.K., F. Bernard, B. Mitrevski, L.P. Steele, C.M. Trudinger, S. Reimann, R.L. Langenfelds, P.B. Krummel, P.J. Fraser, D.M. Etheridge, M.A.J. Curran, and J.B. Burkholder, Abundances, emissions, and loss processes of the long-lived and potent greenhouse gas octafluorooxolane (octafluorotetrahydrofuran, c-C_4F_8O) in the atmosphere, ***Atmos. Chem. Phys.***, ***19***, 3481–3492, doi:10.5194/acp-19-3481-2019, 2019.

Wahner, A., and C. Zetzsch, Rate constants for the addition of OH to aromatics (benzene, p-chloroaniline, and o-, m-, and p-dichlorobenzene) and the unimolecular decay of the adduct. Kinetics into a quasi-equilibrium. 1, ***J. Phys. Chem.***, ***87***, 4945–4951, doi:10.1021/j150642a036, 1983.

Wallington, T.J., M.D. Hurley, O.J. Nielsen, and M.P. Sulbaek Andersen, Atmospheric chemistry of $CF_3CFHCF_2OCF_3$ and $CF_3CFHCF_2OCF_2H$: Reaction with Cl atoms and OH radicals, degradation mechanism, and global warming potentials, ***J. Phys. Chem. A***, ***108***, 11333–11338, doi:10.1021/jp046454q, 2004.

WMO (World Meteorological Organization), ***Scientific Assessment of Ozone Depletion: 2014***, Global Ozone Research and Monitoring Project–Report No. 55, 416 pp., Geneva, Switzerland, 2014.

WMO (World Meteorological Organization), ***Scientific Assessment of Ozone Depletion: 2018***, Global Ozone Research and Monitoring Project–Report No. 58, 588 pp., Geneva, Switzerland, 2018.

Wuebbles, D.J., D. Youn, K. Patten, D. Wang, and M. Martinez-Aviles, Metrics for Ozone and Climate: Three-Dimensional Modeling Studies of Ozone Depletion Potentials and Indirect Global Warming Potentials, in ***Twenty Years of Ozone Decline: Proceedings of the Symposium for the 20th Anniversary of the Montreal Protocol***, edited by C. Zerefos, G. Contopoulos, and G. Skalkeas, Springer, Dordrecht, Netherlands, 297–326 pp., doi:10.1007/978-90-481-2469-5_23, 2009.

Youn, D., K.O. Patten, D.J. Wuebbles, H. Lee, and C.-W. So, Potential impact of iodinated replacement compounds CF_3I and CH_3I on atmospheric ozone: a three-dimensional modeling study, ***Atmos. Chem. Phys.***, ***10***, 10129–10144, doi:10.5194/acp-10-10129-2010, 2010.

Young, C.J., R.F. Gómez Biagi, M.D. Hurley, T.J. Wallington, and S.A. Mabury, Paint solvent to food additive: An environmental route of dehalgenation for 4-chlorobenzotrifluoride, ***Environ. Tox. Chem.***, ***27***, 2233–2238, doi:10.1897/08-051.1, 2008.

Young, C.J., M.D. Hurley, T.J. Wallington, and S.A. Mabury, Atmospheric lifetime and global warming potential of a perfluoropolyether, ***Environ. Sci. Technol.***, ***40***, 2242–2246, doi:10.1021/es052077z, 2006.

Young, C.J., M.D. Hurley, T.J. Wallington, and S.A. Mabury, Atmospheric chemistry of CF_3CF_2H and $CF_3CF_2CF_2CF_2H$: Kinetics and products of gas-phase reactions with Cl atoms and OH radicals, infrared spectra, and formation of perfluorocarboxylic acids, ***Chem. Phys. Lett.***, ***473***, 251–256, doi:10.1016/j.cplett.2009.04.001, 2009.

Yvon-Lewis, S.A., and J.H. Butler, Effect of oceanic uptake on atmospheric lifetimes of selected trace gases, ***J. Geophys. Res.***, ***107***, 4414, doi:10.1029/2001JD001267, 2002.

Zhang, M., and Y. Huang, Radiative forcing of quadrupling CO_2, ***J. Climate***, ***27***, 2496–2508, doi:10.1175/jcli-d-13-00535.1, 2014.

Zhang, N., L. Chen, T. Uchimaru, F. Qing, J. Mizukado, H. Quan, and H. Suda, Kinetics of gas-phase reactions of cyc-$CF_2CF_2CF_2CHFCH_2$ and trans-cyc-$CF_2CF_2CF_2CHFCHF$ with OH radicals between 253 and 328 K, ***Chem. Phys. Lett.***, ***639***, 199–204, doi:10.1016/j.cplett.2015.09.020, 2015.

Zhang, N., T. Uchimaru, Q. Guo, F. Qing, L. Chen, and J. Mizukado, Atmospheric chemistry of perfluorocyclopentene (cyc-$CF_2CF_2CF_2CF$=CF-): Kinetics, products and mechanism of gas-phase reactions with OH radicals, and atmospheric implications, ***Atmos. Environ.***, ***160***, 46–54, doi:10.1016/j.atmosenv.2017.04.012, 2017.

Zhang, Q., C. Y., S. Tong, M. Ge, J. Shenolikar, M.S. Johnson, Y. Wang, N.T. Tsona, A. Mellouki, and L. Du, Atmospheric oxidation of selected chlorinated alkenes by O_3, OH, NO_3 and Cl, ***Atmos. Environ.***, ***170***, 12–21, doi:10.1016/j.atmosenv.2017.09.031, 2017.

Zhang, S., R. Strekowski, L. Bosland, A. Monod, and C. Zetzsch, Kinetic study of the reaction of OH with CH_2I_2, ***Phys. Chem. Chem. Phys.***, ***13***, 11671–11677, doi:10.1039/c1cp20885c, 2011.

Zhang, S., R. Strekowski, A. Monod, L. Bosland, and C. Zetzsch, Temperature-dependent kinetics study of the reactions of OH with C_2H_5I, ***n***-C_3H_7I, and ***iso***-C_3H_7I, ***J. Phys. Chem. A***, ***116***, 9497–9506, doi:10.1021/jp300575f, 2012.

APPENDIX A:
CHEMICAL FORMULAE AND NOMENCLATURE

Reactive Halogen-Containing Species

Cl	atomic chlorine	Br	atomic bromine
Cl_y	total inorganic chlorine	Br_y	total inorganic bromine
Cl_2	molecular chlorine	Br_2	molecular bromine
ClO	chlorine monoxide	BrO	bromine monoxide
ClO_x	(ClO + 2 ClOOCl)	Br_2O	dibromine monoxide
Cl_2O_2, ClOOCl	dichlorine peroxide (ClO dimer)	BrO_x	(Br, BrO, $BrONO_2$, HOBr, ...)
$ClONO_2$, $ClNO_3$	chlorine nitrate	$BrONO_2$, $BrNO_3$	bromine nitrate
HCl	hydrogen chloride (hydrochloric acid)	HBr	hydrogen bromine
HOCl	hypochlorous acid	HOBr	hypobromous acid
F	atomic fluorine	I	atomic iodine
F_2	molecular fluorine	I_2	molecular iodine
F_y	total inorganic fluorine	I_y	total inorganic iodine
HF	hydrogen fluoride (hydrofluoric acid)	IO	iodine monoxide
FO_x	F + FO	IO_x	iodine radicals

Other Reactive Species

O	atomic oxygen	H	atomic hydrogen
$O(^3P)$	atomic oxygen (ground state)	H_2	molecular hydrogen
$O(^1D)$	atomic oxygen (first excited state)	OH	hydroxyl radical
O_2	molecular oxygen	HO_2	hydroperoxyl radical
O_3	ozone	H_2O	water
O_x	odd oxygen (O, $O(^1D)$, O_3)	HO_x	odd hydrogen (H, OH, HO_2, H_2O_2)
N	atomic nitrogen	HNO_2, HONO	nitrous acid
N_2	molecular nitrogen	HOONO	pernitrous acid
N_2O	nitrous oxide	HNO_3	nitric acid
NO	nitric oxide	HNO_4, $HOONO_2$	peroxynitric acid
NO_2	nitrogen dioxide	NH_3	ammonia
NO_3	nitrogen trioxide, nitrate radical	NH_4NO_3	ammonium nitrate
N_2O_5	dinitrogen pentoxide	NO_x	nitrogen oxides (NO + NO_2)
$HNO_3 \cdot 3H_2O$	nitric acid trihydrate condensate (NAT)	NO_y	total reactive nitrogen (NO, NO_2, NO_3, N_2O_5, $ClONO_2$, HNO_4, HNO_3)
S	atomic sulfur		
SO_2	sulfur dioxide	H_2S	hydrogen sulfide
H_2SO_4	sulfuric acid	CS_2	carbon disulfide
CH_3SCH_3	dimethyl sulfide (DMS)	COS, OCS	carbonyl sulfide
C	carbon atom		
CO	carbon monoxide	CO_2	carbon dioxide
CH_3	methyl radical	CH_3CH_3	ethane
CH_4	methane	$CH_3CH_2CH_3$	propane
CH_3OH	methyl alcohol, methanol	$CH_3CH_2CH_2CH_3$	butane
$CF_3C(O)OH$, CF_3CO_2H	trifluoroacetic acid (TFA)	CH_2O	formaldehyde
$CaCO_3$	calcite, calcium carbonate		
TiO_2	titanium dioxide		
Al_2O_3	aluminum oxide		

Note: Table A-5 in the *Annex* provides an extensive listing of chemical names and formulas, including many ozone depleting substances, their replacements, and other substances of interest to the Montreal Protocol.

APPENDIX B:
2022 Ozone Assessment Acronym Dictionary

A

A5	Article 5 countries of the Montreal Protocol
AAO	Antarctic oscillation
ACCESS	Australian Community Climate and Earth System Simulator
ACCMIP	Atmospheric Chemistry and Climate Model Intercomparison Project
ACE-FTS	Fourier Transform Spectrometer instrument on the Atmospheric Chemistry Experiment satellite
AEAP	Atmospheric Effect of Aviation Project
AerChemMIP	Aerosol and Chemistry Model Intercomparison Project
AGAGE	Advanced Global Atmospheric Gases Experiment (atmospheric monitoring surface sites)
AGTP	absolute global temperature change potential
AGWP	absolute global warming potential
AI	artificial intelligence
AIMS	Atmospheric chemical Ionization Mass Spectrometer
AMSU	Advanced Microwave Sounding Unit (satellite-based instrument)
ANY	Australian New Year (fire event January 2020)
AO	Arctic oscillation
AoA	age of stratospheric air
AOD	aerosol optical depth
APEEP	Ap-driven energetic electron precipitation (model)
AR5	IPCC Fifth Assessment Report
AR6	IPCC Sixth Assessment Report
ARISE	Assessing Responses and Impacts of Solar climate intervention on the Earth system
ASOPOS	ASsessment of Operating Procedures for Ozone Sondes
ATom	Atmospheric Tomography Mission (aircraft-based field campaign)
ATTREX	Airborne Tropical TRopopause Experiment (aircraft-based field campaign)

B

BASIC	BAyeSian Integrated and Consolidated composite ozone time-series (data product)
BC	black carbon aerosol
BDC	Brewer-Dobson circulation
BECCS	bioenergy with carbon capture and storage
BNN	Bayesian neural network
BU	bottom-up (estimate based on observations)
BUV	Backscatter Ultraviolet (satellite-based instrument)

C

CALIOP	Cloud-Aerosol Lidar with Orthogonal Polarization (satellite-based instrument)
CALIPSO	Cloud-Aerosol Lidar and Infrared Pathfinder Satellite Observations (satellite-based instrument)
CAM-Chem	Community Atmosphere Model with Chemistry (CAM-chem), a component of the NCAR Community Earth System Model (CESM)
CanESM	Canadian Earth System Model
CAO	cold air outbreak
CARIBIC	Civil Aircraft for the Regular Investigation of the Atmosphere Based on an Instrument Container (aircraft-based observational campaign)
CAS RN	Chemical Abstracts Service registry number
CAST	Coordinated Airborne Studies in the Tropics (aircraft-based field campaign)
CAVA	Central American Volcanic Arc
CCI	Climate Change Initiative of the European Space Agency
CCM	chemistry-climate model

CCMI	Chemistry-Climate Model Initiative
CCMVal	Chemistry-Climate Model Validation Activity (e.g. CCMVal-2 = Phase 2 of CCMVal)
CCT	cirrus cloud thinning
CDM	Clean Development Mechanism of the Kyoto Protocol
CDR	carbon dioxide removal
CESM	Community Earth System Model
CFCs	chlorofluorocarbons
CFSR	NCEP Climate Forecast System Reanalysis (data product)
CGAA	Cape Grim Air Archive (atmospheric monitoring surface sites)
CGTP	combined global temperature change potential
CI	climate intervention
CLaMS	Chemical Lagrangian Model of the Stratosphere
CMEs	coronal mass ejections
CMIP	Climate Model Intercomparison Project (e.g. CMIP6 = Phase 6 of CMIP)
CNRM	National Centre for Meteorological Research (France)
CONTRAST	Convective Transport of Active Species in the Tropics (aircraft-based field campaign)
COP	Conference Of the Parties of the United Nations Framework Convention on Climate Change (UNFCCC)
COS	carbonyl sulfide
CPT	cold point tropopause
CR-AVE	Costa Rica Aura Validation Experiment (aircraft-based field campaign)
CSIRO	Commonwealth Scientific and Industrial Research Organisation (Australia)
CTM	chemistry transport model
CUE	critical use exemption

D

DJF	December-January-February
DLM	dynamic linear model
DMS	dimethyl sulfide
DOE	Department of Energy (United States)
DU	Dobson Units

E

ECMWF	European Centre for Medium-Range Weather Forecasts (forecast model)
ECS	equilibrium climate sensitivity
EDC	ethylene dichloride
EECl	equivalent effective chlorine
EEMD	ensemble empirical model decomposition
EEP	energetic electron precipitation
EESBnC	Equivalent Effective Stratospheric Benchmark-normalized Chlorine
EESC	equivalent effective stratospheric chlorine
EHF	eddy heat flux
EMAC	ECHAM/MESSy Atmospheric Chemistry
ENSO	El Niño-Southern Oscillation
EOF	empirical orthogonal function
EPA	Environmental Protection Agency (United States)
EPP	energetic particle precipitation
ERA	ECMWF Re-Analysis (a global atmospheric reanalysis data product)
ERF	effective radiative forcing
ESM	Earth system model
EU	European Union

F

FDH	fixed dynamical heating
FIREBIRD	Focused Investigations of Relativistic Electron Burst Intensity, Range, and Dynamics (CubeSat dual satellite mission)
FRF	fractional release factor
FTIR	Fourier transform infrared
FZH	Forschungszentrum Jülich institute (Germany)

G

GAW	Global Atmosphere Watch programme of WMO
GC-ECD	gas chromatography-electron capture detection (instrument)
GCM	global circulation model
GDP	gross domestic product
GEISA	Gestion et Etude des Informations Spectroscopiques Atmosphériques / Management and Study of Atmospheric Spectroscopic Information
GeoMIP	Geoengineering Model Intercomparison Project
GEOSCCM	Goddard Earth Observing System Chemistry Climate Model
GFDL-EM	Geophysical Fluid Dynamics Laboratory (of NOAA) Earth system Model
GHG	greenhouse gas
GISSTEMP	Goddard Institute for Space Studies (GISS) Surface Temperature Analysis (data product)
GLENS	Geoengineering Large ENSemble project
GLORIA	Global Limb Radiance Imager for the Atmosphere (satellite-based instrument)
GloSSAC	Global Space-based Stratospheric Aerosol Climatology (data product)
GMI	Global Modeling Initiative
GOME	Global Ozone Monitoring Experiment spectrometer (satellite-based instrument)
GOMOS	Global Ozone Monitoring by Occultation of Stars (satellite-based instrument)
GOZCARDS	Global OZone Chemistry And Related trace gas Data records for the Stratosphere
GPS	global positioning system
GR	growth rate
GSFC2D	Goddard Space Flight Center 2-D model
GSG	GOME-SCIAMACHY-GOME-2 merged dataset
$GtCO_2$-eq	gigatonnes of carbon dioxide equivalent
GTO	GOME-type Total Ozone column ozone product
GTP	global temperature change potential
GWP	global warming potential

H

HadGEM	Hadley Centre Global Environment Model
HadISST	Hadley Centre Sea Ice and Sea Surface Temperature (data product)
HALO	High-Altitude and LOng range (research aircraft)
HALOE	HALogen Occultation Experiment (satellite-based instrument)
HBFO	hyrobromofluoroolefin
HCFC	hydrochlorofluorocarbon
HCFO	hydrochlorofluoroolefin
HF	hydrogen fluoride/hydrofluoric acid
HFC	hydrofluorocarbon
HFE	halogenated ether
HFO	hydrofluoroolefin
HFP	hexafluoropropylene
HIAPER	High-performance Instrumented Airborne Platform for Environmental Research
HIPPO	HIAPER Pole-to-Pole Observations (aircraft-based field campaign)
HITRAN	high-resolution transmission molecular absorption database
HSCT	High Speed Civil Transport (category of aircraft)
HST	hypersonic transport (category of aircraft)
HTOC	Halon Technical Options Committee

I

IAGOS	In-service Aircraft for a Global Observing System
IASI	Infrared Atmospheric Sounding Interferometer (satellite-based instrument)
ICR	industrial and commercial refrigeration
IEA	International Energy Agency
IGAC	International Global Atmospheric Chemistry project
IHD	interhemispheric difference
ILT	independent linear trend
IOD	integrated ozone depletion
IO3C	International Ozone Commission
IPCC	Intergovernmental Panel on Climate Change

I

IRF	instantaneous radiative forcing
ISS	International Space Station
ITCZ	intertropical convergence zone

J

JJA	June-July-August
JRA-55	the 55-year Japanese ReAnalysis project conducted by the Japan Meteorological Agency (JMA)

L

LBL	line-by-line
LOTUS	Long-term Ozone Trends and Uncertainties in the Stratosphere (a SPARC activity)
LS	lower stratosphere
LW	longwave (radiation wavelength range)
LZRH	level of zero radiative heating

M

MAC	mobile air conditioner
MAGICC	Model for the Assessment of Greenhouse Gas Induced Climate Change
MAM	March-April-May
MBL	marine atmospheric boundary layer
MCB	marine cloud brightening
MEGRIDOP	MErged GRIdded Dataset of Ozone Profiles
MERRA	Modern Era Retrospective-analysis for Research and Applications (e.g. MERRA-2 = version 2 of MERRA)
MF	mole fraction
MIPAS	Michelson Interferometer for Passive Atmospheric Sounding
ML	machine learning
MLF	Montreal Protocol's Multilateral Fund
MLR	multiple linear regression
MLS	Microwave Limb Sounder (satellite-based instrument)
MMM	multi-model mean
MRI-ESM	Meteorological Research Institute (of Japan) Earth System Model
MSR	Multi-sensor reanalysis
MSU	Microwave Sounding Unit (satellite-based instrument)

N

NAM	northern annular mode
NAO	North Atlantic oscillation
NASA	National Aeronautics and Space Administration (United States)
NAT	nitric acid trihydrate
NCAR	National Center for Atmospheric Research (United States)
NCEP	National Centers for Environmental Prediction (United States)
NDACC	Network for the Detection of Atmospheric Composition Change
NH	Northern Hemisphere
NIES	National Institute for Environmental Studies (Japan)
NIWA-BS	National Institute of Water and Atmospheric Research - Bodeker Scientific (dataset)
NOAA	National Oceanic and Atmospheric Administration (United States)
NTCF	near-term climate forcer

O

OCS	carbonyl sulfide (also COS)
ODP	ozone depletion potential
ODS	ozone-depleting substance
OECD	the Organization for Economic Cooperation and Development
OHP	Observatorie de Haute-Provence (observatory in France)

OLP	ozone loss potential
OMD	ozone mass deficit
OMI	Ozone Monitoring Instrument (satellite-based instrument)
OMPS	Ozone Mapping Profiler Suite (satellite-based instrument)
OMPS-LP	OMPS Limb Profiler (satellite-based instrument)
ORM	Ozone Research Managers of the parties to the Vienna Convention
OSIRIS	Optical Spectrograph and InfraRed Imaging System (satellite-based instrument)

P

PAR	photosynthetically active radiation
PCE	perchloroethylene, also known as tetrachloroethylene
PFC	perfluorocarbon
PFP	PSC formation potential
PG	product gas
PGI	product gas injection
PNE	Pacific Northwest Event (2017 wildfire event)
POSIDON	Pacific Oxidants, Sulfur, Ice, Dehydration, and cONvection (aircraft-based field campaign)
Pre-AVE	Pre-Aura Validation Experiment (aircraft-based field campaign)
PSC	polar stratospheric cloud
PTFE	polytetrafluoroethylene/polytetrafluoroethene
PWT	piecewise trend
PWLT	piecewise linear trend
pyroCb	pyrocumulonimbus cloud

Q

QBO	Quasi-Biennial Oscillation
QPS	quarantine and pre-shipment

R

RAOBCORE	RAdiosone OBservation COrrection using REanalyses (data product)
RCP	Representative Concentration Pathway scenario (used by IPCC)
RE	radiative efficiency
RF	radiative forcing
RICH	Radiosonde Innovation Composite Homogenization reanalysis (data product)
RSS	Remote Sensing Systems renanlysis (data product)

S

S2S	sub-seasonal to seasonal
SABER	Sounding of the Atmosphere using Broadband Emission Radiometry (satellite-based instrument)
SAD	aerosol surface area density
SAGE	Stratospheric Aerosol and Gas Experiment (satellite-based instrument)
SAI	stratospheric aerosol injection
SAM	southern annular mode
SAOZ	Système D'Analyse par Observations Zénithales (type of spectrometer instrument)
SAP	UNEP Scientific Assessment Panel to the Parties of the Montreal Protocol
SARF	stratospheric-temperature-adjusted radiative forcing
SBUV	Solar Backscatter Ultraviolet (satellite-based instrument)
SBUV MOD	SBUV Merged Ozone Data (MOD) product
SBUV COH	SBUV Cohesive dataset (COH)
SCIAMACHY	SCanning Imaging Absorption spectroMeter for Atmospheric CHartographY (satellite-based instrument)
SCISAT	SCIence SATellite
SEANY	Southeast Australia New Year (2020 wildfire event)
SG	source gas
SGI	source gas injection
SH	Southern Hemisphere
SHIVA	Stratospheric ozone Halogen Impacts in a Varying Atmosphere (field campaign)
SIC	sea ice concentration

SLIMCAT Single-Layer Isentropic Model of Chemistry and Transport
SLP sea level pressure
SMR Sub-Millimetre Radiometer (satellite-based instrument)
SODP stratospheric ozone depletion potential
SON September-October-November
SORCE SOlar Radiation and Climate Experiment
SPARC Stratospheric Processes And their Role in Climate (project of WCRP)
SPE solar proton event
SRES Special Report on Emissions Scenarios (used by IPCC)
S-RIP SPARC Reanalysis Intercomparison Project
SRM solar radiation modification
SSA stratospheric sulfuric acid aerosols
SSI solar spectral irradiance
SSP Shared Socioeconomic Pathway scenarios (used by IPCC)
SST sea surface temperature or supersonic transport (aircraft)
SSTA SST anomaly
SSU Stratospheric Sounding Unit (satellite-based instrument)
SSW sudden stratospheric warming
STAR The NOAA Center for Satellite Applications and Research
STE stratosphere-troposphere exchange
STS supercooled ternary solution
STT stratosphere-to-troposphere transport
Suomi NPP Suomi National Polar-orbiting Partnership (satellite)
SW shortwave (radiation wavelength range)
SWOOSH Stratospheric Water and OzOne Satellite Homogenized (merged data record)
SWV stratospheric water vapor

T

TACTS Transport and Composition in the UT/LMS (aircraft-based field experiment)
TC4 Tropical Composition, Cloud and Climate Coupling (aircraft-based field experiment)
TCE trichloroethene
TCO total column ozone
TEAP UNEP Technology and Economic Assessment Panel to the Parties of the Montreal Protocol
TFA trifluoroacetic acid
TFE tetrafluoroethylene/ tetrafluoroethene
TOA top of the atmosphere
TOAR Tropospheric Ozone Assessment Report
TOMCAT Toulouse Off-line Model of Chemistry and Transport
TOMS Total Ozone Mapping Spectrometer (satellite-based instrument)
TORERO Tropical Ocean tRoposphere Exchange of Reactive halogen species and Oxygenated VOC (aircraft-based field experiment)
TOVS/ATOVS TIROS Operational Vertical Sounder / Advanced TOVS (satellite-based instrument)
TP tropopause pressure
TROPOMI TROPOspheric Monitoring Instrument (satellite-based instrument)
TSI total solar irradiance
TTL tropical tropopause layer

U

UAH University of Alabama Huntsville
UARS Upper Atmosphere Research Satellite
UBDC upper branch of the Brewer-Dobson Circulation (BDC)
UCI University of California Irvine
UEA University of East Anglia
UKCA United Kingdom Chemistry and Aerosols model
UKESM United Kingdom Earth System Model
UNEP United Nations Environment Programme
UNFCCC United Nations Framework Convention on Climate Change
USA United States of America
UT upper troposphere

UTLS	upper troposphere/lower stratosphere
UV	ultraviolet (wavelength range)

V

VCM	vinyl chloride/vinyl chloride monomer
VDC	1,1-dichlorothene
VIRGAS	Volcano-plume Investigation Readiness and Gas-phase and Aerosol Sulfur (field campaign)
VIS/Vis	visible-wavelength radiation
VolMIP	Volcanic Forcings Model Intercomparison Project
VSL SG	very short-lived source gas
VSLS	very short-lived substance

W

WACCM	Whole Atmosphere Community Climate Model
WCRP	World Climate Research Programme
WDCGG	World Data Centre for Greenhouse Gases (a World Data Centre (WDC) operated by the Japan Meteorological Agency (JMA) under WMO-GAW)
WISE	Wave-driven ISentropic Exchange (aircraft-based field campaign)
WMO	World Meteorological Organization
WOUDC	World Ozone and Ultraviolet Radiation Data Centre of WMO/GAW

AUTHORS, CONTRIBUTORS, AND REVIEWERS

Co-Chairs of the Scientific Assessment Panel (SAP) of the Montreal Protocol and Assessment Co-Chairs

David W. Fahey	NOAA Chemical Sciences Laboratory	USA
Paul A. Newman	NASA Goddard Space Flight Center	USA
John A. Pyle	University of Cambridge and the National Centre for Atmospheric Science (NCAS)	UK
Bonfils Safari	University of Rwanda, College of Science and Technology	Rwanda

Assessment Scientific Steering Committee

David W. Fahey	NOAA Chemical Sciences Laboratory	USA
Paul A. Newman	NASA Goddard Space Flight Center	USA
John A. Pyle	University of Cambridge and the National Centre for Atmospheric Science (NCAS)	UK
Bonfils Safari	University of Rwanda, College of Science and Technology	Rwanda
Julie Arblaster	Monash University	Australia
Lucy Carpenter	University of York	UK
Jianxin Hu	Peking University, College of Environmental Sciences and Engineering	China
Ken Jucks	NASA Headquarters	USA
David A. Plummer	Environment and Climate Change Canada, Climate Research Division	Canada

Assessment Coordinator

Sarah J. Doherty	University of Colorado, Cooperative Institute for Research in Environmental Sciences (CIRES) at NOAA Chemical Sciences Laboratory	USA

Graphics and Layout Coordinator

Chelsea R. Thompson	NOAA Chemical Sciences Laboratory	USA

Lead Authors

Chapter 1: Update on Ozone-Depleting Substances (ODSs) and Other Gases of Interest to the Montreal Protocol

Johannes C. Laube	Forschungszentrum Jülich, Institute for Energy and Climate Research: Stratosphere (IEK-7)	Germany
Susann Tegtmeier	University of Saskatchewan, Institute of Space and Atmospheric Studies	Canada

Chapter 2: Hydrofluorocarbons (HFCs)

Qing Liang	NASA Goddard Space Flight Center	USA
Matt Rigby	University of Bristol, School of Chemistry	UK

Chapter 3: Update on Global Ozone: Past, Present, and Future

Birgit Hassler	Deutsches Zentrum für Luft und Raumfahrt (DLR), Institut für Physik der Atmosphäre (IPA)	Germany
Paul J. Young	Lancaster University	UK

Chapter 4: Polar Stratospheric Ozone: Past, Present, and Future

Martyn P. Chipperfield	University of Leeds	UK
Michelle L. Santee	NASA Jet Propulsion Laboratory, California Institute of Technology	USA

Chapter 5: Stratospheric Ozone Changes and Climate

Hella Garny	Deutsches Zentrum für Luft und Raumfahrt (DLR), Institut für Physik der Atmosphäre (IPA)	Germany
Harry Hendon	Bureau of Meteorology and Monash University	Australia

Chapter 6: Stratospheric Aerosol Injection and Its Potential Effect on the Stratospheric Ozone Layer

James Haywood	University of Exeter and Met Office Hadley Centre	UK
Simone Tilmes	National Center for Atmospheric Research (NCAR), Atmospheric Chemistry Observations & Modeling	USA

Chapter 7: Scenarios and Information for Policymakers

John S. Daniel	NOAA Chemical Sciences Laboratory	USA
Stefan Reimann	Swiss Federal Laboratories for Materials Science and Technology (Empa)	Switzerland

Annex: Summary of Abundances, Lifetimes, ODPs, REs, GWPs, and GTPs

James B.Burkholder	NOAA Chemical Sciences Laboratory	USA
Øivind Hodnebrog	CICERO Center for International Climate Research	Norway

Twenty Questions and Answers About the Ozone Layer: 2022 Update

Ross J. Salawitch	University of Maryland College Park	USA

Co-Authors

Chapter 1: Update on Ozone-Depleting Substances (ODSs) and Other Gases of Interest to the Montreal Protocol

Rafael Pedro Fernandez	Institute for Interdisciplinary Science (ICB), National Research Council (CONICET)	Argentina
Jeremy Harrison	National Centre for Earth Observation (NCEO)	UK
Lei Hu	University of Colorado, Cooperative Institute for Research in Environmental Sciences (CIRES) at NOAA Global Monitoring Laboratory	USA
Paul Krummel	Commonwealth Scientific and Industrial Research Organisation (CSIRO) Oceans and Atmosphere, Climate Science Centre	Australia
Emmanuel Mahieu	University of Liège	Belgium
Sunyoung Park	Kyunpook National University, School of Earth System Sciences, Department of Oceanography	South Korea
Luke Western	University of Bristol, School of Chemistry	UK

Chapter 2: Hydrofluorocarbons (HFCs)

Xuekun Fang	Zhejiang University	China
Dave Godwin	U.S. Environmental Protection Agency, Stratospheric Protection Division	USA
Jens Mühle	University of California San Diego, Scripps Institution of Oceanography	USA
Takuya Saito	National Institute for Environmental Studies	Japan
Kieran Stanley	Institute of Atmospheric and Environmental Sciences	Germany
Guus J. M. Velders	National Institute for Public Health and the Environment (RIVM) & Utrecht University	Netherlands

Chapter 3: Update on Global Ozone: Past, Present, and Future

William T. Ball	Delft University of Technology, Department of Geoscience and Remote Sensing	Netherlands
Robert Damadeo	NASA Langley Research Center	USA
James Keeble	National Centre for Atmospheric Science (NCAS)	UK
Elaine Maillard Barras	Federal Office of Meteorology and Climatology MeteoSwiss	Switzerland
Viktoria F. Sofieva	Finnish Meteorological Institute (FMI)	Finland
Guang Zeng	National Institute of Water and Atmospheric Research (NIWA)	New Zealand

Chapter 4: Polar Stratospheric Ozone: Past, Present, and Future

Simon P. Alexander	Australian Antarctic Division	Australia
A. T. J. de Laat	Royal Netherlands Meteorological Institute	Netherlands
Doug E. Kinnison	National Center for Atmospheric Research (NCAR)	USA
Jayanarayanan Kuttippurath	Centre for Oceans, Rivers, Atmosphere and Land Services (CORAL), Indian Institute of Technology Kharagpur	India
Ulrike Langematz	Freie Universtät Berlin	Germany
Krzysztof Wargan	Science Systems and Applications Inc. (SSAI) at NASA Goddard Space Flight Center	USA

Chapter 5: Stratospheric Ozone Changes and Climate

Marta Abalos	Universidad Complutense de Madrid, Department of Earth Physics and Astrophysics, Facultad de CC. Fisicas	Spain
Gabriel Chiodo	ETH Zürich, Institute for Atmospheric and Climate Science	Switzerland
Ariaan Purich	ARC Centre of Excellence for Climate Extremes and Climate Change Research Centre	Australia
William J. Randel	National Center for Atmospheric Research (NCAR)	USA
Karen L. Smith	University of Toronto Scarborough, Department of Physical and Environmental Sciences	Canada
David Thompson	Colorado State University	USA

Chapter 6: Stratospheric Aerosol Injection and Its Potential Effect on the Stratospheric Ozone Layer

Anthony Jones	Met Office	UK
Frank Keutsch	Harvard University, Department of Chemistry and Chemical Biology	USA
Anton Laakso	Finnish Meteorological Institute (FMI), Atmospheric Research Centre of Eastern Finland	Finland
Ulrike Niemeier	Max Planck Institute for Meteorology	Germany
Anja Schmidt	Deutsches Zentrum für Luft und Raumfahrt (DLR), Institut für Physik der Atmosphäre (IPA); Ludwig Maximilian University of Munich, Meteorological Institute; and University of Cambridge, Yusuf Hamied Department of Chemistry	Germany
Daniele Visioni	Cornell University, Sibley School of Mechanical and Aerospace Engineering	USA
Pengfei Yu	Jinan University, Institute for Environmental and Climate Research	China

Chapter 7: Scenarios and Information for Policymakers

Paul Ashford	Anthesis Consulting Group	UK
Eric Fleming	Science Systems and Applications, Inc. (SSAI) at NASA Goddard Space Flight Center	USA
Ryan Hossaini	Lancaster University	UK
Megan Lickley	Massachusetts Institute of Technology	USA
Robyn Schofield	The University of Melbourne	Australia
Helen Walter-Terrinoni	The Air Conditioning, Heating, and Refrigeration Institute (AHRI) and Technology and Economic Assessment Panel (TEAP) of the Montreal Protocol	USA

Twenty Questions and Answers About the Ozone Layer: 2022 Update

Sarah J. Doherty	University of Colorado, Cooperative Institute for Research in Environmental Sciences (CIRES) at NOAA Chemical Sciences Laboratory	USA
David W. Fahey	NOAA Chemical Sciences Laboratory	USA
Eric Fleming	Science Systems and Applications, Inc. (SSAI) at NASA Goddard Space Flight Center	USA
Laura McBride	University of Maryland, College Park	USA

Richard McKenzie	National Institute of Water and Atmospheric Research (NIWA)	New Zealand
Karen H. Rosenlof	NOAA Chemical Sciences Laboratory	USA
Chelsea R. Thompson	NOAA Chemical Sciences Laboratory	USA

Contributing Authors

Chapter 1: Update on Ozone-Depleting Substances (ODSs) and Other Gases of Interest to the Montreal Protocol

Elliot Atlas	University of Miami, Rosenstiel School of Marine and Atmospheric Science	USA
Peter Bernath	Old Dominion University, Department of Chemistry & Biochemistry	USA
Geoff Dutton	NOAA Global Monitoring Laboratory	USA
Lucien Froidevaux	NASA Jet Propulsion Laboratory	USA
Ryan Hossaini	Lancaster University	UK
Timo Keber	Institute for Atmospheric and Environmental Sciences	Germany
Theodore K. Koenig	Peking University, College of Environmental Sciences and Engineering and State Key Joint Laboratory of Environmental Simulation and Pollution Control	China
Stephen A. Montzka	NOAA Global Monitoring Laboratory	USA
Jens Mühle	University of California San Diego, Scripps Institution of Oceanography	USA
Simon O'Doherty	University of Bristol, School of Chemistry	UK
David E. Oram	University of East Anglia, School of Environmental Sciences	UK
Klaus Pfeilsticker	University of Heidelberg, Institut für Umweltphysik	Germany
Maxime Prignon	Chalmers University of Technology, Department of Earth, Space and Environment	Sweden
Birgit Quack	GEOMAR, Helmholtz Centre for Ocean Research Kiel	Germany
Matt Rigby	University of Bristol, School of Chemistry	UK
Meike Rotermund	University of Heidelberg, Institut für Umweltphysik	Germany
Takuya Saito	National Institute for Environmental Studies	Japan
Isobel J. Simpson	University of California Irvine, Department of Chemistry	USA
Dan Smale	National Institute of Water and Atmospheric Research (NIWA)	New Zealand
Martin K. Vollmer	Swiss Federal Laboratories for Materials Science and Technology (Empa)	Switzerland
Dickon Young	University of Bristol, School of Chemistry	UK

Chapter 2: Hydrofluorocarbons (HFCs)

Peter Bernath	Old Dominion University, Department of Chemistry & Biochemistry	USA
Nada Derek	Commonwealth Scientific and Industrial Research Organisation (CSIRO)	Australia
Vladimir Orkin	National Institute of Standards and Technology (NIST)	USA
Stefan Reimann	Swiss Federal Laboratories for Materials Science and Technology (Empa)	Switzerland
Isobel J. Simpson	University of California Irvine, Department of Chemistry	USA
Luke Western	University of Bristol, School of Chemistry	UK

Chapter 3: Update on Global Ozone: Past, Present, and Future

Matt Amos	Lancaster University, Lancaster Environment Centre	UK
Niramson Azouz	Laboratoire Atmosphères, Milieux, Observations Spatiales (LATMOS)	France
Melanie Coldewey-Egbers	Deutsches Zentrum für Luft und Raumfahrt (DLR), Remote Sensing Technology Institute	Germany
Lawrence Coy	Science Systems and Applications, Inc. (SSAI) at NASA Goddard Space Flight Center	US
Simone Dietmüller	Deutsches Zentrum für Luft und Raumfahrt (DLR), Institut für Physik der Atmosphäre (IPA)	Germany
Sandip S. Dhomse	University of Leeds, School of Earth and Environment	UK
Sophie Godin-Beekman	Laboratoire Atmosphères, Milieux, Observations Spatiales (LATMOS), Centre National de la Recherche Scientifique (CNRS), Sorbonne University	France
Daan Hubert	Royal Belgian Institute for Space Aeronomy (BIRA-IASB)	Belguim
Mahesh Kovilakam	Science Systems and Applications, Inc. (SSAI) at NASA Langley Research Center	USA
Paul A. Newman	NASA Goddard Space Flight Center	USA
Clara Orbe	NASA Goddard Institute for Space Studies and NASA Goddard Space Flight Center	USA
Irina Petropavlovskikh	University of Colorado, Cooperative Institute for Research in Environmental Sciences (CIRES) at NOAA Global Monitoring Laboratory	USA
William J. Randel	National Center for Atmospheric Research (NCAR)	USA
Wolfgang Steinbrecht	Meteorological Observatory Hohenpeissenberg Deutscher Wetterdienst (DWD)	Germany
Monika E. Szelag	Finnish Meteorological Institute (FMI)	Finland
Kleareti Tourpali	Aristotle University of Thessaloniki, Laboratory of Atmospheric Physics	Greece
Corinne Vigouroux	Royal Belgian Institute for Space Aeronomy (BIRA-IASB)	Belguim
Mark Weber	Universität Bremen, Institute of Environmental Physics	Germany

Chapter 4: Polar Stratospheric Ozone: Past, Present, and Future

Sandip S. Dhomse	University of Leeds	UK
Jens-Uwe Grooß	Forschungszentrum Jülich	Germany
James Keeble	University of Cambridge, Department of Chemistry	UK
Zachary D. Lawrence	University of Colorado, Cooperative Institute for Research in Environmental Sciences (CIRES) at NOAA Physical Sciences Laboratory and NorthWest Research Associates	USA
Gloria L. Manney	NorthWest Research Associates and New Mexico Institute of Mining and Technology	USA
Rolf Müller	Forschungszentrum Jülich	Germany
Eric Nash	Science Systems and Applications, Inc. (SSAI)	USA
Paul A. Newman	NASA Goddard Space Flight Center	USA
David A. Plummer	Environment and Climate Change Canada, Climate Research Branch	Canada
Sarah Safieddine	Laboratoire Atmosphères, Observations Spatiales (LATMOS)/IPSL, Sorbonne Université, Université de Versailles Saint Quentin-en-Yvelines (UVSQ), Centre National de la Recherche Scientifique (CNRS)	France

Ines Tritscher	Forschungszentrum Jülich	Germany
Peter von der Gathen	Alfred Wegener Institute, Helmholtz Centre for Polar and Marine Research	Germany
Mark Weber	Universität Bremen, Institute of Environmental Physics	Germany
Ingo Wohltmann	Alfred Wegener Institute, Helmholtz Centre for Polar and Marine Research	Germany

Chapter 5: Stratospheric Ozone Changes and Climate

James A. Anstey	Environment and Climate Change Canada, Canadian Centre for Climate Modelling and Analysis	Canada
Blanca Ayarzagüena	Universidad Complutense de Madrid	Spain
Antara Banerjee	University of Colorado, Cooperative Institute for Research in Environmental Sciences (CIRES) at NOAA Chemical Sciences Laboratory	USA
Martyn P. Chipperfield	University of Leeds	UK
Martin Dameris	Deutsches Zentrum für Luft und Raumfahrt (DLR), Institut für Physik der Atmosphäre (IPA)	Germany
Ramiro Checa Garcia	University of Vienna	Austria
Rishav Goyal	University of New South Wales, Climate Change Research Centre	Australia
Paul A. Newman	NASA Goddard Space Flight Center	USA
Felix Plöger	Forschungszentrum Jülich	Germany
Lorenzo Polvani	Columbia University, Department of Applied Physics and Applied Mathematics	USA
Karen H. Rosenlof	NOAA Chemical Sciences Laboratory	USA
Anja Schmidt	Deutsches Zentrum für Luft und Raumfahrt (DLR), Institut für Physik der Atmosphäre (IPA); Ludwig Maximilian University of Munich, Meteorological Institute; and University of Cambridge, Yusuf Hamied Department of Chemistry	Germany
William Seviour	University of Exeter	UK
Keith Shine	University of Reading, Department of Meteorology	UK
Neil Swart	Environment and Climate Change Canada, Canadian Centre for Climate Modelling and Analysis	Canada
Paul J. Young	Lancaster University	UK

Chapter 6: Stratospheric Aerosol Injection and Its Potential Effect on the Stratospheric Ozone Layer

John Dykema	Harvard University, John A. Paulson School of Engineering and Applied Sciences	USA
Anthony Jones	Met Office	UK
Anton Laakso	Finnish Meteorological Institute (FMI), Atmospheric Research Centre of Eastern Finland	Finland
Catherine Anne Wilka	Stanford University	USA

Chapter 7: Scenarios and Information for Policymakers

Laura McBride	University of Maryland, College Park	USA
Martin N. Ross	The Aerospace Corporation	USA
Sunyoung Park	Kyungpook National University, School of Earth System Sciences, Department of Oceanography	South Korea
Susann Tegtmeier	University of Saskatchewan, Institute of Space and Atmospheric Studies	Canada
Ross J. Salawitch	University of Maryland, College Park	USA
David Sherry	NSA Ltd (Nolan Sherry & Associates)	UK
Guus J. M. Velders	National Institute for Public Health and the Environment (RIVM) & Utrecht University	Netherlands

Annex: Summary of Abundances, Lifetimes, ODPs, REs, GWPs, and GTPs

Brian McDonald	NOAA Chemical Sciences Laboratory	USA
Vladimir Orkin	NIST Chemical Science and Technology Laboratory	USA
Vassilis C. Papadimitriou	University of Crete, Department of Chemistry and University of Colorado, Cooperative Institute for Research in Environmental Sciences (CIRES)	Greece
Daniel Van Hoomissen	University of Colorado, Cooperative Institute for Research in Environmental Sciences (CIRES) at NOAA Chemical Sciences Laboratory	USA

Review Editors

Chapter 1: Update on Ozone-Depleting Substances (ODSs) and Other Gases of Interest to the Montreal Protocol

Andreas Engel	Institute for Atmospheric and Environmental Sciences, University of Frankfurt	Germany
Bo Yao	Fudan University	China

Chapter 2: Hydrofluorocarbons (HFCs)

Stephen A. Montzka	NOAA Global Monitoring Laboratory	USA
Martin K. Vollmer	Swiss Federal Laboratories for Materials Science and Technology (Empa)	Switzerland

Chapter 3: Update on Global Ozone: Past, Present, and Future

Jessica Neu	NASA Jet Propulsion Laboratory, California Institute of Technology	USA
Wolfgang Steinbrecht	Meteorological Observatory Hohenpeissenberg Deutscher Wetterdienst (DWD)	Germany

Chapter 4: Polar Stratospheric Ozone: Past, Present, and Future

Susan Solomon	Massachusetts Institute of Technology, Department of Earth, Atmospheric, and Planetary Sciences	USA
Mark Weber	Universität Bremen, Institute of Environmental Physics	Germany

Chapter 5: Stratospheric Ozone Changes and Climate

Amy H. Butler	NOAA Chemical Sciences Laboratory	USA
Amanda Maycock	University of Leeds, School of Earth and Environment	UK

Chapter 6: Stratospheric Aerosol Injection and Its Potential Effect on the Stratospheric Ozone Layer

Valentina Aquila	American University, Department of Environmental Science	USA
Karen H. Rosenlof	NOAA Chemical Sciences Laboratory	USA

Chapter 7: Scenarios and Information for Policymakers

Lambert Kuijpers	A/gent b.v. Environmental Consultancy	Netherlands
Donald J. Wuebbles	University of Illinois, Department of Atmospheric Sciences	USA

Reviewers

Hideharu Akiyoshi	National Institute for Environmental Studies (NIES)	Japan
Mads P. Sulbaek Andersen	California State University, Northridge	USA
Stephen O. Andersen	Institute for Governance and Sustainable Development (IGSD)	USA
Tim Arnold	National Physical Laboratory and University of Edinburgh	UK
Alkiviadis F. Bais	Aristotle University of Thessaloniki, School of Physics, Laboratory of Atmospheric Physics	Greece
Govindasamy Bala	Indian Institute of Science, Center for Atmospheric and Oceanic Sciences	India
Antara Banerjee	University of Colorado, Cooperative Institute for Research in Environmental Sciences (CIRES) at NOAA Chemical Sciences Laboratory	USA
Tina Birmpili	UNEP Multilateral Fund Secretariat for the Implementation of the Montreal Protocol	Canada
Adam Bourassa	University of Saskatchewan, Institute of Space and Atmospheric Studies	Canada
Peter Braesicke	Karlsruher Institut für Technologie (KIT)	Germany
Amy H. Butler	NOAA Chemical Sciences Laboratory	USA
Natalia Calvo	Universidad Complutense de Madrid, Department of Earth Physics and Astrophysics	Spain
Long Cao	Zhejiang University, Department of Atmospheric Sciences, School of Earth Sciences	China
Martin Dameris	Deutsches Zentrum für Luft und Raumfahrt (DLR)	Germany
Sean Davis	NOAA Chemical Sciences Laboratory	USA
Anne Douglass	NASA Goddard Space Flight Center (emeritus)	USA
Vitali Fioletov	Environment and Climate Change Canada	Canada
Paul Fraser	Commonwealth Scientific and Industrial Research Organisation (CSIRO) Oceans and Atmosphere	Australia
Lucien Froidevaux	NASA Jet Propulsion Laboratory, California Institute of Technology	USA
Jan Fuglestvedt	Centre for International Climate and Environmental Research (CICERO)	Norway
Rolando Garcia	National Center for Atmospheric Research (NCAR)	USA
Chaim Garfinkel	Hebrew University of Jerusalem	Israel
Nathan P. Gillett	Environment and Climate Change Canada	Canada
Sophie Godin-Beekman	Laboratoire Atmosphères, Milieux, Observations Spatiales (LATMOS), Centre National de la Recherche Scientifique (CNRS), Sorbonne University	France
William Goetzler	Guidehouse	USA
Neil Harris	Cranfield University	USA
Peter Hitchcock	Cornell University, Department of Earth and Atmospheric Sciences	USA
Peter Irvine	University College London, Department of Earth Sciences	UK
Martin Jucker	Climate Change Research Centre, , University of New South Wales	Australia
David Karoly	Commonwealth Scientific and Industrial Research Organisation (CSIRO)	Australia
Alexey Yu. Karpechko	Finnish Meteorological Institute (FMI)	Finland
Jooil Kim	University of California San Diego, Scripps Institution of Oceanography	USA
Andrew Klekociuk	Australian Antarctic Division	Australia
Ben Kravitz	Indiana University	USA
Lambert Kuijpers	A/gent b.v. Environmental Consultancy	Netherlands
Susan Gabriela Lakkis	Pontificia Universidad Católica Argentina, Facultad de Ingeniería y Ciencias Agrarias and Universidad Tecnológica Nacional, Facultad Regional Buenos	Argentina
Jean-Francois Lamarque	National Center for Atmospheric Research (NCAR)	USA
Sunday Leonard	UN Environment Programme (UNEP) Scientific & Technical Advisory Panel to the Global Environment Facility (STAP-GEF),	Kenya
Eun-pa Lim	Bureau of Meteorology	Australia
Jintai Lin	Peking University, School of Physics, Department of Atmospheric and Oceanic Sciences	China
Pu Lin	Princeton University, Program in Atmospheric and Oceanic Sciences and NOAA Geophysical Fluid Dynamics Laboratory	USA
Nathaniel Livesey	NASA Jet Propulsion Laboratory, California Institute of Technology	USA
Diego Loyola	Deutsches Zentrum für Luft und Raumfahrt (DLR)	Germany
Doug MacMartin	Cornell University	USA
Sasha Madronich	National Center for Atmospheric Research (NCAR)	USA
Michela Maione	University of Urbino, Department of Pure and Applied Sciences and National Research Council of Italy, Institute for Climate and Atmospheric Sciences	Italy
Archie McCulloch	University of Bristol, Atmospheric Chemistry Research Group (retired)	UK
Sophia Mylona	UN Environment Programme (UNEP) Ozone Secretariat	Kenya
Hiroaki Naoe	Meteorological Research Institute (MRI)	Japan
Simon O'Doherty	University of Bristol	UK
David Oram	University of East Anglia	UK
Marisol Osman	Karlsruher Institut für Technologie (KIT)	Germany
Prabir Patra	Japan Agency for Marine-Earth Science and Technology (JAMSTEC)	Japan
Andrea Pazmiño	Laboratoire Atmosphères, Milieux, Observations Spatiales (LATMOS), Centre National de la Recherche Scientifique (CNRS), Université de Versailles Staint Quentin-en-Yvelines (UVSQ)	France
Thomas Peter	ETH Zürich	Switzerland
Damaris Kirsch Pinheiro	Federal Univeristy of Santa Maria, Chemical Engineering Department, Center of Technology	Brazil
Marta Pizano	Consultant	Colombia

Felix Plöger	Forschungszentrum Jülich	Germany
Michael Prather	University of California Irvine, Earth System Science Department	USA
A.R. Ravishankara	Colorado State University	USA
Claire Reeves	University of East Anglia (emeritus)	UK
Laura Revell	University of Canterbury	New Zealand
Rob Rhew	University of California, Berkeley	USA
Jadwiga Richter	National Center for Atmospheric Research (NCAR)	USA
Harald Rieder	University of Natural Resources and Life Sciences, Vienna	Austria
Martin Riese	Forschungszentrum Jülich	Germany
Alan Robock	Rutgers University	USA
Alfonso Saiz-Lopez	Spanish National Research Council, Instituto de Química Física Rocasolano, CSIC	Spain
Nihar Shah	Lawrence Berkeley National Laboratory	USA
Jonathan Shanklin	British Antarctic Survey (BAS) (Emeritus Fellow)	UK
Keith Shine	University of Reading, Department of Meteorology	UK
Michael Sigmond	Environment and Climate Change Canada, Canadian Centre for Climate Modelling and Analysis	Canada
Björn-Martin Sinnuber	Karlsruher Institut für Technologie (KIT)	Germany
Keith Solomon	University of Guelph, Center for Toxicology	Canada
Gabi Stiller	Karlsruher Institut für Technologie (KIT), IMK-ASF	Germany
Kane Stone	Massachusetts Institute of Technology, Department of Earth, Atmospheric, and Planetary Sciences	USA
Susan Strahan	University of Maryland, Baltimore County and NASA Goddard Space Flight Center	USA
William Sturges	University of East Anglia	UK
Matt Tully	Bureau of Meteorology	Australia
Jean-Paul Vernier	National Institute of Aerospace and NASA Langley Research Center	USA
Timothy Wallington	Ford Motor Company, Research & Advanced Engineering	USA
Shingo Watanabe	Japan Agency for Marine-Earth Science and Technology (JAMSTEC)	Japan
Ray Weiss	University of California San Diego, Scripps Institution of Oceanography	USA
David Wilmouth	Harvard University	USA
Shigeo Yoden	Kyoto University	Japan
Durwood Zaelke	Institute for Governance and Sustainable Development (IGSD)	USA
Yanli Zhang	Chinese Academy of Science (CAS), Guangzhou Institute of Geochemistry (GIG)	China

Editorial Team

Sarah J. Doherty	University of Colorado, Cooperative Institute for Research in Environmental Sciences (CIRES) at NOAA Chemical Sciences Laboratory	USA
Chelsea R. Thompson	NOAA Chemical Sciences Laboratory	USA
Jacquelyn Crossman	MPF-ZAI	USA
Mark Essig	North Carolina State University, Cooperative Institute for Satellite Earth System Studies	USA
Thomas K. Maycock	North Carolina State University, Cooperative Institute for Satellite Earth System Studies	USA
Andrea L. McCarrick	North Carolina State University, Cooperative Institute for Satellite Earth System Studies	USA
Brooke C. Stewart	North Carolina State University, Cooperative Institute for Satellite Earth System Studies	USA

Administrative and Technical Support

Catherine Burgdorf Rasco	University of Colorado, Cooperative Institute for Research in Environmental Sciences (CIRES) at NOAA Chemical Sciences Laboratory	USA
Ronda Knott	NOAA Chemical Sciences Laboratory	USA
Douglas Ohlhorst	NOAA Chemical Sciences Laboratory	USA
Albert Romero	NOAA Office of the Chief Administrative Officer	USA
Kathy A. Thompson	Science Systems and Applications, Inc. (SSAI)	USA
Richard Tisinai	University of Colorado, Cooperative Institute for Research in Environmental Sciences (CIRES) at NOAA Chemical Sciences Laboratory	USA
Catherine Weable	NOAA Chemical Sciences Laboratory	USA

Photo Credits

Cover	Johannes Werthebach, Ice Cube / NSF
Remembrances	Crutzen: Getty Images; McFarland: M. McFarland; Molina: Getty Images
Chapter 1 Cover	Paedii Luchs via Stocksy
Chapter 2 Cover	skyNext via Adobe Stock
Chapter 3 Cover	Jonathan Kingston
Chapter 4 Cover	Ryan Skorecki, NSF, via U.S. Antarctic Program Photo Library
Chapter 5 Cover	Elizabeth Asher, NOAA CSL / CIRES
Chapter 6 Cover	NASA
Chapter 7 Cover	MyCreative via Adobe Stock
Annex	Daniel Van Hoomissen, NOAA CSL / CIRES

Final Author Meeting

Geneva, Switzerland, 25 – 29 July 2022

Stephen O. Andersen	Institute for Governance & Sustainable Development (IGSD)	USA
Valentina Aquila	American University, Department of Environmental Science	USA
Julie Arblaster	Monash University	Australia
Tina Birmpili	UNEP Multilateral Fund Secretariat for the Implementation of the Montreal Protocol	Canada
Peter Brasicke	Karlsruher Institut für Technologie (KIT)	Germany
Amy H. Butler	NOAA Chemical Sciences Laboratory	USA
Lucy Carpenter	University of York	UK
Gabriel Chiodo	ETH Zürich, Institute for Atmospheric and Climate Science	Switzerland
Martyn P. Chipperfield	University of Leeds	UK
Robert Damedeo	NASA Langley Research Center	USA
John S. Daniel	NOAA Chemical Sciences Laboratory	USA
Sarah J. Doherty	University of Colorado, Cooperative Institute for Research in Environmental Sciences (CIRES) at NOAA Chemical Sciences Laboratory	USA
Andreas Engel	University of Frankfurt, Institute for Atmospheric and Environmental Sciences	Germany
David W. Fahey	NOAA Chemical Sciences Laboratory	USA
Vitali Fioletov	Environment and Climate Change Canada (ECCC)	Canada
Paul Fraser	Climate Science Centre, Commonwealth Scientific and Industrial Research Organization (CSIRO)	Australia
Hella Garny	Deutsches Zentrum für Luft und Raumfahrt (DLR), Institut für Physik der Atmosphäre (IPA)	Germany
Sophie Godin-Beekman	Laboratoire Atmosphères, Milieux, Observations Spatiales (LATMOS), Centre National de la Recherche Scientifique (CNRS), Sorbonne University	France
Marco Gonzales	United Nations Environment Programme (UNEP) Ozone Secretariat (retired)	Costa Rica
Neil Harris	Cranfield University	UK
Birgit Hassler	Deutsches Zentrum für Luft und Raumfahrt (DLR), Institut für Physik der Atmosphäre (IPA)	Germany
James Haywood	University of Exeter and Met Office Hadley Centre	UK
Harry Hendon	Bureau of Meteorology and Monash University	Australia
Jianxin Hu	Peking University, College of Environmental Sciences and Engineering	China
Ken Jucks	NASA Headquarters	USA
Doug E. Kinnison	National Center for Atmospheric Research (NCAR)	USA
Ronda Knott	NOAA Chemical Sciences Laboratory	USA
Lambert Kuijpers	A/gent b.v. Environmental Consultancy	Netherlands
Johannes C. Laube	Forschungszentrum Jülich, Institute for Energy and Climate Research: Stratosphere (IEK-7)	Germany
Qing Liang	NASA Goddard Space Flight Center	USA
Megan Lickley	Massachusetts Institute of Technology	USA
Bella Maranion	U.S. Environmental Protection Agency (EPA) and Technology and Economic Assessment Panel (TEAP) of the Montreal Protocol	USA
Amanda Maycock	University of Leeds, School of Earth and Environment	UK
Stephen A. Montzka	NOAA Global Monitoring Laboratory	USA
Rolf Mueller	Forschungszentrum Jülich	Germany
Jens Mühle	University of California San Diego, Scripps Institution of Oceanography	USA
Sophia Mylona	United Nations Environment Programme (UNEP) Ozone Secretariat	Kenya
Stoyka Netcheva	World Meteorological Organization (WMO)	Switzerland
Jessica Neu	NASA Jet Propulsion Laboratory, California Institute of Technology	USA
Paul A. Newman	NASA Goddard Space Flight Center	USA
Simon O'Doherty	University of Bristol	UK
David A. Plummer	Environment and Climate Change Canada, Climate Research Division	Canada
Michael Prather	University of California Irvine, Earth System Science Department	USA
John A. Pyle	University of Cambridge and the National Centre for Atmospheric Science (NCAS)	UK
William J. Randel	National Center for Atmospheric Research (NCAR)	USA
A. R. Ravishankara	Colorado State University	USA
Stefan Reimann	Swiss Federal Laboratories for Materials Science and Technology (Empa)	Switzerland
Matt Rigby	University of Bristol, School of Chemistry	UK
Karen H. Rosenlof	NOAA Chemical Sciences Laboratory	USA
Bonfils Safari	University of Rwanda, College of Science and Technology	Rwanda
Ross J. Salawitch	University of Maryland College Park	USA
Michelle L. Santee	NASA Jet Propulsion Laboratory, California Institute of Technology	USA

Megumi Seki	United Nations Environment Programme (UNEP) Ozone Secretariat	Kenya
Keith Shine	University of Reading, Department of Meteorology	UK
Susan Solomon	Massachusetts Institute of Technology, Department of Earth, Atmospheric, and Planetary Sciences	USA
Wolfgang Steinbrecht	Meteorological Observatory Hohenpeissenberg Deutscher Wetterdienst (DWD)	Germany
Susan Strahan	University of Maryland, Baltimore County	USA
Susann Tegtmeier	University of Saskatchewan, Institute of Space and Atmospheric Studies	Canada
Chelsea R. Thompson	NOAA Chemical Sciences Laboratory	USA
Kathy A. Thompson	Science Systems and Applications, Inc. (SSAI)	USA
Simone Tilmes	National Center for Atmospheric Research (NCAR), Atmospheric Chemistry Observations & Modeling	USA
Matt Tully	Bureau of Meterology	Australia
Guus J. M. Velders	National Institute for Public Health and the Environment (RIVM) & Utrecht University	Netherlands
Daniele Visioni	Cornell University, Sibley School of Mechanical and Aerospace Engineering	USA
Martin Vollmer	Swiss Federal Laboratories for Materials Science and Technology (Empa)	Switzerland
Helen Walter-Terrinoni	The Air Conditioning, Heating, and Refrigeration Institute (AHRI) and Technology and Economic Assessment Panel (TEAP) of the Montreal Protocol	USA
Catherine Weable	NOAA Chemical Sciences Laboratory	USA
Mark Weber	Universität Bremen, Institute of Environmental Physics	Germany
Ray Weiss	University of California San Diego, Scripps Institution of Oceanography	USA
Luke Western	University of Bristol	UK
Donald J. Wuebbles	University of Illinois, Department of Atmospheric Sciences	USA
Bo Yao	Fudan University	China
Paul J. Young	Lancaster University	UK

Highlights of the Executive Summary

Tina Birmpili	UNEP Multilateral Fund Secretariat for the Implementation of the Montreal Protocol	Canada
Neil Harris	Cranfield University	UK
Karen H. Rosenlof	NOAA Chemical Sciences Laboratory	USA
Susan Solomon	Massachusetts Institute of Technology, Department of Earth, Atmospheric, and Planetary Sciences	USA
Donald J. Wuebbles	University of Illinois, Department of Atmospheric Sciences	USA

World Meteorological Organization
United Nations Environment Programme
National Oceanic and Atmospheric Administration
National Aeronautics and Space Administration
European Commission